AFRL-PR-WP-TM-2005-2083

APPLICATIONS OF LASER DIAGNOSTICS

Larry P. Goss, Ph.D.

Innovative Scientific Solutions, Inc.
2766 Indian Ripple Road
Dayton, OH 45440-3638

MARCH 2005

Final Report for 21 July 2000 - 20 February 2005

Approved for public release; distribution is unlimited.

STINFO FINAL REPORT

PROPULSION DIRECTORATE
AIR FORCE RESEARCH LABORATORY
AIR FORCE MATERIEL COMMAND
WRIGHT-PATTERSON AIR FORCE BASE, OH 45433-7251

NOTICE

Using Government drawings, specifications, or other data included in this document for any purpose other than Government procurement does not in any way obligate the U.S. Government. The fact that the Government formulated or supplied the drawings, specifications, or other data does not license the holder or any other person or corporation; or convey any rights or permission to manufacture, use, or sell any patented invention that may relate to them.

This report was cleared for public release by the Air Force Research Laboratory Wright Site (AFRL/WS) Public Affairs Office (PAO) and is releasable to the National Technical Information Service (NTIS). It will be available to the general public, including foreign nationals.

PAO Case Number: AFRL/WS-05-0006, 4 Jan 2005

THIS TECHNICAL REPORT IS APPROVED FOR PUBLICATION.

//s//
VINCENT M. BELOVICH, Ph.D.
Project Monitor
Combustion Branch

//s//
ROBERT D. HANCOCK, Ph.D.
Chief
Combustion Branch

//s//
JEFFREY M. STRICKER
Chief Engineer
Turbine Engine Division
Propulsion Directorate

This report is published in the interest of scientific and technical information exchange and its publication does not constitute the Government's approval or disapproval of its ideas or findings.

REPORT DOCUMENTATION PAGE

Form Approved
OMB No. 0704-0188

The public reporting burden for this collection of information is estimated to average 1 hour per response, including the time for reviewing instructions, searching existing data sources, searching existing data sources, gathering and maintaining the data needed, and completing and reviewing the collection of information. Send comments regarding this burden estimate or any other aspect of this collection of information, including suggestions for reducing this burden, to Department of Defense, Washington Headquarters Services, Directorate for Information Operations and Reports (0704-0188), 1215 Jefferson Davis Highway, Suite 1204, Arlington, VA 22202-4302. Respondents should be aware that notwithstanding any other provision of law, no person shall be subject to any penalty for failing to comply with a collection of information if it does not display a currently valid OMB control number. **PLEASE DO NOT RETURN YOUR FORM TO THE ABOVE ADDRESS**.

1. REPORT DATE *(DD-MM-YY)*	2. REPORT TYPE	3. DATES COVERED *(From - To)*
March 2005	Final	07/21/2000 – 02/20/2005

4. TITLE AND SUBTITLE
APPLICATIONS OF LASER DIAGNOSTICS

5a. CONTRACT NUMBER
F33615-00-C-2068

5b. GRANT NUMBER

5c. PROGRAM ELEMENT NUMBER
65503F

6. AUTHOR(S)
Larry P. Goss, Ph.D.

5d. PROJECT NUMBER
3048

5e. TASK NUMBER
04

5f. WORK UNIT NUMBER
ET

7. PERFORMING ORGANIZATION NAME(S) AND ADDRESS(ES)

Innovative Scientific Solutions, Inc.
2766 Indian Ripple Road
Dayton, OH 45440-3638

8. PERFORMING ORGANIZATION REPORT NUMBER
2068 Final

9. SPONSORING/MONITORING AGENCY NAME(S) AND ADDRESS(ES)

Propulsion Directorate
Air Force Research Laboratory
Air Force Materiel Command
Wright-Patterson AFB, OH 45433-7251

10. SPONSORING/MONITORING AGENCY ACRONYM(S)
AFRL/PRTC

11. SPONSORING/MONITORING AGENCY REPORT NUMBER(S)
AFRL-PR-WP-TM-2005-2083

12. DISTRIBUTION/AVAILABILITY STATEMENT
Approved for public release; distribution is unlimited.

13. SUPPLEMENTARY NOTES
Report contains color.

14. ABSTRACT

This report describes the results of experimental and numerical investigations on gas-turbine combustion and fuel processes. The purpose of this program is the advancement of the "state-of-the-art" in laser diagnostics, modeling and simulations, propulsion sciences, advanced propulsion concepts, current and next-generation gas-turbine-engine components, and high-impact revolutionary technologies for air-breathing propulsion systems. The objectives of this research program include:

1) Development, evaluation, and utilization of state-of-the-art-laser diagnostic techniques and analytical simulations and models in the study of combustion, fuel, turbine, and compressor processes that are important to current and future propulsion systems.
2) Performance of fundamental experiments that will advance the understanding of critical combustion and fuel processes.
3) Identification and development of the critical-technology needs of pulsed-detonation engines.
4) Performance of advanced-cycle-aero and aerospace-propulsion-system studies that will result in high-impact revolutionary technologies.
5) Evaluation of potential commercial applications of advanced technologies developed during the program.

15. SUBJECT TERMS
Advanced Laser Diagnostics, Fuel Diagnostics, Computational Fluid Dynamics with Chemistry, Vortex-Flame Interactions, Pulsed-Detonation Engines, Trapped-Vortex Combustor, Advanced Engine Technology, Advanced Cycle Analysis

16. SECURITY CLASSIFICATION OF:			17. LIMITATION OF ABSTRACT:	18. NUMBER OF PAGES	19a. NAME OF RESPONSIBLE PERSON (Monitor) / 19b. TELEPHONE NUMBER *(Include Area Code)*
a. REPORT	b. ABSTRACT	c. THIS PAGE			
Unclassified	Unclassified	Unclassified	SAR	712	Vincent M. Belovich (937) 255-4229

Standard Form 298 (Rev. 8-98)
Prescribed by ANSI Std. Z39-18

TABLE OF CONTENTS

Section		Page
1	INTRODUCTION	1
2	ADVANCED DIAGNOSTIC TECHNIQUE DEVELOPMENT AND EVALUATION	2
2.1	General Overview	2
2.1.1	Pointwise Diagnostic Techniques	2
2.1.1.1	Chemiluminescence as Measurement of Local Equivalence Ratio	2
2.1.1.2	Dual-Pump, Dual-Broadband Coherent Anti-Stokes Raman Scattering (CARS)	2
2.1.2	Imaging-Based Diagnostic Techniques	3
2.1.2.1	Studies of Ignition and Vortex-Flame Interaction in Starting Jets	3
2.1.2.2	Velocity Measurements in Millimetric Areas [Millimetric DPIV (Digital Particle Image Velocimetry)]	3
2.1.2.3	Progress and Recent Advances in PIV	4
2.1.2.4	Milli-DPIV Approaches for Studying Boundary-Layer-Based Flow-Control Systems	4
2.1.2.5	Studies of Vortex-Induced Flame Extinction in Counterflow Diffusion Flames Using CH PLIF and PIV	4
2.1.2.6	Laser-Based Measurements in Wrinkled Two-Phase Counterflow Diffusion Flames	5
2.1.2.7	Application of Optical Diagnostics for Combustion and Fluid Flows	5
2.1.2.8	Effects of Ignition Delay on Impulsively Initiated Premixed Jets	6
2.1.2.9	Simultaneous PLIF/PIV Investigation of Vortex-Flame Extinction in H2-Air Counterflow Diffusion Flames	6
2.1.2.10	Combustion and Laser Diagnostics at AFRL	7
2.1.2.11	Experimental Study of Two-Phase Vortex-Flame Interactions by Laser-Induced Fluorescence (LIF) of OH and CH	7
2.1.2.12	Real-Time Combustor Diagnostics Using High-Speed Digital Imaging	8
2.1.2.13	Single-Shot LII Measurements in Reaction Zone of Model Combustor	8

TABLE OF CONTENTS (Continued)

Section **Page**

2.1.3 Picosecond Techniques 8
2.1.3.1 Terahertz Radiation Measurements in Combustion Environments 8
2.1.3.2 Terahertz Studies of Gas and Condensed Phases 9
2.1.3.3 Recent Applications of Terahertz-Radiation (T-Ray) Technology to Studies of Combustion and Fuel 9
2.1.3.4 Current and Future Applications of Ultrafast Lasers for Propulsion Diagnostics 10
2.1.4 Fuel Diagnostic Techniques 11
2.1.4.1 Micro to Nano - Small Research for Fuels and Combustion 11
2.1.4.2 Evaluation of Electrochemical Release of Self-Assembled Reagents as Component of Proconcentrator for Flow-Injection Analysis 11
2.1.4.3 Highly Luminescent CdS Nanoparticles: Effect of Particle Size and Preparation Method on Photoenhancement Process 12
2.1.4.4 Highly Luminescent CdS Nanoparticles Applied Toward Development of Chemical Sensors 12
2.1.4.5 Temperature Effects on Fluorescence Lifetimes of CdS Nanoparticles 13
2.1.4.6 Applying Chemometrics to Prediction of Aviation-Fuel Properties 13
2.1.4.7 Kinetic Behavior of Long-Period-Grating Fiber-Optic Sensors 14
2.1.4.8 Crystallographic and Spectroscopic Investigations of Effect of Preparation Procedure on CdS Nanoparticles Made in Reverse Micelles 14
2.1.4.9 Quenching Studies of Highly Luminescent CdS Nanoparticles in Presence of Sulfur-Containing Compounds 15
2.1.5 Facility Upgrade 16
2.1.5.1 Expanding Combustion and Laser Diagnostics Research Complex 16

3 SIMULATION AND MODEL DEVELOPMENT AND EVALUATION 17

3.1 General Overview 17
3.1.1 Jet Diffusion Flames 17
3.1.1.1 Role of CHF_3 in Extinguishing Diffusion and Premixed Flames 17

TABLE OF CONTENTS (Continued)

Section **Page**

3.1.1.2 Effects of C_2-Chemistry on Structure of Partially Premixed Methane-Air Flames 18
3.1.1.3 Ignition and Flame Propagation in Impulsively Started Fuel Jet 19
3.1.1.4 PAH Formation in Inverse Diffusion Flame 19
3.1.1.5 Effect of Gravity on Burner-Stabilized and Lifted Partially Premixed Flames 20
3.1.1.6 Investigation of PAH Formation in Different Flames Using UNICORN 20
3.1.1.7 Triple-Flame Propagation and Stabilization in Laminar Axisymmetric Jet 21
3.1.2 Opposed Jet Flames 21
3.1.2.1 Behavior of Jet Diffusion Flame in Multi-Vortex Flow Field 21
3.1.2.2 Curved Hydrogen Diffusion Flames Formed behind Bluff Body 21
3.1.2.3 Insights into Non-adiabatic-Equilibrium Flame Temperatures During Millimeter-Size Vortex/ Flame Interactions 22
3.1.2.4 Extinction Criterion for Unsteady, Opposing-Jet Flames 23

4 FUNDAMENTAL EXPERIMENTS 24

4.1 General Overview 24
4.1.1 Jet Diffusion Flames 24
4.1.1.1 Combustion in Impulsively Initiated Vortex Rings 24
4.1.1.2 Visualization and Two-Color DPIV Measurements of Flows in Circular and Square Coaxial Nozzles 24
4.1.1.3 Experimental and Numerical Investigation of Vortex-Flame Interactions in Impulsively Initiated Premixed and Non-Premixed Jets 25
4.1.1.4 Comparisons of Initially Turbulent, Low-Velocity-Ratio Circular and Square Coaxial Jets 25
4.1.1.5 Study of Vortex Shedding of Jet in Crossflow 26
4.1.1.6 Experimental Investigation of Vortex Shedding in Crossflow 26
4.1.2 Opposed Jet Flames 27
4.1.2.1 Vortex-Flame Interactions: Experimental Observations of Annular Local Extinction 27

TABLE OF CONTENTS (Continued)

Section **Page**

4.1.2.2 Flame Propagation and Morphology in Premixed Vortex Rings 27
4.1.2.3 Simultaneous PLIF/PIV Investigation of Vortex-Flame Interactions 28
4.1.2.4 Performance of CH PLIF and PIV in Two-Phase Methane/n-Heptane/Air Vortex-Flame Interactions 28
4.1.2.5 Effects of Ignition on Premixed Vortex Rings 29
4.1.2.6 Study of Multi-Vortex/Flame Interactions in Opposing-Jet Diffusion Flame 30
4.1.2.7 Vortex-Induced Flame Extinction in Two-Phase Counterflow Diffusion Flames with CH PLIF and PIV 30
4.1.3 Model Combustors 31
4.1.3.1 LII Measurements in Reaction Zone of Model Gas-Turbine Combustor 31
4.1.3.2 Combustion-Air-Jet Influence on Primary-Zone Characteristics for Gas-Turbine Combustors 31
4.1.3.3 Particulate Matter and PAH Determination Using Well-Stirred Reactor 31
4.1.3.4 Multi-Component Laser-Doppler-Velocimetry (LDV) Measurements Downstream of Gas-Turbine-Engine Nozzle/Air Swirler 32

5 PULSED-DETONATION-ENGINE TECHNOLOGY 33

5.1 General Overview 33
5.1.1 Engine Development 33
5.1.1.1 Detonation-Initiation Studies and Performance Results for PDE Applications 33
5.1.1.2 Evaluation of Self-Aspirated PDE 33
5.1.1.3 Evaluation of Hybrid PDE 34
5.1.1.4 Quad-4-Based Research PDE 34
5.1.1.5 Detonation Wave Propagation through Tube Array 35
5.1.1.6 AFRL PDE Research Application 35
5.1.1.7 Integration of PDE with Ejector Pump and with Turbo-Charger as Methods to Self-Aspirate 36
5.1.1.8 Evaluation of Hybrid-Piston PDE 36

TABLE OF CONTENTS (Continued)

Section **Page**

5.1.1.9 Effects of Exit Geometry on Performance of PDE 37
5.1.1.10 Valve-Pressure-Drop Analysis of Quad-4 PDE PDE at Wright-Patterson Air Force Base 37
5.1.1.11 Performance Enhancement of PDE Ejector 37
5.1.1.12 Evaluation of Hybrid-Piston PDE 38
5.1.1.13 Experimental Study of Deflagration-to-Detonation (DDT) Enhancement Techniques in H_2/Air PDE 38
5.1.1.14 Detonation Studies and Performance Results for Research PDE 39
5.1.1.15 Interaction of PDE with Turbine 39
5.1.1.16 Heat Transfer and Thermal Management of PDE 39
5.1.2 Application of Optical and Numerical Diagnostic Methods to PDE 40
5.1.2.1 Optical Diagnostics for Characterizing Advanced Combustors and PDEs 40
5.1.2.2 Emission- and Absorption-Based Sensors for PDE . . . 40
5.1.2.3 Computational and Experimental Studies of PDE 40
5.1.2.4 OH-Based Fuel/Air-Ratio Monitor for PDE 41
5.1.2.5 Fiber-Coupled Laser Sensor for In-Situ Measurement of Hydrocarbon Fuels in PDEs 41
5.1.2.6 Computational and Experimental Studies of PDEs . . . 42

6 ADVANCED-ENGINE-CONCEPT STUDIES 43

6.1 General Overview 43
6.1.1 General Liquid-Fueled Combustor 43
6.1.1.1 Computational and Experimental Study of Aerodynamics and Heat Release in Liquid-Fueled Combustor 43
6.1.2 Ultra-Compact Combustor 44
6.1.2.1 Ultra-Compact Combustors: Main and Inter-Turbine Burner Concepts 44
6.1.2.2 Ultra-Compact Combustion Technology Using High Swirl for Enhanced Burning Rate 44
6.1.3 Trapped-Vortex Combustor 45
6.1.3.1 Trapped-Vortex-Combustor (TVC) Concept for Gas-Turbine Engines 45
6.1.3.2 Optical Diagnostics and Numerical Characterization of TVC 45

TABLE OF CONTENTS (Continued)

Section		Page
7	LIST OF PUBLICATIONS, PRESENTATIONS, AND SIGNIFICANT ACCOMPLISHMENTS	47
	APPENDIX: Publications and Presentations	69

PREFACE

This report was prepared by Dr. Larry P. Goss of Innovative Scientific Solutions, Inc., and covers work performed during the period 21 July 2000 through 20 February 2005 under Air Force Contract F33615-00-C-2068. The contract was administered under the direction of the Air Force Research Laboratory, Wright-Patterson Air Force Base, Ohio, with Dr. Vincent Belovich as Government Project Monitor.

1. INTRODUCTION

This report describes the results of experimental and numerical investigations on gas-turbine combustion and fuel processes. The purpose of this program was the advancement of the state-of-the-art in laser diagnostics, modeling and simulations, propulsion sciences, advanced propulsion concepts, current and next-generation gas-turbine-engine components, and high-impact revolutionary technologies for air-breathing propulsion systems.

The objectives of this research program were to:

1) Develop, evaluate, and utilize state-of-the-art laser diagnostic techniques and analytical simulations and models in the study of combustion, fuel, turbine, and compressor processes that are important to current and future propulsion systems.
2) Conduct fundamental experiments that will advance the understanding of critical combustion and fuel processes.
3) Identify and develop the critical technology needs of pulsed-detonation engines.
4) Conduct advanced-cycle aero- and aerospace-propulsion-system studies that will result in high-impact revolutionary technologies.
5) Evaluate potential commercial applications of the advanced technologies developed during the program.

The research conducted during this program resulted in more than 140 publications and presentations, a complete list of which can be found in Section 7. Complete copies of 75 of these presentations and publications are included in the Appendix. In this report the research efforts are summarized in Sections 2-6. Section 2 details the advanced-diagnostic-technique development and evaluation. Section 3 describes the effort on simulation and model development and evaluation. Section 4 documents the fundamental experiments. Section 5 details the pulsed-detonation-engine technology. Section 6 describes the advanced-engine-concept studies.

2. ADVANCED-DIAGNOSTIC-TECHNIQUE DEVELOPMENT AND EVALUATION

2.1 General Overview

The objectives of this portion of the program were to develop and apply advanced diagnostic techniques for fundamental experiments, fuel-related issues, and advanced component concept studies. The diagnostic techniques developed under this task were to support directly the other major tasks of the program. A wide variety of point-wise, imaging, picosecond, and fuels-specific techniques were developed and evaluated. A summary of the work accomplished on this task during the program follows.

2.1.1 Pointwise Diagnostic Techniques

2.1.1.1 Chemiluminescence as Measurement of Local Equivalence Ratio

Measurements were made of the chemiluminescence of OH*, CH*, and C2* in laminar laboratory propane/air flames and a liquid-fueled model combustor. Ratios of the emission intensity for the three species were found to be a strong function of equivalence ratio. Results of the laboratory measurements were used to infer conditions within the model combustor. The measurements and their utility were considered in the context of previous studies. The results of this investigation were documented by M. S. Brown, T. R. Meyer, G. J. Sturgess [all of Innovative Scientific Solutions, Inc. (ISSI)], J. Zelina, and J. R. Gord [both of the Air Force Research Laboratory (AFRL)] in AIAA Paper No. 2002-3865 that was presented at the 38th AIAA/ASME/SAE/ASEE Joint Propulsion Conference and Exhibit, 7-10 July 2002, Indianapolis, IN. The paper is included in the Appendix.

2.1.1.2 Dual-Pump, Dual-Broadband Coherent Anti-Stokes Raman Scattering (CARS) for Measurement of Temperature and Multiple-Species Concentrations

In a collaborative effort among ISSI, Purdue University, and AFRL, the application of dual-pump dual-broadband (DPDB) (or dual-broadband triple-pump) CARS measurements in reacting flows was demonstrated. The DPDB CARS technique allows detection of temperature and the concentration of three species simultaneously. The results of this investigation were documented by S. Roy, T. R. Meyer, M. S. Brown (all of ISSI), R. P. Lucht (Purdue University), J. R. Gord, V. M. Belovich, and E. Corporan (all of AFRL) in 1) a paper that was presented at the 28th Annual Dayton-Cincinnati Aerospace Science Symposium, which was held 4 March 2003 in Dayton, OH and 2) a poster that was presented at the Joint Poster Session of the Dayton Section of the American Chemical Society and the Ohio Valley Section of the Society for Applied Spectroscopy, which was held 6 March 2003 in Dayton. The visual materials for the presentation are included in the Appendix.

2.1.2 Imaging-Based Diagnostic Techniques

2.1.2.1 Studies of Ignition and Vortex-Flame Interaction in Starting Jet

The behavior of starting jets has been the subject of a number of previous investigations in non-reacting environments. In the current investigation, ignition and combustion in starting fuel jets were studied experimentally using planar laser-induced fluorescence (PLIF) imaging of OH. Well-characterized vortex rings of fuel and air were generated at the exit of an axisymmetric nozzle using a solenoid-driven piston to pulse a reservoir of methane fuel. Ignition was initiated at various locations downstream of the nozzle exit and at various times relative to vortex initiation, pinch-off, and propagation. Several parameters affecting vortex propagation and mixing were also studied, including piston speed and stroke length. Results from PLIF visualizations were compared with corresponding data from non-reacting starting jets and with numerical simulations from a time-dependent computational-fluid-dynamics-with-chemistry (CFDC) code. The results of this study were documented by T. R. Meyer (ISSI), J. R. Gord (AFRL), V. R. Katta (ISSI), W. M Roquemore (AFRL), G. L. Switzer (ISSI), and G. J. Fiechtner (ISSI) in a poster, which was presented at the 2001 Poster Session of the Dayton Section of the American Chemical Society and the Ohio Valley Section of the Society for Applied Spectroscopy, 22 March 2001, Dayton, OH. These results were also presented at the 26th Annual Dayton-Cincinnati Aerospace Science Symposium, 30 March 2001, Dayton, OH. The visual materials for this presentation are included in the Appendix.

2.1.2.2 Velocity Measurements in Millimetric Areas [Milimetric DPIV (Digital Particle Image Velocimetry)]

A flow-control system for a high-turning-stator cascade was investigated using DPIV. The system employs small (millimetric) blowing cavities and suction holes in the blades. Velocity measurements on these small areas and at the thin boundary layer during blow-down tests are necessary for verifying the flow-control-device performance and also for yielding details of the flow very near the blade. The millimetric size of the viewing areas prevents the direct application of standard DPIV since the laser thickness is typically greater than the hole size and because regular optics cannot be used in a standard manner for viewing very small areas. Issues related to volumetric illumination, fiber-optic delivery, particle-seeding image size, scattering direction, optical focusing, and speckle and glare reduction were explored. An advantage of making measurements in small areas is that high resolution can be accomplished with regular lk x 1k CCD sensors (e.g., 1000 pix/mm). This also makes feasible the use of digital-holography approaches for measuring velocities in small volumes and micro-volumes. The results of this investigation were documented by J. Estevadeordal (ISSI) and W. W. Copenhaver (AFRL) in a paper that was presented at the 55th Annual Meeting of the American Physical Society/Division of Fluid Dynamics, which was held 24-26 November 2002 in Dallas, TX. The visual materials for this presentation are included in the Appendix.

2.1.2.3 Progress and Recent Advances in PIV

It is of great importance to fluid-dynamics and combustion experimentalists to be able to measure complex, three-dimensional turbulent flowfields globally, with high spatial and temporal resolution. While we are still far from fully realizing this objective, significant progress has been made during the last decade toward accomplishing this goal, especially in optical diagnostic techniques because of their nonintrusive nature. One of these techniques, PIV, allows one to measure both two- and three-dimensional velocities in a wide variety of flowfields ranging from subsonic to hypersonic and also in reacting flows. The progress and recent advances in this technique such as stereoscopic, defocused, holographic, and micro-PIV and its application to combustion, turbomachinery, micro-pumps, and large-scale wind-tunnels as well as practical issues such as seeding, illumination, accuracy, and resolution were documented by S. P. Gogineni, J. Estevadeordal (both of ISSI), and J. R. Gord (AFRL) in a paper that was presented at the 28th Annual Dayton-Cincinnati Aerospace Sciences Symposium, which was held 4 March 2003 in Dayton, OH. The visual materials for this presentation are included in the Appendix.

2.1.2.4 Milli-DPIV Approaches for Studying Boundary-Layer-Based Flow-Control Systems

Flow-control systems that employ small (millimetric) blowing cavities and suction holes in the blades were investigated using DPIV. Velocity measurements on the small areas and at the thin boundary layer during blowndown tests are necessary for verifying the flow-control device performance and also for yielding details of the flow very near the blade. The millimetric size of these viewing areas prevents the direct application of standard DPIV since the laser thickness is typically greater than the hole size and because regular optics cannot be used in a standard manner for viewing very small areas. Issues related to volumetric illumination, fiber-optic delivery, particle-seeding image size, scattering direction, optical focusing, and speckle and glare reduction were explored. An advantage of making measurements in small areas is that high resolution can be accomplished with regular 1k x 1k CCD sensors (e.g., 1000 pix/mm). This also makes it feasible to use digital-holography approaches for measuring velocities in small volumes and micro-volumes. The results of this investigation were documented by J. Estevadeordal (ISSI), W. W. Copenhaver, and D. Car (both of AFRL) in a paper that was presented at 28th Annual Dayton-Cincinnati Aerospace Science Symposium, which was held 4 March 2003 in Dayton, OH. The visual materials for this presentation are included in the Appendix.

2.1.2.5 Studies of Vortex-Induced Flame Extinction in Counterflow Diffusion Flames Using CH Planar Laser-Induced Fluorescence (PLIF) and PIV

The interaction of a laminar non-premixed flame and a vortex was examined. The CH-radical layer produced by the flame was imaged, for the first time in this configuration, using PLIF. Simultaneous measurements using PIV yielded flow-field data. The methane-air flame was supported in a non-premixed opposed-jet burner. The extinction

processes that occurred during the interaction were analyzed. Also, in the experiments, it appeared that polycyclic-aromatic-hydrocarbon (PAH) fluorescence strongly perturbed CH LIF measurements. To clarify this, the effects of equivalence ratio, droplet seeding, and laser energies on CH vs. PAH fluorescence were studied. The results of this investigation were documented by A. Lemaire (Ecole Centrale Paris), T. R. Meyer (ISSI), K. Zahringer (Ecole Centrale Paris), J. R. Gord (AFRL), and J. C. Rolon (Ecole Centrale Paris) in a poster and a paper that were presented at the 8th Topical Meeting on Laser Applications to Chemical and Environmental Analysis (Optical Society of America), 7-10 February 2002, Boulder, CO. The paper was published in the conference proceedings (*Laser Applications to Chemical and Environmental Analysis)*, and the poster is included in the Appendix.

2.1.2.6 Laser-Based Measurements in Wrinkled Two-Phase Counterflow Diffusion Flames

Vortex-induced flame wrinkling and extinction represent fundamental turbulent flame phenomena that must be understood for the development of accurate numerical models. In the current study, repeatable flame wrinkling and extinction were produced using a two-phase counterflow diffusion flame and a piston-actuated vortex. PLIF of CH was used to mark the flame front, and PIV was employed to obtain information concerning the flow field. The phase-correlated CH PLIF and PIV results showed that flame extinction occurs within 1 ms after the vortex begins to wrinkle the flame. Velocity measurements showed that a five-fold increase in the fuel-side peak strain rate occurs during this extinction process. In addition to flame wrinkling and extinction, the effects of fuel equivalence ratio, droplet seeding, and PAH fluorescence on the CH PLIF measurements were studied. The results of this investigation were documented by T. R. Meyer (ISSI), A. Lemaire, K. Zahringer (both of Ecole Centrale Paris and CNRS), J. R. Gord (AFRL), and J. C. Rolon (Ecole Centrale Paris and CNRS) in a poster that was displayed at the American Chemical Society/Society for Applied Spectroscopy Annual Poster Session and Patterson College Chemistry Awards Night, which was held 5 March 2002 in Dayton, OH. The visual materials for this poster are included in the Appendix.

2.1.2.7 Application of Optical Diagnostics for Combustion and Fluid Flows

Over the past few years, emphasis in fluid-mechanics measurement techniques has shifted from obtaining pointwise to whole-flowfield information. Advanced optical diagnostic techniques such as PIV and PLIF have played a critical role in obtaining whole-flowfield data. These techniques were simultaneously applied in combusting flowfields in an attempt to understand vortex-flame interactions and the flame-extinction process. In addition, PIV has been applied to transitional wall jets, jet-in-a-cross flow, and transonic turbomachinery flowfields. These experimental results have had a significant impact on the development and validation of computational-fluid-dynamics (CFD) codes. Holographic flow visualization has also been applied to both reacting and non-reacting flowfields. The results of this investigation were documented by S. P. Gogineni (ISS), J. R. Gord, and B. V. Kiel (both of AFRL) in an invited presentation at

the Delft Institute of Technology in The Netherlands on 4 June 2002. The visual materials for this presentation are included in the Appendix.

2.1.2.8 Effects of Ignition Delay on Impulsively Initiated Premixed Jets

An experimental and numerical investigation was performed to explore methods for achieving flame speeds that are much greater than laminar burning velocities. A premixed-fuel jet was impulsively issued into a low-speed annular airflow, and ignition was provided after a preset delay time. The temporally varying structure of the propagating flame in and around the jet was measured using OH and acetone PLIF and PIV. Experiments were performed by varying the equivalence ratio, ignition delay time, and jet momentum. Calculations were also performed using a time-dependent two-dimensional code that incorporates 17-species finite-rate chemistry for methane fuel. The ignition process was simulated by temporarily increasing the temperature in a small region within the jet column. Calculations were performed for the stoichiometric fuel/air mixture with varying ignition delay times. Instantaneous structures of the simulated and measured flames were compared. Flame-propagation speeds were obtained from the numerical results by tracking the flame location along the centerline. It was observed that flame speed increased with ignition delay. An order-of-magnitude increase in flame speed was achieved by igniting the jet after a delay of ~ 6 ms. Further increase in ignition delay created unburned fuel pockets and decreased the flame speed. The results of this investigation were documented by T. R. Meyer, S. P. Gogineni, V. R. Katta (all of ISSI), and J. R. Gord (AFRL) in a paper that was presented at the 11th International Symposium on Applications of Laser Techniques to Fluid Mechanics, which was held 8-11 July 2002 in Lisbon, Portugal,. The paper is included in the Appendix.

2.1.2.9 Simultaneous PLIF/PIV Investigation of Vortex-Induced Annular Extinction in H_2-Air Counterflow Diffusion Flames

High-temporal-resolution measurements of scalars and velocity were used to study vortex-induced annular (off-centerline) flame extinction during the interaction of a propagating vortex with an initially stationary counterflow hydrogen-air diffusion flame. Such an extinction process differs from classical one-dimensional descriptions of strained flamelets in that it captures the effects of flame curvature as well as dynamic strain. PLIF measurements of the hydroxyl radical (OH) were used to track flame development, and simultaneous PIV was used to characterize the two-dimensional flowfield. Measurements revealed differences in local and normal strain-rate profiles along and across the reaction zone and indicated that vortex-induced curvature in the annular region may initiate the extinction process. In addition, the effect of local flame extinction on vortex evolution and dissipation was determined from measured vorticity data. The results of this study were documented by T. R. Meyer (ISSI), G. J. Fiechtner (Sandia National Laboratories), S. P. Gogineni (ISSI), J. C. Rolon (Ecole Central Paris), C. D. Carter, and J. R. Gord (both of AFRL) in a paper that was submitted in September 2002 for publication in Experiments in Fluids.

2.1.2.10 Combustion and Laser Diagnostics at AFRL

The Combustion and Laser Diagnostics Research Complex (CLDRC) supports the experimental and computational study of fundamental combustion phenomena to expand the scientific knowledge base, validate combustor-design codes, and improve the performance of future-generation propulsion systems for military and commercial aviation This state-of-the-art complex provides unique laboratory tools for the experimental characterization of combustion processes through the development, demonstration, and application of advanced laser-based/optical diagnostic techniques such as PLIF, Coherent Anti-Stokes Raman Spectroscopy (CARS), PIV, LII, Holography, TeraHertz Time-Domain Spectroscopy, and diode-laser-based sensors. These capabilities are complemented by a suite of specialized modeling and simulation methodologies for assessing and predicting the detailed chemistry and physics of combustion processes. The above techniques have been employed in both fundamental studies (vortex-flame interactions) and applied systems (Trapped-Vortex Combustor). Through recently completed construction, the CLDRC has been expanded to include seven new combustion laboratories at WPAFB. Next-generation diagnostics developments and combustion studies slated for performance in the new facilities were documented by J. R. Gord (AFRL), T. R. Meyer, M. S. Brown, S. Roy, and S. P. Gogineni (all of ISSI) in a paper for presentation at the 55th Annual Meeting of the Division of Fluid Dynamics of the American Physical Society, 24-26 November 2002, Dallas, TX. The visual materials for this presentation are included in the Appendix.

2.1.2.11 Experimental Study of Two-Phase Vortex-Flame Interactions by LIF of OH and CH

The interaction between a vortex and a flat laminar diffusion flame is generally used to simulate a number of features that are common in turbulent combustion such as dynamic strain, stretch, and curvature. Using well-controlled experiments to verify numerical simulations, phenomena such as flame extinction and micro-vortex-flame behaviour can be studied. The dynamic interaction between a laminar flame and a vortex may be examined by LIF of the OH layer produced by the flame--OH being a marker of long-living intermediates--or by the CH radical, which is considered to be a good marker of the primary reaction zone and a representative of the flame surface. The goal of the present investigation was to study two-phase vortex-flame interactions using both OH and CH PLIF. As with previous measurements in premixed flames, our results indicated that gaps in the CH PLIF layer do not always correspond to gaps in the OH layer. The results of this study were documented by A. Lemaire, K. Zahringer (both of Ecole Centrale Paris), T. R. Meyer (ISSI), J. R. Gord (AFRL), and J. C. Rolon (Ecole Centrale Paris) in a paper that was presented at the 4th Pacific Symposium on Flow Visualization and Image Processing (PSFVIP-4), which was held 3-5 June 2003 in Chamonix, France. The paper was published in the Conference Proceedings and is included in the Appendix.

2.1.2.12 Real-Time Combustor Diagnostics Using High-Speed Digital Imaging

Improved fuel-air mixing and subsequent flame propagation are essential for enhanced combustor performance. The use of high-speed digital imaging as a real-time diagnostic for such processes was demonstrated in three configurations--a single swirl-cup combustor, a trapped-vortex combustor, and a pulsed-detonation engine. Imaging rates of up to 40,500 frames/s and exposure times as low as 10 μs surpass the capabilities of conventional high-speed photography and provide new insight into processes such as soot formation, flame morphology at elevated pressures, and deflagration-to-detonation transition. In addition to its use for real-time combustor diagnostics, the high-speed digital imaging has been employed for coherent-structure velocimetry (CSV). The results of this investigation were documented by T. R. Meyer, M. S. Brown, J. Hoke, S. Fonov (all of ISSI), F. Schauer, and J. R. Gord (both of AFRL) in a paper that was presented at the 27th Annual Dayton-Cincinnati Aerospace Science Symposium, which was held 5 March 2002 in Dayton, OH. The visual materials for this presentation are included in the Appendix.

2.1.2.13 Single-Shot LII Measurements in Reaction Zone of Model Combustor

In an investigation of the effect of additives on particulate production, LII measurements were performed in a JP-8-fueled single swirl-cup combustor with a central nozzle. Single-shot LII images of the soot exhibited localized high concentrations with varying spatial and temporal behavior. High-speed luminescence images revealed a similar complex soot structure driven by local fluid and chemical behavior. Averages of the single-shot images permitted parametric studies of the LII signal on laser fluence, camera gate and delay settings, and global equivalence ratio. Examples of single-shot LII signals as well as the results of the parametric studies were examined in the context of the additive study. The results of this investigation were documented by M. S. Brown, T. R. Meyer (both of ISSI), J. R. Gord, and V. M. Belovich (both of AFRL) in a poster that was displayed at the American Chemical Society/Society for Applied Spectroscopy Annual Poster Session and Patterson College Chemistry Awards Night and in a paper that was presented at the Twenty-Seventh Annual Dayton-Cincinnati Aerospace Science Symposium. These meetings were held on 5 March 2002 in Dayton, OH. The visual materials for these presentations are included in the Appendix.

2.1.3 Picosecond Techniques

2.1.3.1 Terahertz Radiation Measurements in Combustion Environments

A novel, broadband source of terahertz (THz) radiation was employed to detect water vapor in room air and in a stable hydrogen/air flame. The semiconductor-based transmitter produced a spatially coherent, pulsed THz beam, and line-of-sight detection was made with a similar semiconductor-based gated detector. Transmission signals were acquired in the time domain and then Fourier transformed to the spectral-frequency domain. Measurements were performed on two hardware platforms, both pumped by ultrafast lasers. One platform demonstrated, for the first time, the technical marriage of a

THz transmitter/receiver pair with the asynchronous-optical-sampling (ASOPS) technique. This measurement approach required no opto-mechanical delay, facilitating rapid scanning of the full THz temporal signal. Additionally, use of ASOPS promised a means of "freezing" rapid dynamics in the THz regime for close study. A second platform utilized a now commercially available system comprised of a fiber-coupled transmitter/receiver pair along with an integrated optical delay. Transmission measurements performed on a ceramic combustion liner and neat polar and non-polar solvents were made. Efforts to date were in the context of Air Force diagnostic needs and the rapid evolution of THz hardware. The results of this study were documented by M. S. Brown (ISSI), J. V. Rudd, D. Zimdars, M. Warmuth (all of Picometrix, Inc.), and J. R. Gord (AFRL) and presented at the 26th Annual Dayton-Cincinnati Aerospace Science Symposium, which was held 30 March 2001 in Dayton, OH. This presentation received the Award for Best Paper in Instrumentation I Session. The visual materials for this presentation are included in the Appendix.

2.1.3.2 Terahertz Studies of Gas and Condensed Phases for Combustion Application

Rapid advances in Terahertz (THz) source and receiver technology are enabling the application of these devices to activities ranging from fundamental spectroscopy to product quality assurance. Application to combustion environments stems from some general observations: 1) water (both gas and liquid phase) is a strong absorber in the THz region, and 2) aviation fuel, soot, and many solids (e.g., ceramics) are transparent in the THz region. Using packaged, modular transmitter/receiver pairs based on advanced antennae structures, we are conducting studies that address issues relevant to the application of such hardware to combustion efforts. Time-domain measurements have been made on two hardware platforms. One platform employs two ultrafast pump lasers in the asynchronous-optical-sampling technique, while the other makes use of a more traditional single-pump-laser optical-delay line. Spectra of water vapor in a hydrogen/air flame have been recorded along with spectra of fuel surrogates and ceramics. System performance has been assessed in terms of bandwidth and collection time. The results of this study were documented by M. S. Brown (ISSI), D. Zimdars (Picometrix, Inc.), and J. R. Gord (AFRL) in an invited paper that was presented at the 11th Gordon Research Conference on Laser Diagnostics in Combustion, which was held 1-6 July 2001 in South Hadley, MA.

2.1.3.3 Recent Applications of Terahertz-Radiation (T-Ray) Technology to Studies of Combustion and Fuel

A novel, broadband source of terahertz (THz) radiation was employed to detect water vapor in room air and in a stable hydrogen/air flame. The semiconductor-based transmitter produced a spatially coherent, pulsed THz beam; line-of-sight detection was accomplished with a similar semiconductor-based gated detector. Transmission signals were acquired in the time domain and then Fourier transformed to the spectral-frequency domain. Measurements were performed on two hardware platforms, both pumped by ultrafast lasers. One platform demonstrated, for the first time, the technical marriage of a THz transmitter/receiver pair with the asynchronous-optical-sampling (ASOPS)

technique. This measurement approach requires no opto-mechanical delay, thus facilitating rapid scanning of the full THz temporal signal. Additionally, use of ASOPS promises a means of "freezing" rapid dynamics in the THz regime for close study. A second platform utilized a now commercially available system comprised of a fiber-coupled transmitter/receiver pair along with an integrated optical delay. Transmission measurements were performed on a ceramic combustion liner and neat polar and non-polar solvents. Efforts to date have been performed in the context of AF diagnostic needs and the rapid evolution of THz hardware. The results of this study were documented by M. S. Brown (ISSI), J. V. Rudd, D. Zimdars, M. Warmuth (all of Picometrix, Inc.), and J. R. Gord (AFRL) in a paper that was presented at the Luminescence Symposium, 43rd Rocky Mountain Conference on Analytical Chemistry, which was held 29 July - 2 August 2001 in Denver, CO. The visual materials for this presentation are included in the Appendix.

2.1.3.4 Current and Future Applications of Ultrafast Lasers for Propulsion Diagnostics

Over the course of the past several decades, lasers have been critical to the development and application of optical diagnostics for nonintrusive investigation of advanced propulsion systems. While many of these techniques have traditionally been designed around cw and nanosecond-pulsed sources, the emergence of robust picosecond- and femtosecond-pulsed ultrafast lasers is driving the development and application of powerful new diagnostics. In facilities at Wright-Patterson Air Force Base, we have been exploiting modelocked Ti:sapphire lasers and regenerative chirped-pulse amplifiers to explore the fundamental chemistry and physics of combusting flowfields and aviation fuels. Techniques based on ultrashort pulses, including pump/probe spectroscopy, time-correlated single-photon counting, picosecond time-resolved LIF, and time-domain terahertz spectroscopy, have been applied to quantify chemical species in fuels and flames and to capture the associated kinetics and dynamics. In other experiments the tremendous repetition rates of these modelocked systems have been employed to achieve high-speed digital imaging of fluid-dynamic events at ultrafast framing rates. As the peak powers and focused intensities delivered by ultrasfast-laser systems continue to skyrocket, new diagnostics will be achieved. We have been currently expanding our laboratory facilities to include a multi-terawatt laser system for fundamental studies of laser-matter interactions. The Propulsion and Materials Directorates are planning joint studies that will fuel the development of next-generation combustion diagnostics and innovative techniques for non-destructive evaluation of propulsion-system hardware and other high-value manufactured assets of interest to the Air Force. The current ultrafast diagnostics and plans for future development have been documented by J. R. Gord, W. M. Roquemore (both of AFRL), M. S. Brown (ISSI), and J. L. Blackshire (AFRL, Materials and Manufacturing Directorate) in a paper for presentation at the Directed Energy Professional Society (DEPS) Ultrashort Pulse Laser Materials Interaction Workshop, 25 September 2003, Boulder, CO. The visual materials for this presentation are included in the Appendix.

2.1.4 Fuel Diagnostic Techniques

2.1.4.1 Micro to Nano - Small Research for Fuels and Combustion

The Fuels and Combustion Branches of AFRL have been actively investigating micro and nanoscopic materials as they pertain to fuel chemistry, sensor development, and MEMS devices. At these dimensions, surface interactions (e.g., surface chemistry, viscosity, and heat transfer) are extremely important in understanding the macroscopic chemical and physical processes that occur. In some cases current models used to predict chemical or physical properties are inadequate because of a lack of information concerning these surface effects. In this study we examined both physical and chemical processes occurring within and about micro and nanoscopic materials. Specifically, microfluidic results were obtained using an LIF technique within a Si substrate Y-channel (~ 100 μm across and 30 μm deep) coupled with simple CFD calculations. In addition, spectroscopic results (steady-state and time-resolved) were obtained for model nanoparticles, and a novel pyrene-dendromer-modified carbon nanotube was used. The results of this investigation were documented by C. E. Bunker, J. R. Gord (both of AFRL), T. R. Meyer, M. S. Brown, V. R. Katta (all of ISSI), D. A. Zweifel (Clemson University), B. A. Harruff (AFRL), and Y-P Sun (Clemson University) in a paper that was presented at the TMS Annual Meeting, Symposium on Surface Engineering: Science and Technology II, 17-22 February 2002, Seattle, WA. The paper was published in the conference proceedings [*Surface Engineering: Science and Technology of Interfaces II* (A. Kumar, Y-W. Chung, J. J. Moore, G. L. Doll, K. Yasui, and D. S. Misera, Eds.) (The Minerals, Metals and Materials Society, Warrendale, PA, 2002), pp. 25-34]. The paper is included in the Appendix. These results were also presented at the 27th Annual Dayton-Cincinnati Aerospace Science Symposium, which was held 5 March 2002 in Dayton, OH.

2.1.4.2 Evaluation of Electrochemical Release of Self-Assembled Reagents as Component of Proconcentrator for Flow-Injection Analysis

It was demonstrated that self-assembled monolayers anchored to gold by a thiolate can trap an analyte and that electrochemical release of the assembly into a carrier allows determination at a downstream detector. Quantitative potentiostatic release of a coumarin derivative was demonstrated by fluorometry. The capture of $PMo_{12}O_{40}^{3-}$ on a monolayer of 4-aminothiophenol, followed by oxidative release, results in a 4.8-nA peak (1.6-s width at 1 mL $min^{-1)}$ for the four-electron reduction of $PMo_{12}O_{40}^{3-}$. The sensitivity is increased by forming multilayers on the preconcentrator. Release of 10 layers of $P_2W_{18}O_{62}^{6-}$ yields a 12.4-nA peak, even though only a one-electron reduction occurs at the potential employed. The results of this study were documented by L. Cheng, J. Seneviratne, G. E. Pacey (all of Miami University), J. R. Gord (AFRL), M. S. Brown, and T. R. Meyer (both of ISSI) in a paper that was published in Electroanalysis (Vol. 14, pp. 1339-1343, November 2002). The paper is included in the Appendix.

2.1.4.3 Highly Luminescent CdS Nanoparticles: Effect of Particle Size and Preparation Method on Photoenhancement Process

CdS nanoparticles were prepared with emission properties characteristic of trap states (i.e., broad, Gaussian-like, and red shifted from the absorption-band onset) using the reverse-micelle method. Luminescence quantum yields for freshly prepared particles were independent of particle size or the quantum-confinement effect, with the quantum yields being 0.02 – 0.04 for particles prepared with w_o values of 2 - 10 (w_o = $[H_2O]/[AOT]$). Irradiation of the particles at the absorption maxima resulted in an increase in the quantum yields (Φ_L = ~ 0.12 for w_o = 4). The increase was found to be a function of the particle size, with smaller particles undergoing greater photoenhancement. The degree of enhancement also correlated with observed spectral shifts; particles displaying a greater spectral shift with irradiation experienced a greater enhancement in the quantum efficiency. The effect of the irradiation process on CdS nanoparticles prepared at w_o values of 4, 5, 6, and 8 was studied. These data along with supporting TEM and x-ray powder-diffraction results were considered within the context of the quantum-confinement effect, the role of surface properties, and crystal structure. The results of this study were documented by C. E. Bunker (AFRL), B. A. Harruff, P. Pathak, Y. Lin (all of Clemson University), J. Widera (ISSI), J. R. Gord (AFRL), and Y.-P. Sun (Clemson University) in a paper that was presented at the Inter-American Photochemical Society Meeting, which was held 3 January 2003 in Clearwater Beach, FL. The extended abstract is included in the Appendix.

2.1.4.4 Highly Luminescent CdS Nanoparticles Applied Toward Development of Chemical Sensors

Nanoparticles have recently attracted much scientific attention because of their small size, unusual electronic and optical properties, and potential applications as sensors, catalysts, light-weight structures, and pharmaceuticals. Our research has focused on using these materials to design small sensors for chemical detection. We have the ability to synthesize highly luminescent CdS nanoparticles by photoirradiation and drying the stock solution of the CdS nanoparticles prepared in AOT reverse micelles. The synthesis produces particles with Φ_L values of ~ 40% after photoirradiation and drying. These nanoparticles are characterized by high surface areas. It is also known that the quantum efficiency of trap-state emission from CdS nanoparticles is sensitive to environmental perturbations. Such particles have potential applications for the development of gas sensors. We have been investigating the influence of compounds that contain S, O, and N atoms that are present in aviation fuel on the phenomenon of dynamic quenching of long-lived states of highly luminescent CdS nanoparticles. Applying chemometric methods to the data permits the accurate determination of fuel composition. The long-term goal is to develop small, portable, inexpensive, and easy-to-operate chemical sensors for fuel diagnostics. The results of this investigation were documented by J. Widera, J. J. Karnes (both of ISSI), J. R. Gord, and C. E. Bunker (both of AFRL) in 1) a paper that was presented at 28th Annual Dayton-Cincinnati Aerospace Science Symposium, which was held 4 March 2003 in Dayton, OH and 2) a poster that was presented at the Joint Poster Session of the Dayton Section of the American Chemical

Society and the Ohio Valley Section of the Society for Applied Spectroscopy, which was held 6 March 2003 in Dayton, OH. The visual materials for the presentation are included in the Appendix.

2.1.4.5 Temperature Effects on Fluorescence Lifetimes of CdS Nanoparticles

Synthesis, characterization, and application of nanoparticles continue to be rapidly growing areas of study in the larger field of nanotechnology. Motivated by a desire to develop fuel-sensor platforms that exploit the unique optical characteristics of these nanomaterials, we have made substantial effort to prepare highly luminescent CdS nanoparticles through reverse-micelle techniques and to explore the spectroscopic features of these chemical species. One such study involves the effects of temperature on the fluorescence lifetimes of laser-excited CdS nanoparticles. Particles were subjected to nanosecond-pulsed excitation at 337 nm using a nitrogen laser. Time-resolved fluorescence decays were recorded at a series of temperatures from 20 to 80°C using a fast-wired photomultiplier tube and a digital storage oscilloscope. The lifetimes of the CdS fluorescence decay were observed to decrease with increasing temperature, as expected, based on classical photophysical theory. The results of this investigation were documented by Joseph R. Gord (Dayton Christian Middle School), J. Widera (ISSI), James R. Gord, and C. E. Bunker (both of AFRL) in a poster that was presented at the Joint Poster Session of the Dayton Section of the American Chemical Society and the Ohio Valley Section of the Society for Applied Spectroscopy, which was held 6 March 2003 in Dayton, OH.

2.1.4.6 Applying Chemometrics to Prediction of Aviation-Fuel Properties

The Fuels Branch of AFRL is actively seeking methodologies for the rapid and accurate determination of fuel properties and characteristics “at the skin of the aircraft.” Currently fuel properties and characteristics are determined using well-established ASTM-type methods; however, such techniques suffer from slow response (require sampling coupled with laboratory analysis), high cost (complex instrumentation), and poor accuracy (outdated technology). In an effort to improve the speed of analysis, reliability, and accuracy and to better support field operations, we investigated several analytical methods that are suitable for use in the field. For example, the fast-GC method has converted a powerful laboratory tool (standard gas chromatography) into an analytical technique that is sufficiently rapid to be included in pre-flight inspections. NIR, IR, and Raman-spectroscopy analysis can also be performed in a matter of minutes. Physical-property information and data from the above-mentioned analytical techniques were collected for more than 100 different aviation fuels. Chemometric techniques were used to correlate the known physical properties of the fuels and the data obtained from the analytical methods. The results of this study were documented by J. J. Karnes (ISSI), G. Bota, P. de B. Harrington (both of Ohio University), and C. E. Bunker (AFRL) in a poster that was presented at the Joint Poster Session of the Dayton Section of the American Chemical Society and the Ohio Valley Section of the Society for Applied Spectroscopy, which was held 6 March 2003 in Dayton, OH.

2.1.4.7 Kinetic Behavior of Long-Period-Grating Fiber-Optic Sensors

A new mode of analysis using long-period-grating (LPG) fiber-optic sensors based on their time-dependent response was developed. In contrast to all previous studies in which LPG sensing elements operate in the equilibrium mode based on Langmuir adsorption behavior, the current kinetic approach allows analysis of the early-time wavelength shift of the sensor. This is particularly useful for low-concentration measurements where the response of the system can be very slow. The model is based on diffusion of the analyte through the outer protective membrane and into the active binding-membrane region, which is bound to the fiber cladding. The model fits the time-dependent behavior well and provides a means for calibration of the concentration-dependent time response. Copper concentrations of 0.6 ppm were reliably detected. The kinetic mode should be applicable to other affinity-coated LPG fiber-optic sensors. The results of this investigation were documented by S. W. Buckner (St. Louis University), J. Widera (ISSI), J. R. Gord, C. E. Bunker (both of AFRL), G. E. Pacey (Miami University), and V. R. Katta (ISSI) in a paper that was presented at the 225th American Chemical Society National Meeting, which was held 23-27 March 2003 in New Orleans, LA.

2.1.4.8 Crystallographic and Spectroscopic Investigations of Effect of Preparation Procedure on CdS Nanoparticles Made in Reverse Micelles

Nanoparticles, because of their small size and unusual electronic and optical properties, have received considerable scientific attention. Of the many materials investigated, CdS may be considered a model compound. Numerous methods for the preparation of CdS nanoparticles have been demonstrated.[1-3] Reverse micelles have shown great versatility in the ability to control particle size through manipulation of the internal water-core dimensions of the micelle or nanoreactor. Optical characterization of CdS particles prepared in reverse micelles of different sizes shows a strong correlation between the absorption-edge onset or absorption-band maximum vs. particle size.[4-5] The phenomenon is attributed to the quantum-confinement effect. Recently it has been shown that the quantum efficiency of trap-state emission from CdS nanoparticles prepared with diameters on the order of 2 - 3 nm in reverse micelles can be significantly increased through a photo-irradiation procedure.[5] The result is highly luminescent (~ 18% quantum yield) CdS nanoparticles that display trap-state emissions. Such particles have potential applications to the development of gas sensors and electro-optical devices.[6] A detailed investigation of the quantum-efficiency-enhancement phenomenon has revealed a strong dependence of the optical characteristics on preparation procedure.[1] The dependence correlates with an interesting finding that the initial crystal structure of the CdS nanoparticles is an apparent function of the mixing dynamics of two precursor solutions for the reverse-micelle method. The ability to alter crystal structure through simple changes in preparation procedure (inadvertently or by design) can play an important role, in addition to the quantum-confinement effect, in determining the optical and electronic properties of nanoparticles.[1] A systematic investigation was conducted on the effects of preparation procedure on the crystal structure of CdS nanoparticles prepared using the reverse-micelle method. The results were considered within the context of the observed optical properties and the quantum-yield-enhancement phenomenon.

References
1. Y. Wang, N. Herron, *Phys. Rev. B* **42**, 7253 (1990).
2. N. Pinna, K. Weiss, H. Sack-Kongehl, W. Vogel, J. Urban, M. P. Pileni, *Langmuir* **17**, 7982 (2001).
3. Y.-P. Sun, H. W. Rollins, *Chem. Phys. Lett.* **288**, 585 (1998).
4. H. Weller, *Phil. Trans. R. Soc. Lond. A* **354**, 757 (1996).
5. B. A. Harruff, C. E. Bunker, *Langmuir*, in press.
6. F. Seker, K. Meeker, T. F. Kuech, A. B. Ellis, *Chem. Rev*. **100**, 2505 (2000).

The results of this investigation were documented by C. E. Bunker (AFRL), P. Pathak, B. A. Harruff, Y. Lin (all of Clemson University), J. Widera (ISSI), J. R. Gord (AFRL), and Y.-P. Sun (Clemson University) in a paper that was presented at the 203rd Meeting of the Electrochemical Society (ECS), which was held 27 April – 2 May 2003 in Paris. The visual materials for the presentation at the ECS meeting are included in the Appendix.

2.1.4.9 Quenching Studies of Highly Luminescent CdS Nanoparticles in Presence of Sulfur-Containing Compounds

Nanoparticles have recently attracted a great deal of scientific attention because of their small size, unusual electronic and optical properties, and potential applications as sensors, catalysts, light-weight structures, and pharmaceuticals.[1-2] These materials were used in our laboratory to design sensors for chemical detection. CdS nanoparticles were synthesized using the reverse-micelle method and then treated by a photo-irradiation and vacuum-drying procedure, resulting in highly luminescent particles with quantum efficiencies of ~ 35%.[3] The nano particles are characterized by uniform size distributions (~ 3 - 5 nm diameter), high surface areas, and trap-state emissions. A systematic investigation was conducted of the luminescence quenching of the CdS nanoparticles by different sulfur-containing compounds. The system (CdS nanoparticles – quencher) was characterized by means of UV-Vis absorption and steady-state and time-resolved luminescence spectroscopy. The results were considered within the context of both static and dynamic quenching processes.

References
1. F. Seker, K. Meeker, T. F. Kuech, A. B. Ellis, *Chem. Rev.* **100**, 2505 (2000).
2. A. Henglein, *Chem. Rev*. **89**, 1861 (1989).
3. B. A. Harruff, C. E. Bunker, *Langmuir* **19**(3), 893 (2003).

The results of this study were documented by J. Widera (ISSI), J. R. Gord, and C. E. Bunker (both of AFRL) in a paper that will be presented at the Rocky Mountain Conference on Analytical Chemistry, which will be held 27-31 July 2003 in Denver, CO. The visual materials for this presentation are included in the Appendix.

2.1.5 Facility Upgrade

2.1.5.1 Expanding Combustion and Laser Diagnostics Research Complex

The Combustion and Laser Diagnostics Research Complex (CLDRC) supports the experimental and computational study of fundamental combustion phenomena to expand the scientific- knowledge base, validate combustor-design codes, and improve the performance, reduce the pollutant emissions, and enhance the affordability, maintainability, and reliability of current and future-generation propulsion systems for military and commercial aviation. This state-of-the-art complex provides unique laboratory tools for the experimental characterization of combustion through the development, demonstration, and application of advanced laser-based/optical diagnostic techniques. These capabilities are complemented by a suite of specialized modeling and simulation methodologies for assessing and predicting the detailed chemistry and physics of combustion processes. Through recently completed construction, the CLDRC has been expanded to include seven new combustion laboratories in the Building 5 complex at Area B, Wright-Patterson Air Force Base. Next-generation diagnostics developments and combustion studies slated for performance in the new facilities were documented by J. R. Gord, R. D. Hancock, W. M. Roquemore (all of AFRL), M. S. Brown, T. R. Meyer, S. P. Gogineni, and S. Roy (all of ISSI) in a poster that was displayed at the American Chemical Society/Society for Applied Spectroscopy Annual Poster Session and Patterson College Chemistry Awards Night and in a paper that was presented at the 27th Annual Dayton-Cincinnati Aerospace Science Symposium. These meetings were held on 5 March 2002 in Dayton, OH. The visual materials for these presentations are included in the Appendix.

3. SIMULATION AND MODEL DEVELOPMENT AND EVALUATION

3.1 General Overview

The objectives of this portion of the program concerned the development and application of simulations and models for the study of combustion and fuel processes.

3.1.1 Jet Diffusion Flames

3.1.1.1 Role of CHF_3 in Extinguishing Diffusion and Premixed Flames

Studies of laminar, buoyant jet diffusion flames provide information that is important for understanding combustion phenomena, formulating theories of combusting processes, and developing and evaluating CFD codes for practical combustion systems. Because of the similarities between buoyant jet diffusion flames and practical uncontrolled fires, it has been suggested that studies of fire-suppressing agents in the former system could provide valuable information on the behavior of such agents in actual fires. A periodically oscillating, pure-methane-air jet diffusion flame was simulated using GRI Version 1.2 chemistry. This flame had been investigated previously using the Reactive-Mie-Scattering technique, and excellent agreement was found between predictions and measurements. To explore the chemical inhibition resulting from the use of CHF_3 fire suppressant, it was added to the air flow in such a way that its addition did not change the molar concentration of oxygen.

Two-dimensional calculations for the CHF_3-affected dynamic flames were made using GRI-NIST chemistry having 82 species and 1510 elementary reactions. It was found that for concentrations of up to 26% CHF_3, the diffusion-flame base shifted slowly toward a downstream location and became stabilized within ~ 40 mm of the jet exit. For concentrations greater than 27%, the flame base moved downstream rapidly until it was cleared from the computational domain. On the other hand, for concentrations greater than 65%, the flame appeared to extinguish at locations other than the base. Flame structures obtained with different concentrations of CHF_3 were compared with those obtained for the pure methane-air jet diffusion flame. Calculations for stoichiometric premixed flames with different concentrations of fire-suppressing agent were also made. The chemical steps that were affected most significantly by fluorine reactions were identified in both the diffusion and the premixed flames. It was found that in addition to a considerable decrease in OH radicals in the ethane-air-CHF_3 flame, the concentration of H_2 decreased significantly. Unlike in premixed flames, the peak concentration of O radicals did not change significantly with the addition or small amounts of CHF_3 in the air stream of a diffusion flame. The results of this investigation were presented in AIAA Paper No. 2001-1075, which was co-authored by V. R. Katta (ISSI) and W. M. Roquemore (AFRL). This paper was presented at the 39th AIAA Aerospace Sciences Meeting and Exhibit, which was held 8-11 January 2001 in Reno, NV. The paper is included in the Appendix.

3.1.1.2 Effects of C_2-Chemistry on Structure of Partially Premixed Methane-Air Flames

Partially premixed flames (PPF) can contain multiple reaction zones, e.g., one or two with a premixed-like structure and one being a nonpremixed reaction zone. An intrinsic feature of these flames pertains to the synergistic interactions between these two types of reaction zones that are characterized by the heat and mass transfer between them. Since these interactions are strongly dependent on the distribution of the radical and stable species concentrations, an accurate representation of the flame chemistry involving these species is critical for simulating their behavior. The role of C_2-chemistry in determining the structure of partially premixed methane-air flames was investigated by employing two relatively detailed chemical mechanisms. The first involves only C_2-containing species and consists of 52 reactions involving 17 species, while the second mechanism represents both C_1- and C_2-chemistry and consists of 81 reactions that involve 24 species.

A planar, two-dimensional, partially premixed flame established on a rectangular slot burner was simulated. The simulation was based on the numerical solution of the time-dependent conservation equations for mass continuity, momentum, species, and energy. The computations were validated by comparison with the experimentally obtained chemiluminescent emission from excited-C_2* free-radical species as well as with velocity measurements using PIV.

A numerical study was then conducted to examine the applicability of C_1- and C_2-mechanisms for predicting the structure of partially premixed flames for different levels of partial premixing and reactant velocity. The results indicated that both mechanisms reproduce the global structure of PPF over a wide range of reactant velocity and stoichiometry. Since the C_1-mechanism is known to be inadequate for fuel-rich premixed flames, its relatively good performance can be attributed to the interactions between the two reaction zones that characterize the PPF structure. However, important quantitative differences exist between the predictions of the two mechanisms. Overall, the C_2-mechanism is superior to the C_1-mechanism in that its predictions are in closer agreement with our experimental results. The rich, premixed reaction-zone height obtained using the C_2-mechanism is more sensitive to variations in the equivalence ratio than predictions obtained using the C_1-mechanism. In addition, for high levels of partial premixing, the methane consumption in the inner reaction zone is significantly increased when the C_2-mechanism, rather than the C_1-mechanism, is employed. Consequently, the amount of methane that leaks from the rich premixed to the non-premixed reaction zone is significantly lower when the C_2-mechanism is used. Interactions between the inner and outer reaction zones are stronger when the C_2-mechanism is employed. Finally, the maximum temperature predicted by the C_2-mechanism is slightly lower than that obtained using the C_1-chemistry alone. These differences are attributed to the presence of the C_2-chain in the 81-step mechanism, which strongly affects the inner premixed reaction zone. The results of this effort were documented in a paper by Z. Shu (University of Illinois at Chicago), V. R. Katta (ISSI), I. K. Puri, and S. K. Aggarwal (both of the University of Illinois at Chicago), which was published in *Combustion*

Science and Technology (Vol. 157, pp. 185-211, August 2000). This paper is included in the Appendix.

3.1.1.3 Ignition and Flame Propagation in Impulsively Started Fuel Jet

The burning velocity of premixed gas can be increased by moving the flame into a region where fuel is traveling at a higher velocity. In studies by McCormack et al.,[1] flame speeds up to 15 m/s were obtained in vortices, suggesting a linear dependence of flame speed on vortex circulation. Ishizuka et al.[2] also reported super-laminar flame speeds along the vortex core but observed a somewhat reduced dependence on vortex circulation. Cattolica and Vosen[3] performed studies of premixed flame propagation in the wake of a vortex for a combustion-torch configuration in which ignition of lean premixed gases within a combustion chamber generated a vortex ring of unburned, premixed methane and air. The flame following in the wake of the vortex eventually propagated through the vortex rollers. A numerical investigation was performed in our laboratory to understand the various flame-propagation patterns that were observed in our experimental work on impulsively started jets and vortices.[4]

References
1. P. D. McCormack, K. Scheller, G. Muller, and R. Tisher, *Combustion and Flame* **19**, 297 (1972).
2. S. Ishizuka, M. Takahiro, H. Takahashi, K. Kiminori, and H. Ryo, *Combustion and Flame* **113**, 542 (1997).
3. R. J. Cattolica and S. R. Vosen, *Combustion Science and Technology* **48**, 77 (1986).
4. T. R. Meyer, J. R. Gord, V. R. Katta, and W. M. Roquemore, "Combustion in Impulsively Initiated Vortex Rings," 2nd Joint Meeting of the U. S. Sections of the Combustion Institute, Oakland, CA, 2001.

The results of this study were documented by V. R. Katta, T. R. Meyer (both of ISSI), J. R. Gord, and W. M. Roquemore (both of AFRL) in a paper that was presented at the 9th International Conference on Numerical Combustion, 7-10 April 2002, Sorrento, Italy. The paper was published in the conference proceedings and is included in the Appendix.

3.1.1.4 PAH Formation in Inverse Diffusion Flame

Particle residence time, thermal environment, and chemical environment are important factors in soot-formation processes in flames. Recent experimental studies on inverse diffusion flames revealed that the soot generated in these flames in not fully carbonized. To understand the chemical and physical structure of the early soot formed in these flames, knowledge of the flow dynamics is required. A time-dependent, detailed-chemistry CFD model was developed for simulation of an ethylene-air inverse jet diffusion flame. Steady-state simulations showed that all of the PAH species are produced outside the flame surface on the fuel side. Unsteady simulations revealed that buoyancy-induced vortices establish outside the flame as a result of the low fuel velocity (~ 7 cm/s). Unlike in the case of normal diffusion flames, these vortices appear mainly in the exhaust jet. The 17.2-Hz vortices increase mixing, which causes PAH species to

distribute more evenly in downstream locations than in upstream ones. Computed trajectories of 20-nm particles injected along the 1200-K fuel-side contour line indicate that soot-precursor particles are alternately reheated and cooled while being entrained into and advected by the buoyancy-induced vortices. This flow pattern could explain the experimentally observed large size and slight carbonization of inverse-diffusion-flame soot. The results of this study were documented by V. R. Katta (ISSI), L. G. Blevins (Sandia National Laboratories), and W. M. Roquemore (AFRL) in AIAA Paper No. 2003-0666, which was presented at the 41st AIAA Aerospace Sciences Meeting and Exhibit, which was held 6-9 January 2003 in Reno, NV. The paper is included in the Appendix.

3.1.1.5 Effect of Gravity on Burner-Stabilized and Lifted Partially Premixed Flames

The effect of gravity on burner-stabilized and lifted methane-air partially premixed flames was investigated numerically. A comprehensive, time-dependent computational model was used to simulate the flame transition from normal gravity to zero gravity. The model employs a detailed description of methane-air chemistry and transport properties, with the effect of thermal radiation being modeled by the optically thin assumption. The amount of radiative heat loss is quantified in terms of a radiation fraction (χ_{rad}), which is defined as the ratio of total radiation heat loss to total heat release. It was found that the effect of radiation is small for 1-g partially premixed flames, i.e., $\chi_{rad} \approx 0.1$. However, for the corresponding 0-g flames, the thermal-radiation effect is significantly higher, $\chi_{rad} \approx 0.5$, since the flame volume increases in the absence of buoyancy. This, in turn, causes the flame temperature to decrease and results in weaker reaction activity. The effect of coflow is to counteract the effect of gravity on partially premixed flames since the former enhances the advection of oxidizer to the outer non-premixed reaction zone and, thus, increases the overall reaction rate. The results of this investigation were documented by X. Qin, I. K. Puri, S. K. Aggarwal (all of the University of Illinois at Chicago), and V. R. Katta (ISSI) in AIAA Paper No. 2003-1018, which was presented at the 41st AIAA Aerospace Sciences Meeting and Exhibit, which was held 6-9 January 2003 in Reno, NV. The paper is included in the Appendix.

3.1.1.6 Investigation of PAH Formation in Different Flames Using UNICORN

Residence time and thermal environment are important factors in soot formation. To understand the chemical and physical structures of soot formed in different flames, knowledge is required on the flow dynamics that govern these flames. A time-dependent, detailed-chemistry CFD model was developed for the simulation of different types of ethylene-air flames. Calculations were made for burner-stabilized, opposing-jet, co-axial jet, diffusion, and premixed flames using this code and the results compared. It was observed that the fuel-lean premixed flames yield negligible amounts of PAH species, while the fuel-rich premixed and jet-diffusion flames yield similar amounts. The results of this study were documented by V. R. Katta (ISSI) and W. M. Roquemore (AFRL) in a paper that was presented at the 3rd Joint Meeting of the U. S. Sections of the Combustion Institute on Combustion Fundamentals and Applications, which was held in Chicago, IL, on 16-19 March 2003. The paper is included in the Appendix.

3.1.1.7 Triple-Flame Propagation and Stabilization in Laminar Axisymmetric Jet

Methane-air triple-flame propagation and stabilization was investigated experimentally and numerically in both partially premixed and non-premixed jet modes. The objective was to examine characteristics such as local flame-displacement speed, flame stretch, and curvature of the propagating flame at the triple points (or the leading edge). Following ignition in a non-uniform mixture, well-defined triple flames are formed that propagate upstream toward the burner. During flame propagation the flame is subjected to the effects of unsteady stretch, especially for the non-premixed jet, which causes ambiguity in defining the triple points since the flame shape and structure change. A low-stoichiometry region around the triple points was found, which has an important implication for flame propagation near the triple point. The results of this investigation were documented by X. Qin, I. K. Puri, S. K. Aggarwal (all of the University of Illinois at Chicago), and V. R. Katta (ISSI) in a paper that was presented at the 3rd Joint Meeting of the U. S. Sections of the Combustion Institute on Combustion Fundamentals and Applications, which was held in Chicago, IL, on 16-19 March 2003. The paper is included in the Appendix.

3.1.2 Opposed Jet Flames

3.1.2.1 Behavior of Jet Diffusion Flame in Multi-Vortex Flow Field

Studies on single vortex-flame interactions are important to the understanding of turbulent-flame behavior. However, construction of the mathematical and physical models for turbulent flames based on the understanding gained from single-vortex-flame interactions is rather difficult. A natural remedy to this difficulty is to acquire understanding of multi-vortex-flame interactions. A numerical investigation was performed to generate the interaction of a flame surface with multiple vortices simultaneously. This turbulent-like flow field in an opposing-jet diffusion flame was generated by driving two vortices simultaneously from the air and fuel sides toward the flame surface with different velocities. Changes in the structure of the flame during its interaction with the incoming vortices and the instability that generated multiple vortices were investigated using a time-dependent CFDC code that incorporates 13 species and 74 reactions. The results of this investigation were documented in a paper and a poster by V. R. Katta (ISSI) and W. M. Roquemore (AFRL) and presented at the 2nd Joint Meeting of the U. S. Sections of the Combustion Institute, 25-28 March 2001, Oakland, CA. The paper is included in the Appendix.

3.1.2.2 Curved Hydrogen Diffusion Flames Formed behind Bluff Body

Vortex-flame interactions are often considered to be the building blocks for statistical theories of turbulence. During these interactions the flame surface is subjected not only to unsteadiness but also to deformation. Studies of Law,[1] Mizomoto et al.,[2] Takagi and Xu,[3] and Katta and Roquemore[4] have shown that the structure of a flamelet depends on the curvature and the preferential diffusion associated with species having different molecular weights. To investigate the effects of curvature on flame structure, both

theoretical and experimental studies have been initiated. In particular, experiments designed by Roberts et al.[5] and Rolon et al.[6] have created great interest, especially because of their unique abilities to shoot a well-characterized vortex toward the flame surface. To separate unsteady effects from those of curvature, Finke and Grunefeld[7] recently established an experimental setup. By placing a bluff body either in the fuel or oxidizer stream of an opposing-jet diffusion flame, they generated various steady curved flames. A numerical study was performed in this laboratory on the curved diffusion flames formed between the opposing jets of hydrogen fuel and oxidizer. The calculated flame structures match very well with those obtained in the experiment. Numerical experiments were performed to determine the role of curvature and preferential diffusion on these flames.

References
1. C. K. Law, *Progress in Energy and Combustion Science* **10**, 295 (1984).
2. M. Mizomoto, Y. Asaka, S. Ikai, and C. K. Law, in *Proceedings of the 20th Symposium (International) on Combustion* (The Combustion Institute, Pittsburgh, PA, 1984), p. 1933.
3. T. Takaga and Z. Xu, *Combustion and Flame* **96**, 50 (1994).
4. V. R. Katta and W. M. Roquemore, *Combustion and Flame* **100**, 61 (1995).
5. W. L. Roberts, J. F. Driscoll, M. C. Drake, and J. W. Ratcliffe, in *Proceedings of the 24th Symposium (International) on Combustion* (The Combustion Institute, Pittsburgh, PA, 1992).
6. J. C. Rolon, F. Aguerre, and S. Candel, *Combustion and Flame* **100**, 422 (1995).
7. H. Finke and G. Grunefeld, *Proceedings of the Combustion Institute* **28**, 2133 (2000).

The results of this study were documented by V. R. Katta (ISSI) and W. M. Roquemore (AFRL) in a paper that was presented at the Fall Technical Meeting of the Eastern States Section of the Combustion Institute, 3-5 December 2001, Hilton Head, SC. The paper is included in the Appendix.

3.1.2.3 Insights into Non-adiabatic-Equilibrium Flame Temperatures during Millimeter-Size Vortex/Flame Interactions

Previous experimental and numerical studies have demonstrated that local flame temperatures can significantly increase above or decrease below the adiabatic flame temperature during millimeter-size vortex/flame interactions. Such large excursions in temperature are not observed in centimeter-size vortex/flame interactions. To identify the physical mechanisms responsible for these super- or sub-adiabatic flame temperatures, numerical studies were conducted for millimeter-size vortex/flame interactions in a hydrogen-air, opposing-jet diffusion flame. Contrary to expectations, preferential diffusion between H_2 and O_2 and geometrical curvature are not responsible for these variations in local flame temperature. This was demonstrated through simulations made by forcing the diffusion coefficients of H_2 and O_2 to be equal, thereby eliminating preferential diffusion. Propagation of the flame into small (~ l mm) vortices suggested that the amount of reactant carried by such a small vortex is not sufficient to feed the flame with fresh reactant during the entire vortex/flame-interaction process. Various

numerical experiments showed that the reactant-limiting characteristics associated with the millimeter-size vortices and the local Lewis number--not preferential diffusion--are responsible for the generation of flame temperature that is different from the adiabatic value. The reactant-deficient nature of the millimeter-size vortices forces the combustion products to be entrained into the vortex. While a greater-than-unity Lewis number causes pre-heating of the reactant through the product entrainment, a less-than-unity Lewis number causes cooling of the reactant. Contrary to this behavior, a centimeter-size large vortex wraps and maintains the flame around its outer perimeter by feeding the flame with fresh reactant throughout the interaction process, thereby rendering the flame unaffected by the Lewis number. Since turbulent flames generally involve interactions with small-size vortices, the physical mechanisms described here should be considered when developing mathematical models for turbulent flames. The results of this investigation were documented by V. R. Katta, T. R. Meyer (both of ISSI), J. R. Gord, and W. M. Roquemore (both of AFRL) in a paper that was published in *Combustion and Flame* [Vol. 132, pp. 639-651 (March 2003)]. The paper is included in the Appendix.

3.1.2.4 Extinction Criterion for Unsteady, Opposing-Jet Diffusion Flames

Dynamic flames are known to survive at strain rates that are much higher than those associated with steady-state flames. A numerical and experimental investigation was performed to aid the understanding of the extinction process associated with unsteady flames. Spatially locked unsteady flames in an opposing-jet-flow burner were established and stretched by simultaneously driving one vortex from the air side and another from the fuel side. Changes in the structure of the flame during its interaction with the incoming vortices and with the instability-generated secondary vortices were investigated using a time-dependent CFDC code known as UNICORN (UNsteady Ignition and COmbustion with ReactioNs). The combustion process was simulated using a detailed-chemical-kinetics model that incorporates 13 species and 74 reactions. Slow-moving vortices produce a wrinkled but continuous flame, while fast-moving vortices create a locally quenched flame with its edge wrapped around the merged vertical structures. In an attempt to characterize the observed quenching process, five variables—namely, air-side, fuel-side, and stoichiometric strain rates and maximum and stoichiometric scalar dissipation rates—were investigated. It was found that these characteristic parameters cannot be used to describe the quenching process associated with unsteady flames. The flow and chemical nonequilibrium states associated with the unsteady flames are responsible for changes in the extinction values of these traditional characteristic variables. However, even though the quenching values of the scalar dissipation rates increase with the velocity of the incoming vortices, the variations are much smaller than those observed in the strain rates. It was proposed that a variable that is proportional to the air-side strain rate and inversely proportional to the rate of change in the flame temperature can be used to characterize the unsteady quenching process uniquely. The results of this investigation were documented by V. R. Katta, T. R. Meyer, M. S. Brown (all of ISSI), J. R. Gord, and W. M. Roquemore (both of AFRL) in a paper that was submitted in April 2003 for publication in *Combustion and Flame.*

4. FUNDAMENTAL EXPERIMENTS

4.1 General Overview

The purpose of this portion of the program was to conduct fundamental experiments that would aid the understanding of all processes required for advanced-propulsion-system technologies. This effort required a close coupling of numerical and experimental studies, and thus required a multi-disciplinary team.

4.1.1 Jet Diffusion Flames

4.1.1.1 Combustion in Impulsively Initiated Vortex Rings

Ignition and flame propagation in premixed methane-air vortex rings were investigated while the equivalence ratio, ignition timing, and vortex propagation velocity were varied. This study significantly extended the work of several investigators who mainly considered the effect of exit velocity. Because ignition is initiated at various stages of vortex development, this study contained elements of flame propagation along the vortex axis as well as in the wake and roller structures. Results were compared with numerical simulations from a time-dependent CFDC code. In addition to useful insight into ignition and flame propagation in the field of a premixed vortex, practical insight was gained into the feasibility of a vortex-assisted ignition system for high-speed combustor applications. The results of this study were documented in a paper and a poster by T. R. Meyer (ISSI), J. R. Gord (AFRL), V. R. Katta (ISSI), W. M. Roquemore (AFRL), G. L. Switzer (ISSI), and G. J. Fiechtner (ISSI) and presented at the 2nd Joint Meeting of the U. S. Sections of the Combustion Institute, 25-28 March 2001, Oakland, CA. The paper is included in the Appendix.

4.1.1.2 Visualization and Two-Color DPIV Measurements of Flows in Circular and Square Coaxial Nozzles

High-resolution, reactive Mie scattering laser-sheet visualizations, two-color DPIV, and thermal-anemometry measurements in flows generated by equivalent coaxial circular and square jets were conducted. Visualization results were obtained for three square coaxial configurations and a reference circular coaxial nozzle at two Reynolds numbers of the outer jet (19,000 and 29,000) and for inner-to-outer jet velocity ratios of 0.15, 0.22, and 0.3. These results indicated that the internal unmixed region diminished with decreasing velocity ratio. Strong evidence of unsteady recirculation and back-flow was observed at the end of the core of the inner jet for the low-velocity ratios. Comparisons between circular and square jet configurations indicated considerable mixing enhancement when square nozzles were used. Low-coherence, organized large-scale structure was evident from the visualizations and DPIV measurements near the origin of the inner mixing-region shear layers and was even more pronounced in the core region of the near field. These observations were confirmed by velocity spectra, which displayed peaks corresponding to a free shear-layer instability mode in the inner mixing-region shear layers, and a wake-type mode in the core region where the mean flow has a wake-like

character. Although some large-scale structure was observed in the outer mixing layer during the visualizations, this was found to be incoherent on the basis of the DPIV measurements and the velocity spectra. It should be noted that no axis-switching phenomena were observed in the square-nozzle flows examined here. This is attributed to the absence of an organized structure in the outer shear layer, which was initially highly turbulent, and the weakly coherent nature of the organized structure observed in the inner mixing-region near field. The results of this study were documented by J. W. Bitting, D. E. Nikitopoulos (both of Louisiana State University), S. P. Gogineni (ISSI), and E. J. Gutmark (Louisiana State University) in a paper that was published in *Experiments in Fluids* [Vol. 31, pp. 1-12 (July 2001)]. This paper is included in the Appendix.

4.1.1.3 Experimental and Numerical Investigation of Vortex-Flame Interactions in Impulsively Initiated Premixed and Non-Premixed Jets

The effects of ignition and subsequent flame propagation in a pseudo-turbulent premixed flow field were investigated using PIV, PLIF, and a CFD code with chemistry. Premixed jets of methane and air were generated at the exit of an axisymmetric nozzle using a solenoid-driven piston, and ignition was initiated at various phases with respect to vortex formation using a pair of electrodes. Previous investigations in this area focused on the effects of spark timing, equivalence ratio, and vortex strength on global flame morphology. In the current study a more detailed analysis was made of the simultaneous OH PLIF and PIV data to explore flame propagation and vortex structure. Successful comparisons between experiments and numerical simulations were also made, and these data provide further insight into the effects of turbulence on premixed flame stability and heat release. The results of this investigation were documented by S. P. Gogineni, T. R. Meyer, V. R. Katta (all of ISSI), and J. R. Gord (AFRL) in a poster that was displayed at the American Chemical Society/Society for Applied Spectroscopy Annual Poster Session and Patterson College Chemistry Awards Night and in a paper that was presented at the 27^{th} Annual Dayton-Cincinnati Aerospace Science Symposium. These meetings were held on 5 March 2002 in Dayton, OH. The visual materials for these presentations are included in the Appendix.

4.1.1.4 Comparisons of Initially Turbulent, Low-Velocity-Ratio Circular and Square Coaxial Jets

A qualitative and quantitative comparison of unforced flows emanating from equivalent geometries of axisymmetric (circular) and square coaxial nozzles was made. The initial state of the jets is turbulent, as in nozzles relevant to practical applications. Flow visualization and velocity measurements were performed at a coflow-jet Reynolds number of 1.9×10^4 and at an inner-to-outer jet velocity ratio of 0.3. Scaling of mean velocity and turbulence profiles was examined for the three shear layers formed in the near field of axisymmetric and square coaxial flows. Visualizations and local velocity measurements have indicated modest mixing enhancement when square nozzle are used compared to axisymmetric ones, and this is largely attributed to differences in the initial velocity profiles of these two configurations. Low-coherence, large-scale periodic

structures were observed for both nozzle configurations in the midfield of the inner mixing region, which has wake characteristics. The outer mixing region, which was initially highly turbulent, showed no signs of an "indigenous" organized structure. The spectral characteristics of the circular and square nozzle combinations were qualitatively similar. However, the discrete frequency peaks associated with the wake of the inner mixing region were much broader in the case of the square nozzles. What is more important is that the dominant frequency at the end of the midfield within the inner mixing region was lower in the case of the square nozzles, as compared to the circular ones. Spectra from the turbulent shear layers of the middle mixing region in the near field indicated the presence of a short-lived shear-layer preferred mode at a much higher frequency than the one associated with the subsequent development of the wake downstream. The existence of axis switching--a phenomenon observed in single non-axisymmetric nozzles--was not evident from visualizations and measurements in the square coaxial nozzle, presumably due to the initial low coherence of large-scale structures in the shear layers. The results of this study were documented by D. E. Nikitopoulos, J. W. Bitting (both of Louisiana State University), and S. P. Gogineni (ISSI) in a paper that was published in the *AIAA Journal* [Vol. 41, No. 2, pp. 230 – 239, (February 2003)]. The paper is included in the Appendix.

4.1.1.5 Study of Vortex Shedding of Jet in Crossflow

An experimental investigation of a circular jet issuing from a wall normal to a crossflow was conducted over a momentum-ratio range of 2.0 - 15 for various jet and crossflow Reynolds numbers. The flowfield was interrogated using split-film and DPIV techniques to characterize the various regimes of the flow. The analyzed data revealed the three classic vortices that are present in a jet-in-cross-flow environment: the leading-edge horseshoe vortex, Karman-Street vortices, and the combined Kelvin-Helmholtz/Counter-Rotating Vortex Pair (K-H/CVP). It was observed that the penetration is a function not only of momentum ratio and axial location but also of both jet and crossflow Reynolds Numbers. The DPIV data qualitatively indicated an increase in the Kelvin-Helmholtz vortex-shedding frequency with crossflow Reynolds number. The results of this study were documented by B. Kiel, C. Murawski, M. Flanagan, A. Cox (all of AFRL), and S. Gogineni (ISSI) in a paper that was presented at the 28th Annual Dayton-Cincinnati Aerospace Science Symposium, which was held 4 March 2003 in Dayton, OH.

4.1.1.6 Experimental Investigation of Vortex Shedding of Jet in Crossflow

An experimental investigation of a circular jet emitting from a wall into a crossflow was conducted. The analyzed data revealed the three classic vortices that are present in a jet-in-crossflow environment: leading-edge horseshoe vortex, the Karman-Street vortices, and the combined Kelvin-Helmholtz/Counter Rotating Vortex Pair (K-H/CVP). The focus of this investigation was to study the frequency content of these vortices over a wide range of momentum ratios and Reynolds Number. A circular jet at room temperature and ambient pressure was investigated over a range of momentum ratios from 2.0 to 15. The range of crossflow Reynolds numbers based on crossflow velocity and jet diameter was 3,000 - 18,000. The flowfield was interrogated using a TSI 1288

split-film probe. From the split-film data Discrete Fast Fourier Transforms (DFFT) of the velocity data were performed. Diagrams of Fourier spectra and energy spectra were constructed using the DFFT data. From the Fourier spectra, the Strouhal number of each of the vortices was discerned. Plots of Strouhal number versus Reynolds number were also made for each type of vortex. All three types of vortices showed some sensitivity to crossflow Reynolds number. This was especially true at higher Reynolds number where the Strouhal number decreased significantly. Finally, the K-H/CVP Fourier spectra displayed two distinct peaks for nearly every Reynolds number tested. These peaks are associated with the frequency of the ring vortex and the frequency that the ring vortex was shed from the jet. The results of this investigation were documented by B. Kiel, C. Murawski, M. Flanagan, A. Cox (all of AFRL), and S. Gogineni (ISSI) in AIAA Paper No. 2003-0182 that was presented at the 41st AIAA Aerospace Sciences Meeting and Exhibit, which was held 6-9 January 2003 in Reno, NV. The paper is included in the Appendix.

4.1.2 Opposed Jet Flames

4.1.2.1 Vortex-Flame Interactions: Experimental Observation of Annular Local Extinction

An experiment was conducted to observe the dynamic interaction of a laminar flame and a vortex. The OH layer produced by the flame was imaged using PLIF, and vortex-characterization data were acquired using digital, two-color PIV. The PIV and PLIF measurements of OH were performed simultaneously. The hydrogen-air flame was supported in a non-premixed opposed-jet burner. The apparatus produced highly repeatable events under most circumstances. Conditions were chosen to enable the observation of a distinct annular extinction of the OH layer. The temporal behavior of the extinction evolution agrees with prior modeling predictions--a conclusion drawn after implementation of a novel pre-emptive triggering scheme that improves temporal resolution to ~10 ns electronically. Practical repeatability of the vortex-flame interactions was demonstrated for the temporal evolution of the annular break with 10-μs time steps. The pre-emptive triggering scheme enables the identification of other interaction behavior, based on temporal features such as non-repeatable observations that are sensitive to experimental perturbations. The results of this investigation were documented by G. J. Fiechtner, C. D. Carter (both of ISSI), J. R. Gord (AFRL), P.-H. Renard, D. Thevenin, J. C. Rolon (all of (Ecole Centrale Paris and CNRS), and T. R. Meyer (ISSI) in a paper that was accepted in May 2001 for publication in *Combustion and Flame*.

4.1.2.2 Flame Propagation and Morphology in Premixed Vortex Rings

Ignition and combustion in starting fuel jets were studied experimentally using PLIF imaging of OH. Well-characterized vortex rings of fuel and air were generated at the exit of an axisymmetric nozzle using a solenoid-driven piston to pulse a reservoir of methane fuel. Ignition was initiated at various locations downstream of the nozzle exit and at

various times relative to vortex initiation, pinch-off, and propagation. The effects of stoichiometry on vortex flame propagation were then studied for various ignition regimes. Results from PLIF visualizations were compared with corresponding numerical simulations from a time-dependent CFD code with chemistry. The results of this investigation were documented by T. R. Meyer (ISSI), J. R. Gord (AFRL), V. R. Katta, G. J. Fiechtner, G. L. Switzer (all of ISSI), and W. M. Roquemore (AFRL) in an invited paper that was presented at the 11th Gordon Research Conference on Laser Diagnostics in Combustion, 1-6 July 2001, South Hadley, MA.

4.1.2.3 Simultaneous PLIF/PIV Investigation of Vortex-Flame Interactions

Recent studies of vortex-flame interactions have advanced the understanding of isolated turbulent events and their impact on local non-premixed flame fronts. In the current investigation vortex-flame interactions in a counterflow Rolon Burner developed at Ecole Centrale Paris/CNRS were investigated using a simultaneous PLIF/PIV technique. The OH layer produced by a hydrogen-air flame was imaged using PLIF, and vortex-characterization data were acquired using two-color DPIV. Experiments were performed for cases with and without flame extinction. Results showed that the case with flame extinction has higher initial vortex strength but experiences greater levels of energy dissipation at later times as a result of flame propagation within the vortex rollers. Measurements at high temporal resolution showed that the extinction process takes place in an annular region at the leading edge of the vortex rather than at the centerline for the conditions investigated in the present experiment. Local normal strain rates computed from the PIV data showed higher *fuel-side* normal strain rates in the annular region of the vortex-perturbed flame but higher *air-side* normal strain rates at the centerline. The results of this investigation were documented by T. R. Meyer (ISSI), G. J. Fiechtner (formerly of ISSI), C. D. Carter (ISSI), J. R. Gord (AFRL), and S. P. Gogineni (ISSI) in PIV'01 Paper 1055 that was presented at the 4th International Symposium on Particle Image Velocimetry, 17-19 September 2001, Gottingen, Germany. The paper is included in the Appendix.

4.1.2.4 Performance of CH PLIF and PIV in Two-Phase Methane/n-Heptane/Air Vortex-Flame Interactions

A thorough understanding of turbulent mixing is critical to the continued development of high-performance, low-emissions propulsion systems for both military and commercial aviation applications. Such an understanding will enable the production of compact gas-turbine combustors that are designed for maximum heat release with minimum pollutant emissions and reduced infrared signature. Turbulent mixing can provide tremendous combustor performance gains through reduced weight and increased thrust-to-weight ratio.

In an effort to reduce the complexity of these systems while capturing the essential features that define the physics and chemistry of turbulent reacting flows, we have reduced the study of fully developed turbulence to experimental and computational characterization of isolated vortex-flame interactions. These studies have been conducted

at AFRL, in collaboration with an international team of researchers that includes scientists and engineers at Ecole Centrale Paris (ECP) and ONERA. Developing predictive understanding of turbulent mixing as it applies to reacting flows is the overall goal of this research.

Efforts to date have been focused on computational and experimental studies of the interaction of a single vortex and a flat hydrogen/air diffusion flame stabilized between two counterflow nozzles. Extensive research in this configuration using PLIF, Rayleigh-scattering thermometry, and PIV has allowed the development of combustion diagrams that outline various regimes of flame extinction due to vortex size, strength, and fuel mixture fraction. The effects of fire suppressants and local strain rates on flame extinction have also been the subjects of detailed study and have provided useful phenomenological data for the development of more accurate numerical models.

The next phase of research on vortex-flame interactions is underway in two main areas: 1) studies of multiple-vortex-flame interactions at AFRL and 2) studies of two-phase vortex-flame interactions at ECP. Both configurations are designed to advance our understanding of turbulent combustion under conditions that more closely reflect those of real gas-turbine combustors. Through the collaborative program, each research team develops expertise in these separate configurations and shares this expertise through on-site visits and personnel exchange programs to reduce development time and redundancy.

In November of 2001, Dr. T. R. Meyer (ISSI) joined the research team at ECP for a two-month period to help perform CH PLIF and PIV in two-phase methane/n-heptane/air vortex-flame interactions. Thorough analyses of the effects of vortex size, vortex strength, and fuel mixture fraction were performed to extend our understanding of single-phase hydrogen/air vortex-flame interactions to more realistic liquid-fueled conditions. Another milestone of this effort included the first application of CH PLIF during a non-premixed vortex-flame interaction as well as the simultaneous application of CH PLIF and PIV during that interaction. The experimental findings of this effort will be presented at the following technical meetings: 8th Topical Meeting on Laser Applications to Chemical and Environmental Analysis (Optical Society of America) (7-10 February 2002, Boulder, CO), the Dayton-Cincinnati Aerospace Science Symposium (5 March 2002, Dayton, OH), the Joint Poster Session of the Dayton Section of the American Chemical Society and the Ohio Valley Section Society for Applied Spectroscopy (5 March 2002, Dayton, OH), and the 11th International Symposium on Applications of Laser Techniques to Fluid Mechanics (8-11 July 2002, Lisbon, Portugal).

4.1.2.5 Effects of Ignition on Premixed Vortex Rings: Simultaneous PLIF and PIV Investigation

Preliminary studies of reacting, premixed vortex rings have shown that flame propagation is highly sensitive to ignition timing, equivalence ratio, and vortex strength. A variety of divergent phenomena have been observed, such as interior/exterior flame propagation, vortex-induced flame bridging across the jet column, and the formation of unburned pockets. PLIF of acetone and OH was performed to study the non-reacting and reacting

regions, respectively, and PIV was used to study the effects of reaction on the flow field. The flow field consisted of well-characterized vortex rings of premixed methane and air generated at the exit of an axisymmetric nozzle using a solenoid-driven piston. Ignition was initiated at various phases of vortex development and propagation. Results were compared with corresponding numerical simulations from a time-dependent computational-fluid-dynamics code with chemistry. The results of this investigation were documented by T. R. Meyer (ISSI), J. R. Gord (AFRL), V. R. Katta, and S. P. Gogineni (both of ISSI) in a paper that was presented at the 54th Annual Meeting of the American Physical Society, Division of Fluid Dynamics, 18-20 November 2001, San Diego, CA. The visual materials for this presentation are included in the Appendix.

4.1.2.6 Study of Multi-Vortex/Flame Interactions in Opposing-Jet Diffusion Flame

A numerical and experimental investigation was performed to generate interaction of a flame surface with multiple vortices. This unsteady flame in an opposing-jet-flow burner was established by driving two vortices simultaneously from the air and fuel sides. Changes in the structure of the flame during its interaction with the incoming vortices and the instability-generated secondary vortices were investigated using the time-dependent CFDC code known as UNICORN. The combustion process was simulated using a detailed-chemical-kinetics model that incorporates 13 species and 74 reactions. While the slowly moving vortices resulted in a wrinkled but continuous flame, the fast-moving vortices created a locally quenched flame, with its edge being wrapped around the merged vertical structures. Three variables, namely, air and fuel-side strain rates and scalar dissipation rate, were investigated to characterize the observed quenching processes. It was found that none of these variables can characterize the quenching process associated with the unsteady flames. Even though the quenching value of the scalar dissipation rate increased with the velocity of the incoming vortices, its variation was much smaller than that obtained in air- or fuel-side strain rates. It is proposed that a variable proportional to the air-side strain rate and inversely proportional to the temperature-drop rate at extinction could characterize the unsteady quenching process. The results of this study were documented by V. R. Katta, M. S. Brown, T. R. Meyer (all of ISSI), J. R. Gord, and W. M. Roquemore (both of AFRL) in AIAA Paper No. 2002-0479 that was presented at the 40th AIAA Aerospace Science Meeting and Exhibit, 14-17 January 2002, Reno, NV. This paper is included in the Appendix

4.1.2.7 Vortex-Induced Flame Extinction in Two-Phase Counterflow Diffusion Flames with CH PLIF and PIV

The interaction between a laminar, two-phase, non-premixed counterflow flame and a vortex was examined. Special emphasis was placed on the influence of different flame and vortex parameters on the extinction behavior of the flame. Simultaneous PLIF of the CH radical layer produced by the flame and PIV measurements of the flowfield were used to characterize the flame-vortex interaction. These simultaneous diagnostics were used for the first time in this configuration. The extinction processes occurring during the flame-vortex interaction can be analyzed by this method, especially the effect of strain at the flame surface. The influence of the droplets on the extinction behavior is

apparent, in comparison with a fully gaseous flame. The spray flame is weaker and extinguishes earlier than a gaseous flame. In the measurements an additional broadband signal in the vicinity of the CH layer is probably due to the induced fluorescence of polycyclic aromatic hydrocarbons that are excited at the same wavelength. The results of this study were documented by A. Lemaire (Ecole Centrale Paris), T. R. Meyer (ISSI), K. Zahringer, J. C. Rolon (both of Ecole Centrale Paris), and J. R. Gord (AFRL) in a paper that was published in *Applied Optics* [Vol. 42, No. 12, pp. 2063-2071 (20 April 2003)]. One of the figures from this paper was chosen to appear on the cover of the 20 April 2003 issue. The paper is included in the Appendix.

4.1.3 Model Combustors

4.1.3.1 LII Measurements in the Reaction Zone of a Model Gas-Turbine Combustor

In concert with an Air Force program designed to study the effect of additives on particulate production, LII measurements were performed in a JP-8-fueled, single swirl-cup combustor with a central nozzle. Single-shot and averaged LII images of soot were obtained along with high-speed luminescence images. Performance of the LII system was evaluated as well as its utility in augmenting extractive-sampling approaches to particulate measurements. The results of this study were documented by M. S. Brown, T. R. Meyer (both of ISSI), J. R. Gord, V. M. Belovich, and W. M. Roquemore (all of AFRL) in AIAA Paper No. 2002-0393 that was presented at the 40th AIAA Aerospace Science Meeting and Exhibit, which was held 14-17 January 2002 in Reno, NV. This paper is included in the Appendix.

4.1.3.2 Combustion-Air-Jet Influence on Primary-Zone Characteristics for Gas-Turbine Combustors

Emissions and lean-blowout measurements were performed in a generic-combustor primary zone of an aircraft gas-turbine engine to determine the effects of opposed, circular combustion air jets of a range of sizes, positioned half a dome height downstream from the dome. The primary zone was operated at simulated engine high-power conditions and representative dome and liner pressure drops. Most of the NO_x was generated in the jets. Although an optimum jet size was identified, the lowest overall emissions resulted from a no-combustion air-jet configuration; air jets were necessary, however, to confer lean-blowout stability and short flame length. The results of this investigation were documented by S. Gogineni (ISSI), D. Shouse, C. Frayne, J. Stutrud (all of AFRL), and G. Sturgess (ISSI) in a paper that was published in the *Journal of Propulsion and Power* [Vol. 18, No. 2, pp. 407-416, (March-April 2002)]. This paper is included in the Appendix.

4.1.3.3 Particulate Matter and PAH Determination Using Well-Stirred Reactor

Combustion-generated particulates from gas-turbine combustors can have adverse effects on engine-maintenance costs, plume visibility, and the environment. Research is being conducted to provide an understanding of the mechanisms of soot formation and identify mitigation strategies. A cooled well-stirred reactor, which simulates the primary zone of

a gas-turbine combustor, was used in experiments carried out with premixed, fuel-rich ($1.9 < \varphi < 2.6$) ethylene-air and ethylene-ethanol-air mixtures. Multiple physical characteristics, including particle number density, particle-size distribution, total-carbon mass, and PAH content, were used to quantify soot. A unique instrument, the Particulate Matter Characterization and Monitoring System, was utilized for determination of the particle-size distribution and the chemical characterization of the soot and gaseous emissions. The results of the study showed that the benzene concentration in the gas phase increased monotonically with equivalence ratio, while the pyrene correlated with soot content. The results suggest that pyrene and other PAH species can be used to predict soot formation for more complex combustion systems. For the conditions of the present study, the addition of ethanol to ethylene was shown to lower soot production. The results of this investigation were documented by R. F. Reich (AFRL), S. D. Stouffer [University of Dayton Research Institute (UDRI)], V. R. Katta (ISSI), H. T. Mayfield (AFRL at Tyndall AFB), C. W. Frayne, and J. Zelina (both of AFRL) in AIAA Paper No. 2003-0664, which was presented at the AIAA Reno Meeting in January 2003. The paper is included in the Appendix.

4.1.3.4 Multi-Component Laser-Doppler-Velocimetry (LDV) Measurements Downstream of Gas-Turbine-Engine Nozzle/Air Swirler

LDV measurements were performed downstream of a gas-turbine-engine nozzle/air swirler to determine the appropriate boundary conditions for use in a three-dimensional numerical model. Three components of velocity were obtained using a two-component LDV system. A variety of numerical filtering techniques was used to increase the accuracy of velocity measurements near scattering surfaces. Measurements were made for two different fuel nozzles, two different pressure drops, and a variety of geometrical configurations. The data were used to determine a number of important flow parameters, including nozzle exit velocities, swirl angles, recirculation zones, and reattachment regions. Probability density functions were analyzed to detect regions with bimodal velocity statistics indicative of possible vortex shedding. These measurements can be used not only to understand the overall flow structure but also to anchor the numerical model. The results of this study were documented by J. D. Miller [Universal Technology Corporation (UTC)], T. R. Meyer, M. S. Brown (both of ISSI), A. Lynch, J. R. Gord, J. Zelina, D. T. Shouse, V. M. Belovich, and R. D. Hancock (all of AFRL) in a paper that was presented at the 28th Annual Dayton-Cincinnati Aerospace Science Symposium, which was held 4 March 2003 in Dayton, OH. The visual materials for this presentation are included in the Appendix.

5. PULSED-DETONATION-ENGINE TECHNOLOGY

5.1 General Overview

The purpose of this portion of the program was to identify the critical technology needs of pulsed-detonation engines (PDEs). The four areas examined in this task were engine development, fuel type, detonation initiation and propagation, and performance and emissions.

5.1.1 Engine Development

5.1.1.1 Detonation-Initiation Studies and Performance Results for PDE Applications

An in-house computational and experimental program to investigate and develop an air-breathing PDE that uses a practical fuel (kerosene-based, fleet-wide use, "JP" type) was conducted at the Combustion Sciences Branch of the Turbine Engine Division of AFRL (AFRL/PRTC). PDE's have the potential of high thrust, low weight, low cost, high scalability, and wide operating range; but several technological hurdles must be overcome before a practical engine can be designed. This research effort involved investigating such critical issues as 1) detonation initiation and propagation; 2) valving, timing, and control; 3) instrumentation and diagnostics; 4) purging, heat transfer, and repetition rate; 5) noise and multi-tube effects; 6) detonation and deflagration-to-detonation transition modeling; and 7) performance prediction and analysis. An innovative, four-detonation-tube engine design was tested and evaluated. Preliminary data were obtained with premixed hydrogen/air as the fuel/oxidizer to demonstrate proof of concept and verify models. Techniques for initiating detonations in hydrogen/air mixtures were developed without the use of oxygen-enriched air. The results of this effort were presented in AIAA Paper No. 2001-1129, co-authored by F. Schauer, J. Stutrud (both of AFRL), and R. Bradley (ISSI), which was presented at the AIAA Aerospace Sciences Meeting in Reno and is included in the Appendix.

Portions of these results were also presented in two invited papers: 1) "Pulse-Detonation-Engine In-House Research at AFRL" (by the same authors), which was presented at the 13th ONR Propulsion Meeting, 10-12 August 2000, Minneapolis, MN, and 2) "AFRL/PRSC Pulse Detonation Engine Research Program" [by these authors and V. R. Katta (ISSI)], which was presented at the 12th PERC Symposium, Ohio Aerospace Institute, 26-27 October 2000, Cleveland, OH. The second paper is included in the Appendix.

5.1.1.2 Evaluation of Self-Aspirated PDE

Self-aspiration in a PDE was evaluated. Two possible self-aspiration methods were examined--a turbo-charger and a supersonic pulsed ejector pump (SPEP). The effectiveness of the turbo-charger and SPEP operating in a PDE environment were evaluated as well as the performance and noise level of the hybrid PDE. In the turbo-charged PDE, a portion of the exhaust gasses is used to turn a centrifugal turbine. The

power produced by the turbine is used to drive a centrifugal compressor. Air flow through the compressor is measured by an automotive-style hot wire. The supersonic pulsed ejector was evaluated in an experiment, independent of the turbo-charger. Two configurations involve the SPEP. In the first the SPEP is placed at the exit of a straight detonation tube to augment thrust and reduce noise. In the second, the SPEP is connected to the detonation tube via a 45-deg lateral pipe fitting; in this configuration, a portion of the exhaust gas from the detonation is used to drive the SPEP. Performance under a variety of operating conditions was evaluated. The results of this investigation were documented by J. L. Hoke (ISSI), J. S. Stutrud (AFRL), R. P. Bradley (ISSI), and F. R. Schauer (AFRL) and presented at the 26th Annual Dayton-Cincinnati Aerospace Science Symposium, 30 March 2001, Dayton, OH. The visual materials for this presentation are included in the Appendix.

5.1.1.3 Hybrid Piston PDE

A hybrid Piston-PDE was evaluated. At low air speeds a pure PDE requires that pressurized fuel and oxidizer be carried onboard, mitigating the specific thrust and flight time of the engine. By combining the PDE with a piston engine, shaft work and thrust can be obtained. Shaft work from the piston engine can be used to supercharge the PDE, making it self-aspirating. The goal of this study was to evaluate the thrust and shaft work produced from a hybridized Piston-PDE. Analytical calculations were made and the early stages of experimental testing documented. The block and head of a motorcycle engine were separated, and detonation tubes were inserted in a spacer block. For the initial experiments both fuel (hydrogen) and air were supplied under pressure to the detonation tubes. The original starter motor was used for turning the pistons and cam shaft to start the engine. Pre-mixed air and hydrogen were fed through the intake manifold, and purge air was fed through the "exhaust" manifold. A hybrid Piston-PDE is a possible means of creating shaft work and thrust from pulsed detonations. The results of this study were documented by B. M. Frankey (AFRL), J. L. Hoke (ISSI), J. S. Stutrud (AFRL), R. P. Bradley (ISSI), and F. R. Schauer (AFRL) and presented at the 26th Annual Dayton-Cincinnati Aerospace Science Symposium, 30 March 2001, Dayton, OH. The visual materials for this presentation are included in the Appendix.

5.1.1.4 Introduction to a PDE

A General Motors Quad-4 engine, as commonly found in the Pontiac Grand-Am and Chevrolet Cavalier, was adapted to make an extremely low-cost, high-performance propulsion system. Cycle frequency was controlled with an electric motor driving dual overhead cam shafts. The four-cylinder, 16-valve engine was converted into a four-tube PDE by replacing the cylinder block with four lengths of common pipe and using intake-valve pairs to feed premixed fuel and air. By flowing clean air backward through them, exhaust valve pairs were used to create a purge cycle which cooled the detonator tube walls and acted as a buffer between hot detonation products and incoming subsequent fuel-air charges. Weak ignition was accomplished via a common automotive ignition system. A Shelkin spiral was used to accelerate the transition of deflagration combustion to detonation. Thrust was measured via a damped thrust stand. Detonation wave speeds

were determined by measuring time-of-flight between high-frequency pressure transducers separated by a known distance. Because of the hazardous environment associated with detonations, extremely flexible virtual instrumentation and controls were used remotely. The Quad-4-based research PDE has proven to be a versatile and robust test bed for detonation experiments. Many concepts key to the viability of future PDE propulsion systems have been developed using these tools. The results of this study were documented by M. Slagel (ISSI), F. Schauer, J. Stutrud (both of AFRL), and R. Bradley (ISSI) and presented at the 26th Annual Dayton-Cincinnati Aerospace Science Symposium, 30 March 2001, Dayton, OH. The visual materials for this presentation are included in the Appendix.

5.1.1.5 Detonation Wave Propagation through Tube Array

Pulse detonation engines derive thrust from the momentum flux behind a traveling shock-detonation wave. Detonation occurs in a tube where a fuel-air mix is ignited at discrete time intervals. Pulse-detonation tubes currently have individual ignition sources, and a multi-tube array would require multiple ignition sources. Of interest is the possibility of developing a multi-tube array with a single ignition source. One concept would be to pulse-ignite and detonate a high-energy wave that would, in turn, initiate detonation in joined parallel tubes. The initial effort underway involves the building and testing of a goal-post arrangement of tubes in which the cross connector has a detonation wave propagating across the open-ended secondary (upright) tubes. Of concern is quenching (attenuation) of the original detonation wave. Pressure transducers will be installed to detect wave-passing events and the resulting wave strengths propagated into open-ended uprights. Successful development will lead to tests involving detonation in the secondary tubes--a necessary ingredient for full-up parallel tube detonations from a single ignition source. The results of this investigation were documented by A. J. Rolling, P. I. King [both of the Air Force Institute of Technology (AFIT)], F. Schauer (AFRL), J. Hoke, R. Bradley, M. Slagel, V. Katta (all of ISSI), and J. Stutrud (AFRL) and presented at the 26th Annual Dayton-Cincinnati Aerospace Science Symposium, 30 March 2001, Dayton, OH. The visual materials for this presentation are included in the Appendix.

5.1.1.6 AFRL PDE Research Application

Various experiments employing the in-house research PDE at Wright-Patterson Air Force Base were conducted to examine aspiration and power-extraction issues. Nozzle effectiveness was tested for a variety of geometries including straight, diverging, and converging nozzles. The resulting impact upon both thrust and detonator-tube blow down was assessed. A detonation-driven ejector was examined using the detonation as the primary driver flow to entrain secondary air flow. The interaction of the detonation with the primary exit region was found to be critical for ejector operation. Preliminary studies were conducted on a PDE-driven turbine. Detonations bled from a detonator tube were employed to spin a centrifugal turbine which, in turn, spooled-up a compressor. By matching compressor mass flow and outlet pressure to PDE manifold conditions, self-aspiration was achieved. Detonation pressure was also employed to drive pistons in a hybrid PDE-piston engine. The results of this study were documented by J. Hoke, R.

Bradley (both of ISSI), and F. Schauer (AFRL) in an invited paper that was presented at the European Office of Aerospace Research and Development (EOARD) and EADS-Aerospatiale Matra Missiles (AMM) Workshop on Pulse Detonation Engines, 28-29 August 2001, Bourges, France. The visual materials for this presentation are included in the Appendix

5.1.1.7 Integration of PDE with Ejector Pump and with Turbo-Charger as Methods to Self-Aspirate

Two methods, an ejector pump and a turbo-charger, were evaluated as a means of self-aspirating a PDE. For the experiments pertaining to the ejector pump, a PDE was run on hydrogen and air at frequencies up to 40 Hz, equivalence ratios from 0.5 to 1.0, and fill fractions from 0.25 to 1.0. Flow visualization was used to determine the combination of fill fraction and equivalence ratio that would successfully induce a secondary flow in the ejector pump. Pressure traces at the inlet and along the ejector pump were used to elucidate the performance of the ejector pump. The induced secondary flow was found to be approximately triple the primary detonation flow. Fill fraction and equivalence ratio were found to affect the performance of the ejector. High fill fractions and high equivalence ratios resulted in an oscillatory flow at the ejector inlet. Hydrogen and air were used as the fuel and oxidizer during the experiment with the turbo-charger also. Air flow and pressure at the exit of the compressor were employed to evaluate the potential for self-aspirating the PDE. By running two detonation tubes simultaneously through the turbo-charger, self-aspiration was achieved. The centrifugal-style turbine and compressor of the turbo-charger were not discolored or pitted after a 25-min. self-aspiration run where the detonation tube and turbo-charger attained thermal equilibrium. Throughout the tests the turbine experienced 35K-plus detonation events and reached a rotational operating speed of 80K rpm. The results of this study were documented by J. Hoke, R. Bradley (both of ISSI), J Stutrud, and F. Schauer (both of AFRL) in AIAA Paper No. 2002-0615 that was presented at the 40th AIAA Aerospace Science Meeting and Exhibit, 14-17 January 2002, Reno, NV. This paper is included in the Appendix.

5.1.1.8 Evaluation of Hybrid-Piston PDE

Experiments were conducted on a hybrid piston-PDE to evaluate the power-extraction and system-interaction issues. The hybrid engine was constructed using a four-cylinder motorcycle engine, with a spacer block between the valves and pistons. Four detonation tubes--one for each cylinder--were placed perpendicular to the direction of the piston travel. A deflagration-to-detonation transition (DDT) was used to achieve detonations. The piston is in the deflagration region of the DDT. This hybrid engine has a critical starting frequency. Above this frequency the engine will self-actuate and produce excess power. Below this frequency the power produced is less than that required for self-actuation, and the engine decelerates after the starter motor is disengaged. The hybrid piston-PDE constructed for these experiments is capable of producing 20 hp and 50 lbf of thrust simultaneously. The results of this investigation were documented by B. Frankey, F. Schauer (both of AFRL), R. Bradley, and J. Hoke (both of ISSI) in AIAA Paper No.

2002-0474 that was presented at the 40th AIAA Aerospace Science Meeting and Exhibit, 14-17 January 2002, Reno, NV. This paper is included in the Appendix.

5.1.1.9 Effects of Exit Geometry on Performance of PDE

A preliminary analysis of a PDE-driven ejector was performed. The thrust augmentation provided by a constant-area cross-section ejector was computed. A range of partial-tube fill fractions and ejector diameters was simulated in this study. During the initial phase of this effort, important issues associated with the imposed exit boundary conditions were addressed. Final analysis showed a rapid decrease in the PDE-ejector-system performance as the ratio of the ejector to detonation-tube diameter was increased. The thrust augmentation at small ejector diameters was attributed to a compression wave that reflected off the ejector wall and propagated back into the detonation tube. In addition, the sensitivity of the PDE-ejector-system performance to the detonation-tube fill fraction for all diameter ratios studied was observed to be similar to the case of the PDE without an ejector. Good agreement was found between the simulations and available experimental data. The results of this study were documented by D. Allgood, E. Gutmark (both of the University of Cincinnati), and V. Katta (ISSI) in AIAA Paper No. 2002-0613 that was presented at the 40th AIAA Aerospace Science Meeting and Exhibit, 14-17 January 2002, Reno, NV. This paper is included in the Appendix.

5.1.1.10 Valve-Pressure-Drop Analysis of PDE

The pressure drop of a research PDE valve train was investigated experimentally. A General Motors Quad-4 engine, commonly found in the Pontiac Grand-Am, was adapted to make an extremely low cost research PDE. Cycle frequency was controlled with an electric motor that was driving duel overhead cam shafts. The four-cylinder, 16-valve engine was converted to a four-tube PDE by replacing the cylinder block with four lengths of common pipe and using intake-valve pairs to feed premixed fuel and air. Exhaust-valve pairs with clean air flowing backward through them were used to create a purge cycle that cooled the detonator-tube walls and acted as a buffer between the hot detonation products and the incoming subsequent fuel-air charge. Data were obtained on the pressure drop across the intake and exhaust valves. The pressure drop depends on factors including engine frequency, fill fraction, and tube geometry. Increasing the frequency of the engine or the volume of the detonator tube increases the thrust, the amount of required air, and the pressure drop. Although the results obtained were relative to a research engine with non-ideal valves, similar trends are expected for realistic valve configurations. The results of this investigation were documented by M. Slagel (ISSI) and F. Schauer (AFRL) in a paper that was presented at the 27th Annual Dayton-Cincinnati Aerospace Science Symposium, 5 March 2002, Dayton, OH. The visual materials for this presentation are included in the Appendix.

5.1.1.11 Performance Enhancement of PDE Ejector

A preliminary analysis of a PDE-driven ejector was performed. The thrust augmentation provided by a constant-area cross-section ejector was computed. A range of partial tube

fill fractions and ejector diameters was simulated. During the initial phase of this study, important issues associated with the imposed exit-boundary conditions were addressed. The final analysis showed a rapid decrease in the PDE-ejector system performance as the ratio of ejector to detonation-tube diameter was increased. The thrust augmentation at the small ejector diameters was attributed to a compression wave that reflected off the ejector wall and propagated back into the detonation tube. In addition, the sensitivity of the PDE-ejector system performance to the detonation tube fill fraction for all diameter ratios studied was found to be similar to the case of the PDE without an ejector. Good agreement was observed between the simulations and available experimental data. The results of this investigation were documented by D. Allgood, E. Gutmark (both of the University of Cincinnati) and V. Katta (ISSI) in a paper that was presented at the 27th Annual Dayton-Cincinnati Aerospace Science Symposium, 5 March 2002, Dayton, OH.

5.1.1.12 Evaluation of Hybrid-Piston PDE

Experiments were conducted on a hybrid-piston PDE to evaluate the power-extraction and system-interaction issues. The hybrid engine was constructed using a four-cylinder motorcycle engine with a spacer block between the valves and the pistons. Four detonation tubes--one for each cylinder--were placed perpendicular to the direction of the piston travel. A DDT was used to achieve detonations. The piston is in the deflagration region of the DDT. This hybrid engine has a critical starting frequency. Above this frequency the engine will self-actuate and produce excess power. Below this frequency the power produced is less than that required to self-actuate, and the engine decelerates after the starter motor is disengaged. The hybrid-piston PDE constructed for these experiments is capable of producing 20 hp and 50 lbf of thrust simultaneously. The results of this investigation were documented by B. Frankey, F. Schauer (both of AFRL), R. Bradley, and J. Hoke (both of ISSI) in a paper that was presented at the 27th Annual Dayton-Cincinnati Aerospace Science Symposium, 5 March 2002, Dayton, OH. The visual materials for this presentation are included in the Appendix.

5.1.1.13 Experimental Study of DDT Enhancement Techniques in H_2/Air PDE

Experiments were performed on a number of DDT-enhancement techniques for use in a H_2/air PDE. The mechanism, speed, and location of DDT for three configurations were considered, including a Shchelkin spiral, an extended cavity/spiral, and a co-annulus. High-speed digital imaging was used to track flame propagation, and simultaneous time-correlated pressure traces were used to record progress of the shock structure. It was found that DDT is initiated primarily through local explosions that are highly dependent on the particular geometry. In addition to various geometries, the effect of equivalence ratio and spark timing were also investigated for three configurations. The results of this study were documented by T. R. Meyer, J. L. Hoke, M. S. Brown (all of ISSI), J. R. Gord, and F. R. Schauer (both of AFRL) in AIAA Paper No. 2002-3720 that was presented at the 38th AIAA/ASME/SAE/ASEE Joint Propulsion Conference and Exhibit, 7-10 July 2002, Indianapolis, IN. The paper is included in the Appendix.

5.1.1.14 Detonation Studies and Performance Results for Research PDE

A combined computational and experimental investigation of an air-breathing PDE was conducted. Models and hardware developed under the AFRL in-house PDE program were used to examine critical technology issues such as detonation initiation and propagation; valving; timing and control; instrumentation and diagnostics; variation in tube fill, equivalence ratio, and repletion rate; detonation and deflagration-to-detonation transition; and performance prediction and analysis. An innovative, premixed four-detonation-tube engine design was employed for experimental research and evaluation. Specialized instrumentation and measurement techniques were developed to investigate unsteady PDE processes. Research objectives included detonation initiation in air without the use of excess oxygen and performance results for various operating conditions. Data were obtained with hydrogen/air as well as hydrocarbon/air mixtures and compared with theoretical results. An invited presentation [co-authored by F. Schauer, J. Stutrud (both of AFRL), R. Bradley, V. Katta, and J. Hoke (all of ISSI)] documenting the results of this study was made at the International Colloquium on Advances in Confined Detonations, 2-5 July 2002, Moscow, Russia. The presentation is included in the Appendix.

5.1.1.15 Interaction of PDE with Turbine

A PDE blowing down through a turbine was evaluated. In previous experiments a coupled PDE-turbocharger demonstrated shaft-power extraction and self-aspiration (AIAA Paper No. 2002-0615). The present study involves additional instrumentation, configurations, and operating conditions for further study of the detonation-driven turbine. A PDE detonator-tube exhaust drives a centrifugal turbine. A connected centrifugal compressor with regulated outlet pressure and measured inlet flow enables the determination of the achieved operating conditions. The turbine was spun to over 130,000 rpm and was studied at virtually all significant conditions on the turbine operating map, including high compressor flow rates and outlet pressures. In addition, significant back-pressurization of the detonation tube was demonstrated under some operating conditions. Selected operating conditions were compared to theoretical calculations, demonstrating high losses through the expansion throughout the turbine. The turbine survived all testing, despite detonation in the inlet. The turbine significantly attenuated the strength of detonation-driven shocks in the exhaust nozzle. The results of this investigation were documented by F. Schauer (AFRL), R. Bradley, and J. Hoke (both of ISSI) in AIAA Paper No. 2003-0891 that was presented at the 41st AIAA Aerospace Sciences Meeting and Exhibit, which was held 6-9 January 2003 in Reno, NV. The paper is included in the Appendix.

5.1.1.16 Heat Transfer and Thermal Management in PDE

The unsteady nature of the PDE cycle creates a thermal environment that is fundamentally different from steady flow cycles. Gas velocities in a detonation tube range from O(-1) to O(1000) within a single cycle. This broad range of velocities and flow reversal makes it difficult to determine analytically the contribution to the heat load

from the purging, filling, detonating, and blow-down portions of the cycle. The overall heat load on a detonation tube was measured calorimetrically in an aluminum water-cooled detonation tube. The effects of operating parameters such as fill fraction, purge fraction, ignition delay, equivalence ratio, and cycle frequency were examined. Equivalence ratio and cycle frequency were found to have the most significant effect on detonator-tube heat load. The results of this study were documented by J. Hoke, R. Bradley (both of ISSI), and F. Schauer (AFRL) in AIAA Paper No. 2003-0852 that was presented at the 41st AIAA Aerospace Sciences Meeting and Exhibit, which was held 6-9 January 2003 in Reno, NV. The paper is included in the Appendix [number on paper in Appendix is in error (AIAA 2003-6486); correct number is AIAA 2003-0852, as above].

5.1.2 Application of Optical and Numerical Diagnostic Methods to PDE

5.1.2.1 Optical Diagnostics for Characterizing Advanced Combustors and PDEs

Optical diagnostic techniques have been applied with great success to the fundamental study of combustion chemistry and physics in the laboratory; however, the challenges afforded by real-world propulsion systems demand continuing innovation if such techniques are to be adapted and transitioned for use in engineering tests and on-board monitoring and control applications. Efforts continued on transitioning aerodynamic measurement technologies from diagnostics-development laboratories to combustor test-and-evaluation facilities in the AFRL Propulsion Directorate's Combustion Science Branch (Turbine Engine Division). Various optical diagnostic techniques were applied to visualize flowfields and quantify temperatures and key species concentrations in several advanced combustors. A number of next-generation diagnostics are targeted for laboratory-to-facility transition in the near future. The results of this effort were documented by J. R. Gord (AFRL), M. S. Brown, and T. R. Meyer (both of ISSI) in AIAA Paper No. 2002-3039 that was presented at the 22nd AIAA Aerodynamic Measurement Technology and Ground Testing Conference, 24-26 June 2002, St. Louis, Missouri. The paper is included in the Appendix.

5.1.2.2 Emission- and Absorption-Based Sensors for PDE

Emission- and absorption-based sensors for tube fill and equivalence-ratio measurements were successfully demonstrated for the PDE. Simple hardware platforms were used repeatedly without failure. The results of this investigation were documented by M. S. Brown (ISSI) in a paper that was presented at the Turbine Engine Technology Symposium, 9-12 September 2002, Dayton, OH. The visual materials for this presentation are included in the Appendix.

5.1.2.3 Computational and Experimental Studies of PDE

Shadowgraph visualizations of PDE exhaust flowfields were performed using a new nanosecond-duration light source. The shadowgraph system was developed at the University of Cincinnati and tested using the research PDE at AFRL. The complete detonation and blow-down process of the PDE was visualized and reconstructed by

synchronizing the shadowgraph system with separate but repeatable detonation events. No visible smear or distortion of the detonation front and shock waves was observed as a result of the extremely short duration of each light pulse. Preliminary comparisons between the experimental visualizations and computational modeling results also showed good agreement. The structure and development of the exiting detonation was accurately predicted in the modeling. The results of this investigation were documented by D. Allgood, E. Gutmark (both of the University of Cincinnati), T. Meyer, J. Hoke, V. Katta (all of ISSI), F. Schauer, and J. R. Gord (both of AFRL) in AIAA Paper No. 2003-0889, which was presented at the 41st AIAA Aerospace Sciences Meeting and Exhibit, which was held 6-9 January 2003 in Reno, NV. The paper is included in the Appendix.

5.1.2.4 OH-Based Fuel/Air-Ratio Monitor for PDE

The fuel-to-air ratio is an important operating parameter for the PDE. Its value, in part, determines the delivered thrust and can be varied as a means of throttling the engine. In addition, fuel-to-air ratios must be maintained within detonation limits for a given fuel. It is desirable, therefore, to have a robust measure of this quantity for both the research test stand and the eventual field-test aircraft. To this end we collected emission from the A-X electronic transition of the OH as a function of PDE operating conditions for three fuels--hydrogen, propane and aviation gasoline. OH is an intermediate product of all hydrocarbon combustion chemistry and serves as a monitor of the overall combustion process. Our collected OH emission signals correlated well with the amount of delivered hydrogen and with estimated signals based on simulated Chapman-Jouguet detonations. Similar functional dependencies between the OH emission signal and the amount of propane and aviation gasoline used were observed. Future plans include a hardened emission monitor that is suitable for flight tests. The results of this study were documented by M. S. Brown, T. R. Meyer, J. L. Hoke, and J. T. Parker (all of ISSI), J. R. Gord, and F. R. Schauer (both of AFRL) in 1) a paper that was presented at the 28th Annual Dayton-Cincinnati Aerospace Science Symposium, which was held 4 March 2003 in Dayton, OH, and 2) a poster that was presented at the ACS/SAS Poster Session and Patterson College Chemistry Awards, which was held on 6 March 2003 in Dayton, OH. The presentation received the AIAA Best Technical Presentation Award, and the visual materials are included in the Appendix.

5.1.2.5 Fiber-Coupled Laser Sensor for In-Situ Measurement of Hydrocarbon Fuels in PDEs

The fuel-air ratio and intake-charge uniformity are parameters that strongly affect the performance and control of PDEs. A simple laser-based sensor for real-time in-situ measurement of PDE fuel concentrations was developed and applied using line-of-sight absorption at 3.39 μ. The commercial-grade continuous-wave laser source, PDE measurement volume, and dual-wavelength detector were fiber optically coupled, resulting in a robust sensor that is capable of withstanding significant acoustic vibrations during PDE operation. Interference from particulate and droplet scattering was measured using visible laser light at 0.633 μ that is fiber-coupled into the same hardware. This sensor is capable of detecting a number of hydrocarbon fuels and, thus far, has been used

successfully to quantify propane and aviation-gasoline fuel-air ratios under cold-flow and detonating conditions. The effects of locally varying temperature and pressure on signal interpretation and measurement accuracy were considered. Sensor capabilities include characterization of rates of tube fill and purge as well as qualitative measurement of charge uniformity and stratification. The results of this investigation were documented by T. R. Meyer, M. S. Brown, J. L. Hoke, and J. T. Parker (all of ISSI), J. R. Gord, and F. R. Schauer (both of AFRL) in 1) a paper that was presented at the 28th Annual Dayton-Cincinnati Aerospace Science Symposium, which was held 4 March 2003 in Dayton, OH, and 2) a poster that was presented at the ACS/SAS Poster Session and Patterson College Chemistry Awards, which was held on 6 March 2003 in Dayton, OH. The visual materials for the presentation are included in the Appendix.

5.1.2.6 Computational and Experimental Studies of PDEs

Shadowgraph visualizations of PDE exhaust flowfields were performed using a new nanosecond-duration light source. The shadowgraph system was developed at the University of Cincinnati and tested using the research PDE at the Air Force Research Laboratory. The complete detonation and blow-down process of the PDE was visualized and reconstructed by synchronizing the shadowgraph system with separate but repeatable detonation events. No visible smear or distortion of the detonation front and shock waves was observed because of the extremely short duration of each light pulse. Preliminary comparisons between the experimental visualizations and computational modeling results also showed good agreement. The structure and development of the existing detonation wave was accurately predicted in the modeling. The results of this study were documented by D. Allgood, E. Gutmark (both of the University of Cincinnati), T. Meyer, J. Hoke, V. Katta (all of ISSI), F. Schauer, and J. Gord (both of AFRL) in a paper that was presented at the 28th Annual Dayton-Cincinnati Aerospace Science Symposium, which was held 4 March 2003 in Dayton, OH. The visual materials are included in the Appendix.

6. ADVANCED-ENGINE-CONCEPT STUDIES

6.1 General Overview

The purpose of this portion of the program was to identify the critical technology needs of advanced engine concepts (except the PDE). The three areas examined in this task were the general liquid-fueled combustor, the ultra-compact combustor, and the trapped-vortex combustor.

6.1.1 General Liquid-Fueled Combustor

6.1.1.1 Computational and Experimental Study of Aerodynamics and Heat Release in Liquid-Fueled Combustor

This study involved a diverse examination of CFD modeling issues related to the prediction of multi-phase reacting flows as applied to combustion-system research and development. The objectives of this effort included 1) performing validation simulations for the CFD flow solver for two-phase flow dynamics and chemically reacting flows and 2) applying the CFD code in support of an experimental program to develop instrumentation for *in situ* optical measurement of combustion instabilities, with the ultimate goal being to develop active combustion control systems to dampen or eliminate large-amplitude combustion oscillations. The flow solver used in this study is the second-generation solver of the NASA Glenn Research Center (GRC) National Combustion Code (NCC) called FPVortex^{TM}. Flow Parametrics, LLC independently developed this solver.

To achieve the first objective, FPVortex^{TM} was applied to simulate gas-phase and particle dynamics in a swirling co-annular, particle-laden sudden-pipe-expansion flow. Detailed comparisons were made with experimental data for gas-phase and particle mean velocities. Good agreement was observed for mean axial and tangential velocity components of both phases at various downstream measurement locations.

In support of the second objective, a staged approach was taken, beginning with validation studies of the liquid-spray droplet flow, calculations of gaseous-fueled combustion, and simulations of the full liquid-spray droplet-fueled combustion flow. Comparisons of predictions and data were made for gas-phase velocity in the liquid-spray droplet flow and also for axial heat release in the liquid-fueled combustor. The combustion system, developed at the Georgia Tech Combustion Laboratory, was evaluated experimentally using an optical CH*-emissions measurement technique in which the output voltage is proportional to the heat release in a reacting flow. Comparisons were made at two equivalence ratios that are characteristic of stable and unstable modes of combustion. The measured heat-release profile was considered with respect to the CFD results.

Near-term experimental efforts under this collaborative project were aimed at acquiring more detailed gas-phase and liquid-droplet data, including all three components of mean

and RMS velocities for both phases. Additional experimental data acquisition and data reduction for CH* emissions in the combustor are also in progress. Near-term computational efforts on this program involve parametric studies on the sensitivity of results due to variations of inlet-liquid-spray droplet boundary conditions, including the use of stochastic methods for initial velocities and starting locations. Fundamental studies of single liquid-droplet dynamics and evaporation are being conducted using existing experimental data for comparison. The experimental and computational efforts are being coordinated and are directed toward unsteady, multi-phase combustion-dynamics cases that provide data and design guidance for active control of combustion instabilities.

The results of this study were documented in AIAA Paper No. 2001-0976 by A. Brankovic, R. C. Ryder, Jr. (both of Flow Parametrics, LLC), G. J. Sturgess (ISSI), J. Lee, A. Kushari, E. Lubarsky, and B. T. Zinn (all of the Georgia Institute of Technology). The paper was presented at the AIAA 39th AIAA Aerospace Sciences Meeting and Exhibit, which was held 8-11 January 2001 in Reno, NV. The paper is included in the Appendix.

6.1.2 Ultra-Compact Combustor

6.1.2.1 Ultra-Compact Combustors: Main and Inter-Turbine Burner Concepts

Dr. G. J. Sturgess was invited to present a paper entitled, "Ultra Compact Combustor: Main and Inter-Turbine Burner Concepts," at the Intelligent Turbine Engines (MITE) Workshop on Goals and Technologies for Future Gas Turbines, which was held 4-5 December 2000 in Atlanta, GA. The co-authors of this presentation were R. A. Anthenien and W. M. Roquemore (both of AFRL). The visual materials for this presentation are included in the Appendix.

6.1.2.2 Ultra-Compact Combustion Technology Using High Swirl for Enhanced Burning Rate

A gas-turbine engine was proposed that utilizes a near constant-temperature (CT) cycle and an Inter-Turbine Burner (ITB) to provide large amounts of power extraction from the low-pressure turbine. This level of energy is achieved with a modest temperature rise across the ITB. The additional energy can be used to power a large fan for a high-bypass-ratio transport aircraft or to drive a generator for electrical-power extraction. Conventional gas-turbine engines cannot meet such power extraction demands without a loss of engine thrust. A second power source to provide energy for such applications would be necessary, adding considerable cost and weight to the system. Efforts were focused on Ultra-Compact Combustor (UCC) technology to serve as an ITB or main combustor in the CT engine. Reducing the size of the main combustor and ITB is essential to reducing or maintaining overall engine weight and size. Concepts for a UCC were explored experimentally. CFD was used to guide combustor design modifications. The modified combustor hardware was tested in the Atmospheric Pressure Combustor Research Complex (APCRC) at AFRL. Experimental results indicated that the

combustion-system flame-holding zone operated at 99+% combustion efficiency over a wide range of operating conditions. Flame lengths were extremely short, at about 50% that of conventional systems. High heat-release rates were observed while maintaining high combustion efficiencies. Combustor cavity g-loading enhanced reaction rates, thereby increasing the combustion efficiency. The results of this study were documented by J. Zelina, J Ehret, R. D. Hancock, D. T. Shouse, W. M. Roquemore (all of AFRL), and G. J. Sturgess (ISSI) in AIAA Paper No. 2002-3725 that was presented at the 38th AIAA/ASME/SAE/ASEE Joint Propulsion Conference and Exhibit, 7-10 July 2002, Indianapolis, IN. The paper is included in the Appendix.

6.1.3 Trapped-Vortex Combustor

6.1.3.1 Trapped-Vortex-Combustor (TVC) Concept for Gas-Turbine Engines

A TVC concept for low-emissions, high-performance, gas-turbine combustors is being developed and evaluated. This concept was first evaluated in an Air Force Office of Scientific Research program in 1993 and has evolved from a fundamental study to a development/evaluation program involving sector-rig experiments under realistic operating conditions. Its development is motivated, in part, by concerns about NOx emissions generated by gas-turbine engines used for aircraft and stationary power. The TVC offers the potential of a simple, compact, and less-expensive low-emissions combustor. It departs from the traditional swirl-stabilized designs used in gas-turbine engines for the past 40 years. It has two parts--a pilot combustor for stability and a main combustor for power. The pilot utilizes cavities to establish the recirculation zones needed for stable combustion. Each cavity is sized to provide a stable recirculation zone that is referred to as a "trapped vortex." Fuel and air are injected into the cavities in a way that reinforces the vortex that is naturally formed in these cavities.

The following characteristics of a TVC have been demonstrated under realistic conditions: 1) up to a 50% improvement in ignition, blow out, and altitude re-light over current-technology (conventional swirl-stabilized) combustors; 2) NOx-emission reduction ranging from 40% to 60% of the 1996 ICAO standard; and 3) an operating range that is 40% wider than that of conventional combustors, with a combustion efficiency at or above 99%. The results of this effort were presented in AIAA Paper No. 2001-0483, which was co-authored by W. M. Roquemore, D. Shouse (both of AFRL), D. Burrus, A. Johnson, C. Cooper, B. Duncan [all of General Electric Aircraft Engines (GEAE)], K.-Y. Hsu, V. R. Katta, G. J. Sturgess (all of ISSI), and I. Vihinen (GE Industrial Products). The paper was presented at the 39th AIAA Aerospace Sciences Meeting and Exhibit, which was held 8-11 January 2001, in Reno, NV. The paper is included in the Appendix.

6.1.3.2 Optical Diagnostics and Numerical Characterization of TVC

Optical diagnostics were performed in concert with numerical simulations to characterize a new TVC for gas-turbine engines. Variable parameters included the fuel composition, inlet pressure, inlet-pressure drop, inlet temperature, and fuel-injection scheme. A

number of experimental techniques were employed, such as high-speed digital imaging, CSV, PIV, and PLIF of OH. The experimental data compared well with results from a CFDC code and were used to understand the flow pattern and flame location within the combustor. The utility of advanced diagnostics and simulations during the design and testing phase of combustor development was considered. The results of this study were documented by T. R. Meyer, M. S. Brown, S. Fonov, and L. P. Goss (all of ISSI), J. R. Gord, D. T. Shouse, V. M. Belovich, W. M. Roquemore (all of AFRL), C. S. Cooper, E. S. Kim (both of GE Aircraft Engines), and J. M. Haynes (GE Global Research) in AIAA Paper No. 2002-3863 that was presented at the 38th AIAA/ASME/SAE/ASEE Joint Propulsion Conference and Exhibit, 7-10 July 2002, Indianapolis, IN. The paper is included in the Appendix.

7. LIST OF PUBLICATIONS, PRESENTATIONS, AND SIGNIFICANT ACCOMPLISHMENTS

"Effects of C_2-Chemistry on the Structure of Partially Premixed Methane-Air Flames," Z. Shu, V. R. Katta, I. K. Puri, and S. K. Aggarwal, Combust. Sci. Tech. 157, 185 (August 2000).

"Pulse Detonation Engine In-House Research at AFRL," F. Schauer, J. Stutrud, and R. Bradley, Invited presentation at the 13th ONR Propulsion Meeting, 10-12 August 2000, Minneapolis, MN.

"AFRL/PRSC Pulse Detonation Engine Program," F. Schauer, J. Stutrud, R. Bradley, and V. Katta, Invited presentation at the 12th PERC Symposium, Ohio Aerospace Institute, 26-27 October 2000, Cleveland, OH.

"Modeling, CFD, and Kinetics," G. J. Sturgess, Invited presentation at the United Engineering Foundation Conference on Lean Combustion Technology and Its Control, 6-9 November 2000, Santa Fe, NM.

"Ultra Compact Combustors: Main and Inter-Turbine Burner Concepts," G. J. Sturgess, R. A. Anthenien, and W. M. Roquemore, Invited presentation at the Intelligent Turbine Engines (MITE) Workshop on Goals and Technologies for Future Gas Turbines, 4-5 December 2000, Atlanta, GA.

"Detonation Initiation Studies and Performance Results for Pulsed Detonation Engine Applications," F. Schauer, J. Stutrud, and R. Bradley, AIAA Paper No. 2001-1129 presented at the 39th AIAA Aerospace Sciences Meeting and Exhibit, 8-11 January 200l, Reno, NV.

"Trapped Vortex Combustor Concept for Gas Turbine Engines," W. M. Roquemore, D. Shouse, D. Burrus, A. Johnson, C. Cooper, B. Duncan, K.-Y. Hsu, V. R. Katta, G. J. Sturgess, and I. Vihinen, AIAA Paper No. 2001-0483 presented at the 39th AIAA Aerospace Sciences Meeting and Exhibit, 8-11 January 2001, Reno, NV.

"Role of CHF_3 in Extinguishing Diffusion and Premixed Flames," V. R. Katta and W. M. Roquemore, AIAA Paper No. 2001-1075 presented at the 39th AIAA Aerospace Sciences Meeting and Exhibit, 8-11 January 2001, Reno, NV.

"Computational and Experimental Study of Aerodynamics and Heat Release in a Liquid Fueled Combustor," A. Brankovic, R. C. Ryder, Jr., G. J. Sturgess, J. Lee, A. Kushari, E. Lubarsky, and B. T. Zinn, AIAA Paper No. 2001-0976 presented at the 39th AIAA Aerospace Sciences Meeting and Exhibit, 8-11 January 2001, Reno, NV.

"Gaseous Transport Properties Measurements in High Pressure Environment by Transient Grating Spectroscopy," Y. Li, W. L. Roberts, and M. S. Brown, AIAA Paper No. 2001-0849 presented at the 39th AIAA Aerospace Sciences Meeting and Exhibit, 8-11 January 2001, Reno, NV.

"Analysis of Transition Process in a Forced Wall Jet Using High Resolution PIV and 3D DNS," S. P. Gogineni, Invited presentation at NIST, Process Measurements Division, 31 January 2001, Gaithersburg, MD.

"Absorption and the Dimensionless Overlap Integral for Two-Photon Excitation," G. J. Fiechtner and J. R Gord, J. Quant. Spectrosc. Rad. Trans. 68, 543 (1 March 2001).

"Effects of Stoichiometry on Vortex Ignition and Flame Propagation," T. R. Meyer, J. R. Gord, V. R. Katta, W. M. Roquemore, G. L. Switzer, and G. J. Fiechtner, Presented at the 2001 Poster Session of the Dayton Section of the American Chemical Society and the Ohio Valley Section of the Society for Applied Spectroscopy, 22 March 2001, Dayton, OH.

"Combustion in Impulsively Initiated Vortex Rings," T. R. Meyer, J. R. Gord, V. R. Katta, W. M. Roquemore, G. L. Switzer, and G. J. Fiechtner, Presented at the 2nd Joint Meeting of the U. S. Sections of the Combustion Institute, 25-28 March 2001, Oakland, CA; also presented as a poster.

"Behavior of a Jet Diffusion Flame in a Multi-Vortex Flow Field," V. R. Katta and W. M. Roquemore, Presented at the 2nd Joint Meeting of the U. S. Sections of the Combustion Institute, 25-28 March 2001, Oakland, CA.

"Evaluation of a Self-Aspirated Pulse Detonation Engine," J. L. Hoke J. S. Stutrud, R. P. Bradley, and F. R Schauer, Presented at the Twenty-Sixth Annual Dayton-Cincinnati Aerospace Science Symposium, 30 March 2001, Dayton, OH.

"Transonic-Flow Control," J. Estevadeordal, W. W. Copenhaver, W. Ng, and C. Carter, Poster presented at the Twenty-Sixth Annual Dayton-Cincinnati Aerospace Science Symposium, 30 March 2001, Dayton, OH.

"A PIV Study of a Flow Control System in a High Turning Stator Cascade," J. Estevadeordal, W. W. Copenhaver, W. Ng, and C. Carter, Presented at the Twenty-Sixth Annual Dayton-Cincinnati Aerospace Science Symposium, 30 March 2001, Dayton, OH. Received Award for Best Paper in Turbomachinery Session.

"Studies of Ignition and Vortex-Flame Interaction in a Starting Jet," T. R. Meyer, J. R. Gord, V. R. Katta, W. M. Roquemore, G. L. Switzer, and G. J. Fiechtner, Presented at the Twenty-Sixth Annual Dayton-Cincinnati Aerospace Science Symposium, 30 March 2001, Dayton, OH.

"Evaluation on a Hybrid Piston-Pulse Detonation Engine," B. M. Frankey, J. L. Hoke, J. S. Stutrud, R. P. Bradley, and F. R. Schauer, Presented at the Twenty-Sixth Annual Dayton-Cincinnati Aerospace Science Symposium, 30 March 2001, Dayton, OH.

"An Introduction to a Pulsed Detonation Engine," M. Slagel, F. Schauer, J. Stutrud, and R. Bradley, Presented at the Twenty-Sixth Annual Dayton-Cincinnati Aerospace Science Symposium, 30 March 2001, Dayton, OH.

"Detonation Wave Propagation through Tube Array," A. J. Rolling, P. King, F. Schauer, J. Hoke, R. Bradley, M. Slagel, V. Katta, and J. Stutrud, Presented at the Twenty-Sixth Annual Dayton-Cincinnati Aerospace Science Symposium, 30 March 2001, Dayton, OH.

"Terahertz Radiation Measurements in Combustion Environments," M. S. Brown**,** J. V. Rudd, D. Zimdars, M. Warmuth, and J. R. Gord, Presented at the Twenty-Sixth Annual Dayton-Cincinnati Aerospace Science Symposium, 30 March 2001, Dayton, OH. Received Award for Best Paper in Instrumentation I Session.

"Experimental Results for a Novel, High Swirl, Ultra-Compact Combustor for Gas Turbine Engines," R. A. Anthenien, R. A. Mantz, W. M. Roquemore, and G. Sturgess, Presented at the Meeting of the Western States Section of the Combustion Institute, April 2001, Berkeley, CA.

"DPIV Study of Wake-Rotor Synchronization in a Transonic Compressor," J. Estevadeordal, S. Gogineni, L. Goss, W. Copenhaver, and S. Gorrell, AIAA Paper No. 2001-3095 presented at the 31st AIAA Fluid Dynamics Conference and Exhibit, 11-14 June 2001, Anaheim, CA.

"Investigation of Complex Fluid Flows Using PIV, Holography, and DNS," S. Gogineni, Invited presentation at Rutgers University, 28 June 2001, New Brunswick, NJ.

"Visualization and Two-Color DPIV Measurements of Flows in Circular and Square Coaxial Nozzles," D. Nikitopoulos, J. Bitting, S. Gogineni, and E. Gutmark, Exp. Fluids 31(1), 1 (July 2001).

"Flame Propagation and Morphology in Premixed Vortex Rings," T. R. Meyer, J. R. Gord, V. R. Katta, G. J. Fiechtner, G. L. Switzer, and W. M. Roquemore, Invited presentation at the 11th Gordon Research Conference on Laser Diagnostics in Combustion, 1-6 July 2001, South Hadley, MA.

"Terahertz Studies of Gas and Condensed Phases for Combustion Application," M. S. Brown, D. Zimdars, and J. R. Gord, Invited presentation at the Gordon Research Conference on Laser Diagnostics in Combustion, 1-6 July 2001, South Hadley, MA.

"Detonation Initiation and Performance in Complex Hydrocarbon Fueled Pulsed Detonation Engines," F. Schauer J. Stutrud, R. Bradley, V. Katta, and J. Hoke, Presented at the 50th JANNAF Propulsion Meeting, 11-13 July 2001, Salt Lake City, UT.

"Recent Applications of T-Ray Technology to Studies of Combustion and Fuel," M. S. Brown, J. V. Rudd, D. Zimdars, M. Warmuth, and J. R. Gord, Presented at the Luminescence Symposium, 43rd Rocky Mountain Conference on Analytical Chemistry, 29 July - 2 August 200l, Denver, CO.

"In-House Pulse Detonation Engine Research at AFRL Wright-Patterson AFB," F. Schauer, J. Stutrud, R. Bradley, V. Katta, and J. Hoke," Invited presentation at the 14th ONR Propulsion Meeting, 10 August 2001, Chicago, IL.

"In-House Pulse Detonation Engine Research at Wright-Patterson AFB," F. Schauer, J. Stutrud, R. Bradley, V. Katta, and J. Hoke, Invited presentation at the European Office of Aerospace Research and Development and EADS-Aerospatiale Matra Missiles Workshop on Pulse Detonation Engines, 28-29 August 2001, Bourges, France.

"AFRL Pulse Detonation Engine Research Applications," J. Hoke R. Bradley, and F. Schauer, Invited presentation at the European Office of Aerospace Research and Development and EADS-Aerospatiale Matra Missiles Workshop on Pulse Detonation Engines, 28-29 August 2001, Bourges, France.

"Combustion Diagnostics," S. Gogineni and J. Gord, Invited lecture at the International Workshop on Modern Advances in Combustion, Indian Institute of Technology, 31 August - 1 September 2001, Madras, India.

"Investigation of Wake-Shock Interactions in a Transonic Compressor Using DPIV," S. Gogineni, J. Estevadeordal, W. Copenhaver, and S. Gorrell, Presented at the 15th International Symposium on Air Breathing Engines (ISOABE), 2-7 September 2001, Bangalore, India; published as ISOABE Paper No. 2001-1196.

"Simultaneous PLIF/PIV Investigation of Vortex-Flame Interactions," T. R. Meyer, G. J. Fiechtner, C. D. Carter, J. R. Gord, and S. P. Gogineni, PIV'01 Paper 1055, Presented at the 4th International Symposium on Particle Image Velocimetry, 17-19 September 2001, Gottingen, Germany. Dr. Gogineni was Chairman of the Session on Complex Engineering Flow Fields.

"Effects of Ignition on Premixed Vortex Rings: A Simultaneous PLIF/PIV Investigation," T. R. Meyer, J. R. Gord, V. R. Katta, and S. P. Gogineni, Presented at the 54th Annual Meeting of the American Physical Society, Division of Fluid Dynamics, 18-20 November 2001, San Diego, CA.

"Study of a Flow Control System in a High Turning Stator Cascade Using DPIV," J. Estevadeordal, W. Copenhaver, C. Carter, Presented at the 54th Annual Meeting of the American Physical Society, Division of Fluid Dynamics, 18-20 November 2001, San Diego, CA.

"On Curved Hydrogen Diffusion Flames Formed behind a Bluff Body," V. R. Katta and W. M. Roquemore, Presented at the Fall Technical Meeting of the Eastern States Section of the Combustion Institute, Chemical and Physical Processes in Combustion, 3-5 December 2001, Hilton Head, SC; published in the Conference Proceedings.

"Numerical and Experimental Study of Heat Transfer through Ceramics Disk under Combusting-Flow Environment," V. R. Katta, T. R. Meyer, T. A. Parthasarathy, J. Knoop, J. R. Gord, W. M. Roquemore, and R. J. Kerens, Presented at the ACS 26th Annual International Conference on Advanced Ceramics and Composites, 13-18 January 2002, Cocoa Beach, FL.

"Laser-Induced Incandescence Measurements in the Reaction Zone of a Model Gas Turbine Combustor," M. S. Brown, T. R. Meyer, J. R. Gord, V. Belovich, and W. Roquemore, AIAA Paper No. 2002-0393 presented at the 40th AIAA Aerospace Sciences Meeting and Exhibit, 14-17 January 2002, Reno, NV.

"Effects of Exit Geometry on the Performance of a Pulse Detonation Engine," D. Allgood, E. Gutmark, and V. R. Katta, AIAA Paper No. 2002-0613 presented at the 40th AIAA Aerospace Sciences Meeting and Exhibit, 14-17 January 2002, Reno, NV.

"Integration of Pulsed Detonation Engine with an Ejector Pump and with a Turbo-Charger as Methods to Self-Aspirate," J. Hoke, R. Bradley, J. Stutrud, and F. Schauer, AIAA Paper No. 2002-0615 presented at the 40th AIAA Aerospace Sciences Meeting and Exhibit, 14-17 January 2002, Reno, NV.

"Study of Multi-Vortex/Flame Interactions in an Opposing Jet Diffusion Flame," V. R. Katta, M. S. Brown, T. R. Meyer, J. R. Gord, and W. M. Roquemore, AIAA Paper No. 2002-0479 presented at the 40th AIAA Aerospace Sciences Meeting and Exhibit, 14-17 January 2002, Reno, NV.

"Evaluation of a Hybrid-Piston Pulsed Detonation Engine," B. Frankey, F. Schauer, R. Bradley, and J. Hoke, AIAA Paper No. 2002-0474 presented at the 40th AIAA Aerospace Sciences Meeting and Exhibit, 14-17 January 2002, Reno, NV.

"Studies of Vortex-Induced Flame Extinction in Counterflow Diffusion Flames Using CH PLIF and PIV," A. Lemaire, T. Meyer, K. Zahringer, J. Gord, and J. C. Rolon, Presented at the 8th Topical Meeting on Laser Applications to Chemical and Environmental Analysis (Optical Society of America), 7-10 February 2002, Boulder, CO, and published in Laser Applications to Chemical and Environmental Analysis. Also presented as a poster.

"Micro to Nano - Small Research for Fuels and Combustion," C. E. Bunker, J. R. Gord, T. R. Meyer, M. S. Brown, V. R. Katta, D. A. Zweifel, B. A. Harruff, and Y-P Sun, Presented at the TMS Annual Meeting, Symposium on Surface Engineering: Science and Technology II, 17-22 February 2002, Seattle, WA. Published in Surface Engineering: Science and Technology of Interfaces II (A. Kumar. Y-W. Chung, J. J. Moore, G. L. Doll, K. Yasui, and D. S. Misra, Eds.) (The Minerals, Metals, and Materials Society, Warrendale, PA, 2000), pp. 25-34.

"Study of Wake-Blade Interactions in a Transonic Compressor Using Flow Visualization and DPIV," J. Estevadeordal, S. Gogineni, L. Goss, W. Copenhaver, and S. Gorrell, J. Fluids Eng. 124, 1 (March 2002).

"Combustion Air Jet Influence on Primary Zone Characteristics for Gas Turbine Combustors," S. Gogineni, D. Shouse, C. Frayne, J. Stutrud, and G. Sturgess, J. Propul. Power 18(2), 407 (March-April 2002).

"Laser-Induced Incandescence (LII) for Soot Studies in a Model Combustor," M. S. Brown, T. R. Meyer, J. R. Gord, and V. Belovich, Poster presented at the American Chemical Society/Society for Applied Spectroscopy Annual Poster Session and Patterson College Chemistry Awards Night, 5 March 2002, Dayton, OH.

"Expanding the Combustion and Laser Diagnostics Research Complex (CLDRC)," J. R. Gord, R. D. Hancock, W. M. Roquemore, M. S. Brown, T. R. Meyer, S. P. Gogineni, and S. Roy, Poster presented at the American Chemical Society/Society for Applied Spectroscopy Annual Poster Session and Patterson College Chemistry Awards Night, 5 March 2002, Dayton, OH.

"Laser-Based Measurements in Wrinkled Two-Phase Counterflow Diffusion Flames," S. Roy, M. S. Brown, V. N. Velur, R. P. Lucht, and J. R. Gord, Poster presented at the American Chemical Society/Society for Applied Spectroscopy Annual Poster Session and Patterson College Chemistry Awards Night, 5 March 2002, Dayton, OH.

"Vortex-Flame Interactions in Impulsively Initiated Premixed Jets," S. P. Gogineni, T. R. Meyer, V. R. Katta,, and J. R. Gord, Poster presented at the American Chemical Society/Society for Applied Spectroscopy Annual Poster Session and Patterson College Chemistry Awards Night, 5 March 2002, Dayton, OH.

"High-Speed Digital Imaging for Characterizing Advanced Combustors," T. R. Meyer, M. S. Brown, J. L. Hoke, S. Fonov, F. R. Schauer, and J. R. Gord, Poster presented at the American Chemical Society/Society for Applied Spectroscopy Annual Poster Session and Patterson College Chemistry Awards Night, 5 March 2002, Dayton, OH.

"Real-Time Combustor Diagnostics Using High-Speed Digital Imaging," T. R. Meyer, M. S. Brown, J. L. Hoke, S. Fonov, F. R. Schauer, and J. R. Gord, Presented at the Twenty-Seventh Annual Dayton-Cincinnati Aerospace Science Symposium, 5 March 2002, Dayton, OH.

"A Valve Pressure Drop Analysis of the Quad-4 Pulsed Detonation Engine at Wright-Patterson AFB," M. Slagel and F. R. Schauer, Presented at the Twenty-Seventh Annual Dayton-Cincinnati Aerospace Science Symposium, 5 March 2002, Dayton, OH.

"New Facilities in the Combustion and Laser Diagnostics Research Complex," J. R. Gord, R. D. Hancock, W. M. Roquemore, M. S. Brown, T. R. Meyer, S. P. Gogineni, and S. Roy, Presented at the Twenty-Seventh Annual Dayton-Cincinnati Aerospace Science Symposium, 5 March 2002, Dayton, OH.

"Experimental and Numerical Investigation of Vortex-Flame Interactions in Impulsively Initiated Premixed and Non-premixed Jets," S. P. Gogineni, T. R. Meyer, V. R. Katta, and J. R. Gord, Presented at the Twenty-Seventh Annual Dayton-Cincinnati Aerospace Science Symposium, 5 March 2002, Dayton, OH.

"Single-Shot LII Measurements in the Reaction Zone of a Model Combustor," M. S. Brown, T. R. Meyer, J. R. Gord, and V. M. Belovich, Presented at the Twenty-Seventh Annual Dayton-Cincinnati Aerospace Science Symposium, 5 March 2002, Dayton, OH.

"Investigation of Micro and Nano Materials for Fuels and Combustion Research," C. E. Bunker, J. R. Gord, T. R. Meyer, M. S. Brown, V. R. Katta, D. A. Zweifel. B. A. Harruff, and Y-P Sun, Presented at the Twenty-Seventh Annual Dayton-Cincinnati Aerospace Science Symposium, 5 March 2002, Dayton, OH.

"Performance Enhancement of a Pulse Detonation Engine Ejector," D. Allgood, E. Gutmark, and V. R. Katta, Presented at the Twenty-Seventh Annual Dayton-Cincinnati Aerospace Science Symposium, 5 March 2002, Dayton, OH

"Evaluation of a Hybrid-Piston Pulsed Detonation Engine," B. Frankey, F. Schauer, R. Bradley, and J. Hoke, Presented at the Twenty-Seventh Annual Dayton-Cincinnati Aerospace Science Symposium, 5 March 2002, Dayton, OH.

"Basic Research Studies in Compressor Flow Control," W. Copenhaver, D. Car, P. Koch, J. Estevadeordal, S. Guillot, and W. Ng, Presented at the Twenty-Seventh Annual Dayton-Cincinnati Aerospace Science Symposium, 5 March 2002, Dayton, OH.

"Crash and Burn," V. R. Katta, T. R. Meyer, J. R. Gord, and W. M. Roquemore, Poster presented at the Twenty-Seventh Annual Dayton-Cincinnati Aerospace Science Symposium, 5 March 2002, Dayton, OH. Poster received Art-in-the-Science Award (Third-Place).

"Ignition and Flame Propagation in an Impulsively Started Fuel Jet," V. R. Katta, T. R. Meyer, J. R. Gord, and W. M. Roquemore, Presented at the 9th International Conference on Numerical Combustion, 7-10 April 2002, Sorrento, Italy; published in Conference Proceedings.

"Improvement of a Counter-Swirl Stator Section with Ejector Pump Based Boundary Layer Control," W. W. Copenhaver, W. Ng, J. Estevadeordal, and C. Carter, Presented at the ASME Turbo Expo 2002, 3-6 June 2002, Amsterdam, The Netherlands.

"Application of Optical Diagnostics for Combustion and Fluid Flows," S. P. Gogineni, J. R. Gord, and B. V. Kiel, Invited Seminar, Delft Institute of Technology, 4 June 2002, The Netherlands.

"Flow-Control of a Transonic, High-Turning-Stator Cascade," W. W. Copenhaver, J. Estevadeordal, P. Koch, D. Car, W. Ng, S. Guillot, and C. Carter, Poster presented at the 1st AIAA Flow Control Conference, 24-26 June 2002, St. Louis, MO.

"Counter-Flow Blowing for Counterswirl Designs/Vectoring," W. Copenhaver, D. Car, J. Estevadeordal, and S. Guillot, Presented at the 1st AIAA Flow Control Conference, 24-26 June 2002, St. Louis, MO.

"Optical Diagnostics for Characterizing Advanced Combustors and Pulsed-Detonation Engines," J. R. Gord, M. S. Brown, and T. R. Meyer, AIAA Paper No. 2002-3039 presented at the 22nd AIAA Aerodynamic Measurement Technology and Ground Testing Conference, 24-26 June 2002, St. Louis, MO.

"Detonation Studies and Performance Results for a Research Pulse Detonation Engine," F. Schauer, J. Stutrud, R. Bradley, V. Katta, and J. Hoke, Invited Paper at the International Colloquium on Advances in Confined Detonations, 2-5 July 2002, Moscow, Russia; published in the Conference Proceedings.

"Ultra-Compact Combustion Technology Using High Swirl for Enhanced Burning Rate," J. Zelina, J. Ehret, R. D. Hancock, D. T. Shouse, W. M. Roquemore, and G. J. Sturgess, AIAA Paper No. 2002-3725 presented at the 38th AIAA/ASME/SAE/ASEE Joint Propulsion Conference and Exhibit, 7-10 July 2002, Indianapolis, IN.

"Optical Diagnostics and Numerical Characterization of a Trapped-Vortex Combustor," T. R. Meyer, M. S. Brown, S. Fonov, L. P. Goss, J. R. Gord, D. T. Shouse, V. M. Belovich, W. M. Roquemore, C. S. Cooper, E. S. Kim, and J. M. Haynes, AIAA Paper No. 2002-3863 presented at the 38th AIAA/ASME/SAE/ASEE Joint Propulsion Conference and Exhibit, 7-10 July 2002, Indianapolis, IN.

"Experimental Study of Deflagration-to-Detonation Enhancement Techniques in a H_2/Air Pulsed-Detonation Engine," T. R. Meyer, J. L. Hoke, M. S. Brown, J. R. Gord, and F. R. Schauer, AIAA Paper No. 2002-3720 presented at the 38th AIAA/ASME/SAE/ASEE Joint Propulsion Conference and Exhibit, 7-10 July 2002, Indianapolis, IN.

"Chemiluminescence as a Measurement of Local Equivalence Ratio," M. S. Brown, T. R. Meyer, G. J. Sturgess, J. Zelina, and J. R. Gord, AIAA Paper No. 2002-3865 presented at the 38th AIAA/ASME/SAE/ASEE Joint Propulsion Conference and Exhibit, 7-10 July 2002, Indianapolis, IN.

“Effects of Ignition Delay on Impulsively Initiated Premixed Jets,” T. R. Meyer, S. P. Gogineni, V. R. Katta, and J. R. Gord, Presented at the 11th International Symposium on Applications of Laser Techniques to Fluid Mechanics, 8-11 July 2002, Lisbon, Portugal; individual papers on CD.

"PIV/PLIF Investigation of Two-Phase Vortex-Flame Interactions,” A. Lemaire, T. R. Meyer, J. R. Gord, and J. C. Rolon, Presented at the 11th International Symposium on Applications of Laser Techniques to Fluid Mechanics, 8-11 July 2002, Lisbon, Portugal; individual papers on CD.

“Macro- and Milli-DPIV Studies of a Boundary-Layer-Based Flow-Control System for a Transonic Cascade,” J. Estevadeordal, W. W. Copenhaver, D. Car, P. Koch, W. Ng, S. Guillot, and C. Carter, Presented at the 11th International Symposium on Applications of Laser Techniques to Fluid Mechanics, 8-11 July 2002, Lisbon, Portugal; individual papers on CD.

“DPIV Study of a Boundary-Layer-Based Flow-Control System for a High-Turning Stator Cascade” W. W. Copenhaver, W. Ng, J. Estevadeordal, and C. Carter, Presented at the 11th International Symposium on Applications of Laser Techniques to Fluid Mechanics, 8-11 July 2002, Lisbon, Portugal; individual papers on CD.

“Effects of Unsteady Strain Rate on OH and CH LIF in Counterflow Diffusion Flames,” T. R. Meyer, V. R. Katta, J. R. Gord, A. Lemaire, K. Zähringer, and J. C. Rolon, Presented at the 44th Rocky Mountain Conference on Applied Spectroscopy, 28 July - 1 August 2002, Denver, CO.

“Qualitative Studies of Unsteady Combustion Processes Through High-Speed Imaging of Flame Luminosity,” J. Miller, J. R. Gord, and T. R. Meyer, Presented at the 44th Rocky Mountain Conference on Applied Spectroscopy, 28 July - 1 August 2002, Denver, CO.

“Laser-Induced Incandescence (LII) for Soot Measurements in Combusting Flows,” J. R. Gord, M. S. Brown, and T. R. Meyer, Presented at the 44th Rocky Mountain Conference on Applied Spectroscopy, 28 July - 1 August 2002, Denver, CO.

“Simultaneous PLIF/PIV Investigation of Vortex-Induced Annular Extinction in H_2-Air Conterflow Diffusion Flames,” T. R. Meyer, G. J. Fiechtner, S. P. Gogineni, J. C. Rolon, C. D. Carter, and J. R. Gord, Submitted in September 2002 for publication in Experiments in Fluids.

“Emission and Absorption Based Sensors for the Pulsed Detonation Engine,” M. S. Brown, Presented at the Turbine Engine Technology Symposium, 9-12 September 2002, Dayton, OH.

"Evaluation of Electrochemical Release of Self-Assembled Reagents as a Component of a Proconcentrator for Flow-Injection Analysis," L. Cheng, J. Seneviratne, G. E. Pacey, J. R. Gord, M. S. Brown, T. R. Meyer, and J. A. Cox, Electroanal. 14, 1339 (November 2002).

"The Effect of the Dynamic Filling Process on PDE Performance and Nozzle Selection," J. Hoke, R. Bradley, and F. Schauer, Presented at the 51st JANNAF Propulsion Meeting, 18-21 November 2002, Lake Buena Vista, FL.

"Development of Optical Diagnostics for Combusting Flows," J. R. Gord, T. R. Meyer, M. S. Brown, S. Roy, and S. P. Gogineni, Presented at the 55th Annual Meeting of the American Physical Society, Division of Fluid Dynamics, 24-26 November 2002, Dallas, TX; abstract published in Bull. Am. Phys. Soc. 47(10), 109 (2002).

"Milli-DPIV Studies of a Boundary-Layer Based Flow Control System for a Transonic Cascade," J. Estevadeordal and W. Copenhaver, Presented at the 55th Annual Meeting of the American Physical Society, Division of Fluid Dynamics, 24-26 November 2002, Dallas, TX; abstract published in Bull. Am. Phys. Soc. 47(10), 174 (2002).

"Highly Luminescent CdS Nanoparticles: Effect of Particle Size and Preparation Method on the Photoenhancement Process," C. E. Bunker, B. A. Harruff, P. Pathak, Y. Lin, J. Widera, J. R. Gord, and Y.-P Sun, Presented at the Inter-American Photochemical Society Meeting, 3 January 2003, Clearwater Beach, FL.

"Interaction of a Pulsed Detonation Engine with a Turbine," F. Schauer, R. Bradley, and J. Hoke, AIAA Paper No. 2003-0891 presented at the 41st AIAA Aerospace Sciences Meeting and Exhibit, 6-9 January 2003, Reno, NV.

"Effect of Gravity on Burner-Stabilized and Lifted Partially Premixed Flames," X. Qin, I. K. Puri, S. K. Aggarwal, and V. R. Katta, AIAA Paper No. 2003-1018 presented at the 41st AIAA Aerospace Sciences Meeting and Exhibit, 6-9 January 2003, Reno, NV.

"PAH Formation in an Inverse Diffusion Flame," V. Katta. L. G. Blevins, and W. M. Roquemore, AIAA Paper No. 2003-0666 presented at the 41st AIAA Aerospace Sciences Meeting and Exhibit, 6-9 January 2003, Reno, NV.

"Particulate Matter and Polycyclic Aromatic Hydrocarbon Determination Using a Well-Stirred Reactor," R. F. Reich, S. D. Stouffer, V. R. Katta, H. T. Mayfield, C. W. Frayne, and J. Zelina, AIAA Paper No. 2003-0664 presented at the 41st AIAA Aerospace Sciences Meeting and Exhibit, 6-9 January 2003, Reno, NV.

"Computational and Experimental Studies on the Performance of Pulse Detonation Engines," D. Allgood, E. Gutmark, T. Meyer, J. Hoke, V. Katta, F. Schauer, and J. R. Gord, AIAA Paper No. 2003-0889 presented at the 41st AIAA Aerospace Sciences Meeting and Exhibit, 6-9 January 2003, Reno, NV.

"Heat Transfer and Thermal Management in a Pulsed Detonation Engine," J. Hoke, R. Bradley, and F. Schauer, AIAA Paper No. 2003-0852 presented at the 41st AIAA Aerospace Sciences Meeting and Exhibit, 6-9 January 2003, Reno, NV.

"Experimental Investigation of Vortex Shedding of a Jet in Crossflow," B. Kiel, C. Murawski, M. Flanagan, A. Cox, and S. Gogineni, AIAA Paper No. 2003-0182 presented at the 41st AIAA Aerospace Sciences Meeting and Exhibit, 6-9 January 2003, Reno, NV.

"Comparisons of Initially Turbulent, Low-Velocity-Ratio Circular and Square Coaxial Jets," D. E. Nikitopoulos, J. W. Bitting, and S. Gogineni, AIAA J. 41(2), 230 (February 2003).

"Insights into Non-adiabatic-Equilibrium Flame Temperatures during Millimeter-Size Vortex/Flame Interactions," V. R. Katta, T. R. Meyer, J. R. Gord, and W. M. Roquemore, Combust. Flame 132, 639 (March 2003).

"Dual-Pump Dual-Broadband Coherent Anti-Stokes Raman Scattering for the Measurement of Temperature and Multiple Species Concentrations," S. Roy, T. R. Meyer, M. S. Brown, R. P. Lucht, J. R. Gord, V. M. Belovich, and E. Corporan, Presented at the 28th Annual Dayton-Cincinnati Aerospace Science Symposium, 4 March 2003, Dayton, OH. Received AIAA Best Technical Presentation Award.

"Multi-Component LDV Measurements Downstream of a Gas Turbine Engine Nozzle/Air Swirler," J. D. Miller, T. R. Meyer, M. S. Brown, A. Lynch, J. R. Gord, J. Zelina, D. T. Shouse, V. M. Belovich, and R. D. Hancock, Presented at the 28th Annual Dayton-Cincinnati Aerospace Science Symposium, 4 March 2003, Dayton, OH.

"Experimental Investigation of Vortex Shedding of a Jet in Cross Flow," B. Kiel, C. Murawski, M. Flanagan, A Cox, and S. Gogineni, Presented at the 28th Annual Dayton-Cincinnati Aerospace Science Symposium, 4 March 2003, Dayton, OH.

"Progress and Recent Advances in Particle Image Velocimetry," S. P. Gogineni, J. Estevadeordal, and J. R. Gord, Presented at the 28th Annual Dayton-Cincinnati Aerospace Science Symposium, 4 March 2003, Dayton, OH.

"Experimental and Computational Studies of Pulse Detonation Engines," D. Allgood, E. Gutmark, T. Meyer, J. Hoke, V. Katta, F. Schauer, and J. Gord, Presented at the 28th Annual Dayton-Cincinnati Aerospace Science Symposium, 4 March 2003, Dayton, OH.

"OH-Based Fuel/Air Ratio Monitor for the Pulsed-Detonation Engine," M. S. Brown, T. R. Meyer, J. L. Hoke, J. T. Parker, and J. R. Gord, Presented at the 28th Annual Dayton-Cincinnati Aerospace Science Symposium, 4 March 2003, Dayton, OH. Received AIAA Best Technical Presentation Award.

“Fiber-Coupled Laser Sensor for In-situ Measurement of Hydrocarbon Fuels in Pulsed-Detonation Engines,” T. R. Meyer, M. S. Brown, J. L. Hoke, and J. T. Parker, Presented at the 28th Annual Dayton-Cincinnati Aerospace Science Symposium, 4 March 2003, Dayton, OH.

“Highly Luminescent CdS Nanoparticles Applied Toward the Development of Chemical Sensors,” J. Widera, J. J. Karnes, J. R. Gord, and C. E. Bunker, Presented at the 28th Annual Dayton-Cincinnati Aerospace Science Symposium, 4 March 2003, Dayton, OH.

"Milli-DPIV Approaches for Studying Boundary-Layer Based Flow Control Systems," J. Estevadeordal, W. Copenhaver, and D. Car, Presented at the 28th Annual Dayton-Cincinnati Aerospace Science Symposium, 4 March 2003, Dayton, OH.

“OH*-Based Equivalence Ratio Monitor,” M. S. Brown, T. R. Meyer, J. L. Hoke, J. T. Parker, J. R. Gord, and F. R. Schauer, Poster presented at the ACS-SAS Poster Session and Patterson College Chemistry Awards, 6 March 2003, Dayton, OH.

“Quantifying Hydrocarbon Fuels in Pulsed-Detonation Engines through Laser-Based Absorption Measurements,” T. R. Meyer, M. S. Brown, J L. Hoke, J. T. Parker, J. R. Gord, and F. R Schauer, Poster presented at the ACS-SAS Poster Session and Patterson College Chemistry Awards, 6 March 2003, Dayton, OH.

“Temperature Effects on the Fluorescence Lifetimes of CdS Nanoparticles,” J. R. Gord, J. Widera, J. R. Gord, and C. E. Bunker, Poster presented at the ACS-SAS Poster Session and Patterson College Chemistry Awards, 6 March 2003, Dayton, OH.

“Photophysical Properties of Highly Luminescent CdS Nanoparticles,” J. Widera, J. J. Karnes, J. R. Gord, and C. E. Bunker, Poster presented at the ACS-SAS Poster Session and Patterson College Chemistry Awards, 6 March 2003, Dayton, OH.

“Multi-Pump CARS Techniques for Measuring Temperature and Species Concentrations in Combusting Flows,” S. Roy, T. R. Meyer, M. S. Brown, R. P. Lucht, J. R. Gord, V. M. Belovich, and E. Corporan, Poster presented at the ACS-SAS Poster Session and Patterson College Chemistry Awards, 6 March 2003, Dayton, OH.

“Applying Chemometrics to the Prediction of Aviation-Fuel Properties,” J. J. Karnes, G. Bota, P. de B. Harrington, and C. E. Bunker, Poster presented at the ACS-SAS Poster Session and Patterson College Chemistry Awards, 6 March 2003, Dayton, OH.

“Highly Luminescent CdS Nanoparticles Applied toward the Development of Chemical Sensors,” J. Widera, J. J. Karnes, J. R. Gord, and C. E. bunker, Poster presented at the ACS-SAS Poster Session and Patterson College Chemistry Awards, 6 March 2003, Dayton, OH.

"Triple Flame Propagation and Stabilization in a Laminar Axisymmetric Jet," X. Qin, I. K. Puri S. K. Aggarwal, and V. R. Katta, Presented at the 3rd Joint Meeting of the U. S. Sections of the Combustion Institute, 16-19 March 2003, Chicago, IL.

"Investigation of PAH Formation in Different Flames Using UNICORN," V. R. Katta and W. M. Roquemore, Presented at the 3rd Joint Meeting of the U. S. Sections of the Combustion Institute, 16-19 March 2003, Chicago, IL.

"Kinetic Behavior of Long-Period Grating (LPG) Fiber-Optic Sensors," S. W. Buckner, J. Widera, J. R. Gord, C. E. Bunker, G. E. Pacey, and V. R. Katta, Presented at the 225th ACS National Meeting, 23-27 March 2003, New Orleans, LA.

"Extinction Criterion for Unsteady Opposing-Jet Diffusion Flames," V. R. Katta, T. R. Meyer, M. S. Brown, J. R. Gord, and W. M. Roquemore, Submitted in April 2003 for publication in Combustion and Flame.

"Emission, Thermocouple, and Electrical Measurements in $SF_6/Ar/O_2$ SiC Etching Discharges," M. S. Brown, J. D. Scofield, and B. N. Ganguly, Accepted in April 2003 for publication in the Journal of Applied Physics.

"Dual-Pump Coherent Anti-Stokes Raman Scattering Temperature and CO_2 Concentration Measurements," R. P Lucht, V. N. Velur, C. D. Carter, K. D. Grinstead, J. R. Gord, P. M. Danehy, G. J. Fiechtner, and R. L. Farrow, AIAA J. 41, 679 (April 2003).

"Vortex-Induced Flame Extinction in Two-Phase Counterflow Diffusion Flames with CH Planar Laser-Induced Fluorescence and Particle-Image Velocimetry," A. Lemaire, T. R. Meyer, K. Zahringer, J. C. Rolon, and J. R. Gord, Appl. Opt. 42(12), 2063 (20 April 2003).

"Crystallographic and Spectroscopic Investigations of the Effect of Preparation Procedure on CdS Nanoparticles Made in Reversed Micelles," C. E. Bunker, P. Pathak, B. A. Harruff, Y. Lin, J. Widera, J. R. Gord, and Y.-P. Sun, Presented at the 203rd Meeting of the Electrochemical Society, 27 April – 2 May 2003, Paris, France.

"Triple-Pump Coherent Anti-Stokes Raman Scattering (CARS): Temperature and Multiple-Species Concentration Measurements in Reacting Flows," S. Roy, T. R. Meyer, M. S. Brown, V. N. Velur, R. P. Lucht, and J. R. Gord, Submitted to Optics Communications in May 2003.

"Experimental Study of Two-Phase Vortex-Flame Interactions by Laser Induced Fluorescence of OH and CH," A. Lamaire, K. Zahringer, T. R. Meyer, J. R. Gord, and J. C. Rolon, Presented the 4th Pacific Symposium on Flow Visualization and Image Processing, 3-5 June 2003, Chamonix, France, and published in the Conference Proceedings.

”Stator Cascade Flow Vectoring through Counter-Flow Blowing.” M. R. Harff, J. M. Wolff, W. W. Copenhaver, D. Car, and J. Estevadeordal, AIAA Paper No. 2003-3408 to be presented at the 33rd AIAA Fluid Dynamics Conference and Exhibit, 23-26 June 2003, Orlando, FL.

“Crystallographic and Spectroscopic Investigations of the Effect of Preparation Procedure on CdS Nanoparticles Made in Reverse Micelles,” C. E. Bunker, P. Pathak, B. A. Harruff, Y. Lin, J. Widera, J. R. Gord, and Y.-P. Sun, To be presented at the AIAA/ ICAS International Air and Space Symposium and Exposition, 14-17 July 2003, Dayton, OH.

“Dynamics of Vortex-Flame Interactions and Implications for Turbulent Combustion,” T. R. Meyer, V. R. Katta, M. S. Brown, J. R. Gord, W. M. Roquemore, A. Lemaire, K. Zahringer, and J. C. Rolon, AIAA Paper No. 2003-4633, Invited paper to be presented at the 39th AIAA/ASME/SAE/ASEE Joint Propulsion Conference and Exhibit, 20-23 July 2003, Huntsville, AL.

“Quenching Studies of Highly Luminescent CdS Nanoparticles in the Presence of Sulfur Containing Compounds,” J. Widera, J. R. Gord, and C. E. Bunker, To be presented at the 45th Rocky Mountain Conference on Analytical Chemistry, 27-31 July 2003, Denver, CO.

“Optical Sensor Platforms for Quantifying Pollutant Emissions in Combustion Exhausts,” J. R. Gord, R. Barron-Jimenez, T. N. Anderson, R. P. Lucht, S. Roy, M. S. Brown, and S. Stouffer, To be presented at the 45th Rocky Mountain Conference on Applied Spectroscopy, 27-31 July 2003, Denver, CO.

“Dual-Pump, Dual-Broadband Coherent Anti-Stokes Raman Scattering for Characterization of Liquid-Fueled Combustors,” S. Roy, T. R. Meyer, R. P. Lucht, V. M. Belovich, E. Corporan, and J. R. Gord, To be presented at the 45th Rocky Mountain Conference on Applied Spectroscopy, 27-31 July 2003, Denver, CO.

“Effects of Dynamic Strain on OH* and CH* Luminescence in Counterflow Diffusion Flames,” J. Miller, A. Lynch, J. R. Gord, T. R. Meyer, M. S. Brown, and V. Katta, To be presented at the 45th Rocky Mountain Conference on Applied Spectroscopy, 27-31 July 2003, Denver, CO.

“Initiation of Detonation in a Large Tube,” V. Katta, C. Tucker, J. Hoke, and F. Schauer, To be presented at the 19th International Colloquium on the Dynamics of Explosions and Reactive Systems, 27 July-1 August 2003, Hakone, Japan.

“Application of Advanced Optical Diagnostics for Combustion and Fluid Flows,” S. P. Gogineni and J. R. Gord, Invited Seminar to be presented at the University of Texas at Austin, 12 August 2003, Austin, TX.

"Modeling of Two-Photon Absorption Processes: Direct Numerical Integration of the Time-Dependent Density Matrix Equations," R. P. Lucht, S. Roy, J. R. Gord, and T. B. Settersten, Invited paper to be presented at the Gordon Research Conference on Laser Diagnostics in Combustion, 17-22 August 2003, Oxford, England.

"Triple-Pump CARS Techniques: From Laboratory Flames to JP-8-Fueled Combustors," T. R. Meyer, S. Roy, M. S. Brown, R. P. Lucht, and J. R. Gord, Invited paper to be presented at the Gordon Research Conference on Laser Diagnostics in Combustion, 17-22 August 2003, Oxford, England.

"Simultaneous CH PLIF and PIV for the Investigation of Two-Phase Vortex-Flame Interactions," A. Lemaire, K. Zahringer, T. Meyer, J. Gord, and J. C. Rolon, Invited paper to be presented at the Gordon Research Conference on Laser Diagnostics in Combustion, 17-22 August 2003, Oxford, England.

"DPIV Measurements of the Flow Field between a Transonic Rotor and an Upstream Stator," S. Gorrell, W. Copenhaver, and J. Estevadeordal, To be presented at the ISUAAAT 03 International Symposium on Unsteady Aerodynamics, Aeroacoustics, and Aeroelasticity of Turbomachines, 7-11 September 2003, Durham, NC, and published in Conference Proceedings.

"Experimental Investigation of Two-Phase Vortex-Flame Interactions by PIV and PLIF," K. Zahringer, A. Lemaire, T. R. Meyer, J. R. Gord, and J. C. Rolon, To be presented at the German Association of Engineers Society of Energy Technology (VDI) 21st German Flame Day Meeting (21 Deutscher Flammentag), 9-10 September 2003, Cottbus, Germany.

"PIV Investigation on the Vortex Shedding of a Jet-in-a-Cross Flow," B. Kiel, A. Cox, J. Estevadeordal, and S. Gogineni, To be presented at the 5th International Symposium on PIV, 22-24 September 2003, Busan, Korea.

"Current and Future Applications of Ultrafast Lasers for Propulsion Diagnostics," J. R. Gord, W. M. Roquemore, M. S. Brown, and J. L. Blackshire, To be presented at the Directed Energy Professional Society (DEPS) Ultrashort Pulse Laser Materials Interaction Workshop, 25 September 2003, Boulder, CO.

"Temperature and CO_2 Concentration Measurements in the Exhaust Stream of a Liquid-Fueled Combustor Using Dual-Pump Coherent Anti-Stokes Raman Scattering (CARS) Spectroscopy," S. Roy, T. R. Meyer, R. P. Lucht, V. M. Belovich, E. Corporan, and J. R. Gord, To be submitted to Combustion and Flame.

Significant Accomplishments

Dr. Sivaram Gogineni (ISSI) was elected to serve as President of the Dayton Area Defense Contractors Association for FY 2000-2001.

Dr. Sivaram Gogineni (ISSI) serves on two AIAA Technical Committees--Fluid Dynamics and Aerodynamic Measurement Technology.

An invited paper entitled, "Pulse Detonation Engine In-House Research at AFRL," co-authored by F. Schauer, J. Stutrud (both of AFRL), and R. Bradley (of ISSI), was presented at the 13th ONR Propulsion Meeting, 10-12 August 2000, Minneapolis, MN.

Photographs from two efforts were selected for publication on the frontispiece of the Journal of Visualization [Vol. 3, No. 2, p. 95, September 2000)]: 1) "Modeling and Measurement of the Interaction of Starting Jets and Flames," that was conducted by G. J. Fiechtner, V. R. Katta, C. D. Carter (all of ISSI), J. R. Gord, W. M. Roquemore (both of AFRL), and J. C. Rolon (Ecole Centrale Paris and CNRS) and 2) "Visualization of Vortex-Shedding and Blade Synchronization in a Transonic Compressor," by J. Estevadeordal, S. Gogineni, L. Goss (all of ISSI), W. Copenhaver, and S. Gorrell (both of AFRL).

An invited paper entitled, "AFRL/PRSC Pulse Detonation Engine Program," co-authored by F. Schauer, J. Stutrud (both of AFRL), R. Bradley, and V. Katta (both of ISSI), was presented at the 12th PERC Symposium, Ohio Aerospace Institute, 26-27 October 2000, Cleveland, OH.

Dr. Geoffrey. J. Sturgess (ISSI) was invited to present a paper entitled, "Modeling, CFD, and Kinetics," at the United Engineering Foundation Conference on Lean Combustion Technology and Its Control, 6-9 November 2000, Santa Fe, NM.

Dr. Geoffrey. J. Sturgess (ISSI) was invited to present a paper entitled, "Ultra Compact Combustor: Main and Inter-Turbine Burner Concepts," at the Intelligent Turbine Engines (MITE) Workshop on Goals and Technologies for Future Gas Turbines, 4-5 December 2000, Atlanta, GA.

Dr. Sivaram Gogineni (ISSI) was Chairman of the Session on Jet Flows II at the 39th AIAA Aerospace Sciences Meeting and Exhibit, 8-11 January 2001, Reno, NV.

Dr. Sivaram Gogineni (ISSI) was invited to present a paper entitled, "Analysis of Transition Process in a Forced Wall Jet Using High Resolution PIV and 3D DNS," at NIST, Process Measurements Division, 31 January 2001, Gaithersburg, MD.

A photograph entitled, "Vortex Shedding in a Transonic Compressor," by J. Estevadeordal, S. Gogineni, L. Goss (all of ISSI), W. Copenhaver, and S. Gorrell (both of AFRL) was selected for publication on the frontispiece of the Journal of Visualization [Vol. 3, No. 4, March 2001].

Dr. Sivaram Gogineni (ISSI) was Chairman of the Instrumentation II Session at the Twenty-Sixth Annual Dayton-Cincinnati Aerospace Science Symposium, 30 March 2001, Dayton, OH. He also served as Membership Chairman and Registration Co-Chairman for this symposium.

Dr. Sivaram Gogineni (ISSI) was invited to present a paper entitled, "Investigation of Complex Fluid Flows Using PIV, Holography, and DNS," at Rutgers University, 28 June 2001, New Brunswick, NJ.

A photograph from the article entitled, "Role of Flow Visualization in the Development of UNICORN," by W. M. Roquemore (AFRL) and V. R. Katta (ISSI), which appeared in the Journal of Visualization [Vol. 2, Nos. 3/4 (2000)], was selected in July of 2001 to receive the Kodak Award for Excellent Visualized Image in 2000. This photograph was selected by the Visualization Society of Japan from photographs appearing in all of their publications during 2000.

In 2001 Dr. Sivaram Gogineni (ISSI) nominated Dr. W. M. Roquemore (AFRL) for the Propellants and Combustion Award.

An invited paper entitled, "Flame Propagation and Morphology in Premixed Vortex Rings," co-authored by T. R. Meyer (ISSI), J. R. Gord (AFRL), V. R. Katta, G. J. Fiechtner, G. L. Switzer (all of ISSI), and W. M. Roquemore (AFRL), was presented at the 11th Gordon Research Conference on Laser Diagnostics in Combustion, 1-6 July 2001, South Hadley, MA.

An invited paper entitled, "Terahertz Studies of Gas and Condensed Phases for Combustion Application," by M. S. Brown (ISSI), D. Zimdars (Picometrix, Inc.), and J. R. Gord (AFRL), was presented at the Gordon Research Conference on Laser Diagnostics in Combustion, 1-6 July 2001, South Hadley, MA.

An invited paper entitled, "In-House Pulse Detonation Engine Research at AFRL Wright-Patterson AFB," co-authored by F. Schauer, J. Stutrud (both of AFRL), R. Bradley, V. Katta, and J. Hoke (all of ISSI)," was presented at the 14th ONR Propulsion Meeting, 10 August 2001, Chicago, IL.

An invited paper entitled, "In-House Pulse Detonation Engine Research at Wright-Patterson AFB," co-authored by F. Schauer, J. Stutrud (both of AFRL), R. Bradley, V. Katta, and J. Hoke (all of ISSI), was presented at the European Office of Aerospace Research and Development and EADS-Aerospatiale Matra Missiles Workshop on Pulse Detonation Engines, 28-29 August 2001, Bourges, France.

An invited paper entitled, "AFRL Pulse Detonation Engine Research Applications," co-authored by J. Hoke, R. Bradley (both of ISSI), and F. Schauer (AFRL), was presented at the European Office of Aerospace Research and Development and EADS-Aerospatiale Matra Missiles Workshop on Pulse Detonation Engines, 28-29 August 2001, Bourges, France.

Dr. Sivaram Gogineni (ISSI) was invited to give a lecture entitled, "Combustion Diagnostics," at the International Workshop on Modern Advances in Combustion, Indian Institute of Technology, 31 August - 1 September 2001, Madras, India.

Dr. Sivaram Gogineni (ISSI) was Chairman of the Session on Complex Engineering Flow Fields at the 4th International Symposium on Particle Imaging Velocimetry, 17-19 September 2001, Gottingen, Germany.

Dr. Terry Meyer (ISSI) joined the research team of Ecole Centrale Paris (ECP) in November of 2001 for a two-month period to assist with the performance of CH planar laser-induced fluorescence and particle-image velocimetry in two-phase methane/n-heptane/air vortex-flame interactions.

Dr. Sivaram Gogineni (ISSI) served as Session Chair at the 54th Annual Meeting of the American Physical Society, Division of Fluid Dynamics, 18-20 November 2001, San Diego, CA.

Dr. Viswanath Katta (ISSI) served as a committee member for doctoral candidate Julian de Charentenay and attended his dissertation defense on 18 January 2002 at Ecole Centrale de Paris in Paris, France; his dissertation is entitled, "Numerical Simulations of Unsteady Reacting Flows."

Dr. Viswanath Katta (ISSI) was selected as one of the winners of the Engineers and Scientists Outstanding Achievement Award given by the Affiliate Societies Council of the Engineering and Science Foundation of Dayton for the year 2002. Dr. Katta received this award for his pioneering efforts in developing and applying sophisticated computer codes for the study of combustion and fuels. The 43rd Annual Awards Banquet was held on 21 February 2002 at Sinclair Community College in Dayton, OH.

Dr. Sivaram Gogineni (ISSI) served as Registration Co-Chairman and Sponsorship Chairman at the Twenty-Seventh Annual Dayton-Cincinnati Aerospace Science Symposium, 5 March 2002, Dayton, OH.

Dr. Sivaram Gogineni (ISSI), representing the American Institute of Aeronautics and Astronautics, attended Congressional Visits Day on 20-22 March 2002 in Washington, D.C.

Dr. Geoffrey Sturgess (ISSI) was elected a Fellow of the American Institute of Aeronautics and Astronautics in 2002. He was inducted at the AIAA Global Air and Space 2002 Conference, 22-24 April 2002 in Washington, D. C.

In April 2002 photographs from the following three previously published articles were selected for inclusion in "Best-of-the-Gallery," a book to be published by the American Physical Society/Division of Fluid Dynamics (APS/DFD). This book will contain photographs from award-winning posters submitted over the past 18 years at the APS/DFD Annual Meetings.

1. "High Free-Stream Turbulence Influence on Turbine Film Cooling Flows," by S. Gogineni (ISSI), R. Rivir, D. Pestian (both of AFRL), and L. Goss (ISSI)

2. "Comparison of Transitional Free Jet and Wall Jet," by S. Gogineni (ISSI), C. Shih, and A. Krothapalli (both of Florida State University)

3. "Dynamics of Jet in Cross Flow," by S. Gogoineni, M. Whitaker, L. Goss (all of ISSI), and W. M. Roquemore (AFRL).

On 22 May 2002 at the Dayton-Cincinnati AIAA Annual Honors and Awards Program, it was announced that on 1 June 2002, Dr. Sivaram Gogineni (ISSI) would be the new Section Chair for AIAA. He received the Chairman's Award for supporting the local section and the Aerospace Science Symposium as Membership Chair, Registration Co-chair, and Corporate-Sponsorship Chair and for spearheading numerous membership upgrades, developing and maintaining a first-class membership database, and contributing immeasurably to symposium success and funding.

On 22 May 2002 at the Dayton-Cincinnati AIAA Annual Honors and Awards Program, Dr. Viswanath Katta, Dr. Terrence Meyer (both of ISSI), Dr. James R. Gord, and Dr. W. Mel Roquemore (both of AFRL) received the Art-in-the-Science Award (third place) for a poster entitled, "Crash and Burn," which was presented at the Twenty-Seventh Annual Dayton-Cincinnati Aerospace Science Symposium, 5 March 2002, Dayton, OH.

Dr. Geoffrey Sturgess (ISSI) was invited to present a lecture course on combustion at Pratt and Whitney, Canada, in June 2002.

Dr. Sukesh Roy (ISSI) was selected in June 2002 to participate in the National Academy of Engineering's Frontiers of Engineering Program that brings together the best young engineering talent in the United States to discuss topics of current interest in the field.

Dr. Sivaram Gogineni (ISSI) was elected in June 2002 to serve as Honors and Awards Chairman of the Dayton Section of the ASME.

Dr. Sivaram Gogineni (ISSI) attended a Technical Committee Meeting in conjunction with the ASME Turbo Expo 2002, 3-6 June 2002, Amsterdam, The Netherlands.

Dr. Geoffrey Sturgess (ISSI) was Organizer and Chairman of the Session on Flame Stability and Co-Chairman of the Panel Session on Combustion Processes and Their Reliability at the ASME Turbo Expo 2002, 3-6 June 2002, Amsterdam, The Netherlands. He also attended a meeting of the Combustion and Fuels Committee in conjunction with this conference.

Dr. Sivaram Gogineni (ISSI) was invited to present a seminar on 4 June 2002 entitled, "Advanced Optical Diagnostic Techniques for Complex Fluid Flows;" at the Delft Institute of Technology in The Netherlands; the seminar was co-authored by J. Gord and B. Kiel (both of AFRL).

Dr. Sivaram Gogineni (ISSI) chaired two sessions at the AIAA St. Louis Conference, which was held in St. Louis, MO, 23-27 June 2002: 1) Advanced Flow Control Techniques and Technologies and 2) Shock Wave/Viscous Flow Interaction.

In July 2002 Dr. Sivaram Gogineni (ISSI) participated as an Executive Committee Member in planning-committee meetings for the AIAA/ICAS Symposium to be held in Dayton in July 2003 and for the Twenty-Eighth AIAA Dayton-Cincinnati Aerospace Science Symposium to be held in Dayton on 4 March 2003. For the latter conference, he will serve as Corporate Sponsorship Chair and Registration Co-chair.

An invited paper entitled, "Detonation Studies and Performance Results for a Research Pulse Detonation Engine," co-authored by F. Schauer, J. Stutrud (both of AFRL), R. Bradley, V. Katta, and J. Hoke (all of ISSI) was presented at the International Colloquium on Advances in Confined Detonations, 2-5 July 2002, Moscow, Russia, and published in the Conference Proceedings.

In August 2002, Dr. Sivaram Gogineni (ISSI) successfully nominated Commander Maj. Gen. Paul D. Nielsen for the AIAA Hap Arnold Award for Excellence in Aeronautical Program Management. He received the award at the AIAA Aircraft Technology, Integration, and Operations Forum in Los Angeles, CA, on 1 October 2002.

Dr. Sivaram Gogineni (ISSI) successfully nominated Dr. W. M. Roquemore (AFRL) as an ASME Fellow in October 2002. He has successfully nominated seven persons to Fellow Grade.

Dr. Sivaram Gogineni (ISSI) served as Chair for two sessions at the ASME Winter Annual Meeting, 17-21 November 2002, New Orleans, LA.

In January 2003 the following ISSI employees were nominated for the AFRL Simpson Award for their team efforts on Room 20 High Pressure Combustion Research: Charles Abel, Brad Day, Roger Mears, Richard Ryman, Ronald Britton, Steve Pennington, and Karl Shoffstall.

Dr. Sivaram Gogineni (ISSI) served as Section Vice-Chair of the Dayton Section of ASME during 2003.

Dr. Sivaram Gogineni (ISSI) served as Chair of both the AIAA Information and Publications Subcommittee and the AIAA Web Development Team for the year 2003.

Two photographs from previously published joint studies by Dr. Viswanath R. Katta (ISSI) and Dr. W. Mel Roquemore (AFRL) are included in the AFRL/Propulsion Directorate brochure entitled, "Modeling and Simulation: Applications for Propulsion and Power Research and Development." This brochure was displayed and distributed at the 41st AIAA Aerospace Sciences Meeting and Exhibit, 6-9 January 2003, Reno, NV.

Dr. Sivaram Gogineni (ISSI) served as a Session Chair at the 41st AIAA Aerospace Sciences Meeting and Exhibit, 6-9 January 2003, Reno, NV.

Dr. Geoffrey Sturgess (ISSI) has been invited by the American Institute of Aeronautics and Astronautics to write an extensive paper on gas-turbine combustion for publication in the AIAA Journal of Propulsion and Power in the year 2003 as part of the celebration of the centennial of the first flight by the Wright Brothers. An entire issue of the journal will be devoted to this paper.

Dr. Sivaram Gogineni (ISSI) was notified in February 2003 that a photograph from his article entitled, "Double Helix Instability in Forced Wall Jet" (Phys. Fluids, Sept. 2002) would appear on cover of the AIP publication entitled, "2004 Graduate Programs in Physics, Astronomy, and Related Fields."

In February 2003, Dr. Sivaram Gogineni (ISSI) successfully nominated Dr. W. M. Roquemore (AFRL) as an APS Fellow.

Dr. Sivaram Gogineni (ISSI) was an Executive Committee Member for TechFest 2003, which was held in February 2003 under the sponsorship of the Engineers Club of Dayton.

A photograph from a paper entitled, "Vortex-Induced Flame Extinction in Two-Phase Counterflow Diffusion Flames with CH Planar Laser-Induced Fluorescence and Particle-Image Velocimetry," by A. Lemaire (Ecole Centrale Paris), T. R. Meyer (ISSI), K. Zahringer, J. C. Rolon (both of Ecole Centrale Paris), and J. R. Gord (AFRL) (published in Applied Optics, Vol. 42, No. 12, pp. 2063-2071, 20 April 2003), was chosen to appear on the cover of the 20 April 2003 issue of Applied Optics.

In May 2003 Dr. Sivaram Gogineni (ISSI) became a panel member of the NASA-Sponsored Advanced Sensors Consortium in Huntsville, AL.

At the AIAA Dayton-Cincinnati/ASME Dayton Annual Honors and Awards Program on 21 May 2003, Dr. Sivaram Gogineni (ISSI) received the Special Service Citation for Dedication to the Aerospace Profession and Outstanding Leadership of and Support to the AIAA Dayton/Cincinnati Section, was recognized for being Section Chair for the Dayton/Cincinnati Section for 2002-2003, and also received the Third-Place Award in the AIAA Art-in-the-Science Competition.

At the AIAA Dayton-Cincinnati/ASME Dayton Annual Honors and Awards Program on 21 May 2003, Drs. Sukesh Roy and Terrence Meyer (both of ISSI) received the Outstanding Technical Contribution Award for significant contributions in the development of dual-pump, dual-broadband Coherent Anti-Stokes Raman Spectroscopy (CARS) and its application to practical gas-turbine combustors.

At the AIAA Dayton-Cincinnati/ASME Dayton Annual Honors and Awards Program on 21 May 2003, AIAA Best Technical Presentation Awards were received by Michael Brown, Terry Meyer, and John Hoke (all of ISSI) [in conjunction with. J. T. Parker (OSU) and J. R. Gord (AFRL)] for their paper entitled, "OH-Based Fuel/Air Ratio Monitor for the Pulsed-Detonation Engine," and by Sukesh Roy, Terry Meyer, and Michael Brown (all of ISSI) [in conjunction with R. P. Lucht (Purdue University), J. R. Gord, V. M. Belovich, and. E. Corporan (all of AFRL)] for their paper entitled, "Dual-Pump Dual-Broadband Coherent Anti-Stokes Raman Scattering for the Measurement of Temperature and Multiple Species Concentrations."

At the AIAA Dayton-Cincinnati/ASME Dayton Annual Honors and Awards Program on 21 May 2003, a photograph entitled, "Transonic Scenery," by Jordi Estevadeordal (ISSI) [in conjunction with A. Breeze-Stringfellow (GE Aircraft Engines) and M. Langford (Virginia Tech)] won the Second-Place Award in the AIAA Art-in-the-Science Competition.

In 2003 Dr. Sivaram Gogineni (ISSI) successfully nominated 12 scientists for upgrade to Associate Fellow Status in AIAA and one scientist for the Outstanding Engineers and Scientists Award sponsored by the Affiliate Societies Council of the Engineering and Science Foundation of Dayton.

Dr. Sivaram Gogineni (ISSI) will serve as Session Organizer and Session Chair for the ASME/IGTI Turbo Expo, which will be held 16-19 June 2003 in Atlanta, GA. He is a member of the ASME/IGTI Technical Committee for Fuels and Combustion.

Dr. Sivaram Gogineni (ISSI) will serve as a Session Organizer and Session Chair at the 33rd AIAA Fluid Dynamics Conference and Exhibit, which will be held 23-26 June 2003 in Orlando, FL.

An invited paper entitled, "Dynamics of Vortex-Flame Interactions and Implications for Turbulent Combustion," by T. R. Meyer V. R. Katta, M. S. Brown (all of ISSI), J. R. Gord, W. M. Roquemore (both of AFRL), A. Lemaire, K. Zahringer, and J. C. Rolon (all of Ecole Centrale Paris) will be presented at the 39th AIAA/ASME/SAE/ASEE Joint Propulsion Conference and Exhibit, 20-23 July 2003, Huntsville, AL. The paper will be published as AIAA Paper No. 2003-4633.

An invited seminar entitled, "Application of Optical Diagnostics to Combustion and Fluid Flows," by S. P. Gogineni (ISSI) and J. R. Gord (AFRL) will be presented at the University of Texas at Austin, 12 August 2003, Austin, TX.

APPENDIX

Publications and Presentations

38th AIAA/ASME/SAE/ASEE Joint Propulsion Conference & Exhibit
7-10 July 2002, Indianapolis, Indiana

AIAA 2002-3865

CHEMILUMINESCENCE AS A MEASUREMENT OF LOCAL EQUIVALENCE RATIO

Michael S. Brown,* Terrence R. Meyer,† and Geoffrey J. Sturgess‡
Innovative Scientific Solutions, Inc.
Dayton, Ohio 45440-3638

Joseph Zelina§ and James R. Gord¶
Air Force Research Laboratory
Propulsion Directorate
Wright-Patterson Air Force Base, OH 45433-7103

ABSTRACT

Measurements of the chemiluminescence of OH*, CH*, and C_2* in laminar laboratory propane/air flames and a liquid-fueled model combustor are presented. Ratios of the emission intensity for the three species are a strong function of equivalence ratio. Results of the laboratory measurements are used to infer conditions within the model combustor. Discussion of the measurements and their utility is made in the context of previous studies.

I. INTRODUCTION

One of the goals of advanced gas turbine development is the realization of intelligent active control. Work in this area seeks to establish methods of monitoring all aspects of gas turbine performance and health, algorithms to assess engine function and efficiency, and actuators to make real-time operation adjustments. Passive optical sensors can play a significant role in active control by providing an inexpensive means of monitoring flame emission inside the combustor. We present here results of an ongoing investigation in the use of optical emission as a means of measuring the local equivalence ratio (Φ) in a model liquid-fueled combustor.

*Physicist, Senior Member AIAA
†Research Engineer, Member AIAA
‡Senior Research Engineer, Fellow AIAA
§Research Engineer, Senior Member AIAA
¶Principal Research Chemist, Associate Fellow AIAA

To date, our efforts in developing this optical sensor have been concentrated on two complementary activities. First, we have made calibration measurements in laminar laboratory flames. The focus of these studies is the identification of particular signal ratios that are indicative of changes in Φ. Fluctuations in Φ reflect transients in mixing or fuel atomization as well as on-demand changes in supplied fuel. These studies also seek to establish the applicability of emission signal ratios as a measure of equivalence ratio across a broad spectrum of fuel/oxidizer combinations. Secondly, we have performed measurements in a liquid-fueled model combustor (see Figure 1) to establish the utility of the sensor as part of the research and development of advanced combustor designs and to test approaches to making a hardened optical sensor.

The optical emission from flames has long been a subject of study.[1] Numerous intermediate as well as stable species emit light over the full optical spectrum ranging from the vacuum ultraviolet to the far infrared. The particular emission spectrum detected is a strong function of the chemistry present in a flame and thus reflects the particular fuel, oxidizer, mixture ratio, pressure and temperature. In this sense, emission spectra serve as fingerprints for local flame environments. Studies employing emission signals range from applied efforts in commercial engines to fundamental work in vortex-flame interaction. Broadband emission images have been used to characterize the pre-ignition sequence in a direct-inject diesel engine[2] and charge stratification in a spark-ignited engine.[3] CO_2* chemiluminescence images have been used to study vortex-flame interaction as a function of Lewis number and heat release.[4] UV and IR emission from OH* has been used to delineate the radii of flame balls in microgravity studies.[5]

This material is declared a work of the U.S. Government and is not subject to copyright protection in the United States.

In recent years there has been a renewed interest in optical emission as a flame monitor for the purpose of feedback control. A complete monitoring and feedback system based on CH* emission was recently demonstrated in a partially premixed methane/air laboratory flame.[6] Neural network processing of OH* emission images has also been used for feedback control of a model industrial burner.[7] In our ongoing work, we are making emission measurements in model combustors and calibrating them with measurements from laboratory flames in an effort to provide useful information to the hardware designers. In particular, we are aiming to determine the local equivalence ratio in the partially confined volume near the fuel injectors of an advanced combustor. The status of these efforts is presented here.

II. EXPERIMENTAL APPROACH

A sample, averaged emission spectrum acquired in the model combustor is shown in Figure 2. The spectrum was acquired using a fixed-grating, off-the-shelf spectrometer. The response at the blue end of the spectrum is largely determined by the blaze angle of the grating while the red response is largely determined by the silicon-based linear ccd detector. The spectrum has not been corrected for nonuniform response. Six molecular emission bands due to OH*, CH*, and C_2* are clearly visible in the spectrum. With increasing equivalence ratio, a broad structureless background appears along with these molecular features. For the combustor condition of Figure 2, this background extends from ~ 480 nm to nearly 900 nm. The broad background likely has contributions from polycyclic aromatic hydrocarbon (PAH) emission and particulate incandescence. A weaker broadband emission background possibly due to CO_2* is seen extending from the OH* band at 308 nm into the stronger PAH background. Strong unstructured CO_2* emission is typically seen in lean hydrocarbon flames peaking near 430 nm.[1,8] As the local equivalence ratio changes, the relative strength of the emission features as well as the broad background change as a consequence of changes in the local combustion chemistry—in particular, changes in the production and destruction rates of chemical intermediates. The CH* emission at 430 nm from the $A^2\Delta$ state follows oxidation of C_2H,[9]

$$C_2H + O \rightarrow CO + CH^* \qquad (1)$$

A significantly smaller amount of CH* is produced via the reaction of C_2H and O_2. The OH* emission originates from the $A^2\Sigma$ state produced by the oxidation of CH,[10]

$$CH + O_2 \rightarrow CO + OH^* \qquad (2)$$

The precise chemical origin of C_2* chemiluminescence is unknown[1] although reactions between CH and CH or C have been suggested.[11] All of the excited radical states are collisionally quenched at rates faster than their chemical removal. Hence, emission signal strengths track production rates very closely.[12] While some uncertainties in the temperature dependence of the production rates exist, they are known well enough that a recent comparison between experimental and model absolute emission signal strengths of OH and CH in a laminar methane/air flame were found to agree to within a factor of six.[13]

To establish spectral metrics for determining Φ in the model combustor, emission spectra similar to that shown in Figure 2 have been acquired in a laminar, propane/air, laboratory flame above a Hencken burner. Most recent laboratory-flame emission studies have been conducted in laminar, premixed methane/air flames.[6,10,13-16] For our initial laboratory measurements, propane was chosen because it more closely represents the carbon-to-hydrogen ratio in the JP-8-fueled combustor. The emission data were taken from the flame region located roughly one centimeter above the surface of the burner as a function of Φ. In this region, the flame gases are well mixed but little or no co-flow (N_2) has been drawn into the flame. Calibrated mass-flow controllers were used to adjust the equivalence ratio over the stable operating condition of the burner. The emission signals were collected using a silica-core/silica-cladding fiber bundle coupled to a small, fixed-grating, commercial spectrometer package that collects light between 190 and 870 nm. Bundles of four and five fiber strands were used—each fiber collecting line-of-sight emission with an acceptance angle of ~12°. Under laboratory conditions, it is straightforward to maintain a fixed spatial relationship between the collection end of the fiber and the flame zone, and to keep the end of the bundle free of particulates and other obscurants. Such conditions are difficult to control or monitor in a combustor test facility. For this reason, the emission data collected in the laboratory flame were analyzed from the perspective of finding various spectral ratios that correlate well with Φ. Use of ratios normalizes out to a large extent signal strength changes due simply to changes in the location of the flame front or transmission changes at the entrance face of the fiber bundle. This analysis necessarily assumes that any change in transmission is wavelength independent.

Similar fiber bundles were used to make emission measurements in a model combustor; specifically, the inter-turbine burner (ITB) test rig at WPAFB. The ITB testing is part of an ongoing project to develop an ultra-compact combustor. The silica/silica fibers are robust to temperatures of ~1100° C. The flame temperatures exceed this value, so the fibers were not placed in direct contact with the flame front. Using ceramic standoffs, fiber bundles were sleeved inside ¼-in stainless steel tubes that were inserted through holes in the fore wall of the ITB combustor. The light collection end of the bundles were located flush to the surface of the fore wall and gathered emission across the flame-holding annular cavity of the combustor. One sleeved fiber bundle was located opposite one of the circumferential fuel injectors. A second was located between two adjacent injectors. The aft wall of the annular cavity was lined with a ceramic ring. The free-space distance between the fiber bundles and the ceramic ring amounted to one inch. Though in contact with the flame, no emission from the surface of the ceramic piece was discernible in the collected spectra. This was verified by observing the disappearance of all signal features (molecular and broadband) as the combustor flame was extinguished. A purge flow of dry nitrogen was directed through the ¼-in tubes during ignition and relighting to prevent sooting of the fiber ends. While the fibers rarely came in direct contact with the flame front, they did degrade over time due to the heat load. The functional lifetime of the fiber bundles was typically found to be about four hours of combustor operation.

Since the emission signals are collected in a line-of-sight fashion, it is impossible to ascertain exactly where along the optical axis the signals originated or whether or not signals from different species are co-located. However, evidence from several other studies strongly suggests that the emission of OH*, CH* and C_2* emanates from coincident spatial regions. The OH* and CH* emission should be highly coupled since CH is the precursor to OH* (see Eqn. 2). The same may be true of CH* and C_2*, since CH may be a precursor of C_2* as well.[11] Simultaneous images of OH*, CH* and C_2* (470 nm) taken in a premixed acetylene/oxygen flame are spatially coincident in both the radial and axial directions.[17] Similar results have been seen in laminar methane/air flames—the authors noting that in the radial dimension all three species show a sharp cutoff on the fuel lean side of the reaction zone.[16] Yoshida *et al.* collected OH*, CH* and C_2* emission images in a turbulent premixed propane/air flame.[18] Their system consisted of annular opposed jets. In both the radial and axial directions average images of all three radical emission patterns are coincident. In the radial direction, the CH* emission exhibits the narrowest intensity distribution. The C_2* emission lies directly on top of the CH* emission between the centerline and peak intensity region while exhibiting a somewhat broader spatial distribution for the outer region of the annular flame zone. The OH* emission closely follows the CH* emission distribution between the outermost regions of the flame zone and the peak intensity region while extending closer to the axial centerplane than the CH* emission. The Kobe University group has developed an imaging system that efficiently collects light from only a small sample volume roughly 1 mm in the axial direction and 0.8 mm in the radial direction.[16,19] Their calibration work in laminar premixed methane/air flames was used to analyze emission data collected in a turbulent premixed methane/air flame. The turbulent emission data strongly suggest that peak emission from OH*, CH* and C_2* is co-located in the flame front. Planar laser-induced fluorescence (PLIF) measurements detect the ground-state populations of target molecules. Simultaneous PLIF images of CH and OH in a lifted jet diffusion flame reveal that CH and OH are found together in the flame front with the CH appearing predominantly on the fuel rich side and the OH appearing predominantly on the fuel lean side. Both radicals accurately locate the flame front.[20] In a vortex-flame interaction study of methane/air flames, images of the CH* emission were found to mimic the CH PLIF images in that the emission was found only in the primary reaction zone and disappeared at about the same time as the CH fluorescence after interaction of the vortex with the flame front.[12] All of these considerations strongly suggest that, while our particular emission probe is a line-of-sight diagnostic, the collected emission signals for the three principal radicals are emanating from the same spatial location or locations along the light collection axis and therefore reflect the same local flame chemistry.

In general, radical concentrations reflect the local flame environment as defined by the local pressure, temperature, velocity field and fuel/air mixture ratio. Fluctuations in the local mixture fraction (or equivalence ratio) manifest themselves as fluctuations in the local radical concentration. This behavior has been recently quantified in the case of OH by a group using short-pulse laser-induced fluorescence to track the temporal behavior of OH concentrations in non-premixed turbulent flames.[21,22] The temporal statistics of the OH fluorescence agree well with statistics (at least to zeroth order) of the local mixture fraction. While it has not been directly demonstrated to date, it is reasonable to assume that the radical chemiluminesence will be closely coupled to the local equivalence ratio in the turbulent non-premixed flame zone of the model combustor. Fluctuations in one should accompany

fluctuations in the other. Recently, a group at Kobe University has demonstrated local equivalence ratio measurements in a turbulent premixed methane/air flame.[19] Based on their previous emission correlation work in a laminar methane/air flame, the local equivalence ratio was determined at three spatial locations as the local flame front moved through the observation volume. For a global equivalence ratio of 1, probability distributions of time series measurements of three ratios (OH*/CH*, C_2*/OH* and C_2*/CH) had mean equivalence ratio values between 0.95 and 1.06.

III. EXPERIMENTAL RESULTS AND DISCUSSION

It was known *a priori* that, while the model combustor was to be operated at overall lean conditions, the fuel/air ratio in the annular cavity would be rich. Consequently, the calibration emission spectra were acquired under laminar flame conditions on both the lean and rich side of stoichiometry. Figure 3 displays the raw signals for OH*, CH* (430 nm), C_2* (550 nm) and the total signal (molecular plus broadband). The emission signals for the other CH* band as well as the other two C_2* bands show the same species functional behavior with equivalence ratio as those plotted. The OH*, CH* and total emission signals increase with equivalence ratio on the lean side peaking at $\Phi = 1$. This is consistent with radical production rates being maximized at stoichiometry. The C_2* signal peaks at $\Phi = 1.4$ consistent with the fact that C_2* tends to be strongest at high temperature and carbon availability.

Measurements in premixed laminar methane/air flames show similar but not identical functional dependences on equivalence ratio for OH* and CH*.[14-16] Likewise, C_2* emission peaks near $\Phi = 1.35$ in the same flames.[16]

Figure 4 and Figure 5 display four spectral signal ratios generated from the raw data for equivalence ratios extending from 0.7 to 1.8. The ratios CH*/OH* and C_2*/OH* increase nonlinearly with increasing equivalence ratio. These trends are similar to those seen in methane/air flames, though the exact functional dependences differ.[16]

Previous studies in laminar flames have also shown that both OH* and CH* emission scale linearly with the total mass flow rate.[6,14,15] Ratios of the two emission signals are therefore independent of flow rate.

Time-averaged emission signals were acquired in the model combustor using integration times of two to five seconds. The residence time of the gases in the annular cavity is roughly 1-4 ms. Turbulent time scales will be on this order and shorter. All short-lived temporal fluctuations are thus completely averaged over in the acquisition. The A/D conversion time of the spectrometer/detector package employed was limited to sampling times ≥30 ms. The autocorrelation of time series of OH* and CH* emission taken with the minimum sampling time were constant exhibiting no slowly varying temporal behavior, at least for durations on the order of a few tens of seconds. Hence, there is no reason to suspect that the individual signal averages of two to five seconds are in anyway biased.

For most operating conditions of the combustor, the flame front in the annular cavity was anchored in the shear layer between the injected fuel spray (at each injector location) and the adjacent injected air stream. As flow rates and pressure drops across the injectors were changed, the location of the anchoring region moved. Larger pressure drops pushed the flame toward the axial centerline of the combustor. This movement of the flame zone alters the sample captured by the light collection cone of the fiber bundles.

Three examples of CH*/OH* emission ratios taken in the model combustor are shown in Figure 6 and Figure 7. They were acquired for three different pressure drops across the injector. Trace sets A, B and C correspond to pressure drops of 2%, 2.3% and 3%, respectively. For each of the three conditions, two traces are shown, one for the on-injector fiber bundle and one for the in-between fiber bundle. Using the results from the propane/air study, the observed combustor emission ratios have been converted to equivalence ratio and plotted against the equivalence ratio derived from the known mass flow rates into the cavity. In this way the plots indicate the relative mixing of the fuel and air in the probe volume sampled by the fiber bundles. As seen, the optically derived equivalence ratios are larger than the mass flow ratios suggesting incomplete mixing in the annular cavity. As anticipated the sample volume captured by the on-injector fiber bundle is always richer than that of the in-between bundle. The three sets of traces decrease in magnitude as the pressure drop increases. The increased pressure drop pushes the fuel stream closer to the axial centerline and thus leans out the mixture in the cavity.

Interestingly, the C_2*/OH* ratios measured in the combustor are very large, lying outside the range measured in the propane/air study. In general, C_2* emission increases with temperature and carbon availability.[1] Since the fuel feed to the combustor is preheated and since the fuel is on average a significantly heavier hydrocarbon than propane, the

significant relative increase in C_2* emission intensity is not too surprising. It does demonstrate the difficulty in transferring results from laminar flames burning simple single-component fuels to a turbulent JP-8-fueled combustor.

IV. FUTURE WORK

As noted by example above, direct transfer of laboratory laminar flame emission results to a liquid-fueled turbulent combustor is not straightforward. To this end we plan to acquire more laboratory data using more complex fuels and a vortex-flame interaction geometry to begin to address the impact of turbulence on chemiluminescence signals. Additionally, the model combustor will be fitted with a quartz aft wall making it easy to move the fiber-optic probes around to multiple spatial locations and map out the spatial dependence of the emission signal.

V. ACKNOWLEDGMENTS

The authors would like to acknowledge Lt. Jeffrey Ehret of WPAFB and Glen Boggs of ISSI for their assistance with various aspects of the model combustor tests. This work is supported in part by U. S. Air Force Contract F33615-00-C-2068.

VI. REFERENCES

1. Gaydon, A. G., *The Spectroscopy of Flames*. 1974, New York: Wiley and Sons. 412.
2. Dec, J. E. and Espey, C., *Chemiluminescence Imaging of Autoignition in a DI Diesel Engine*. in *SAE International Fall Fuels and Lubricants Meeting and Exposition*. 1998. San Francisco, CA.
3. Kuwahara, K. and Ando, H., *Analysis of Barrel-Stratified Lean-Burn Flame Structure by Two-Dimensional Chemiluminescence Measurement.* JSME International Journal, Series B, 1994. **37**: pp. 650-658.
4. Samaniego, J. M. and Mantel, T., *Fundamental Mechanisms in Premixed Turbulent Flame Propagation via Flame-Vortex Interactions Part I: Experiment.* Combustion and Flame, 1999. **118**.
5. Abid, M., Wu, M. S., Liu, J. B., Ronney, P. D., Ueki, M., Maruta, H., Kobayashi, H., Niioka, T., and Vanzandt, D. M., *Experimental and Numerical Study of Flame Ball IR and UV Emissions.* Combustion and Flame, 1999. **116**: pp. 348-359.
6. Scott, D. A., King, G. B., and Laurendeau, N. M., *Chemiluminescence-Based Feedback Control of Equivalence Ratio for a Continuous Combustor.* Journal of Propulsion and Power, 2002. **18**.
7. Allen, M. G., Butler, C. T., Johnson, S. A., Lo, E. Y., and Russo, F., *An Imaging Neural Network Combustion Control System for Utility Boiler Applications.* Combustion and Flame, 1993. **94**: pp. 205-214.
8. Samaniego, J. M., Egolfopoulos, F. N., and Bowman, C. T., *CO_2* Chemiluminescence in Premixed Flames.* Combustion Science and Technology, 1995. **109**: pp. 183-203.
9. Devriendt, K., Van Look, H., Ceursters, B., and Peeters, J., *Kinetics of Formation of Chemiluminescent CH(A2Delta) by the Elementary Reactions of $C_2H(X2Sigma+)$ with O(3P) and $O_2(X3Sigma)$; a Pulse Laser Photolysis Study.* Chemical Physics Letters, 1996. **261**: pp. 450-456.
10. Dandy, D. S. and Vosen, S. R., *Numerical and Experimental Studies of Hydroxyl Radical Chemiluminescence in Methane-Air Flames.* Combustion Science and Technology, 1992. **82**: pp. 131-150.
11. Bowman, C. T. and Seery, D. G., Combustion and Flame, 1968. **12**: pp. 611-614.
12. Najm, H. N., Paul, P. H., Mueller, C. J., and Wyckoff, P. S., *On the Adequacy of Certain Experimental Observables as Measurements of Flame Burning Rate.* Combustion and Flame, 1998. **113**: pp. 312-332.
13. Luque, J., Jeffries, J. B., Smith, G. P., Crosley, D. R., Walsh, K. T., Long, M. B., and Smooke, M. D., *CH(A-X) and OH(A-X) Optical Emission in an Axisymmetric Laminar Diffusion Flame.* Combustion and Flame, 2000. **122**.
14. Higgins, B., McQuay, M. Q., Lacas, F., Rolon, J. C., Darabiha, N., and Candel, S., *Systematic Measurements of OH Chemiluminescence for Fuel-Lean, High-Pressure, Premixed, Laminar Flames.* Fuel, 2001. **80**: pp. 67-74.
15. Higgins, B., McQuay, M. Q., Lacas, F., and Candel, S., *An Experimental Study on the Effect of Pressure and Strain Rate on CH Chemiluminescence of Premixed Fuel-Lean Methane/Air Flames.* Fuel, 2001. **80**: pp. 1583-1591.
16. Kojima, J., Ikeda, Y., and Nakajima, T., *Spatially Resolved Measurements of OH*, CH*, and C_2* Chemiluminescence in the Reaction Zone of Laminar Methane/Air Premixed Flames*. in

International Combustion Symposium. 2000.

17. Kauranen, P., Andersson-Engels, S., and Svanberg, S., *Spatial Mapping of Flame Radical Emission Using a Spectroscopic Multi-Colour Imaging System.* Appl. Phys. B, 1991. **53**: pp. 260-264.

18. Yoshida, A., Narisawa, M., Tsuji, H., and Hirose, T., *Chemiluminescence Emission of C_2, CH and OH Radicals from Opposed Jet Burner Flames.* JSME International Journal, Series B, 1995. **38**: pp. 222-229.

19. Ikeda, Y., Kojima, J., and Nakajima, T., *Chemiluminescene Based Local Equivalence Ratio Measurement in Turbulent Premixed Flames*. in *40th Aerospace Sciences Meeting and Exhibit.* 2002. Reno, NV.

20. Watson, K. A., Lyons, K. M., Donbar, J. M., and Carter, C. D., *Scalar and Velocity Field Measurements in a Lifted CH_4-Air Diffusion Flame*. Combustion and Flame, 1999. **117**: pp. 257-271.

21. Renfro, M. W., Gore, J. P., King, G. B., and Laurendeau, N. M., *Self-Similarity of Hydroxyl-Concentration Temporal Statistics in Turbulent Nonpremixed Jet Flames.* AIAA Journal, 2000. **38**: pp. 1230-1236.

22. Renfro, M. W., Sivathanu, Y. R., Gore, J. P., King, G. B., and Laurendeau, N. M. *Time-Series Analysis and Measurements of Intermediate-Species Concentration Spectra in Turbulent Non-Premixed Flames*. in *Twenty-Seventh Symposium (International) on Combustion*. 1998. Boulder, CO (USA): The Combustion Institute.

VII. FIGURES

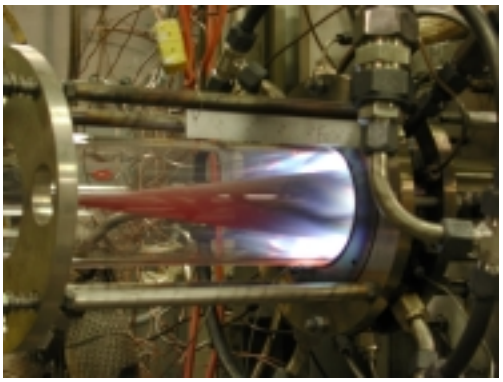

Figure 1. Model combustor used in emission study. The fiber probes were inserted through the fore wall of the annular cavity.

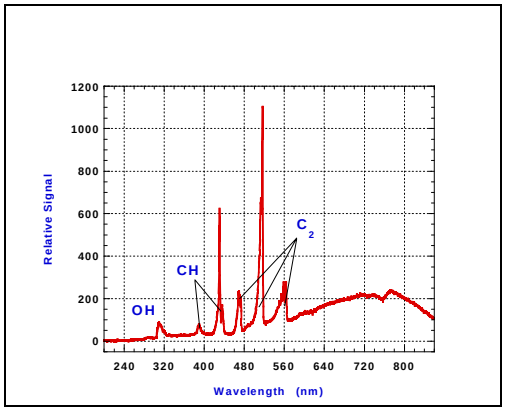

Figure 2. Emission spectrum acquired in the inter-turbine burner test rig at a local equivalence ratio of ~ 1.5.

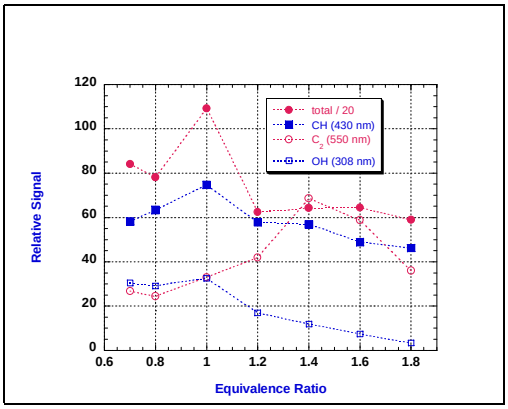

Figure 3. Emission signals from laminar propane/air flame.

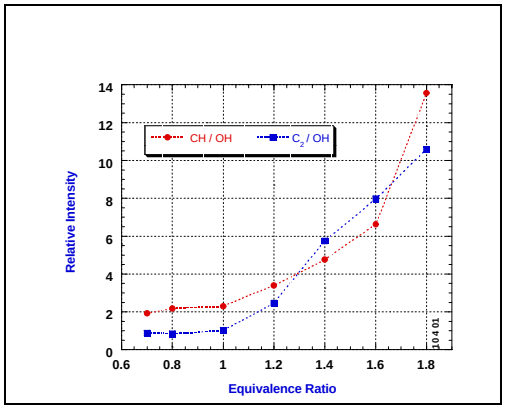

Figure 4. Emission signal of CH* (435 nm) and C_2* (550 nm) ratioed to OH* (308 nm).

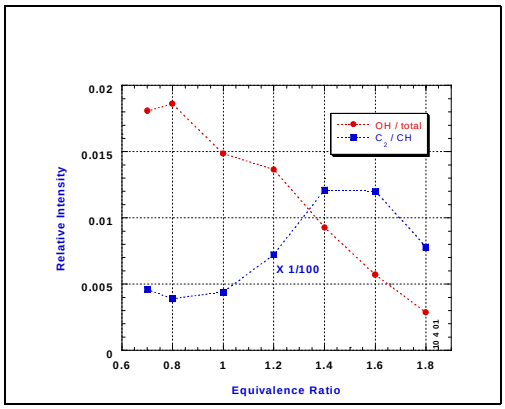

Figure 5. Emission signal from C_2* (550 nm) normalized to CH* (435 nm) and OH* emission normalized to the total emission—molecular plus broadband.

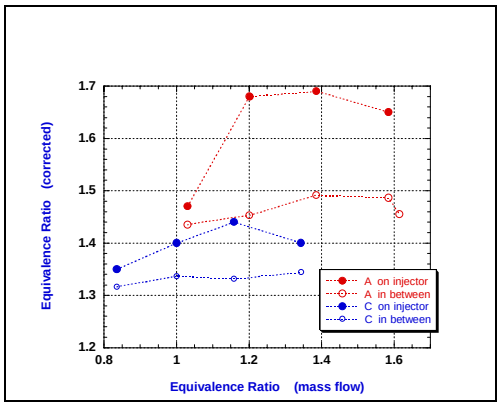

Figure 6. Corrected equivalence ratios based on averaged CH*/OH* emission intensities for signals collected in the model combustor. A and C denote pressure drops across the injectors of 2% and 3%, respectively.

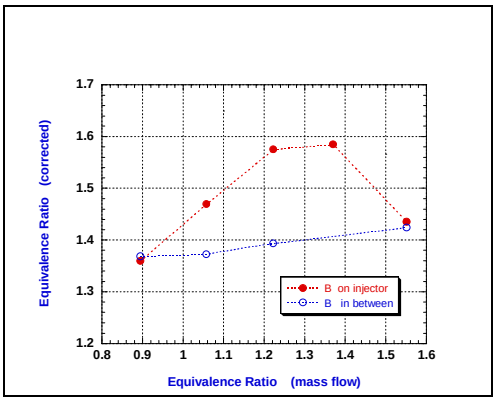

Figure 7. Same as in Figure 6 for a pressure drop of 2.3%.

Dual-Pump Dual-Broadband Coherent Anti-Stokes Raman Scattering For The Measurement of Temperature and Multiple Species Concentrations

Sukesh Roy, Terrance R. Meyer, and Michael S. Brown
Innovative Scientific Solutions, Inc.

Robert P. Lucht
Purdue University

James R. Gord, Vincent M. Belovich, and Edwin Corporan
Air Force Research Laboratory, Propulsion Directorate

This is a collaborative work between ISSI, Purdue University and Air Force Research Laboratory. The objective of this work is to demonstrate the application of dual-pump dual-broadband (or dual broadband triple-pump CARS) CARS measurement in reacting flows. DPDB CARS technique allows us to detect temperature and the concentration of three species simultaneously.

Motivation

Simultaneous single-shot measurements of temperature and species concentrations (Both at Low and High Temperatures)

↓

Measurement of performance and efficiency

↓

Characterization of advanced propulsion system

The motivation for this experiment is to get the information of temperature and the concentration of three species simultaneously from a single laser-shot. These measurements allow us to evaluate the efficiency of the combustion system which in turn helps to characterize advance propulsion system.

Significance

- **Monitoring of temperature and three species simultaneously with a single hardware platform**
- **Provides accurate temperatures both at low and high temperatures**
- **Minimizing the number of diagnostics**
- **High spatial and temporal resolution**
- **Simultaneous acquisition of single-shot spectra in two spectral regions will provide better temperature accuracy in dynamic reacting flows**

The main advantage of DPDB CARS system is that you can monitor the temperature and the concentration of three species using single hardware platform.

Another advantage of this technique is that, it provides accurate measurements both at low and high temperatures.

This technique will allow us to get all the required information form reacting flows with minimum number of diagnostics.

The CARS technique will provide the required spatial and temporal resolution.

In DPDB CARS we acquire signal at two different spectral region of the spectrum. Simultaneous acquisition of single-shot spectra at two different spectral regions will provide better temperature accuracy in dynamically reacting flows.

Combustor Test Facilities

Goal: execute measurements in combustion hardware test stands

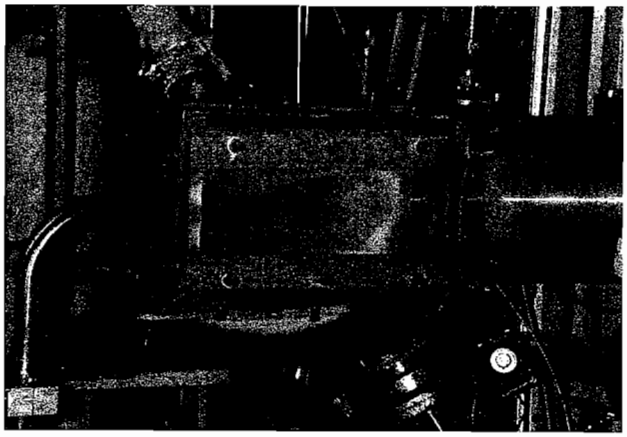

The picture shows the photograph of a GE CFM-56 gas turbine combustor. The ultimate goal is to apply this technique in a real gas turbine combustor rig like this one at Wright-Patterson AFB.

Features of CARS

Advantages

- **Non-invasive Technique**
- **Coherent (laser-like) signal (good background discrimination)**
- **Spatially and temporally resolved**
- **Excellent temperature measurement technique**

–Like all laser-based techniques CARS is a non-invasive technique: this allows us to diagnose reacting flows without disturbing the flow chemistry

- In CARS, the signal comes out as a coherent laser-like signal which is advantageous for discriminating the signal against highly luminous flame emission i.e., better signal-to-noise ratio (SNR)

-With CARS high spatial and temporal resolution are achievable. Spatial resolution of approximately 25 micron is achieved. The temporal resolution is limited by the laser repetition rate.

- CARS is an excellent temperature measurement technique with an accuracy of ± 2%

Features of CARS

Disadvantages

- **Not very sensitive (concentrations > 1%)**
- **Complex**
- **Spatial resolution along beam path is ~2 mm**

CARS is applicable only to detect molecules with high concentrations and the technique is not sensitive for the detection trace gas molecules due to inherent non-resonant background signal generation.

It is a very complex technique especially compared to Laser Induced Fluorescence (LIF)

Spatial resolution along the beam path is approximately 2 milimeters.

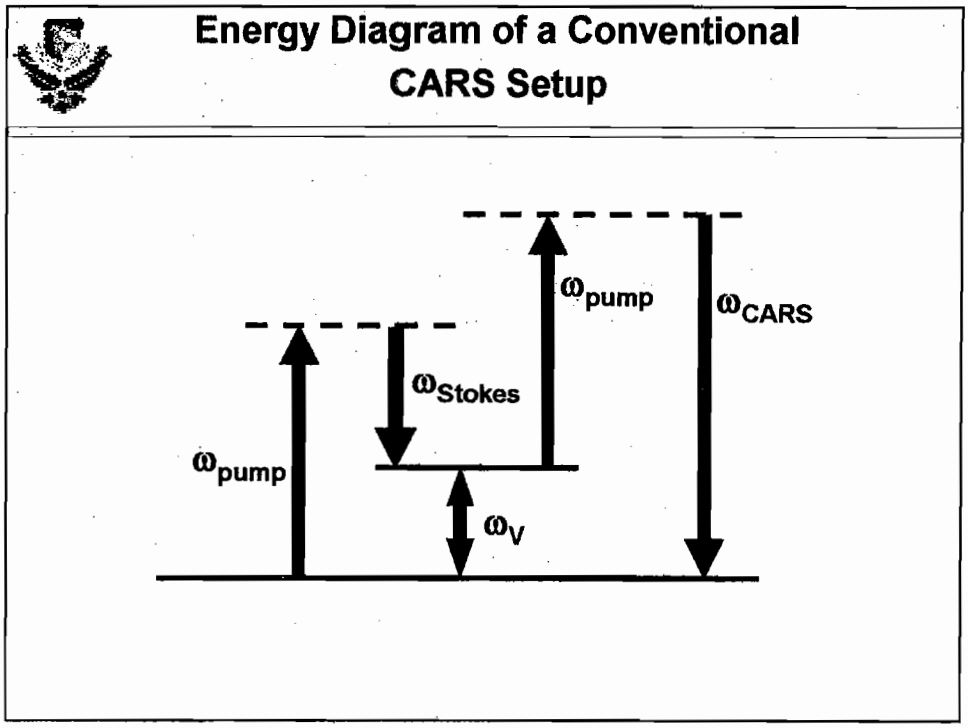

In conventional CARS, a single-longitudinal-mode (SLM) laser provides the two pump beam and a broadband dye laser provides the Stokes' beam. A polarization is induced in the medium when the frequency difference between the pump and the Stokes beam become equal to the vibrational frequency of the probe molecule. The second pump beam then scatters of the molecule at a shifted frequency, which is the CARS signal. In Conventional CARS we get the information about temperature and the concentration of one species from a single laser shot. Now we will see what happens when the two pump beam become different.

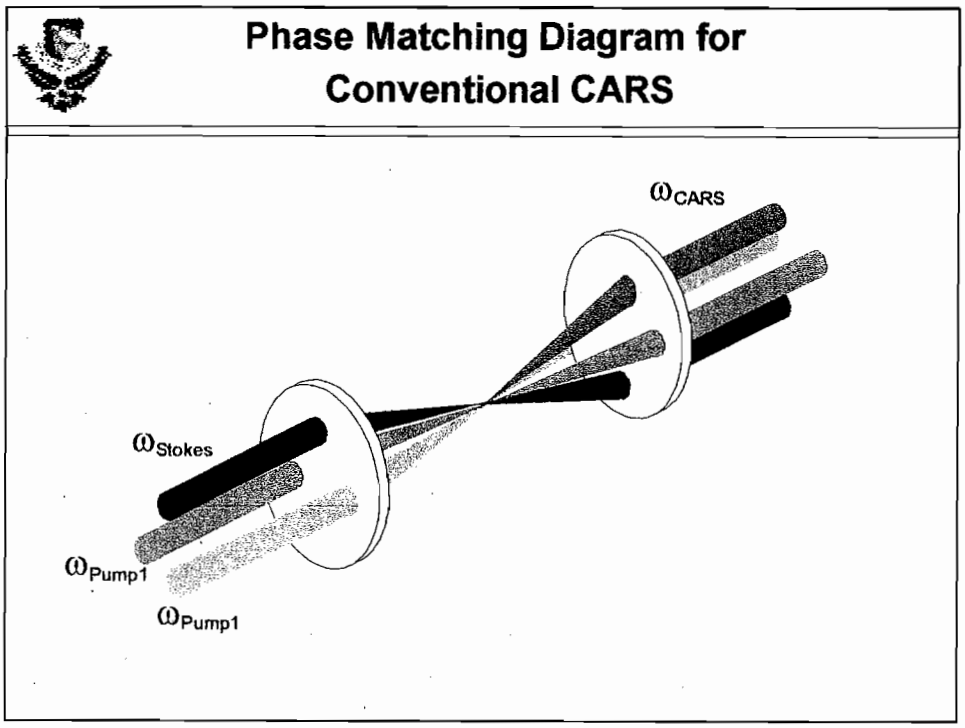

This is a three-dimensional phase-matching diagram of the folded-box CARS system.

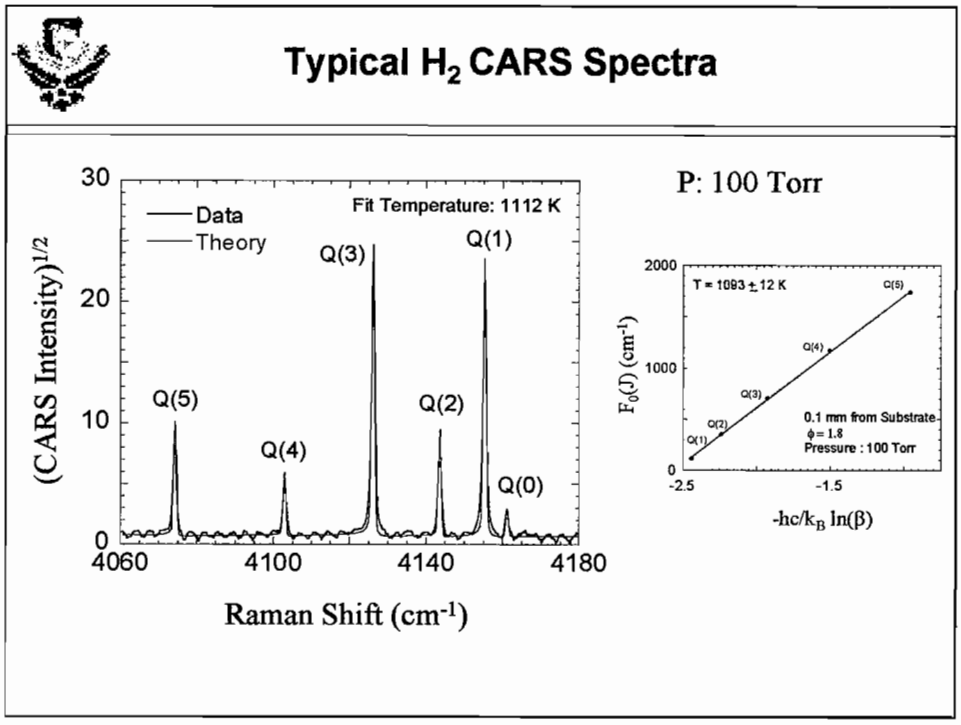

This is a typical Hydrogen CARS spectrum taken in a low-pressure diamond-forming flame. The temperature from the CARS spectra can be evaluated either by fitting a theoretical CARS spectra with the experimental one or by means of a Boltzmann plot. If the spectral lines are well isolated like hydrogen CARS spectrum, then Boltzmann plots are sufficient to evaluate the temperature. A typical Boltzmann plot for the CARS spectrum is shown on the right hand side.

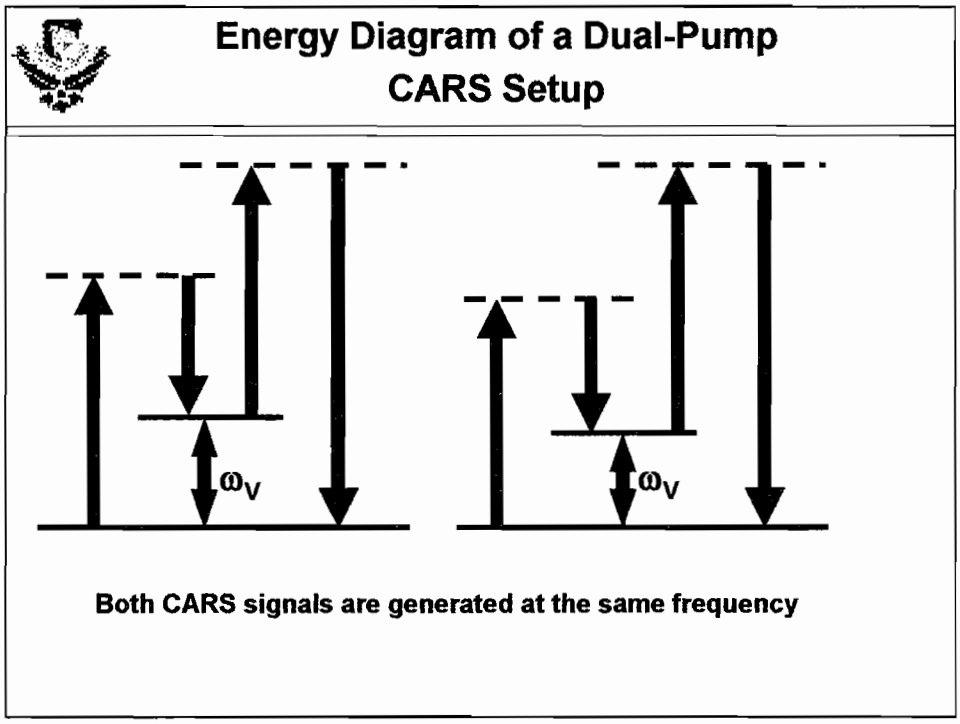

In dual-pump CARS we get the concentration of two species and temperature from a single laser shot. Here instead of using the same pump beam, two different pump beams are used in such a way that the frequency difference between each pump beam and the Stokes' beam become equal to the vibrational frequency of the two molecules being probed. Each molecule then scatter the other pump beam at a shifted frequency. The main advantage of dual pump CARS is that the both CARS signals generate at the same frequency. This completely eliminate the needs of using two different detector or correcting the signal for detector efficiency at different wavelengths.

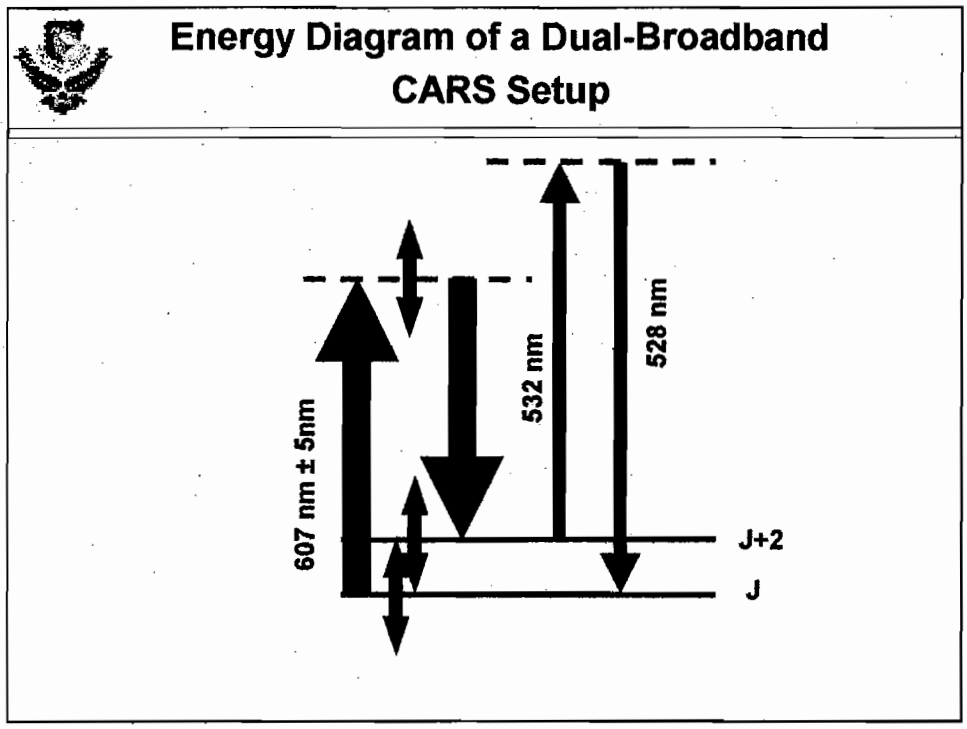

Most of the broadband dye laser has a bandwidth of the order of 200 -400 cm^{-1}. This bandwidth is wide enough to excite the rotational transitions of several molecules simultaneously.

Here the same BB dye laser acts both as a pump beam and as a Stokes beam.

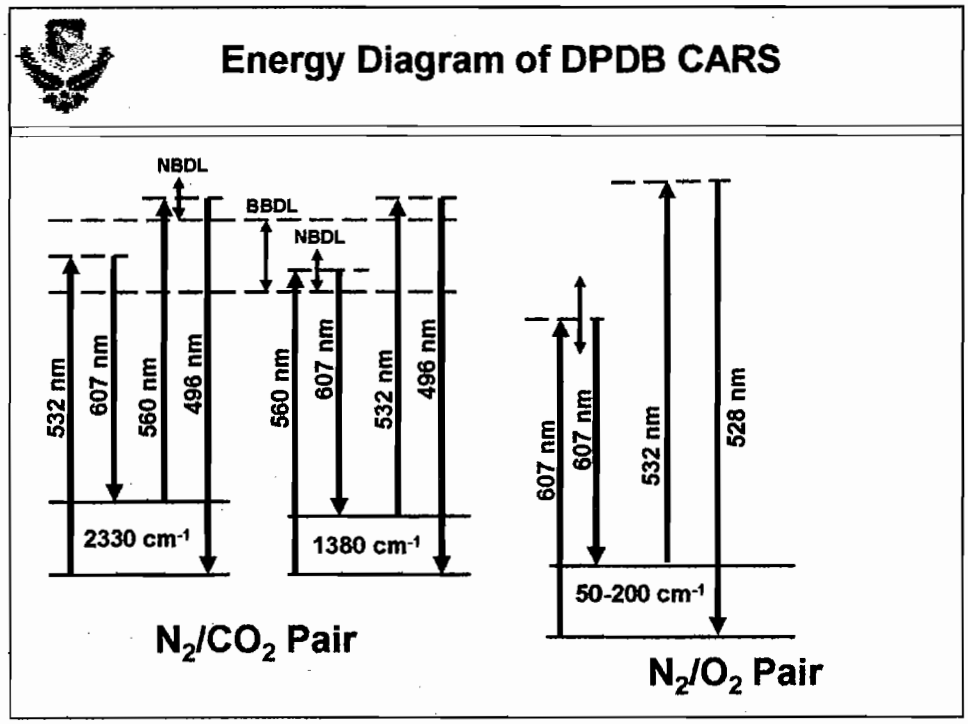

DPDB CARS is essentially a dual pump CARS system superimposed on top of a dual-broadband rotational CARS system. This is an energy diagram for N2, CO2 and O2 molecules. As evident from the energy diagram, that nitrogen CARS signal is generating at two different wavelength. By comparing the single-shot nitrogen spectra acquired at these two different wavelength we would be able to improve the accuracy of temperature measurements using single-shot CARS measurements in dynamic reacting flows.

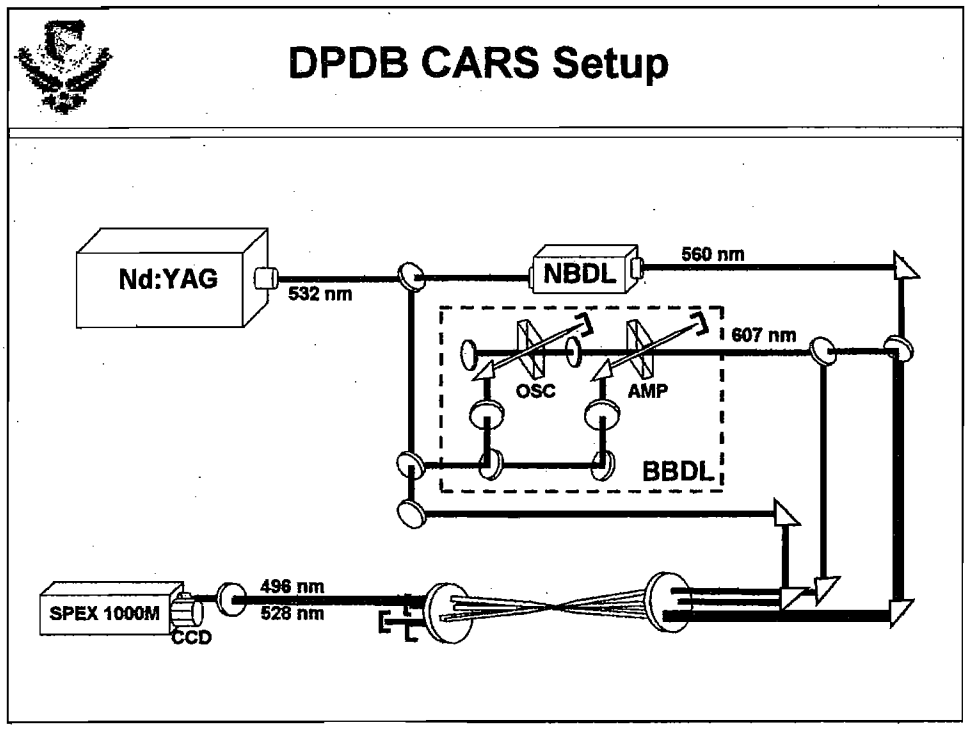

This is a schematic diagram of the DPDB CARS system. Here 532-nm output beam from the YAG laser is used to pump a narrowband dye laser and a broadband dye laser. The narrowband dye laser provide one pump beam and the 532-nm beam acts as the second pump beam. The broadband dye laser provides the pump beam for the rotational CARS system also the Stokes's beam for both CARS system. In this setup CARS signals are generated at 496 nm and 528 nm. These two signals are separated with a dichroic and detected with two back-illuminated unintensified CCD camera after dispersing with a 1-m spectrometer.

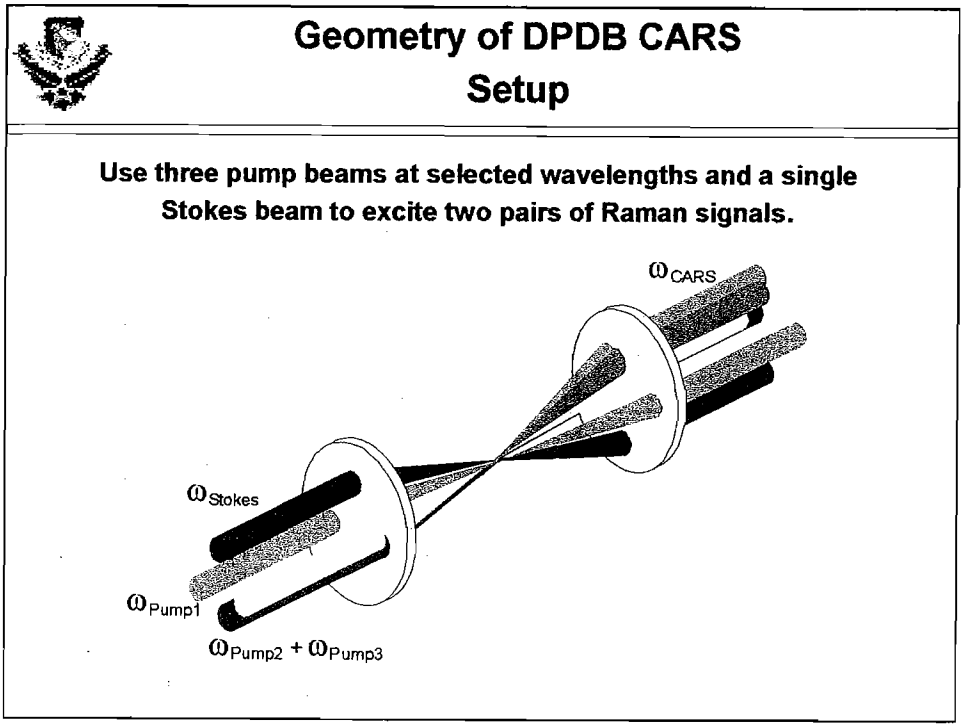

The phase-matching diagram for the DPDB CARS experiment is shown here. The incident beams are phase-matched using the folded boxcars geometry with the 560-nm and 607-nm beams arranged co-linearly. The laser beams were focused and re-collimated using 500- mm focal-length lenses.

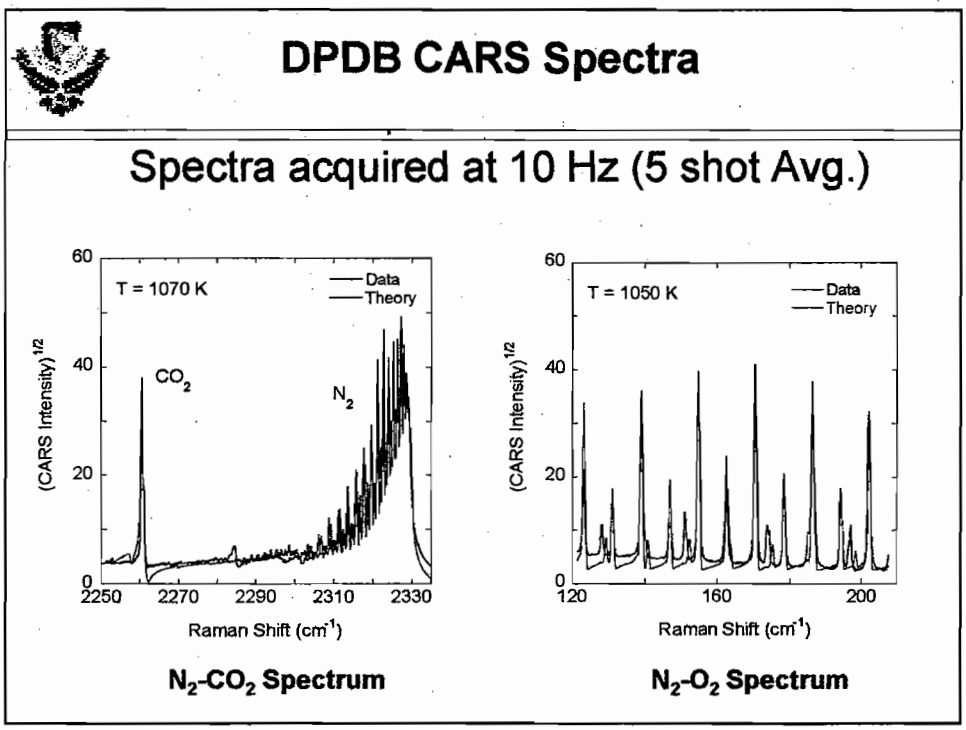

Single-shot and averaged nitrogen-CO2 CARS spectra are shown here.

The figure shows an N2-CO2 CARS spectrum (average of 100 laser shots) generated near 496 nm and acquired 7 mm above the Hencken burner. This spectra is acquired in a lean hydrogen-air flame seeded with carbon dioxide.

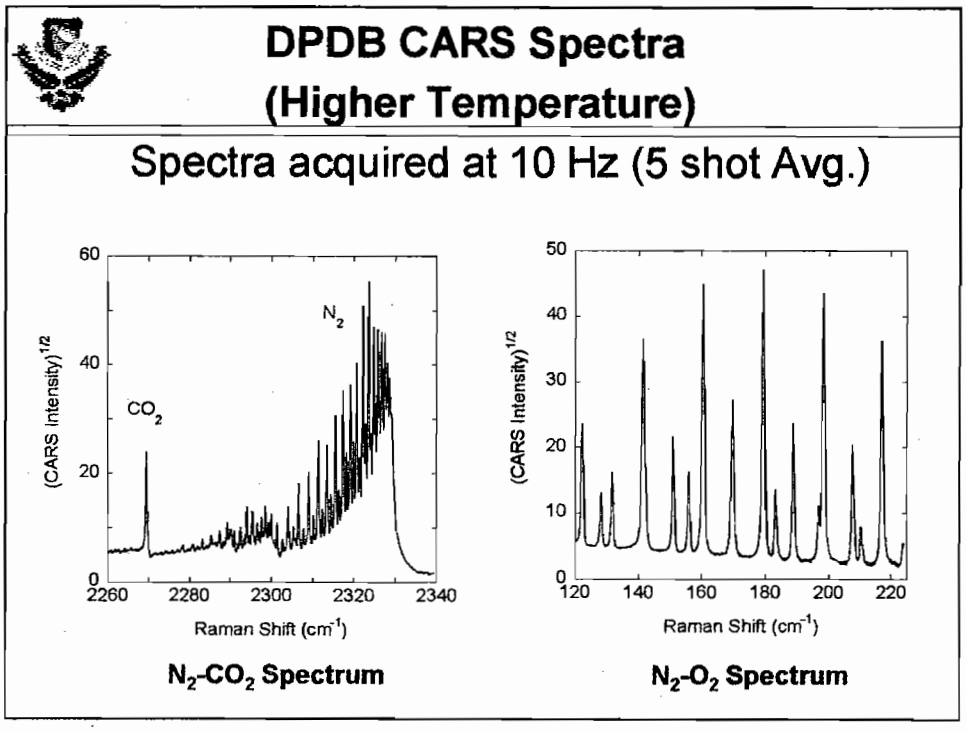

Single-shot and averaged nitrogen-CO2 CARS spectra are shown here.

The figure shows an N2-CO2 CARS spectrum (average of 100 laser shots) generated near 496 nm and acquired 7 mm above the Hencken burner. This spectra is acquired in a lean hydrogen-air flame seeded with carbon dioxide.

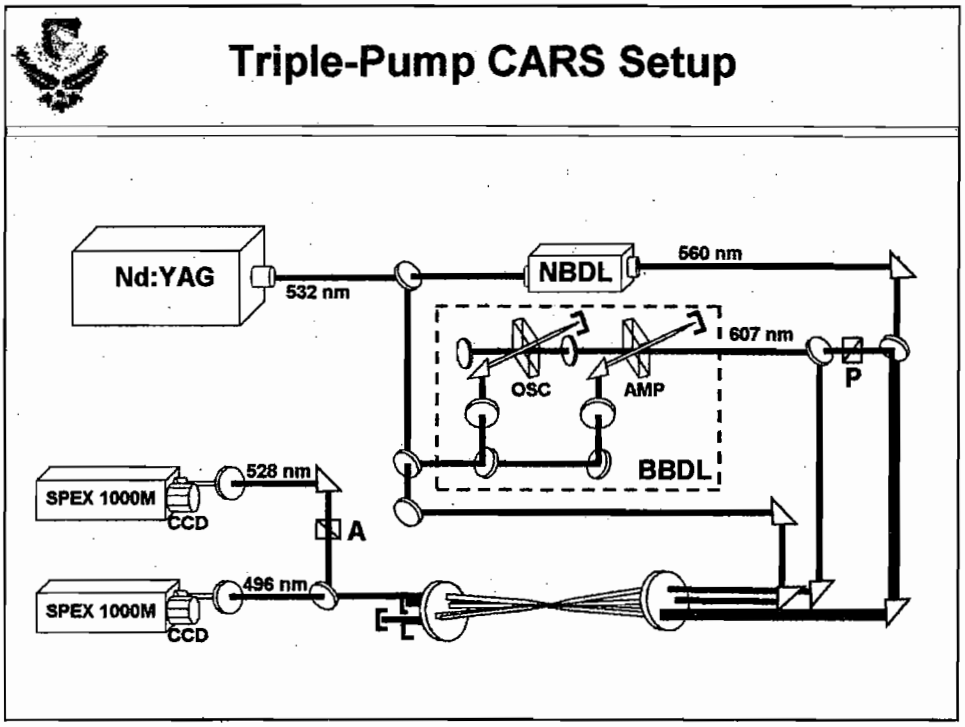

This is a schematic diagram of the DPDB CARS system. Here 532-nm output beam from the YAG laser is used to pump a narrowband dye laser and a broadband dye laser. The narrowband dye laser provide one pump beam and the 532-nm beam acts as the second pump beam. The broadband dye laser provides the pump beam for the rotational CARS system also the Stokes's beam for both CARS system. In this setup CARS signals are generated at 496 nm and 528 nm. These two signals are separated with a dichroic and detected with two back-illuminated unintensified CCD camera after dispersing with a 1-m spectrometer.

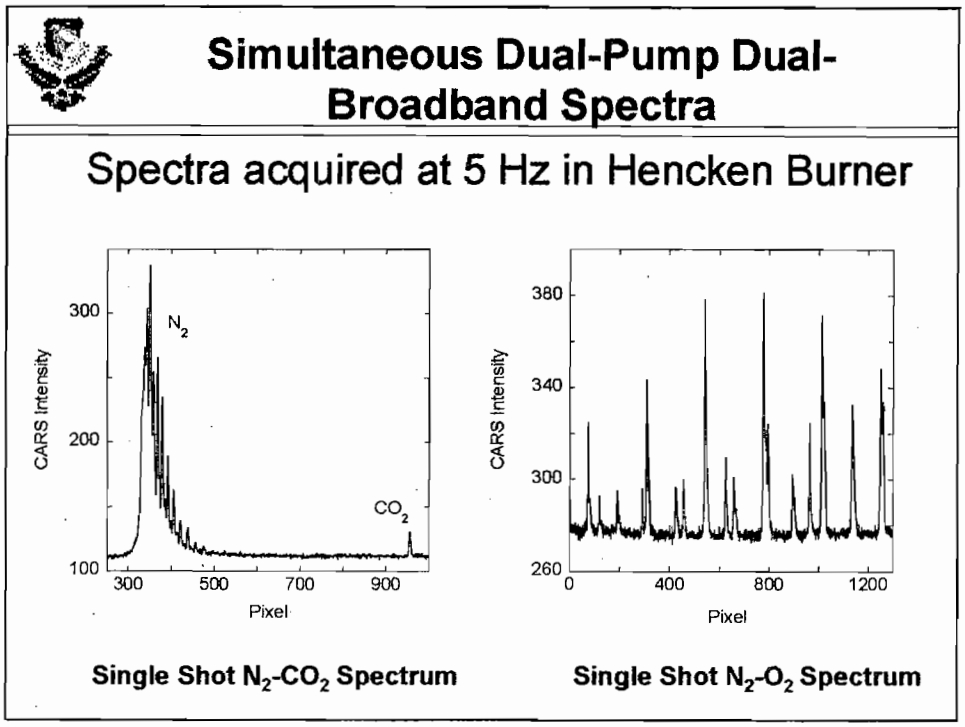

The rotational spectra of nitrogen and oxygen are shown here.

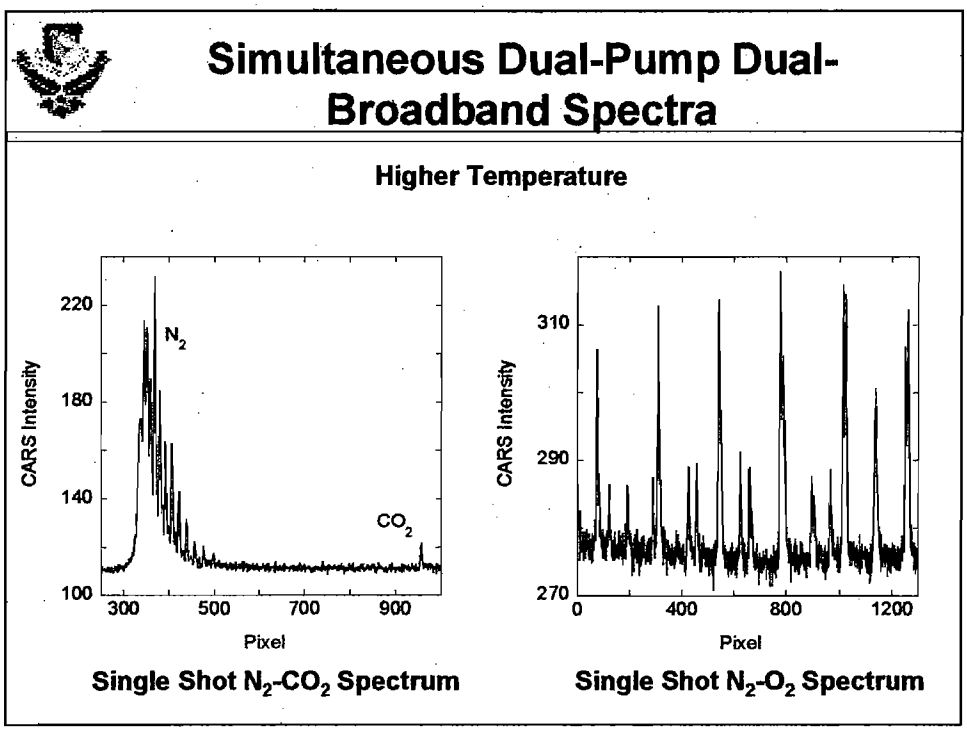

The rotational spectra of nitrogen and oxygen are shown here.

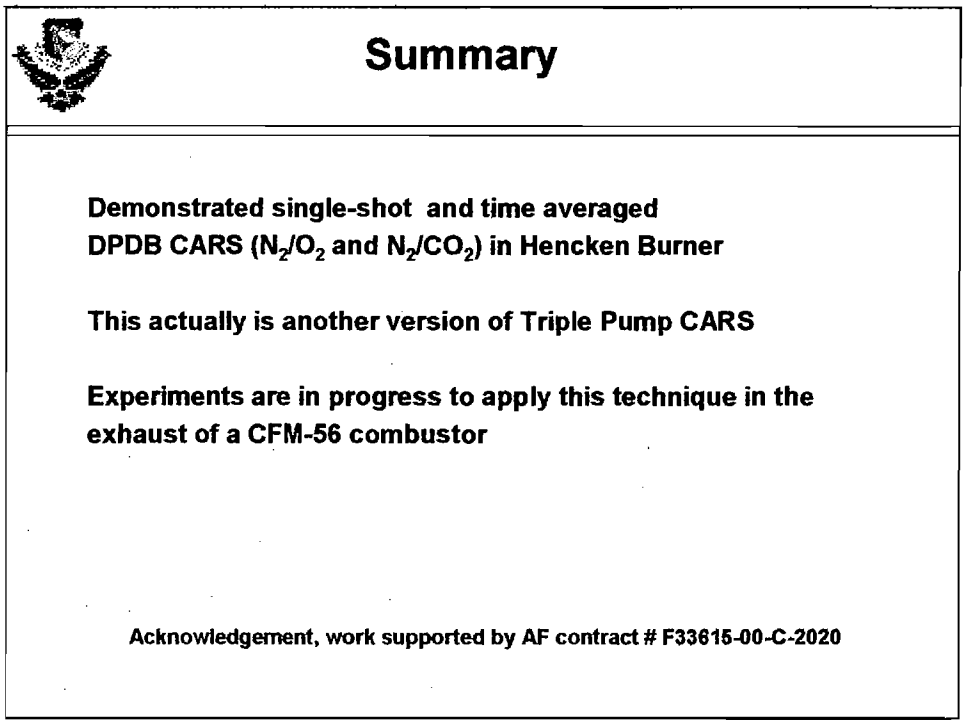

The DPDB CARS technique was demonstrated through simultaneous acquisition of N2-O2 and N2-CO2 spectra in an atmospheric-pressure hydrogen-air premixed flame seeded with CO2. This technique provides measurements of temperature along with concentrations of two target species.

Studies of Ignition and Vortex-Flame Interaction in a Starting Jet

T.R. Meyer, J.R. Gord,
V.R. Katta, W. M. Roquemore,
G.L. Switzer, and G.J. Fiechtner

ISSI / PRTS
Air Force Research Laboratory

26th Annual Dayton-Cincinnati Aerospace Science Symposium
March 30, 2001

Background and Motivation

- High-speed combustors demand fast and reliable ignition.
- Vortices found to be effective "flame holders" (e.g. trapped vortex, pulsed combustion).
- Vortices greatly enhance mixing and reaction.
- Flame propagation in vortex rings also useful for basic combustion studies.

Objectives

- Evaluate feasibility of vortex-assisted ignition.
- Generate well-controlled vortex ignition and combustion events.
- Study effects of equivalence ratio, spark timing, and vortex strength.
- Perform OH and acetone PLIF.
- Compare with direct numerical simulations (DNS).

Jet-in-Co-Flow Burner

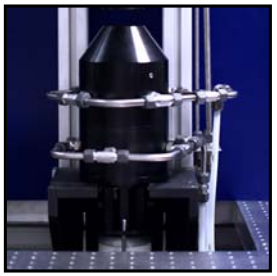

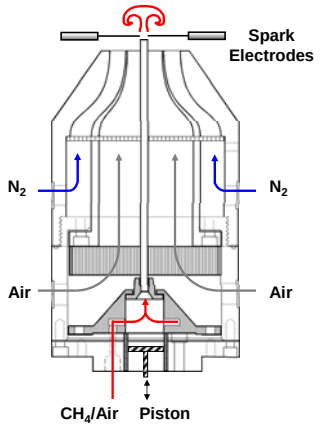

Experimental Facility

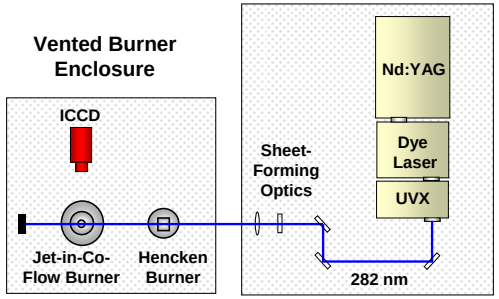

OH Absorption Spectrum
1-0 Band of the A-X System

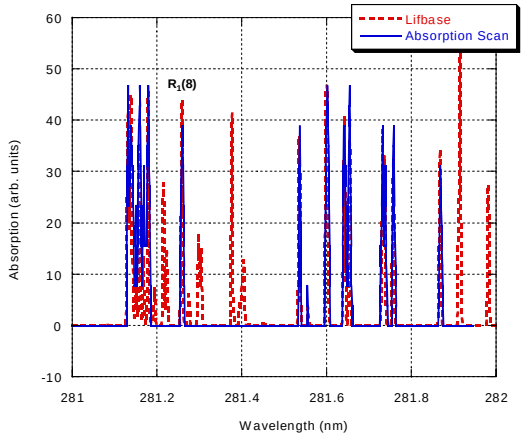

Timing and Electronics

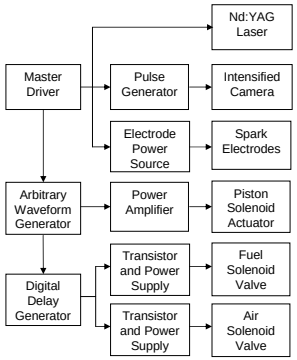

Operating Conditions

Ignition Timing (ms)*	Equivalence Ratio	Piston Stroke (mm)	Vortex Velocity (m/s)
2.5	1.0	3.3	5
4	0.75, 1.0, 1.25, 1.5	3.3	5
4	1.0	1.6	2.5
5	1.0	5	6.5
6	1.0	1.6, 3.3, 5	2.5, 5, 6.5
8	1.0	3.3	5

* Relative to piston actuation

Cold-Flow Vortex Propagation

ISSI

Vortex 1:
Piston Stoke of 1.6 mm

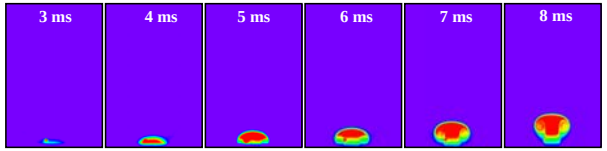

Vortex 2:
Piston Stoke of 3.3 mm

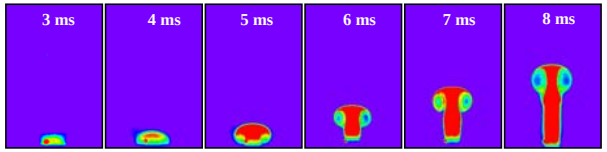

Vortex 3:
Piston Stoke of 5 mm

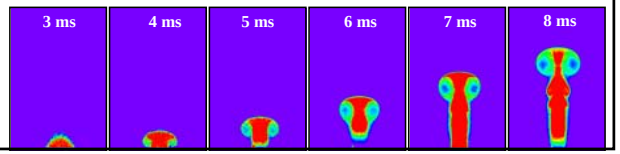

Interior Flame Propagation

Phi = 1, Vortex 2, Spark at 6 ms

ISSI

OH PLIF

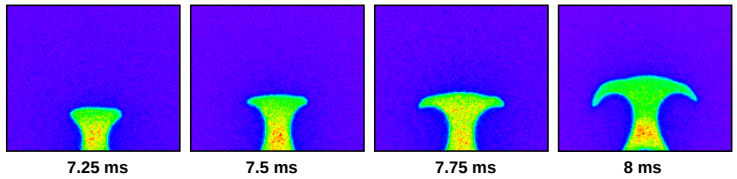

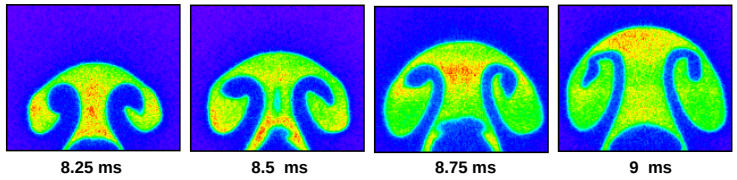

Bridging of Exterior Flame

Phi = 1, Vortex 2, Spark at 4 ms

ISSI

OH and Acetone PLIF

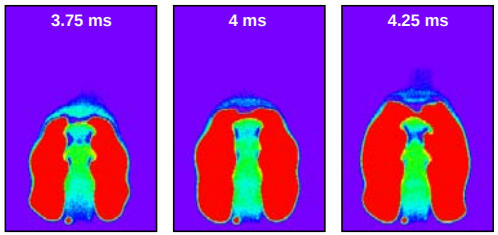

Comparison with DNS

Phi = 1, Vortex 1

ISSI

Experiment

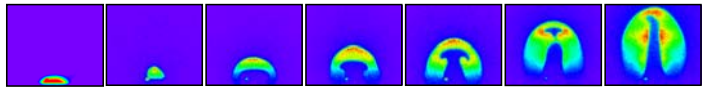

Simulation

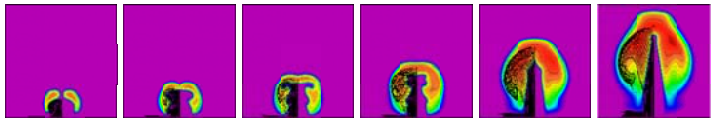

Effect of Spark Timing
Phi = 1, Vortex 2

ISSI

Spark at 2.5 ms

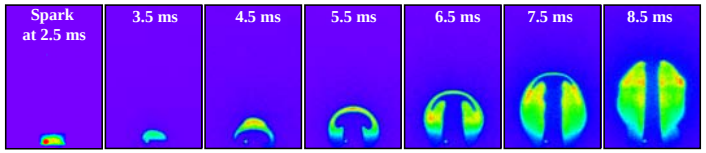

Spark at 4 ms

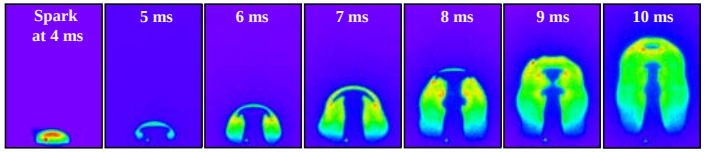

Effect of Spark Timing
Phi = 1, Vortex 2

ISSI

Spark at 6 ms

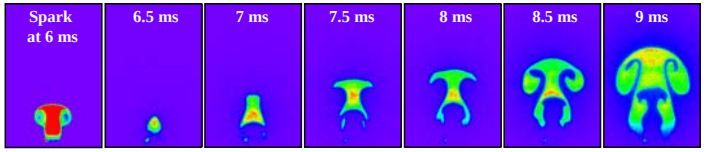

Spark at 8 ms

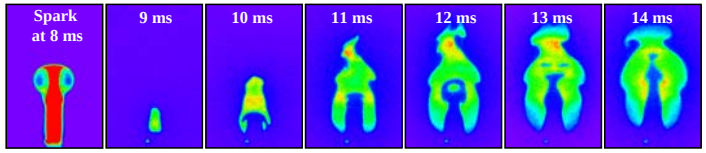

Effect of Equivalence Ratio
Vortex 2, Spark at 4 ms

ISSI

Phi = 0.75

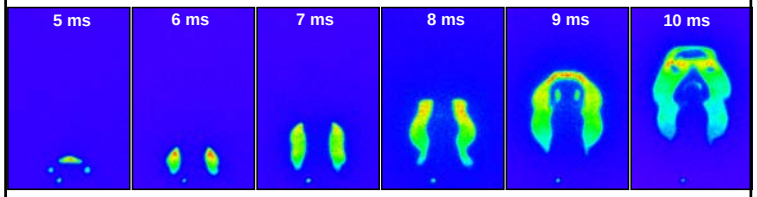

Phi = 1.0

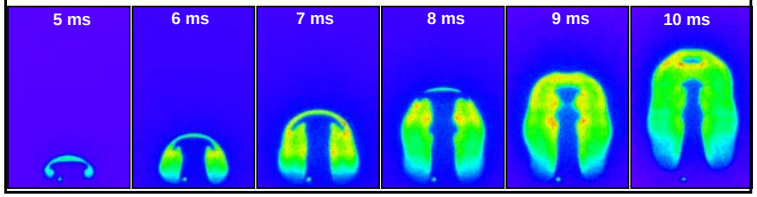

Effect of Equivalence Ratio
Vortex 2, Spark at 4 ms

ISSI

Phi = 1.25

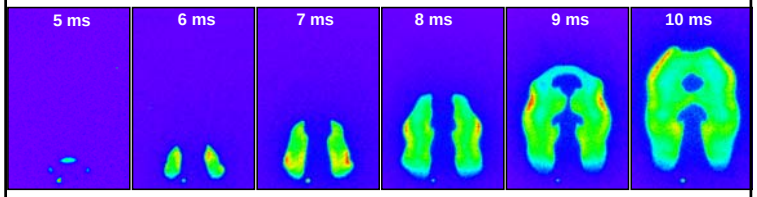

Phi = 1.5

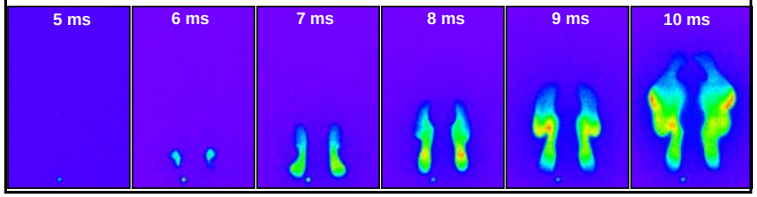

Effect of Vortex Strength

ISSI

Vortex 1

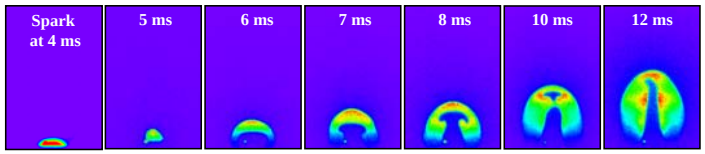

Vortex 2

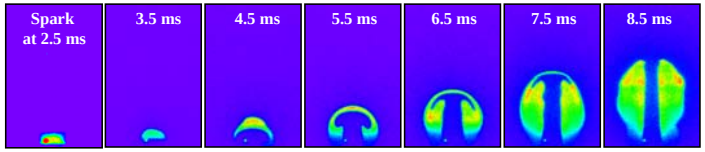

Effect of Vortex Strength

ISSI

Vortex 2

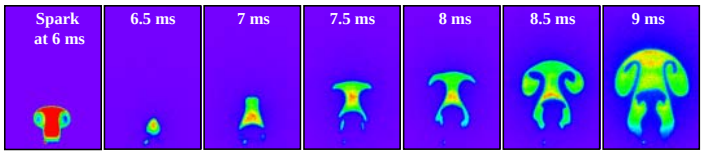

Vortex 3

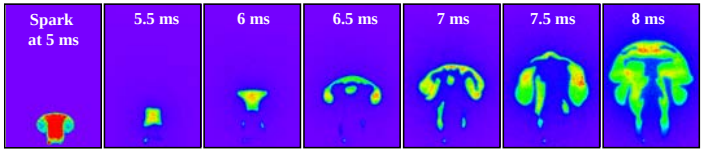

Conclusions

ISSI

- Ideal vortex ignition possible only under certain conditions.
- Spark timing leads to either interior or exterior flame propagation.
- Ideal flame entrainment and product formation at stoichiometric conditions.
- Vortex ignition possible at high vortex strengths and high jet velocities.
- Preliminary DNS results promising.

Future Work

ISSI

- Measurement of velocity using PIV to set DNS conditions.
- Study Lewis number effects and test DNS performance with different fuels.
- Quantify product formation.
- Two-camera visualization of cold vortex and flame regions.

VELOCITY MEASUREMENTS IN MILLIMETRIC AREAS
(millimetric DPIV)

Jordi Estevadeordal,(1) William W. Copenhaver,(2)

(1) Innovative Scientific Solutions Inc., 2766 Indian Ripple Rd., Dayton, OH 45440, USA
E-mail: jordi@innssi.com
(2) AFRL/PRTF, Bldg. 18; 1950 Fifth St., Wright-Patterson AFB, OH 45433-7251, USA
E-mail: william.copenhaver@wpafb.af.mil

MOTIVATION

- A flow-control system for a high-turning-stator cascade is investigated using **PIV**.
- The system employs small **(millimetric) blowing and suction** cavities and holes.
- Objective is perform velocity measurements in these small areas and in the **boundary layer** to complement *simultaneous* **standard PIV** and conventional pressure and temperature measurements.
- Issues include **volumetric illumination, sharp DOF, image processing and Digital Holography.**

Example of flow-control configuration within the cascade blade

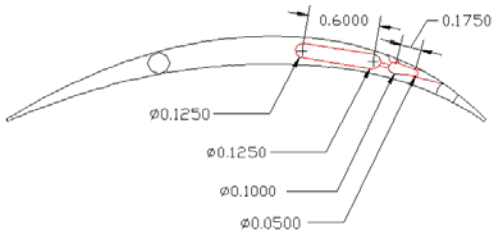

CFD

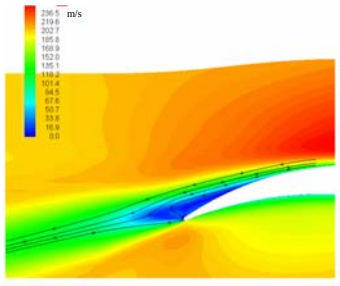

Without Flow Control

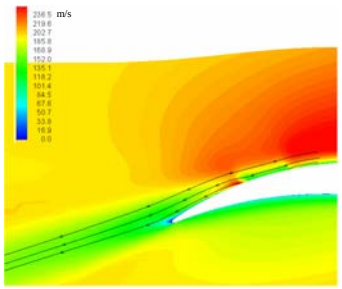

With Flow Control
(.8 Motive, 1.2 Blow)

STANDARD PIV (Macro Views)

Schematic of DPIV setup for cascade velocity measurements

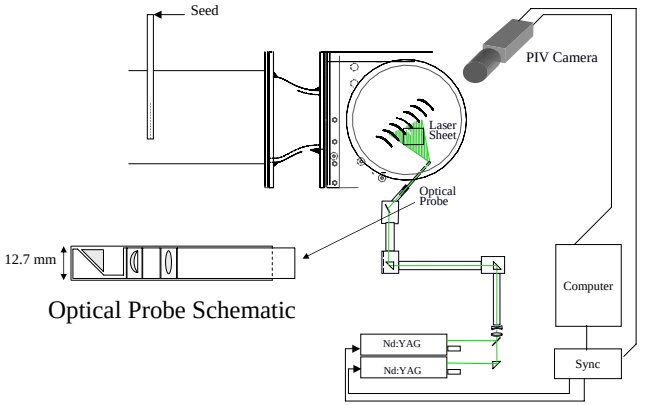

FLOW VISUALIZATION

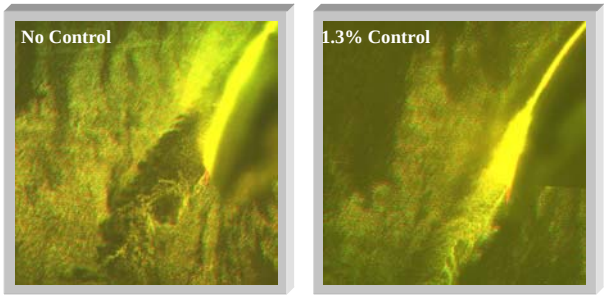

DPIV

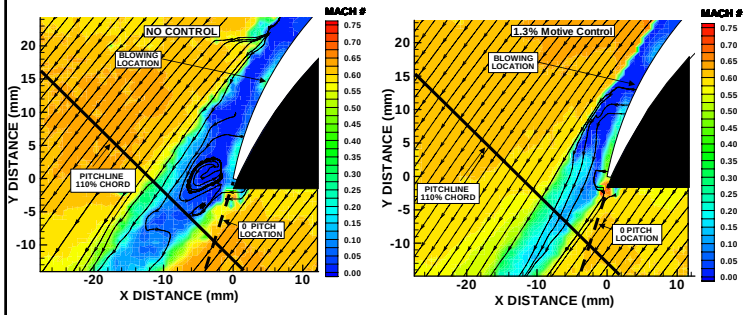

MILLIMETRIC PIV

(boundary layer, fluidic ports)

APPROACHES TO VELOCITY MEASUREMENTS IN MILLIMETRIC AREAS (blowing, suction, boundary layer)

- Volumetric Illumination
- Sharp DOF
- Partial-coherence
- Digital In-Line Holography

- Image processing (background substraction, images substraction, images multiplication, etc.) provides improvements in SNR and contrast
- Seeding strategy
- Bonuses: -high resolution with 1k x 1k CCD sensors
  -ambient light has negligible effect.

Volume Illumination with Sharp DOF

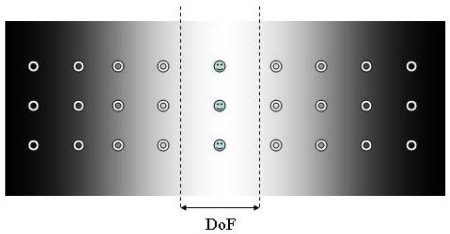

All particles in the illuminated volume scatter light but the diffraction pattern has a maximum intensity (Airy function) at the **focal plane of the lenses**. **DOF** is defined as a specified fraction of that maximum.

Ref: Meinhart et al. 2000 "Volume illumination for two-dimensional particle image velocimetry" *Meas. Sci. tech. 11, p. 809*

Milli-DPIV setup for *single-focused plane* with *Off-Axis* volume illumination

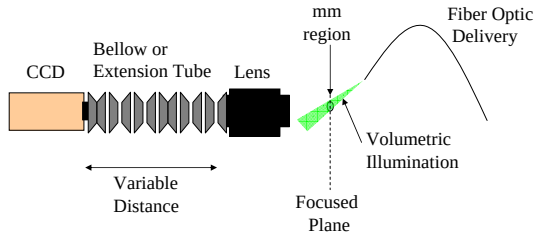

Effect of volume-illumination *direction* for a bubble emanating from a *2-mm*-diameter orifice

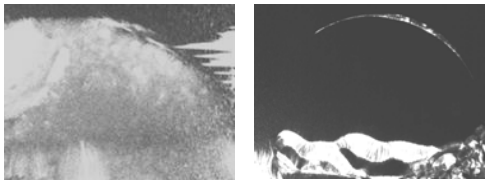

a b

The sharp focused plane is at the center of the bubble.
A few degrees off in-line produces speckle (a);
optimal value for single focused plane occurs for near-forward scattering
and occurs at few degress from forward (in-line) (b).

Volume Illumination with Sharp DOF: DPIV examples

Uniform flow (Res = 1000 pix/mm)

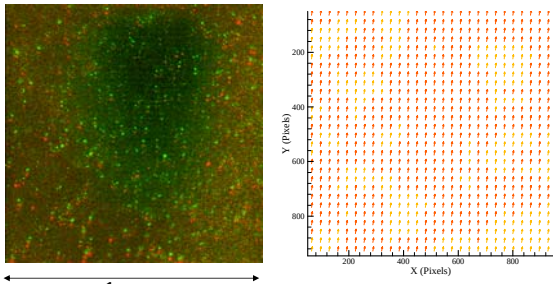

1 mm

Seed: 0.5 microns particles Vel Max = 1 m/s

Volume Illumination with Sharp DOF: DPIV examples

Jet (Res = 255 pix/mm)

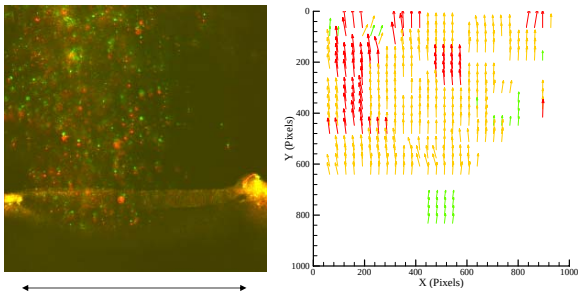

3 mm

Seed: 15 microns particles Vel Max = 30 m/s

A **3D** approach for **mill** and **micro** volumes:

digital holography

Digital In-line Holography (LEEPS)

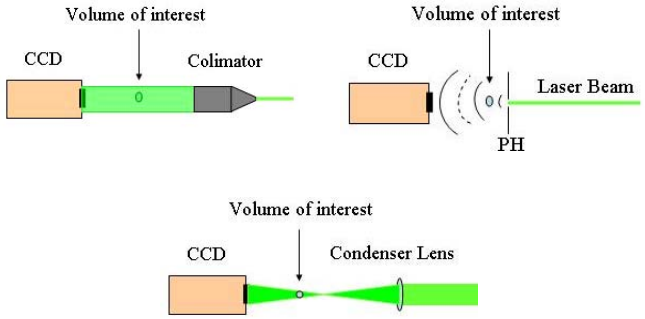

DIH reconstruction of 2mm bubble (b)

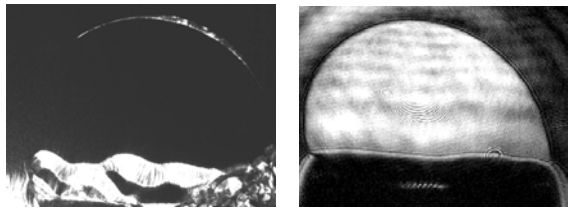

a b

single focused plane near-forward scattering (a) and DIH reconstruction of a similar bubble (b).

Digital In-line Holography: Numerical Interrogation

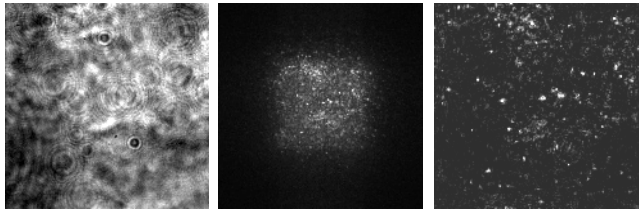

a b c

Interrogation of a **spray** hologram (a) from two different magnifications, showing the full spray (b) and a region inside (c).

Ref: Kreuzer et al 2001 "Digital in-line holography with photons and electrons" *J. Phys.:Cond. Matter 13, p. 10729*

Digital In-line Holography: PARTICLE SIZING

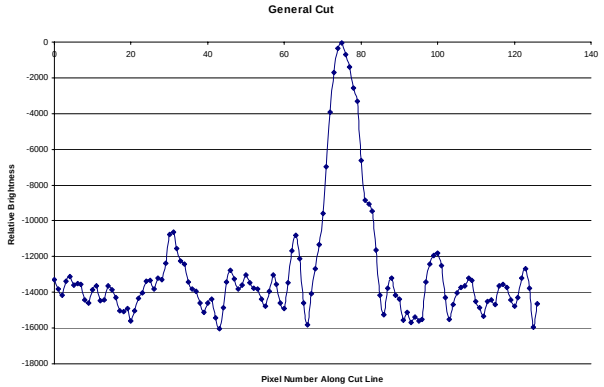

a cut through one plane to get an estimate of particle size: typically 5-10 microns

Digital In-line Holography: VELOCITY

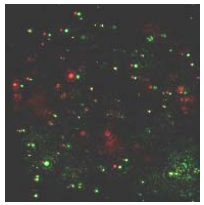

9 mm

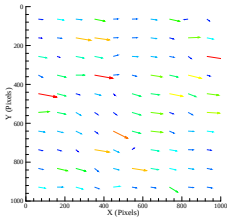

Conclusions

Approaches of Digital Particle Image Velocimetry (DPIV) in the mm range 'millimetric PIV' were introduced to complement Standard-PIV results aimed to study thin boundary layers and flow-control systems that employ small blowing cavities and suction holes in the blades.

Standard PIV (MACRO VIEWS) ⟷ Mill Metric PIV (MILL/MICRO VIEWS)

↓ ↓

Wake ⟷ Boundary layer, fluidics

PROGRESS AND RECENT ADVANCES IN PARTICLE IMAGE VELOCIMETRY

S. Gogineni and J. Estevadeordal
Innovative Scientific Solutions, Inc.
Dayton, OH 45440

J. R. Gord
Air Force Research Laboratory
Wright-Patterson Air Force Base, OH 45433

Outline

- Brief History
- Principle of PIV
- Two-Dimensional PIV
- Three-Dimensional PIV
- MicroPIV
- Summary

Brief History

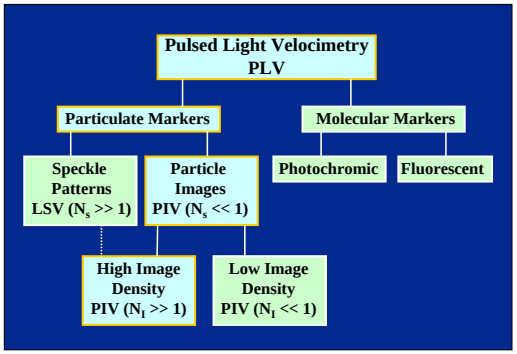

Principle of PIV

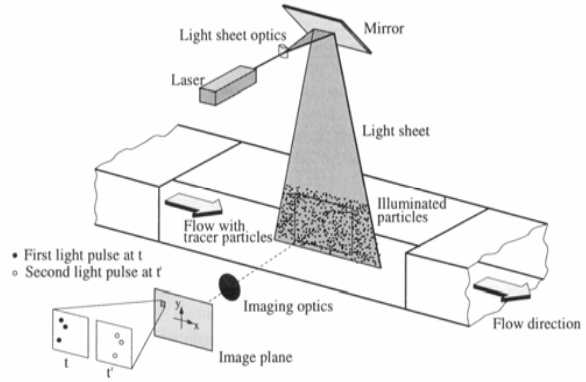

Components of PIV System

- Seeding
- Light Source
- Recording Devices
- Processing and Post-Processing

Stereoscopic PIV

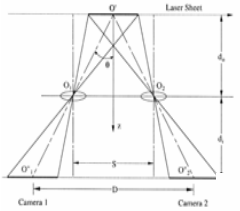

Translational System

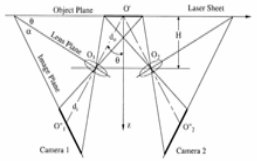

Angular Displacement System

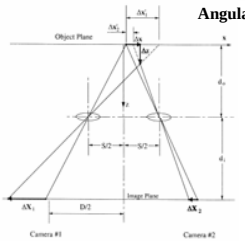

Geometrical configuration of cameras and particle shifts in a translational System (Prasad, 2000)

Angular Displacement Systems

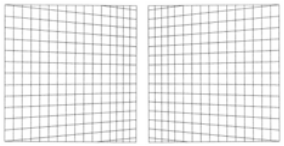

Distortions of left and right cameras due to Scheimpflug condition (Prasad & Jenson, 1995)

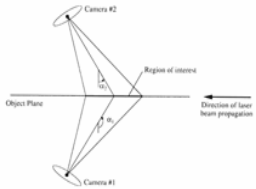

Alternative Scheimpflug condition implementation (Prasad, 2000)

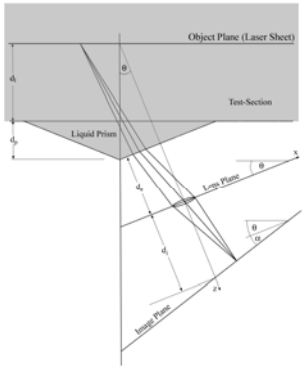

Usage of a liquid prism to eliminate distortions due to viewing through an air-liquid interface (Prasad & Jenson, 1995)

3-D Volumetric Measurements

Multiple Cameras – Triangulation Methods

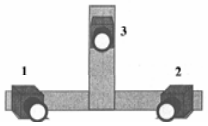

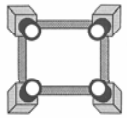

Various setups for 3-D triangulation methods using 3 cameras and 4 cameras

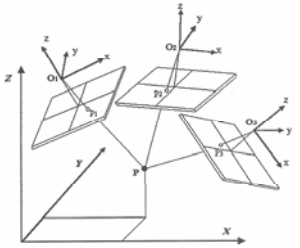

Perspective rays as seen from each of the three triangulation cameras

3-D Volumetric Measurements

Multiple Cameras – Defocusing Methods

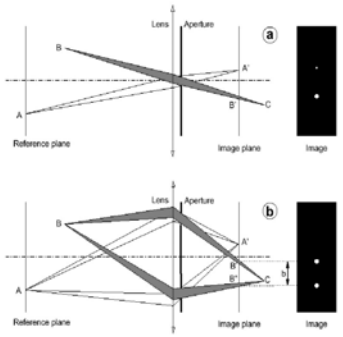

Defocusing concept for 3D Defocusing PIV (Pereira et al. 2000)

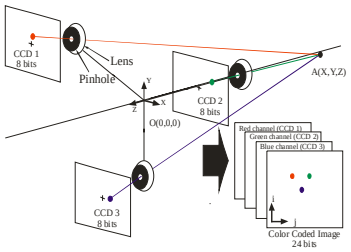

Defocusing PIV with the use of off-the-shelf hardware items (Pereira et al. 2000)

Principle of holography

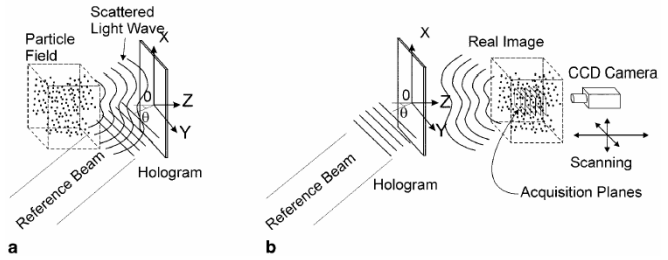

Principle of Holographic PIV. (a) recording (b) reconstruction

In-line holographic PIV

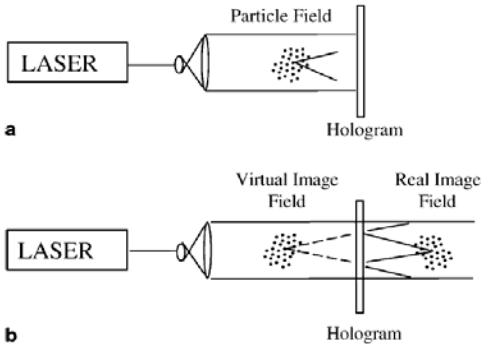

In-line holographic PIV recording setup

Off-line holographic PIV

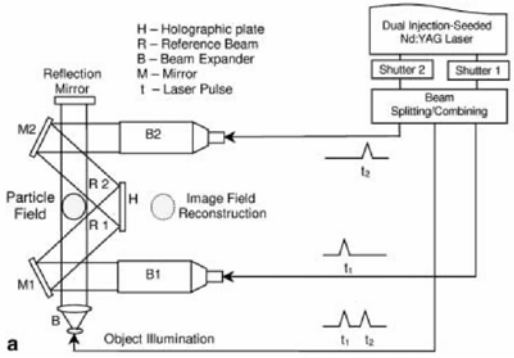

Off-line holographic PIV recording setup (Pu et al. 2000)

Multi-beam holographic PIV systme

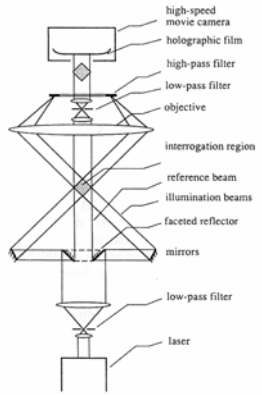

Multi-beam holographic PIV system with IROV (Zimin et al. 1993)

Holography (Reconstruction)

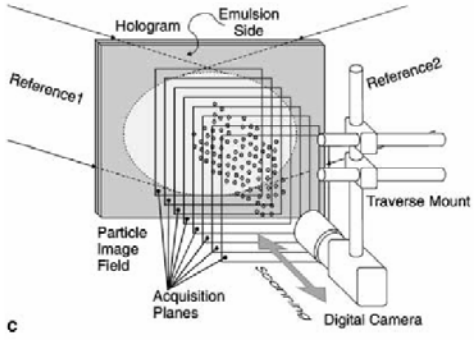

Reconstruction of volumetric data by slice extraction (Pu et al. 2000)

Micro-PIV System

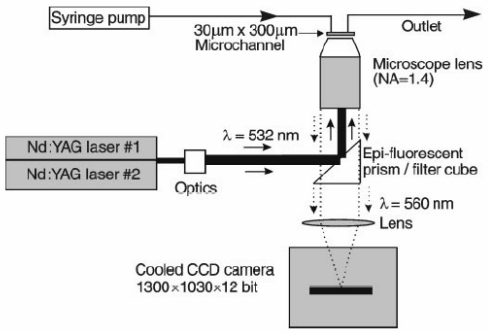

(Meinhart et al. 1999)

Ensemble Averaging Methods

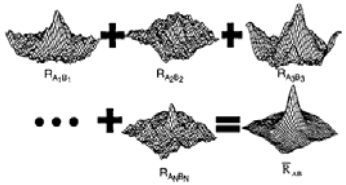

Averaged instantaneous cross-correlation domains (Meinhart et al., 2000)

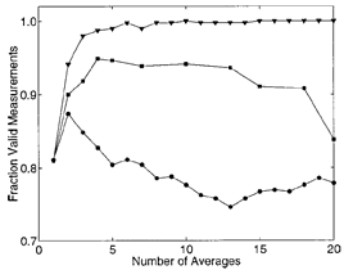

Comparison of the three averaging methods: average velocity , average image , average correlation (Meinhart et al., 2000)

Summary

- PIV is an established technique and is a valuable tool for measuring 2-D and 3-D flowfields.
- Several advances have been made on this technique over the past two decades in terms of sophisticated software, advanced imaging systems, and light sheet illumination.
- Future research involves implementing the technique to large-scale flowfields and microfluidics.

Milli-DPIV approaches for studying boundary-layer-based flow-control systems

Jordi Estevadeordal,(1) William W. Copenhaver,(2) Dave Car,(2)

(1) Innovative Scientific Solutions Inc., 2766 Indian Ripple Rd., Dayton, OH 45440, USA
E-mail: jordi@inssi.com
(2) AFRL/PRTF, Bldg. 18, 1950 Fifth St., Wright-Patterson AFB, OH 45433-7251, USA
E-mail: william.copenhaver@wpafb.af.mil; david.car@wpafb.af.mil

MOTIVATION

- Study of flow-control and boundary-layer systems such as high-turning stator in transonic cascades using **PIV**.
- The systems employs small **(millimetric) blowing and suction** cavities, slots, holes, etc. at the blade surface.
- Objective is perform velocity measurements in these small areas and in the **boundary layer** to complement *simultaneous* **standard PIV** and conventional pressure and temperature measurements.
- Issues include **volumetric illumination, sharp DOF, image processing and Digital Holography.**

Example of flow-control configuration within a cascade blade

Chord is 4 in.; span is 6 in.

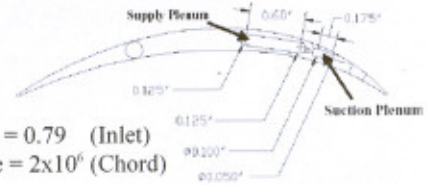

M = 0.79 (Inlet)
Re = $2x10^6$ (Chord)

CFD

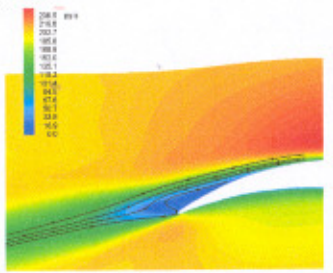

Without Flow Control

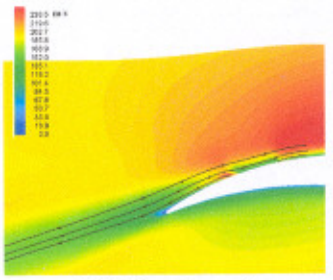

With Flow Control
(.8 Motive, 1.2 Blow)

STANDARD PIV (Macro Views)

Schematic of DPIV setup for cascade velocity measurements

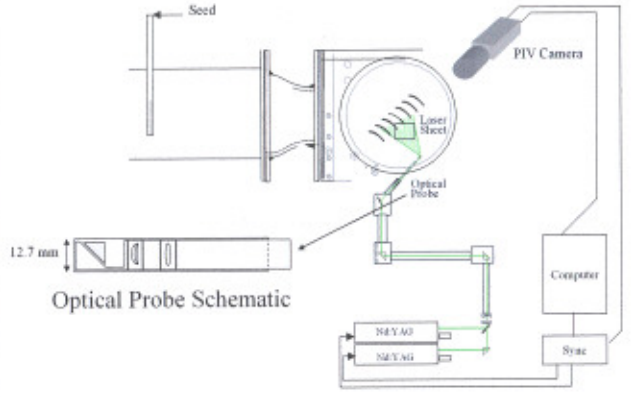

FLOW VISUALIZATION

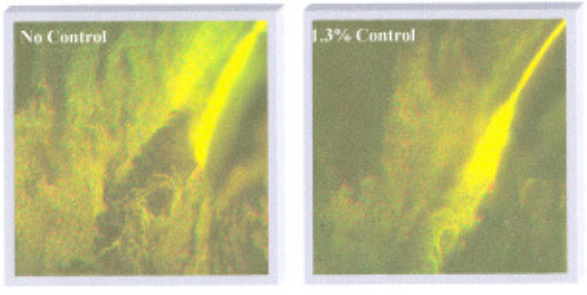

DPIV

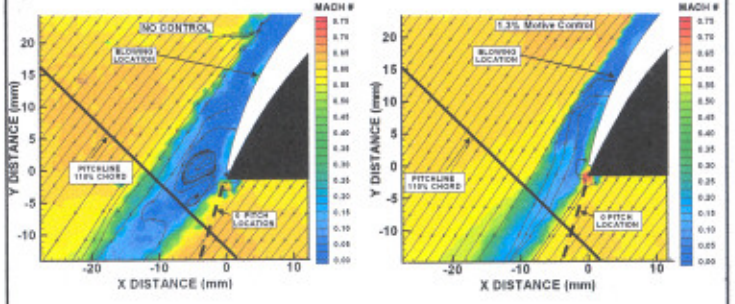

MILLIMETRIC PIV

(boundary layer, fluidic ports)

APPROACHES TO VELOCITY MEASUREMENTS IN MILLIMETRIC AREAS (blowing, suction, boundary layer)

- Volumetric Illumination
- Sharp DOF
- Partial-coherence
- Digital In-Line Holography

- Image processing (background substraction, images substraction, images multiplication, etc.) provides improvements in SNR and contrast
- Seeding strategy
- Bonuses: -high resolution with 1k x 1k CCD sensors
  -ambient light has negligible effect.

Volume Illumination with Sharp DOF

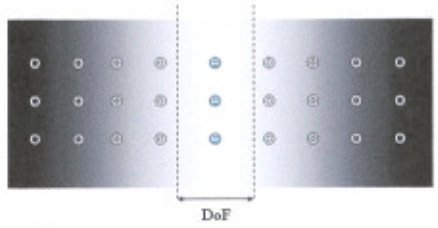

All particles in the illuminated volume scatter light but the diffraction pattern has a maximum intensity (Airy function) at the **focal plane of the lenses**. **DOF** is defined as a specified fraction of that maximum.

Ref: Meinhart et al. 2000 "Volume illumination for two-dimensional particle image velocimetry" *Meas. Sci. tech. 11, p. 809*

Milli-DPIV setup for *single-focused plane* with *Off-Axis* volume illumination

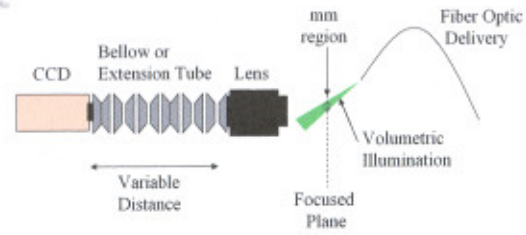

Effect of volume-illumination *direction* for a bubble emanating from a *2-mm*-diameter orifice

a b

The sharp focused plane is at the center of the bubble.
A few degrees off in-line produces speckle (a);
optimal value for single focused plane occurs for near-forward scattering
and occurs at few degrees from forward (in-line) (b).

Volume Illumination with Sharp DOF: DPIV examples

Uniform flow (Res = 1000 pix/mm)

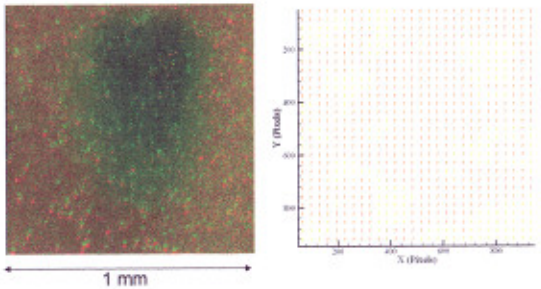

1 mm

Seed: 0.5 microns particles

Vel Max = 1 m/s

Volume Illumination with Sharp DOF: DPIV examples

Jet (Res = 255 pix/mm)

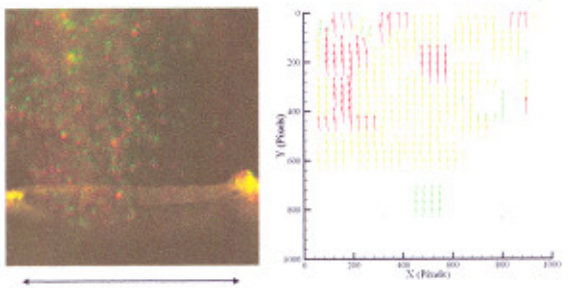

3 mm

Seed: 15 microns particles

Vel Max = 30 m/s

A **3D** approach for **mill** and **micro** volumes:

digital holography

Digital In-line Holography (LEEPS)

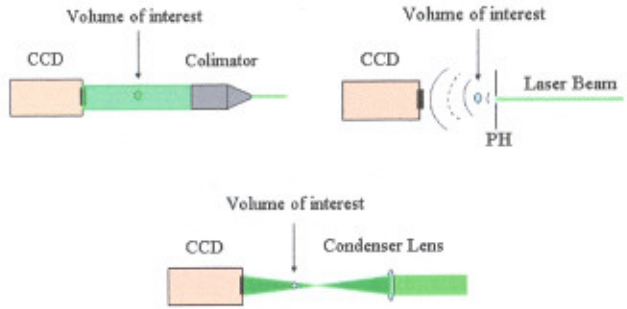

DIH reconstruction of 2mm bubble (b)

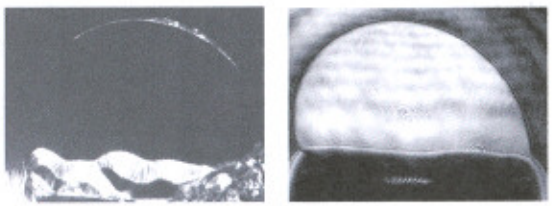

a b

single focused plane near-forward scattering (a) and DIH reconstruction of a similar bubble (b).

Digital In-line Holography: Numerical Interrogation

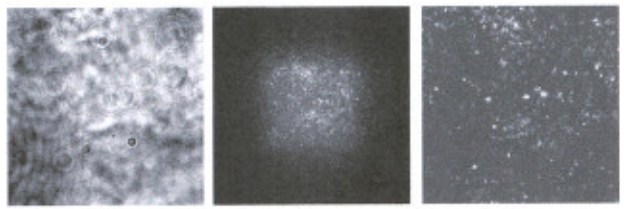

a b c

Interrogation of a **spray** hologram (a) from two different magnifications, showing the full spray (b) and a region inside (c).

Ref: Kreuzer et al 2001 "Digital in-line holography with photons and electrons" *J. Phys.:Cond. Matter 13, p. 10729*

Digital In-line Holography: PARTICLE SIZING

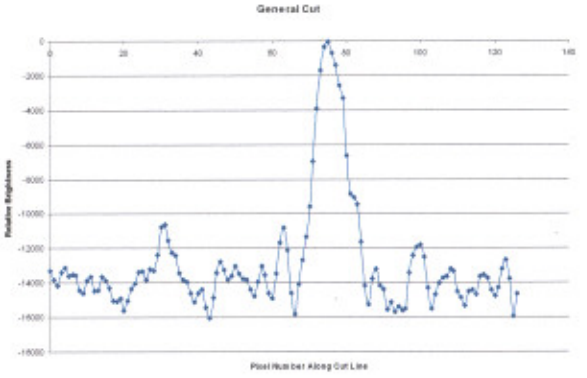

a cut through one plane to get an estimate of particle size: typically 5-10 microns

Digital In-line Holography: VELOCITY

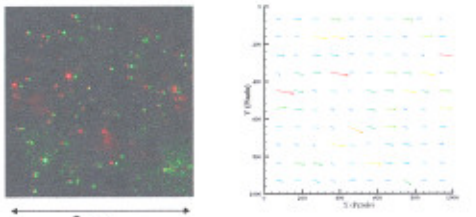

Conclusions

Approaches of Digital Particle Image Velocimetry (DPIV) in the mm range 'millimetric PIV' were introduced to complement Standard-PIV results aimed to study thin boundary layers and flow-control systems that employ small blowing and suction cavities, slots, holes etc. in the blades.

Standard PIV (MACRO VIEWS)	⟷	Mill Metric PIV (MILL/MICRO VIEWS)
↓		↓
Wake	⟷	Boundary layer, fluidics

Studies of Vortex-Induced Flame Extinction in Counterflow Diffusion Flames Using CH PLIF and PIV

A. Lemaire†, T.R. Meyer*, K. Zähringer†, J.R. Gord*, and J.C. Rolon†

†Laboratoire E.M2.C,
Ecole Centrale Paris and CNRS
F-92295 Châtenay-Malabry Cedex, France

* Air Force Research Laboratory
Wright-Patterson AFB
Dayton, OH 45440

Objectives : Perform systematic studies on vortex-flame interactions

Introduction

- Vortex-induced flame extinctions represent important fundamental turbulent flame phenomena
- Vortex-induced flame extinctions can provide a repeatable time sequence for detailed study
- CH planar laser-induced fluorescence (PLIF) is useful for marking the flame front and particle-image velocimetry (PIV) gives flowfield dat
- Effects of fuel equivalence ratio, droplet seeding, and PAH fluorescence also of interest

Lasers and Optics for CH PLIF and PIV

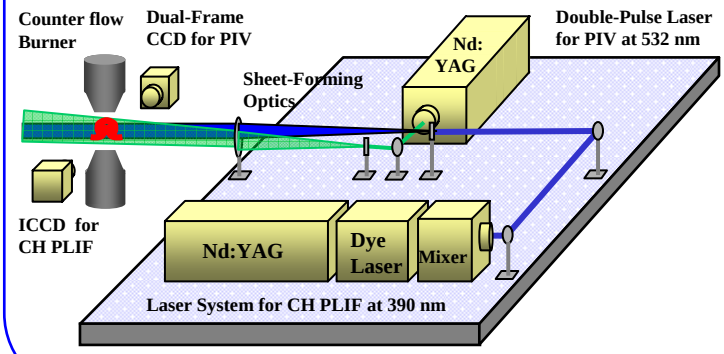

Main results :

Effect of Laser Energy on Relative CH-PAH PLIF and Scattering at Phi = 5

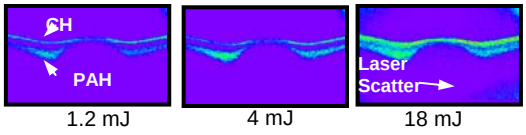

Line Plots of CH PLIF and PAH Fluorescence at phi = 5 and 1.2 mJ

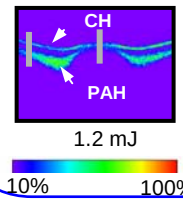

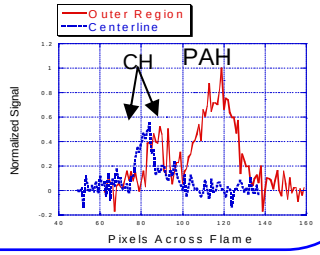

Single-Shot Vs. Average Images

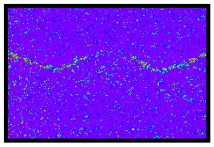

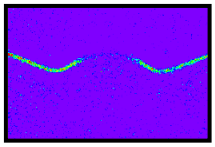

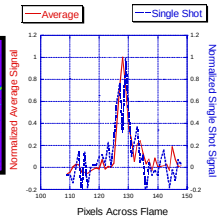

Single Shot Image Average of 20 Images

Mie Scattering on Ethanol Droplets and CH PLIF / PIV During Flame Extinction

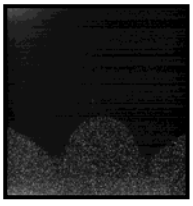

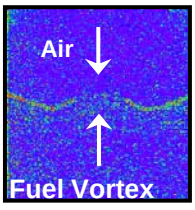

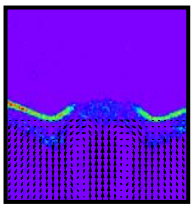

Mie Scattering from Ethanol Droplets

Raw Single Shot CH PLIF

20-Shot Average CH PLIF and PIV

Time-Correlated Sequence of CH PLIF / PIV at Phi = 4

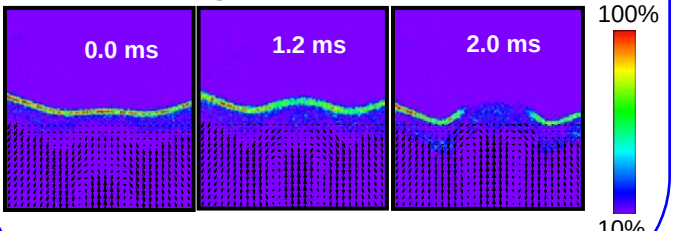

Conclusion :

- CH PLIF / PIV performed for the first time during vortex interaction in a counter flow diffusion flame
- Semi-quantitative results from CH PLIF show flame extinction occurs within 1 ms
- PIV shows increase in fuel side strain during extinction
- Overall PAH fluorescence much lower at Global Phi = 4 and during vortex interaction, but is non-negligible
- Greater separation of CH PLIF and PAH fluorescence occurs at lower laser energy

Laser-Based Measurements in Wrinkled Two-Phase Counterflow Diffusion Flames

T. R. Meyer,[1] A. Lemaire,[2] K. Zähringer,[2]
J. R. Gord,[3] and J. C. Rolon[2]

[1]Innovative Scientific Solutions, Inc.
[2]Ecole Centrale Paris / CNRS
[3]Air Force Research Laboratory / PRTS

Joint Poster Session of the Dayton Section American Chemical Society and the Ohio Valley Section Society for Applied Spectroscopy

Dayton, OH, March 5, 2002

Motivation

Study vortex-induced flame wrinkling and extinction in *two-phase* counterflow diffusion flames for use in turbulent combustion models.

- Use hydrocarbon gaseous and liquid fuels.
- Obtain time-correlated sequences of flamelet wrinkling and extinction at various operating conditions.
- Look for a correlation with peak fuel-side strain rate obtained from particle-image velocimetry (PIV).
- Evaluate suitability of CH planar laser-induced fluorescence (PLIF) as a combustion diagnostic.
- Characterize interferences from PAH fluorescence.

Test Facility and Conditions

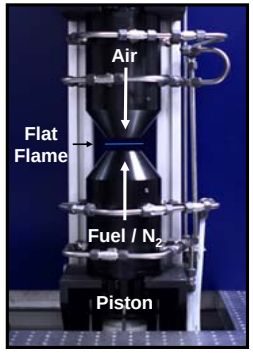

Counterflow Burner

- Equal upper and lower velocities of 0.7 m/s.
- 3 cm burner separation.
- Vortex velocity of 4.5 m/s.
- Global methane-air equivalence ratio of 4 (4.4 with ethanol droplets).
- Nitrogen co-flow.

Set-up for CH PLIF and PIV

- Exciting B-X transition of CH and detecting emission from A-X.
- PIV collected simultaneously with 2nd laser and camera system.

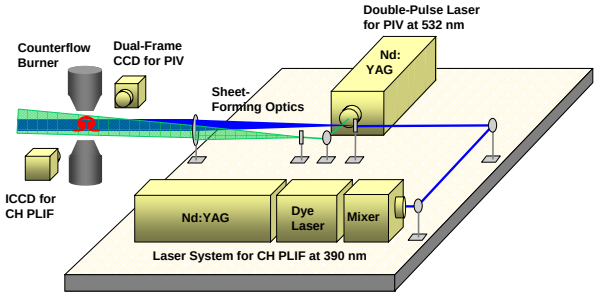

Raw and Processed Data

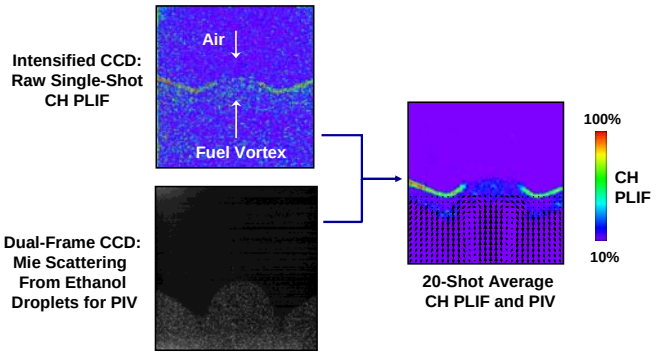

Single-Shot vs. Average Images

- Line plots of CH PLIF across the flame during vortex interaction.
- Match of spatial profiles indicates low system jitter and good vortex-flame phase correlation.

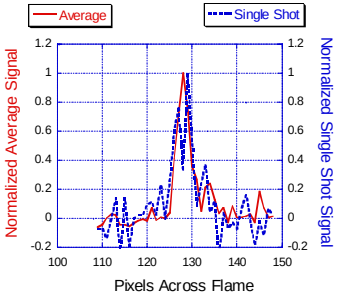

Time-Correlated Sequence

- Fuel-side vortex induces flame wrinkling and extinction of flamelet.

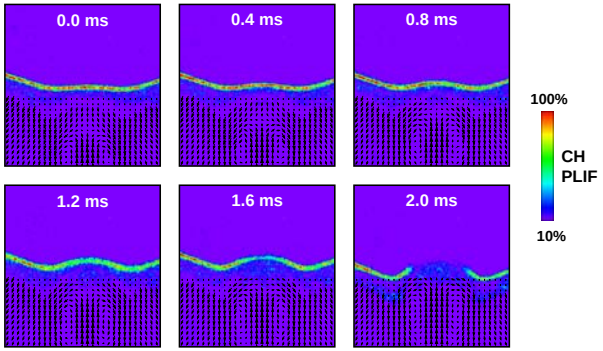

CH PLIF and Strain Rate vs. Time

- Measurements made at burner centerline.
- Time = 0 ms is at start of flame wrinkling.
- Extinction time scale is about 1 ms.
- Peak fuel-side strain increases to 2000 s^{-1} during extinction.

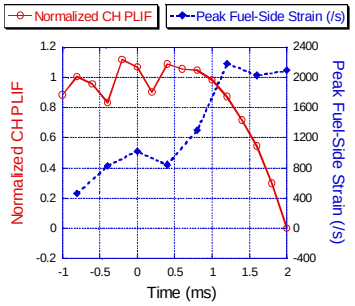

PAH Characterization
(Relative CH and PAH)

- Methane-air global equivalence ratio is 5.
- PAH fluorescence is much larger in unperturbed regions.

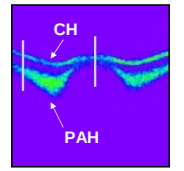

1.2 mJ

10% 100%
CH PLIF

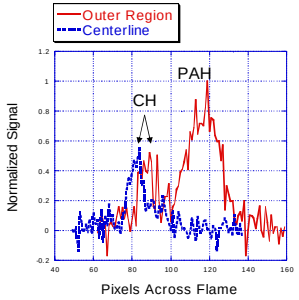

PAH Characterization
(Laser Energy)

- Methane-air global equivalence ratio is 5.
- More favorable CH PLIF – PAH discrimination at lower laser energy.

1.2 mJ | 4 mJ | 18 mJ

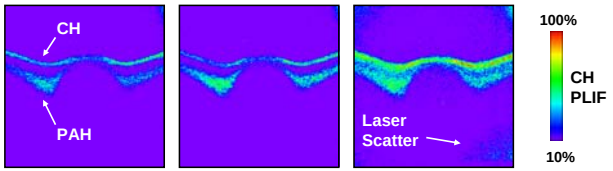

PAH Characterization
(Equivalence Ratio)

- PAH fluorescence has sharp increase at about Phi = 5.
- PAH fluorescence decreases during vortex interaction.

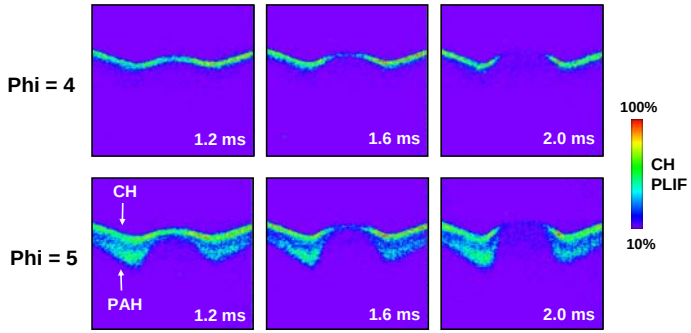

PAH Characterization
(Equivalence Ratio)

- Laser energy is 18 mJ.
- Very little difference in CH to PAH ratio near centerline.

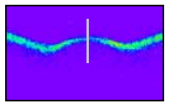

Phi = 4

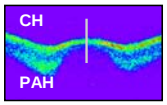

Phi = 5

10% 100%
CH PLIF

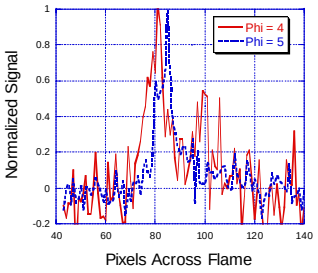

Summary and Conclusions

- CH PLIF / PIV performed for the first time during vortex interaction in a counterflow diffusion flame.
- Semi-quantitative results from CH PLIF show time scale of flame extinction is less than 1 ms.
- PIV shows five-fold increase in fuel side strain rate during extinction to about 2000 s^{-1}.
- Large increase in PAH fluorescence observed for global equivalence ratio of about Phi=5.
- More favorable separation of CH PLIF and PAH fluorescence occurs as laser energy is reduced.

Future Work

- Perform systematic study with different fuels and equivalence ratios.
- Study the effect of vortex size and strength.
- Use solid particle seeding to obtain peak air-side strain rate.
- Compare experimental results with numerical simulation.

APPLICATION OF OPTICAL DIAGNOSTICS FOR COMBUSTION AND FLUID FLOWS

Sivaram P. Gogineni
Innovative Scientific Solutions, Inc.
2766 Indian Ripple Road
Dayton, Ohio, 45440, U.S.A.

James R. Gord and Barry V. Kiel
Propulsion Directorate
Air Force Research Laboratory
Wright-Patterson Air Force Base, Ohio, 45433, U.S.A.

Acknowledgments
Drs. M. Roquemore, W. Copenhaver, M. Visbal, D. Gaitonde, and Dr. C. Carter, AFRL
Drs. L. Goss, T. Meyer, V. Katta, J. stevadeordal, G. Fiechnter, ISSI
Dr. H. Meng, SUNY, Buffalo, Dr. A. Krothapalli, L. Lourenco, and C. Shih, FAMU/FSU

OUTLINE OF THE PRESENTATION

- **Particle Image Velocimetry**
  - → Wall jet
  - → Jet-in-a-Crossflow
  - → Turbomachinery
- **Planar Laser Induced Fluorescence**
  - → Vortex-Flame Interactions
- **Holographic Flow Visualization**
  - → Vortex-ring and Bag-shaped Instability
  - → Diffusion Flame

Transition Process in a Wall Jet

SINGLE-COLOR PIV WITH IMAGE SHIFTING

TRANSITIONAL WALL JET

- To provide a detailed knowledge of the wall jet flow behavior during the transition process using a combination of Flow Visualization, PIV and DNS.

Specifically to understand the:

- Mechanism involved for the formation of initial vortex in the inner region
- Non-linear process by which the spanwise rollers breakdown into small-scale structures

DEFINITION OF A PLANE WALL JET

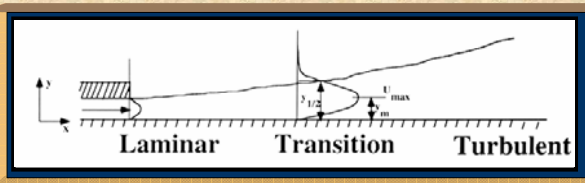

A plane wall jet is a stream of fluid blown tangentially along a plane wall. It consists of:

(i) an inner region (boundary layer) and

(ii) an outer region (free shear layer)

SCHEMATIC OF THE FACILITY

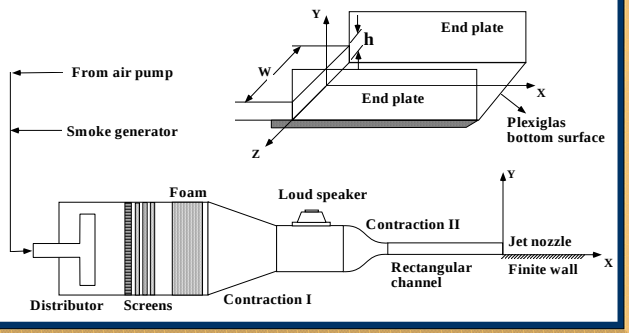

PHOTOGRAPH OF THE FACILITY

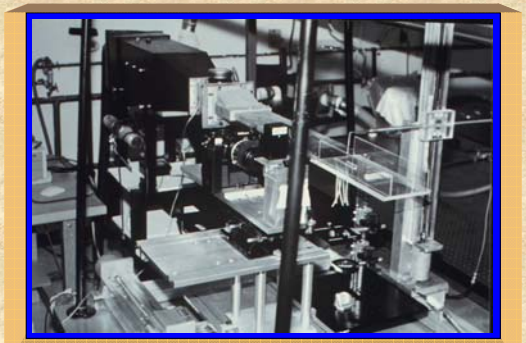

COMPARISON OF TRANSITIONAL FREE JET AND WALL JET

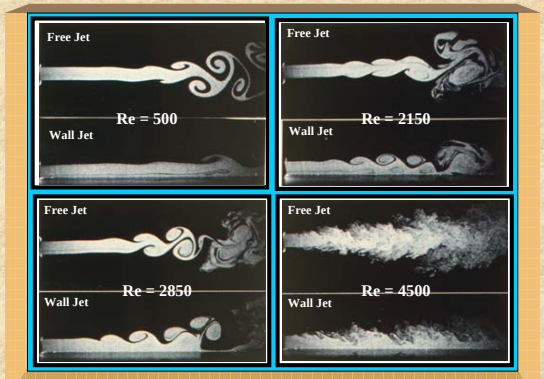

Winner of the 10th Annual Fluid Mechanics Photo Contest, Nov. 1992

STREAMWISE (X-Y PLANE) FLOW VISUALIZATION

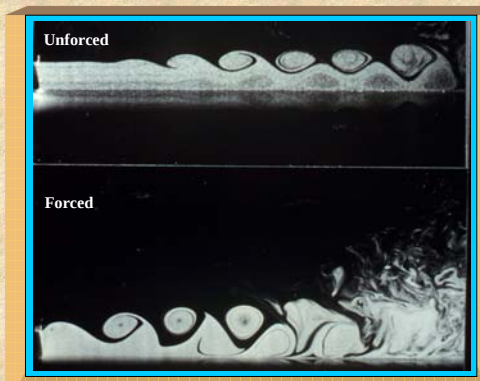

SCHEMATIC OF THE PIV SYSTEM

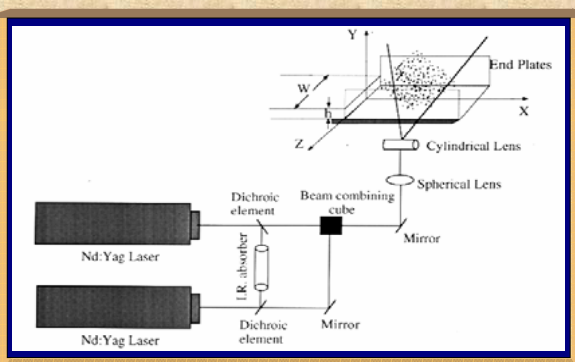

TYPICAL DOUBLE-EXPOSED PIV IMAGE

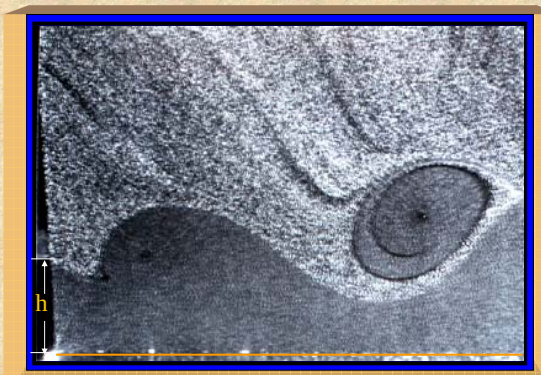

SCHEMATIC OF COMPUTATIONAL DOMAIN

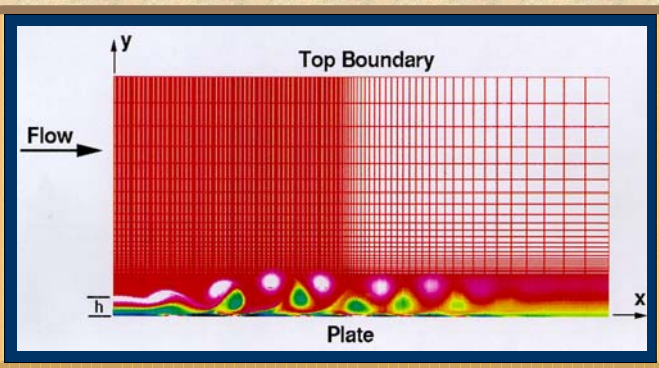

INSTANTANEOUS VORTICITY DISTRIBUTION

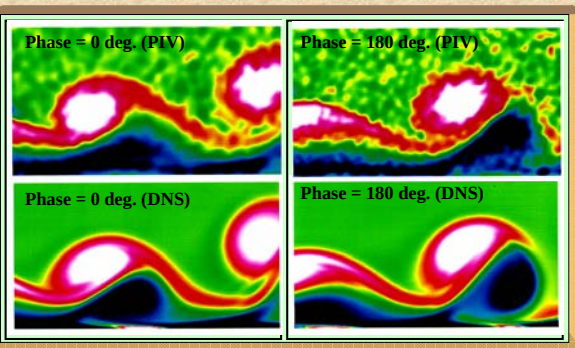

STREAKLINE VISUALIZATION

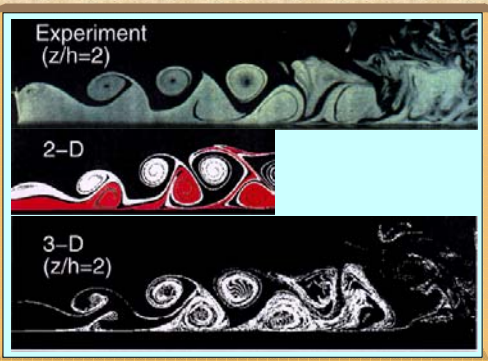

SPANWISE FLOW VISUALIZATION AND VORTICITY DISTRIBUTION

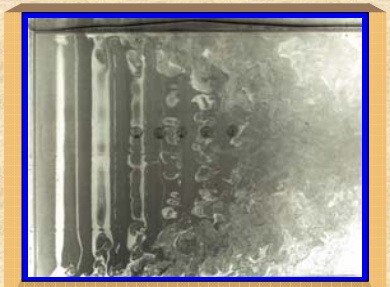

Laser Sheet/Smoke Visualization

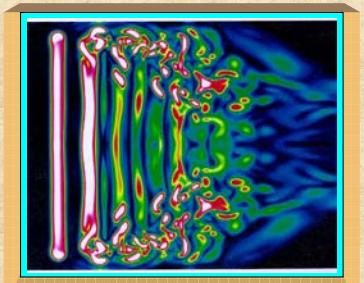

Vorticity Distribution (3D-DNS Simulation)

SPATIAL VORTICITY DISTRIBUTION

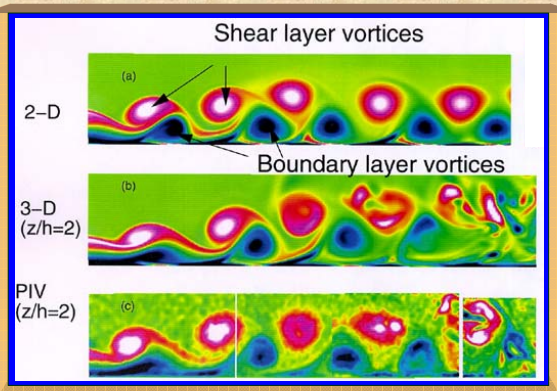

Iso-surface of Vorticity Magnitude for Shear-Layer Vortical Structures

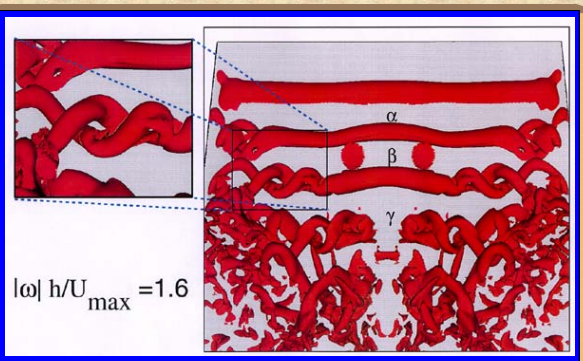

TRANSITION PROCESS IN A PLANE WALL JET

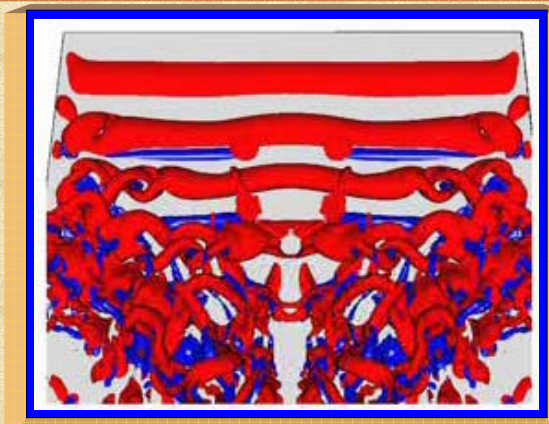

Double-Helix Instability in a Forced Wall Jet

ISSI

Winner of the 16th Annual Fluid Mechanics Photo Contest, Nov. 1998

M. Visbal and D. Gaitonde
Air Force Research Laboratory
Wright-Patterson AFB, OH 45433

S. Gogineni
Innovative Scientific Solutions, Inc.
Dayton, OH 45440

Flow visualization [x-z plane]

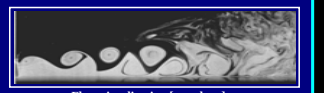
Flow visualization [x-y plane]

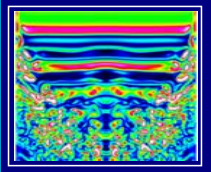
Vorticity magnitude (DNS)

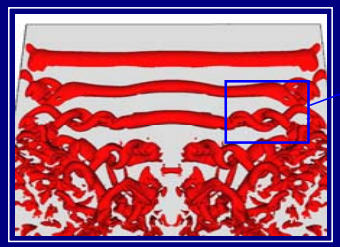
Iso-surface of vorticity magnitude (DNS)

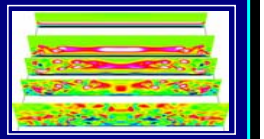
Vorticity contours [y-z planes: (DNS)]

Jet in a Cross Flow

SCHEMATIC OF THE TWO-COLOR PIV

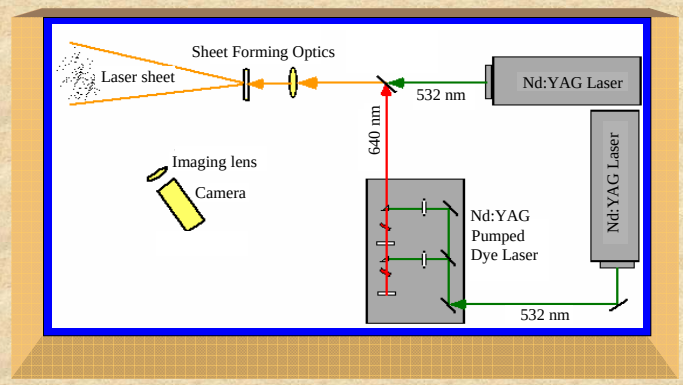

JET-IN-A-CROSSFLOW

Winner of the 12th Annual Fluid Mechanics Photo Contest, Nov. 1994

FLOW VISUALIZATION AND PIV IMAGES (X-Z PLANE)

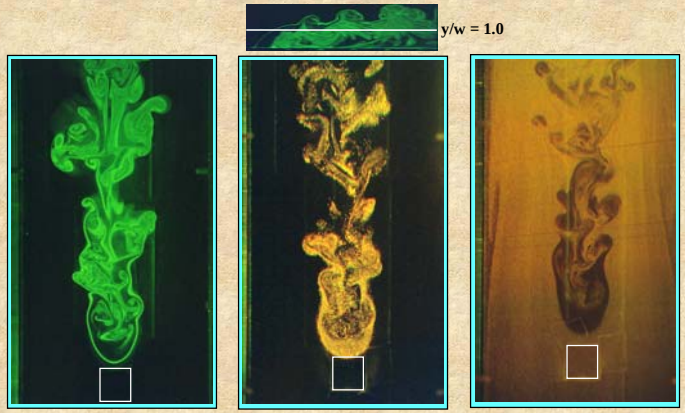

DOUBLE EXPOSED TWO-COLOR PIV IMAGES OF JET IN A CROSS FLOW (X-Y PLANE)

DOUBLE EXPOSED PIV IMAGES (Y-Z PLANE)

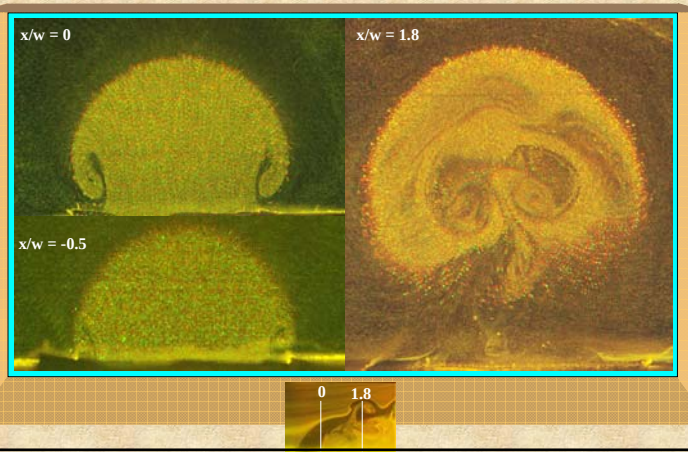

INSTANTANEOUS VELOCITY AND VORTICITY DISTRIBUTIONS

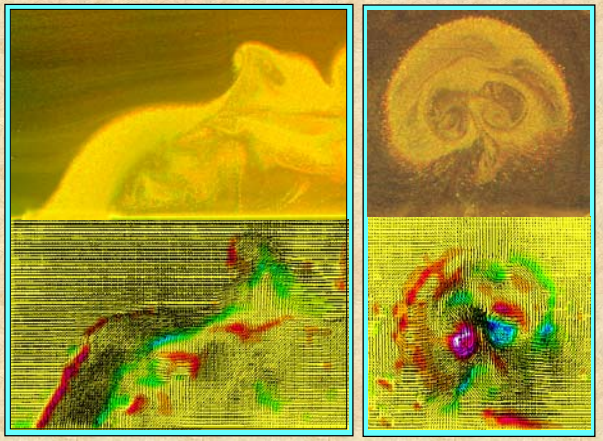

Wake Vortex and Rotor Blade Interactions In Turbomachinery Flow Fields

MOTIVATION

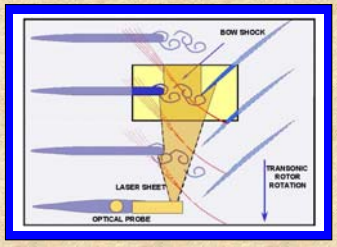

- Measuring velocity fields in rotating blade rows is extremely important to evaluate and improve design systems
- Turbomachinery flowfields are highly unsteady
- DPIV offers the potential to investigate the effect of unsteady flowfields on blade loading, blade structural response, wake transport, boundary-layer transition, and flow separation.

WHY DPIV?

- Significantly reduces the facility run time compared to point based techniques such as LDV
- Offers the potential to obtain measurements closer to the surface
- High-resolution data can be used to aid the development and assessment of CFD codes
- Instantaneous data from DPIV is extremely valuable in understanding the unsteady nature of the turbomachinery flow fields

COMPRESSOR AERO RESEARCH LAB

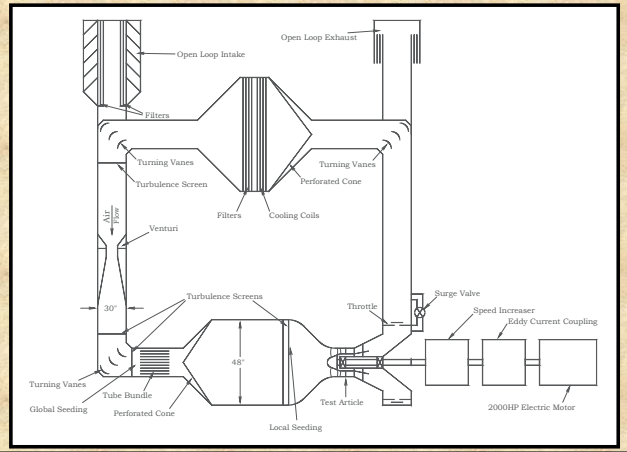

STAGE MATCHING INVESTIGATION RIG

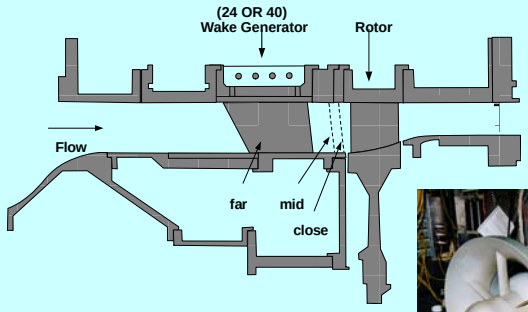

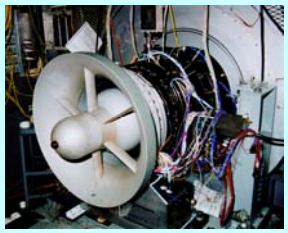

	x/c
Close	0.12
Mid	0.26
Far	0.56

WAKE GENERATOR/ROTOR

Design Inlet Mach # = 0.568

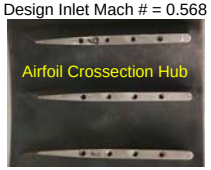

40 Strut Configuration

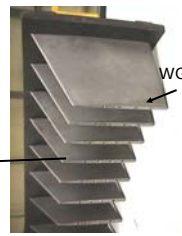

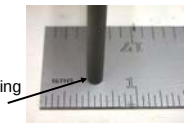

WG Trailing Edge

Trailing Edge Thickness /Mid Chord -- 6%

Core Rotor

CORE ROTOR	
TIP RELATIVE MACH #	1.19
HUB RELATIVE MACH #	0.96
ASPECT RATIO	0.96
INLET HUB/TIP RATIO	0.75
PRESSURE RATIO	1.86
DESIGN RPM	13,532

DPIV ISSUES FOR TURBOMACHINERY

- OPTICAL ACCESS
- SEEDING STRATEGIES
- MINIMIZATION OF SURFACE GLARE
- BLADE-PASSAGE SYNCHRONIZATION
- MEASUREMENT-FRAME POSITIONING

LASER BEAM DELIVERY SYSTEM

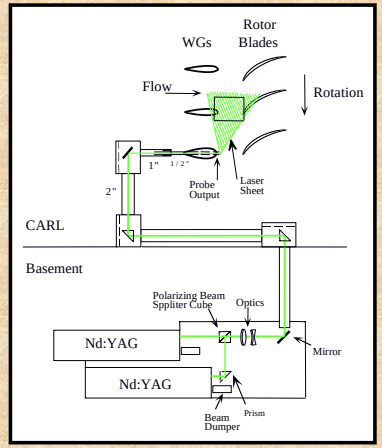

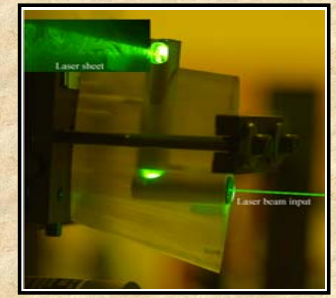

PHOTOGRAPH OF THE CARL FACILITY

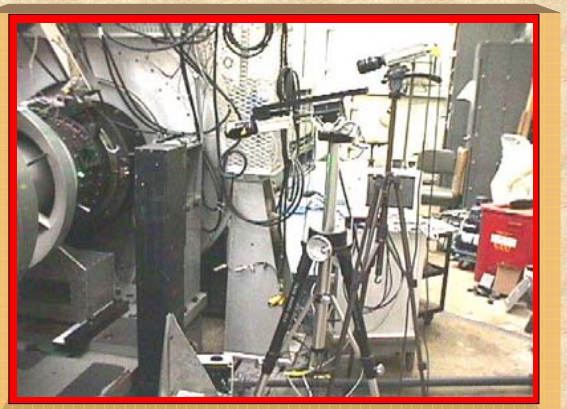

OVERALL STAGE PRESSURE RATIO

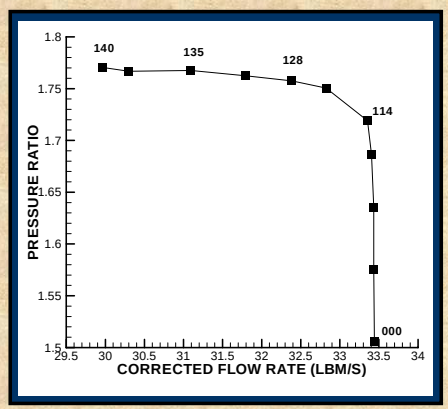

EFFECT OF THROTTLE VARIATION

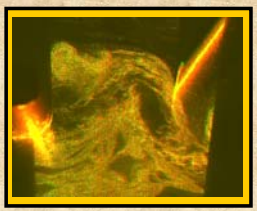

Choking

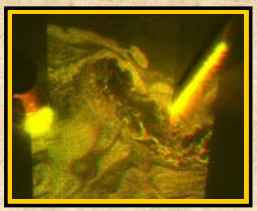

Peak Efficiency

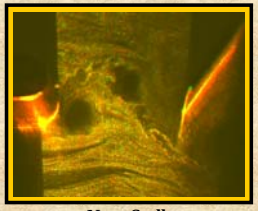

Near Stall

FLOW VISUALIZATIONS OF THE WAKE STRUCTURE

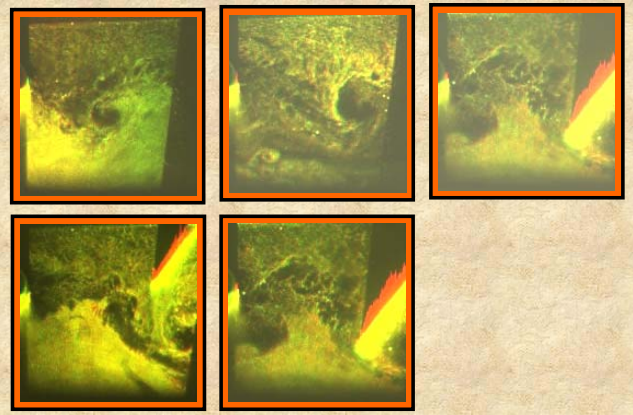

INSTANTANEOUS VELOCITY DISTRIBUTIONS (CLOSE SPACING, 90% SPAN)

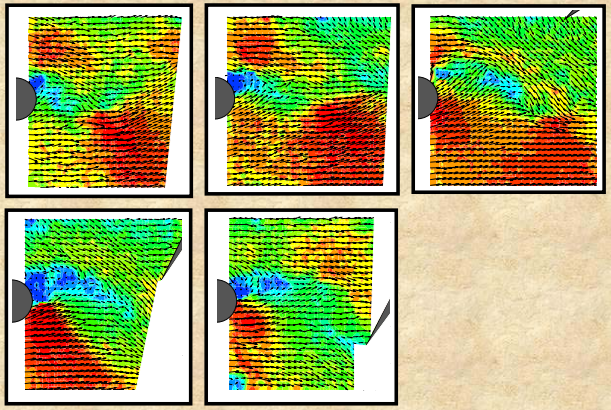

AVERAGE VELOCITY DISTRIBUTIONS (CLOSE SPACING, 90% SPAN)

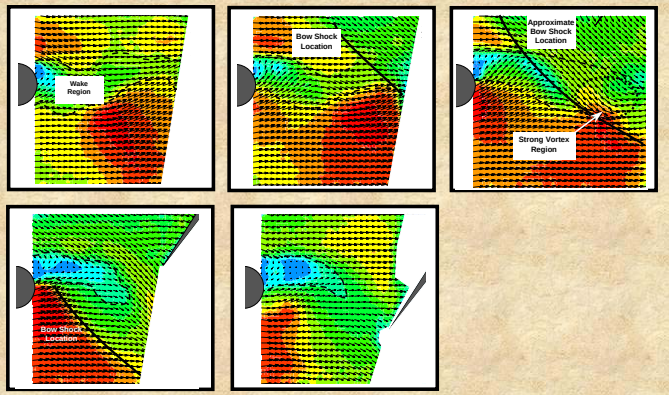

AVERAGE VELOCITY DISTRIBUTIONS (MID SPACING, 90%)

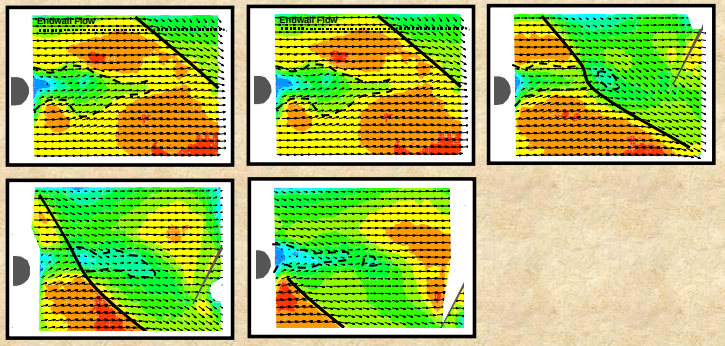

AVERAGE VELOCITY DISTRIBUTIONS (MID SPACING, 75% SPAN)

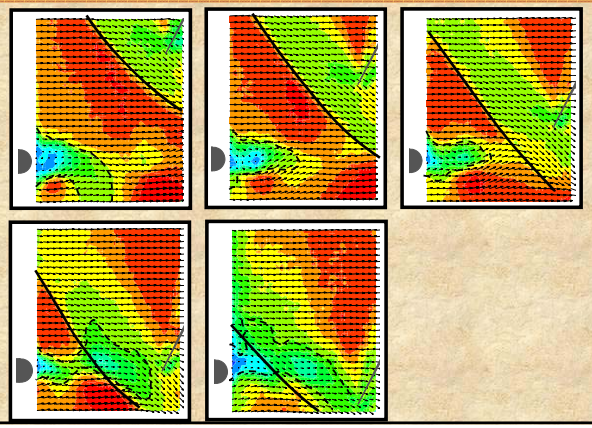

SUMMARY

- A DPIV system was developed for investigating the transonic turbomachinery flow fields
- Specifically, the unsteady phenomena in the wake region and the interaction of the wake with the blade leading edge of a transonic rotor at near-stall was investigated
- DPIV system captured the vortex shedding, the vortex-blade synchronization, the wake chopping, and the wake-shock interaction
- Results clearly showed that the wake is turned and spread after passage of the moving rotor bow shock
- DPIV results also indicated that the rotor bow shock is weaker at 90% span but extends farther forward of the rotor than at 75% span

Vortex Flame Interactions

TRANSITION TO TURBULENCE

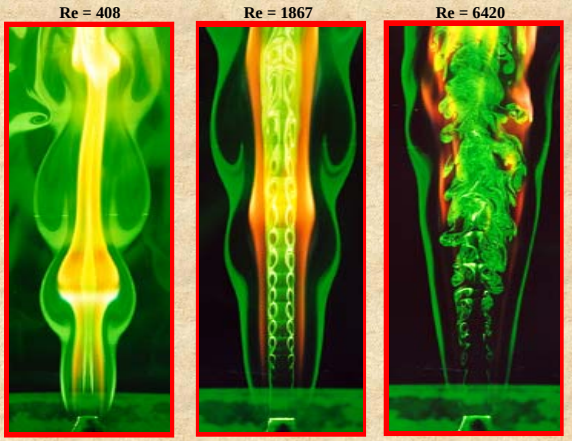

SCHEMATIC OF THE ROLON BURNER

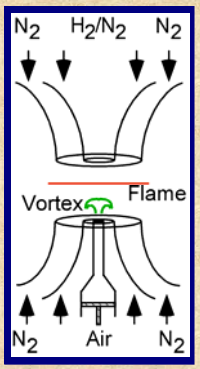

VORTEX FORMATION

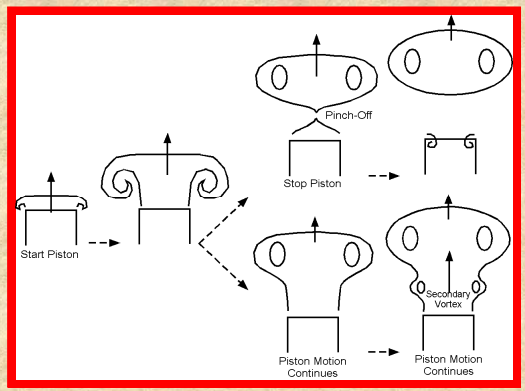

VORTEX HISTORY

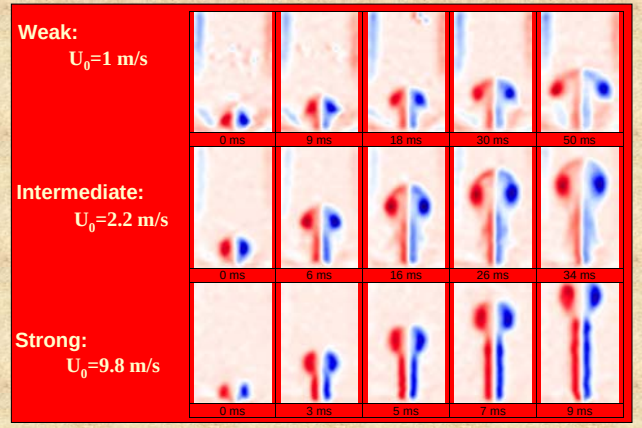

ANNULAR EXTINCTION OF OH LAYER

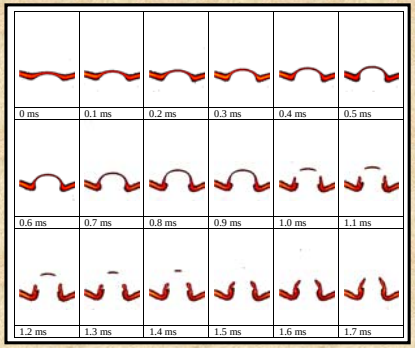

OH Layer Reconnection

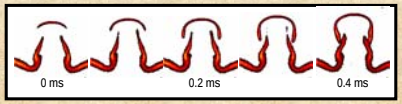

FLOW ANIMATIONS

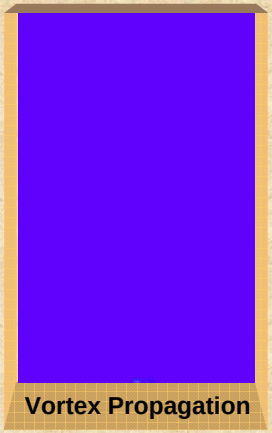

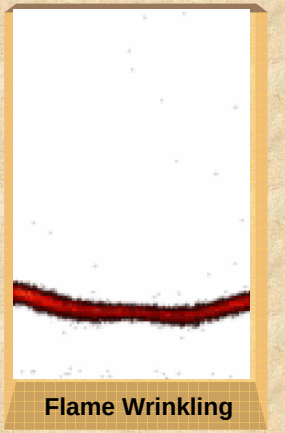

FLOW ANIMATIONS

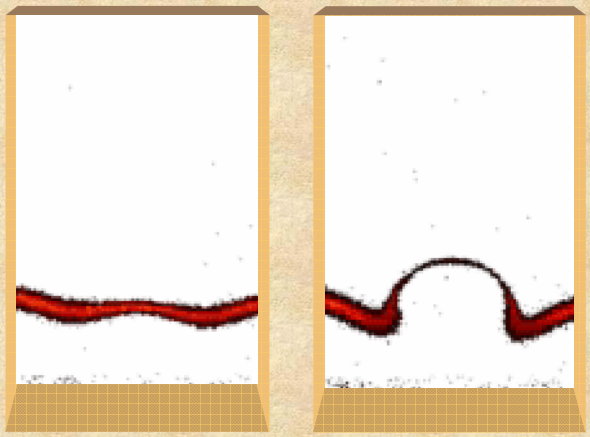

SIMULTANEOUS OH-PLIF AND VELOCITY DISTRIBUTIONS

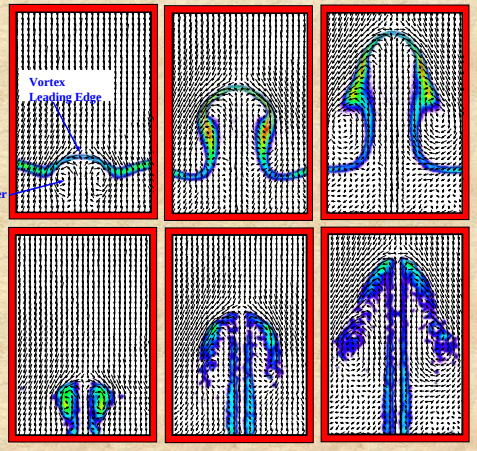

FOR A CASE
WITH
NO FLAME EXTINCTION

SUPERPOSED VELOCITY AND VORTICITY DISTRIBUTIONS

SIMULTANEOUS OH-PLIF AND VELOCITY DISTRIBUTIONS

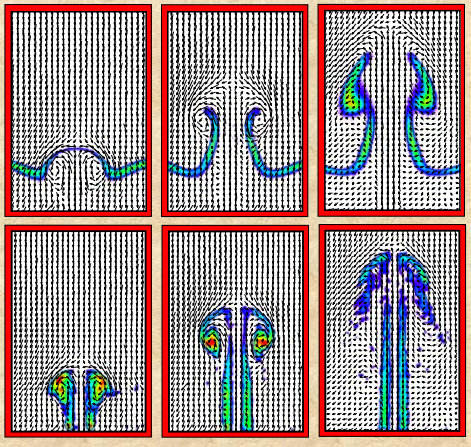

FOR A CASE WITH FLAME EXTINCTION

SUPERPOSED VELOCITY AND VORTICITY DISTRIBUTIONS

SUPERPOSED VELOCITY AND VORTICITY DISTRIBUTIONS

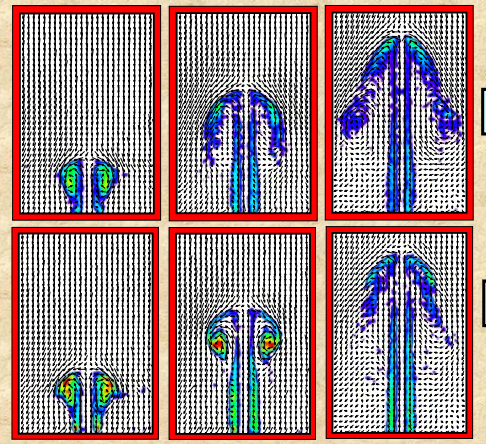

FOR A CASE WITH NO FLAME EXTINCTION

FOR A CASE WITH FLAME EXTINCTION

SIMULTANEOUS OH-PLIF AND PIV DATA SHOWING THE TIME RESOLUTION REQUIRED TO CAPTURE FLAME EXTINCTION

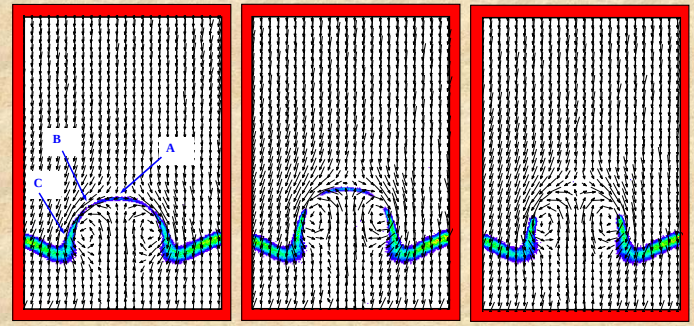

VELOCITY GRADIENT NORMAL TO THE FLAME SURFACE

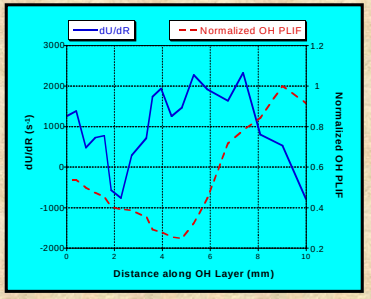

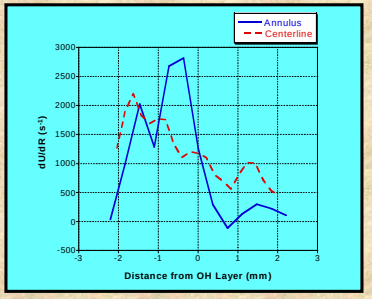

COMPARISON BETWEEN EXPERIMENTAL RESULTS AND COMPUTATIONS

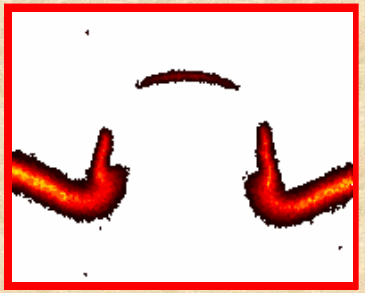

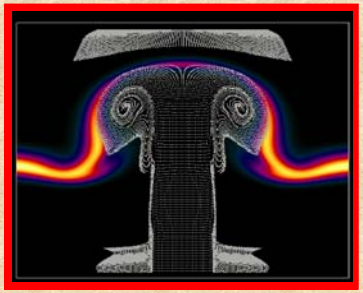

Katta 1998

COMPARISON BETWEEN EXPERIMENT AND COMPUTATIONS

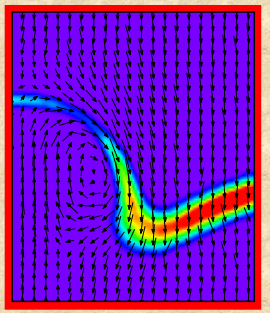

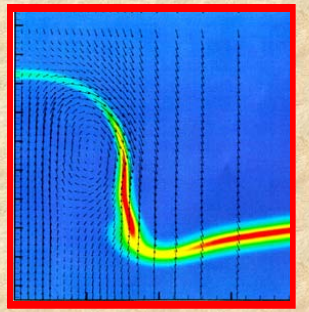

PRINCIPLE OF HOLOGRAPHY

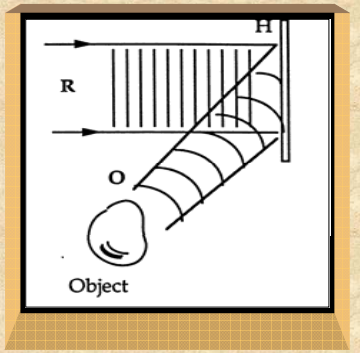

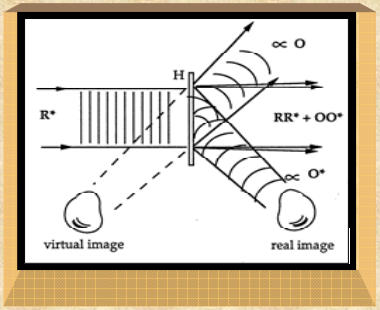

EXPERIMENTAL SETUP

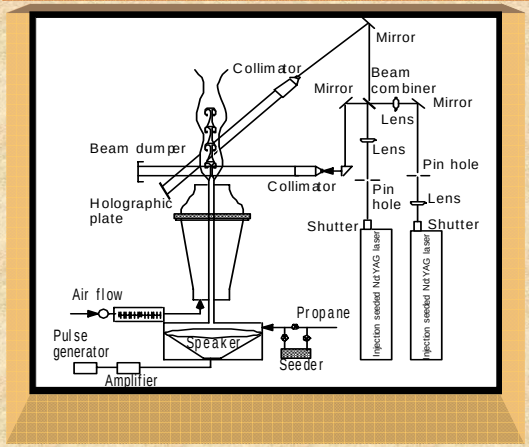

RECONSTRUCTION SYSTEM

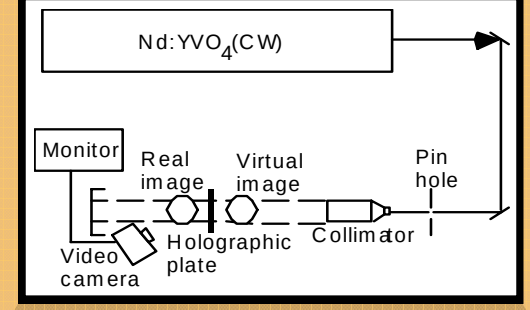

3D VISUALIZATION OF VORTEX-RING INSTABILITY USING HOLOGRAPHY (IROV)

3D VISUALIZATION OF VORTEX-RING AND BAG-SHAPED INSTABILITIES USING HOLOGRAPHY

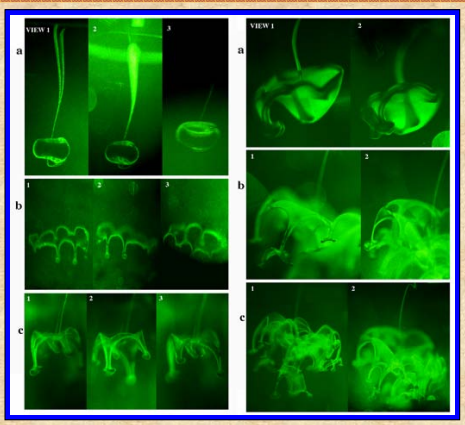

PHOTOGRAPHS OF THE HOLOGRAPHIC PLATES AND THE RECONSTRUCTED IMAGES (IROV)

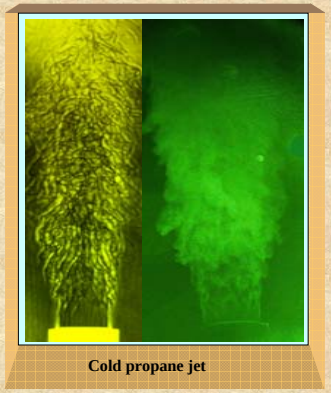

Cold propane jet

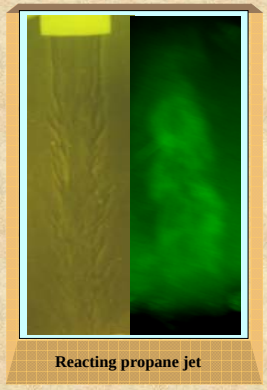

Reacting propane jet

COMPARISON OF LASER SHEET VISUALIZATION AND RECONSTRUCTED IMAGE FROM HOLOGRAM

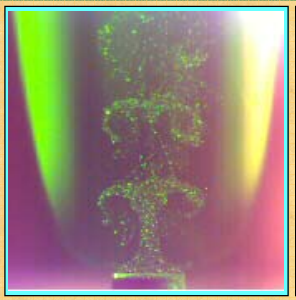

2D Laser sheet visualization

Reconstructed image (cold jet)

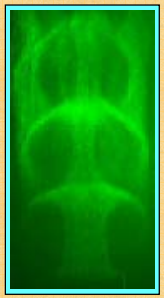

Reconstructed image (reacting jet)

RECONSTRUCTED IMAGE OF COLD PROPANE JET ISSUING INTO CO-FLOWING AIR

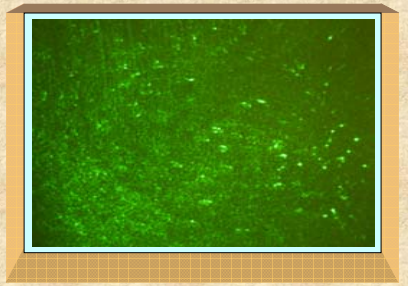

DOUBLE EXPOSED PARTICLE IMAGES SUITABLE FOR OBTAINING VELOCITY DISTRIBUTION

Two Color PIV for Large-Scale Wind Tunnel Facility

SARL WIND TUNNEL FACILITY

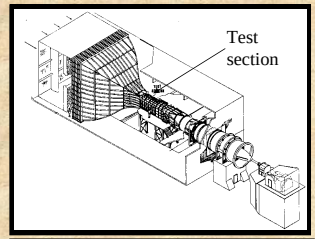

FLOW CONDITIONS

Angle of Attack: 23 deg.

Mach Number: 0.2

Reynolds Number: 1.87 x 10^6

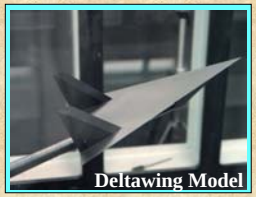

LASER SHEET ORIENTATION

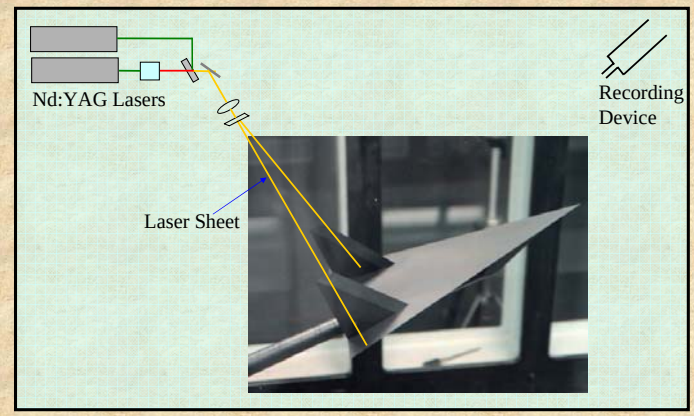

FLOW OVER DELTAWING WITH TAILS

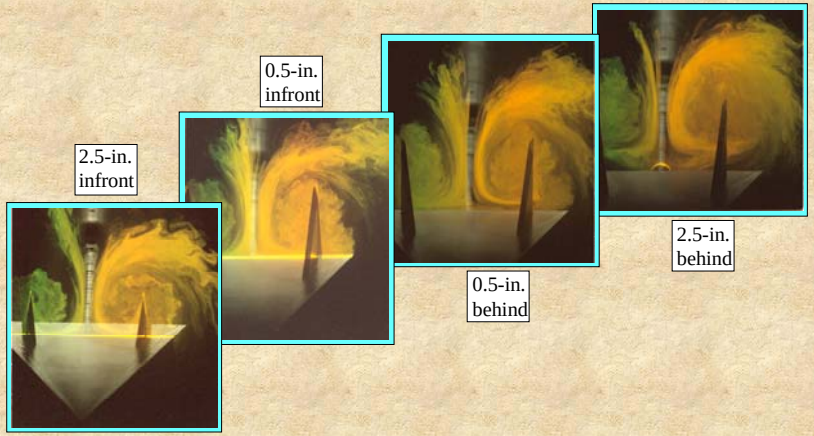

11th International Symposium on Applications of Laser Techniques to Fluid Mechanics
Lisbon, Portugal, July 8-11, 2002

Effects of Ignition Delay on Impulsively Initiated Premixed Jets

T. R. Meyer, S. P. Gogineni, V. R. Katta
Innovative Scientific Solutions, Inc.
2766 Indian Ripple Road
Dayton, OH 45440-3638, USA

J. R. Gord
Air Force Research Laboratory
Propulsion Directorate
Wright-Patterson Air Force Base, OH 45433-7103, USA

ABSTRACT

An experimental and numerical investigation is performed to explore the methods for achieving flame speeds that are much greater than laminar burning velocities. A premixed fuel jet is impulsively issued into a low-speed annular airflow, and ignition is provided after a preset delay time. The temporally varying structure of the propagating flame in and around the jet is measured using OH and acetone planar laser-induced fluorescence (PLIF) and particle-image velocimetry (PIV). Experiments are performed by varying the equivalence ratio, ignition delay time and jet momentum. Calculations are also performed using a time-dependent two-dimensional code that incorporates seventeen-species finite-rate chemistry for methane fuel. The ignition process is simulated by temporarily increasing the temperature in a small region within the jet column. Calculations are performed for the stoichiometric fuel/air mixture with varying ignition delay times. Instantaneous structures of the simulated and measured flames are compared. Flame propagation speeds are obtained from the numerical results by tracking the flame location along the centerline. It is observed that flame speed increases with ignition delay. An order of magnitude increase in flame speed is achieved by igniting the jet after a delay of ~ 6 ms. Further increase in ignition delay creates unburned fuel pockets and decreases the flame speed.

1. Introduction

Premixed flames in which fuel and oxidizer are mixed prior to burning have considerable industrial importance as they produce clear flames with intense combustion and little soot. These premixed combustion systems are commonly used in applications such as domestic heating and gas fires. Most large-scale practical combustors also contain flame zones, especially near the flame base, that are of the premixed type. Even though the laminar burning velocities of hydrocarbon fuels are only on the order of 1 m/s, the vortex-flame interactions in turbulent combustor flows can increase flame propagation velocities to several tens of m/s. Due to the severe geometrical restrictions placed on ultra-compact combustors such as inter-turbine and trapped-vortex combustors (Katta et al., 2000), it is necessary to increase the flame propagation velocities beyond the typical turbulent burning velocities. In this context knowledge of flame propagation through vortices filled with combustible mixture plays a key role in the development of ultra-compact combustors.

Due to the frequent occurrence of such vortex-flame interactions in reacting flows of technological interest, they have received considerable attention in recent years. Renard et al. (2000) provided a comprehensive review of numerical, theoretical, and experimental investigations of vortex-flame interactions and their effects on flame dynamics, extinction, ignition, mixing, baroclinic torque, and thermal diffusion. These investigations typically involved either collisions between laminar flame fronts and vortices or flame propagation within the vortices. The current study falls into the latter category, which is useful for studying the effects of flow structure, vorticity, and curvature on flame ignition and propagation. Previous studies have demonstrated that premixed burning velocity increases when the flame is moved into a region where fuel is traveling at a higher velocity. Studies by McCormack et al. (1972) addressed flame speeds up to 15 m/s in vortices and suggested a linear dependence of flame speed on vortex circulation. Ishizuka et al. (1997) also reported super-laminar flame speeds along the vortex core, but observed a somewhat reduced dependence on vortex circulation. Cattolica and Vosen (1986) performed studies of premixed flame propagation in the wake of a vortex for a combustion-torch configuration in which ignition of lean premixed gases within a combustion chamber generated a vortex ring of unburned, premixed methane and air. The flame followed in the wake of the vortex and eventually propagated though the vortex rollers.

In the present paper experimental and numerical investigations have been performed to identify and understand the various flame propagation patterns that arise in impulsively started jets and associated vortices. Parametric studies are performed on ignition and flame propagation by varying equivalence ratio, ignition timing, and vortex propagation velocity (Meyer et al., 2001). Instantaneous flames and flow structures are measured using OH planar laser-induced fluorescence (PLIF) and particle-image velocimetry (PIV), respectively. A time-dependent multi-dimensional model known as UNICORN (UNsteady Ignition and COmbustion with ReactioNs) (Katta et al., 1994) is used for the simulation of ignition and flame propagation in vortices. This model has been extensively validated through the simulation of various steady and unsteady flames associated with diffusion (Katta et al., 1998) and premixed (Katta et al., 1995; Katta et al., 2000) combustion systems.

2. Experimental Set-Up and Conditions

The jet-in-co-flow burner of the current study has been used in a number of previous investigations of vortex-flame interactions (Rolon et al., 1995, Fiechtner et al., 2000). In the current configuration, shown in Fig. 1, repeatable vortex rings of premixed methane and air were formed at the exit of a 5-mm-diameter central nozzle using a solenoid-driven 25-mm-diameter piston at the bottom of the fuel tube. Ignition was initiated at various phases with respect to vortex formation and propagation using a pair of electrodes located near the nozzle periphery. A co-flow of air surrounded the fuel-air jet, and a shroud flow of nitrogen was used to reduce external disturbances. A steady background flow rate of 0.14 m/s was maintained for all flows when the piston was not being actuated. When acetone planar laser-induced fluorescence (PLIF) measurements were performed, the nozzle air supply was diverted into an acetone-seeding system prior to premixing with methane.

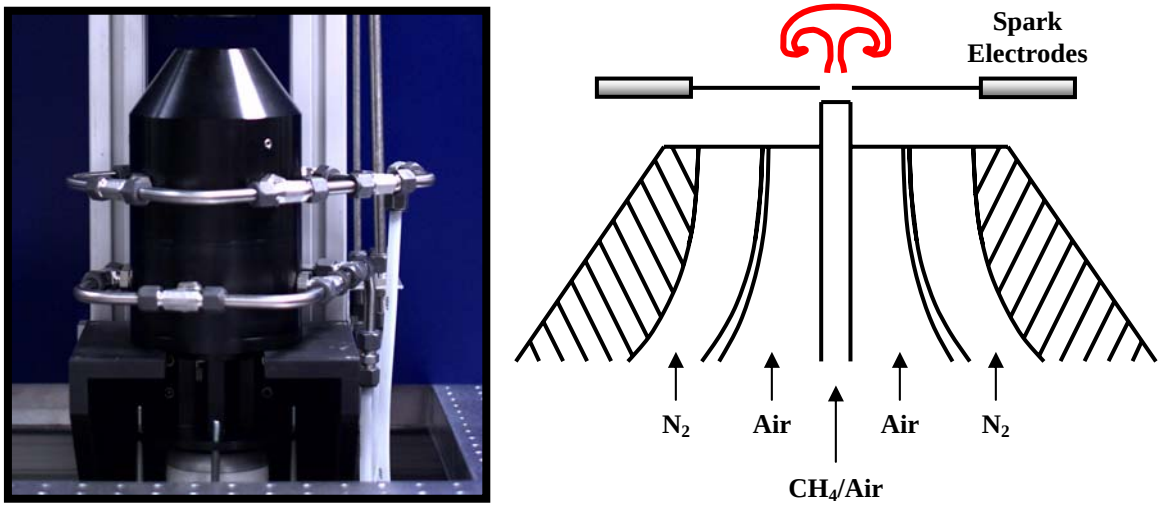

Fig. 1. Jet-in-co-flow burner used for vortex ignition experiments.

PLIF of the hydroxyl radical (OH) was accomplished by exciting the $R_1(8)$ transition of the (1,0) band in the A-X system. The requisite 281.3414-nm laser sheet was generated using the frequency-doubled output of a Nd:YAG pumped dye laser, and subsequent fluorescence from the A-X (1,1) and (0,0) bands was detected at right angles using a f/1.4 UV lens and an intensified charge-coupled-device (ICCD) camera. The 576×384 pixel array was binned in 2×2 groups, and the imaged area was 26.5 mm wide × 40 mm high. Prior to detection by the ICCD, the OH PLIF signal was filtered using UG-11 and WG-295 colored glass filters to remove visible and laser scattered light, respectively. Acetone PLIF was accomplished using the same laser wavelength and camera system (without the UG-11 filter), eliminating any uncertainties due to misalignment and variations in signal generation. Although most acetone PLIF measurements were performed to characterize the *cold-flow* conditions, the 300-ns gate of the ICCD allowed the UG-11 filter to be removed for simultaneous OH and acetone PLIF. A timing circuit driven by a Quantum Composer, Inc., pulse generator allowed for synchronization of the laser pulse, camera gate, spark ignition, and piston actuation.

For PIV measurements, the flow was seeded with aluminum-oxide particles, and the images were acquired using a Kodak ES 4.0 camera and Micro-Nikkor f/2.8 lens. A schematic diagram of the simultaneous OH PLIF and PIV image acquisition system is shown in Fig. 2. Cross-correlation processing of PIV images was performed using custom software developed at Innovative Scientific Solutions, Inc. (Gogineni et al., 1998).

As shown in Table 1, three main parameters were varied during the experiments: spark timing, equivalence ratio, and vortex strength. The equivalence ratio was varied from 0.75 to 1.5, and the spark timing was varied from 2.5 ms to 8 ms after the piston stroke. The effect of vortex strength was studied by varying the piston stroke from 1.6 to 5 mm while keeping the rise time constant. This resulted in vortex propagation velocities ranging from 2.5 to 6.5 m/s, which for constant ratios of vortex core diameter to toroidal ring diameter, is proportional to the maximum tangential velocity in the vortex as well as the circulation. Since flame propagation is very sensitive to the location of the spark, the position of the electrodes was kept constant for all runs at 2-3 mm above the fuel-air nozzle, 3.5 mm apart, and just outside of the central jet. Thus, a flame could be initiated prior to, during, or after the vortex formation and propagation stages.

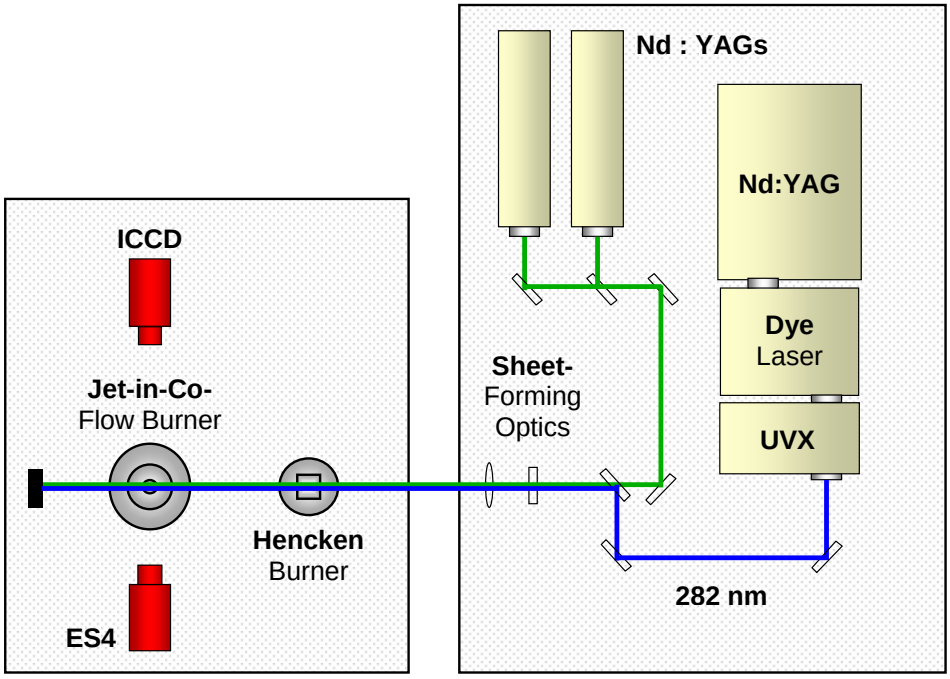

Fig. 2. Schematic of the simultaneous PLIF/PIV system.

Table 1. Experimental Conditions.

Ignition Timing (ms)*	Equivalence Ratio	Piston Stroke (mm)	Vortex Velocity (m/s)
2.5	1.0	3.3	5
4	0.75, 1.0, 1.25, 1.5	3.3	5
4	1.0	1.6	2.5
5	1.0	5	6.5
6	1.0	1.6, 3.3, 5	2.5, 5, 6.5
8	1.0	3.3	5

* Relative to piston actuation

3. Numerical Model

Ignition and flame propagation in the starting jets was simulated using an unsteady two-dimensional code known as UNICORN (Katta et al., 1994; Roquemore and Katta, 2000). The time-dependent governing equations are expressed in a cylindrical-coordinate system. Temperature- and species-dependent transport coefficients are used. The enthalpy of each species is calculated from polynomial curve fits. A stoichiometric methane/air mixture was used as the fuel. The detailed chemistry model (Peters and Rogg, 1993) used for describing methane combustion consists of 17 species and 52 elementary reaction steps. The finite-difference forms of the momentum equations were integrated using an implicit QUICKEST scheme, and those of the species and energy equations were obtained using a hybrid scheme of upwind and central differencing.

Computations were performed using a 571x151 non-uniform grid system covering a physical domain of 70x20 mm. The grid system was clustered in such way that the local grid spacing in the axial and radial directions in the flame zone was 0.1 mm to resolve substantial gradients in the flow variables. The burner

diameter was 5 mm, and a flat velocity profile with U_{ave} = 0.135 m/s was used as the initial flow condition. A fuel jet consisting of stoichiometric CH_4/O_2 and 71.5% N_2 was issued into the flow by suddenly increasing the fuel-mixture velocity to 6.5 m/s. A steady annular airflow of 0.135 m/s was used throughout the calculation. Ignition was initiated at a location that is 2 mm above the inflow boundary and at the axis of symmetry. The delay between the initiation of ignition and the start of the fuel jet (ignition-delay time, τ) was varied to investigate flame propagation through the injected premixed gases.

4. Results and Discussion

4.1 PLIF and PIV Results

A series of acetone PLIF images was collected for each of the three piston strokes in order to document the cold-flow conditions. As shown in Fig. 3, the piston stroke has a significant impact on the vortex convection velocity, although the ratio of the vortex-core diameter to toroidal-ring diameter as a function of distance from the nozzle exit remains fairly constant. This confirms that vortex circulation should be approximately proportional to the vortex convection velocity and, thus, piston stroke. Note that the nozzle exit is aligned with the bottom of each image and that the red dot near the bottom marks the location of one of the electrodes.

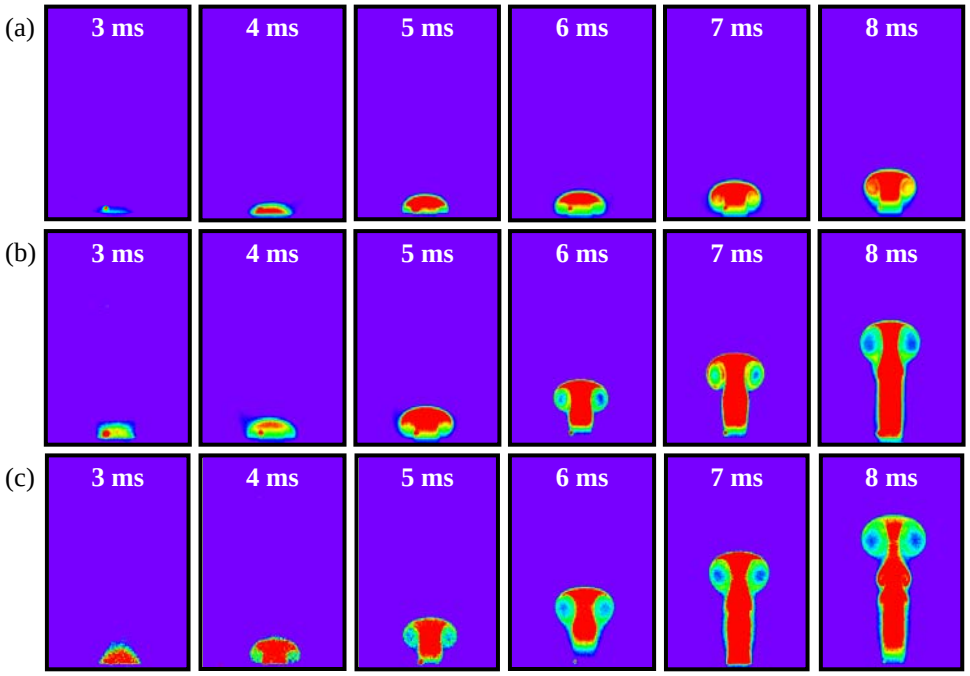

Fig. 3. Acetone PLIF images of cold-flow vortex propagation as a function of time after the piston is actuated for piston strokes of (a) 1.6 mm, (b) 3.3 mm, and (c) 5 mm.

The effect of spark timing is presented in Fig. 4, which shows a sequence of OH PLIF images for each of the spark timings listed in Table 1. The vortex propagation prior to ignition is shown in Fig. 3b, with an equivalence ratio of 1.0 and piston stroke of 3.3 mm. For a spark timing of 2.5 ms, ignition is initiated just ahead of the approaching vortex. The flame propagates quickly into the vortex rollers and remains on the exterior of the jet column where fluid velocity is low. The vortex continues to stretch the flame ahead of the vortex between 4.5 and 7.5 ms and quenches the flame between 7.5 and 8.5 ms. For a spark timing of 4 ms, ignition is initiated as the tip of the vortex passes the electrodes. Vortex-flame propagation is similar to that of the previous case, and a clear annular extinction of the flame is shown at 8 ms. This type of extinction is also observed under certain conditions when a vortex of cold fuel impinges

on flat counterflow diffusion flames (Katta et al., 1998). For a spark timing of 6 ms, the vortex is beyond the formation stage, and the flame propagates within the jet column and into the vortex rollers. Interestingly, the flame does not propagate down into a second approaching vortex, but remains on the exterior. For a spark timing of 8 ms, the vortex is 4-5 diameters downstream of the electrodes and is unable to propagate into the rollers.

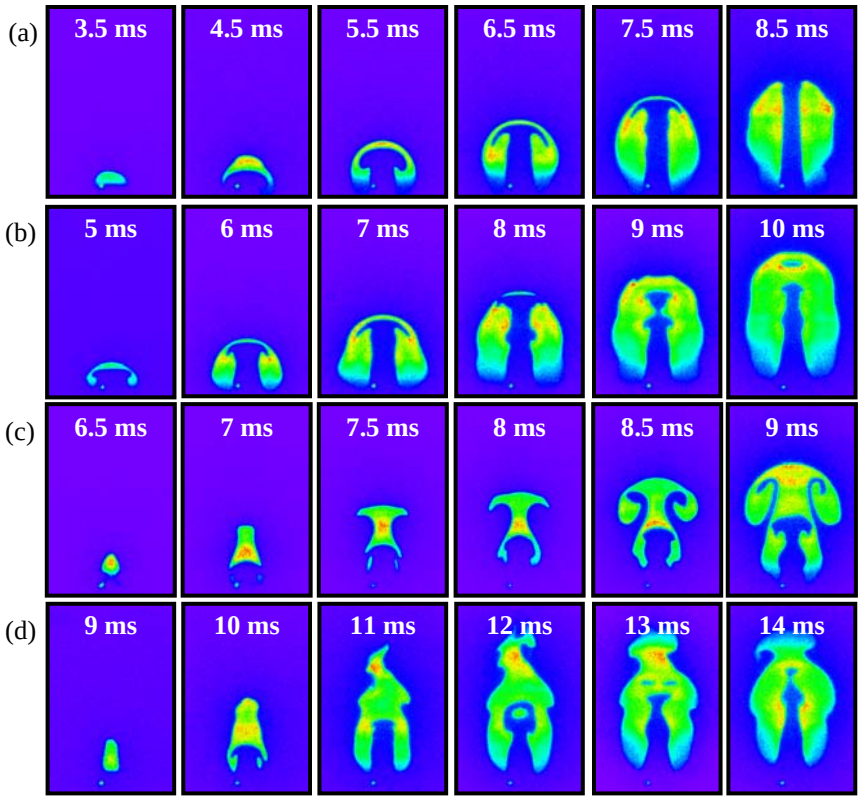

Fig. 4. OH PLIF image sequence for spark timings of (a) 2.5 ms, (b) 4 ms, (c) 6 ms, and (d) 8 ms after piston actuation. Equivalence ratio is 1.0 and piston stroke is 3.3 mm.

The effect of equivalence ratio is shown in Fig. 5. The spark occurs 4 ms after piston actuation and the piston stroke is 3.3 mm. Unlike the stoichiometric conditions shown in Fig. 4b, the lean and rich flames are almost immediately quenched after initial flame formation ahead of the vortex. Flame propagation along the exterior of the jet column is quite similar for equivalence ratios of 0.75 and 1.25 (Figs. 5a and 5b, respectively), but is greatly diminished for an equivalence ratio of 1.5 (Fig. 5c), as expected. Flame bridging occurs across the jet column in Figs. 5a and 5b, but is suppressed in Fig. 5c.

Figure 6 shows Mie scattering from a typical PIV image and the corresponding velocity distribution. An OH image is also superimposed to display the flame-front location. This image was taken 8.5 ms after piston actuation with an equivalence ratio of 1.0.

4.2 Computational Results

To understand further the ignition delay and flame propagation in impulsively initiated premixed jets, computations are performed using an unsteady two-dimensional code (UNICORN). The flow and geometric parameters are chosen to be close to the experimental conditions. A 6.6-m/s jet initiated into a stagnant or low-speed parallel flow generates a large mushroom-shaped vortex at the tip. As the jet pushes into this nearly stagnant flow, the vortex increases in size through entrainment. In addition, impulsively started jets generate smaller vortices on the jet column just upstream of the larger vortex. As the primary vortex convects downstream, it entrains not only the surrounding air but also the secondary vortices on the

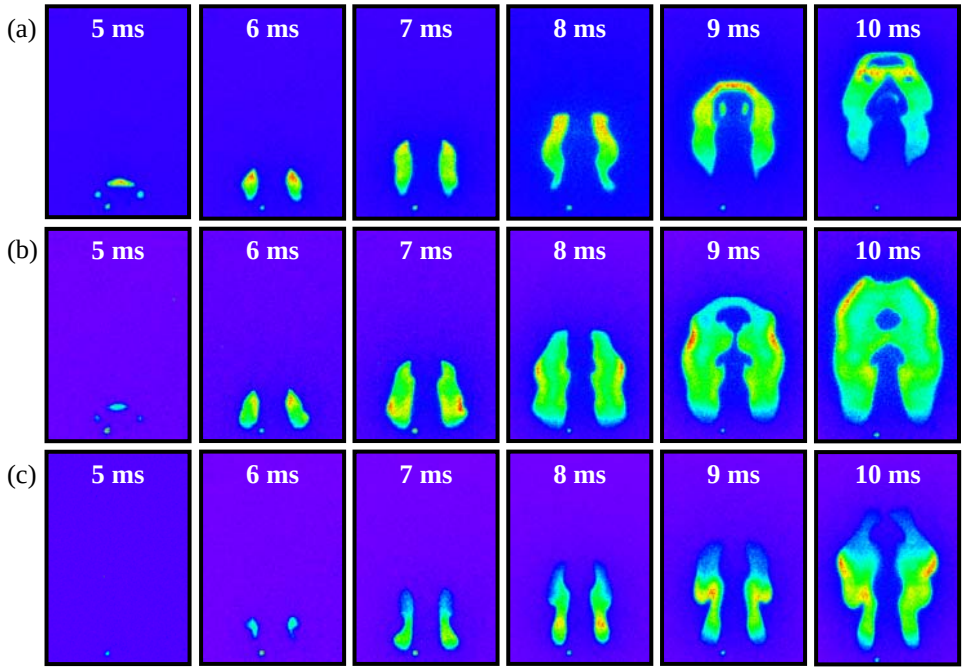

Fig. 5. OH PLIF image sequence for equivalence ratios of (a) 0.75, (b) 1.25, and (c) 1.5. Spark timing is 4 ms after piston actuation and piston stroke is 3.3 mm.

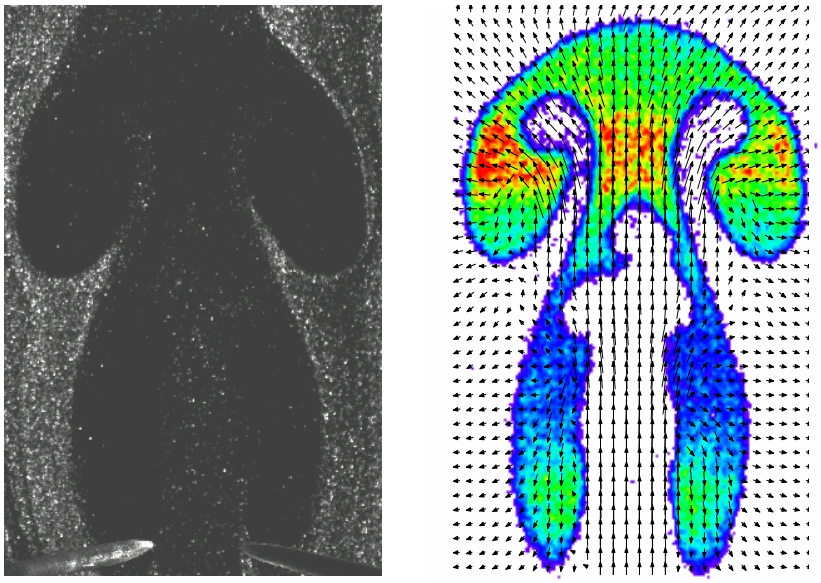

Double Exposed PIV Image

Instantaneous Velocity Field with Superimposed OH-PLIF Image

Fig. 6. Typical PIV image and corresponding instantaneous velocity distribution (Phi=1.0, 8.5 ms after piston actuation).

jet column. As a result of this entrainment, the jet of 6.6 m/s velocity penetrates through the nearly stagnant flow at a velocity of about 4.1 m/s.

Ignition in the calculations is initiated within the jet column τ ms after the start of the jet. During this process the temperature within a region of 5 grid points is held at 1600 K for five time-steps. Small

amounts of H and OH radicals (< 0.5%) are also introduced within this region to initiate the methane-air combustion chemistry. Calculations were made for different ignition-delay times and the results for four cases are shown in Fig. 7 in the form of temperature distributions and fuel-jet structures. These cases were selected to illustrate the different flame-propagation mechanisms. In Case 1, ignition was initiated 0.75 ms after the jet was started. By this time, the tip of the jet has traveled ~ 1 mm past the spark location and provided combustible mixture at the time of ignition. The flame and jet structures at 3.5 ms and 12.3 ms for this case are shown in Fig. 7a in the left and right halves, respectively. The average velocity of the flame propagation in the axial direction is ~ 3.4 m/s, which is ~ 17% lower than that of the cold jet. This reduction in propagation speed results because the flame established along the outer core of the fuel column acts like a barrier to jet propagation. Nevertheless, as the laminar burning velocity of the stoichiometric methane-air mixture is only 0.38 m/s, the impulsively started jet has increased the flame propagation velocity by an order of magnitude. Similar ignition and flame propagation are observed in Fig. 7b when the ignition delay is increased to 1.5 ms. The average flame propagation velocity increases slightly to 3.5 m/s and the flame is wrapped around the jet similarly to that seen in Case 1. However, there is a significant difference in the structure of the burning jet when it is compared to the one obtained in Case 1. The jet in the 1.5-ms case becomes transitional with the formation of 420-Hz organized structures, while the jet in the 0.75-ms case becomes laminar by t = 12.3 ms. Calculations made for these two cases simulated the flow features observed in the experiment (Fig. 4b).

As shown in Fig. 7c, the flame-propagation mechanism completely changes when the ignition delay is increased to 6 ms. Similar to the experiment shown in Fig. 4c, the head of the jet has traveled 24 mm past the ignition location by the time ignition is initiated. The flame rapidly propagates downstream within the jet column and reaches the tip of the jet with an average burning velocity of 6.5 m/s. As the flame propagates into the lead vortex and burns the entrained fuel, the size of the lead vortex increases significantly. The jet in this case also becomes transitional with the formation of organized secondary vortices. The flame structure matches that shown previously in Fig. 4c. When the ignition delay is further increased to 9 ms, the flame is unable to reach the jet tip Fig. 7d. As a result the initial fuel vortex formed at the tip of the jet detaches from the fuel jet and travels as a pocket of unburned gas. This flame-propagation

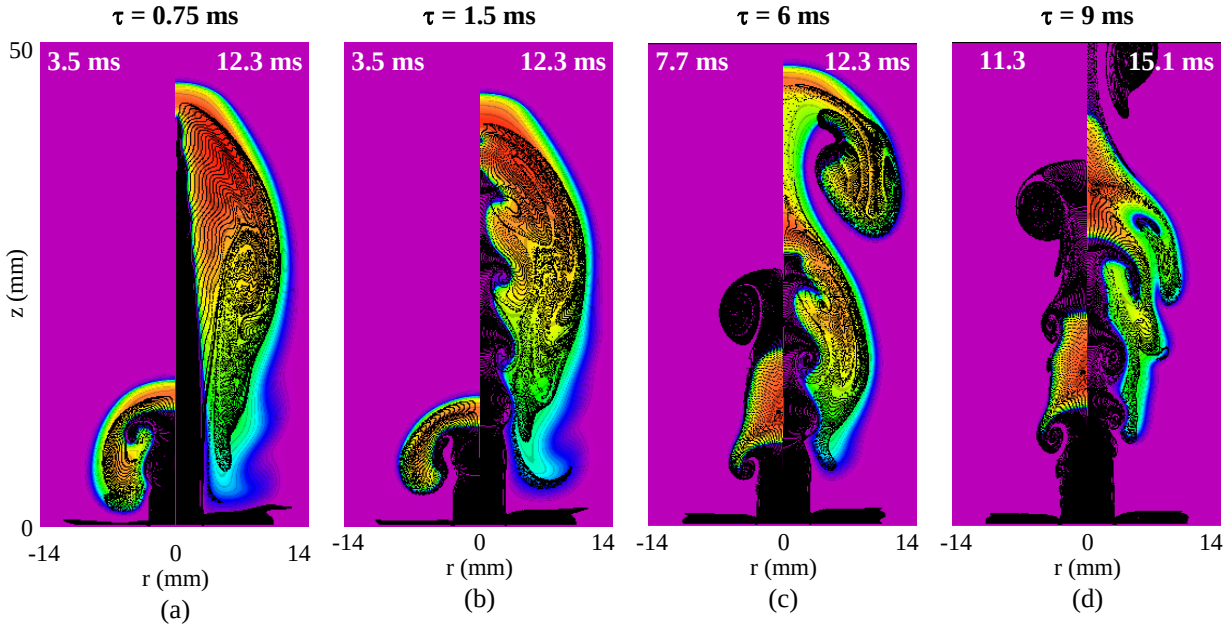

Fig. 7. Influence of ignition-delay on flame propagation through a 5-mm-diameter fuel jet. Velocity of the jet is 6.5 m/s. In each picture locations of particles injected from the fuel jet are superimposed on the temperature distribution. The ignition delays (a) 0.75 ms, (b) 1.5 ms, (c) 6.0 ms, and (d) 7.0 ms represent the time lapses between initiation of ignition and start of the jet. Left- and right-half images represent flame structures during the early and later stages of flame propagation, respectively.

mechanism is similar to that observed in the experiments in Fig. 4d. The average burning velocity in this case has dropped back to 5.5 m/s.

Traces of the flame locations at the centerline for the four cases considered are shown in Fig. 8. It is evident from this figure that the flame speed (slope), in general, is decreases with time. The flame speed at the end of the calculation is lower than that obtained at the time of ignition. Also, two regimes for initial flame speeds may be identified. When ignition occurs close to the vortex source (τ = 0.75 and 1.5 ms), the initial flame speed reaches a value of ~ 4.4 m/s, whereas when ignition takes place in the jet column (τ = 6.0 and 9.0 ms), it jumps to ~ 8.2 m/s. It may be recalled that the cold-flow velocities in these two regions are 4.1 and 6.6 m/s, respectively. Thus, when ignition occurs in the jet column, the flame speed increases above the combined value of jet and laminar burning velocities. The instabilities that are generated when the ignition takes place in the jet column (Figs. 7c and 7d) may contribute to this enhancement in flame speed.

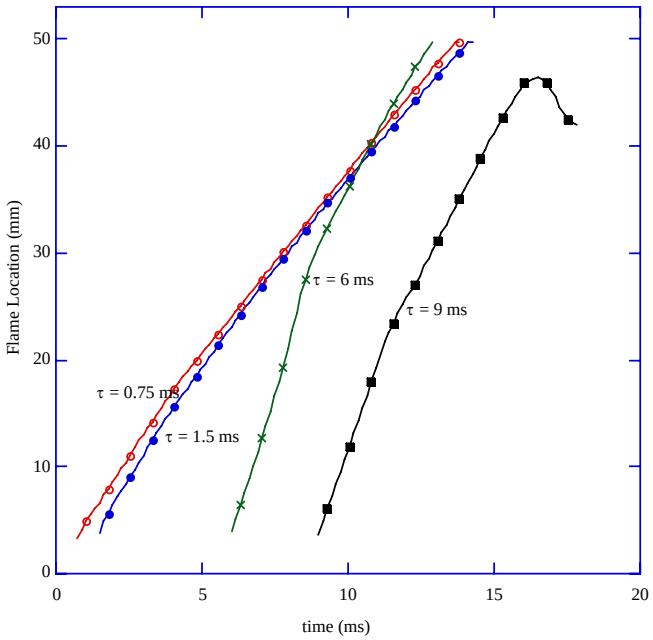

Fig. 8. Traces of the flame along the centerline for different ignition delays.

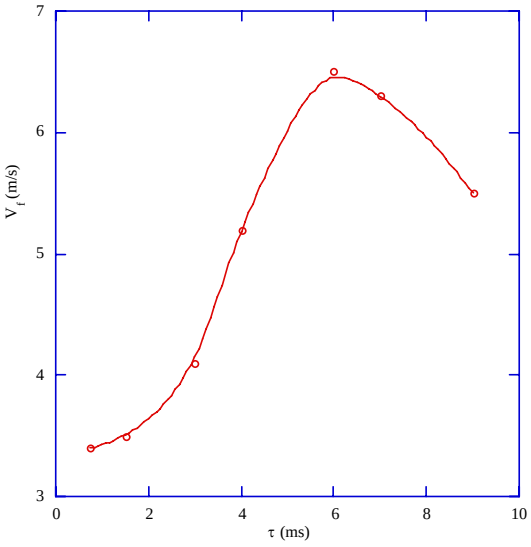

Fig. 9. Average flame speeds obtained for different ignition delays.

The variation of average flame speed with ignition delay is plotted in Fig. 9. It shows that for the given fuel-jet-injection scheme: (1) the flame velocity can be significantly increased by changing the ignition delay and (2) there exists a maximum in flame velocity that one can achieve in the laminar flow regime using large-scale vortices.

5. Conclusions

The current study explores several important parameters that affect flame propagation in ignited jets. Flame propagation is highly sensitive to spark timing and takes place in two distinct regions: (a) within the jet column and vortex rollers and (b) on the vortex exterior. Ignition after the passage of a vortex leads to the former type of flame propagation, and ignition ahead of a vortex leads to the latter type of flame propagation. The equivalence ratio affects the stability and speed of flame propagation, with ideal conditions found at stoichiometric to slightly rich conditions. Higher vortex strength causes localized extinction in the flames formed outside the vortex and causes more wrinkling to the flames formed within the jet column. Calculations for the ignition and flame propagation in stoichiometric fuel are performed using a well-tested CFD code. These time-dependent calculations with detailed chemical kinetics successfully simulate the experimentally observed flame-propagation mechanisms. It is found that propagation speed can be increased significantly by impulsively starting the fuel jet. However, for the given

jet injection, flame speed can only be increased to a maximum value by varying the ignition delay. Further delay in ignition leaves unburned fuel in the exhaust, and flame speed drops quickly.

Acknowledgments

The authors wish to thank Dr. C. D. Carter for use of the ES4 camera. The authors also acknowledge the assistance of Dr. R. D. Hancock and Mr. I. Vihinen in the assembly and construction of the burner. This work is supported by U.S. Air Force Contract F33615-00-C-2068 and through funding from the Air Force Office of Scientific Research (Dr. Julian Tishkoff, Program Manager).

References

Cattolica, R. J. and Vosen, S. R. (1986), *Combustion Science and Technology*, 48:77.

Fiechtner, G. J., Renard, P. H., Carter, C. D., Gord, J. R. and Rolon, J. C. (2000), "Injection of Single and Multiple Vortices in an Opposed-Jet Burner," *Journal of Visualization*, 2:331-341.

Gogineni, S., Goss, L., Pestian, D., and Rivir, R. (1998), "Two-Color Digital PIV Employing a Single CCD Camera," *Experiments in Fluids*, 25:320-328.

Ishizuka, S., Takahiro, M., Takahashi, H., Kiminori, K. and Ryo, H. (1997), *Combustion and Flame*, 113:542.

Katta, V. R., Anthenien, R., Mantz, R., Roquemore, W. M., Brockman, R. A., John, R., Zawanda, L. P., Parthasarathy, T. A., and Kerans, R., "Influence of Ceramix-Matrix-Composite Wall Plates on Combustor Performance" AIAA Paper 2000-3351, *36th Joint Propulsion Conference and Exhibit*, Huntsville, AL, July 17-19, 2000.

Katta, V. R., Brenez, L., and Rolon, J. C. (2000), "Experimental and Numerical Investigation of Structures of Two-Dimensional Partially Premixed Methane/Air Flames," *Proceedings of the Combustion Institute*, 28:1909-1916.

Katta, V. R., Goss, L. P. and Roquemore, W. M. (1994), "Numerical Investigations of Transitional H_2/N_2 Jet Diffusion Flames," *AIAA Journal*, 32:84-94.

Katta, V. R., Hsu, K. Y., and Roquemore, W. M. (1998), "Local Extinction in an Unsteady Methane-Air Jet Diffusion Flame," *Proceedings of the Combustion Institute*, 27:1121-1129.

Katta, V. R., and Roquemore, W. M. (1998), "Simulation of Dynamic Methane Jet Diffusion Flame Using Finite-Rate Chemistry Model," *AIAA Journal*, 36(11):2044-2054.

Katta, V. R., and Roquemore, W. M. (1995), "Numerical Studies on the Structure of Two-Dimensional H_2/Air Premixed Jet Flame," *Combustion and Flame*, 102(1/2):21.

McCormack, P. D., Scheller, K., Muller, G. and Tisher, R., *Combustion and Flame*, 19:297 (1972).

Meyer, T. R., Gord, J. R., Katta, V. R., and Roquemore, W. M., "Combustion in Impulsively Initiated Vortex Rings," *2nd Joint Meeting of the US Sections of Combustion Institute*, Oakland, CA, 2001.

Peters, N. (1993), "Reduced Kinetic Mechanisms for Applications in Combustion Systems," Lecture Notes in Physics (N. Peters and B. Rogg, Eds.), Springer-Verlag, Berlin, Vol. m15, pp. 3-14.

Renard, P. H., Thevenin, D., Rolon, J. C. and Candel, S. (2000), "Dynamics of Flame/Vortex Interactions," *Progress in Energy and Combustion Science*, 26:225-282.

Rolon, J. C., Aguerre, F. and Candel, S. (1995), *Combustion and Flame*, 100:422-429.

Roquemore, W. M. and Katta, V. R. (2000), "Role of Flow Visualization in the Development of UNICORN," *Journal of Visualization*, 2:257.

COMBUSTION & LASER DIAGNOSTICS AT AIR FORCE RESEARCH LABORATORY

James R. Gord
Propulsion Directorate
Air Force Research Laboratory
Wright-Patterson Air Force Base, OH

Michael S. Brown
Terry R. Meyer
Sukesh Roy
Sivaram P. Gogineni
Innovative Scientific Solutions, Inc.
Dayton, OH

Mission

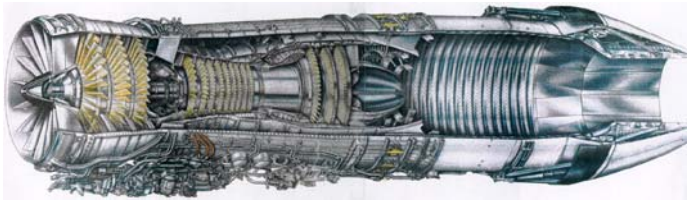

- **Improved Propulsion-System Performance (Thrust/Weight, SFC, etc.)**
- **Reduced Pollutant Emissions**
- **Enhanced Maintainability, Reliability, Affordability**

2

Combustor Technology Development

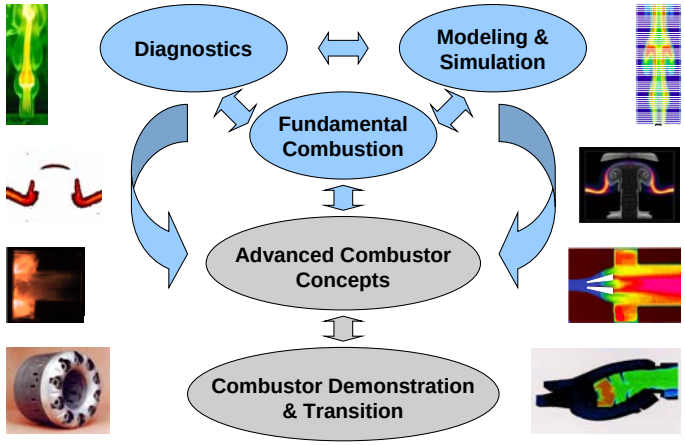

3

Phased Diagnostics Approach

Combustion Research in the Laboratory

Performance Evaluation in the Engine Test Cell

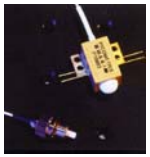

Real-Time Control on the Flight Line and in the Air

4

Turbulence (Vortex-Flame Interactions)

- Predictive understanding of turbulent combustion
- Detailed chemistry and physics
- Improved engine performance

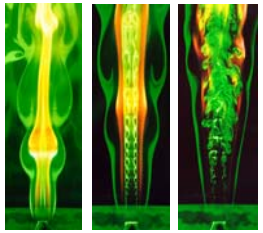

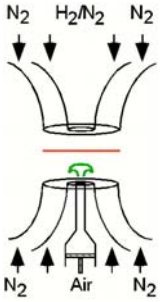

5

Flow Visualization

- Acetone Planar Laser-Induced Fluorescence (PLIF)
- Planar Rayleigh Scattering (PRS)
- Simultaneous OH PLIF/ Particle Image Velocimetry (PIV)

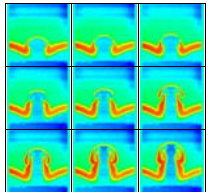

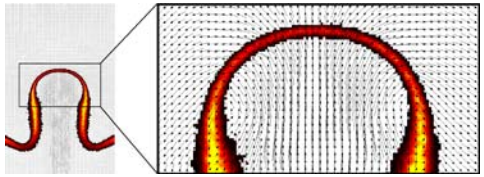

6

SIMULTANEOUS OH-PLIF AND VELOCITY DISTRIBUTIONS

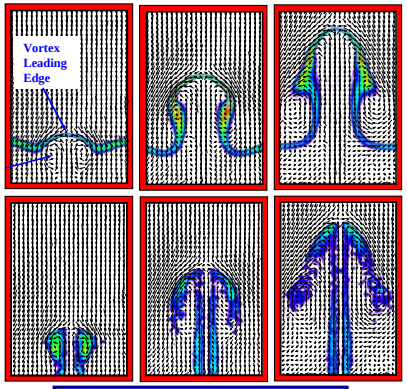

FOR A CASE WITH NO FLAME EXTINCTION

SUPERPOSED VELOCITY AND VORTICITY DISTRIBUTIONS

SIMULTANEOUS OH-PLIF AND VELOCITY DISTRIBUTIONS

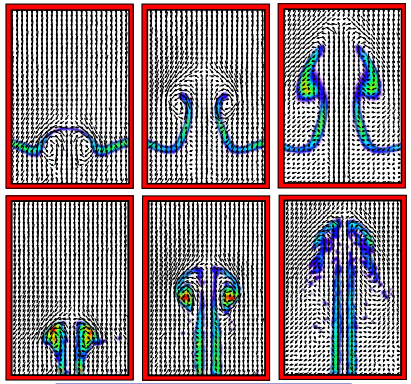

FOR A CASE WITH FLAME EXTINCTION

SUPERPOSED VELOCITY AND VORTICITY DISTRIBUTIONS

8

FLAME EXTINCTION PROCESS

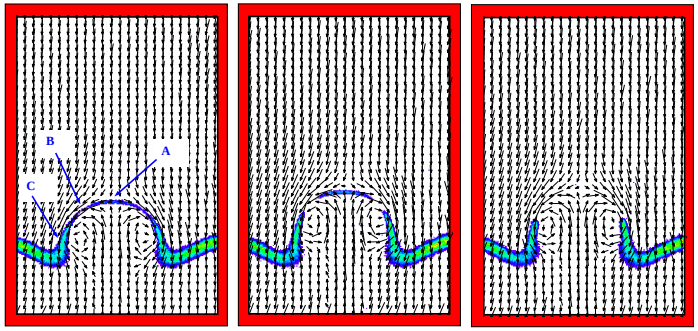

9

Triple-Pump CARS Instrumentation

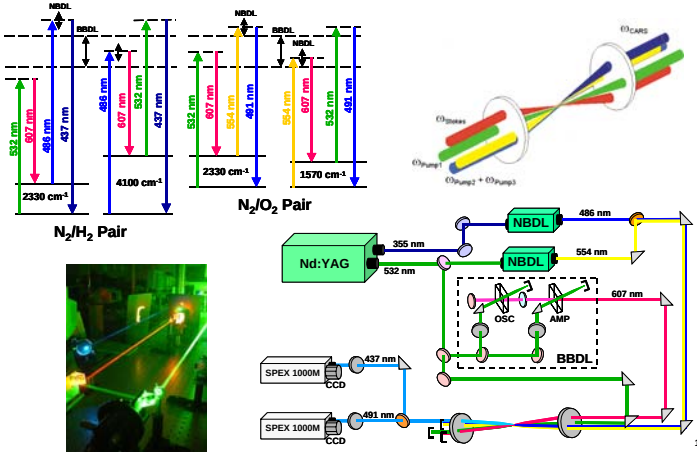

10

Triple-Pump CARS Application

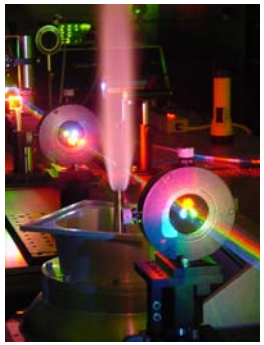

Quantitative, Single-Shot Temperatures & Species w/ High Spatial & Temporal Resolution

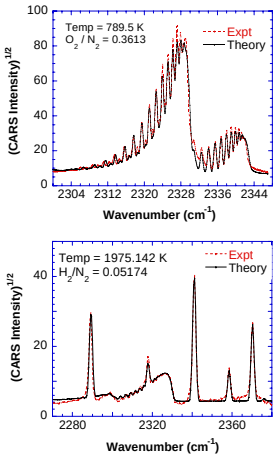

11

Solid-State-Laser-Based Sensors

- **Pollutant-Emissions Measurements**
- **CO, NO Absorption Spectroscopy**
- **Ruggedization, Miniaturization**
- **Well-Stirred Reactor Applications at WPAFB**
- **Auxiliary Power Unit Applications at Honeywell**

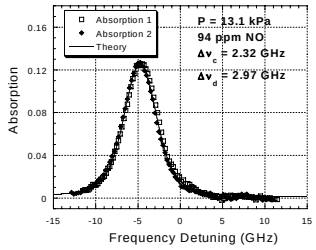

12

Frequency-Mixing Schemes (CO)

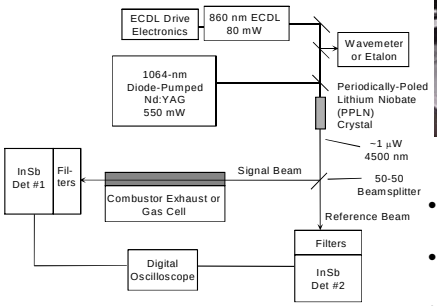

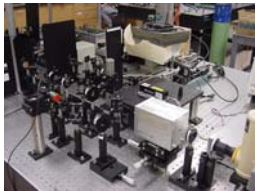

- 860-nm ECDL w/ 1064-nm YAG
- PPLN DFG Yields 1 μW @ 4.5 μm
- Preliminary Measurements in CO/N_2 Mixtures

Frequency-Mixing Schemes (NO)

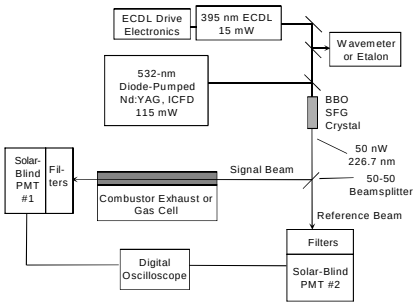

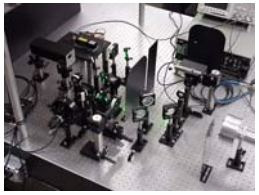

- 395-nm ECDL w/ 532-nm YAG
- BBO SFG Yields 50 nW @ 226.7 nm
- Preliminary Measurements in NO/N_2 Mixtures
- 0.2-ppm NO LOD (1-m Path)

Nitric Oxide Sensor at Honeywell

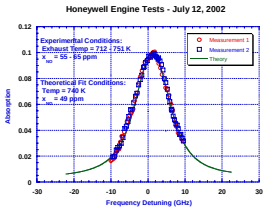

Continuous, Nonintrusive Monitoring of Pollutant Emissions in a Real-World APU

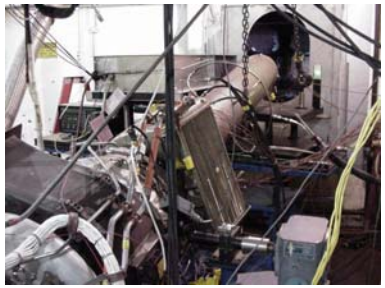

Terahertz Radiation ("T-Rays")

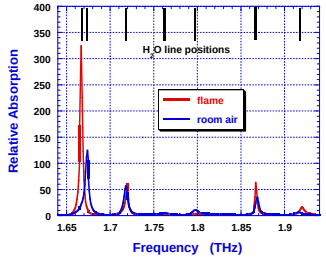

- Far Infrared
- Absorption Lines
- Transmission Properties
- Packaging

2000
R&D 100
Award Winner

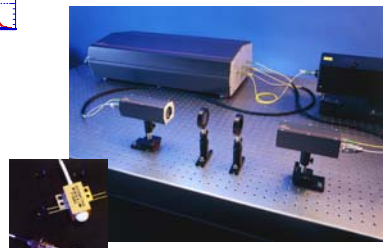

Other Ultrafast Spectroscopies

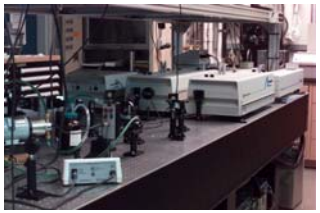

- Pico/Femtosecond Pump-Probe Spectroscopy
- Asynchronous Optical Sampling
- Picosecond Time-Resolved Laser-Induced Fluorescence
- Polarization Spectroscopy

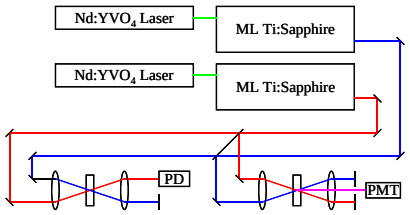

17

OVERVIEW OF CLDRC

18

Summary

- CLDRC provides diagnostic support for advanced combustor development.
- Three-phased approach features fundamental studies and diagnostics development, test-cell applications, and on-board integration.
- New facilities in CLDRC will permit next-generation experimental studies.

19

Acknowledgments

- AFRL: Cam Carter, Jeff Donbar
- Innovative Scientific Solutions, Inc.: Vish Katta, Larry Goss, Mark Hsu
- Sandia CRF: Greg Fiechtner
- NASA Langley: Keith Grinstead
- École Centrale Paris: Juan Carlos Rolon, Dominique Thévenin, Paul-Henri Renard, Julien de Charentenay, Alix Lemaire, Katharina Zähringer

20

Acknowledgments

- Purdue: Bob Lucht, Thomas Walther
- Aculight, Inc.: Angus Henderson, Pam Roper, Roy Mead
- Picometrix, Inc.: Van Rudd, Dave Zimdars, Matt Warmuth
- Air Force Office of Scientific Research: Julian Tishkoff, Charbel Raffoul (EOARD)

Hydrocarbon Fuel Sensor

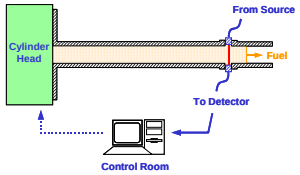

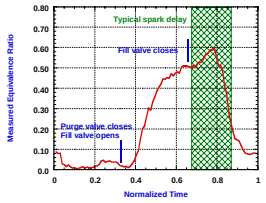

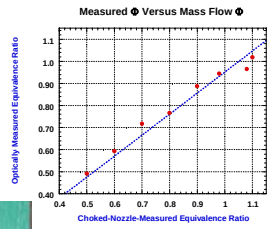

Real-Time Optical Determination of Fuel/Air Equivalence Ratio and Tube Fill-Fraction

Emission Sensor for Φ & Fill

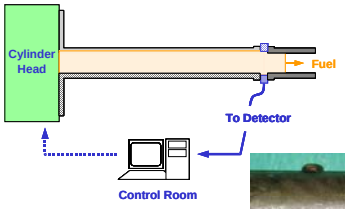

Potential for Active Control through On-Board Monitoring of Φ and Fill

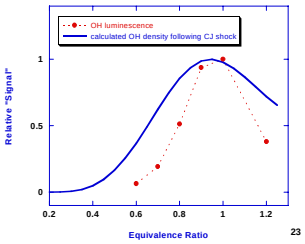

Ultranarrowband Doubly Resonant OPO

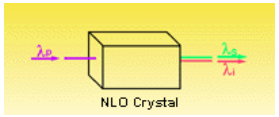

$\omega_{pump} = \omega_{signal} + \omega_{idler}$

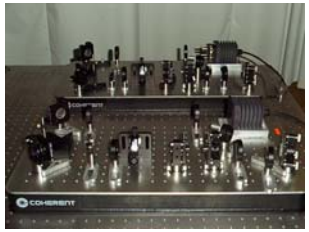

Proceedings of PSFVIP-4
June 3-5, 2003, Chamonix, France.
F4009

Experimental study of two-phase vortex-flame interactions by laser induced fluorescence of OH and CH

A. Lemaire [1], K. Zähringer [1,2], T. R. Meyer [3], J. R. Gord,[4] and J. C. Rolon [1]

[1] Laboratoire d'EM2C, CNRS/École Centrale Paris, Grande Voie des Vignes, 92295 Chatenay-Malabry Cedex, France.
[2] now at : Lehrstuhl für Strömungsmechanik und Strömungstechnik, Universität Magdeburg, 39106 Magdeburg, Germany.
[3] Innovative Scientific Solutions Inc., 2766 Indian Ripple Road, Dayton, OH 45440, USA.
[4] Air Force Research Laboratory, Propulsion Directorate Wright-Patterson Air Force Base, OH 45433-7103, USA

KEYWORDS*:*
Main subject(s): *Combustion,*
Fluid: *Aerodynamics,*
Visualisation method: Laser Induced Fluorescence

ABSTRACT : The interaction between a vortex and a flat laminar diffusion flame is generally used to simulate a number of features that are common in turbulent combustion, such as dynamic strain, stretch, and curvature. Using well-controlled experiments to verify numerical simulations, phenomena such as flame extinction and micro-vortex-flame behaviour can be studied. The dynamic interaction between a laminar flame and a vortex may be examined by laser induced fluorescence of the hydroxyl (OH) layer produced by the flame, OH being a marker of long living intermediates, or by the CH radical which is considered to be a good marker of the primary reaction zone and a representative of the flame surface. The goal of the present investigation is to study two-phase vortex-flame interactions using both, OH and CH planar laser-induced fluorescence (PLIF). Like previous measurements in premixed flames, our results indicate that gaps in the CH PLIF layer do not always correspond to gaps in the OH layer.

1. Introduction

In the flamelet model for turbulent non-premixed combustion the flame surface is supposed to interact with turbulent vortices. The induced local strain and curvature can result in reduced overall reaction rates, local flame extinction, and decreased flame stability. Using well-controlled vortex injection to perturb steady counterflow diffusion flames and simulate the mentioned unsteady local extinction process in a repeatable manner, helped to generate turbulent combustion diagrams (Thévenin et al., 2000), and to study the time evolution of flame surface area during vortex-flame interaction (Renard et al., 1999). Two-phase vortex-flame interactions in counterflow diffusion flames were reported by Santoro et al. (2000 and 2002), who used methanol-air spray flames to capture flame phenomena found in practical devices.

Nguyen and Paul (1996) showed through measurements of OH and CH PLIF in premixed flames, that breakage of the CH radical front during vortex interaction may not be associated with a rupture of the OH-front. Donbar et al. (2000) showed the different features of the CH and OH layers in a turbulent nonpremixed methane-air flame. The CH layer can be considered as a proof that the flame exists. It appears in a narrow region of the flame near the location of peak temperature. OH may show either a flame location, an interface between OH and entrained air or a fuel-air interface where the flame is extinguished. In our study, the controlled vortex-flame interaction in a two-phase methane/n-heptane flame is visualised by these two radicals.

The goal of the current investigation is to study the flame structure and shape during two-phase vortex-flame interaction with a vortex coming from the droplet laden fuel side of the burner. CH and OH planar laser-induced fluorescence (PLIF) is used to visualise the flame front during vortex impingement and the different behaviour of these radicals as representatives of the reaction zone is discussed. Flame-surface evolution and relative radical mole fractions as a function of time relative to vortex perturbation can be determined from these images for different flame and vortex conditions.

Copyright ©2003 by PSFVIP-4

2. Experimental device

The burner apparatus and diagnostic approach have previously been described by Lemaire et al. (2002) for CH PLIF experiments. Thus, only a brief description is included here, with the changes necessary for the OH-PLIF study.

2-1 Burner apparatus and flow conditions

The experimental device used for this work was previously modified from a gaseous counterflow burner design (Rolon et al. 1991) to include a piston-actuated vortex injection system (Rolon et al. 1995). Several experimental studies using this apparatus have been reported previously in the literature (Renard, et al. 1999; Fiechtner et al. 2000). The burner consists of two axisymmetric, 20-mm diameter counterflow nozzles, with air in the upper flow and a nitrogen-fuel mixture in the lower flow. A two-phase methane with n-heptane fuel mixture is produced inside an atomizer system, creating a mono-disperse field of droplets (2.43-2.83 m in diameter) for the current flow conditions. The spray is diluted to a non-dense condition. A 40-mm diameter flow of nitrogen surrounds each nozzle to shield the flame from ambient disturbances. The nozzle separation is set to 30 mm in this study. A vortex tube of 2 mm is added along the centerline of the fuel nozzle, fed by an electronically controlled piston-actuation system. Vortices of varying strength can be generated by controlling the stroke, and rise time of the piston. In this paper we concentrate on flames with an overall mixture ratio of 3.44 and a vortex size of 2 mm with a piston rise time of 10 ms. The initial mass fraction of fuel is 0.21 and the mass fraction of methane in the fuel is 0.48. The steady nozzle velocities of the fuel and oxyder stream are respectively 0.59 m/s and 0.61 m/s. The varying vortex parameters are given in table 1 including the ejected volume ΔV. The vortex propagation velocity U_T has been determined previously by PIV measurements (Lemaire et al., 2002). The 2-mm-tube vortices structure showing a spherical pattern, the vortex circulation (Γ_{Vort} is calculated using a spherical vortex model (($\Gamma_{Vort} = U_T D/5$ where D is the vortex diameter equal to 4mm).

Vortex	ΔV (mm^3)	U_T ($m.s^{-1}$)	Γ_{Vort} ($cm^2.s^{-1}$)
A	10	0.4	3.2
B	14	0.7	5.6
C	38	1.0	8.0

Table 1 : Vortex features.

2-2 LIF-System

CH PLIF is achieved using the $Q_1(5)$ transition (389.5 nm) in the $B^2\ ^{\sim}\ ^2$ (0,0) absorption band of CH. The OH-PLIF technique uses the $Q_1(6)$ band of the $A^2\ ^+$--X^2 (1,0) transition of OH at 283 nm. The laser pulses of about 7 ns in duration and mean energies between 15 and 20 mJ for both CH and OH are formed into 0.3 mm thick sheets of 20-mm height for CH and of 50-mm height for OH. The power density variation inside the measurement region has been minimised by controlling it with Rayleigh scattering from nitrogen and Mie scattering from the droplets, by centering the laser sheet on the flame region during the entire vortex-flame interaction and by partially saturating the transitions. The high laser energy allows to diminish quenching and pulse-to-pulse laser fluctuation. Thus laser-sheet intensity variations did not exceed 5% in the whole measurement region.

Fluorescence of CH is collected from the A--X(0,0) and A--X(1,1) bands around 430 nm by using a combination of a 410 nm high-pass and a 450 nm low-pass filter. OH-Fluorescence is observed from the A--X(0,0) and A--X(1,1) bands through a filter combination of a 250-400-nm band-pass filter and a 285-nm high-pass filter. The CH PLIF signal is collected during 20 ns using a 2 x 2 binned 512 x 512 array PI-Max intensified CCD camera with a 58-mm f/1.2 Noct-Nikkor lens and 20-mm extension ring, while the OH signal is recorded during 80 ns using the same camera with a UV 105-mm f/4.5 Nikkor lens and a 36-mm extension ring. The region of interest is of 25 x 25 mm for CH detection and of 20 x 20 mm for OH.

Observation of vortex interactions also requires the synchronisation of several events, including vortex generation, laser pulse, and camera exposure. The vortex-flame interaction can then be imaged at various phases of its development by adjusting relative timing of piston actuation and laser diagnostics. The OH and CH PLIF measurements have not been realised simultaneously, but on similar vortices whose parameters are controlled and repeatable. The propagation velocities and circulations have been deduced from PIV measurements simultaneously with the CH-LIF.

Copyright ©2003 by PSFVIP-4

3. Results and discussion

Figures 1 to 3 show the series of LIF images for three different vortex conditions. These images are raw images, where no background has been subtracted and no normalisation with respect to the laser power has been done. The CH images are mean images of 10 raw images due to the low signal level of CH-LIF, the OH images are single-shot images. On the left side the CH-LIF images are represented, on the right side the OH-LIF is shown together with Mie diffusion on the n-heptane droplets. This allows the visualisation of the evaporation front, which is situated under the flame front represented by the OH layer, and the vortex position and structure.

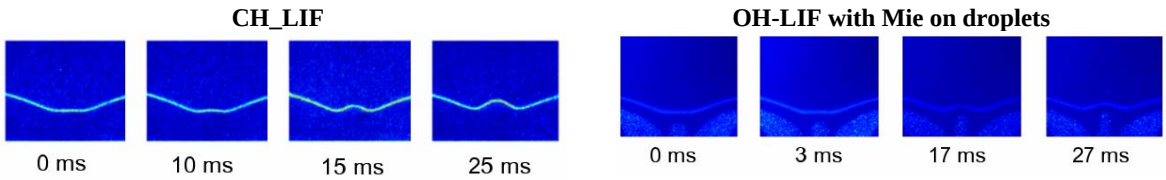

Fig. 1 : Vortex-flame interaction with weak deformation and no extinction (Vortex A)

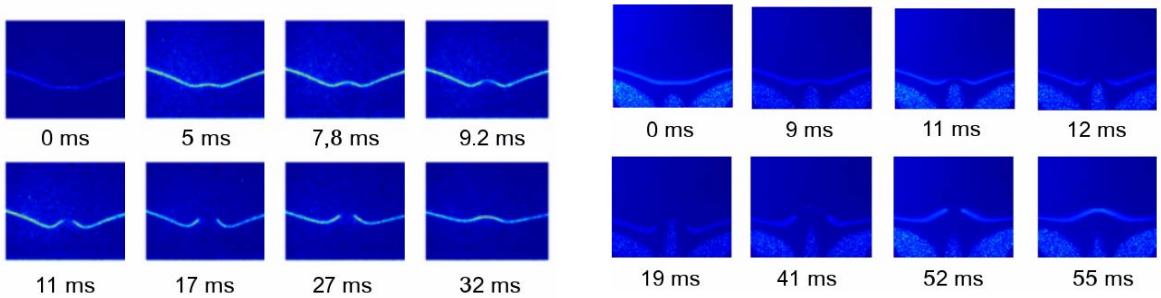

Fig. 2 : Vortex-flame interaction with weak deformation, extinction and reconnection (Vortex B)

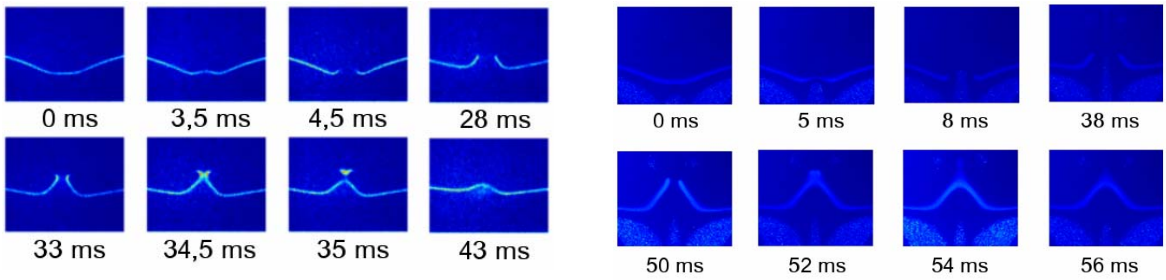

Fig. 3 : Vortex-flame interaction with weak deformation, extinction, elongation, junction and formation of small flame pocket (Vortex C)

In the first case (Fig.1) the flame is deformed very weakly during vortex impingement (Vortex). There is no extinction and after about 40 ms the flame has once more its initial form. Figure 2 shows a series of images with flame extinction. The vortex (Vortex B) first weakly deforms the flame, which thins in the centre and disrupts. The initial OH-layer thickness is about 1 mm, the CH-layer is much thinner (0.2 mm). The vortex passes through the flame but is not strong enough to propagate against the air flow. The flame edges at the extinction hole remain in the vortex core, and non–vaporized droplets continue to feed the flame (Fig 2, time 41 ms). Then the flame reconnects propagating towards the mixed reactants accumulated by the absence of flame interface. If the vortex circulation is rather strong (Vortex C), flame extinction takes place much earlier. Then the vortex core propagates far inside the air flow, elongating strongly the flame edges. The conical flame shape elongates strongly under the induced vortex strain with its upper side becoming smaller; so that the flame fronts collapse. This collapse highly increases the flame intensity, leading rapidly to the formation of a small flame pocket. These is entrained by the vortex inside the air flow until extinction by lack of fuel. The OH and CH behaviours are slightly different during the collapse process. The CH signal clearly disappears at the collapse point separating a small flame pocket, while OH does not disappear completely and is present, with a weak signal, in a wide area from the collapse point to the flame pocket.
When comparing the two corresponding series for CH and OH, one can recognise that the CH-layer seems to extinguish before the OH-layer. For vortex B the CH front disrupts between 9 and 11 ms, for OH this takes place

Copyright ©2003 by PSFVIP-4

about 2 ms later. In the case of vortex C the difference is even bigger, CH-extinction is visualised after about 4 ms, whereas the OH-layer stays intact nearly until 8ms. The same fact can be remarked for the reconnection or junction of the flame front. The CH layer is re-established before the OH-layer.
These differences between OH and CH are known in the literature for local extinction processes in turbulent premixed jet flames (Nguyen and Paul,1996; Donbar et al.,2000). Here the same differences are found during dynamic vortex-flame interactions in diffusion flames. The earlier extinction of the CH-layer is due to the kinetic differences of CH and OH formation in the flame. CH is formed in the very early stage of the chemical reaction on the fuel-side of the flame and thus touched first by the vortex. OH is formed later, has a longer lifetime and diffuses into the hot burnt gasses. Therefore the OH layer is broader and it can exist for a while even after extinction of the primary reaction, as it can be seen during the collapse process. Watson et al. (1999) showed some images of reconnected CH-layers wrapping around broken OH-layers in their study of turbulent diffusion jet flames. This could corresponds to our finding of a later reconnection of the extinguished OH front compared to CH. The CH-layer has a faster chemistry and seems to be more sensitive to the vortex movement and therefore re-establishes earlier after the vortex has passed.

4. Conclusions and prospects

Laser-induced fluorescence measurements of CH and OH in a two-phase, laminar, non-premixed counterflow flame, interacting with a vortex have been done in this study. Different interaction regimes exhibit different ways of flame surface evolution with wrinkling, elongation, extinction and collapse processes. Both radicals are representatives of the reaction region, CH on the fuel-rich side, OH for the fuel-lean side of the flame. They show global behaviour similarities, however their local behaviour during transient process is clearly different. In order to get a more accurate depiction of the regions of extinction and reconnection or junction of disrupted flame fronts, simultaneous CH and OH measurements would be necessary on the same configuration. This would finally exclude any doubt about repeatability of the vortex generation and its influence on the interaction behaviour.

Acknowledgments

This work was supported by French DGA / ONERA PEA-number 98703-TITAN and by U.S. Air Force Contract F33615-00-C-2068 in a French-U.S. collaborative program.

References

Donbar J.M., Driscoll J.F., and Carter C.D.: Reaction Zone Structure in Turbulent Nonpremixed Jet Flames - From CH-OH PLIF Images, *Combustion and Flame*, Vol. 122, pp. 1-19, 2000.

Fiechtner G. J., Renard P. H., Carter C. D., Gord J. R. and Rolon J. C.: Injection of Single and Multiple Vortices in an Opposed-Jet Burner, *Journal of Visualization*, Vol. 2, pp. 331-341, 2000.

Lemaire, A., Meyer, T. R., Zähringer, K., Gord, J. R. and Rolon, J.-C.: PIV/PLIF-Investigation of two-phase vortex-flame interactions : effects of vortex size and strength, *Experiments in Fluids*, accepted for publication, 2002.

Nguyen Q.-V., Paul P. H.: The time evolution of a vortex-flame interaction observed via planar imaging of CH and OH, *Proceedings of the Combustion Institute*, Vol. 26, pp. 357-364, 1996.

Renard P. H., Rolon, J. C., Thevenin, D., and Candel, S.: Investigations of heat release, extinction, and time evolution of the flame surface for a non-premixed flame interacting with a vortex, *Combustion and Flame*, Vol. 117, pp. 189-205, 1999.

Rolon J.C., Veynante, D., Martin, J.-P. and Durst F.: Counter Jet Stagnation Flows, *Experiments in Fluids*, Vol. 11, pp. 313-324, 1991.

Rolon, J. C., Aguerre, F. and Candel, S. Experiments on the Interaction between a Vortex and a Strained Diffusion Flame, *Combustion and Flame*, Vol. 100, pp. 422-429, 1995.

Santoro V.S., Kyritsis D.C. and Gomez A.: An Experimental Study of Vortex-Flame Interaction in Counterflow Spray Diffusion Flames, *Proc. Combust. Inst.*, Vol. 28, pp. 1023-1030, 2000.

Santoro V.S. and Gomez A.: Extinction and Reignition in Counterflow Diffusion Spray Flames interacting with Laminar Vortices, *Proc. Combust. Inst.*, Vol. 29, 2002.

Thévenin D., Renard P.-H., Fiechtner G.J., Gord J.R. and Rolon J.C.: Regimes of Non-Premixed Flame-Vortex Interactions, *Proc. Combust. Inst*., Vol. 28, pp. 2101-2108, 2000.

Watson K.A., Lyons K.M., Donbar J.M., and Carter C.D.: Scalar and velocity measurements in a lifted CH4-air diffusion Flame, *Combustion and Flame*, Vol. 117, pp. 257-271, 1999.

Copyright ©2003 by PSFVIP-4

REAL-TIME COMBUSTOR DIAGNOSTICS USING HIGH-SPEED DIGITAL IMAGING

Terrence R. Meyer, Michael S. Brown, John L. Hoke, and Sergey Fonov
Innovative Scientific Solutions, Inc.

Frederick R. Schauer and James R. Gord
Air Force Research Laboratory / PRTS

27th Annual Dayton-Cincinnati Aerospace Sciences Symposium
Dayton, Ohio, March 5, 2002

Acknowledgements

D. Shouse, V. Belovich, and M. Roquemore
Air Force Research Laboratory / PRTS

R. Bradley, G. Boggs, R. Britton, R. Ryman, K. Shoffstall, B. Day, J. Parker, and M. Slagel
Innovative Scientific Solutions, Inc.

C. Cooper
GE Aircraft Engines

C. Tenney
Photo-sonics / IMC

U.S. Air Force Contract F33615-00-C-2068

Background and Motivation

- **Many combustors of practical interest are highly intermittent and three-dimensional.**
- **Such combustors are difficult to study with single-frame laser-based imaging.**
- **High-speed digital imaging is now capable of 60,000 fps with 10 μs exposure.**
- **High-speed digital imaging can offer convenient real-time diagnostics for combustor research and development.**

Applications

Pulsed-Detonation Engine

- **Supersonic combustion**
- **High pressure flame structure**
- **Dynamics of soot formation**

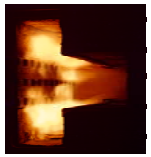

Trapped-Vortex High-Pressure Combustor

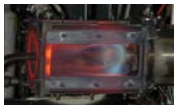

Single Swirl Cup CFM-56 Atmospheric Combustor

Equipment

ISSI

	Photron FASTCAM-Ultima SE 1	Photo-sonics Phantom v5.0	Redlake HG-100K Imager
Maximum Speed	40,500 fps	60,000 fps	100,000 fps
Minimum Shutter	24.7 µs	10 µs (Indep.)	10 µs (Indep.)
Chip	NMOS 256 x 256	CMOS 1024 x 1024	CMOS 1508 x 1100
Sensitivity	Good Visible Only	Low Visible Only	Low Visible Only

PDE Exhaust

ISSI

Image from Conventional Video Camera

Exhaust Flow from High-Speed Camera (18,000 fps)

PDE Detonation Transition

ISSI

Side-View of Full Tube with Shelkin Spiral (18,000 fps)

0.0 µs

55.5 µs

111.0 µs

166.5 µs

222.0 µs

PDE Detonation Transition

ISSI

Side-View of Transition Region with Shelkin Spiral (18,000 fps)

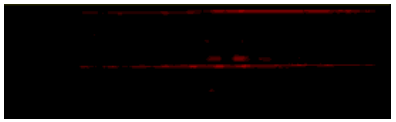

0.0 µs

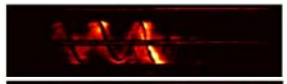

55.5 µs

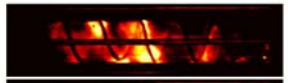

111.0 µs

166.5 µs

PDE Detonation Transition

ISSI

- Endview images collected in conjunction with high-speed pressure traces.

Endview of PDE Tube with Shelkin Spiral (40,500 fps)

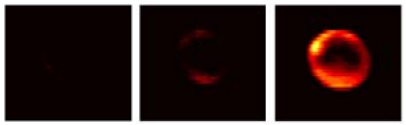

0 µs 25 µs 50 µs

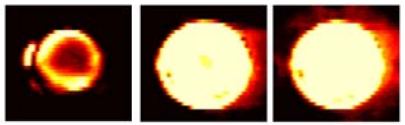

75 µs 100 µs 125 µs

Trapped-Vortex Combustor

ISSI

- High-speed imaging shows vortex circulation and roll-over time.
- High pressure leads to more uniformly distributed heat release.

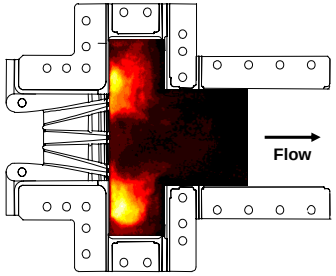

Atmospheric Pressure

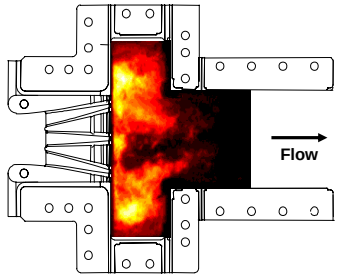

High Pressure

Coherent-Structure Velocimetry

ISSI

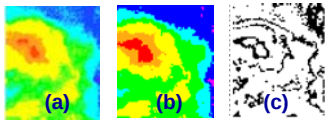

Step (a): Obtain source image.
Step (b): Increase contrast.
Step (c): Calculate iso-contours.
Step (d): Cross-correlate for velocity.

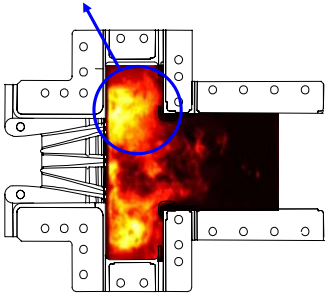

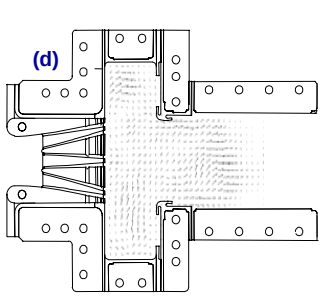

CFM56 Atmospheric Combustor

ISSI

- Filtered high-speed images can highlight CH^* fluorescence in the fuel-spray region.
- Fuel-spray intermittency evident in time-correlated images.

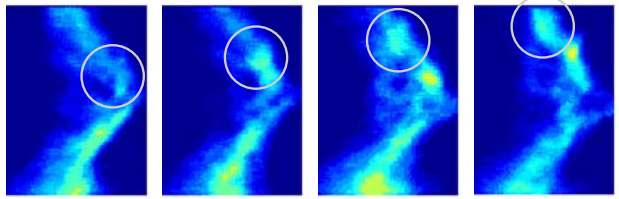

CFM56 Soot Formation

ISSI

Soot Luminescence

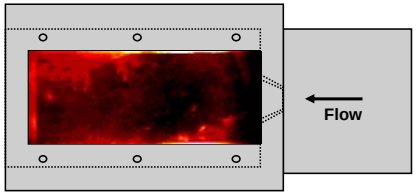

Instantaneous Velocity

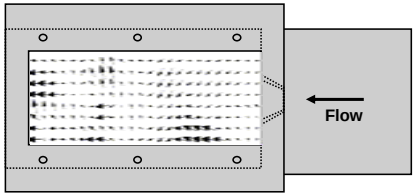

Influence of Streamwise Vortices in Soot Formation

ISSI

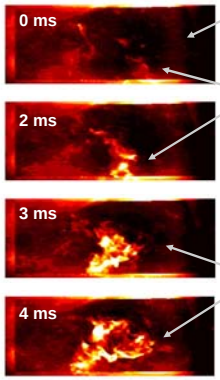

Conical mixing layer induced by fuel injector

Apparent initiation and growth of soot structure

Evidence of soot formation associated with streamwise vortices

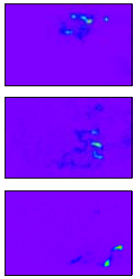

Comparison with uncorrelated single-shot LII

Conclusions

ISSI

High-speed digital imaging demonstrated in the following areas:

- **Imaging highly transient processes in a pulsed-detonation engine.**
- **Analyzing the effect of various operating conditions on the flame structure of a high-pressure trapped-vortex combustor.**
- **Providing a time-averaged and instantaneous estimate of the velocity field using coherent-structure velocimetry.**
- **Analyzing the coupling of fluid dynamics and soot formation in a CFM56 atmospheric combustor.**

SINGLE-SHOT LII MEASUREMENTS IN THE REACTION ZONE OF A MODEL COMBUSTOR

M. Brown and T. Meyer
Innovative Scientific Solutions, Inc.
Dayton, OH

J. Gord, V. Belovich
Air Force Research Laboratory
Wright-Patterson AFB, OH

27th Annual Dayton-Cincinnati
Aerospace Sciences Symposium
March 2002
Dayton, OH

Motivation

Part of an Air Force program to evaluate fuel additives for particulate reduction.

Specific Goals:

Obtain single-shot LII images in reaction zone of JP-8-fueled combustor,

Look for correlation with extractive sampling results,

Look for correlation with fluid behavior (high speed imaging),

Determine soot volume fraction.

2

Combustor Test Facility

Single Swirl Cup CFM-56 Atmospheric Combustor

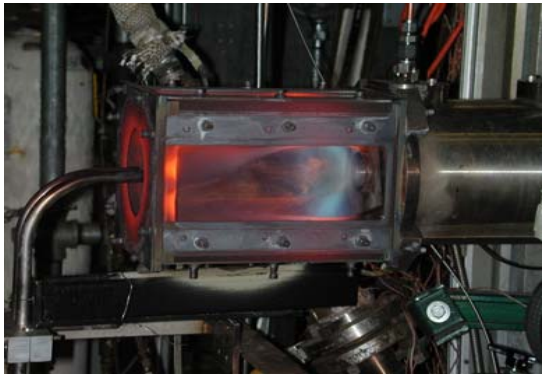

3

Experimental Setup

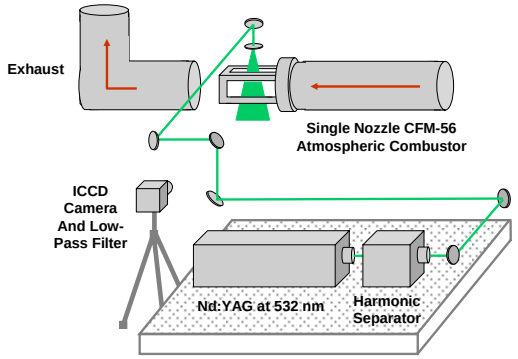

4

Experimental Setup - B

Image Field of View

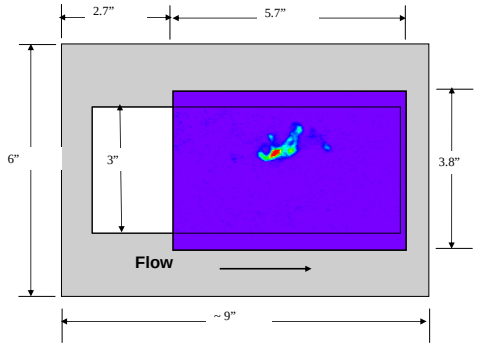

5

LII Data Generation & Collection

Typical Operational Envelope

Laser power	100 – 600 mJ
Camera delay	20 – 60 ns
Camera gate width	200 – 400 ns
Spectral filters	spf 500 (<500 nm)

6

Single-Shot LII Images

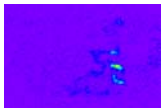

Scale 0 – 3,000

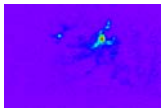

Scale 0 – 5,000

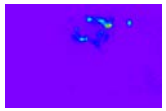

Scale 0 – 15,000

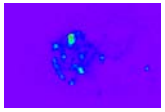

Scale 0 – 15,000

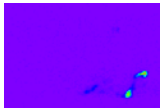

Scale 0 – 20,000

7

Single-Shot LII Images

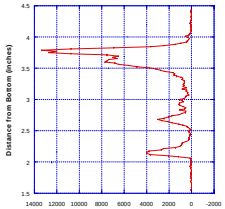

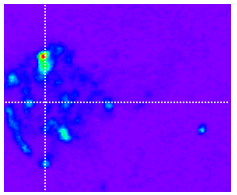

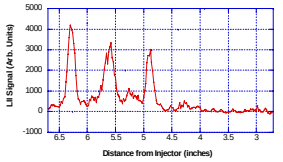

8

High Speed Images of Combustor

High-speed imaging system: captures full window area, 9000 fps, no filters (luminescence and chemiluminescense).

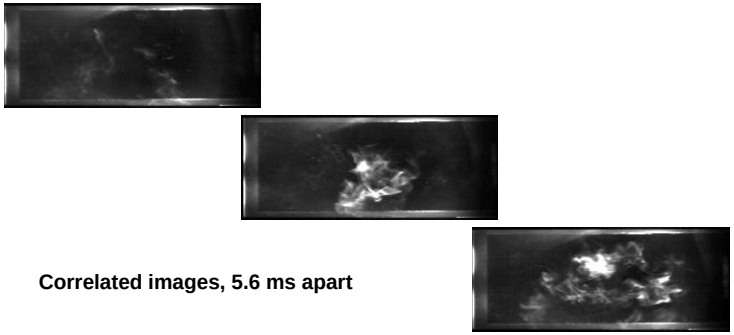

Correlated images, 5.6 ms apart

9

Average LII Image

Average from 795 of 800 Single-Shot Images

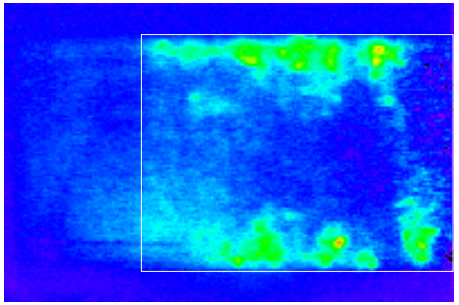

White line denotes area used for reduction to scalar average.

10

Results from Averaged Images

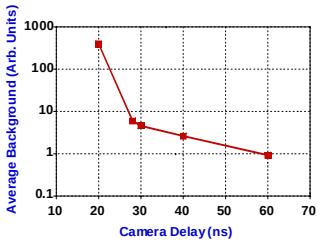

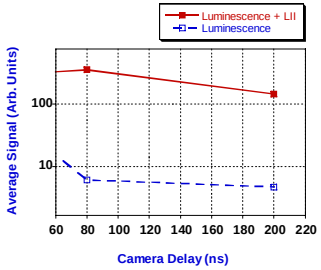

Flame Off

Flame On

11

Results from Averaged Images

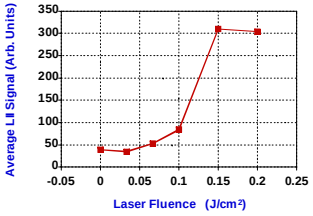

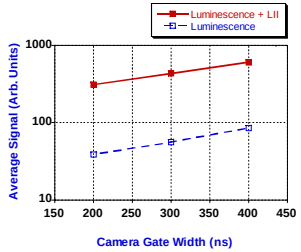

12

Comparison with Probe Sampling

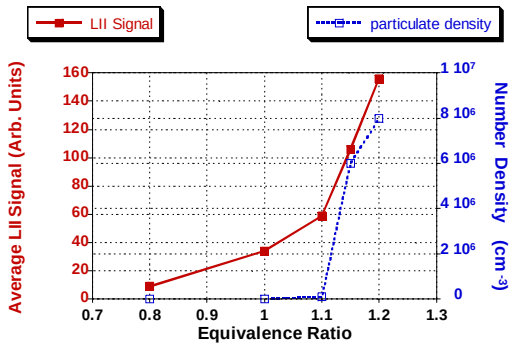

13

Effect of Additive

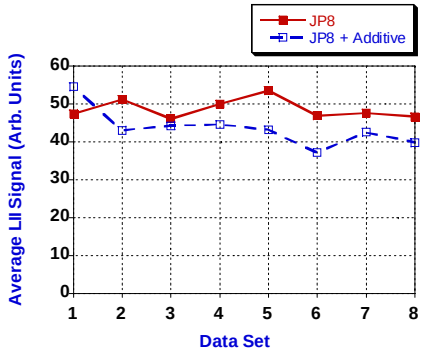

14

Summary and Future Work

Demonstrated single-shot acquisition of LII images in reaction zone of JP-8-fueled swirl-inlet combustor ($0.8 \leq \varphi \leq 1.2$),

Performed parametric studies of LII signal on camera gate delay, gate width, and laser fluence,

Optimized spectral filtering and gate delay to minimize laser scatter and background luminescene,

Single-shot LII images reveal a complex structure that changes shot-to-shot similar to high-speed images of flame emission,

For $\phi \geq 1.1$, averaged LII signal trend similar to probe-sampled particulate density,

LII images indicate possibility of characterizing additive effects on soot volume fraction.

Future work: use 1064-nm excitation, establish calibration procedure, and continue correlation Study with probe-sampling.

Acknowledgement, work supported in part by AF contract # F33615-00-C-2068.

15

TERAHERTZ RADIATION MEASUREMENTS IN COMBUSTION ENVIRONMENTS

30 Mar 01

Michael S. Brown
Innovative Scientific Solutions, Inc.
J. Van Rudd, David Zimdars & Matt Warmuth
Picometrix, Inc.
James R. Gord
Air Force Research Laboratory, Propulsion Directorate

THz Spectral Territory

Hardware-Based Delineation

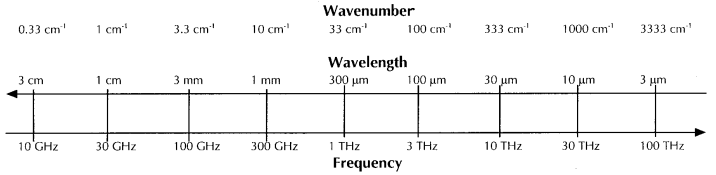

Microwave Spectroscopy — FTIR

Material Resonances: gases – rotations
liquids – hindered motions
solids – electron bound states

2

THz Hardware Evolution

practical fs lasers + low temp GaAs + microfabrication + substrate lenses — *yesterday*

↓

practical THz transmitters / receivers

↓

THz time domain spectroscopy (THz-TDS)

↙ ↘

hardened, user-friendly systems (Picometrix)

applications ISSI/AFRL — *today*

3

Picometrix Hardware Approach

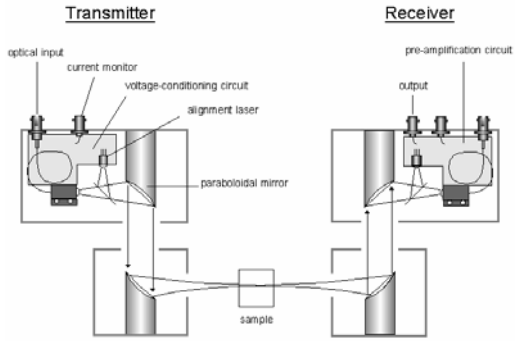

Fiber-Coupled Transmitter / Receiver Pair

4

Soot Absorption

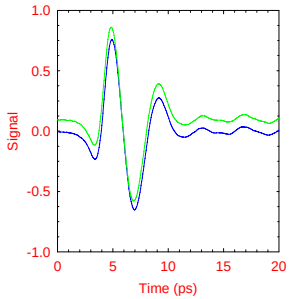

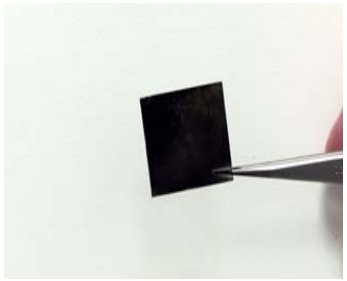

Test Case: Soot film on substrate.

5

Fuel / Water

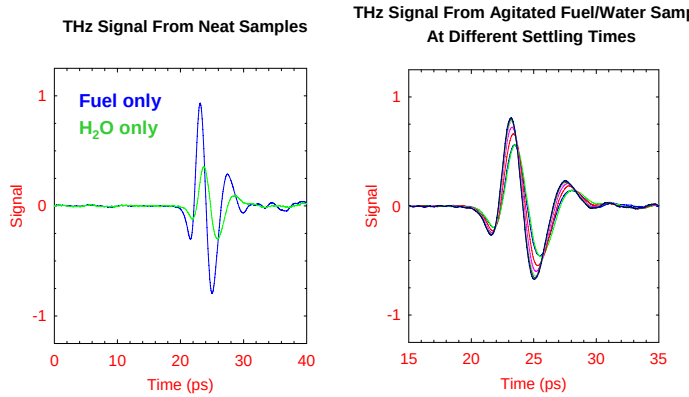

6

THz Time Domain Spectroscopy (THz-TDS)

Pro :

- time-based & coherent,
- measure real & imag parts of dielectric response,
- material transparencies,
- small footprint,
- $I / Io \sim N_g - N_{ex}$

Con :

- $\alpha(\omega) \sim \omega$,
- modest spatial resolution,
- $I / Io \sim N_g - N_{ex}$

7

Operational Characteristics

Transmitter bandwidth	20 GHz - 5 THz
Receiver time response	280 fs
Avg output power	10 nW
Peak output power	10 mW
Signal / Noise	$10^3 – 10^6$
Required input	5 – 20 mW
	50 – 150 fs pulse

8

Hardware Platforms

Measurements performed on two hardware platforms.

1) **Conventional – one pump laser, scanning optical delay**

2) **ASOPS – two asynchronous pump lasers, no optical delay**

ASOPS: ASynchronous OPtical Sampling

9

ASOPS Platform

Two ultrafast lasers independently pump the transmitter & receiver.

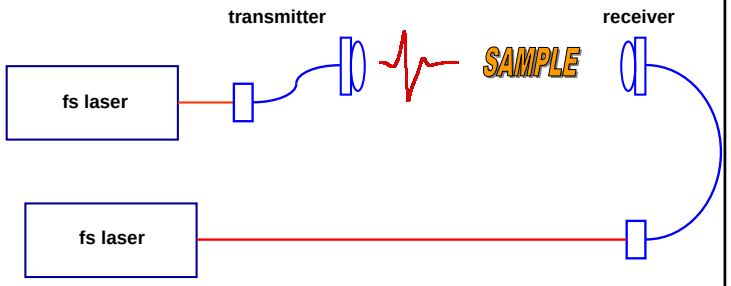

10

ASOPS Technique

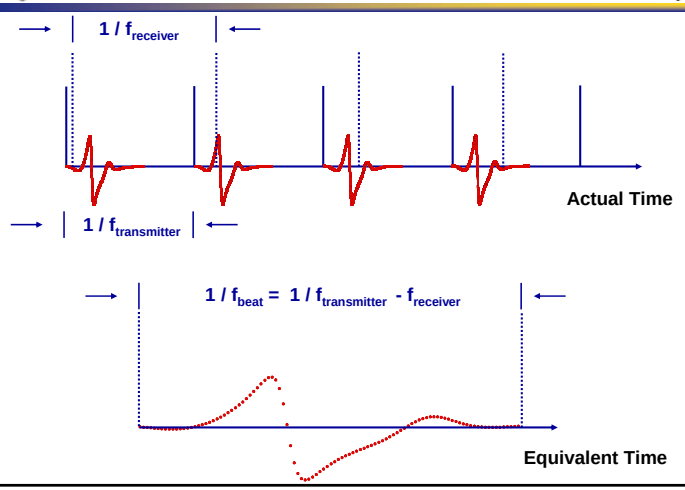

11

Combining THz Hardware With ASOPS Technique

Time Domain Signals

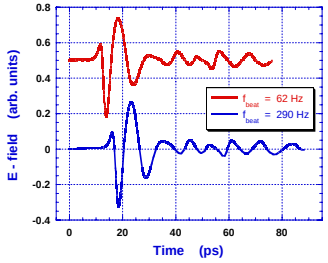

Corresponding Power Spectra

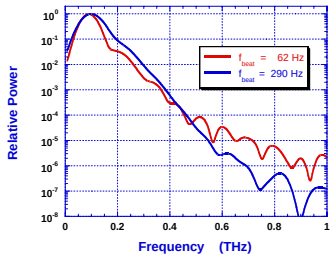

12

THz Transmission of Ceramic Combustor Liner (alumina)

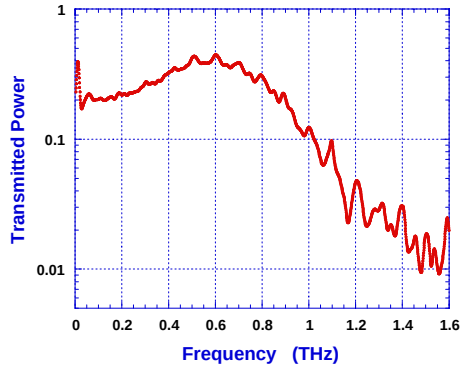

13

Conventional Platform

One ultrafast laser pumps both the transmitter & receiver.

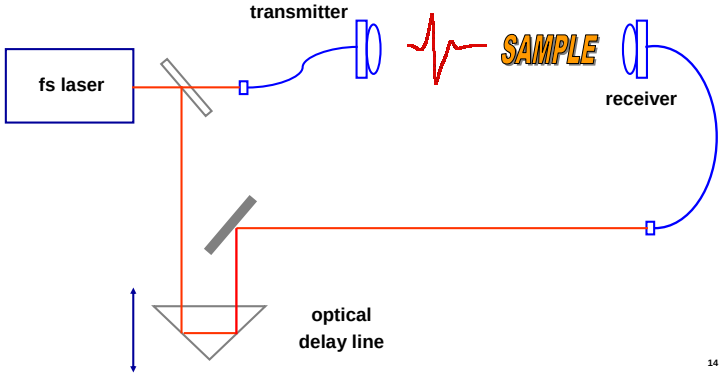

14

Water Vapor in Room Air

Improved spectral bandwidth permits detection of H_2O.

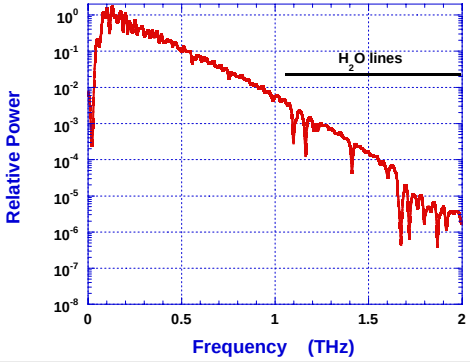

15

Absorption in Liquids

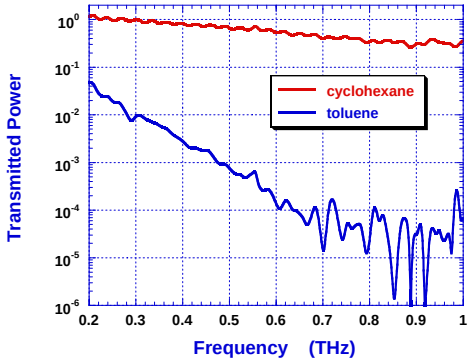

16

Water Vapor in a Flame

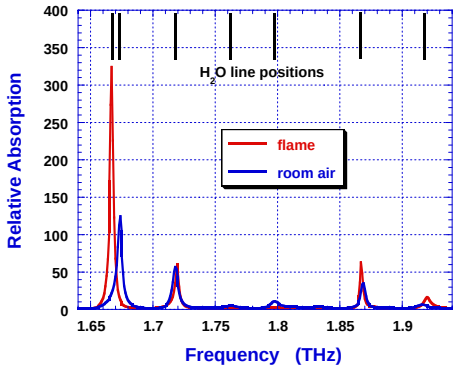

17

Summary

- THz hardware is rapidly developing.
- Proof-of-concept measurements made using two different hardware platforms.
- Measurements indicate sensitivity to water vapor in “opaque” environments.
- Improved spectral bandwidth will enhance THz utility for AF applications.

18

RECENT APPLICATIONS OF T-RAY TECHNOLOGY TO STUDIES OF COMBUSTION AND FUEL

43rd Rocky Mountain Conference on Analytical Chemistry

29 July – 2 August 2001

Michael S. Brown
Innovative Scientific Solutions, Inc.
J. Van Rudd, David Zimdars & Matt Warmuth
Picometrix, Inc.
James R. Gord
Air Force Research Laboratory, Propulsion Directorate

THz Spectral Territory

Hardware-Based Delineation

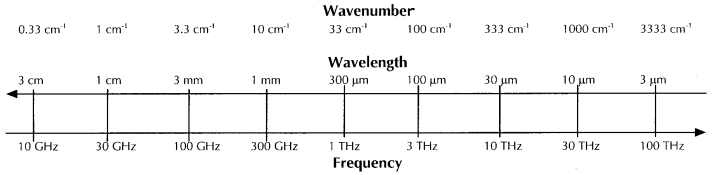

Microwave Spectroscopy — FTIR

Material Resonances: gases – rotations
liquids – hindered motions
solids – electron bound states

2

THz Hardware Evolution

practical fs lasers + low temp GaAs + microfabrication + substrate lenses — *yesterday*

↓

practical THz transmitters / receivers

↓

THz time domain spectroscopy (THz-TDS)

↙ ↘

hardened, user-friendly systems (Picometrix)

applications ISSI/AFRL — *today*

3

Picometrix Hardware Approach

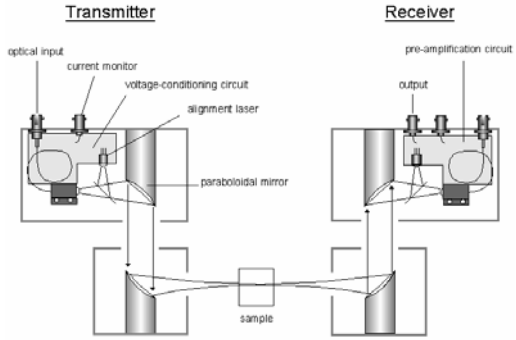

Fiber-Coupled Transmitter / Receiver Pair

4

Soot Absorption

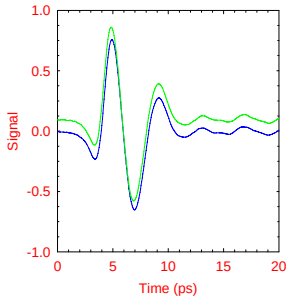

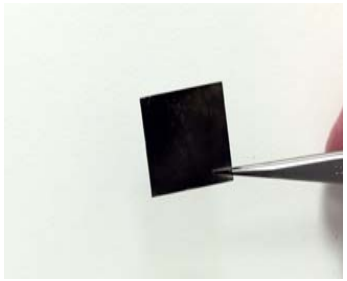

Test Case: Soot film on substrate.

5

Fuel / Water

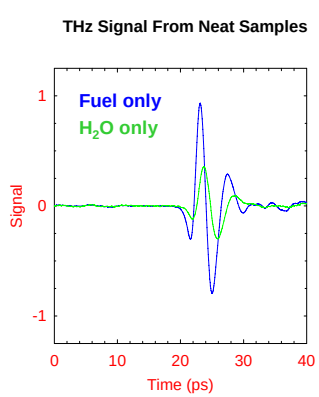

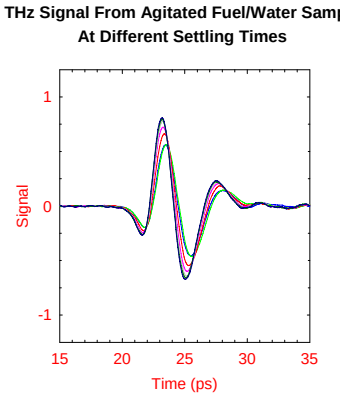

6

THz Time Domain Spectroscopy (THz-TDS)

Pro :

- time-based & coherent,
- measure real & imag parts of dielectric response,
- material transparencies,
- small footprint,
- $I / Io \sim N_g - N_{ex}$

Con :

- $\alpha(\omega) \sim \omega$,
- modest spatial resolution,
- $I / Io \sim N_g - N_{ex}$

7

Operational Characteristics

Transmitter bandwidth	20 GHz - 5 THz
Receiver time response	280 fs
Avg output power	10 nW
Peak output power	10 mW
Signal / Noise	$10^3 – 10^6$
Required input	5 – 20 mW
	50 – 150 fs pulse

8

Hardware Platforms

Measurements performed on two hardware platforms.

1) **Conventional – one pump laser, scanning optical delay**

2) **ASOPS – two asynchronous pump lasers, no optical delay**

ASOPS: ASynchronous OPtical Sampling

9

ASOPS Platform

Two ultrafast lasers independently pump the transmitter & receiver.

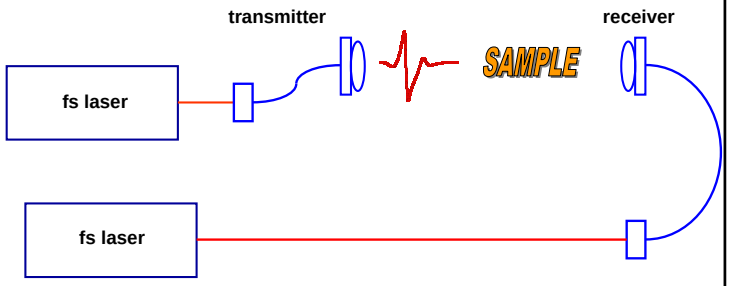

10

ASOPS Technique

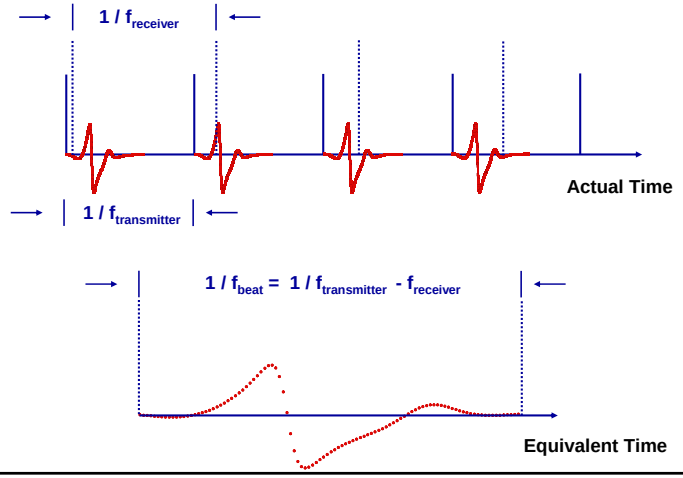

11

Combining THz Hardware With ASOPS Technique

Time Domain Signals

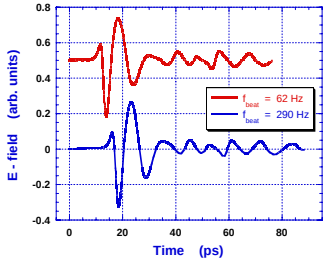

Corresponding Power Spectra

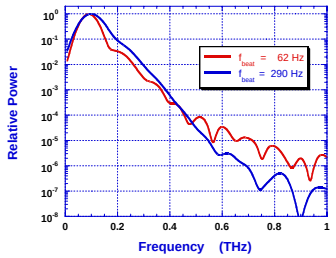

12

THz Transmission of Ceramic Combustor Liner (alumina)

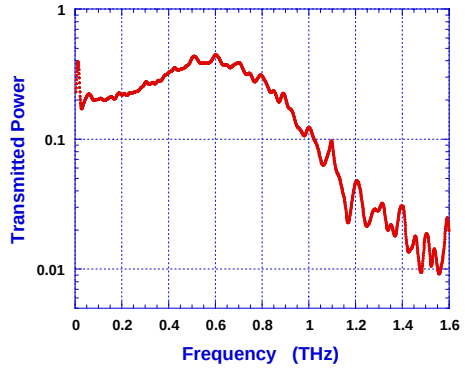

13

Conventional Platform

One ultrafast laser pumps both the transmitter & receiver.

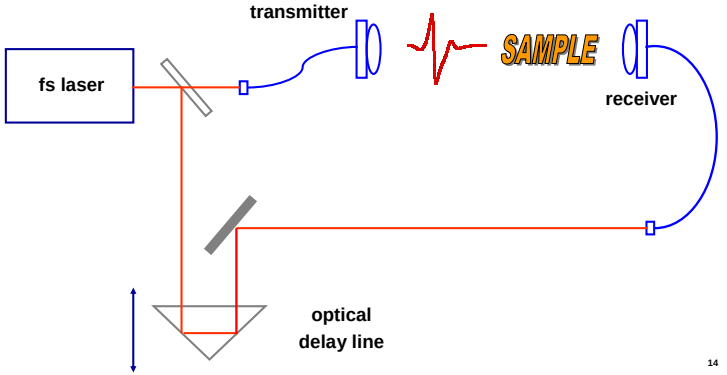

14

Water Vapor in Room Air

Improved spectral bandwidth permits detection of H_2O.

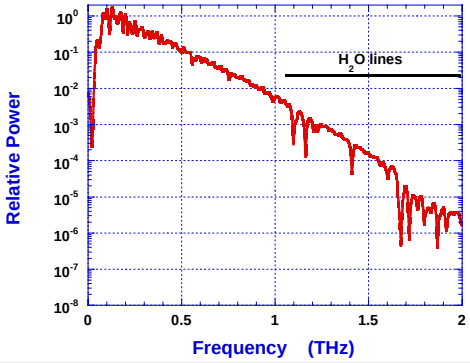

15

Absorption in Liquids

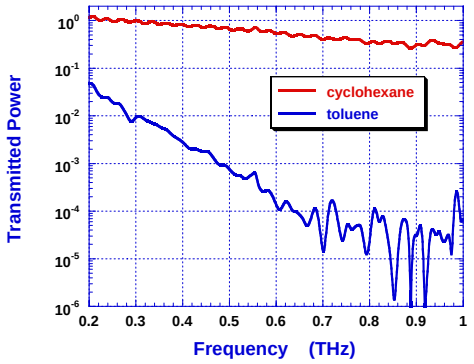

16

Water Vapor in a Flame

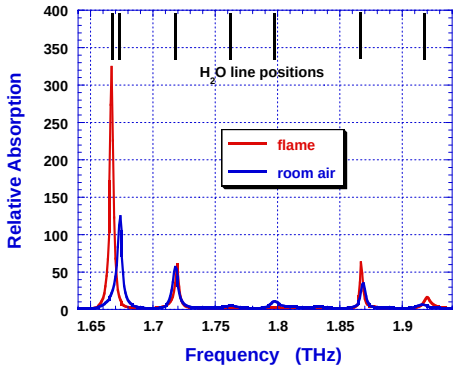

17

Summary

- THz hardware is rapidly developing.
- Proof-of-concept measurements made using two different hardware platforms.
- Measurements indicate sensitivity to water vapor in “opaque” environments.
- Improved spectral bandwidth will enhance THz utility for AF applications.

18

Current and Future Applications of Ultrafast Lasers for Propulsion Diagnostics

Ultrashort Pulse Laser Materials Interaction Workshop
Thursday 25 September 2003

James R. Gord and W. M. Roquemore
AFRL, Propulsion Directorate

Michael S. Brown
Innovative Scientific Solutions, Inc.

James L. Blackshire
AFRL, Materials and Manufacturing Directorate

Acknowledgments

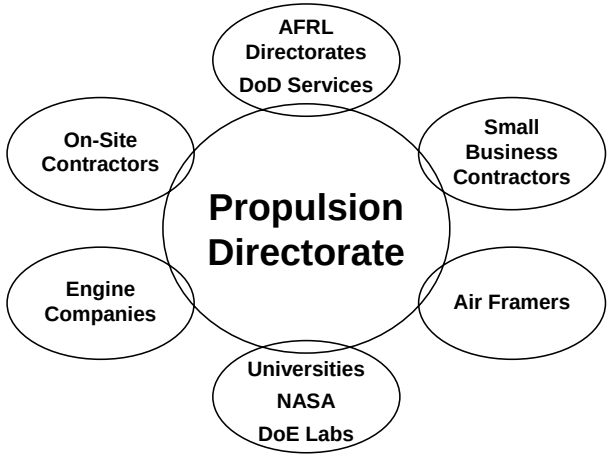

Combustion Science Branch Mission

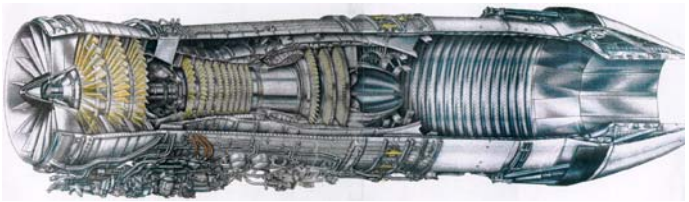

- **Improved Propulsion-System Performance (Thrust/Weight, SFC, etc.)**
- **Reduced Pollutant Emissions**
- **Enhanced Maintainability, Reliability, Affordability**

Combustor Technology Development

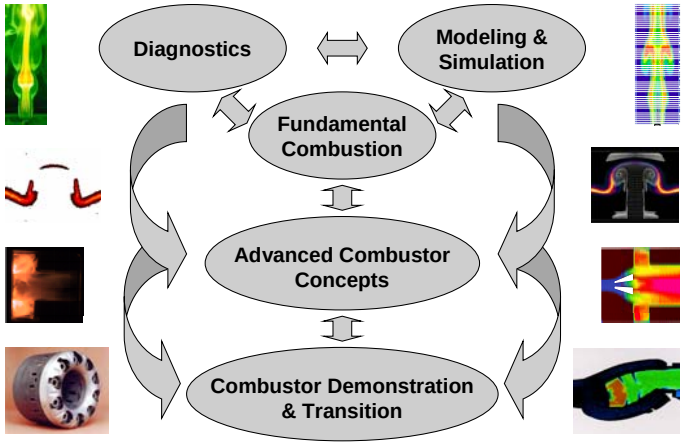

Selected Combustor Rigs

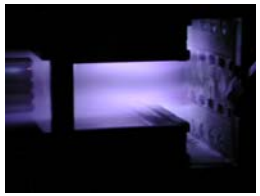

Trapped-Vortex Combustor

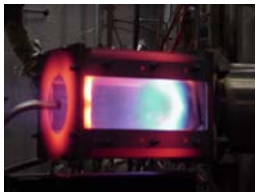

CFM56 Generic Combustor

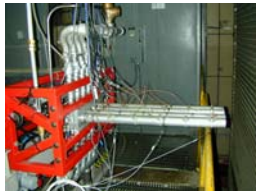

Pulsed-Detonation Engine

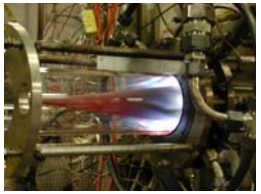

Ultra-Compact Combustor

Phased Diagnostics Approach

Combustion Research in the Laboratory

Performance Evaluation in the Engine Test Cell

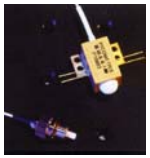

Real-Time Control on the Flight Line and in the Air

Not-So-Ultrafast Diagnostic Efforts

- Two-Dimensional Flow Visualization
  - High-Speed Digital Imaging
  - Planar Laser-Induced Fluorescence
  - Particle-Image Velocimetry
  - Coherent-Structure Velocimetry
  - Laser-Induced Incandescence
- Multi-Pump Coherent Anti-Stokes Raman Scattering
- Transient-Grating Spectroscopy
- Laser Doppler Velocimetry
- Point Emission Measurements
- Pulsed-Detonation Engine Diagnostics
- Mid-IR Doubly Resonant, Ultranarrowband OPO
- Particulate-Mitigation Efforts
- Turbulence and Vortex-Flame Interactions
- Predictive M&S Development & Application
- Diode-Laser-Based Sensors
- Combustor Development (TVC, ITB/UCC)

Ultrafast Hardware

- Tsunami 80-MHz Ti:Sapphire Oscillator (4)
  - Operation at 80 fs, 2 ps, 30 ps, and 80 ps
  - Millennia Nd:VO_4 Pumped
- Spitfire 50-kHz Ti:Sapphire Regenerative Amp
  - Operation from 2 ps to 80 ps
  - Frequency Doubled to Visible, Tripled to UV
  - Merlin ND:YLF Pumped
- 20-Hz Distributed Feedback Dye Laser
  - Nominal 100-ps Pulsewidth
  - Continuously Tunable for Spectroscopy
  - Nd:YAG Regen Pumped
- Legend 1-kHz Ti:Sapphire Regenerative Amp
  - <30 fs Pulsewidth
  - >2.5 mJ/Pulse
  - Evolution Nd:YLF Pumped
  - Front End for Proposed 20-TW System

Ultrafast Diagnostic Efforts

- **Aviation Fuels, Additives, and Supercritical Fluids**
  - Two-Photon Fluorescence
  - Time-Correlated Single-Photon Counting
  - Pump/Probe (Synchronous, Asynchronous)
  - Terahertz Time-Domain Spectroscopy
- **Combustion and Related Reacting Flowfields**
  - MHz-Rate Digital Imaging
  - Picosecond Time-Resolved Laser-Induced Fluorescence
  - Pump/Probe (Synchronous, Asynchronous)
  - Terahertz Time-Domain Spectroscopy
  - Polarization Spectroscopy

TCSPC in Supercritical Fuels

Diffusional Quenching

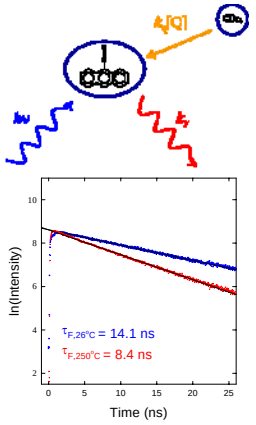

Rotational Anisotropy

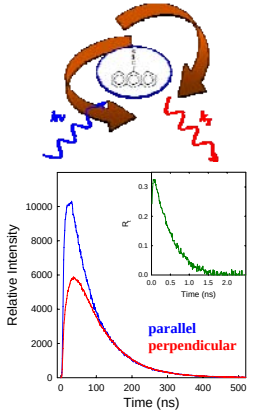

Trapped-Vortex Combustor

High-Speed Digital Imaging
JP-8-Fueled TVC at Pressure

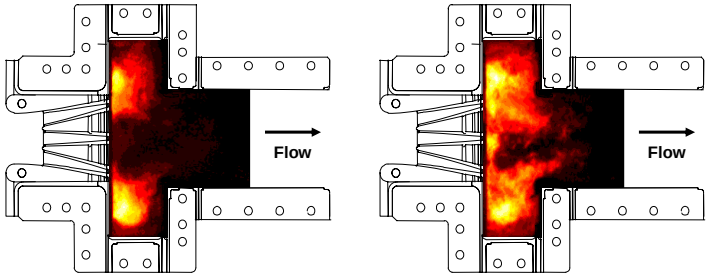

8.5 Atmospheres | 12 Atmospheres

Turbulence (Vortex-Flame Interactions)

Reproducible, Periodic

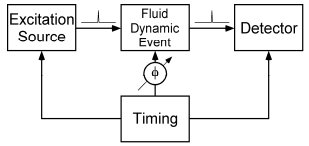

Transient, Unsteady

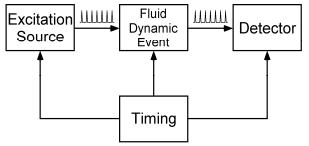

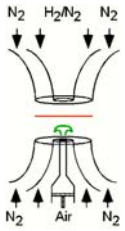

Phase-Locked Acetone PLIF

Phase-Locked Hydroxyl PLIF

High-Speed Imaging of Spark Ignition

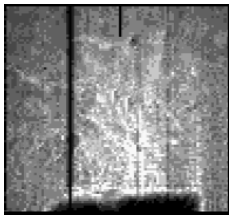

- Laser Schlieren
- 1-MHz Framing Rate
- 32-Frame Capacity

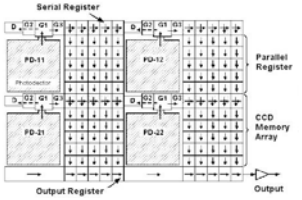

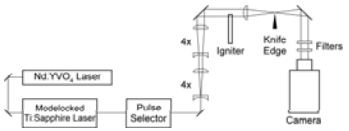

PITLIF in the Rolon Burner

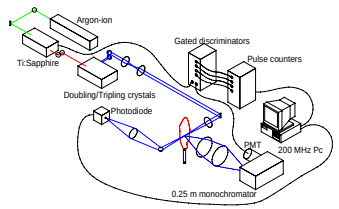

- Purdue, Connecticut
- Picosecond Time-Resolved Laser-Induced Fluorescence
- Tremendous Data-Acquisition Bandwidth
- Lifetime/Quenching Data
- Absolute Number Densities
- Time Series, PSD's

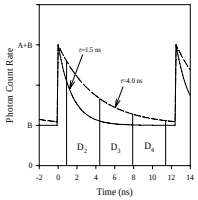

Photon-Counting Bins

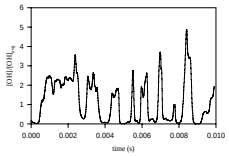

Hydroxyl Time Series

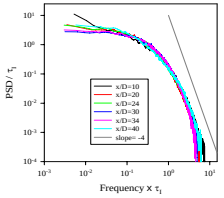

Power Spectral Densities (OH)

Synchronous Pump/Probe

- Absorbing Analytes
- Coherent Signal
- Tremendous Data-Acquisition Bandwidth
- Quenching-Free Measurements
- Absolute Number Densities
- Time-Series, PSD's

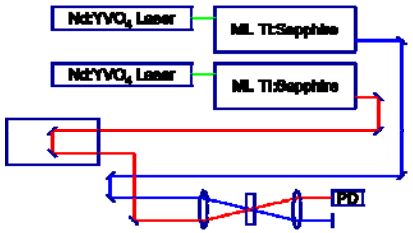

Asynchronous Pump/Probe (ASOPS)

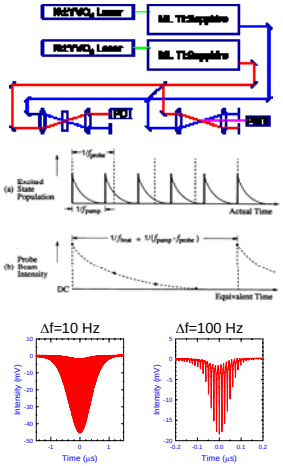

- Asynchronous Optical Sampling
- No-Moving-Parts Delay Line
- Potential for Rapid Scanning of Full Free Temporal Range
- Trade Off Between Temporal Resolution & Scanning Rate

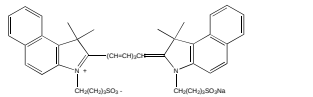

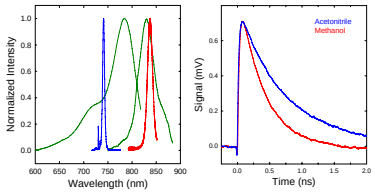

Terahertz Radiation ("T-Rays")

- Unexplored Spectral Territory
- Absorption Lines of Interest for Studying Combustion and Fuels
- Advantageous Transmission Properties (Ceramics, Soot, Aviation Fuels, Etc.)
- Potential Imaging Applications
- Robust Packaging Continues to Evolve

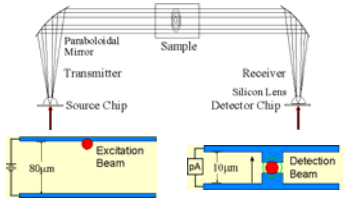

Dr. Dan Grischkowsky, et al., http://elec-engr.okstate.edu/thzlab/

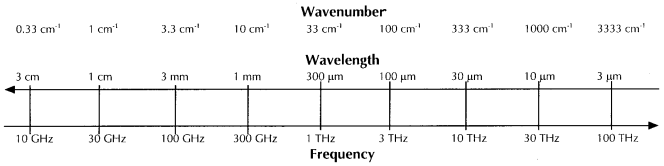

THz Combustion Data

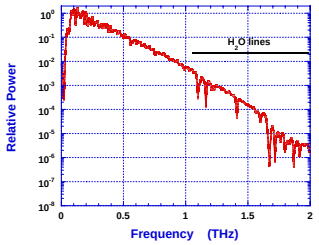

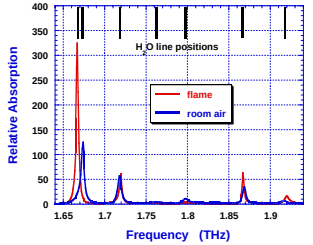

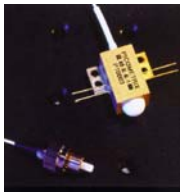

2000 R&D 100 Award Winner (Picometrix, Inc.)

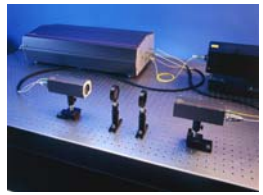

Picosecond Polarization Spectroscopy

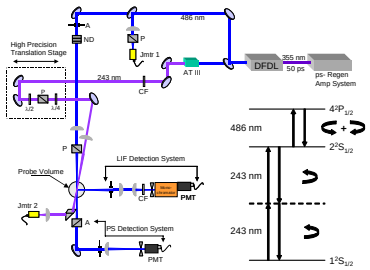

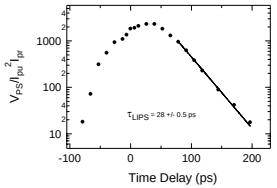

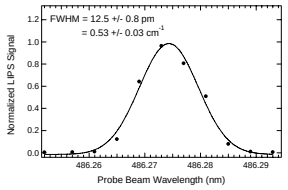

- Purdue, Sandia CRF
- Picosecond Nd:YAG Regen, DFDL
- Hencken Flame
- Two-Color, Two-Photon H Atom Detection
- Absolute Number Densities
- Energy Transfer
- Code Development and Validation

High-Intensity-Laser/Matter Interactions

- "Relativistic" Optics
- New Physical Phenomena
- AFRL Team (PR, ML, DE, SN, HE, AFOSR)
- DARPA Interest
- Near-Term: Machining
- Mid-Term: Non-Destructive Evaluation, Materials Processing, Weapons, Stand-Off Detection
- Long-Term: Space Propulsion
- "Extreme Light," Mourou & Umstadter, Sci Am 286, 80 (May 2002)

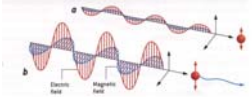

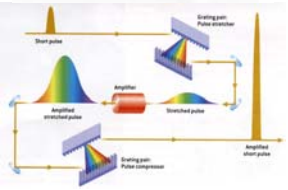

Ultrafast Laser Machining

- Manufacturing Cost Savings
- Engineering/Performance Benefits
  - Flexible Hole Geometry (shaped and cylindrical)
  - Drill After Thermal Barrier Coating
  - Drill Advanced Materials (Ceramics, CMC's)
  - No Cracks, Remelt, or Spalling
  - Improved Thrust to Weight
  - Improved Fuel Savings

Courtesy Pratt & Whitney

Courtesy KML, Inc.

CLDRC Expansion

New Facilities for Combustion Research & Diagnostics Development

Continuing Research Activity

- Provide diagnostic support for advanced combustor development.
- Develop and apply novel diagnostics with an emphasis on new spectral territory, ultrashort pulsewidths, and high intensities.
- Pursue a three-phased approach through basic laboratory research, test-cell applications, and on-board integration.

Better Engines through Light!

Ultrafast Pump/Probe Measurements of Combustion Kinetics & Dynamics

Transient-Grating Spectroscopy in a High-Pressure Combustor

Triple-Pump Coherent Anti-Stokes Raman Scattering (CARS)

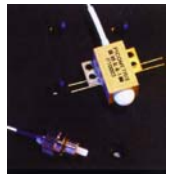

Terahertz (T-Ray) Transmitter
Courtesy Picometrix, Inc.

PRTS Mission (IHPTET/VAATE)

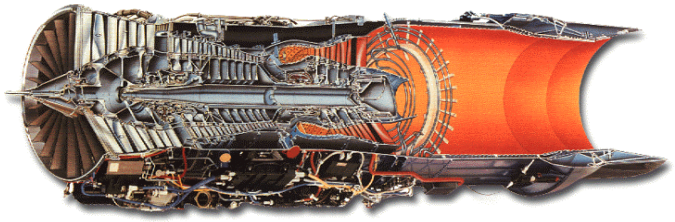

- Improved Propulsion-System Performance (Thrust/Weight, SFC, etc.)
- Reduced Pollutant Emissions
- Enhanced Maintainability, Reliability, Affordability

PRTS Turbine Engine Research Center (TERC) Facilities

- Combustion & Laser Diagnostics Research Complex (CLDRC) - Dr. Jim Gord
- Atmospheric-Pressure Combustor Research Complex (APCRC) - Dr. Vince Belovich
- High-Pressure Combustor Research Facility (HPCRF) - Mr. Dale Shouse
- Pulsed-Detonation Research Facility (PDRF) - Dr. Fred Schauer

PITLIF in the Rolon Burner

PITLIF Electronics

Third Harmonic Generator @ 307 nm

Picosecond Modelocked Ti:Sapphire Laser @ 921 nm

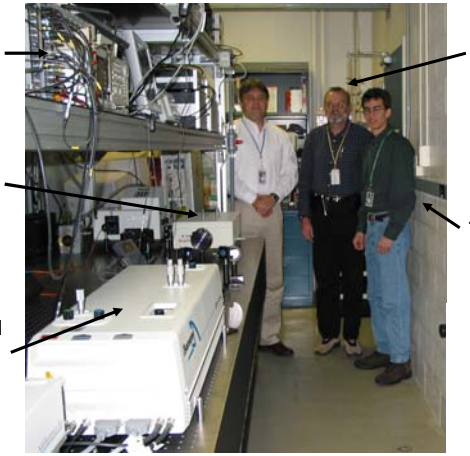

Galen King

Terry Meyer

Picosecond Polarization Spectroscopy

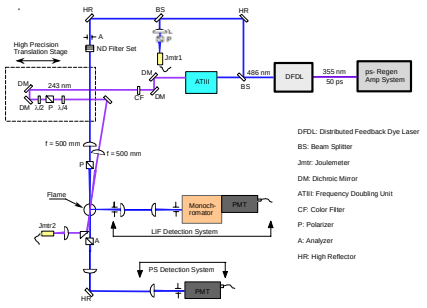

- Purdue, Sandia CRF
- Picosecond Nd:YAG Regen, DFDL
- Hencken Flame
- Two-Color, Two-Photon H Atom Detection
- Absolute Number Densities
- Energy Transfer
- Code Development and Validation

Better Engines through Light!

Ultrafast Pump/Probe Measurements
of Combustion Kinetics & Dynamics

Transient-Grating Spectroscopy
in a High-Pressure Combustor

Triple-Pump Coherent Anti-Stokes
Raman Scattering (CARS):
Temperature and Species

Combustion & Laser Diagnostics
CLDRC
Research Complex

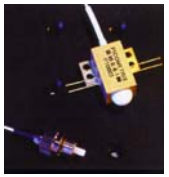

Terahertz Radiation
(T-Ray) Transmitter
Courtesy Picometrix, Inc.

MICRO TO NANO—SMALL RESEARCH FOR FUELS AND COMBUSTION

Christopher E. Bunker[1]; James R. Gord[1]; Terrence R. Meyer[2]; Michael S. Brown[2]; Viswanath R. Katta[2]; Daniel A. Zweifel[3]; Barbara A. Harruff[1]; Ya-Ping Sun[3]

[1]Air Force Research Laboratory, Propulsion Directorate, Wright-Patterson AFB OH 45433
[2]Innovative Scientific Solutions, Inc., 2766 Indian Ripple Rd., Dayton OH, 45440
[3]Clemson University, Chemistry Department, Clemson SC 29634

Abstract/Introduction

The Fuels and Combustion Branches of the Air Force Research Laboratory have been actively investigating micro and nanoscopic materials as they pertain to fuel chemistry, sensor development, and MEMS devices. At these dimensions, surface interactions (*e.g.*, surface chemistry, viscosity, and heat transfer) take on tremendous importance in understanding the macroscopic chemical and physical processes that occur. In some cases, current models used to predict chemical or physical properties are inadequate due to a lack of information concerning these surface effects. In this paper, we will detail some of our efforts to examine both physical and chemical processes occurring within and about micro and nanoscopic materials. Specifically, microfluidic results obtained using a LIF technique within a Si substrate Y-channel (~100 μm across and 30 μm deep) coupled with simple CFD calculations will be presented. In addition, spectroscopic results (steady-state and time-resolved) for model nanoparticles and a novel pyrene-dendromer-modified carbon nanotube will be discussed.

Experimental

Microfluidics. The Y-shaped micro-channels used in this program were obtained from Research International, Woodinville WA. The channels (depth ~30 μm, width ~100 μm) were prepared in thin quartz substrates using a diamond-tipped tool, then attached to thick Si substrates by anodic bonding. Holes drilled through the quartz at the termination of the channels provide a means of delivering fluid to and from the channels. Imaging measurements were performed on the micro-channels using methanol as the test fluid. Magnification was achieved using microscope objectives with long working distances in concert with commercial camera lenses. Images were acquired using analog and digital video cameras as well as a high-resolution digital still camera. Image contrast between the target fluid stream and its surroundings was achieved through laser-induced fluorescence [1]

Surface Engineering: Science & Technology of Interfaces II
Edited by A. Kumar, Y-W. Chung,
J.J. Moore, G.L. Doll, K. Yasui and D.S. Misra
TMS (The Minerals, Metals & Materials Society), 2002

using common organic dyes dissolved in the methanol. Dichroic mirrors and colored-glass filters were used to discriminate the fluorescent signal from specular and diffuse reflection of the incident laser light. To help delineate edges of hardware elements in the images, incoherent light from a low-power lamp was often employed along with the laser excitation. Broad-area imaging was achieved using one-photon excited fluorescence with unfocused incident laser light. The 532-nm output of a cw vanadate ($Nd:YVO_4$) laser operating at outputs of 10-30 mW was employed to excite fluorescence.

CdS Nanoparticles. CdS nanoparticles were prepared using the reverse-micelle method.[2-4] In a typical experiment, two separate solutions of $CdNO_3$ and Na_2S (both at 0.2 M) are prepared in one mL of water. These solutions are then employed to prepare two additional solutions: one by injecting 36 μL of the $CdNO_3$ solution into 5 mL of 0.1-M dioctyl sulfosuccinate sodium salt (AOT) solution in heptane, and the other by injecting 36 μL of the Na_2S solution into 5 mL of 0.1-M AOT solution in heptane. In each case the final solution, which was allowed to equilibrate for one hour prior to further use, is characterized by a $[H_2O]/[AOT]$ ratio of 4 (w_o). The two solutions are then mixed and left to stand for ~5 min. A 1-mL portion of the CdS/AOT/heptane solution is added to 10 mL of hexane and used in the investigations. Uv-vis absorption spectra were recorded using a Perkin Elmer λ900 Uv-Vis/Nir-IR spectrometer. Luminescence spectra and photoirradiations were conducted with a Spex Fluorolog-3 single-photon-counting spectrometer, equipped with a 450-W Xe lamp, double monochromators for excitation and emission wavelength selection, and a Hamamatzu R928 photomultiplier tube as detector. All spectra have been corrected for the non-linear response of the instrument. Luminescence decays were obtained using a home-assembled system consisting of a N_2 laser (Laser Science, Inc., VSL-337ND-S, λ_{ex} 337 nm), an R928p photomultiplier tube wired for fast response as detector, and a Tektronics oscilloscope for data collection.

Carbon Nanotube. The SWNT samples were obtained from the Department of Physics at Clemson University and were purified using procedures similar to those reported in the literature.[5-7] In a typical experiment, a purified SWNT sample (15.0 mg) was treated in concentrated HCl solution to recover fully the carboxylic acid groups on the nanotube surface, followed by refluxing in thionyl chloride for 24 h to convert the carboxylic acids into acyl chlorides. After a complete removal of residual thionyl chloride on a rotary evaporator with a vacuum pump, the sample was mixed well with carefully dried dendron (150 mg, 0.26 mmol) in a flask, heated to 90°C, and vigorously stirred for 24 h under nitrogen protection. The reaction mixture was extracted with chloroform to obtain a dark homogeneous solution. The solution was dried on a rotatory evaporator with a vacuum pump and purified by Soxhlet extraction with acetone for 48 hrs. The final product was obtained after drying at 60°C under vacuum for 24 hrs. Spectroscopic measurements were made using the instruments described in the previous section.

Results and Discussion

Microfluidics. Micro- and nano-scale sensors sought for fuel evaluation or monitoring will likely employ both static and dynamic fluid systems. As the characteristic channel width decreases, micro-fluidic behavior becomes increasingly sensitive to surface characteristics (physical and chemical), as well as bulk fluid characteristics such as thermal transport and viscosity. Various tools are needed to evaluate the performance of existing micro-fluidic devices and aid in the design of future devices. We have undertaken both experimental and

computational approaches to develop tools for such applications. Fluorescence-based microscopy was used to obtain images of fluid flow in a Y-shaped micro-channel to study multi-component flow phenomena. A computational fluid dynamics (CFD) code[8] developed in-house was used to examine various aspects of fluid behavior in micro-environments, including Y-channels and micro-jets.

Figures 1 and 2 provide two examples of broad-area imaging of the Y-shaped micro-channel using one-photon excited fluorescence. Using a peristaltic pump, methanol and dye-tagged methanol were pumped into the upper and lower arms, respectively, of the 70-degree Y. The velocities of the two streams could be varied independently and mean velocities amounted to about 10 mm/s with corresponding Reynolds numbers of ~0.1. Reflected light levels from the quartz slab and underlying Si substrate were considerable. Colored glass filters were used to reject the reflected light. The bright areas interior to the channels in Figures 1 and 2 are due to fluorescence from the dye-tagged methanol stream. The faint outline of the channel is due to incoherent illumination.

In the image sequence of Figure 1, both a neat and a dye-tagged methanol stream are flowing (left to right) with varying relative velocities. A diffusive mixing layer is established between the two streams. As the lower stream velocity is increased in the image sequence, the mixing layer moves toward the low speed stream. The exact position of the mixing layer is sensitive to the relative stream velocities as well as the relative viscosity and therefore serves as a monitor of these two physical parameters.

CFD modeling of the fluid behavior in the micro-channels was achieved through modifications to our in-house CFD code, Unicorn, which solves the full Navier-Stokes equations. Two-dimensional calculations of the flow velocity and mixing of the dye-tagged methanol stream with the pure methanol stream were performed with the following inputs: 1) boundary condition (slip no/slip), 2) channel dimensions, 3) liquid diffusion coefficient and viscosity, and 4) the center-line flow velocity of the two streams. For the micro-channel used in the imaging experiments, the no-slip boundary condition was found to work well. Examples of the calculations for the Y-channel can be seen in Figure 3 for the case of a 3:1 stream velocity ratio. The calculations should be compared to the images in Figures 1 and 2. Both the calculations and the acquired images indicate weak diffusive mixing downstream of the Y. The image sequence of Figure 2 was taken at three different spatial locations. The first image was acquired at the Y apex and the two subsequent images were acquired 20 and 70 channel widths downstream. All three images were taken with the same relative flow velocity. The apparent movement in the mixing layer is suggestive of mixing by diffusion. Line profiles taken across the channel confirm this, as shown in Figure 4. The fluorescence signal has spatially broadened at the downstream location with respect to the apex position. Within the experimental uncertainty, the computed profiles (Figure 4b) indicate mixing at the same level as the acquired images (Figure 4a).

Not all microfluidic applications will call for enclosed channels carrying single-phase fluids. Numerous potential applications exist for micro-jets ranging from printer technologies to drug delivery to micro-thruster needs. We have applied our CFD code to examine some of the various physical processes encountered in micro-jets. Figure 5 shows the fluid behavior of an air micro-jet impinging on quiescent air. Such studies can be used to investigate the effects of wall boundary conditions on the flow. Vortex formation, as

seen in the image sequence, has a significant impact on local fluid mixing. The computational study that generated the image sequence of Figure 6 examines the role of surface tension on droplet formation. The sequence traces the injection of a water micro-jet into air with subsequent droplet formation, propagation, and coalescence.

The fluorescence-based micro-imaging along with the CFD modeling constitute a pair of tools that we plan to use in evaluating micro-fluidic hardware for fuel testing and monitoring. The imaging provides a means to measure relative fluid stream velocities and viscosities and evaluate stream mixing. The CFD modeling permits the rapid evaluation of different channel geometries and the behavior of two-phase flows with the inclusion of surface-tension effects. Future work will include the development of techniques, such as two-photon fluorescence microscopy, for studying sub-micron flow and surface-interaction phenomena.

CdS Nanoparticles. Absorption spectra, luminescence spectra, and luminescence quantum yields (Φ_L) have been measured for model CdS nanoparticles prepared in AOT reverse micelles. Based on the λ_{max} of the freshly produced particles (~340 nm), the average diameter of the CdS nanoparticles used in this study is ~6 nm.[9] This observation was confirmed by TEM analysis. In the course of investigating freshly prepared CdS nanoparticles, it was observed that successive measurements of the luminescence spectrum produced an increase in the observed intensity. To investigate the phenomenon, freshly prepared particles were photoirradiated at the absorption maximum for intervals of either 15 or 60 min using the fluorescence spectrometer with 5-nm-bandpass excitation slits. After each irradiation interval, quantitative absorption and luminescence spectra were acquired and Φ_L determined (standardized against 9-cyanoanthracene). The plot in Figure 7 shows the typical trend for the absorption spectra with irradiation—the band maximum is observed to shift toward the red (~25 nm total) and decrease in intensity. A similar shift in the luminescence-band maximum is also observed (Figure 7, inset); however, the intensity increases substantially with irradiation. This phenomenon is more evident in the plot of Φ_L vs. irradiation time (Figure 8). The observed trend is similar to those observed in chemical-passivation studies.[10,11] Apparently two regions of differing behavior exist for CdS nanoparticles when photoirradiated: an early region where irradiation of the particles results in a significant and monotonic increase in quantum efficiency, and a plateau region where the particles become photo-stable. The increase in quantum efficiency is approximately an order of magnitude, with freshly prepared particles exhibiting Φ_L values of ~ 1% and plateau particles exhibiting Φ_L values between 9 and 14 percent.

Preliminary data describing the luminescent decays of these particles indicate multi-exponential character and an increase in the long-lived component's contribution for the red-shifted plateau particles (Figure 9). Such observations are in good agreement with theoretical explanations of the luminescent behavior of CdS clusters.[12-15] The observed red shift in the luminescence spectra may be due to changing particle size (quantum confinement effect) or due to a change in the excited-state dynamics brought on by photoinduced surface modification. Further investigations to determine the underlying mechanism, including studies of the effects of concentration and w_o, are underway.

Carbon Nanotubes. Bimolecular energy-transfer reactions can serve as useful probes of local polarities, viscosities, temperatures, and in some cases indicate specific contaminants. The ability to control the location of the reaction is critical to the development of MEMS-

and NEMS-based chemical sensors. Here we report the investigation of a unique carbon-nanotube molecule that has been functionalized with a dendromer-containing pyrene (Figure 10).

The photophysics of pyrene are well known and well understood.[16] At high concentrations, pyrene undergoes a diffusion-controlled excited-state reaction to form an excimer. Because the photophysical properties of the pyrene excimer are distinct from the pyrene monomer and because the reaction is diffusion controlled, the formation of the pyrene excimer has been used as a probe of local solvent environment. The properties of the pyrene-functionalized dendromer are similar to those of pyrene monomer; therefore, the pyrene-functionalized dendromer attached to a carbon nanotube should also serve as a probe of the local solvent environment.

Uv-Vis absorption and fluorescence-emission spectra were collected for the pyrene-functionalized dendromer attached to the carbon nanotube in toluene (Figure 11). The emission spectra are characterized by contributions from both the pyrene monomer and excimer (broad, red-shifted, Gaussian-like band). The estimated concentration of pyrene in the dendromer/carbon-nanotube solution is several orders of magnitude below that at which pyrene displays excimer emission. Figure 11 also demonstrates the effect of concentration of the pyrene-dendromer-modified carbon nanotube on the relative yields of monomer-to-excimer emission—no change is observed. The formation of the excimer at very low pyrene concentrations indicates a high local concentration of the dendromer on the carbon nanotube. The lack of concentration effects on the relative monomer-to-excimer yield indicates that the excimer is intramolecular in nature (*i.e.*, originating from a single carbon nanotube). To explore the dynamics of the excimer formation process, fluorescence emission and excitation spectra were recorded for the pyrene-dendromer-modified carbon nanotube in toluene at 77K. At this temperature, molecular motion is arrested; therefore observation of excimer would indicate preassociation of the pyrene molecules (ground state dimer complex). As can be seen in Figure 12, the emission spectrum obtained at 77K shows a substantial decrease in the excimer intensity. This reduced excimer contribution clearly indicates that a portion of the excimer yield originates from a dynamic process; however, the fact that not all of the emission intensity is lost suggests that some ground-state complexation may occur. Further characterization of the excited-state dynamics of this novel molecule using time-resolved techniques is under way.

Conclusion

The techniques and results presented herein represent some of our efforts aimed at understanding micro- and nanoscopic materials. Future research will seek to couple these tools with actual MEMS- or NEMS-based devices. The potential for application of these materials and techniques in Air-Force platforms is very high. Propulsion will be enhanced through incorporation of these technologies into combustion, fuel, and thermal-management systems.

Acknowledgments

The authors would like to acknowledge the contributions of Prof. Gilbert E. Pacey, Department of Chemistry and Biochemistry, Miami University, to the microfluidics studies described in this paper and Liangwei Qu and Brad Martin at Clemson University to the preparation, purification, and study of dendromer/carbon-nanotube samples.

References

1) P. H. Paul, M. G. Garguilo, and D. J. Rakestraw, "Imaging of Pressure- and Electrokinetically Driven Flows Through Open Capillaries," *Anal. Chem.* **1998**, *70*, 2459.
2) Lianos, P.; Thomas, J. K. "Cadmium Sulfide of Small Dimensions Produced in Inverted Micelles" *Chem. Phys. Lett.* **1986**, *125*, 299.
3) Lianos, P.; Thomas, J. K. "Small CdS Particles in Inverted Micelles" *J. Coll. Inter. Sci.* **1987**, *117*, 505.
4) Petit, C.; Jain, T. K.; Billoudet, F.; Pileni, M. P. "Oil-in-Water Micellar Solution used to Synthesize CdS Particles—Structural Study and Photoelectron Transfer-Reaction" *Langmuir*, **1994**, *10*, 4446.
5) Liu, J.; Rinzler, A. G.; Dai, H.; Hafner, J. H.; Bradley, R. K.; Boul, P. J.; Lu, A.; Lverson, T.; Shelimov, K.; Huffman, C. B.; Rodriguez-Macias, F.; Shon, Y.-S.; Lee, T. R.; Colbert, D. T.; Smalley, R. E. *Science* **1998**, 280, 1253.
6) (a) Tsang, S. C.; Chen, Y. K.; Harris, P. J. F.; Green, M. L. H. *Nature*, **1994**, *372*, 159. (b) Hiura, H.; Ebbesen, T. W.; Tanigaki, K. *Adv. Mater.* **1995**, 7, 275.
7) Rinzler, A. G.; Liu, J.; Dai, H.; Nikolaev, P.; Huffman, C. B.; Rodriguez-Macias, F. J.; Boul, P. J.; Lu, A. H.; Heymann, D.; Colbert, D. T.; Lee, R. S.; Fischer, J. E.; Rao, A. M.; Eklund, P. C.; Smalley, R. E. *Appl. Phys. A* **1998**, 67, 29.
8) W. M. Roquemore and V. R. Katta, "Role of Flow Visualization in the Development of UNICORN," J. Visual. **2000**, *2*, 257.
9) Weller, H. "Optical Properties of Quantized Semiconductor Particles" *Phil. Trans. R. Soc. Lond. A* **1996**, *354*, 757.
10) Dannhauser, T.; O'Neil, M.; Johansson, K.; Whitten, D.; McLendon, G. "Photophysics of Quantized Colloidal Semiconductors Dramatic Luminescence Enhancement by Binding of Simple Amines" *J. Phys. Chem.* **1986**, *90*, 6074.
11) Chandler, R. R.; Coffer, J. L. "Antiquenching Effect of Lanthanide b-Diketonate Complexes on the Photoluminescence of Quantum-Confined Cadmium Sulfide Clusters" *J. Phys. Chem.* **1991**, *95*, 4.
12) Rossetti, R.; Brus, L. "Electron-Hole Recombination Emission as a Probe of Surface Chemistry in Aqueous CdS Colloids" *J. Phys. Chem.* **1982**, *86*, 4470.
13) Brus, L. "Electronic Wave Functions in Semiconductor Clusters: Experiment and Theory" *J. Phys. Chem.* **1986**, *90*, 2555.
14) Chestnoy, N; Harris, T. D.; Hull, R.; Brus, L. E. "Luminescence and Photophysics of CdS Semiconductor Clusters: The Nature of the Emitting State" *J. Phys. Chem.* **1986**, *90*, 3393.
15) Logunov, S.; Green, T.; Marguet, S.; El-Sayed, M. A. "Interfacial Carriers Dynamics of CdS Nanoparticles" *J. Phys. Chem. A* **1998**, *102*, 5652.
16) Sun, Y.-P.; Bunker, C. E. "Quantitative Spectroscopic Investigation of Enhanced Excited-State Complex-Formation in Supercritical Carbon Dioxide under Near-Critical Conditions—Inconsistency between Experimental-Evidence and Classical Photophysical Mechanism" *J. Phys. Chem.* **1995**, *99*, 13778, and refs cited therein.

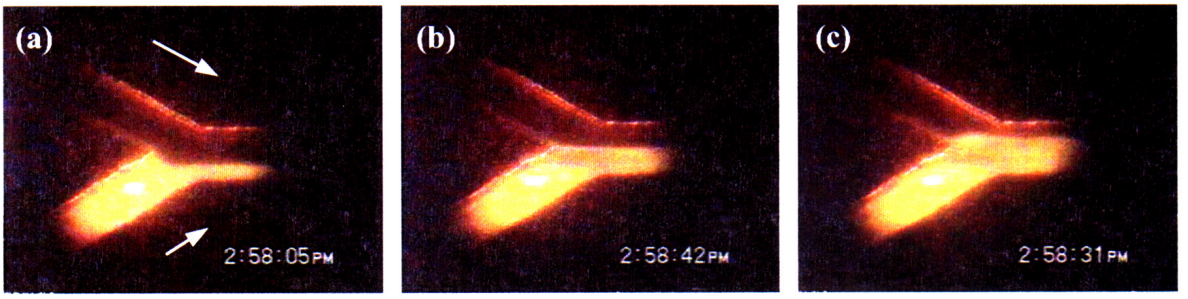

Figure 1. Laser-induced fluorescence measurements of steady flow in a 100-micron wide × 30-micron deep Y-channel with upper stream to lower stream velocity ratios of (a) 3:1, (b) 1:1, and (c) 1:3. Upper stream consists of pure methanol and lower stream is dye-tagged methanol. The location of the interface can be used to infer the relative velocity ratio or relative viscosity of the fluids.

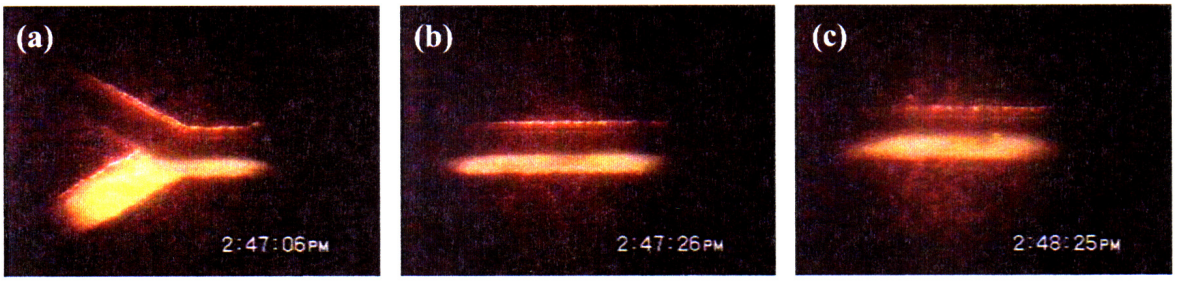

Figure 2. Evidence of slow diffusive mixing for steady Y-channel flow at a 3:1 upper stream to lower stream velocity ratio. The sequence shows locations near (a) the Y-channel intersection, (b) 20 channel widths downstream, and (c) 70 channel widths downstream.

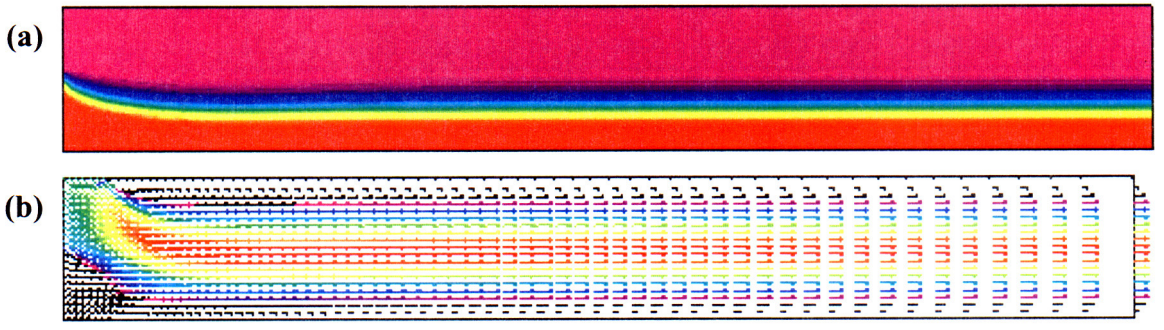

Figure 3. CFD computations of (a) mixture fraction and (b) velocity for steady Y-channel flow at a 3:1 upper stream to lower stream velocity ratio. The left edge corresponds to the plane at the apex of the Y-channel.

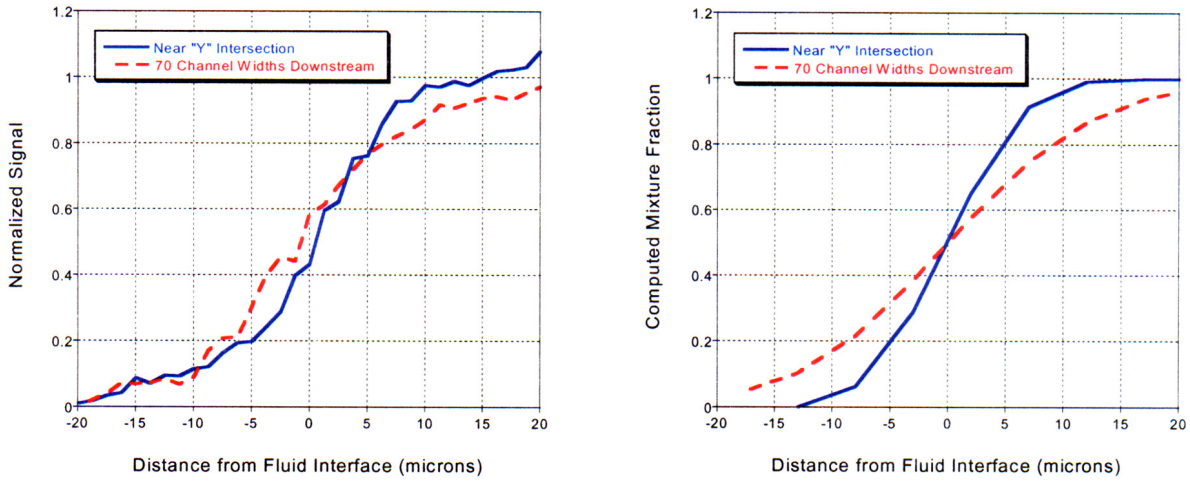

Figure 4. (a) Measured and (b) predicted diffusive mixing for steady Y-channel flow at a 3:1 upper stream to lower stream velocity ratio. Upper stream is pure methanol at 10 mm/s and lower stream is dye-tagged methanol at 3 mm/s.

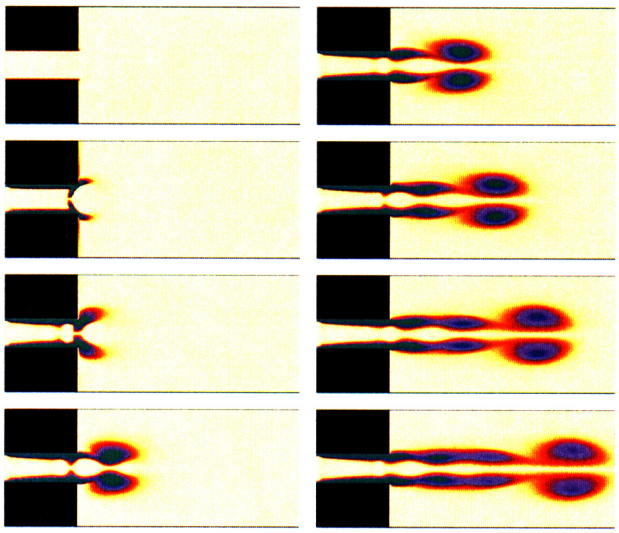

Figure 5. Computed flow field of a pulsed micro-scale air jet showing vortex formation and propagation similar to that of typical macro-scale air jets. Such computations can be used to evaluate the effects of different slip conditions on the vortex-development process.

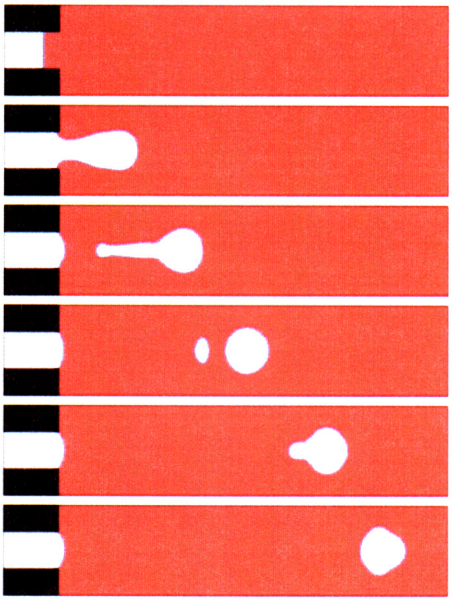

Figure 6. Computed flow field of a pulsed micro-scale water jet showing droplet development and coalescence. The computations include the effects of surface tension on droplet formation.

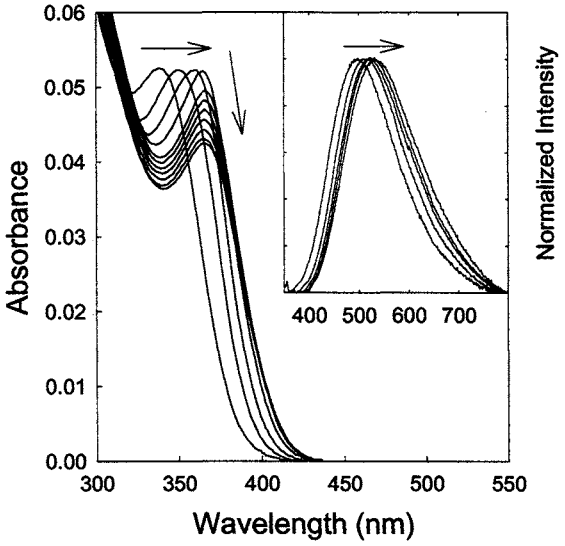

Figure 7. Uv-vis absorption and luminescence emission (inset) spectra of CdS nanoparticles (w_o = 4) obtained as a function of irradiation time.

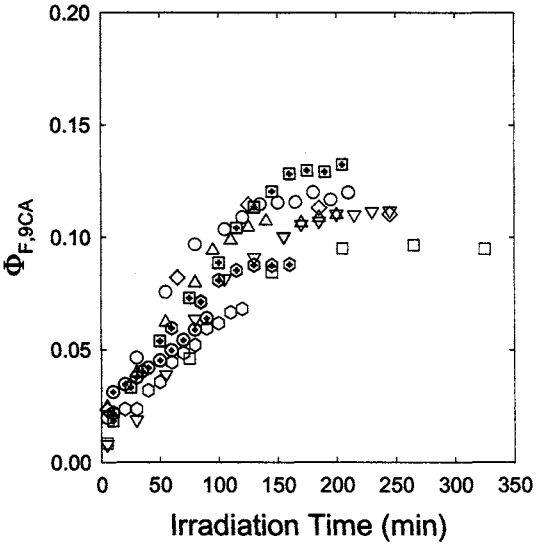

Figure 8. Fluorescence quantum yields of the CdS nanoparticles (w_o = 4) measured as a function of irradiation time. Symbols represent separate experiments.

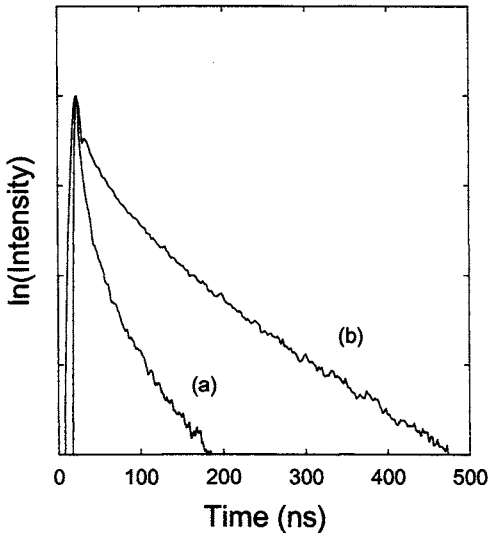

Figure 9. Luminescence decays for CdS nanoparticles (w_o = 4) prior to (a) and after (b) photoirradiation.

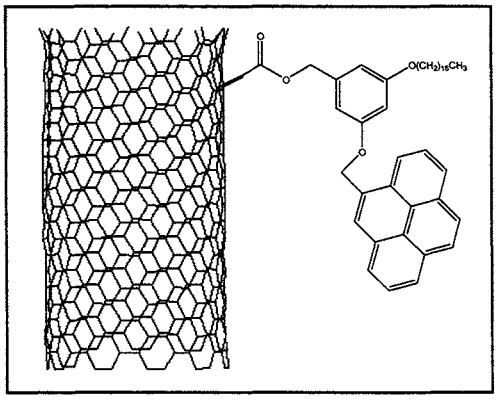

Figure 10. Pyrene-dendromer-modified single-walled carbon nanotube.

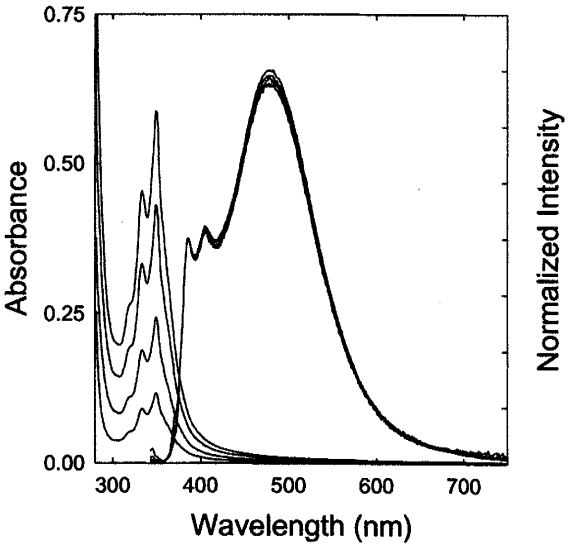

Figure 11. Uv-vis absorption and fluorescence emission spectra of the SWNT-Py-dendromer recorded as a function of concentration.

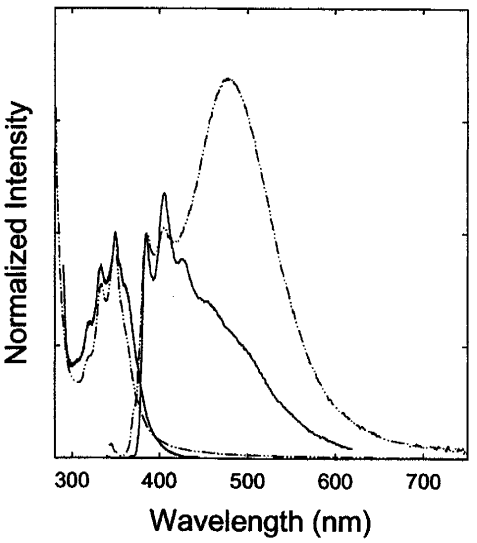

Figure 12. Uv-vis absorption and fluorescence excitation and emission spectra of the SWNT-Py-dendromer measured in room-temperature toluene (-·-·-) and in 77K toluene solid (—).

Feature Article

Evaluation of Electrochemical Release of Self-Assembled Reagents as a Component of a Preconcentrator for Flow-Injection Analysis

Long Cheng,[a] *Janaki Seneviratne*,[a] *Gilbert E. Pacey*,[a] *James R. Gord*,[b] *Michael S. Brown*,[c] *Terrence S. Meyer*,[c] *James A. Cox**[a]

[a] Department of Chemistry and Biochemistry, Miami University, Oxford, OH 45056, USA; e-mail: coxja@muohio.edu
[b] Air Force Research Laboratory, Propulsion Directorate, Wright-Patterson Air Force Base, OH 45433-7103, USA
[c] Innovative Scientific Solutions, Inc., 2766 Indian Ripple Road, Dayton, OH 45440-3638, USA

Received: December 19, 2001
Final version: February 8, 2002

Abstract
Demonstrated is that self-assembled monolayers anchored to gold by a thiolate can trap an analyte and electrochemical release of the assembly into a carrier allows determination at a downstream detector. Quantitative potentiostatic release of a coumarin derivative is demonstrated by fluorometry. The capture of $PMo_{12}O_{40}^{3-}$ on a monolayer of 4-aminothiophenol followed by oxidative release results in a 4.8 nA peak (1.6-s width at 1 mL min^{-1}) for the four-electron reduction of $PMo_{12}O_{40}^{3-}$. The sensitivity is increased by forming multilayers on the preconcentrator. Release of 10 layers of $P_2W_{18}O_{62}^{6-}$ yields a 12.4 nA peak even though only a one-electron reduction occurs at the potential employed.

Keywords: Preconcentration, Self-assembled monolayers, Flow-injection, Amperometry

Dedicated to Professor Gary Christian on the Occasion of His 65th Birthday

1. Introduction

The development of preconcentrators that are suited for microscale Total Analytical Systems, μ-TAS, requires a capture phase with dimensions that are small relative to the size of the channels. Any means of modifying a portion of the surface of the channel with a capture agent potentially can be used to meet this need. Self-assembled monolayers, SAMs, in which an analytical reagent is tethered to the channel wall, have characteristics that meet this requirement. As detailed in a recent review [1], SAMs are commonly formed by spontaneous reaction between an alkanethiol and gold. Thus, tagging an analytical reagent with a thiol provides a route to tethering a capture agent to an electrode. Turyan and Mandler [2] demonstrated this concept by self-assembling a ω-mercaptocarboxylic acid on a mercury electrode and applying the system to the accumulation and voltammetric determination of Cd^{2+}. The detection limit was 4×10^{-12} M. Flink et al. [3, 4] employed SAMs with crown ether functionalities for the determination of electrochemically inactive cations on the basis of changes in the electrode capacitance or in the charge-transfer of a redox probe added to the sample solution. The controllable permselectivity of SAMs also has been exploited to improve the performance of amperometric detectors in flow streams [5]. Of particular importance in that study was that the SAM was stable for at least 6 h under flow rates of 1 mL min^{-1}. Further examples on analytical applications of SAMs, especially to the design of biosensors, are summarized in recent reviews [6, 7].

For use as a preconcentrator in a flow system, a requirement is the facile, controlled release of the analyte from the capture site. Controlled electrochemical release of reagents from polymer-coated electrodes [8, 9] and from polyelectrolyte microcapsules on electrodes [10] has been studied; however, to our knowledge, applications that involve interaction between the analyte and a functional group tethered by a SAM have been limited to sensor development where preconcentration and measurement are in the same physical domain. A fundamental problem is that in a microscale preconcentrator with the capture reagent confined to a surface the interaction between the analyte and the capture reagent must be strong to minimize breakthrough of the analyte, which exacerbates the release of the analyte into the detection stream. A potential solution is to release the analyte by breaking the bond between the SAM and the surface.

Electrochemical oxidation or reduction can reverse the formation of a SAM by spontaneous reaction between a thiol and gold [11, 12]. In alkaline media, the gold-thiolate is oxidized by a three-electron process to Au and a sulfonate or is reduced by a one-electron process to Au and a sulfide. The general process of formation and destruction of a SAM on an electrode typically is monitored by voltammetry of a liquid-phase redox probe. The formation of the SAM is accompanied by attenuation of the voltammetric current for a reversible system such as $Fe(CN)_6^{3-,4-}$, and removal of the film results in restoration of that current [13, 14]. In addition, other methods such as capacitance measurements and

 © 2002 WILEY-VCH Verlag GmbH & Co. KGaA, Weinheim 1040-0397/02/1910-1339 $ 17.50+.50/0

infrared spectroscopy have been used to evaluate SAM chemistry [11].

An objective of the present study is to employ laser fluorescence measurements in the evaluation of the efficiency of electrochemical desorption of SAMs from gold. In this regard, the proposed applications require quantitative displacement of the captured analyte on a time scale that is short relative to the flow rate of the FIA carrier solution. The test system for these experiments is coumarin that is tethered to gold by an octanethiol chain. Fox and co-workers have described the synthesis of these SAMs on gold [15, 16]. Coumarin served as fluorescence probes of the structure of the SAM [16].

In the present study, coumarin was used as a surrogate capture agent. Its fluorescence was used to evaluate the efficiency of electrochemical release from gold. A proof of concept on the use of SAMs as preconcentrators for FIA was performed with a polyoxometalate as the analyte and 4-aminothiolphenol, which is tethered to gold, as the capture reagent. In addition, the proof of concept study was extended to include organized multilayers. These assemblies, which consisted of a polyoxometalate as the analyte and a polyamidoamine dendrimer as the spacer, were formed by layer-by-layer electrostatic deposition.

2. Experimental

Unless otherwise stated, all chemicals were ACS reagent grade, which were used as received. Acetonitrile, ethanol, sulfuric acid, and phosphomolybdic acid, $H_3PMo_{12}O_{40}$, were from Fisher Scientific Company (Fair Lawn, NJ). The generation-4 polyamidoamine (G4-PAMAM), 1,8-dibromooctane (98%), DBO, and 7-hydroxy-4-methyl coumarin (97%), HMC, were from Aldrich Chemical Co. (Milwaukee, WI), and the 4-aminothiophenol (4-ATP), from Alfa AESAR (Ward Hill, MA). $K_6P_2W_{18}O_{62}$ was prepared by a published procedure [17].

To obtain a coumarin derivative that was suited for formation of a SAM, an octanethiol tag was attached by a method based on a recent report [15]. A solution containing 34 mmol HMC, 121 mmol DBO, and 72 mmol K_2CO_3 in 100 mL of acetone was heated at reflux temperature for 48 h. After removal of the solvent, 50 mL of water were added, and the product was extracted with CH_2Cl_2. The extract was dried and the residue was separated on a silica gel column. The conversion to 7-(8-(thioacetyl)octoxy)-4-methylcoumarin, MCSH, was by reflux in ethanol in the presence of potassium thioacetate. The product was verified by ^{1}H NMR.

Gold electrodes were modified by formation of a thiolate [1]. When MCSH was the assembled reagent, only one monolayer was attached. Approximately 5 mg of the MCSH was dissolved in 1 mL of ethyl acetate, and a freshly cleaned gold electrode was placed in the solution for 5 days. The formation of monolayers and multilayers that contained a polyoxometalate used a layer-by-layer electrostatic deposition in accord with earlier reports [18, 19]. Briefly, the electrodes were soaked overnight in a freshly prepared solution of 5 mM 4-ATP in ethanol to obtain a positively charged precursor film (Au | 4-ATP) for anchoring either $PMo_{12}O_{40}^{3-}$ (PMo_{12}) or $P_2W_{18}O_{62}^{6-}$ (P_2W_{18}). For preparing a PMo_{12} monolayer, the Au | 4-ATP electrode was immersed in 5 mM PMo_{12} dissolved in a mixed 0.5 M H_2SO_4 (aqueous) – acetonitrile (v/v = 1:1) solution for 30 min. For the modification of a gold electrode with multilayer films of P_2W_{18} and G4-PAMAM, the Au | 4-ATP electrode was placed for 30 min in 3.4 mM P_2W_{18} – 0.1 M HCl to deposit a negatively charged P_2W_{18} layer. Next, after thoroughly rinsing with water, the electrode was transferred to a 1.0 wt% PAMAM – 0.1 M HCl solution for another 30 min, during which a positively charged G4-PAMAM layer was deposited. Between each step, the surface was dried with a stream of nitrogen gas. Repetition of the immersion and drying steps yielded multilayer films.

Voltammetry experiments were performed with a CH Instruments Model 750 electrochemical workstation (Austin, TX) in a conventional three-electrode cell. The working electrode was gold (1 mm diameter) from Cypress Systems (Lawrence, Kansas). Prior to use, the electrode surfaces were polished successively with 1.0, 0.3 and 0.05 micron alpha alumina powder (Mark V Laboratory, East Granby, CT) and were sonicated in water. The counter and reference electrodes were platinum wire and Ag | AgCl (Bioanalytical Systems, West Lafayette, IN), respectively. The formal potentials, E_f, of the redox couples were determined as the average of the cathodic and anodic peak potentials, E_{pc} and E_{pa}. The fluorescence experiments were performed with a Jobin Yvon/Horiba Fluorolog 3 instrument (Edison, NJ). Gold wires (0.127 mm diameter) were coated with the SAM that contained a coumarin fluorophore. The formation and release of MCSH was studied with the hexacyanoferrate redox probe. The fluorescence from a 10-mm cuvet filled with 0.1 M sulfuric acid, in which MCSH was electrochemically released, was measured.

The flow injection analysis (FIA) experiments were conducted with an Eldex Laboratory pump (Model A-120-S, Napa, CA), a Rheodyne 7125 injection valve (Cotati, CA), and a CH Instruments Model 800 electrochemical detector (Austin, TX). A commercial flow cell (BAS, West Lafayette, IN) was used for amperometric detection with a silver working electrode (3 mm diameter) and a stainless steel counter electrode. The Ag | AgCl reference electrode was placed downstream of the working electrode. Analytical measurements were made at a constant applied potential, 0.0 V. Preconcentration was performed in a second flow cell (Cypress Systems, Lawrence, Kansas) that was placed upstream from the detector. Here, gold disks (1 mm diameter) that were modified as described above were the working electrodes. When this cell was the source of electrochemically released polyoxometalates, a potential step from 0.5 to 1.5 V was applied. The release of the polyoxometalate-containing SAM was into a carrier stream, 0.5 M H_2SO_4 (1:1 aqueous – acetonitrile), that was flowed at 1.0 mL min^{-1}.

3. Results and Discussion

Initial experiments were performed with the Au | MCSH system. The successful formation of a SAM was suggested by cyclic voltammetry of a probe species, $Fe(CN)_6^{3-}$ [13, 14]. As shown in Figure 1, contacting the gold electrode to the MCSH solution as described in Section 2, yielded a SAM with sufficient surface coverage to block the outer sphere electron transfer of 10 mM $Fe(CN)_6^{3-}$ with the substrate Au electrode. Here, the potential window was 0.0 to 0.5 V. Increasing the window to 0.0 to 1.8 V in 1.0 M H_2SO_4 apparently oxidized the thiolate to the corresponding oxide of sulfur [12], thereby releasing the MCSH. The alternative of using reductive desorption was not used because of potential interference from the hydrogen evolution reaction. The electrode subsequently was transferred into the $Fe(CN)_6^{3-}$ solution and scanned over the 0.0 to 0.5 V range. Reversible voltammetry of the $Fe(CN)_6^{3-,4-}$ couple was again observed; the separation between E_{pc} and E_{pa} was 70 mV at 100 mV s^{-1}, which is nearly identical to that at bare Au electrode.

To determine the efficiency of removal of the MCSH, the current for the oxidation of the thiolate was monitored during continuous cycling. The data in Figure 2 suggest that the MCSH layer was depleted by the fifth scan. The initial voltammogram showed a peak for the oxidation of the thiolate at about 1.7 V; however, the current in that region was dominated by the oxidation of gold after five scans. A limitation of the data in Figure 2 is that the signal-to-background ratio in the region of the thiolate oxidation is low.

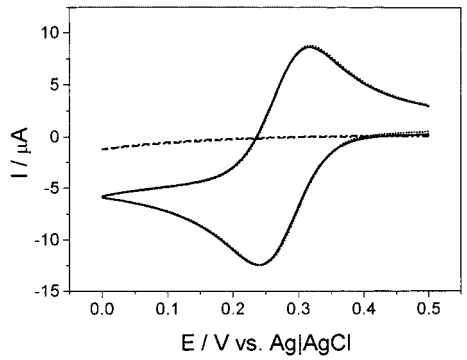

Fig. 1. Cyclic voltammetry at 0.1 V $s^{-1}$of 10 mM $Fe(CN)_6^{3-}$ in 0.5 M KCl on a bare Au electrode (solid line) and on a Au | MCSH before (dashed line) and after (dotted line) a potential scan over the range of 0.0 and 1.8 V for 5 cycles in 1.0 M H_2SO_4 at 0.1 V s^{-1}.

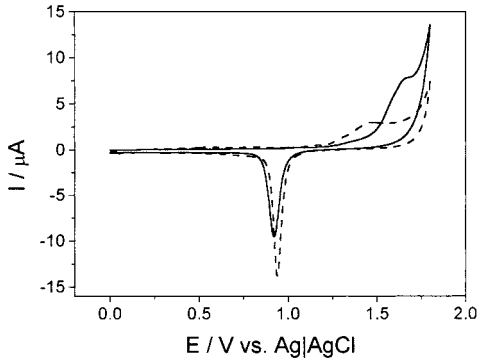

Fig. 2. Cyclic voltammetry of Au | MCSH in 1.0 M H_2SO_4 over the range of 0.0 – 1.8 V at 0.1 V s^{-1}. Only the first cycle (solid line) and the fifth cycle (dashed line) of a continuous scan are shown.

The release of MCSH was studied further by a combination of potentiostatic oxidation of the thiolate and fluorescence measurements on the medium. An Au | MCSH electrode (0.1 cm^2) was transferred into 0.1 M H_2SO_4 for 5 min. The fluorescence spectrum of the liquid phase (Figure 3a) was featureless, which suggests that the SAM is chemically stable under these conditions. After momentary application of 1.7 V to the electrode, a spectrum was again obtained. An emission peak at 380 nm was observed (Figure 3b). The electrode was rinsed and transferred to a fresh aliquot of solution. A repeat of the potential application and fluorescence measurement showed no evidence of a signal at 380 nm (Figure 3c). These results support the hypothesis that oxidation at 1.7 V rapidly removes the entire MCSH assembly from the gold. Moreover, the fluorescence spectra (emission and excitation) matched those of a standard MCSH solution, which is evidence that the coumarin is not oxidized under these conditions.

The second step in the development of the method is a demonstration of trapping by a SAM. The test system was a 4-ATP SAM on a gold electrode. The model analyte was the Keggin-type polyoxometalate, PMo_{12}, which was attached electrostatically to the 4-ATP. Cyclic voltammetry of the Au | 4-ATP | PMo_{12} assembly exhibited three redox couples with formal potentials at 0.381, 0.238 and 0.012 V (Figure 4A, curve a). They correspond to three, two-electron redox processes involving Mo centers. The influence of scan rate on peak current was investigated. A linear regression

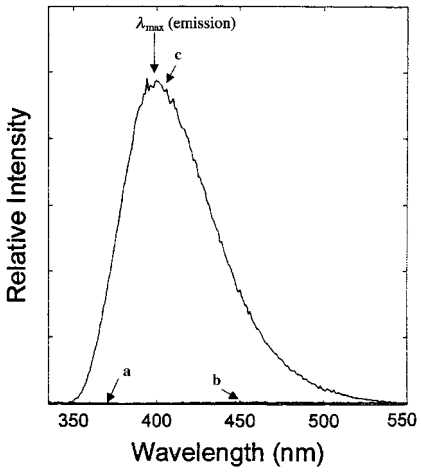

Fig. 3. Fluorescence spectra of a) 0.1 M H_2SO_4, b) 0.1 M H_2SO_4 after contact with Au | MCSH for 5 minutes, and c) same as (b) except that ca. 1.7 V was applied to the Au | MCSH electrode prior to the measurement. The solvent was methanol.

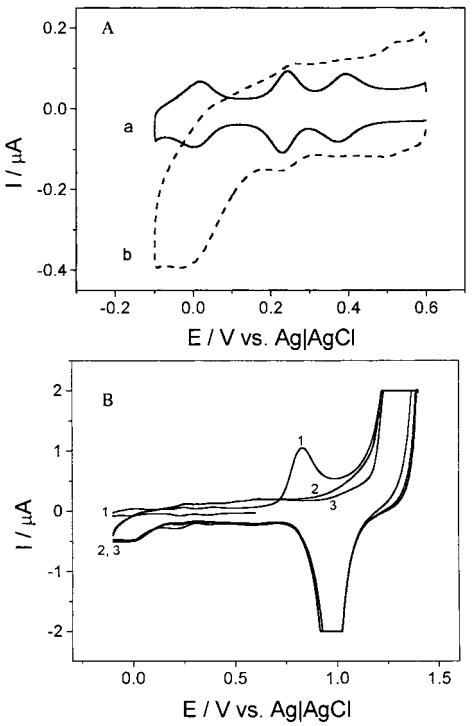

Fig. 4. Cyclic voltammetric (CV) study of the release of 4-ATP | PMo_{12} from Au into 1.0 M H_2SO_4. A) CVs of Au | 4-ATP | PMo_{12} a) before and b) after the electrochemical release conducted in (B). B) CV of Au | 4-ATP | PMo_{12} with numbers indicating the sequence of potential scans. All data were recorded at 0.1 V s^{-1} negative-going scans initiated at 0.6 V.

analysis (10 points) of log-log plot of peak current for the process near 0.2 V vs. scan rate yielded a slope of 0.946 (r, 0.999). The range of scan rates studied was 20 to 1000 mV s^{-1}. The direct proportionality between current and scan rate is indicative of reduction of a surface confined species, so charge transport across the 4-ATP layer is facile. By scanning the potential up to 1.4 V, an oxidation peak appeared at 0.83 V during the first cycle; this peak was not developed during subsequent scans (Figure 4B). The anodic process at 0.83 V was postulated as the oxidation of the thiol group of 4-ATP, which will result in the release of the SAM from the Au. This hypothesis was supported by the fact that the well-defined redox couples of PMo_{12} disappeared (Figure 4A, curve b) after the above-described excursion to 1.4 V (Figure 4B).

Proof of concept of this trap-release method was performed using Au | 4-ATP as the preconcentrator and PMo_{12} as the model analyte. The experiment was performed by accumulating PMo_{12} from a 5 mM solution, releasing the 4-ATP | PMo_{12} assembly into a flowing stream of 0.5 M H_2SO_4 in a 1:1 (vol.) water:acetonitrile mixture, and detecting the released material by amperometry at 0.0 V. The release was by stepping the potential from 0.5 to 1.5 V for ten seconds. The detection potential was a compromise between that for the four-electron reduction of Mo centers and the hydrogen evolution reaction. The signal at the detector is shown in Figure 5. The sharp peak, for which the

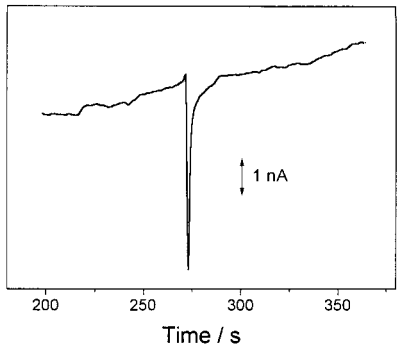

Fig. 5. Flow-injection amperometry of PMo_{12} released from a Au | 4-ATP | PMo_{12} electrode by a 10-s potential step from 0.5 to 1.5 V. Amperometric detection was at a Ag working electrode at 0.0 V. Carrier solution, 0.5 M H_2SO_4 in 50% (vol.) acetonitrile; flow rate, 1.0 mL min^{-1}.

full width at half maximum (FWHM) is 1.6 s, is indicative of a prompt releasing of the 4-ATP | PMo_{12} film. The peak current is 4.8 nA. This current is entirely due to the reduction of the PMo_{12}; in this regard, the oxidized form of the 4-ATP, in which the thiolate is converted to an oxide [12], is not reducible at the potential employed here. While these data demonstrate the concept of the SAM-based trap-release method, calibration information cannot be obtained with PMo_{12} as the analyte. At concentrations where this polyoxometalate is stable, the surface coverage, Γ, approaches 1.0 in a matter of seconds.

A potential route to increasing the attainable current density is to use multilayer trapping of the analyte. This approach was tested using a Dawson-type polyoxometalate, P_2W_{18}, and G4-PAMAM as the components of the deposit. As described in the Experimental section, the assembly, Au | 4-ATP | nP_2W_{18} | $(n-1)$G4-PAMAM, was made ($n=10$). Cyclic voltammetry of P_2W_{18} dissolved in aqueous solution and immobilized in the multilayer assembly was compared in Figure 6. P_2W_{18} in 1.0 M H_2SO_4 (Figure 6A) exhibits four reversible redox waves with E_f at 0.078, −0.082, −0.333 and −0.568 V on a glassy carbon electrode, corresponding to one-, one-, two- and two-electron redox processes, respectively [20]. However, the P_2W_{18} multilayer film deposited on Au (Figure 6B) only shows two main redox waves with E_f at −0.186 and −0.464 V, corresponding to a pair of two-electron redox processes. The first redox wave corresponds to the merging of the first two one-electron redox waves shown in solution [20]. Taking into account the pH effect on E_f, the second redox wave corresponds to the third redox process observed in solution.

The potentiostatic release and the amperometric measurement were performed as described above. The peak current (12.4 nA) for the reduction of the W centers (Figure 7) was greater than that observed for the release of Mo centers from a monolayer (Figure 5). The higher sensitivity in the former case is noteworthy in that at the measurement potential, 0.0 V, four electrons are transferred per mole of PMo_{12} while only one electron is transferred per mole of P_2W_{18}. The peak width was approximately the same

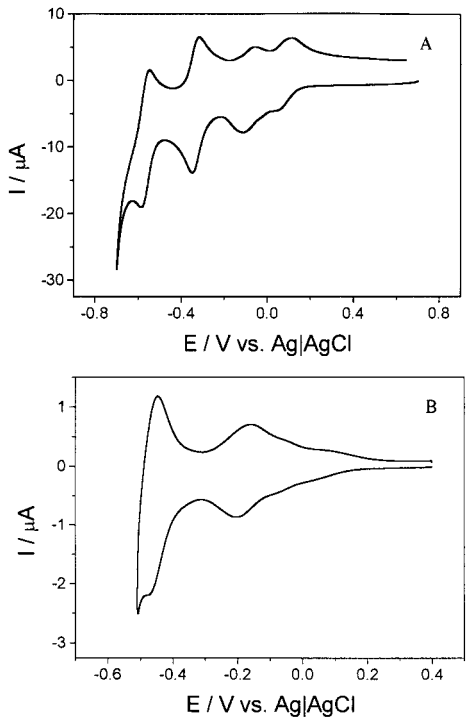

Fig. 6. Cyclic voltammetry of P_2W_{18} as A) a 3.5 mM solute in 1.0 M H_2SO_4 and B) a component of the multilayer assembly, Au | 4-ATP | $10P_2W_{18}$ | 9G4-PAMAM with 0.2 M Na_2SO_4 at pH 1.1 as the supporting electrolyte. Scan rate, 0.1 V s^{-1}.

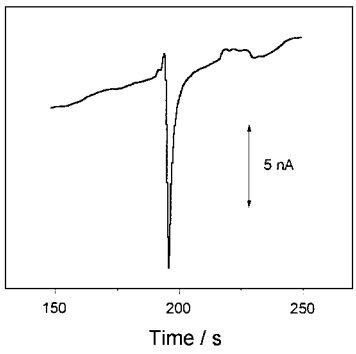

Fig. 7. Flow-injection amperometry of P_2W_{18} released from a multilayer assembly, Au | 4-ATP | $10P_2W_{18}$ | 9PAMAM, by a 30-s potential step from 0.5 to 1.5 V. The other conditions are the same as in Fig. 5.

as that in the former case; here, FWHM was 2.0 s. The onset of the hydrogen evolution reaction precluded applying a more negative potential for detection of P_2W_{18}. The relative sensitivities suggest that a strategy such as sequential exposure of the upstream electrode to solutions of analyte and spacer may provide efficient preconcentration of an analyte.

4. Conclusions

The above results suggest that self-assembled monolayers can be used as preconcentrators in flow-injection analysis (FIA) systems. An important feature is that rapid release of the analyte is accomplished by oxidizing the thiolate anchor to gold. With a traditional system, the bond between the analyte and the host phase is broken; here, the more favorable the capture chemistry, the more difficult it is to accomplish release. The SAM-based system is attractive for application to micromachined FIA systems in that the physical size of the capture phase is small relative to the micron-level channels used in these devices. Presently, we are extending this study to the use of self-assemblies of crown ethers and of functionalities that capture analytes by formation of β-donor complexes. These trapping agents will be evaluated as preconcentrators in microscale Total Analytical Systems.

5. References

[1] A. Ulman, *Chem. Rev.* **1996**, *96*, 1533.
[2] I. Turyan, D. Mandler, *Anal. Chem.* **1994**, *66*, 58.
[3] S. Flink, B. A. Boukamp, A. van den Berg, F. C. J. M. van Veggel, D. N. Reinhoudt, *J. Am. Chem. Soc.* **1998**, 4652.
[4] S. Flink, F. C. J. M. van Veggel, D. N. Reinhoudt, *J. Phys. Chem. B* **1999**, *103*, 6515.
[5] J. Wang, H. Wu, L. Agnes, *Anal. Chem.* **1993**, *65*, 1893.
[6] D. Mandler, I. Turyan, *Electroanalysis* **1996**, *8*, 207.
[7] Th. Wink, S. J. van Zuilen, A. Bult, W. P. van Bennekom, *Analyst* **1997**, *122*, 43R.
[8] L. L. Miller, B. Zinger, Q. X. Zhou, *J. Am. Chem. Soc.* **1987**, *109*, 2267.
[9] T. Komura, K. Kijima, T. Tamaguchi, K. Takahashi, *J. Electroanal. Chem.* **2000**, *486*, 166.
[10] X. Shi, F. Caruso, *Langmuir* **2001**, *17*, 2036.
[11] C. A. Widrig, C. Chung, M. D. Porter, *J. Electroanal. Chem.* **1991**, *310*, 335.
[12] M. A. Walczak, D. D. Popenoe, R. S. Deinhammer, B. D. Lamp, C. Chung, M. D. Porter, *Langmuir* **1991**, *7*, 2687.
[13] M. D. Porter, T. B. Bright, D. L. Allara, C. E. D. Chidsey, *J. Am. Chem. Soc.* **1987**, *109*, 3559.
[14] S. Berchmans, V. Vegnaraman, G. P. Rao, *J. Solid State Electrochem.* **1998**, *3*, 52.
[15] W. Li, V. Lynch, H. Thompson, M. A. Fox, *J. Am. Chem. Soc.* **1997**, *119*, 7211.
[16] M. A. Fox, W. Li, M. Wooten, A. McKerrow, J. W. Whitesell, *Thin Solid Films* **1998**, *327–329*, 477.
[17] H. Wu, *J. Biol. Chem.* **1920**, *43*, 189.
[18] L. Cheng, J. A. Cox, *Electrochem. Commun.* **2001**, 285.
[19] L. Cheng, G. E. Pacey, J. A. Cox, *Electrochim. Acta* **2001**, *46*, 4223.
[20] M. Sadakane, E. Steckhan, *Chem. Rev.* **1998**, *98*, 219.

Highly Luminescent CdS Nanoparticles: Effect of Particle Size and Preparation Method on the Photoenhancement Process

C. E. Bunker[†], B. A. Harruff[‡], P. Pathak[‡], Y. Lin[‡],
J. Widera[†], J. R. Gord[†], and Y.-P. Sun[‡]

[†]Air Force Research Laboratory, Propulsion Directorate, Wright-Patterson Air Force Base, OH 45433
[‡]Department of Chemistry, Clemson University, Clemson, SC 29634

CdS nanoparticles have been prepared with emission properties characteristic of trap states (*i.e.*, broad, Gaussian-like, and red shifted from the absorption band onset) using the reverse micelle method. Luminescence quantum yields for freshly prepared particles are independent of particle size or quantum-confinement effect with the quantum yields being 0.02 – 0.04 for particles prepared with w_o values of 2 to 10 (w_o = $[H_2O]/[AOT]$). Irradiation of the particles at the absorption maxima results in an increase in the quantum yields (Φ_L = ~0.12 for w_o = 4). The increase is found to be a function of the particle size; smaller particles undergo greater photoenhancement. The degree of enhancement also correlates with observed spectral shifts; particles displaying a greater spectral shift with irradiation undergo a greater enhancement in the quantum efficiency. The effect of the irradiation process on CdS nanoparticles prepared at w_o values of 4, 5, 6, and 8 will be presented. The data will be discussed along with supporting TEM and x-ray powder diffraction results within the context of the quantum-confinement effect, the role of surface properties, and crystal structure.

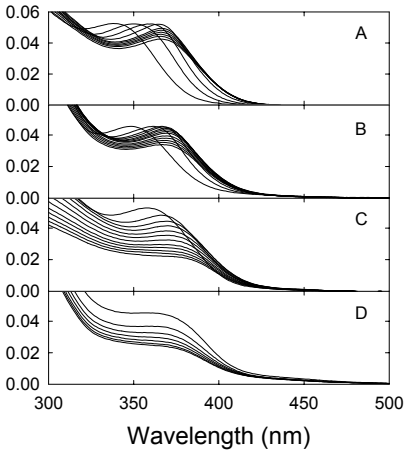

Figure 1

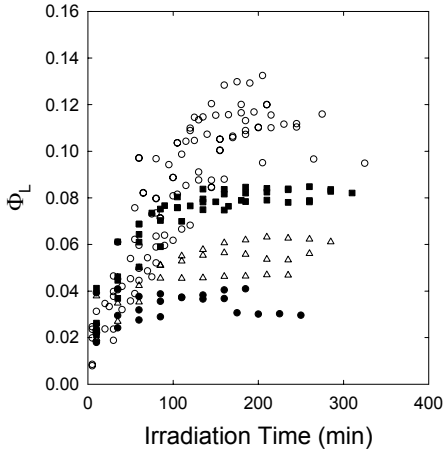

Figure 2

Figure 1. Absorption spectra collected as a function of irradiation time for AOT-protected CdS nanoparticles in hexane solution with w_o = 4 (A), 5 (B), 6 (C), and 8 (D).

Figure 2. Quantum yields determined as a function of irradiation time for AOT-protected CdS nanoparticles with w_o = 4 (○), 5 (■), 6 (Δ), and 8 (●).

Highly Luminescent CdS Nanoparticles Applied Toward the Development of Chemical Sensors

Justyna Widera
John J. Karnes, James R. Gord
Christopher E. Bunker*

Propulsion Directorate
Air Force Research Laboratory
Wright-Patterson Air Force Base OH

Introduction

- **Smart Nozzle**
  - **Develop fuel-quality diagnostics**
  - **Enhance the versatility of the fuel**
  - **Additize as needed at the skin of the aircraft**
  - **Reduce costs of operation and maintenance**
  - **Use nanoparticles as sensors**

- **CdS nanoparticles demonstrate luminescence characteristics applicable to the development of fuel-quality sensors**

Spectral Properties of AOT Protected CdS Nanoparticles

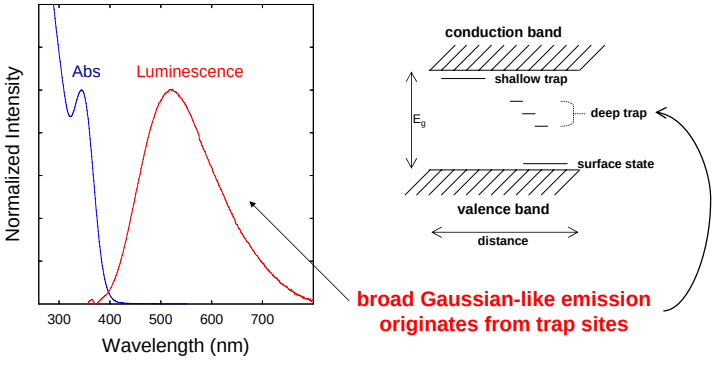

1) Rossetti, R.; Brus, L. *J. Phys. Chem.* 1982, *86*, 4470. 2) Brus, L. *J. Phys. Chem.* 1986, *90*, 2555. 3) Chestnoy, N.; Harris, T. D.; Hull, R.; Brus, L. E. *J. Phys. Chem.* 1986, *90*, 3393.

Effect of Particle Size on Absorption and Emission Spectra

Quantum Confinement Effect

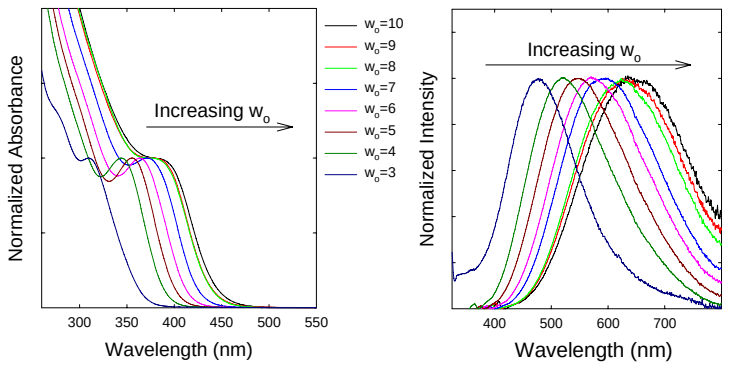

Time vs Irradiation

During the course of the luminescence investigation, it was observed that successive measurements of the same CdS solution resulted in an increase in the observed luminescence intensity (yield). Samples measured individually as a function of time-since-preparation showed no increase in yield. The observed effect is therefore attributed to photoirradiation.

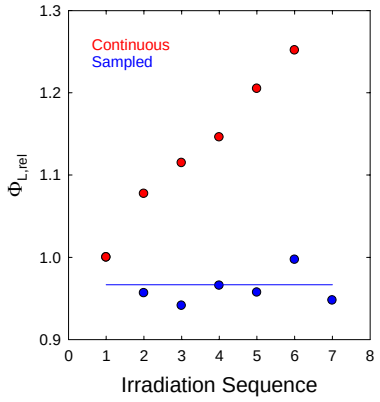

Irradiation Effect on Absorption Spectra vs. w_o

absorption spectra recorded at 15 min intervals throughout the irradiation process

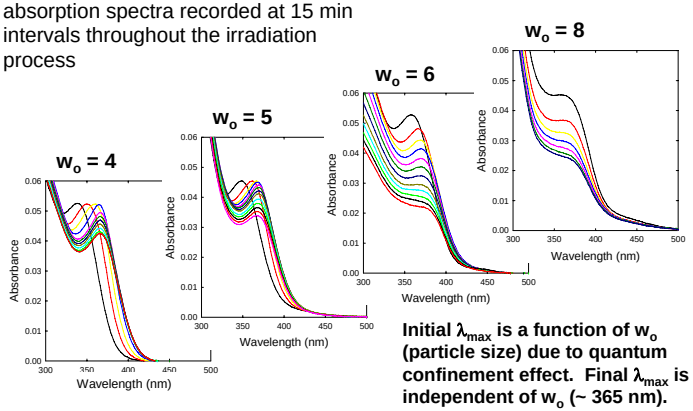

Initial λ_{max} is a function of w_o (particle size) due to quantum confinement effect. Final λ_{max} is independent of w_o (~ 365 nm).

Irradiation Effect vs w_o

Luminescence yields are determined for replicate CdS particles at different w_o values. As can be seen, the initial luminescence yield for the freshly prepared particles is independent of w_o, ranging between 1 and 4%. The effects of irradiation, however, are highly dependent on w_o with higher w_o values corresponding to larger particles and lower plateau luminescence yields.

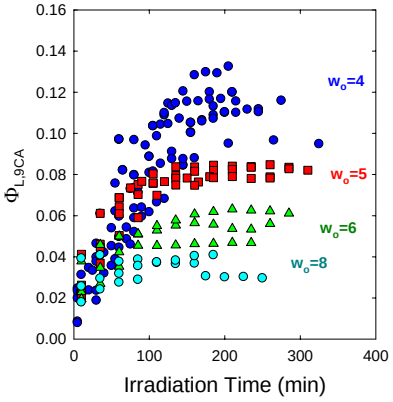

Did Particle Size Change with Irradiation?

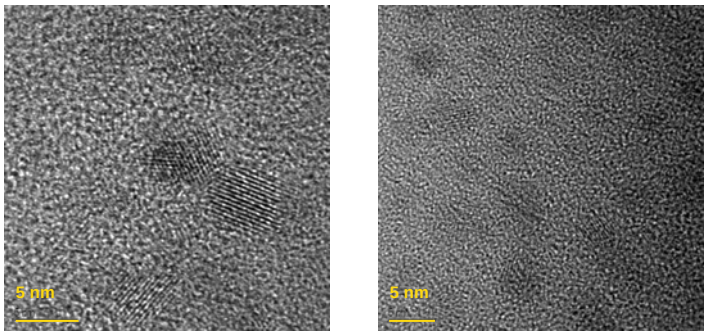

Fresh **Plateau**

particle size ~2 - 4 nm

Effect of Preparation Volume

small volume preparation

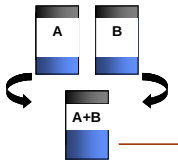

large volume preparation

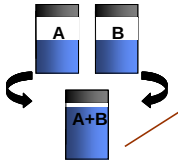

X-ray powder diffraction

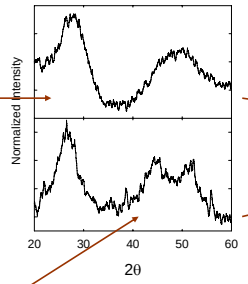

absorption

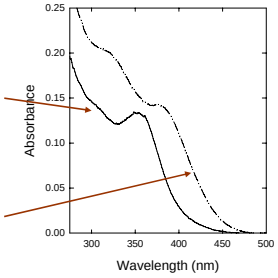

(all concentrations held constant)

Summarized Results

Table 1. Effect of Preparation Volume on Crystal Structure and Absorption Maximum

$CdNO_3$[a]	Na_2S[a]	Structure	d (nm)	λ_{max} ABS	
5 mL	5 mL	cubic	1.39	335	(fresh)
5 mL	5 mL	cubic	2.29	360	(irradiated)
5 mL	5 mL			333	(drop wise)
5 mL	5 mL			333	(drop/mix)
5 mL	5 mL		2.15		(aged)
10 mL	10 mL	cubic/hex[b]	2.0	345	
15 mL	15 mL	cubic/hex[b]	2.8	355	
20 mL	20 mL	cubic/hex[b]	1.98	360	

a) Cd^{2+} and S^{2-} concentrations are constant and all solutions are prepared with $w_o = 4$.
b) cubic/hex indicates observation of the bimodal x-ray spectrum which could be either hexagonal or cubic.

Even Higher Quantum Yields!

small volume preparation

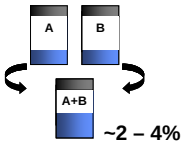

~2 – 4%

irradiated

~12%

dried (temp, vac)

~42% ⟸ *stable*

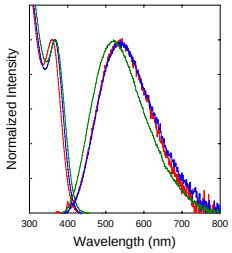

fresh
plateau
dried

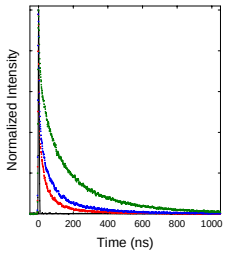

Absorption Spectra *f*(solvent)

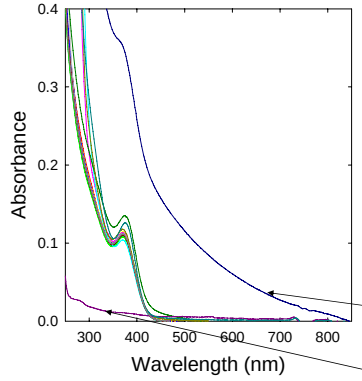

Cyclohexane
Pentane
Hexane
Heptane
Toluene
Benzene
THF
Ethyl acetate
Chloroform
Dichloromethane
Acetone
DMSO
Propylene carbonate
Benzyl alcohol
Ethanol
Methanol
Octanol
Dodecane
Acetonitrile

Luminescence Spectra *f*(solvent)

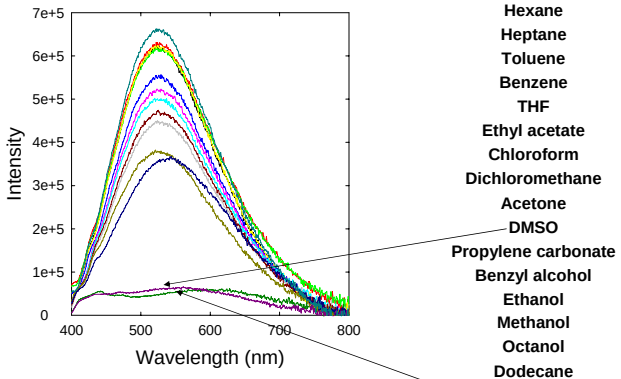

Cyclohexane
Pentane
Hexane
Heptane
Toluene
Benzene
THF
Ethyl acetate
Chloroform
Dichloromethane
Acetone
DMSO
Propylene carbonate
Benzyl alcohol
Ethanol
Methanol
Octanol
Dodecane
Ethylene glycol

Summarized QY Results

Table 1. CdS Quantum Yields in Different Solvents

Solvent	ABS Max	FLSC Max	Φ_L	E^T_N
Cyclohexane	371	526	0.320	0.006
Pentane	371	525	0.348	0.009
Hexane	371	525	0.361	0.009
Heptane	371	527	0.362	0.012
Toluene	370	527	0.318	0.099
Benzene	371	527	0.300	0.111
THF	370	525	0.215	0.207
Ethyl acetate	371	526	0.223	0.228
Chloroform	370	528	0.266	0.259
Dichloromethane	370	529	0.280	0.309
Acetone	371	529	0.189	0.355
DMSO	375	556	0.043	0.444
Propylene carbonate	no peak	432		0.491
Benzyl alcohol	371	528	0.198	0.608
Ethanol	368	528	0.151	0.654
Methanol	369	538	0.073	0.762
Octanol	371	533	0.332	
Dodecane	371	525	0.363	

QY vs. Solvent Polarity Metric

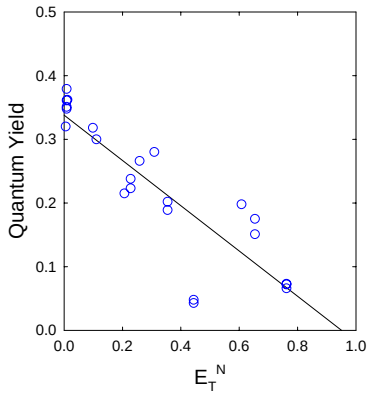

Conclusions

We have prepared highly luminescent CdS nanoparticles with emission properties characteristic of trap states. The particles are easily prepared, are reproducible, and are stable on the order of days.

The initial spectral properties are clearly a function of particle size (quantum confinement effect), surface chemistry, and to some extent crystal structure.

Changes in the spectral properties (*i.e.*, photoenhancement procedure) are influenced by particle size, but, are clearly due to surface effects (no change to particle size or crystal structure was observed with irradiation).

The solvent dependent behavior seems to indicate the particles act as simple molecules.

Acknowledgments

Air Force Office of Scientific Research
Air Force Research Laboratory, PRTG

B. A. Harruff
P. Pathak
Y. Lin
Prof. Y.-P. Sun
(Clemson University)

Crystallographic and Spectroscopic Investigations of the Effect of Preparation Procedure on CdS Nanoparticles Made in Reversed Micelles

203rd Meeting of the ECS Paris France, 2003

Christopher E. Bunker†

P. Pathak‡, B. A. Harruff‡, Y. Lin‡, J. Widera†, J. R. Gord†, and Y.-P. Sun‡

†Air Force Research Laboratory
Propulsion Directorate
Wright-Patterson Air Force Base OH

‡Department of Chemistry
Clemson University
Clemson SC

Introduction

- CdS can serve as a model compound
  - numerous preparation methods available
  - electro/optical properties tunable (QCE)
  - luminescence is well defined
    - excitonic
    - trap state
  - trap-state emissions sensitive to chemical perturbation
- use CdS nanoparticles as chemical sensors
- luminescence yields typically low
- surface chemistry not defined

Spectral Properties

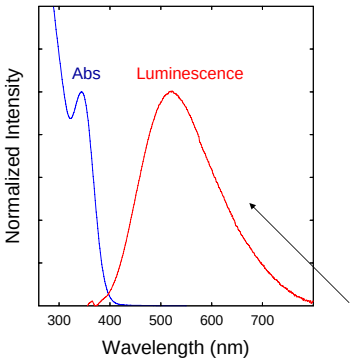

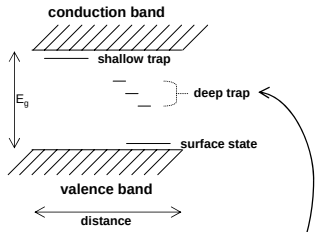

broad Gaussian-like emission originates from trap sites

1) Rossetti, R.; Brus, L. *J. Phys. Chem.* 1982, *86*, 4470. 2) Brus, L. *J. Phys. Chem.* 1986, *90*, 2555. 3) Chestnoy, N.; Harris, T. D.; Hull, R.; Brus, L. E. *J. Phys. Chem.* 1986, *90*, 3393.

Effect of Particle Size on Absorption and Emission Spectra

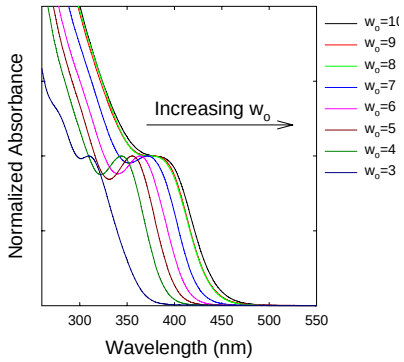

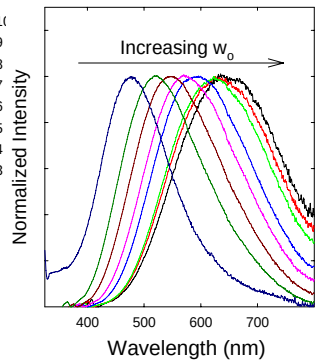

Time vs Irradiation

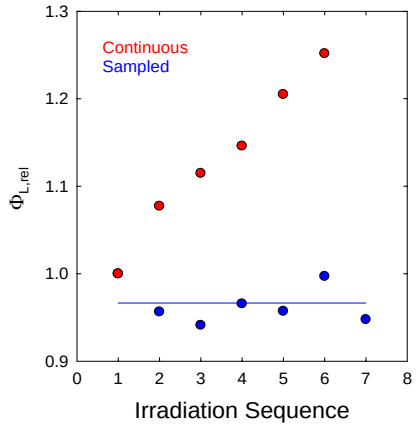

Irradiation Effect on Absorption Spectra vs. w_o

absorption spectra recorded at 15 min intervals throughout the irradiation process

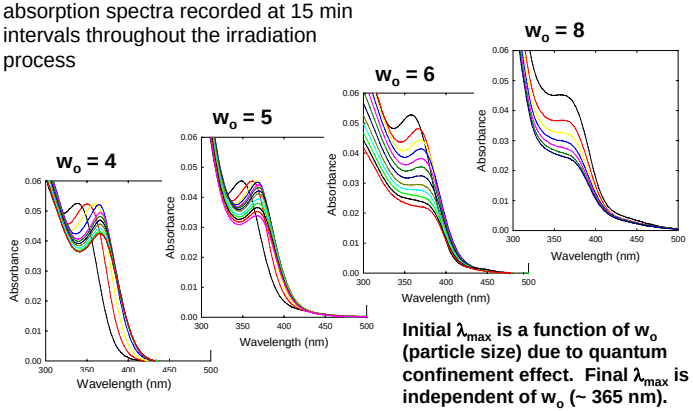

Initial λ_{max} is a function of w_o (particle size) due to quantum confinement effect. Final λ_{max} is independent of w_o (~ 365 nm).

Absorption Maximum Shift with Irradiation

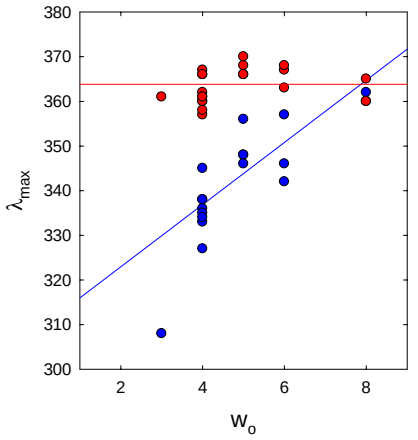

Initial λ_{max}
Final λ_{max}

final position independent of particle size

Irradiation Effect vs w_o

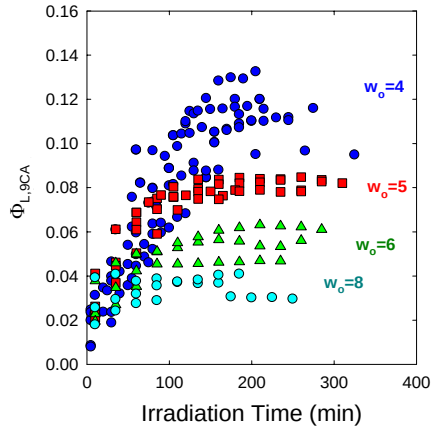

Did Particle Size Change with Irradiation?

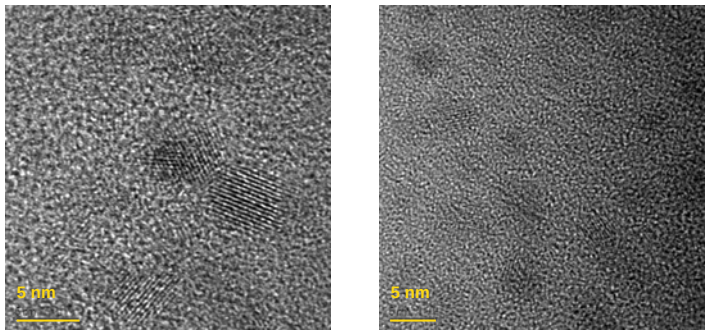

Fresh Plateau

particle size ~2 - 4 nm

Effect of Preparation Volume

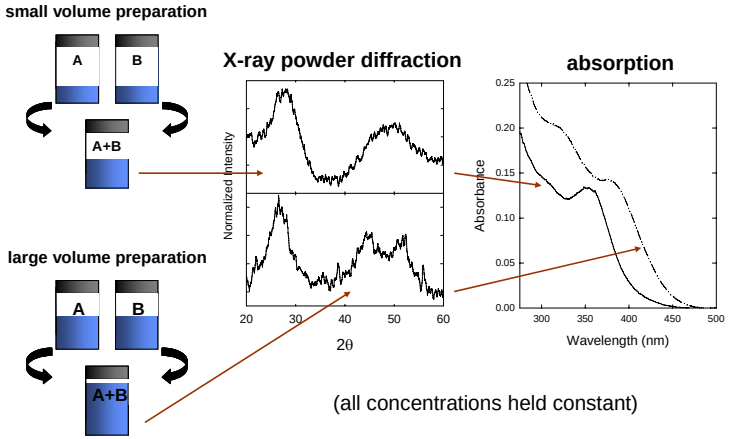

(all concentrations held constant)

Summarized Results

Table 1. Effect of Preparation Volume on Crystal Structure and Absorption Maximum

$CdNO_3$[a]	Na_2S[a]	Structure	d (nm)	λ_{max} (nm)	
5 mL	5 mL	cubic	1.2	335	(fresh)
5 mL	5 mL	cubic	2.3	365	(irradiated)
5 mL	5 mL	cubic		335	(drop wise)
5 mL	5 mL	cubic/hex[b]		335	(drop/mix)
5 mL	5 mL	cubic/hex[b]	2.2	357	(aged)
10 mL	10 mL	cubic/hex[b]	2.0	345	
15 mL	15 mL	cubic/hex[b]	2.8	355	
20 mL	20 mL	cubic/hex[b]	2.0	360	

a) Cd^{2+} and S^{2-} concentrations are constant and all solutions are prepared with $w_0 = 4$.
b) Cubic/hex indicates observation of the bimodal x-ray spectrum which could be either hexagonal or cubic.

Even Higher Quantum Yields!

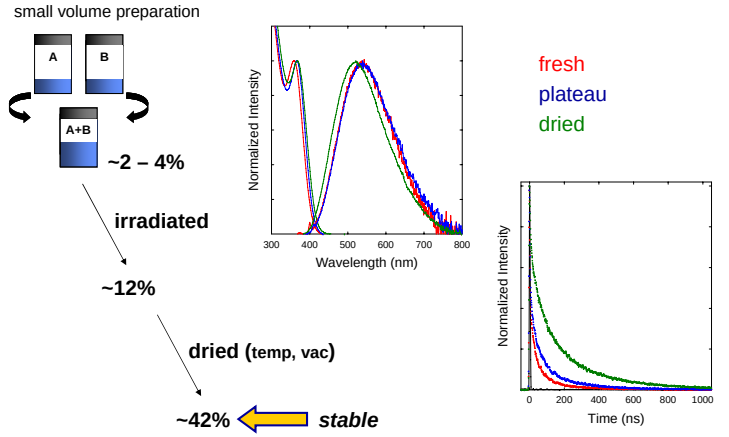

Conclusions

We have prepared highly luminescent CdS nanoparticles with emission properties characteristic of trap states. The particles are easily prepared, are reproducible, and are stable on the order of days.

The initial spectral properties are clearly a function of particle size (quantum confinement effect), surface chemistry, and to some extent crystal structure.

Changes in the spectral properties (*i.e.*, photoenhancement procedure) are influenced by particle size, but are clearly due to surface effects (no change to particle size or crystal structure was observed with irradiation).

Acknowledgments

Air Force Office of Scientific Research
Air Force Research Laboratory, PRTG

Dr. Larry Allard, Oak Ridge National Laboratory
Dr. Donald Phelps, AFRL

Rocky Mountain Conference on Analytical Chemistry
27-31 July 2003
Denver, CO

Quenching Studies of Highly Luminescent CdS Nanoparticles in Presence of Sulfur-Containing Compounds

J. Widera

Innovative Scientific Solutions, Inc.
2766 Indian Ripple Road
Dayton, OH 45440

J. R. Gord and C. E. Bunker

Air Force Research Laboratory
Propulsion Directorate
Wright-Patterson AFB, OH 45433

Nanoparticle Preparation Capabilities

Reverse Micelle (Pileni Method)

- Characterized by a confined-space reaction (nanoreactors)
- metal reductions: $A^{n+} \rightarrow A^{o}$
- multicomponent reactions: A + B -> AB
- core-shell structures: $A^{n+} \rightarrow A^{o} + B \rightarrow B(A^{o})$

Sonochemical (Suslick Method)

- characterized by a nanometer sized high-temperature reaction zone created through cavitation
- metal reductions: $A^{n+} \rightarrow A^{o}$
- degradation and nucleation: AB -> A^{o}

Rapid Expansion of a Supercritical Solution (RESS) (Sun Method)

- characterized by precipitation through rapid depressurization
- modified to include expansion into a receiving solution (RESSolve)
- metal reductions: $A^{n+} \rightarrow A^{o}$
- multicomponent reactions: A + B -> AB
- mixed metals of non-equilibrated compositions: $A_{m}B_{n}$

CdS Nanoparticles

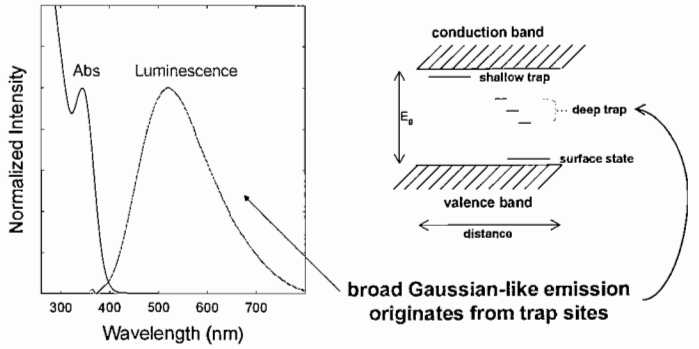

1) Rossetti, R.; Brus, L. *J. Phys. Chem.* 1982, *86*, 4470. 2) Brus, L. *J. Phys. Chem.* 1986, *90*, 2555. 3) Chestnoy, N.; Harris, T. D.; Hull, R.; Brus, L. E. *J. Phys. Chem.* 1986, *90*, 3393.

Nanoreactors

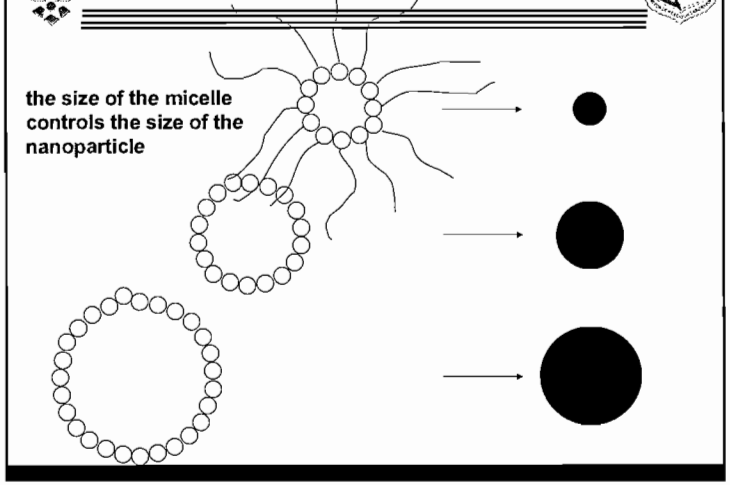

Effect of Particle Size on Absorption and Emission Spectra

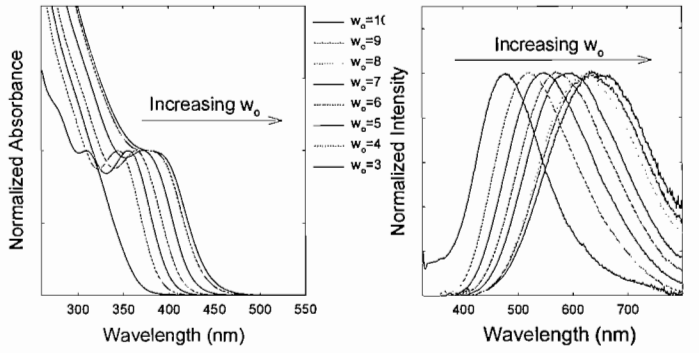

quantum confinement effect

Time vs Irradiation

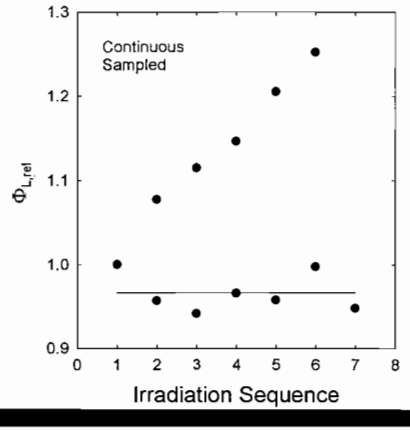

Irradiation Effect on Absorption Spectra vs. w_o

absorption spectra recorded at 15 min intervals throughout the irradiation process

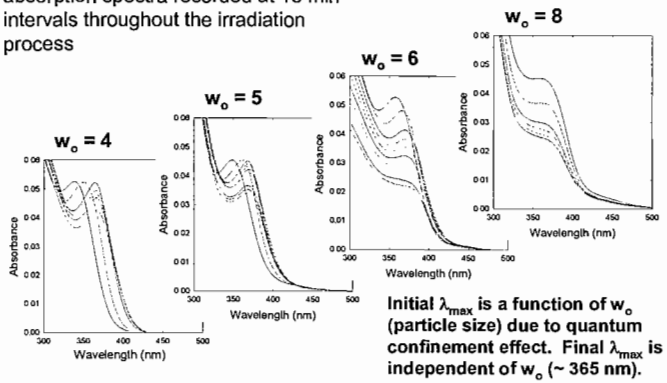

Initial λ_{max} is a function of w_o (particle size) due to quantum confinement effect. Final λ_{max} is independent of w_o (~ 365 nm).

Absorption Maximum Shift with Irradiation

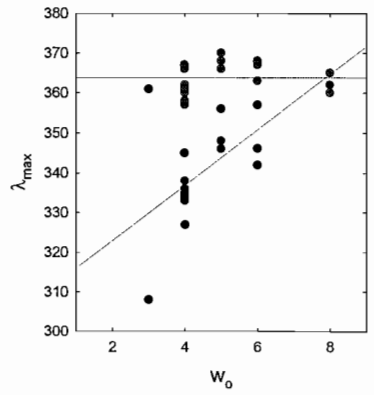

Initial λ_{max}
Final λ_{max}

final position independent of particle size

Irradiation Effect vs w_o

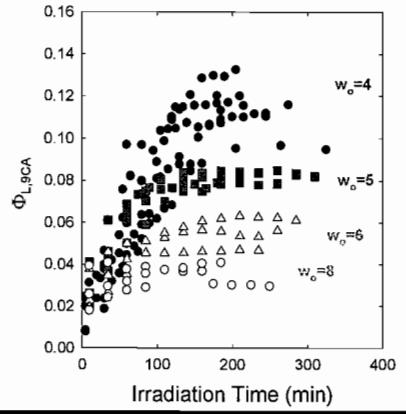

Did Particle Size Change with Irradiation?

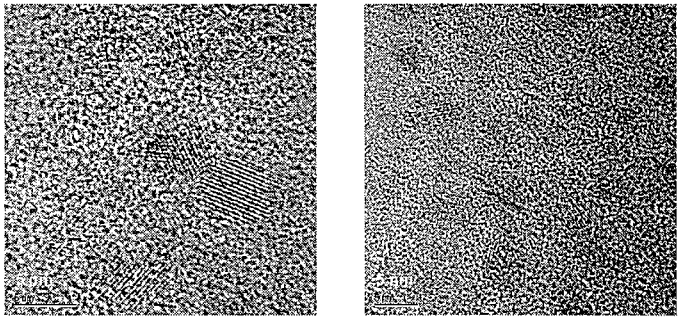

Fresh

Plateau

particle size ~2 - 4 nm

Effect of Preparation Volume

small volume preparation

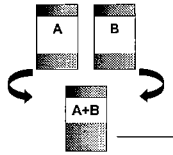

X-ray powder diffraction

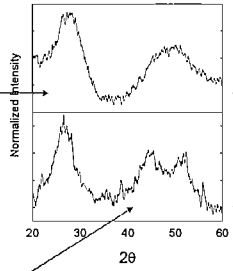

absorption

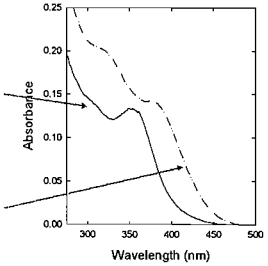

large volume preparation

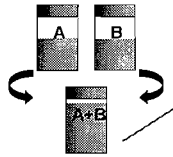

(all concentrations held constant)

Summarized Results

Table 1. Effect of Preparation Volume on Crystal Structure and Absorption Maximum

$CdNO_3$[a]	Na_2S[a]	Structure	d (nm)	λ_{max} (nm)	
5 mL	5 mL	cubic	1.2	335	(fresh)
5 mL	5 mL	cubic	2.3	365	(irradiated)
5 mL	5 mL	cubic		335	(drop wise)
5 mL	5 mL	cubic/hex[b]		335	(drop/mix)
5 mL	5 mL	cubic/hex[b]	2.2	357	(aged)
10 mL	10 mL	cubic/hex[b]	2.0	345	
15 mL	15 mL	cubic/hex[b]	2.8	355	
20 mL	20 mL	cubic/hex[b]	2.0	360	

a) Cd^{2+} and S^{2-} concentrations are constant and all solutions are prepared with $w_0 = 4$.
b) Cubic/hex indicates observation of the bimodal x-ray spectrum which could be either hexagonal or cubic.

Even Higher Quantum Yields!

small volume preparation

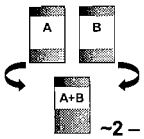

~2 – 4%

irradiated

~12%

dried (temp, vac)

~42% ⇐ *stable*

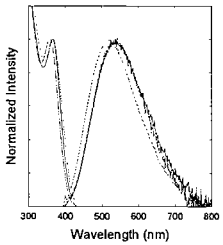

fresh
plateau
dried

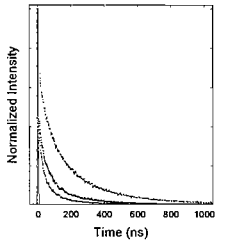

Fresh-Plateau-Thermal

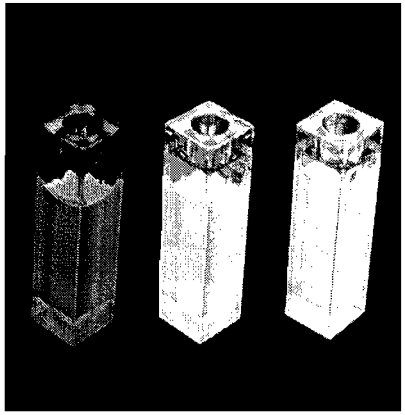

Luminescence Quenching

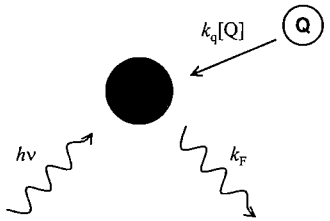

$\Phi_F^o/\Phi_F = 1 + K_{SV}[Q]$

where

$K_{SV} = k_q\tau_F^o$

Emission *f*(DMSO)

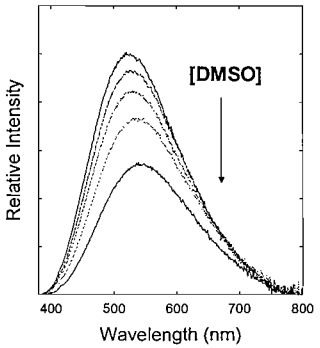

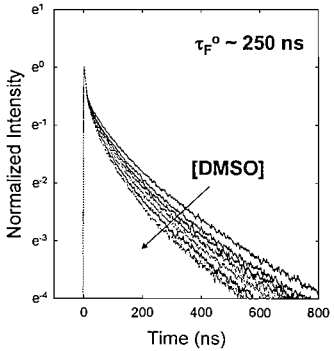

Stern-Volmer Plot w/DMSO

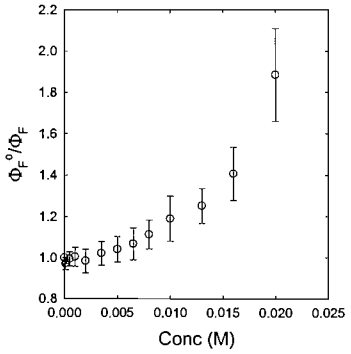

Stern-Volmer Plot w/Hexanethiol

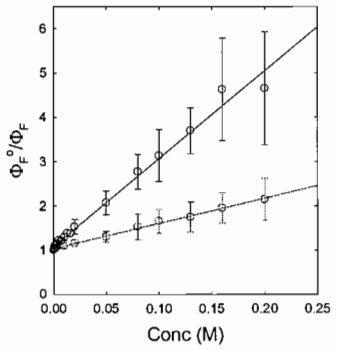

K_{sv} = 19.8

$k_q \sim 7.9 \times 10^7$ ns

K_{sv} = 5.7

$k_q \sim 2.3 \times 10^7$ ns

Conclusions

We have prepared highly luminescent CdS nanoparticles with emission properties characteristic of trap states. The particles are easily prepared, are reproducible, and are stable on the order of days.

The initial spectral properties are clearly a function of particle size (quantum confinement effect), surface chemistry, and to some extent crystal structure.

Changes in the spectral properties (*i.e.*, photoenhancement procedure) are influenced by particle size, but are clearly due to surface effects (no change to particle size or crystal structure was observed with irradiation).

Acknowledgments

Dr. James R. Gord (AFRL/PRTS)
Dr. Donald K. Phelps (AFRL/PRTG)
Prof. Ya-Ping Sun (Clemson Univ.)
Prof. Steven W. Buckner (St. Louis Univ.)

Barbara Harruff	**P. Pathak**	**AFOSR**
Y. Lin	**Dr. Justyna Widera**	**AFRL/PRTG**
John Karnes	**Nathan Sanders**	**AFRL/PRTS**
Brad Martin	**Matt Rabe**	
Sophie Rozenzhak	**Dan Zweifel**	

EXPANDING THE COMBUSTION AND LASER DIAGNOSTICS RESEARCH COMPLEX (CLDRC)

Annual Joint ACS/SAS Poster Session
5 March 2002

J. R. Gord, R. D. Hancock, & W. M. Roquemore
AFRL, Propulsion Directorate
M. S. Brown, T. R. Meyer, S. P. Gogineni, & S. Roy
Innovative Scientific Solutions, Inc.

PRTS Mission (IHPTET/VAATE)

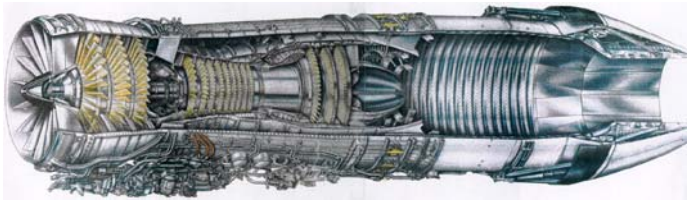

- **Improved Propulsion-System Performance (Thrust/Weight, SFC, etc.)**
- **Reduced Pollutant Emissions**
- **Enhanced Maintainability, Reliability, Affordability**

2

PRTS Turbine Engine Research Center (TERC) Facilities

- **Combustion & Laser Diagnostics Research Complex (CLDRC) - Dr. Jim Gord**
- **Atmospheric-Pressure Combustor Research Complex (APCRC) - Dr. Vince Belovich**
- **High-Pressure Combustor Research Facility (HPCRF) - Mr. Dale Shouse**
- **Pulsed-Detonation Research Facility (PDRF) - Dr. Fred Schauer**

3

Combustor Technology Development

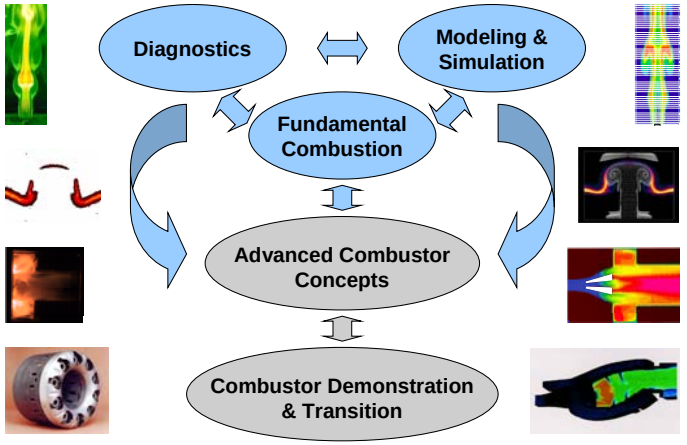

4

Phased Diagnostics Approach

Combustion Research in the Laboratory

Performance Evaluation in the Engine Test Cell

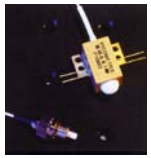

Real-Time Control on the Flight Line and in the Air

5

CLDRC

Bldg 490 Rms 108, 151-153

Bldg 18 Rm 20

Combustion & Laser Diagnostics Research Complex

CLDRC

D-Bay

Bldg 5

6

Bldg 5 CLDRC Floor Plan

Office Space		Instrumentation & Electronics Shop, Laser Staging & Maintenance, Calibration			
Hallway					
Lobby with Displays		Combustion Laboratories			

7

Turbulence (Vortex-Flame Interactions)

- Predictive understanding of turbulent combustion
- Detailed chemistry and physics
- Improved engine performance

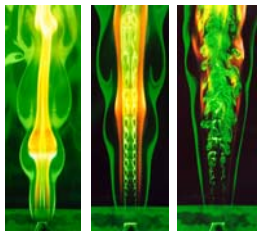

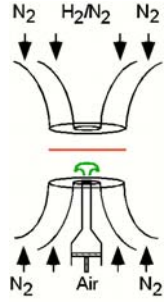

8

Flow Visualization

- Acetone Planar Laser-Induced Fluorescence (PLIF)
- Planar Rayleigh Scattering (PRS)
- Simultaneous OH PLIF/ Particle Image Velocimetry (PIV)

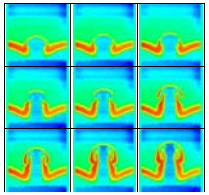

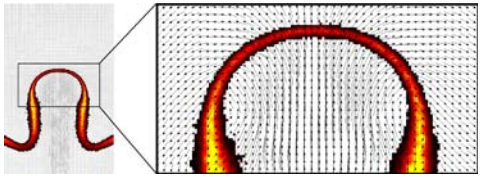

9

New Directions

- Two-Phase Flows
- Multiple-Vortex Interactions
- Elevated Pressures
- Quantitative Techniques

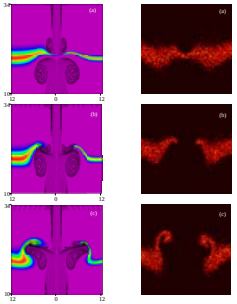

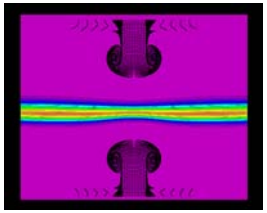

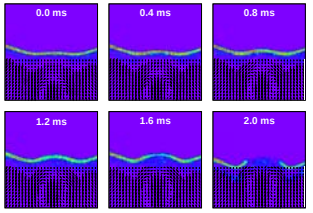

10

Triple-Pump CARS

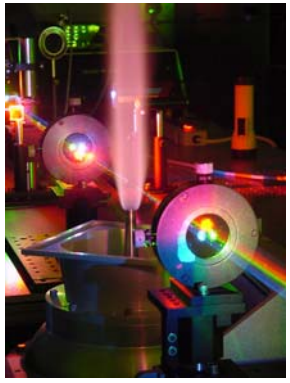

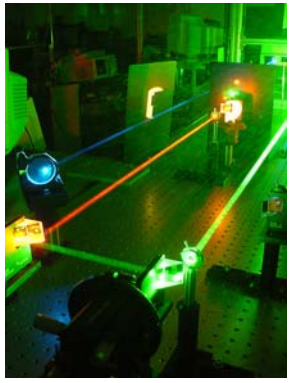

11

Ultranarrowband Doubly Resonant OPO

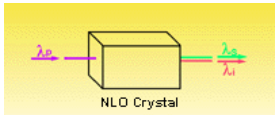

$\omega_{pump} = \omega_{signal} + \omega_{idler}$

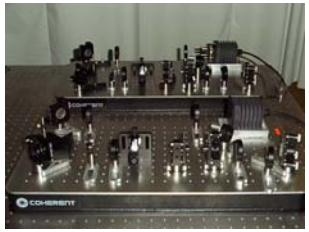

12

Diode-Laser-Based Sensors

- Absorption Spectroscopy
- Measurements of CO, NO
- Potential for Ruggedization, Miniaturization

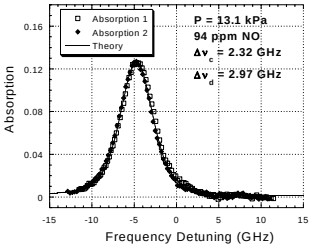

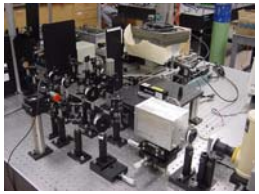

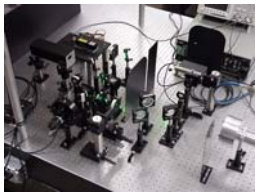

Terahertz Radiation ("T-Rays")

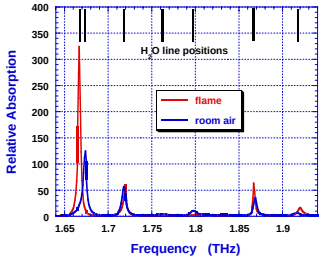

- Far Infrared
- Absorption Lines
- Transmission Properties
- Packaging

2000
R&D 100
Award Winner

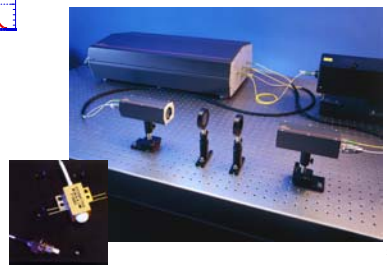

Other Ultrafast Spectroscopies

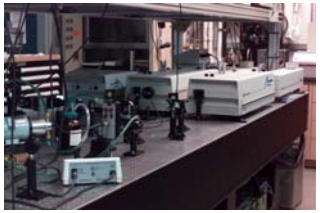

- Pico/Femtosecond Pump-Probe Spectroscopy
- Asynchronous Optical Sampling
- Picosecond Time-Resolved Laser-Induced Fluorescence
- Polarization Spectroscopy

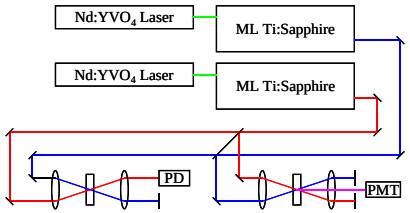

Summary

- CLDRC provides diagnostic support for advanced combustor development.
- Three-phased approach features fundamental studies and diagnostics development, test-cell applications, and on-board integration.
- New facilities in Bldg 5 will permit next-generation experimental studies.

(c)2001 American Institute of Aeronautics & Astronautics or Published with Permission of Author(s) and/or Author(s)' Sponsoring Organization.

A01-16860

AIAA 2001-1075

Role of CHF_3 in Extinguishing Diffusion and Premixed Flames

V. R. Katta
W. M. Roquemore
Air Force Research Laboratory
Wright-Patterson AFB, OH

39th AIAA Aerospace Sciences Meeting & Exhibit
8-11 January 2001 / Reno, NV

For permission to copy or republish, contact the American Institute of Aeronautics and Astronautics
1801 Alexander Bell Drive, Suite 500, Reston, VA 20191

(c)2001 American Institute of Aeronautics & Astronautics or Published with Permission of Author(s) and/or Author(s)' Sponsoring Organization.

Role of CHF_3 in Extinguishing Diffusion and Premixed Flames

V. R. Katta* and W. M. Roquemore+
Propulsion Directorate
Air Force Research Laboratory
Wright-Patterson Air Force Base, OH 45433-7103

Abstract:

Studies of laminar, buoyant jet diffusion flames play an important role in understanding combustion phenomena, formulating theories of combusting processes, and developing and evaluating CFD codes for practical combustion systems. Because of the similarities between buoyant jet diffusion flames and practical uncontrolled fires, it is suggested that studies of fire-suppressing agents in the former system could provide valuable information on the behavior of such agents in actual fires. A periodically oscillating, pure-methane-air jet diffusion flame is simulated using GRI Version 1.2 chemistry. This flame was investigated previously using the Reactive-Mie-Scattering technique, and excellent agreement was found between predictions and measurements. To explore the chemical inhibition resulting from the use of CHF_3 fire suppressant, it is added to the air flow in such a way that its addition does not change the molar concentration of oxygen. Two-dimensional calculations for the CHF_3-affected dynamic flames are made using GRI+NIST chemistry, having 82 species and 1510 elementary reactions. It is found that for concentrations of up to 26% CHF_3 the diffusion-flame base shifts slowly toward a downstream location and becomes stabilized within ~40 mm of the jet exit. For concentrations > 27%, the flame base moves downstream rapidly until it is cleared from the computational domain. On the other hand, for concentrations > 65%, the flame appeared to extinguish at locations other than the base. Flame structures obtained with different concentrations of CHF_3 are compared with those obtained for the pure methane-air jet diffusion flame. Calculations for stochiometric premixed flames with different concentrations of fire-suppressing agent are also made. The chemical steps that are affected most significantly by fluorine reactions are identified in both the diffusion and premixed flames. It is found that in addition to a considerable decrease in OH radicals in the methane-air-CHF_3 flame, the concentration of H_2 decreases significantly. Unlike in premixed flames, the peak concentration of O radicals does not change significantly with the addition of small amounts of CHF_3 in the air stream of a diffusion flame.

* AIAA Associate Fellow
Senior Engineer, Innovative Scientific Solutions, Inc.,
2766 Indian Ripple Road, Dayton, OH 45440,
e-mail: vrkatta@erinet.com
+ Senior Scientist, AIAA Fellow

This paper is declared a work of the U. S. Government and is not subjected to copyright protection in the United States.

Introduction:

Effective fire-extinguishing agents are known to act primarily through chemical mechanisms. Trifluorobromomethane (CF_3Br, Halon 1301) is a widely used [1] fire-suppressing agent and studies have been conducted on understanding its inhibitory mechanism in premixed flames [2-4]. However, it is also extremely effective for depleting stratospheric ozone. Consequently, with the current ban on the production of CF_3Br, replacements are being considered that are predominantly fluorinated hydrocarbons [5]. Understanding the inhibition mechanisms of these replacements along with CF_3Br is important for their efficient use and for developing new agents. Past studies on CF_3Br have provided insight into the inhibiting action of CF_3, even though the chemical inhibition with this agent is dominated by the brominated species. On the other hand, experimental studies on premixed CO and H_2 flames have identified the key decomposition steps of CHF_3 leading to CF_3. Therefore, although the agents being considered as replacements for CF_3Br are predominantly two- and three-carbon fluorinated molecules [5], insight into the chemical paths that are important in their fire-suppressing capability can be obtained from the study of simpler species such as CHF_3, which are more amenable to modeling. Recently, a comprehensive kinetic mechanism for fluorine-species inhibition has been developed [5,6].

Most of the studies conducted to gain an understanding of the inhibitory effects of halogenated or fluorinated hydrocarbons on flames were performed in premixed systems [7,8]. These flames were selected mainly because the overall reaction rate, heat release, and heat and mass transport can be described with a fundamental parameter--laminar burning velocity. On the other hand, most of the common uncontrolled fires are of the diffusion type and often become dynamic in nature, with large vortical structures entraining additional surrounding air.

(c)2001 American Institute of Aeronautics & Astronautics or Published with Permission of Author(s) and/or Author(s)' Sponsoring Organization.

Studies of jet diffusion flames plays an important role in understanding combustion phenomena, formulating theories of combusting processes, and developing and evaluating design codes for practical combustion systems. A laminar jet diffusion flame established with a low-speed fuel and a negligibly small annular air flow generates large-scale, low-frequency (1-40 Hz), organized buoyancy-induced vortices on the air side of the flame--very similar to pool fires. Because of the similarities between buoyant jet diffusion flames and practical uncontrolled fires, the former are often investigated to understand the effect of gravity on vortical structures, flame-vortex interactions, and entrainment characteristics of the latter. Following a similar strategy, it is suggested that studies of the effects of fire-suppressing agents on buoyant jet flames provide valuable information on the behavior of such agents in actual fires.

Several numerical investigations of dynamic jet flames using the conserved-scalar, global-chemistry, and detailed chemistry models have revealed important aspects of combustion such as the effect of heat-release rate [9,10], the role of buoyancy [11-13], enhancement of soot formation [14], and Lewis-number effects [15,16]. However, the authors are not aware of any computation performed for the prediction of the effects of fire-suppressing agents on jet diffusion flames--mainly, because of the large chemical kinetics required for describing the inhibition action of these agents in hydrocarbon flames.

This paper describes the first numerical simulation for a dynamic jet diffusion flame inhibited by a fire suppressant using detailed chemical kinetics. This study also demonstrates that using today's desktop computers and an efficient CFD code, one can simulate the chemical structure of a complex unsteady flow. For comparison purpose, steady-state premixed flames are also computed for various fire-suppressant concentrations.

Numerical Model:

A time-dependent, axisymmetric mathematical model known as UNICORN (Unsteady Ignition and Combustion using ReactioNs) [17] is used to simulate the unsteady jet diffusion flames considered in this study. It solves for u- and v-momentum equations, continuity, and enthalpy- and species-conservation equations on a staggered-grid system. The body-force term due to the gravitational field is included in the axial-momentum equation for simulating vertically mounted flames. A clustered mesh system is employed to trace the large gradients in flow variables near the flame surface. Two detailed chemical-kinetics models are incorporated in UNICORN for the investigation of fluoromethane effects on methane combustion: 1) GRI-V1.2 compiled by the Gas Research Institute (GRI) [18]--the most comprehensive mechanism, with 31 species and 346 elementary-reaction steps, recommended by several investigators [18] for computing the structures of methane flames; and 2) GRI-HFC model [19] developed by National Institute of Standards and Technology (NIST) through addition of fluoromethane-related inhibition reactions to the GRI-V1.2 combustion mechanism--a model having 82 species and 1510 elementary-reaction steps. Thermo-physical properties such as enthalpy, viscosity, thermal conductivity, and binary molecular diffusion of all the species are calculated from the polynomial curve fits developed for the temperature range 300 - 5000 K. Mixture viscosity and thermal conductivity are then estimated using the Wilke and Kee expressions, respectively. Molecular diffusion is assumed to be of the binary-diffusion type, and the diffusion velocity of a species is calculated using Fick's law and the effective-diffusion coefficient of that species in the mixture.

The finite-difference forms of the momentum equations are obtained using an implicit QUICKEST scheme [12], and those of the species and energy equations are obtained using a hybrid scheme of upwind and central-differencing. At every time-step, the pressure field is accurately calculated by solving all the pressure Poisson equations simultaneously and utilizing the LU (Lower and Upper diagonal) matrix-decomposition technique. The boundary conditions are treated in the same way as that reported in earlier papers [20].

The flow field considered in the present study has vortical structures outside the flame surface that are > 30 mm in length. Unsteady axisymmetric calculations are made on a physical domain of 250 x 150 mm utilizing a 201 x 71 non-uniform grid system. The computational domain is bounded by the axis of symmetry and an outflow boundary in the radial direction and by the inflow and another outflow boundary in the axial direction. The outer boundaries in the z and r directions are located sufficiently far from the nozzle exit (~ 30 nozzle diameters) and the symmetry axis (~ 20 nozzle diameters), respectively, that propagation of boundary-induced disturbances into the region of interest is minimized. Flat velocity profiles are imposed at the fuel and air inflow boundaries, while an extrapolation procedure with weighted zero- and first-order terms is used to estimate the flow variables at the outflow boundary.

The simulations presented here are performed on a Pentium II 300-MHz-based Personal Computer with 524 MB of memory. Typical execution times using the GRI-V1.2 and GRI+HFC mechanisms are ~220 and ~650 s/time-step, respectively. Stably oscillating flames are usually obtained in about 1000 time steps (which corresponds to approximately five flicker cycles), starting from the solution obtained with a 24-species-chemistry model [21]. It is worth noting that an unsteady two-

(c)2001 American Institute of Aeronautics & Astronautics or Published with Permission of Author(s) and/or Author(s)' Sponsoring Organization.

dimensional flame under the influence of fire suppressant can be calculated using an 82-species, 1510-elementary-reactions mechanism (GRI+HFC) on a personal computer in ~ 200 h. Capabilities demonstrated in this paper will revolutionize the way in which combustion processes are investigated in the future.

Code Preparation:

Incorporating large chemical-kinetics mechanisms in CFD codes is a formidable task and is highly susceptible to typographical and programming errors--mainly because of the implicit treatment of the reaction-rate terms for a stable solution procedure. To avoid such errors in the present 25,000-line code, software that generates the FORTRAN code for a given chemical-kinetics model has been developed. It directly reads the data published on the web [19] by NIST and writes the modified UNICORN code for that chemistry. This software has been rigorously tested on smaller mechanisms and to ensure that it generates an error-free code for the given chemistry. In this way, human involvement in preparing the CFD code is minimized; hence, errors associated with it are eliminated.

Results and Discussion:

The experimental setup used for the studies on buoyant jet diffusion flames consists of vertically mounted coannular tubes and is described in detail in Ref. 21. The central fuel jet is issued from a 25.4-mm-diameter tube that contracts to a 10-mm-diameter nozzle. The nozzle is designed to provide a flat laminar velocity profile at the nozzle exit. The annular-air jet has a diameter of 245 mm. An air velocity of 15 cm/s is used to reduce room-air disturbances without significantly affecting the visible flame structure. The fuel-jet velocity is 0.5 m/s. Because of the buoyancy forces and the shear-layer instability, this flame became a dynamically oscillating one.

An instantaneous image of the flame obtained with the Reactive-Mie-Scattering (RMS) technique [22] is shown in Fig. 1(a). With this method micron-sized TiO_2 particles, formed from the spontaneous reaction between the seeded-$TiCl_4$ vapor and the water vapor produced during combustion, are visualized by the Mie-scattered light from a laser sheet. $TiCl_4$ is seeded into both the fuel and the annular-air flows. The bright-orange region is the luminous flame surface captured simultaneously with the Mie-scattered light. The buoyant jet flame shown in Fig. 1 has important features such as low-velocity fuel and air flows, large vortical structures entraining air, and flame acceleration with height--often observed in pool fires.

Because of the gravity term in the axial-momentum equation and the low-speed annular-air flow (~ 0.15 m/s), solution of the governing equations resulted in a dynamic flame, with large toroidal vortices forming naturally outside the flame surface. The computed instantaneous temperature field using GRI-V1.2 chemical kinetics is shown in color in Fig. 1(b). The iso-molar-concentration contours of the CH_3 and OH radicals are shown in 1(c) on the left and right halves, respectively. It is important to note that no artificial perturbation is required for the formation of the outer vortices. In the presence of gravitational force, acceleration of hot gases along the flame surface generated the outer structures as part of the solution. As these vortices are convected downstream, they cause the flame to squeeze at certain locations (z = 58 and 150 mm in the computed flame) and bulge at others (z = 35 and 90 mm in the computed flame). The frequency corresponding to the passage of these outer vortices (also known as the flame-flickering frequency) is ~ 12 Hz. The predicted flame structure compares well with that obtained in experiments. Calculations for this flame were also made using GRI+HFC chemical kinetics, and essentially the same results as shown in Fig. 1 were obtained since the fire suppressant was not used in this flame.

The computed flame in Fig. 1 is well anchored to the inflow boundary. The flame structure in the stretched (squeezed) region at z = 58 mm above the inflow boundary is shown in Fig. 1(d). As expected, both the OH and O radicals are concentrated on the airside of the flame surface (high-temperature surface). It is noted that their concentrations decrease when the flame is bulging outward (for example at z = 90 mm).

To evaluate the performance of a fire suppressant on this flame, fluoromethane (CHF_3) was added to air at different concentration levels, and calculations were performed for the modified flow conditions using GRI+HFC chemical kinetics. In experimental studies involving fire suppressants, researchers typically replace part of the air with the agent. Even though such a practice represents a practical fire-extinction procedure, the data generated in those studies become complicated with simultaneous effects of deoxygenation and agent chemistry. To isolate the effects of the latter, calculations were performed by replacing part of the nitrogen with CHF_3, without altering the concentration of oxygen.

Since the annular air velocity is only 0.15 m/s, the agent introduced into the calculations from the inflow boundary requires about 1.6 s (i.e., ~4200 time steps) to reach the exit boundary. To expedite the calculations, new initial data were generated by replacing the corresponding amount of nitrogen with the specified amount of agent in the pure methane-air-flame data in regions where the free stream oxygen was not affected. In calculations made with this new initial data, the agent entered the flame zone through diffusion very quickly (in about 300 time steps) and all along the flame simultaneously.

(c)2001 American Institute of Aeronautics & Astronautics or Published with Permission of Author(s) and/or Author(s)' Sponsoring Organization.

Calculations made with different amounts of CHF_3 suggest that when the concentration is < 10% (i.e, oxygen 21% and nitrogen 59%), no visible effects on the flame are observed. For concentrations between 10 and 26%, the flame is separated slightly (< 40 mm) from the inflow boundary and stabilized at a new location. However, when the concentration is increased to a value > 27%, the flame completely blown out of the computational domain.

Instantaneous solutions obtained for 20% and 35% concentrations of CHF_3 are shown in Figs. 2 and 3, respectively. Here, temperatures are plotted in (a)'s, OH and CH_3 concentrations are plotted in (b)'s, and CHF_3 and C_2F_6 concentrations are shown in (c)'s. The flame base in Fig. 2 is stabilized at z ~ 32 mm above the nozzle while that in Fig. 3 is moving downstream with time. Results shown in Fig. 3 were obtained after 0.14 s of calculation and the flame was found to clear the computational domain in another 0.2 s.

As mentioned earlier, 20% CHF_3 was not sufficient to quench the flame completely. Even though its base is shifted downstream, it is well anchored at ~32 mm above the inlet. A comparison of pure methane-air [Fig. 1(b)] flame with those with 20% [(Fig. 2(a)] and 35% [Fig. 39a)] of CHF_3 revels three important characteristics: 1) Oxygen and CHF_3 are entering the flame through the separation established between the base and inlet, 2) flame temperature is not affected significantly, and 3) vortical structures became larger with the addition of the agent.

Because of weak mixing in the shear layer near the jet exit, the diffusion flame near the jet exit is always stained to a greater extent than that located further downstream [23]. The presence of CHF_3 in the annular flow quenched the strained flame near the jet exit. The flame is stabilized 32-mm above the jet exit, which led to leakage of oxygen and CHF_3 into the flame. In general the concentrations of H_2, OH and H decreased with the addition of CHF_3. However, the concentration of O is not changed much, especially, with the addition of small amount of CHF_3.

The computed time evolution of the temperature as the large outer structures are convected past fixed radial lines at 20, 30, 40, 60, 80, and 100 mm above the inflow boundary are visualized for a 20%-CHF_3 flame in Figs. 4(a) ~ 4(f), respectively. Bulging and squeezing of the flame due to the convective motion of the outer vortices cause the periodic oscillation in the flame surface. As discussed previously, the pure methane/air flame is subjected to 20% agent concentration at t = 0. Even though the vortical structures developed (Figs. 1-3) in the presence of CHF_3 are larger, the flame oscillations actually decrease at a fixed height (Fig. 4) as the flames with CHF_3 are shifted downstream. Figures 4(d) ~ 4(f) indicate that the period of flame oscillation has decreased from 84 to 79 ms (frequency has increased from 12 to 12.6 Hz.). The sudden disappearance of high-temperature region in Figs 4(a) and 4(b) is resulting from the passage of the flame base at that location.

Since the gaseous CHF_3 is heavier than N_2, the molecular weight of the O_2+N_2+CHF_3 mixture (32 gmole) is ~10% greater than that of the O_2+N_2 mixture of air. The effects of denser annular flow on the flame are similar to those observed with gravitational force as far as buoyancy forces are concerned. Therefore, the denser annular flow generates greater buoyancy forces on the flame which, in turn, results in larger vortical structures. As a result, the flicker frequency of the 20% CHF_3 flame increased to 12.6 Hz compared to the 12 Hz obtained for the flame that is surrounded by air (Fig. 1).

When the CHF_3 concentration is increased to a value > 27%, the flame base moved rapidly downstream; and after a few milliseconds the entire flame cleared the computational domain. The rate at which the flame base moves clearly depends on the concentration of the added CHF_3. Higher the concentration of the agent (CHF_3) in the annular air the faster the flame blown out of the computational domain. Interestingly, flame was not actually quenched by the fire suppressant as seen in Fig. 3. In order to observe the quenching process due to fire suppressant, its concentration needed to be increased to ~ 65%. The flame obtained with 65% fire suppressant in the air stream (i.e., 21% oxygen, 51% CHF_3 and 28% N_2) is shown in Fig. 5. The high temperature and OH concentration in the flame zone are continuous along the flame length—confirming that the flame has not been quenched anywhere. The flame structures in the base region (z = 88.5 mm) and stretched region (z = 123 mm) are compared in Figs. 5(c) and 5(d). These plots indicate that 1) the concentrations of radicals (such as O, H, and OH) decreased significantly compared to those obtained with pure methane flame (Fig. 1) and 2) the concentrations of these radicals in the stretched region are much lower than those at the flame base. The latter observation further suggests that the flame in the stretched region is very close to the quenching limit. In deed, further increase in CHF_3 concentration generated regions of quenched flame.

The computed time evolution of the temperature as the large outer structures are convected past fixed radial lines at 20, 40, 60, 80, 100, and 120 mm above the inflow boundary are shown for the 65%-CHF_3 flame in Figs. 6(a) ~ 6(f), respectively and for the 70% CHF_3 flame in Figs. 7(a)~7(f), respectively. A comparison between flame evaluations obtained for 65% and 70% CHF3 flames suggests the following; 1) flame base moves faster in the 70% CHF3 flame [took 91 ms to reach to the height of 80 mm in Fig. 6(d) while it took only 89 ms in Fig. 7(d)]. This is because of the higher buoyancy force acting on the virtually the same flame by the heavier annular flow. Secondly, the flame in the stretched region is quenched for 70% CHF_3 concentration [Fig. 7(e) and 7(f)].

(c)2001 American Institute of Aeronautics & Astronautics or Published with Permission of Author(s) and/or Author(s)' Sponsoring Organization.

Over all, the calculations made for a buoyant jet diffusion flame suggests that when the agent concentration is slightly above the critical value (required to extinguish a flame), then the flame quenches through a blowout process. That is, the base of the flame becomes unstable and moves downstream in search of a stabilizing point. This 27% concentration is not sufficient to quench the weakly strained flame (Fig. 1). However, additional simulations made with > 65% CHF_3 concentration quenched the flame at squeezed locations within 0.1 s from the start of the calculations. It is important to note that 1) this concentration may not be the critical concentration to extinguish the flame as it certainly depends on the location of the outer vortex or in other words the strain rate applied on the flame by the outer vortex and 2) part of 0.1 s time was needed for the agent to diffuse radially into the flame zone.

To further understand the role of CHF3 on flame quenching, calculations were made for a stationary premixed flame. The Bunsen flame formed with a 5-mm nozzle is first simulated using GRI mechanism. Stoichiometric fuel-air ratio was considered while a parabolic profile was used for the velocity. The simulated steady Bunsen flame is plotted in Fig. 8(a) with the upper image showing the temperature distribution and the lower one giving the OH concentration field. The maximum temperature was 2240 K and it appeared just above the tip of the inner cone.

Calculations were made by adding CHF_3 to the fuel stream. Here also, the concentrations of CH_4 and O_2 were not changed while adding CHF_3. Only the concentration of N_2 was reduced to compensate the addition of CHF_3. Flames obtained with 5%, 10%, 20% and 30% CHF_3 are shown in Figs. 8(b)-8(e), respectively. The important observations made from these figures are 1) the cone height increases with CHF_3 addition suggesting that the burning velocity is decreasing, 2) flame is getting fatter with CHF_3, 3) flame base is shifting toward a downstream location and 4) OH is forming along the outer edge of the flame in the products indicating a secondary combustion process from the products.

The flame structure close to the tip of the cone obtained for the pure methane-air and methane-air-10%-CHF_3 flame are shown in Figs. 9(a) and (b), respectively. In contrast with that observed from diffusion flame calculations, the concentrations of H, O, and OH radicals are decreasing with the addition of CHF_3. On the other hand, the concentrations of hydrocarbon radicals seem increasing. Interestingly, the temperature has increased by ~ 30K with the addition of 10% CHF_3. The variations of flame temperature and peak OH concentrations with the concentration of CHF_3 are plotted in Fig. 9(c). This indicates that the flame temperature initially increases and then decreases for CHF_3 concentrations > 15%. It is interesting to recall that in diffusion flame simulations, the flame temperature and concentration of O radicals did not change with the small addition of CHF_3.

The reactions that yield rates greater than $5x10^{-5}$ mole/cm^3/s in the pure methane-air flame are listed in Figure 10(a), along with their rates (dark-colored bars). The rates of these reactions in a 20%-CHF_3 diffusion flame are also shown using light-colored bars. The reactions involving fluorine are not shown here since they are absent in the pure methane-air flame. Figure 10(a) suggests that all major reactions are significantly pacified by the fire suppressant. The rates of the chain-branching reactions (R5, R73 and R168) have been significantly reduced in the flame with CHF_3, leading to lower concentrations of OH in the flame zone. The reduction of the chain branching reaction rate (R73) was also observed in studies with CF_3Br [24]. Similar plot for the premixed flame is shown in Fig. 10(b). A comparison between figures 10(a) and 10(b) suggests that more reactions are affected by the addition of CHF_3 in premixed flame, especially, the once involving hydrocarbons. A detailed analysis of the reaction paths is needed to understand the differences in the role of CHF_3 in premixed and diffusion flames.

Conclusions:

A periodically oscillating, pure-methane-air jet diffusion flame was used to explore the inhibition chemistry of CHF_3. This laminar flame, established with a low-speed fuel and a negligibly small annular air flow, generated large-scale, low-frequency (0-40 Hz), organized buoyancy-induced vortices on the air side of the flame that are similar to those observed in pool fires. Two detailed chemical-kinetics models--1) GRI-V1.2 having 31 species and 346 elementary-reaction steps and 2) GRI-HFC model developed by NIST that has 82 species and 1510 elementary-reaction steps--were incorporated into an axisymmetric CFD model for the investigation of the effects of fluoromethane on methane combustion. The simulations were performed on a Pentium II 300-MHz-based Personal Computer, and the typical execution time using GRI+HFC mechanism was ~200 h per case.

Calculations made for the pure methane-air jet diffusion flame yielded a flame structure very near that measured using Reactive-Mie-Scattering technique. To explore the chemical inhibition resulting from CHF_3 fire suppressant, this suppressant was added to the air flow in such a way that its addition did not change the molar concentration of oxygen. It was observed that the size of the outer vortices and the flicker frequency increase with the addition CHF_3. It was also found that the presence of CHF_3 did not affect the flame temperature significantly. Calculations made with different concentrations of CHF_3 revealed that for concentrations up to 26% the diffusion flame base shifts slowly toward a downstream location

(c)2001 American Institute of Aeronautics & Astronautics or Published with Permission of Author(s) and/or Author(s)' Sponsoring Organization.

and becomes stabilized within 40 mm of the jet exit; for concentrations > 27%, the flame base moves downstream rapidly until it clears the computational domain. Flame structures obtained with 20%, 35% and 50% CHF_3 are compared with those obtained for the pure methane-air jet diffusion flame. Calculations were also made for a stoichiometric premixed flame with different concentrations of CHF_3 added to the fuel jet. It was found that in addition to a considerable decrease in OH radicals in the methane-air-CHF_3 flame, the concentration of H_2 also decreases significantly. Unlike in premixed flames, the peak concentration of the O radical does not change significantly with the addition of small CHF_3 in the air stream of a diffusion flame.

Acknowledgments:

This work was supported, in part, by U. S. Air Force Contract F33615-95-C-2507 and the Air Force Office of Scientific Research. The authors would like to thank Dr. Fumi Takahashi for stimulating discussions.

References:

1. Anderson, S. O., *Fire J.*, Vol. 81, 1987, p. 56 and 118.
2. Gann, R. G. (Ed), Halogenated Fire Suppressants, ACS Symposium Series No. 16, The American Chemical Society, 1975.
3. Biordi, J. C., Lazzara, C. P., and Papp, J. F., *Fourteenth Symposium (International) on Combustion*, The Combustion Instituite, Pittsburgh, 1973, p. 367.
4. Westbrook, C. K., *Combust. Sci. Technol.* Vol. 34, 1983, p. 201.
5. Nyden, M. R., Linteris, G. T., Burgess, D. R. F., Jr., Westmoreland, P. R., Tsang, W., and Zachariah, M., in *Evaluation of Alternative In-Flight and Dry Bays* (Eds. W. L. Grosshandler, R. G. Gann, and W. M. Pitts), National Institute of Standards and Technology, Gaithersburg, MD, 1994, NIST SP 861, p. 467.
6. Burgess, D. R. F., Jr., Zachariah, M. R., Tsang, W., and Westmoreland, P. R., Thermochemical and Chemical Kinetic Data for Fluorinated Hydrocarbons, *Prog. Energy Combust. Sci.*, Vol. 21, 1996, p. 453.
7. Linteris, G. T., and Truett, L., *Combust. Flame*, Vol. 105, 1996, p. 15.
8. Linteris, G. T., Burgess, D. R., Jr., Babushok, V., Zachariah, M., Tsang, W., and Westmoreland, P., *Combust. Flame*, Vol. 113, 1998, p. 164.
9. Ellzey, J. L., Laskey, K. J., and Oran, E. S., (1989), in *Dynamics of Deflagrations and Reactive Systems: Flames*, A. L. Kahl, J. C. Leyer, A. A. Borisov, and W. A. Sirgnano, Eds., Vol. 131, Progress in Astronautics and Aeronautics, American Institute of Aeronautics and Astronautics, Washington, D. C., 1989, p. 179.
10. Yamashita, H., Kushida, G., and Takeno, T., *Proce Roy Soc of London A*, Vol. 431, No. 1882, 1990, p. 301.
11. Davis, R. W., Moore, E. F., Roquemore, W. M., Chen, L.-D., Vilimpoc, V., and Goss, L. P., *Combustion and Flame*, Vol. 83, Nos. 3/4, 1991, pp. 263-270.
12. Katta, V. R., Goss, L. P., and Roquemore, W. M., *AIAA Journal*, Vol. 32, No. 1, 1994, p. 84.
13. Patnaik, G, and Kailasanath, K., *Combustion and Flame*, Vol. 99, No. 10, 1994, p. 247.
14. Kaplan, C. R., Oran, E. S., Kailasanath, K., and Ross, H. D., *26th Symposium (International) on Combustion*, The combustion Institute, Pittsburgh, PA, 1996, p. 1301.
15. Takagi T., and Xu, Z., *Combustion and Flame*, Vol. 96, Nos. 1 and 2, 1994, p. 50.
16. Katta, V. R., and Roquemore, W. M., *Combustion and Flame*, Vol. 100, No. 1, 1995, p. 61.
17. Roquemore W. M., and Katta, V. R., *Journal of Visualization*, in press Jan. 2000.
18. Frenklach, M., Wang, H., Goldenberg, M., Smith, G. P., Golden, D. M., Bowman, C. T., Hanson, R. K., Gardiner, W. C., V. Lissianski, V., Technical Report No. GRI-95/0058, Gas Research Institute, Chicago, IL, November 1, 1995.
19. NIST WWW CKMech (Thermochemistry, Kinetics, Mechanisms) *http://fluid.nist.gov/ckmech.html.*
20. Katta, V. R., Goss, L. P., and Roquemore, W. M., *Int. J. Num. Methods Heat Fluid Flow*, Vol. 4, No. 5, 1994, p. 413.
21. Katta, V. R., and Roquemore W. M., *AIAA J*, Vol. 36, No. 11, 1998, p. 2044.
22. Roquemore, W. M., Chen, L-D., Goss, L. P., and Lynn, W. F., *Turbulent Reactive Flows*, edited by R. Borghi and S. N. B. Murthy, *Vol. 40, Lecture Notes in Engineering*, Springer-Verlag, Berlin, 1989, p. 49.
23. Katta, V. R., Goss, L. P., and Roquemore W. M., *Combustion and Flame*, Vol. 96, No. 1-2, 1994, p. 60.
24. Westbrook, C. K., in *Ninteenth Symposium (International) on Combustion*, The Combustion Institute, Pittsburgh, 1982, p. 127.

(c)2001 American Institute of Aeronautics & Astronautics or Published with Permission of Author(s) and/or Author(s)' Sponsoring Organization.

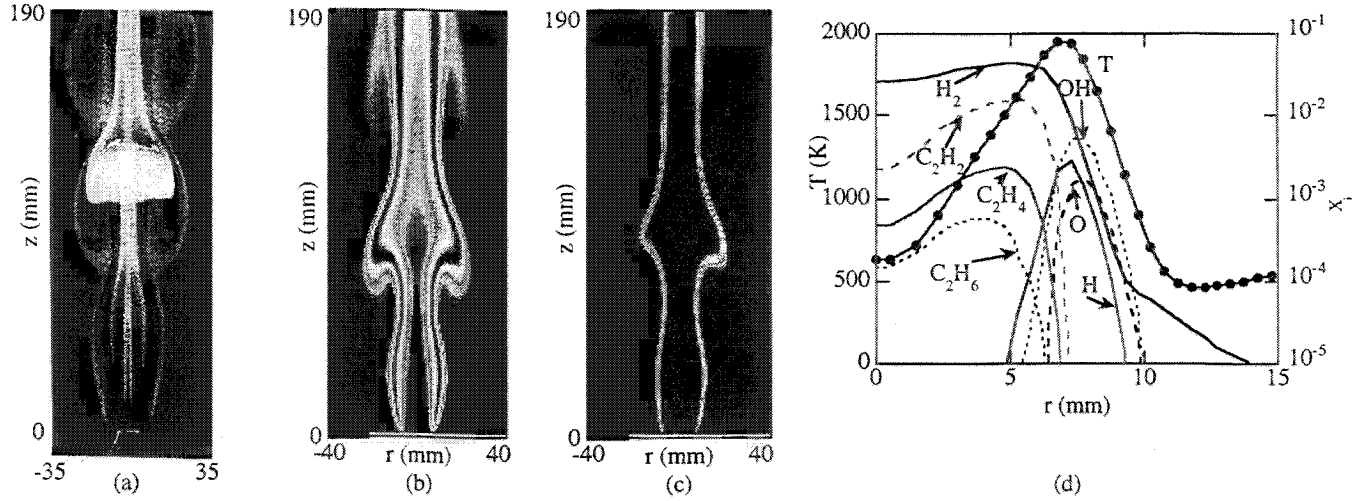

Fig. 1. Vertically mounted methane-air jet diffusion flame. (a) Reactive-Mie-Scattering image of experimental flame, (b) instantaneous temperature field of computed flame, (c) instantaneous CH_3 (left) and OH (right) concentration fields, (d) flame structure at z = 58 mm.

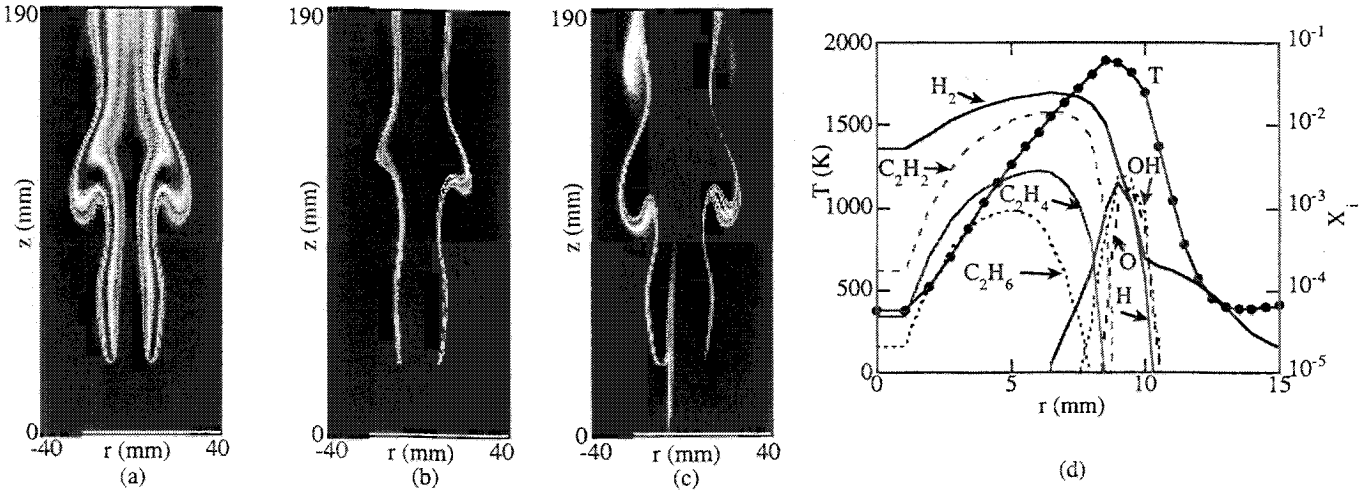

Fig. 2. Computed methane-air-CHF_3 jet diffusion flame for 20% fire suppressant. Instantaneous (a) temperature field, (b) CH_3 (left) and OH (right) concentration fields, (c) CHF_3 (left) and C_2F_6 (right) concentration fields, and (d) flame structure at z = 88 mm.

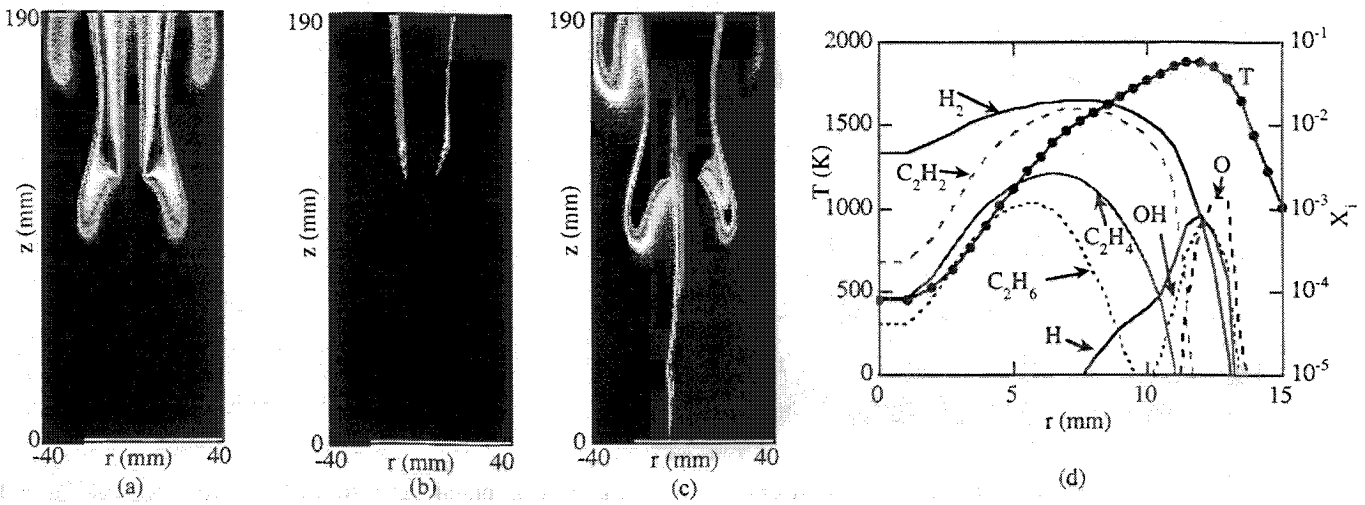

Fig. 3. Computed methane-air-CHF_3 jet diffusion flame for 35 % fire suppressant. Instantaneous (a) temperature field, (b) CH_3 (left) and OH (right) concentration fields, (c) CHF_3 (left) and C_2F_6 (right) concentration fields, and (d) flame structure at z = 145 mm.

(c)2001 American Institute of Aeronautics & Astronautics or Published with Permission of Author(s) and/or Author(s)' Sponsoring Organization.

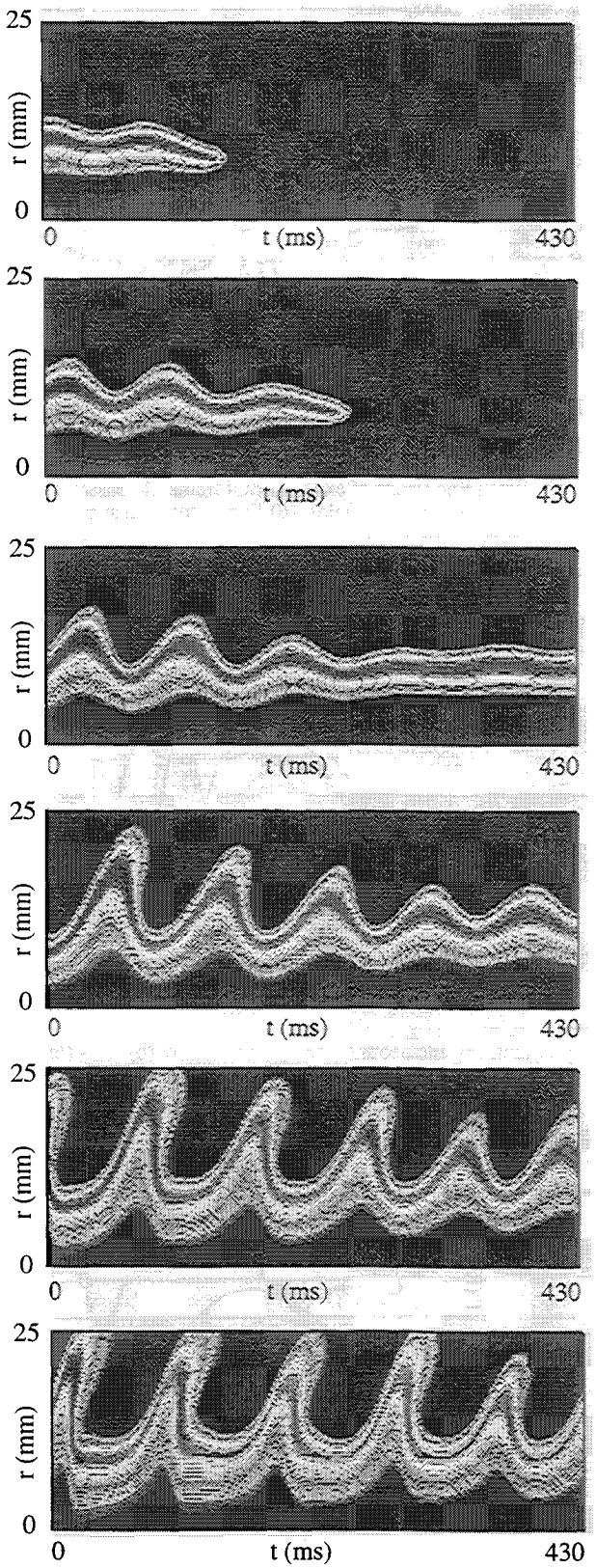

Fig. 4. Variation of temperature with time at different heights in methane-air-CHF_3 jet diffusion flame for 20% fire suppressant. z = (a) 20 mm, (b) 30 mm, (c) 40 mm, (d) 60 mm, (e) 80 mm, (f) 100 mm.

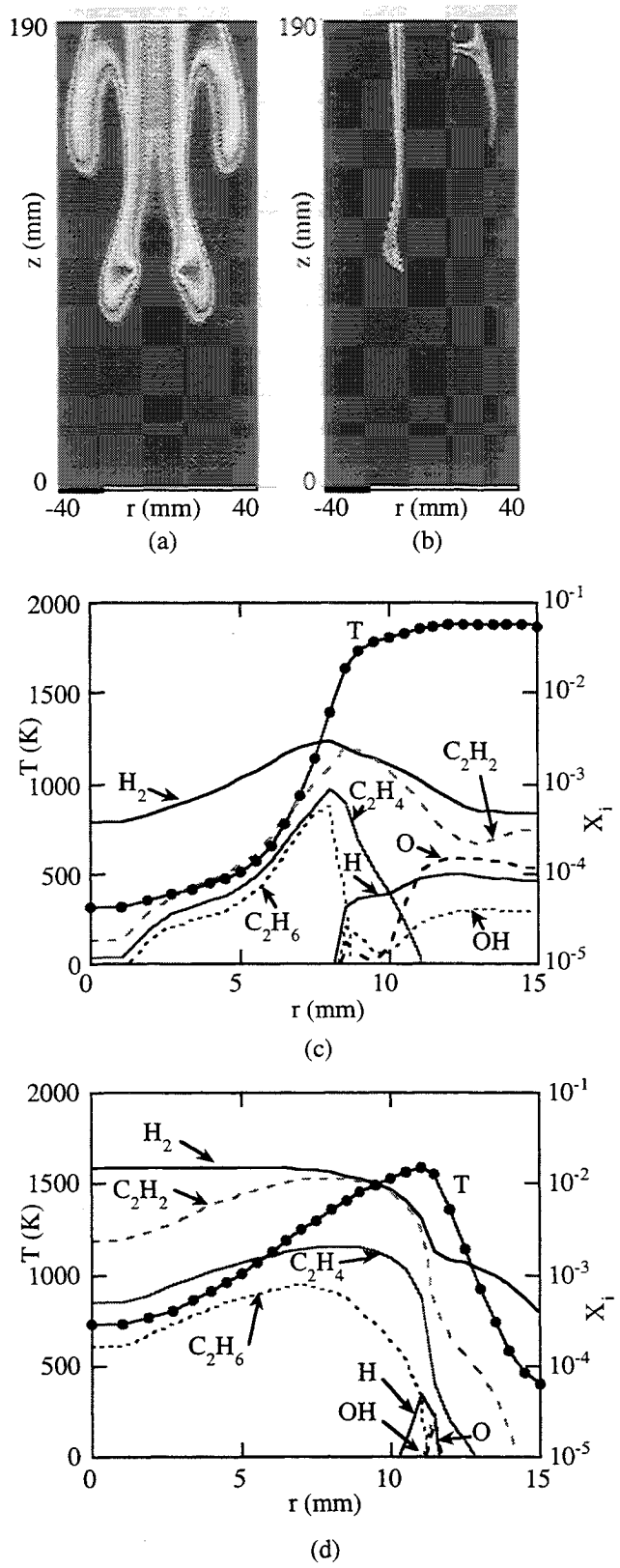

Fig. 5. Computed methane-air-CHF_3 jet diffusion flame for 50% fire suppressant. Instantaneous (a) temperature field, (b) CH_3 (left) and OH (right) concentration fields, and flame structures at (c) z = 88.5 mm, and (d) z = 123 mm.

(c)2001 American Institute of Aeronautics & Astronautics or Published with Permission of Author(s) and/or Author(s)' Sponsoring Organization.

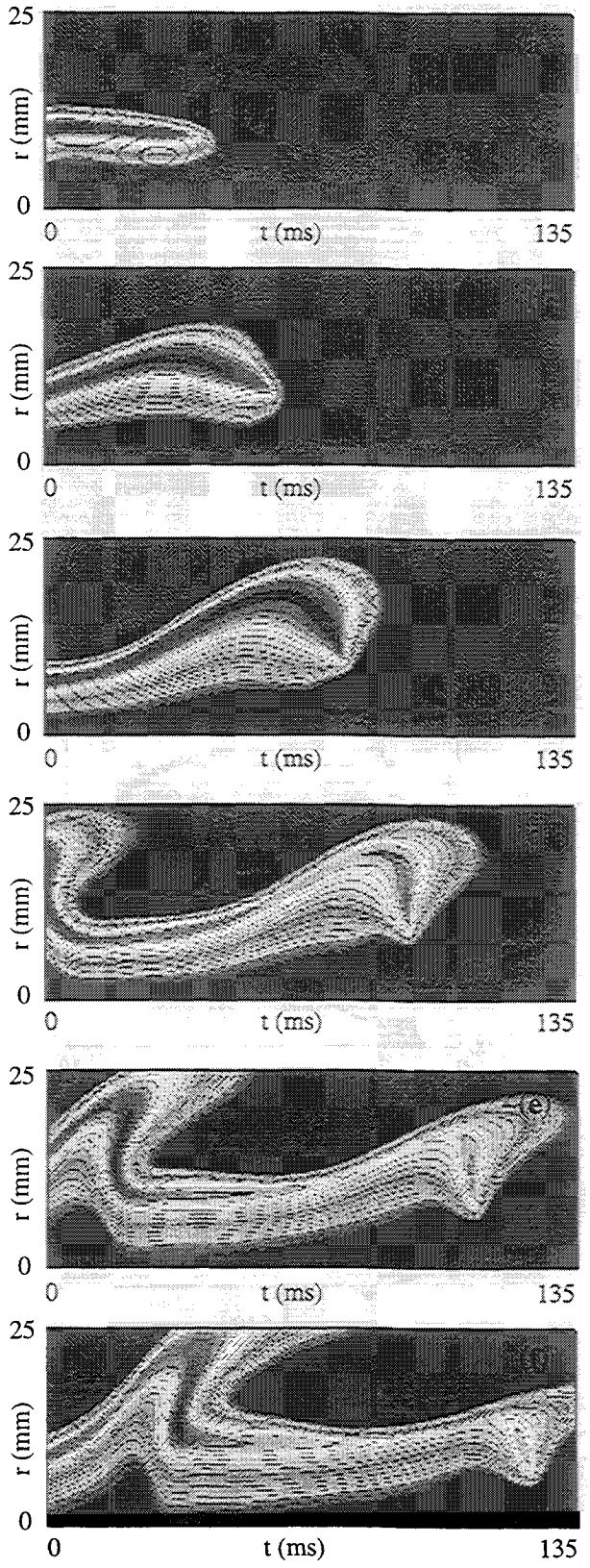

Fig. 6. Variation of temperature with time at different heights in methane-air-CHF_3 jet diffusion flame for 65% fire suppressant. z = (a) 20 mm, (b) 40 mm, (c) 60 mm, (d) 80 mm, (e) 100 mm, (f) 120 mm.

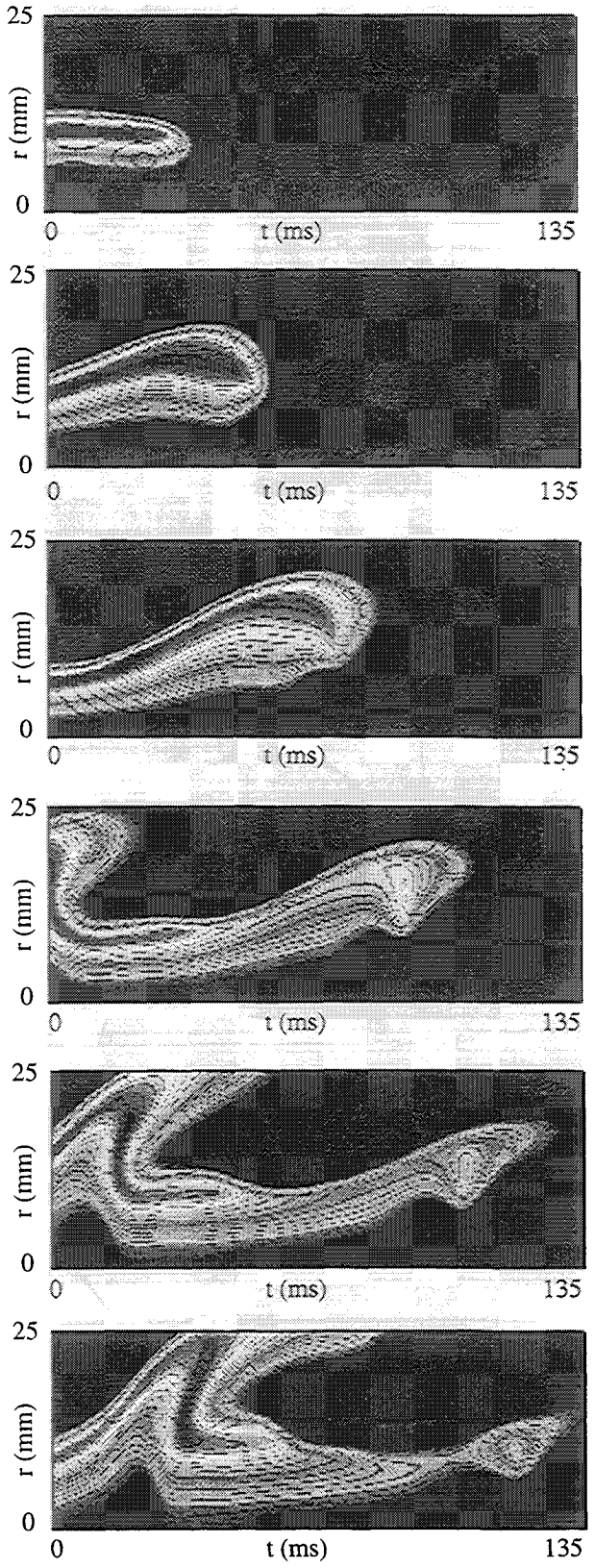

Fig. 7. Variation of temperature with time at different heights in methane-air-CHF_3 jet diffusion flame for 70% fire suppressant. z = (a) 20 mm, (b) 40 mm, (c) 60 mm, (d) 80 mm, (e) 100 mm, (f) 120 mm.

(c)2001 American Institute of Aeronautics & Astronautics or Published with Permission of Author(s) and/or Author(s)' Sponsoring Organization.

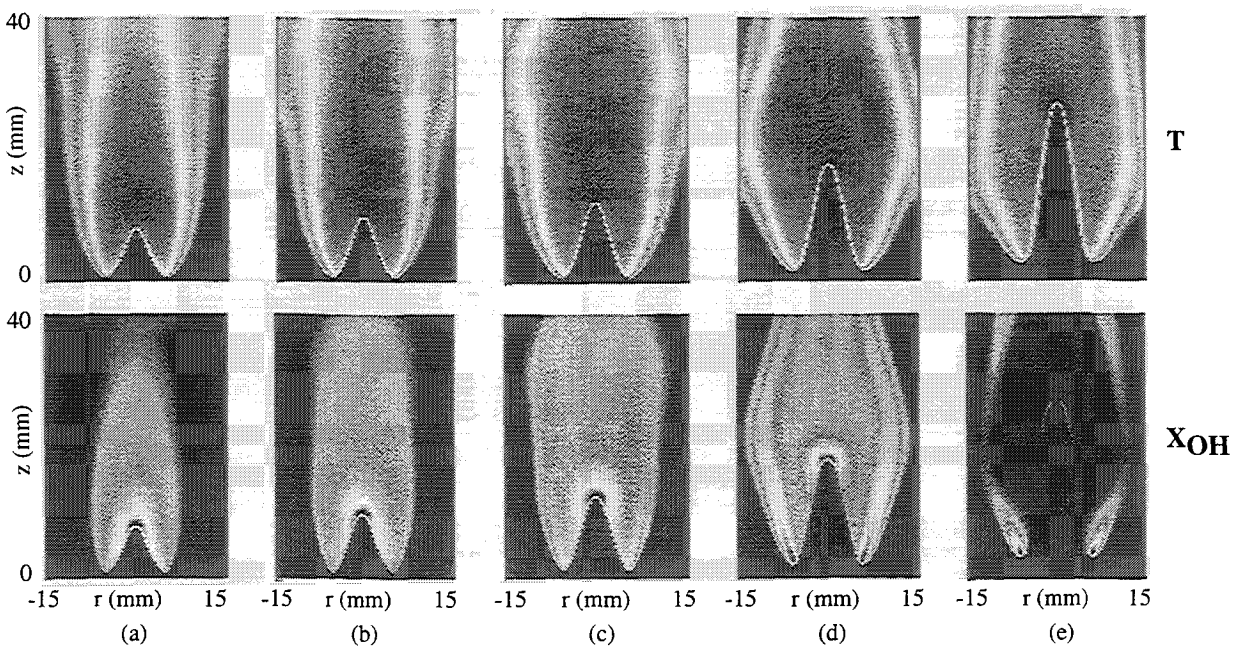

Fig. 8. Computed methane-air-CHF_3 stoichiometric premixed flame for various fire-suppressant concentrations. (a) 0, (b) 5%, (c) 10%, (d) 20% and (e) 30%. Upper images represent temperature fields and lower ones represent OH concentrations.

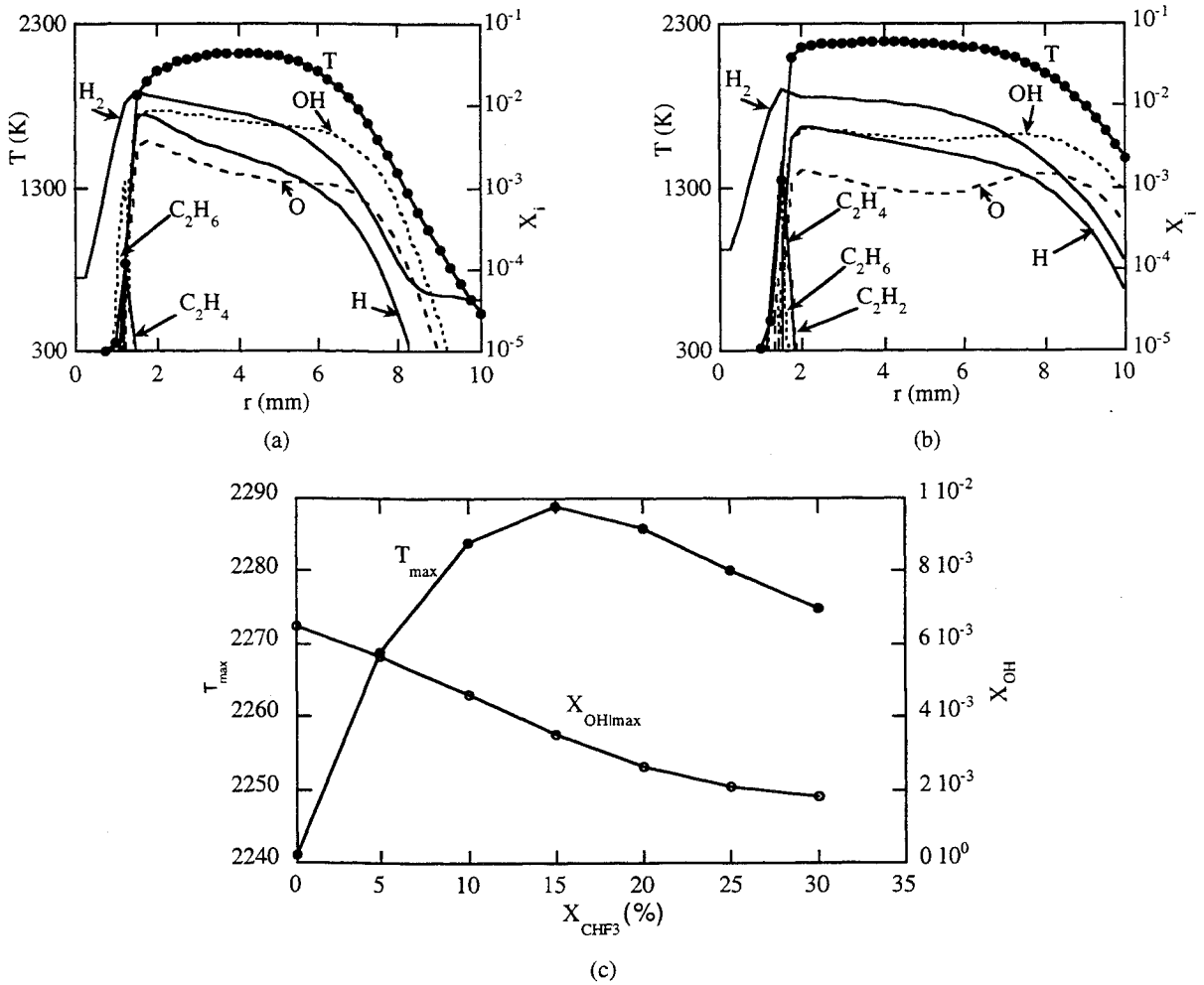

Fig. 9. Radial distributions of temperature and species in (a) methane-air and (b) methane-air-CHF_3 stoichiometric premixed flames. (c) Variation of flame temperature and peak-OH concentration with the addition of fire-suppressing agent.

(c)2001 American Institute of Aeronautics & Astronautics or Published with Permission of Author(s) and/or Author(s)' Sponsoring Organization.

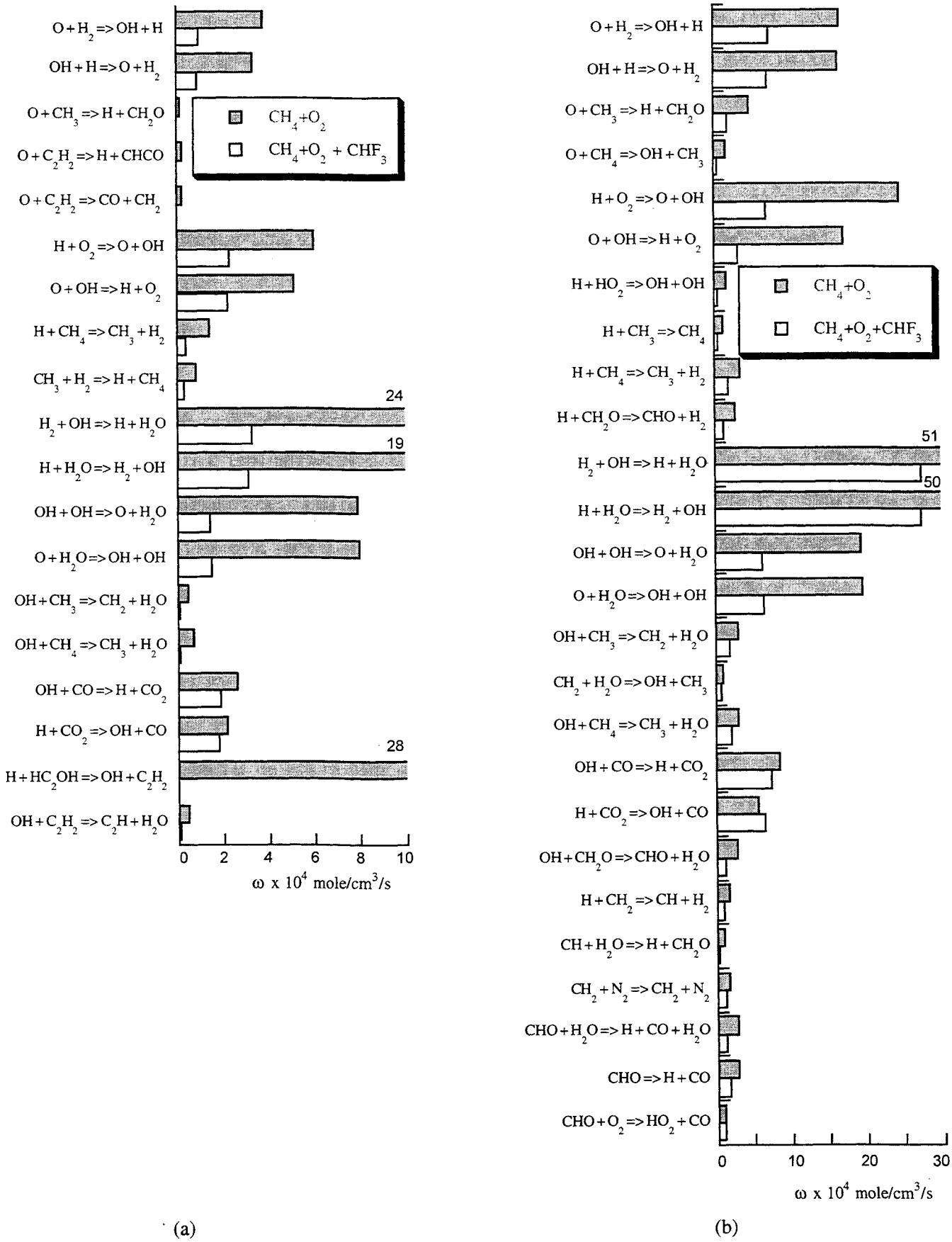

Fig. 10. Major reactions affected by the addition of CHF_3 in (a) a diffusion flame and (b) stoichiometric premixed flame. Bar lengths correspond to specific reaction rates.

Combust. Sci. and Tech., 2000, Vol. 157, pp. 185-211
Reprints available directly from the publisher
Photocopying permitted by license only

© 2000 OPA (Overseas Publishers Association) N.V.
Published by license under the
Gordon and Breach Science Publishers imprint.
Printed in Malaysia

Effects of C_2-Chemistry on the Structure of Partially Premixed Methane-Air Flames

ZHUANG SHU, VISWANATH R. KATTA*, ISHWAR K. PURI and SURESH K. AGGARWAL†

Department of Mechanical Engineering, University of Illinois at Chicago M/C 251, 842 W. Taylor St., Chicago, IL 60607–7022

(Received March 03, 1999; In final form January 31, 2000)

Partially-premixed flames (PPF) can contain multiple reaction zones, e.g., one or two with a premixed-like structure and one being a nonpremixed reaction zone. An intrinsic feature of partially premixed flames pertains to the synergistic interactions between these two types of reaction zones that are characterized by heat and mass transfer between them. Since these interactions are strongly dependent on the distribution of the radical and stable species' concentrations, an accurate representation of the flame chemistry involving these species is critical for simulating their behavior. The role of C_2-chemistry in determining the structure of partially premixed methane-air flames is investigated herein by employing two relatively detailed chemical mechanisms. The first involves only C_1-containing species and consists of 52 reactions involving 17 species, while the second mechanism represents both C_1- and C_2-chemistry and consists of 81 reactions that involve 24 species. A planar two-dimensional partially premixed flame established on a rectangular slot burner is simulated. The simulation is based on the numerical solution of the time-dependent conservation equations for mass continuity, momentum, species, and energy. The computations are validated by comparison with the experimentally-obtained chemiluminescent emission from excited-C_2^* free radical species, as well as with velocity measurements using particle image velocimetry. A numerical study is then conducted to examine the applicability of C_1 and C_2 mechanisms for predicting the structure of partially premixed flames for different levels of partial premixing and reactant velocity. Results indicate that both the mechanisms reproduce the global structure of PPF over a wide range of reactant velocity and stoichiometry. Since the C_1 mechanism is known to be inadequate for fuel-rich premixed flames, its relatively good performance can be attributed to the interactions between the two reaction zones that characterize the PPF structure. There are, however, important quantitative differences between the predictions of the two mechanisms. The C_2 mechanism is overall superior compared to the C_1 mechanism in that its predictions are in closer agreement with our experimental results. The rich premixed reaction zone height obtained with the C_2 mechanism is more sensitive to variations in the equivalence ratio as compared with predictions that are obtained using the C_1-mechanism. In addition, for high levels of partial premixing, the methane consumption in the inner reaction zone is significantly increased when the C_2-mechanism is employed, compared to when the C_1-mechanism is used. Con-

* Innovative Scientific Solutions, Inc. Dayton, OH 45430.
† Corresponding author. email: ska@uic.edu

sequently, the amount of methane that leaks from the rich premixed to nonpremixed reaction zone is significantly lower when the C_2-mechanism is used. The interactions between the inner and outer reaction zones are stronger when the C_2-mechanism is employed. Finally, the maximum temperature predicted by the C_2-mechanism is slightly lower as compared to that obtained using the C_1-chemistry alone. These differences are attributed to the presence of the C_2-chain in the 81-step mechanism, which strongly affects the inner premixed reaction zone.

INTRODUCTION

Partially premixed flames (PPF) occur in many practical systems that include Bunsen burners, industrial furnaces, and gas-fired domestic burners. In ultra-lean premixed combustors, a promising new concept to significantly reduce pollutant emissions, partially premixed combustion is an important phenomenon due to the inherent unmixedness of fuel and oxidizer. Partial premixing is an important process in lifted flames since the reactants can mix prior to ignition. Partial premixing also occurs in turbulent combustion and in spray combustion systems. The partial premixing of laminar diffusion flamelets has been considered essential for the modeling and prediction of turbulent flame structure. Consequently, a fundamental understanding of the structure of partially premixed flames is important from both practical and scientific considerations.

Previous investigations of partially premixed flames have employed both counterflow (Yamaoka and Tsuji 1978; Hamins et al. 1985; Seshadri et al. 1985; Law et al. 1989; Li et al. 1997) and coflow (Gore and Zhan 1996; Shu et al. 1997a and 1997b; Shu et al. 1998) configurations. A counterflow partially premixed flame can be established by flowing two opposing jets, one containing a rich fuel-air mixture and the other containing air. Similarly, a partially premixed flame can be stabilized in a coflow configuration, with the inner flow containing a rich fuel-air mixture and the outer flow containing air. A general finding in these studies is that for certain range of equivalence ratios, partially premixed flames are characterized by the existence of two distinct reaction zones; an inner rich premixed zone which is synergistically coupled to an outer nonpremixed zone. Since an important part of these interactions involves the exchange of key radical species, it is essential that a detailed reaction mechanism be employed for an accurate prediction of the double-flame structure. Li and Williams (1998) examined the double-flame structure in a counterflow configuration by employing a detailed CH_4-air chemistry involving C_1-, C_2-, and C_3-species. Shu et al. (1997a, 1997b, 1998) employed a 52-step reaction mechanism, involving C_1-species, to simulate steady two-dimensional partially-premixed methane-air flames.

The present study extends our previous analysis to include an 81-step mechanism, which contains both C_1- and C_2-species, for the simulation of two-dimen-

sional PPFs stabilized on a Wolfhard-Parker slot burner. The major objective is to examine the applicability of C_1- and C_2-mechanisms for predicting the structure of PPFs for different levels of partial premixing and reactant velocity. Since the C_2-chemistry provides an important pathway for fuel consumption through the $CH_3 + CH_3 \Leftrightarrow C_2H_6$ reaction, it is known to play a significant role in predicting the characteristics of fuel-rich premixed combustion; for example, the laminar premixed flame speed as a function of equivalence ratio for rich methane-air mixtures. It is, therefore, important to examine as to why the C_1-mechanism can adequately reproduce the measured structure of PPFs, while it fails to accurately predict the laminar flame speed under fuel-rich conditions. Another consideration for including the C_2-mechanism is that C_2-species represent a major source of CH_2 and CH radicals that are largely responsible for the "prompt" mechanism of NO_x production. The C_2-containing species also play a major role in soot formation.

THE COMPUTATIONAL MODEL

The simulation considers a planar 2-D partially premixed flame established on a rectangular Wolfhard-Parker slot burner that is schematically depicted in Fig. 1(a), and described elsewhere (Shu et al. 1998). A fuel-rich mixture is introduced from the inner slot, and air from either side of it. Identical two-dimensional flames are established on either side of the centerline. Numerical simulations are conducted on one side of the symmetry plane (plane 1). The other three planes bounding the domain are the free surface (plane 2), the inflow boundary (plane 3), and the outflow boundary (plane 4). Figure 1(b) contains a schematic illustration of the computational domain.

The flame simulation is based on a numerical solution of the time-dependent governing equations for a two-dimensional reacting flow. The governing equations and the numerical model have been previously described (Shu et al. 1997a and 1998). We have also previously presented a detailed experimental-computational study of the double-flame structure for different velocities and levels of partial premixing (Shu et al. 1998). The focus of this investigation is to examine the effects of C_2-chemistry on the double-flame structure of partially premixed methane-air flames. Two detailed mechanisms for CH_4-air chemistry, as compiled by Peters (1993), are employed. The first mechanism involves C_1-chemistry alone, comprising of 52 reactions that involve 17 species, while the latter mechanism represents both C_1- and C_2-chemistry and consists of 81 reactions and 24 species.

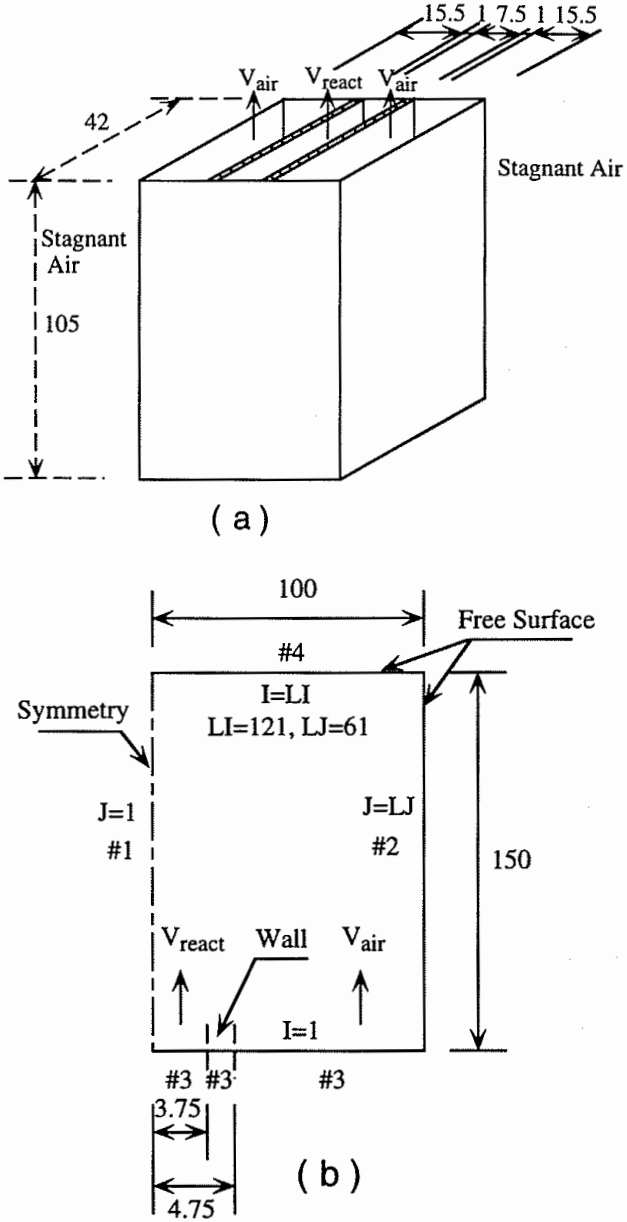

FIGURE 1 Schematic diagram of the 100 mm × 150 mm (or 61 × 121 gridline) computational domain. The symbols I and J, respectively, represent the axial and transverse gridlines. The boundary conditions are also specified. The simulated burner consists of an inner 7.5 mm slot with two 15.5 mm outer slots on either side of it. The wall thickness separating the slots is 1 mm

The thermodynamic and transport properties, such as the viscosity, thermal conductivity, and binary diffusion coefficients that are required in the computations are considered to be temperature- and species-dependent. The methodology to calculate these properties has been described in previous publications (Shu et al. 1997a; Katta et al. 1994). The enthalpy h and specific heat for each species are calculated using the polynomial curve fits complied by Kee et al. (1983). An implicit algorithm is employed to solve the time-dependent governing equations, which are integrated by using a "finite control volume" approach with a staggered, nonuniform grid system. Further details about the numerical procedure and the treatment of boundary conditions are discussed by Katta et al. (1994).

RESULTS

Figure 2 contains a comparison between the experimental and predicted (using the C_1-mechanism*) images of partially premixed flames for three different cases. The experimental images are represented in terms of the excited C_2^*-chemiluminescence signal, while the computed flames are depicted in terms of the heat release rate contours. The C_2^*-chemiluminescence images (Shu et al. 1998) were obtained using a 513×480 pixel intensified and gated solid-state camera (ITT F4577). As discussed by Shu et al. (1998), the C_2^*-emission signal has shown to be a marker of the heat release rate in partially premixed flames. Both the C_2^*-signal and the predicted heat release clearly depict two reaction zones, one an inner premixed reaction zone and the other an outer nonpremixed reaction zone. As we have previously discussed (Shu et al. 1997a and 1997 b; Shu et al. 1998). the two distinguishing features of a partially premixed flame are the existence of spatially-separated reaction zones, and the synergistic interactions between these regions. For the three cases depicted in Fig. 2, the simulation and experiment show good agreement with respect to the spatial location of the reaction zones, implying that the C_1-mechanism is capable of reproducing the PPF structure that is observed in laboratory experiments. The region near the apex of the nonpremixed reaction zone has a weaker chemiluminescent intensity than the predictions indicate. This is due to the fact that C_2^* radicals are relatively weaker in this region

Figure 3 compares reaction rate contours of the major fuel decomposition reactions, namely (a) $CH_4 + H \Leftrightarrow CH_3 + H_2$, (b) $CH_4 + OH \Leftrightarrow CH_3 + H_2O$, and (c) the net fuel consumption rate predicted by two mechanisms. The flame condi-

* In the following discussion, the term C_2-mechanism refers to the 81-step mechanism that represents both the C_1- and C_2-chemistry, while C_1-mechanism refers to the 52-step mechanism that only involves the C_1-chemistry.

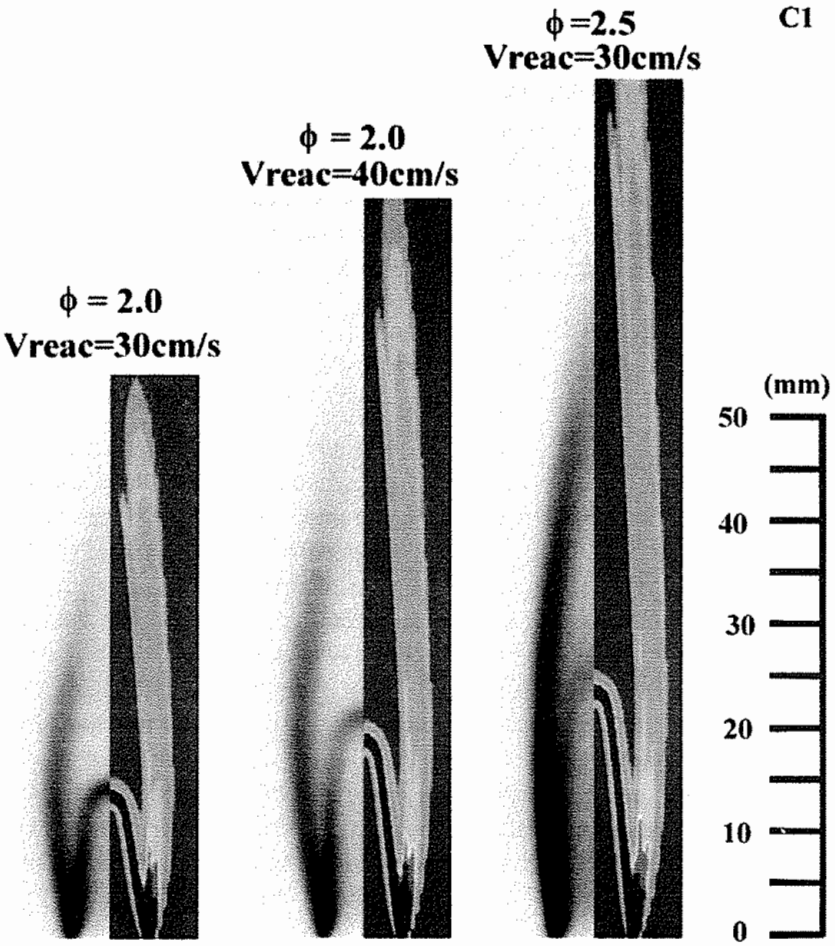

FIGURE 2 Comparison of the predicted heat release rates (obtained by using the C_1-mechanism) with the experimentally-obtained C_2-chemiluminescence images of partially premixed flames for three different cases: (a) $\phi = 2.0$, $V_{react} = 30$ cm s^{-1}; (b) $\phi = 2.0$, $V_{react} = 40$ cm s^{-1}; and (c) $\phi = 2.5$, $V_{react} = 30$ cm s^{-1}. The outer slot velocity in all cases $V_{air} = 30$ cm s^{-1} (See Color Plate XI at the back of this issue)

tions correspond to a mixture equivalence ratio $\phi = 2.5$ in the inner slot, and reactant and air velocities, V_{reac} and V_{air} both equal to 30 cm s^{-1}. The reaction rate contours clearly indicate that for C_2-mechanism, methane is completely consumed in the inner premixed region with very little CH_4 escaping into the outer nonpremixed region. In contrast, when the C_1-mechanism is employed, methane

is only partly consumed in the inner premixed reaction zone, with the remaining methane being consumed in the outer nonpremixed reaction region. Further evidence of this is provided by the methane concentration contours depicted in Fig. 4. The higher fuel consumption in the inner reaction zone for the C_2-mechanism is attributable to the C_2-chemistry, which provides an additional pathway for methyl consumption through the reaction $CH_3 + CH_3 \Leftrightarrow C_2H_6$. Further discussion on this aspect is provided in a later section.

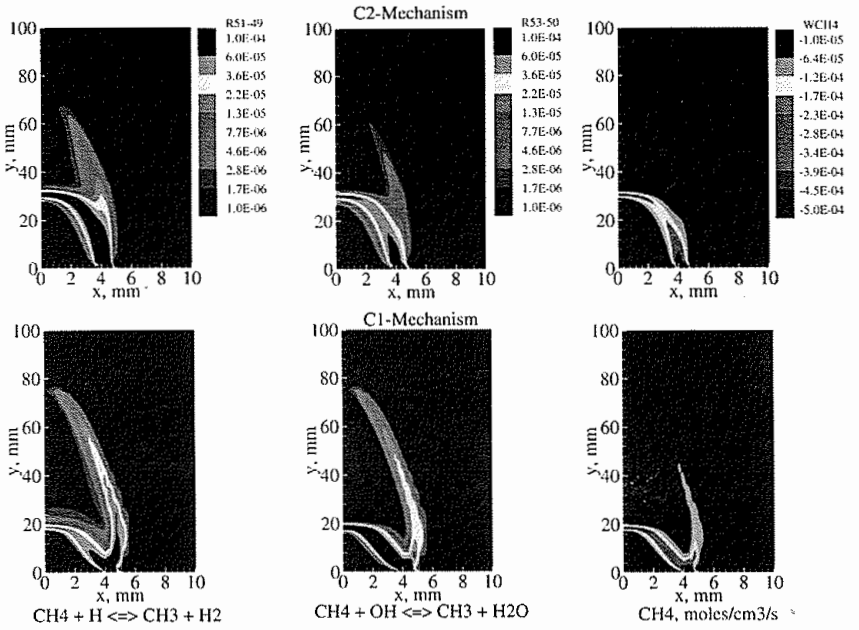

FIGURE 3 Comparison of the reaction-rate contours of major fuel decomposition reactions: (a) $CH_4 + H \Leftrightarrow CH_3 + H_2$, (b) $CH_4 + OH \Leftrightarrow CH_3 + H_2O$, and (c) the net consumption rate of methane as predicted by the C_1- and C_2-mechanisms. $\phi = 2.5$, $V_{react} = V_{air} = 30$ cm s^{-1} (See Color Plate XII at the back of this issue)

The reaction rate contours presented in Fig. 3 also indicate that the two mechanisms differ with respect to the major methane consumption reaction in the inner premixed reaction zone. For the C_2-mechanism, methane consumption by H atoms dominates that by OH radicals, while for the C_1-mechanism, the corresponding reaction with hydroxyl radicals is more important reaction. This can be attributed to the higher concentration of H atoms for the C_2-mechanism compared with that predicted by the C_1-mechanism. The concentrations of H and OH predicted by the two mechanisms are presented in Fig. 4. Another factor contributing to the difference in the fuel-consumption chemistry is that the interactions

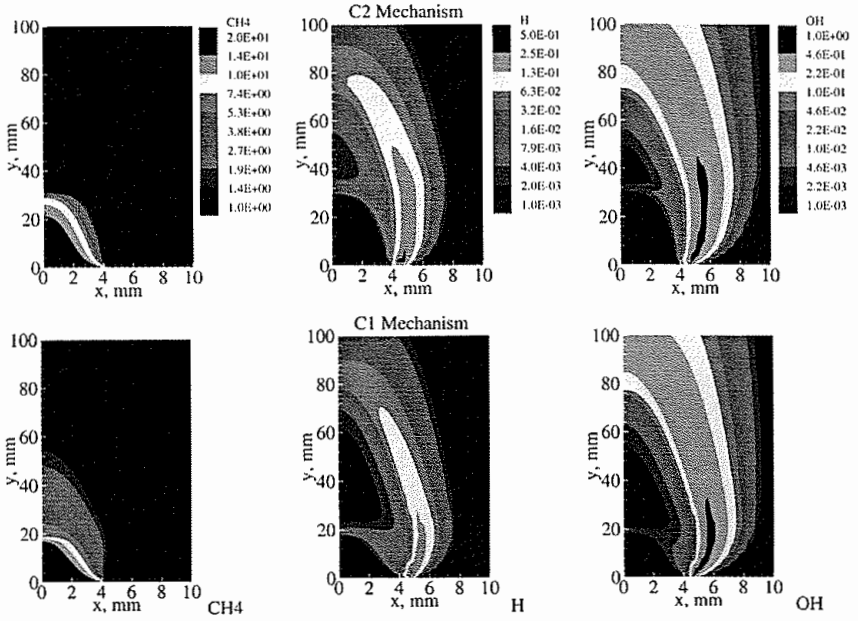

FIGURE 4 Contours of the CH_4, H-atom, and OH concentrations predicted by the two mechanisms for the case discussed in context of Fig. 3 (See Color Plate XIII at the back of this issue)

between the inner and outer reaction zones are stronger when the C_2-mechanism is employed.

The heat release rate and CHO-concentration contours for the conditions corresponding to Fig. 3 are presented in Fig. 5. The heat release rate contours clearly indicate that interactions between the inner and outer reaction zones are stronger when the C_2-mechanism is used than that with the C_1-mechanism. (This is represented at the base of the rich premixed and outer nonpremixed reaction zones through the existence of a broadened and connected heat release zone.) These synergistic interactions involve the exchange of energy and species (which include radical species such as H and OH, and stable intermediate species such as $H_2$and CO) between the two reaction zones. The degree of interaction can be illustrated by considering the separation distance between the two reaction zones. Use of the C_2-mechanism results in a smaller separation distance compared to that obtained after employing the C_1-mechanism. The inner and outer reaction zones heights can be based on the heat release rate contours. The premixed zone height can also be deduced from the CHO concentration contours that are presented in Fig. 5, and from the methane-consumption-rate contours contained in Fig. 3. These contours indicate that the premixed zone height predicted by the

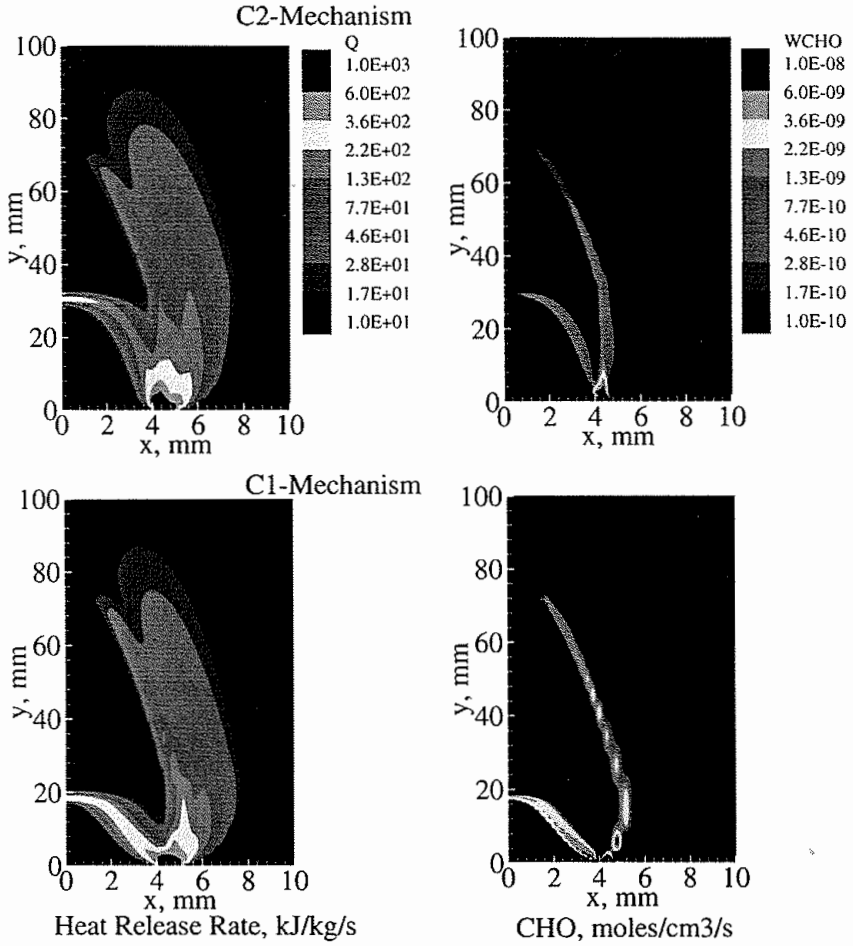

FIGURE 5 Contours of heat release rate and CHO concentration predicted by the two mechanisms for the case discussed in context of Fig. 3 (See Color Plate XIV at the back of this issue)

C_2-mechanism is higher than that simulated with the C_1-mechanism. However, the (outer) nonpremixed zone heights are essentially similar when either mechanism is used, although the outer zone is somewhat broader upon application of the C_2-mechanism. Additional discussion on the effects of C_2-chemistry on the inner and outer zone heights is provided later.

Another important observation pertains to the correlation between the CHO concentration and the heat release rate contours. As discussed by Najm et al.

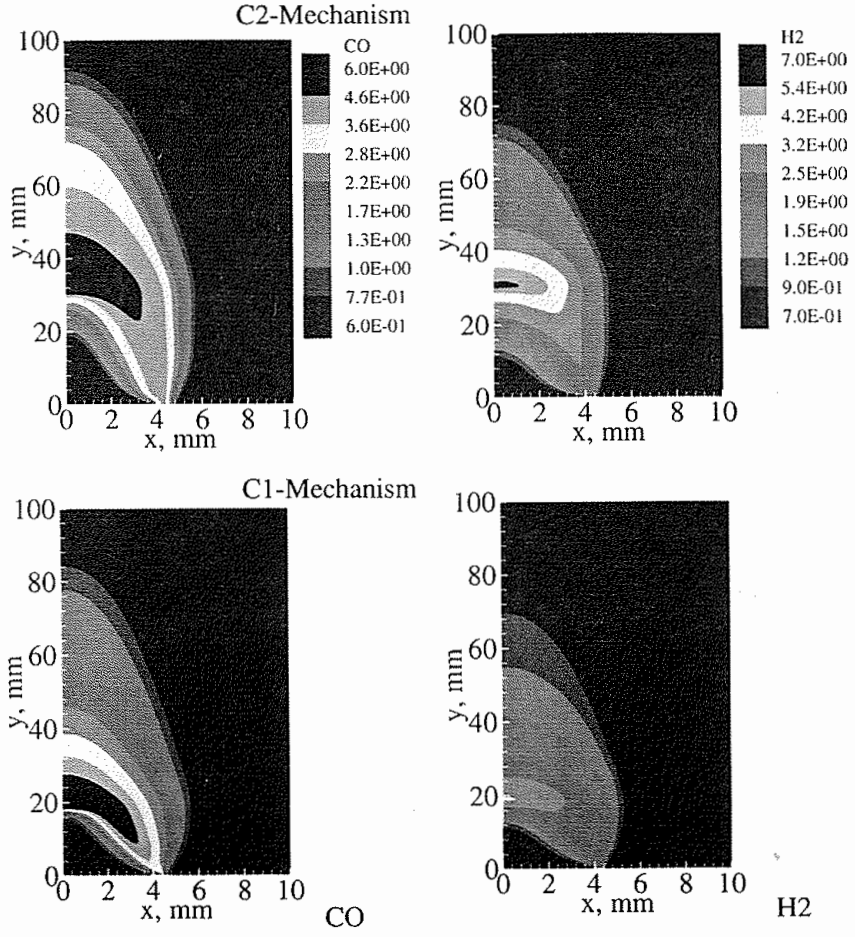

FIGURE 6 Contours of the CO and H_2 mole fractions predicted by the two mechanisms for the case discussed in context of Fig. 3 (See Color Plate XV at the back of this issue)

(1998), CHO is an excellent marker of heat release rate in premixed methane-air flames. In the present case, which focuses on partially premixed flames, CHO is found to be an excellent marker of heat release in the inner premixed region. However, it seems to be a relatively poorer indicator of heat release in the outer nonpremixed reaction zone, since its concentration is negligible in that region where the dominant heat release reactions involve the HO_2 chemistry (Lee et al. 1996). It is also interesting to note that the CHO concentration in the outer region is significantly higher when the C_1-mechanism is used due to the consumption of the "leaked" methane there.

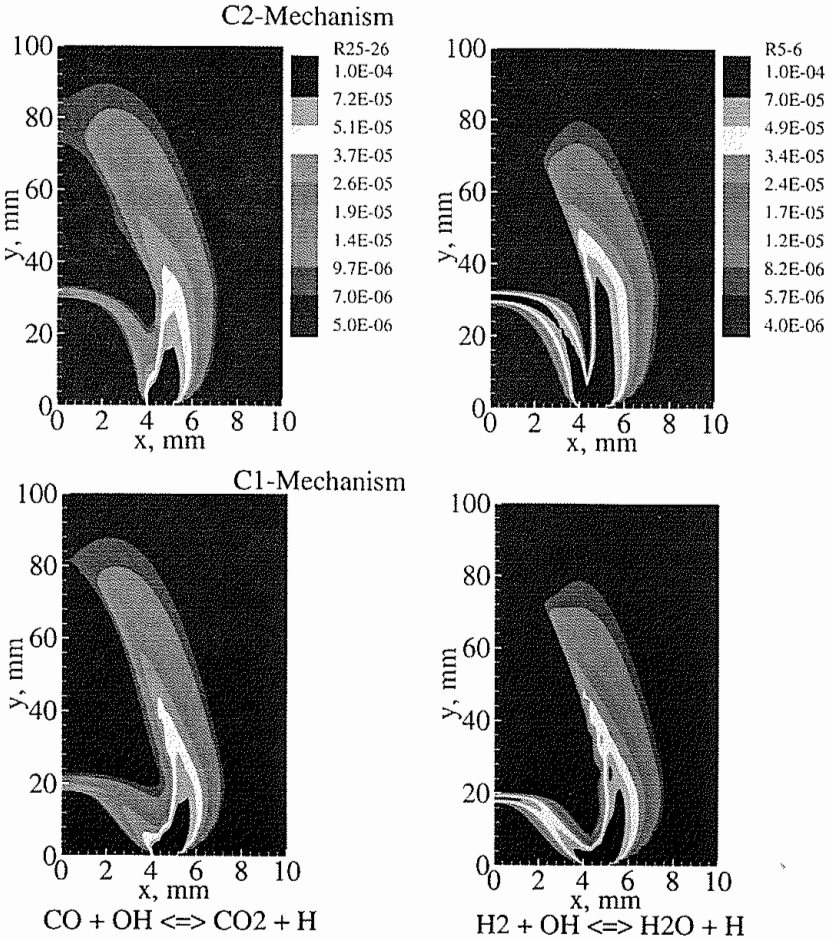

FIGURE 7 Comparison of the rate contours of the reactions CO + OH ⇔ CO_2 + H and H_2 + OH ⇔ H_2O + H predicted by the two mechanisms for the case discussed in context of Fig. 3 (See Color Plate XVI at the back of this issue)

Figure 6 contains contours of the CO and H_2 concentrations predicted by the two mechanisms for the flame discussed in the context of Fig. 3. Note that CO and H_2 are the "product" species that are formed in the inner premixed reaction zone and are also the reactant or "fuel" species that are provided to the outer non-premixed reaction zone. The C_2-mechanism predicts significantly higher concentrations of CO and H_2 compared with the C_1-mechanism. This is attributable to the fact that the amount of methane consumed in the inner reaction region is sig-

nificantly higher due to the C_2-chemistry. The reaction rate contours of the CO- and H_2-oxidation reactions, $CO + OH \Leftrightarrow CO_2 + H$ and $H_2 + OH \Leftrightarrow H_2O + H$, are presented in Fig. 7. For both mechanisms, the CO- and H_2-oxidation contours through these reactions strongly correlate with the heat release rate contours contained in Fig. 5. While the first reaction appears to be similar for both mechanisms, the second reaction is relatively stronger in both the inner and outer reaction zones when the C_2-mechanism is used. This can be attributed to the significantly higher concentration of H_2 in the inner flame and that of OH in the outer flame for this mechanism. The stronger interactions between the inner and outer flames for C_2-mechanism is also clearly illustrated in these plots.

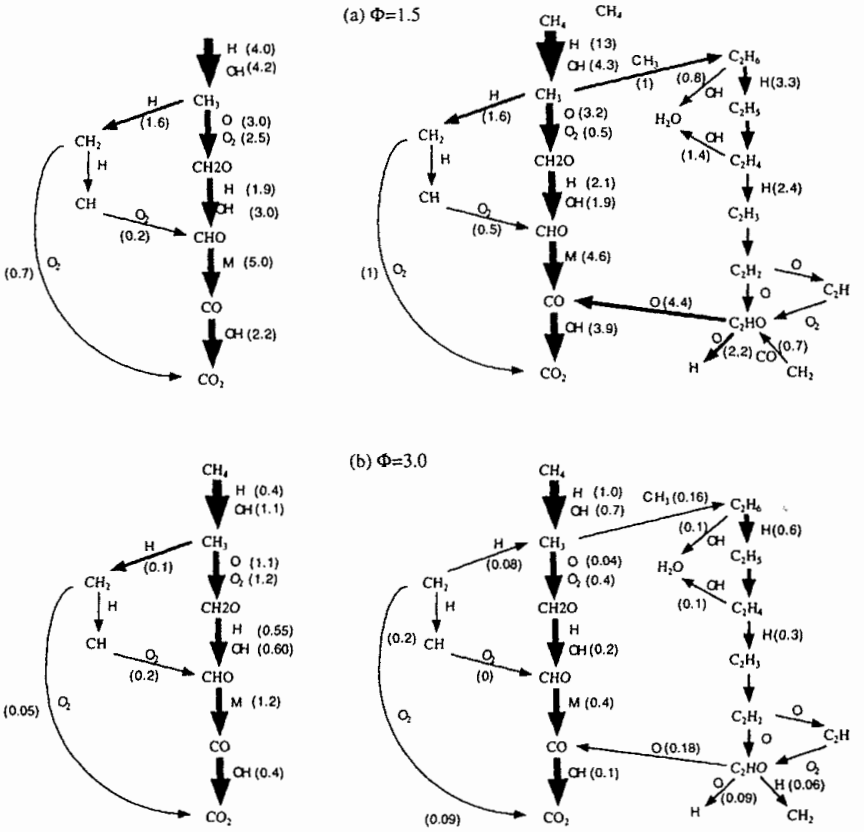

FIGURE 8 Schematic illustration of the dominant reaction pathways involved with the two mechanisms for a flame established with an inner flow equivalence ratios $\phi = 3.0$, and with $V_{react} = V_{air} = 30$ cm s^{-1}. The numbers in parentheses indicate the relative magnitude of the reaction rate. The thickness of the arrows is also used to indicate the relative magnitudes of the species consumption rates

Based on the rate distributions of the various reactions, the important pathways leading to the formation of CO and H_2 in the inner reaction zone can be described as follows. (1) Methane is converted to methyl (CH_3) radicals mainly through its reactions with H and OH. As indicated in Fig. 3, these reactions are relatively stronger in case of the C_2-mechanism than when the C_1-mechanism is used, due to the faster consumption of methyl radicals through the $CH_3 + CH_3 \Leftrightarrow C_2H_6$ channel. (2) The conversion of CH_3 to CO follows three separate routes in C_2-mechanism, and two separate paths in the C_1-mechanism. These pathways are schematically illustrated in Fig. 8. The first two paths are common to both mechanisms, while the third route involving C_2-species is obviously relevant in the C_2-mechanism alone. The first pathway involves the decomposition of CH_3 into CH_2, which is converted to CH, that then reacts with O_2 to form CHO which is subsequently converted to CO (the dominant reaction in the conversion of CHO to CO is $CHO + M \Leftrightarrow CO + H + M$). The second route dominates the first path, and involves the oxidation of CH_3 with O and O_2 to form CH_2O, which then reacts with H and OH to form CHO, that forms CO in the manner described above. (3) The third route involves C_2-containing species, and begins with the formation of C_2H_6. The ethane forms C_2H_5, mainly through the reaction $C_2H_6 + H \Leftrightarrow C_2H_5 + H_2$, and the C_2H_5 radicals decompose into C_2H_4, that then forms C_2H_3 (predominantly through the reaction $C_2H_4 + H \Leftrightarrow C_2H_3 + H_2$). The C_2H_3 radicals decompose to form C_2H_2, which produces C_2HO and, subsequently, CO. The chemical paths are schematically illustrated in Fig. 8.

In Fig. 9, we present reaction rate profiles of the two major chain-branching reactions, (a) $H + O_2 \Leftrightarrow OH + O$ and (b) $H_2 + O \Leftrightarrow OH + H$, and of the reaction $O_2 + H + M \Leftrightarrow HO_2 + M$. Clearly, these three reactions are important in both the inner and outer reaction zones. While the reaction rate distributions are qualitatively similar for the two mechanisms, the first two chain branching reactions are stronger in the inner zone when the C_2-mechanism is used. This is partly responsible for the relatively complete consumption of methane in the inner flame in case of the C_2-mechanism. In addition, the rate contours clearly indicate stronger interactions between the two reaction zones when the C_2-mechanism is employed compared to those obtained with the C_1-mechanism.

Figure 10 contains a comparison between the measured C_2^*-chemiluminescence and the predicted heat release rate profiles (obtained both by using the C_1- and C_2-mechanisms) for various partially premixed flames. While the predicted and measured reaction zone topography shows excellent qualitative agreement over a wide range of equivalence ratios, there are quantitative differences with respect to the spatial location of the inner premixed reaction zone. At higher levels of air addition to the inner flow (i.e., $\phi \leq 1.5$), the inner reaction zone height predicted by both the C_1- and C_2-mechanisms is larger than that obtained from

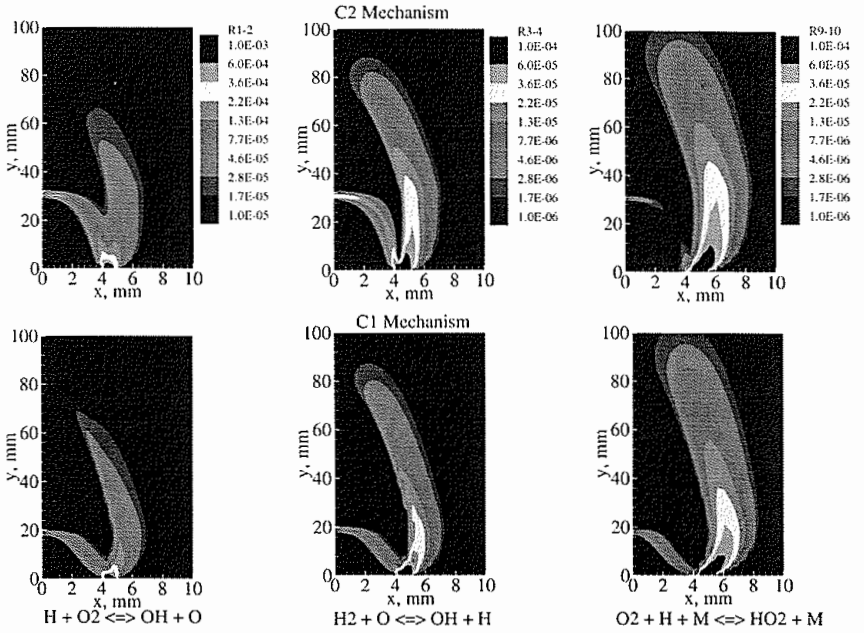

FIGURE 9 Comparison of contours of the reactions (a) $H + O_2 \Leftrightarrow OH + O$, (b) $H_2 + O \Leftrightarrow OH + H$, and (c) $O_2 + H + M \Leftrightarrow HO_2 + M$ predicted by the two mechanisms for the case discussed in context of Fig. 3 (See Color Plate XVII at the back of this issue)

measurements. As ϕ is increased, the inner reaction zone heights predicted by the C_1-mechanism exhibits a relatively weaker dependence on variations in the equivalence ratio compared with those obtained using the C_2-mechanism or with the measured results. As discussed in the following section, this can be attributed to the absence of C_2-chemistry in the C_1-mechanism. As a consequence, at low levels of air premixing ($\phi \geq 3.0$), predictions using the C_1-mechanism yield lower inner reaction zone heights compared with measurements or those obtained using the C_2-mechanism.

Figure 11 shows the inner and outer reaction zone topographies in terms of the heat release rate contours predicted by both mechanisms for different levels of partial premixing. The global partially premixed flame structure regarding the existence of two reaction zones is predicted in a qualitatively similar manner by the two mechanisms. With both mechanisms the heights of the two reaction zones increase as the level of air premixing decreases (or as ϕ increases), since the chemical time required for the global chemistry to occur increases with larger values of ϕ. In addition, the inner reaction zone is observed to play a more impor-

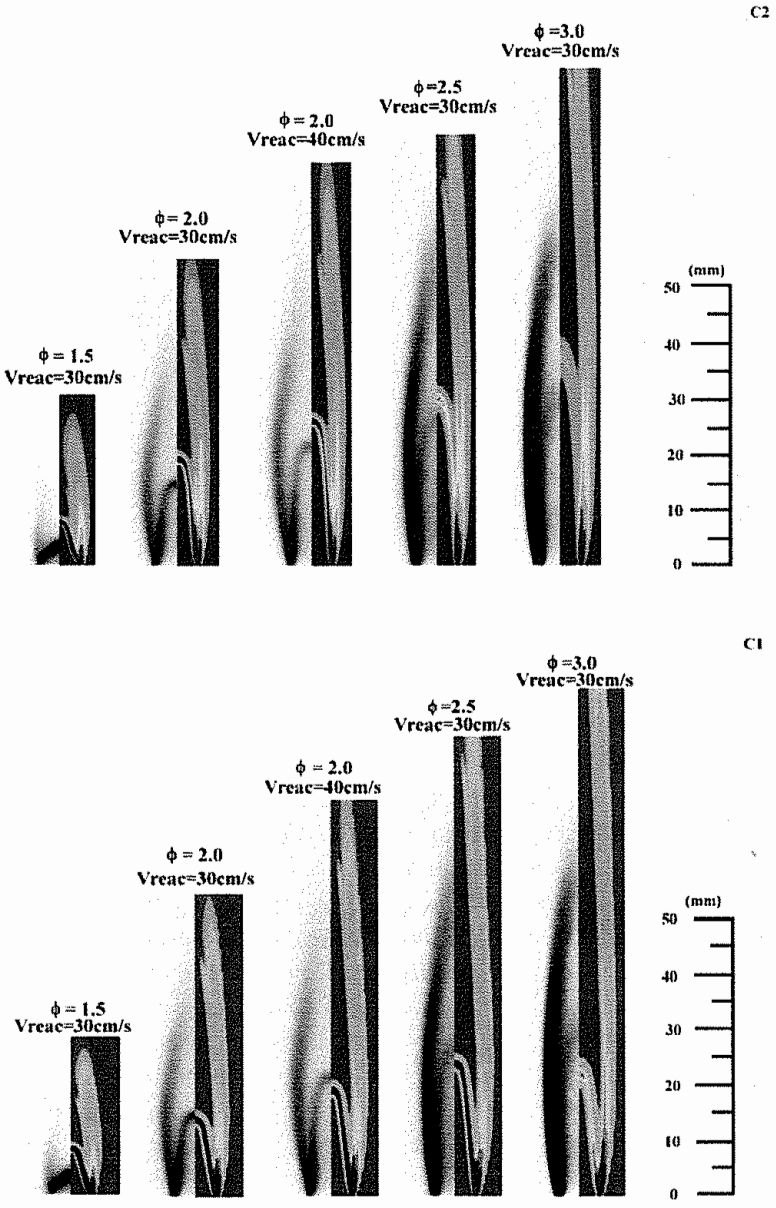

FIGURE 10 Comparison of the predicted heat release rates, obtained by using the C_1- and C_2-mechanisms, with the experimentally-obtained C_2-chemiluminescence images of partially premixed flames for five different cases. The outer slot velocity in all cases $V_{air} = 30$ cm s^{-1} (See Color Plate XVIII at the back of this issue)

tant role at higher levels of air premixing ($\phi \leq 2.0$), while the outer reaction zone is relatively stronger at lower level of air premixing ($\phi > 2.5$).

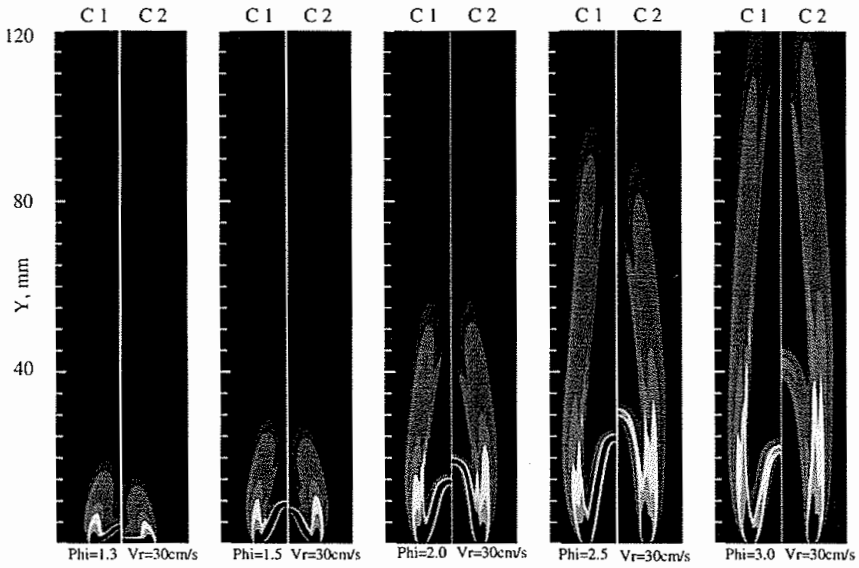

FIGURE 11 Predicted heat release rate contours for the two mechanisms for different levels of partial premixing. For all cases, $V_{react} = V_{air} = 30$ cm s^{-1} (See Color Plate XIX at the back of this issue)

It is apparent from Fig. 11 that there are quantitative differences in the flame structure predicted by the two mechanisms. These differences can be attributed to the C_2-path in the C_2-mechanism, which has a relatively stronger influence on the inner reaction zone. In particular, the inner reaction zone height exhibits a far stronger sensitivity to variations in the equivalence ratio when the C_2-mechanism is used compared with the C_1-mechanism. Consequently, at high levels of air premixing ($\phi \leq 1.5$), the C_2-mechanism yields a lower inner reaction zone height, while at lower levels of premixing ($\phi \geq 2.0$), it yields a higher inner zone height compared the predictions obtained with the C_1-mechanism. The outer (non-premixed) reaction zone height is relatively unaffected by the mechanism that is used, although it is slightly lower in case of the C_2-mechanism. However, due to the synergistic interactions between the two reaction zones, the spatial topography of the outer reaction zone is noticeably affected by the choice of reaction mechanism.

The global characteristics of partially premixed flames predicted by the two mechanisms are depicted in Fig. 12, which shows the temperature and the mole

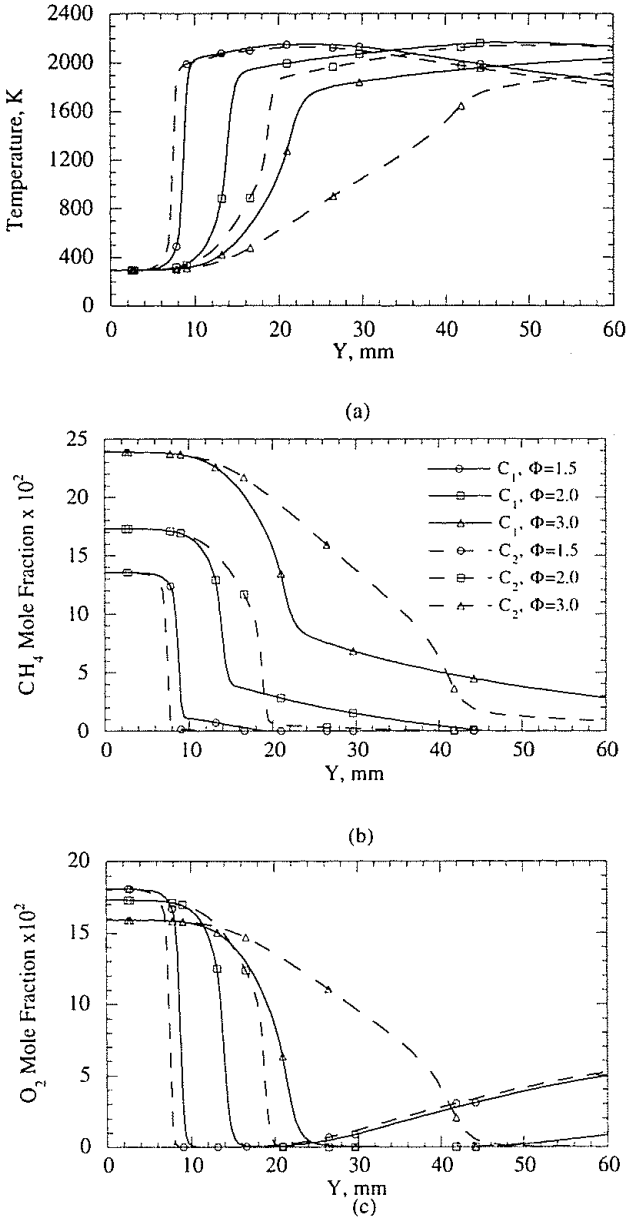

FIGURE 12 Temperature and mole fraction distributions of the reactants (CH_4 and O_2) along the centerline as predicted by using the C_1- and C_2-mechanisms for three different equivalence ratios, and $V_{react} = V_{air} = 30$ cm s^{-1}

fraction of CH_4 and O_2 along the centerline for three different cases. Consistent with the results discussed earlier, the flames predicted by using the C_1-mechanism exhibit less sensitivity to the equivalence ratio. In addition, for high levels of partial premixing, the methane consumption in the inner premixed zone is significantly higher for the C_2-mechanism compared to that when C_1-mechanism is used. Consequently, for high levels of partial premixing, the amount of methane that leaks from the rich premixed to nonpremixed reaction zone is significantly lower when the C_2-mechanism is used. The maximum temperature obtained with the C_2-mechanism is slightly lower compared to that obtained using the C_1-mechanism. This is due to the endothermic effects (Lee et al. 1996) caused by the C_2-pathway.

In general, quantitative differences in the predictions of the two mechanisms are relatively small at high level of partial premixing (ϕ=1.5), i.e., when interactions between the two reaction zones of partially premixed flames are strong. Since the C_1-mechanism is known to be inadequate for fuel-rich premixed flames (Xue and Aggawal, 2000), its relatively good performance in the context of PPFs can be attributed to the interactions between the two reaction zones. As the level of partial premixing is reduced, e.g. ϕ is increased, these interactions become weaker, and quantitative differences between the two mechanisms become more significant. This is clearly depicted in the plots of temperature and species mole fractions for ϕ=3.0 shown in Fig. 12. In this context, it is important to note that while the rich premixed flames are chemistry dominated, the corresponding PPFs are characterized by both chemistry and transport. Consequently, any conclusions regarding the applicability of reduced or detailed reactions mechanisms, that are based on premixed combustion phenomena, may not be extended to partially premixed combustion.

REACTION PATHWAYS IN C_1- AND C_2-MECHANISMS

As illustrated in Fig. 8, the C_1-pathway involves two routes, i.e.,

$$CH_3 \rightarrow CH_2O \rightarrow CHO, \text{and} \qquad \text{(PI)}$$

$$CH_3 \rightarrow CH_2 \rightarrow CH \rightarrow CHO \qquad \text{(PII)}$$

These formyl radicals subsequently produce CO, which is further oxidized to form CO_2. The first of these two paths is faster, since formyl production through the reactions

$$CH_2O + H \rightarrow CHO + H_2, \text{and} \qquad \text{(RI)}$$

$$CH_2O + OH \rightarrow CHO + H_2O, \qquad \text{(RII)}$$

is more significant than its formation through the reaction

$$CH + O_2 \rightarrow CHO + O. \qquad \text{(RIII)}$$

The C_2-pathway involves an additional route, i.e.,

$$CH_3 \rightarrow C_2H_6 \rightarrow C_2H_5 \rightarrow C_2H_4 \rightarrow C_2H_3 \rightarrow C_2H_2 \rightarrow C_2HO \rightarrow CO. \qquad \text{(PIII)}$$

Although the path PIII is typically slower than the two C_1-channels PI and PII, it is nonetheless significant since (1) it introduces endothermic effects (Lee et al. 1996), and (2) because the rate of CO formation through the reaction

$$C_2HO + O \rightarrow CO + CO + H \qquad \text{(RIV)}$$

has an equal magnitude to the rate of the reaction

$$CHO + M \rightarrow CO + H + M. \qquad \text{(RV)}$$

The C_2-pathway PIII also affects the C_1-channel PII by increasing H-atom formation through reaction RIV and the reaction

$$C_2HO + H \Leftrightarrow CH_2 + CO. \qquad \text{(RVI)}$$

As illustrated in Table I, this reaction results in a net production of H-atoms at lower equivalence ratios ($\phi \leq 1.5$), but a net consumption of these atoms at higher equivalence ratios ($\phi \geq 3.0$).

Therefore, the major effect of the C_2-pathway PIII at lower equivalence ratios ($\phi \leq 1.5$) is to increase the overall reaction rates by increasing H-atom formation and, thereby, augmenting the effect of the chain-branching reactions by raising the net availability of radical species. This is illustrated by the data presented in Table I for some key reaction rates for flames established at ϕ= 1.5 and 3.0, and computed by using both the C_1- and C_2-mechanisms. Reaction rates are presented in an integrated form, i. e., $(1/A)\int_A \dot{w}_i dA$ where $\dot{w}_i$ is the rate of production (consumption) of species i, and the area A is selected to include a significant part of the inner or outer flames respectively.

The increase in H-atom formation is largely due to the effect of reactions RIV and RVI. Reaction RIV is also responsible for an increase in CO production, the oxidation of which through the reaction

$$CO + OH \Leftrightarrow CO_2 + H \qquad \text{(RVII)}$$

is also responsible for H-atom formation. The increase in H-atom formation has a feedback effect, since, as illustrated in Table I, it synergistically raises the rates of the initiation reactions

$$CH_4 + H \rightarrow CH_3 + H_2, \text{and} \qquad \text{(RVIII)}$$

$$O_2 + H \rightarrow OH + O \qquad \text{(RIX)}$$

This in turn increases the rates of the other initiation reactions (cf. Table I), namely,

$$H_2 + O \Leftrightarrow OH + H, \text{and} \qquad \text{(RX)}$$

$$H_2 + OH \rightarrow H_2O + H \qquad \text{(RXI)}$$

and, thus, enhances the rate of H-atom formation. In summary, the C_2-chemistry is responsible for an overall increase in the reaction rates by increasing H-atom formation and, thereby, the radical pool. Consequently, for flames established at $\phi \leq 1.5$, as shown in Fig. 11, the inner reaction zone is located upstream when it is modeled using the C_2-chemistry as compared to when the C_1-chemistry is employed in the simulations.

The data contained in Table I also illustrates that the impact of C_2-chemistry is larger on the inner premixed reaction zone than its influence on the outer non-premixed reaction zone. Since the C_2-chemistry is "faster", methane leakage to the outer reaction zone is negligible when it is employed. The increase in the radical pool in the inner reaction zone due to the C_2-chemistry synergistically influences the outer reaction region, eventually resulting in a higher product (CO_2 and H_2O) formation rate in that zone.

At higher equivalence ratios, the overall reaction rate is lower than at higher levels of air premixing (i.e., lower ϕ), since the flame is influenced relatively more by transport and less by the premixed methane-air chemistry. In addition, the fuel flux through the inner slot also rises as the equivalence ratio increases. Consequently, the flame occupies a larger overall spatial volume. At $\phi = 3$, the effect of the C_2-chemistry again occurs due to reaction RIV that produces H-atoms, and reaction RVI that consumes H-atoms. Once again, the rate of the initiation reactions RVIII-RXI increases. However, as illustrated in Fig. 8 and Table I, the role of reaction RIV in augmenting H-atom formation is relatively diminished due to the paucity of the O-atom pool at higher ϕ. In addition, the smaller increase in the H-atom pool at $\phi = 3$ (in comparison with $\phi = 1.5$) is offset by H-atom consumption through the reactions RVI and

$$C_2H_6 + H \rightarrow C_2H_5 + H_2, \text{and} \qquad \text{(RXII)}$$

$$C_2H_5 + H \rightarrow C_2H_4 + H_2. \qquad \text{(RXIII)}$$

TABLE I Integrated species consumption (or production) rates for dominant reaction in the inner and outer flames at Φ=1.5 and 3.0 computed by using the C_1- and C_2-mechanisms

Reactions	*Φ=1.5*				*Φ=3.0*			
	Inner		*Outer*		*Inner*		*Outer*	
	C_1	C_2	C_1	C_2	C_1	C_2	C_1	C_2
CH_4								
1. $CH_4 + H \Leftrightarrow CH_3 + H_2$	−4.0	−13	−0.06	0	−0.4	−1.0	−0.2	0
2. $CH_4 + OH \Leftrightarrow CH_3 + H_2O$	−4.2	−4.3	−0.02	0	−1.1	−0.7	−0.15	0
O_2								
1. $O_2 + H \Leftrightarrow OH + O$	−6.0	−14.7	−0.5	−0.15	−0.5	−0.9	−1.0	−0.6
2. $O_2 + H + M \Leftrightarrow HO_2 + M$	0	−0.7	−0.4	−0.13	0	0	−0.45	−0.4
3. $HO_2 + OH \rightarrow H_2O + O_2$	0	0.12	0.3	0	0	0	0.35	0.3
4. $CH_3 + O_2 \rightarrow CH_2O + OH$	−2.5	−1.0	0	0	−1.2	−0.4	−0.25	0
CO								
1. $CO + OH \Leftrightarrow CO_2 + H$	−2.2	−3.9	−0.6	−0.16	−0.4	−0.1	−0.85	−0.7
2. $CHO + M \rightarrow CO + H + M$	5.0	4.6	0.1	0	1.2	0.4	0.4	0
3. $CH_2 + O_2 \rightarrow CO + OH + H$	0.5	1.0	0.03	0	0	0.09	0	0
4. $C_2HO + H \Leftrightarrow CH_2 + CO$	/	−0.7	/	0	/	0.06	/	0
5. $C_2HO + O \rightarrow 2CO + H$	/	4.4	/	0	/	0.18	/	0
6. $C_2H_2 + O \rightarrow CH_2 + CO$	/	2.0	/	0	/	0.2	/	0
H_2								
1. $H_2 + O \Leftrightarrow OH + H$	−0.8	−3	−0.15	0	−0.05	−0.1	−0.2	−0.2
2. $H_2 + OH \Leftrightarrow H_2O + H$	−4.2	−13.4	−0.35	−0.12	−0.3	−0.8	−0.55	−0.3
3. $CH_2O + H \rightarrow CHO + H_2$	1.9	2.1	0	0	0.55	0.2	0	0
4. $CH_3 + H \Leftrightarrow CH_2 + H_2$	1.6	1.6	0	0	0.10	−0.08	0.15	0
5. $CH_4 + H \Leftrightarrow CH_3 + H_2$	4.0	13	0.06	0	0.4	1.0	0.2	0
6. $C_2H_4 + H \rightarrow C_2H_3 + H_2$	/	2.4	/	0	/	0.3	/	0
7. $C_2H_6 + H \rightarrow C_2H_5 + H_2$	/	3.3	/	0	/	0.6	/	0
CO_2								
1. $CO + OH \Leftrightarrow CO_2 + H$	2.2	3.9	0.6	1.5	0.4	0.1	0.85	0.7
2. $CH_2 + O_2 \rightarrow CO_2 + 2H$	0.7	1	0	0	0.05	0.09	0	0
H_2O								
1. $H_2 + OH \Leftrightarrow H_2O + H$	4.2	13.4	0.35	0.12	0.3	0.8	0.55	0.3
2. $H_2O + O \Leftrightarrow 2OH$	−0.7	−1.5	−0.30	0	0	−0.07	−0.4	−0.3
3. $HO_2 + H \rightarrow H_2O + O$	0	0.1	0.3	0	0	0	0.35	0
4. $CH_2O + OH \rightarrow CHO + H_2O$	3	1.9	0	0	0.6	0.2	0.4	0

Reactions	*Φ=1.5*				*Φ=3.0*			
	Inner		*Outer*		*Inner*		*Outer*	
	C_1	C_2	C_1	C_2	C_1	C_2	C_1	C_2
5. $CH_4 + OH \Leftrightarrow CH_3 + H_2O$	4.2	4.3	0.02	0	1.1	0.7	0.15	0
6. $C_2H_4 + OH \rightarrow C_2H_3 + H_2O$	/	1.4	/	0	/	0.1	/	0
7. $C_2H_6 + OH \rightarrow C_2H_5 + H_2O$	/	0.8	/	0	/	0.1	/	0
CH_3								
1. $CH_3 + H \Leftrightarrow CH_2 + H_2$	−1.6	−1.6	0	0	−0.10	0.07	−0.15	0
2. $CH_3 + O \rightarrow CH_2O + H$	−3.0	−3.2	0	0	−1.1	−0.04	0	0
3. $CH_3 + O_2 \rightarrow CH_2O + OH$	−2.5	−0.5	0	0	−1.2	−0.4	−0.25	0
4. $CH_4 + H \Leftrightarrow CH_3 + H_2$	4.0	13	0.06	0	0.4	1.0	0.2	0
5. $CH_4 + OH \Leftrightarrow CH_3 + H_2O$	4.2	4.3	0.02	0	1.1	0.7	0.15	0
6. $2CH_3 \rightarrow C_2H_6$	/	−1	/	0	/	−0.16	/	0
CHO								
1. $CH + O_2 \rightarrow CHO + O$	0.2	0.5	0	0	0	0	0	0
2. $CO_2 + CH \rightarrow CHO + CO$	0.1	0.3	0	0	0	0	0	0
3. $CHO + M \rightarrow CO + H + M$	−5.0	−4.6	−0.1	0	−1.2	−0.4	− 0.4	0
4. $CH_2O + H \rightarrow CHO + H_2$	1.9	2.1	0	0	0.55	0.2	0	0
5. $CH_2O + OH \Leftrightarrow CHO + H_2O$	3	1.9	0	0	0.6	0.2	0.4	0
6. $CHO + H \rightarrow CO + H_2$	0	−0.1	0	0	0	0	0	0
H								
1. $O_2 + H \Leftrightarrow OH + O$	−6.0	−14.7	−0.5	−0.15	−0.5	−0.9	−1.0	−0.6
2. $H_2 + O \Leftrightarrow OH + H$	0.8	3	0.15	0	0.05	0.1	0.2	0.2
3. $H_2 + OH \Leftrightarrow H_2O + H$	4.2	13.4	0.35	0.12	0.3	0.8	0.55	0.3
4. $O_2 + H + M \Leftrightarrow HO_2 + M$	0	−0.7	−0.4	−0.13	0	0	−0.45	−0.4
5. $CO + OH \Leftrightarrow CO_2 + H$	2.2	3.9	0.6	0.16	0.4	0.1	0.85	0.7
6. $CHO + M \rightarrow CO + H + M$	5.0	4.6	0.1	0	1.2	0.4	0.4	0
7. $CH_3 + O \rightarrow CH_2O + H$	3.0	3.2	0	0	1.1	0.04	0	0
8. $CH_4 + H \Leftrightarrow CH_3 + H_2$	−4.0	−13	−0.06	0	−0.4	−1.0	−0.2	0
9. $C_2HO + O \rightarrow 2CO + H$	/	2.2	/	0	/	0.09	/	0
10. $C_2H_4 + H \rightarrow C_2H_3 + H_2$	/	−2.4	/	0	/	−0.3	/	0
11. $C_2H_6 + H \rightarrow C_2H_5 + H_2$	/	−3.3	/	0	/	−0.6	/	0
OH								
1. $O_2 + H \Leftrightarrow OH + O$	6.0	14.7	0.5	0.15	0.5	0.9	1.0	0.6
2. $H_2 + O \Leftrightarrow OH + H$	0.8	3	0.15	0	0.05	0.1	0.2	0.2
3. $H_2 + OH \Leftrightarrow H_2O + H$	−4.2	−13.4	−0.35	−0.12	−0.3	−0.8	−0.55	−0.3

Reactions	Φ=*1.5*				Φ=*3.0*			
	Inner		*Outer*		*Inner*		*Outer*	
	C_1	C_2	C_1	C_2	C_1	C_2	C_1	C_2
4. $CO + OH \Leftrightarrow CO_2 + H$	−2.2	−3.9	−0.6	−0.16	−0.4	−0.1	−0.85	−0.7
5. $CH_4 + OH \Leftrightarrow CH_3 + H_2O$	−4.2	−4.3	−0.02	0	−1.1	−0.7	−0.15	0
6. $C_2H_4 + OH \rightarrow C_2H_3 + H_2O$	/	−1.4	/	0	/	−0.1	/	0
7. $C_2H_6 + OH \rightarrow C_2H_5 + H_2O$	/	−0.8	/	0	/	−0.1	/	0
O								
1. $O_2 + H \Leftrightarrow OH + O$	6.0	14.7	0.5	0.15	0.5	0.9	1.0	1.0
2. $H_2 + O \Leftrightarrow OH + H$	−0.8	−3	−0.15	0	−0.05	−0.1	−0.2	−0.25
3. $CH_3 + O \rightarrow CH_2O + H$	−3.0	−3.2	0	0	−1.1	−0.04	0	0
4. $C_2HO + O \rightarrow 2CO + H$	/	−2.2	/	0	/	−0.09	/	0

Note:
1. The unit of the species consumption (or production) rate is 10^{-5} moles m^{-3} s^{-1}.
2. The "0" indicates a small value, and "/" indicates that the reaction is not included in the C_1-mechanism.

The two C_1-pathways PI and PII and the C_2-path PIII are distinguished by a competition between the following reactions

$$CH_3 + O \rightarrow CH_2O + H, \qquad \text{(RXIV)}$$

$$CH_3 + O_2 \rightarrow CH_2O + OH, \qquad \text{(RXV)}$$

$$CH_3 + H \rightarrow CH_2 + H_2, \text{and} \qquad \text{(RXVI)}$$

$$CH_3 + CH_3 + (M) \rightarrow C_2H_6 + (M). \qquad \text{(RXVII)}$$

The reactions RXIV and RXV occur along path PI, RXVI along path PII, and RXVII along PIII. When C_2-chemistry is employed, reaction RXIV dominates RXV at lower values of ϕ due to the relative abundance of O atoms.

There is a competition for O-atom consumption between reactions RXIV and RX. Reaction RVIII results in the formation of H_2 and, since, H-atoms are in greater abundance when C_2-chemistry is employed, so is molecular hydrogen. However, at the higher equivalence ratio ($\phi = 3$), the O-atom pool is not sufficiently enhanced in the inner reaction zone due to the relative paucity of molecular oxygen. Therefore, the two reactions RXIV and RX compete with each other to consume O-atoms and, consequently, the path PI diminishes in importance, rendering the path PIII of comparable magnitude. This decreases the overall reaction rates for the C_2-mechanism, since path PIII is slower compared to path

PI. This also leads to a reduction in CO formation through reaction RV that is not offset by either reaction RIV or the reaction

$$C_2H_2 + O \rightarrow CH_2 + CO, \qquad \text{(RXVIII)}$$

both of which occur along the C_2-pathway PIII.

In addition, the lower concentration of O_2 at higher ϕ reduces the formation of hydroxyl radicals through the reaction RIX. This leads to a reduction in the consumption rates of methane and CO (through reactions RXIX and RVII respectively) for both the C_1- and C_2-mechanisms. However, this effect is relatively more significant in case of the latter mechanism due to the competing reactions

$$CH_4 + OH \rightarrow CH_4 + H_2O, \text{ and} \qquad \text{(RXIX)}$$

$$C_2H_4 + OH \rightarrow C_2H_3 + H_2O. \qquad \text{(RXX)}$$

In summary, the use of C_2-chemistry enhances the overall reaction rate in the inner flame at lower equivalence ratios by increasing the radical pool in comparison with the C_1-mechanism. However, due to a paucity in the O-atom pool at higher equivalence ratios, this effect is significantly diminished in richer flames, such that the slower path PIII becomes comparable to the path PI. In addition, as indicated in Table I, reaction RVI produces H-atoms at lower ϕ, but consumes them at higher ϕ. The net effect is that the methane consumption rate is reduced when the C_2-mechanism is used. In addition, the use of C_2-chemistry further retards the CO-formation rate in richer flames due to a reduction in the OH-radical pool. As a result, the inner reaction zone in the $\phi = 3.0$ flame exists at higher (more downstream) locations when the C_2-mechanism is employed, but at lower locations when the simpler mechanism is used.

CONCLUSIONS

In the present study, the role of C_2-chemistry in determining the structure of partially premixed methane-air flames has been investigated by employing two detailed mechanisms. The first mechanism involves only C_1-chemistry and comprises 52 reactions that involve 17 species, while the second mechanism contains both C_1- and C_2-chemistry and C_2-chemistry and consists of 81 reactions and 24 species. The simulation model has been validated by comparing the predicted and measured planar partially premixed flames (PPFs) established on a rectangular Wolfhard-Parker slot burner. A detailed numerical study has been conducted to examine the effects of C_2-chemistry on the structure of partially premixed flames for different levels of partial premixing and reactant velocities. The important observations from this investigation are as follows:

1. Both the C_1- and C_2-mechanisms are capable of reproducing the global features of PPFs that are observed in laboratory experiments. These include: (1) the existence of an inner premixed reaction zone and an outer non-premixed reaction zone; (2) synergistic interactions between these two reaction zones, whereby the inner zone provides CO and H_2(intermediate fuels) to the outer zone, which in turn provides radical species (H and OH) to the inner zone; (3) variation of the inner and outer reaction zone heights with changes in the equivalence ratio and reactant velocity; and (4) the relative dominance of the inner zone chemistry at higher levels of air premixing (i.e., lower ϕ) and of the outer zone at higher values of ϕ. Since the C_1-mechanism has been shown to be inadequate for fuel-rich premixed flames, its relatively good performance in the context of PPFs can be attributed to the synergistic interactions between the two reaction zones.
2. There are important quantitative differences in the PPF structures predicted by the two reaction mechanisms. First, the inner reaction zone height predicted by the C_1-mechanism is less sensitive to variations in the equivalence ratio as compared with the C_2-mechanism. At high levels of air premixing ($\phi \leq 1.5$), the C_2-mechanism yields a lower inner reaction zone height, while at lower levels of air premixing ($\phi \geq 2.0$), it yields a higher inner zone height compared with predictions obtained by using the C_1-mechanism. The predictions using the C_2-mechanism are more consistent with the experimental results. Second, methane consumption in the inner reaction zone is significantly higher when the C_2-mechanism is used as compared to results obtained with C_1-mechanism. Consequently, for high levels of partial premixing, the amount of methane that leaks from the rich premixed to non-premixed zone is significantly lower when the C_2-mechanism is used.. Third, a smaller separation distance between the inner and outer reaction zones is predicted by the C_2-mechanism, compared to the C_1-mechanism results. This indicates stronger interactions between the inner and outer reaction zones when the C_2-mechanism is used. Finally, the maximum temperature predicted by the C_2-mechanism is slightly lower as compared to that obtained using the C_1-mechanism. The various differences are due to the presence of C_2-chain in the 81-step mechanism, which strongly affects the structure of the inner premixed reaction zone.
3. The C_1-pathway, involved in the conversion of methane to CO and H_2, consists of two channels. The first channel involves $CH_3 \rightarrow CH_2O \rightarrow CHO$, while the second channel involves $CH_3 \rightarrow CH_2 \rightarrow CH \rightarrow CHO$. The formyl radicals subsequently form CO, which is further oxidized to produce CO_2, while H_2 is oxidized to form H_2O. The C_2-route in the C_2-mechanism involves an additional path $CH_3 \rightarrow C_2H_6 \rightarrow C_2H_5 \rightarrow C_2H_4 \rightarrow C_2H_3 \rightarrow C_2H_2$

$\rightarrow C_2HO \rightarrow CO$. At lower equivalence ratios ($\phi \leq 1.5$), the major effect of the C_2-pathway is to increase the overall reaction rates by increasing H-atom formation and, thereby, augmenting the effect of the chain-branching reactions by raising the net availability of radical species. Consequently, the inner reaction zone is located further upstream when the C_2-mechanism used, and further downstream when C_1-mechanism is employed. However. at higher equivalence ratios this effect is significantly diminished due to the paucity of O-atoms, so that the slower C_2-path becomes comparable to the C_1-path. In addition, the reaction $C_2HO + H \Leftrightarrow CH_2 + CO$ produces H-atoms at lower ϕ, but consumes them at higher ϕ. The C_2-path also retards the CO-formation rate in richer flames due to a reduction in the OH-radical pool. The net effect is that at higher equivalence ratios, the methane consumption rate is reduced, and the inner reaction zone exists at higher axial locations when C_2-mechanism is employed.

4. The C_2-pathway has no direct effect on the outer nonpremixed reaction zone. However, the spatial location of this zone is indirectly affected, as it is located closer to the inner reaction zone, by the C_2-pathway.

Acknowledgements

This research was supported by the National Science Foundation Combustion and Plasma Systems Program through Grant No. CTS-9707000 for which Dr. Farley Fisher is the Program Director. Simulations were performed on the SGI workstations at NCSA at Urbana-Champaign.

References

Gore, J. P., and Zhan, N. J. (1996), NOx Emission and Major Species Concentrations in Partially Premixed Laminar Methane/Air Co-flow Jet Flames, *Combust. Flame*, **115**, 414–427.

Hamins, A., Thridandam, H., and Seshadri, K. (1985), Structure and Extinction of a Counterflow Partially-Premixed, Diffusion Flame, *Chem. Eng. Sci.*, **40**, 2027–2038.

Katta, V. R., Goss, L. P., and Roquemore, W. M. (1994), Effect of Nonunity Lewis number and Finite-Rate Chemistry on the Dynamics of a Hydrogen-Air Jet Diffusion Flame, Combust. Flame, **96**, 60–74.

Kee, R. J, Miller, J. A., and Warnatz, J. (1983), A Fortran Program Package for the Evaluation of Gas-phase Viscosities, Conductivities, and Diffusion Coefficients, Sandia National Laboratories Report SAND83–8209.

Law, C. K., Li, T. X., Chung, S. H., Kim, J. S., and Zhu, D. L. (1989), On the Structure and Extinction Dynamics of Partially-Premixed Flames: Theory and Experiment, *Combust. Sci. Tech.*, **64**, 99–232.

Lee, K. Y., Cha, D. J., Hamins, A., and Puri, I. K. (1996), An Investigation of the Role of Radiative Thermal Loss in Inhibited Counterflow Flames," *Combust. Flame*, Vol. **104**, 27–40.

Li, S. C., Illincic, N., and Williams, F. A. (1997), Reduction of NOx Formation by Water Sprays in Strained Two-Stage Flames, ASME J. of Engineering for Gas Turbines and Power, **119**, 836–843.

Li, S. C. and Williams, F. A. (1998), Experimental and Numerical Studies of NOx Formation in Two-Stage Methane-Air Flames, ASME Paper 98-GT-73, IGTI Congress and Exhibition, Stockholm, Sweden.

Najm, H. N., Paul, P. H., Mueller, C. J., and Wyckoff, P. S. (1998), On the Adequacy of Certain Experimental Observables as Measurements of Flame Burning Rate, *Combust. Flame*, **113**, 312–332.

Peters, N. (1993), Reduced Kinetic Mechanisms for Applications in Combustion Systems, Lecture Notes in Physics, N. Peters and B. Rogg (Eds.), Springer-Verlag, **m15**, 3–14.

Seshadri, K., Puri, I., and Peters, N. (1985), Experimental and Theoretical Investigations of Partially Premixed Diffusion Flames at Extinction, *Combust. Flame*, **61**, 237–249.

Shu, Z., Aggarwal, S. K., Katta, V. R., and Puri, I. K. (1997a), Flame-Vortex Dynamics in an Inverse Partially Premixed Combustor: The Froude Number Effects, *Combust. Flame*, **111**, 276–295.

Shu, Z., Aggarwal, S. K., Katta, V. R., and Puri, I. K. (1997b), A Numerical Investigation of the Flame Structure of an Unsteady Inverse Partially-Premixed Flame," *Combust. Flame*, **111**, 296–311.

Shu, Z., Krass, B. J., Choi, C. W., Aggarwal, S. K., Katta, V. R., and Puri, I. K. (1998), Investigation of the Flame Structure of a Steady Two-Dimensional Partially-Premixed Methane-Air Slot Flame, Twenty-seventh Symposium (International) on Combustion, The Combustion Institute, Pittsburgh, 625–632.

Yamaoka, I., and Tsuji, H. (1978), An Experimental Study of Flammability Limits Using Counterflow Flames, Seventeenth Symposium (International) on Combustion, The Combustion Institute, Pittsburgh,, pp. 843–855.

Xue, H., and Aggarwal, S. K. (2000), Effects of Reaction Mechanisms on the Structure and Extinction of Partially Premixed Counterflow Flames, Paper 2000–0578, 38th Aerospace Sciences Meeting, Reno, Nevada, Jan. 10–13.

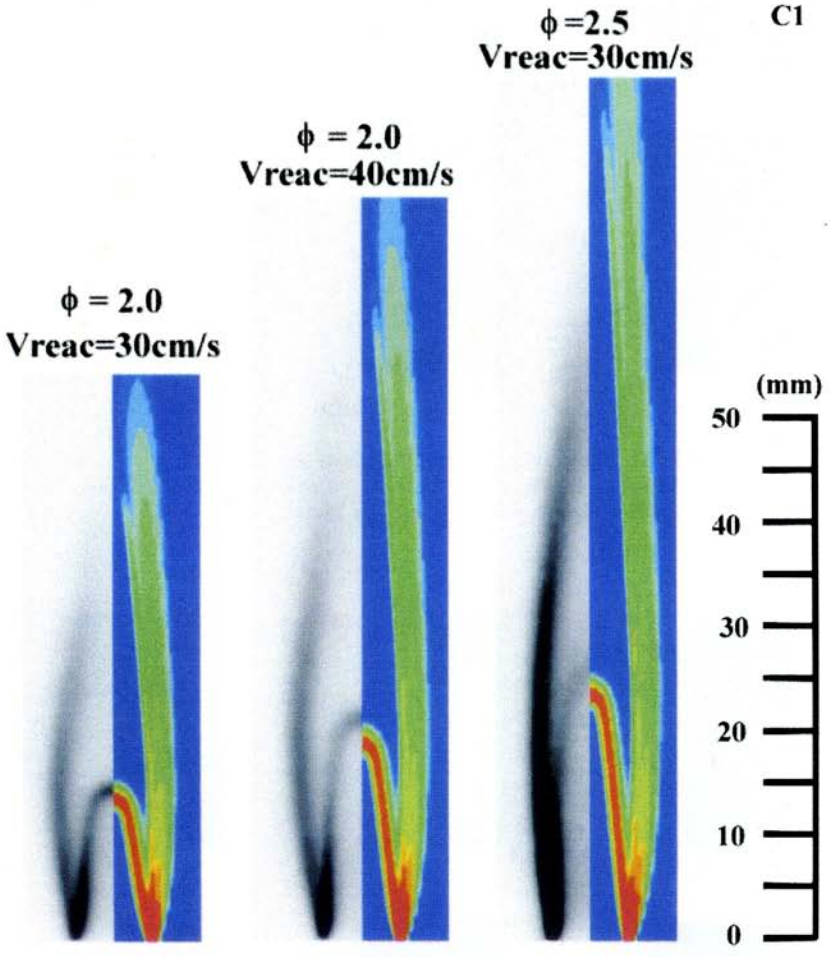

Color Plate XI (See page 190, Figure 2) Comparison of the predicted heat release rates (obtained by using the C_1-mechanism) with the experimentally-obtained C_2-chemiluminescence images of partially premixed flames for three different cases: (a) $\phi = 2.0$, $V_{react} = 30$ cm s^{-1}; (b) $\phi = 2.0$, $V_{react} = 40$ cm s^{-1}; and (c) $\phi = 2.5$, $V_{react} = 30$ cm s^{-1}. The outer slot velocity in all cases $V_{air} = 30$ cm s^{-1}

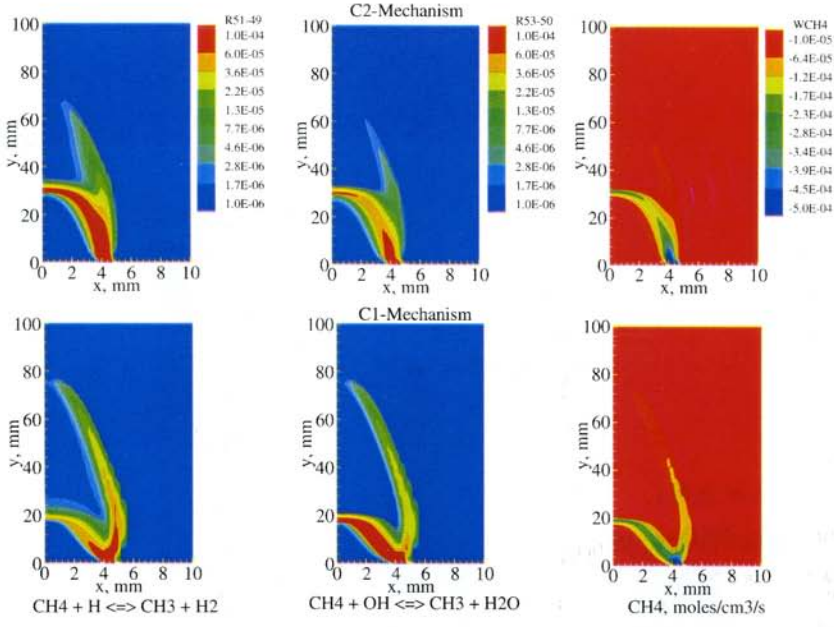

Color Plate XII (See page 191, Figure 3) Comparison of the reaction-rate contours of major fuel decomposition reactions: (a) $CH_4 + H \Leftrightarrow CH_3 + H_2$, (b) $CH_4 + OH \Leftrightarrow CH_3 + H_2O$, and (c) the net consumption rate of methane as predicted by the C_1- and C_2-mechanisms. $\phi = 2.5$, $V_{react} = V_{air} = 30$ cm s^{-1}

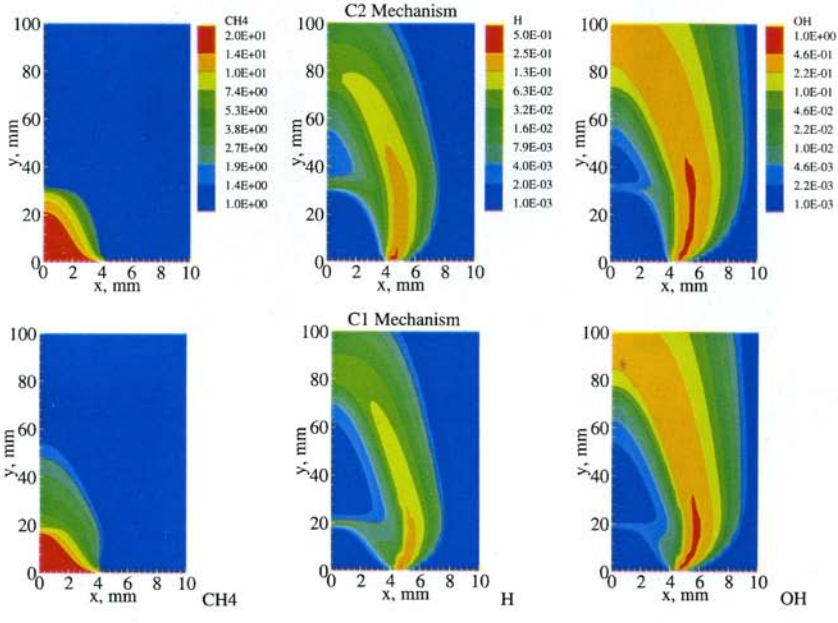

Color Plate XIII (See page 192, Figure 4) Contours of the CH_4, H-atom, and OH concentrations predicted by the two mechanisms for the case discussed in context of Fig. 3

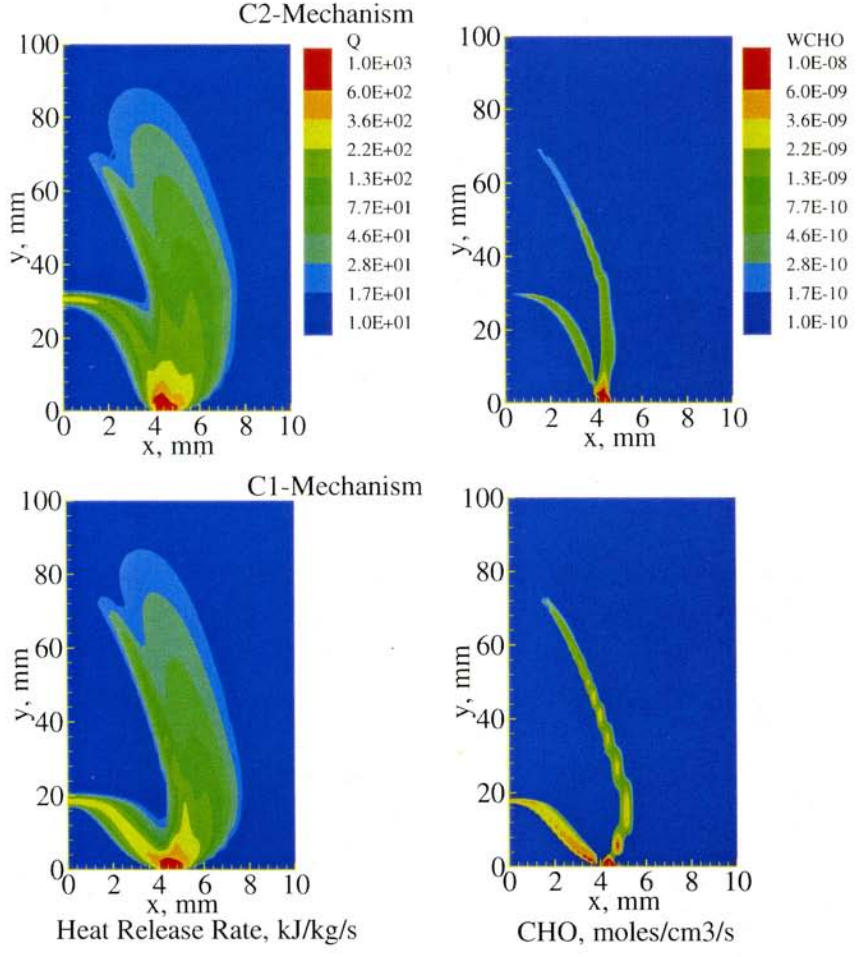

Color Plate XIV (See page 193, Figure 5) Contours of heat release rate and CHO concentration predicted by the two mechanisms for the case discussed in context of Fig. 3

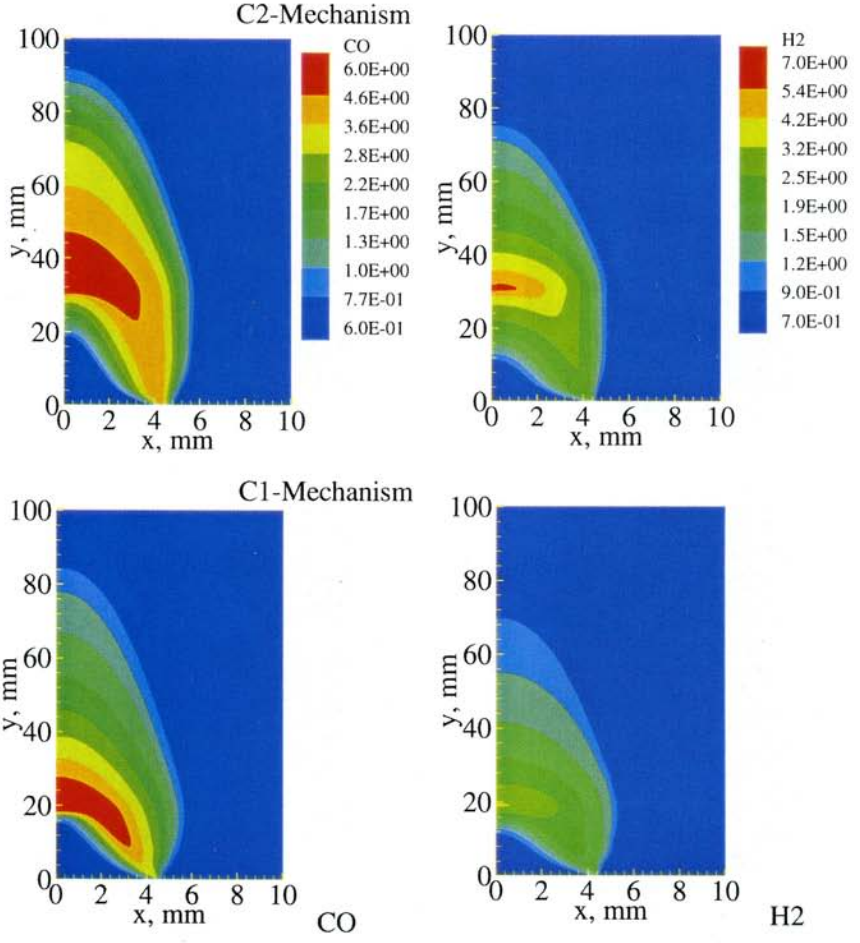

Color Plate XV (See page 194, Figure 6) Contours of the CO and H_2 mole fractions predicted by the two mechanisms for the case discussed in context of Fig. 3

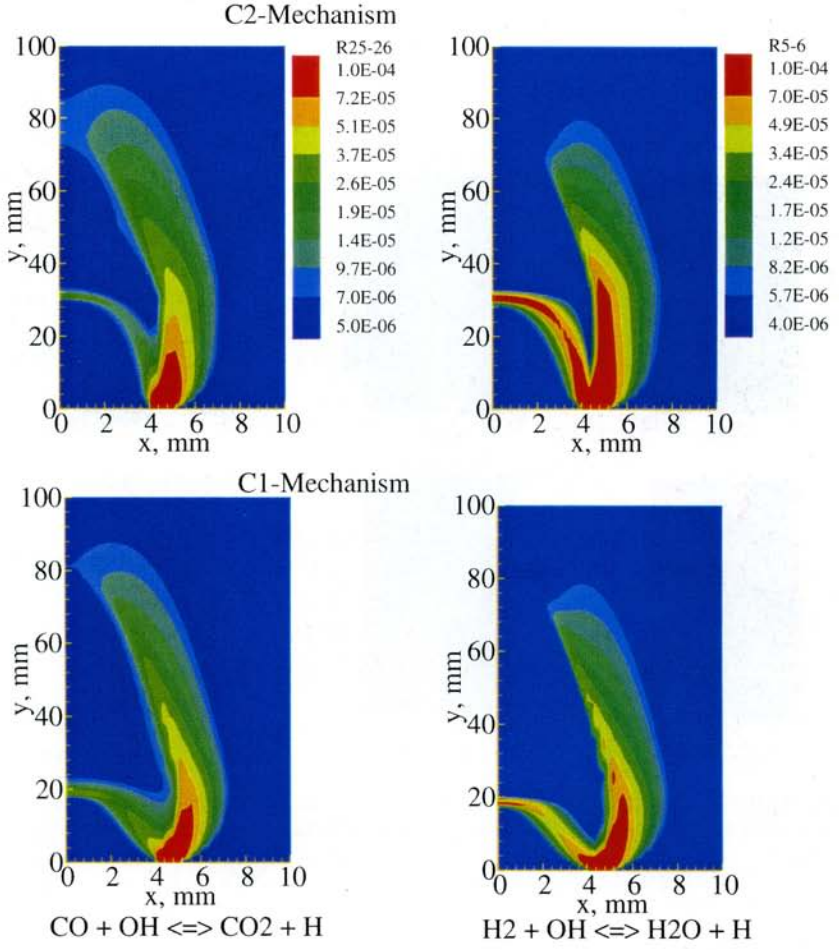

Color Plate XVI (See page 195, Figure 7) Comparison of the rate contours of the reactions CO + OH ⇔ CO_2 + H and H_2 + OH ⇔ H_2O + H predicted by the two mechanisms for the case discussed in context of Fig. 3

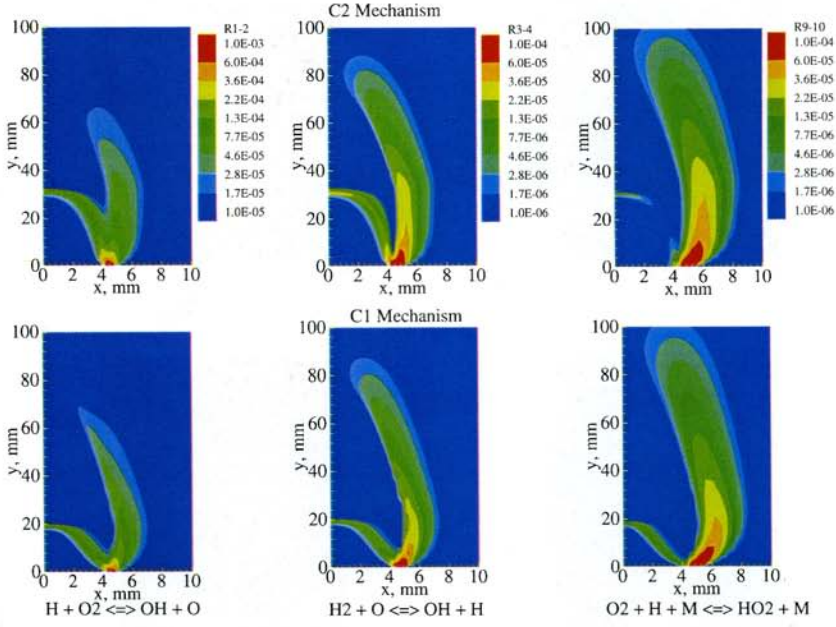

Color Plate XVII (See page 198, Figure 9) Comparison of contours of the reactions (a) $H + O_2 \Leftrightarrow OH + O$, (b) $H_2 + O \Leftrightarrow OH + H$, and (c) $O_2 + H + M \Leftrightarrow HO_2 + M$ predicted by the two mechanisms for the case discussed in context of Fig. 3

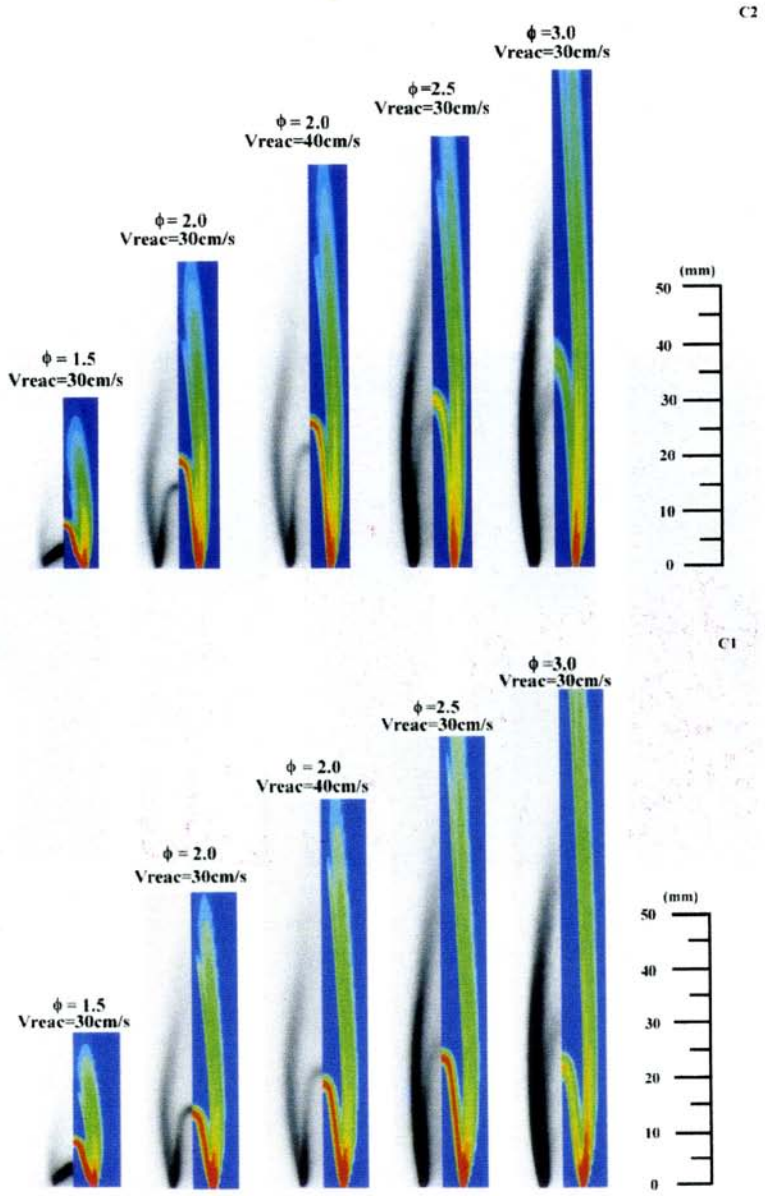

Color Plate XVIII (See page 199, Figure 10) Comparison of the predicted heat release rates, obtained by using the C_1- and C_2-mechanisms, with the experimentally-obtained C_2-chemiluminescence images of partially premixed flames for five different cases. The outer slot velocity in all cases V_{air} = 30 cm s^{-1}

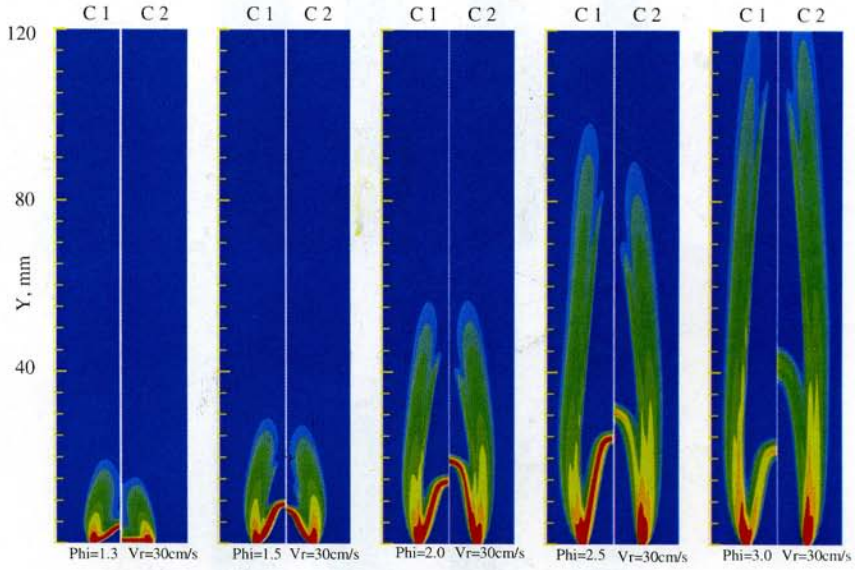

Color Plate XIX (See page 200, Figure 11) Predicted heat release rate contours for the two mechanisms for different levels of partial premixing. For all cases, $V_{react} = V_{air} = 30$ cm s^{-1}

Ninth International Conference on Numerical Combustion, April 7-10, 2002, Sorrento, Italy, pp. 427-428

Ignition and Flame Propagation in an Impulsively Started Fuel Jet

V. R. Katta*, T. R. Meyer*, J. R. Gord, and W. M. Roquemore
Propulsion Directorate, Air Force Research Laboratory, Wright-Patterson Air Force Base, OH
Correspondence E-Mail Address: vrkatta@erinet.com
*Innovative Scientific Solutions, 2766 Indian Ripple Road, Dayton, OH.

Introduction:

It is possible to increase the burning velocity by moving the flame into a region where fuel is traveling at a higher velocity. Studies by McCormack et al.[1] obtained flame speeds up to 15 m/s in vortices and suggested a linear dependence of flame speed on vortex circulation. Ishizuka et al.[2] also reported super-laminar flame speeds along the vortex core, but observed a somewhat reduced dependence on vortex circulation. Cattolica and Vosen[3] performed studies of premixed flame propagation in the wake of a vortex for a combustion-torch configuration in which, ignition of lean premixed gases within a combustion chamber generated a vortex ring of unburned, premixed methane and air. The flame followed in the wake of the vortex eventually propagated though the vortex rollers. In the present paper a numerical investigation has been performed to understand the various flame propagation patterns that were observed in our experimental work on impulsively started jets and the vortices.[4]

Mathematical Model:

The ignition and flame propagation was simulated using an unsteady two-dimensional code known as UNICORN.[5,6] The time-dependent governing equations were expressed in cylindrical-coordinate system. Time and species dependent transport coefficients were employed. The detailed chemistry model employed for describing methane combustion consists of 17 species and 52 elementary reaction steps. The finite-difference forms of the momentum equations were integrated using an implicit QUICKEST scheme, and those of the species and energy equations were obtained using a hybrid scheme of upwind and central differencing. Computations were performed using a 571 X 151 non-uniform grid system covering a physical domain of 70 X 20 mm. The grid system was clustered to yield a local grid spacing of 0.1 mm in both the axial and radial directions. The burner diameter was 5 mm and a flat velocity of 0.135 m/s was used as initial flow condition. A fuel jet was issued into the flow by suddenly increasing the fuel velocity to 6.5 m/s. It consists of CH_4 and O_2 at stoichiometric proportions and 71.5% N_2. A steady annular air flow of 0.135 m/s was used throughout the calculation. Ignition was initiated at a location that is 2 mm above the inflow boundary and at the axis of symmetry. The delay between the start of the jet and the vortex (ignition-delay time, ?) was varied to investigate flame propagation through the injected premixed gases.

Results and discussion:

A jet having a velocity of 6.6 m/s issued into a low-speed parallel flow generates a large mushroom-shaped vortex ahead of the jet. As the jet pushes into this nearly stagnant flow the size of the head vortex increases quickly. Impulsively started jets also generate smaller vortices on the jet column just upstream of the larger vortex. As the head vortex convects downstream it entrains not only the surrounding air but also the secondary vortices on the jet itself. The jet tip is penetrating at a velocity of ~ 4.1 m/s.

Calculations were made for different ignition-delay times and the results for four different cases are shown in Fig. 1 in the form of temperature distributions and fuel-jet structures. These cases were selected to illustrate the different flame-propagation mechanisms. In Case 1, ignition was initiated 0.75 ms after the jet was started. By this time, the tip of the jet has traveled ~ 1 mm past the spark location and provided combustible mixture at the time of ignition. The flame and jet structures at 3.5 ms and 12.3 ms are shown in Fig. 1(a). The average velocity of the flame propagation in the axial direction is ~ 3.4 m/s, which is ~ 17% lower than the cold-jet propagation velocity. Flame in this case is established along the outer core of the fuel jet and is acting like a barrier to the fuel jet. On the other hand, as the laminar burning velocity of the stoichiometric methane-air mixture (0.38 m/s) is much less than the jet velocity, the flame is

propagating with the jet, but at a reduced velocity. This is the case even when the ignition delay was increased to 1.5 ms [Fig. 1(b)]. The average flame propagation velocity remained at 3.4 m/s as the flame wraps around the jet. However, there is a significant difference in the jet structure when it is compared with the one obtained for 0.75-ms ignition delay. Jet in the 1.5-ms case became transitional with the formation of ~ 420-Hz organized structures, while the jet in the 0.75-ms case became laminar at t = 12.3 ms. Flame propagation completely changed when the ignition delay was increased to 6 ms [Fig. 1(c)]. Here, the head of the jet has traveled 24 mm past the ignition location by the time ignition was initiated. Flame has rapidly propagated downstream and caught up with the tip of the jet and the average burning velocity has reached a value 6.5 m/s. Since flame propagated into the head vortex from the wake region the former got expanded. Jet in this case also became transitional with the formation of organized structures. When the ignition delay was increased to 7 ms, flame tried to catch up with the jet tip but could not succeed [fig. 1(d)]. As a result, the initial fuel vortex formed at the tip of the jet got detached from the fuel jet and traveled as a pocket of unburned gas. The average burning velocity for this case has dropped back to 5.5 m/s.

References:

1. McCormack, P. D., Scheller, K., Muller, G. and Tisher, R., *Combustion and Flame*, 19:297 (1972)
2. Ishizuka, S., Takahiro, M., Takahashi, H., Kiminori, K. and Ryo, H. *Combustion and Flame*, 113:542 (1997).
3. Cattolica, R. J. and Vosen, S. R., *Combustion Science and Technology*, 48:77 (1986).
4. Meyer, T. R., Gord, J. R., Katta, V. R., and Roquemore, W. M., Combustion in Impulively Initiated Vortex Rings, 2nd Joint Meeting of the Combustion Institute, 2001
5. Roquemore, W. M., and Katta, V. R., *Journal of Visualization*, 2:257 (2000)
6. Katta, V. R., Goss, L. P. and Roquemore, W. M., *AIAA Journal*, 32:84 (1994).

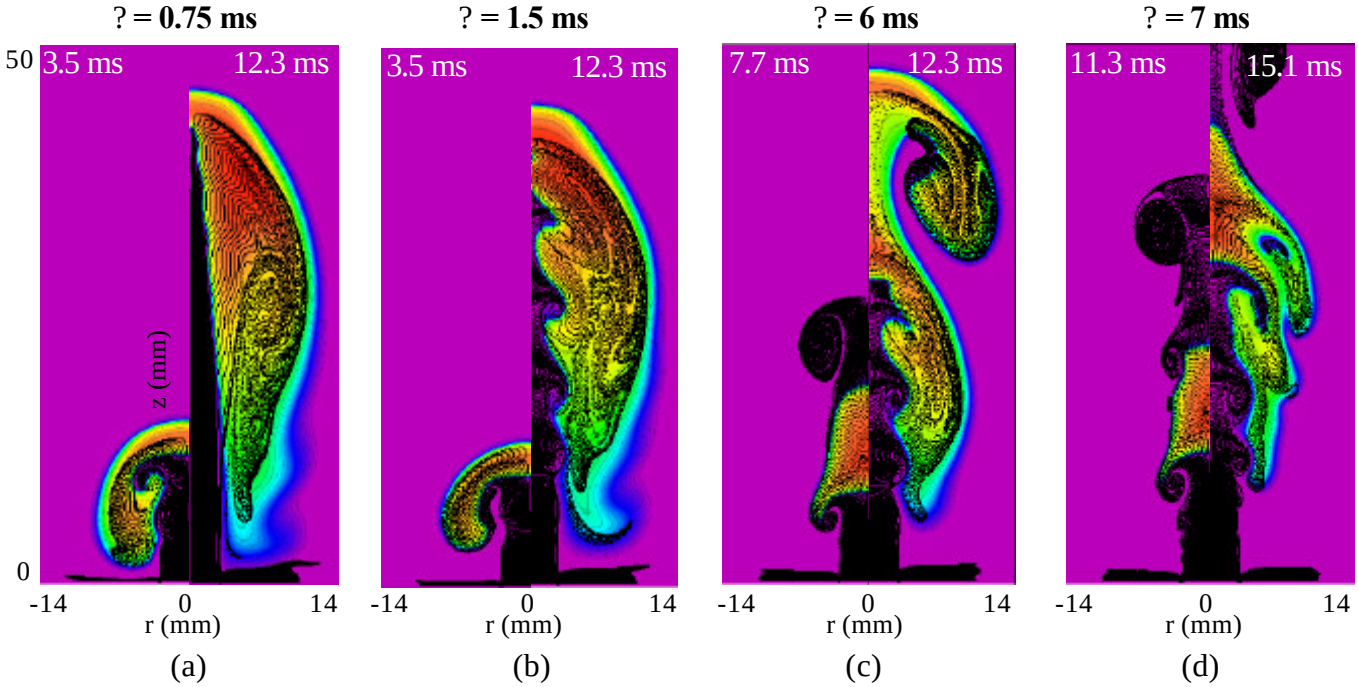

Fig. 1. Influence of ignition-delay time on flame propagation through a 5-mm-diameter fuel jet. Velocity of the jet is 6.5 m/s. In each picture locations of particles injected from fuel jet are superimposed on the temperature distribution. The ignition delays (a) 0.75 ms, (b) 1.5 ms, (c) 6.0 ms, and (d) 7.0 ms represent the time lapses between initiation of ignition and start of jet. Left- and right-half images represent flame structures during the early and later stages of flame propagation, respectively.

41st Aerospace Sciences Meeting and Exhibit
6-9 January 2003, Reno, Nevada

AIAA 2003-666

PAH Formation in an Inverse Diffusion Flame

Viswanath R. Katta*
Innovative Scientific Solutions, Inc.
2766 Indian Ripple Road
Dayton, OH 45440-3638

Linda G. Blevins
Combustion Research Facility
Sandia National Laboratories
Livermore, CA 94550-0969

and

William M. Roquemore
Propulsion Directorate
Air Force Research Laboratory
Wright-Patterson Air Force Base, OH 45433

Abstract:

Particle residence time, thermal environment, and chemical environment are important factors in soot formation processes in flames. Recent experimental studies on inverse diffusion flames revealed that the soot generated in these flames is not fully carbonized. To understand the chemical and physical structure of the early soot formed in these flames, knowledge of the flow dynamics of inverse diffusion flames is required. A time-dependent, detailed-chemistry computational-fluid-dynamic (CFD) model is developed for simulation of the ethylene-air inverse jet diffusion flame. Steady-state simulations show that all the polycyclic aromatic hydrocarbon (PAH) species are produced outside the flame surface on the fuel side. Unsteady simulations reveal that buoyancy-induced vortices establish outside the flame due to the low fuel velocity (~7 cm/s). Unlike in normal diffusion flames, these vortices appear mostly in the exhaust jet. The 17.2 Hz vortices increase mixing, causing PAH species to distribute more evenly in downstream locations than in upstream locations. Computed trajectories of 20 nm particles injected along the 1200-K fuel-side contour line indicate that soot precursor particles are alternately reheated and cooled while they are entrained into and advected by the buoyancy-induced vortices. This flow pattern could explain the experimentally observed large size and slight carbonization of IDF soot.

Introduction:

Soot is an undesirable combustion product and its formation represents one of the most complex chemical systems in flames. Considerable progress has been made in recent years on understanding the chemical and physical aspects of soot formation in hydrocarbon flames. Soot particles containing several thousand carbon atoms are formed from simple fuel molecules within a few milliseconds. After the first aromatic rings (such as benzene and small PAHs) are formed in the gas phase, acetylene and other molecules react with these small PAHs to form larger PAHs[1]. The first soot particles are thought to be formed when two or more PAHs react to form a three dimensional particle. This process is known as particle inception[2]. The soot particles formed interact with the gas-phase molecules by the addition of acetylene to their surfaces (surface growth) and by the reaction with molecular oxygen and/or hydroxyl radical (oxidation). Another process thought to increase soot mass is the collision of PAHs with a soot particle.

Several experimental and numerical investigations of soot formation have been performed using coflow and counterflow diffusion flames[3-6]. A few have focused on the importance of soot particle pathways (i.e., residence time, temperature, and chemistry)[7-8]. Santoro et al.[7] used soot volume fraction, temperature, and velocity measurements from an ethylene-air jet diffusion flame to examine the soot growth process along individual particle paths. Based on experimental data, they argued that the soot formation rate increases in the annular region of the flame due to an increase in residence time. Lin and Faeth[8] found that the direction of soot particle movement with respect to the flame sheet is important. They argued that if soot particles forming on the fuel rich side of the flame remained entrained in the fuel-rich region for a long time before crossing the flame surface, then surface growth could be enhanced. In contrast, Lin and Faeth[8] argued that the amount of soot generated could be reduced if the soot particle is made to cross the flame surface quickly.

This material is declared a work of the U.S. Government and is not subject to copyright protection in the United States.

One way to alter the soot particle pathway is to use inverse diffusion flames. Wu and Essenhigh[9] studied inverse diffusion flames by exchanging the fuel and air jets of normal jet diffusion flames. They found that, in some cases, inverse diffusion flames are essentially non-luminous with no apparent soot formation. However, in some other cases, especially at higher air jet velocities, a luminous region forms with an orange-yellow cap on top of the blue cone-shaped flame. Recently, Blevins et al.[10] further investigated inverse diffusion flames under high-air-flow-rate conditions and found that the soot exiting an ethylene inverse flame is high in hydrogen and PAH content and is chemically similar to precursor particles. These authors termed the particles "young soot." The authors found that the soot was large and partially carbonized relative to precursor particles from normal flames. A complementary numerical study was performed by Davis et al.[11] Thermal and fluid dynamic aspects of the flame were investigated by incorporating a global chemical kinetics model. Particle tracking in the steady state simulations showed that inverse flame soot is expected to cool and quench immediately after formation; it should not grow excessively or carbonize. The experimentally observed soot maturation may be caused by unsteadiness not captured in the steady-state solutions. The purpose of this paper is to use time-dependent numerical modeling with detailed chemistry to examine this possibility.

In the present work, a numerical simulation of the inverse diffusion flame examined by Blevins et al.[10-12] is made using a well-tested CFD code and a detailed chemical kinetics model for PAH formation in ethylene flames. Numerical results obtained for the steady-state and unsteady flames are compared. Calculations were also made by injecting nanometer-size particles to determine the thermal and chemical time histories for precursor particles in the dynamic inverse flame.

Experiment:

A tri-axial inverse diffusion flame (IDF) burner having 1-cm-diameter central air jet and a 3-cm-diameter co-annular fuel jet is used[10-12]. The airflow was 32 mg/s (~35 cm/s) and the ethylene (C_2H_4) flow was 49 mg/s (~7 cm/s). The visible flame height was 3.5 cm, and an orange cap constituted 90% of the height. A N_2 blanket flow necessary to prevent flame formation between the fuel and room air was passed through the outer annulus of the burner. A nearly invisible soot stream exits the flame. The flame was photographed for comparison with predictions. Extensive experiments have been previously performed with this flame[10-12].

Mathematical Model:

A time-dependent, axisymmetric mathematical model known as UNICORN (Unsteady Ignition and Combustion using ReactioNs)[13,14] is used to simulate the potentially unsteady jet diffusion flames considered in this study. It solves for u- and v-momentum equations, continuity, and enthalpy- and species-conservation equations on a staggered-grid system. The body-force term due to the gravitational field is included in the axial-momentum equation for simulating vertically mounted flames. A clustered mesh system is employed to trace the large gradients in flow variables near the flame surface. A detailed chemical-kinetics model of Wang and Frenklach[15] is incorporated into UNICORN for the investigation of PAH formation in C_2H_4 flames. It consists of 99 species and 1066 elementary-reaction steps. Thermo-physical properties such as enthalpy, viscosity, thermal conductivity, and binary molecular diffusion of all the species are calculated from the polynomial curve fits developed for the temperature range 300 - 5000 K. Mixture viscosity and thermal conductivity are then estimated using the Wilke and Kee expressions, respectively. Molecular diffusion is assumed to be of the binary-diffusion type, and the diffusion velocity of a species is calculated using Fick's law and the effective-diffusion coefficient of that species in the mixture. A simple radiation model based on the optically thin-media assumption is incorporated into the energy equation. Only radiation from CH_4, CO, CO_2, and H_2O is considered in the present study[16].

The finite-difference forms of the momentum equations are obtained using an implicit QUICKEST scheme[17], and those of the species and energy equations are obtained using a hybrid scheme of upwind and central differencing. At every time step, the pressure field is accurately calculated by solving all the pressure Poisson equations simultaneously and using the LU (Lower and Upper diagonal) matrix-decomposition technique. The boundary conditions are treated in the same way as that reported in earlier papers[18].

The IDF[10-12] considered in the present study has a computed flame height of ~ 20 mm. Since the formation of PAHs is important not only in the flame zone but also in the exhaust products, axisymmetric calculations are made on a physical domain of 200 mm x 50 mm using a 401 x 121 non-uniform grid system. The computational domain is bounded by the axis of symmetry and an outflow boundary in the radial direction and by the inflow and another outflow boundary in the axial direction. The outer boundaries in the z and r directions are located sufficiently far from the burner exit (~ 20 inner-tube diameters) and the symmetry axis (~ 5 inner-tube diameters), respectively, such that propagation of boundary-induced disturbances into the region of interest is minimized. Flat velocity profiles are imposed at the fuel and air inflow boundaries, while an extrapolation procedure with weighted zero- and first-order terms is used to estimate the flow variables at the outflow boundary.

The simulations presented here are performed on a Pentium III 1-GHz Personal Computer with 1.2 GB of memory. Typical execution time is ~120 s/time-step.

Steady state flames are usually obtained in about 1000 time steps starting from the solution obtained using the combustion part of the kinetics (i.e., not including PAH).

Results and Discussion:

A direct photograph of the experimental flame is shown in Fig. 1 along with computed temperature contours. This luminous flame is well attached to the burner rim and has a flame height of about 18 mm based on the lower bright yellow region of the computation. The blue emission in the base region of the photographed flame (where very little soot is generated) indicates that the flame slightly curves in as the air jet emerges from the burner. Unlike a normal diffusion flame, the IDF doesn't expand in the radial direction. This is partially due to the low stoichiometric equivalence ratio of 0.292 for C_2H_4-air combustion, which establishes the flame surface on the air side. The flame shape may also be caused by the high air-to-fuel velocity ratio (5:1) used for this flame. Overall, the simulated flame shape matches well with that of the experiment. The yellow contour, which represents a temperature of 1800 K, matches with the outer surface of the orange emission in the experiment.

Model Validation Studies:

The CFD model UNICORN has been extensively validated in the past by simulating various steady and unsteady counterflow[13,19] and coflow[13,20] jet diffusion flames and by comparing the results with experimental data. This gives confidence that UNICORN can simulate the structure of dynamic flames accurately. However, the integration of C_2H_4 and PAH chemistry into UNICORN needs to be validated to establish the accuracy of the present predictions. Validation is achieved by simulating the burner-stabilized flame extensively investigated by Harris et al.[21] and Wang and Frenklach.[15]

The flame chosen is a premixed C_2H_4/O_2/Ar flame with an equivalence ratio of 2.76. The velocity of the cold reactants is 7.8 cm/s. The Ar:O_2 mole ratio is 79:21. Two-dimensional calculations for this burner-stabilized flame are made by enforcing periodic boundary conditions at the two boundaries in the axial direction and by using the measured temperature profile as input. These two-dimensional calculations eventually resulted in a one-dimensional flame with all the variations in the radial direction diminished.

Variations in concentrations of several species with respect to flame height are compared with experimental data in Fig. 2. The temperature profile used in these calculations has a peak value of 1901 K [Fig. 2(a)]. The calculations predict the proper trends in major species concentrations, such as the decrease in O_2 and C_2H_4 concentrations and the increase in CO and CO_2 concentrations. However, the computed H_2 concentrations are somewhat lower than the measurements. This discrepancy was also observed by Wang and Frenklach[15] while modeling this flame using CHEMKIN and was attributed to the higher concentrations of OH obtained with the present chemical mechanism.

The experimental and measured mole fractions of CH_4, C_2H_2, C_4H_4, and C_4H_6 at different heights are compared in Fig. 2(b). The key intermediate species are generally predicted well by the model. The computed peak concentrations of these species are within a factor of two of the measured values, which is probably within experimental uncertainty. Similarly, the predicted concentration profiles of one-ring aromatics compare well with the measured ones shown in Fig. 2(c). The steady rise of aromatics is typical of C_2H_4 burner-stabilized flames and is well reproduced by the Wang/Frenklach mechanism. Based on the comparisons shown in Fig. 2 it is assumed that the modified UNICORN model can reasonably simulate an C_2H_4 flame.

Grid Independence:

To determine the grid sensitivity in simulating the IDF shown in Fig. 1, several calculations using UNICORN and adopting different grid systems were performed. The photograph of the flame in Fig. 1 suggests that the surface of the flame is smooth and its structure resembles that of a laminar steady state flame. Calculations were initially performed on a 100 mm x 50 mm physical domain using a 251 x 91 grid system omitting the unsteady terms in the model. The resulting laminar flame is shown in Fig. 1. The minimum spacing achieved with this grid system was 0.2 mm in both the r and z directions. To minimize the grid-stretching effects on the simulations, this minimum spacing was enforced everywhere in the neighborhood of the high-temperature region. Even though the simulated flame matched well with that of the experiment (Fig. 1), calculations were also made on a 401 x 121 grid system to determine the grid sensitivity of the results. The minimum spacing achieved with this grid system was 0.05 mm and 0.2 mm in the r and z directions, respectively. The physical domain was extended to 200 mm in the axial direction for this fine grid system.

The steady state flames obtained with the coarse and fine mesh systems are compared in Fig. 3 by plotting iso-temperature color contours. Both grid systems predicted the same flame height and peak temperature (2440 K). On the other hand, the fine grid system seems to yield slightly sharper temperature profiles on the fuel side and a shorter core length of the air jet for this IDF.

The temperature and species distributions along the centerline obtained with the coarse and fine meshes are compared in Fig. 4. While most of the species are predicted similarly by the two mesh systems, the fine

mesh predicts lower concentrations of heavier aromatics such as pyrene compared to those predicted by the coarse mesh. Similar observations can be made by comparing the radial distributions (Fig. 5) of various species obtained with these two grid systems at 16 mm above the burner. The biphenyl concentration computed with the fine mesh is slightly lower than that computed with the coarse mesh. The comparisons shown in Figs. 3-5 suggest that the results obtained with the 251 x 91 grid system are nearly grid independent. However, to avoid any concerns that might arise in the predictions of PAH concentrations, the 401 x 121 grid system is used throughout the present work.

Dynamics of the Inverse Diffusion Flame:

Various studies of normal jet diffusion flames (i.e., with the fuel jet at the center) suggest that when the annular air flow is low (< 40 cm/s), the flame tends to flicker with the development of buoyancy induced vortices outside the flame surface. Generally, the flickering frequency for these flames is independent of or weakly dependent on fuel-jet diameter, fuel type, and air-flow velocity. The low annular fuel velocity of ~7 cm/s and the high-enthalpy C_2H_4 fuel (flame temperatures are about 2400 K) used for the IDF create an appropriate environment for the flame to flicker. The experimental image shown in Fig. 1 was obtained with a long shutter opening (~ 1 s); hence, the photo would not capture the instantaneous structure of a flame that might be oscillating at a frequency of 10-20 Hz.

To investigate the possibility that the IDF oscillates naturally, unsteady calculations were performed for the same flow conditions. Surprisingly, the unsteady simulations resulted in a flame with large vortices forming outside the flame surface. However, unlike in normal diffusion flames, formation and advection of these vortices is seen only in locations downstream of the flame tip. An instantaneous image of the simulated unsteady IDF is shown in Fig. 6. Here, iso-contours of temperature and benzene concentration are plotted in the left and right halves, respectively. The temperature field upstream of the flame tip is similar to that of the steady state flame shown in Fig. 3. On the other hand, a large vortical structure of ~ 30 mm in length is evident in the downstream locations. Even though the temperature of the gases contained in the vortex is less than 1000 K at this instant, a significant amount of benzene is entrained in the vortex.

The unsteady flame in Fig. 6 is oscillating at a low frequency with large toroidal vortices forming naturally outside the flame surface. It is important to note that no artificial perturbation is introduced in the calculations for the development of these outer vortices. In the presence of gravitational force, the acceleration of hot gases along the flame surface generates the outer structures as part of the solution. However, since the flame height is only 18 mm, much of the vortex (or instability) growth takes place downstream of the flame tip in the exhaust gases. A close examination of the flame images obtained at several instants suggest that the flame tip is also oscillating weakly. The computed frequency corresponding to the passage of these outer vortices (also known as the flame-flickering frequency) is 17.2 Hz.

Evolutions of the flame at 40 mm and 120 mm above the burner are shown in Figs. 7(a) and 7(b), respectively. These plots represent the changes in radial distributions of naphthalene (left) and benzene (right) concentrations with time as seen by an observer looking at the flame at a given height. The changes in temperature at these heights are also shown by superimposing iso-temperature contour lines. Strong fluctuations in PAH species concentrations are evident at z = 40 mm. It is interesting to note that an island of high temperature (> 1200 K) appears at the center between 20 ms and 45 ms where naphthalene and benzene concentrations are low. The strong vortex is pinching off the products from the jet and rolling them into itself. This is also evident in the instantaneous plot shown in Fig. 6. At this instant, hot products and benzene are cut off by the vortex at z = 50 mm. The vortex has dissipated significantly by the time it reaches the height of 120 mm above the burner. Only a weak roll-up of PAH species by the vortices is observed at this location [Fig. 7(b)]. The remnant of the jet pinching that occurred at upstream locations causes the species concentrations to fluctuate at the center. In contrast to those observed at z = 40 mm, the concentrations of naphthalene and benzene at 120 mm are high in the island of high temperature (> 750 K) at the center between 27 ms and 42 ms.

Inadequacy of Steady-State Simulations:

The instantaneous temperature field of the unsteady flame (Fig. 6) downstream of the flame tip is different from that of the steady state flame (Fig. 3). However, such comparison between the steady state and unsteady flows is not justified as the solution shown in Fig. 6 exists only during a fraction of a second. Solutions plotted at other instants look very different from that shown in Fig. 6. To determine the significance of flow unsteadiness on the generation of PAH species, a more reasonable comparison was made by constructing a time-averaged flame from several instantaneous solutions. For example, time-averaged temperature (T_{ave}) at each grid point is obtained using the formula

$$T_{ave} = \frac{1}{\tau}\int_{t_0}^{t_0+\tau} T \cdot dt$$

Here, τ is the period of oscillation and t_0 is an arbitrary time in the simulation.

The distribution of the time-averaged temperature of the unsteady flame and the temperature distribution of the steady flame are compared in Fig. 8(a). The peak temperatures in both images are the same and are equal

to 2440 K. As expected, these distributions are similar in the regions upstream of the flame tip where the flame oscillations are negligibly weak. The low temperature region outside the flame surface and the high temperature region near the axis of symmetry are broader and more diffuse in the time-averaged result than in the steady result. The formation and advection of vortices outside the flame surface (i.e., on the fuel side) enhances mixing between the high-temperature products and cold fuel.

Distribution of time-averaged benzene concentration of the unsteady flame and that of the steady state flame are compared in Fig. 8(b). Since most of the benzene is produced in the low-temperature region (< 1200 K) on the fuel side of the flame, its concentration distribution is significantly affected by the vortex dynamics. The peak benzene concentration for the steady flame is reduced by ~20% from its value of 150 ppm in the time-averaged flame. The flame radius based on benzene concentration at a flame height of 40 mm increases from 7.5 mm for the steady calculation to 10 mm for the time-averaged calculation. Weak oscillations of the flame at locations upstream of the tip are evident in the benzene concentration at z = 8 mm. The comparisons made in Fig. 8 suggest that unsteady effects can not be ignored, especially in the low-temperature regions of the IDF. They further suggest that a steady state simulation is not adequate in predicting the distributions of species, especially those formed in temperatures < 1200 K.

In recent measurements of IDF PAH amounts,[10] species samples were collected in the exhaust products at locations downstream from the high-temperature flame (~ 150 mm from the burner). To understand the differences one might expect by performing a steady state simulation of this flame rather than an unsteady one, time-averaged radial distributions of several species at 180 mm above the burner are compared with the steady state solutions in Fig. 9. In general, the concentration of every species is over predicted by the steady state simulations. The products that are generated inside and within the high-temperature region, such as CO and CO_2, appear in higher concentrations everywhere in the steady state simulations. On the other hand, PAH species, which are generated outside the flame in the lower temperature regions, appear in higher concentrations in the steady-state flame at the center and in lower concentrations away from the center. The combustion products CO and CO_2 are generated in large quantities and are diffused significantly on a molecular level. As a result, the vortices appearing in the unsteady simulation do not effectively distribute these abundant species. On the other hand, PAH species are generated in small quantities and are confined close to the center; hence, they are mixed more effectively by the vortices. A close examination of the results in Fig. 9 suggests that a 15 % to 20 % reduction in PAH concentrations at the center occurs due to the presence of vortices in the unsteady simulation.

Prediction of Thermal Environment for PAH's:

The formation of benzene in flames initiates the generation of PAH species from fuel molecules. Some of the lower-weight PAH's are likely to remain in the gaseous state, while some of the heavier PAH's may condense on particles. Small and large PAH may also participate in surface growth. Particle tracking is used to examine the time/temperature/PAH chemistry pathways of incipient soot particles placed in the flow.

The unsteady IDF calculations are continued from the solution shown in Fig. 6 by introducing 20 nm particles into the flowfield. Since soot inception is thought to occur around 1200 K on the fuel side, these nanoparticles are introduced along the 1200-K contour line. Motion of the particles at every particle time step (which is set as $1/10^{th}$ of the flow time step) is calculated by including thermophoretic, gravitational, drag and viscous forces.[22] The instantaneous distribution of the particles after 120 ms of real-time calculations is shown in Fig. 10 along with the instantaneous temperature (left) and benzene concentration (right) fields. While particle locations are shown in black, the line (1200-K contour) along which these particles were released is shown in white. No particles were released from the air-side 1200-K line.

Figure 10 suggests that particles nearly follow the gas flow. Particles enter the vortex along with the gaseous benzene. This is an important feature of the dynamic flame as the entrained particles have longer residence times in the vortex and are more susceptible to coagulation, surface condensation, and/or surface growth. This trend may explain the experimentally observed large size of soot emitted by the IDF. The residence times and the temperature history of the particles are shown in Fig. 11 for particles released from different locations. All the particles start with a temperature of 1200 K; however, their temperatures decrease rapidly initially as they move away from the flame. As the particles are entrained into the vortex, they are brought closer to the flame and their temperatures increase by more than 100 K. This reheating of particles may lead to a slight degree of carbonization of the particles relative to precursor particles, consistent with the experimental finding. Particle trajectories in the steady state flame did not show reheating of particles.

The spikes in temperature for the particles injected from different heights indicate that all the particles formed along the 1200-K line are entrained into the vortices and are subjected to the reheating process. In fact, Fig. 11 further suggests that the particles entrained into the vortices roll inside the vortex and are reheated again and again as they advect downstream. This is consistent with the peaks appearing in the benzene concentration and temperature distributions shown in Figs. 6 and 7. Therefore, the vortices appearing in IDFs not only increase the mixing between the species but

also alter the thermal environment for the entrained species and particles. The latter process could lead to additional soot formation, enhanced surface growth, more coagulation, and/or partial carbonization of the young soot. Experimental verification of the computed flow field is in progress.

Conclusions:

A time-dependent, axisymmetric, detailed-chemistry CFD model was developed for the simulation of C_2H_4-air inverse jet diffusion flames. PAH formation was simulated using the 99-species, 1066-reactions mechanism of Wang and Frenklach. The CFD model (UNICORN) was validated by simulating a burner-stabilized premixed flame and comparing the results with measurements. Both the steady-state and unsteady simulations for the IDF were performed. Steady-state simulations yielded a laminar flame and predicted that all PAH species are produced outside the flame surface on the fuel side. Unsteady simulations revealed that buoyancy-induced vortices established outside the flame surface due to the low fuel jet velocity. No artificial perturbation was used in these unsteady simulations. Unlike in normal diffusion flames, vortices in the IDF appeared mostly in the exhaust gases. It was found that the advection of these vortices at 17.2 Hz increased mixing of species and caused PAH species to distribute more uniformly in downstream locations. Trajectories of 20 nm particles injected along the fuel-side 1200-K contour line indicated that soot-precursor particles can be reheated while they are entrained into and advected by the buoyancy-induced vortices. The computed unsteady flow field may explain the slight maturation of young soot from IDFs observed experimentally.

Acknowledgement:

Financial support for this work was provided by Strategic Environmental Research and Development Program (SERDP), the Air Force Office of Scientific Research (AFOSR), the Air Force Contract #F33615-00-C-2068, and the National Aeronautics and Space Administration (NASA).

References:

1. Richter, H. and Howard, J. B., Prog. *Energy Combust. Sci.* 26:565 (2000)

2. Kennedy, I. M., Prog. *Energy Combust. Sci.* 23:95 (1997)

3. Kaplan, C. R., and Kilasanath, K., Combustion and Flame, Vol. 124, 2001, pp. 275-294.

4. Smooke, M. D., Mcenally, C. S., Pfefferle, L. D., Hall, R. J., and Colket, M. B., Combustion and Flame, Vol. 117, 1999, pp. 117-139.

5. Sugiyama, G., Proceedings of the Combustion Institute, The Combustion Institute, PA, Vol. 25, 1994, pp. 601-608.

6. Du, J., and Axelbaum, R. L., Combustion and Flame, Vol. 100, 1995, pp. 367-375.

7. Santoro, R. J., Yeh, T. T., Horvath, J. J., and Semerjian, H. G., Combustion Science and Technology, Vol. 53, 1987, pp. 89-115.

8. Lin, K.-C., and Faeth, G. M., Journal of Propulsion and Power, Vol. 12, 1996, pp. 10-17.

9. Wu, K._T., and Essenhigh, R. H., Proceedings of the Combustion Institute, The Combustion Institute, PA, Vol. 20, 1984, pp. 1992-1932.

10. Blevins, L. G.; Fletcher, R. A.; Benner, B. A.; Steel, E. B.; Mulholland, G. W. *Proceedings of the Combustion Institute,* Vol. 29, 2002.

11. Blevins, L. G., Yang, N. Y. C., Mikofski, M. A., Mulholland, G. W., and Davis, R. W., Paper AIAA-003-0985, AIAA 41st Aerospace Sciences Meeting and Exhibit, Reno, Nevada, January 2003.

12. Blevins, L. G., Yang, N. Y. C., Mulholland, G. H., and Davis, R. W., and Steel, E. B., Preprints of Symposia-American Chemical Society, Division of Fuel Chemistry, 2002, 47(2), pp. 740-744.

13. Roquemore W. M., and Katta, V. R., *Journal of Visualization*, in press Jan. 2000.

14. Katta, V. R., and Roquemore, W. M., *Combustion and Flame*, Vol. 100, No. 1, 1995, p. 61.

15. Wang, H., and Frenklach, M., *Combustion and Flame*, Vol. 110, No. 1, 1997, p. 173.

16. Annon., Computational Submodels, International Workshop on Measurement and Computation of Turbulent Nonpremixed Flames., http://www.ca.sandia.gov/tdf/Workshop/Submodels.html, 2001.

17. Katta, V. R., Goss, L. P., and Roquemore, W. M., *AIAA Journal*, Vol. 32, No. 1, 1994, p. 84.

18. Katta, V. R., Goss, L. P., and Roquemore, W. M., *Int. J. Num. Methods Heat Fluid Flow*, Vol. 4, No. 5, 1994, p. 413.

19. Katta, V. R., Carter, C. D., Fiechtner, G. J., Roquemore, W. M., Gord, J. R., and Rolon, J. C., in *Twenty-seventh Symposium (International) on Combustion*, The Combustion Institute, Pittsburgh, PA, 1998, p. 98.

20. Katta, V. R., and Roquemore W. M., *AIAA Journal*, Vol. 36, No. 11, 1998, p. 2044.

21. Harris, S., Weiner, A. M., and Blint, R., Combustion and Flame, Vol. 72, 1988, pp. 91-109.

22. Waldmann, and Schmit, K. H., "Therophoresis and Diffusiophoresis of Aerosols," in Aerosol Science, Edited by Davies, C. N., Academic Press, 1966, pp. 137-162.

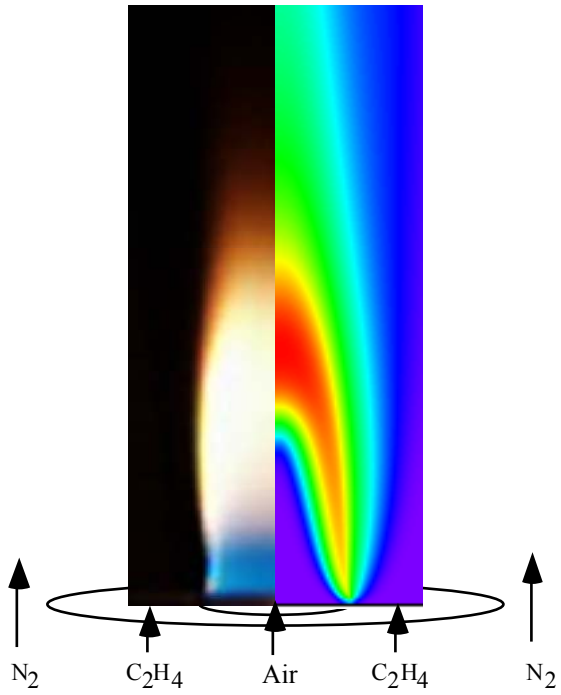

Fig. 1. Inverse diffusion flame (IDF) setup. Direct photograph of the experimental flame (left) and steady-state solution obtained using UNICORN.

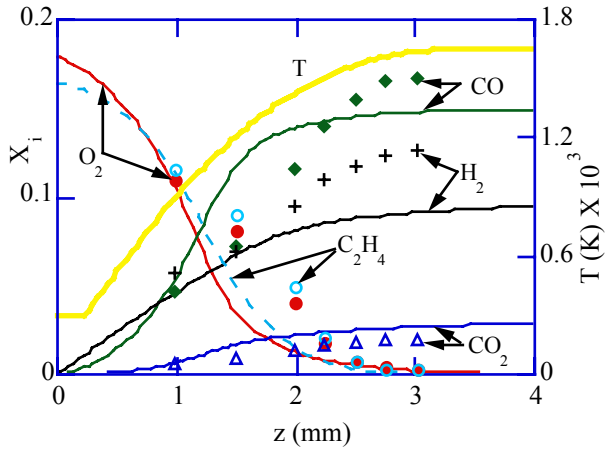

(a)

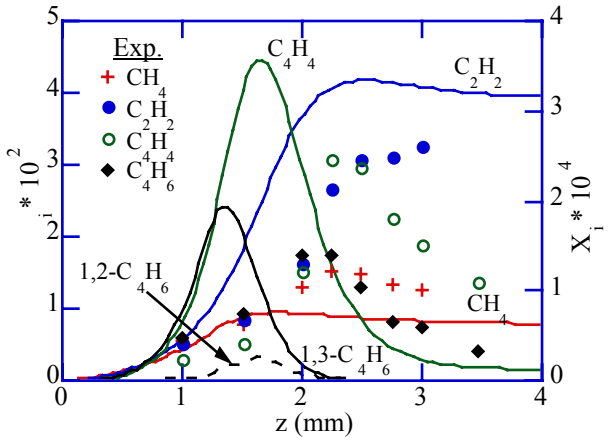

(b)

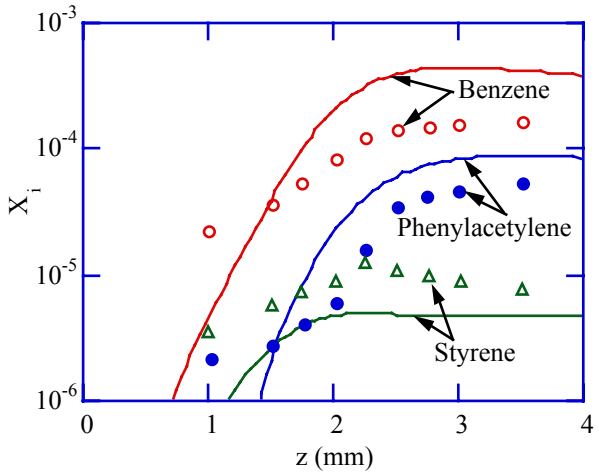

(c)

Fig. 2. Comparison between measured and computed species distributions for the burner-stabilized premixed flame. Calculations for this one-dimensional flame were made using UNICORN and by imposing temperature profile shown in (a).

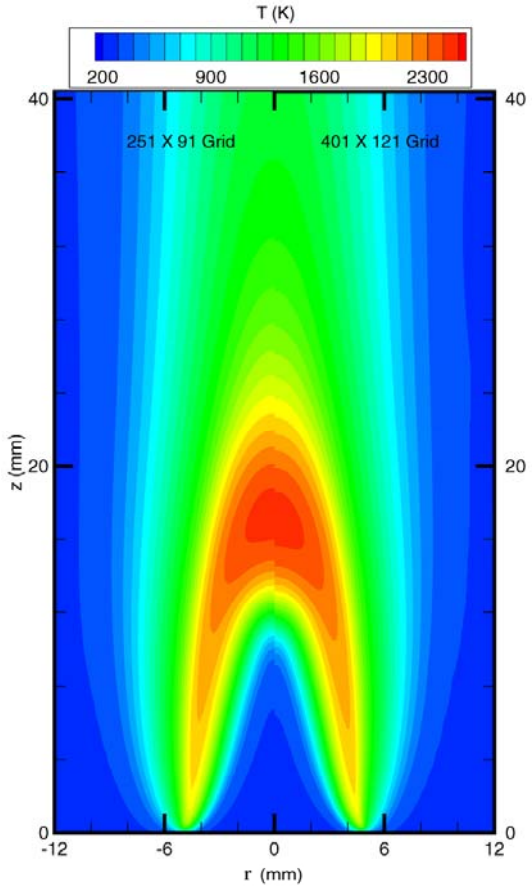

Fig. 3. Effect of grid resolution on temperature field computed for IDF. Coarse-mesh (left) and fine-mesh (right) calculations utilized grid spacings of 0.2 and 0.05 mm, respectively.

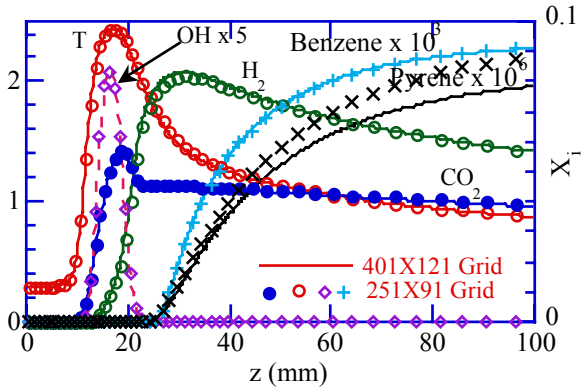

Fig. 4. Effect of grid resolution on temperature and species distributions along the centerline.

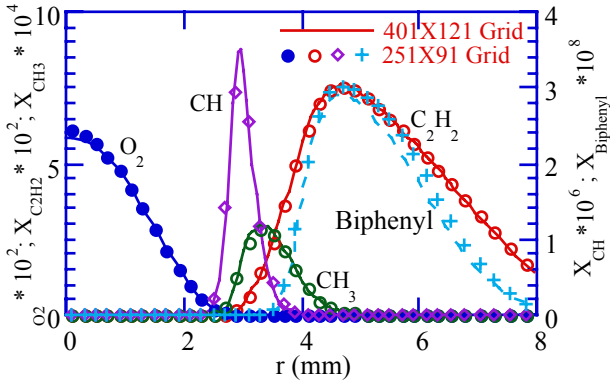

Fig. 5. Effect of grid resolution on species distributions in radial direction at z = 16 mm.

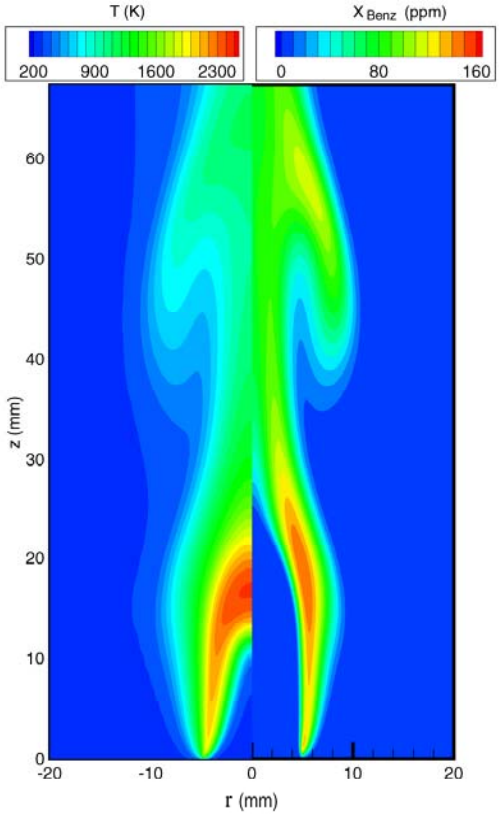

Fig. 6. Instantaneous temperature (left) and benzene concentration (right) obtained in unsteady simulations.

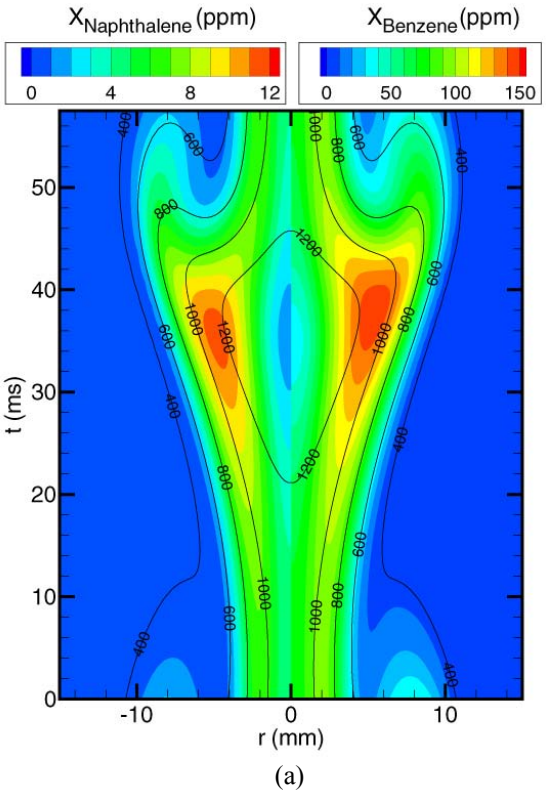

(a)

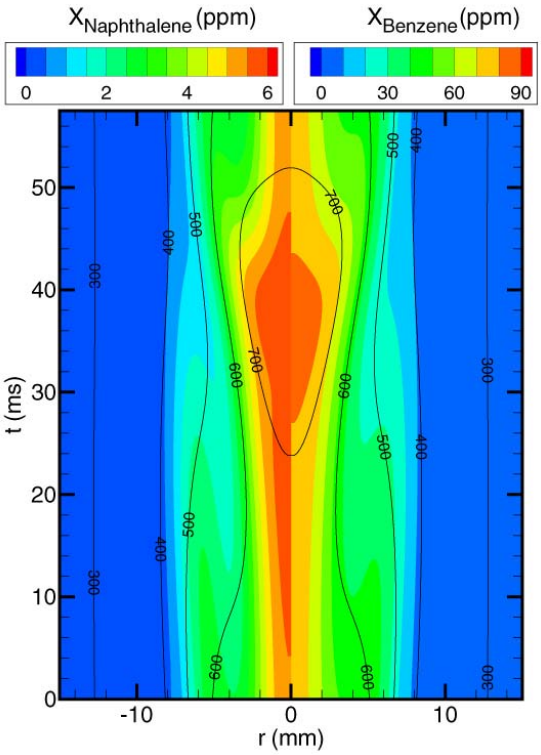

(b)

Fig. 7. Evolutions of benzene (right) and naphthalene (left) concentrations at axial distances of (a) 40 and (b) 120 mm from the burner exit.

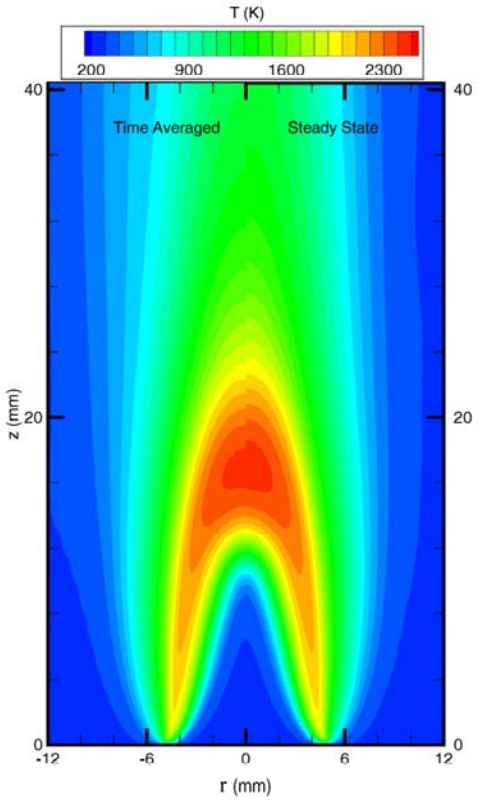

Fig. 8. Time-averaged (left) and steady-state (right) data for IDF. (a) Temperature, (b) benzene concentration.

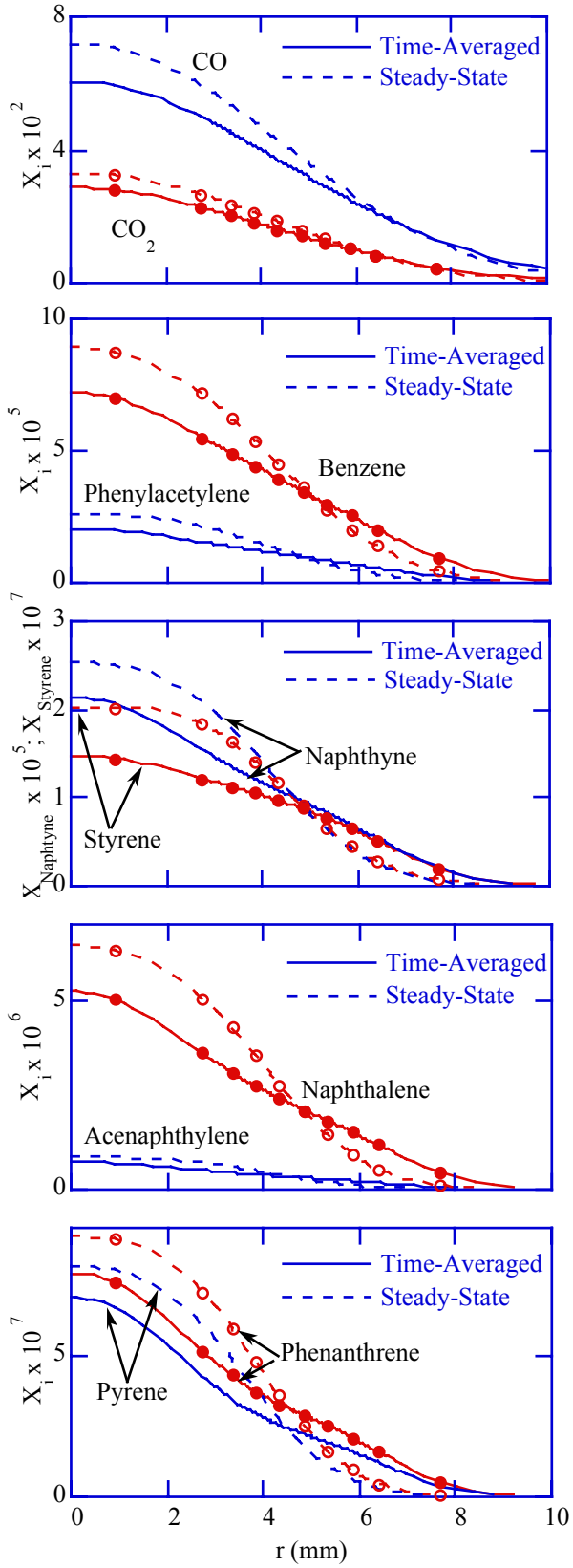

Fig. 9. Comparison of time-averaged and steady-state data for different species at z = 180 mm. Time averaged data was generated from several instantaneous solutions obtained during one flicker period of 58 ms.

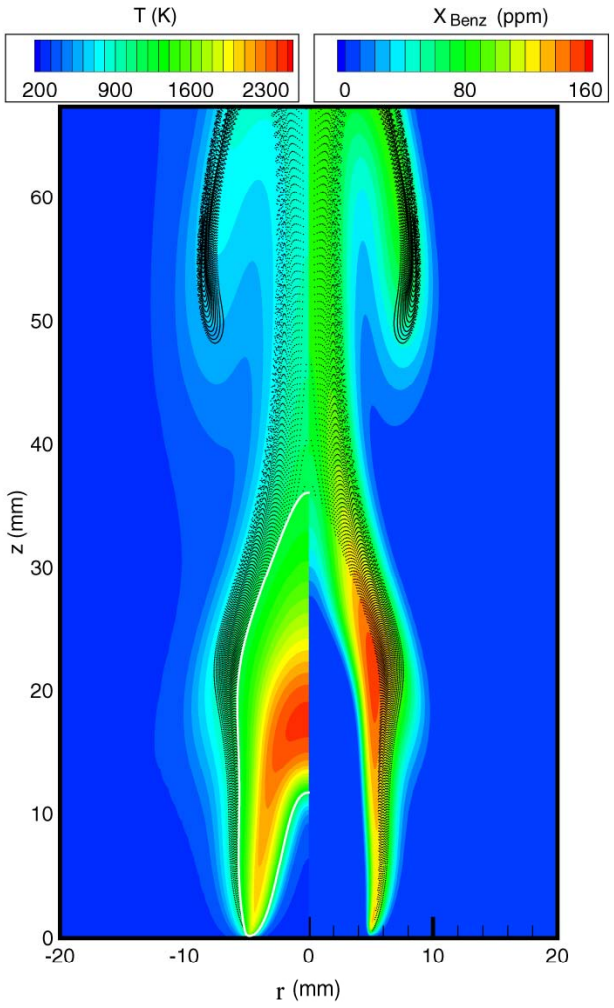

Fig. 10. Instantaneous locations of 20-nm-size particles superimposed on temperature (left) and benzene concentration (right). Nanoparticles were injected from 1200-K-iso-temperature line on fuel side (outer white line).

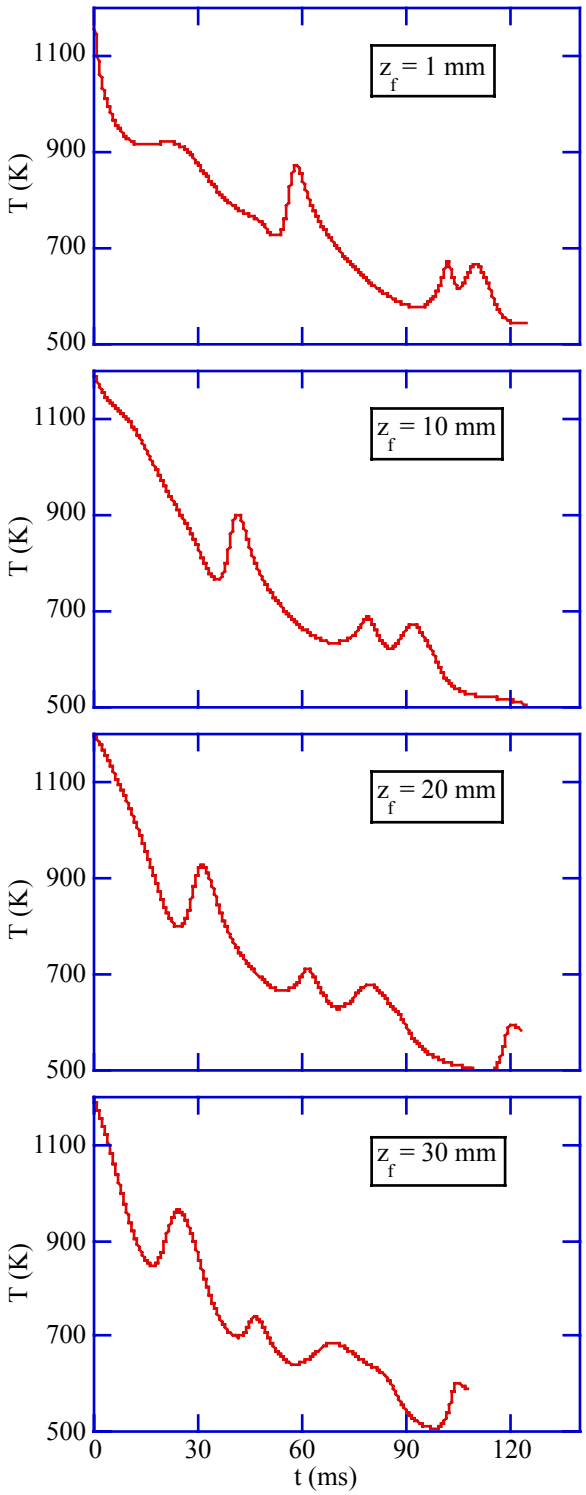

Fig. 11. Temperature history of the particles released from 1200-K location at different heights above the burner exit.

41st Aerospace Sciences Meeting and Exhibit
6-9 January 2003, Reno, Nevada

AIAA 2003-1018

Effect of Gravity on Burner-Stabilized and Lifted Partially Premixed Flames

Xioa Qin, Ishwar K. Puri*, Suresh K. Aggarwal, and V. R. Katta†

Department of Mechanical and Industrial Engineering m/c 251
University of Illinois at Chicago, 842 W. Taylor St., Chicago, IL 60607–7022, USA

ABSTRACT

The effect of gravity on burner-stabilized and lifted methane–air partially premixed flames is numerically investigated. A comprehensive, time-dependent computational model is used to simulate the flame transition from normal gravity to zero gravity. The model employs a detailed description of methane-air chemistry and transport properties, with the effect of thermal radiation modeled by the optically-thin assumption. The amount of radiative heat loss is quantified in terms of a radiation fraction (c_{rad}), defined as the ratio of total radiation heat loss to the total heat release. It is found that the effect of radiation is small for 1–g partially premixed flames, i.e., $c_{\mathrm{rad}} \approx 0.1$. However, for the corresponding 0–g flames, the thermal radiation effect is significantly higher, $c_{\mathrm{rad}} \approx 0.5$, since the flame volume increases in the absence of buoyancy. This in turn causes the flame temperature to decrease and results in weaker reaction activity. The effect of coflow is to counteract the effect of gravity on PPFs, as the former enhances the advection of oxidizer to the outer nonpremixed reaction zone, and thus, increases the overall reaction rate.

INTRODUCTION

Partially premixed flames (PPFs) are hybrid flames containing multiple reaction zones. They can exploit the advantages of both nonpremixed and premixed flames regarding safety, lower pollutant emission levels, and flame stability [1,2]. A double (or triple) flame can be established on an axisymmetric burner by introducing a fuel rich mixture through an inner tube and air (or a lean mixture) from a concentric outer tube [3]. Partially premixed flames occur in many applications including gas-fired domestic burners, industrial furnaces, and Bunsen burners. Partially premixed combustion may also be encountered in future space applications or spaceship fires, and it is meaningful to investigate gravitational effects on partially premixed flame from this perspective [4,5].

The effects of gravity on both premixed and nonpremixed flames have been extensively investigated during the last decade. Law and Faeth [5], Kono et al. [6], and Ronney [7] have provided reviews of experimental and computational studies dealing with 1–g and microgravity (μ–g) flames under different configurations. However, the corresponding literature regarding partially premixed flames under 1– and μ–g conditions is sparse. It is known [1,2,8,9,10] that partially premixed flames contain multiple reaction zones and that their structure is determined by the transport and thermo-chemical interactions between these reaction zones. We have previously presented numerical results [8] concerning the effects of gravity on these interactions. That study pertained to the structure of two-dimensional partially premixed methane-air double flames established on a slot burner. For double flames, i.e., partially premixed flames containing two reaction zones, it was observed that the absence of gravity increases the spatial separation between the reaction zones, since diffusive transport is enhanced relative to advection, and entrainment of the outer fluid caused by buoyancy is eliminated. These effects increase the effective flame volume in a μ–g flame compared to its 1–g counterpart. In addition, the spatial characteristics of the inner premixed region were found to be mostly unaffected by gravitational effects, while the outer nonpremixed zones exhibited significant differences. In a subsequent investigation [9], the effect of gravity on both the spatial and temporal characteristics of a burner-stabilized methane-air triple flame was investigated.

Since the high temperature regions are much broader at 0–g, thermal radiation effects can become significant as the role of gravity is diminished. The radiative cooling time τ_{rad} for a gaseous volume of combustion products that is

* Corresponding author. E-mail: ikpuri@uic.edu
† Innovative Scientific Solutions, Inc.

Copyright © 2003 by the American Institute of Aeronautics and Astronautics, Inc. All rights reserved.

initially at its adiabatic flame temperature T_f is $t_{rad} = (g/(g-1))P/(4sK_p(T^4 - T_0^4))$ [7]. Assuming P = 1 atm, K_p= 56 cm^{-1}, γ = 1.35, T_0 = 298 K, and partially–premixed "flame" temperatures to vary from 1650 to 2200 K (in the inner premixed and outer nonpremixed reaction zones), the corresponding τ_{rad} values lie in the range 0.3–0.09 s. The diffusive transport time scale $\tau_d = d^2/a$, and the buoyant transport time scale $\tau_b \approx L/U_b$, where $U_b \approx (gL(Dr/r))^{1/2}$ is the buoyancy–induced velocity. In general, $Dr/r \approx 1$, so that $t_b \approx (L/g)^{1/2}$ [7]. Represen-tative values for a and g, are taken to be 1.5 cm^2/s and 980 cm/s^2, respectively. For 1 = L = 10 cm, τ_b varies from 0.03–0.1 s. For τ_d to lie within these bounds, d = 2–4 mm. This thickness depends on the level of partial premixing and the velocities of the reactant streams. Therefore, if the transport zone thickness exceeds 4 mm (as is the norm in the flames that we have investigated [9]), $\tau_b < \tau_d$, i.e., gravitational effects overwhelm transport effects.

Radiation effects are relatively unimportant at normal gravity, since $\tau_b < \tau_{rad}$. However, $\tau_b \to 8$ as $g \to 0$, and radiation effects can become significant under microgravity conditions. As $g \to 0$, our previous numerical study [9] has shown that the role of molecular transport becomes more important so that it is possible that $\tau_{rad} \sim \tau_d$. Therefore, a careful investigation of the interactions between transport, buoyancy, and thermal radiation will increase our understanding of partially premixed flames, thereby resulting in better combustor design and fire safety solutions. In addition, it is important to quantify these effects under different flow conditions. It is also pertinent to compare the thermal radiation effects for the rich premixed zone, nonpremixed zone, and the region between them for both 1– and μ–g flames. Moreover, previous investigations have not considered the effect of gravity on flame stretch in PPFs (especially on the inner premixed reaction zone), as well as on flame liftoff and stabilization due to the limitation of experimental facilities.

The objective of this investigation is to examine gravity effects on the structure of laminar methane-air partially premixed flames established on an axisymmetric burner. By comparing the results for normal gravity flames with corresponding flames established at zero gravity, we will focus on thermal radiation effects and on quantifying the heat loss from radiation. We will also investigate flame lift-off and blow-off of PPFs to understand the flame stabilization mechanism under the interactions of buoyancy, flame stretch and curvature.

NUMERICAL METHOD

The computational model is based on the algorithm developed by Katta et al. [11] and the simulation method is described in detail elsewhere [1-3, 8-10]. The numerical model solves time–dependent governing equations for an axisymmetric reacting flow. Using cylindrical coordinates (z, r), these equations can be written in the form

$$\frac{\partial(rf)}{\partial t} + \frac{\partial(rvf)}{\partial r} + \frac{\partial(ruf)}{\partial z} = \frac{\partial}{\partial r}\left(\Gamma^f \frac{\partial f}{\partial r}\right) + \frac{\partial}{\partial z}\left(\Gamma^f \frac{\partial f}{\partial z}\right) - \frac{rvf}{r} + \frac{\Gamma^f}{r}\frac{\partial f}{\partial r} + S^f. \quad (1)$$

The general form of the equation represents conservation of mass, momentum, species, or energy conservation equation, depending on the variable used for f. Introducing the overall species conservation equation and the state equation $p = rR_uT\sum_k Y_k/M_k$ completes the set of equations. The transport coefficient Γ^ϕ and source terms S^ϕ appearing in the above equation is provided in Table 1 of Ref. [1]. In addition, a sink term based on an optically-thin gas assumption is included in the energy equation to account for thermal radiation in the flame. This is described in the next section. The methane–air chemistry is modeled using a detailed mechanism that considers 24 species and 81 elementary reactions [12]. The mechanism has been validated for the computation of premixed flame speeds and the structure of nonpremixed and partially premixed flames [13,14].

Figure 1 presents the geometry of the axisymmetric burner and computational domain. The computational domain of 100 mm × 50 mm in the axial (z) and radial (r) directions, respectively, is represented by a staggered, non-uniform 201 × 101-grid system. The inner burner wall of 0.8 mm thickness is simulated by an insert body maintained at an isothermal temperature. The outflow boundaries in both directions are located sufficiently far from the respective inflow and symmetric boundaries so that the propagation of boundary–induced disturbances is minimized. At the inflow

boundary, the fully developed pipe flow in the inner tube and flat-velocity profiles outside the inner tube (when V_{out} is not zero) were used. The temperature and species mass fraction profiles are assumed to be uniform at the inflow boundary.

Thermal Radiation Model

An optically-thin radiation model has been frequently used in the computational studies of flames in a variety of situations. These include investigations on the flammability limit for premixed flames [15,16,17,18,19], and on the study of NOx formation [20,21], flame structure [22] and extinction [13] for partially premixed flames. According to optical thin approximation, the sink term due to the radiation heat loss, q_{rad}, may be calculated as [23]

$$q_{rad} = -4\sigma K_p (T^4 - T_0^4) . \quad (2)$$

The Planck mean absorption coefficient K_p accounts for the absorption and emission from the participating gaseous species CO_2, H_2O, CO and CH_4, and is expressed as

$$K_p = p\sum_k x_k K_{p,k} , \quad (3)$$

where $K_{p,k}$ denotes the mean absorption coefficient of species k and its value is obtained by using a polynomial approximation to the experimental data given in Ref. [24].

To characterize the effect of radiation on flames, we define the radiation fraction as the ratio of total radiation heat loss to total heat released (heat of combustion), i.e.,

$$\chi_{rad} = Q_{rad} / Q , \quad (4)$$

The heat of combustion is calculated by integrating the local heat release rate in the volume encompassed by the computational domain, i.e.,

$$Q = \int_V q\, dV \approx \sum_{i,j=1}^{NI,NJ} q_{i,j} \Delta V_{i,j} , \quad (5)$$

where $\Delta V = \pi (r_{i+1,j}^2 - r_{i,j}^2)(z_{i,j+1} - z_{i,j})$, and NI and NJ are the numbers of grid points in the z and r directions, and $q_{i,j}$ is the local heat release rate expressed as

$$q = q_{i,j} = \sum_{k=1}^{K} H_k w_k . \quad (6)$$

The total radiation heat loss can be obtained by integrating the local radiation heat loss over the volume, i.e.

$$Q_{rad} = \int_V q_{rad}\, dV \approx \sum_{i,j=1}^{NI,NJ} q_{rad} \Delta V . \quad (7)$$

RESULTS AND DISCUSSION

Validation of Numerical Model

The numerical model has been previously validated for both burner-stabilized and lifted methane-air partially premixed flames [2,3,25]. Additional validation of the model is provided by comparing the predicted and measured flame topologies and temperature distributions for a 1-g partially premixed methane-air flame containing two reaction zones. Figure 2 presents a comparison of the predicted heat release rate contours with the experimentally obtained C_2^*–chemiluminescence intensities for this flame. The flow conditions are f_{in} = 2.0, V_{in} = 0.6 m/s, f_{out} = 0, and V_{out} = 0.5 m/s. The optically-thin radiation model was included in the simulation. In our previous study [25], the C_2^*–chemiluminescence has been shown to be a good marker of the heat-release or reaction zones. In Fig. 2, the C_2^*–chemiluminescence image has been normalized by multiplying each pixel intensity by a constant value, which is the ratio of the maximum heat release rate to the maximum pixel intensity. The measurements and prediction are in very good agreement with respect to the topologies of both the inner rich premixed and outer nonpremixed reaction zones. Both the simulated heat release rates and the chemiluminescence image indicate that the reaction intensities peak at the flame base, where the inner and outer reactions are merged. This high reactivity region has been termed as the "reaction kernel" by Takahashi et al. [26], and is due to the combined effect of flame curvature and premixing, which is primarily due to the diffusive transport behind the burner rim. The reaction intensities decrease along the sides of the inner premixed zone, and the heat-release rate progressively decreases along the outer nonpremixed reaction zone at downstream locations. The nonpremixed reaction zone exhibits a weak tip

in Fig. 2 for both the chemiluminescence image and the simulation.

Figure 3 presents a comparison between the measured, using the technique of Rainbow Schlieren Deflectometry [27] and predicted temperature distributions for the flame considered in the context of Fig. 2. The measured temperatures near the burner rim increase more gradually in comparison with the predictions, and are distributed in a broader region around the rim. Regardless of these differences in the upstream region, there is generally good qualitative and quantitative agreement between the measured and predicted temperatures at downstream locations. Both the simulations and the predictions indicate that the premixed reaction zone is relatively thin, and the region with the highest temperatures lies between the inner premixed and outer nonpremixed reaction zones. The measured maximum temperature is slightly higher (2159 K *vs.* 2021 K) compared to the predicted value. This is attributed to the uncertainties and resolutions in both the measurements and predictions (e.g., related to the chemical mechanism and the thermodynamic and transport properties). In general, the maximum error lies in the rich side of the flame near the centerline because of the assumption of constant refractivity throughout the flame [28].

Simulations of 0-g Partially Premixed Flames

Since the numerical solution employs a time-accurate algorithm, two different approaches can be used to obtain a stable partially premixed flame at 0–g. One is to ignite the mixture at the beginning of the simulations, and then compute the 0-g flame until it attains a steady state structure. The other approach is to first compute a steady flame at 1–g, and then change gravity to zero and perform simulations until a steady flame at 0–g is obtained. Both methods have been used in drop-tower experiments, and their differences have been discussed by Bahadori *et al*. [29]. It was observed that laminar jet nonpremixed flames did not reach steady state, as the temperature fields were still evolving at the end of the drop period. On the other hand, Urban *et al.* [30] and Lin *et al.* [31] conducted long-duration tests in the space shuttle, and observed that the nonpremixed soot-containing hydrocarbon flames were almost twice as long as μ–g flames observed in ground-based drop-tower facilities. Similar trends may be expected for partially premixed flames and it is worthwhile to examine these transient aspects in order to understand the influence of changing gravitational acceleration.

Figure 4 presents the temporal evolution for a 0–g partially premixed flame in terms of a selected value of the heat release rate and temperature contours when it is computed using the second approach, i.e. when a corresponding stable 1–g flame is subjected to a sudden 0-g condition at t = 0. The flow conditions are f_{in} = 2.5, V_{in} = 0.3 m/s, f_{out} = 0, and V_{out} = 0. The specified heat release rate contour has a value of 100 kW/m^3, while the temperature contour has a value of 600 K. The initial 1–g flame at t = 0 is represented by broken line contours. As indicated in Fig. 4, the initial 1–g flame becomes rounder and broader during its evolution to a steady 0–g flame. The inner premixed reaction zone reaches its steady state rather quickly, while the outer nonpremixed flame evolves over a longer duration. In addition, the heat release rate contour reaches steady state much faster than the temperature contour. For example, the heat release rate contour at t = 0.4 s is relatively close to those at t = 1.8 s and 2.2 s, while the temperature contour at t = 0.4 s is still developing. This implies that radiation effects influence the flame temperature and the diffusion time scale is larger than the reaction time scale, since the isotherm is influenced both by diffusion and radiation (the time scale for which is also larger than reaction time scale). The isotherms at t = 1.8 s and 2.2 s are nearly identical, suggesting that a nearly steady state is established at t = 2.2 s. Therefore, the steady 0–g flames discussed in the following sections are those corresponding to t = 2.2s.

Effect of Radiation on 1-g and 0-g Flames

Fig. 5 presents the flame structures in terms of the heat release rate and temperature contours for 1– and 0–g flames computed with and without radiation in order to characterize the effect of thermal radiation on 1– and 0–g partially premixed flames. The flow conditions are the same as those in the context of Fig. 4. The flames exhibit a double flame structure with an inner rich premixed reaction zone and an outer nonpremixed reaction zone. For the 1–g flame (cf. Figs. 5(a) and (b)), the heat release rate contours indicate that with radiation included, the heights of both the inner premixed and

outer nonpremixed zones slightly increase, implying a small increase in the chemical time. The radiation also decreases the temperature in high-temperature regions, as indicated by the 1400 K and 1800 K isotherms along the centerline. However, the overall effect of radiation on the structure of 1–g flame is relatively insignificant. In contrast, the structure of the corresponding 0–g flame is strongly influenced by radiation. As indicated by the heat release rate contours (cf. Figs. 5(c) and (d)), with radiation included, the heights of both the inner premixed and outer nonpremixed reaction zones increase by about 2 mm (>10%), implying that the chemical time scale increases significantly due to radiation. In addition, the intensity of heat release rate near the flame tip decreases, and the region occupied by the 1800 K isotherm shrinks to a fraction of that without radiation. These changes are easy to understand since when radiation heat loss is considered in the numerical model, the flame temperature and the reaction rates decrease and the residence time of fuel increases, which results in a relatively longer and thicker flame. The 0–g flame with radiation appears to be longer but more compact; the latter effect may be attributed to the decrease in the thermal and mass diffusivities caused by the reduced temperatures.

Figure 6 presents temperature profiles along the centerline and along a radial segment at z = 6 mm for both the 1– and 0–g flames discussed in Fig. 5. The temperature profiles reach their peaks right after the inner premixed reaction zone and then exhibit a gradual decrease downstream. The shift in the maximum temperature locations is indicative of the increase in the flame height for 0–g flames. Without radiation, the peak temperatures are essentially identical for 1– and 0–g flames (2028 K *vs.* 2020 K). However, when radiation is included, the difference between the peak temperatures for 1– and 0–g flames becomes quite significant (1973 K *vs.* 1760 K). More importantly, the decrease in the peak temperature caused by radiation is 260 K for the 0–g flame, compared to a value of 55 K for the 1–g flame. This clearly demonstrates that radiation effect on partially premixed flames is significantly enhanced under μ–g conditions. This is primarily due to the significantly enlarged reaction zone volume of the 0–g partially premixed flame as compared to that of 1–g flame. As indicated in Figs. 6(a) and 6(b), the 0–g flame is taller and significantly broader compared to the 1–g flame.

Figure 7 presents heat release rate profiles corresponding to the temperature profiles discussed in Fig. 6. The peak in the heat release rate profile along the centerline (cf. Fig. 7(a)) corresponds to the tip of the inner premixed flame, while the two peaks in the radial profiles (cf. Fig. 7(b)) correspond to the inner premixed and outer nonpremixed reaction zones, respectively. The comparison of heat release rate profiles in both Fig. 7(a) and 7(b) for the 1– and 0–g flames indicates that in the absence of radiation the peak heat release rate for the 0–g flame is only one half of that for the 1–g flame. This difference can be attributed to two factors. First, the 0–g flame is spatially broader and taller than the 1–g flame, and second, the reactivity at the premixed flame tip is weaker for the 0–g flame due to a decrease in oxidizer advection in the absence of buoyancy. Regarding the effect of radiation, Fig. 7 corroborates results discussed in the context of Figs. 5 and 6. As indicated in Fig. 7(a), the effect of radiation is much stronger for the 0–g flame compared to that for the 1–g flame. For the former, the peak heat release rate with radiation is less than half of that without radiation, indicating that the reactivity at the premixed flame tip is significantly weakened due to thermal radiation. Another important observation from the comparison of radial heat release rate profiles in Fig. 7(b) is that the radiation does not have any significant effect on the total heat release rate in the 1– and 0–g partially premixed flames.

Validity of the Optically-Thin Gas Assumption

In order to assess the validity of the optically-thin gas assumption, the maximum optical thickness is calculated along the axial (z) direction by [23]

$$k_z(r) = \int_0^Z K_p dz \,, \tag{8}$$

and along the radial (r) direction by

$$k_r(z) = \int_0^R K_p dr \,. \tag{9}$$

Figure 8 presents the variation of k_z and k_r for the flames corresponding to Figs. 5(b) and 5(d). The value of k_z is much larger than that of k_r, since the Planck mean coefficients are function of the local

species concentration and temperature and the flames are "thicker" in the axial direction than in the radial direction. The fact that k_z is larger than k_r is also partly due to the high concentration of CH_4, H_2O, CO, and CO_2 along the axial segment that is considered. An important observation from Fig. 8 is that the optical thickness is significantly larger for the 0–g flame as compared to that for the 1–g flame. The peak value of k_z occurs near the centerline with values of 0.132 and 0.162 for the 1– and 0–g flames, respectively. Although these values are not insignificant, they are nevertheless much smaller than unity, and thus justify the optically thin gas assumption.

The global effect of radiation on 1– and 0–g partially premixed flames is summarized in Table 1, which presents the computed values of the maximum flame temperature T_{max}, maximum heat release rate q_{max}, total heat of combustion Q, total thermal radiation heat loss Q_{rad}, radiation fraction χ_{rad}, maximum optical thickness $k_{z,max}$, and flame height H (which is defined by the peak heat release rate along the centerline), for five flames. The computed radiation fraction values for 1–g flames are in good agreement with those reported in literature for laminar methane-air nonpremixed flames [32]. It is logical that corresponding values for PPFs should be of the same order. A comparison of χ_{rad} for 1– and 0–g flames again demonstrates that the effect of radiation on partially premixed flames is significantly enhanced in the absence of gravity for which the χ_{rad} value can be as high as 50.5%., although it drops to roughly 22.9% in the presence of a coflow. The optically-thin gas model is known to overpredict the radiation heat loss in flames. Nevertheless, it provides a limiting value for the radiation loss, and can be used to compare the effects of radiation in 1– and 0–g flames. We now discuss the results of the effect of gravity and coflow on the structures of 1– and 0–g partially premixed flames.

Effect of Gravity and Inner/Outer Jet Velocities

Shu et al [8] have reported detailed numerical results concerning the effects of gravity, equivalence ratio and velocity on the structure of burner-stabilized, 2-D planar double flames. A corresponding investigation on triple flames was conducted by Azzoni et al [9]. In general, the presence of gravity has a significant effect on the outer nonpremixed reaction zone in the case of double flames, and on both the outer nonpremixed and the lean premixed zones in the case of triple flames. The region downstream of the inner premixed reaction zone is also noticeably influenced by gravity, since enhanced advection and entrainment due to buoyancy in this region reduces the residence time available for the oxidation of CO and H_2 that are produced in the inner rich premixed zone, resulting in a more compact flame at 1–g.

We have observed that the differences between the 1– and 0–g flames are enhanced when radiation is included. Figure 9 presents velocity vectors along with temperature and heat release rate contours for the 1– and 0–g flames discussed in the context of Figs. 5(b) and (d). The base of the 0–g flame moves further away from the centerline and stabilizes below the burner rim, and the height of the inner premixed reaction zone is significantly increased compared to that for the 1–g flame (14.4 *vs.* 10.7 mm). The flame base movement is due to the entrainment of air. In 1–g, entrainment produces a flow that pushes the flame closer to the centerline, and which also pulls the base towards the burner wall. In 0–g, the buoyant entrainment flow disappears so that the flame base moves away from the centerline. In addition, the maximum flame temperature and heat release rate are significantly lower in the absence of gravity (cf. Table 1). The effect of gravity on the flame volume was quantified by calculated the volume occupied by isotherms with temperature T = 1000 K. The calculated flame volume of the 0–g flame was 3.9 times larger than that of the 1–g flame (9.298 *vs.* 2.381 cm^3). This again indicates the necessity of considering thermal radiation in the numerical simulations for micro-gravity flames.

For the 1–g flame, the Froude number ($Fr = V_{in}^2 / gD$) has a value of 2.0, implying that the gravitational and inertial effects are of similar magnitude. The velocity vector plots in Fig. 9 indicate that while flow fields upstream of the inner premixed reaction zone are nearly identical for the 1– and 0–g flames, they are markedly different in regions between the two reaction zones as well as downstream of the outer nonpremixed reaction zone. For the 1–g flame, buoyancy accelerates the product species flow rates (CO and H_2 from the inner premixed zone, and CO_2 and H_2O from the

outer nonpremixed zone) downstream of the two respective reaction zones. In addition, the entrainment due to by buoyant acceleration makes the velocity vectors in these regions bend toward the centerline. This causes the outer reaction zone to move closer to the inner reaction zone, and thus making 1–g flame compact compared to the 0–g flame.

In order to examine the effect of coflow on the structures of 1– and 0–g partially premixed flames, we have simulated flames for the coflow velocities V_{out} = 0.3 m/s, and 0.6 m/s. There is little difference between the flames with the 0.3 and 0.6 m/s coflow velocities, and both flames are shorter and more compact. Figure 10 presents velocity vectors along with temperature and heat release rate contours for the flame of V_{out} = 0.3 m/s. The coflow velocity is assumed to have a top hat flat velocity profile that ends at the outer burner wall. The outer ambient flow is considered to be quasi-quiescent air with an axial velocity 0.001 m/s at the inflow boundary. Other conditions pertaining to this flame are f_{in} = 2.5, V_{in} = 0.3 m/s, and f_{out} = 0. Although, the presence of a coflow makes both the 1– and 0–g flames shorter and more compact, its effect is more pronounced for the 0–g flame. The flame base is pushed closer to the centerline by the presence of coflow. Another noteworthy result is that the difference in the structures of 1– and 0–g flames is less pronounced as the coflow velocity is increased. Table 1 presents some global properties of these flames. Both the maximum flame temperature and heat release rate become higher in the presence of a coflow, since the coflow increases the advective flux of oxidizer, and thus enhances the global reaction rate in the flame. Takahashi and Katta [33] have reported a similar "blowing effect" for laminar methane jet nonpremixed flames. In addition, as indicated in the table, the radiation fraction decreases with increasing coflow, and the differences between the maximum flame temperatures and heat release rates for the 1– and 0–g flames become less pronounced.

Figure 11 illustrates the effect of varying inner jet velocities on the 1– and 0–g partially premixed flames. The heat release rate contours, velocity vectors and isotherms are presented for three cases: (a) V_{in} = 0.1 m/s; (b) 0.4 m/s; and (c) 0.8 m/s. Other conditions for all three flames are f_{in} = 2.5, f_{out} = 0, and V_{out} = 0. The values of the Froude number of the 1–g flames for these three cases are 0.23, 3.63, and 14.51, respectively, demonstrating the increasingly larger inertial effect as compared to buoyancy effect. For all the flames, the heights of both the inner and outer reaction zones heights increase as the jet velocity is increased, since the fuel residence time which is determined by the reaction time remains invariant. The difference between the 1– and 0–g flame heights becomes more pronounced at higher jet velocities. The dependence of the inner flame height on the reactant is attributed to the residence time, since the chemical reaction time essentially depends only on the equivalence ratio. The increase in the height of the outer flame is attributed to the strong synergistic interaction between the two flames and to the enhanced advection fluxes of CO and H_2 from the inner reaction zone. In 0–g, due to the absence of buoyancy acceleration, the weaker air entrainment and the enhancement of radiation heat loss, the flame heights further increase at higher inner flow rates.

Gravity Effect of Lifted Triple Flames

Lifted partially premixed methane/air triple flames under normal gravity have been investigated by the authors recently [34]. It is found that the liftoff heights of triple flames increase linearly with the inner flow velocity V_{in} at relatively low values. As V_{in} exceeds a critical velocity the flame becomes unstable and oscillates, with blowout occurring occasionally after some periodic displacements. At even higher velocities the flame directly blows out.

Figure 12 illustrates lifted methane-air triple flames at different gravity levels of 0–g, 1–g, and 1.5–g, respectively, at the flow conditions of f_{in} = 2.5, with 25% N_2 dilution in volume, V_{in} = 0.6 m/s, f_{out} = 0.35, and V_{out} = 0.5 m/s. In Figs. 13(b) and 13(c), since the flame is oscillating, only a transient flame is shown here. In 1–g, the lifted flame stabilizes at a height of z ≈ 5.0 mm. The inner rich premixed flame is relatively stable, but the nonpremixed and outer lean premixed flame oscillates at a frequency of 13.5 Hz. Large vortex evolution process in the outer lean flame can be clearly identified from temperature contours and velocity vector fields which are not shown here. The oscillation is mainly due to buoyancy induced instability and can be verified by its disappearance

when gravity level changes into 0–g. The 0–g lifted triple flame is stable and stabilizes at a height about 2.0 mm which is lower than that in 1–g condition. However, from the temperature history profile of the outer lean flames, small amplitude oscillation (< 5%) is observed and can be attributed to velocity shear layer induced Kelvin-Helmholtz instability [9]. The frequency of this kind of oscillation is 8.0 Hz. On the other hand, due to the enhancement of buoyancy effect in 1.5–g, although the liftoff height of the triple flame does not change much, the oscillation amplitude intensifies, especially in the nonpremixed and outer lean premixed reaction zones, and the oscillating frequency increases to 15.4 Hz. At 2–g condition, the flame can not stabilized itself and blows out directly. Further studies on lifted triple flames are under performance.

CONCLUSIONS

The effect of gravity on burner-stabilized and lifted methane–air partially premixed flames is numerically investigated. The model employs a detailed description of methane-air chemistry and transport properties, with the effect of thermal radiation modeled by the optically-thin assumption. The presence of gravity has a significant effect on the outer nonpremixed reaction zone in the case of double flames, and on both the outer nonpremixed and the lean premixed zones in the case of triple flames. It is found that the effect of radiation is small for 1–g partially premixed flames, i.e., $c_{\text{rad}} \approx 0.1$. However, for the corresponding 0–g flames, the thermal radiation effect is significantly higher, $c_{\text{rad}} \approx 0.5$, since the flame volume increases in the absence of buoyancy. This in turn causes the flame temperature to decrease and results in weaker reaction activity. The effect of coflow is to counteract the effect of gravity on PPFs, as the former enhances the advection of oxidizer to the outer nonpremixed reaction zone, and thus, increases the overall reaction rate. The 0–g lifted triple flames are stable and their liftoff height is lower than that of 1–g flame.

ACKNOWLEDGMENT

This research was supported by the National Science Foundation Combustion and Plasma Systems Program for which Dr. Farley Fisher is the Program Director, and by the NASA Microgravity Research Division for which Dr. Uday Hegde serves as the technical monitor. We thank Dr. X. Xiao for assisting with the experiment of Rainbow Schlieren Deflectometry temperature measurements.

Nonmenclature

H_k	Specific enthalpy of species k (kJ/kmol)
i	Axial grid index
j	Radial grid index
K	Number of species
K_p	Planck mean absorption coefficient (1/m-atm)
$K_{p,k}$	Planck mean absorption coefficient of species k (1/m-atm)
M_k	Molecular weight of species k (kg/kmol)
p	Pressure (Pa)
Q	Total heat release (heat of combustion) (W)
q	Local heat release rate (W/cm^3)
Q_{rad}	Total radiation heat loss (W)
q_{rad}	Radiation heat loss rate (W/cm^3)
r	Radial coordinate
R_u	The universal gas constant (J/kmol-K)
T	Temperature.
t	Time
T_0	The ambient temperature
u	Axial velocity component (m/s)
v	Radial velocity component (m/s)
x_k	Mole fraction of species k
Y_k	Mass fraction of species k
z	Axial coordinate
S^f	Source terms
Γ^f	The transport coefficient
w_k	Net production rate of species k
g	Dynamic viscosity (N-s/m^2)
r	Density (kg/m^3)

s Stefan–Boltzmann constant

c_{rad} Radiation fraction

REFERENCES

1. Shu, Z., Aggarwal, S. K., Katta, V. R., and Puri, I. K., *Combust. Flame* 111: 296-311 (1997).
2. Azzoni, R., Ratti, S., Aggarwal, S. K., and Puri, I. K., *Combust. Flame* 119: 23–40 (1999).
3. Qin, X., Puri, I. K., and Aggarwal, S. K., 2nd Joint Meeting of the US Sections of the Combustion Institute, Oakland, CA, March 25-28, 2001, Paper No. 228.
4. Sacksteder, K. R., *Proc. Combust. Inst*. 23: 1589–1597 (1990).
5. Law, C. K., and Faeth, G. M., *Prog. Energy Combust. Sci*. 20: 65–113 (1994).
6. Kono, M., Ito, K., Niioka, T., Kadota, T., and Sato, J., *Proc. Combust. Inst*. 26: 1189–1199 (1996).
7. Ronney, P. D., *Proc. Combust. Inst*. 27: 2485–2506 (1998).
8. Shu, Z., Chun, C. W., Aggarwal, S. K., Katta, V. R., and Puri, I. K., *Combust. Flame* 118: 91-107 (1999).
9. Azzoni, R., Ratti, S., Puri, I. K., and Aggarwal, S. K., *Phys. Fluids* 11: 3449-3464 (1999).
10. Aggarwal, S. K., Puri, I. K., and Qin, X., *Phys. Fluids* 13:265-275 (2001).
11. Katta, V. R., Goss, L. P., and Roquemore, W. M., *Combust. Flame* 96:60 (1994).
12. Peters, N., *Reduced Kinetic Mechanisms for Applications in Combustion Systems*, Lecture Notes in Physics, N. Peters and B. Rogg (Eds.), Springer–Verlag, Vol. m15, 1993, p. 3.
13. Xue. H., and Aggarwal, S. K., *AIAA Journal* 39-4: 637-645 (2001).
14. Shu, Z., Katta, V. R., Puri, I. K., and Aggarwal, S. K., *Combust. Sci. and Tech.* 157: 185 (2000).
15. Sibulkin, M., and Frendi, A., *Combust. Flame* 82: 334 (1990).
16. Lakshmisah, K. N., Paul, P. J. and Mukunda, H. S., *Proc. Combust. Inst*. 23: 433-440 (1990).
17. Platt, J. A., and Tien, J. S., Chemical *and Physical Processes in Combustion, 1990 Fall Technical Meeting, Eastern Section of the Combustion Institute*, 1990.
18. Sung, C. J., and Law, C. K., *Proc. Combust. Inst*. 26: 865-873 (1996).
19. Guo, H, Ju, Y., Maruta, K., Niioka, T., and Liu, F., *Combust. Flame* 109: 639-646 (1997).
20. Ravikrishna, R. V., and Laurendeau, N. M., *Combust. Flame* 122: 474-482 (2000).
21. Barlow, R. S., Karpetis, A. N., Frank, J. H, and Chen, J. Y., *Combust. Flame* 127: 2021-2118 (2001).
22. Bennett, B. A. V., McEnally, C. S., Pfefferle, L. D., and Smooke, M. D., *Combust. Flame* 123: 522-546 (2000).
23. Siegel, R., and Howell, J. R., *Thermal Radiation Heat Transfer*, Hemisphere Publishing Corporation, New York, 1981.
24. Smith, N., Gore, J., Kim, J., and Tang, Q., Radiation Models, International Workshop on Measurement and Computation of Turbulent Nonpremixed Flames, http://www.ca.sandia.gov/tdf/Workshop/Submodels.html, 2001.
25. Shu, Z., Krass, B. J., Choi, C. W., Aggarwal, S. K., Katta, V. R., and Puri, I. K., *Proc. Combust. Inst*. 27: 625-632 (1998).
26. Takahashi, F., Schmoll, W. J., and Katta, V. R., *Proc. Combust. Inst*. 27: 675-684 (1998).
27. Xiao, X., and Puri, I. K. and Agrawal, A., *Applied Optics* 41-10: 1922-1928 (2002).
28. Qin, X., Xiao, X. Puri, I. K., and Aggarwal, S. K., *Combust. Flame* 128: 121-132 (2002).
29. Bahadori, M. Y., Edelman, R. B., Stocker, D. P., and Olson, S. L., *AIAA Journal* 28: 236-244 (1990).
30. Urban, D. L., Yuan, Z. -G., Sunderland, P. B., Linteris, G. T., Voss, J. E., Lin, K.-C., Dai, Z., Sun, K., and Faeth, G. M., *AIAA Journal* 36: 1346–1360 (1998).
31. Lin, K.-C., Faeth, G. M., Sunderland, P. B., Urban, D. L., and Yuan, Z.-G., *Combust. Flame* 116:415–431 (1999).
32. Markstein, G. H., *Proc. Combust. Inst*. 20: 1055-1061 (1984).
33. Takahashi, F., and Katta, V. R., Proceedings of the 2002 Spring Technical Meeting of the Central State Section, The Combustion Institute, paper No. B1-4, 2002.
34. Qin, X., Puri, I. K., and Aggarwal, S. K., "Characteristics of lifted triple flames stabilized in the near field of a partially premixed axisymmetric jet flows," to appear in *Proc. Combust. Inst*. 29.

Table 1: Properties of double. For all the cases, f_{in} = 2.5, V_{in} = 0.3 m/s, and f_{out} = 0.

V_{out} ($m\ s^{-1}$)	Gravity (g)	T_{max} (K)	q_{max} ($W\ cm^{-3}$)	Q (W)	Q_{rad} (W)	χ_{rad} (%)	$k_{z,max}$	H (mm)
0	1	1974	632	32.78	3.03	9.2	0.132	10.7
0	0	1811	268	32.02	16.17	50.5	0.162	14.4
0.3	1	1989	1008	32.90	2.69	8.2	0.130	8.2
0.3	0	1954	890	32.78	7.51	22.9	0.149	8.6
0.6	0	1990	1264	32.66	4.02	12.3	0.135	9.7

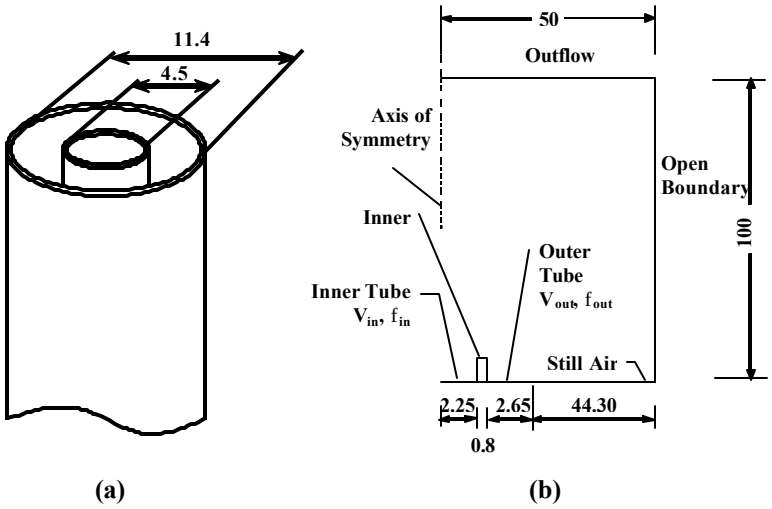

Fig. 1: A schematic diagram of the axisymmetric burner (a) and computational domain (b). The dimensions are in unit of mm.

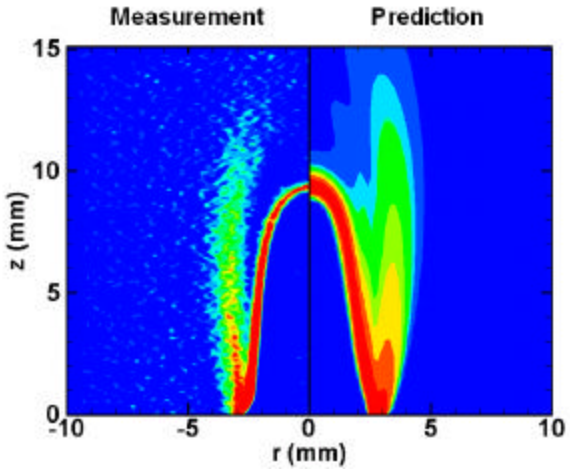

Fig. 2: Comparison between measured C_2^*-chemiluminescence intensity (left) and predicted heat release rates (right) for a methane/air double flame of ϕ_{in} = 2.0 and ϕ_{out} = 0, with V_{in} = 0.6 m/s and V_{out} = 0.5 m/s.

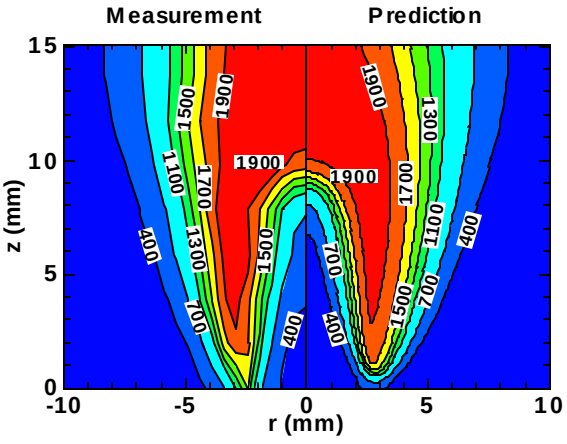

Fig. 3: Comparison between predicted (left) and measured (right) temperature distributions for the flame corresponding to Fig. 2.

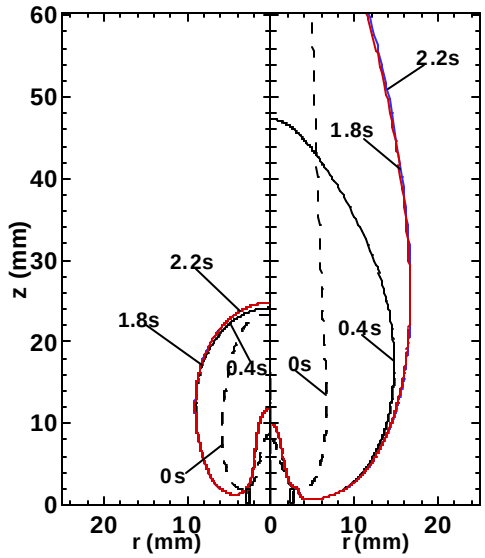

Fig. 4: Temporal evolution of the selected heat release rate and temperature contours for a 0–g partially premixed flame at the conditions of f_{in} = 2.5, V_{in} = 0.3 m/s, f_{out} = 0, and V_{out} = 0. The heat release rate contour has a value of 100 kW/m^3, while the temperature contour has a value of 600 K.

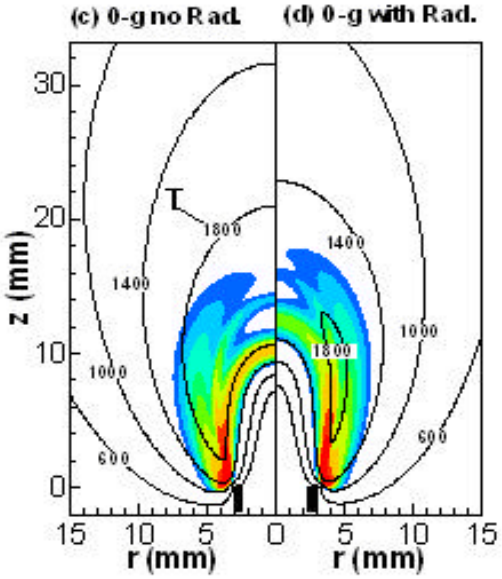

Fig. 5: Double flame structure in terms of the heat release rate and temperature contours for 1– and 0–g flames computed with and without radiation. The flow conditions are the same as those in Fig. 4.

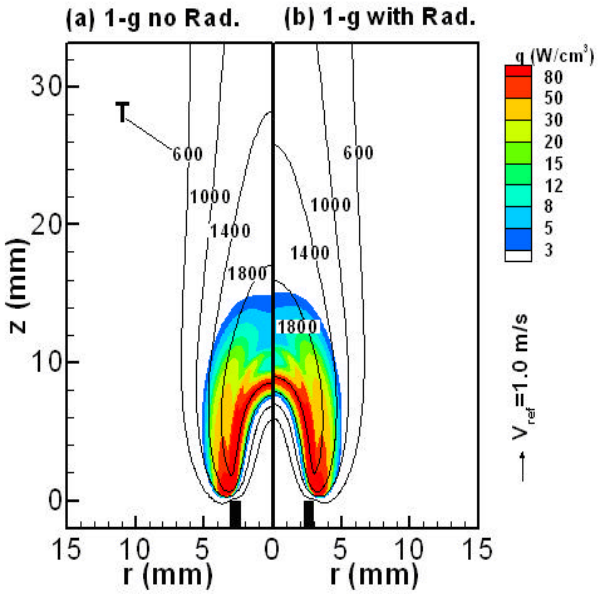

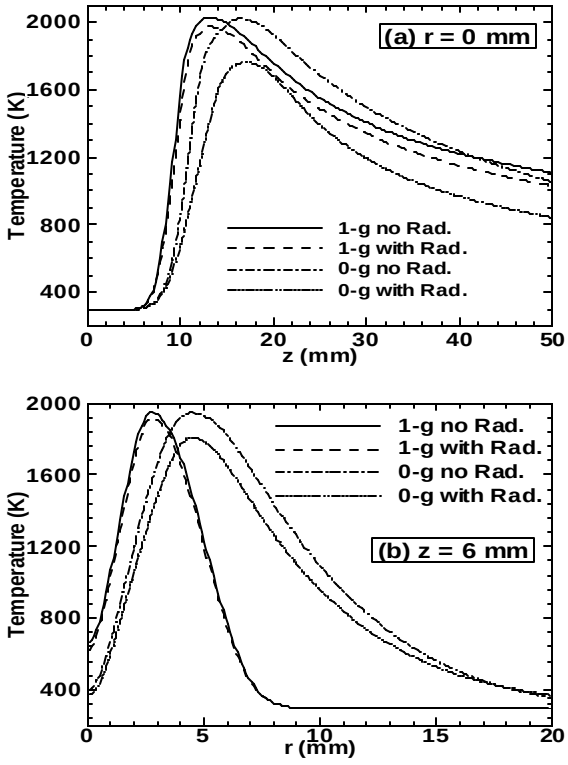

Fig. 6: Temperature profiles along the centerline and along a radial cut at z = 6 mm for both the 1– and 0–g flames discussed in Fig. 5.

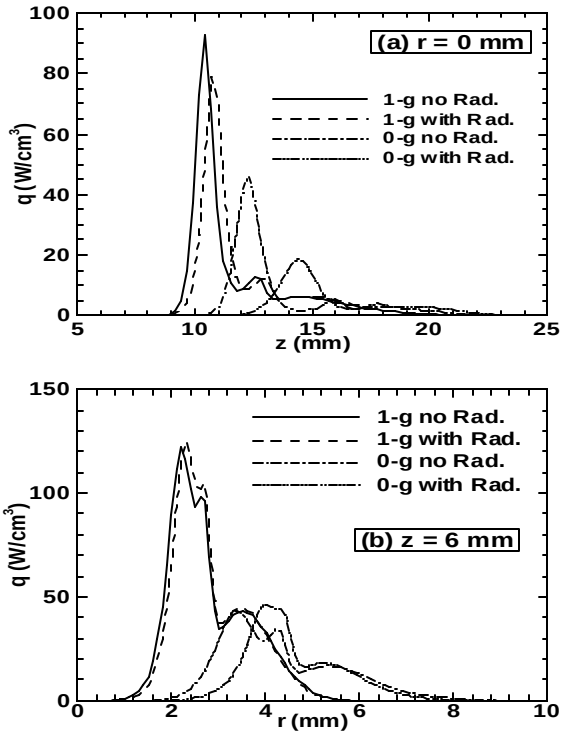

Fig. 7: Heat release rate profiles along the centerline and along a radial cut at z = 6 mm for both the 1– and 0–g flames discussed in Fig. 5.

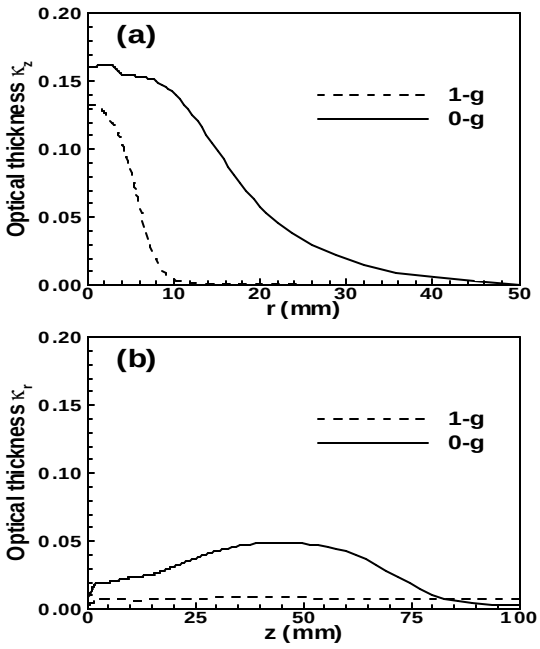

Fig. 8: Variation of k_z and k_r for the flames corresponding to Figs. 5b and 5d, respectively.

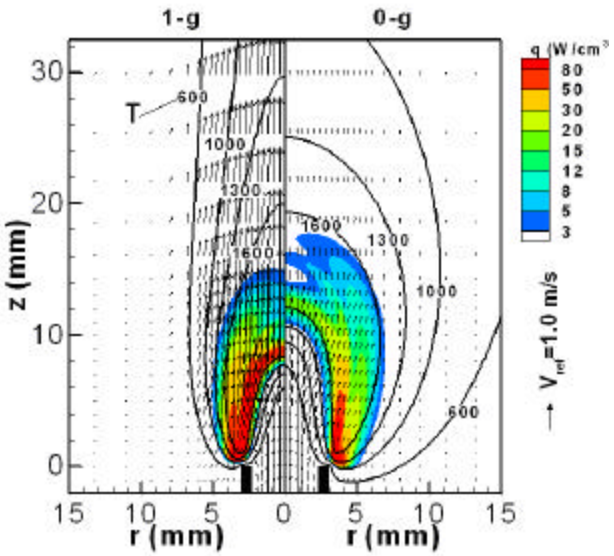

Fig. 9: Velocity vector fields, temperature and heat release rate contours for the 1– and 0–g flames discussed in the context of Fig. 5(b) and 5(d), respectively.

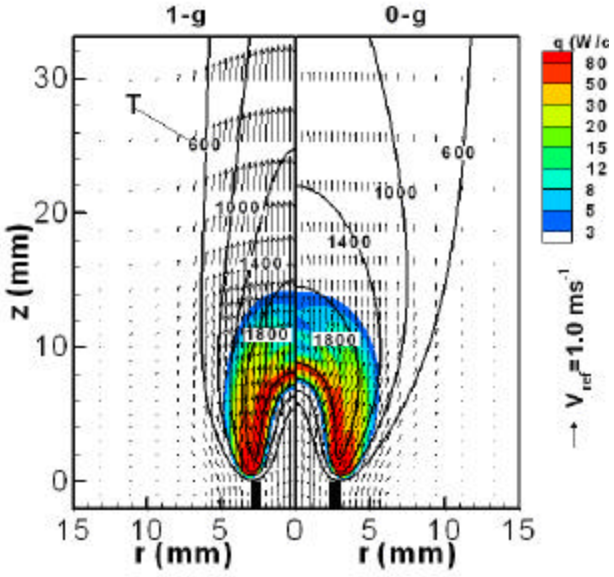

Fig. 10: Effect of coflow on the structures of 1– and 0–g double flames in terms of velocity vectors fields, temperature and heat release rate contours for the condition of f_{in} = 2.5, V_{in} = 0.3 m/s, f_{out} = 0, and V_{out} = 0.3 m/s.

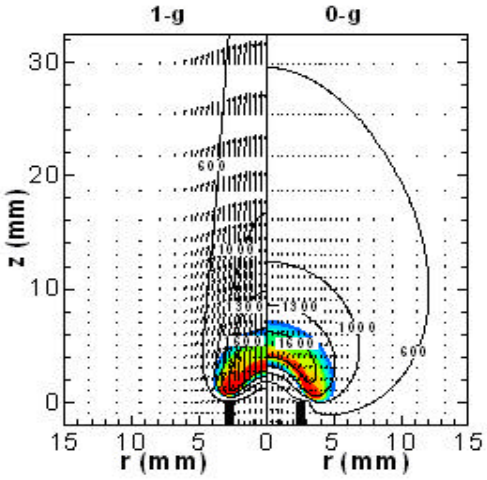

(a) V_{in} = 0.1 m/s

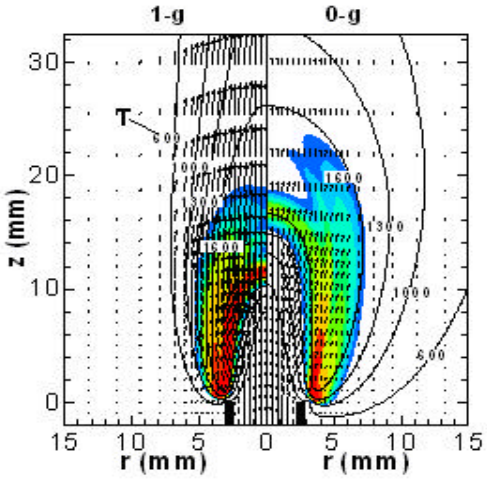

(b) V_{in} = 0.4 m/s

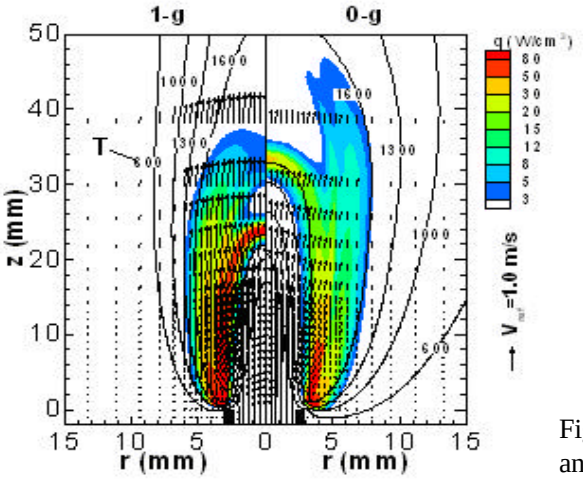

(c) V_{in} = 0.8 m/s

Fig. 11: Effect of inner jet velocities on the 1– and 0–g partially premixed flames. Other conditions are f_{in} = 2.5, f_{out} = 0, and V_{out} = 0.

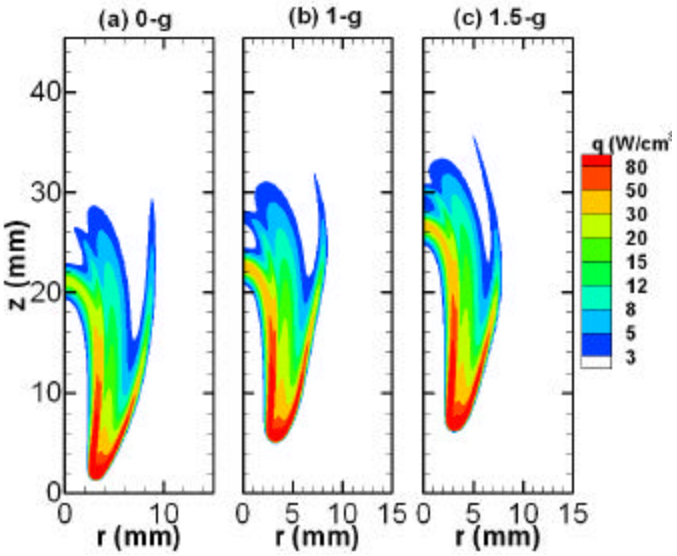

Fig. 12: Effect of gravity on lifted triple flames of conditions at f_{in} = 2.5, 25% N2 dilution in volume, V_{in} = 0.6 m/s, f_{out} = 0.35, and V_{out} = 0.5 m/s.

Investigation of PAH Formation in Different Flames using UNICORN

Viswanath R. Katta*
Innovative Scientific Solutions Inc.
2766 Indian Ripple Road, Dayton, OH 45440

and

William M. Roquemore
Propulsion Directorate, Air Force Research Laboratory
Wright Patterson Air Force Base, OH 45433

Abstract

Residence time and thermal environment are important factors in the soot formation. To understanding the chemical and physical structures of the soot formed in different flames knowledge on flow dynamics governing these flames is required. A time-dependent, detailed-chemistry CFD model is developed for the simulation of different types of ethylene-air flames. Calculations are made for the burner-stabilized, opposing jet, co-axial jet, diffusion, and premixed flames using the same code and the results are compared with each other. It is observed that the fuel-lean premixed flames yield negligible amounts of PAH species, while the fuel-rich premixed and jet-diffusion flames result similar amounts of PAHs.

Introduction

Soot is an undesirable combustion product and its formation represents one of the most complex chemical systems in flames. Considerable progress has been made in recent years on the chemical and physical aspects of the soot formation in hydrocarbon flames. Soot particles containing several-thousand carbon atoms are formed from simple fuel molecules within a few microseconds. While the first aromatic rings (such as benzene and small PAHs) are formed in the gas phase, acetylene molecules react with these small PAHs and polymerize to larger PAHs[1]. The first soot particles are formed when two PAHs collide and form a three dimensional particle. This process is also known as particle inception[2]. The soot particles formed interact with the gas-phase molecules by the addition of acetylene to their surfaces (surface growth) and by the reaction with molecular oxygen and the hydroxyl-radical (oxidation). Another process which increases the soot mass is the collision of a PAH with a soot particle.

Several experimental and numerical investigations have been made in the past on soot formation in co- and counter-flow diffusion flames[3-6]. Santoro et al.[7] made temperature and velocity measurements in a ethylene-air jet diffusion flame for studying the soot growth process along individual particle paths. Based on the experimental data they argued that soot formation increases in the annular region of the flame due to an increase in residence time. Lin and Faeth[8] found that direction of soot particle movement with respect to the flame sheet is important in the generation of soot. If the soot particle forming on the fuel rich side of the flame stay entrained in the fuel-rich region for a long time before crossing the flame surface then its surface growth could be enhanced. In contrast, Lin and Faeth[8] argued that the soot generation could be reduced if the soot particle is made to cross the flame surface quickly. Wu and Essenhigh[9] and Blevins et al.[10] have studied the inverse diffusion flames by reversing the fuel and air jets of a normal jet diffusion flame. To further understand the soot characteristics of an inverse diffusion flame numerical studies have been performed by Blevins et al.[11] and Katta et al.[12]

In the present work, several ethylene laminar flames were numerically simulated using a well-tested CFD code and a detailed chemical kinetics model for PAH formation. The resulted structures of the flames were compared to identify the fluid dynamics effects on PAH formation.

Description of UNICORN

A time-dependent, axisymmetric mathematical model known as UNICORN (Unsteady Ignition and Combustion using ReactioNs)[13,14] is used to simulate various flames considered in the present study. It solves for u- and v-momentum equations, continuity, and enthalpy- and species-conservation equations on a staggered-grid system. The body-force term due to the gravitational field is included in the axial-momentum equation while simulating vertically mounted flames. A clustered mesh system is employed to trace the large gradients in flow

* Corresponding author: vrkatta@erinet.com

variables near the flame surface. A detailed chemical-kinetics model of Wang and Frenklach[15] is incorporated in UNICORN for the investigation of PAH formation in acetylene and ethylene flames. It consists of 99 species and 1066 elementary-reaction steps. Thermo-physical properties such as enthalpy, viscosity, thermal conductivity, and binary molecular diffusion of all the species are calculated from the polynomial curve fits developed for the temperature range 300 - 5000 K. Mixture viscosity and thermal conductivity are then estimated using the Wilke and Kee expressions, respectively. Molecular diffusion is assumed to be of the binary-diffusion type, and the diffusion velocity of a species is calculated using Fick's law and the effective-diffusion coefficient of that species in the mixture. A simple radiation model based on optically thin-media assumption is incorporated into the energy equation. Only radiation from CH_4, CO, CO_2, and H_2O is considered in the present study[16].

The finite-difference forms of the momentum equations are obtained using an implicit QUICKEST scheme[17], and those of the species and energy equations are obtained using a hybrid scheme of upwind and central differencing. At every time-step, the pressure field is accurately calculated by solving all the pressure Poisson equations simultaneously and utilizing the LU (Lower and Upper diagonal) matrix-decomposition technique. The boundary conditions are treated in the same way as that reported in earlier papers.[18]

Results and Discussion

The CFD model UNICORN has been extensively validated in the past by simulating various steady and unsteady counterflow[13,19] and coflow[13,20] jet diffusion flames and by comparing the results with experimental data. This gives confidence that UNICORN can simulate the structure of dynamic flames accurately. However, the integration ethylene+PAH chemistry to UNICORN code needs to be validated in order to establish the accuracy of the predictions made in the present work. It is achieved by simulating the burner-stabilized flame that was extensively investigated by Harris et al.[21] and Wang and Frenklach.[15]

The flame chosen is a premixed $C_2H_4/O_2/Ar$ flame with an equivalence ratio of 2.76. Velocity of the cold reactants is 7.8 cm/s. The $Ar:O_2$ mole ratio used was 79:21. Two-dimensional calculations for this burner-stabilized flame are made by enforcing periodic boundary conditions at the two boundaries in the axial direction and by using the measured temperature profile as an input quantity. These two-dimensional calculations eventually resulted in one-dimensional flame with all the variations in the radial directions being vanished.

Variations in concentrations of several species with respect to height in the flame are compared with the experimental data in Fig. 1. The temperature profile used in these calculations has a peak value of 1901 K [Fig. 1(a)]. Calculations have predicted the variations in major species concentrations; such as, drop in O_2 and C_2H_4 and growth in CO and CO_2, reasonably well. However, the computed concentrations of H_2 are somewhat lower than the measurements. This discrepancy was also observed by Wang and Frenklach[15] while modeling this flame using CHEMKIN and attributed it to the higher concentrations of OH obtained with the present chemical mechanism.

The experimental and measured mole fractions of CH_4, C_2H_2, C_4H_2, C_4H_4, and C_2H_6 at different heights are compared in Fig. 1(b). The key intermediate species, in general, are well predicted by the model. The computed peak concentrations of these radicals are within a factor of 2 of the measured values, which is probably of the order of the experimental uncertainty. Similarly, the predicted concentration profiles of one-ring aromatics compare well with the measured ones as shown in Fig. 1(c). The steady rise of aromatics is typical of ethylene burner-stabilized flames and is well reproduced by the Wang-and-Frenklach mechanism. Based on the comparisons shown in Fig. 1 it may be assumed that the modified UNICORN model can reasonably simulate an ethylene flame.

Two-dimensional calculations were made for a low-strained, opposing-jet diffusion flame using UNICORN. The separation used between the 1-cm-diameter fuel and oxidizer nozzles was 2 cm. Pure ethylene was used as fuel. The 0.5 m/s fuel and air jets established global and air-side strain rates of 50 and 100 s^{-1}, respectively. The flow field, temperature and benzene- and OH-concentration distributions are plotted in Fig. 2. Here, fuel and air are injected from the bottom and top, respectively. As expected (since the stoichiometric fuel/air ratio is 0.2917), flame is formed on the air side of the stagnation plane.

Significant amount of benzene is formed in this diffusion flame on the fuel side while almost all the OH is generated outside and on the air side of benzene. Distributions of various species along the stagnation line are shown in Fig. 3. It is interesting to note that all the carbonaceous species are located on the fuel side of the peak temperature. When compared to the fuel-rich, burner-stabilized flame (Fig. 1), diffusion flame generated lesser amounts of PAH species.

The simulated fuel-rich (ϕ = 2.4)) and fuel-lean (ϕ = 0.6) opposing-jet premixed flames are shown in Figs. 4 and 6, respectively. Velocities used for these two flames are the same ($V_f = V_a =$ 0.8 m/s) and both the flames resulted in nearly identical temperatures (~ 1800 K) as shown in Figs. 5(a) and 7(a). Dramatic differences in PAH species produced by these rich and lean flames may be noted from Figs. 5(c) and 7(c). Negligible amounts of PAHs are generated in the fuel-lean case. A comparison of chemical structures of diffusion (Fig. 3) and fuel-rich premixed (Fig. 3) flames suggests that the radicals such as O, H, and OH are nearly separated from the carbonaceous species in the former cases while all these species coexist

in the latter. However, similar amounts of PAHs are found in these two types of flames.

Calculations for the co-axial diffusion and fuel-lean-premixed jet flames are performed using UNICORN and the results are shown in Figs. 8 and 10, respectively. Chemical structures of the diffusion flame at a height of 20 mm above the exit and that of the premixed flame at a height of 10 mm above the exit are shown in Figs. 9 and 11, respectively. In line with the results obtained for opposing jet flames, these co-axial jets also yielded higher PAHs in the case of diffusion flame compared to the premixed (fuel lean) one. In fact, the PAHs produced in the premixed co-axial jet flame are even lower than those produced in the opposing jet flame even though both the flames have fuels with identical equivalence ratios and injection velocities.

Conclusions

A time-dependent, axisymmetric, detailed-chemistry CFD model is developed for the simulation of ethylene-air flames. PAH formation is simulated using the 99-species, 1066-reactions model of Wang and Frenklach. The CFD model (UNICORN) was validated by simulating a burner-stabilized premixed flame and comparing the results with the measurements. Both the diffusion-type and premixed-type flames were simulated for the opposing and co-axial jet configurations. In general, fuel-lean premixed flames yielded extremely low concentrations of PAH species. Unlike in fuel-rich premixed flames, the radicals such as O, H, and OH are nearly separated from the carbonaceous species in diffusion flames; however, similar amounts of PAHs are produced in these two types of flames.

Acknowledgement

Financial support for this work was provided by Strategic Environmental Research and Development Program (SERDP), Air Force Office of Scientific Research (AFOSR), and the Air Force Contract #F33615-00-C-2068.

References

1. Richter, H. and Howard, J. B., Prog. *Energy Combust. Sci.* 26:565 (2000)
2. Kennedy, I. M., Prog. *Energy Combust. Sci.* 23:95 (1997)
3. Kaplan, C. R., and Kilasanath, K., "Flow-Field Effects on Soot Formation in Normal and Inverse Methane-Air Diffusion Flames," Combustion and Flame, Vol. 124, 2001, pp. 275-294.
4. Smooke, M. D., Mcenally, C. S., Pfefferle, L. D., Hall, R. J., and Colket, M. B., "Computational and Experimental Study of Soot Formation in a Coflow, Laminar Diffusion Flame," Combustion and Flame, Vol. 117, 1999, pp. 117-139.
5. Sugiyama, G., Proceedings of the Combustion Institute, The Combustion Institute, PA, Vol. 25, 1994, pp. 601-608.
6. Du, J., and Axelbaum, R. L., Combustion and Flame, Vol. 100, 1995, pp. 367-375.
7. Santoro, R. J., Yeh, T. T., Horvath, J. J., and Semerjian, H. G., Combustion Science and Technology, Vol. 53, 1987, pp. 89-115.
8. Lin, K.-C., and Faeth, G. M., Journal of Propulsion and Power, Vol. 12, 1996, pp. 10-17.
9. Wu, K._T., and Essenhigh, R. H., Proceedings of the Combustion Institute, The Combustion Institute, PA, Vol. 20, 1984, pp. 1992-1932.
10. Blevins, L. G.; Fletcher, R. A.; Benner, B. A.; Steel, E. B.; Mulholland, G. W. *Proceedings of the Combustion Institute,* Vol. 29, 2002.
11. Blevins, L. G., Yang, N. Y. C., Mulholland, G. H., and Davis, R. W., and Steel, E. B., "Early Soot from Inverse Diffusion Flames," Fuel Chemistry Division Preprints, 47(1), 2002.
12. Katta, V. R., Blevins, L. G., and Roquemore, W. M., AIAA Paper 2003-0666, Reno, NV.
13. Roquemore W. M., and Katta, V. R., *Journal of Visualization*, Vol. 2, Nos. 3/4, 2000, pp.257-272.
14. Katta, V. R., and Roquemore, W. M., *Combustion and Flame*, Vol. 100, No. 1, 1995, p. 61.
15. Wang, H., and Frenklach, M., *Combustion and Flame*, Vol. 110, No. 1, 1997, p. 173.
16. Annon., Computational Submodels, International Workshop on Measurement and Computation of Turbulent Nonpremixed Flames., http://www.ca.sandia.gov/tdf/Workshop/Submodels.html, 2001.
17. Katta, V. R., Goss, L. P., and Roquemore, W. M., *AIAA Journal*, Vol. 32, No. 1, 1994, p. 84.
18. Katta, V. R., Goss, L. P., and Roquemore, W. M., *Int. J. Num. Methods Heat Fluid Flow*, Vol. 4, No. 5, 1994, p. 413.
19. Katta, V. R., Carter, C. D., Fiechtner, G. J., Roquemore, W. M., Gord, J. R., and Rolon, J. C., in *Twenty-seventh Symposium (International) on Combustion*, The Combustion Institute, Pittsburgh, PA, 1998, p. 98.
20. Katta, V. R., and Roquemore W. M., *AIAA Journal*, Vol. 36, No. 11, 1998, p. 2044.
21. Harris, S., Weiner, A. M., and Blint, R., "Formation of Small Aromatic Molecules in a Sooting Ethylene Flame," *Combustion and Flame*, Vol. 72, 1988, pp. 91-109.

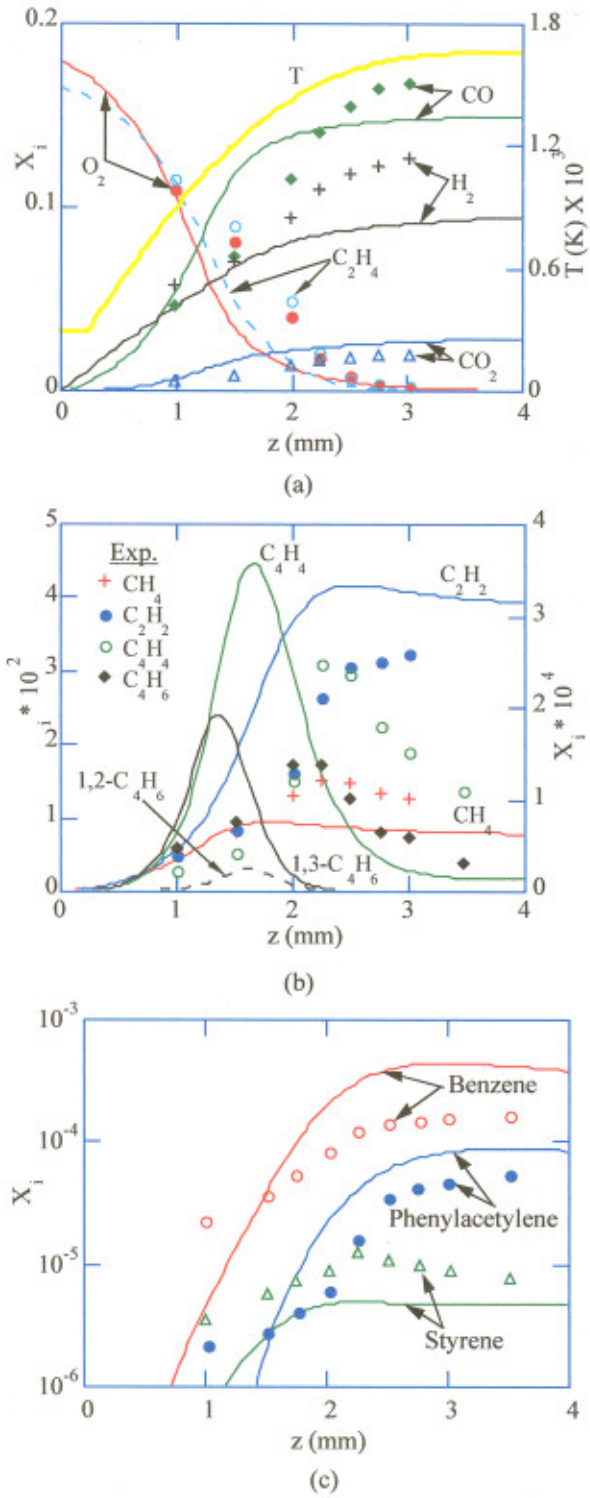

Fig. 1. Comparison between measured and computed species distributions for the burner-stabilized premixed flame. Calculations for this one-dimensional flame were made using UNICORN and by imposing temperature profile shown in (a).

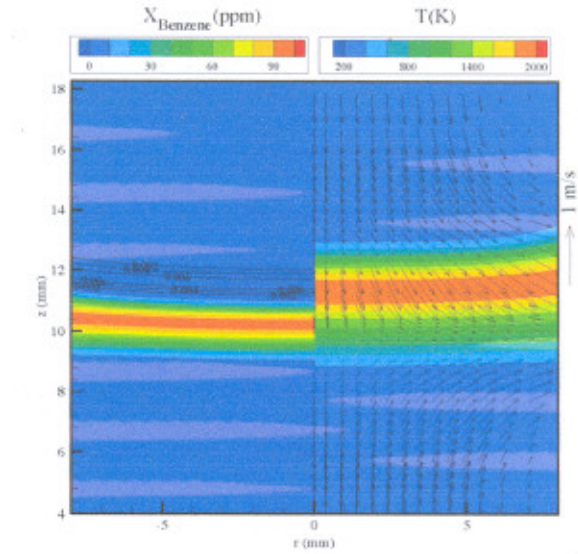

Fig. 2. A low-strained, opposing-jet diffusion flame. T and V are plotted on right and $X_{benzene}$ and X_{OH} on left.

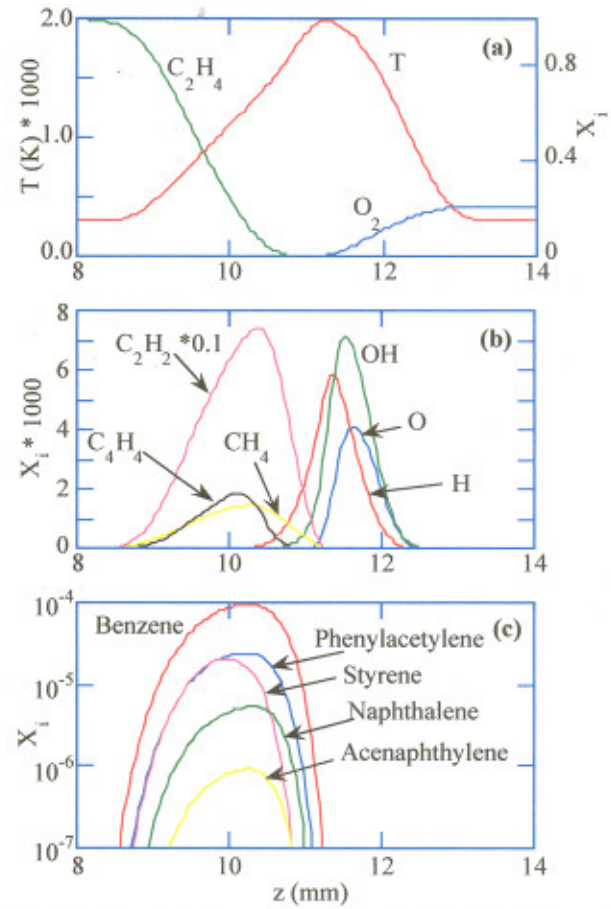

Fig. 3. Flame structure along the centerline. Variations of (a) T and reactants, (b) minor species, and (c) PAH species across the flame surface.

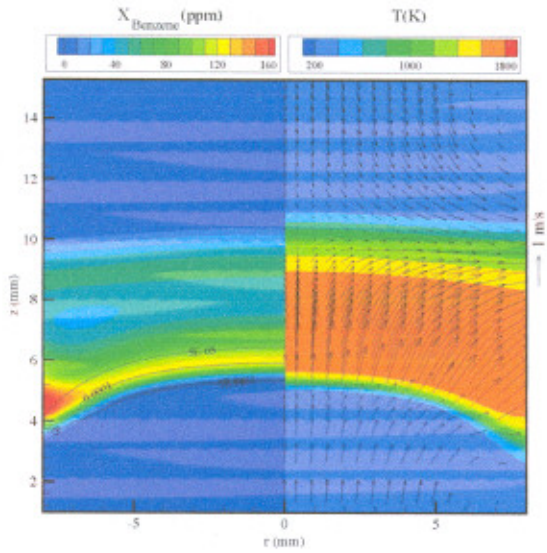

Fig. 4. A fuel-rich, opposing-jet premixed flame. T and V are plotted on right and $X_{benzene}$ and X_{OH} on left.

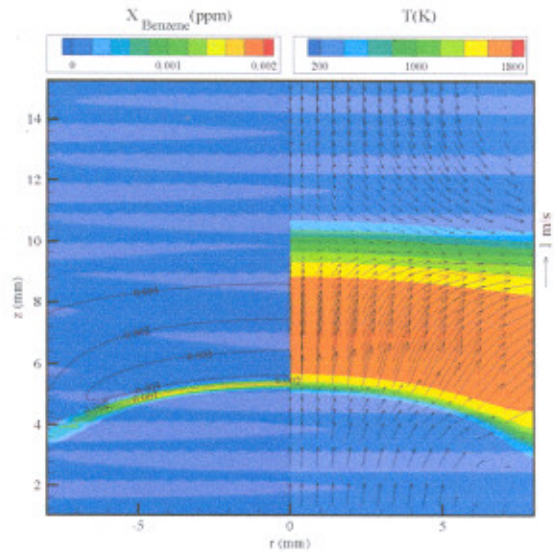

Fig. 6. A fuel-lean, opposing-jet premixed flame. T and V are plotted on right and $X_{benzene}$ and X_{OH} on left.

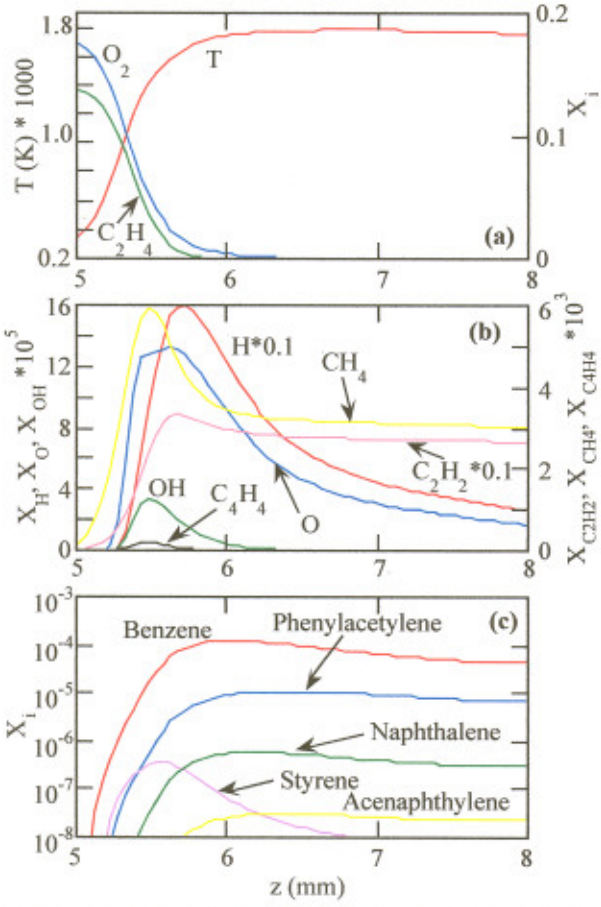

Fig. 5. Flame structure along the centerline. Variations of (a) T and reactants, (b) minor species, and (c) PAH species across the flame surface.

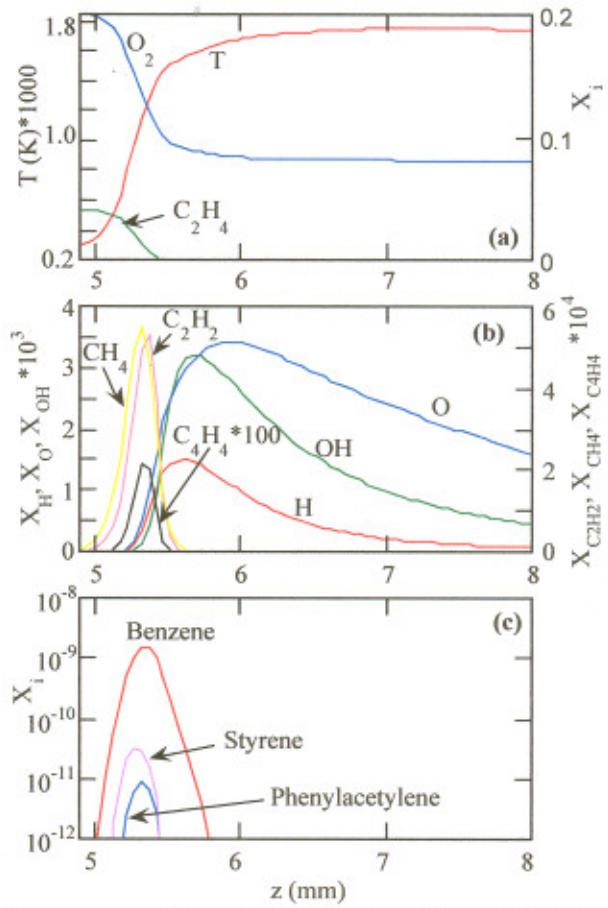

Fig. 7. Flame structure along the centerline. Variations of (a) T and reactants, (b) minor species, and (c) PAH species across the flame surface.

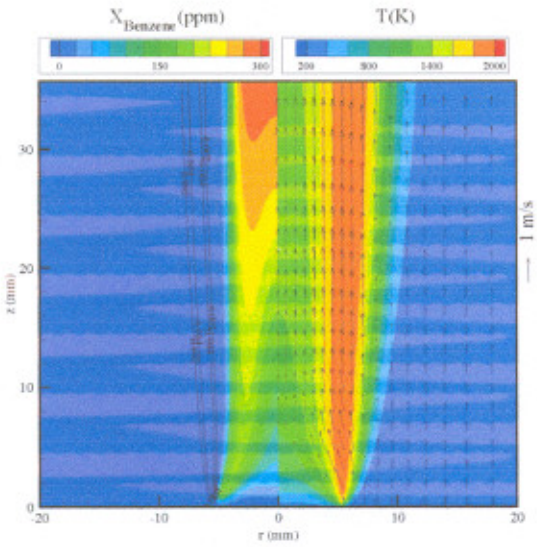

Fig. 8. A low-speed, coaxial-jet diffusion flame. T and V are plotted on right and $X_{benzene}$ and X_{OH} on left.

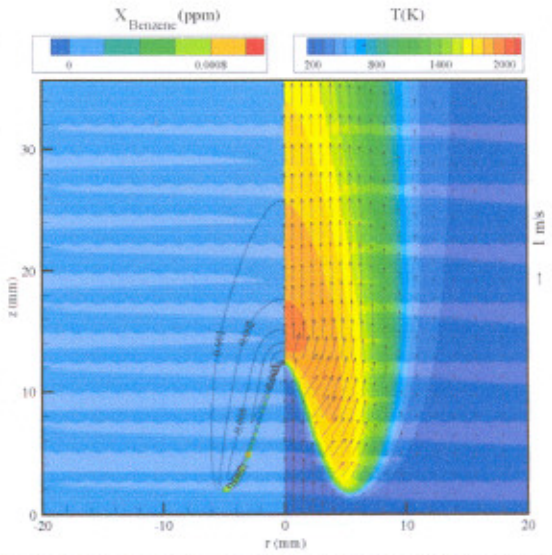

Fig. 10. A low-speed, coaxial-jet premixed flame. T and V are plotted on right and $X_{benzene}$ and X_{OH} on left.

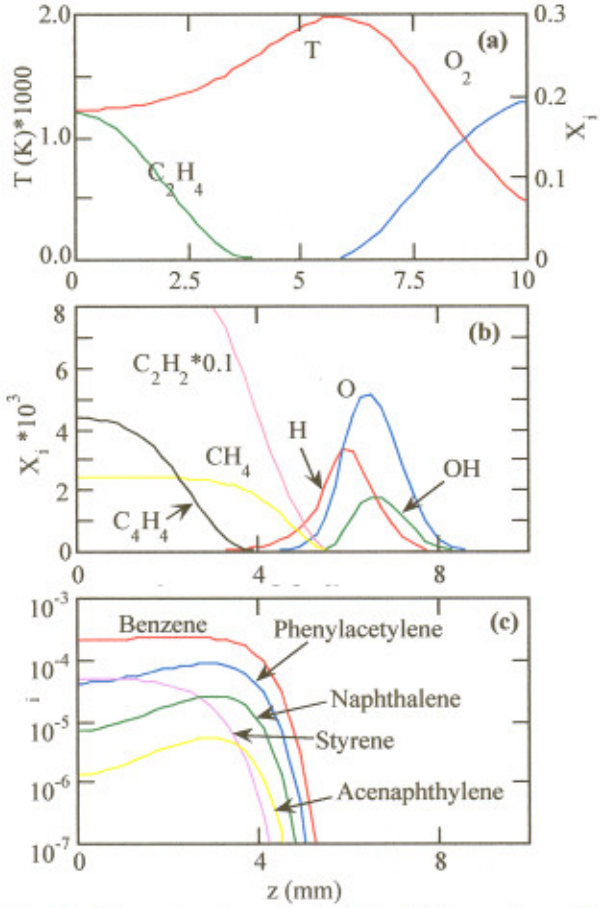

Fig. 9. Flame structure at a height of 20-mm above the burner. Variations of (a) T and reactants, (b) minor species, and (c) PAH species across the flame surface in the radial direction.

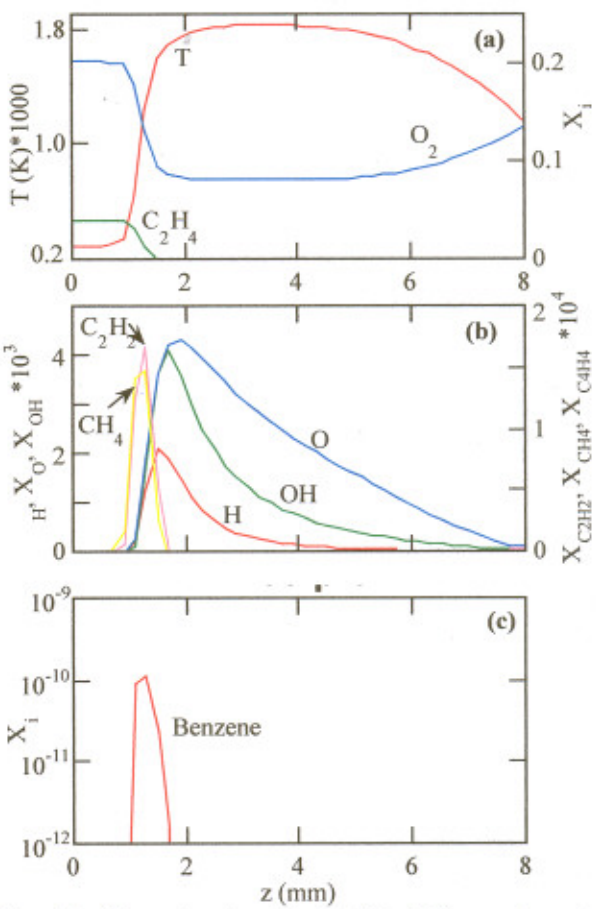

Fig. 11. Flame structure at a height of 10-mm above the burner. Variations of (a) T and reactants, (b) minor species, and (c) PAH species across the flame surface in the radial direction.

Triple Flame Propagation and Stabilization in a Laminar Axisymmetric Jet

X. Qin, I. K. Puri*, S. K. Aggarwal, V. R. Katta†
Department of Mechanical Engineering
University of Illinois at Chicago
842 W. Taylor St., Chicago, IL 60607-7022

Abstract
Methane-air triple flame propagation and stabilization is investigated experimentally and numerically in both partially premixed and nonpremixed jet modes. The objective is to examine the characteristics (such as local flame displacement speed, flame stretch, curvature, etc.) of the propagating flame at the triple points (or the leading edge). Following ignition in a nonuniform mixture, well defined triple flames are formed that propagate upstream toward the burner. During the flame propagation, it undergoes effects of unsteady stretch, especially for the nonpremixed jet, and this brings ambiguity in defining the triple points since the flame shape and structure changes. A low stoichiometry region around the triple points was found and this has an important implication for the flame propagation near the triple point.

Introduction

Triple flame behavior has been extensively studied because of the important role of these flames during flame stabilization, flame spread, and re-ignition in turbulent combustion [1]. Kioni *et al*. [2], and Plessing *et al*. [3] investigated the formation of triple flames in a nitrogen-diluted methane stream. They concluded that the existence of a fuel mass fraction gradient normal to the flow direction, along which the equivalence ratio varies from fuel rich to fuel lean, is an essential condition for the formation of a triple flame. The ability to propagate in a non-uniform mixture is an important characteristic of a triple flame. The flame can propagate with either a positive or a negative flame speed, depending upon various system parameters, such as the Lewis number, flame stretch, and heat loss [4].

Triple flames occur in many combustion devices, such as various industrial burners, and IC and aircraft engines. The process of re-ignition can involve the formation of a triple flame that may lose its characteristics during propagation [1]. Under certain conditions a propagating triple flame may lose one or both of its premixed wings and degrade into an "edge flame" [5,6]. This transition is of both fundamental and practical interest and it is worthwhile to verify the validity of the various theories that seek to explain this phenomenon.

Hartley and Dold [7] and Ruetsch *et al*. [8] have reported analytical and numerical investigations of triple flame propagation in nonuniform mixtures. They found that the flame propagation speed decreases as the mixture fraction gradient is increased. However, their results were obtained using a single-step global reaction model with idealized assumptions that ignored the effects of unequal species diffusivities. Furthermore, realistic flames are stretched, and experience time-varying mixture fraction gradients and changes in their shape and curvature, factors that have not previously been addressed in detail. Echekki and Chen [9] numerically investigated the influence of gravity in the upward and downward propagation and structure of triple flames. However, they too considered single step chemistry and diffusionally neutral mixtures. Their investigation considered freely propagating triple flames and, hence, those results are inapplicable for flame positions in proximity to a burner.

Kioni *et al*. [2] conducted a numerical investigation of a propagating triple flame, and observed that with increasing strain rate the complex structure of a triple flame transforms into that of a conventional nonpremixed flame. Im and Chen [10] investigated the effect of flow strain on triple flame propagation and showed that the precise identification of the triple point of a propagating triple flame that is subject to a large strain field becomes ambiguous. They demonstrated that large discrepancies arise in the flame displacement speeds determined at the triple point that is variously defined as the location of the maximum curvature or by the maximum heat release. Ko and Chung [11] investigated the propagation of laminar triple flames in nonpremixed methane jets, and examined the correlations for flame propagation speed with respect to flame curvature, stretch, and fuel mass fraction gradient. However, they focused on the far field of various axisymmetric jets and did not address the transition of a triple flame into a nub, which is expected to occur near a burner rim.

Despite the abundance of the literature related to the phenomenon, it is still difficult to compare experimental measurements of triple flame propagation with analytical or numerical results due to a lack of quantitative data in

* Corresponding author: ikpuri@uic.edu
† Innovative Scientific Solutions, Inc. Dayton, Ohio 45440.
Proceedings of the Third Joint Meeting of the U.S. Sections of The Combustion Institute

idealized configurations. Therefore, it is necessary to further study the flame propagation phenomenon and clarify the transition of propagating triple flames into other structures in the vicinity of a burner.

Our objective in this context is to examine the characteristics of a propagating triple flame that is ignited downstream of a burner in the nonuniform mixture of an axisymmetric jet. The flame propagation speed is measured using a high-speed camera. A time-dependent computational model is used to simulate the transient ignition and flame propagation phenomena under normal-gravity conditions. The numerical results are validated through a comparison with experimental measurements and then used to investigate the characteristics in the vicinity of the triple point of a propagating triple flame.

Experimental and Numerical Methods

The transient processes associated with ignition and flame propagation in methane-air mixtures were investigated using an annular concentric burner that is schematically presented in Fig.1. The brass burner consists of a central tube with an inner diameter of 4.5 mm and an outer diameter of 6.1 mm, which is surrounded by a concentric outer tube of 11.4 mm diameter. The burner has a length of 200 mm to ensure fully developed Poiseuille flow at the exit. A hollow acrylic cylinder with a diameter of 120 mm was placed concentrically around the burner to minimize the effect of outside disturbances. Either methane or methane-air fuel-rich mixtures were introduced from the inner tube, while air was introduced from the outer tube.

The methane-air mixtures were ignited 35 mm downstream from the burner by a pulsed Nd:YAG laser (Continuum, Surelite SL II-10) with a maximum power of 300 mJ at 532 nm. The laser ignition system is also shown schematically in Fig. 1. The laser beam was focused with a convex lens and the mixture was ignited at the focal point using a single pulse with duration of 6 ns. A successful ignition event was generally followed by the formation of a triple flame that propagated upstream and eventually stabilized at the burner exit. Flame propagation images were recorded by a high-speed video camera (Kodak EktaPro) with a 1 ms exposure time (at 1000 frames per second).

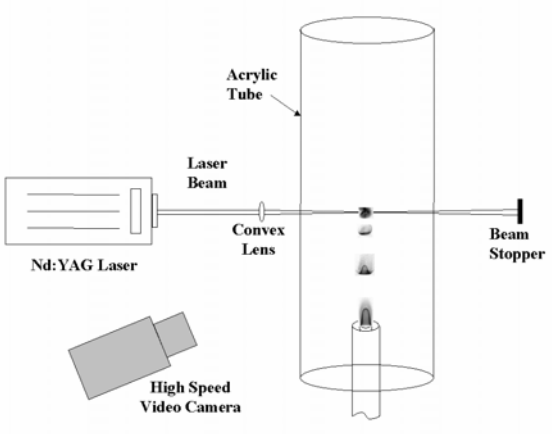

Fig.1: Schematic Diagram of experimental set-up.

The computational model employs an implicit algorithm to solve the unsteady gas–phase equations. The simulation method, which is described in detail elsewhere [12], solves the time–dependent governing equations for a two–dimensional, axisymmetric reacting flow. The methane–air chemistry is modeled using a detailed C2 mechanism that considers 24 species and 81 elementary reactions [13]. The mechanism has been validated for the computation of premixed flame speeds and the structure of nonpremixed and partially premixed flames [14,15].

The computational domain of 100 mm × 50 mm in the axial (z) and radial (r) directions, respectively, is represented by a staggered, non-uniform 591×125-grid system. The domain is bounded by a symmetry axis and an outflow boundary in the radial direction, and by an inflow and another outflow boundary in the axial direction. The outflow boundaries in both directions are located sufficiently far from the respective inflow and symmetric boundaries so that the propagation of boundary–induced disturbances is minimized. At the inflow boundary, a fully developed pipe flow in the inner tube and flat-velocity profiles outside the inner tube were used. The temperature and species-mass-fraction profiles are assumed to be uniform at the inflow boundary.

Results and Discussion

Flame Propagation

Two cases were considered in this investigation of triple flames. For case A, a methane-air mixture at an equivalence ratio of 2.0 and with a mean burner exit velocity of 0.5 m/s was introduced from the inner tube and air was supplied from the outer tube. The observations from this case allowed us to examine the formation and propagation of a triple flame in a partially premixed jet. For case B, pure methane was introduced from the inner tube at a mean burner exit velocity of 0.1 m/s and air was provided from the outer tube. This case allowed an examination of the propagation of a triple flame in a nonpremixed jet mode. For both cases, the mean velocity of the outer airflow was 0.3 m/s.

Methane-air mixtures were ignited at a 35 mm height downstream of the burner exit. Figure 2 presents the temporal evolution of the flame topology for case A in the form of high-speed video images. The images begin with flame ignition and subsequently show the flame propagating to a stationary burner–stabilized state. In general, two reacting volumes (or kernels) are formed following ignition. One propagates downstream and is quickly extinguished. The other propagates upstream and develops into a triple flame, which is the focus of this investigation. The triple point is clearly established by $t \approx$

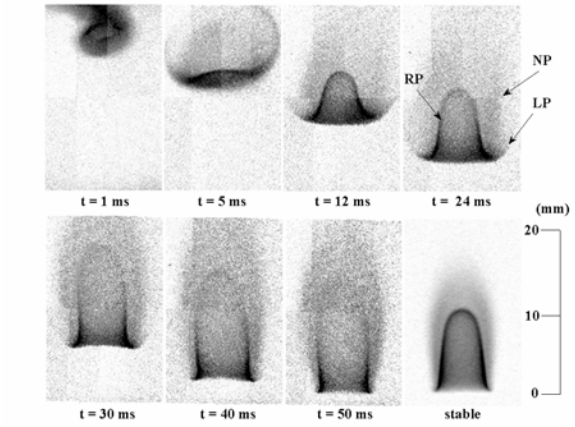

Fig. 2: Experimental images showing the temporal evolution of ignition and flame propagation for case A. The notation RP, NP, and LP is used to represent the rich premixed, nonpremixed, and lean premixed reaction zones, respectively.

5ms and a well-defined triple flame develops at ≈ 12 ms. The rich-premixed (RP) and lean-premixed (LP) reaction zones, as well a nonpremixed (NP) reaction zone that is established between the RP and LP reaction zones can be readily identified in the 12 and 24 ms images. As the flame propagates upstream, the inner RP and the NP reaction zones become longer and globally they both appear to move more slowly than the triple point or leading edge of the flame. Simultaneously, the flame curvature around the triple point increases significantly. When the triple flame approaches the burner and is stabilized near its exit, it transforms into a double flame due to the absence of the mixing layer, i.e., the outer lean

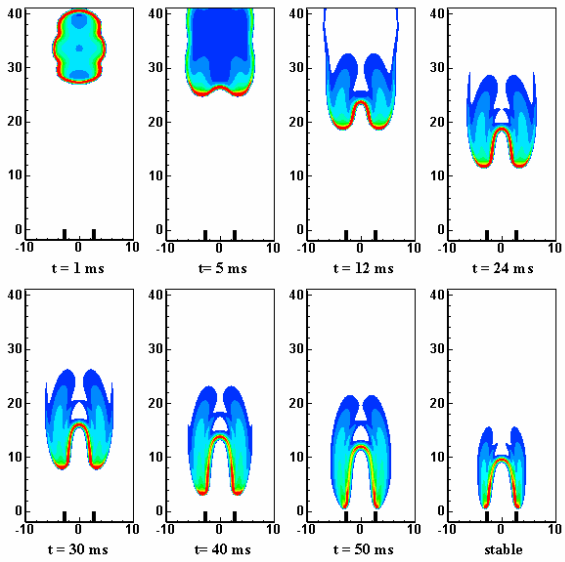

Fig.3: Simulated images showing the temporal evolution of ignition and flame propagation in terms of heat release rate contours for case A.

premixed reaction zone loses its distinct identity and becomes merged with the NP reaction zone.

Figure 3 presents the simulated transient ignition and flame propagation processes for case A. These processes are represented through the heat release rate contours for the same incremental times corresponding to Fig. 2. The transient processes associated with the formation of a reacting volume, its evolution into a triple flame followed by the upstream propagation of the triple flame, and its stabilization near the burner exit in the form of a double flame are clearly reproduced by the simulation. Comparing Figs. 2 and 3, we observe that despite some differences in the flame topology, the simulated results are in good agreement with the experimental observations with respect to the position of the propagating flame and the corresponding flame speed, the flame height and width, and the final shape of the burner–stabilized flame.

Figure 4 presents the simulated results for the nonpremixed jet (case B) in terms of the heat release rate (right) and normalized oxygen mass fraction (left) contours during the ignition and flame propagation processes. Again, ignition results in the formation of two reacting volumes, one moving upstream and the other downstream. The upstream volume develops into a triple flame as clearly shown by the heat release rate contours at t = 3.5 and 12 ms. However, in a spatial sense, the two premixed reaction zones and the nonpremixed flame are closely connected, especially at the flame base. It may, therefore, be more appropriate to use the term “edge flame” to describe this case. As the flame propagates

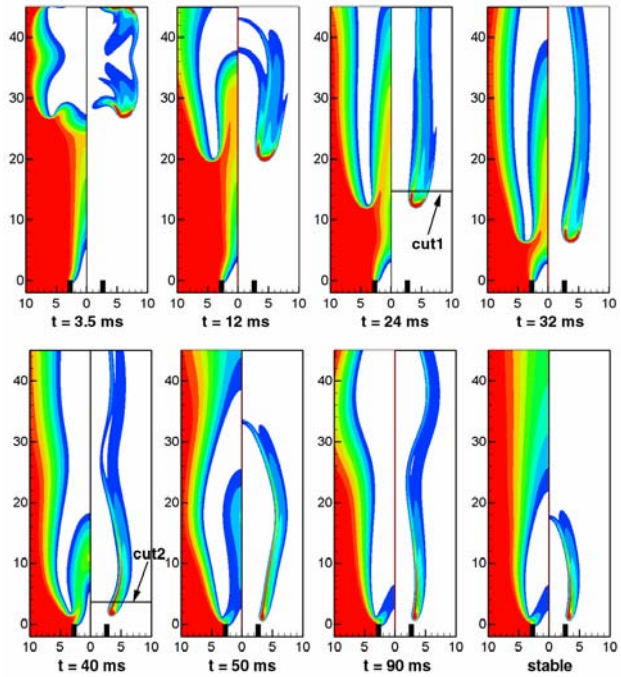

Fig. 4: Computed heat release rate (right) and normalized O_2 mass fraction (left) contours for case B.

upstream, the curvature in the vicinity of the triple point becomes larger, and the flame experiences increasing curvature-induced stretch. After t = 40 ms, when the flame is close to the burner rim, the inner RP and outer LP reaction zones merge with the NP zone.

Comparing Figs. 3 and 4, we observe that the triple flame established for case A (in the partially premixed mixing layer) propagates more evenly than the flame established for case B (in the pure methane/pure air mixing layer). Here, use of the term "even" implies that the flame propagates along a more linear path for case A as compared to the S-shaped path followed by the case B flame. The propagation of the flame base (which is really the "leading edge" of the triple flame) for case B occurs along a complex contour. The leading edge first moves towards the centerline, then moves outwards or away from it, then once again towards the centerline, and finally stabilizes just above the outer periphery of the burner rim. The relatively low fuel velocity for case B allows the flame to propagate closer to the centerline. The irregular flame propagation for this case occurs mainly due to the differences in the inner and outer flow velocities rather than the dissimilarities in the mixing layers.

The nonpremixed flame for case B has a longer "tail" than the flame for case A. From the oxygen mass fraction contours presented in Fig. 4, we observe that, due to the entrainment of air, oxygen penetrates into the mixing layer and forms a relatively oxygen-rich region near the triple point. For both cases, the flame loses its triple reaction zone structure before it reaches the burner rim. The approximate location where this occurs is at z ≈ 5 mm for case A and z ≈ 10 mm for case B.

Characteristics at the Triple Point

Triple Point Location

The triple point at the flame base is defined as the location of the intersection of stoichiometric mixture fraction line and the specified OH isocontour. The definition of mixture fraction follows Bilger [16]. This definition is generally employed to investigate non-premixed flames, but we have previously shown that mixture fraction based state relationships can also be developed for partially premixed flames [17,18,19].

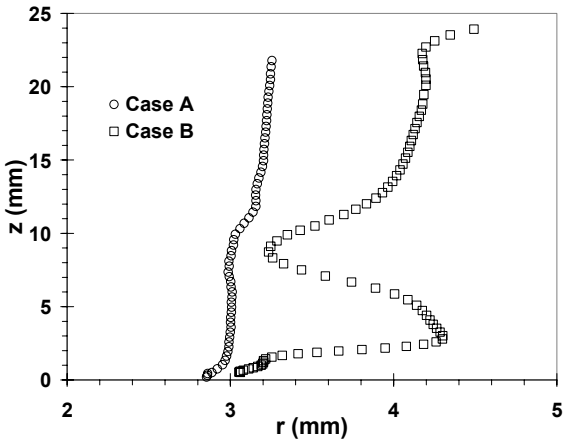

Fig. 5: Loci of triple points from the simulations.

Figure 5 presents the loci of triple points during flame propagation for both cases A and B. Several observations can be made from this figure. First, the triple points for case B are located far from the centerline as compared with those for case A. This is attributed to the addition of air to the fuel jet in case A that brings the stoichiometric mixture fraction location closer to the centerline. Second, the flame propagates relatively smoothly for case A as compared to case B (refer to Figs. 3 and 4). For the latter, the propagation contour follows an "S" shape. The complex path traversed by the flame for case B is related to interactions between the propagating flame and the vortical flow ahead of the flamefront, as discussed in the following section. Third, for both cases, as the flames approach the burner, they oscillate near the burner surface before stabilizing above it. This oscillation is more prominent for case B. As mentioned in the context of Figs. 3 and 4, the flame undergoes a significant transition near the burner rim. Therefore, although it may not be entirely meaningful to use the term triple point after its transition to an edge flame, we will continue to apply that terminology in order to be consistent and compare our results at various axial locations.

We have selected two instances for case B and plotted the velocity vectors near the flame base in Fig. 6 in order to observe the flame propagation and flow behavior near the flame base more closely.The flamefront is represented

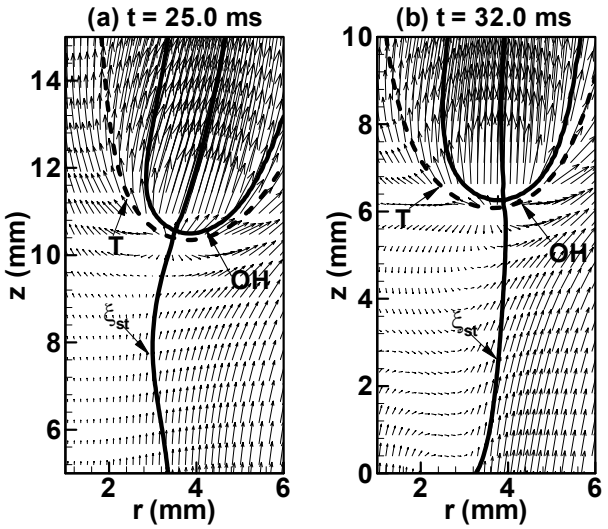

Fig. 6: Simulated velocity field near the triple points at two instances during flame propagation for case B. The flamefront is represented by the OH isocontour of 3×10^{-5}. The solid line represents the stoichiometric mixture fraction contour. The dashed line is the 600 K isotherm.

by the OH mass fraction isocontour of 3×10^{-5}. We can see from Fig. 6 that as the flame proceeds into the unburned gases it behaves much like a solid body traveling against the incoming flow. In general, the volumetric expansion resulting from a stationary flame generates a positive pressure gradient for the incoming reactant flow, which, in turn, decelerates and/or deflects the fluid entering the flame zone. The velocity of a stretched propagating flame is higher than that of a corresponding unstretched stationary flame. The higher burning velocity causes stronger volumetric expansion and generates larger pressure gradients in the incoming flow. When the flow velocity is small, this large pressure gradient causes flow reversal in the upstream region of the flame edge as seen in Fig. 6. However, as the flame becomes stationary when it reaches the burner tip, a decrease in the flow velocity occurs in the region upstream of the flame edge.

Even though the velocity vector maps of the propagating flame shown at 25 and 32 ms in Figs. 6(a) and (b), respectively, are similar in the locations downstream of the flame edge, important differences in the velocity fields can be observed at upstream locations. In Fig. 6(a), the stoichiometric mixture fraction line bends towards the centerline (or is concave to it) at $z \approx 8$ mm due to strong entrainment of coflow air at t = 25 ms, consequently, the leading edge of the flame moves towards the centerline. There is a low velocity region just ahead of the triple point and the streamlines diverge upstream of this area. Since the outer air coflow has a higher mean velocity, the velocity gradient also aids in bending the ξ_{st} line towards the centerline.

Vorticity Evolution

In Fig. 6(b), when the flame propagates past $z \approx 7$ mm (at t = 32 ms), there is flow circulation ahead of its leading edge, forcing the stoichiometric mixture fraction line away from the centerline (or convex to it) and causing the flame to propagate outwards. In Fig. 7, we present the instantaneous vorticity contours, isotherms and velocity vector plots at different times during the development and propagation of triple flame for case B in order to examine the vorticity field near the triple point. Figures 7(a) and 7(b) present the flame development process, Figs. 7(c) to 7(e) the triple flame propagation, and Fig. 7(f) a nonpremixed flame during the process of stabilization near a burner wall. A vortex is established following ignition at (z, r) ≈ (28 mm, 6 mm), i.e., in the lower portion of the ignition kernel or reacting volume (cf. Fig. 7(a)). The ignition kernel subsequently develops into a triple flame (cf. Fig. 7(c)), and, as this flame propagates upstream, the vortex stays ahead of the flame front as indicated in Figs. 7(c) and 7(d). Although the vortex becomes weaker as it moves upstream, it nevertheless influences the mixing behavior upstream of the triple point, and, thereby, its propagation characteristics. Eventually the vortex is dissipated as the triple flame approaches the burner and undergoes transition to a nonpremixed flame near the burner wall (cf. Fig. 7(f)).

Figures 7(c) and 7(d) also indicate regions of large positive and negative vorticity near the RP and LP zones, respectively. This vorticity is generated by flow expansion or dilatation due to heat release in the two reaction zones. As the flame approaches the burner and the RP reaction zone merges with the NP reaction zone, the positive vorticity field interacts with the vorticity field generated at the burner wall, which is shown in Fig. 7(e). A small recirculation zone is established downstream of the wall that aids in the flame stabilization process (cf. Fig. 7(f)) as the nonpremixed flame stabilizes near the burner wall.

The flame propagation speed V_f can be determined experimentally from the high-speed camera images, i.e. $V_{f,exp} = \Delta z / \Delta t$, where Δz denotes the distance between two sequential triple points along the direction normal to the leading edge, and Δt the time difference. Equation (2) treats the flame globally as a solid object and provides an average flame speed along the axial (z) direction. However, this equation cannot accurately provide information about the local flame propagation speed if the flame does not move linearly along z, such as in case B.

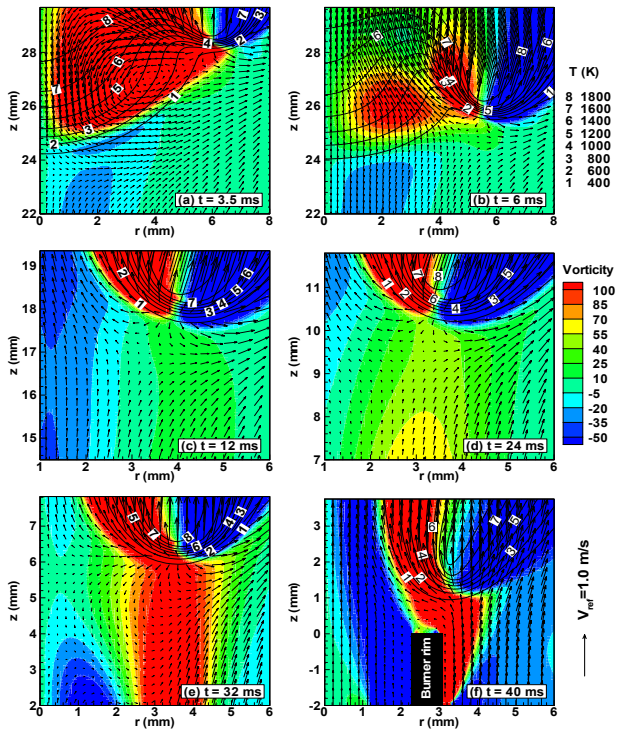

Fig. 7: Simulated vorticity contours, temperature contours and velocity field showing the vorticity evolution at six different times during triple flame development and propagation for case B.

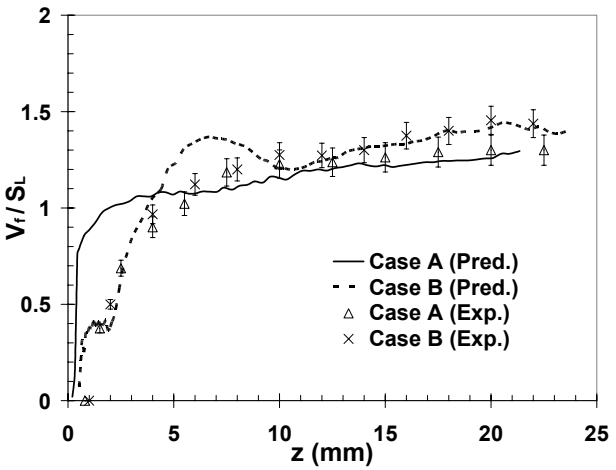

Fig. 8: Flame propagation speeds along the axial distance.

Figure 8 presents the flame propagation speed V_f obtained from high-speed video images and from the simulated triple point locations in Fig. 5. The flame speeds are normalized by the stoichiometric laminar burning velocity S_L of methane-air mixtures (assumed to have a value of 0.4 m/s). For both cases, the measured and predicted flame propagation speeds decrease monotonically as the flame approaches the burner. This is in accord with Ko and Chung's results [11] and the predictions of Hartley et al. [7] and Ruetsch et al. [8]. Moreover, there is good agreement between the measured and predicted flame speeds, except for a small discrepancy near the burner rim.

Conclusions

The characteristics of propagating triple flames and of the transition from a triple flame structure to partially premixed and nonpremixed structures are investigated. There is good qualitative agreement between the measured and predicted flame propagation characteristics, including (i) the global features such as flame topology, (ii) temporal characteristics such as flame location with respect to time and global (1-D) flame speed.

The simulations indicate that the flame leading edge or triple point, which can be defined by the intersection of the stoichiometric mixture fraction line and the specific OH isocontour, propagates along the stoichiometric mixture fraction line. This result is in accord with our previous investigation concerning flame liftoff and downstream propagation. Following ignition, a vortex forms ahead of the ignition kernel or reacting volume. As the ignition kernel develops into a propagating triple flame, the vortex propagates with the flame front, but ahead of it. Although the vortex becomes weaker during its propagation, it nevertheless influences the mixing behavior upstream of the triple point and, thereby, its propagation characteristics (especially for the case when triple flame undergoes transition to nonpremixed flame). When the flame approaches the burner wall, the mixture fraction gradient increases and the two premixed wings of the triple flame diminish in size and finally merge with the nonpremixed wing to form a double flame (for case A) or a nonpremixed flame (in case B).

Acknowledgements

This research was supported by the National Science Foundation Combustion and Plasma Systems Program for which Dr. Farley Fisher is the Program Director, and by the NASA Microgravity Research Division for which Dr. Uday Hegde serves as the technical monitor.

References

1. Vervisch, L., Proc. Combust. Inst. 28:11 (2000).
2. Kioni, P. N., Rogg, B., Bray, K. N. C., and Liñán, A., Combust. Flame 95:276 (1993).
3. Plessing, T., Terhoeven, P., Peters, N., and Mansour, M. S., Combust. Flame 115:335 (1998).
4. Thatcher, R. W. and Dold, J. W., Combust. Theory Modell. 4:435 (2000).
5. Buckmaster, J., Combust. Sci. Technol. 115:41 (1996).
6. Buckmaster, J., J. Eng. Math. 31:269 (1997).
7. Hartley, L. J., and Dold, J. W., Combust. Sci. Technol. 80:23 (1991).
8. Ruetsch, G. R., Vervisch, L., and Liñán, A., Phys. Fluids 7:1447 (1995).
9. Echekki, T. and Chen, J.-Y., Combust. Theory Modell. 5: 499 (2001).
10. Im, H. G., and Chen, J. H., Combust. Flame 126: 1384 (2001).
11. Ko, Y. S. and Chung, S. H., Combust. Flame 118: 151 (1999).
12. Shu, Z., Aggarwal, S. K., Katta, V. R., and Puri, I. K., Combust. Flame 111: 276 (1997).
13. Peters, N., Reduced Kinetic Mechanisms for Applications in Combustion Systems, Lecture Notes in Physics, N. Peters and B. Rogg (Eds.), Springer–Verlag, Vol. m15, 1993, p. 3.
14. Xue. H., and Aggarwal, S. K., AIAA Journal 39-4: 637 (2001).
15. Shu, Z., Katta, V. R., Puri, I. K., and Aggarwal, S. K., Combust. Sci. Technol. 157:185 (2000).
16. Bilger, R. W., Proc. Combust. Inst. 22:475 (1988).
17. Aggarwal, S. K., and Puri, I. K., AIAA J. 36: 1190 (1998).
18. Puri, I. K., Aggarwal, S. K., Ratti, S., and Azzoni, R., Combust. Flame 124: 311 (2001).
19. Qin, X., Puri, I. K., and Aggarwal, S. K., Phys. Fluids, 40: 731 (2001).

Ninth International Conference on Numerical Combustion, April 7-10, 2002, Sorrento, Italy, pp. 427-428

Behavior of a Jet Diffusion Flame in a Multi-Vortex Flow Field

V. R. Katta
Innovative Scientific Solutions, Inc.
2766 Indian Ripple Road
Dayton, OH 45440

and

W. M. Roquemore
Air Force Research Laboratory
Propulsion Directorate
Wright-Patterson Air Force Base, OH 45433

Abstract:

Studies on single vortex-flame interactions are important to the understanding of turbulent-flame behavior. However, construction of the mathematical and physical models for turbulent flames based on the understanding gained from single vortex-flame interactions seems rather difficult. A natural remedy to this difficulty is to acquire understanding on multi-vortex-flame interactions. A numerical investigation is performed in this study to generate interaction of a flame surface with multiple vortices simultaneously. This turbulent-like flow field in an opposing-jet diffusion flame is generated by driving two vortices simultaneously from the air and fuel sides toward the flame surface with different velocities. Changes in the structure of the flame during its interaction with the incoming vortices and the instability that generated multiple vortices are investigated using a time-dependent CFDC code that incorporates 13 species and 74 reactions.

Introduction:

Studies on the structure of dynamic flames are important to the understanding of fundamental combustion processes; they provide insights into turbulent combustion phenomena and help developing and evaluating simplified models that can be used in design codes for practical combustion systems. Unsteady flames are subjected to stretching that varies in time; typically, the time scale for the changes in strain rate is comparable to the chemical response time of the system. Numerous investigations (experimental and numerical)[1-3] have been performed to quantify the scalar structure of steady state, aerodynamically strained, planar diffusion flames. Such studies on counterflow diffusion flames have not only provided benchmark experimental data but also yielded valuable insight into the flame behavior in response to strain rate. However, in practical combustion devices, flames are subjected to severe unsteadiness that results from the random motion of vortices;[4,5] this led to studies of unsteady counterflow flames. To retain the simplicity offered by planar diffusion flames, unsteadiness is imposed on counterflow flames by fluctuating the fuel and air jets simultaneously and sinusoidally.[6,7] These studies have demonstrated that the unsteady flames can be stretched beyond the steady-state extinction limit.

During vortex-flame interactions, which are often considered to be the building blocks for statistical theories of turbulence, the flame surface is subjected not only to unsteadiness but also to deformation. To investigate the effects of curvature on unsteady flames, both theoretical and

experimental studies have been initiated.[8,9] In particular, experiments designed by Roberts et al.[10] and by Rolon[11] have created great interest, especially because of their unique ability to inject a well-characterized vortex toward the flame surface.

Several investigators have developed models[12-14] for the study of single vortex-flame interactions in opposing-jet flames. In all of these models, it is assumed that an artificially created (by specifying the vorticity field) vortex pair interacts with a flat flame formed in a parallel flow. Although such an assumption has advantages in exploring interesting aspects of vortex-flame interactions, investigations employing this assumption do not represent actual interactions in opposing-jet flames and hence, they could not facilitate direct comparisons between predictions and measurement results and make verification of the predictions difficult.

Recent advances in computer-hardware technology and the need to improve the understanding of combustion phenomena under complex practical situations have led to the development of two- and three-dimensional Computational Fluid Dynamics models that incorporate detailed chemical kinetics (CFDC).[15,16] Complete simulation of the counterflow diffusion flame using multi-dimensional models would not only eliminate the concerns regarding the simplified analyses but also provide a valuable tool for studies of vortex-flame interactions in counterflow premixed[10] and diffusion[11] flames.

Structures of different types of unsteady flames have been studied recently by the authors[17] by issuing vortices from the fuel and air sides of an opposing-flow jet diffusion flame. They treated the unsteady flames into two categories--namely, traveling and stationary. In the first type not only the strain rate on the flame but also its location changes with time. On the other hand, in the second type, only the strain rate on the flame varies with time, while the flame itself is locked spatially. Issuing equal strength vortices simultaneously from the fuel and air sides toward the flame surface generated the latter type unsteady flames. In certain situations, this collision of vortices leads to the generation of multiple vortices and, thereby, a turbulent like flow field. This paper describes a numerical study of a flame subjected to interaction with multiple vortices, simultaneously, in a hydrogen opposing-jet diffusion flame.

Numerical Model:

Time-dependent, axisymmetric Navier-Stokes equations written in the cylindrical-coordinate (z-r) system are solved along with species- and energy-conservation equations.[18] A detailed-chemical-kinetics model has been used to describe hydrogen-air combustion. This model consists of thirteen species--namely, H_2, O_2, H, O, OH, H_2O, HO_2, H_2O_2, N, NO, NO_2, N_2O, and N_2. A detailed-chemical-kinetics model having 74 reactions among the constituent species is used, and the rate constants for this H_2-O_2-N_2 reaction system were obtained from Ref. 19.

Temperature- and species-dependent property calculations are incorporated in the model. The governing equations are integrated on a nonuniform staggered-grid system. An orthogonal grid having rapidly expanding cell sizes in both the axial and radial directions is employed. The finite-difference forms of the momentum equations are obtained using an implicit QUICKEST scheme,[20,21] and those of the species and energy equations are obtained using a hybrid scheme of upwind and central differencing. At every time step, the pressure field is calculated by solving the pressure Poisson equations simultaneously and utilizing the LU (Lower and Upper diagonal) matrix-decomposition technique. This model has been validated previously by simulating various steady and unsteady counterflow[22] and coflow[18,23] jet diffusion flames.

Results and Discussion:

The opposing-jet-flame burner used for the studies of unsteady flame structures was designed by Rolon[11] and is shown in Fig. 1(a) and is described in Ref. 11. A flat flame is formed between the fuel and air jets having velocities of 0.69 and 0.5 m/s, respectively. The hydrogen-to-nitrogen ratio used for the fuel jet is 0.38. Calculations for this axisymmetric flame were made using a non-uniform 301 x 241 mesh system distributed over a physical domain of 40 x 40 mm, which yielded a mesh spacing of 0.1 mm in both the axial (x) and the radial (r) directions in the region of interest.

The computed steady-state flame structure along the stagnation line is shown in Figs. 1(b) and 1(c). The 48-s^{-1} air-side strain rate of this flame represents a weakly strained one. The flame (peak-temperature region) is located at z = 19.2 mm, and its temperature of 1560 K is only slightly lower than the corresponding adiabatic temperature of 1614 K. In general, the peak strain rate on the fuel side (K_f = 60 s^{-1}) will be greater than that on the air side as a result of the difference in the density of the two jets. Even at this low strain rate, the fuel and oxidizer are not completely consumed simultaneously in the flame zone. In an overlap region of ~1 mm, both H_2 and O_2 are present.

The steady-state strain rate of the opposing-jet flame can be increased by gradually increasing the velocities of the fuel and air jets. Calculations were repeated by varying the jet velocities, and it was found that a stable steady-state flame could be obtained for fuel and air jet velocities of 16 and 14 m/s, respectively. These velocities yielded an air-side strain rate (K_a) and flame temperature of 1410 s^{-1} and 1130 K, respectively; these values agree favorably with calculations made by Gutheil et al.[24]

Vortices are shot toward the flame surface from both the air and fuel sides by injecting specific amounts of air and fuel, respectively, through the respective syringe tubes. In contrast to our earlier studies on single vortex-flame interactions,[17] very small size vortices are generated in this study to simulate a turbulent like flow field. The diameters of the injection tubes used for generating the fuel and air vortices are 2.8 and 1.4 mm, respectively. Evolution of the vortices and their interaction with the flame surface depend on the injection times. In general, with the shorter injection times, the generated vortices travel faster toward the flame surface and affect its structure as the local flow time scales approach the chemical time scales. Unsteady flame simulations were made by injecting air and fuel through the respective syringe tubes in such a way that the velocity at the exit increased linearly at a rate of 10^3 m/s/s. However, due to the differences in the sizes of the injection tubes, the vortex generated from the fuel tube dominated that generated from the air side.

An unsteady stationary flame was established initially as the two vortices approached the flame surface nearly at the same time. The interaction of the vortex-flame-vortex is shown in Fig. 2. The instantaneous locations of the particles indicate that the vortex originated from the fuel side is slightly smaller than the twice the diameter of the air-side vortex. The interaction of the two vortices with the flame surface resulted in point extinction. In this case, extinction first occurred at the stagnation line and then extended radially outward. This is in contrast to the annular extinction observed in the case of the air-side-vortex/flame interaction.[22]

As the interaction progressed further, a ring-type mushroom vortex was formed (Fig. 3). The flame is wrapped around this mushroom vortex. Two important points may be noted from Fig. 3. The impact of fuel and air side vortices at the stagnation plane resulted in secondary vortices on the fuel jet while the air jet maintains its laminar shear layer. Secondly, a flamelet was cut-off from the original flame and wrapped in the lower part of the mushroom vortex.

Figure 4 depicts the interaction of the flame with multiple vortices. The impingement of fuel and air jets resulted in a stream of vortices that are wrapped into a larger vortex. The typical size of the smaller vortex is ~1 mm while the larger vortex is about 7 mm in diameter. Because of the

presence of the smaller vortices, the flame became thicker and longer. Note, the extent of white particles (originated on the air side) spread on the flame surface.

The interaction at a much later stage is shown in Fig. 5. The vortices seem to be getting weaker due to two reasons. Firstly, the fuel jet shear-layer instabilities have dampened out as no source perturbation was added for continuous generation of these vortices. Secondly, the higher viscosity associated with the combustion products is dissipating the vorticity.

Conclusions:

Unsteady flames are often studied to gain a better understanding of turbulent-flame structures and, hence, facilitate the development of accurate turbulence-chemistry interaction models. A time-dependent CFDC code that incorporates 13 species and 74 reactions among the constituent species has been developed for simulation of unsteady flames resulting from different vortex-flame interactions in opposing-flow hydrogen jet diffusion flames. The model has been validated by direct simulation of several steady state and unsteady axisymmetric counterflow and coflow jet diffusion flames.

A steady-state opposing-flow jet flame was established using the Rolon-burner geometry. Several unsteady flames were then obtained by injecting vortices into the flow by ramping the velocity at the center portion of the air- and fuel-jet exits. Calculations are performed for the flame evolution in a turbulent-like flow field. The fluctuating quantities resulting from this flame-multi-vortex interaction will be compared with those obtained with single-vortex-flame interactions in the future.

Acknowledgments:

This work was supported, in part, by the Air Force Office of Scientific Research.

References:

1. Kee, R. J., Miller, J. A., Evans, G. H., and Dixon-Lewis, G., *Proc. Combust. Inst.* 22: 1479-1486 (1988).
2. Dixon-Lewis, G., *Proc. Combust. Inst.* 23: 305-324 (1990).
3. Chelliah, H. K., Law, C. K., Ueda, T., Smooke, M. D., and Williams, F. A., *Proc. Combust. Inst.* 23: 503-510 (1990).
4. Hottel, H. C., and Hawthorne, W. R. *Proc. Combust. Inst.* 3: 254-266 (1949).
5. Roquemore, W. M., Chen, L.-D., Goss, L. P., and Lynn, W. F. in *Turbulent Reactive Flows*, Lecture Notes in Engineering (R. Borghi and S. N. B. Murthy, Eds.) (Springer-Verlag, Berlin, 1989), Vol. 40, p. 49.
6. Darabiha, N., *Comb. Sci. Technol.*, 86: 163 (1992).
7. Egolfopoulos, F. N., and C. S. Campbell, *J. Fluid Mech.*, 318: 1 (1996).
8. Paul, P. H., and Najm, H. N., *Proc. Combust. Inst.* 27: 43-50 (1998).
9. Patnaik, G., and Kailasanath, K., *Proc. Combust. Inst.* 27: 711-717 (1998).
10. Roberts, W. L., Driscoll, J. F., Drake, M. C., Ratcliffe, J. W., *Proc. Combust. Inst.* 24: 169-176 (1992).
11. Rolon, J. C., Aguerre, F., and Candel, S., *Combust. Flame* 100:422 (1995)
12. Ashurst, W. T., *Combust. Sci. Technol.* 92:87 (1993).
13. Poinsot, T., Trouve, A., Veynante, D., Candel, S., and Esposito, E., *J. Fluid Mech.* 177:265 (1987).
14. Rutland, C. J., and Ferziger, J. H., *Combust. Flame* 84:343 (1991).
15. Smooke, M. D., Ern, A., Tanoff, M. A., Valdati, B. A., Mohammed, R. K., Marran, D. F., Long, M. B., *Proc. Combust. Inst.* 26: 2161-2168 (1996).
16. Katta, V. R., and Roquemore, W. M., AIAA Paper 97-0904, Jan., 1997.
17. Katta, V. R., Roquemore, *Proc. Combust. Inst.* 28 (2000).
18. Katta, V. R., and Roquemore, W. M., *Combust. Flame* 100:61 (1995).
19 Frenklach, M., Wang, H., Goldenberg, M., Smith, G. P., Golden, D. M., Bowman, C. T., Hanson, R. K., Gardiner, W. C., V. Lissianski, V., Gas Research Institute Technical Report No. GRI-95/0058, November 1, 1995.
20. Leonard, B. P., *Comput. Meth. Appl. Mech. Eng.*, 19:59 (1979).
21. Katta, V. R., Goss, L. P., and Roquemore, W. M., *AIAA J.*, 32:84 (1994).
22. Katta, V. R., Carter, C. D., Fiechtner, G. J., Roquemore, W. M., Gord, J. R., and Rolon, J. C., *Proc. Combust. Inst.* 27: 587-594 (1998).
23. Grisch, F., Attal-Tretout, B., Bouchardy, P., Katta, V. R., and Roquemore, W. M., *J. Nonlin. Opt. Phys. Mater.,* 5:505 (1996)
24. Gutheil, E., Balakrishnan, G., and Williams, F. A., in *Lecture Notes in Physics* (N. Peters and B. Rogg, Eds.) (Springer-Verlag, New York, 1993), pp. 177-195.

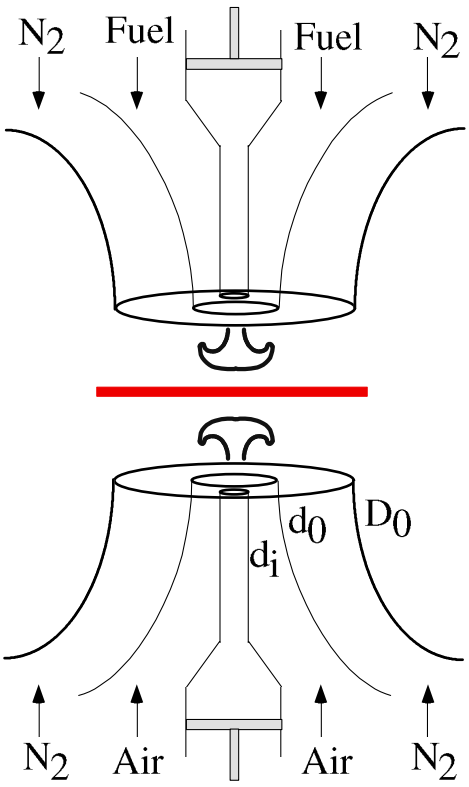

(a)

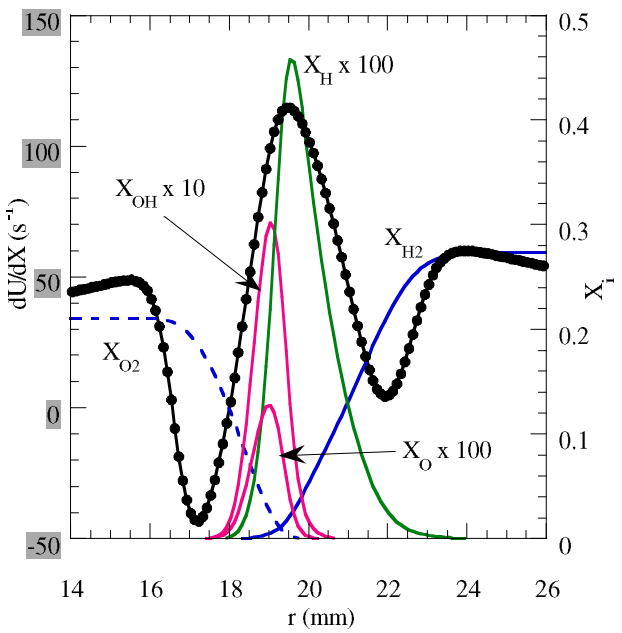

(b)

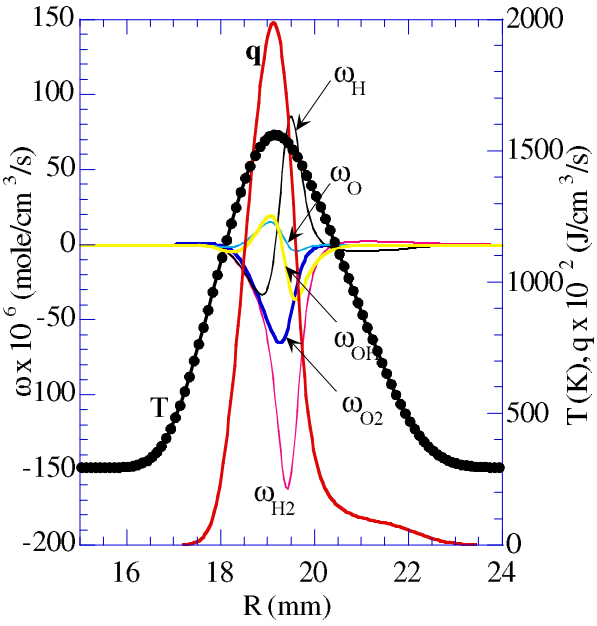

(c)

Figure 1. (a) Opposing-jet flame burner designed by Rolon, (b), (c) steady-state flame structure obtained for air and fuel jet velocities of 0.5 and 0.69 m/s, respectively.

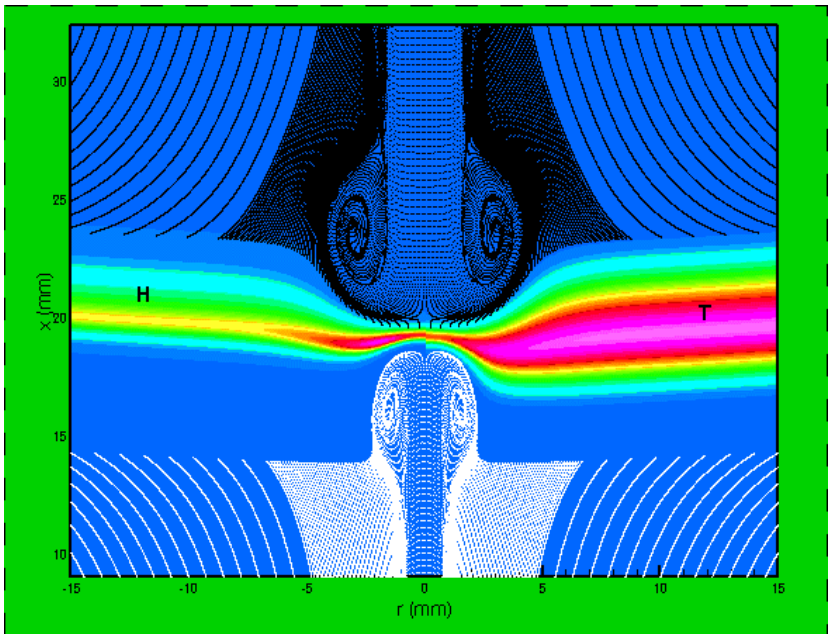

Fig. 2. Flame sandwiched between two colloiding vortices. Instantaneous locations of the particles are superimposed on temperature field (right) and H-mole concentration (left). Black particles represent those originated on fuel side and white ones represent those originated on the air side..

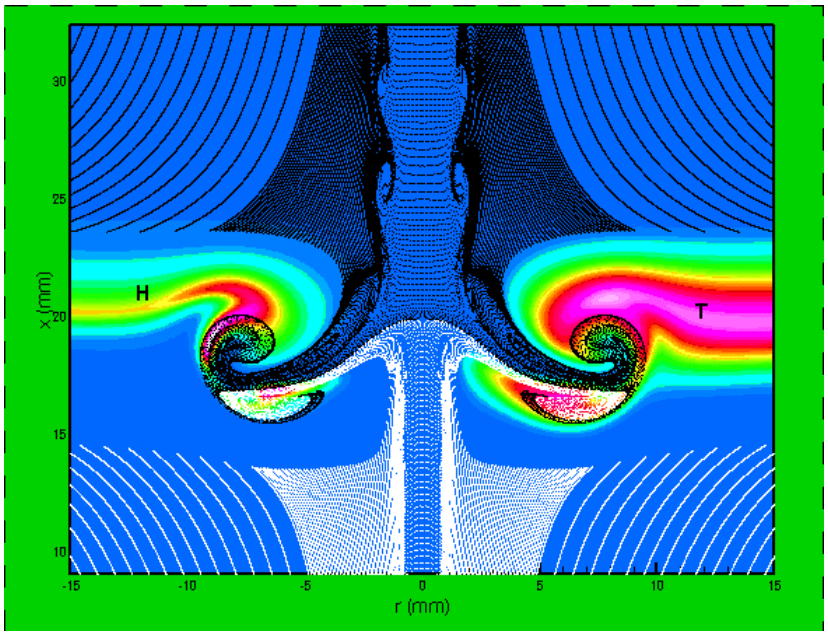

Fig. 3. Broken flame wrapped into the mushroom vortex. Legend is same as that of Fig. 2.

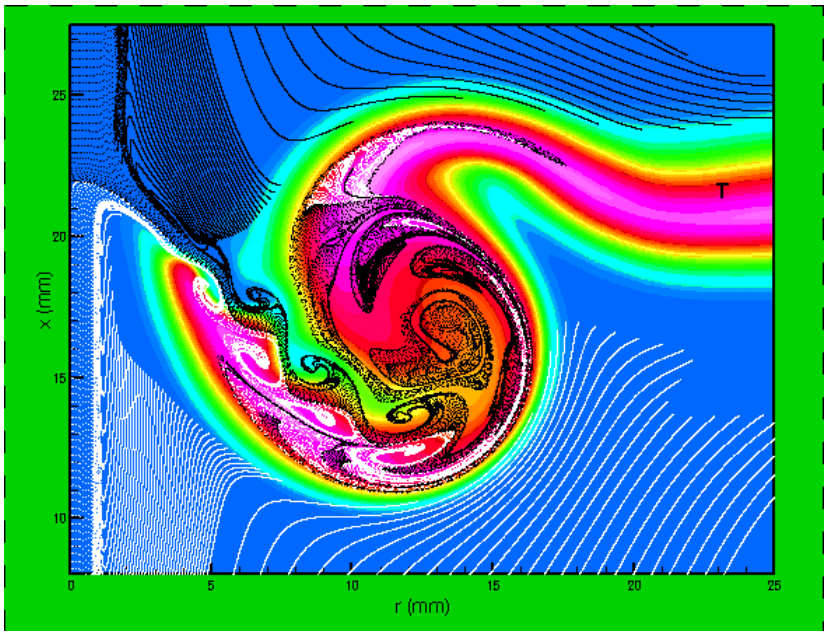

(a)

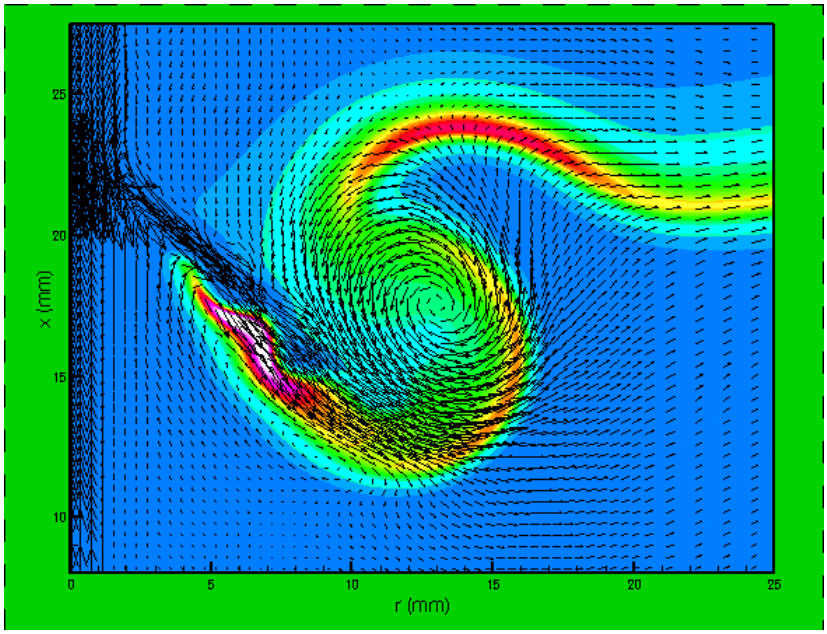

(b)

Fig. 4. Flame broadening with the generation of multiple new vortices. (a) Instantaneous locations of the particles are superimposed on temperature field and (b) instantaneous velocity field is superimposed on H-mole concentration.

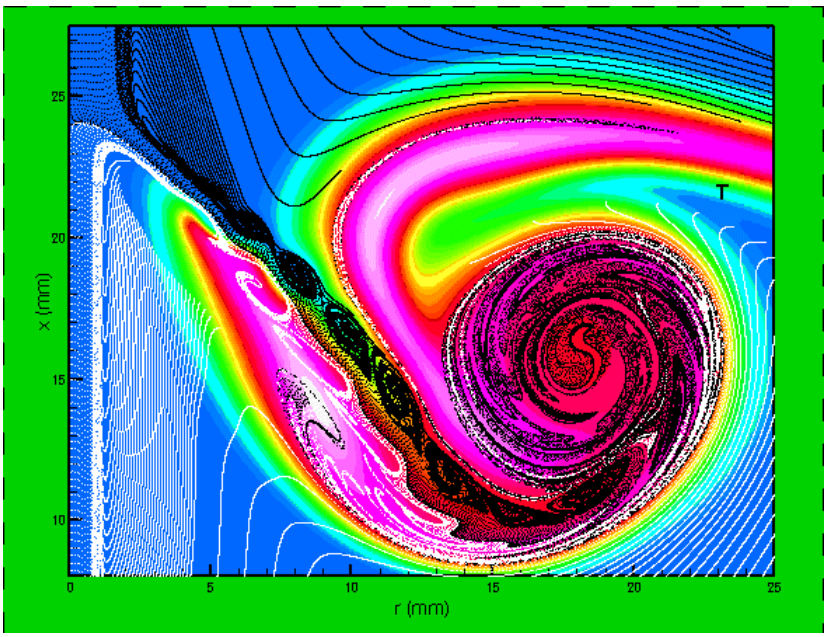

(a)

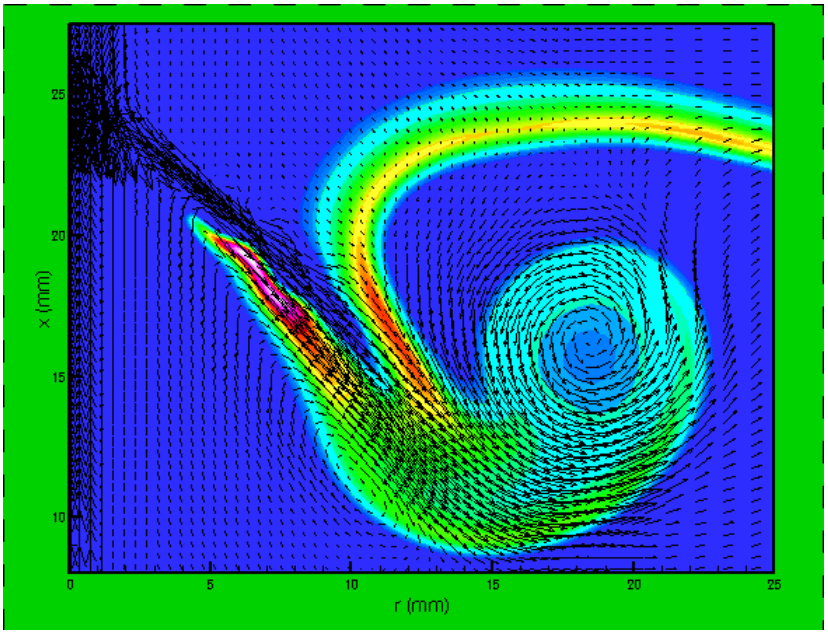

(b)

Fig. 5. Dissipation of vortices in the viscous burnt products. (a) Instantaneous locations of the particles are superimposed on temperature field and (b) instantaneous velocity field is superimposed on H-mole concentration.

ELSEVIER

Combustion and Flame 132 (2003) 639–651

Combustion and Flame

Insights into non-adiabatic-equilibrium flame temperatures during millimeter-size vortex/flame interactions

V. R. Katta[a,*], T. R. Meyer[a], J. R. Gord[b], W. M. Roquemore[b]

[a]*Innovative Scientific Solutions, Inc., 2766 Indian Ripple Rd., Dayton, OH 45440 U.S.A.*
[b]*Air Force Research Laboratory, Propulsion Directorate, Wright-Patterson Air Force Base, OH 45433 U.S.A.*

Received 29 April 2002; received in revised form 30 September 2002; accepted 7 October 2002

Abstract

Previous experimental and numerical studies have demonstrated that local flame temperatures can significantly increase above or decrease below the adiabatic-equilibrium flame temperature during millimeter-size vortex/flame interactions. Such large excursions in temperature are not observed in centimeter-size vortex/flame interactions. To identify the physical mechanisms responsible for these super- or sub-adiabatic-equilibrium flame temperatures, numerical studies have been conducted for millimeter-size vortex/flame interactions in a hydrogen-air, opposing-jet diffusion flame. Contrary to expectations, preferential diffusion between H_2 and O_2 and geometrical curvature are not responsible for these variations in local flame temperature. This was demonstrated through simulations made by forcing the diffusion coefficients of H_2 and O_2 to be equal and thereby eliminating preferential diffusion. Propagation of flame into small (~1 mm) vortices suggested that the amount of reactant carried by such a small vortex is not sufficient to feed the flame with fresh reactant during the entire vortex/flame interaction process. Various numerical experiments showed that the reactant-limiting characteristics associated with the millimeter-size vortices and the local Lewis number (not preferential diffusion) are responsible for the generation of flame temperature that is different from the adiabatic-equilibrium value. The reactant-deficient nature of the millimeter-size vortices forces the combustion products to be entrained into the vortex. While a greater-than-unity Lewis number results in pre-heating of the reactant through the product entrainment, a less-than-unity Lewis number causes cooling of the reactant. Contrary to this behavior, a centimeter-size large vortex wraps and maintains the flame around its outer perimeter by feeding the flame with fresh reactant throughout the interaction process, thereby rendering the flame unaffected by the Lewis number. Since turbulent flames generally involve interactions with small-size vortices, the physical mechanisms described here should be considered when developing mathematical models for turbulent flames. © 2003 The Combustion Institute. All rights reserved.

Keywords: Diffusion flames; Vortex/flame interactions; Non-adiabatic temperature; Preferential diffusion; Turbulence

1. Introduction

Vortex/flame interactions are often considered to be the building blocks for statistical theories of turbulence. During these interactions, the flame surface is subjected not only to unsteadiness but also to deformation. To investigate the effects of curvature on unsteady flames, both theoretical and experimental studies have been initiated [1,2]. Experiments designed by Roberts et al. [3] and by Rolon [4] are particularly interesting because of their unique ability to inject a well-characterized vortex toward the flame surface. Using a counter-flow burner similar to that of

*Corresponding author. Tel.: +937-255-8781; fax: +937-255-3139.
E-mail address: vrkatta@erinet.com (V.R. Katta).

0010-2180/03/$ – see front matter © 2003 The Combustion Institute. All rights reserved.
doi:10.1016/S0010-2180(02)0517-5

Nomenclature

d_i	Syringe tube diameter
d_o	Nozzle diameter
D_o	Outer nozzle diameter
H	Total enthalpy
H_0	Heat of formation
K	Strain rate
K_a	Air-side strain rate
Le	Lewis number
q	Heat-release rate
r	Radius
R	Radius of curvature
V_f	Flame transitional velocity
t	Time
T	Temperature
T_f	Flame (peak) temperature
T_0	Room temperature
u	Velocity in z direction
X	Mole fraction
z	Axial distance
ϕ	Equivalence ratio

Rolon, several investigators have studied vortex/flame interactions in which the flame surface is subjected to stretch, deformation, and translation. In general, these studies suggest that 1) moving curved flames can withstand strain rates that are much greater than the corresponding maximum strain rate of a steady planar flame and 2) vortices originating at the air side can quench the flame much easier than those originating at the fuel side. Takagi et al. [5] and Yoshida and Takagi [6] have investigated the effect of curvature on temperature by injecting micro-jets toward the flame surface. Their studies on hydrogen-air diffusion flames revealed that 1) a micro-jet issued from the air side increases the flame temperature at the tip by ~300 K and 2) a micro-jet issued from the fuel side decreases the temperature and may cause local extinction. They speculated that this behavior of hydrogen flames is the result of the combined effect of preferential diffusion and flame curvature with respect to the in-coming fuel. They argued that the higher diffusivity of hydrogen renders the region at the tip of a concave (negative-curvature) flame fuel-rich and that at the tip of a convex (positive-curvature) flame fuel-lean. Calculations made for these micro-jet/flame interactions by Yoshida and Takagi [6] and Lee et al. [7] also predicted this behavior. However, insufficient analysis of the results did not validate the conclusions of Takagi et al. [5] regarding the effects of preferential diffusion on flames.

Motivated by these observations, Finke and Grunefeld [8] modified the counter-flow burner to generate stationary curved flames. Using a 5-mm bluff body embedded in fuel flow or in airflow, they obtained either a concave or a convex flame with respect to the in-coming fuel. Noting that a concave flame extinguished annularly and that a convex flame extinguished at the center, they also surmised that flame curvature and preferential diffusion are responsible for such flame behavior.

The objective of this study was to employ numerical simulations to gain a more precise understanding of the physical processes responsible for the observed super- and sub-adiabatic-equilibrium flame temperatures during millimeter-size vortex/flame interactions. Several investigators have developed models [9–11] for studying vortex/flame interactions in opposing-jet flames. In all of these models, it is assumed that a vortex pair created through the superimposition of a synthesized-vorticity field interacts with a flat flame formed in a parallel flow. Although such an assumption has advantages when exploring interesting aspects of vortex/flame interactions, investigations employing this assumption may not represent actual experimental vortex/flame interactions. Hence, this approach does not facilitate direct comparisons between predictions and experimental results and makes verification of the former difficult. However, multidimensional models that incorporate detailed chemical kinetics [12,13] are capable of simulating the vortex evolution in an opposing-jet-flow configuration and its interaction with the flame simultaneously.

In the present study, such simulations of the millimeter-size vortex/flame interaction were made to validate the numerical model employed. Computational experiments were then performed to lend new insight into the role of preferential diffusion, curvature, strain rate, and Lewis number in generating super- or sub-adiabatic-equilibrium flame temperatures during these vortex/flame interactions.

2. Numerical model

Time-dependent, axi-symmetric Navier-Stokes equations written in the cylindrical-coordinate (*z-r*) system are solved along with species- and energy-conservation equations [14]. A detailed chemical-kinetics model is used to describe the hydrogen-air combustion process. This model consists of thirteen species—namely, H_2, O_2, H, O, OH, H_2O, HO_2, H_2O_2, N, NO, NO_2, N_2O, and N_2. A detailed chemical-kinetics model having 74 reactions among the constituent species is used; the rate constants for this H_2-O_2-N_2 reaction system were obtained from [15].

Temperature- and species-dependent property calculations are incorporated. The governing equations are integrated on a non-uniform staggered-grid system. An orthogonal grid having rapidly expanding cell sizes in both the axial and radial directions is employed. The finite-difference forms of the momentum equations are obtained using an implicit QUICKEST scheme [16,17], and those of the species and energy equations are obtained using a hybrid scheme of up-wind and central differencing. At every time step, the pressure field is calculated by solving the pressure Poisson equations simultaneously and utilizing the LU (lower and upper diagonal) matrix-decomposition technique. This model, called UNICORN (UNsteady Ignition and COmbustion with ReactioNs), has been extensively validated [18] by simulating various steady and unsteady counter-flow [19] and co-flow [14,20] jet-diffusion flames and by comparing the results with experimental data.

3. Modeling Rolon-burner flames

The opposing-jet-flame burner used for these studies was designed by Rolon [4] and is shown in Fig. 1, along with the experimental and computational results for a millimeter-size vortex/flame interaction. The burner assembly consists of 25-mm-diameter nozzles (d_o), 40-mm-diameter outer nozzles (D_o), and syringe tubes of 0.2-mm to 5-mm diameter (d_i). A flat flame is formed between the fuel and air jets having velocities of 0.69 and 0.5 m/s, respectively. An annular nitrogen flow of 0.1 m/s is used from both the fuel and air-side nozzles. The hydrogen-to-nitrogen ratio employed for the fuel jet is 0.38. Only the region between the lower and upper nozzle exits was modeled in the present study. The fuel (d_o), air (d_o), nitrogen (D_o), and injection (d_i) jet diameters used in the simulations were identical to those used in the experiment. Calculations for the steady-state axi-symmetric flame were made using a non-uniform 801 × 336 mesh system distributed over a physical domain of 20 × 20 mm, which yielded a mesh spacing of 0.02 mm in both the axial (z) and the radial (r) directions in the region of interest. A flat profile for the velocity is used in the computations at the exit of each nozzle. The computed air-side strain rate along the stagnation line is 48 s^{-1}. Here and throughout this paper, the strain rate (K) along the stagnation line is calculated from the rate of change in the axial velocity (u) with respect to the distance (z). The peak temperature of 1560 K of this weakly strained flame is only slightly lower than the corresponding adiabatic-equilibrium flame temperature of 1598 K.

4. Results and discussion

Experiments and computations are performed for vortex/flame interactions using the Rolon burner for different flow conditions and vortex sizes.

4.1 Air-side-vortex/flame interaction

Vortices are shot toward the flame surface from the air-side by injecting a specified amount of air through the syringe tube (Fig. 1) and then through a 0.2-mm-diameter micro-injection tube. Evolution of the injected micro-vortex (initial diameter <1 mm) and its interaction with the flame surface is dependent on the injection duration. In general, with shorter injection times, the generated vortices travel faster toward the flame surface and influence the flame structure as the local-flow time-scales approach the chemical time-scales. A typical experimental image of the millimeter-size vortex/flame interaction is shown in Fig. 1. This represents the OH-concentration field captured using the planar laser-induced fluorescence (PLIF) measurement technique and clearly shows the significant increase in OH concentration in the head region of the vortex. Results obtained from the calculations made for the millimeter-size vortex/flame interaction in Fig. 1 are shown on the right-hand side of the experimental image. Calculations also predicted the significant increase in the concentration of OH in the head region. The computed OH distribution matches qualitatively the uncorrected experimental OH-PLIF data. The somewhat broad and diffused distribution of OH in the vortex-head region in the experiment could be attributed to the alignment of the laser sheet with the axis of the injection tube. The inner and outer radii of the protrusion of the OH layer that occurred as a result of the vortex penetration are only ~0.3 and 0.7 mm, respectively, on the order of the laser-sheet thickness (~0.4 mm). A small misalignment of the laser sheet with the center-line of the OH protrusion could cause the capture of OH signal that is present circumferentially and blurs the fluorescence image.

Both in the experiment and the calculations, the interaction between the millimeter-size vortex and the flame resulted in local quenching (break in the flame surface) along the stagnation line during the early stages; then the flame was re-connected within 1 ms. The temperature and OH concentration began to increase soon after the re-connection of the extinguished flame, and this increase continued monotonically with time and further propagation of the vortex. Calculations as well as experiments [21] using different injection velocities resulted in very similar interaction sequences; namely, quenching, re-ignition, and an increase in temperature above the adia-

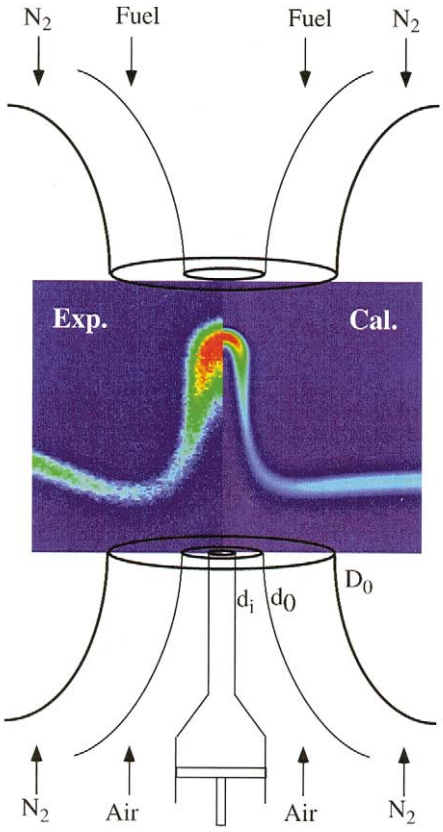

Fig. 1. Schematic diagram of opposing-jet burner used in studies of vortex/flame interactions. Inserted images (measured and computed on left and right halves, respectively) are those of typical protruded flame obtained with millimeter-size air-side vortex, showing increase in concentration of OH at tip.

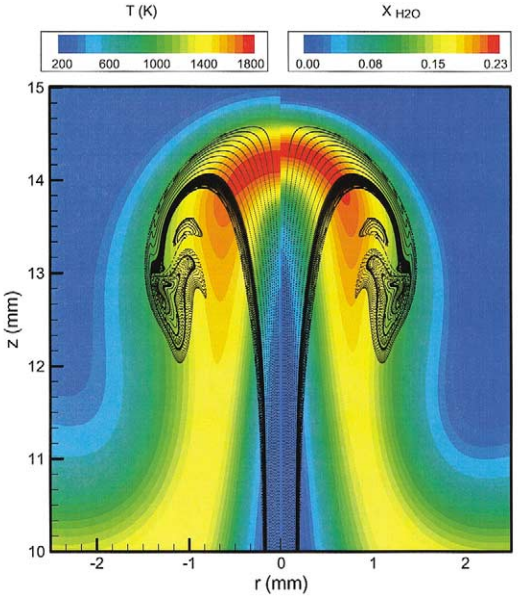

Fig. 2. Structure of flame computed during interaction with millimeter-size air-side vortex. Temperature (T_{min} = 294 K and T_{max} = 1800 K) and H_2O concentration ($X_{H2O}|_{min}$ = 0 and $X_{H2O}|_{max}$ = 22.8%) plotted on the left and right halves, respectively. Linear-rainbow color scale is used to represent various contour levels. Instantaneous locations of particles injected from air nozzle are superimposed.

batic-equilibrium value in the head region of the vortex.

A detailed view of the millimeter-size air-vortex/flame interaction at 2.8 ms after the start of air injection is shown in Fig. 2. The structure of the vortex is identified through a plot of the instantaneous locations of the particles that were injected from the air nozzle. The vortex initiated by the 0.2-mm-diameter micro-tube has grown in size to a diameter of 2.9 mm. Instantaneous temperature and H_2O-concentration distributions are plotted in Fig. 2 on the left and right sides, respectively. The temperature of the flame in the head region has increased to 1792 K, which is ~194°K higher than the adiabatic-equilibrium flame temperature obtained based on cold reactants. Also, the flame has propagated into the core of the vortex. The instantaneous curvature of this flame is ~1.5 mm^{-1}. Earlier calculations [19] made with a 5-mm injection tube that generated a ~15-mm-diameter vortex (shown in Fig. 3) did not reveal this behavior. Even though calculations and the corresponding experiments for this centimeter-size vortex/flame interaction did not reveal temperatures that are greater than the adiabatic-equilibrium value, a significant amount of curvature (~0.14 mm^{-1}) to the flame surface was generated. This indicated that the curvature alone may not be responsible for the increase in temperature observed during the millimeter-size vortex/flame interactions. Note that the vortex diameter of 15 mm in Fig. 3 is nearly five times larger than the stretched-flame thickness (~3 mm, based on the full width of the temperature profile) at the center-line, while the vortex diameter of 3 mm in Fig. 2 is the same as the flame thickness.

In addition to the difference in the flame-thickness-to-vortex-diameter ratios for millimeter-size (Fig. 2) and centimeter-size (Fig. 3) vortex/flame interactions, the structure of these two flames varies significantly. As mentioned earlier, the temperature at the head of the millimeter-size vortex has increased, while that of the centimeter-size vortex has decreased. The flame in Fig. 2 has penetrated significantly into the vortex and distorted it. On the other hand, the flame in Fig. 3 has remained near the periphery of the vortex. A view along the center-line

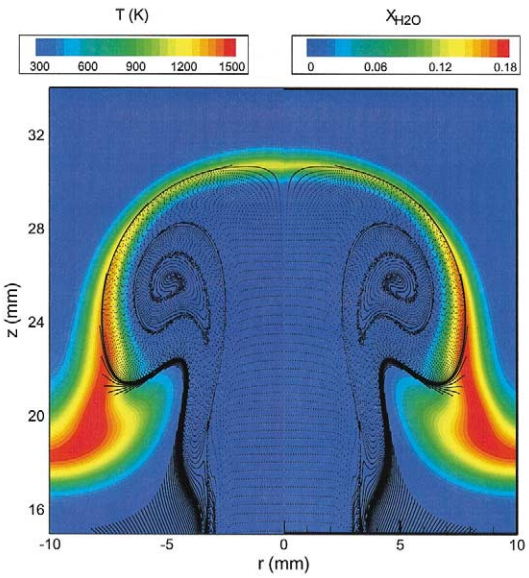

Fig. 3. Structure of flame computed during interaction with centimeter-size air-side vortex. Temperature (T_{min} = 294 K and T_{max} = 1600 K) and H_2O concentration ($X_{H2O}|_{min}$ = 0 and $X_{H2O}|_{max}$ = 20.0%) plotted on the left and right halves, respectively. Linear-rainbow color scale is used to represent various contour levels. Instantaneous locations of particles injected from air nozzle are superimposed.

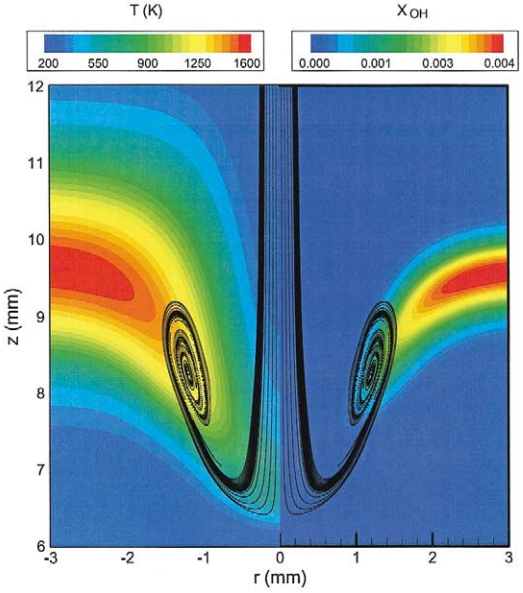

Fig. 4. Structure of flame computed during interaction with millimeter-size fuel-side vortex. Temperature (T_{min} = 294 K and T_{max} = 1600 K) and OH concentration ($X_{OH}|_{min}$ = 0 and $X_{OH}|_{max}$ = 0.41%) plotted on left and right halves, respectively. Linear-rainbow color scale is used to represent various contour levels. Instantaneous locations of the particles injected from fuel nozzle are superimposed.

in Fig. 2 reveals a shift in the distribution of H_2O with respect to the distribution of the temperature, with the peak in the former appearing 0.1 mm downstream of that in the latter. On the other hand, no shift in the locations of the peaks in H_2O and temperature distribution is observed in Fig. 3.

4.2 Fuel-side-vortex/flame interaction

Calculations were made for the interaction of a millimeter-size fuel-side vortex and the flame using the injection scheme shown in Fig. 1, except that the injector-tube assembly is now placed in the fuel nozzle. The velocity of the injected fuel was chosen to be only 12 m/s [which was significantly lower than that used for the air-side vortex (20 m/s)] since the fuel-side millimeter-size vortex/flame interactions seem to promote local extinction. The instantaneous temperature and OH-concentration distributions simulated 5 ms after the start of fuel injection are shown in Fig. 4 on the left and right sides, respectively. The millimeter-size vortex (~3.0-mm diameter) that developed from the injection of fuel is also shown in Fig. 4 via a plot of the instantaneous locations of the particles that were injected from the fuel nozzle. Even this slowly moving vortex extinguished the flame at the center (peak temperature dropped to 720 K) and did not promote to re-connection of the flame hole or temperature build-up. In fact, calculations made with various injection velocities failed to generate a case in which the extinguished flame hole is re-connected while the fuel-side vortex is still traveling through the flame.

4.3 Discussion on super-adiabatic-equilibrium flame temperatures

4.3.1 Inconsistency in existing theory

The differences in the interactions of air-side and fuel-side millimeter-size vortices with a diffusion flame were described earlier by Yoshida and Takagi [6] and Lee et al. [7]. They attributed these differences to the preferential diffusion among H_2, O_2, and N_2 and the focusing/de-focusing nature of the curved flame.

The diffusion coefficient of hydrogen is ~3.5 times larger than that of oxygen. Yoshida and Takagi [6] speculated that this difference in diffusion coefficients generates regions with high concentrations of H_2 in the concave flame (with respect to the fuel), as in Fig. 2, and lower concentrations of H_2 in the convex flame, as in Fig. 4. They used the H_2 ratio (the mole-fraction of H_2 in the fuel that should have been available locally before combustion) to identify the

fuel-rich and fuel-lean regions. This variable estimates the concentration of H_2 from the local product composition. If all of the products are produced locally, then the H_2 ratio exactly yields the amount of H_2 present locally before combustion takes place. However, if the products formed at one location are transported to another through convection and diffusion, then the H_2 ratio computed at the latter location represents not only H_2 that was available there before combustion but also part of the H_2 that was available at the former location. The major product in a hydrogen flame is H_2O. Water formed at one location and transported to another would yield higher values of the H_2 ratio and, thereby, erroneously higher concentrations of H_2 in the latter region. A view of the H_2O distribution in Fig. 2 suggests that variation in its concentration generally follows the variation in temperature. The H_2 ratio calculated from this high concentration of H_2O certainly indicates the presence of a greater amount of fuel in the region before combustion. However, such interpretation from H_2O is incorrect, since an appreciable amount of H_2O was transported from up-stream locations to the head of the vortex. The mechanism responsible for this transport of H_2O will be discussed later.

4.3.2. Role of preferential diffusion

In a pre-mixed flame, a difference in the diffusion velocities of the reactants can cause an increase or decrease in the reactant concentration in the cusp region, depending on the curvature of the flame with respect to the reactants. On the other hand, since the amount of fuel or oxygen that is able to cross the stoichiometric surface in a diffusion flame is negligible, a diffusion flame is not subjected to the focusing or de-focusing effect in the creation of higher- or lower-concentration regions of reactants, respectively. If the fuel flux into the flame zone increases for some reason (for example, injection), then the diffusion flame moves to a new location to achieve a balance with the stoichiometric air flux. To demonstrate that preferential diffusion in conjunction with the flame curvature does not lead to fuel-rich and fuel-lean regions in a diffusion flame, calculations were repeated for the millimeter-size vortex/diffusion-layer interaction by turning off the chemical reactions associated with the simulation shown in Fig. 2. Results in the form of H_2-concentration and equivalence-ratio distributions are plotted in Fig. 5 on the left and right sides, respectively. The iso-equivalence contour showing the location of the stoichiometric mixture is plotted by a white line. The vortex structure at the same instant is represented with black dots. Note that the vortex in Fig. 5 is only 1.9 mm in diameter and, thus, has a curvature (1.1 mm^{-1}) for

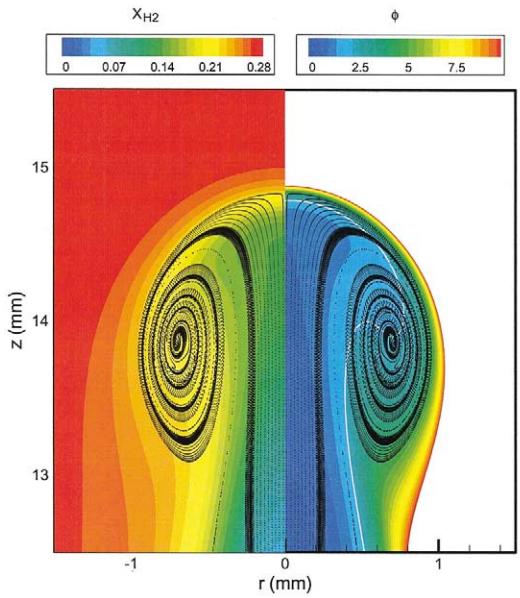

Fig. 5. Mixing between fuel (H_2) and oxygen during propagation of millimeter-size air-side vortex. Concentrations of H_2 ($X_{H2}|_{min} = 0$ and $X_{H2}|_{max} = 27.4\%$) and equivalence ratio ($\phi_{min} = 0$ and $\phi_{max} = 10.0$) plotted on left and right halves, respectively. Linear-rainbow color scale is used to represent various contour levels. White contour line represents stoichiometric-mixture location. Instantaneous locations of particles injected from air nozzle are superimposed.

the diffusion layer that is comparable to that of the flame in Fig. 2. The limited growth for the vortex in the non-reacting case (Fig. 5) resulted from lack of volumetric expansion that was present in the flame simulation (Fig. 2). At room temperature, the ratio of H_2 to O_2 diffusion coefficients is 3.66, which is slightly higher than the ratio obtained at 2200 K. Therefore, the cold-flow simulation in Fig. 5 includes preferential-diffusion effects that are equal to or greater than those that one would expect in the combusting flow. Figure 5 shows that neither the concentration of H_2 nor the equivalence ratio increased as a result of the combined effect of curvature and high preferential diffusion between H_2 and O_2. Note that in the absence of chemical reactions, the mole-fraction of H_2 (X_{H2}) and the H_2 ratio become identical, since the concentration of H_2O is zero everywhere. Based on the cold-flow results, one would not expect the H_2 concentration (or H_2 ratio)—and, thus, the flame temperature—to increase in a curved diffusion flame. Therefore, it appears that curvature and preferential diffusion are not responsible for the super-adiabatic-equilibrium flame temperatures shown in Fig. 2.

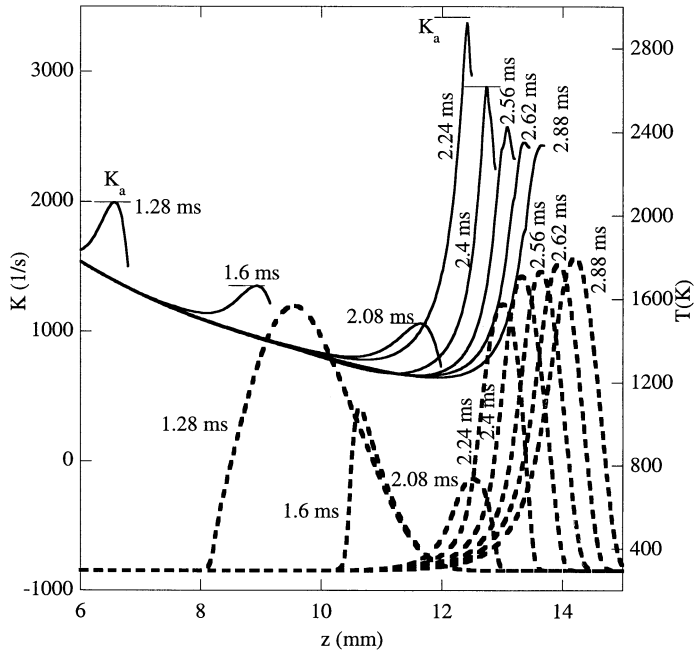

Fig. 6. Temperature profiles (broken lines) and corresponding applied air-side strain rates (solid lines) along the center-line at different instants during interaction process between millimeter-size air-side vortex and flame. Times are with respect to start of issuance of air-side vortex.

4.3.3 Roles of strain rate and curvature

To examine further whether variations in strain rate ($K = du/dz$), curvature ($1/R$), and flame translational velocity (V_f) are responsible for the temperature excursions noted in Fig. 2, these variations along with those in temperature are plotted (see Figs. 6 and 7). First, variations of strain rate and temperature along the center-line at several instants are shown in Fig. 6. Since the air-side strain rate [22,23] is often used in describing the structure of a flame influenced by the air-side vortex, only the portions of the strain-rate curves in the neighborhood of the air-side value were plotted in Fig. 6. Flame stretching began at ~1.28 ms when the air-side strain rate was increased to 2000 s^{-1}. However, this value decreased as the flame underwent the extinction process and the vortex faced increasingly less obstruction from the viscous fluid generated at the flame surface. At ~2.08 ms, re-ignition occurred, and the flame temperature and strain rate increased rapidly. After $t = 2.24$ ms, the air-side strain rate decreased gradually, while the flame temperature increased beyond the adiabatic-equilibrium value.

Next, the flame temperature, velocity, air-side strain rate, and curvature as functions of time were plotted (see Fig. 7). Since the flame around the vortex is not perfectly circular in shape, the average curvature ($1/R$) of the flame is obtained through integration of the local curvature along the flame surface as follows

$$\frac{1}{R} = \frac{1}{r_{\max}} \int_0^{r_{\max}} \frac{\sin(\theta)}{r}\, dr$$

$$= \frac{1}{r_{\max}} \int_0^{r_{\max}} \frac{1}{r\sqrt{1 + \left(\frac{dr}{dz}\right)^2}}\, dr.$$

Here, r_{max} is the radius of the flame where the vortex is largest in diameter, and the lower limit of zero for the integral represents the flame at the apex (head of the vortex). The flame surface was identified by tracing the peak temperature location as a function of r. Note that for a concavely curved flame with respect to the air flow (from bottom to top in Fig. 1), the above expression for curvature gives a positive value. Figure 7 shows that during the vortex/flame-interaction process, the flame temperature at the head of the vortex is increasing while the curvature of the flame is decreasing. Note that the flame curvature decreases as the flame increases in size, while the interacting vortex entrains increasingly more of the surrounding fluid. The relationship between the flame curvature and temperature observed in Fig. 7 does not

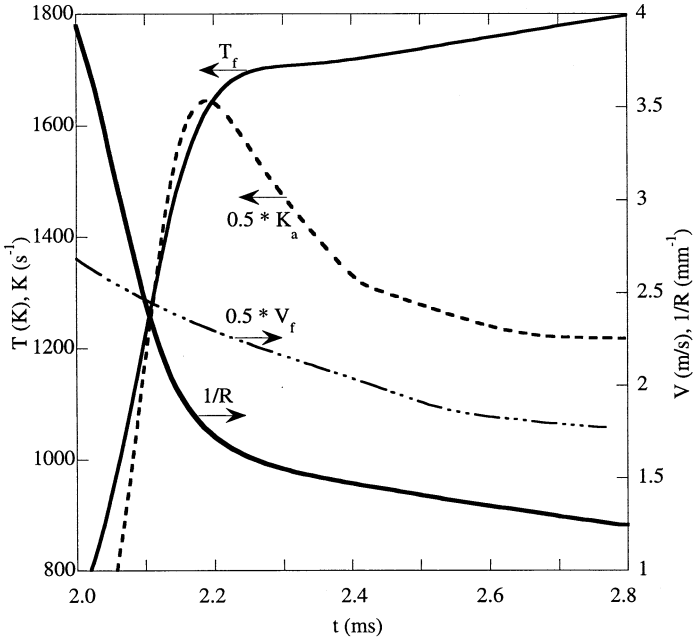

Fig. 7. Variations of center-line flame (peak) temperature (T_f), air-side strain rate (K_a), flame translational velocity (V_f), and flame curvature ($1/R$) with time during air-side millimeter-size vortex/flame interaction.

follow the preferential-diffusion-flame-curvature theory proposed by Takagi et al. [5,6]. The latter suggests that the flame temperature should increase with curvature in the case of air-side vortex/flame interaction. This controversy in theory and predictions suggests that curvature may not be the cause of the observed increase in flame temperature. In fact, the studies of Finke and Grunefeld on steady-state curved flames that employed various inert gases [8] could not establish a relationship between flame curvature and quenching limit.

Figure 7 could also suggest that the decrease in air-side strain rate with time after $t = 2.24$ ms could cause an increase in flame temperature. However, the strain rates (>2500 s^{-1}) to which the flame is subjected between 2.1 and 2.8 ms are well above the quenching limit (1770 s^{-1}) [23] and would not yield temperatures that are above adiabatic-equilibrium values; hence, the possibility that the strain rate causes the super-adiabatic-equilibrium flame temperature can be ruled out. Similarly, since the flame is traveling with the vortex, the translational velocity of the former reaches a very high ($\sim$3.5 m/s) value and, hence, its role in causing a diffusion flame to burn intensely can also be ruled out.

4.3.4 Role of chemical activity

Another method of identifying the possibility of increased H_2 concentration generating higher temperature in the tip region is to study the chemical activity in that region. This can be accomplished by calculating the heat-release rate through chemical kinetics. Figure 8 shows the variations of peak temperature and peak heat-release rate along the center-line with time for the air-side millimeter-size vortex/flame interaction. Various regimes of the interaction process are also indicated in this figure. Note that the peaks in temperature and heat-release rate along the center-line do not necessarily occur at the same location in the flame. A low peak-heat-release rate of 32 J/cm^3/s appears when the flame is in steady state, i.e., before being affected by the in-coming vortex. The flame is stretched and becomes unsteady as the vortex begins to interact with it. The heat-release rate increases during this stretching phase as increasingly more fuel and oxidizer are transported into the flame zone and burned. However, since the chemical kinetics cannot consume all of the increased reactant flow, the flame temperature decreases, falling below the quenching limit by t $\sim$1.59 ms. In the absence of flame, the heat-release rate rapidly decreased initially and then gradually reached a minimum value of 8 J/cm^3/s by $t = 2.02$ ms. During this no-flame phase, the chemical kinetics among the residual product species was responsible for the release of heat.

Interesting temperature behavior is noted during the no-flame phase. Figure 8 shows that after $t = 1.85$ ms, the temperature began to rise even when the

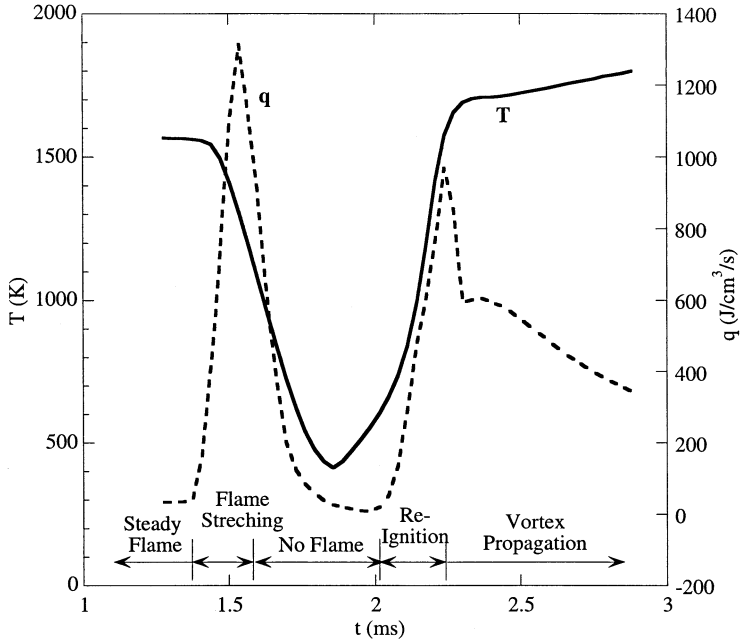

Fig. 8. Peak heat-release rate (q_{max}) and flame temperature (T_f) at different times during air-side millimeter-size vortex/flame interaction process.

heat-release rate was still decreasing. This indicates that hot products were being brought into the head region of the vortex and increased the temperature. The heat-release rate began to rise after $t = 2.02$ ms as a result of the flame propagation from the sides, and eventually re-ignition took place at $t = 2.08$ ms. Because of the pre-mixing between the fuel and air that occurred in the absence of the flame, a spike in the peak heat-release rate was established during the re-ignition process. Note that the peak heat-release rate following the spike ($\sim$600 J/cm^3/s) did not reach the value experienced by this flame before extinction, even though the stretch on the flame had increased to a value ($\sim$3300 s^{-1}) that was much higher than the peak strain rate ($\sim$2000 s^{-1}) imposed on the flame before extinction (cf. Fig. 6). Typically, the heat-release rate in a pure diffusion flame increases with strain rate as reactant fluxes increase with strain rate. The failure to generate a higher heat-release rate in the diffusion flame in Fig. 6 after the re-ignition suggests that the strain rate, in fact, did not produce higher reactant fluxes—which, may occur if the reactant in the vortex is partially depleted.

Figure 8 also shows that during the vortex-propagation stage ($t > 2.24$ ms) while the heat release rate was decreasing, the temperature continued to increase. This behavior suggests that the reactant fluxes (H_2 and O_2) into the flame zone are decreasing and, in turn, the heat-release rate. Therefore, the increase in flame temperature for $t > 2.24$ ms is due neither to an increase in chemical activity nor to an increase in H_2 mole-fraction, as was suggested previously [5,6].

4.3.5 Role of Lewis number

To gain insight into the origin of the super-adiabatic-equilibrium flame temperature, numerical experiments were performed where certain physical or chemical processes were turned off. Figure 9 shows the air-side millimeter-size-vortex/flame interaction simulated by forcing the Lewis number to unity. Lewis number (Le) is defined as the ratio between the heat- and mass-diffusive transport. In a multi-component mixture, one should expect several Lewis numbers—each one corresponds to a specific species in the mixture. There fore, the diffusion coefficient of every species is made equal to that of hydrogen while forcing the heat-transfer rate to be equal to the mass-diffusion rate to achieve the unity-Lewis-number condition in the multi-component mixture. Because of this higher diffusion coefficient, the flame became thicker than the normal one shown in Figs. 2 through 4. Note that the chemical kinetics was not altered in this simulation. The temperature of the stationary flame decreased to 1400 K with the unity-Lewis-number assumption. This results from the flame shifting to the fuel side of the stagnation plane where the N_2 concentration is higher (nearer that in the fuel stream). Figure 9 shows that the temperature near the tip of the millimeter-size vortex is $\sim$50 K above the

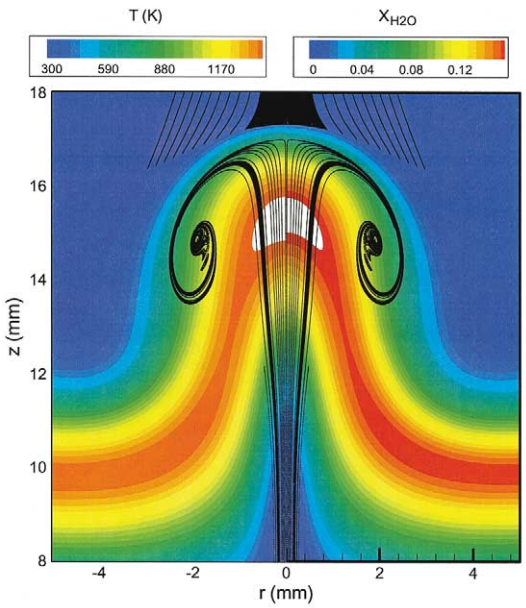

Fig. 9. Structure of flame computed using unity-Lewis-number assumption during interaction with millimeter-size air-side vortex. Temperature (T_{min} = 294 K and T_{max} = 1410 K) and H_2O concentration ($X_{H2O}|_{min}$ = 0 and $X_{H2O}|_{max}$ = 16.2%) plotted on left and right halves, respectively. Linear-rainbow color scale is used to represent various contour levels. Regions where temperature is in excess of 1410 K are shown in white. Instantaneous locations of particles injected from both air and fuel nozzles are superimposed.

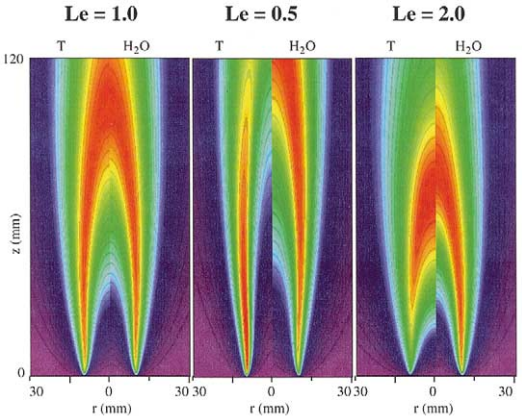

Fig. 10. Steady-state flames calculated using different Lewis-number assumptions. Fuel (H_2) jet is located at center (i.e., inside flame). Temperature and H_2O concentration are plotted on left and right halves, respectively, in each case. Linear-rainbow color scale is used between the minimum and maximum values to represent various contour levels.

stationary-flame temperature. Although this increase in temperature in unity-Lewis-number simulation is not so high as that observed in Fig. 2, the result does suggest that preferential diffusion among species is not important in explaining the super-adiabatic-equilibrium flame temperatures. The role of non-unity Lewis number in increasing temperature by 194 K in Fig. 2 is examined later.

Unity-Lewis-number calculations made by setting the diffusion coefficients of all the species equal to that of oxygen also yielded similar excursions in temperature during the interactions between the air-side millimeter-size vortex and the flame. Furthermore, a unity-Lewis-number calculation was also made for the fuel-side millimeter-size-vortex/flame interaction described in Fig. 4. This simulation also resulted in an increase in flame temperature similar to that observed with an air-side vortex. For the calculation shown in Fig. 4, the Lewis number is actually lower than one, and the flame was quenched. These simulations with the unity-Lewis-number assumption suggest that the Lewis number contributes to the super- and sub-adiabatic-equilibrium flame temperatures observed during millimeter-size-vortex/flame interactions. However, in earlier studies [19] on interactions of larger vortices with the same flame, excursions in flame temperature did not result. This suggests that some characteristics of millimeter-size vortices in conjunction with non-unity Lewis number are responsible for the super- and sub-adiabatic-equilibrium flame temperatures noted in Figs. 2 and 4. The question remains concerning which characteristic associated with vortex size contributes to the temperature changes.

4.3.6 Impact of limited supply of reactants

Re-examination of the vortex and flame structures associated with the millimeter-size vortex/flame (Figs. 2 and 9) and the centimeter-size vortex/flame (Fig. 3) [19,23] interactions brought to light a unique feature associated with the former. During the centimeter-size vortex/flame interaction, the flame always remains near the head of the vortex. This suggests that the vortex contains an abundant quantity of reactant. Also, during this interaction, the vortex always transports cold reactant into the flame. However, when the vortex is small, the flame moves into the vortex. This suggests that the diffusion flame is depleting the reactant contained within the millimeter-size vortex, consistent with the heat-release-rate data presented in Fig. 8. This case represents a reactant-limited interaction. As the reactant mass is depleted, the vortex transports products (which include product species and heat) along with the remaining reactant into the flame. The flame temperature de-

pends on the composition of fluid that is transported into the flame by the vortex. For example, if the vortex transports heated mass into the flame, then one should expect an increase in flame temperature. If it transports cold products (water gas), then a decrease in flame temperature should occur. The composition of the products generated in a diffusion flame depends on how the reactants and heat are transported in and out, respectively, i.e., on the local Lewis number.

4.4 Lewis number and reactant-limitedness in jet flames

To explain the role of the Lewis number and the characteristics associated with the millimeter-size vortices in altering the flame temperature, a simple case that eliminates unsteady, non-equilibrium chemistry and non-uniform transport properties was selected. Numerical simulations for an axi-symmetric, reactant-limited jet flame were performed using constant properties and Lewis number and infinitely fast global-reaction assumptions. Calculations made for a jet flame with either fuel or air inside yielded identical results. The temperature and H_2O-concentration fields obtained for three steady-state flames having different Lewis numbers are shown in Fig. 10 for the fuel-inside-flame case. The velocity of the fuel and air jets is 0.2 m/s, which yielded complete burning of the fuel within a 130-mm height. Calculations made with higher velocities and larger fuel-tube diameters yielded perfectly straight flames, with no change in flame temperature with height. The normalized temperature and H_2O-concentration distributions at a height of 50 mm above the inlet for the three flames are compared in Fig. 11.

Two important points must be highlighted in the results shown in Fig. 10. First, the flames are fuel-limited and, therefore, converge toward the axis of symmetry. Second, the water concentration is always highest at the flame tip. This is due to the cumulative process of water formation in the flame (H_2O in these flames has an infinite lifetime). When Le = 1 [Fig. 10(a)], the flame temperature increases with height and reaches a peak value at the tip—consistent with the unity-Lewis-number simulation made for the air-side millimeter-size vortex/flame interaction in [Fig. 9]. The reason for this behavior becomes clear when the temperature and H_2O distributions in Fig. 10(a) are compared. By definition, in the case of Le = 1, both product (H_2O) and heat diffuse similarly. However, Fig. 10(a) suggests that the temperature is diffusing faster than the H_2O (distribution of temperature is wider at the center compared to that of H_2O). The reason for such behavior in Le = 1 diffusion flames will now be discussed.

When the Lewis number is equal to unity, heat and mass diffuse similarly, provided the gradients for heat and mass are also the same. The reason for this is that the diffusive flux is the product of the diffusion coefficient and the mass (or enthalpy) gradient. It is known that the specific heat of water is significantly higher than that of either H_2 or O_2. Thus, at room temperature, the enthalpy ($H–H^0$) of H_2O will be higher than that of H_2 or O_2. The enthalpy gradient

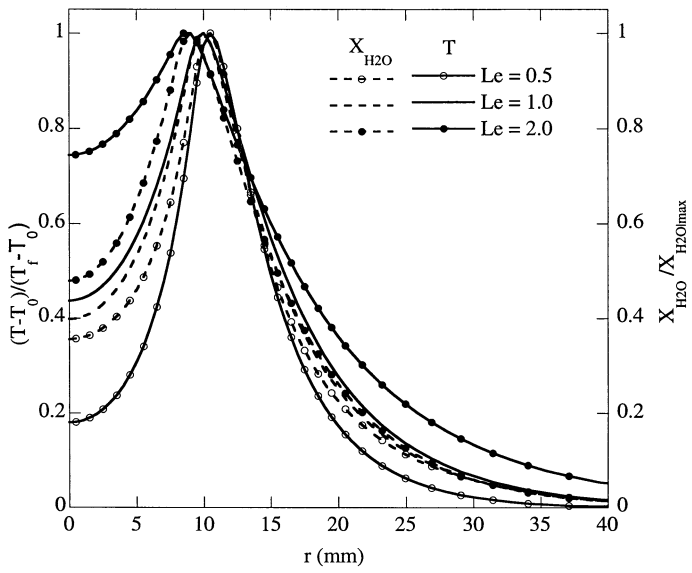

Fig. 11. Normalized temperature and H_2O distributions across flame at axial height of 50 mm above inlet for flames obtained with different Lewis-number assumptions.

between H_2O in the flame zone and cold reactants away from the flame would be the same as the mass gradient for the generated H_2O if and only if the enthalpy of the cold reactants is the same as that of cold H_2O. Because of the difference in specific heats, the enthalpy of H_2 or O_2 is lower than that of cold (room-temperature) H_2O. As a result, the enthalpy (or temperature) gradient is greater than the mass gradient. This higher enthalpy gradient produces higher heat flux and, thus, more diffusion of heat than of mass, even when the Lewis number is unity. This results in pre-heating of the reactants. Since specific heats of both H_2 and air are lower than that of H_2O, this pre-heating should occur on both sides of the diffusion flame, no matter which reactant is at the center, as is evident in Fig. 11. The temperature profile for the Le = 1 flame is more diffused on both sides of the flame than the H_2O distribution. In a perfectly flat flame, both reactants are in abundance, and the pre-heated reactants do not enter the flame zone to raise the flame temperature, which results in a self-similar solution. However, if these pre-heated reactants enter the flame at down-stream locations, the temperature of the flame can increase beyond the adiabatic-equilibrium value. This can happen when one of the reactants is deficient. Flames naturally curve toward the deficient reactant at down-stream locations. As seen in Fig. 10(a), the pre-heating of the deficient reactant (fuel) at the center has caused the temperature to increase at the tip of the flame.

When Le = 0.5, heat diffuses much more slowly than the products (H_2O), resulting in more H_2O at the axis of symmetry [Fig. 10(b)]. The water that diffuses beyond the heat acts as a diluent to the fuel since it is not transporting heat with it. In fuel-limited flames, such as in Fig. 10, this diluted fuel enters the flame at down-stream locations and cools the flame. Because of the accumulation effect, the flame tip is the coldest flame region. On the other hand, when Le = 2.0, heat diffuses faster than the products (H_2O) and pre-heats the fuel at the center. Again, in a fuel-limited flame, this heated fuel eventually enters the flame at down-stream locations, making the flame hotter. Because of the accumulation effect, the flame tip is the hottest flame region.

In a hydrogen-air diffusion flame, the Lewis number on the fuel side is near 0.5 and that on the air side is slightly above unity. The amount of fuel or air contained in a millimeter-size vortex or jet is quite small, and the protruded flame becomes reactant-limited. Because of these combined effects, the temperature at the tip of the air-side millimeter-size vortex/flame interaction increases (Le is slightly greater than unity, and the flame is air-limited), as seen in Fig. 2. The temperature at the head of the fuel-side millimeter-size vortex/flame interaction decreases (Le $\sim$ 0.5 and the flame is fuel-limited), as seen in Fig. 4. Even though the Lewis number is greater or smaller than unity in the case of centimeter-size vortex/flame interactions, the protruded flame contains sufficient reactant; thus, the flame temperature does not change as a result of the non-unity Lewis number. It may decrease because of strain, but it does not increase. Geometrical curvature ($1/R$) does not impact these diffusion flames. Only curvature resulting from reactant deficiency plays a role in altering the flame temperature. To further verify this hypothesis, a calculation for a millimeter-size air-vortex/flame interaction in a planar 2-D flow was performed. Consistent with the above arguments, the flame was significantly curved, but the temperature did not increase at the tip since the planar vortex contained more air and the protruded flame did not become air-limited.

5. Conclusions

Vortex/flame interactions are often studied to gain an understanding of complex, turbulent reaction processes. A millimeter-size vortex shot toward a flame generates a protruded flame very similar to the flame bump observed on a turbulent flame. Earlier studies of millimeter-size vortex/flame interactions suggested that when the vortex originates on the air side, it can increase the flame temperature above the adiabatic-equilibrium value by as much as 300 K. Even though the consequences of these interactions are significant and play a major role in describing a turbulent flame, the exact cause of such variations in flame temperature is not well understood. In the present study, a well-tested CFD model was used to investigate millimeter-size vortex/flame interactions. Calculations performed for the air-side and fuel-side millimeter-size vortex/flame interactions revealed an increase and decrease in flame temperature, respectively. These results qualitatively agree with the experiments and the simulations of Takagi et al. [6] and Lee at al [7]. Numerical experiments were performed to identify the physical mechanisms responsible for generating these super- and sub-adiabatic-equilibrium flame temperatures. The results indicated that the geometrical curvature of the flame and preferential diffusion between H_2 and O_2 are not responsible for the super-adiabatic-equilibrium flame temperature. Based on studies conducted using vortices of different sizes and various Lewis numbers and changing the origin of the vortices, the following conclusions have been derived:

1. Both the millimeter- and centimeter-size vortex/flame interactions generate curvature to the flame surface. Preferential diffusion or curvature in a diffusion flame does not cause an increase or decrease in the flame temperature.

2. It is known that a less-than-unity Lewis number renders a diffusion flame (whether curved or not) hotter and a greater-than-unity Lewis number renders it cooler, compared to the similarly stretched unity-Lewis-number flame.
3. A centimeter-size vortex possesses reactant in abundance and, hence, its interaction with a diffusion flame could be described by the changes in air-side strain rate. Consequently, the flame temperature decreases as the flame is stretched by the vortex, despite of its origin (fuel- or air-side) or curvature.
4. During its interaction with a diffusion flame, a millimeter-size vortex becomes reactant-limited and promotes entrainment of combustion products into the vortex. The heat content of the entrained products (mostly water gas in hydrogen flames) depends on the local Lewis number. If the Lewis number is less than unity, then the vortex entrains cold products and renders the flame cooler. Similarly, if the Lewis number is greater than unity, then the vortex entrains hot (pre-heated) products and renders the flame hotter.
5. Geometrical curvature generated during the vortex/flame interactions has no significance in diffusion flames. It becomes important only when the reactant contained in the vortex becomes insufficient during the interaction process. Naturally, the higher the curvature, the more rapidly the vortex becomes reactant-limited.

Although this study was conducted with hydrogen fuel, it is felt that the results are applicable to hydrocarbon diffusion flames also.

Acnowledgment

This work was supported, in part, by Air Force Contract F33615-00-C-2068 and the Air Force Office of Scientific Research (Dr. Julian Tishkoff). The experimental image shown in Fig. 1 was obtained at the Air Force Research Laboratory by Drs. P. H. Renard, J. C. Rolon, and G. J. Fiechtner under a Joint US-French Collaborative Program. The authors would like to thank Marian Whitaker for editorial help.

References

[1] P.H. Paul, H.N. Najm, Twenty-Seventh Symposium (International) on Combustion, The Combustion Institute, Pittsburgh, 1998, p. 43.
[2] G. Patnaik, K. Kailasanath, Twenty-Seventh Symposium (International) on Combustion, The Combustion Institute, Pittsburgh, 1998, p. 711.
[3] W.L. Roberts, J.F. Driscoll, M.C. Drake, J.W. Ratcliffe, Twenty-Fourth Symposium (International) on Combustion, The Combustion Institute, Pittsburgh, 1992, p. 169.
[4] J.C. Rolon, F. Aguerre, S. Candel, Combust. Flame 100 (1995) 422.
[5] T. Takagi, Y. Yoshikawa, K. Yoshida, M. Komiyama, S. Kinoshita, Twenty-Sixth Symposium (International) on Combustion, The Combustion Institute, Pittsburgh, 1996, p. 1101.
[6] K. Yoshida, T., Takagi, Twenty-Seventh Symposium (International) on Combustion, The Combustion Institute, Pittsburgh, 1998, p. 685.
[7] J.C. Lee, C.E. Frozakis, K. Boulouchos, Seventeenth International Colloquium on the Dynamics of Explosions and Reactive Systems (ICDERS), Heidelberg, Germany, July 25–30, 1999.
[8] H. Finke, G. Grunefeld, Proceedings of the Combustion Institute, Vol. 28, The Combustion Institute, Pittsburgh, 2000, p. 2133.
[9] W.T. Ashurst, Combust. Sci. Technol. 92 (1993) 87.
[10] T. Poinsot, A. Trouve, D. Veynante, S. Candel, E. Esposito, J. Fluid Mech. 177 (1987) 265.
[11] C.J. Rutland, J.H. Ferziger, Combust. Flame 84 (1991) 343.
[12] M.D. Smooke, A. Ern, M.A. Tanoff, B.A. Valdati, R.K. Mohammed, D.F. Marran, M.B. Long, Twenty-Sixth Symposium (International) on Combustion, The Combustion Institute, Pittsburgh, 1996, p. 2161.
[13] V.R. Katta, W.M. Roquemore, AIAA paper 97-0904, Aerospace Sciences Meeting, Reno, American Institute of Aeronautics and Astronautics, 1997.
[14] V.R. Katta, W.M. Roquemore, Combust. Flame 100 (1995) 61.
[15] M. Frenklach, H. Wang, M. Goldenberg, G.P. Smith, D.M. Golden, C.T. Bowman, R.K. Hanson, W.C. Gardiner, V.V. Lissianski, Gas Research Institute technical report No. GRI-95/0058, Gas Research Institute, Chicago, IL (1995).
[16] B.P. Leonard, Comput. Methods Appl. Mech. Eng. 19 (1979) 59.
[17] V.R. Katta, L.P. Goss, W.M. Roquemore, AIAA J. 32 (1994) 84.
[18] W.M. Roquemore, V.R. Katta, J. Visualiz. 2 (2000) 257.
[19] V.R. Katta, C.D. Carter, G.J. Fiechtner, W.M. Roquemore, J.R. Gord, J.C. Rolon, Twenty-Seventh Symposium (International) on Combustion, The Combustion Institute, Pittsburgh, 1998, p. 98.
[20] F. Grisch, B. Attal-Tretout, P. Bouchardy, V.R. Katta, W.M. Roquemore, J. Nonlin. Opt. Phys. Mater. 5 (1996) 505.
[21] P.H. Renard, D. Thevenin, J.C. Rolon, S. Candel, Prog. Energy Combust. Sci. 26 (2000) 225–282.
[22] H.K. Chelliah, C.K. Law, T. Ueda, M.D. Smooke, F.A. Williams, Twenty-Third Symposium (International) on Combustion, The Combustion Institute, Pittsburgh, 1990, p. 503.
[23] V.R. Katta, W.M. Roquemore, Proceedings of the Combustion Institute, Vol. 28, The Cumbustion Institute, Pitsburgh, 2000, p. 2055.

COMBUSTION IN IMPULSIVELY INITIATED VORTEX RINGS

T. R. MEYER,[1] J. R. GORD,[2] V. R. KATTA,[1] W. M. ROQUEMORE,[2]
G. L. SWITZER,[1] AND G. J. FIECHTNER[1]
[1]*Innovative Scientific Solutions, Inc.*
2766 Indian Ripple Road
Dayton, OH 45440-3638, USA
[2]*Air Force Research Laboratory*
Propulsion Directorate
Wright-Patterson Air Force Base, OH 45433-7103, USA

1. Introduction

Due to their frequent occurrence in reacting flows of technological interest, vortex-flame interactions have received considerable attention in recent years. Renard et al.[1] provide a comprehensive review of numerical, theoretical, and experimental investigations of vortex-flame interactions and their effects on flame dynamics, extinction, ignition, mixing, baroclinic torque, and thermal diffusion. These investigations typically study the collision of a laminar flame front with a vortex or burning within the vortex itself. The current study falls into the latter category, which is useful for studying the effects of flow structure, vorticity, and curvature on flame ignition and propagation. Within this important subset are a number of studies of flame propagation along the axis of a premixed vortex ring. Early studies by McCormack and coworkers[2,3] reported flame speeds of up to 15 m/s, with a linear dependence on vortex circulation. Ishizuka et al.[4] also report super-laminar flame speeds along the vortex core, but propose a somewhat reduced dependence on vortex circulation. Cattolica[5] and Cattolica and Vosen[6] performed studies of premixed flame propagation in the wake of a vortex for a combustion-torch configuration. Ignition of lean premixed gases within a combustion chamber generated a vortex ring of unburned, premixed methane and air. The flame follows in the wake of the vortex and eventually propagates though the vortex rollers. Wilson et al.[7] used a similar method of generating premixed vortex combustion for use in active combustion control.

In the current study, ignition and flame propagation in premixed methane-air vortex rings are investigated while varying the equivalence ratio, ignition timing, and vortex propagation velocity. This significantly extends the work of Cattolica[5] and Cattolica and Vosen,[6] who mostly considered the effect of exit velocity. Because ignition is initiated at various stages of vortex development, this investigation contains elements of flame propagation along the vortex axis as well as in the wake and roller structures. Results are compared with numerical simulations from a time-dependent computational fluid dynamics code with chemistry. In addition to giving useful insight into ignition and flame propagation in the field of a premixed vortex, practical insight is gained into the feasibility of a vortex-assisted ignition system for high-speed combustor applications.

2. Experimental Set-Up and Conditions

The jet-in-co-flow burner of the current study has been used in a number of previous investigations of vortex-flame interactions.[8,9] In the current configuration, shown in Fig. 1, repeatable vortex rings of premixed methane and air were formed at the exit of a 5 mm-diameter

central nozzle using a solenoid-driven 25 mm-diameter piston at the bottom of the fuel tube. Ignition was initiated at various phases with respect to vortex formation and propagation using a pair of electrodes located near the nozzle periphery. A co-flow of air surrounded the fuel-air jet, and a shroud flow of nitrogen was used to reduce external disturbances. A steady background flow rate of 0.14 m/s was maintained for all flows when the piston was not being actuated. When acetone planar laser-induced fluorescence (PLIF) measurements were performed, the nozzle air supply was diverted into an acetone seeding system prior to premixing with methane.

PLIF of the hydroxyl radical (OH) was accomplished by exciting the $R_1(8)$ transition of the (1,0) band in the A-X system. The requisite 281.3414 nm laser sheet was generated using the frequency doubled output of a Nd:YAG pumped dye laser, and subsequent fluorescence from the A-X (1,1) and (0,0) bands was detected at right angles using a f/1.4 UV lens and an intensified charge-coupled device (ICCD) camera. The 576×384 pixel array was binned in 2×2 groups, and the imaged area was 26.5 mm wide × 40 mm high. Prior to detection by the ICCD, the OH PLIF signal was filtered using UG-11 and WG-295 colored glass filters to remove visible and laser scattered light, respectively. Acetone PLIF was accomplished using the same laser wavelength and camera system (without the UG-11 filter), eliminating any uncertainties due to misalignment and variations in signal generation. Although most acetone PLIF measurements were performed to characterize the *cold-flow* conditions, the 300 ns gate of the ICCD allowed the UG-11 filter to be removed for simultaneous OH and acetone PLIF. A timing circuit driven by a Quantum Composer, Inc. pulse generator allowed for synchronization of the laser pulse, camera gate, spark ignition, and piston actuation.

As shown in Table 1, three main parameters were varied during the experiments: spark timing, equivalence ratio, and vortex strength. The equivalence ratio was varied from 0.75 to 1.5, and the spark timing was varied from 2.5 ms to 8 ms after the piston stroke. The effect of vortex strength was studied by varying the piston stroke between 1.6 to 5 mm while keeping the rise time constant. This resulted in vortex propagation velocities ranging from 2.5 to 6.5 m/s, which for constant ratios of vortex core diameter to toroidal ring diameter, is proportional to the maximum tangential velocity in the vortex as well as the circulation.[4] Since flame propagation is very sensitive to the location of the spark, the position of the electrodes was kept constant for all runs at 2-3 mm above the fuel-air nozzle, 3.5 mm apart, and just outside of the central jet. Thus, a flame could be initiated prior to, during, or after the vortex formation and propagation stages.

3. Numerical Model

Ignition and propagation of a premixed flame in the flow field of a vortex induced by a starting jet was investigated using a transient two-dimensional code known as UNICORN,[10] which solves the time-dependent, axisymmetric Navier-Stokes equations along with the species- and energy-conservation equations. The chemical kinetics model for methane-air combustion consists of 17 species and 52 elementary reaction steps. Transport coefficients and properties were estimated using molecular dynamics, mixing rules, and polynomial curve-fits. An implicit QUICKEST scheme was used to solve the finite difference forms of the momentum equations, and a hybrid scheme of upwind and central differencing was used for the species and energy equations.[11] The 50×20 mm computational domain meshed with a 201×81 grid system was clustered to resolve the large gradients in flow variables near the flame zone such that the local grid spacing in the axial and radial directions was 0.2 mm. A nozzle diameter of 5 mm and initial flow velocity of 0.14 m/s was used to match the experimental conditions. A vortex was

issued into the flow by suddenly increasing the nozzle exit velocity to 4.5 m/s with a top-hat velocity profile. Ignition was simultaneously initiated 3 mm above the inflow boundary and 2 mm away from the axis in the radial direction. To simulate secondary instabilities induced by velocity fluctuations, a secondary perturbation was applied to the nozzle exit velocity in the numerical model.

4. Results and Discussion

A series of acetone PLIF images was collected for each of the three piston strokes in order to document the cold-flow conditions. As shown in Fig. 2, the piston stroke has a significant impact on the vortex convection velocity, although the ratio of the vortex core diameter to toroidal ring diameter as a function of distance from the nozzle exit remains fairly constant. This confirms that vortex circulation should be approximately proportional to the vortex convection velocity and, thus, piston stroke.[4] Note that the nozzle exit is aligned with the bottom of each image and that the red dot near the bottom marks the location of one of the electrodes.

The effect of spark timing is presented in Fig. 3, which shows a sequence of OH PLIF images for each of the spark timings listed in Table 1. The vortex propagation prior to ignition is shown in Fig. 2b, with an equivalence ratio of 1.0 and piston stroke of 3.3 mm. For a spark timing of 2.5 ms, ignition is initiated just ahead of the approaching vortex. The flame propagates quickly into the vortex rollers and remains on the exterior of the jet column where fluid velocity is low. The vortex continues to stretch the flame ahead of the vortex between 4.5 and 7.5 ms and quenches the flame between 7.5 and 8.5 ms. For a spark timing of 4 ms, ignition is initiated as the tip of the vortex passes the electrodes. Vortex-flame propagation is similar to that of the previous case, and a clear annular extinction of flame is shown at 8 ms. This type of extinction is also observed under certain conditions when a vortex of cold fuel impinges on flat counter-flow diffusion flames.[12] For a spark timing of 6 ms, the vortex is beyond the formation stage, and the flame propagates within the jet column and into the vortex rollers. Interestingly, the flame does not propagate down into a second approaching vortex, but remains on the exterior. For a spark timing of 8 ms, the vortex is 4-5 diameters downstream of the electrodes and is unable to propagate into the rollers.

Simultaneous acetone/OH PLIF images are shown in Fig. 4, which allows one to observe the burned and unburned regions simultaneously. The color scaling is adjusted to give contrast between the two signals, with OH PLIF regions appearing red. The images in Fig. 4a correspond to the sequence in Fig. 3b and show the fate of the vortex after the flame is quenched at 8 ms. Note that secondary vortices lead to flame bridging across the jet column and the formation of an island of unburned fuel and air. The images of Fig. 4b show the distortion of the vortex caused by flame propagation.

The effect of equivalence ratio is shown in Fig. 5. The spark timing is at 4 ms after piston actuation and the piston stroke is 3.3 mm. Unlike the stoichiometric conditions shown in Fig. 3b, the lean and rich flames are almost immediately quenched after initial flame formation ahead of the vortex. Flame propagation along the exterior of the jet column is quite similar for equivalence ratios of 0.75 and 1.25 (Figs. 5a and 5b, respectively), but is greatly diminished for an equivalence ratio of 1.5 (Fig. 5c), as expected. Flame bridging, as described previously, occurs across the jet column in Figs. 5a and 5b, but is suppressed in Fig. 5c.

To study the effects of vortex strength on vortex ignition and flame propagation, the ignition timing relative to vortex location was matched for the case shown previously in Fig. 3a (piston

stroke of 3.3 mm) and that of Fig. 6a (piston stroke of 1.6 mm). This can be verified by comparing Fig. 2a at 4 ms and Fig. 2b at 3 ms. Flame propagation is similar for both cases, but the weaker vortex of Fig. 6a does not penetrate the flame ahead of it. The same vortex of Fig. 6a, which is ignited just prior to reaching the electrodes, is ignited just past the electrodes in Fig. 6b. The resulting flame propagates within the jet column and into the vortex rollers, underscoring the need to match ignition timing to the correct phase of vortex development. The conditions for Fig. 7 (piston stroke of 5 mm) were selected such that ignition took place in a similar phase of vortex development as Fig. 3c (piston stroke of 3.3 mm). Again, this can be verified by comparing Fig. 2b at 6 ms and Fig. 2c at 4 ms. For the stronger vortex of Fig. 7, the flame propagates within the jet column and into the vortex rollers much more quickly than in Fig. 3c. In addition, the initial flame lift-off is more dramatic for the stronger vortex of Fig. 7, and local flame perturbations become more apparent. For a spark timing 1 ms later than that of Fig. 7 (see Fig. 2c at 6ms), the flame burns within the jet column but is unable to reach the vortex.

The conditions of the computational model were chosen to simulate flame propagation in the weaker vortex of Fig. 6a. The numerical configuration differs somewhat from experimental conditions because of the asymmetric nature of the ignition process. The presence of a boundary layer at the nozzle exit, uncertainty in the nozzle exit velocity, and nozzle exit velocity fluctuations may also lead to differences in the numerical and experimental results. Nonetheless, the results of the model, shown in Fig. 8, are quite promising. Differences in the selected timing are due to the 0.4 ms time step of the computations. The model predicts flame propagation ahead of the vortex and in the wake region and correctly predicts flame bridging across the jet column. As expected, flame bridging does not take place when the secondary perturbation in the exit velocity is removed.

5. Conclusions

The current study explored several important parameters that affect flame propagation in ignited vortex rings. Flame propagation was found to be highly sensitive to spark timing and was found to take place in two distinct regions: (A) within the jet column and vortex rollers, and (B) on the vortex exterior. Ignition after the passage of a vortex led to Type A flame propagation, and ignition ahead of a vortex led to Type B flame propagation. The equivalence ratio affects the stability and speed of flame propagation, with ideal conditions found at stoichiometric to slightly rich conditions. Higher vortex strength correlated with a higher likelihood of flame extinction for Type A flame propagation, and with faster, more highly wrinkled flame layers for Type B flame propagation. Preliminary results from the numerical model were promising, given uncertainties in boundary and ignition conditions. Future work will focus on obtaining particle image velocimetry data to aid in the computations, as well as more quantitative analysis of product formation.

Acknowledgments

The authors wish to thank Dr. C. D. Carter for his advice in setting up the OH PLIF experiments. The authors also acknowledge the assistance of Dr. R. D. Hancock and Mr. I. Vihinen in the assembly and construction of the burner. This work is supported by U. S. Air Force Contract F33615-00-C-2068.

References

1. Renard, P. H., Thevenin, D., Rolon, J. C. and Candel, S. (2000), "Dynamics of flame/vortex interactions," *Progress in Energy and Combustion Science*, Vol. 26, pp. 225-282.
2. McCormack, P. D. (1971), "Combustible Vortex Rings," *Proceedings of the Royal Irish Academy*, Vol. 71, pp. 73-83.
3. McCormack, P. D., Scheller, K., Muller, G. and Tisher, R. (1972), "Flame propagation in a vortex core," *Combustion and Flame*, Vol. 19, pp. 297-303.
4. Ishizuka, S., Takahiro, M., Takahashi, H., Kiminori, K. and Ryo, H. (1997), "Flame Speeds in Combustible Vortex Rings," *Combustion and Flame*, Vol. 113, pp. 542-553.
5. Cattolica, R. J. (1986), "Combustion-Torch Ignition: Fluorescence Imaging of NO_2," Twenty-First Symposium (International) on Combustion, The Combustion Institute, pp. 1551-1559.
6. Cattolica, R. J. and Vosen, S. R. (1986), "Two-Dimensional Fluorescence Imaging of a Flame-Vortex Interaction," *Combustion Science and Technology*, Vol. 48, pp. 77-87.
7. Wilson, K. J., Gutmark, E., Yu, K. H. and Schadow, K. C. (1994), "Active Control of Bluff-Body Flame Holder Combustor," AIAA Paper No. 940215, 32nd Aerospace Sciences Meeting & Exhibit, Reno, NV.
8. Rolon, J. C., Aguerre, F. and Candel, S. (1995), *Combustion and Flame*, Vol. 100, pp. 422-429.
9. Fiechtner, G. J., Renard, P. H., Carter, C. D., Gord, J. R. and Rolon, J. C. (2000), "Injection of Single and Multiple Vortices in an Opposed-Jet Burner," *Journal of Visualization*, Vol. 2, pp. 331-341.
10. Katta, V. R., Goss, L. P. and Roquemore, W. M. (1994), "Effect of non-unity Lewis number and finite-rate chemistry on the dynamics of a hydrogen-air jet diffusion flame," *Combustion and Flame*, Vol. 96, pp. 60-74.
11. Katta, V. R., Goss, L. P. and Roquemore, W. M. (1994), "Numerical Investigations ofTransitional H_2/N_2 Jet Diffusion Flames," *AIAA Journal*, Vol. 32, pp. 84-94.
12. Katta, V. R., Carter, C. D., Fiechtner, G. J., Roquemore, W. M., Gord, J. R. and Rolon, J. C. (1998), "Interaction of a Vortex with a Flat Flame Formed Between Opposing Jets of Hydrogen and Air," Twenty-Seventh Symposium (International) on Combustion, The Combustion Institute, pp. 587-594.

Table 1. Experimental Conditions.

Ignition Timing (ms)*	Equivalence Ratio	Piston Stroke (mm)	Vortex Velocity (m/s)
2.5	1.0	3.3	5
4	0.75, 1.0, 1.25, 1.5	3.3	5
4	1.0	1.6	2.5
5	1.0	5	6.5
6	1.0	1.6, 3.3, 5	2.5, 5, 6.5
8	1.0	3.3	5

*** Relative to piston actuation**

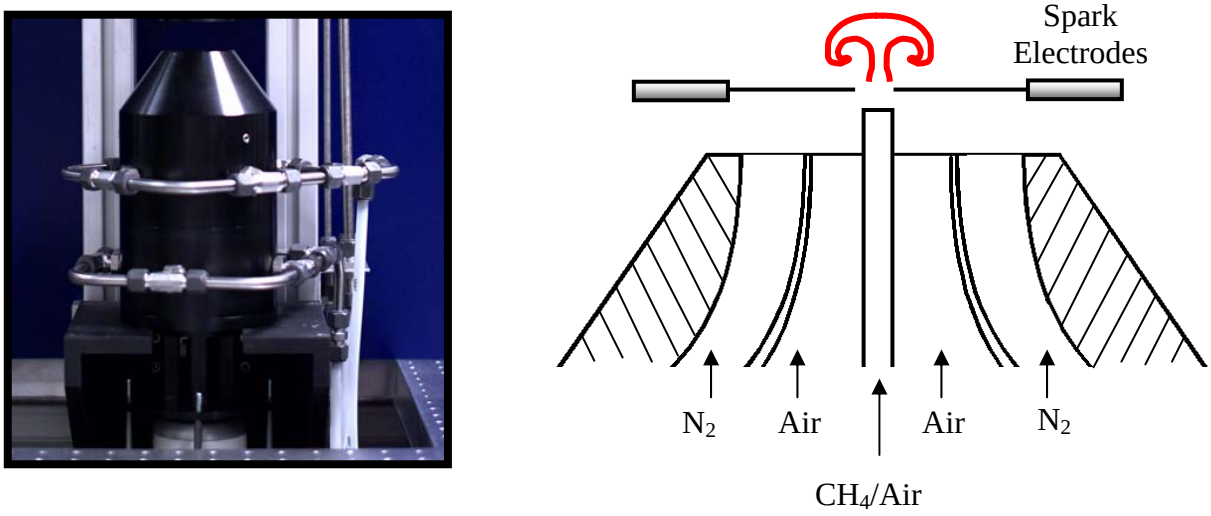

Fig. 1. Jet-in-co-flow burner used for vortex ignition experiments

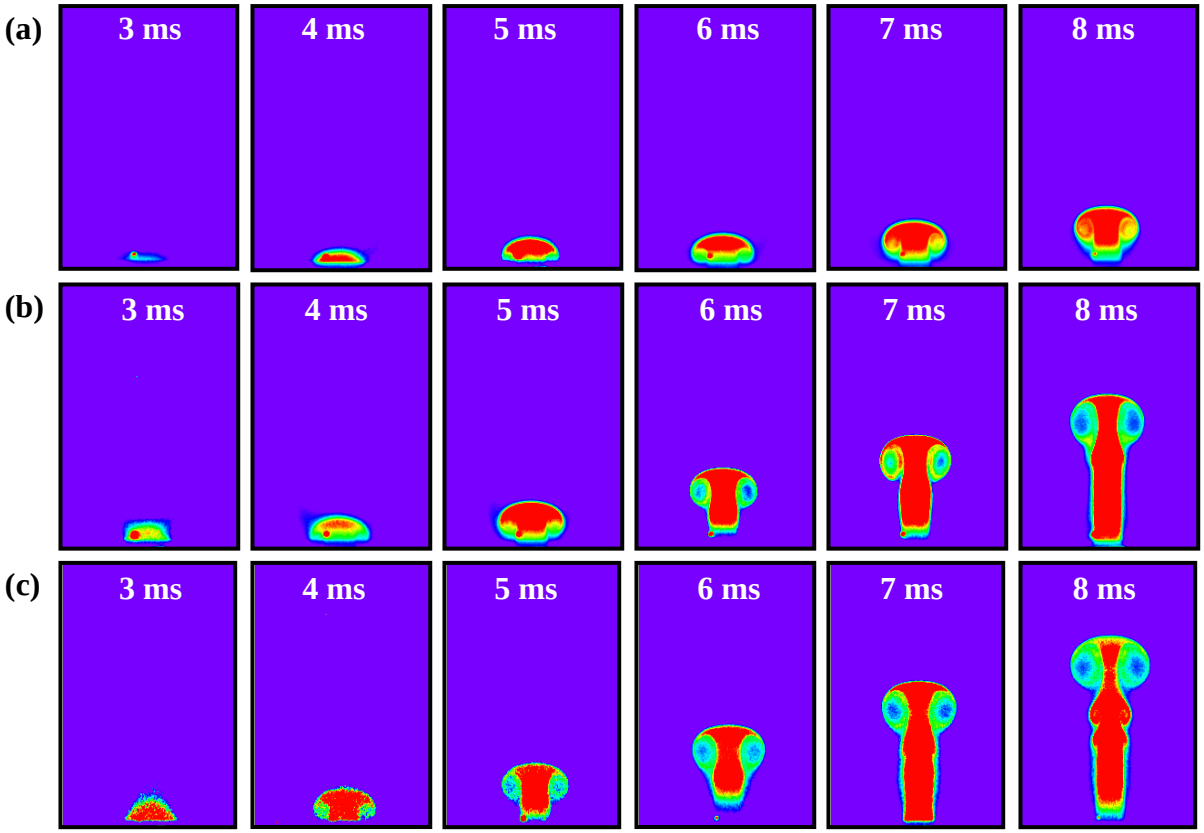

Fig. 2. Acetone PLIF images of cold-flow vortex propagation as a function of time after the piston is actuated for piston strokes of (a) 1.6 mm, (b) 3.3 mm, and (c) 5 mm.

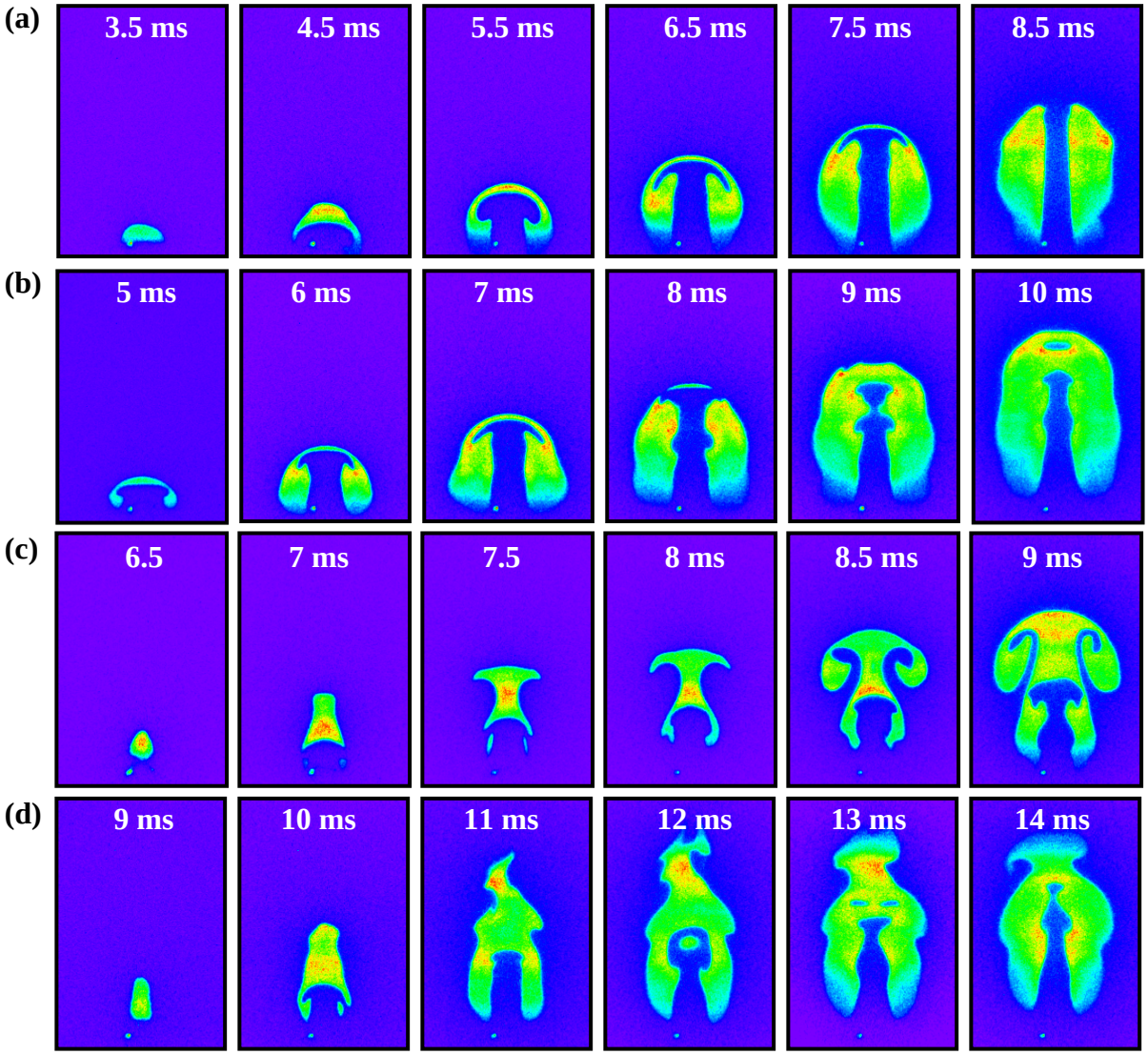

Fig. 3. OH PLIF image sequence for spark timings of (a) 2.5 ms, (b) 4 ms, (c) 6 ms, and (d) 8 ms after piston actuation. Equivalence ratio is 1.0 and piston stroke is 3.3 mm.

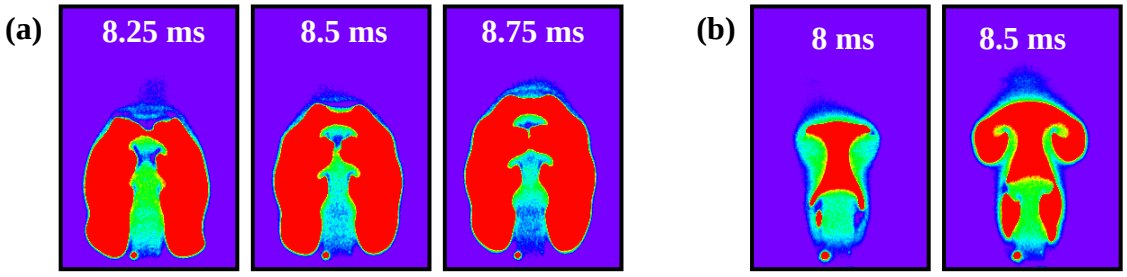

Fig. 4. Partial sequence of Acetone/OH PLIF images for spark timings of (a) 4 ms and (b) 6 ms after piston actuation. Equivalence ratio is ~1.0 and piston stroke is 3.3 mm. Images scaled such that regions of OH appear red.

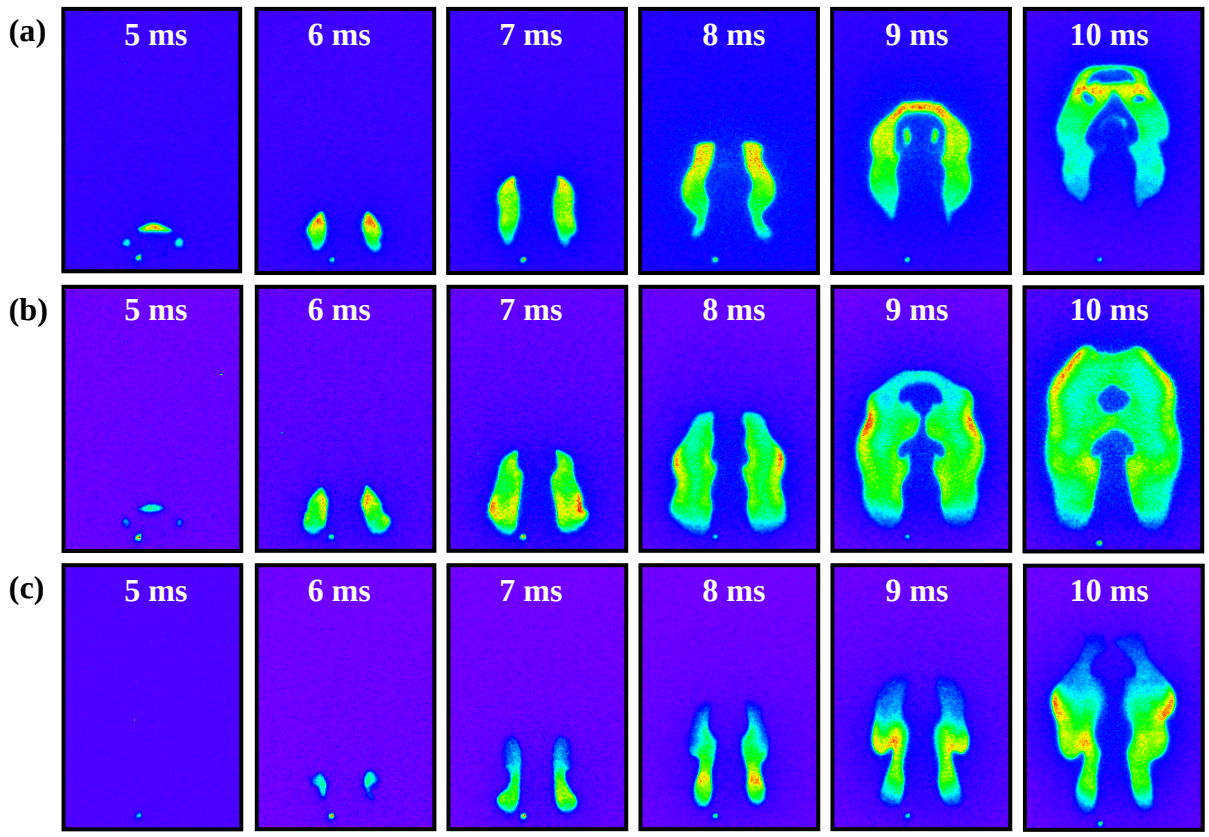

Fig. 5. OH PLIF image sequence for equivalence ratios of (a) 0.75, (b) 1.25, and (c) 1.5. Spark timing is 4 ms after piston actuation and piston stroke of 3.3 mm.

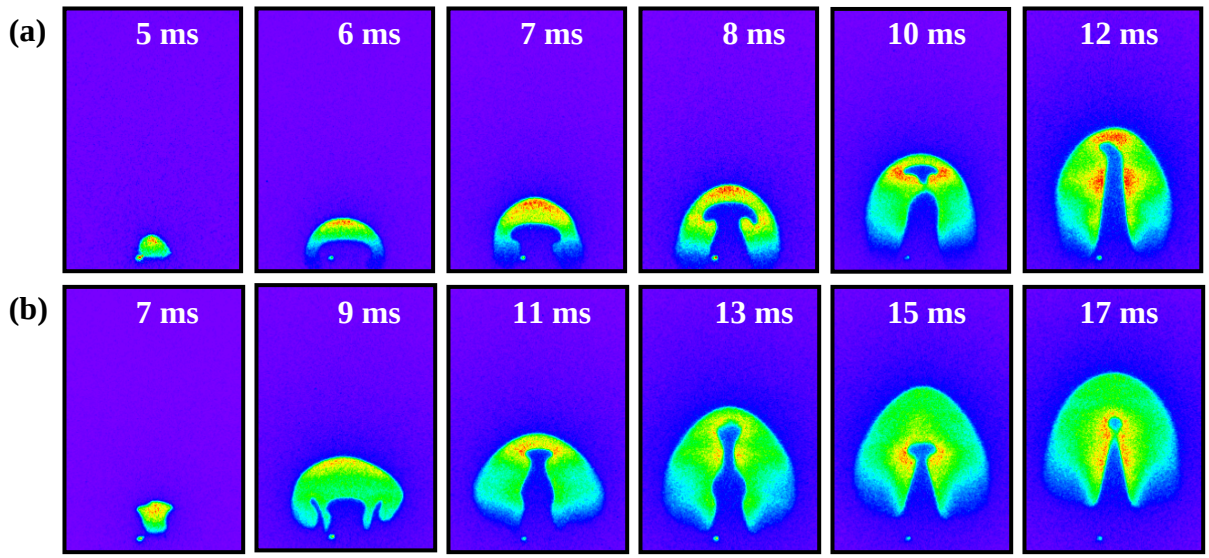

Fig. 6. OH PLIF image sequence for a piston stroke of 1.6 mm and spark timings of (a) 4 ms and (b) 6 ms after piston actuation. Equivalence ratio is 1.0.

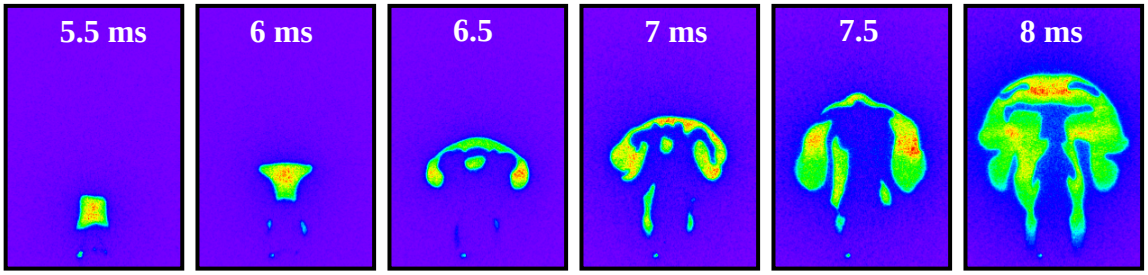

Fig. 7. OH PLIF image sequence for a piston stroke of 5 mm and spark timing of 6 ms for comparison with Fig. 3c. Equivalence ratio is 1.0.

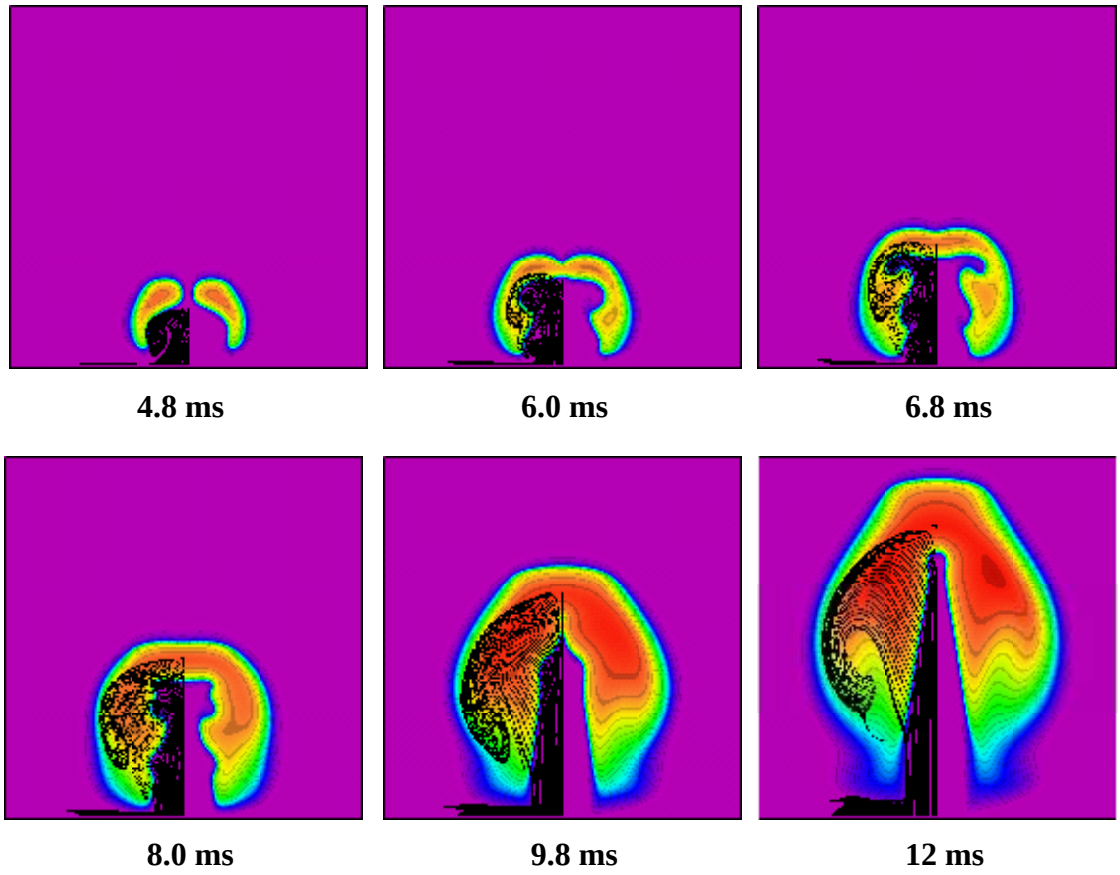

Fig. 8. Computed temperatures and particle traces simulating a 1.6 mm piston stroke. Ignition is initiated as the vortex exits the nozzle at ~4.0 ms. Image width and height are 20 mm.

Experiments in Fluids 31 (2001) 1–12 © Springer-Verlag 2001

Visualization and two-color DPIV measurements of flows in circular and square coaxial nozzles

J. W. Bitting, D. E. Nikitopoulos, S. P. Gogineni, E. J. Gutmark

Abstract High-resolution, reactive Mie scattering laser-sheet visualizations, two-color digital particle image velocimetry (DPIV) and thermal anemometry measurements in flows generated by equivalent coaxial circular and square jets are presented. Visualization results were obtained for three square, coaxial configurations, and a reference circular coaxial nozzle, at two Reynolds numbers of the outer jet (19,000 and 29,000) and for inner-to-outer jet velocity ratios of 0.15, 0.22, and 0.3. These indicated that the internal unmixed region diminished with decreasing velocity ratio. Strong evidence of unsteady recirculation and back-flow was observed at the end of the core of the inner jet, for the low velocity ratios. Comparisons between circular and square jet configurations indicated considerable mixing enhancement when square nozzles were used. Low-coherence, organized large-scale structure was evident from the visualizations and DPIV measurements near the origin of the inner mixing-region shear layers, and more so in the core region of the near field. These observations were confirmed by velocity spectra, which displayed peaks corresponding to a free shear-layer instability mode in the inner mixing-region shear layers, and a wake-type mode in the core region where the mean flow has a wake-like character. Although some large-scale structure was observed in the outer mixing layer during the visualizations, this was found to be incoherent on the basis of the DPIV measurements and the velocity spectra. It is noted that no axis-switching phenomena were observed in the square nozzle flows examined here. This is attributed to the absence of an organized structure in the outer shear layer, which was initially highly turbulent, and the weakly coherent nature of the organized structure observed in the inner mixing-region near field.

Received: 2 November 1998/Accepted: 8 September 2000

J. W. Bitting, D. E. Nikitopoulos (✉), E. J. Gutmark
Mechanical Engineering Department
Louisiana State University, Baton Rouge
LA 70803, USA

S. P. Gogineni
Innovative Scientific Solutions Inc.
Dayton, OH 45430, USA

This work has been carried out with funding from NASA EPSCoR and the Louisiana Board of Regents LEQSF to D.E. Nikitopoulos. The support of the Louisiana State University Dean's Fellowship Program and the AFOSR Graduate Summer Research Program is also gratefully acknowledged, as is the help of Dr. W.M. Roquemore of Wright Laboratory.

1 Introduction

Coaxial nozzles are an integral part of many engineering systems where mixing of streams of different fluids is required. They are used to provide the mixing between fuel and oxidizer in gas turbine combustors for propulsion and power producing systems, as well as waste thermal treatment systems. Another application is in jet exhaust noise reduction and control. Single non-circular nozzles have been shown to have better mixing characteristics than axisymmetric counterparts. Therefore, combinations of such nozzles in coaxial configurations can be of practical interest. The present work aims at investigating the use of non-circular coaxial nozzles as a method of passively controlling the mixing process between two coaxial jet flows.

Numerous studies have been performed to date on single circular jets, the dynamics of which are fairly well understood. Coaxial circular jets, which have a much more complex structure, have not been as widely investigated. Early studies, such as those by Forstall and Shapiro (1950), Chigier and Beer (1964), and Williams et al. (1969), were primarily concerned with the mean flow aspects of coaxial jet flow and covered various jet exit Reynolds numbers and mean-velocity ratios for several circular nozzle-exit geometries. Ko and his co-workers in a series of articles that span a 15-year period conducted much of the systematic early work on this subject. Ko's work on coaxial nozzles includes investigations of annular jets (e.g., Ko and Chan 1979; Ko and Lam 1984), as well as coaxial jets. The latter are of more direct relevance to the present study and will be discussed in some detail. Ko and Kwan (1976) and Kwan and Ko (1977) experimentally studied the near field of circular, coaxial jets at inner-to-outer velocity ratios, λ, greater than unity (1.4 to 3.3) and a co-flow Reynolds numbers, Re_{oh}, based on hydraulic diameter, ranging from 21,000 to 49,000. Coaxial nozzle flows at inner-to-outer velocity ratios less than unity (0.15 to 0.8) and at a fixed Reynolds number of $Re_{oh} = 58{,}000$ have been examined by Ko and Au (1985). These studies presented mean velocity, turbulence intensity, and pressure measurements, including velocity and pressure spectra. In most free shear flows, the development of the flow, and particularly of the large-scale coherent structures in the early stages of development, depends on the initial conditions (Nikitopoulos and Liu 1987). This is also true for the near field of coaxial jets

where shear layers are developing and merging. The exit shear-layer thickness, the turbulence intensity and spectral signature of the ensuing jets play an important role. A thorough flow visualization study by Dahm et al. (1992) shows the large-scale vortical structures in a nozzle of low outer-to-inner area ratio. Their study clearly illustrates possible mutual interactions between the mixing regions and the corresponding large-scale structures depending on the velocity ratio, λ, and Reynolds number. Tang and Ko (1993) have performed further research on excited coaxial jets at a velocity ratio of 0.3. They showed that the initial region of the jet plays an important role in the downstream formation of large-scale structures. They also identified vortex interaction processes resulting in incomplete coalescence.

Non-circular jets are also relevant to the present study, considering their unique characteristics of vortex evolution by self-induction, and the subsequent higher entrainment rates, which makes them good candidates for passive control of the jet flow. Several single-jet, non-circular configurations have been researched to date: rectangular/square, triangular, lobed, and elliptic. The rectangular and square nozzles produce non-circular vortex rings at the exit, which then deform and, under certain conditions, can lead to a switching of the jet axis. The axis switching is due largely to deformation and self-induction produced by the sharp corners of the nozzle, and depends on the initial velocity profile characteristics. Early studies by Sforza et al. (1966), Trentacoste and Sforza (1976), and duPlessis et al. (1974) investigated square jets but no insight was given into the underlying fundamental behavior of the square jet vortical interactions. Quinn and Militzer (1988) showed that for a square jet of the same hydraulic diameter as a circular jet, the square jet had a faster spreading rate at similar distances from the jet exit as compared to the circular jet. A detailed numerical simulation followed by experimental investigation illustrated that the axis switching is due to self-induction governed by the Biot–Savart Law with hairpin vortices developing along the diagonals of the square jets (Grinstein et al. 1995). Quinn (1992) has also observed off-center velocity peaks for a square slot orifice exit, caused by the "vena contracta" effect. A further study by Grinstein and Kailasanath (1995) on reactive square jets showed higher entrainment rates in the regions where the vortices roll up.

Triangular jets have also been investigated by Schadow et al. (1988). The process of self-induction in the corners of the triangle produced enhanced mixing in that region. The flow results were different between triangular orifice exits and pipe/nozzle exits, emphasizing the importance of initial conditions. A numerical and experimental study by Koshigoe et al. (1988) explained the differences and formulated conditions for which axis switching occurs. Enhancements in the fine scale mixing and combustion stability in the corner regions of the triangular jet were verified by Schadow et al. (1990). Large-scale mixing was accomplished on the flat sides with reduced pressure oscillations as compared to the circular jet. Fuel injection in the corners of the jet produced the best combustion results for the triangular jet.

Elliptic jets have also been studied, and have exhibited the same axis-switching and self-induction phenomena as found in triangular and rectangular jets. Gutmark and Ho (1986) demonstrated axis switching of the elliptic jet, resulting in an entrainment rate eight times higher than a circular jet.

Although single non-circular nozzles have been shown to be effective in terms of improved mixing, coaxial configurations of such nozzles have hardly been studied. Recently Bitting et al. (1997) presented flow visualization results for various combinations of non-circular (square, triangular, and lobed) and circular coaxial nozzles for various intermediate Reynolds numbers (up to 29,000) and low velocity ratios (inner mean velocity to outer mean velocity) less than unity. Most of these combinations seemed to enhance mixing compared to their circular counterparts. This paper presents reactive, Mie-scattering, laser-sheet visualizations in flows generated by coaxial square jets in three different configurations. Of these, one is examined in more detail through visualizations at two different Reynolds numbers and three different velocity ratios. Comparisons between the square coaxial nozzles and their axisymmetric counterpart are carried out, and results from two-color digital particle image velocimetry (DPIV) are presented for these two geometries. Comparisons of the DPIV mean velocities and those measured by a hot-wire sensor are also presented in an attempt to validate the accuracy of the DPIV technique when applied to a complex three-dimensional flow such as the present one.

2 Experimental setup and methods

A test facility was designed and built to carry out the research in non-circular, coaxial nozzle flows using air as the working fluid. This facility incorporates a modular design that allows easy exchange of inner and outer nozzles with different lip geometries. The test facility uses two independent air-flow supplies. On each supply line an orifice flow meter is used to determine the air-flow rate corresponding to a desired mass averaged jet flow velocity. Valved, bypass ports allow the use of part of the metered air streams for seeding purposes. The inner-jet flow passes through a flow-straightening honeycomb screen prior to entering the jet contraction with a contraction ratio of approximately 19:1. The outer jet flow reaches the outer jet through an annular passage with a contraction ratio of approximately 8:1. Provisions for aerodynamically adding swirl to the jet flows have been made, but have not been used for the present experiments. Ports for speakers are also provided so that the flow can be acoustically excited at appropriate frequencies, but have not been used during the present experiments.

A circular coaxial nozzle with an inner diameter of 15.24 mm (0.6 in) and an outer diameter of 38.1 mm (1.5 in) has been used as the baseline nozzle for the non-circular, coaxial nozzle flow study. The wall thickness of the inner nozzle is 1.905 mm (0.075 in). With the above dimensions, the hydraulic (effective) diameter of the inner jet and outer jet is $d_i = 15.26$ mm (0.6 in) and $d_o = 19.05$ mm (0.75 in) respectively. For the square nozzles, the hydraulic diameters are the same as for the

circular jet in order to allow for proper comparison between the circular and square jet flows. The outer-to-inner area ratio is also preserved at 4.69. The orientation of the inner square jet can be changed with respect to the outer square jet to give a centerline angular orientation offset of 22.5° (square I), 0° (square II) or 45° (square III) as depicted in Fig. 1.

Visualizations have been carried out using a pulsed laser sheet and seeding with $TiCl_4$, which upon reaction with moisture produces fine sub-micron TiO_2 particles. Several seeding strategies have been used to visualize the shear layers in the near field of the nozzles. Flow visualization of the inner and outer shear layers has been performed using $TiCl_4$ as seed in the dry co-flow air, with water vapor in the inner-jet air flow. Reversing the seeding of the streams has isolated the inner shear layer, and removing the moisture from the inner nozzle has isolated the outer shear layer. Instantaneous and time-averaged cuts have been made with a 1-mm thick laser sheet from a Nd-YAG laser pulsing at 10 Hz. Visualizations on a horizontal plane (perpendicular to the jet axis) have also been carried out at various distances form the jet exit. These were achieved by using a horizontal laser sheet and a mirror positioned above the laser-sheet plane at an angle of 45° with respect to the jet axis. Thus the top-view image was reflected horizontally into the receiving camera lens. The distance between the mirror and the exit of the jet was adequately large to avoid interference with the flow. Short (10 ns) exposures have been taken with a high-resolution Kodak CCD array (3,060 × 2,036) camera, to visualize the instantaneous structure of the jets, while long exposures (2 s) have been used to provide a 20-realization average of the mixing regions.

Two-color, digital particle image velocimetry (DPIV) measurements have also been carried out on vertical planes for the axisymmetric and square II configurations. A Nd-YAG laser provided one color at 532 nm and a sulforhodamine-640 dye laser pumped by a second Nd-YAG laser was used to provide the second color. The laser-sheet thickness was 1 mm and the laser pulse time separation was 20 μs. More details of the two-color DPIV system can be found in Gogineni et al. (1998). Both nozzles were seeded with Al_2O_3 particles for the DPIV measurements. The average diameter of the Al_2O_3 particles was 1 μm, which provides for an adequate particle response time for the measurement of the flows at hand. The DPIV images were analyzed using cross-correlation software (see Gogineni et al. 1998) on a Macintosh Power PC. The interrogation window size was 64 × 64 pixels with 50% overlap between adjacent interrogation windows. The spatial resolution was 5% of d_o in each direction on the laser-sheet plane and 2.5% of d_o across it. The displacement resolution for the velocity measurements was 1.2 μm (or 0.006% of d_o). Thus, the velocity resolution was 0.13 m/s (or 1% of the co-flow average velocity). The latter was based on a sub-pixel resolution of 0.1 as per Gogineni et al. (1998). Up to 113 samples (images) were used to determine the mean-velocity field of the flows examined. Thus, the DPIV measurements are useful in providing a qualitative picture of the mean-flow field in two dimensions, and are adequate for a quantitative analysis of the mean flow. The DPIV mean-flow results are evaluated by comparing with constant-temperature anemometry (CTA) measurements carried out using a TSI 1260A-10 probe (sensing length of 0.508 mm) with a 2.7% of d_o spatial resolution and approximately half the DPIV velocity resolution. The CTA measurements were carried out using equipment manufactured by TSI and were based on 10,000 samples with a sampling rate of 10 kHz and a low-pass filter cut-off of 5 kHz.

3
Results and discussion

In the results discussed in this section, each flow condition will be characterized by the Reynolds number of the outer jet flow based on the outer jet hydraulic diameter, and the inner-to-outer-flow velocity ratio, λ. The stream-wise direction, z, when scaled, will be given in outer jet hydraulic diameters, d_o. Unlike the studies of Ko and collaborators, and Dahm et al. (1992), the boundary layers of the outer nozzle exit are turbulent and the turbulence level in the outer jet is considerable (of the order of 20%). Thus, the exit flow condition is closer to what is encountered in practical applications.

Time-averaged and instantaneous planar flow visualization on a cross-flow plane of flows generated by the three square nozzle combinations of Fig. 1, are shown in Fig. 2. The Reynolds number of the outer nozzle flow is 19,000 and the velocity ratio is 0.3. The visualization was done at a plane located 1 in. (or $z/d_o = 2/3$) above the nozzle exit plane. At this elevation the unmixed regions in the core of the inner nozzle and between the inner and outer shear layers of the coaxial nozzle are to a great extent still present as it is evident from the averaged images in

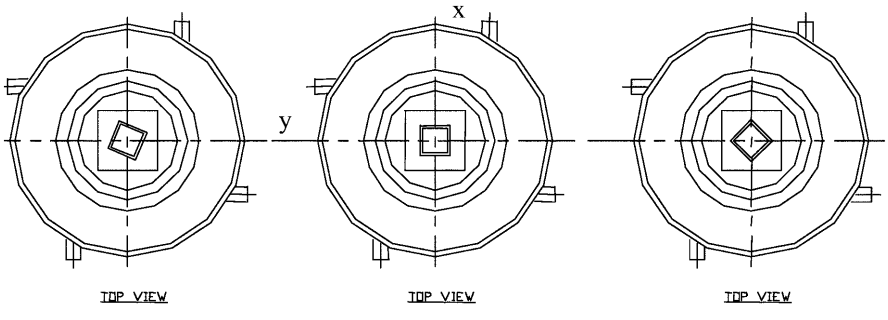

Fig. 1. Square coaxial nozzle configurations: *left* square I, *center* square II, *right* square III

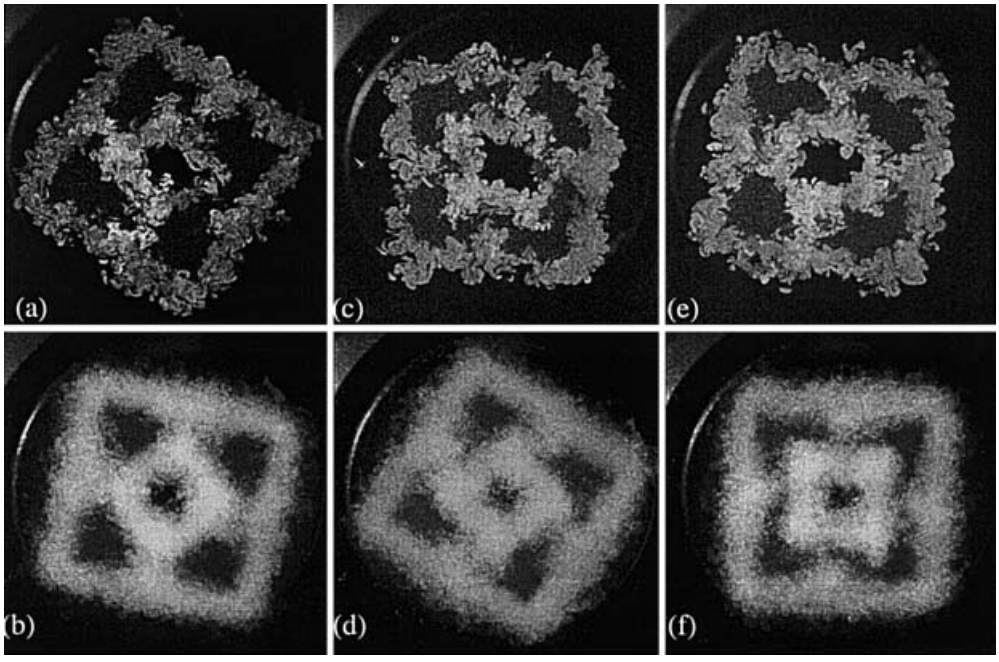

Fig. 2a–f. Cross-flow plane visualizations of three square, coaxial nozzle configurations: cuts at $z/d_o = 2/3$; **a, c, e** instantaneous images and **b, d, f** averaged images; $Re = 19{,}000$, $\lambda = 0.3$

Fig. 2b, d, f. Both instantaneous and averaged images indicate significant localized interactions between the inner and outer shear layers. In the case of the square II configuration (Fig. 2c, d) these shear layers are almost fully connected, with the outer shear layer growing into the inner one. This is, largely, due to the shape of the mean-velocity profile in the plane jet formed between the outer and inner square sides. Real-time observations during the visualization experiments indicated that the interaction between the inner and outer shear layers is intermittent in the near field of the jet. At one instant the seeded inner and outer shear layers would be fully connected, as in the case of the upper and right sides of the jet in Fig. 2c. At another instant, the seeded inner and outer shear layers would be separated by an unmixed region as in the lower and left sides of the jet in Fig. 2c. In the other two square nozzle configurations the same type of interaction is observed between the outer shear layer and the corner flows of the inner jet. The outer shear layer, in general, maintains the square geometrical shape of its origin. There is no visible evidence of distortion that could indicate that axis switching is in progress. The inner jet also maintains the geometrical shape of its origin although some distortion is observed. As shown by Grinstein et al. (1995) the development of axis switching for single non-circular nozzles is strongly dependent on the initial flow conditions. Therefore, in addition to the presence of coaxial flow, which changes the shear stress on the inner jet and the physics considerably, it is possible that the initial conditions for this experiment do not promote this phenomenon.

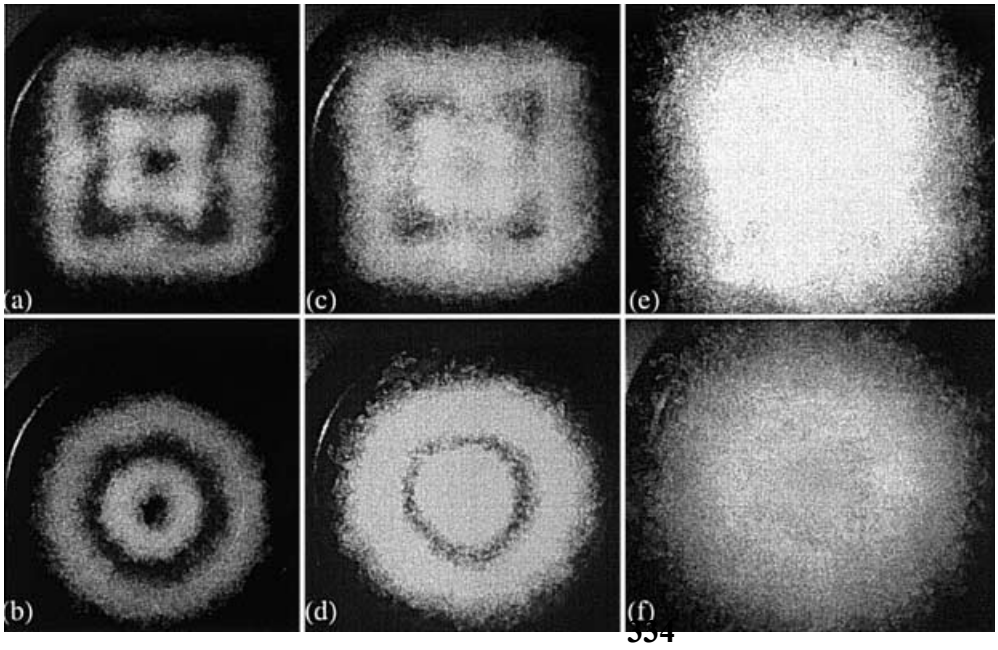

Fig. 3a–f. Averaged cross-flow plane visualizations of **a, c, e** square II and **b, d, f** axisymmetric, coaxial nozzle flows: cuts at $z/d_o = 2/3$, **a, b**; $z/d_o = 1$, **c, d**; $z/d_o = 2$, **e, f**; $Re = 19{,}000$, $\lambda = 0.3$

Another possibility is that the phenomenon has not yet developed at the axial distance of this visualization. Local injection of small-scale "mushroom" shaped vortical structures from the mixing regions into the unmixed areas is clearly visible in all instantaneous images. The fine-grained structure of the shear layers in the instantaneous visualizations is indicative of a highly turbulent flow, which impairs the development of clearly defined (coherent) large-scale vortical structures at the exit of the jet. Bearing in mind the observations of Grinstein et al. (1995), the highly turbulent shear layers generated at the exit of the square coaxial nozzles examined here, along with the low level of coherence of the associated large-scale structures, may also be responsible for the apparent absence of axis switching.

Averaged, cross-flow-plane visualizations at three different planes located at heights of $z/d_o = 2/3$, 1, and 2 above the exit of the jet for the circular and square II jet configurations are shown in Fig. 3. The Reynolds number is 19,000 and the velocity ratio 0.3. It is evident from the comparison that interactions of the inner and outer shear layers are absent at the lower levels in the case of the circular jet. The mixing regions in the case of the square jet combinations are more substantial and there is qualitative evidence that mixing at the flat sections of the jet is improved in this case. For example, the inner-jet unmixed core size is substantially diminished in the square nozzle flow (Fig. 3a) compared to the corresponding circular one (Fig. 3b). Also the interaction between outer and inner mixing regions, which is present in the square nozzle flow (Fig. 3a, c) is absent in the circular one (Fig. 3b,d). The inner jet at $z/d_o = 1$ and the outer jet at the highest elevation show evidence that the square jets are losing the correlation with the geometrical shape of their origin.

A center-plane visualization of the stream-wise evolution of the flow for the square II and axisymmetric coaxial

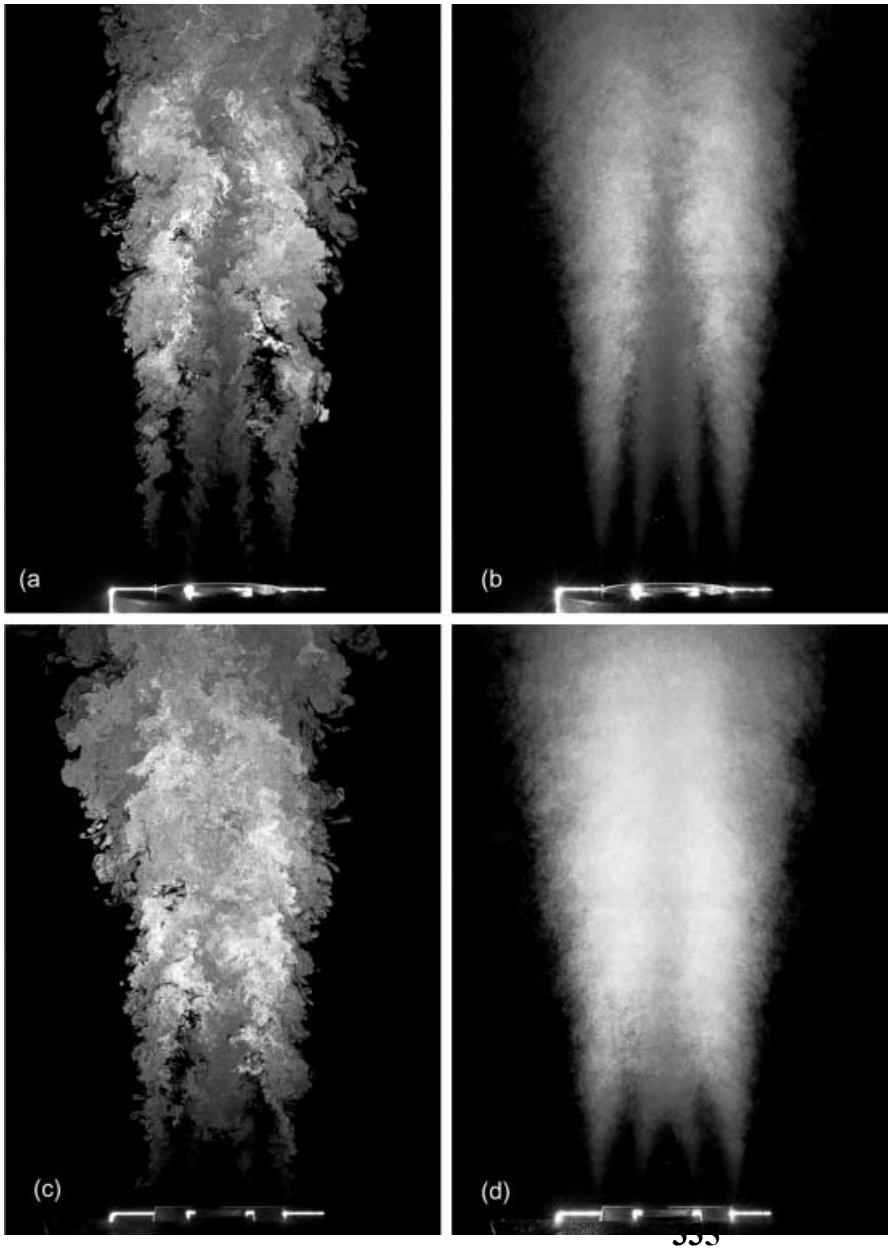

Fig. 4a–d. Center-plane visualizations of **a, b** axisymmetric, and **c, d** square II, coaxial nozzle flows; **a, c** instantaneous images, and **b, d** averaged images. $Re = 29{,}000$, $\lambda = 0.3$

jets is given in Fig. 4, at a Reynolds number of 29,000 and velocity ratio of 0.3. The scale for all images is identical, and the visualized center-plane for the square II jet is normal to the square sides. It is clearly visible from the averaged images (Fig. 4b, d) that better mixing is achieved by the square nozzle combination. The inner and co-flowing unmixed regions disappear sooner in the square II case than the axisymmetric one, and the inner and outer shear-layer growth appears to be faster. Also, the outer square jet spread is considerably faster than its axisymmetric counterpart. The instantaneous realizations illustrate the same effect. The shear layers near the exit of both jets indicate the presence of large-scale structures, masked by smaller turbulent scales. The presence of this underlying organized structure in the inner region of the jet is more apparent in the DPIV results that will be discussed later, and clearly manifested in velocity spectra. The characteristic intermittent ejection of "mushroom" shaped eddies is particularly evident in the outer shear-layer boundary. The scale of the vortices is larger in the far field of the outer jet compared to the near-field shear layers indicating the change of scale that accompanies the transition from a shear-layer character to that of a jet.

Figure 5 depicts superposition of averaged visualizations from the circular (Fig. 5a for diametrical plane) and square II (Fig. 5b, c for center-plane and diagonal views respectively) coaxial jet flows, at three different velocity ratios for a Reynolds number of 29,000. The mixing region for $\lambda = 0.15$ appears as light gray, the overlap of the mixing regions from the flows with $\lambda = 0.15$ and 0.22 appears as dark gray, and the overlap of the mixing regions from all three flows ($\lambda = 0.15$, 0.22, and 0.3) appears as black. Basic qualitative features are common to the circular and square cases. It is observed that strong backflow develops downstream of the inner jet as the velocity ratio is decreased (light gray and dark gray mixing regions in Fig. 5). At the lowest velocity ratio the inner-jet unmixed core disappears immediately after the inner-jet exit (light gray mixing region in Fig. 5). Inspection of instantaneous realizations of the square II jet shown in Fig. 6, and real-time observations during the experiments, indicate the presence of unstable recirculation vortices in that region, which is reminiscent of the near-field, bluff-body wake flow. This recirculation was observed at $\lambda = 0.15$ and 0.22 in both the square II and the axisymmetric jets, and was absent at $\lambda = 0.3$ for both Reynolds numbers examined. It is also manifested by the flat termination of the unmixed core for the two lower velocity ratios in Fig. 5. This wake-like behavior of the inner mixing region at low velocity ratios has been identified by Ko and Au (1985) and is similar to what is observed behind the solid core of an annular jet (Ko and Chan 1979). At the highest velocity ratio (0.3) there is no evidence of near-field, wake-like behavior, and the inner shear layers that are initiated as asymmetric wakes at the lip of the inner nozzle evolve gradually and merge to end the unmixed core of the inner jet. As we will see later, wake characteristics still exist in this region and at this velocity ratio, but the character is

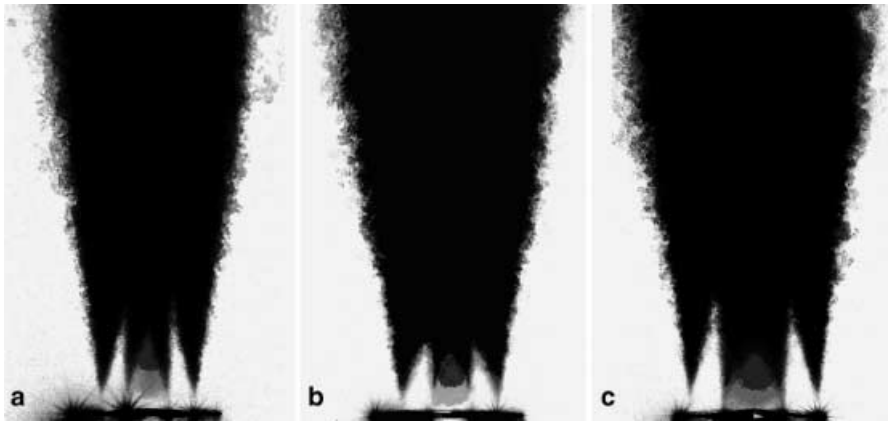

Fig. 5a–c. Superposition of averaged visualizations of coaxial nozzle flows with three different velocity ratios at a $Re = 29{,}000$; **a** circular diametrical plane, **b** square II center-plane, and **c** square II diagonal plane. The mixing region for $\lambda = 0.15$ is light gray, the overlap of the mixing regions from the flows with $\lambda = 0.15$ and 0.22 appears as dark gray, and the overlap of the mixing regions from all three flows ($\lambda = 0.15$, 0.22, and 0.3) appears as black

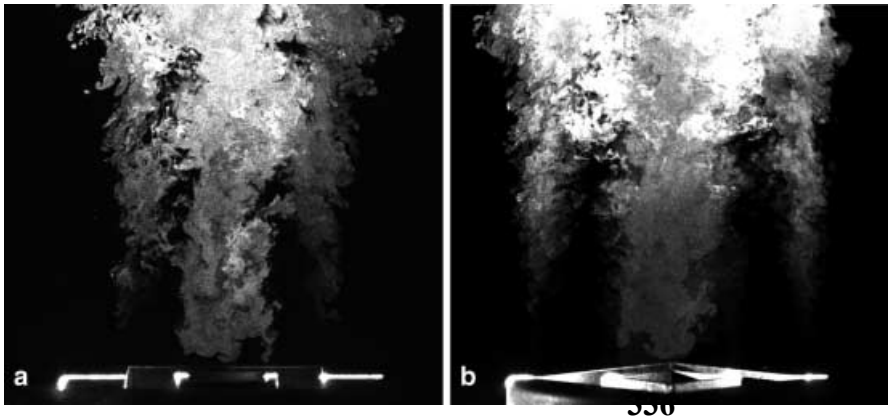

Fig. 6a, b. Near-field visualizations of square II coaxial nozzle flow at a $Re = 29{,}000$ and $l = 0.15$, illustrating wake-like character of inner mixing region; **a** centerline plane, **b** diagonal plane

reminiscent of far-field wake behavior rather than near field. Figure 5 also indicates that varying the velocity ratio within the range examined while keeping the outer Reynolds number fixed primarily impacts the evolution of the inner mixing region. The outer mixing region, which is dominated by the strong outer shear layer, remains unaffected on the basis of this qualitative method of examination. A comparison between the circular and square cases presented in Fig. 5 clearly indicates that enhanced mixing exists in the inner mixing region of the square jets for all three velocity ratios. The same is observed in the near-field outer mixing region on the square jet center-plane. The co-flow unmixed core on the center-plane (Fig. 5b) is destroyed earlier in the square jet relative to the circular jet (Fig. 5a), but also relative to the square jet diagonal-plane (Fig. 5c). The spread of the outer jet is also enhanced in the square case (Fig. 5b) relative to the circular case (Fig. 5a) for all velocity ratios.

Averaged and instantaneous visualizations of the inner-jet shear layer alone, the outer shear layer alone, and both of them combined are rendered in Fig. 7 for the square II jet at a Reynolds number of 19,000 and a velocity ratio of 0.3. This figure also illustrates the success of the different seeding strategies used here, in selectively visualizing parts of the co-axial flow. The inner-jet flow (Fig. 7a, d) is rapidly mixed with the co-flow air, as seen by the brighter areas at the end of the jet potential core. As expected because of the higher co-flow velocity, the "outwards" transport is limited as shown by the tracer pattern. The shear layer between the co-flow and inner-jet flow exhibits fine-scale structures that seem to be more stretched. These observations are also evident in Fig. 7b, e, where the visualization of the outer shear layer alone is shown. The "wispy" fine scale structures indicate a very strong dynamic interaction between co-flow and inner-jet flow. The instantaneous realization of the inner jet in Fig. 7d bears evidence of a large-scale varicose instability mode manifested by the stream-wise wavering of the mixed region. This is seen more clearly in Fig. 7e from the low concentration tracer signature along the centerline of the jet. This signature can be attributed to the fact that in that region where the inner shear layers are merging, the inner velocity profile assumes a far-field, wake-like shape, which supports a varicose mode.

Two-color DPIV mean-velocity vector fields on a centerline plane in the near field of the axisymmetric and square II flow cases are respectively shown in Figs. 8 and 9 for the same conditions as the visualizations of Fig. 7, but with different magnification. In both Figs. 8 and 9, the vector fields are superposed on constant axial mean-velocity gray-scale-flooded contours. The mean DPIV results for the axisymmetric case are based on a 113-image

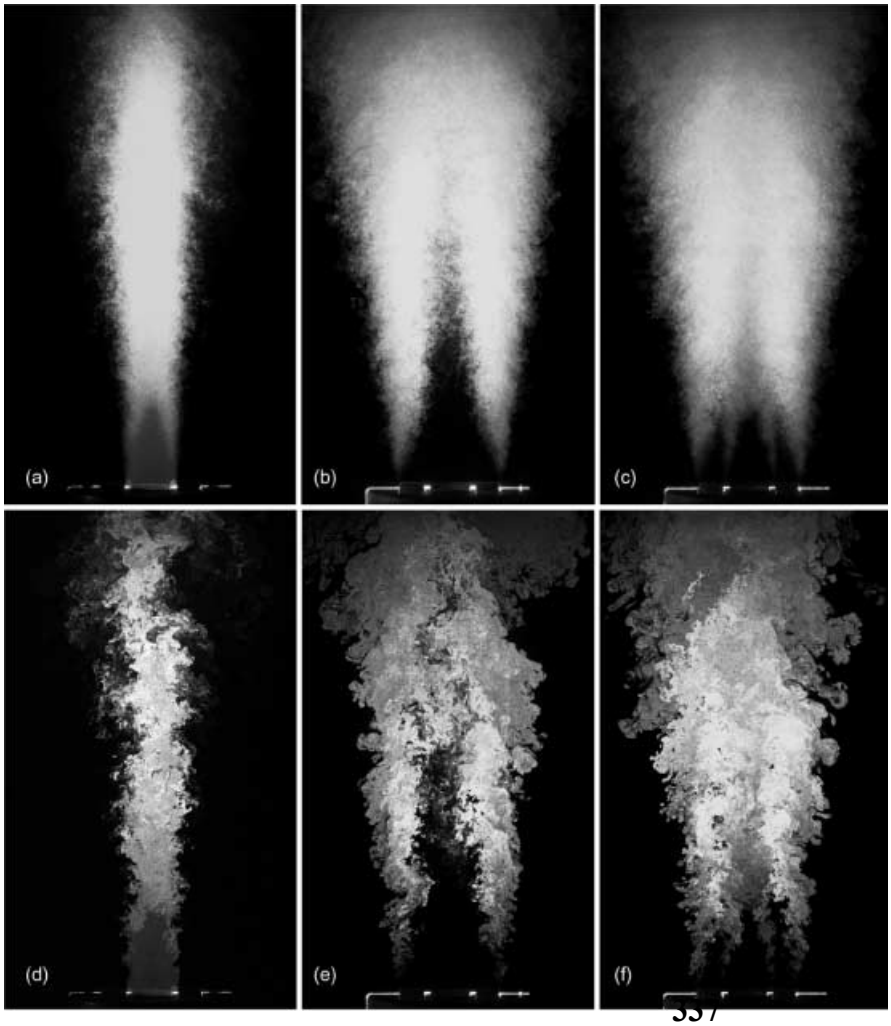

Fig. 7. **a–c** Averaged and **d–f** instantaneous center-plane visualizations of square II coaxial flows at $Re = 19{,}000$, $\lambda = 0.3$: **a, d** inner mixing region; **b, e** outer mixing region; **c, f** both

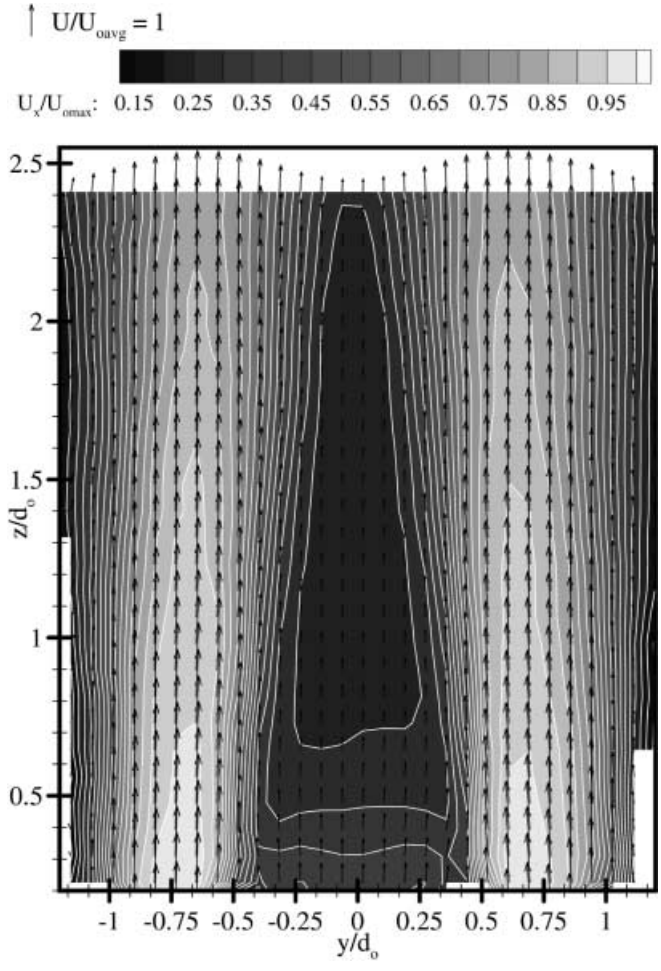

Fig. 8. Average velocity vector field and axial velocity contours from two-color, DPIV measurements for the axisymmetric coaxial nozzle flow; $Re = 19{,}000$, $\lambda = 0.3$

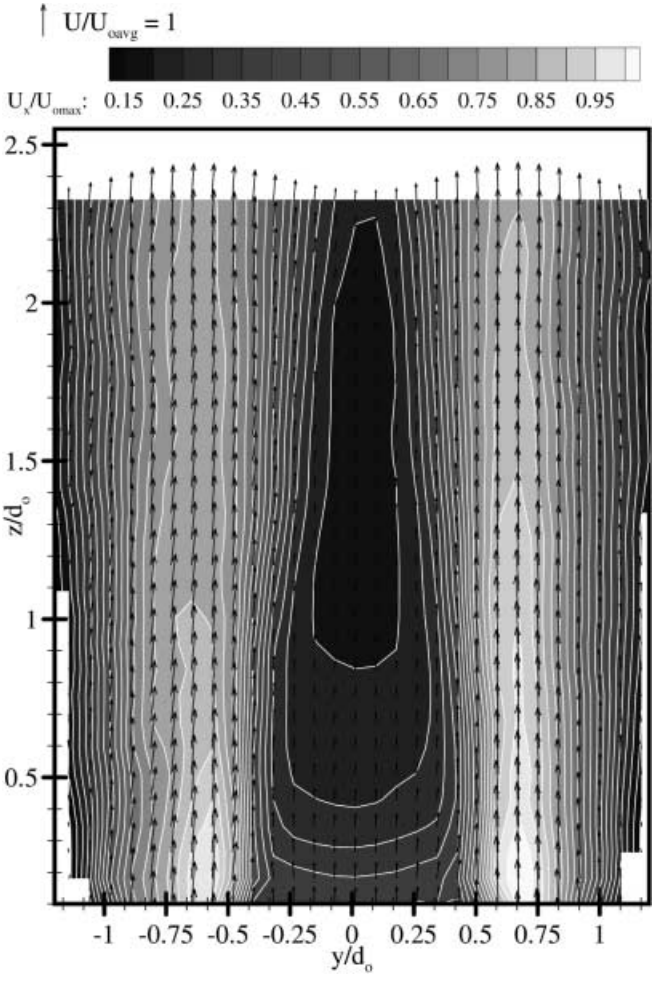

Fig. 9. Average velocity vector field and axial velocity contours from two-color, DPIV measurements for the square II, coaxial nozzle flow; $Re = 19{,}000$, $\lambda = 0.3$

average and for the square II case on a 41-image average. Before proceeding to the discussion of the DPIV results we present typical comparisons between the DPIV and CTA axial mean-velocity profile measurements for both nozzle geometries in Figs. 10 (axisymmetric) and 11 (square II along-side) at one downstream location. Included are the CTA measurements of the local turbulence intensity. It is evident that the agreement between DPIV and CTA measurements is very good, in spite of the limited DPIV sample sizes. This is especially true for the square II case where the sample size is smallest. Some differences are observed particularly in regions of high shear and/or turbulence intensity but are within the limits imposed by a combination of positional and statistical uncertainty as well as velocity and spatial resolution. The horizontal and vertical spatial resolution for DPIV and the horizontal spatial resolution for CTA were of the order of 5% of the inner nozzle diameter. The error bars in Figs. 10 and 11 are based on statistical uncertainty only. Comparisons of DPIV and CTA mean profiles at other distances from the jet exit are equally good, indicating that the performance of the two-color, DPIV technique in measuring these turbulent, complex, three-dimensional flows is satisfactory.

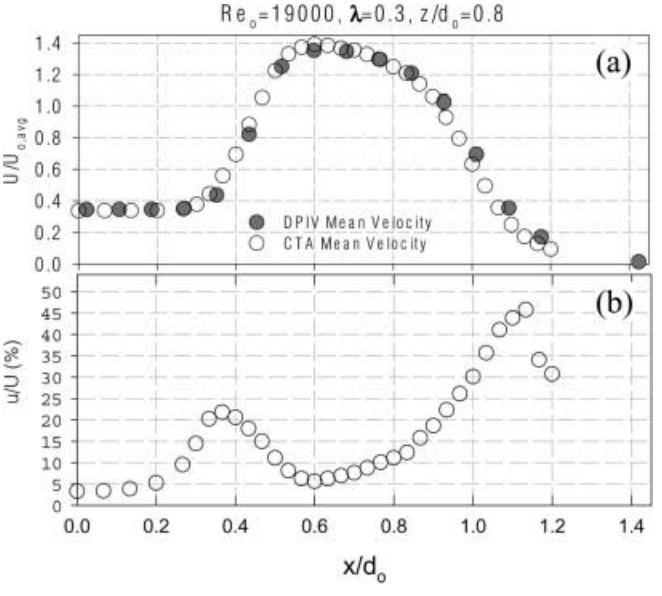

Fig. 10a, b. Comparisons between two-color, DPIV, and CTA mean-velocity measurements **a** in an axisymmetric, coaxial nozzle flow, **b** local turbulence intensities. Error bars are at 95% confidence level

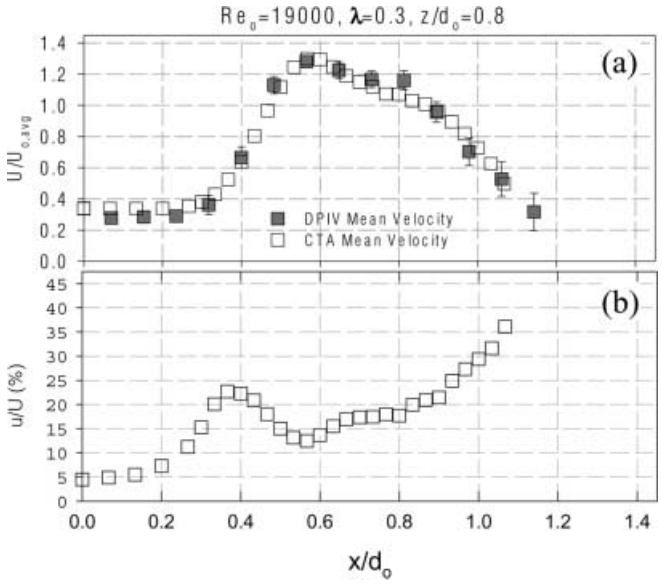

Fig. 11a, b. Comparisons between two-color, DPIV, and CTA mean-velocity measurements **a** in a square II, coaxial nozzle flow, **b** local turbulence intensities. Error bars are at 95% confidence level

The DPIV results of Figs. 8 and 9 also indicate that the velocity profiles of the co-flow are initially flatter in the axisymmetric case compared to the square II one, and that in this region a mean-velocity gradient exists over most of the outer part of the co-flowing jet. This difference in initial conditions accounts for the more rapid decrease of the co-flow core velocity observed for the square II case in Fig. 9 and the faster reduction of the corresponding co-flow unmixed region indicated by the visualizations of Figs. 4 and 5. The co-flow is seen to decelerate downstream as the flow stream spreads both inwards and outwards. A 5% asymmetry is also observed in the initial region of the square II co-flow, while the symmetry of the axisymmetric flow is excellent. The inner-jet potential core velocity is seen to decrease downstream in both cases, as the faster co-flow stream suppresses the weaker inner jet. This deceleration of the inner-jet potential core causes a local increase of the inner shear-layer velocity ratio (strength) that influences its dynamics. The mean velocity of the inner-jet core remains fairly constant, after the initial rapid deceleration of the inner core, within the range $0.5 < z/d_o < 1.6$, for both axisymmetric and square II jets. The deceleration of the inner jet is more rapid in the case of the square II nozzle, and the corresponding value of the flat core-velocity minimum is 20% lower than the axisymmetric nozzle case. Further downstream, recovery of the velocity in the central region takes place, due to the merging of the opposite co-flowing shear layers. This merging occurs earlier for the square II nozzle than the axisymmetric one, indicating a stronger interaction and mixing between the inner and outer co-flowing jets for this geometry. This is corroborated by the visualizations of Figs. 4 and 5, which indicate that the unmixed core is smaller for the square II case compared to the axisymmetric one. It should be noted that, although the visualizations of Figs. 4 and 5 are at a $Re = 29{,}000$, the qualitative features of the flows are the same as those observed for the $Re = 19{,}000$ condition of the measurements. The velocity profiles in the core region at the highest elevation from the jet exit shown in Figs. 8 and 9 bear the signature of the far field of a wake. However, unlike the case of the traditional wake, both the centerline and "free-stream" velocities are evolving, and this may have a considerable influence on the flow dynamics. The instantaneous visualizations of Fig. 7 discussed previously have indicated the presence of a wake-like large-scale structure in the near-field core region of the jets. This is confirmed by instantaneous vorticity distributions obtained from the DPIV measurements and presented in Figs. 12 and 13. The two instantaneous vorticity distributions from the axisymmetric case shown in Fig. 12 indicate that a fairly symmetric large-scale structure of free shear-layer character is developing very

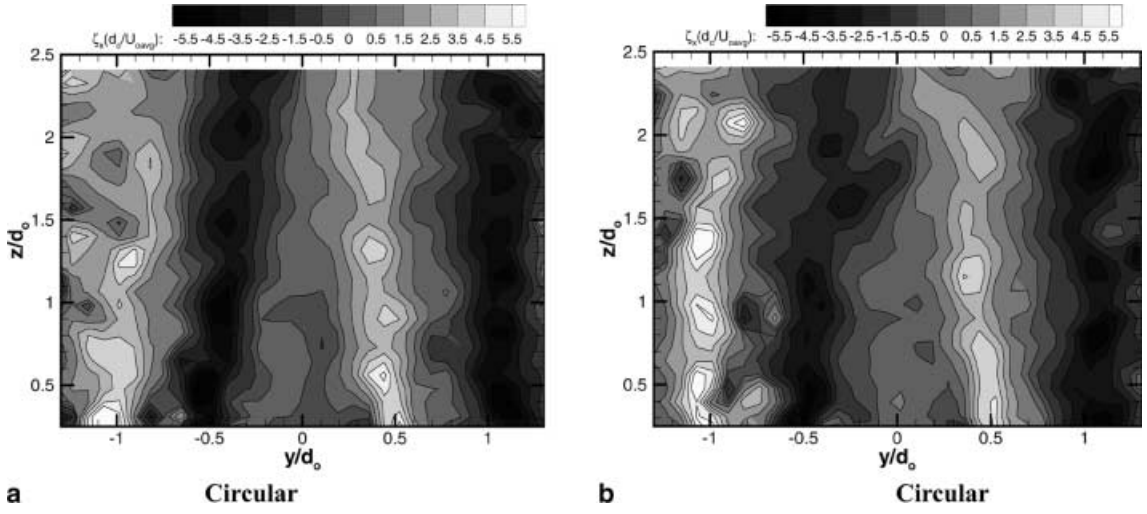

Fig. 12a, b. Instantaneous vorticity distributions from two-color, DPIV measurements for the axisymmetric, coaxial nozzle flow. $Re = 19{,}000$, $\lambda = 0.3$

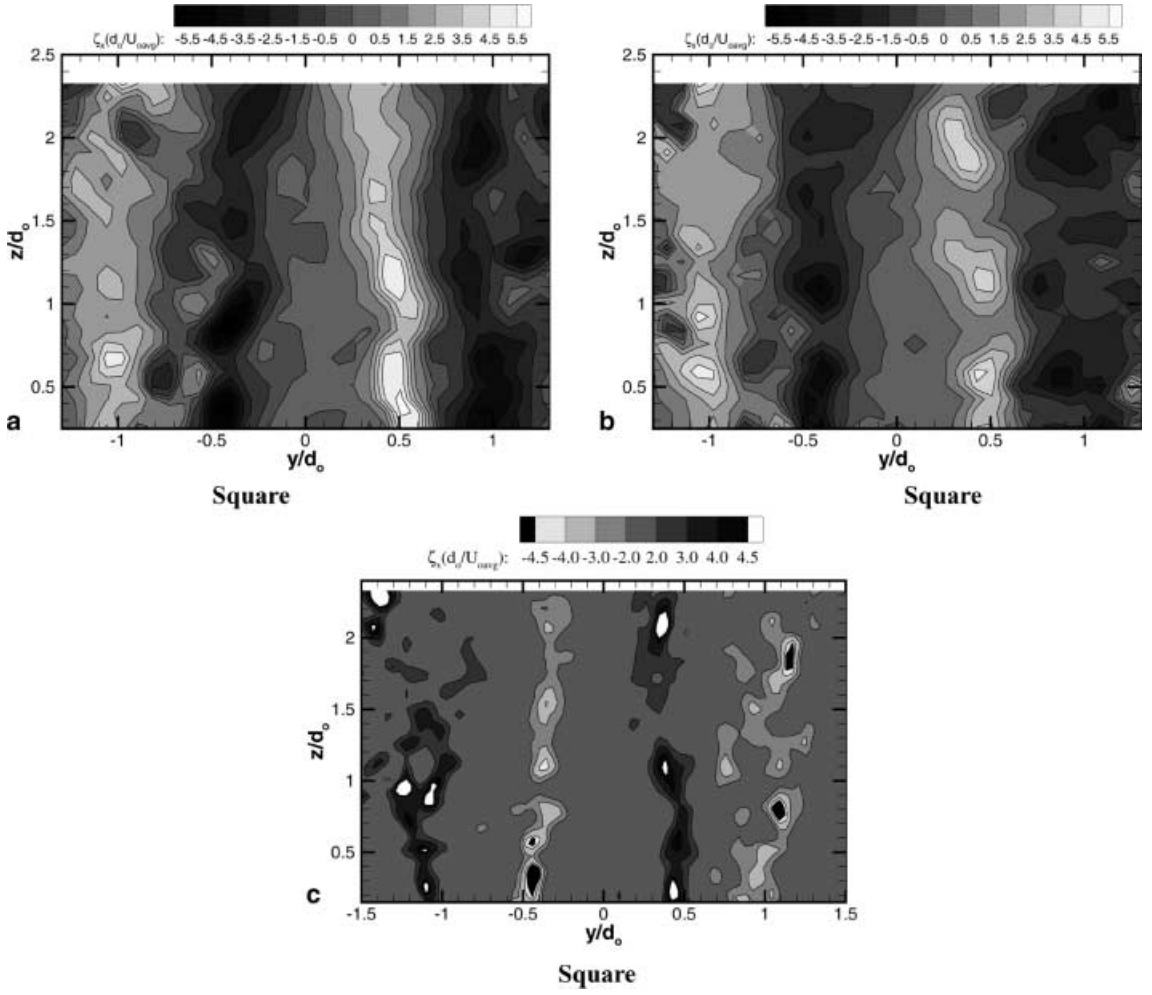

Fig. 13a–c. Instantaneous vorticity distributions from two-color, DPIV measurements for the square II, coaxial nozzle flow. $Re = 19{,}000$, $\lambda = 0.3$

close to the exit inside the inner region where the potential core is intact and the inner shear layers are well separated (see mean-velocity distributions in Fig. 8). This is evidenced by the vorticity concentrations in that region. Further downstream the symmetry in the vorticity distributions appears to be breaking down as the inner shear layers come together forming a wake-like profile. Comparison between Fig. 12a and b brings forth the intermittent nature of the wake-like large-scale structure that forms at the end of the inner core. Similar qualitative observations indicating the evolution of a wake-like, large-scale structure from the initial shear-layer related, large-scale structure can be made for the square (II) coaxial jet as evidenced by Fig. 13a, b. It should be noted that seeding was not present in the ambient air for the realizations of Figs. 12 and 13a, b. Thus, the outer shear-layer instantaneous vorticity distributions in these figures do not represent well the structure of the outer mixing region. For this reason an attempt was made to obtain two-color, DPIV measurements using smoke as the ambient air seed. An instantaneous vorticity distribution from such a measurement is shown in Fig. 13c for the square nozzle case. The outer shear layer is adequately represented and indicates the presence of vorticity concentrations that are rather incoherent. This leads to the conclusion that there is no organized large-scale structure associated with the outer shear layer. This is justified by the fact that the outer shear layer was highly turbulent from its onset.

The observations made on the basis of the visualizations and the DPIV results relative to large-scale coherent structure within the jets is confirmed from the analysis of velocity spectra obtained through CTA from the regions of interest. The amplitudes are presented relative to the rms (A_o) at the center point at the exit of the jet. The short-lived appearance of a weakly coherent shear-layer mode in the inner mixing layer of the near field of the coaxial jets is manifested by a broad local peak in the spectra of Fig. 14a, b for the circular and square II cases respectively. Shear-layer scaling has been used for the frequency, which appears on the horizontal axis as a Strouhal number based on initial momentum thickness (θ_o) and velocity difference. The Strouhal number corresponding to the observed spectral peaks, at 1,024 Hz for the circular and 1,150 Hz for the square II cases, is consistent with the most amplified shear-layer mode as predicted by linear stability

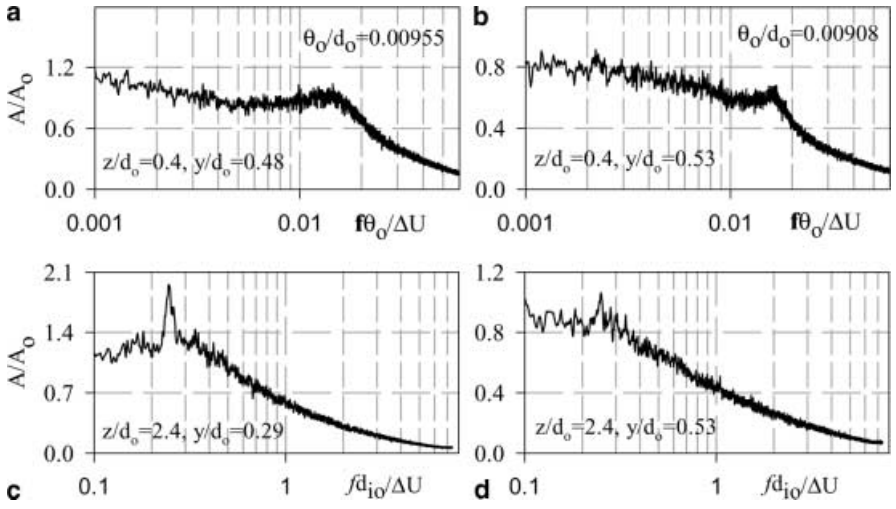

Fig. 14a–d. Spectra from the inner mixing region of the **a, c** circular and **b, d** square II, coaxial nozzle flows at $Re = 19{,}000$, $\lambda = 0.3$

analysis (e.g., see Nikitopoulos and Liu 1987). Spectra obtained from the inner shear region of both jets after the merging of the inner shear layers and the formation of the wake-like mean-velocity profile, are shown in Fig. 14c, d for the circular and square II jets respectively. The scaling of the frequency is consistent with the wake-like nature of the flow using a Strouhal number based on the inner nozzle outer lip dimension ($d_{io} = 19$ mm) and the initial velocity difference. The presence of the large-scale structure observed in the visualizations is manifested by distinct spectral peaks, at 166 Hz for the circular and 169 Hz for the square II cases, with a Stouhal number magnitude consistent with that expected in a wake. DPIV instantaneous visualizations such as that of Fig. 13c indicate the absence of an organized large-scale structure in the near-field, outer shear layer. This can be explained by a highly turbulent boundary layer at the nozzle exit. Indeed, as shown in Fig. 15, velocity spectra obtained inside the outer shear layer at the exit of both the circular and square nozzles, reveal a nearly fully developed turbulence spectrum with evidence of an inertial range present.

In view of the combined visualization, DPIV and spectra evidence, the absence of an organized structure in the outer shear layer and the weakly coherent nature of the organized structure observed in the inner mixing-region near field are the most probable reasons for the absence of axis switching in the square nozzle flows examined here.

4
Concluding remarks

Reactive Mie scattering laser-sheet visualizations, two-color DPIV, and thermal anemometry measurements in flows generated by coaxial circular and square jets have been carried out. A series of different seeding strategies were used to selectively visualize the different mixing regions of the coaxial jets. Results were presented for the three square coaxial configurations and a reference circular coaxial nozzle at two Reynolds numbers of the outer jet (19,000 and 29,000) and for inner-to-outer jet velocity ratios of 0.15, 0.22, and 0.3. The internal unmixed regions of these low-velocity-ratio jet flows diminished with decreasing velocity ratio. At the lowest velocity ratios, strong evidence of unsteady wake-like recirculation was observed at the end of the core of the inner jet. The measurements also indicate a rapid deceleration of the inner-jet core, saturation to a minimum, and subsequent increase of the velocity as the inner shear layers merge to destroy it. The mean-velocity and turbulence-intensity record correlates well with the observations made during the visualizations. The visualizations also revealed interesting interactions between the inner and outer square-nozzle shear layers in the near field. The region of interaction and overlap of the inner and outer shear layers are characterized by more stretched-out structures than those observed in the regions where such direct interaction is absent. Low-coherence, organized, large-scale structure was evident from the visualizations and DPIV measurements near the origin of the inner mixing-region shear layers and more so in the core region of the near field. These observations were confirmed by velocity spectra, which displayed peaks corresponding to a free shear-layer instability mode in the inner mixing-region shear layers, and a wake-type mode in the core region where the mean flow has a wake-like character. Although some large-scale structure was ob-

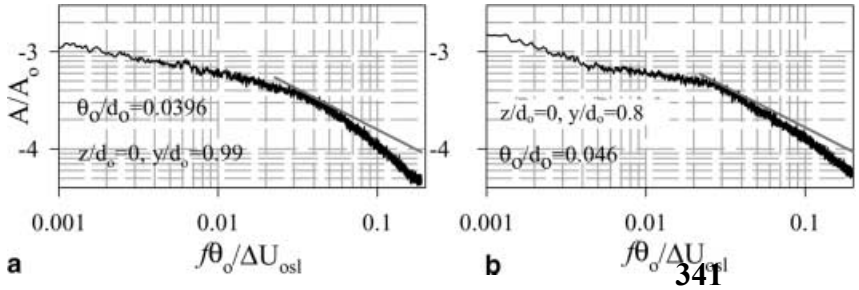

Fig. 15a, b. Spectra from the onset of the outer mixing layer of the **a** circular and **b** square II, coaxial nozzle flows at $Re = 19{,}000$, $\lambda = 0.3$. The straight line indicates the −5/3 inertial range slope

served in the outer mixing layer during the visualizations, this was found to be incoherent on the basis of DPIV vorticity distributions and the velocity spectra. It is noted that no axis-switching phenomena were observed in the square nozzle flows examined here. This is attributed to the absence of an organized structure in the outer shear layer, which was initially highly turbulent, and the weakly coherent nature of the organized structure observed in the inner mixing-region near field. However, comparisons between the circular and square jet flow-visualizations and DPIV measurements indicated considerable local mixing enhancement when square nozzles were used. The measurements indicate that the major contributor to the observed differences in the near-field mixing patterns between the axisymmetric and square II nozzles may be attributed to initial velocity profile effects in the co-flow.

Non-circular coaxial jets are flows of considerable complexity which have received very little attention thus far. The results presented here provide a first glimpse into these flows of potentially significant practical interest. Important questions related to the possible existence of axis switching in these nozzles, the role of the initial conditions and the relevant bulk flow parameters remain to be answered through further research.

References

Au H; Ko NWM (1987) Coaxial jets of different mean velocity ratios: Part 2. J Sound Vibr 116(3): 427–443

Bitting JW; Nikitopoulos DE (1997) Visualization and two-color digital PIV measurements in circular and square coaxial nozzles. Final Report, AFOSR GSRP, Wright Laboratory, Wright-Patterson AFB, August

Bitting JW; Nikitopoulos DE; Gogineni SP; Gutmark EJ (1997) Visualization of non-circular, coaxial nozzle flow structure. Bull Am Phys Soc 42: 23–25

Chigier NA; Beer JM (1964) The region near the nozzle in double concentric jets. Trans ASME, J Bas Eng 86: 797–804

Dahm WJA; Frieler CE; Tryggvason G (1992) Vortex structure and dynamics in the near field of a coaxial jet. J Fluid Mech 241: 371–402

duPlessis MP; Wang RL; Kahawita R (1974) Investigation of the near-region of a square jet. Trans ASME, J Fluids Eng 74(6): 246–251

Forstall W; Shapiro HH (1950) Momentum and mass transfer in coaxial gas jets. Trans ASME, J Appl Mech 10: 399–408

Gogineni S; Goss L; Pestian D; Rivir R (1998) Two-color digital PIV employing a single CCD camera. Exp Fluids 25: 320–328

Grinstein FF; Gutmark E; Parr T (1995) Near field dynamics of subsonic free square jets. A computational and experimental study. Phys Fluids 7(6): 1483–1497

Grinstein FF; Kailasanath K (1995) Three-dimensional numerical simulations of unsteady reactive square jets. Combust Flame 100: 2–10

Gutmark E; Ho C (1986) Visualization of a forced elliptic jet. AIAA J 24(4): 684–685

Ko NWM; Au H (1985) Coaxial jets of different mean velocity ratios. J Sound Vibr 100(2): 211–232

Ko NWM; Chan WT (1979) The inner regions of annular jets. J Fluid Mech 93(3): 549–584

Ko NWM; Kwan ASH (1976) The initial region of subsonic coaxial jets. J Fluid Mech 73(2): 305–332

Ko NWM; Lam KM (1984) Further measurements in the initial region of an annular jet. J Sound Vibr 93(3): 333–348

Koshigoe S; Gutmark E; Schadow KC; Tubis A (1988) Wave structures in jets of arbitrary shape. III. Triangular jets. Phys Fluids 31(6): 1410–1419

Kwan ASH; Ko NWM (1977) The initial region of subsonic coaxial jets: Part II. J Fluid Mech 82(2): 273–287

Nikitopoulos DE; Liu JTC (1987) Nonlinear binary-mode interactions in a developing mixing layer. J Fluid Mech 179: 345–370

Quinn WR (1992) Streamwise evolution of a square jet cross section. AIAA J 30(12): 2852–2857

Quinn WR; Militzer J (1988) Experimental and numerical study of a turbulent free square jet. Phys Fluids 31(5): 1017–1025

Schadow KC; Gutmark E; Parr DM; Wilson KJ (1988) Selective control of flow coherence in triangular jets. Exp Fluids 6: 129–135

Schadow KC; Gutmark E; Wilson KJ; Smith RA (1990) Noncircular inlet duct cross-section to reduce combustion instabilities. Combust Sci Technol 73: 537–553

Sforza PM; Steiger MH; Trentacoste N (1966) Studies on three-dimensional viscous jets. AIAA J 4(5): 800–806

Tang DK; Ko NWM (1993) Coherent structure interactions in excited coaxial jet of mean velocity ratio of 0.3. AIAA J 31(8): 1521–1524

Trentacoste N; Sforza P (1967) Further experimental results for three-dimensional free jets. AIAA J 5(5): 885–891

Williams TJ; Ali MR; Anderson JS (1969) Noise and flow characteristics of coaxial jets. J Mech Eng Sci 11: 133–142

Experimental and Numerical Investigation of Vortex-Flame Interactions in Impulsively Initiated Premixed and Non-Premixed Jets

S.P. Gogineni, T.R. Meyer, V.R. Katta
Innovative Scientific Solutions, Inc.
Dayton, OH 45440

J. R. Gord
Air Force Research Laboratory

Objectives

- To evaluate the effects of ignition and subsequent flame propagation in premixed flow field using PIV, LIF, and DNS.
- To gain an insight into the effects of turbulence on premixed flame stability and heat release.
- To analyze the effects of strain rate on flame extinction during vortex-flame interaction.
- To provide input parameters for developing direct numerical simulations (DNS).

Experimental Setup

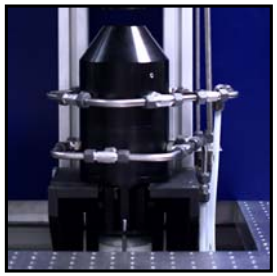

Jet-in-Co-Flow Burner

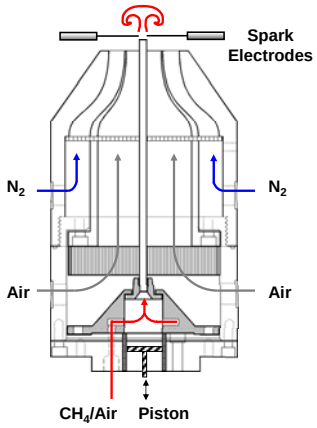

Schematic of the Lasers and Image Acquisition System

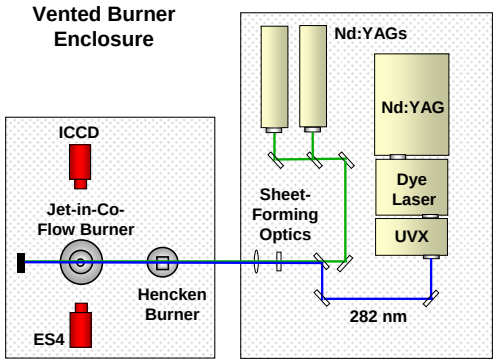

OH Absorption Spectrum
1-0 Band of the A-X System

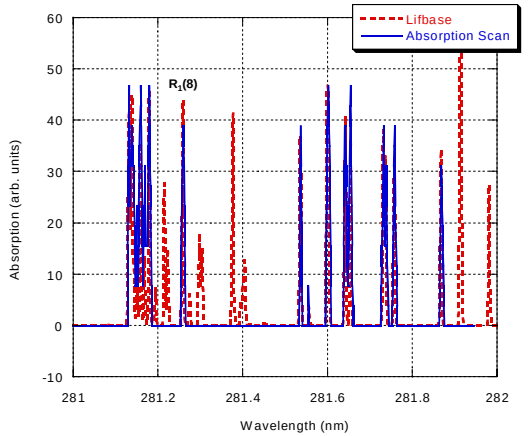

Operating Conditions

Ignition Timing (ms)*	Equivalence Ratio	Piston Stroke (mm)	Vortex Velocity (m/s)
2.5	1.0	3.3	5
4	0.75, 1.0, 1.25, 1.5	3.3	5
4	1.0	1.6	2.5
5	1.0	5	6.5
6	1.0	1.6, 3.3, 5	2.5, 5, 6.5
8	1.0	3.3	5

*** Relative to piston actuation**

Cold-Flow Vortex Propagation

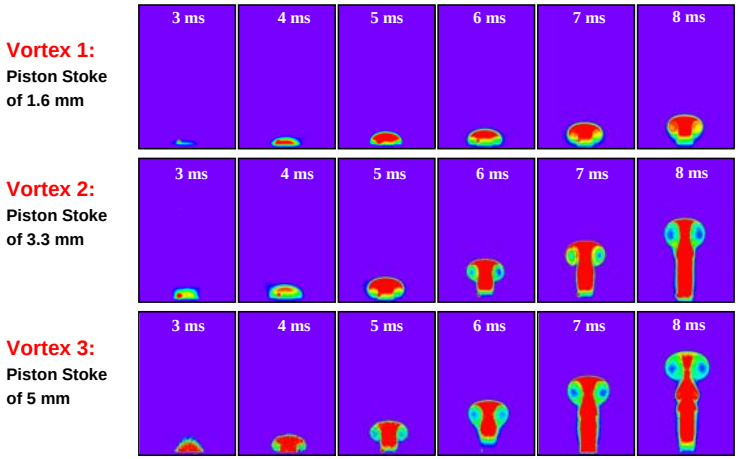

Effect of Vortex Strength

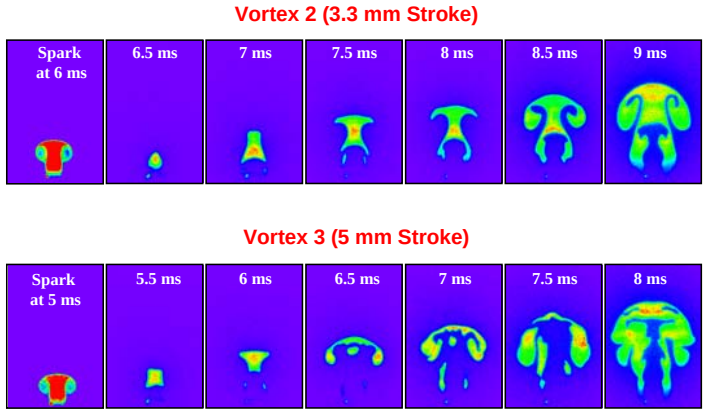

Effect of Equivalence Ratio

Vortex 2, Spark at 4 ms

Phi = 0.75

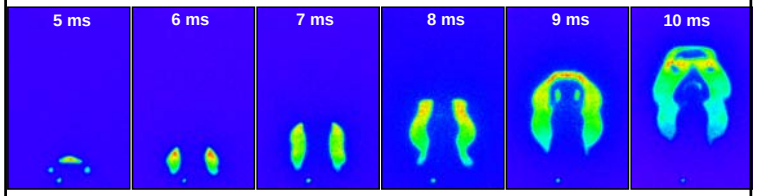

Phi = 1.0

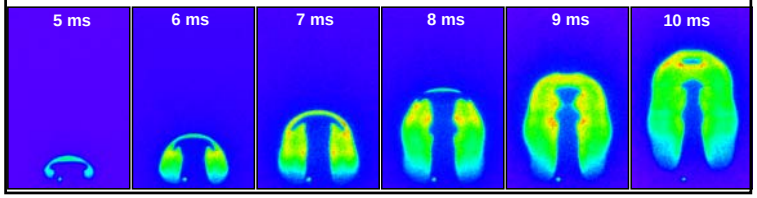

Effect of Spark Timing

Phi = 1, Vortex 2

Spark at 4 ms

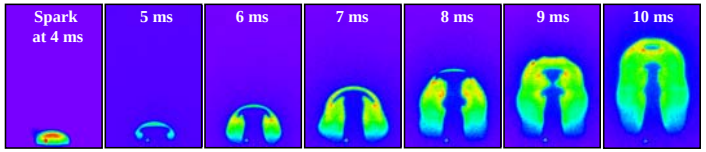

Spark at 6 ms

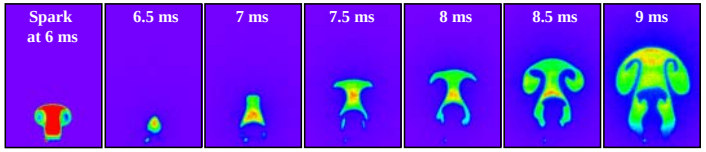

Simultaneous OH and PIV Data

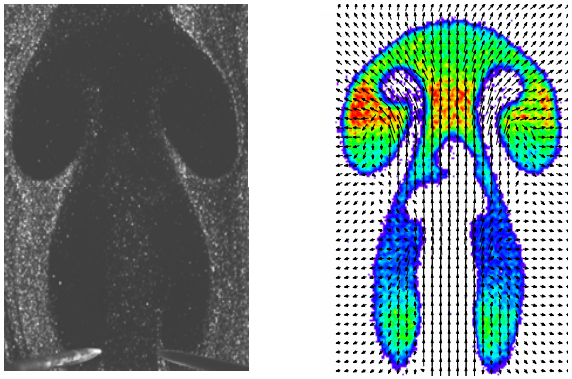

Phi 1.0 Vortex 2 Image taken 8.5 ms after piston actuation

Direct Numerical Simulations

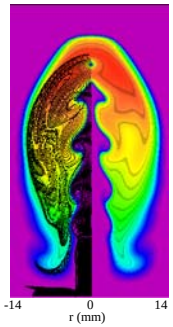

Spark timing 4 msec

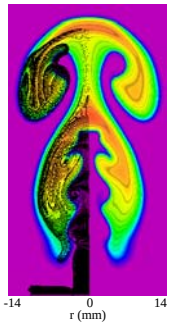

Spark timing 6 msec

Experiment vs. Computation

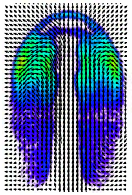

Experiment

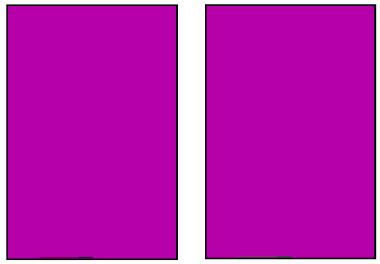

Computation

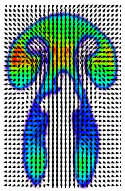

Experiment

Analysis of Flame Exctinction

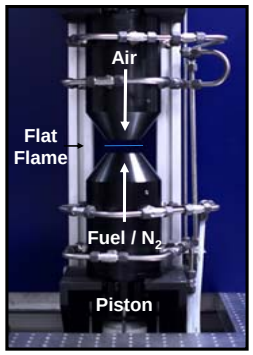

Counterflow Burner

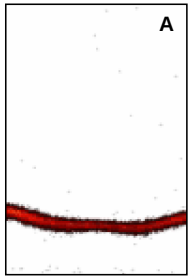

OH PLIF – No Flame Extinction

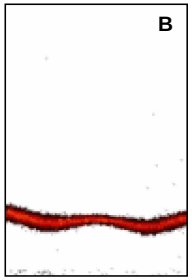

OH PLIF – with Flame Extinction

Simultaneous OH PLIF and PIV

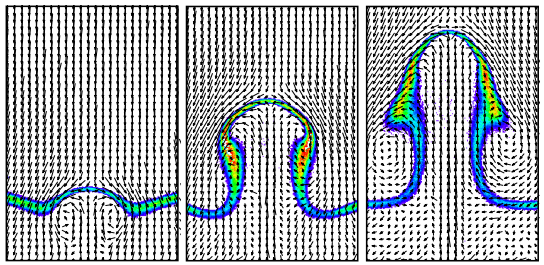

No Flame Extinction Condition
(Images are spaced 9 ms apart)

Simultaneous OH PLIF and PIV

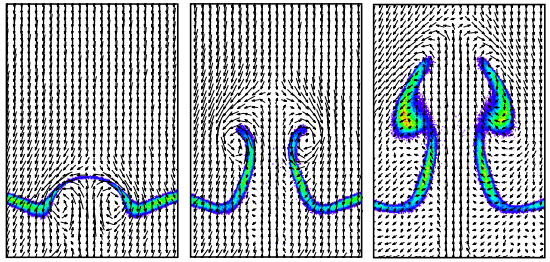

Flame Extinction Condition
(Images are spaced 6 ms apart)

Simultaneous OH PLIF and PIV

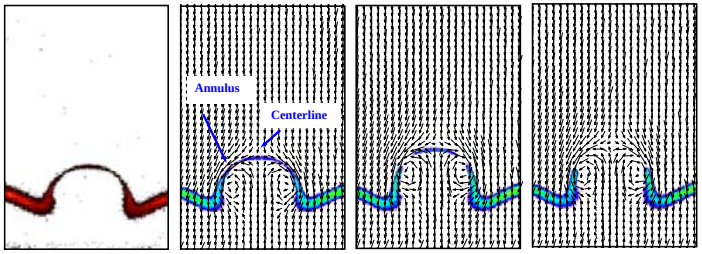

OH PLIF

Flame Extinction Condition
(Images are spaced 0.3 ms apart)

Effect of Strain Rate

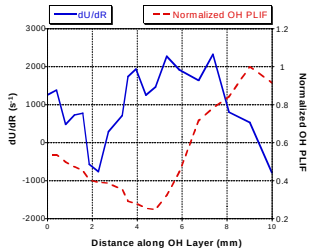

(a)

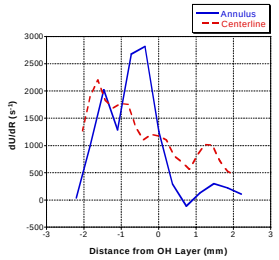

(b)

Conclusions

- Current study explored several important parameters that affect flame propagation in premixed jets
- Flame propagation is highly sensitive to spark timing and takes place in two distinct regions: (A) within the jet column and vortex rollers (B) on the vortex exterior
- Computations show very good overall agreement with experimental results.
- Flame extinction studied using simultaneous OH PLIF and PIV shows higher non-centerline strain causing annular extinction.

AIAA JOURNAL
Vol. 41, No. 2, February 2003

Comparisons of Initially Turbulent, Low-Velocity-Ratio Circular and Square Coaxial Jets

Dimitris E. Nikitopoulos* and Jason W. Bitting†
Louisiana State University, Baton Rouge, Louisiana 70803
and
Sivaram Gogineni‡
Innovative Scientific Solutions, Inc., Dayton, Ohio 45430

A qualitative and quantitative comparison between unforced flows emanating from equivalent geometries of axisymmetric (circular) and square coaxial nozzles is presented. The initial state of the jets is turbulent, as in nozzles relevant to practical applications. Flow visualization and velocity measurements were performed at a coflow-jet Reynolds number of 1.9×10^4 and at an inner-to-outer jet velocity ratio of 0.3. Scaling of mean velocity and turbulence profiles has been examined for the three shear layers formed in the near field of axisymmetric and square coaxial flows. Visualizations and local velocity measurements have indicated modest mixing enhancement when square nozzles are used compared to the axisymmetric ones, and this is largely attributed to differences in initial velocity profiles between these two configurations. Low-coherence, large-scale periodic structures were observed for both nozzle configurations in the midfield of the inner mixing region, which has wake characteristics. The outer mixing region, which is initially highly turbulent, shows no signs of an "indigenous" organized structure. The spectral characteristics of the circular and square nozzle combinations are qualitatively similar. However, the discrete frequency peaks associated with the wake of the inner mixing region are much broader in the case of the square nozzles. More important, the dominant frequency at the end of the midfield within the inner mixing region is lower in the case of the square nozzles compared to that of the circular ones. Spectra from the turbulent shear layers of the middle mixing region in the near field indicate the presence of a short-lived shear layer preferred mode at a much higher frequency than the one associated with the subsequent development of the wake downstream. The existence of axis switching, a phenomenon observed in single nonaxisymmetric nozzles, is not evident from visualizations and measurements in the square coaxial nozzle, presumably due to the initial low coherence of large-scale structures in the shear layers.

Nomenclature

A	=	amplitude
D	=	hydraulic diameter or length scale
f	=	frequency
Re	=	Reynolds number
U	=	mean velocity
u'	=	rms velocity fluctuation
x	=	streamwise coordinate
y	=	cross-stream coordinate
ΔU	=	mean velocity difference across the shear layer at its origin
δ	=	shear-layer thickness $\lvert y_{0.9} - y_{0.1} \rvert$
η	=	dimensionless cross-stream coordinate (shear-layer scaling)
λ	=	inner-to-outer jet average velocity ratio

Subscripts

avg	=	arithmetic average of inner and outer jet flow peak values
cl	=	centerline value
io	=	outer dimension of inner nozzle
max	=	maximum
min	=	minimum
o	=	outer jet quantity
oo	=	outer nozzle dimension
0.1	=	mean velocity is 10% of the shear-layer velocity difference
0.5	=	mean velocity is 50% of the shear-layer velocity difference
0.9	=	mean velocity is 90% of the shear-layer velocity difference

Received 1 May 2001; revision received 25 June 2002; accepted for publication 1 July 2002. Copyright © 2002 by the American Institute of Aeronautics and Astronautics, Inc. All rights reserved. Copies of this paper may be made for personal or internal use, on condition that the copier pay the $10.00 per-copy fee to the Copyright Clearance Center, Inc., 222 Rosewood Drive, Danvers, MA 01923; include the code 0001-1452/03 $10.00 in correspondence with the CCC.

*Voorhies Associate Professor, Center for Turbine Innovation and Energy Research, Mechanical Engineering Department. Member AIAA.
†Graduate Student, Mechanical Engineering Department.
‡Senior Research Engineer. Associate Fellow AIAA.

Introduction

COAXIAL nozzles are an integral part of many engineering systems where mixing of different fluid streams is required. They are used to provide mixing between fuel and oxidizer in combustors of propulsion systems and power-producing gas-turbine systems, as well as waste combustion and incineration systems. Single noncircular nozzles have been shown to have better mixing characteristics than their axisymmetric counterparts. Therefore, combinations of such nozzles into coaxial configurations is promising. The present work aims at qualitatively and quantitatively investigating the near-field flow structure of square coaxial nozzles relative to equivalent axisymmetric coaxial jets under turbulent initial conditions, which are more typical of practical nozzles.

A good deal of work on circular coaxial nozzles has been performed as described in a series of papers. Ko and Kwan[1] provide information about the velocity and turbulence fields of coaxial jets with different inner to annular air velocity ratios λ. Subsequent work by Ko and Au[2] has examined mean flow and turbulence scaling for the same flows. A thorough flow visualization study by Dahm et al.[3] shows the large-scale vortical structures and their interactions for various λ at low Reynolds numbers. Tang and Ko[4] studied forced coaxial jets for a velocity ratio of 0.3 and showed that the initial region of the jet plays an important role in the downstream development of large-scale structures.

Regarding noncircular nozzles, several configurations have been researched to date for a single jet, including rectangular/square, triangular, lobed, and elliptic.

The rectangular and square nozzles produce noncircular vortex rings at the exit, which then deform and, under certain conditions, can lead to a switching of the jet axis. The axis switching is caused primarily by deformation and self-induction in regions of high curvature on the vortex ring produced by the sharp corners of the nozzle and depends on the initial velocity and vorticity characteristics.[5] Early studies by Sforza et al.,[6] Trentacoste and Sforza,[7] and duPlessis et al.[8] investigated square jets, but no insight was given to the underlying fundamental behavior of the square jet vortical interactions. Quinn and Militzer[9] showed that the square jet had faster spreading rates at similar distances from the exit as compared to an equivalent circular jet. A detailed numerical simulation by Grinstein et al.,[10] accompanied by an experimental investigation, illustrated that the axis switching is due to self-induction governed by the Biot–Savart law with hairpin vortices developing along the diagonals of the square jets. Their study also highlighted the effect of initial conditions and concluded that azimuthal uniformity in shear-layer momentum thickness, low small-scale turbulence levels, and a high level of shear-layer large-scale structure at the exit are favorable to the development of axis switching. Off-center velocity peaks (vena contracta effect) have been observed by Quinn[11] for a square slot orifice exit, which also favored the development of axis switching. Zaman's[5] study of rectangular jets, with and without tabs, has also provided valuable insight into the role of initial conditions and streamwise vorticity in promoting or suppressing axis switching through coupling with azimuthal vorticity dynamics.

The triangular jet has also been investigated by Schadow et al.[12] The process of self-induction in the corners of the triangle produced enhanced mixing in that region. The flow results were different for triangular orifice exits or pipe/nozzle, emphasizing the importance of initial conditions. A numerical and experimental study by Koshigoe et al.[13] explained the differences and formulated conditions for which axis switching occurs. Enhancement in the fine-scale mixing and combustion stability in the corner regions of the triangular jet were verified by Schadow et al.[14] Large-scale mixing was accomplished on the flat sides with reduced pressure oscillations as compared to the circular jet.

Elliptic jets have been studied extensively,[15–19] exhibiting axis switching and self-induction characteristics as in triangular and rectangular jets. Indeed, Husain and Hussain[16–18] have identified and described the axis-switching mechanism and its relation to azimuthal vortex dynamics, providing the basis for similar interpretations in other geometries. In terms of mixing enhancement, Gutmark and Ho[19] have documented entrainment rates in 2:1 elliptic jets that are eight times higher than a similar circular jet.

Although single noncircular nozzles have been shown to be promising in terms of improved mixing, coaxial configurations of such nozzles have hardly been studied. Bitting et al.[20] presented flow visualization results for various combinations of noncircular (square, triangular, lobed) and axisymmetric coaxial nozzles for various intermediate Reynolds numbers and low velocity ratios and made preliminary comparisons between circular and square geometries.[21] In this paper, we have studied the flow structure of a square coaxial nozzle at a single coflow Reynolds number and two inner-jet velocity ratios and have compared the results with the corresponding axisymmetric coaxial jet flows.

Experimental Setup and Methods

The test facility used for this study incorporates a modular design that allows easy exchange of inner and outer nozzles with different lip geometries. The test facility uses two independent airflow supplies. Four 25.4-mm (1-in.) lines provide air to the inner nozzle, and eight 6.35-mm ($\frac{1}{4}$-in.) lines provide air to the outer nozzle. On each main supply line, an orifice flow meter is used to determine the airflow rate. Valved, bypass ports allow the use of part of the metered air streams for seeding purposes. The inner jet flow passes through a flow-straightening honeycomb screen before entering the jet contraction with a contraction ratio of approximately 19:1. The outer jet flow reaches the outer jet through an annular passage with a contraction ratio of approximately 8:1. No attempt was made to condition the flow in either nozzle, other than the flow straightener of the inner flow, as would be the case in a practical situation. Furthermore, the flow conditions were selected so that the estimated shear-layer modes at the exit would not resonate with acoustic modes of the facility, which would be tantamount to "passive" forcing of the shear-layer, large-scale structure.

A circular coaxial nozzle with an inner diameter of 15.24 mm (0.6 in.) and an outer diameter of 38.1 mm (1.5 in.) has been used as the baseline nozzle for the square, coaxial nozzle flow study. With the preceding dimensions, the hydraulic (effective) diameter of the inner jet and outer jet is 15.24 and 19.05 mm, respectively. For the square nozzles, the hydraulic diameters are the same as for the circular jet for proper near-field comparisons between the two nozzles. The inner-to-outer-area ratio is preserved at 0.213. Note that matching the hydraulic diameters between the circular and square nozzles was deemed appropriate for the near-field comparisons of the present study. The reasoning behind this is that the flow in the near field is influenced by the conditions at the exit, which are a product of an internal flow. Thus, the hydraulic diameter is more relevant to the near field.[21] The traditional matching of nozzle flow areas is more relevant to the far field.

Visualizations have been carried out using a pulsed laser sheet and seeding with $TiCl_4$, which, on reaction with moisture produces fine submicrometer TiO_2 particles. A summary of seeding strategies that have been used to visualize selectively the shear layers in the near field of the nozzles are presented in Table 1. Instantaneous and time-averaged cuts have been made with a laser sheet from a Nd-YAG laser pulsing at 10 Hz. Visualizations on a horizontal plane (perpendicular to the jet axis) have also been carried out at various distances form the jet exit. These were achieved by a horizontal laser sheet and a mirror positioned above it at an angle of 45 deg with respect to the vertical jet axis. Thus, the top-view image was reflected horizontally into the receiving camera lens. The distance between the mirror and the exit of the jet was adequately large to avoid interference with the flow. Short (10-ns) exposures have been taken with a high-resolution Kodak charge-coupled device (CCD) array (3060 × 2036) camera, to visualize the instantaneous structure of the jets, whereas long exposures (2 s) have been used to provide a 20-realization average of the mixing regions. The resolution of the visualization images ranged from 63 μm/pixel for the side views (streamwise planes) to 33 μm/pixel for the top views (cross-stream planes).

Constant-temperature anemometry (CTA) measurements were carried out using a properly calibrated single-element probe with a spatial resolution of 2.7% of the outer hydraulic diameter (sensing length of 0.508 mm). The sensor was oriented parallel to the direction of traverse and perpendicular to the dominant direction of the airflow. The directions of the traverses used to determine velocity profiles across the jets are shown in Fig. 1. Data were collected using the TSI IFA300 system with a sampling rate of 10,000 Hz,

Table 1 Seeding strategy for visualization of the various mixing regions of the coaxial jets

Strategy no.	Visualization domain/airstream	Inner	Outer	Ambient
1	Inner and outer jet shear regions combined	H_2O (v)	$TiCl_4$	H_2O (v)
2	Outer jet shear regions only	Dry air	$TiCl_4$	H_2O (v)
3	Inner jet shear regions only	$TiCl_4$	H_2O (v)	H_2O (v)
4	Merged outer shear regions	$TiCl_4$	Dry Air	H_2O (v)

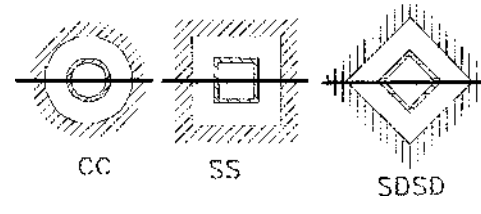

Fig. 1 Laser sheet cuts and hot-wire traverses.

low-pass filter cutoff of 5000 Hz, and sample size of 10,000 points for mean flow and turbulence intensity measurements. The velocity resolution was approximately 0.1 m/s (or 0.8% of the outer flow average velocity) with an accuracy of the same magnitude. Velocity spectra were acquired along the jet centerline and in the shear layers at the location of maximum turbulent rms fluctuation. The sample size was increased to 256,000, and the spectra were calculated for blocks of 10,000 points with 50% overlap and ensemble averaged over approximately 50 blocks.

Results and Discussion

The visualization results and local quantitative measurements to be presented here are from axisymmetric and square coaxial nozzle flows at an outer flow $Re_0 = 1.9 \times 10^4$. This Reynolds number is based on the outer nozzle hydraulic diameter and average velocity. The inner-to-outer jet average velocity ratio λ was 0.3.

Flow Visualizations

An instantaneous planar flow visualization along the center plane of the square coaxial nozzle is shown in Fig. 2. This visualization was achieved through strategy 1 (Table 1) and reveals the fine structure of the shear layers due to the initially highly turbulent and three-dimensional flowfield. Evidence of a somewhat organized large-scale structure, obscured by smaller-scale eddies, can be observed in the shear layers of the near field. Many well-defined, apparently three-dimensional, vortical structures are seen to be injected into the ambient air, which is an indication of the strongly intermittent character of the mixing process. Similar features were observed for the axisymmetric coaxial nozzle, the visualizations of which are not shown here for the sake of brevity.

In Fig. 3, instantaneous planar visualizations perpendicular to the jet axis, taken with the same seeding strategy as in Fig. 2, visually show the variation of the jet shear-layer cross sections in the near field at various distances from the jet exit. The axisymmetric (circular) jet exhibits, on average, an axisymmetric flow pattern (Figs. 3Ca and 3Cb), whereas the square jet shear layers retain the geometrical shape of their origin for several outer hydraulic diameters (Figs. 3Sa and 3Sb). However, at the farthest location from the jet exit (Fig. 3Sc), the square jet mixing regions evidently tend to loose the memory of the original shape. Intense intermittency, manifested by injections of three-dimensional vortical structures of various scales, is evident at the edges of both the inner and outer shear layers, as also seen in the axial plane visualization of the square jet in Fig. 2. The injected structures often penetrate from one mixing layer to the other, across the outer jet unmixed region, as evidenced, for example, in Figs. 3Cb, 3Sa, and 3Sb. A region of interaction between the inner and outer shear layers of the coflow is observed in the middle of the sides of the outer shear layer. This indicates strong interaction between the inner and outer shear layers in the square jet, which was not observed in the axisymmetric jet until further downstream, and this is indicative of faster merging of the outer and inner mixing regions in the case of the square nozzle geometry. The horizontal planar visualizations of Fig. 3 also show that the large-scale symmetries of the flow expected on the basis of the nozzle geometry are still present in the near field, whereas no strong evidence of azimuthal organized large-scale structures can be observed. In addition, no strong visual evidence of axis switching is present in the visualizations of the square jets in the near field.

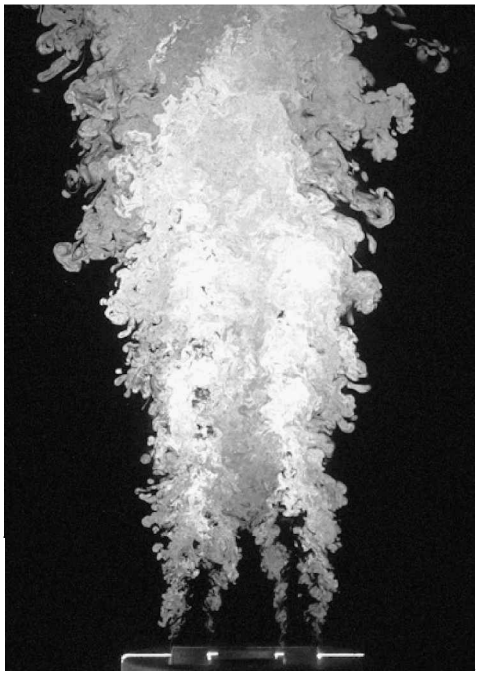

Fig. 2 Instantaneous visualization of a coaxial square jet ($Re_0 = 1.9 \times 10^4$ and $\lambda = 0.3$).

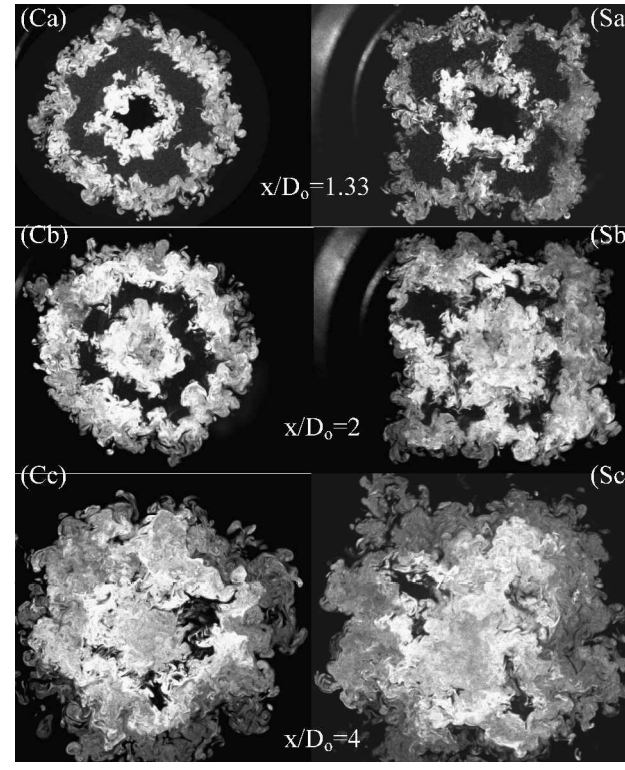

Fig. 3 Instantaneous horizontal laser sheet visualizations of equivalent circular (Ca, Cb, and Cc) and square (Sa, Sb, and Sc) coaxial jets ($Re_0 = 1.9 \times 10^4$ and $\lambda = 0.3$).

Figure 4 presents instantaneous visualizations of the outer shear layer (Figs. 4a, 4c, and 4e) and inner jet mixing region (Figs. 4b, 4d, and 4f) separately for the square (Figs. 4a and 4b on a centerplane perpendicular to the square sides and Figs. 4c and 4d on a diagonal plane) and axisymmetric (Figs. 4e and 4f on a diametral center plane) coaxial nozzles. The outer shear layer was visualized using seeding strategy 2 (Table 1) and the inner shear layer and jet was visualized using seeding strategy 3. Two planar visualization cuts are shown for the square nozzle, one perpendicular to the square side through the centerline (Figs. 4a and 4b) and one on the diagonal plane (Figs. 4c and 4d). Only half of each jet field is shown. Figures 4b, 4d, and 4f indicate that the inner jet flow is rapidly mixed with the coflow air, as seen by the brighter (heavily seeded) areas at the end of the jet unmixed core. As expected, because of the higher coflow velocity, the "outward" transport is limited as shown by the tracer pattern. The mixing boundary between the coflow and inner jet flow exhibits fine-scale, "wispy" structures that seem to be more stretched. This is also evident from the outer shear-layer visualizations of Figs. 4a, 4c, and 4e. The instantaneous realizations of the outer shear layer bear evidence of large-scale structures obscured by smaller scales, as in Fig. 2. A streamwise instability of the inner jet is also outlined by the streamwise wavering of the inner jet column. The outer shear layer appears thickest across the side of the square nozzle (Fig. 4a) and is thinner along the diagonal (Fig. 4c), as it is for the axisymmetric

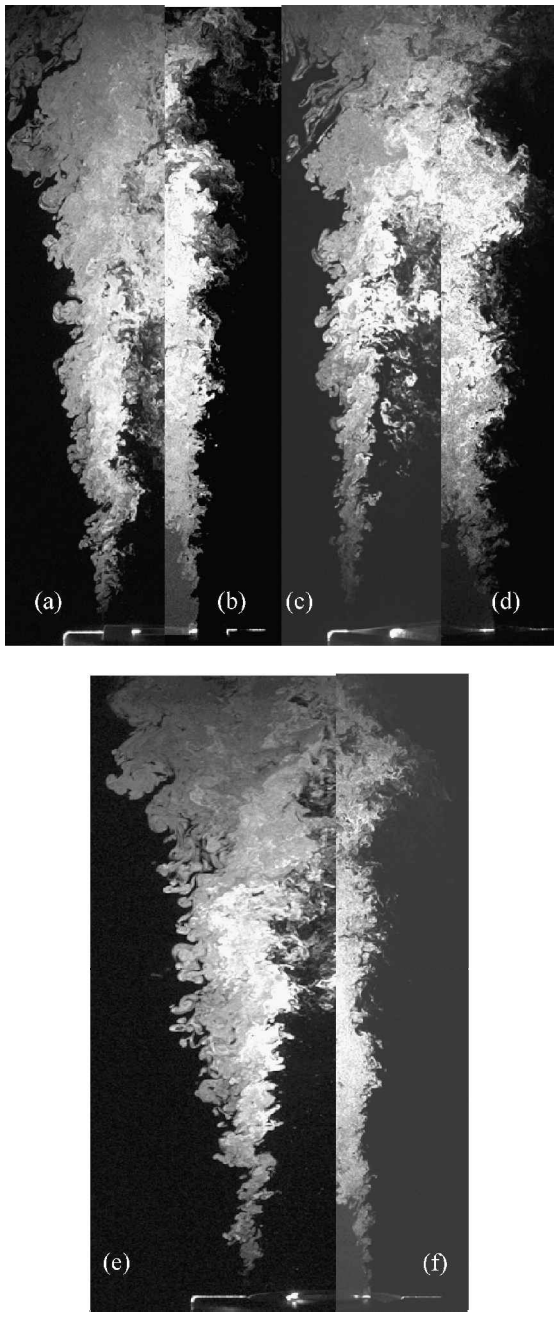

Fig. 4 Instantaneous coaxial jet flow visualizations ($Re_0 = 1.9 \times 10^4$ and $\lambda = 0.3$): a) square side, outer mixing region; b) square side, inner mixing region; c) square diagonal, outer mixing region; d) square diagonal, inner mixing region; e) axisymmetric, outer mixing region; and f) axisymmetric, inner mixing region.

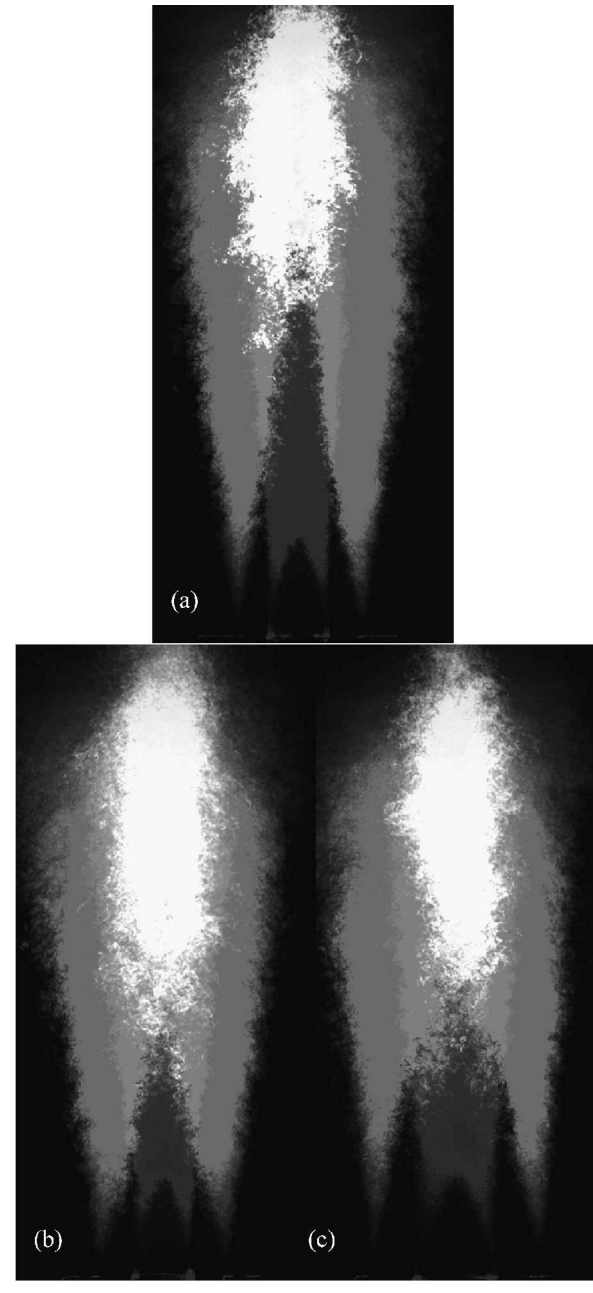

Fig. 5 Averaged visualizations of the mixing regions of a) circular coaxial nozzle flow (diametric plane-section CC in Fig. 1), b) square coaxial nozzle (center plane-section SS in Fig. 1), and c) square coaxial nozzle (diagonal plane-section SDSD in Fig. 1). $Re_0 = 1.9 \times 10^4$ and $\lambda = 0.3$.

nozzle (Fig. 4e). The intermittent presence of the tracer in the central region of the jet in Figs. 4a, 4c, and 4e, indicates that transport from the outer shear layers has started. It is evident from Figs. 4a, 4c, and 4e that such transport is somewhat delayed in the axisymmetric case compared to the square. The outer shear layer inward growth appears to be more rapid for the square nozzle in the near field.

Time-averaged visualizations of the mixing regions for the square and the corresponding circular coaxial nozzle flows are shown in Fig. 5. Each image is a gray-scale superposition of three separate time-averaged visualizations. The outer mixing region appears as gray. The inner mixing region appears as a darker shade of gray. The fully mixed region, visualized using seeding strategy 4 (Table 1) appears as white. In this last case, the reaction between $TiCl_4$ and moisture can take place to produce the visible titanium oxide seed particles only when moist ambient air penetrates the outer mixing region into the core of the jet. The overlap between the inner and outer mixing regions appears as light gray. The unmixed cores (inner and outer) and the ambient region are black.

It appears from Fig. 5 that the fully mixed region begins at an earlier location for the square nozzles compared to the circular ones. The outer unmixed cores disappear sooner for the square nozzles in the region between the parallel square sides (Fig. 5b) compared to the diagonal plane (Fig. 5c) and the circular nozzles (Fig. 5a). This indicates improved, yet localized, mixing with the square nozzles. The velocity measurements presented in the next section indicate that this improved mixing stems from higher outer-flow initial turbulence levels in the region between the parallel square-nozzle sides compared to those of the circular one.

Velocity and Turbulence Profiles

Axial mean velocity and velocity fluctuation profiles have been measured across the jets at various downstream locations from the jet origin covering the near field of the coaxial jets. Samples of these profiles are shown in Fig. 6, superimposed on time-averaged

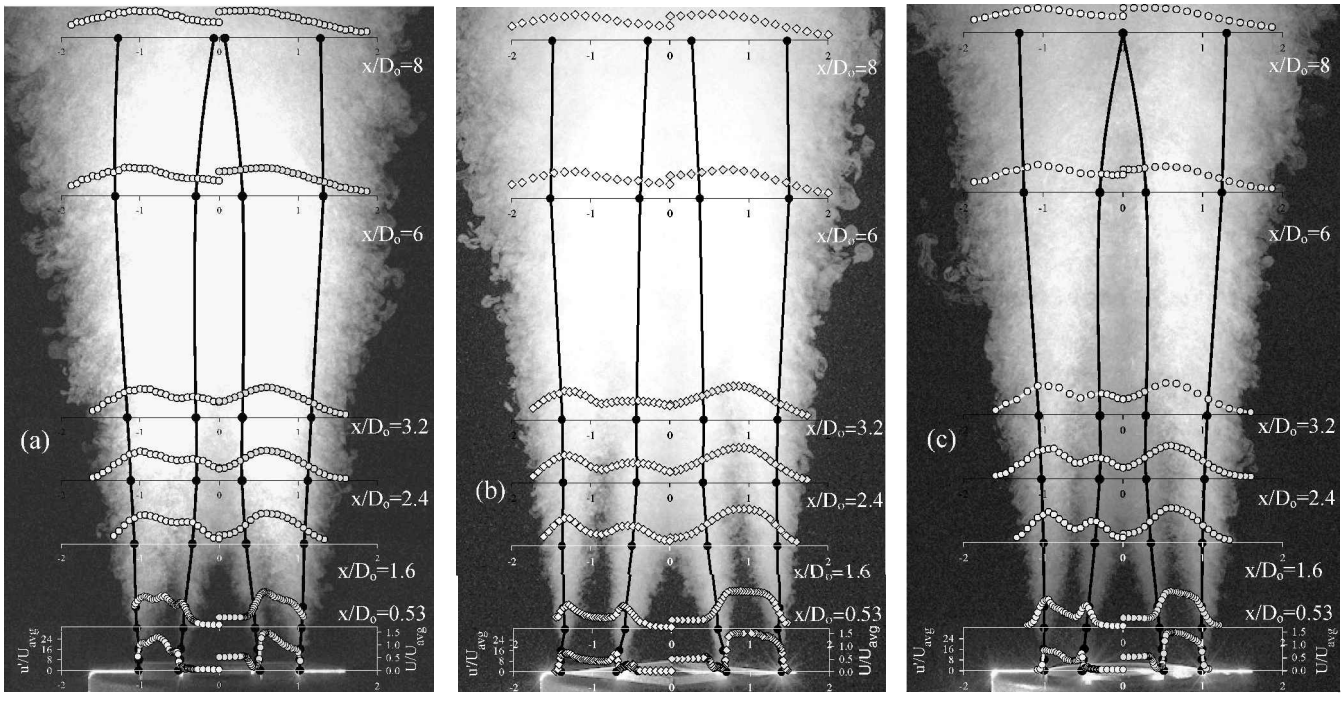

Fig. 6 Visualization and measurement of the flow evolution in coaxial nozzles at $Re_0 = 1.9 \times 10^4$ and $\lambda = 0.3$: a) square SS plane, b) square SDSD plane, and c) axisymmetric CC plane: ○, streamwise mean velocity; ⊖, streamwise velocity fluctuation; –●–, outer shear layer ($U_{max} - U_{min}$)/2 width; and –●- -, middle shear layer ($U_{max} - U_{min}$)/2 width.

visualizationsof the flow. Two sets of profiles are given for the square nozzle case; one parallel to the square jet sides along the plane of symmetry (SS in Fig. 1) and one along the diagonal (SDSD in Fig. 1), as is customary in previous single square jet investigations.[10] The velocities are scaled with the arithmetic average of the maximum velocities of the inner and coflow streams at the exit of the coaxial jets. The difference between these average velocity scales between the axisymmetric and square cases is less than 3%, and so this scaling does not produce a misleading picture. All lengths are scaled with the outer jet hydraulic diameter D_o.

The streamwise development of the shear layers existing in the near field of the axisymmetric and square coaxial jets examined appears quantitatively in Fig. 6 and was shown qualitatively in Fig. 5. At the onset of the jets, three shear layers are identified: the inner shear layer of the inner jet, a middle shear layer on the inside of the coflow jet, and the outer shear layer of the coflow jet. The middle and inner shear layers form the wake of the inner nozzle lip. The development of the shear layers is tracked by recording the "radial" location ($y_{0.5}/D_o$) of the point, which has a velocity equal to 50% of the maximum velocity difference across each shear region.

A defining factor in the downstream development of a jet is the initial condition at the exit. The shape and details of the initial mean velocity and the turbulence intensity profiles are of critical importance in interpreting the observed differences in the development of the axisymmetric and square coaxial nozzles. Note from Fig. 6 that the initial mean profiles ($x/D_o = 0$) of the axisymmetric and square (SS scan) nozzles are almost identical in the inner nozzle region and the wake created after the inner nozzle lip. The core of the inner jet is uniform and the fluctuation level low (fraction of a percent), with a small peak inside the inner shear layer near the inner jet wall. However, a considerable difference exists between the mean profiles in the core of the coflow region. The axisymmetric coflow jet core is considerably more uniform than its square counterpart, which has the shape of a simple shear flow, more so than the one from the circular jet. In both cases, the maximum velocity occurs closer to the inner wall. The difference between the axial fluctuation profiles in this region is more substantial. The maximum fluctuation level is observed near the middle of the coflow core for the square nozzle case with secondary peaks inside the two bounding shear layers, the middle shear layer near the inner wall of the outer jet, and the outer shear layer of the outer jet. No such peak is present in the core of the axisymmetric coflow, and the highest fluctuation levels are observed inside the bounding shear layers. Contrary to the square-jet side scan (SS), the shapes of the initial mean and fluctuation profiles along the square-jet diagonal scan (SDSD) are almost exactly similar to those of the axisymmetric jet, and the fluctuation levels are of the same magnitude. In the case of the square nozzle, the side-to-diagonal ratio of the outer shear-layer momentum thickness was approximately three. Thus, there is a significant azimuthal nonuniformity of the outer shear-layer thickness. Such a condition has been found to be detrimental to the development of axis switching[10] and may be a contributing reason to the absence of axis switching in our experiments.

On the basis of the measured profiles and with the aid of the time-averaged visualization, the coaxial jets can be divided into distinct regions, in a manner similar to that carried out by Ko and Au.[2] The first region is the one immediately downstream of the jet exit (approximately $0 < x/D_o < 0.5$), where the inner jet core decelerates. At the end of this region, the wake of the inner jet has completely disappeared as the inner and middle mixing layers merge, as evidenced in Fig. 6. In the second region (approximately $0.5 < x/D_o < 1.6$), the potential core of the inner jet persists at a fixed centerline velocity. At the end of this second region this potential core disappears, and the middle shear regions merge. This is evident in Fig. 6 from the time-averaged visualization and the velocity profiles at $x/D_o = 1.6$. The potential core of the inner jet disappears somewhat faster in the case of the square nozzle. The relative shapes of the coflow jet core profiles are preserved in these two regions, whereas the peak mean velocity remains more or less fixed. By the end of the second region, the original middle peak in fluctuation intensity has disappeared, and the highest fluctuation intensity is observed inside the outer coflow shear layer thereafter. In the same neighborhood, the averaged visualization (Fig. 6) indicates that outer and middle shear layers merge. This occurs earlier for the square nozzle across its sides (SS scans in Fig. 6a). The fluctuation level in the core of the square-jet coflow is initially considerably higher (by more than a factor of two) than that observed in the same region of the axisymmetric jet. The significant differences observed in the initial region profiles between the axisymmetric and square- (SS scan) jet coflows explain the higher mixing and inward spread of the outer

coflow shear layer qualitatively documented by the visualizations of Figs. 3 and 4. Such significantly enhanced growth was not observed along the diagonal of the square jet where the initial profile of the coflow mean velocity is more uniform, fluctuation level lower, and the profile shapes similar to the axisymmetric ones. The turbulence intensity along the centerline increases steadily within both initial regions described earlier, much like in a single jet.

The process of gradual merging of the opposite middle shear layers takes place within the third region of the coaxial jet (approximately $1.6 < x/D_o < 8$), as seen in Fig. 6. The centerline velocity minimum increases gradually until it becomes an absolute maximum at the end of the region. As the middle shear layers weaken, the corresponding maximum in turbulence intensity is eliminated until only one peak remains at the end of this region, corresponding to the outer shear layer. The centerline turbulence intensity reaches a peak in the beginning of this third region and gradually decays to a plateau at the end of the region (near $x/D_o = 8$, as seen in Fig. 6). Note from Fig. 6 that, after the middle shear-layer growth has completely overwhelmed the core of the inner jet (near $x/D_o = 2.4$), the axisymmetric and square- (SS scan) jet mean and fluctuation profiles become very nearly identical in magnitude and shape. The fourth region beyond $x/D_o = 8$ displays the characteristics of a "single jet" with a single centerline maximum of the mean velocity and a single off-center peak in turbulence intensity associated with the outer shear layer (see Fig. 6). In this region, the centerline turbulence intensity remains approximately constant as the centerline velocity begins to decay. Note that, on superposition, the square-jet diagonal profiles (SDSD scan) collapse onto those obtained from the SS scan and the axisymmetric nozzle case in the beginning of this fourth region. This indicates that the memory of the geometrical origin of the jet is being lost, or it could be construed as weak evidence of an "axis-switching" phenomenon in progress.

Figure 6 also indicates that the middle shear-layer development is nearly identical between the axisymmetric and square (SS scan) jets. This is in agreement with the mean and fluctuation profiles being nearly identical between the two jets within the middle shear layer. The middle shear layer on the diagonal of the square jet exhibits a much faster inward growth than that in the SS direction. The inward growth of the middle shear layers is slowed down considerably past the end of the second region, where the inner jet is completely overwhelmed and the mean shear is diminished. These discussed trends are quantified in Table 2, where the growth rates of the half-width ($dy_{0.5}/dx$) and the thickness ($d\delta/dx$) of the shear layers are listed. The middle shear layer for the axisymmetric nozzle and the SS direction of the square nozzle ceases to exist at around $x/D_o = 8$. However, it persists past that point on the diagonal, as is also insinuated by Fig. 3Sc. The growth of the outer shear layer is distinctly different between the axisymmetric and square nozzle in the SS direction. The initial location of the half-velocity point is also different as a consequence of the difference in the initial profiles. As observed qualitatively in the visualizations in the background of the profiles of Fig. 6 and quantitatively in Table 2, the near-field growth of the outer shear layer for the square nozzle in the SS direction is somewhat faster than that in the axisymmetric case. This can again be explained by virtue of the difference in the corresponding initial profiles. The growth of the outer shear layer on the diagonal is quite different. It is seen in Fig. 6b and Table 2 that, after a short period of no growth, a local contraction (negative growth) of the outer shear layer is documented, followed by a second region of growth. That the outer shear-layer half-width on the side (SS) increases, whereas it diminishes on the diagonal (SDSD), is a possible indication of a weak tendency toward axis switching near the exit of the nozzle. However, in the absence of strong visualization and quantitative evidence (crossover of the half-widths), one cannot conclude that this phenomenon actually takes place. This is not surprising given that it has been shown in single noncircular jets that axis switching is very sensitive to the initial conditions and the degree of large-scale structure coherence in the near field, which is very low in our case.

Scaled velocity and turbulence intensity profiles from the three shear regions of the coaxial flow are presented in Fig. 7. Scaling typically used in shear layers has been employed, following the example of Ko and Au.[2] The trends of their scaled data from axisymmetric

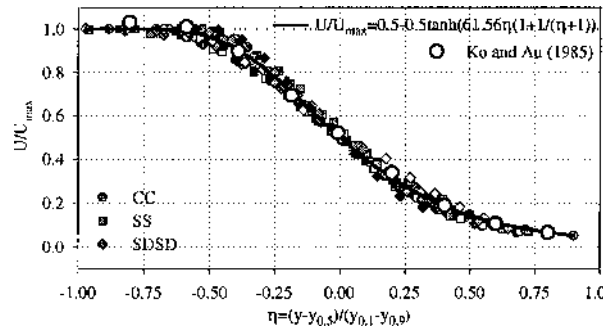

a) Outer shear layer mean velocity (x/D_o = 1.6, 2.4, 3.2, 6, 8)

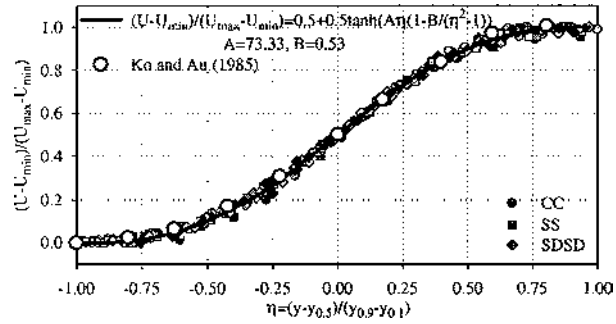

b) Middle shear layer mean velocity (x/D_o = 0, 0.13, 0.27, 0.53, 0.8, 1.6, 2.4, 3.2)

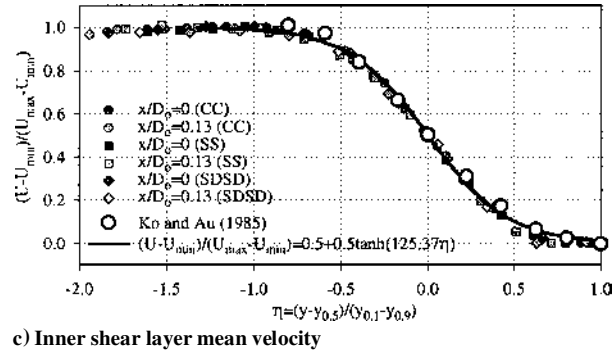

c) Inner shear layer mean velocity

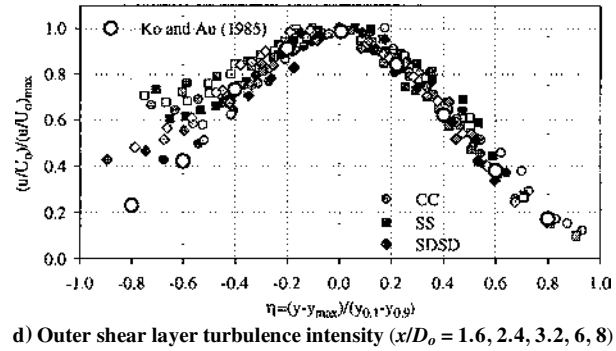

d) Outer shear layer turbulence intensity (x/D_o = 1.6, 2.4, 3.2, 6, 8)

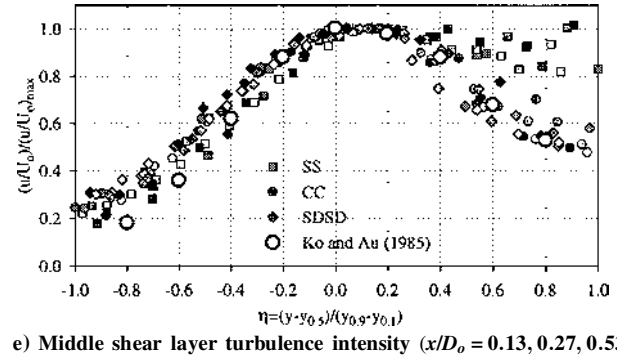

e) Middle shear layer turbulence intensity (x/D_o = 0.13, 0.27, 0.53, 0.8, 1.6)

Fig. 7 Scaled velocity and turbulence intensity profiles for square and circular coaxial nozzles: $Re_0 = 1.9 \times 10^4$ and $\lambda = 0.3$.

Table 2 Shear-layer growth rates

	Middle shear layer						Outer shear layer					
	$dy_{0.5}/dx(\times 10^3)$			$d\delta/dx(\times 10^2)$			$dy_{0.5}/dx(\times 10^3)$			$d\delta/dx(\times 10^2)$		
x/D_o	CC	SS	SDSD	CC	SS	SD	CC	SS	SD	CC	SS	SDSD
0.27	105	85	225	19	19	35	5	38	−98	3	35	2
0.53	105	100	155	22	20	33	0	56	−48	25	38	14
1.6	88	92	92	10	11	16	17	40	−12	18	18	19
2.4	37	31	34	4	5	5	33	48	8	16	12	17

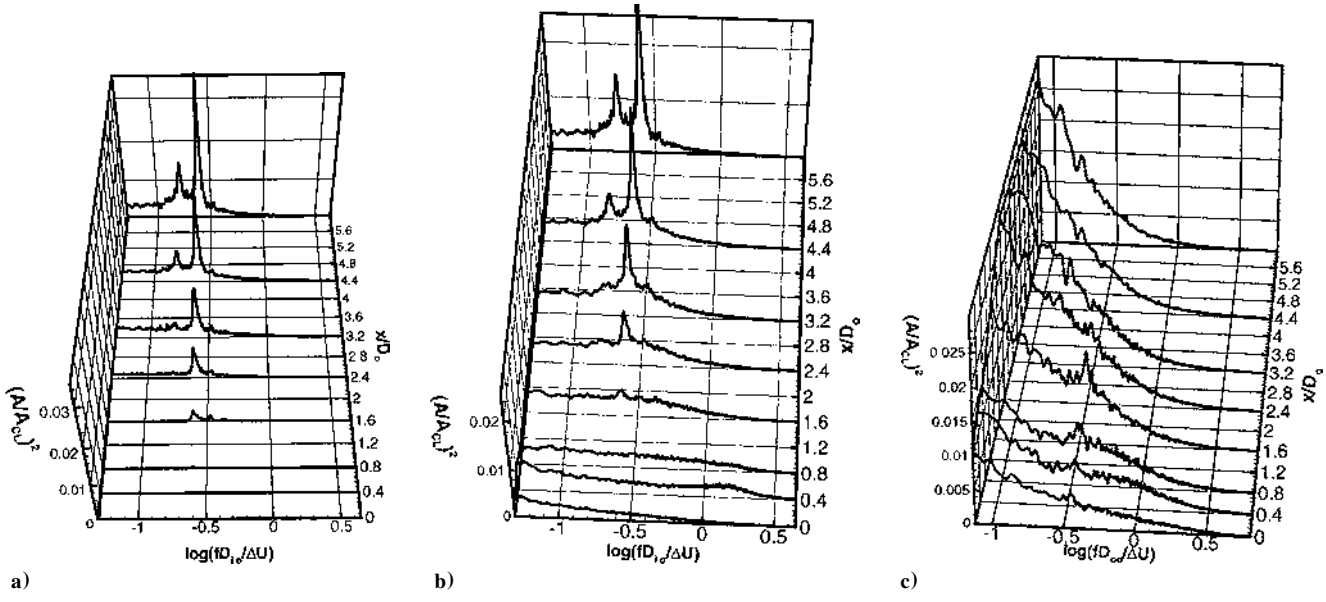

Fig. 8 Velocity spectra from a circular coaxial nozzle flow at $Re_0 = 1.9 \times 10^4$ and $\lambda = 0.3$: a) centerline, b) middle mixing region, and c) outer mixing region.

coaxial nozzles at various velocity ratios less than unity have been used for comparisons and to put the present data into perspective. Best fits of the scaled mean velocity profiles with typical hyperbolic tangent profiles are also included in Figs. 7a–7c. It is evident from Fig. 7 that the scaled mean profiles from both the axisymmetric and square (SS and SDSD scans) nozzle flows collapse on a single trend to a very satisfactory extent for all shear layers. This is more so for the middle and inner shear layers. The outer shear layer displays a higher degree of scatter. This is so primarily because the outer shear layer is less cleanly defined at the onset of the coflow jet flow as discussed earlier. The agreement with Ko and Au[2] is also very good. The scaling of the turbulence intensity is somewhat less clean. In the case of the outer layer, the scaling is good, whereas some deviations are observed, primarily for the SS scans of the square nozzles. It is speculated that this is the case for the same reason that causes the higher scatter in the mean scaled profiles. The agreement with Ko and Au[2] is reasonable considering that their turbulence profiles also displayed some scatter and that fewer downstream locations were included in their scaling. The turbulence intensity scaling is also good for the middle shear layer. In fact, it is very good to the left of the turbulence peak, whereas it breaks down for the SS scan of the square nozzle to the right of the peak for the same reason discussed earlier. The comparison to Ko and Au[2] is quite good considering the difference in coflow initial conditions between our study and theirs.

Velocity Spectra

Scaled velocity spectra obtained along the centerlines, as well as the inner and outer mixing regions, of both circular and square nozzles (SS section) are shown in Figs. 8 and 9, respectively. The spectra for each axial location from all mixing regions were taken at a transverse location corresponding to the point of maximum velocity fluctuation in the neighborhood of the corresponding shear-layer midpoint. The amplitude scaling is such that all spectral amplitudes are referred to the initial centerline point for each nozzle geometry. Thus, relative comparisons of spectral magnitude characteristics are possible between the two geometries examined. The frequencies are scaled to reflect the Strouhal number based on a relevant geometrical length scale and the velocity difference between the maximum and minimum across the corresponding shear region. Note that the centerline spectra at the exit of the jets have several peaks at frequencies that match the acoustic characteristics of the nozzle chamber. These peaks are not visible in Figs. 8a and 9a due to the nature of the scaling. In the immediate near field of the nozzles at $x/D_o = 0.4$ within the middle mixing region, a broad peak is observed in both the circular (Fig. 8b) and square (Fig. 9b) nozzle flows. At this downstream location, the inner core of the velocity profile is still flat, and the middle shear layer has its own identity, unlike further downstream where a wakelike profile develops as the inner uniform core disappears (see Fig. 6). Consequently, the observed local peak in the spectrum should be associated with the shear-layer preferred mode. Indeed, the observed frequency peaks at 1024 Hz for the circular nozzle and 1150 Hz for the square one correspond to the preferred modes of the corresponding shear layers. This is revealed by examining the associated Strouhal numbers. These were calculated using classical shear-layer scaling, based on the initial momentum thickness and the velocity jump magnitude, and they are in reasonably good agreement with linear stability estimates of the dominant shear-layer mode Strouhal numbers calculated by a linear stability code previously used by Nikitopoulos and Liu[22,23] and Nikitopoulos and Seo.[24] Downstream of the exit, prominent frequency peaks appear in the centerline (Figs. 8a and 9a) and middle mixing region (Figs. 8b and 9b) spectral records of both the circular and square nozzle flows. The individual peaks correspond to initial peaks at the exit and are both within a range in the neighborhood of the most amplified frequency for the wakelike profile that develops in the midfield of the inner mixing region based on linear stability. The frequencies with the peak amplitudes are virtually identical for the circular (111- and 166-Hz) and square (115- and 169-Hz)

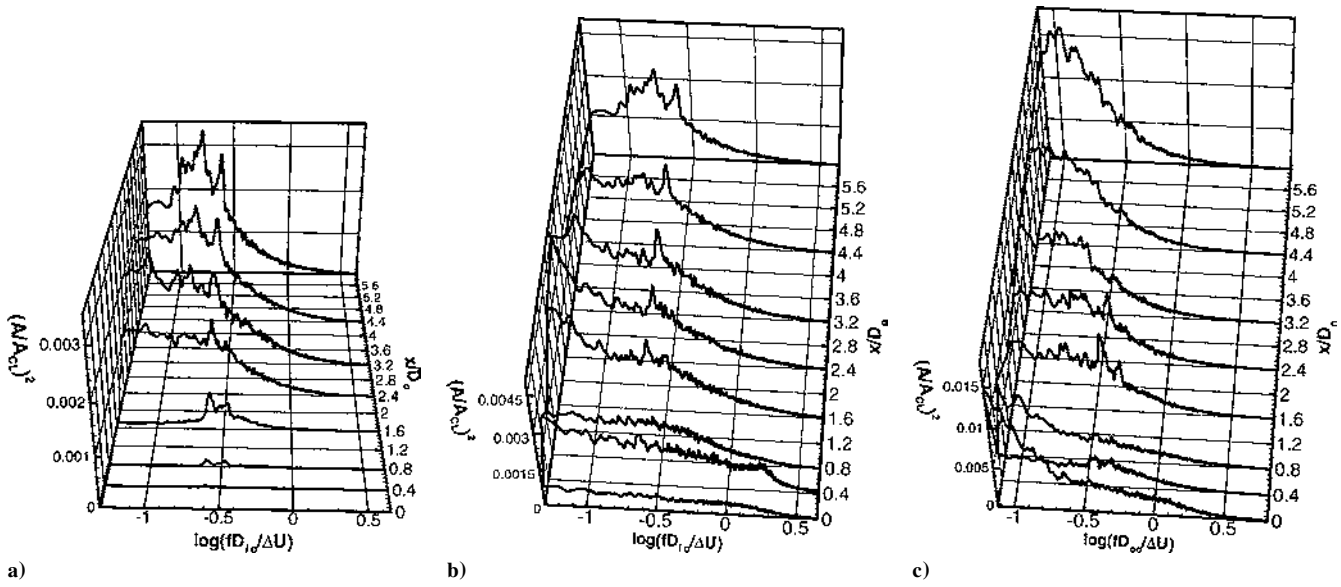

Fig. 9 Velocity spectra from a square coaxial nozzle flow at $Re_0 = 1.9 \times 10^4$ and $\lambda = 0.3$: a) centerline, b) middle mixing region (SS), and c) outer mixing region (SS).

configurations. They are amplified throughout the evolution of the inner region in the near and midfield, as are the less prominent frequencies in that neighborhood of the spectrum. This is not unusual because the frequency-amplification rate curve, as predicted by linear stability, is relatively flat in the neighborhood of the most amplified frequency, allowing amplification of a band of frequencies around the preferred mode. The main differences in the spectra of the inner region midfield between the circular and square nozzle flows are in the breadth and magnitude of the peak frequencies as they evolve downstream. The spectral peaks are sharper and stronger in the case of the circular nozzles compared to the broader and weaker ones of the square nozzles. In both geometries, the higher of the two observed discrete frequencies becomes dominant in the near field of the inner region, whereas the lower one, which is approximately $\frac{2}{3}$ of the higher, emerges. In the midfield of the inner region, the higher frequency remains dominant in the case of the circular geometry, whereas it assumes a secondary role in the case of the square geometry. In the latter case, the lower discrete frequency becomes dominant in the midfield, although its peak is much broader than its counterpart of the circular nozzle.

The shear layer of the outer mixing region is initially highly turbulent at the exit, more so than the one in the middle mixing region. Therefore, the initial spectra at the exit are broadband and were found to display a $-\frac{5}{3}$ inertial range when plotted on a log–log scale. The discrete peaks observed in the near field of the outer shear layers of both circular (Fig. 8c) and square (Fig. 9c) configurations are at 166 Hz. By the application of shear-layer scaling, it was determined that this frequency is too low to be related to the outer shear-layer preferred mode. It is apparent that its appearance is a reflection of the development of the wake mode of the middle mixing region in the beginning of the coaxial jet midfield. This notion is reinforced by this discrete frequency peak occuring in the neighborhood where the outer mixing layer meets the inner mixing region at the end of the coflow unmixed core, as observed in Fig. 4. As the already turbulent outer shear layer grows and develops further downstream, all spectral peaks disappear, and the $-\frac{5}{3}$ inertial range is fully reestablished. Note that no local peak is observed at a frequency corresponding to the preferred mode of the outer shear layer. This is justified by this shear layer being initially highly turbulent and the flow being unforced, other than the acoustic modes of the nozzle interior, which are weak compared to the broadband turbulent spectrum strength in the outer shear layer and not tuned to the outer shear-layer mode.

Similar trends to those described for the SS section of the square nozzle are observed when examining the spectral evolution in the middle and outer mixing regions of the SDSD (diagonal) section. The spectral evolution on the diagonal plane is shown in Fig. 10. The

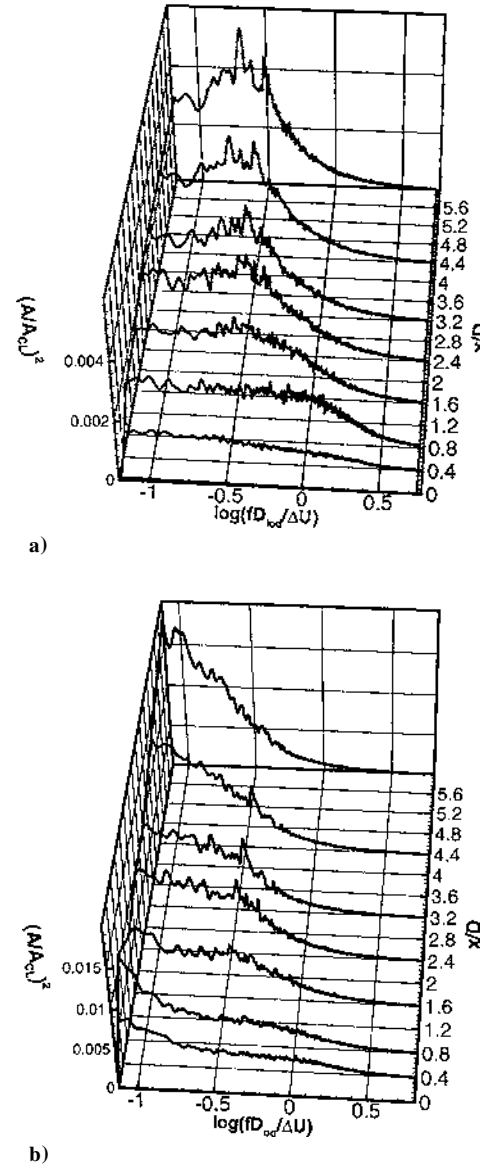

Fig. 10 Velocity spectra from a square coaxial nozzle flow at $Re_0 = 1.9 \times 10^4$ and $\lambda = 0.3$: a) middle mixing region (SDSD) and b) outer mixing region (SDSD).

middle mixing region of Fig. 10a displays two broad, yet discrete, peaks (115 and 169 Hz) in the same fashion as in the center plane according to Fig. 9b. The initial emergence of the higher frequency in the beginning of the jet midfield and the shift toward the lower frequency further downstream are consistent with the centerline and center plane behaviors. Unlike the case of the square nozzle center plane, a distinct preferred mode associated with the middle shear layer is not observed along the diagonal. Instead, a rapid "filling" of the spectrum appears in the range of frequencies commensurate with the expected preferred mode based on a Strouhal number calculated from free mixing layer scaling. The absence of a discrete preferred mode can be attributed to the more vigorous production of smaller scales due to the corner flows on the diagonal. The outer shear-layer spectra shown in Fig. 10b also reveal the same features observed before on the center plane. The initial shear layer is highly turbulent and the frequency peak, which appears in the midfield at a distance from the exit corresponding to the merging of the outer and middle mixing regions, is a reflection of the middle mixing region wake mode. No local spectral peak associated with the shear layer is observed on this plane either. A $-\frac{5}{3}$ inertial range is observed from the onset of the outer shear layer at the outer nozzle exit and is maintained throughout its evolution.

Conclusions

A qualitative and quantitative investigation of unforced, initially turbulent flows emanating from equivalent geometries of axisymmetric (circular) and square coaxial nozzles has been carried out. Flow visualization and velocity measurements were performed at a coflow jet Reynolds number of 1.9×10^4 and at an inner-to-outer jet velocity ratio of 0.3. Scaling of mean velocity and turbulence profiles for the three shear layers formed in the near field of axisymmetric and square coaxial flows was found to be consistent between the two geometries and with previously reported trends for axisymmetric coaxial jets.

Large-scale periodic structures were identified for both nozzle configurations in the midfield of the inner mixing region, which has wake characteristics. The frequency of the observed spectral peaks in this region scaled using wake scales correspond to Strouhal number values consistent with those expected for a wake on the basis of linear stability. The outer mixing region, which is highly turbulent, displays a $-\frac{5}{3}$ inertial range from its onset at the nozzle exit and shows no signs of an indigenous coherent organized structure. The spectra obtained in the square nozzle mixing regions both on the center plane and the diagonal planes are mutually consistent, indicating the same broad frequency peaks. The spectra from the turbulent shear layers of the middle mixing region near field indicate the presence of a short-lived shear-layer preferred mode at a much higher frequency than the one associated with the subsequent development of the wake downstream. The spectral characteristics of the circular and square nozzle combinations are qualitatively similar. However, the discrete frequency peaks associated with the wake of the inner mixing region are much broader in the case of the square nozzles, and the dominant frequency at the end of the midfield within the inner mixing region is lower than that of the circular ones. This is explained by the higher overall turbulence intensity in the inner mixing region of the square nozzles.

The existence of axis switching, a phenomenon observed in single nonaxisymmetric nozzles, is not evident from visualizations and measurements in the square coaxial nozzle. The lack of axis switching is attributed to the initial low coherence of large-scale structures (azimuthal vorticity) in the shear layers, the initially high small-scale turbulence levels in the outer flow, and strong azimuthal nonuniformity of the outer shear layers. These factors have been identified in past studies[5,10] of single noncircular jets as factors detrimental to axis switching. Thus, it is not surprising that this phenomenon did not occur. In spite of the absence of axis switching, visualizations and local velocity measurements have indicated modest mixing enhancement on the side plane in the square nozzles compared to the circular ones. This can be largely attributed to local differences in the initial velocity profiles between these two configurations and, particularly, to the higher initial turbulence intensity levels in the outer flow on the side of the square nozzle. The potential for development of axis switching in coaxial noncircular nozzle flows needs further investigation. Thus, additional work is necessary to determine to what extent mixing enhancement, other than the geometrical increase of the area subjected to shear or that caused by differences in initial conditions, can be produced using square coaxial nozzles as opposed to axisymmetric ones. Nozzles with initial conditions more favorable to axis switching and/or application of active forcing could answer this question and reveal if this phenomenon is at all possible in noncircular coaxial nozzle flows.

Acknowledgments

This work has been supported by NASA, the Louisiana Board of Regents Louisiana Education Quality Support Fund, and the U.S. Air Force Office of Scientific Research Graduate Student Research Program. The guidance and help of W. M. Roquemore of the U.S. Air Force Research Laboratory and helpful discussions with E. J. Gutmark while at Louisiana State University are also gratefully acknowledged.

References

[1]Ko, N. W. M., and Kwan, A. S. H., "The Initial Region of Subsonic Coaxial Jets," *Journal of Fluid Mechanics*, Vol. 73, 1976, pp. 305–332.

[2]Ko, N. W. M., and Au, H., "Coaxial Jets of Different Mean Velocity Ratios," *Journal of Sound and Vibration*, Vol. 100, No. 2, 1985, pp. 211, 212.

[3]Dahm, W. J. A., Frieler, C. E., and Tryggvason, G., "Vortex Structure and Dynamics in the Near Field of a Coaxial Jet," *Journal of Fluid Mechanics*, Vol. 241, 1992, pp. 371–402.

[4]Tang, D. K., and Ko, N. W. M., "Coherent Structure Interactions in Excited Coaxial Jet of Mean Velocity Ratio of 0.3," *AIAA Journal*, Vol. 31, No. 8, 1993, pp. 1521–1524.

[5]Zaman, K. B. M. Q., "Axis Switching and Spreading of an Asymmetric Jet: The Role of Coherent Structure Dynamics," *Journal of Fluid Mechanics*, Vol. 316, 1996, pp. 1–27.

[6]Sforza, P. M., Steiger, M. H., and Trentacoste, N., "Studies on Three-Dimensional Viscous Jets," *AIAA Journal*, Vol. 4, No. 5, 1966, pp. 800–806.

[7]Trentacoste, N., and Sforza, P., "Further Experimental Results for Three-Dimensional Free Jets," *AIAA Journal*, Vol. 5, No. 5, 1967, pp. 885–891.

[8]duPlessis, M. P., Wang, R. L., and Kahawita, R., "Investigation of the Near-Region of a Square Jet," *Journal of Fluids Engineering*, Vol. 96, Sept. 1974, pp. 247–251.

[9]Quinn, W. R., and Militzer, J., "Experimental and Numerical Study of a Turbulent Free Square Jet," *Physics of Fluids*, Vol. 31, No. 5, 1988, pp. 1017–1025.

[10]Grinstein, F. F., Gutmark, E., and Parr, T., "Near Field Dynamics of Subsonic Free Square Jets. A Computational and Experimental Study," *Physics of Fluids*, Vol. 7, No. 6, 1995, pp. 1483–1497.

[11]Quinn, W. R., "Streamwise Evolution of a Square Jet Cross Section," *AIAA Journal*, Vol. 30, No. 12, 1992, pp. 2852–2857.

[12]Schadow, K. C., Gutmark, E., Parr, D. M., and Wilson, K. J., "Selective Control of Flow Coherence in Triangular Jets," *Experiments in Fluids*, Vol. 6, 1988, pp. 129–135.

[13]Koshigoe, S., Gutmark, E., Schadow, K. C., and Tubis, A., "Wave Structures in Jets of Arbitrary Shape. III. Triangular Jets," *Physics of Fluids*, Vol. 31, No. 6, 1988, pp. 1410–1419.

[14]Schadow, K. C., Gutmark, E., Wilson, K. J., and Smith, R. A., "Noncircular Inlet Duct Cross-Section to Reduce Combustion Instabilities," *Combustion Science and Technology*, Vol. 73, 1990, pp. 537–553.

[15]Ho, C.-M., and Gutmark, E., "Vortex Induction and Mass Entrainment in a Small-Aspect-Ratio Elliptic Jet," *Journal of Fluid Mechanics*, Vol. 179, 1987, pp. 383–405.

[16]Hussain, F., and Husain, H. S., "Elliptic Jets. Part 1. Characteristics of Unexcited and Excited Jets," *Journal of Fluid Mechanics*, Vol. 208, 1989, pp. 257–320.

[17]Husain, H. S., and Hussain, F., "Elliptic Jets. Part 2. Dynamics of Coherent Structures: Pairing," *Journal of Fluid Mechanics*, Vol. 233, 1991, pp. 439–482.

[18]Husain, H. S., and Hussain, F., "Elliptic Jets. Part 3. Dynamics of Preferred Mode Coherent Structure," *Journal of Fluid Mechanics*, Vol. 248, 1993, pp. 315–361.

[19]Gutmark, E., and Ho, C.-M., "Visualization of a Forced Elliptic Jet," *AIAA Journal*, Vol. 24, No. 4, 1986, pp. 684, 685.

[20]Bitting, J. W., Nikitopoulos, D. E., Gogineni, S. P., and Gutmark, E. J., "Visualization of Non-Circular, Coaxial Nozzle Flow Structure," *Bulletin of the American Physical Society*, Vol. 42, No. 11, 1997, p. 2115.

[21]Bitting, J. W., Nikitopoulos, D. E., Gogineni, S. P., and Gutmark, E. J., "Structure of Square Coaxial Nozzle Flows," AIAA Paper 98-2917, June 1998.

[22]Nikitopoulos, D. E., and Liu, J. T. C., "Nonlinear Binary-Mode Interactions in a Developing Mixing Layer," *Journal of Fluid Mechanics*, Vol. 179, 1987, pp. 345–370.

[23]Nikitopoulos, D. E., and Liu, J. T. C., "Nonlinear Three-Wave Interactions in a Developing Mixing Layer," *Physics of Fluids*, Vol. 13, No. 4, 2001, pp. 966–982.

[24]Nikitopoulos, D. E., and Seo, T., "Two- and Three-Dimensional, Large-Scale Mode Interactions in a Developing Shear Layer," *Bulletin of the American Physical Society*, Vol. 42, No. 11, 1997, p. 2192.

W. J. Devenport
Associate Editor

AIAA 2003-182

AIAA 2003-0182
Experimental Investigation of Vortex Shedding of a Jet in Crossflow

B. Kiel, C. Murawski, M. Flanagan, and A. Cox
Air Force Research Laboratory
Wright Patterson AFB, OH

S. Gogineni
Innovative Scientific Solutions Incorporated
Beavercreek OH

41st Aerospace Sciences Meeting and Exhibit
6-9 Jan 2003

Reno, NV

This material is declared a work of the U.S. Government and is not subject to copyright protection in the United States.

Experimental Investigation of Vortex Shedding in a Jet in Cross-flow

B. Kiel*, C Murawski, M. Flanagan, and A. Cox
Air Force Research Laboratory
Wright Patterson AFB, OH

S. Gogineni
Innovative Scientific Solutions Incorporated
Beavercreek OH

ABSTRACT

An experimental investigation of a circular jet emitting from a wall into a crossflow was completed. The analyzed data revealed the three classic vortices present in a jet-in-cross flow environment: leading edge horseshoe vortex, the Karman-Street vortices, and the combined Kelvin-Helmholtz/Counter Rotating Vortex Pair (K-H/CVP). The focus of this paper was to investigate the frequency content of these vortices over a wide range of momentum ratios and Reynolds Number.

A circular jet at room temperature and ambient pressure was investigated over a range of momentum ratios from 2.0 to 15. The range of crossflow Reynolds numbers based on cross flow velocity and jet diameter was 3,000 to 18,000. The flow field was interrogated using a TSI 1288 split film probe. From the split film data Discrete Fast Fourier Transforms (DFFT) of the velocity data were performed.

Diagrams of Fourier spectra and energy spectra were constructed using the DFFT data. From the Fourier spectra, the Strouhal number of each of the vortices was discerned. Plots of Strouhal number versus Reynolds number were also made for each type of vortex. All three types of vortices showed some sensitivity to cross flow Reynolds number. This was especially true at higher Reynolds number where Strouhal number decreased significantly. Finally the Kelvin-Helmholtz/Counter-rotating Vortex Pair Fourier spectra displayed two distinct peaks for nearly every Reynolds number tested. These peaks are associated with the frequency of the ring vortex and the frequency that the ring vortex was shed from the jet.

NOMENCLATURE

CVP	Counter Rotating Vortex Pair
DFFT	Discrete Fourier Transform
JICF	Jet in Cross Flow
M	Momentum Ratio
k	wave number
Re	Reynolds Number
rms	root mean square
St	Strouhal Number
U	Velocity

Subscripts

c	cross flow
d	dissipation scale
j	jet

INTRODUCTION

Jets in cross flow (JICF) are an important design consideration for many components in a gas turbine engine. For example, in the combustor crossflow jets are introduced into the hot gas path to promote primary zone and dilution zone mixing. The crossflow jets enhance mixing which is required for high combustor efficiencies. Crossflow jets are also used to create exit temperature profiles for the turbine stages to allow for high turbine efficiency and acceptable turbine durability. JICF are also used in the augmentor for the cooling of hot parts. A greater understanding of the design parameters of a JICF can lead to performance improvements in the inlet, combustor, turbine, augmentor and the exhaust nozzle, (Lord, MacMartin, & Tillman 2000).

JICF have been studied for over 70 years, (Sutton 1932 and Bosanquet & Pearson 1936). The 1970s and 1980s brought a tremendous body of work on JICF. This work is very well summarized by Maragason (1993). In this comprehensive paper Maragason reviews many areas including parametric studies associated with jet properties. One of Maragason's conclusions was that there "have only been limited efforts to resolve the unsteady flow features" of a JICF.

More recent papers have addressed several aspects of JICF and the unsteady nature of the flow. Specifically, numerous authors have described a system of four vortices thatemanate from the mixing process between the jet and crossflow: horseshoe vortices,

Address correspondence to barry.kiel@wpafb.af.mil

This Material is a work of the U.S. Government and is not subject to copy write protection in the United States

Karman-Street vortices, Kelvin-Helmholtz vortices, and counter rotating vortex pair (CVP). When the jet issues into the cross flow it initially acts as a semi-rigid column of air. Horseshoe vortices are formed when the approaching cross flow boundary layer rolls up ahead of the stagnation point on the front of the semi-rigid cylinder of air (Figure 1). This is similar to the manner in which

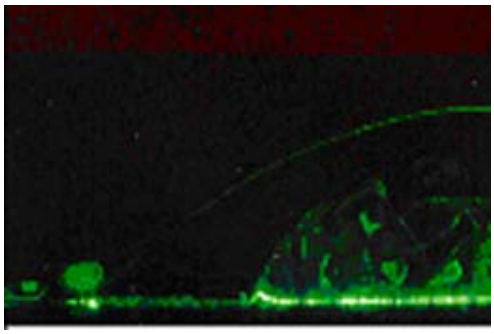

Figure 1 Particle Image Velocimetry (PIV) of Horseshoe Vortices on the Leading Edge of a Jet (Gogineni et al. (1995))

horseshoe vortices are formed on the leading edge of a solid cylinder in cross flow. The size and number of horseshoe vortices is dependant on the cross flow Re (Wei, Chen, & Du 2000 and Kelso & Smits 1995).

Karman-Street vortices form behind the semi-rigid column of air discussed above in the same fashion as they form behind a solid cylinder. Figure 2 depicts these vortices. In their research Moussa, Trischka, & Eskinazi (1977) studied the Karman-Street vortices over a range of momentum ratios of 1.4 to 900. Their data indicated that the St of the Karman-Street vortex generally decreased with increased velocity ratio over the entire range. The results in this paper concentrated on a part of Moussa, Trischka, & Eskinazi (1977)'s data set that is sparsely populated.

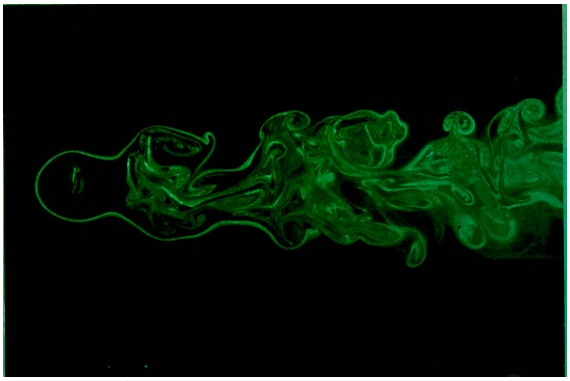

Figure 2 PIV of Karman-Street Vortices Behind a Jet (Gogineni 1et al. (1995))

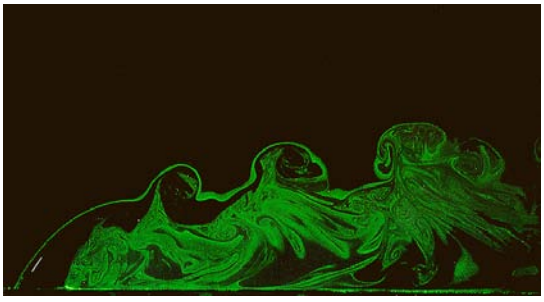

Figure 3 PIV of 3 Kelvin-Helmholtz Vortices (Gogineni et al. (1995))

The last two vortices were the Kelvin-Helmholtz vortices and the CVP. In Figure 3, three Kelvin-Helmholtz vortices with axes of rotation normal to the page are seen. Figure 4 depicts the Counter rotating Vortex Pair. The origins of the Kelvin-Helmholtz and CVP have been debated for well over thirty (30) years. Maragason's (1993) review concluded that the vortices seen in Figure 3 are an artifact of the free jet shear layer while the CVP (Figure 4) develops from the shear layer vorticity of the jet.

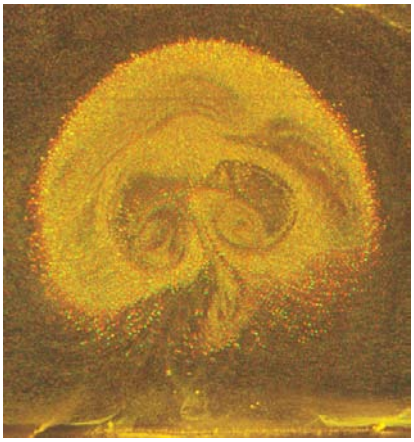

Figure 4 Counter Rotating Vortex Pair (Gogineni et al. (1995))

More recently there have been several papers advocating the origin of both the Kelvin-Helmholtz and CVP as artifacts of the instability manifested as a vortex ring emanating from the jet. The mechanism for the formation of these vortices is the Kelvin-Helmholtz instability at the jet exit. A vortex ring is formed as the jet issues into the cross flow. As the vortex ring convects in the wake, it is amplified by the velocity gradient between the jet and the recirculation zone. The vortex ring is also stretched and tilted by the strong velocity gradient between the free stream and the jet wake.

Several authors; Marzouk &Ghoniem (2002), Lim et al.(2001), Blanchard et al. (1999) and Kelso et al. (1992), have advocated that the Kelvin-Helmholtz and CVP vortices seen in Figures 3 & 4 are of the same origin. They contend that the Kelvin-Helmholtz vortex ring that forms at the jet exit sheds with the jet flow.

The jet is bent over into the cross flow by the pressure gradient between the stagnation point on the leading edge of the jet and the recirculation zone behind the jet. The bending of the jet caused tilted and stretched of the Kelvin Helmholtz vortex ring. The trailing edge of the vortex ring is bent up and forms the CVP. This can clearly be seen in figures 5 &6. Figure 5 depicts the genesis of the Kelvin-Helmholtz vortex ring and its evolution down stream. Figure 6 displays how the circular vortex ring is stretched and tilted resulting in the vortices depicted in Figure 3 and Figure 4. For convention the Kelvin-Helmholtz and CVP vortices will henceforth be referred to as K-H/CVP.

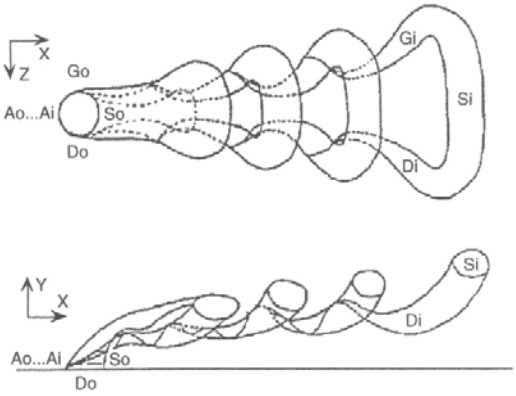

Figure 5 Origin of Kelvin-Helmholtz and CVP Vortices (Brizzi (1995))

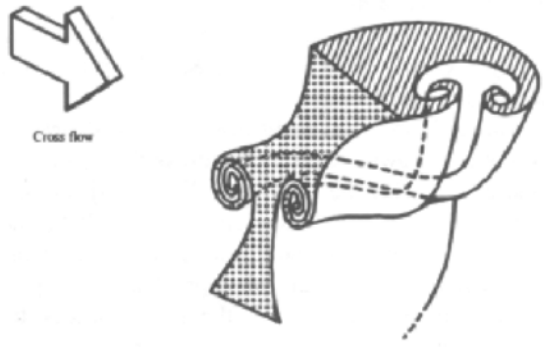

Figure 6 Tilting and Stretching of the Kelvin-Helmholtz vortex Ring (Lim et al, (2001))

SCOPE

Most recent studies of JICF have concentrated ontwo things. First, many studies have concentrated on a specific vortex shedding in the flow. In these studies the effect of Re or momentum ratio on the specific vortex shedding phenomena was studied. Second, other studies use; computations, smoke or LASER to visualize the flow. From that visualization conclusions were made on the nature of the vortices in the JICF interaction. These visualizations were typically at one momentum ratio and one Re. This paper reports the results of an experimental study which determined the frequency content of the vortices formed in the JICF over a wide range of conditions. Data was obtained on all three of the primary vortices in this type of flow. Comparisons to existing horseshoe vortex and cylinder in cross flow data were made.

EXPERIMENTAL APPARATUS

Figure 7 depicts the experimental test rig. The test article (Figure 8) required two sources of air, one for the jet and one for the crossflow. The cross flow air was supplied by a 5.60 kW blower that delivered 0.567 kg/s of air (standard day). The mass flow from the blower was fluctuated by a variable speed motor controller. Jet air was supplied by an 825 kPA air source. Air flow and pressure were then controlled through the use of a pressure regulator and control valve. Subsequently the air was metered by a rotameter with a flow range of .589 m^3/s to 13 m^3/s.

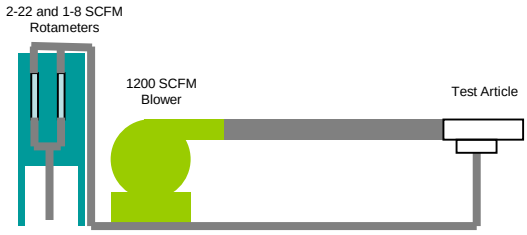

Figure 7 Test Rig

Figure 8 illustrates the test article. Several considerations were used in the design of the test article. The test article was designed such that the Re based on jet velocity and jet diameter was in the range of 13,000 to 34,000. This range was consistent with that of mixing jets, dilution jets, and film cooling flows in the combustor and augmentor. Consideration was

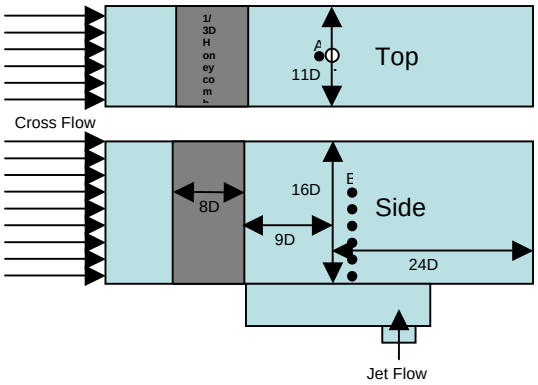

Figure 8 Test Article (D = 1.476e-3 m)

also given to cross flow Re based on channel height. A range of 100,000 to 250,000 was achieved. This too is analogous to combustor and augmentor flows.

A TSI Model 1288 split-film probe was used to collect velocity data in the flow. The split-film sensor had two electrically independent quartz films coating a platinum cylinder (Figure 9). The films were heated using a constant temperature anemometer. Hilpert's Correlation (Incorporera & De Witt 1985) was then used to obtain velocity magnitude and flow angle as a function of the heat transfer of the two probes. Instantaneous velocity data was digitized at a rate of 20 kHz, the highest frequency that the probe could resolve.

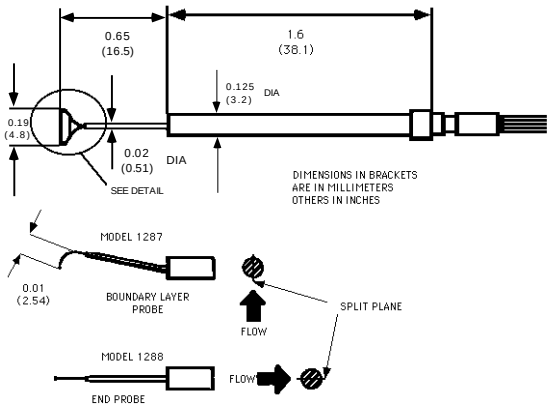

Figure 9 Schematic of TSI Split-film Probes

DATA COLLECTION & PROCESSING

Instantaneous velocity data was collected at several locations in the flow. Horseshoe vortex data was collected ½ diameter ahead of the upstream edge of the jet orifice. This point can be referred to at location 'A' on Figure 8. The split film probe was traversed in the flow to obtain Karmen-Street and K-H/CVP data. Traverses were taken one diameter down stream of the trailing edge of the jet, Figure 8 location 'B'. Traverses proceeded normal to the bottom surface of the test article. The probe was traversed at increments of 2.54e-3 m until the measured velocity was parallel to the inlet crossflow. Rms velocity was also compared with that of the inlet cross flow assuring both matched. Traverses typically contained from 15 to 20 data points.

Frequency domain information was calculated from raw velocity data. Instantaneous velocity data was also squared, yielding instantaneous turbulent kinetic energy. A DFFT of the instantaneous velocity and turbulent kinetic energy was performed for each data point. The frequency domain information was treated in two ways. First, the frequency domain velocity data was studied and information such as dominant frequency data and associated flow conditions were collected. Data was then non-dimensionalized and tabulated for vortex type.

Figure 10 depicts a dimensionless turbulent kinetic energy plot (Tennekes & Lumley 1990). The left hand plot represents data non-dimensionalized by the smallest, or Kolmogorov, scales. Note the plot on the left shows the effect of Re on the turbulent kinetic energy in the large scales. Experimental turbulent kinetic energy data was non-dimensionalized by the Kolmogorov scales. Frequency was converted to wave number. Wave number was then non-dimensionalized using the Kolmogorov scales. Dimensionless wave number and turbulent kinetic energy data were then graphed.

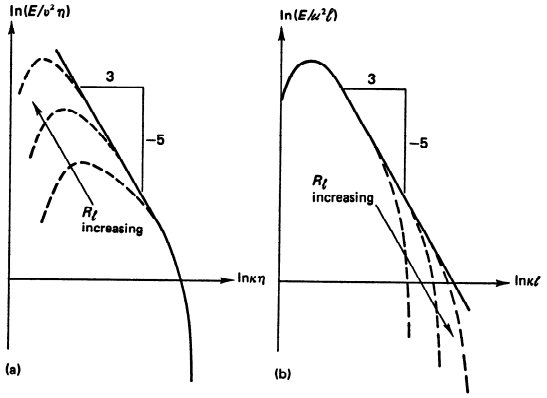

Figure 10 General Normalized Energy Spectra (Tennekes & Lumley, 1990)

RESULTS AND DISCUSSION

In this section there are four subsections. First there is a discussion of the Turbulent Kinetic Energy of the flow. Next the horseshoe vortices are presented. Finally the K-H/CVP and Karman-Street vortices are discussed.

Dimensionless Turbulent Kinetic Energy

To ensure the split film probe was resolving vortices well into the energy containing eddies region DFFTs of the instantaneous turbulent kinetic energy were calculated. The dimensionless data was plotted. Figure 11 is the dimensionless turbulent kinetic energy spectra for a momentum ratio of 10. It was taken one diameter behind the jet and at the point normal to the surface where maximum velocity occurred (approximately 2 3/4 diameters above the surface). Figure 11 is representative of the dimensionless turbulent kinetic energy at all points in the flow. Plots only differed in the magnitude of dimensionless

turbulent kinetic energy in the large eddy region of the flow. This was in excellent agreement with the assertions made about figure 10. Note that the split film probe would only resolve dimensionless wave numbers less than k/kd~0.08. As a result some of the dissipation range was not resolved.

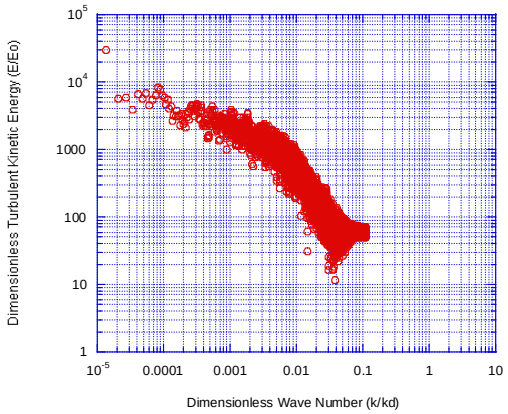

Figure 11 Dimensionless Turbulent Kinetic Energy vs. Dimensionless Wave Number

.

Horseshoe Vortex

A DFFT was also performed on the instantaneous velocity at many points in the flow for many conditions. For the horseshoe vortex instantaneous velocity data were collected over a range of momentum ratios of 3-25, and a range of Re, based on jet diameter and cross flow velocity, of 3,000 to 17,600. Re was varied independent of momentum ratio and visa versa. Four characteristic peaks were discerned in the data between 0 and 50 Hz. For frequencies greater than 50 Hz there was rarely a discernable peak. Figure 12 is a graph of St versus Re for all four peaks. Note in all cases St decreased with increasing Re.

In their paper Kelso & Smits (1995) studied laminar horseshoe vortex in front of the jet. Their data and flow visualization indicated that horseshoe vortices exist in three Re regions: steady, oscillating, and coalescing. For their conditions, they indicated that for Re greater than 3,500 the vortices are a coalescing system. One could speculate that the vortices in this experiment are most likely in the oscillating or coalescing regions. In the oscillating case the vortices oscillate as the Kelvin-Helmholtz vortex ring forms in the jet and sheds. In the coalescing case vortices coalesce and new vortices are constantly being formed. Both regions are characterized by three primary and several secondary vortices.

Figure 12 depicts the St data for the four peaks noted in the frequency data for the horseshoe vortex. As indicated by Kelso & Smits (1995), three of the peaks in the data are associated with the three primary vortices. The fourth can be explained in two ways. Either the fourth vortex is an artifact of the oscillatory nature of the flow (typically these oscillations are very low frequency, corresponding to the lowest St), or the fourth peak corresponds to the formation and shedding of the Kelvin-Helmholtz ring in the jet boundary layer.

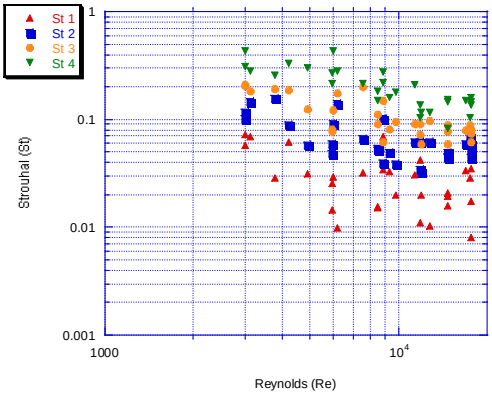

Figure 12 St Versus Re for the Horseshoe Vortex

K-H/CVP

K-H/CVP data was obtained at the point where the mean dimensionless velocity parallel to the cross flow jet velocity profile reached a maximum. Figure 13 depicts dimensionless velocity profiles of the velocity component parallel to the cross flow. The profiles were taken one diameter down stream of the jet trailing edge. Profiles were taken for momentum ratios from 2.5 to 15. Note the maxima occur between 1.5D and 3D.

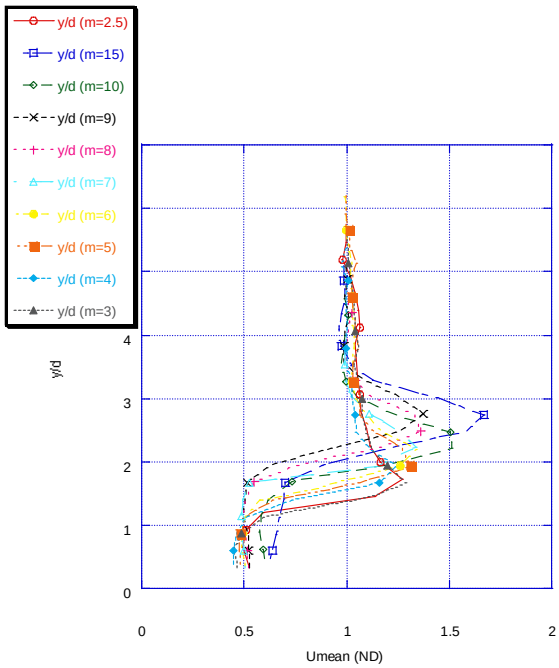

Figure 13 Dimensionless Velocity Profiles at x/D=1

As the momentum ratio increases the location of the maximum velocity increases in height. This was not accurately depicted in Figure 13 due to a lack of resolutiomear the maxim um. Figure 14 depicts the DFFT of instantaneous velocity data in the region of the KH-CVP. This data was taken approximately 1D downstream of the trailing edge of the jet and 3D from the surface. The momentum ratio was 15 and Re

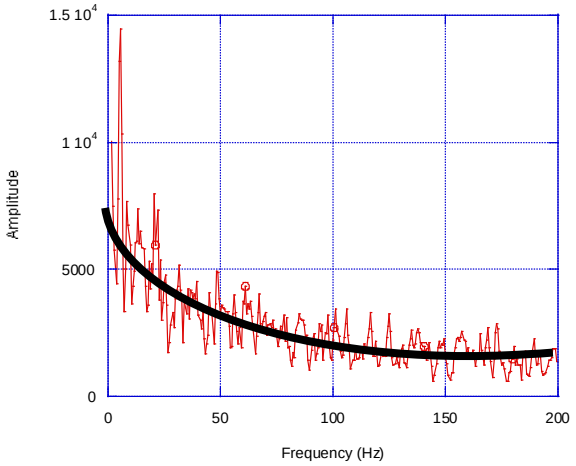

Figure 14 Fourier Spectra of the KH-CVP, M=15

based on jet diameter and mean cross flow velocity was 11,000. The solid line was drawn to demonstrate the mean amplitude. Note the two primary peaks between 0 and 50 Hz. The first occurred at approximately 7.9 Hz while the second occurred at approximately 39.9 Hz. These non-dimensionalize to St of 0.0182, and 0.0685 respectively.

Figure 15 illustrates the KH-CVP St data for the entire range of Re. Note there are two bands of data corresponding to the peaks represented in Figure 14. Careful inspection of the data in Figure 15 reveals the two peaks were not harmonics. Comparing Figure 15 to Figure 12 the open circles in Figure 15 correspond very well to the triangles in Figure 12. This leads one to the assumption that the fourth peak (triangle) in the horseshoe vortex data was associated with the formation or shedding of the of the Kelvin-Helmholtz and not the combination of horseshoe vortices. Further one can conclude from Figures 3, 5, & 15 that the two sets of data correspond to the frequency of the K-H/CVP vortices and the frequency of the shedding of the vortex ring.

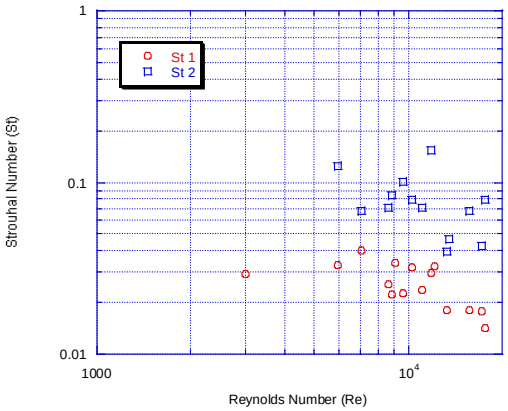

Figure 15 St Versus Momentum ratio for KH-CVP

Karman-Street

Figure 16 displays the dimensionless frequency information found in the wake of the jet. The four peaks found in each set of data between 0 and 50 Hz are plotted. Note the trend of the data in Figure 16 is similar to that of the Figure 12. The last three sets of data in Figure 16; diamonds, squares, and triangles occupy the same area on the plot as the last three sets of data on Figure 12; circles, squares, and triangles.

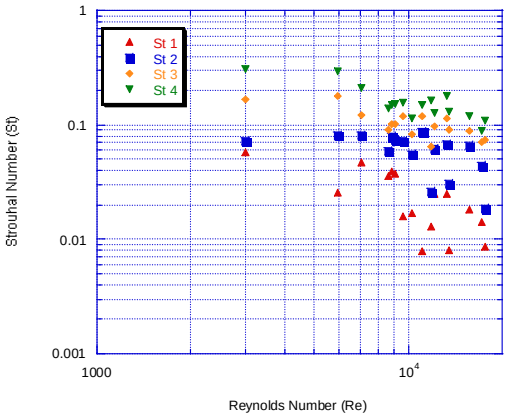

Figure 16 St Versus Re for the Karman Street Vortex

This indicates three things. First some of the horseshoe vortices were being entrained into the wake region. Entrainment of these vortices into the wake of the jet explains the close match in the second and third sets of data on both charts. Second, it was advocated that the last set of data in Figures 12 & 15 are an artifact of the vortex ring shedding from the jet. It was logical that these frequencies would carry over into the wake. Third, these assertions also promoted the notion that the highest band of data on Figure 16 is indicative of the Karman Street vortices.

Figure 17 is a plot of the set of highest St data from Figure 16 (upside down triangles) and the wake

measurements behind a jet in cross flow by Moussa, Trischka, & Eskinazi (1977). Note the data from this experiment (open circles) is in very good agreement with the data of Moussa, Trischka, & Eskinazi (1977) (open squares). This would lead one to attest that the upper most group of data on Figure 16 is in fact the Karman-Street data.

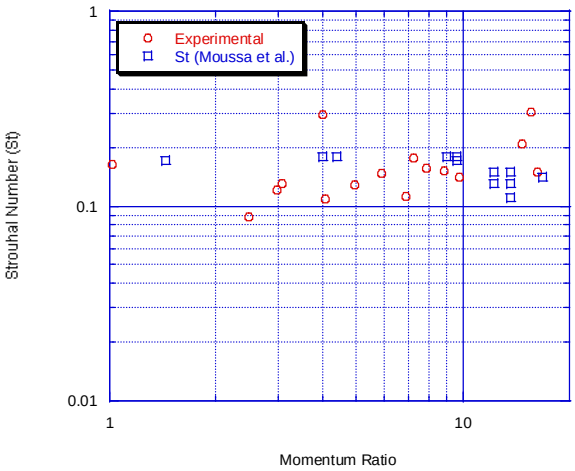

Figure 17 St Versus Reynolds Number for the Karman Street Vortices

CONCLUSION AND RECOMMENDATIONS

An experimental investigation of the vortex shedding phenomena in a JICF was studied. Several interesting things were discerned from the data. First, from the horseshoe vortex data four peaks were noted. When compared to the KH-CVP data it was clearly seen that the last band of data from the horseshoe vortex measurements came from the KH-CVP, while the others were the oscillating horseshoe vortices. Furthermore, when the Karman-Street and horseshoe vortex data are compared with other experimental data one can conclude that the horseshoe vortices convected into the jet wake and were measured along with the Karman-Street vortex shedding. All of the conclusions in this paper were made without flow visualization, but flow visualization was used from several of the papers referenced earlier to augment conclusions.

The ability of these vortices to mix may be enhanced or suppressed with different types of control devices and algorithms. Further efforts will consider the many required aspects of effective control. These efforts will include the development and evaluation of control-oriented modeling based on the data collected in this effort. Studies on controllability and observability with different actuator and sensor configurations will be explored.

To understand the true nature of the jet in crossflow vortices and their interactions further study is required. Flow visualization from smoke, Particle Image Velocimetry (PIV), and/or Computational Fluid Dynamics will bolster conclusions made about the nature of each of the sets of data offered in this paper. Further visualization during control activities will give direct insight into the controllability of the various vortices discussed.

REFERENCES

Blanchard, J., N., et al., 1999, “Influence of a Counter Rotating Vortex Pair on the Stability of a Jet in Cross Flow: an Experimental Study by Flow Visualization”, Experiments in Fluids, Vol. 26, 63-74.

Brizzi, L., E., 1995, “Sur les structures tourbillonnares generees a la fontiere d’ un jet circulaire debouchant perpendiculairement dans une couche limite”, CRSA Paris, 321, II.B, 217-223.

Bosanquet, C., & Pearson, J. L., 1936, ‘The Spread of Smoke and Gasses from Chimneys, Transactions of the Farraday Society, 32, 1249.

Gogineni, S., et al., 1995, “Investigation of a Jet in Cross Flow Using PIV”, AIAA-95-0790.

Incorporera, F., & De Witt, D., 1985, Fundamentals of Heat and Mass Transfer, John Wiley and Sons, New York.

Kelso, R., M., & Smits, A. J., 1995, “Horseshoe Vortex Systems Resulting From the Interaction Between a Laminar Boundary Layer and a Transverse Jet”, Physics of Fluids, 7, 153-158.

Kelso et al., 1992, “A Visual Study of a Round Jet in Cross Flow”, Symposium of Flow Visualization, Yokohama Japan, p 173-177

Lim, T.,et al. 2001, “On the Development of Large-scale Structures of a Jet Normal to a Cross Flow”, Physics of Fluids, Vol. 13, #3, 770-775.

Lord, W.K., MacMartin, D. G., &Tillman, T. G., 2000, “Flow Control Opportunities in Gas Turbine Engines”, AIAA 2000-2234.

Maragason, R., 1993, "Fifty Years of Jet in Cross Flow Research", Proceedings of the 72nd AGARD Fluid Dynamics Panel Meeting", p 1-12 to 1-17.

Marzouk, Y.M, & Ghoniem, A. F., 2002, Mechanism of Streamwise Vorticity Formation in a Transverse Jet”, AIAA 2002-1063

Moussa, Z. M., Trischka, J. W., & Eskinazi, S., 1977, “The near field in the mixing of a round jet with a cross-stream”, Journal of Fluid Mechanics, vol 89, part 1, pp 49-80.

Sutton, O., G., 1932, Proceedings of the Royal Society, A 135, 143.

Tennekes, H., & Lumley, J., 1990, A First Course in Turbulence, MIT Press.

Wei, Q-D., Chen, G., & Du, X-D., 2000, “An experimental Study on the Structure of Juncture Flows”, The Visualization Society of Japan Journal of Visualization, Vol. 3, No. 4, 341-348.

4th International Symposium on Particle Image Velocimetry
Göttingen, Germany, September 17-19, 2001

Simultaneous PLIF/PIV Investigation of Vortex-Flame Interactions

T. R. Meyer, G. J. Fiechtner, C. D. Carter, J. R. Gord, S. P. Gogineni

Abstract Recent studies of vortex-flame interactions have advanced the understanding of isolated turbulent events and their impact on local non-premixed flame fronts. In the current investigation, vortex-flame interactions in a counterflow Rolon Burner developed at École Centrale Paris/CNRS are investigated using a simultaneous PLIF/PIV technique. The hydroxyl (OH) layer produced by a hydrogen-air flame is imaged using planar laser-induced fluorescence (PLIF), and vortex-characterization data are acquired using two-color digital particle-image velocimetry (PIV). Experiments are performed for cases with and without flame extinction. Results show that the case with flame extinction has higher initial vortex strength but experiences greater levels of energy dissipation at later times due to flame propagation within the vortex rollers. Measurements at high temporal resolution show that the extinction process takes place in an annular region at the leading edge of the vortex rather than at the centerline for the conditions investigated in the present experiment. Local normal strain rates computed from the PIV data showed higher *fuel-side* normal strain rates in the annular region of the vortex-perturbed flame, but higher *air-side* normal strain rates at the centerline.

1 Introduction

Recent results of numerical-modeling efforts combined with advanced laser-diagnostic measurements have led to important advances in the understanding of combustion. Numerous investigations have contributed to these advances, including a particular type of study in which the interaction of a laminar, nonpremixed flame and a vortex is examined. The resulting data can be used for a variety of purposes, such as identifying fundamental regimes of vortex-flame interactions (Katta et al. 1998, Fiechtner et al. 2000, Renard et al. 2000). It is well recognized that vortices occur readily in turbulent flows. Vortical structures play an important role in unsteady and turbulent combustion, and experimental data can be used to develop models in combustion areas such as experimental gas-turbine combustors. Experimental study of vortical structures is difficult because of the need to isolate those structures in space and time with respect to a flame front. Therefore, experiments in which a feature of turbulence is isolated and studied are valuable in furthering the understanding of combustion processes, leading to numerous experimental studies of vortex-flame interactions.

Particle-Image Velocimetry (PIV) is an established technique which is being applied to a wide variety of flows including combustion. Planar Laser-Induced Fluorescence (PLIF) has also been in use for a number of years. Recently, several researchers conducted joint PLIF/PIV experiments in flames. Mueller et. al. (1995) performed PIV and OH-PLIF experiments on repeatable vortex-flame interactions. Frank et. al. (1996) reported simultaneous scalar- and velocity-field measurements in turbulent gas-phase flows. Hasselbrink et al. (1997) made simultaneous planar velocity and OH-fluorescence measurements at the base of a lifted, non-premixed, transverse methane jet flame. Rehm & Clemens (1997) made OH-PLIF and PIV measurements in a hydrogen jet flame. Donbar et al. (1998) made simultaneous CH-PLIF and PIV measurements in turbulent flames. Watson et al. (1999) performed scalar- and velocity-field measurements in lifted methane-air diffusion flames. In the present paper, simultaneous OH-PLIF and PIV measurements are made in an opposed-jet Rolon Burner developed at École Centrale Paris/CNRS. A precise control of the relative timing between the laser diagnostics and the vortex-flame event was implemented to explore the time-dependent nature of the vortex-flame interactions.

2 Burner Facility

A schematic of the opposed-jet Rolon Burner is shown in Fig. 1. The flame is supported between upper and lower nozzles that are separated by 40 mm; each nozzle has an exit diameter of 25 mm. The fuel consists of hydrogen

T. R. Meyer, G. J. Fiechtner, C. D. Carter, S. P. Gogineni
Innovative Scientific Solutions Inc., Dayton OH, 45440 USA

J. R. Gord
Air Force Research Laboratory, Propulsion Directorate, Wright Patterson AFB, OH, 45433 USA

Correspondence to:
S. P. Gogineni
Innovative Scientific Solutions. Inc.
2766 Indian Ripple Road, Dayton OH, 45440 USA
Sivaram.gogineni@wpafb.af.mil

diluted with nitrogen and flows from the upper nozzle; air flows from the lower nozzle. A flow of air is supplied to a vortex tube such that in the absence of a vortex, the exit velocity matches the velocity of the air emanating from the surrounding nozzle. Many types of vortices can be produced experimentally, including isolated single vortices and groups of multiple coaxial vortices. As fluid is pumped impulsively from a nozzle or orifice, a single vortex forms, followed by additional vortices in the production of a starting jet. The vortex generator used in the present study can sweep a maximum volume of ~3 cm^3, for a maximum attainable L/D ratio of ~30. For the experiments described here, comparatively strong vortices are generated using a 0.1-ms piston rise-time.

Vortex formations are monitored carefully to avoid the multiple-vortex condition by examining scattering images that are acquired with a color digital camera. Since vortices that are laminar initially can become unsteady and turbulent, these conditions are also avoided in the present study. In addition, the piston/cylinder is aligned and lubricated properly to avoid situations in which an undesired turbulent column of fluid exits the tube. Vortex visualization is accomplished during alignment of the vortex nozzle using PLIF of acetone.

Seed particles are introduced into the burner flows when digital PIV measurements of the vortex velocity are performed. Three particle seeders are installed—one after the air mass-flow controller, a second after the vortex-air mass-flow controller, and a third after the junction where the hydrogen and nitrogen gases are mixed. With the use of three seeders, each flow can be seeded with particles individually, or combinations of the different flowfields can be seeded. Each seeder contains hollow spherical ceramic particles with an approximate mean diameter of 2.4 μm. When PIV studies are not required, the seeders are removed from the apparatus. Experiments are repeated for both seeded and unseeded flows, and no significant change in the results is caused by the presence of seed particles.

Synchronization and Timing

Since data on the time-dependent nature of the vortex-flame interactions are to be compared with computational predictions (in addition to spatial-feature comparisons), precise synchronization of several experimental events is required, including generation and propagation of vortices, production of laser pulses, and activation of the camera shutter and intensifier. A block diagram of the synchronization scheme is shown in Fig. 2. The scheme depicted here provides precise control of the relative timing between the laser diagnostics and the vortex-flame event. To explore the temporal evolution of the event, data are captured utilizing the following phase-locked timing sequence: 1) an image is recorded, 2) the delay between vortex production and the laser/camera events is adjusted, and 3) another vortex is initiated and a second image recorded. This process is repeated to acquire numerous images that are obtained at increasing delays.

3
Measurement Techniques and Data Collection

The PLIF system contains a frequency-doubled, Q-switched Nd:YAG laser that is used to pump a dye laser; this dye laser, in turn, is frequency doubled. The UV radiation is directed through a telescope that is adjusted to produce a light sheet with a height that matches as nearly as possible the 40-mm burner separation. The resulting beam thickness is ~300 μm, which corresponds to the full width (defined as the distance between the locations of the 25%-peak-intensity points).

Hydroxyl radicals absorb the laser radiation at 281.3414 nm via the $R_1(8)$ transition of the (1,0) band in the A-X system. Fluorescence from the A-X (1,1) and (0,0) bands is detected at right angles through WG-295 and UG-11 colored-glass filters using a 105-mm-focal-length f/4.5 UV lens. The resulting light is recorded on an intensified CCD camera with an intensifier gate width of 100 ns. CCD pixels are binned in 2 x 2 groups; the result is an effective array size of 288 x 192 pixels, with an imaged area of 25.6 x 38.4 mm^2. The bottom of the image is flush with the surface of the lower nozzle. A color table is used, with a maximum value set to 95% of the maximum signal for all images taken at a given flame condition. The low-signal color is assigned by calculating the mean background noise and selecting a minimum value that is at least two standard deviations above this level.

Measurements of the velocity field are carried out using two-color digital PIV (Gogineni et al. 1998). A color digital CCD with an array of 3060 x 2036 pixels is used. A magnification of 78 pixels/mm results in an imaged area of 26.0 x 39.0 mm^2. The color CCD camera and the intensified CCD array are aligned using a transparent mask printed with a graduated scale. Further alignment between images is performed after each experiment employing software; a transformation in two-dimensional space is applied to the PIV images relative to the PLIF images. Two lasers are used, with one PIV light sheet produced by frequency doubling the output of a Q-switched Nd:YAG laser (30 mJ/pulse at the test section). The remainder of this beam is used to pump the dye laser that is frequency doubled

to excite OH fluorescence. The second PIV light sheet is produced by pumping a dye laser (employing DCM laser dye) with a second frequency-doubled, Q-switched Nd:YAG laser; this results in laser radiation at 640 nm (40 mJ/pulse at the test section). The thickness of both the red and the green light sheets is set to ~700 μm at the probe region. A digital delay generator is used to drive the timing of the two lasers such that the red pulses are delayed precisely with respect to the green ones. In the absence of a vortex, the underlying counterflow velocity field is probed with red pulses that are delayed by up to 1 ms with respect to the corresponding green pulses. For the fastest vortices studied, the delay between red and green pulses is reduced to 10 μs. The camera shutter is set to open for 1/15 s to permit detection of both laser pulses by the color CCD. Flame emission and light from other devices in the laboratory (monitors, etc.) are attenuated greatly by the shutter.

Velocity vectors are calculated using the custom designed software developed at Stanford (Stan PIV – Hasselbrink 1999). This software incorporates several improvements to standard (single-pass) PIV algorithms and allows recursive estimation of the velocity field. Spurious vectors are filtered using a consistency filter that rejects vectors that are not within a prescribed radius of a prescribed number of the nearest 8 neighboring vectors. The values of the vectors which are invalidated by the filter are interpolated.

4 Results

Figures 3 and 4 show simultaneous images of OH PLIF overlaid with instantaneous velocity vectors from PIV for cases with no flame extinction and with flame extinction, respectively. All OH PLIF images are normalized to the same color scale and represent qualitative OH concentrations. The velocity vectors plotted here correspond to the reference frame of the vortex and are obtained by subtracting its convection velocity. Figures 3 and 4 also show vorticity distributions computed by central differencing of the velocity field.

For the case with no flame extinction, shown in Fig. 3, the vortex velocity is estimated to be 2 m/s, and the spacing is 9 ms between images. As the vortex impinges upon the flame [Fig. 3(a)], the flame surface is wrinkled and wraps around the leading edge of the vortex. The flame then burns through the vortex rollers without being extinguished [see central and rightmost frames of Fig. 3(a)]. The location of the vortex structure is shown more clearly in the vorticity plots of Fig. 3(b). For the case with flame extinction [Fig. 4], the vortex velocity is estimated to be 3 m/s. In order to ensure that each vortex image in Fig. 4 is at the same stage of development as that of Fig. 3, the time spacing is set to 6 ms between frames. However, the vortex shown in Fig. 4(a) breaks the OH layer as it advances toward the upper nozzle. After this initial extinction, the flame propagates into the vortex rollers and begins to reconnect.

The following is a frame-by-frame comparison of Fig. 3 and 4. The plot of vorticity in the *leftmost* frame of Fig. 4(b) shows that the vortex is stronger relative to that of Fig. 3(b). The vortex in the *central frame* of Fig. 4(b) maintains its strength due to early flame extinction, while the vortex in the corresponding frame in Fig. 3(b) is dissipated due to interaction with the flame. In the *rightmost frame* of Fig. 4(b), the vortex is clearly dissipated as the flame propagates into the roller structures. Interestingly, by comparison, the vortex rollers in the rightmost frames of Fig. 3 are less dissipated than those of Fig. 4. This indicates that flame propagation along the vortex rollers plays a more significant role in the dissipation of vorticity when compared with lateral flame propagation across the vortex in Fig. 3.

To explore the flame extinction process further, simultaneous OH PLIF and velocity vectors are plotted with higher temporal resolution (0.3 ms between frames) in Fig. 5. This clearly shows that flame extinction begins in an annular region near the leading edge of the vortex rather than at the centerline. This phenomenon was first observed in the computational results of Katta et al. (1998).

To evaluate further the effect of strain rate on flame extinction, Fig. 6(a) compares the relative OH PLIF signal with the velocity gradient normal to the flame surface (dU/dR) using data from the leftmost image of Fig. 5, where U and R are the velocity and spatial components, respectively, normal to the flame surface. Both the OH PLIF signal and dU/dR are plotted at various points along the center of the OH layer from Point A to C; the velocity gradient is calculated using a combination of central differencing and linear interpolation between grid points. According to the plot of relative OH signal in Fig. 6(a), flame extinction begins to occur near Point B within a region of maximum dU/dR and away from the jet centerline. Because the center of the OH layer does not mark the stoichiometric surface, line plots of dU/dR across Points A and B are shown for comparison in Fig. 6(b). The peak normal strain rate toward the fuel side is higher in the annular region than at the centerline, while the peak normal strain rate toward the air side is higher at the centerline than in the annular region. This supports the findings of Katta et al. (1998), who suggested that the vortex-induced strain rate is not totally responsible for quenching in the latter

Deleted: ¶

location. Also in agreement with Katta et al. (1998), the fuel side peak normal strain rates shown in Fig. 6(b) are within 10% of the calculated values. The computed air side peak normal strain rates show the correct trends, but are higher than the experimental values by 50-100%. These errors may result from slight errors in PIV-OH image matching, relative resolution, thermophoresis, and particle slip. A detailed analysis of these sources of error is the subject of ongoing investigation.

5
Conclusions

A simultaneous OH PLIF and PIV experiment was performed to explore vortex-flame interactions using a counterflow Rolon Burner with a hydrogen-air diffusion flame. PIV images were collected using a high-resolution, two-color CCD sensor and were processed using a recursive estimation technique for higher vector density. It was demonstrated that PIV is extremely valuable when studying vortex dynamics in the presence of a flame front (as marked by OH PLIF) for cases with and without flame extinction. Plots of vorticity show that the case with flame extinction had higher initial vortex strength but experiences greater levels of dissipation at later times due to flame propagation within the vortex rollers. PIV results were also used to compute local normal strain rates and show very good agreement with computational results from the literature.

Acknowledgments

The authors would like to thank Dr. W. M. Roquemore and Dr. V. R. Katta for their guidance and valuable discussions. The authors also thank Dr. R. D. Hancock and Capt. I. Vihinen for assistance in assembly of the burner and Mr. K. D. Grinstead and Dr. J. M. Donbar for technical assistance in setting up the experiments. Finally, the authors thank Prof. Mungal of Stanford University for providing the StanPIV software. This work is supported by U. S. Air Force Contracts F33615-95-C-2507, F33615-97-C-2702, and F33615-00-C-2608.

References

Donbar, J.M.; Driscoll, J.F.; Carter, C.D. (1998) Simultaneous CH Planar Laser-Induced Fluorescence and Particle Image Velocimetry in Turbulent Flames. AIAA 36th Aerospace Sciences Meeting & Exhibit, Jan. 12-15, 1998, Reno, NV, U.S.A. (AIAA 98-0151).

Fiechtner, G.J.; Renard, P.H.; Carter, C.D.; Gord, J.R.; Rolon, J.C. (2000). Journal of Visualization, Vol. 2, No. 3/4, pp. 331-342.

Frank, J.H.; Lyons, K.M.; Long, M.B. (1996) Simultaneous Scalar/Velocity Field Measurements in Turbulent Gas-Phase Flows. Combustion and Flame, Vol. 107, pp. 1-12.

Gogineni, S.; Goss, L.; Pestian, D.; Rivir, R. (1998) Two-Color Digital PIV Employing a Single CCD Camera. Experiments in Fluids, Vol. 25, pp. 320-328.

Hasselbrink, E. (1999) Transverse Jets and Jet Flames: Structure, Scaling, and Effects of Heat Release. Technical Report TSD-121, Dept. of Mechanical Engg., Stanford University, Stanford, CA

Hasselbrink, E.; Mungal, M.; Hanson, R. (1997) Planar Velocity Measurements and OH Imaging in a Transverse Jet. AIAA 35th Aerospace Sciences Meeting & Exhibit, Jan. 6-10, 1997, Reno, NV, U.S.A. (AIAA 97-0118).

Katta, V.R.; Carter, C.D.; Fiechtner, G.J.; Roquemore, W.M.; Gord, J.R.; Rolon, J.C. (1998). 27th Symposium (International) on Combustion, The Combustion Institute, pp.587-594.

Mueller, C.J. et. al. (1995) Effect of Unsteady Stretch Rate on OH Chemistry during a Flame-Vortex Interaction: to assess Flame Models. Combustion and Flame, Vol. 100, pp. 323-331.

Rehm, J.E.; Clemens, N.T. (1997) A PIV/PLIF Investigation of Turbulent Planar Non-Premixed Flames. AIAA 35th Aerospace Sciences Meeting & Exhibit, Jan. 6-10, 1997, Reno, NV, U.S.A. (AIAA 97-0250).

Renard, P.H.; Thevenin, D.; Rolon, J.C.; Candel, S. (2000) Progress Energy Combustion and Science, Vol. 26, pp. 225-282.

Watson, K.A.; Lyons, K.M.; Donbar, J.M.; Carter, C.D. (1999) Scalar and Velocity Field Measurements in a Lifted CH_4-Air Diffusion Flame. Combustion and Flame, Vol. 117, pp. 257-271.

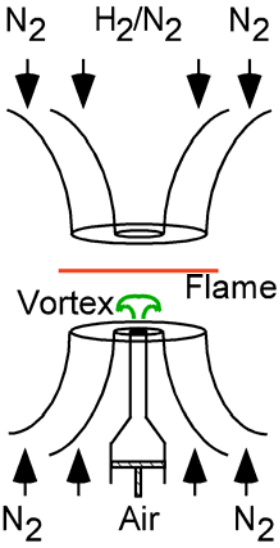

Fig. 1 Schematic of the Rolon Burner.

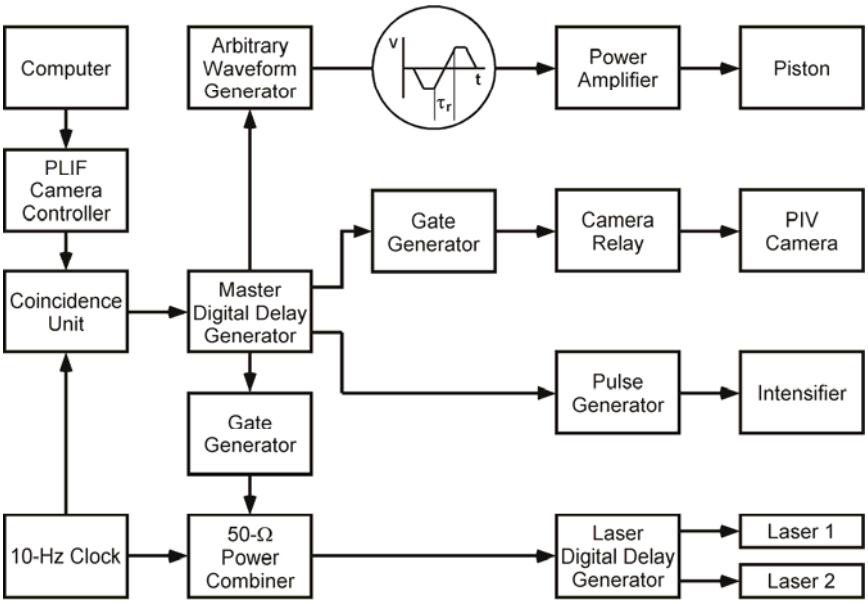

Fig. 2 Block diagram of the synchronization scheme.

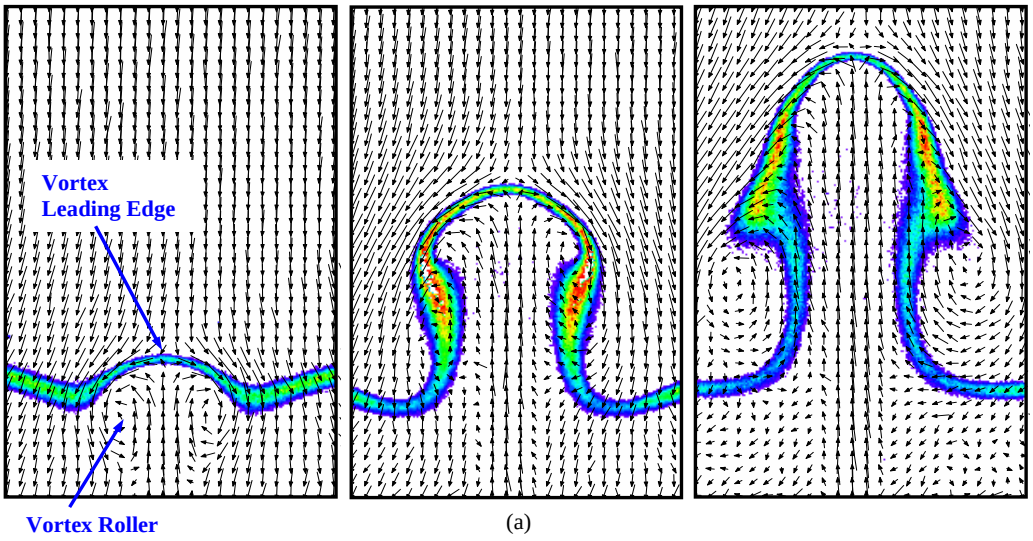

(a)

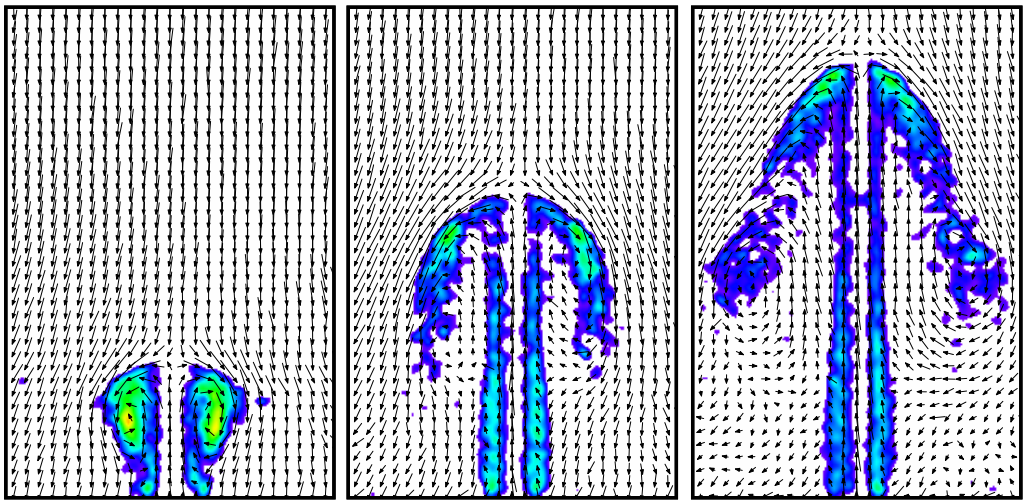

(b)

Fig. 3 (a) Simultaneous OH-PLIF and velocity distributions and (b) superposed velocity and vorticity distributions for a case with no flame extinction. Images progress in time from left to right and are spaced 9 ms apart.

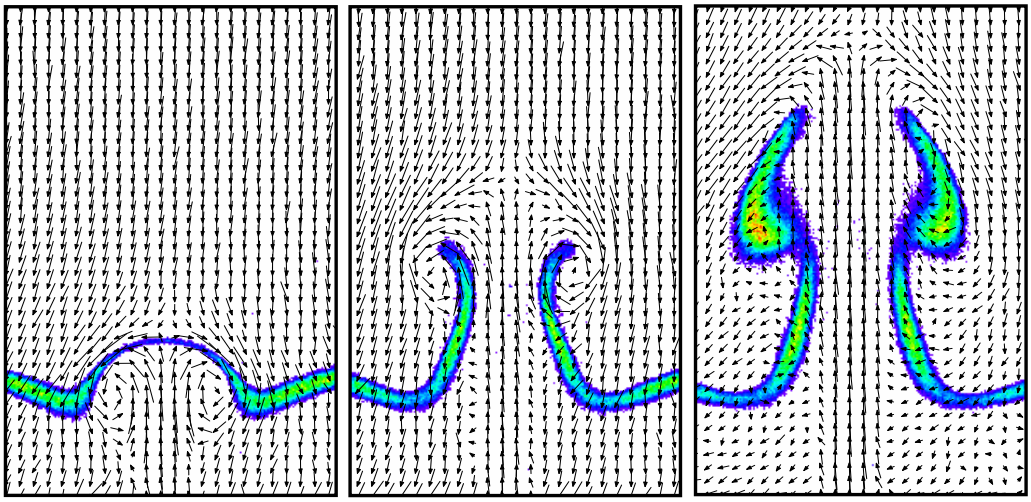

(a)

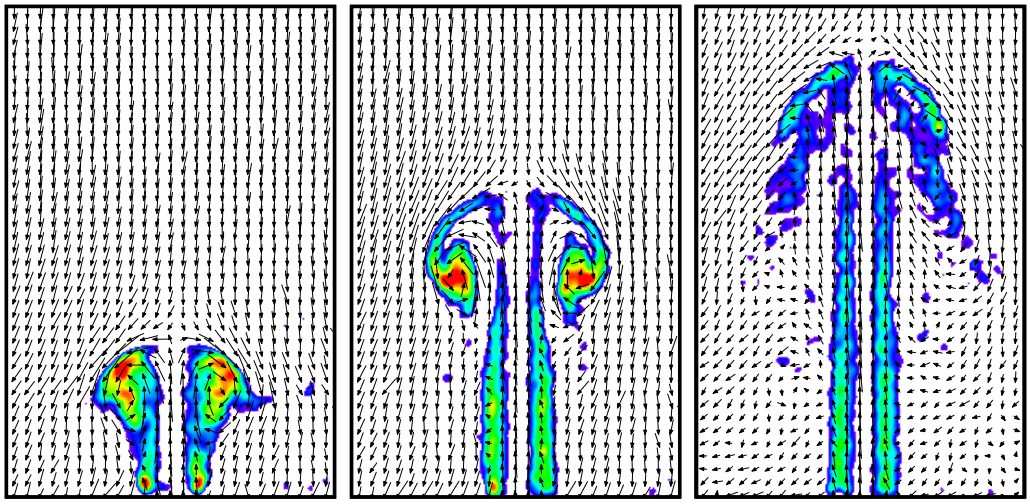

(b)

Fig. 4 (a) Simultaneous OH-PLIF and velocity distributions and (b) superposed velocity and vorticity distributions for a case with flame extinction. Images progress in time from left to right and are spaced 6 ms apart.

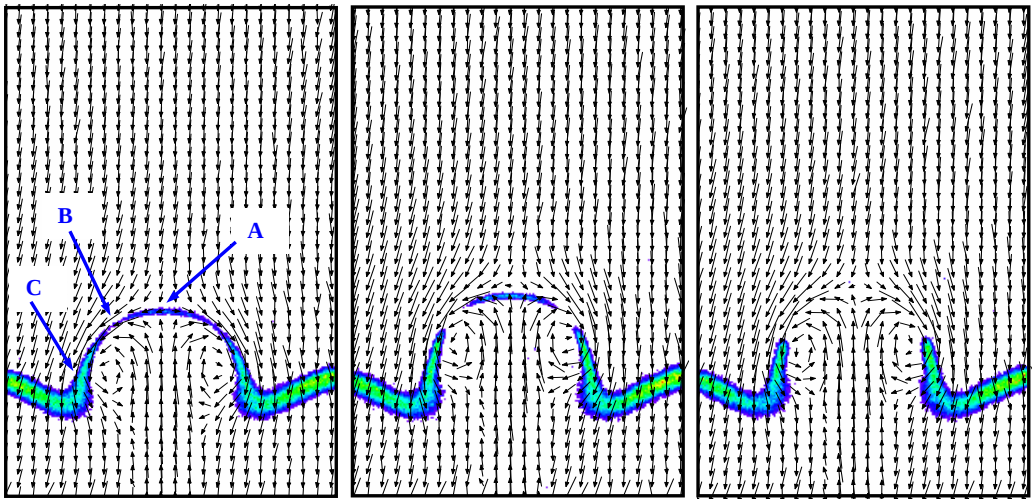

Fig. 5 Simultaneous OH-PLIF and velocity distribution showing the time resolution required to capture the flame extinction. Images progress in time from left to right and are spaced 0.3 ms apart.

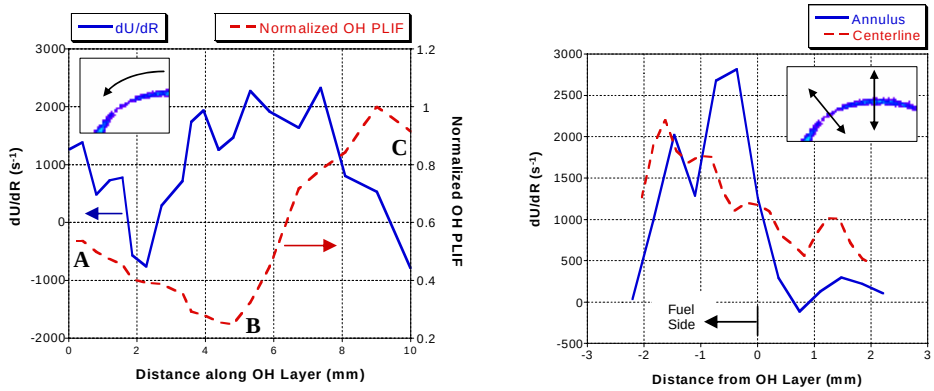

(a) (b)

Fig. 6 (a) Velocity gradient normal to the flame surface (dU/dR) and normalized OH PLIF *along* the flame from Point A to Point C from the leftmost image of Fig. 5; (b) Velocity gradient normal to the flame surface measured *across* Points A (centerline) and B (extinction region) from the leftmost image of Fig. 5.

Effects of Ignition on Premixed Vortex Rings: A Simultaneous PLIF and PIV Investigation

T.R. Meyer, V.R. Katta, S. Gogineni
Innovative Scientific Solutions, Inc.
Dayton, OH 45440

J. R. Gord
Air Force Research Laboratory

Background and Motivation

- Vortices found to be effective "flame holders" (e.g. trapped vortex, pulsed combustion).
- Vortices greatly enhance mixing and reaction.
- Flame propagation in vortex rings also useful for basic combustion studies.

Objectives

- Evaluate feasibility of vortex-assisted ignition.
- Generate well-controlled vortex ignition and combustion events.
- Study effects of equivalence ratio, spark timing, and vortex strength.
- Perform OH, acetone PLIF, and PIV.
- Compare with direct numerical simulations (DNS).

Jet-in-Co-Flow Burner

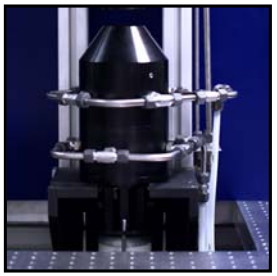

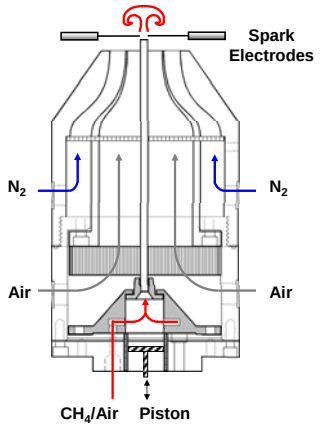

Experimental Facility

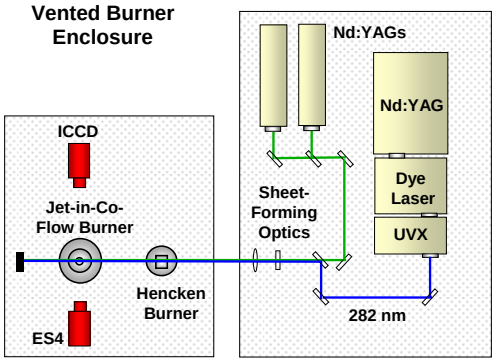

OH Absorption Spectrum
1-0 Band of the A-X System

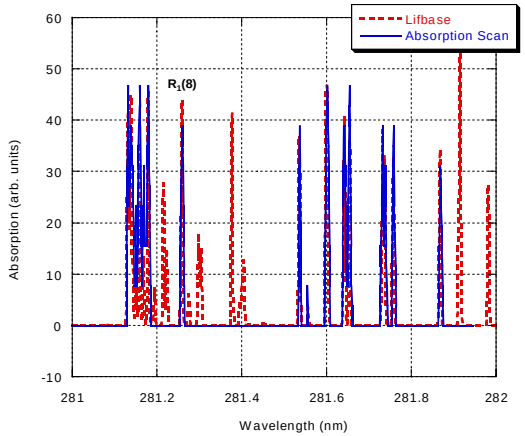

Operating Conditions

Ignition Timing (ms)*	Equivalence Ratio	Piston Stroke (mm)	Vortex Velocity (m/s)
2.5	1.0	3.3	5
4	0.75, 1.0, 1.25, 1.5	3.3	5
4	1.0	1.6	2.5
5	1.0	5	6.5
6	1.0	1.6, 3.3, 5	2.5, 5, 6.5
8	1.0	3.3	5

* Relative to piston actuation

Cold-Flow Vortex Propagation

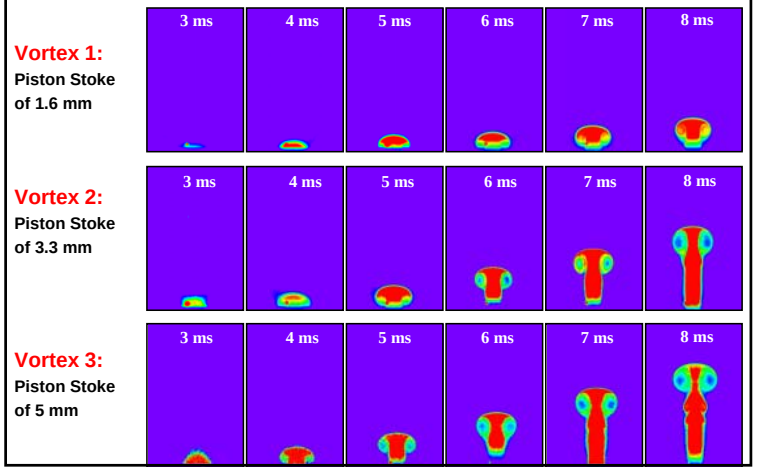

Effect of Vortex Ignition
Phi = 1, Vortex 2, 8 ms After Piston

PIV and Acetone PLIF of Cold Flow

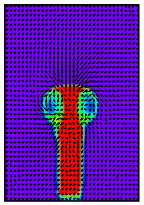

Simultaneous Particle Scattering and OH PLIF

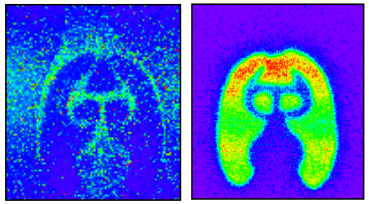

Interior Flame Propagation
Phi = 1, Vortex 2, Spark at 6 ms

OH PLIF

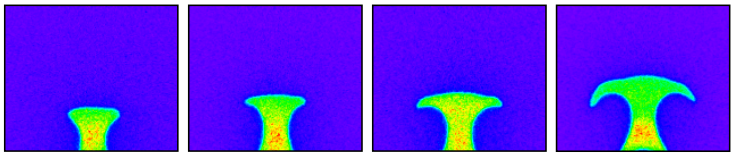

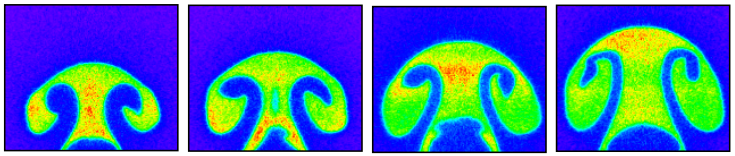

Bridging of Exterior Flame
Phi = 1, Vortex 2, Spark at 4 ms

OH and Acetone PLIF

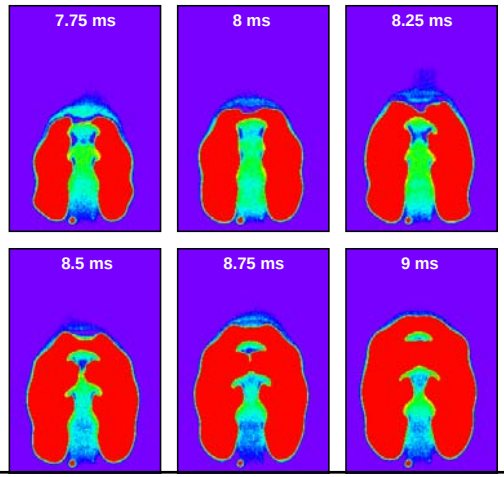

Interior Flame Propagation
Phi = 1, Vortex 2, Spark at 6 ms

OH and Acetone PLIF

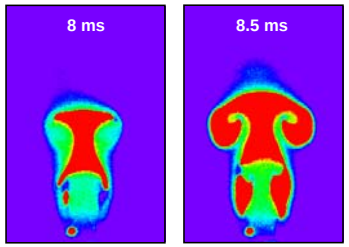

Comparison with DNS

Phi = 1, Vortex 1

Experiment

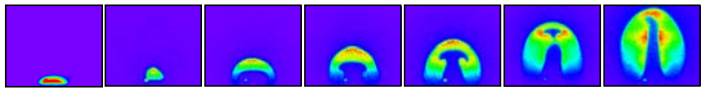

Simulation

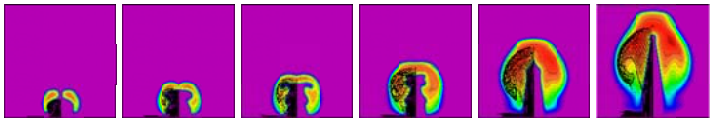

Effect of Spark Timing

Phi = 1, Vortex 2

Spark at 2.5 ms

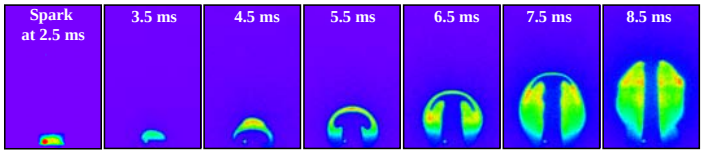

Spark at 4 ms

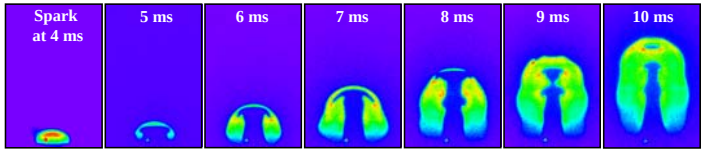

Effect of Spark Timing

Phi = 1, Vortex 2

Spark at 6 ms

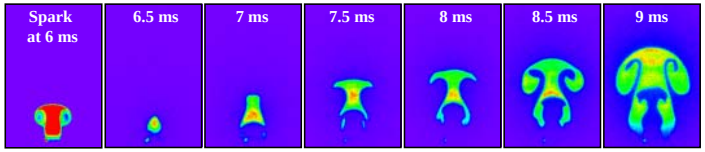

Spark at 8 ms

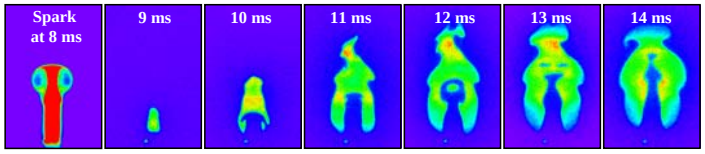

Effect of Spark Timing

Phi = 1, Vortex 2

Spark at 4 ms

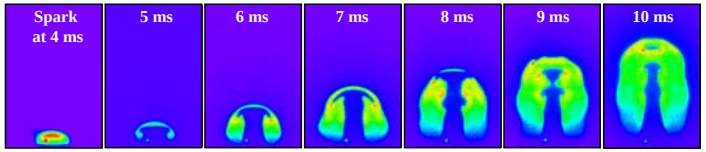

Spark at 6 ms

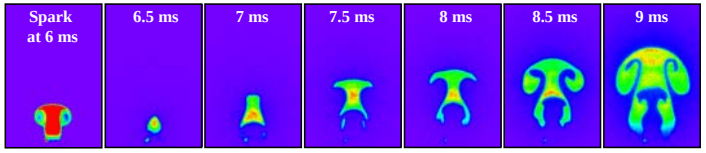

Effect of Equivalence Ratio
Vortex 2, Spark at 4 ms

Phi = 0.75

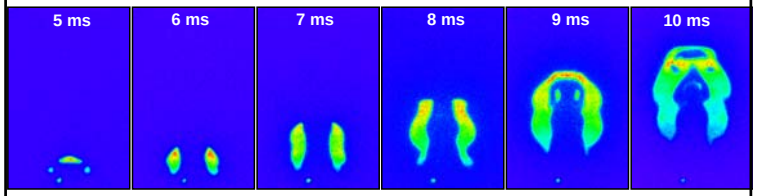

Phi = 1.0

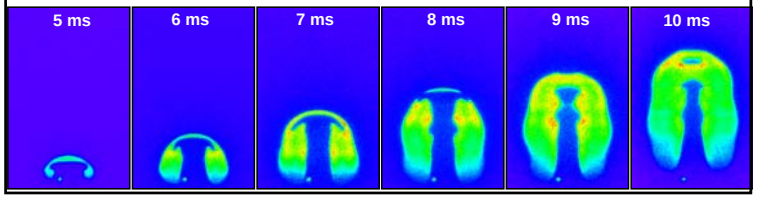

Effect of Equivalence Ratio
Vortex 2, Spark at 4 ms

Phi = 1.25

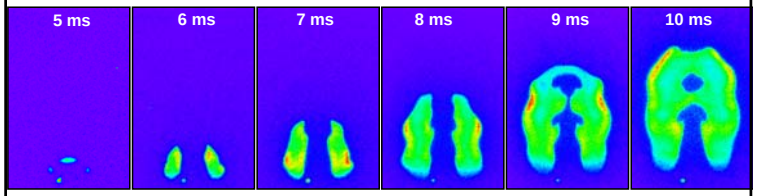

Phi = 1.5

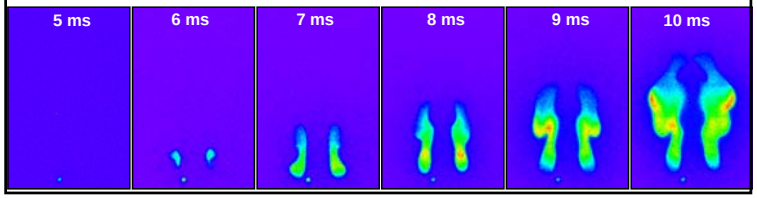

Effect of Vortex Strength

Vortex 1

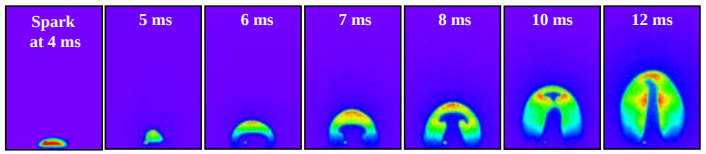

Vortex 2

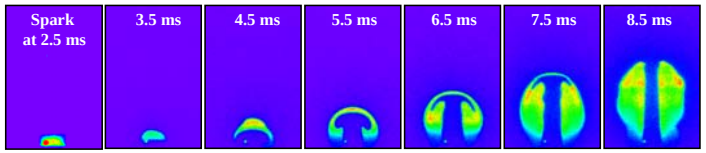

Effect of Vortex Strength

Vortex 2 (3.3 mm Stroke)

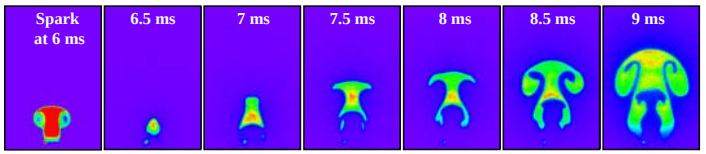

Vortex 3 (5 mm Stroke)

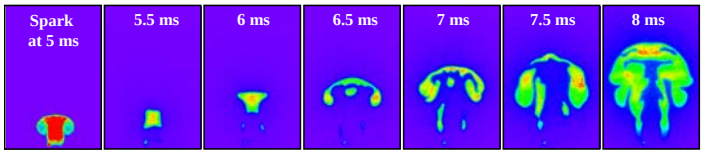

Conclusions

- Ideal vortex ignition possible only under certain conditions.
- Spark timing leads to either interior or exterior flame propagation.
- Ideal flame entrainment and product formation at stoichiometric conditions.
- Vortex ignition possible at high vortex strengths and high jet velocities.
- Preliminary DNS results promising.

Future Work

- Measurement of velocity using PIV to set DNS conditions.
- Study Lewis number effects and test DNS performance with different fuels.
- Quantify product formation.
- Two-camera visualization of cold vortex and flame regions.

(c)2002 American Institute of Aeronautics & Astronautics or Published with Permission of Author(s) and/or Author(s)' Sponsoring Organization.

AIAA 2002-0479 A02-13977

Study of Multi-Vortex/Flame Interactions in an Opposing jet Diffusion Flame

V. R. Katta, M. S. Brown, T. R. Meyer, J. R. Gord,
W. M. Roquemore
Air Force Research Laboratory
Propulsion Directorate
Wright-Patterson AFB, OH 45433

40th Aerospace Sciences Meeting & Exhibit
14-17 January 2002
Reno, Nevada

**For permission to copy or to republish, contact the copyright owner named on the first page.
For AIAA-held copyright, write to AIAA Permissions Department,
1801 Alexander Bell Drive, Suite 500, Reston, VA, 20191-4344.**

(c)2002 American Institute of Aeronautics & Astronautics or Published with Permission of Author(s) and/or Author(s)' Sponsoring Organization.

AIAA-2002-0479

Study of Multi-Vortex/Flame Interactions in an Opposing Jet Diffusion Flame

V. R. Katta*, M. S. Brown*, T. R. Meyer*, J. R. Gord and W. M. Roquemore
Air Force Research Laboratory
Propulsion Directorate
Wright-Patterson Air Force Base, OH 45433
Corresponding e-mail: vrkatta@erinet.com

Abstract:

A numerical and experimental investigation is performed to generate interaction of a flame surface with multiple vortices. This unsteady flame in an opposing-jet-flow burner is established by driving two vortices simultaneously from the air and fuel sides, respectively. Changes in the structure of the flame during its interaction with the incoming vortices and the instability-generated secondary vortices are investigated using a time-dependent CFDC code known as UNICORN. The combustion process is simulated using a detailed-chemical-kinetics model that incorporates 13 species and 74 reactions. While the slowly moving vortices resulted in a wrinkled but continuous flame, the fast moving vortices created a locally quenched flame with its edge being wrapped around the merged vortical structures. Three variables, namely, air and fuel-side strain rates and scalar dissipation rate are investigate to characterize the observed quenching processes. It is found that none of these variables can characterize the quenching process associated with the unsteady flames. Even though, the quenching value of scalar dissipation rate increases with the velocity of the incoming vortices, its variation is much smaller than that obtained in air- or fuel-side strain rates. It is proposed that a variable that is proportional to the air-side strain rate and inversely proportional to the temperature-drop rate at extinction could characterize the unsteady quenching process.

Introduction:

Studies on the structure of dynamic flames are important to the understanding of fundamental combustion processes; they provide insights into the turbulent combustion phenomena and help developing and evaluating simplified models that can be used in design codes for practical combustion systems. Unsteady flames are subjected to stretching that varies in time; typically, the time scale for the changes in strain rate is comparable to the chemical response time of the system. Numerous investigations (experimental and numerical)[1-3] have been performed to quantify the scalar structure of steady-state, aerodynamically strained, planar diffusion flames. Such studies on counterflow diffusion flames have not only provided benchmark experimental data but also yielded valuable insight into the behavior of the flame when it is subjected to higher strain rates. However, in practical combustion devices, flames are subjected to severe unsteadiness that results from the random motion of vortices;[4,5] which led to studies of unsteady counterflow flames. To retain the simplicity offered by planar diffusion flames, unsteadiness was imposed on counterflow flames by fluctuating the fuel and air jets simultaneously and sinusoidally.[6,7] These studies have demonstrated that the unsteady flames can be stretched beyond the steady-state extinction limit.

During vortex-flame interactions, which are often considered to be the building blocks for statistical theories of turbulence, the flame surface is subjected not only to unsteadiness but also to deformation. To investigate the effects of curvature on unsteady flames, both theoretical and experimental studies have been initiated.[8,9] In particular, experiments designed by Roberts et al.[10] and by Rolon[11] have created great interest, especially because of their unique ability to inject a well-characterized vortex toward the flame surface.

Several investigators have developed models[12-14] for the study of interaction between a flat flame and an induced vortex. In all of these models, it was assumed that an artificially created (by specifying the vorticity field) vortex pair interacts with a flat flame formed in a parallel flow. Although such an assumption has advantages in exploring interesting aspects of vortex-flame interactions, investigations employing these synthesized vortices do not represent actual interactions in opposing-jet flames and hence, they could not facilitate direct comparisons between predictions and measurements and make verification of the former very difficult.

Recent advances in computer-hardware technology and the need to improve the understanding of combustion phenomena under complex practical situations have led to the development of two- and three-dimensional Computational Fluid Dynamics

* Innovative Scientific Solutions, Inc.,
2766 Indian Ripple Road, Dayton, OH 45440,

This paper is declared a work of the U. S. Government and is not subjected to copyright protection in the United States.

(c)2002 American Institute of Aeronautics & Astronautics or Published with Permission of Author(s) and/or Author(s)' Sponsoring Organization.

models that incorporate detailed chemical kinetics (CFDC).[15,16] Complete simulation of the counterflow diffusion flame using multi-dimensional models not only eliminated the concerns regarding the simplified analyses but also provided a valuable tool for studies of vortex-flame interactions in counterflow premixed[10] and diffusion[11] flames.

Structures of different types of unsteady flames have been studied recently[17] issuing vortices from the fuel and air sides of an opposing-flow jet diffusion flame. Two types of unsteady flames; namely, traveling and stationary were established during these interactions. In the first type, not only the strain rate on the flame but also its location was changed with time. In the second type, only the strain rate on the flame was varied with time, while the flame itself was locked spatially. The latter unsteady flames were established by issuing vortices simultaneously from the air and fuel sides toward the flame surface. In certain situations, this collision of vortices leads to the generation of multiple vortices and, there by, a turbulent like flow field. This paper describes an experimental and numerical study of a hydrogen opposing-jet diffusion flame subjected to interaction with multiple vortices.

Mathematical model:

A time-dependent, axisymmetric model known as UNICORN (UNsteady Ignition and COmbustion using ReactioNs)[18] was used for the simulations of vortex/flame interactions associated with opposing jet flow burner. This model solves the Navier-Stokes and species- and energy-conservation equations written in the cylindrical-coordinate (z-r) system. A detailed-chemical-kinetics model has been used to describe the hydrogen-air combustion process. This model consists of thirteen species--namely, H_2, O_2, H, O, OH, H_2O, HO_2, H_2O_2, N, NO, NO_2, N_2O, and N_2 and 74 elementary reactions among the constituent species. The rate constants for this H_2-O_2-N_2 reaction system were obtained from Ref. 19.

Temperature- and species-dependent property calculations are incorporated in the model. The governing equations are integrated on a nonuniform staggered-grid system. An orthogonal grid having rapidly expanding cell sizes in both the axial and radial directions is employed. The finite-difference forms of the momentum equations are obtained using an implicit QUICKEST scheme,[20,21] and those of the species and energy equations are obtained using a hybrid scheme of upwind and central differencing. At every time step, the pressure field is calculated by solving the pressure Poisson equations simultaneously and utilizing the LU (Lower and Upper diagonal) matrix-decomposition technique. This model has been validated previously by simulating various steady and unsteady counterflow[22] and coflow[18,23] jet diffusion flames.

Results and Discussion:

The opposing-jet-flow burner used for the studies of unsteady flame structures was designed by Rolon[11] and is shown in Fig. 1(a) and is described in detail in Ref. 11. A flat flame is formed between the fuel and air jets having velocities of 0.69 and 0.5 m/s, respectively. The hydrogen-to-nitrogen ratio used for the fuel jet was 0.38. Vortices are shot toward the flame surface simultaneously from the fuel and air sides. The collision of these vortices with each other at the flame surface quenches the flame locally and generates multiple vortices. Different sizes of fuel- and air-side vortices were used, in part, to establish multiple vortices rapidly and, in part, to mask the errors involved in aligning the upper and lower injection nozzles in the experiment. The air-side vortices were generated by injecting a specified amount of air through the syringe tube (Fig. 1) and then through a 5.0-mm diameter injection-tube. Similarly, the fuel-side vortices were generated by injecting a specified amount of fuel through the syringe tube and then through a 2.0-mm diameter injection-tube. Calculations for these axisymmetric flames were made using a non-uniform 401 x 301 mesh system distributed over a physical domain of 40 x 40 mm, which yielded a mesh spacing of 0.1 mm in both the axial (z) and the radial (r) directions in the region of interest.

Steady-State Flame Structure:

The computed steady-state flame structure along the stagnation line is shown in Fig. 1(b). The 48-s^{-1} air-side strain rate of this flame represents a weakly strained one. The flame (peak-temperature region) is located at z = 19.2 mm, and its temperature of 1560 K is only slightly lower than the corresponding adiabatic temperature of 1598 K. In general, the peak strain rate on the fuel side (K_f = 60 s^{-1}) is greater than that on the air side as a result of the difference in the density of the two jets. Even at this low strain rate, the fuel and oxidizer are not completely consumed simultaneously in the flame zone. In an overlap region of ~1 mm, both H_2 and O_2 are present.

The steady-state strain rate of the opposing-jet flame can be increased by gradually increasing the velocities of the fuel and air jets. Calculations were repeated by varying the jet velocities, and it was found that a stable steady-state flame could be obtained for fuel and air jet velocities of 16 and 14 m/s, respectively. These velocities yielded an air-side strain rate (K_a) and flame temperature of 1410 s^{-1} and 1130

(c)2002 American Institute of Aeronautics & Astronautics or Published with Permission of Author(s) and/or Author(s)' Sponsoring Organization.

K, respectively; these values agree favorably with calculations made by Gutheil et al.[24]

Multi-Vortex/Flame Interactions:

As described earlier, vortices are shot toward the flame surface from both the air and fuel sides simultaneously by injecting specified amounts (2.2 cm^3) of air and fuel through the respective syringe tubes. Evolutions of the vortices and their simultaneous interaction with the flame surface depend on the injection times. In general, with the shorter injection times, the generated vortices travel faster toward the flame surface and affect its structure as the local flow-time scales approach the chemical-time scales. In the present study, various unsteady flames were generated by injecting air and fuel through the respective syringe tubes in such a way that the values of the exit velocities are in between 2 and 10 m/s. Results obtained for nine simulations were discussed in this paper and the exit velocities used for all these simulations are shown in Table 1.

Simulation No.	Exit Velocities	
	Air	Fuel
Case 1	2 m/s	-2 m/s
Case 2	3 m/s	-3 m/s
Case 3	4 m/s	-4 m/s
Case 4	5 m/s	-5 m/s
Case 5	6 m/s	-6 m/s
Case 6	8 m/s	-8 m/s
Case 7	10 m/s	-10 m/s
Case 8	6 m/s	-8 m/s
Case 9	7 m/s	-8 m/s

Table 1. Air and fuel velocities at the injection-tube exits used for generating different multi-vortex/flame interactions.

While the calculations made for Case-1 conditions yielded a flame that is stretched and wrinkled but not extinguished anywhere, the calculations for all other cases resulted flame quenching along the stagnation line. Experiments were also performed for some of these conditions to trace the changes in flame structure during the multi-vortex/flame-interaction process. The computed and experimental results obtained for Case 4 are shown in Figs. 2 and 3, respectively, at different stages of the interaction process. The computed temperature and OH-concentration distributions are plotted on the left and right halves of the images shown in Fig. 2. The instantaneous locations of the particles that were released from the air and fuel nozzles are also shown in Fig. 2 to visualize the flow structures. Air injected from the 5-mm-diameter tube generated a vortex that has grown to a size of 12-mm diameter by the time it reached the flame surface (8.1 ms). Similarly, during the same time period the fuel vortex has grown to 5 mm from its 2 mm initial size. The collision of these two vortices at the flame surface stretched the latter. The temperature of the fame along the stagnation line has decreased to 1140 K, which is close to the quenching limit, in 8.1 ms from the start of the vortex injection. In another ms, the multi-vortex/flame interaction has completely quenched the flame that was sandwiched between the two vortices [Fig. 2(b)]. As the vortices continue to push on to each other in the hole formed on the flame surface, the edge of the flame wrinkled and propagated into the fuel vortex as seen in Fig. 2(c). Similar behavior was observed in the OH-concentration distributions obtained in the experiment (Fig. 3) using PLIF technique. Considering the difficulties associated with aligning the small tubes that are 40-mm apart the symmetricity obtained during the multi-vortex/flame interactions in the experiments is quite good. The simulated results match qualitatively with the measurements. To obtain a better comparison between the experiment and calculation the velocities at the exits of the injector tubes need to be matched. In the present study these velocities were obtained from the total amount of fluid used for injection.

A weak interaction among the opposing vortices and the flame surface was obtained when the injection velocities are low. The computed results obtained for 2 m/s injection velocities (Case 1) are shown in Fig. 4. Significant role ups can be seen in the vortices as these structures travel over longer periods of time. The flame sandwiched between the vortices is stretched significantly, however, is not extinguished [Fig. 4(b)]. Propagation of the combined vortex structure [Fig. 4(c)] broadened the flame as it pulls the products away from the flame zone.

A moderate interaction between the vortices and the flame was obtained for the air-injection velocity of 6 m/s and fuel-injection velocity of 8 m/s (Case 8). The interaction process was visualized in Fig. 5 for this case. As the fuel-injection velocity is greater than that of the air injection, the fuel continued to push toward the air nozzle though the hole formed on the flame surface. During this interaction a small flamelet was separated from the wrinkled main flame [Fig. 5(c)], which got burned at a later time.

A strong interaction between the vortices and the flame was obtained in Case 7 where the injection velocities were 10 m/s. The results for this case are shown in Fig. 6. An important difference between the interaction obtained in Case 7 from the other interactions may be noted from Fig. 6(a). Here, as the air- and fuel-side vortices approach the flame surface, the jet columns are becoming unstable. These instabilities are generating secondary vortices that also

(c)2002 American Institute of Aeronautics & Astronautics or Published with Permission of Author(s) and/or Author(s)' Sponsoring Organization.

travel toward the flame surface. Such secondary vortices were also observed by Fiechtner et al.[25] In 6.2 ms the flame edge has broadened significantly with its interaction with the primary and secondary vortices. In fact, the flame looks like a turbulent one. As expected the vortices trapped in the hot combustion product got dissipated while the ones outside the flame are growing and pulling the flame into them.

Characterization of Extinction:

Simulations made for Cases 2-9 have resulted local flame extinction along the stagnation line. Traditionally, extinction of flames is characterized by the strain rate imposed on them[1,3]. However, it has been shown by several authors that the strain rates at which unsteady flames are extinguished are significantly higher than the corresponding ones for the steady state flames[17,26]. As the strain rate being found to be an inadequate quantity to describe the extinction behavior of an unsteady flame, several researchers have looked into other variables that can be used for this purpose. The one often used is the scalar dissipation rate[27]. The results obtained for Cases 2-9 are used to investigate the validity of the strain rate and scalar dissipation rate for describing the quenching process associated with the unsteady flames.

It is known that the values of strain and scalar-dissipation rates change across the flame width. Typical variations of these quantities are shown in Fig. 7 along the stagnation line for Case 3 at three instants. The temperature profiles are shown in Fig. 7(a). As the flame is squeezed between the vortices its peak temperature also decreased. The flame was near extinction limit at 9.2 ms. Strain rates calculated across the flame at the three instants are shown in Fig. 7(b). As seen from this figure and from the one corresponding to the steady-state flame in Fig. 1(b) it may be noted that strain rate changes significantly across the flame. The presence of vortices further complicates the strain-rate profile. It is argued that the value of the strain rate at a location where the reactants are entering the flame zone represents the strain rate imposed on the flame. However, in diffusion flames, as the fuel and oxidizer enter the flame zone from opposite sides, one would obtain two strain rates. The air-side and fuel-side strain rates at the three instants of Case 3 are shown in Fig. 7(b) with solid and open circles, respectively. In general these strain rates increase rapidly as the flame is squeezed between the vortices. The air- and fuel-side strain rates of 1720 and 2830 s^{-1}, respectively, at the instant of quenching (9.2 ms) are significantly higher than the corresponding ones obtained for the steady state flame.

The scalar dissipation rate is calculated from mixture fraction (ξ) as follows

$$\chi = 2\, D_{eff}\left[\left(\frac{d\xi}{dz}\right)^2 + \left(\frac{d\xi}{dr}\right)^2\right]$$

Here, mixture fraction is defined as the fraction of the mass at any location that originated from the fuel jet[28]. The value of the effective diffusion coefficient is taken to be unity. The variations of scalar dissipation rate across the flame at three instants are shown in Fig. 7(c). Similar to strain rate, scalar dissipation rate also varies across the flame and increases significantly as the flame is squeezed between the vortices. It is relevant to consider peak scalar dissipation rate that occurs at the stoichiometric surface for characterizing a strained flame, as the overall reaction rate also peaks at this location.

The drop in peak temperature with time as the vortices squeeze the flame for all the 7 cases that used equal fuel and air injection velocities are shown in Fig. 8. In general, this drop is more rapid with the faster vortices as in Case 7 and is slower with the weaker vortices as in Case 2. The flame temperature decreased to 1220 K and stayed at this value during the remaining interaction process for Case 1. The flame considered in the present study is known to extinguish (based on the concentrations) when its temperature falls below 1130 K. The times at which the flame temperature decreased to 1130 K can be obtained from Fig. 8 for each case.

The variation of air- and fuel-side strain rates and peak scalar dissipation rate with time for Cases 1-7 are shown in Figs. 9, 10, and 11, respectively. The values corresponding to the quenching times are marked in these plots with solid circles. It may be noted that all these three variables do not yield a single value to describe the flame quenching. The quenching value of air-side strain rate increases with the traveling speed of the vortex. For the highest vortex speed (Case 7) it is ~ 2740 s^{-1}, which is nearly 70% more than that required to quench the flame with the slowly moving vortices (Case 2).

The value of the fuel-side strain rate at quenching condition also increases with the speed of the vortex. In fact, its variation is more than that seen in air-side strain rate. The fuel-side strain rate at the time of quenching for Case 7 is nearly 6 times more than that established with the slowly moving vortices (Case 2).

Even though, the quenching value of scalar dissipation rate also increases with the speed of the vortices (Fig. 11), its variation is less significant when compared to those noted for air- and fuel-side strain rates. The quenching scalar dissipation rate obtained for Case 7 is only ~ 18% higher than that obtained for the slowly moving vortex case (Case 2).

The reason for scalar dissipation rate representing flame quenching better than the strain rate can be

(c)2002 American Institute of Aeronautics & Astronautics or Published with Permission of Author(s) and/or Author(s)' Sponsoring Organization.

understood by looking at the non-equilibrium process associated with chemical- and flow-time scales. As the stretch on the flame is increased, more and more reactants will be transported into the flame zone. At lower strain rates, the chemical kinetics can consume all the reactants entering the flame zone. However, at higher strain rates, chemistry may not cope-up with the reactant fluxes and, there by, flame cooling occurs. As the strain rate (either air or fuel side) represents only the reactant fluxes transported into the flame zone it does not account for the changes in non-equilibrium chemistry that is taking place in highly stained flames. This fact may be demonstrated by plotting the quenching strain rates with respect to the temperature-drop rate at extinction for all the cases considered in this study. Fig. 12 shows that air-side strain rate increases linearly with the temperature-drop rate. As temperature drop directly correlates the balance between the reactant influx and its consumption in the flame zone (extent of non-equilibrium nature of the reactions), Fig. 12 suggests that quenching value of air-side strain rate increases with the extent of non-equilibrium chemistry taking place in the flame zone. Therefore, by defining a variable that is proportional to the air-side strain rate and inversely proportional to the temperature-drop rate one may obtain an universal value for identifying the quenching process in unsteady flames. For example,

$$\sigma = T_\infty \left. \frac{K_a}{\left(dT/dt\right)_{ext}} \right|$$

gives an unique value at extinction condition for all the flames considered in the present study. The applicability of such a variable for different types of unsteady flames will be tested in the future work.

Conclusions:

Unsteady flames are often studied to gain a better understanding of turbulent-flame structures and, hence, facilitate the development of accurate turbulence-chemistry interaction models. An experimental and numerical study has been performed to identify the structural changes that occur during the interactions between multiple vortices and flame surface. A time-dependent model, known as UNICORN, that incorporates 13 species and 74 reactions among the constituent species has been used for simulation of unsteady flames resulting from multi-vortex/flame interactions in opposing-flow hydrogen jet diffusion flames. This model has been validated by direct simulation of several steady-state and unsteady axisymmetric counterflow and coflow jet diffusion flames in the past. OH-concentration measurements were made using PLIF technique.

A steady-state opposing-flow jet flame was established using the Rolon-burner geometry. Several unsteady flames were then obtained by forcing vortices toward the flame surface from both sides simultaneously using injection tubes placed in the fuel and air nozzles. During weak interactions associated with slowly moving vortices the flame surface found to wrinkle and broaden without being extinguished. On the other hand, the strong interactions associated with fast moving vortices yielded secondary flow instabilities and, there by, a turbulent-like flames.

It was found that the air-side strain rate, fuel-side strain rate, or scalar dissipation rate do not characterize the quenching process associated with the unsteady flames. In general, these flames were found to withstand higher strain rates than the steady-state ones and the quenching strain rates increase with the velocity of the incoming vortices. Even though, the quenching value of scalar dissipation rate also increases with the velocity of the incoming vortices, its variation is much smaller than that obtained in air- or fuel-side strain rates. It is proposed that a variable that is proportional to the air-side strain rate and inversely proportional to the temperature-drop rate at extinction could characterize the unsteady quenching process.

Acknowledgments:

This work was supported, in part, by the Air Force Office of Scientific Research.

References:

1. Kee, R. J., Miller, J. A., Evans, G. H., and Dixon-Lewis, G., *Proc. Combust. Inst.* 22: 1479-1486 (1988).
2. Dixon-Lewis, G., *Proc. Combust. Inst.* 23: 305-324 (1990).
3. Chelliah, H. K., Law, C. K., Ueda, T., Smooke, M. D., and Williams, F. A., *Proc. Combust. Inst.* 23: 503-510 (1990).
4. Hottel, H. C., and Hawthorne, W. R. *Proc. Combust. Inst.* 3: 254-266 (1949).
5. Roquemore, W. M., Chen, L.-D., Goss, L. P., and Lynn, W. F. in *Turbulent Reactive Flows*, Lecture Notes in Engineering (R. Borghi and S. N. B. Murthy, Eds.) (Springer-Verlag, Berlin, 1989), Vol. 40, p. 49.
6. Darabiha, N., *Comb. Sci. Technol.*, 86: 163 (1992).
7. Egolfopoulos, F. N., and C. S. Campbell, *J. Fluid Mech.*, 318: 1 (1996).
8. Paul, P. H., and Najm, H. N., *Proc. Combust. Inst.* 27: 43-50 (1998).

(c)2002 American Institute of Aeronautics & Astronautics or Published with Permission of Author(s) and/or Author(s)' Sponsoring Organization.

9. Patnaik, G., and Kailasanath, K., *Proc. Combust. Inst.* 27: 711-717 (1998).
10. Roberts, W. L., Driscoll, J. F., Drake, M. C., Ratcliffe, J. W., *Proc. Combust. Inst.* 24: 169-176 (1992).
11. Rolon, J. C., Aguerre, F., and Candel, S., *Combust. Flame* 100:422 (1995)
12. Ashurst, W. T., *Combust. Sci. Technol.* 92:87 (1993).
13. Poinsot, T., Trouve, A., Veynante, D., Candel, S., and Esposito, E., *J. Fluid Mech.* 177:265 (1987).
14. Rutland, C. J., and Ferziger, J. H., *Combust. Flame* 84:343 (1991).
15. Smooke, M. D., Ern, A., Tanoff, M. A., Valdati, B. A., Mohammed, R. K., Marran, D. F., Long, M. B., *Proc. Combust. Inst.* 26: 2161-2168 (1996).
16. Katta, V. R., and Roquemore, W. M., AIAA Paper 97-0904, Jan., 1997.
17. Katta, V. R., and Roquemore, W. M., *Proc. Combust. Inst.* 28:2055-2062 (2000).
18. Roquemore, W. M., and Katta, V. R., *Journal of Visualization*, 2:257 (2000)
19. Frenklach, M., Wang, H., Goldenberg, M., Smith, G. P., Golden, D. M., Bowman, C. T., Hanson, R. K., Gardiner, W. C., V. Lissianski, V., Gas Research Institute Technical Report No. GRI-95/0058, November 1, 1995.
20. Leonard, B. P., *Comput. Meth. Appl. Mech. Eng.*, 19:59 (1979).
21. Katta, V. R., Goss, L. P., and Roquemore, W. M., *AIAA J.*, 32:84 (1994).
22. Katta, V. R., Carter, C. D., Fiechtner, G. J., Roquemore, W. M., Gord, J. R., and Rolon, J. C., *Proc. Combust. Inst.* 27: 587-594 (1998).
23. Grisch, F., Attal-Tretout, B., Bouchardy, P., Katta, V. R., and Roquemore, W. M., *J. Nonlin. Opt. Phys. Mater.*, 5:505 (1996)
24. Gutheil, E., Balakrishnan, G., and Williams, F. A., in *Lecture Notes in Physics* (N. Peters and B. Rogg, Eds.) (Springer-Verlag, New York, 1993), pp. 177-195.
25. Fiechtner, G. J., Renard, P.-H, Carter, C. D., Gord, J. R., and Rolon, J. C., 1998, *J Visualization* 2: 331-342 (2000)
26. Brown, T. M., Pitz, R. W., and Sung C. J., *Proc. Combust. Inst.* 27: 703-710 (1998).
27. Kyritsis, D. C., Santoro, V. S., and Gomez, A., "Measurements and computations of scalar dissipation rate in vortex perturbed counterflow diffusion flame," Proceedings of the 2001 Technical Meeting of the eastern States Section of the Combustion Institute, Dec. 2-5, 2001.
28. Nandula, S. P., Brown, T. M., and Pitz, R. W., *Combustion and Flame*, Vol. 29, No. 3/4, 1994, p. 445.

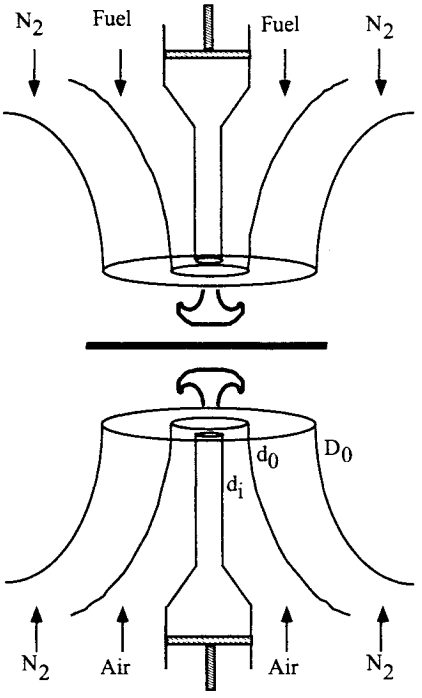

(a)

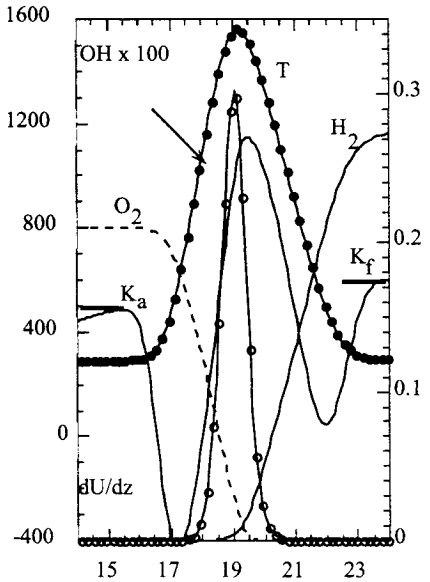

(b)

Fig. 1. Opposing-jet-flow burner used for the investigations of multi-vortex/flame interactions. Nitrogen-diluted hydrogen fuel and air are introduced from the upper and lower nozzles, respectively. (a) Schematic diagram and (b) steady-state flame structure.

(c)2002 American Institute of Aeronautics & Astronautics or Published with Permission of Author(s) and/or Author(s)' Sponsoring Organization.

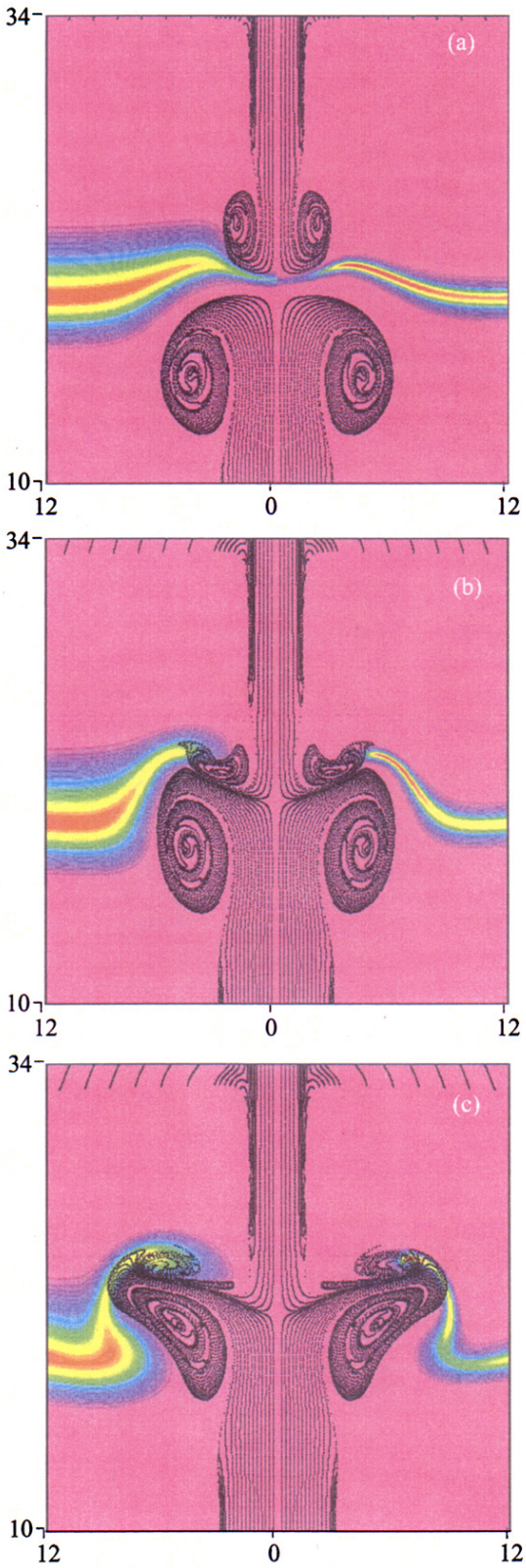

Fig. 2. Simulation of multi-vortex/flame interaction. Particle locations are superimposed on temperature (left) and OH (right) fields. (a) 8.1, (b) 9.1, and (c) 10.1 ms.

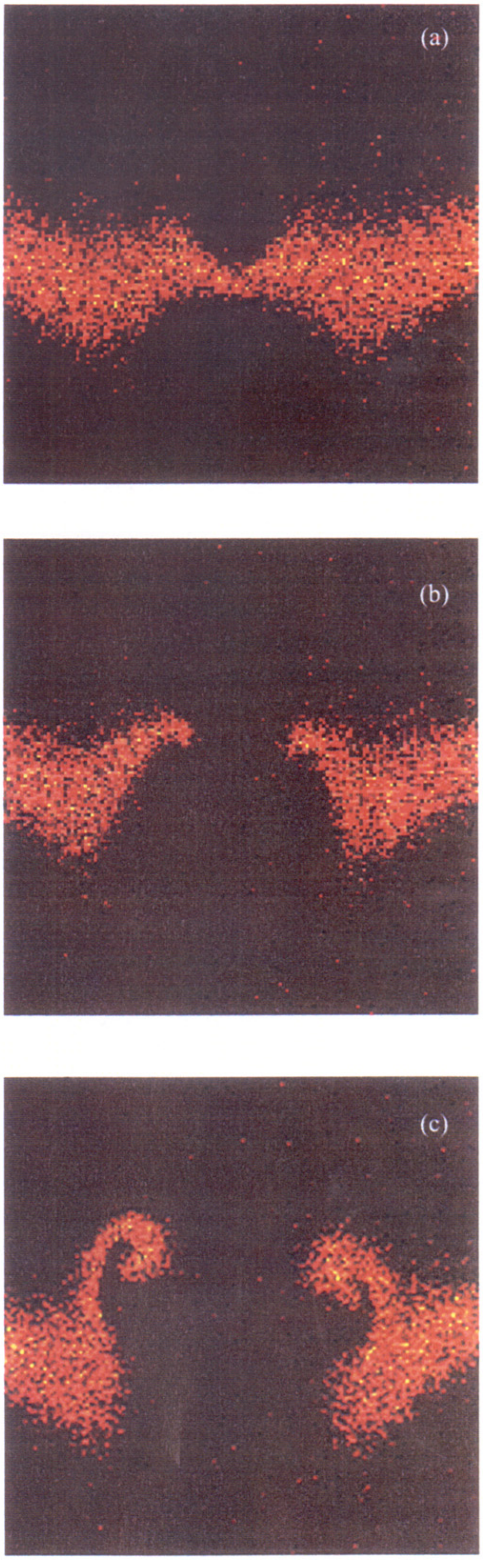

Fig. 3. OH-PLIF images obtained during interaction of flame with vortices coming from both fuel and air sides, simultaneously. (a) t ms, (b) t+1 ms, (c) t+2 ms.

(c)2002 American Institute of Aeronautics & Astronautics or Published with Permission of Author(s) and/or Author(s)' Sponsoring Organization.

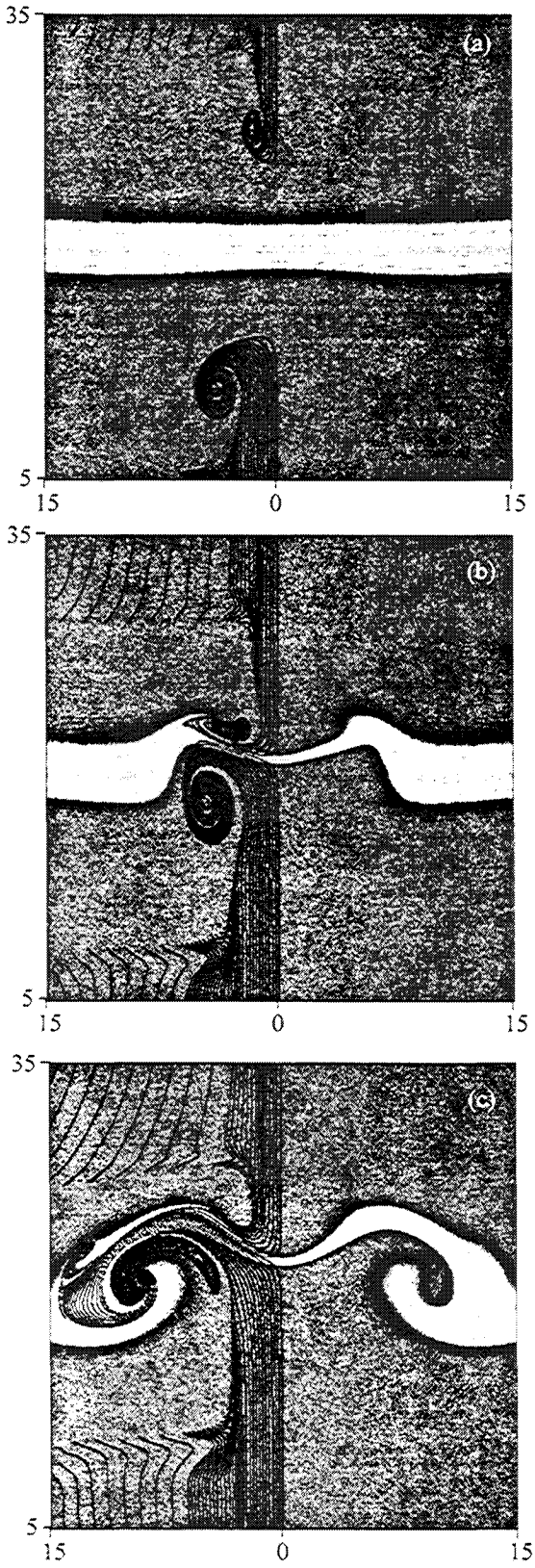

Fig. 4. Weak interaction between slowly traveling vortices and diffusion flame. Particle locations are superimposed on temperature. (a) 10, (b) 16.5, and (c) 23.0 ms.

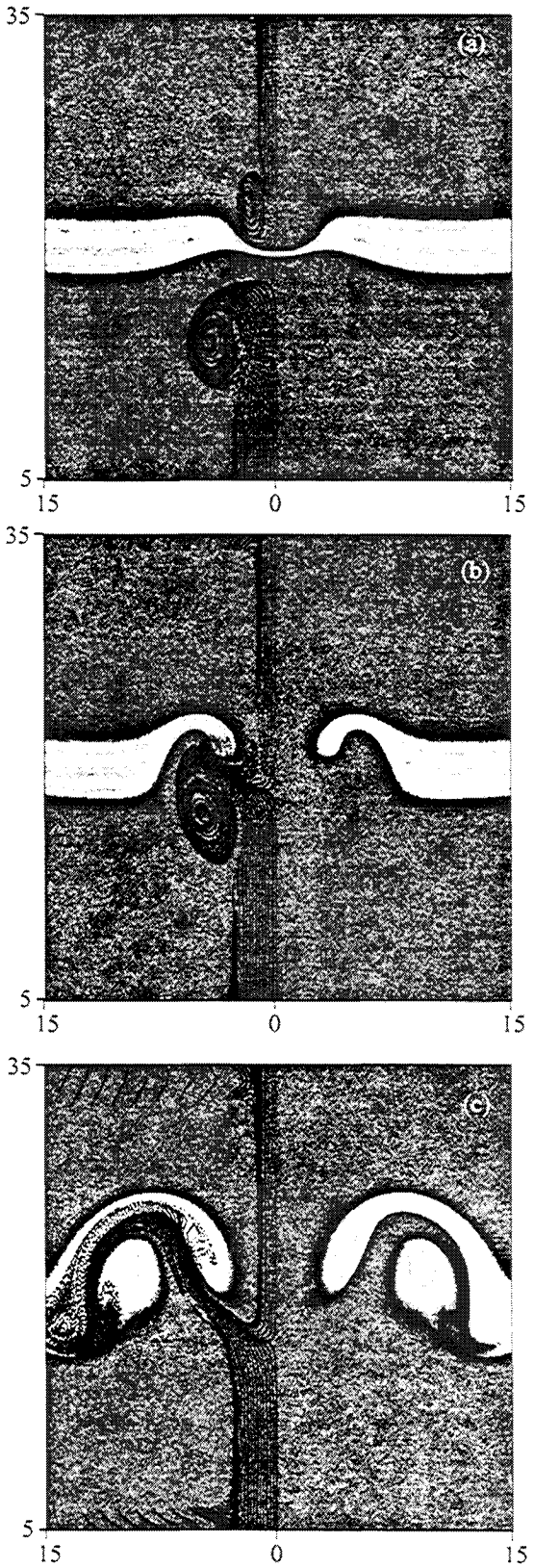

Fig. 5. Moderate interaction between quickly moving vortices and flame. Particle locations are superimposed on temperature. (a) 4, (b) 4.6, and (c) 6.2 ms.

(c)2002 American Institute of Aeronautics & Astronautics or Published with Permission of Author(s) and/or Author(s)' Sponsoring Organization.

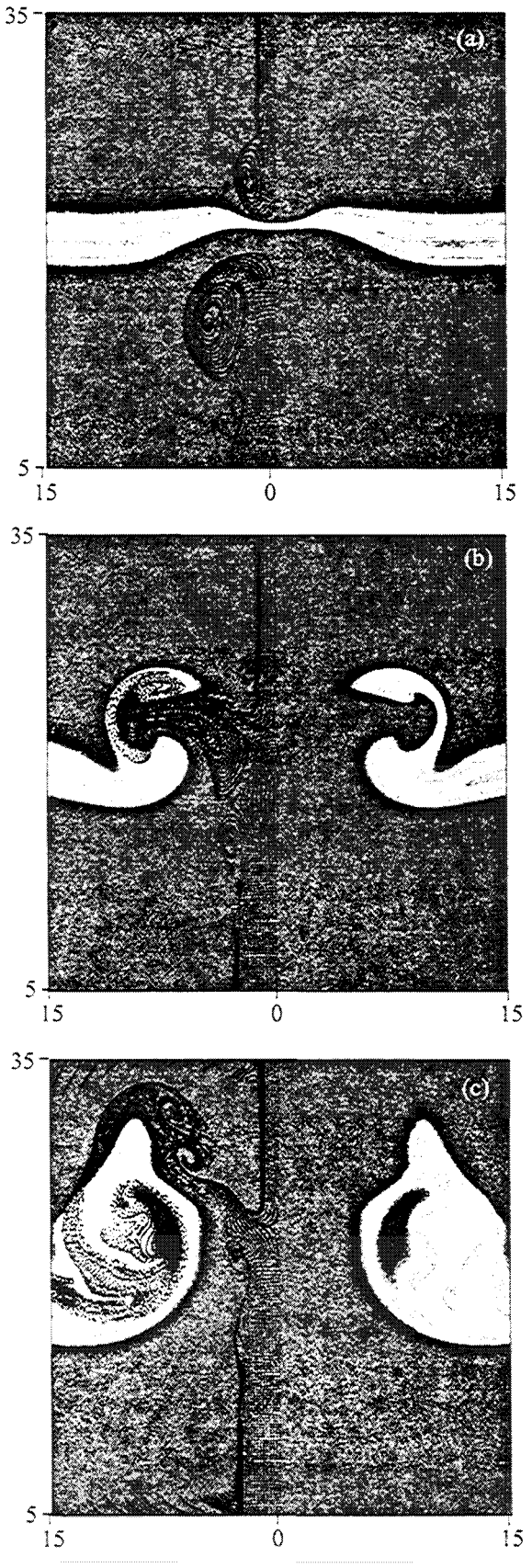

Fig. 6. Strong interaction between quickly moving vortices and flame. Particle locations are superimposed on temperature. (a) 3.7, (b) 4.6, and (c) 6.2 ms.

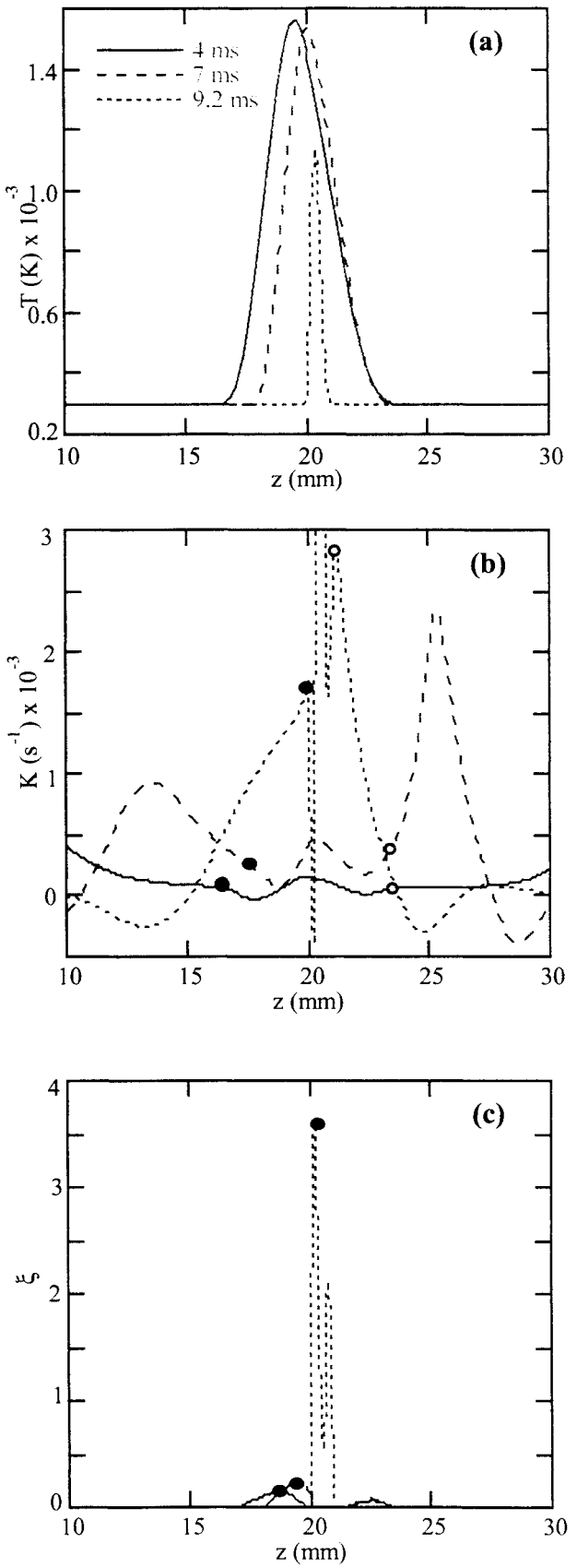

Fig. 7. Flame structure along stagnation line at different phases of multi-vortex/flame interaction of Case 3. (a) Temperature, (b) strain rate, and (c) scalar dissipation rate.

(c)2002 American Institute of Aeronautics & Astronautics or Published with Permission of Author(s) and/or Author(s)' Sponsoring Organization.

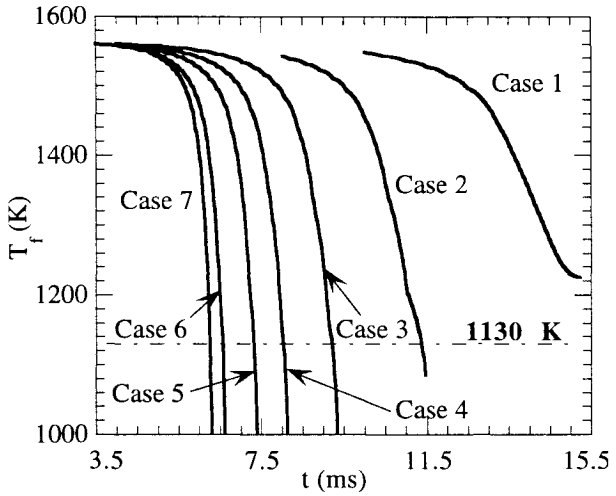

Fig. 8. Fall in peak temperature along stagnation line during interactions of flame with vortices traveling at different velocities.

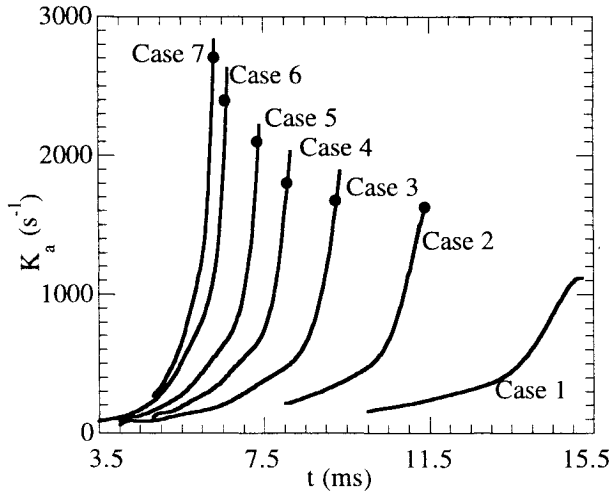

Fig. 9. Increase in air-side strain rate along stagnation line during interactions of flame with vortices traveling at different velocities.

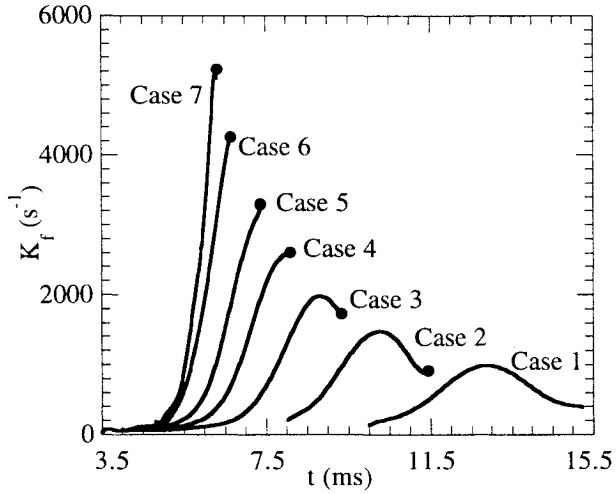

Fig. 10. Increase in fuel-side strain rate along stagnation line during interactions of flame with vortices traveling at different velocities.

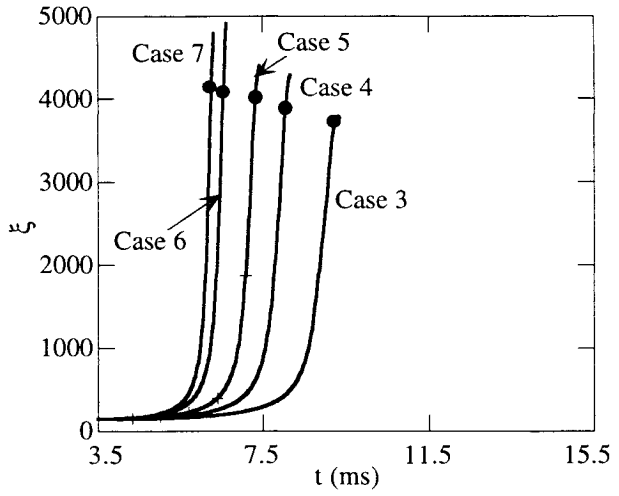

Fig. 11. Increase in scalar dissipation rate at peak-temperature location along stagnation line during interactions of flame with vortices traveling at different velocities.

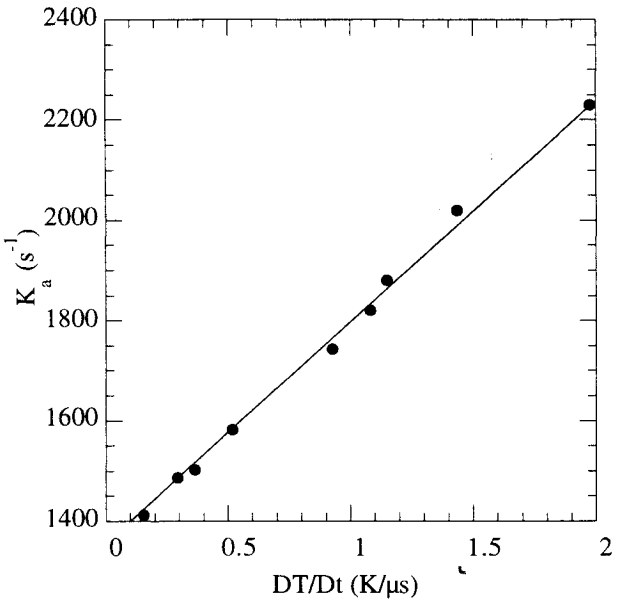

Fig. 12. Relationship between air-side strain rate imposed on flame just prior to its quenching and the rate of decrease in flame temperature.

Vortex-induced flame extinction in two-phase counterflow diffusion flames with CH planar laser-induced fluorescence and particle-image velocimetry

Alix Lemaire, Terrence R. Meyer, Katharina Zähringer, Juan C. Rolon, and James R. Gord

Here the interaction between a laminar two-phase, non-pre-mixed counterflow flame and a vortex is examined. Special emphasis is given to the influence of different flame and vortex parameters on the extinction behavior of the flame. Simultaneaous planar laser-induced fluorescence of the CH radical layer produced by the flame and particle-image velocimetry measurements of the flowfield are used to characterize the flame–vortex interaction. These simultaneous diagnostics are used for the first time in this configuration. The extinction processes occurring during the flame–vortex interaction can be analyzed by this method, especially the influence of strain at the flame surface. The influence of the droplets on the extinction behavior appears clearly compared with a fully gaseous flame. The spray flame is weaker and extinguishes earlier than does a gaseous flame. In the measurements an additional broadband signal in the vicinity of the CH layer is probably due to the induced fluorescence of polycyclic aromatic hydrocarbons, excited at the same wavelength. © 2003 Optical Society of America

OCIS codes: 120.1740, 300.2530, 000.2170, 010.7060, 120.7280.

1. Introduction

The interaction between a vortex and a flat laminar diffusion flame is generally used to simulate a number of features that are common in turbulent combustion, such as dynamic strain, stretch, and curvature.[1] In this investigation the extinction processes during two-phase flame–vortex interactions are studied by use of particle-image velocity (PIV) and planar laser-induced fluorescence (PLIF) in a non-pre-mixed *n*–heptane methane—air flame. Phenomena such as flame extinction and microvortex–flame behavior have been studied by use of gaseous fuels, as well as experiments validating numerical simulations.[2–4] These previous studies have shown that the dynamic interaction between a laminar flame and a vortex may be examined by laser-induced fluorescence of the hydroxyl (OH) layer produced by the flame.

The CH radical is also a good candidate for these dynamic studies, since the concentration distribution constitutes a narrow layer in the flame region. Watson *et al.*[5] and Donbar *et al.*[6] used CH PLIF as a marker for the fuel-decomposition zone in methane–air diffusion flames and found its relatively thin reaction zone to be a good marker for the flame front. Unlike in previous measurements in premixed flames,[7] these studies indicated that CH PLIF did not exhibit "false" flame extinction: Gaps in the CH PLIF layer also corresponded to gaps in the OH layer. In the current study, phase locking of the vortex event and imaging system allows the determination of the time-dependent CH profile during vortex impingement and subsequent local flame extinction. Furthermore, phase locking allows one to obtain average measurements without significant degradation of spatial resolution. Thus CH PLIF in the current study is not just a flame marker but is also a qualitative evaluation of the CH intensification or extinction.

Santoro *et al.*[8,9] performed measurements of formaldehyde PLIF and centerline velocity during extinction of counterflow methanol-spray diffusion flames, considering the effect of air and fuel-side vortices.

At the time of this research, T. R. Meyer (trmeyer@innssi.comis) is with Innovative Scientific Solutions Incorporated, Dayton, Ohio 45440. A. Lemaire, K. Zähringer, and J. Carlos Rolon (rolon@em2c.ecp.fr) were with the Laboratoire E.M2.C., Centre Nationale de la Recherche Scientifique/Ecole Centrale Paris, 92295 Châtenay-Malabry, France. J. R. Gord is with the Air Force Research Laboratory, Propulsion Directorate, Wright-Patterson Air Force Base, Ohio 4533-7103. K. Zähringer is now with Lehrstuhl für Strömungsmechanik, Universität Magdeburg, 39106 Magdeburg, Germany.

Received 20 May 2002; revised manuscript received 10 September 2002.

0003-6935/03/122063-09$15.00/0

© 2003 Optical Society of America

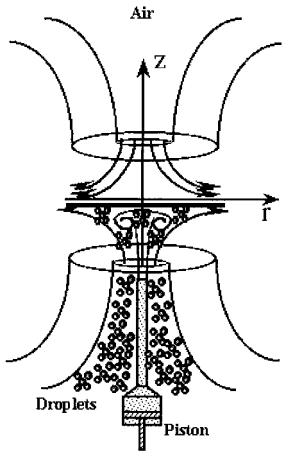

Fig. 1. Two-phase counterflow burner in a non-pre-mixed configuration with liquid fuel coming from the lower nozzle.

In studies of turbulent diffusion flames, however, Watson *et al.*[5] cited the prominence of large-scale fuel-side vortices leading to bulges in the CH profile prior to local extinction. The current study therefore focuses on local flame extinction initiated by fuel-side vortices and further differs from the study of Santoro *et al.*[8] in that it considers the effects of both global mixture ratio and vortex strength on the extinction process.

Since the concentration of the CH radical is rather low, the fluorescence detection is difficult. A second difficulty in the detection of CH fluorescence arises from the short CH fluorescence lifetimes. In a recent study, Renfro *et al.*[10,11] reported CH-LIF concentration measurements in atmospheric hydrocarbon flames by using a picosecond laser. In particular, they reported CH fluorescence lifetimes of the order of 2–5 ns. Finally, the presence of species, which fluoresce with the same UV (390 nm) excitation wavelength, also makes the interpretation of CH fluorescence signals difficult. These additional signals may come from polycyclic aromatic hydrocarbons (PAHs), whose formation is typically observed on the fuel-rich side of diffusion flames.[12] In this paper we show that the fluorescence signals from CH and PAH can be separated and, despite these difficulties, the CH signal may be correctly analyzed.

2. Experimental Setup and Procedure

A. Burner System

The experimental device used for this paper can be compared with the one used in previous studies[2,13] with gaseous flows. The main change in the present case is the addition of an atomizer to generate a spray. The counterflow burner (Fig. 1) comprises two axisymmetric opposite-flow nozzles. Each nozzle has a diameter of 20 mm and is surrounded by a 40-mm-diameter co-flow. The reactant mixture is injected through the central nozzle while a nitrogen co-flow shields the flame from interactions with ambient air. The distance between the nozzle outlets is set to 30 mm. The fuel flow is fed through the lower nozzle while air goes through the upper nozzle, both at room temperature and with atmospheric pressure allowing the stabilization of a flat laminar diffusion flame in the centerplane between the two burners.

To generate the vortex ring, a 3.7-mm inner-diameter tube is installed concentrically within the lower nozzle. It is connected to a cylinder, containing a piston, which in turn is attached to an actuator, supplied by a voltage ramp. When the piston moves upward, a single toroidal vortex is generated at the tip of the tube and travels upward to the flame within the surrounding flow. A continuous flow is supplied to the tube such that, in the absence of a vortex, the exit velocity matches the velocity of the flow from the surrounding injection nozzle. To conserve the total fuel-mass flow rate, the vortex tube flow is supplied from the main fuel flow and is adjusted with a bypass valve to get a flat flame. The vortex properties can be varied by means of changing either the rise time τ_r or the magnitude V_r of the voltage that is fed to the solenoid actuator, obtained by amplifying the output of a digital arbitrary-waveform generator. If full displacement is maintained, the actuator power consumption is considerable. Consequently, a negative potential is first supplied, causing the vortex to be withdrawn from the flame. The flame needs 0.4 s to recover from this initial disturbance. A positive ramp potential with parameters τ_r and V_r is then applied and maintained at the maximum value V_r during the vortex development. The current is set to zero afterward. The total duration of this process is 1 s. In our experiment, the rise time is always equal to 10 ms and only the amplitude is changed.

An air nebulizer provides the liquid fuel spray to the combustible flow. This atomizer consists of two needle tubes placed at an angle of 90° close to each other. The horizontal needle tube creates a high-velocity air jet that creates a depression just above the vertical tube. This depression draws the liquid up by capillarity. The liquid phase breaks up into fine droplets. This system is enclosed in a recipient that contains the liquid *n*–heptane. The largest particles impact the wall, and the finest are entrained in the gas flow. These air nebulizers, widely described in the literature, produce weakly dispersed micrometer-sized sprays. Their mean diameters do not depend on the atomized liquid.[14] The mean droplet diameters in our experiment are between 2.43 and 2.83 μm.

The different interactions used in our study can be characterized by several parameters. The mass fractions $Y_{\mathrm{Ox},0}$ and $Y_{\mathrm{Fu},0}$ of the injected reactant mixtures, the injection velocities V_{Ox} and V_{Fu}, and the ratio y between the mass of doping methane and the total mass of fuel characterize the counterflow diffusion flame. The mass flow rate of *n*–heptane is kept constant and is equal to 32 mg/s. The deduced volumetric density of droplets inside the vortex tube is equal to $9 \times 10^6\ \mathrm{m}^{-3}$. Thus the spray is not a dense spray. From these values the global mixture ratio Φ, defined as the ratio between initial mass fraction

Table 1. Flame Parameters Used in the Experiments Comparing Different Global Mixture Ratios[a]

Case	$Y_{Ox,0}$	$Y_{Fu,0}$	y	v_{Fu} [m s^{-1}]	v_{Ox} [m s^{-1}]	Φ
1	0.232	0.24	0.53	0.7	0.45	3.97
2	0.232	0.27	0.57	0.7	0.45	4.43
3	0.232	0.30	0.60	0.7	0.45	4.90

[a]Vortex A: $\Delta V_{vort} = 38$ [mm^3]; $\Gamma_{vort} = 8$ [cm^2/s].

of fuel $Y_{Fu,0}$ in the fuel side and initial mass fraction of oxygen $Y_{Ox,0}$ in the oxidizer side, divided by the corresponding values for stoichiometric combustion can be deduced. The rise time τ_r of the ramp voltage applied to the piston and the volume ΔV_{vort} of the gas ejected by the piston characterize the vortex. Analytical research[15] has shown that, under conditions that our vortices verify, the vortex circulation Γ_{vort} can be defined as

$$\Gamma_{vort} = \frac{(\Delta V_{vort})^2}{\tau_r d^4}, \quad (1)$$

where d is the inner diameter of the generator vortex tube. Thus the strength of a vortex is higher with high ramp voltage and with small rise time. The parameters used in our experiments are summarized in Tables 1 and 2.

B. Particle Image Velocimetry

Particle image velocimetry (PIV) has been used in studies of premixed[16] and nonpremixed[17,18] vortex–flame interactions to visualize the vortex flow field and to determine the strain field acting on the flame. In the current study, digital cross-correlation PIV is achieved through Mie scattering of silicon dioxide particles in the air stream and of the *n*–heptane droplets in the fuel stream. The silicon dioxide is used because of its relatively low aggregate size (1–5 μm), high melting point (1700 °C), and porous structure. Because the *n*–heptane droplets are sufficiently small (2.43–2.83 μm) and numerous, the spray can be used directly for the PIV measurements.

A double-pulsed Nd:YAG laser is used to generate overlapping 532-nm beams with 200 mJ of energy per beam. As shown in Fig. 2, the PIV beams are expanded in the vertical direction with an $f = -12.7$-mm cylindrical lens and are then recollimated with a spherical lens ($f = 500$ mm). The PIV sheet thickness at the test section is approximately 0.5 mm. Pulse intervals are varied from 0.050 to 0.2 ms depending on the speed of the vortex, in order to keep particle displacements in a reasonable range. Duel-frame digital imaging of the two PIV signals is achieved with a 1008 × 1018 (9.07mm × 9.16mm) array Kodak Megaplus ES1.0 camera with 3.4 μm × 7 μm pixels. An AF Micro Nikkor 105 mm f/2.8 lens and a 36-mm extension ring are used to achieve a 2.2:1 image-to-CCD magnification ratio. Images are processed with custom-designed software at Innovative Scientific Solutions, Incorporated. A 64 × 64 pixel interrogation region and a 50% overlap are used to generate a 30 × 30 vector field across the image.

Table 2. Vortex Parameters Used in the Experiments Comparing Different Vortex Strengths[a]

Case	ΔV_{vort} [mm^3]	Γ_{vort} [cm^2/s]
A	38	8
C	49	13

[a]$Y_{Ox,0} = 0.232$; $Y_{Fu,0} = 0.27$; $y = 0.57$; $v_{Fu} = 0.7$ [m s^{-1}]; $v_{Ox} = 0.45$ [m s^{-1}]; $\Phi = 4.43$.

C. CH Planar Laser-Induced Fluorescence System

The optical arrangement for the CH detection by PLIF is also presented in Fig. 2. The laser system is composed of a Nd:YAG laser (1064 nm), doubled to 532 nm and pumping a tunable dye laser (Rhodamine 640). Finally, the dye laser beam is frequency mixed with the Nd:YAG fundamental in order to obtain a wavelength corresponding to the $B^2\Sigma^- – X^2\Pi(0,0)$ absorption band between 388.5 and 391 nm. The $Q_1(5)$ transition of this band is excited at 389.5 nm. The laser system provides pulses of ~7-ns duration, whose mean energies are between 15 and 20 mJ.

After passage through two prisms, a cylindrical lens ($f = 200$ mm) is used to form a laser sheet that is recollimated by the same spherical lens ($f = 500$ mm) as used for the PIV sheets. This optical system produces parallel and superposed PIV and CH laser sheets in the center of the burner. The CH laser sheet has a height of ~20 mm and a thickness of 0.3 mm. The energy distribution inside the CH laser sheet is measured by Rayleigh scattering on nitrogen. The flame–vortex interaction region has a maximum size of 10 mm. The flame position during the whole interaction remains in the central part of the laser sheet. The power density variation inside this region does not exceed 5%. Spatial wing effects can be excluded in this way.

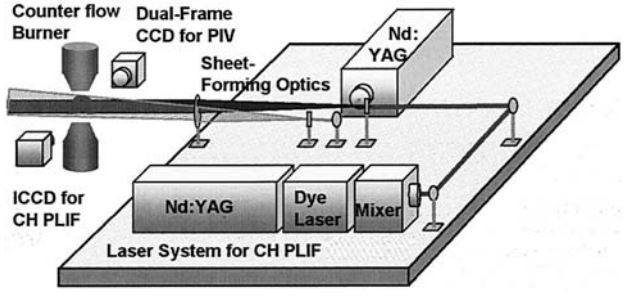

Fig. 2. Experimental setup for the simultaneous PIV and CH-PLIF measurements in two-phase counterflow diffusion flame.

Fluorescence from the A—X (0,0) and A—X (1,1) bands is recorded. These bands are chosen because of their favorable isolation from background scattering.[19] A combination of a 410-nm high-pass and a 450-nm low-pass filter is used to separate the CH LIF signal from the excitation wavelength. Laser-induced fluorescence signals are detected at 90° to the direction of the laser sheet by an intensified CCD camera facing the PIV camera on the other side of the flame (Fig. 2). The intensifier gate width is 20 ns. The CH PLIF signal is collected with a 512 × 512 array Roper Scientific PI-Max intensified CCD camera with a 58-mm $f/1.2$ Noct-Nikkor lens. An image-to-CCD magnification ratio of 2.1:1 is achieved with a 20-mm extension ring. To improve signal-to-noise ratio, 2 × 2 binning of the CCD array is performed. The optical region covered by each binned pixel is 100 μm. The resulting limiting resolution based on the Nyquist criterion and modulation transfer function of the lens was found to be ~215 μm. By definition, this is the smallest object that the camera can resolve. A CH layer thickness that is 234 μm or less cannot reliably be resolved, but the nonperturbed CH layer (thickness, ≈250 μm) is fully resolved by the CH detection scheme.

A region of approximately 20 × 20 mm is imaged. The two cameras are aligned in order to image the same region of the flame, with approximately the same magnification. Their position is calibrated by ruler images. Six characteristic points on these images are chosen to do an image transformation, allowing the exact superposition of the PIV and the CH PLIF images. To avoid the effect of the pulse-to-pulse energy fluctuations, ten images are recorded and averaged.

To minimize effects of reflections and camera noise, a background image is subtracted from the raw image, each time CH data is extracted from the LIF images (e.g., signal intensity during the extinction process). The CH visualization can slightly be influenced by quenching effects even at high laser fluences as used here. However, addressing this issue is beyond the scope of this work.

D. Synchronization System

The CH PLIF and two PIV laser pulses, the PIV and CH LIF imaging systems, and the vortex generation have to be synchronized. These events have two different frequencies, the Nd:YAG lasers nominal repetition rate of 10 Hz and the periodic vortex generation rate of 1 Hz. Owing to the internal synchronization of the PIV system (two lasers, camera, and image acquisition), a rather complicated synchronization scheme was necessary. The core of the PIV system is the PIV processor. Inside the processor, the synchronization unit provides a physical platform for communication signals to and from both PIV lasers and camera and from the external event trigger. The image acquisition has to be synchronized with the vortex event. The synchronization unit instructs the laser cavities when to fire their flash lamps and when to allow their Q switches to emit laser radiation, and it also controls the camera shutter. The Kodak Megaplus ES1.0 camera is run on an asynchronous mode with a short activation delay of 20 μs. Thus when measurements are taken, the delay between the vortex external trigger and the first pulse can be as little as 20 μs.

To synchronize the whole experiment, the PIV YAG laser system served as the main trigger source. Its flash lamp externally triggers a pulse generator, which generates a 10- and a 1-Hz signal. The 10-Hz signal is used to trigger the CH PLIF laser system, by passage through a delay generator, creating the appropriate timing signals for the laser. The timing of the CH laser pulse occurs 20 μs before the second PIV laser pulse to avoid particle scattering. The 1-Hz signal is used to drive the vortex generator, by triggering an arbitrary waveform generator that outputs the 1-s waveform described above, which is amplified and fed into the piston actuator to generate the vortex. The 1-Hz signal also triggers a delay generator, which sends two appropriate signals, one to the controller of the intensified CH camera, another to the PIV synchronization unit that controls PIV imaging. The PIV system is thus triggered by a signal that is linked to itself and to the vortex event.

The initial time of the flame–vortex interaction is defined when the vortex starts to perturb the flame. As discussed in Ref. 2, the vortex generation is perfectly reproducible. To get the temporal evolution of the vortex interacting with the flame, a sequence of images is collected on identical consecutive vortices following a periodic procedure. At each 1-s period, one instant of the vortex life is recorded, giving several images at the same sequence time. The entire vortex sequence is obtained by adjustment of the relative timing of piston actuation and laser diagnostics.

3. Results

As shown on Fig. 3, the typical images registered with the intensified CCD exhibit two different signal layers. The CH radical layer is clearly visible as a thin layer. Underneath this CH layer, an additional signal can be recognized, which is rather strong and whose intensity is also growing with increasing global mixture ratio, n–heptane mass fraction, and laser energy. This signal may be attributed to the fluorescence of polycyclic aromatic hydrocarbons (PAH), which are formed on the fuel side.[12] Because of the rather low CH fluorescence signal, the signal-to-noise ratio is low. Slightly detuning the laser wavelength from the $Q_1(5)$ transition allows us to collect a nonresonant background of the corresponding CH signal (Fig. 3, center). Subtracting the off-resonant averaged image from the on-resonant averaged image results in the difference image shown in Fig. 3 (right), which exhibits a rather good signal-to-noise ratio.

Interference from PAH is evident prior to vortex impingement for all the conditions of the current study. Figure 4 presents the intensity profiles along the center line (labeled pixel 128) and a line in the outer part of the flame (⅔ from the center distance,

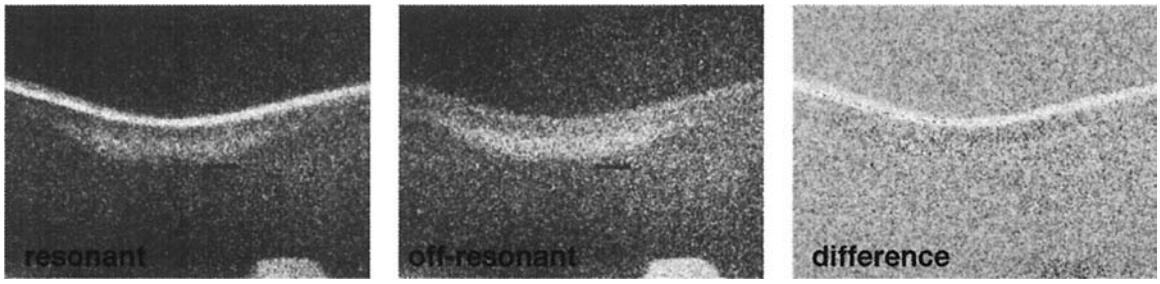

Fig. 3. Raw on-resonant image, raw off-resonant image, and the difference image used for evaluation measurements, for a nonperturbed fully gaseous case with $\Phi = 4$ and $y = 0$.

labeled pixel 42) for two different global mixture ratios 1 and 3 (see Table 1) with the weak vortex A. The left plots correspond to a case in which the vortex has just started to wrinkle the CH layer at 8 ms after vortex arrival, and the right plots correspond to the later time 18 ms. The position shifted from the centerline corresponds to a part of the flame not submitted to the high strain resulting from the vortex. For Case 1, that of a small global mixture ratio and of a weakly wrinkled flame, the CH LIF signal is clearly separated from the PAH signal. As the global mixture ratio increases, the PAH signal increases and thickens. Indeed, for $\Phi = 4.90$ (Case 3) the CH peak is nearly overwhelmed by the PAH signal. It is hard to separate the CH signal from the PAH signal at high global mixture ratio for the flat flame. Yet at the centerline, under the vortex-induced strain (bottom right image), the PAH signal has disappeared

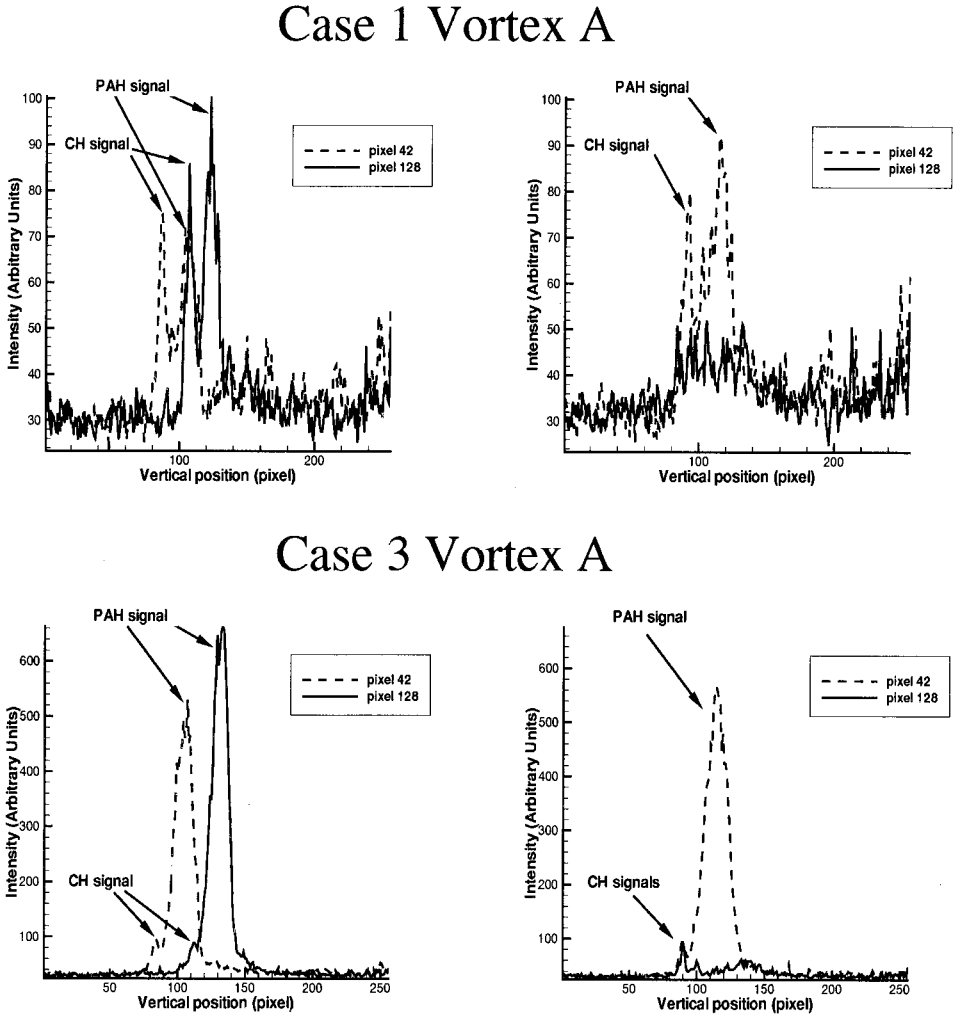

Fig. 4. Intensity profiles for $\Phi = 3.97$ (upper plots) and $\Phi = 4.90$ (lower plots) flames interacting with vortex A at the centerline (labeled pixel 128) and at a location ⅔ shifted from the centerline (labeled pixel 42) at two times $t = 8$ ms (left plots) and $t = 18$ ms (right plots).

faster than the CH signal and during the CH extinction process interference with the PAH signal is very weak. At the shifted position not submitted to vortex strain the PAH signal is quite strong and still overwhelms the CH signal. When the vortex interacts with the flame, the PAH layer disapears and only the CH layer remains visible until the flame extinguishes in the center. The disappearance of the PAH layer prior to the CH layer indicates further that the determination of the relevant time scale of flame response to dynamic strain depends on the selected species. CH PLIF is well suited for the fuel-side vortices of the current study because of is spatial proximity to the fuel inflow (relative to other species such as OH) as well as its presence in the central region of the flame. These plots emphasize that the CH layer supports, more easily and for a longer time, the strain induced by the vortex. The right plots also show that at the later time the CH layer is extinguished (as low as the background) for the global mixture ratio of 3.97, whereas the CH layer is not extinguished for the global mixture ratio of 4.90. The results of a numerical simulation, developed by Katta and Roquemore,[20] and currently including the model of Wang and Frenklach,[21] for the formation of one-to-two–ring PAH species, also show this separation of CH and PAH profiles (Fig. 5). Rather than plot the myriad of PAH compounds against the CH profile, it is sufficient to show the location of benzene (C6H6), which represents the location and spatial width of the entire PAH layer. Figure 5 shows a spatial separation of ~0.7 mm between the CH and C6H6 peaks. In the experimental data, the mean separation of ~1 mm is slightly higher.

Figure 6 represents a complete sequence of flame–vortex interactions at a global mixture ratio of $\Phi = 4.43$ (Case 3) with a strong vortex (C in Table 2). The CH radical layer can be distinguished as the upper signal; the PAH signal is situated below. The PIV measurements are superposed to the PLIF images. It can be seen in these figures that the flame wrinkles more and more as the vortex propagates toward the flame. After ~4 ms the CH layer intensity starts to diminish. The CH layer appears fully extinguished at its center at 5.5 ms and the hole created in the CH layer continuously increases. The vortex core remains under the CH layer until 8 ms, a time when the CH layer is fully extinguished and the hole created is quite large. The vortex passes through the flame between 8 and 13 ms. At 23 ms the vortex, which passed through the flame, entrains and elongates the edges created in the CH layer. These images are raw images from which no dynamic background has been substracted. This is why the PAH signal is visible but maybe also some Mie scattering on droplets in the center of the image. The PAH are formed around the droplets cloud, where the temperature is high and the liquid *n*–heptane evaporates. The high concentration of PAH seems to be located between the cold spray and the high-temperature flame. The thickness of the CH layer does not seem to be affected by the approach of the vortex. Rather, it undergoes a steady decrease in intensity until extinction. Similar results have been reported in turbulent flames, for which the CH layer thickness does not vary as a function of turbulence intensity.[22]

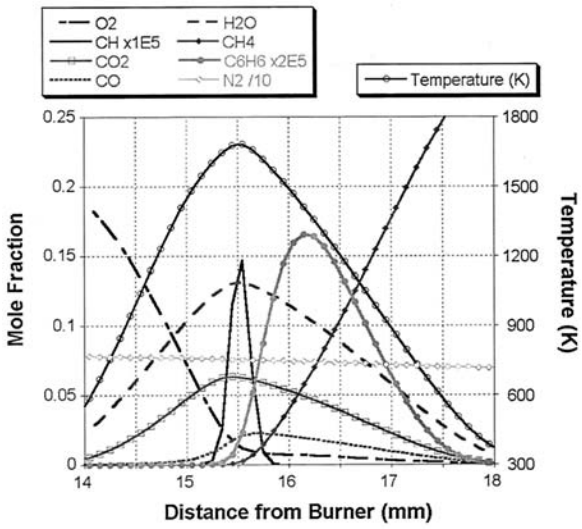

Fig. 5. Numerical calculation of a methane–air counterflow diffusion flame. The separation of the CH and C_6H_6 layers appears clearly in the calculation.

The temporal evolution of the CH signal in the center of the flame is also represented in Fig. 7 for Cases 2A and 2C as well as a fully gaseous flame corresponding to Case 2C. The CH intensity data were calculated with a region of 4×6 pixels at the centerline of the CH layer averaging on ten images. For the stronger vortex C, extinction starts ~5 ms after the vortex has touched the flame, and it is also quicker, which can be seen on the strong negative slope of the curve. In the case of the weak vortex A, the CH intensity decreases from ~8 ms up to 20 ms, where complete extinction is reached. The fully gaseous flame seems to be stronger than the two-phase flame. The two-phase flame extinguishes earlier. The vortex-induced flame's wrinkling and extinction can be explained by the unsteady normal strain rate that acts upon the flame as the vortex approaches.[23] The strain rate data of Fig. 8 were calculated with forward differencing of the normal centerline velocity and an average of five images per data point. As shown in Fig. 7 and 8, a sudden increase in the peak fuel-side normal strain rate leads to a significant drop in the CH LIF intensity. Extinction of the CH layer for vortex A takes ~12 ms. For the case of vortex C the strain rate increase near 5 ms is more dramatic, taking place in less than 1 ms. The CH extinction process appears to begin at nearly the same moment and takes only ~3 ms for completion (rather than the 12 ms for vortex A). This fourfold decrease in the extinction time scale is not expected, considering that vortex C has a peak fuel-side strain rate two times higher than vortex A (750 1/s

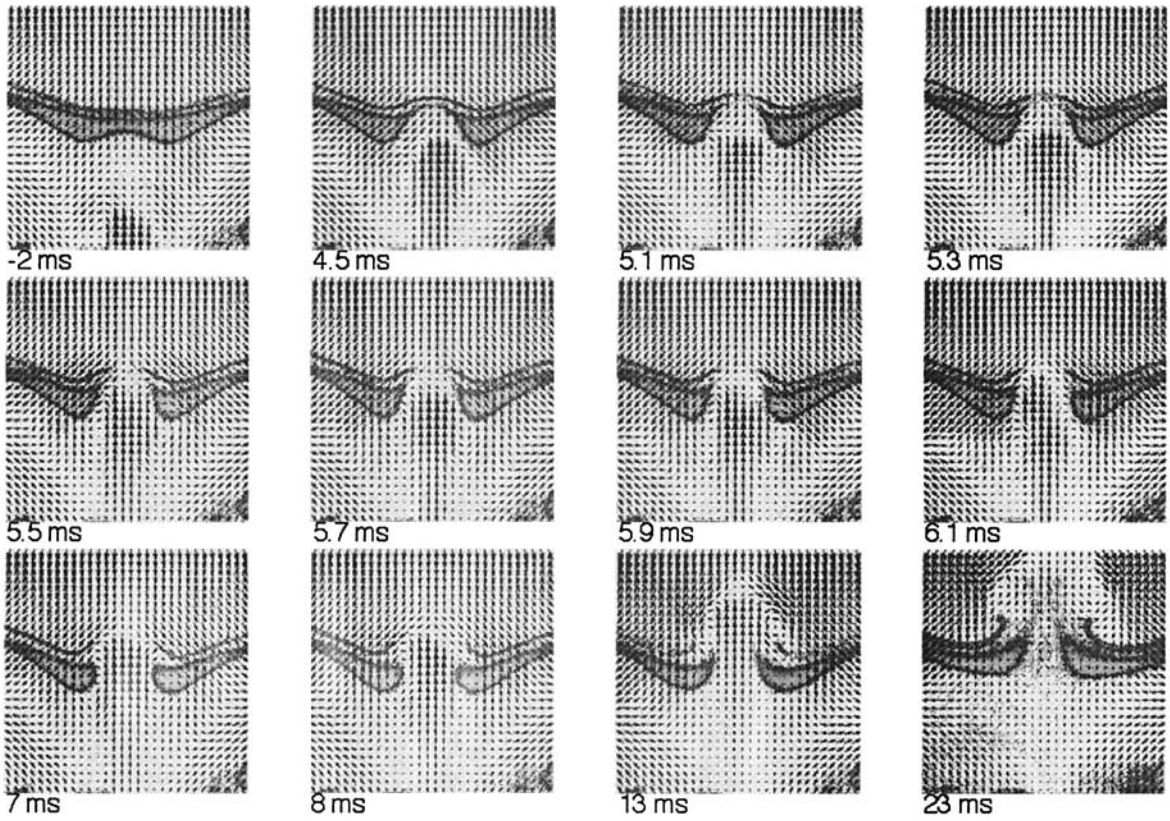

Fig. 6. Time series of flame–vortex interaction at $\Phi = 4.43$ and vortex C (Table 2).

for A and 1573 1/s for C). This suggests that dynamic strain may have an important influence on flamelet behavior. In the gaseous case the peak strain rate is slightly lower than for the spray flame (1363 1/s). This may explain the delay for the beginning of extinction compared with the case of the spray flame. Energy losses due to the evaporation of droplets are also responsible for this delay.

The different extinction behavior of the gaseous and spray flames is also visible in Fig. 9. The normalized flame surface determined from the CH PLIF images at the position of the CH signal maxima decreases earlier for the spray flame. After 8 ms the flame surface area reaches a plateau and increases after 18 ms. This increase occurs because the flame edges are entrained by the vortex after extinction, thereby increasing the total surface area and forming a cylindrical flame in the central region. The flame surface of the methane–air flame starts decreasing ~2 ms later and does not show any constant plateau.

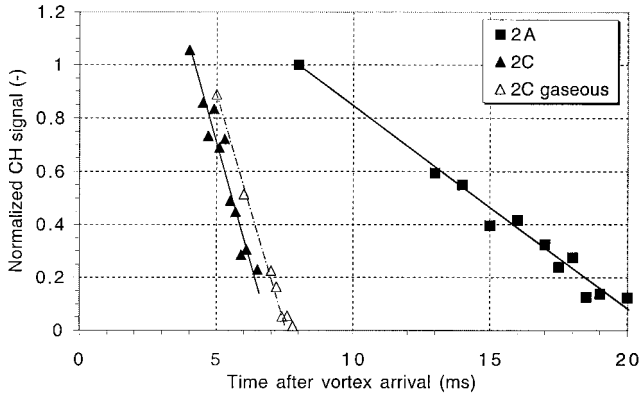

Fig. 7. Temporal evolution of the CH signal in the center of the flame, for the same global mixture ratio of 4.43 and the two-phase flame (Case 2) comparing the influence of two different vortices A and C, and for the same vortex C comparing the influence of the droplets with the fully gaseous flame.

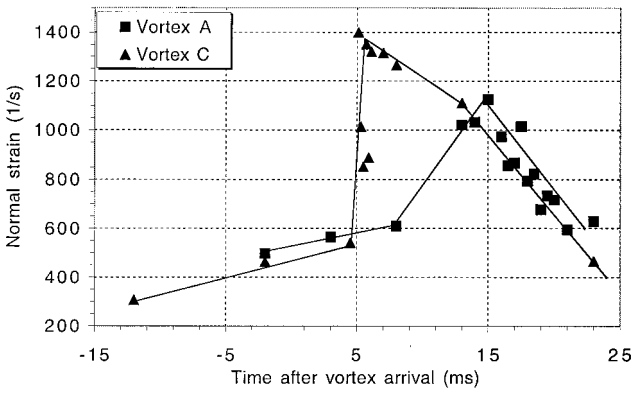

Fig. 8. Temporal evolution of the peak fuel-side normal strain rate in the center of the flame, comparing for the same global mixture ratio of 4.43 and the two-phase flame (Case 2) comparing the influence of two different vortices A and C.

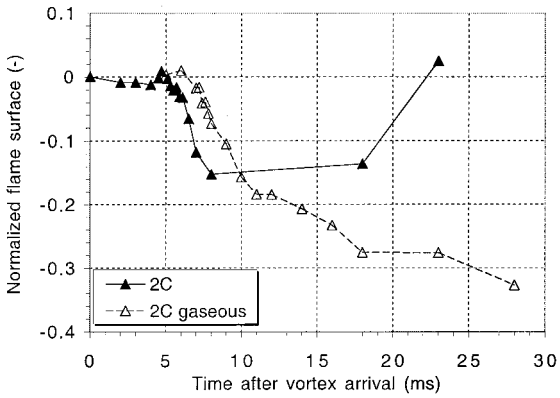

Fig. 9. Temporal evolution of the flame surface during the flame–vortex interaction for the same global mixture ratio of 4.43 and the same vortex C, comparing the influence of the droplets with the fully gaseous flame.

4. Conclusions

The results of the present investigation show that the dependence of extinction on strain can be well illustrated by the simultaneous measurements of velocity by means of PIV and the CH LIF signal evolution. The fluorescence measurements show two different signal layers, the CH layer and a second layer that is probably due to PAH. It is possible to discriminate the CH fluorescence signals from the PAH fluorescence in high-strain fields as induced by a vortex. The global mixture ratio has a strong influence on flame extinction. The transient effects of strong vortices, and the induced flame wrinkling, are represented by the sudden CH fluorescence decay, simultaneously followed by the flame extinction. Despite possible quenching effects on the CH fluorescence signal, the CH layer is clearly sensible to the strain induced by a vortex. The CH disappearance is observed in a region where the dynamic strain rate is high. This is also valid for the PAH disappearance. The droplets convected by the vortices strongly affect the extinction behavior of flames. Flame extinction caused by a two-phase vortex is faster but flame surface recovery is also quicker than in the gaseous flames.

This research was supported by U.S. Air Force Contract F33615-00-C-2068 [U.S. Air Force Office of Scientific Research/International Research Initiative (Julian Tishkoff, Program Manager)] and French DGA/ONERA PEA-number 98703-TITAN in a French–U.S. collaborative program.

We acknowledge V. R. Katta of Innovative Scientific Solutions, Inc., and Campbell Carter of the Air Force Research Laboratory for their help and useful dicussions.

References

1. P. H. Renard, D. Thevenin, J. C. Rolon, and S. Candel, "Dynamics of flame/vortex interactions," Prog. Energy Combust. Sci. **26,** 225–282 (2000).
2. J. C. Rolon, F. Aguerre, and S. Candel, "Experiments on the interaction between a vortex and a strained diffusion flame," Combust. Flame **100,** 422–429 (1995).
3. G. J. Fiechtner, P. H. Renard, C. D. Carter, J. R. Gord, and J. C. Rolon, "Injection of single and multiple vortices in an opposed-jet burner," J. Visualization **2,** 331–341 (2000).
4. P. H. Renard, J. C. Rolon, D. Thevenin, and S. Candel, "Investigations of heat release, extinction, and time evolution of the flame surface for a non-premixed flame interacting with a vortex," Combust. Flame **117,** 189–205 (1999).
5. K. A. Watson, K. M. Lyons, J. M. Donbar, and C. D. Carter, "Scalar and velocity field Measurements in a lifted CH4-air diffusion flame," Combust. Flame **117,** 257–271 (1999).
6. J. M. Donbar, J. F. Driscoll, and C. D. Carter, "Reaction zone structure in turbulent nonpremixed jet flames—from CH-OH PLIF images," Combust. Flame **122,** 1–19 (2000).
7. Q.-V. Nguyen and P. H. Paul, "The time evolution of a vortex-flame interaction observed via planar imaging of CH and OH," Proceedings of the Combustion Institute **26,** 357–364 (1996).
8. V. S. Santoro, D. C. Kyritsis, and A. Gomez, "An Experimental Study of Vortex-Flame Interaction in Counterflow Spray Diffusion Flames," in *Proceedings of the Combustion Institute* (Combustion Institute, Pittsburgh, Pa., 2000), Vol. **28,** pp. 1023–1030.
9. V. S. Santoro and A. Gomez, "Extinction and reignition in counterflow spray diffusion flames interacting with laminar vortices," in *Proceedings of the Combustion Institute* (Combustion Institute, Pittsburgh, Pa., 2002) (to be published).
10. M. W. Renfro, A. Chaturvedy, and N. M. Laurendeau, "Semi-quantitative measurements of CH concentration in atmospheric-pressure counterflow diffusion flames using picosecond laser-induced flourescence," Comb. Sci. Technol. **169,** 25 (2002).
11. M. W. Renfro, G. B. King, and N. M. Laurendeau, "Scalar time-series measurements in turbulent $CH_4/H_2/N_2$ nonpremixed flames: CH," Combust. Flame **122,** 139–150 (2000).
12. H. Böhm and F. Lacas, "On extinction limits and polycyclic aromatic hydrocarbon formation in strained counterflow diffusion flames from 1 to 6 bar," in *Proceedings of the Combustion Institute* (Combustion Institute, Pittsburgh, Pa., 2000), Vol. **28,** pp. 2627–2634.
13. J. C. Rolon, D. Veynante, J.-P. Martin, and F. Durst, "Counter jet stagnation flows," Exp. Fluids **11,** 313–324 (1991).
14. D. Durox, S. Ducrouix, and F. Lacas, "Flow seeding with an air nebulizer," Exp. Fluids **27,** 408–413 (1999).
15. T. Maxworthy, "The structure and stability of vortex rings," J. Fluid Mech. **51,** 15–32 (1972).
16. C. J. Mueller, J. F. Driscoll, D. J. Sutkus, W. L. Roberts, M. C. Drake, and M. D. Smooke, "Effect of unsteady stretch rate on OH chemistry during a flame–vortex interaction: to assess flamelet models," Combust. Flame **100,** 323–331 (1995).
17. D. Thevenin, P. H. Renard, G. J. Fiechtner, J. R. Gord, and J. C. Rolon, "Regimes of non-premixed flame-vortex interactions," in *Proceedings of the Combustion Institute* (Combustion Institute, Pittsburgh, Pa. 2002), Vol. **28,** pp. 2101–2108.
18. T. R. Meyer, G. J. Fiechtner, S. P. Gogineni, J. C. Rolon, C. D. Carter, and J. R. Gord, "Simultaneous PLIF/PIV investigation of vortex-induced annular extinction in H2-Air counterflow diffusion flames," Exp. Fluids (to be published).
19. N. L. Garland and D. R. Crosley, "Energy transfer processes in CH $A^2\Delta$ and $B^2\Sigma^-$ in an atmospheric pressure flame," Appl. Opt. **24,** 4229–4237 (1985).
20. V. R. Katta and W. M. Roquemore, "Extinction in methane–air counterflow diffusion flame—a direct numerical study," in *Proceedings of Central States the Spring Technical Meeting* (Combustion Institute, Pittsburgh, Pa. 1996), pp. 449–454.
21. H. Wang and M. Frenklach, "A detailed kinetic modeling study of aromatics formation in laminar premixed acetylene and ethylene flames," Combust. Flame **100,** 173–221 (1997).

22. A. Ratner, J. F. Driscoll, J. M. Donbar, C. D. Carter, and J. A. Mullin, "Reaction zone structure of non-premixed turbulent flames in the intensely wrinkled regime," in *Proceedings of the Combustion Institute* (Combustion Institute, Pittsburgh, Pa., 2000), Vol. **28,** pp. 245–252.

23. V. S. Santoro, D. C. Kyritsis, A. Linan, and A. Gomez, "Vortex-induced extinction behavior in methanol gaseous flames: a comparison with quasi-steady extinction," in *Proceedings of the Combustion Institute* (Combustion Institute, Pittsburgh, Pa., 2000), Vol. **28,** pp. 2109–2116.

(c)2002 American Institute of Aeronautics & Astronautics or Published with Permission of Author(s) and/or Author(s)' Sponsoring Organization.

A02-13765

AIAA 2002-0393

Laser-Induced Incandescence Measurements in the Reaction Zone of a Model Gas Turbine Combustor

M. Brown and T. Meyer
Innovative Scientific Solutions, Inc.
Dayton, OH

J. Gord, V. Belovich, and W. Roquemore
Air Force Research Laboratory
Wright-Patterson AFB, OH

40th AIAA Aerospace Sciences Meeting and Exhibit
14-17 January 2002
Reno, NV

For permission to copy or to republish, contact the copyright owner named on the first page.
For AIAA-held copyright, write to AIAA Permissions Department,
1801 Alexander Bell Drive, Suite 500, Reston, VA, 20191-4344.

(c)2002 American Institute of Aeronautics & Astronautics or Published with Permission of Author(s) and/or Author(s)' Sponsoring Organization.

AIAA Paper No. 02-0393

LASER-INDUCED INCANDESCENCE MEASUREMENTS IN THE REACTION ZONE OF A MODEL GAS TURBINE COMBUSTOR

Michael S. Brown* and Terrence R. Meyer*
Innovative Scientific Solutions, Inc.
Dayton, Ohio 45440-3638

James R. Gord,** Vincent M. Belovich,* and W. M. Roquemore***
Air Force Research Laboratory
Propulsion Directorate
Wright-Patterson Air Force Base, OH 45433-7103

* Member AIAA ** Associate Fellow AIAA *** Fellow AIAA

ABSTRACT

In concert with an Air Force program designed to study the affect of additives on particulate production, laser-induced incandescence (LII) measurements were performed in a JP-8-fueled, single swirl-cup combustor with a central nozzle. Single-shot and averaged LII images of soot are presented along with high-speed luminescence images. Performance of the LII system is discussed as well as its utility in augmenting extractive sampling approaches to particulate measurements.

I. INTRODUCTION

The contribution of engine-exhaust particulates to atmospheric pollution is the subject of ever-increasing environmental regulation. In addition to contributing to atmospheric pollution, particulates play a key role in radiative heat transfer and can strongly influence local temperatures, engine performance, and infrared signatures.[1] Attempts to reduce particulates have become even more challenging, however, as modern combustors are pushed to higher fuel-air ratios and as further reductions are sought in NOx emissions. Particulate reduction will, therefore, require careful study of the soot-formation process and its mitigation (via additives, for example).

A number of techniques have been used to measure particulates in the reaction zone or burned-gas regions. Physical sampling can be used to obtain the mass fraction of soot as well as other flame species, but it is subject to a number of disadvantages. Physical probes have been found to perturb the thermal and hydrodynamic flowfield,[2] bias particulate measurements,[3] and suffer from poor sensitivity and repeatability as soot emissions are reduced.[4,5] It is also possible to use light scattering and extinction, although these techniques can suffer from low signal-to-noise ratio and beam steering, respectively. Laser-induced incandescence (LII), which occurs when laser-heated soot particles reach 2000-3000 K above the flame temperature, has emerged as a promising diagnostic because it can be used in the reaction zone or burned-gas region, provides relatively high signal levels, and can be insensitive to laser attenuation. Under the proper conditions, LII can be used to measure the soot volume fraction, number density, primary particle size, and particle-size distribution.[6,7,8]

The LII technique has, therefore, received considerable attention in recent years, but relatively few measurements have been made in practical devices.[5,9] The goal of this investigation was to characterize the performance of an LII measurement system for use in the reaction zone of a model gas turbine combustor. An optimal configuration was selected to minimize the effects of laser-intensity variations and interferences from scattering and background luminosity. Experimental results of parametric tests obtained in a JP-8-fueled swirl-inlet combustor are presented including the response of the system to varying equivalence ratio and fuel additives. These measurements were conducted in a survey mode. A second round of more detailed measurements will be conducted later this year.

II. EXPERIMENTAL APPROACH

"This paper is declared a work of the U.S. Government and is not subject to copyright protection in the United States."

(c)2002 American Institute of Aeronautics & Astronautics or Published with Permission of Author(s) and/or Author(s)' Sponsoring Organization.

LII signals have been found to be proportional to the soot volume fraction because the primary particles that comprise soot are typically in the Rayleigh limit and behave approximately as volume absorbers and emitters.[6] The LII technique is somewhat sensitive to local temperature and primary-particle size, however, because heat conduction and soot vaporization scale with surface area.[6] As laser-heated soot cools back down to flame temperatures, its signal weakens and shifts from the visible region into the infrared. Thus, it is important to consider a number of parameters, such as camera timing relative to the incident laser pulse, camera gate width, spectral range of detection, and laser fluence when optimizing an LII measurement setup.

In this investigation, a gated intensified charge-coupled device (ICCD) camera was used to provide control over the timing and gate width, and to improve signal detection. A short-pass filter with a cut-off at 500 nm was used in front of the camera to reduce laser scatter and background soot luminescence and eliminate laser-induced fluorescence from C_2 and PAHs. A visible f/1.2 lens with extension ring was used to achieve a field-of-view 14.4-cm wide by 9.6-cm high.

Due to time and space constraints, it was not feasible to enclose the beam completely during the first set of experiments. Consequently we chose to use visible radiation from a frequency-doubled Nd:YAG laser at 532 nm for safety reasons, even though 1064 nm is better suited for avoiding interferences from background fluorescence and for ensuring that soot particles are within the Rayleigh limit. A cylindrical lens was used to form the 100 – 600 mJ per pulse laser beam into a 12.5-cm wide sheet; the beam was not focused in the transverse direction and had a thickness of 1 cm in the test section. Keeping the laser sheet relatively thick in the transverse direction helped to mitigate damage to the windows, ensured the capture of localized fluidic movement of soot, and helped to keep the laser fluence in the optimal regime. The thickness was chosen to be commensurate with the aperture of the particulate sampling probe. The camera and laser were triggered by a delay generator that enabled continuous variation of the delay between the camera gate and the arrival of the laser pulse in the combustor.

The measurements were made in the Particulate Mitigation Rig, one of several rigs within the Atmospheric Pressure Combustor Research Complex (APCRC) at Wright-Patterson AFB. It is currently used to study the impact of fuel additives on particulate mass and/or number density in the exhaust gases. The additives are generally injected into the fuel stream at concentrations of 1000-10,000 ppm, and particulate measurements are made downstream with a sampling probe.

The rig (see Figure 1) is a single, swirl-cup combustor with a central nozzle. It is similar in configuration to a GE CFM-56 combustor. Radial, counter-rotation swirlers swirl the flow around the nozzle to enhance fuel-droplet breakup and mixing. A flame tube 15.25 cm × 15.25 cm in cross-section and 22.9 cm in length, is attached to help stabilize the flame and allow the exhaust-gas concentration profiles to develop. The flame tube is windowed on the top, bottom, and one side to permit introduction of a laser sheet (top) and viewing of the LII signal (side) at 90° to the sheet. The laser sheet passes completely through the test section significantly reducing interferences from laser reflection. Soot build-up interferes with optical access over about a 12-hr. period, after which the windows must be replaced. In Figure 1, the flow is from right to left. The swirl cup can be seen in the middle of the backward facing wall of the windowed flame tube. CH chemiluminescence (light blue) appears near the cup. Volume emission (light red) is due to nascent particulate luminescence.

The air to the combustor was heated to 350°F and the flow rate was set to approximately 4.5 lbm/min, which produced a 6% pressure drop across the dome. The fuel-flow rate (roughly 0.03 to 0.05 gpm) was varied to produce equivalence ratios from 0.7 to 1.2 (stoichiometric fuel/air ratio equals 0.0681). The oil-cooled particulate-sampling probe, as seen in Figure 1, was placed at the exit plane of the combustor and can be translated to acquire concentration-profile measurements as needed.

A schematic of the experimental setup is shown in Figure 2. A sequence of dichroic mirrors was used to direct the incident laser through a cylindrical lens and into the combustor from the top with the electric field vector parallel to the camera viewing line. This orientation reduces somewhat the Rayleigh scatter present.

Figure 3 shows the field-of-view of the acquired ICCD images. A single-shot LII image (darker blue) is superimposed on the outline (lighter blue) of the combustor. The irregular shape in the LII image is due to a locally high concentration of soot. During this study the relative location of the laser sheet

(c)2002 American Institute of Aeronautics & Astronautics or Published with Permission of Author(s) and/or Author(s)' Sponsoring Organization.

downstream of the swirl cup was adjusted to collect images that included or eliminated CH chemiluminescence.

III. EXPERIMENTAL RESULTS

Examples of an averaged and single-shot LII images are shown in Figure 4 and Figure 5, respectively. The white line in Figure 4 indicates the region of the image delimited top and bottom by the combustor window size and on the left hand side by the uniform region of laser sheet. The average was taken over a series of 800 laser shots acquired at an equivalence ratio of 1.1. Five of the 800 single-shot images exhibited saturation at least over a portion of the full image and were discarded prior to averaging. The average image was background corrected. The regions of highest average LII signal are located toward the top and bottom of the image. This is consistent with the fluid flow from the swirl cup. The nozzle produces a hollow cone of combusting gases that spreads outward toward the walls. The transverse velocity component of the swirl along with a recirculation zone along the combustor centerline complicates the flow pattern. The laser sheet, aligned along the centerline of the combustor, cuts through the swirling, combusting gases near the upper and lower walls of the chamber. Hence, the average LII image appears stronger in these regions. Due to the complexity of the flow-field, soot can be generated throughout the combustor volume.

The three uncorrelated, single-shot LII images appearing in Figure 5 show strong soot incandescence in localized regions throughout the flow-field. (Each of these images has been background corrected.) The isolated convoluted structures appearing in the images are consistent with instantaneous images of the nascent soot luminescence as seen in the three correlated emission images displayed in Figure 6. These flame emission images (laser off) were acquired with no spectral filtering using a high-speed camera operating at 9000 frames per second. The three selected frames are spaced 5.6 ms apart and coarsely show the evolution of a combusting fluid element which is shed from the swirl (lower portion of top frame just to right of midline) and then is distorted by mixing and interaction with the flow-field as the soot luminescence grows in intensity. The complex instantaneous luminescence images are structurally quite similar to the instantaneous LII images. The shot-to-shot variation in the LII signal levels can be quite strong. The upper image in Figure 5 appears with a min/max scaling of 0-3000 while the lower image appears with a scaling of 0-15000.

The shot-to-shot signal from soot in the combustor is clearly intermittent. As a result, it is necessary to resort to statistical means of evaluating the performance of the measurement system. Figures 7 – 12 plot average signal levels under a variety of conditions. The average LII values plotted in these figures were arrived at in a two-step process. First, a background-corrected average image was constructed from several hundred single-shot images after saturated images were discarded. Then, the average value of the individual pixel intensities was calculated within the region indicated by the white line in Figure 4.

Use of a short-pass filter transmitting wavelengths less than 500 nm removed most of the scattered laser light due to specular and diffuse reflection from the interior of the combustor as well as Rayleigh and Mie scattering. The remaining unwanted light was removed by adjusting the delay between the laser pulse and the camera gate. The background signal (combustor off) as a function of delay is shown in Figure 7. A delay setting of 60 ns minimizes the amount of laser scatter in the LII images.

Figure 8 shows the effect of soot-particle vaporization with increasing laser fluence. The roll-off near 0.15 J/cm^2 is consistent with the results obtained recently in laboratory propane/air diffusion flames.[10] Our fluence study was performed using a laser-sheet cross section of 3 cm by 1 cm. Most of the data presented here were recorded with a larger sheet cross section of 12.5 cm by 1 cm. The output energy of the Nd:YAG employed was insufficient to compensate for the increase in beam area, and most of the data shown here were recorded at a fluence of ~0.05 J/cm^2. Consequently, the single-shot image intensities are susceptible to laser intensity fluctuations.

Figure 9 shows the effect of camera gate delay on the LII and background luminescence (laser-off) signals. For delays greater than 50 ns, the nascent luminescence remains unchanged while the LII signal intensity decreases slowly as the laser-heated soot particles begin to cool and approach the temperature of the nascent soot. Thus, one would ideally collect LII for only a short period just after the laser pulse to maximize the signal-to-background ratio. Figure 10 displays the effect of camera gate width on both the LII and luminescence signals and shows that a camera gate width of 200 to 400 ns (used here) does not have a large impact on this ratio.

Figure 11 shows a first look at the average LII signal

(c)2002 American Institute of Aeronautics & Astronautics or Published with Permission of Author(s) and/or Author(s)' Sponsoring Organization.

and particulate number density from extractive sampling as a function of global equivalence ratio. While both signals rise at similar rates for ratios above 1.1, they exhibit dissimilar behavior at lean conditions. Both the sampling probe and the LII laser sheet lie along the centerline of the combustor; however, the probe essentially samples only fluid near the centerline. The LII sheet samples fluid above and below the centerline as well. Fluid motion normal to the centerline will offset somewhat the difference in volumes sampled. The particulates collected by the probe have somewhat longer residences times than those "captured" in the LII image. Further work will be needed to determine if this "sampling" asymmetry is responsible for the signal difference at lean conditions.

Finally, Figure 12 shows preliminary results of the effect of a fuel additive in the swirl-inlet combustor. Due to proprietary concerns, the precise nature of the additive is not discussed here. Eight LII data sets for two run conditions (with and without additive) were acquired over several minutes of run time at an equivalence ratio of 1.1. The runs with neat JP-8 and with JP-8+additive were taken serially several hours apart. Hence, there is no time correlation between the data sets in the two runs. Each data set consists of over a hundred single-shot images averaged together and background corrected. The data taken as a whole suggest that the fuel additive does have a mitigating effect on soot production and/or growth.

IV. CONCLUSIONS, FUTURE WORK

We have demonstrated the acquisition of single-shot LII images in the reaction zone of a JP-8-fueled swirl-inlet combustor over a range of global equivalence ratios (0.8 – 1.2). Suitable choices of spectral filtering and camera gate delay minimize the presence of laser scatter and background luminescence in the LII signal. Single-shot LII images reveal a complex soot structure that changes dramatically shot-to-shot. These structures are similar to those captured by high-speed photography of the nascent flame emission. By reducing averaged images to single-value data points, parametric studies were made of the dependence of the LII signal on camera gate delay, gate width, and incident laser fluence. For equivalence ratios above 1.1, the average LII signal increases at a rate similar to that of the probe-sampled particulate density. A series of runs with and without fuel additive indicate the possibility of characterizing additive effects on soot volume fraction.

Future work will concentrate on establishing a more permanent optical setup with beam enclosure permitting the use of 1064-nm excitation. Additional work will be executed in finding a suitable means to calibrate the LII signal intensity such that the soot volume fraction may be determined on an absolute scale.

V. ACKNOWLEDGMENTS

The authors would like to acknowledge Charles Frayne and Edwin Corporan of WPAFB and Ronald Britton, Glen Boggs, and Darryl Trump of ISSI for their assistance with various aspects of the experimental set-up. We also thank David Snelling of the NRC of Canada for his helpful advice and discussions regarding the LII technique. This work is supported in part by U. S. Air Force Contract F33615-00-C-2068.

VI. REFERENCES

[1] Mewes, B. and Seitzman, J. M., "Soot volume fraction and particle size measurements with laser-induced incandescence," *Applied Optics*, Vol. 36, pp. 709-717 (1997).

[2] Wang, H. and Frenklach, M.. "A Detailed Kinetic Modeling Study of Aromatics Formation in Laminar Premixed Acetylene and Ethylene Flames," *Combustion and Flame*, Vol. 110, pp. 173-221 (1997).

[3] Miller, J. H., Mallard, W. G. and Smyth, K. C., "The Observation of Laser-Induced Visible Fluorescence in Sooting Diffusion Flames," *Combustion and Flame*, Vol. 47, pp. 205-214 (1982)

[4] McManus, K. R., Frank, J. H., Allen, M. G. and Rawlins, W. T., "Characterization of Laser-Heated Soot Particles Using Optical Pyrometry," AIAA 98-0159, 36th Aerospace Sciences Meeting & Exhibit, Reno, Nevada (1998).

[5] Black, J. D., "Laser Induced Incandescence Measurements of Particles in Aero-Engine Exhausts," SPIE Vol. 3821, EUROPTO Conference on Environmental Sensing and Applications, Munich, Germany (1999).

[6] Wainner, R. T., Seitzman, J. M. and Martin, S. R.,"Soot Measurements in a Simulated Engine Exhaust Using Laser-Induced Incandescence," *AIAA Journal*, Vol. 37, pp. 738-743 (1999).

[7] Will, S., Schraml, S. and Leipertz, A., "Two-dimensional soot-particle sizing by time-resolved

(c)2002 American Institute of Aeronautics & Astronautics or Published with Permission of Author(s) and/or Author(s)' Sponsoring Organization.

laser-induced incandescence," *Optics Letters*, Vol. 20, pp. 2342-2344 (1995).

[8] Roth, P. and Filippov, A. V.,"In situ Ultrafine Particle Sizing by a Combination of Pulsed Laser Heatup and Particle Thermal Emission," *Journal of Aerosol Science*, Vol. 27, pp. 97-104 (1996).

[9] Pinson, J. A., Mitchell, D. L., Santoro, R. J. and Litzinger, T. A., "Quantitative, Planar Soot Measurements in a D.I. Diesel Engine Using Laser-Induced Incandescence and Light Scattering," SAE 932650, Fuels and Lubricants Meeting and Exposition, Philadelphia, PA (1993).

[10] Witze, P. O., Hochgreb, S., Kayes, D., Michelson, H. A. and Shaddix, C. R., "Time-Resolved Laser-Induced Incandescence and Laser Elastic Scattering Measurements in a Propane Diffusion Flame," Paper #86, 2nd Joint Meeting of the U.S. Sections of the Combustion Institute, Oakland, CA (March 2001).

(c)2002 American Institute of Aeronautics & Astronautics or Published with Permission of Author(s) and/or Author(s)' Sponsoring Organization.

VII. FIGURES

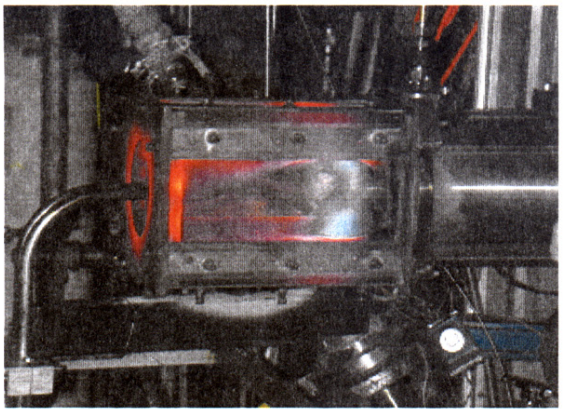

Figure 1. Atmospheric pressure, JP-8-fueled combustor used in this study.

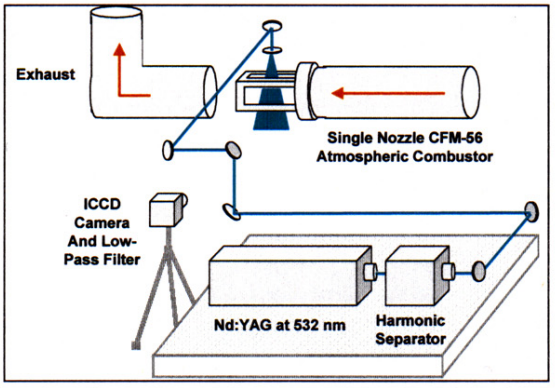

Figure 2. Experimental layout indicating relative location of the laser and camera to the combustor.

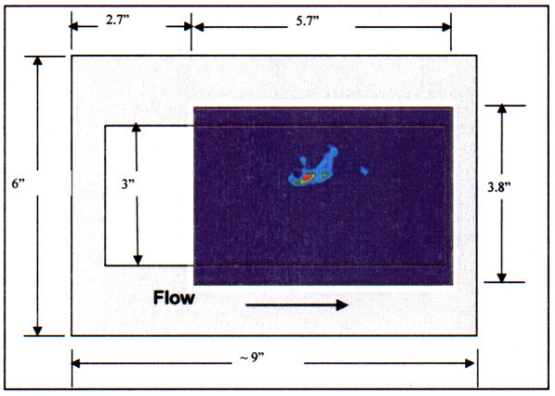

Figure 3. Schematic indicating the field-of-view of the ICCD. Light blue denotes combustor and dark blue indicates area of acquired images.

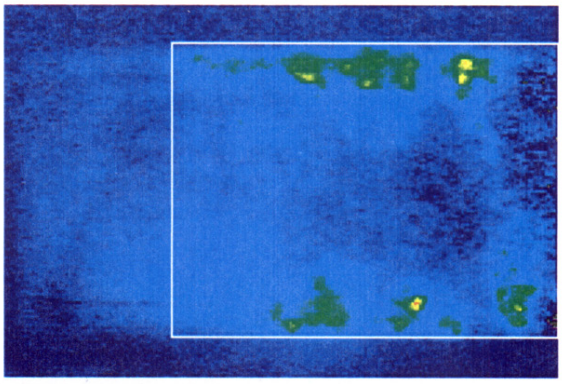

Figure 4. Averaged LII image.

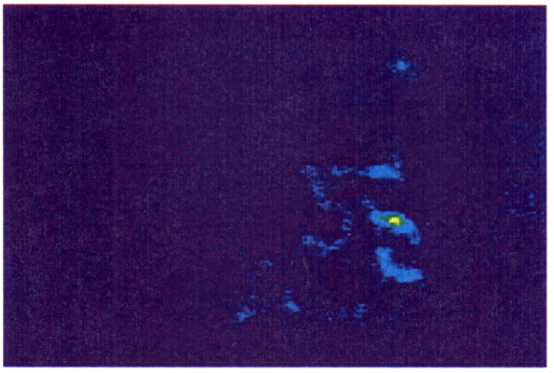

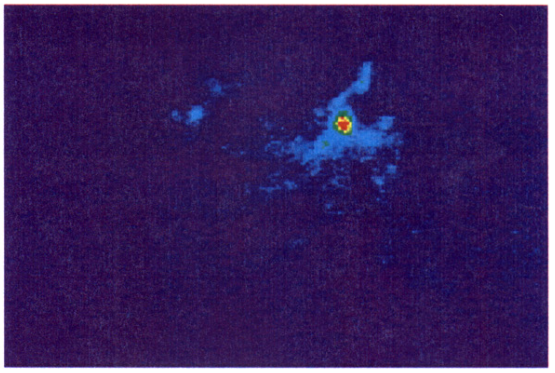

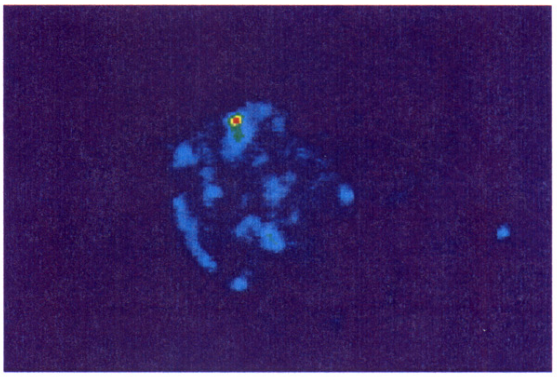

(c)2002 American Institute of Aeronautics & Astronautics or Published with Permission of Author(s) and/or Author(s)' Sponsoring Organization.

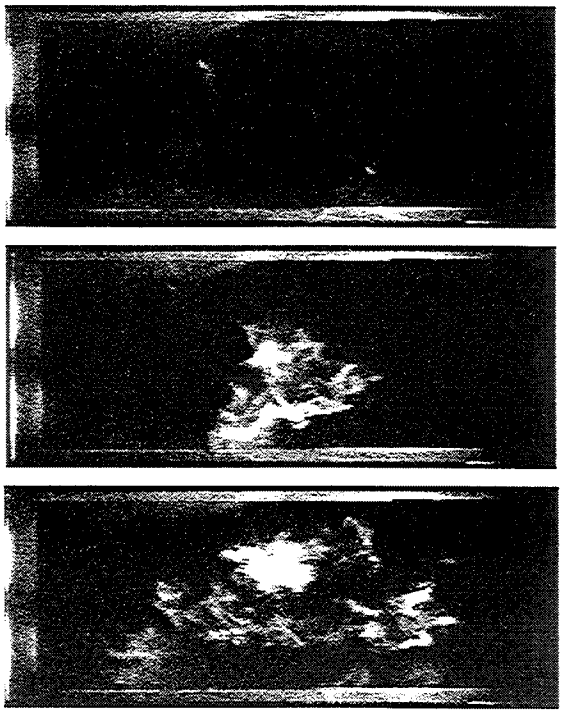

Figure 6. Sequence of high-speed luminescence images (9000 fps) taken 5.6 ms apart indicating the evolution of a combusting fluid element shed from the swirl.

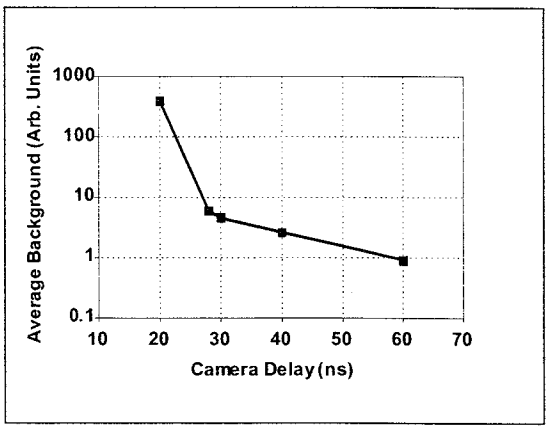

Figure 7. Background laser scatter (combustor off) as a function of delay between laser pulse and camera gate.

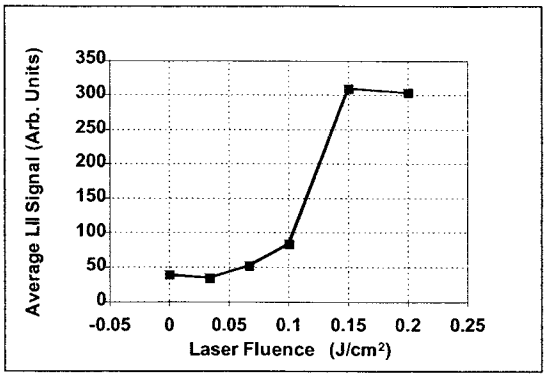

Figure 8. Average LII signal as a function of incident laser fluence. Equivalence ratio = 1.1 .

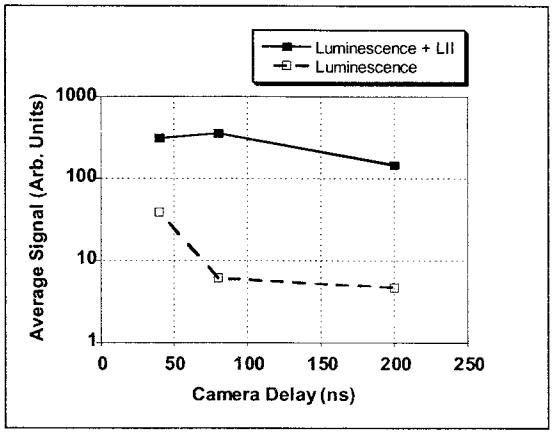

Figure 9. Average LII signal and nascent luminescence as a function of delay between laser-pulse arrival and camera gate.

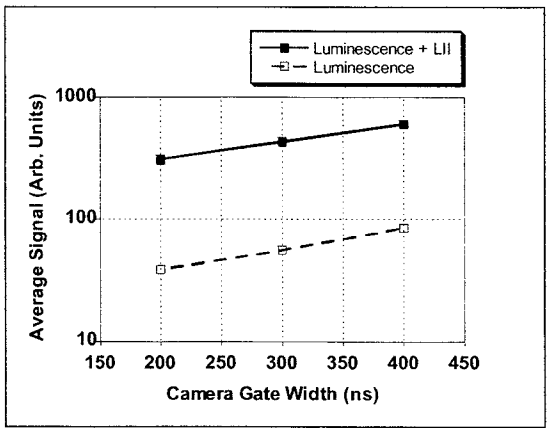

Figure 10. Average LII signal and nascent luminescence as a function of camera gate width.

(c)2002 American Institute of Aeronautics & Astronautics or Published with Permission of Author(s) and/or Author(s)' Sponsoring Organization.

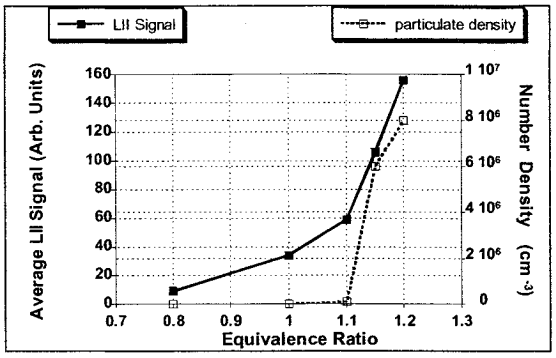

Figure 11. Average LII signal and sampled particulate number density as a function of equivalence ratio.

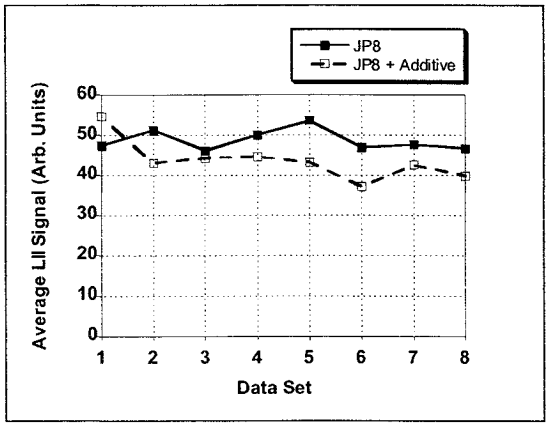

Figure 12. Preliminary test of potential fuel additive for particulate reduction at an equivalence ratio of 1.1 .

JOURNAL OF PROPULSION AND POWER
Vol. 18, No. 2, March–April 2002

Combustion Air Jet Influence on Primary Zone Characteristics for Gas-Turbine Combustors

S. Gogineni*
Systems Research Laboratories, Dayton, Ohio 45440-3696
D. Shouse,† C. Frayne,‡ and J. Stutrud†
U.S. Air Force Research Laboratory, Wright–Patterson Air Force Base, Ohio 45433-7103
and
G. Sturgess§
Pratt & Whitney, East Hartford, Connecticut 06108

Results are presented of emissions and lean blowout measurements in a generic combustor primary zone of an aircraft gas-turbine engine for the effects of opposed, circular combustion air jets of a range of sizes, positioned half a dome height downstream from the dome. The primary zone was operated at simulated engine high-power conditions and representative dome and liner pressure drops. Most of the NO_x is generated in the jets. Although an optimum jet size is identified, the lowest overall emissions resulted from a no-combustion air-jet configuration; air jets are necessary, however, to confer lean blowout stability and short flame length.

Nomenclature

F	=	$10^{0.00143T}/3.72$, temperature correction factor (to 400 K)
H_d	=	combustor dome height
K_f	=	flow criterion
$\dot{m}$	=	mass flow rate through combustor, lbm/s
n	=	apparent reaction order
P	=	combustor pressure, atm
$T_{\dot{m}}$	=	temperature of inlet air, K
V	=	combustor volume, ft^3
Δp	=	pressure drop across combustor
ΔT	=	temperature rise across combustor
$\rho_{\dot{m}}$	=	density of air under combustor inlet conditions
ϕ	=	equivalence ratio

Introduction

DURING development of combustors for industrial and aircraft gas-turbine engines, the issues of adequate lean blowout (LBO) margin and low exhaust emissions are both important aspects in the design process. It is increasingly more difficult to ensure that designs have adequate stability margins concurrently with low emissions and high temperature rise. Achievement of flame stability over wide ranges of engine operating conditions is a function of the primary zone of the combustor; the flame structures established in the primary zone will also control the exhaust emissions. Many aircraft engine combustors use transverse air jets introduced through the liners to provide a nominal termination of the primary zone. These air jets also supply some part of the total air necessary for complete combustion of the fuel. Almost nothing exists in the open literature concerning the interactions of the jet and dome flows in determining emissions or lean blowout stability.

Program Objectives

The overall intent of the study was to understand the detailed behavior of the major flame-holding region (the primary zone) of a generic modern combustor for aircraft gas-turbine engines.

The comprehensive objective was to determine the major flowfield features of a representative primary zone and to understand how they control lean stability together with gaseous emissions generation. It was intended to establish how these specifics are affected by liner and dome pressure drops, and combustion air port positions, shapes, sizes, and arrangements.

Combustor Configuration

The experimental combustor used in this study was modified from one used in an earlier program[1] and was designated the PW 150 technology combustor.[2] The purpose of the combustor was to provide an approximate representation of the salient flame-holding features of a gas-turbine annular combustor in a simplified geometric configuration having high optical access. The combustor cross section, therefore, represented a compromise between the requirements of simplicity for modeling purposes and uncomplicated optical access for application of laser diagnostics. The cross section was square, but generous circular-arc fillets were provided in the corners to suppress vorticity generation that might result in spurious flame holding.

The PW 150 combustor for the present program (Fig. 1) contained a high-swirl (HS) airblast atomizing fuel injector[3] (modified for gaseous fuel operation) and its dome interfacing system. The combustor included uncooled solid metal top and bottom combustor liner plates that accommodated suitable arrays of combustion air jets. Typical flame structures are shown in Fig. 2 for 0.375-in.-(9.53-mm) diam plain circular jets positioned at half-dome height downstream and operating at an overall equivalence ratio of 1.2 with a liner pressure drop of 2.7%. One side combustor liner plate (at 90 deg to the liner plates containing the air jets) contained a fitting for a torch igniter and the other had a quartz window for visual access. The combustor length was 490 mm, and the combustor had a 153-mm hydraulic diameter. The combustor outlet was restricted by a 45% geometric blockage orifice plate[3] to provide representative backpressure of the remainder of a real combustor. The presence of the backpressure plate also prevented the recirculation of external air from downstream back into the combustor.

Received 29 August 1996; revision received 18 October 2001; accepted for publication 20 October 2001. Copyright © 2001 by the authors. Published by the American Institute of Aeronautics and Astronautics, Inc., with permission. Copies of this paper may be made for personal or internal use, on condition that the copier pay the $10.00 per-copy fee to the Copyright Clearance Center, Inc., 222 Rosewood Drive, Danvers, MA 01923; include the code 0748-4658/02 $10.00 in correspondence with the CCC.

*Research Engineer, 2800 Indian Ripple Road; currently Senior Engineer, Innovative Scientific Solutions, Inc., 2766 Indian Ripple Road, Dayton, Ohio 45440-3638. Associate Fellow AIAA.
†Mechanical Engineer, Aero Propulsion and Power Directorate.
‡Electronic Engineer, Aero Propulsion and Power Directorate.
§Fellow; currently Corporate Vice-President, Innovative Scientific Solutions, Inc., 2766 Indian Ripple Road, Dayton, Ohio 45440-3638. Fellow AIAA.

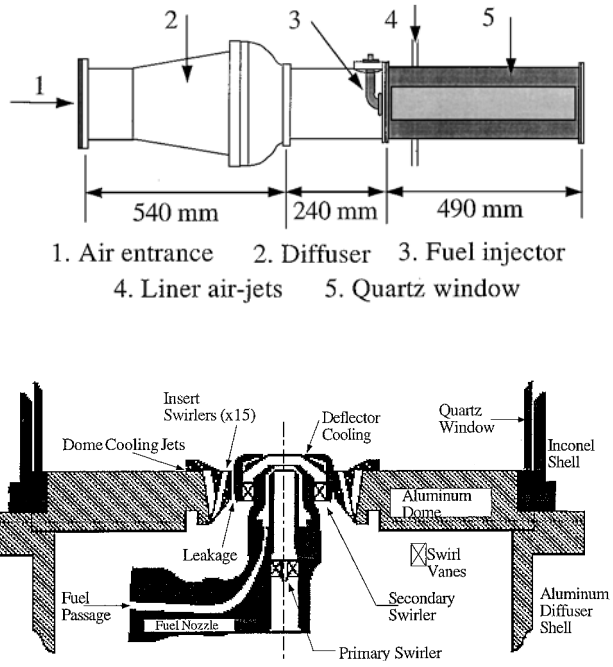

Fig. 1 Laboratory-scale gas-turbine combustor primary zone, showing fuel injector and dome configuration.

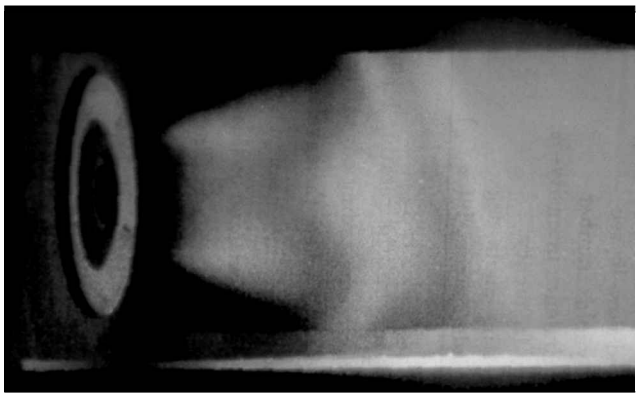

Fig. 2 Natural light flame photograph showing flame structure for the 0.375-in.- (9.53-mm) diam air jets at the half-dome height position.

In the configuration described, the modified combustor represented, in simplified form, the features of the dome and primary zone regions of a generic gas-turbine combustor.

Efficacy of PW 150 Combustor

The PW 150 combustor represented a "single-cup," planar segment of an annular combustor and simulated the primary zone only. It was operated at atmospheric pressure. Therefore, given these limitations it is necessary to justify its acceptability for the intended purpose.

A planar segment of any combustor sacrifices an important aspect of real annular combustors in that the cross-sectional flow areas above and below the combustor midplane surface are symmetrical, which they are not in reality as a result of liner curvatures. The biggest effects of this difference are seen in liner temperatures and the exit mean radial temperature profile, neither of which is of interest to the present program.

Having physical side walls (reflecting), the single-cup combustor has symmetry in lateral boundary conditions rather than periodicity in lateral boundary conditions as in a complete annular system. This means that significant interactions taking place between adjacent cups in a real annular combustor will not be present in the single-cup model combustor. This discrepancy could clearly exert some influence on the overall emissions. However, the general behavior of the individual cup module of an annular combustor that is made up of a circumferential arrangement of such modules should not be substantially changed. Therefore, the single-cup combustor does allow a useful study to be made of the general characteristics pertaining to individual module behavior.

Operation of a study at atmospheric pressure requires that there be no changes in combustor flow patterns between the study and the application operating at high pressures. Application of the laws of partial modeling[4] shows that the aerodynamic processes determining the combustor flow pattern are established by combustor geometry, air pressure drops across the combustor dome and liners, and Reynolds number; Mach numbers are sufficiently low that they exert no effects on flow pattern. Temperature changes caused by heat release from chemical reaction cause changes in velocity and velocity gradients at all points in the combustor, and these can result in some local effects of significance; but if the Reynolds number is high and Mach number is low, these might be neglected overall. Generally, the main features of flow pattern should not be affected. Overall fuel-to-air ratio exerts an effect through the influence of fuel momentum. This has little significance except near the fuel injector where the liquid spray is dense. Fortunately, airblast atomization of liquid fuel from high-flow-number fuel injectors, as used in most modern combustors, ameliorates even this local effect because the fuel has little momentum of its own and is dispersed across the combustor by the air motions. Gaseous propane was used as the fuel for these simulations. Given the fine atomization of liquid fuel achieved by airblast atomization together with the high droplet evaporation rates existing at high-power engine conditions, propane was considered as appropriate for the simulation.

These arguments produce the useful half-truth that, to first order, the flow pattern depends only on the combustor geometry and the air pressure drop across it. Following Spalding,[4] dimensional analysis leads to the flow criterion K_f, where

$$K_f = \frac{\dot{m}^2}{\Delta p \rho_{\dot{m}} D^4 g_0} \tag{1}$$

where the characteristic dimension D is taken as the combustor dome height H_d, and g_0 is Newton's constant if English units are used. The flow criterion should be a constant, as close to unity as possible, between the model combustor and the application. Equation (1) forms the basis for the well-known water-analogy combustion tunnel,[5] through which many successful practical combustors have been developed in the past. The additional term $\Delta T/T_{\dot{m}}$ should also be accounted for.

At conditions representative of the tests, the PW 150 combustor was operated such that the ratio was

$$\frac{(K_f)_{\text{rig}}}{(K_f)_{\text{engine}}} = 1.22 \tag{2}$$

in comparison with a primary zone of a combustor in a 32-atmosphere engine at take-off power, and the ratio,

$$\frac{(\Delta T/T_{\dot{m}})_{\text{rig}}}{(\Delta T/T_{\dot{m}})_{\text{engine}}} = 1.67 \tag{3}$$

The value for the K_f ratio is quite acceptable; the value for the $\Delta T/T_m$ ratio is a little high. However, because $\Delta T/T_m$ only affects the local temperature and velocity gradients but not the overall size and shape of the flame structures, it can be concluded, therefore, that the PW 150 combustor can reproduce reasonably well and, to an acceptable degree, the flow patterns of an engine combustor.

Description of the Rig

The rig was mounted horizontally in a test cell of Wright Laboratory, Wright–Patterson Air Force Base, Ohio. Compressor air after being dried to very low dew points was supplied to the dome region of the combustor by a flow conditioner, passing first through a pressure regulator then through an orifice plate for flow measurement. The flow was controlled with a Fischer controller and valve.

The dome air was then passed through a 48-kW electric heater that utilizes a cascade control system to control the delivered air temperature to the rig. This particular heater could deliver 20 lb/min (9.07 kg/min) of air at 500°F (533 K).

A separate air supply and control system was incorporated to deliver air to the liners. The air was supplied by a 2200 psi bottled air trailer with the flow controlled by pressure and with sonic venturis for flow measurement; it was also dried to very low dew points. The air was then passed through a 15-kW electric heater before the air line was split to deliver air to the top and bottom liner jet bosses. A thermocouple located in the liner jet boss provided temperature feedback to the heater controller. This heater could deliver 5 lb/min (9.27 kg/min) of air at 500°F (533 K). Pressure transducers connected to static-pressure taps located in the dome and liner jet plenum provided a measure of the pressure drops across the dome and liners.

Gaseous propane was supplied from bottles that were ganged together. The propane was metered via turbine flow meters with the flow controlled by Fisher controllers and Badger research valves. The propane was filtered before being delivered to the rig. The fuel-air mixture in the combustor was ignited by a propane torch inserted through a port located in the side wall of the combustor in the near-dome region. The torch was withdrawn, and a blanking plug was inserted into the igniter port following a successful light. Cooling water and glycol for the emissions probe were pumped from a reservoir through the probe where a thermocouple monitored the exiting fluid from the probe. Before returning to the reservoir, the heated glycol was run through a heat exchanger to reduce its temperature.

Range of Experimental Variables

The geometric arrangement of the combustor for this study consisted of the airblast atomizing fuel injector (modified for operation on gaseous propane) mounted with its insert swirler and cooled dome heat shield in the combustor dome (Fig. 1b) and an associated pair of circular combustion air ports contained in the upper and lower walls of the combustor; the air ports were inline with the injector centerline. Although the pair of air ports could be situated 1.0, 0.75, and 0.5 dome heights (H_d) downstream from the dome, only data for the $H_d/2$ position are presently given. Air port diameters were 0.75, 0.5, 0.375, and 0.25 in. (19.05, 12.7, 9.53 and 6.35 mm, respectively), and the equivalent geometric area of the 0.5-in.-diam port in the form of four individual jets of 0.25 in. diam on a pitch circle of 0.575 in. (14.6 mm) diam. Only data for SJ ports are presently given.

The fuel injector was designated as the HS injector, and its design features were representative of current airblast atomizer technology. It had a nominal swirl number (based on vane angles and mass weighted for the swirler flow splits) of 1.41. The total air passage effective area was 0.176 in. (113.55 mm^2), with an outer to inner passage flow split of 2.8. The outer swirler vane angle was 55 deg, and the inner swirler vane angle was 70 deg. The inner passage swirl number was 1.91. The insert swirlers were angled 12.5 deg into the injector centerline, and the swirl angle was zero in this instance. The purpose of the insert swirlers is described in Sturgess et al.[3,6] Dome cooling air was introduced with, but separated from, the insert swirler air and was turned to flow radially outward along the dome surface by a circular deflector plate. The total effective airflow area of the dome excluding the fuel injector was 0.16 in^2 (103.23 mm^2).

The pressure drop across the dome was held fixed at a nominal 4.3% to represent the typical engine experience. To assess its importance, the pressure drop across the air ports was initially varied over the range of 1–5% of the upstream pressure. For the 0.50-in.-(12.7-mm) diam jet, the pressure drop range was extended to as high as 12% in order to explore the effects of jet overpenetration and high turbulence. The dome was also run alone (0% jet pressure drop) to assess the contribution to the total emissions of the injector separate from those of the closely coupled combustion air jets. Pressure drop across a combustor is in practice not a free variable but is set by engine performance considerations. Generally, the allowable pressure drop across a dome is a little higher than that across liners because of the recovery of some dynamic head from the compressor. For much of the work to be presented, the dome pressure drop was held fixed at a nominal value of 4.3% of the upstream pressure, and the liner pressure drop was 3.0%. These values are representative of typical engine conditions. Under these conditions all of the transverse jets with different initial diameters penetrated to the combustor centerline. The inlet air temperatures for the separate dome and transverse jet supplies was a nominal 500°F (533 K). This value was chosen to help satisfy the simulation criteria and to ensure generation of sufficient NO_x without large burn up of CO, so as to permit easy detection of trends and effects in these two pollutants.

With fixed dome and liner pressure drops, for each air-port size, axial position, and pressure drop, the fuel flow rate was varied to cover a range of overall equivalence ratios such that the minimum in the CO curve and the maximum in the NO_x curve could be fully established. It was demonstrated that fuel momentum was not affecting the emissions results.

For the blowout data the air-port pressure drop with a given geometric configuration and inlet air temperature was set in the range of 1–5% at a given dome pressure drop. At each air-port pressure drop the fuel flow was incrementally reduced until a lean blowout occurred.

Description of the Emission Measurements

The emissions sampling probe was a water-cooled quick quench type. This single-point probe was constructed of stainless steel and had an inconel tip. Combustion exhaust was drawn into the probe through a 0.059-in.-(1.5-mm) diam orifice of a converging nozzle. The inside passage diverged to the inside diameter of the sampling tube, which was 0.25 in.-(6.35-mm) diam stainless-steel tubing with a 0.180 in. (4.57 mm) inside diameter. The diverging passage in conjunction with the low pressure inside the probe created a short supersonic expansion, which reduced the temperature of the gas stream. This, combined with the water cooling, effectively quenched the combustion reactions inside the probe. The probe contained a 3-in.-(76.2-mm) diam 90-deg bend and was mounted on a mechanical traversing stand. Figure 3 shows a detail of the emissions probe sampling tip.

The sample transfer system consisted of the sampling probe and heated transfer lines. The probe was connected to $\frac{1}{4}$-in.-(6.35-mm) stainless-steel tubing that was electrically heated and enclosed in an

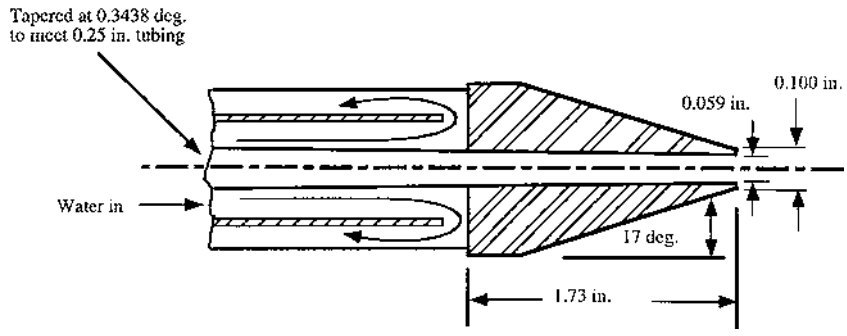

Fig. 3 Sampling tip of the emissions probe.

insulated outer cover. The line was maintained at 320°F (433 K) to prevent condensation of the sample. The line passed from the test cell into the control room and entered an oven, also maintained at 320°F (433 K), where the sample stream was passed through two particulate filters and entered a bellows pump that provided the driving force for the sample flow. The line was then split into two sections, one leading directly to a Beckman Model 402 total hydrocarbon analyzer and the main sample stream leading into a second oven where the line was tapped three more times for delivery to a Beckman Model 955 NO_x analyzer, a Beckman Model 864 CO_2 analyzer, and a Beckman Model 865 CO analyzer, respectively. The sample stream passing into the NO_x analyzer was measured wet. This oven and the lines leading from it were maintained at 160°F (344 K), which is just above the dew point of the exhaust emissions. The sample streams leading to the CO and CO_2 analyzers were first passed through a dryer, where the water content in the sample was extracted through a semipermeable membrane. A hygrometer measured the dew point at the dryer outlet; this temperature was necessary for correcting the dry concentrations back to wet concentrations when making the emissions calculations. The procedures for measuring wet concentrations of hydrocarbons and NO_x emissions and dry concentrations of CO and CO_2 emissions and for controlling the temperatures of the lines are in accordance with the sampling technique and measurement of these emissions as set forth in the Aerospace Recommended Practice, ARP 1256A, and Appendix 3 of International Civil Aviation Organization (ICAO) Annex 16, Volume 2. Although oxygen measurements were not included in any of the emissions calculations, a Beckman Model 755 oxygen analyzer was used to sample the stack exhaust, which contained the accumulated exhaust passed through each of the analyzers, plus any bypassed sample exhaust. NO_x was corrected to a humidity of 0.0063 lbm water per lbm air (0.00286 kg/kg).

In practice, span gases were used to calibrate the emissions analyzers at the ranges of interest. The CO and CO_2 analyzers are nondispersive infrared instruments, and nonlinear calibration curves are used for their calibration over a wide range of span gases. The other analyzers are linear instruments that require a single range calibration. Before each run, the calibrations were performed to less than 3% error. The accuracy of the calibrations was verified both during and after the test runs.

The emissions measurement system was interfaced to a Sun Microsystems computer and data acquisition system that converted analyzer output voltages to concentration values. The emissions calculations made conformed to the methods contained in Aerospace Information Report (AIR) 1533 and Appendix 3 of ICAO Annex 16, Volume 2.

During sampling, an equilibrium test condition was achieved when the analyzers had stabilized; for further accuracy oxygen stability ensured that the sampling system was saturated and an equilibrium condition existed. Further, comparison of the metered fuel-to-air ratio to the measured exhaust fuel-to-air ratio formed an effective representation of the carbon balance between fuel reactants and exhaust products. The agreements were always better than 10% for metered equivalence ratios of unity and less.

For each test condition it was first determined that the emission indices of NO_x (as NO_2), of CO, and of THC (as CH_4) ($EINO_x$, EICO, and EITHC in grams/kilogram of fuel burned) obtained by placing the probe at the center of the test section were the same as those measured by means of an area weighted average procedure. The emission measurements were obtained by traversing the probe both horizontally and vertically through the center of the measurement plane. The measurement plane was 14 in. (355.6 mm) downstream from the dome. Because the emissions probe was introduced into the combustor through the exit orifice plate of 45% blockage, the radial extent of these traverses was determined by this orifice plate. The extent of the radial profile traverses was ±1.75 in. (±44 mm) from the combustor centerline. The area weighted average procedure involved applying a curve fit to the emission measurements obtained in each direction and dividing the area of the combustor exit measurement plane into 11 concentric circles and into 21 sections. The interpolated points were chosen such that each point

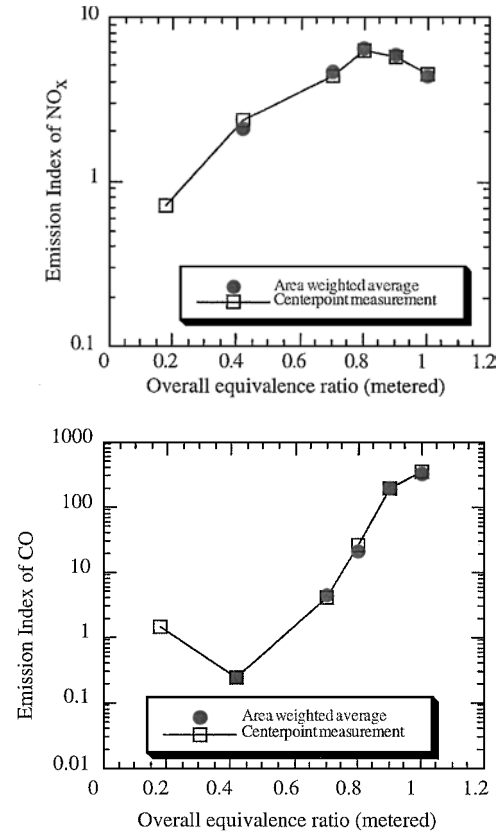

Fig. 4 Example of comparison of area weighted and centerpoint emissions measurements.

represents an equal area of the exit plane. These points were used to find the emission indices from the curve-fitting equation both in the horizontal and vertical directions. An area weighted average was then obtained from the average of these interpolated values. These weighted average emission measurements were compared with the centerpoint measurements, and a typical comparison for $EINO_x$ and EICO is shown in Fig. 4.

The figure indicates that well-mixed conditions occurred at the probe location, and the errors involved were within ±10%. The measurement station of 14 in. (355.6 mm) downstream from the dome was chosen to allow the complex flowfields from the combustion air jet interactions to mix out so that relatively flat emissions profiles were obtained. Such flat profiles, in conjunction with the area-weighting check procedure, allowed single-point measurements to represent the various emissions fields adequately. Of course, chemical reactions could continue beyond the jet-interaction plane before the measurement plane was reached. Check calculations were made, and these showed that CO levels continued to fall from the jet plane to the measurement station but were still reasonably high and that NO_x levels changed very little. The area weighted averaging analysis was performed at each and every test condition and was observed to exhibit the same trends as shown in Fig. 4. Based on this analysis, it was decided to present the emission measurements obtained by placing the probe at the central location of the measurement station in the present investigation.

Effects of Jet Pressure Drop

Figure 5 gives an example of the effect on emission indices of pressure drop across the air ports for the 0.5-in. (12.7-mm) jets as the overall metered equivalence ratio was varied. The transverse air jets were at the $H_d/2$ position, and the fixed dome pressure drop was 4.3%. Minima for carbon monoxide and unburned hydrocarbons are evident at overall equivalence ratios of around 0.42 and 0.7, respectively, and NO_x shows a maximum at an overall equivalence ratio around 0.9. Increasing jet pressure drop increases the peak NO_x significantly, from around 3.4 g/kg at zero pressure drop (dome

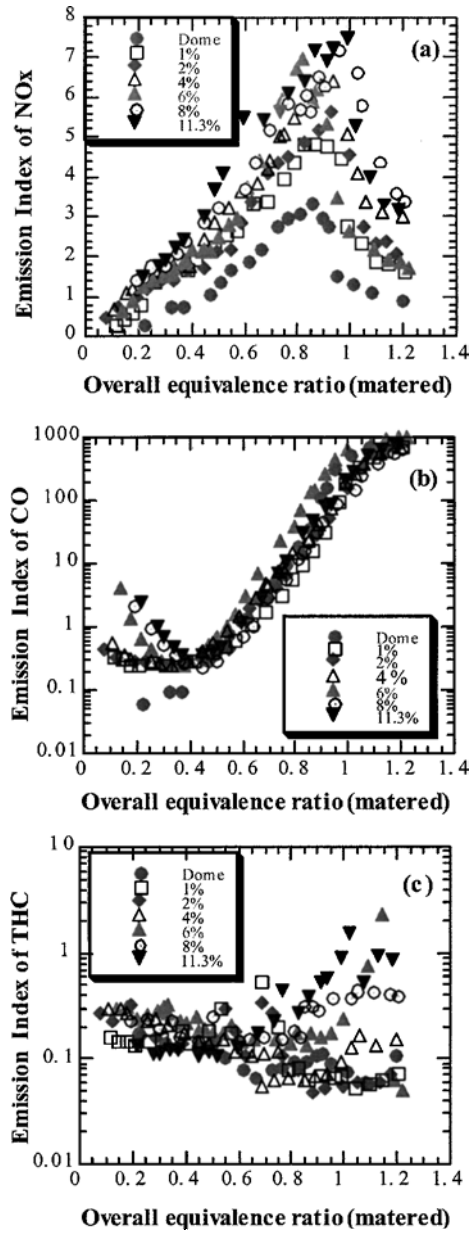

Fig. 5 Effect of liner pressure drop on emission for the 0.50-in. (12.7-mm) opposed air jets at the half-dome height position.

alone) to about 7.5 g/kg at 11.3% pressure drop. When the air jets are present, there is little effect of jet pressure drop on the minimum CO; however, the dome-alone data indicate that a CO minimum has not been reached for overall equivalence ratios down to about 0.2. At all other equivalence ratios the highest CO results from the highest pressure drop. The highest pressure drop also results in the highest emission indices of unburned hydrocarbons over the entire range of overall equivalence ratios. Again, there is no systematic dependence of unburned hydrocarbons on jet pressure drop. The low emissions performance of the dome alone (no transverse air jets) is noteworthy. With the low levels of CO and THC emission indices recorded, the combustion efficiency for all jet pressure drops was about 99.99% up to an overall equivalence ratio of about 0.8 and then decreased for higher equivalence ratios.

Visible in the flame structures seen in Fig. 2 is an intense central flame at the confluence of the opposed air jets that projects upstream slightly into the central region of the conical shear-layer flame from the fuel injector. The size of the central flame increased with increasing pressure drop. Computational fluid dynamics (CFD) analysis of a similar combustor and injector configuration[7] revealed that a football-like (ellipsoidal with the major axis in the same plane but normal to the combustor centerline) recirculation zone was situated immediately upstream of the confluence of the penetrating air jets. Flame appeared to be stabilized around this ball recirculation in a stoichiometric interface. Total emissions from the primary zone will depend on the number, size, and local conditions existing in the flame structures present. Obviously, operating conditions that increase the number or size of flame structures will result in changing emissions values.

Dome Characteristics

The combustor can be operated with zero-combustion air jets to obtain the characteristics of the dome alone. Figure 6 is a plot of the emission index of NO_x for the dome, as a function of metered equivalence ratio taken from Fig. 5; the dome pressure drop was 4.3%. The measured NO_x reaches a peak of about 3.6 g/kg at a dome equivalence ratio of 0.82. As the dome equivalence ratio exceeds unity, NO_x emission index falls as a result of unburned fuel leaving the combustor.

To place the dome NO_x into context with respect to fuel/air mixing and the type of flame resulting, also shown on Fig. 6 are calculated NO_x curves using two approaches: first, assuming "experimentally perfect premixing" of fuel and air, and second, representing the dome flowfield as a reactor network having a degree of partial stirring. For the experimentally perfect premixing case the empirical correlation of Roffe and Venkataramani[8] for lean premixed propane and air systems was used. In this correlation the residence times were estimated for volumes based on observed flame dimensions. The very simple reactor network for the second examination was based on CFD calculations for this injector and hole pattern, with reactor dimensions based on observed flame dimensions and having the fuel heating value reduced to account for estimated heat losses from the combustor. The network consisted of a perfectly stirred reactor with a parallel plug-flow reactor that processed 13% of the total flow that was recirculated back into the perfectly stirred reactor. These two calculations represent perfect premixing in the dome and well mixed but not perfect premixing. The effect of improved mixing as represented by the two calculations is to increase the peak NO_x and to narrow the NO_x curve across equivalence ratio; furthermore, the peak NO_x occurs at dome equivalence ratios around unity.

Comparing the measured dome NO_x against the two calculations demonstrates that the fuel was actually burned in the dome in far from premixed form. The broadened burning limits and the shift of the NO_x down to about 0.8 equivalence ratio indicates this. This behavior occurs despite the use of a gaseous fuel, intimate association of fuel and air in the fuel injector, and the existence of a flame that is lifted from the injector. Nonetheless, although the dome is not premixed, the NO_x emission indices do still show a strong dependence on dome equivalence ratio over the entire range covered. This is indicative of partially premixed burning, with a level of fuel/air

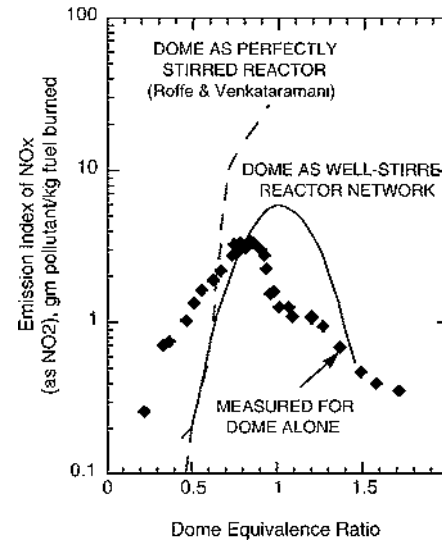

Fig. 6 Assessment of dome mixing characteristics.

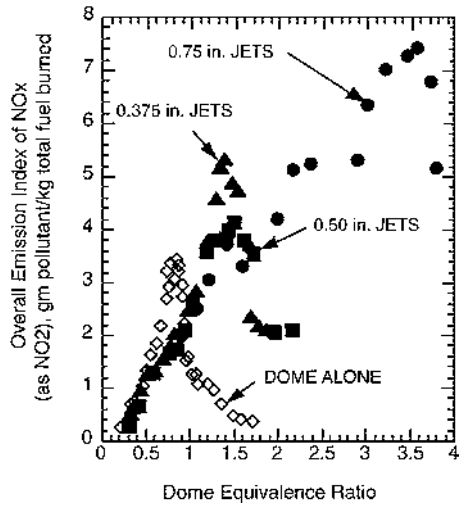

Fig. 7 Overall burning characteristics for NO_x.

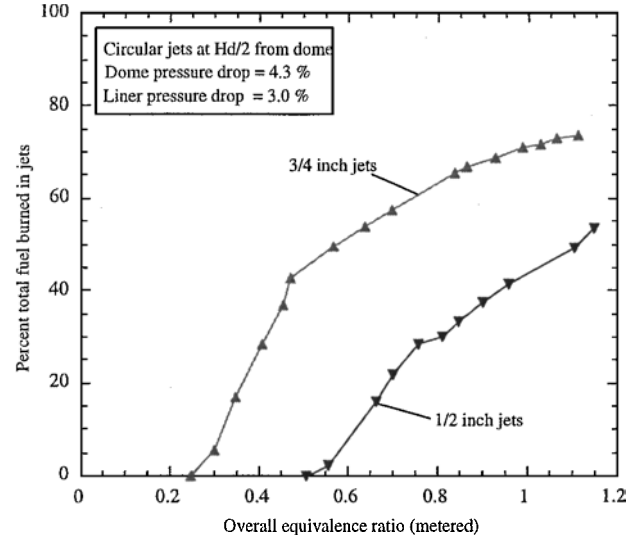

Fig. 8 Dependence of quantity of fuel burned in jets on overall equivalence ratio, for two jet sizes.

unmixedness that is greater than that taken in the reactor network calculations.

Overall Burning Characteristics

If the flame in the dome alone is not premixed, the question must be asked concerning what happens when the air jets are present. Figure 7 is a plot of overall NO_x EIs for several jet systems at $H_d/2$ from the dome, including the dome alone, plotted against dome equivalence ratio, at fixed dome and jet pressure drops. The characteristic of the dome-alone NO_x is that from Fig. 6.

The characteristics for the individual combustion air jets all collapse onto a common curve for dome equivalence ratios up to about 1.15. For dome equivalence ratios of 0.55 and less, this collapsed data is co-incident with the dome-alone data. Such behavior indicates that basic flame characteristics in the dome are unaffected by the presence of the jets.

The NO_x peak for jets being present is shifted from the nominal 0.82 equivalence ratio for the dome-alone to higher dome equivalence ratios, in the range 1.3–1.55 for the smaller jet sizes and to around 3.5 for the largest jet. The levels of NO_x at the peak, and the subsequent behavior on the dome-rich side of the peak, are dependent on the individual jet size. Note, however, that the data for the 0.375-in. (9.53-mm) and 0.50-in. (12.7-mm) jets are virtually co-incident.

The shifted NO_x peak from 0.82 with no jets to 1.3–1.55 dome equivalence ratio with jets indicates that in addition to peak temperatures being reached at lower equivalence ratios (0.82 rather than about 0.92–1.0) as a result of unmixedness effects some of the combustion jet air is actually active in the dome. The co-incidence of the data for individual jets at equivalence ratios less than 1.15 suggests that the dome aerodynamics are not strongly influenced, or least modified, by the details of the air jets, that is, that any additional air introduced into the dome takes part in chemical reactions in a region somewhat separate from the jets themselves and that this region is not far upstream in the dome itself. Flame photographs (Fig. 2) identify a significant luminous region on the injector centerline, just upstream of the confluence of the transverse combustion air jets. This was identified by CFD as burning round a recirculation bubble in this position. This bubble could be where the small quantity of jet air is utilized in the dome. The centerline penetration of all jets at 3% liner pressure drop ensures that this bubble is present whenever the jets are present, although its dimensions depend on the jet size.

Data Analysis Strategy

As Fig. 2 indicates, there are several regions of large heat release existing within the primary zone overall flame structure. To evolve low emissions configurations, it is desirable to understand the separate contributions to overall pollutant formation by these separate burning regions.

A broad bookkeeping strategy was therefore adopted for the data analysis as follows: Because combustion efficiency was 99.99+%, a fuel-rich dome is assumed to burn with 100% oxygen-consumption efficiency at all conditions so that the propane burned in the dome is given by

$$(\dot{m}_{f,\text{dome}})_{\text{burned}} = 0.0638\dot{m}_{a,\text{dome}} \tag{4}$$

and the fuel burned in the jets is

$$(\dot{m}_{f,\text{jets}})_{\text{burned}} = \dot{m}_{f,\text{Tot.}} - (\dot{m}_{f,\text{dome}})_{\text{burned}} \tag{5}$$

Figure 8 shows an example, using the bookkeeping system, of the nominal percent fuel burned in the jets as functions of overall (metered) equivalence ratio for single pairs of opposed circular jets of 0.5 in. (12.7 mm) and 0.75 in. (19.05 mm) diam. The figure shows that for both transverse jets systems the amount of fuel burned in the jets increases with increasing overall equivalence ratio. The 0.75-in. (19.05-mm) jet system at given overall equivalence ratio burns much more of the total fuel supplied than does the 0.50-in. (12.7-mm) jet system. For the 0.75-in. (19.05-mm) jet system all of the fuel supplied is burned in the dome for overall equivalence ratios less than 0.25; for the 0.50-in. (12.7-mm) jet system all of the supplied fuel is burned in the dome for overall equivalence ratios less than 0.5.

Figure 9 shows the burning zone equivalence ratio variations with overall (metered) equivalence ratio for dome and jets at each hole configuration. The relationships between overall and dome and jet equivalence ratios are, respectively, given by

$$\phi_{\text{dome}} = \left(1 + \frac{\dot{m}_{a,\text{jets}}}{\dot{m}_{a,\text{dome}}}\right)\phi_{\text{overall}} \tag{6}$$

and

$$\phi_{\text{jets}} = \frac{\dot{m}_{f,\text{jets}}}{0.0638\dot{m}_{a,\text{jets}}} \tag{7}$$

It can be seen from Fig. 9 that at any overall equivalence ratio the dome with the 0.75-in. (19.05-mm) liner jets is much richer than the dome with 0.5-in. (12.7-mm) jets. For the 0.75-in. (19.05-mm) jets the dome is always above stoichiometric in the range of overall equivalence ratios covered; for the 0.5-in. (12.7-mm) jets the dome is either fuel lean or fuel rich, depending on the overall equivalence ratio. For overall equivalence ratios up to unity, the jets are always fuel lean for either jet size. As a consequence of the stoichiometry distributions for the two jet sizes, the 0.75-in. (19.05-mm) jets burn much more of the total fuel than do the 0.50-in. (12.7-mm) jets.

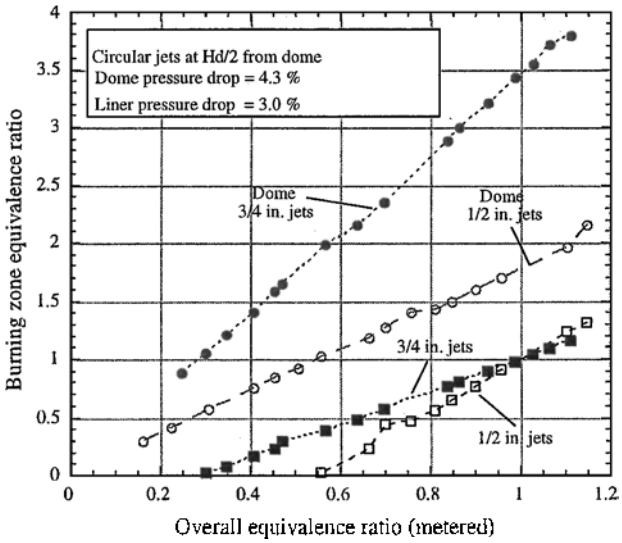

Fig. 9 Stoichiometry breakdowns between dome and jets, for two jet sizes.

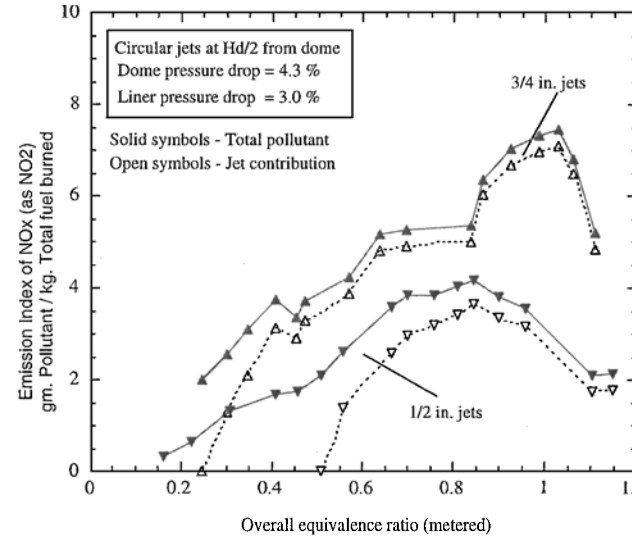

Fig. 10 Contributions of jet NO_x to overall NO_x for two jet systems.

Jet Contribution to NO_x Generation

The principal of superpositions can be used to obtain the separate contributions to total NO_x of the dome alone and then the air jet system. Superpositions depend on the two elements being considered as not substantially changing each other. This has been shown for NO_x in Fig. 7. Therefore, the jet-NO_x EIs were obtained by subtracting from the total NO_x EIs the NO_x EIs for the dome. The dome EIs were obtained from the dome-alone curve in Fig. 6 at the appropriate dome equivalence ratios for each jet system with a particular overall equivalence ratio.

In Fig. 10 the EIs of NO_x, in terms of grams of NO_x per kilogram of total fuel burned, for the 0.50-in. (12.7-mm) and 0.75-in. (19.05-mm) initial diameter transverse combustion air jets are presented with variation in overall (metered) equivalence ratio. For each jet size the total NO_x and the NO_x generated by just the transverse jet systems are given. The figure shows that the jet NO_x reaches zero for the 0.75-in. (19.05-mm) jets at an overall equivalence ratio of 0.25 and for the 0.5-in. (12.7-mm) jets at an overall equivalence ratio of 0.51. These values correspond to zero jet equivalence ratios and zero fuel burned in the jets, as shown in Figs. 8 and 9. These agreements support the use of superpositions as a means to extract jet NO_x. At lower overall equivalence ratios all of the NO_x for both jet systems is generated in the dome, even though the jets are present. For overall equivalence ratios of less than about 0.25, the two overall NO_x curves should run into each other for a common curve representing dome-only (Fig. 6) burning. Although the two curves are converging at lower equivalence ratios, they are not co-incident for overall equivalence ratios less than 0.25. This is because there are slightly different aerodynamic blockage effects resulting from the two transverse jet systems and acting upon the axially directed fuel/air jet from the injector/dome interface region.

The strong jet-NO_x effect is illustrated in Fig. 11, which plots for each jet system the jet NO_x EIs, expressed as grams of NO_x per kilogram of fuel burned in the jets, against the jet equivalence ratio. Expressed in this form, the fact that the 0.75-in. (19.05-mm) jet system burns considerably more of the total fuel supplied than does the 0.50-in. (12.7-mm) jet system (Fig. 8) should be accounted for. Data are shown for all of the jet diameters evaluated. For jet equivalence ratios less than 0.8–0.9 (where a NO_x peak is expected for partially premixed systems) the NO_x for the 0.375-in. (9.53-mm), 0.50-in. (12.7-mm), and 0.75-in. (19.05-mm) jets is essentially independent of jet equivalence ratio. This suggests that the fuel burned in these jet systems at such lower equivalence ratios is in reality reacted in stoichiometric interfaces associated with the fresh air entering through the jets. The jet NO_x EIs consistently begin to decrease at higher jet equivalence ratios. This is because unburned fuel is now exiting the

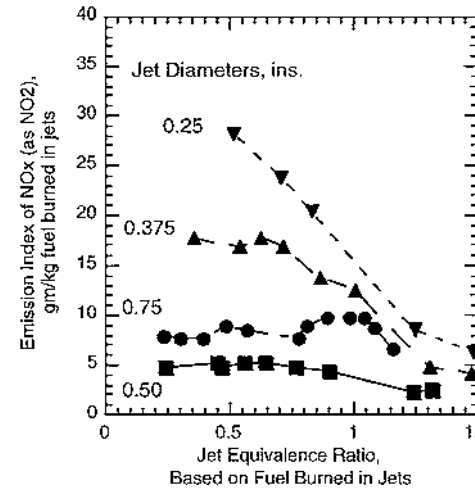

Fig. 11 Demonstration of stoichiometric burning in jet systems.

combustor because the available stoichiometric surfaces are burning all the fuel that they can. The jet NO_x EI plateau levels for the lower jet equivalence ratios decrease with increasing jet initial diameter, with the exception of the 0.50-in. (12.7-mm) jet system, which unexpectedly has the lowest values. For the 0.25-in. (6.35-mm) jets the jet NO_x EIs continuously decrease with increasing jet equivalence ratio over the entire range covered. This suggests that because of its small initial size this jet system might be less coherent than the other jet systems. Although the jet systems are conveniently identified by the jet initial diameters, the flame structures associated with each also include that of the central "football" recirculation zone. For given operating conditions the sizes of these recirculation zones depend on the jet dimensions.

The percentage of total NO_x that is generated in the jets for each initial jet size is plotted in terms of overall equivalence ratio in Fig. 12. The percent jet NO_x was obtained by multiplying the calculated emission indices for the jets by the mass flow rate of fuel burned in the jets, divided by the measured overall emission index for the complete primary zone at the same equivalence ratio, multiplied by the total fuel flow rate. The figure shows that for the 0.75-in. (19.05-mm) initial jet size more than half of the NO_x originates in the jets for all operating equivalence ratios; for the 0.50-in. (12.7-mm) jet the jet NO_x only reaches 50% of the total for a stoichiometric primary zone. The general behavior is for the percent jet NO_x to increase with overall equivalence ratio and to do so rather steeply initially until a plateau level is reached. This behavior is repeated

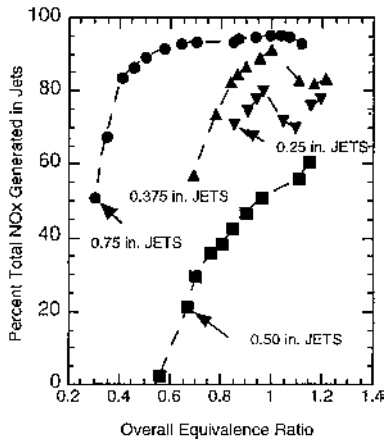

Fig. 12 Contribution of jet-generated NO_x.

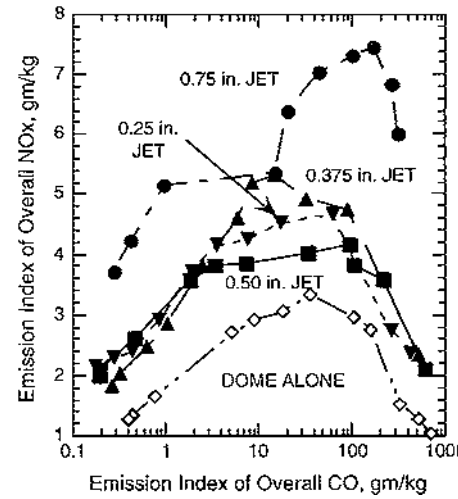

Fig. 13 Overall emissions assessment for range of jet sizes.

for each jet system, and the plateau level is lower for smaller jets than for the larger jets. For the 0.75-in. (19.05-mm) jets the plateau is at about 95% jet NO_x; for the 0.375-in. (9.53-mm) jets it is about 85%, and for the 0.25-in. (6.35-mm) jets it is about 75%. The 0.5-in. (12.70-mm) jet system has not yet reached its plateau level in the range of overall equivalence ratios covered. This jet system appears to be the exception to the general behavior. If overall equivalence ratio is increased above unity, the percent jet NO_x contribution to overall NO_x would eventually start to fall as the jet system became overrich and unburned fuel left the primary zone. This behavior is clearly evident for the two smaller jets and is becoming so for the largest jet. The 50% jet NO_x condition is reached at overall equivalence ratios that increase with decreasing jet size. This corresponds to the condition where the dome equivalence ratio exceeds unity in each case. For the 0.50-in. (12.70-mm) jet system the 50% jet NO_x condition is reached at an overall equivalence ratio of 0.96. From stoichiometry plots (Fig. 9) this corresponds to a dome equivalence ratio of 1.7. This is a very rich dome condition compared to the other jet sizes. This jet system generates lower jet NO_x percentages at all overall equivalence ratios than either larger or smaller jets. Clearly, the 0.5-in. (12.70-mm) jet system behaves differently to all of the others. This different behavior appears to be associated with the football recirculation zone. For the 0.375-in. (9.53-mm) and 0.25-in. (6.35-mm) air jets the recirculation zones are observed to be physically very small. For the 0.75-in. (19.05-mm) air jets although the recirculation zone is physically larger, it is small in relation to the jet structures themselves. In the case of the 0.50-in. jets, the recirculation and jet structures are observed to be comparable in size. The relative dimensions of the recirculation bubble and jet envelope flames can be appreciated from Fig. 2. A clear implication of Fig. 12 in light of these observations concerning the football recirculation bubble is that unburned fuel from the dome is burned differently in the recirculation bubble than it is around the jet structures. It is not difficult to accept that combustion around the highly coherent air jet structures takes place stoichiometrically. This being so, the hypothesis leads to the conclusion that combustion in the recirculation bubble must therefore take place partially premixed and at a local equivalence ratio less than unity. The jet-system net NO_x generated therefore would represent a combination of the NO_x from these two sources, and the amount of NO_x would depend on how much of the fuel is burned around the jets and how much is burned in the recirculation region. If a significant portion of the total fuel processed by the 0.50-in. (12.7-mm) jet system is reacted partially premixed in the recirculation bubble, then the NO_x of this system would be lower than anticipated from just the jet diameter.

Overall Emissions Assessment

Figure 13 is a plot of overall NO_x emissions indices against overall CO emissions indices for each of the jet sizes, including the dome alone. The data for each jet size are limited on the left-hand side by a 0.5 primary zone equivalence ratio and on the right-hand side by 1.1 primary zone equivalence ratio. Such a plot represents the emissions trade between NO_x and CO that might be made. A box can be placed around the data for any particular jet size in the plot, bounded on one side by the maximum CO, on the top by maximum NO_x, and on the remaining side and the bottom by the respective axes. Such a box is a qualitative measure of the total emissions production of the particular jet configuration. Data for any other configuration over the same equivalence ratio range that fall wholly inside the initial box represent a truly lower emissions configuration.

Review of the figure reveals several interesting facts. First, the dome-alone configuration does truly represent the lowest emissions configuration because it has the smallest box. Second, the 0.50-in. (12.70-mm) jet does indeed represent some kind of optimum jet configuration for this primary zone because its box is smaller than the boxes for the other jets. It does not achieve its low NO_x by producing large amounts of CO. Third, the 0.75-in. (19.05-mm) jet is the worst emissions producer, and this is through its jet NO_x generation. The levels of CO over the equivalence ratio range in Fig. 13 are all at or very close to the appropriate equilibrium levels for the test conditions. For lower equivalence levels outside the range, there is an upward departure from equilibrium CO as a LBO condition is approached; similarly, at higher equivalence ratios there is also an upward departure from equilibrium CO as a result of a lack of oxygen.

LBO Considerations

The finding that the dome-alone configuration, that is, no traverse air jets whatsoever, gives the lowest emissions and raises the valid question as to the need for the separate combustion air jets.

The combustion air jets are needed to reduce flame length and to enhance lean stability. These are especially important for aircraft applications. Figure 14 shows some limited stability data for the dome alone and for the dome with the 0.50-in. (12.70-mm) jets at the $H_d/2$ position, in the form of blowout overall equivalence ratio against the air loading parameter (ALP)[9]. The ALP is defined as

$$ALP = m/(VP^n F) \tag{8}$$

The blowouts were conducted at atmospheric pressure, with variation of dome pressure drop for the dome alone and liner pressure drop at fixed dome pressure drop for the with-jet case. In addition for the dome-alone case, two inlet air temperatures were used—ambient and 500°F (533 K). The plot shows that for given ALP the with-jets case blows out at lower equivalence ratio than does the dome alone. For the dome-alone situation there were several flame modes observed. Blowouts for the range of ALPs in Fig. 14 were governed by lifted and attached flame conditions.[2] The presence of the combustion air jets exerts a backpressure on the flame and in addition provides for flame holding on the jets when the flame is lifted from the injector.

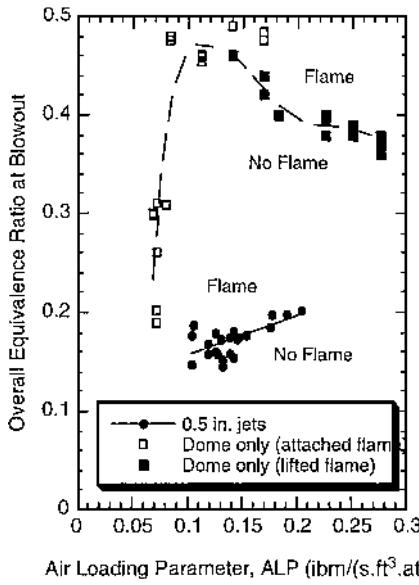

Fig. 14 Stability plot for dome alone and dome with 0.50-in. (12.7-mm) jets at half-dome height position.

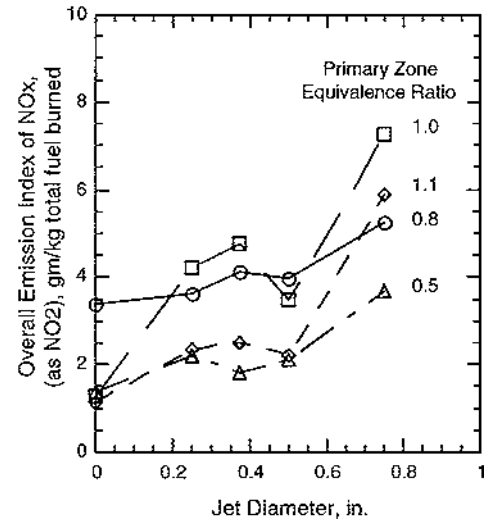

Fig. 15 Optimum jet size for minimum NO_x from overall primary zone.

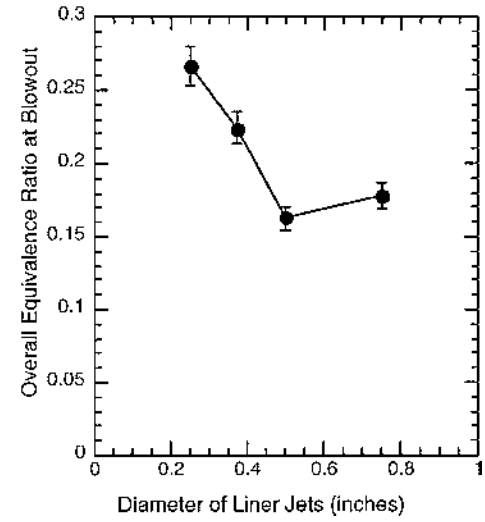

Fig. 16 Optimum jets diameter for blowout stability.

Discussion

The study reveals that the use of transverse combustion air jets to terminate and close the conventional primary zone of an aircraft gas-turbine combustor results in a severe penalty in NO_x emissions as a result of the formation of stoichiometric fuel/air burning interfaces around the jets. Most of the NO_x formed originates in these interfaces. The lowest overall emission characteristic would be achieved from a dome-alone primary zone. However, without the presence of combustion air jets the dome-alone blowout stability is inadequate for the wide turndown ratio necessary for the multipoint operating requirement for aircraft applications. Truly low NO_x dome-alone configurations would demand improved fuel/air mixing compared to conventional primary zones and selection of a fuel-lean design point, together with staged combustion in order to achieve adequate blowout stability. When a conventional dome design is used and the design requirements also include blowout stability as well as low emissions, combustion air jets must be used.

It does appear possible to achieve adequate blowout stability, together with minimized NO_x emissions, by optimizing the combustion air jet system. An example of low NO_x/adequate blowout margin optimization is shown in Figs. 15 and 16. Figure 15 gives the overall emission index of NO_x in terms of primary zone equivalence ratio at a high-power design point for an opposed pair of jets situated in line with the fuel injector at one-half a dome height downstream from the dome. Dome and liner pressure drops are fixed and are in line with current design practice. For a fixed geometry combustor, a primary zone design point equivalence ratio of 1.1 gives a value at engine idle power that will result in low CO emissions. Figure 16 shows that best lean blowout performance would be achieved with 0.50-in.-(12.7-mm) diam circular jets. It can be seen from Fig. 15 that the 0.50-in. (12.7-mm) jets would give a NO_x performance that is equivalent to operating the primary zone very lean (0.5 equivalence ratio) at design point. It should be understood that selection of a 1.1 primary zone equivalence ratio would necessitate the provision of additional combustion air downstream of the primary zone. Again, optimization of this jet system is then necessary.

The optimization involves a minimization of the stoichiometric interfaces formed around the air jets, together with achieving some partial premixing of jet air with unburned combustion products delivered from the dome. This apparently involves careful matching of the jet system to the fuel/air distributions delivered to the air jets by the dome. In the design process a heavy reliance on the computational fluid dynamics tool is essential to achieve the flame structures desired. Experimentally, assessments of local equivalence ratios in the primary zone would be demanded to evaluate these structures. Fortunately, one- and two-color optical diagnostic tools relying on chemiluminescence are now becoming available for this purpose.

A key feature of the optimization appears to be the formation of the football recirculation zones formed on the upstream side of the colliding opposed air jets. The term recirculation zone generally implies a closed volume of fluid, within which little chemical reaction takes place as a result of poor interchange with the surroundings. However, dynamic behavior, wherein the recirculation zone collapses and then reforms at a relatively high frequency, is generally considered to be the mechanism for combustion in such zones. Whereas dynamic behavior is almost certainly of some importance here, it should be accepted the term "recirculation zone" is not a very good descriptor of the "footballs." These are actually highly three-dimensional structures that wrap around the air jets in complicated fashion. They are not closed bodies, but receive fresh air from the colliding jets that give rise to them and discharge products into the wakes of the jets that they wrap around; flow from the dome in engulfed as the footballs roll up.

The study indicates that combustor design requirements, such as blowout stability and emissions, cannot be pursued independently. They must be worked together.

Conclusions

1) Most of the NO_x generated in the generic primary zone appears to originate from stoichiometric burning in interfaces around the combustion air jet system.

2) Minimum total emissions are produced when all of the reactants are introduced through the combustor dome.

3) Combustion air jets are necessary to reduce flame length and confer lean blowout stability.

4) For reasons associated with minimizing the stoichiometric interfaces around the jet and the amount of fuel that is burned in them, the 0.50-in.-(12.70-mm) diam opposed circular jets exhibit a clear optimum for the primary zone when the jets are positioned half a dome height downstream. This optimum is for minimum NO_x and lean blowout stability.

Acknowledgments

The enthusiasm, motivation, support, and contributions of W. M. Roquemore are greatly appreciated. The authors wish to thank R. Britton, M. Burns, and M. Russell for their help in acquiring emission measurements. This research was sponsored by the U.S. Air Force Wright Laboratory, Aero Propulsion and Power Directorate, under Contract F33615-93-C-2304 to Pratt & Whitney, East Hartford, Connecticut (Contract Monitor: Dale Shouse).

References

[1]Sturgess, G. J., Sloan, D. G., Roquemore, W. M., Reddy, V. K., Shouse, D., Lesmerises, A. L., Ballal, D. R., Heneghan, S. P., Vangsness, M. D., and Hedman, P. O., "Flame Stability and Lean Blowout—A Research Program Progress Report," *Proceedings of the 10th International Symposium on Air Breathing Engines*, edited by F. S. Billig, Vol. 1, International Symposium on Air Breathing Engines, Nottingham, England, 1991, pp. 372–384.

[2]Hedman, P. O., Sturgess, G. J., Warren, D. L., Goss, L. P., and Shouse, D. T., "Observations of Flame Behavior from a Practical Fuel Injector Using Gaseous Fuel in a Technology Combustor," *Journal of Engineering for Gas Turbines and Power*, Vol. 117, No. 3, 1995, pp. 441–452.

[3]Sturgess, G. J., Heneghan, S. P., Vangsness, M. D., Ballal, D. R., Lesmerises, A. L., and Shouse, D., "Effects of Back Pressure in a Lean Blowout Research Combustor," *Journal of Engineering for Gas Turbines and Power*, Vol. 115, No. 3, 1993, pp. 486–498.

[4]Spalding, D. B., "Performance Criteria of Gas-Turbine Combustion Chambers—A Method of Comparison and Selection for the Designer," *Aircraft Engineering Monograph*, Bunhill Publications Ltd., London, 1956.

[5]Gerrard, A. J., "Methods of Flow Visualization By Means of Water," *Experimental Methods in Combustion Research*, edited by J. Surugue, Pergamon, New York, 1961, Sec. 1-10, pp. 22–43.

[6]Sturgess, G. J., McKinney, R. G., and Morford, S. A., "Modification of Combustor Stoichiometry for Reduced NO_x Emissions from Aircraft Engines," *Journal of Engineering for Gas Turbines and Power*, Vol. 115, No. 3, 1993, pp. 570–580.

[7]Sturgess, G. J., and Shouse, D. T., "A Hybrid Model for Calculating Lean Blowouts in Practical Combustors," AIAA Paper-96-3125, July 1996.

[8]Roffe, G., and Venkataramani, K. S., "Emissions Measurements for Lean Premixed Propane/Air Systems at Pressure up to 30 Atmospheres," NASA Rept. CR-159421, 1978.

[9]Sturgess, G. J., and Shouse, D., "Lean Blowout in a Generic Gas Turbine Combustor with High Optical Access," *Journal of Engineering for Gas Turbines and Power,* Vol. 119, No. 1, 1997, pp. 108–118.

41st Aerospace Sciences Meeting and Exhibit
6-9 January 2003, Reno, Nevada

AIAA 2003-664

PARTICULATE MATTER AND POLYCYCLIC AROMATIC HYDROCARBON DETERMINATION USING A WELL-STIRRED REACTOR

R. F. Reich[1], S. D. Stouffer[2*], V. R. Katta[3], H. T. Mayfield[4], C. W. Frayne[1*], and J. Zelina[1**]

Air Force Research Laboratory[1]
Wright-Patterson AFB, OH

University of Dayton Research Institute[2]
Dayton, OH

Innovative Scientific Solutions, Inc.[3]
Dayton, OH

Air Force Research Laboratory[4]
Tyndall AFB, FL

*Member AIAA **Senior Member AIAA

ABSTRACT

Combustion generated particulates from gas turbine combustors can cause adverse effects on engine maintenance costs, plume visibility and the environment. Research is being conducted to provide understanding of the mechanisms of soot formation and identify mitigation strategies. A cooled well-stirred reactor (WSR), which simulates the primary zone of a gas turbine combustor, is used in the current study. Experiments have been completed with premixed, fuel-rich ($1.9 < \phi < 2.6$) ethylene-air and ethylene-ethanol-air mixtures. Multiple physical characteristics, including particle number density, particle size distribution, total carbon mass, and (polycyclic aromatic hydrocarbon) PAH content, were used to quantify the soot. A unique instrument, the Particulate Matter Characterization and Monitoring System (PMCMS), was used for the determination of the particle size distribution, and the chemical characterization of the soot and gaseous emissions. The results of the study showed that the benzene concentration in the gas phase increased monotonically with equivalence ratio while the pyrene was shown to correlate with the soot content. The results suggest that pyrene and other PAH species can be used to predict the soot formation for more complex combustion systems. For the conditions of the present study, the addition of ethanol to ethylene was shown to lower soot production compared to pure ethylene.

NOMENCLATURE

CNC	= condensation nuclei counter
GC/MS	= gas chromatograph/mass spectrometer
ICP-MS	= inductively coupled plasma mass spectrometer
RDMA	= radial differential mobility analyzer
m_a	= air mass flow rate (kg/s)
m_f	= fuel mass flow rate (kg/s)
MSVI	= multi-stage virtual impactor
PAH	= polycyclic aromatic hydrocarbon
PFR	= plug flow reactor
PM	= particulate matter
PMCMS	= Particulate Matter Characterization and Monitoring System
R_s	= reflectance of the stained filter
R_w	= reflectance of the unstained filter
SN	= smoke number
T_a	= adiabatic flame temperature (K)
T_f	= reactor temperature (K)
T_o	= inlet temperature (K)
THC	= total hydrocarbons
UNICORN	= UNsteady Ignition and COmbustion with ReactioNs
V	= reactor volume (mL)
WSR	= well-stirred reactor

Symbols

ϕ	= equivalence ratio
ρ	= density (kg/m^3)
τ	= residence time (ms)

This material is declared a work of the U.S. Government and is not subject to copyright protection in the United States.

INTRODUCTION

The accepted process of soot formation (Figure 1) demonstrates the reaction path to soot by which a portion of fuel is broken into unsaturated radicals and intermediates during combustion. These are known as soot precursors, which then react to form small polycyclic aromatic hydrocarbons (PAH). The growth of PAH continues through further reactions and by collisions and nucleation with each other forming larger PAH, becoming incipient soot particles. These particles continue to grow by processes of surface growth, condensation and coalescence, and through reactions with acetylene and smaller PAH, forming particulate matter (PM) < 50 nm in aerodynamic diameter, referred to as primary soot particles. Primary particles collide and coagulate forming PM ranging in size from hundreds of nanometers to microns. Oxidation continues throughout the combustion process, concurrently and within all stages of PM formation, consuming PAH, the growth species and soot particles comprising PM. Oxidation reactions occur by highly reactive radical species containing OH and oxygen atoms, forming primary combustion products, CO_2, H_2O, CO, NOx, unburned total hydrocarbons (THC) and smoke, an aerosol containing soot.

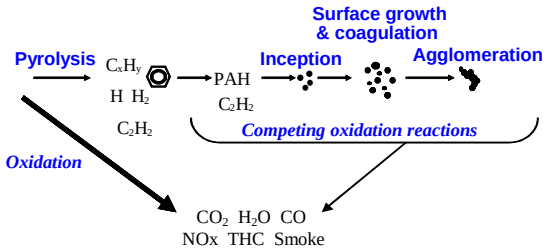

Figure 1: PM Formation Process

To investigate the reduction of PAH and PM due to oxygenates, ethylene fuel (C_2H_4) and ethanol (C_2H_5OH), as an additive, were burned in the Air Force Research Laboratory's Well-Stirred Reactor (WSR)[1-3], while samples were collected from the effluent and analyzed using the Particulate Matter Characterization and Monitoring System (PMCMS)[4]. This study was particularly well-suited for the WSR, which simulates the combustion process in the primary zone of a gas turbine combustor, while eliminating the effects of fuel atomization, evaporation, and mixing processes, and continues the work that was presented in Stouffer et al.[5].

The determination of the PAH and PM generated by the WSR is significant because fundamental information can be evaluated using the PMCMS, before particle inception occurs and after primary particle coagulation into PM. The PMCMS analyses were compared with a predictive model of PAH using UNsteady Ignition and COmbustion using ReactioNs (UNICORN)[6] code which provides quantification and identification of single and multi- ring aromatic hydrocarbons generated in a perfectly stirred reactor.

PM quantification is compared to analyses determined from captured soot and smoke stains, providing further verification of this useful approach and methodology for assessing the validity of experimental and computational results. These results are important for further investigations to determine particulate formation mechanisms, to develop combustion models of pollutant formation and to identify fuel additives to reduce particulate formation.

EXPERIMENTAL APPARATUS

Well-Stirred Reactor

A toroidal-shaped WSR research combustor with a volume of 250 mL was used for the study. A cross section of the reactor and jet ring is shown in Figure 2. The design is a modification of an earlier WSR design by Nenniger[1] and Zelina[2] and features an Inconel jet ring with 48 fuel/air jets. The upper and lower halves of the toroidal reactor are cast from silicon carbide. Silicon carbide was used because of its resistance to thermal cracking. The ceramic reactor is contained inside a steel housing, and has a 2-inch diameter stack connected to the exhaust port which forms the plug flow reactor (PFR) section. The jet ring is cooled by nitrogen impingement cooling to avoid autoignition of the fuel-air mixture within the jet ring manifold.

The two fuels used in the current study were neat ethylene and an ethylene-ethanol mixture with 5% of the fuel mass from the oxygen in the ethanol (14.4% ethanol by mass). With these fuels the WSR operates stably at high equivalence ratios ($1.8 < \phi < 2.6$), which allows measurement of PAH, particulates and smoke in a range of conditions from soot inception through the formation of carbonaceous soot.

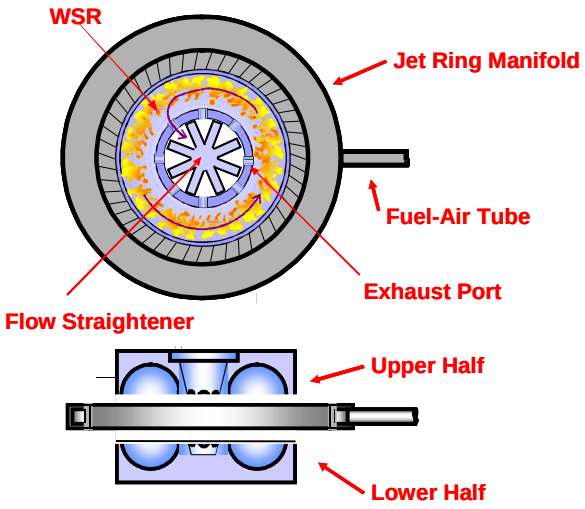

Figure 2: Schematic of WSR Design

Figure 3 is a photograph of the WSR rig during operation which also shows a sampling probe penetrating the exhaust stack, entering the plug flow region above the reactor. Gaseous emissions and smoke were drawn from the PFR section. A port at the bottom of the housing permits probe access to the reactor for obtaining emissions and smoke samples.

Figure 3: WSR Test Rig Burning Ethylene

Experimental Sampling Techniques

Soot samples were collected on filters from both the plug flow region 16 cm downstream of the WSR and from the inside of the toroidal WSR volume on paper or quartz filters by drawing the exhaust gas collected in the probe through the filters. The gas sample was first pulled through a 25 cm-long oil-cooled probe with an inside diameter of 0.47 cm. The probe was cooled to 150°C by circulating oil through the outer jacket. The gas then passed through an electrically heated (constant surface temperature of 150°C) 2-meter long sample line before passing into a Roseco engine smoke emissions sampler.

The volume of the sample gas collected for each test was 7.08 liters. Each sample required 30-60 seconds to collect. The samples acquired on the paper filters (Whatman #4) were analyzed using the SAE ARP1179 procedure[7] to determine the smoke number based on reflected light from the samples:

$$SN = 100\left(1 - \frac{R_s}{R_w}\right)$$

where: R_s= Reflectance of the stained filter
R_w= Reflectance of the unstained filter

The samples acquired on the quartz filters (Whatman type-QMA) were analyzed to determine carbon burn-off in a LECO carbon analyzer. The total carbon analyzer measures the carbon mass deposited on the filter by measuring the CO_2 produced while increasing the temperature of the filter in an oven in the presence of excess oxygen. An advantage of the carbon analyzer is that any inorganic deposits on the filter, caused by erosion of the reactor materials will be ignored in the analysis.

In addition to the carbon burn-off analysis, the quartz filter samples were also analyzed using gas chromatograph/mass spectrometry (GC/MS) Chromatoprobe[8] (Figure 4) analysis to determine the PAH content of the soot. This was performed by placing a 2-mg sample cut from the soot stained quartz filter into the sample vial inside the Chromatoprobe shown in Figure 5. The Chromatoprobe was then inserted into the temperature programmable injector (Figure 6) of the GC/MS, which was rapidly ramped in temperature (150°C/min) from 40 to 320°C. This resulted in the PAH's being thermally desorbed from the quartz filter paper and sequentially injected into the GC/MS for separation and detection.

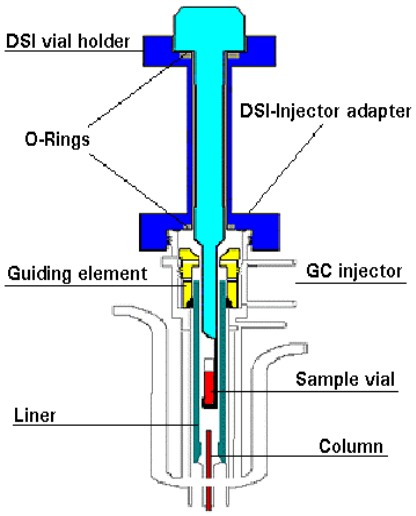

Figure 4: Varian Chromatoprobe

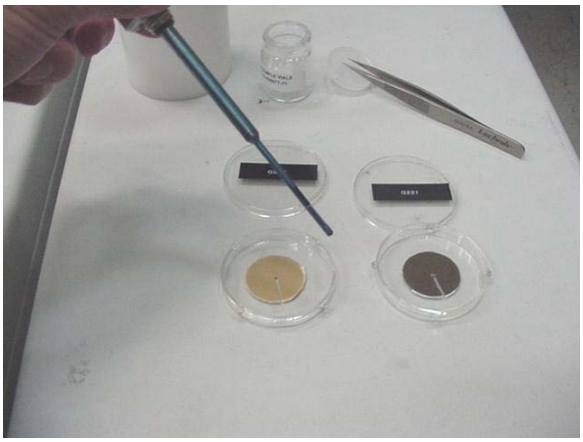

Figure 5: Chromatoprobe Sample

Figure 6: Chromatoprobe in GC/MS

Seventeen different PAH's identified during the Chromatoprobe analysis are listed in Table 1. Also listed are the target ions for each PAH, which are the most abundant ions from the mass spectrum of each PAH used for detection, along with the retention time, which is the time that the PAH is retained on the GC column before detected by the mass spectrometer. The retention time can be used to distinguish between PAH's with the same target ion.

Table 1. PAH Species Identified in the GC/MS Chromatoprobe Analysis

PAH	Target Ion (m/z)	Retention Time (min)
Naphthalene	128	5.367
Acenaphthylene	152	8.191
Acenaphthene	153	8.460
Fluorene	166	9.262
Phenanthrene	178	10.733
Anthracene	178	10.811
1,4-Diphenylbutadiyne	202	12.350
Fluoranthene	202	12.600
Pyrene	202	12.921
Benz [a] anthracene	228	14.899
Chrysene	228	14.951
Benzo [b] fluoranthene	252	16.809
Benzo [k] fluoranthene	252	16.846
Benzo [a] pyrene	252	17.344
Indeno [1,2,3-cd] pyrene	276	19.237
Dibenz [a,h] anthracene	278	19.653
Benzo [g,h,i] perylene	276	19.817

Emissions from the reactor section of the WSR were passed through a quartz filter to remove particulates and then trapped in a 250-mL gas sampling bulb. Gas samples were directly injected into the GC/MS for qualitative and quantitative analysis of combustion gas species. Seven trace combustion gas species were targeted for analysis and are shown in Table 2 along with their corresponding target ions and retention times.

Table 2. Combustion Gas Species Considered in the GC/MS Gas Analysis

Gas Species	Target Ion (m/z)	Retention Time (min)
1,3-Cyclopentadiene	66	0.400
Benzene	78	0.604
Toluene	91	1.094
Ethylbenzene	91	2.164
Phenylacetylene	102	2.485
Styrene	104	2.769
Naphthalene	128	7.980

Particulate and Emissions Measurement Instrumentation

The particulate instrumentation system is composed of a TSI 3022 condensation nuclei counter (CNC) and a sampling system using a vacuum pump to control sample flow through a 10 L/min flow meter and transmitter. This combination of Brooks flow meters is used to set accurate dilution air flows to the particulate sampling probe. The CNC and sampling system are configured to adapt to the PMCMS, shown in Figure 7, used to evaluate particulate species and PAH.

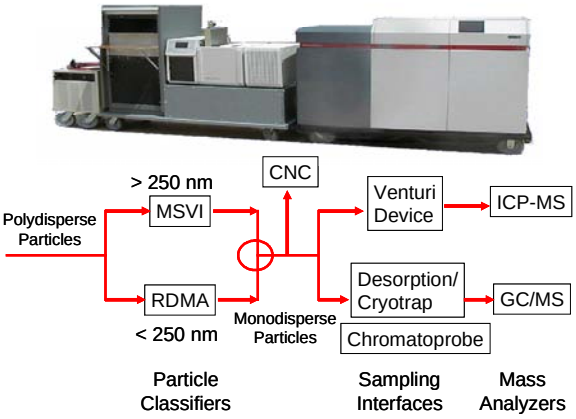

Figure 7: PMCMS and Schematic

Particle size below 250 nm was characterized using the Radial Differential Mobility Analyzer (RDMA)[9] within the PMCMS, shown in Figure 8.

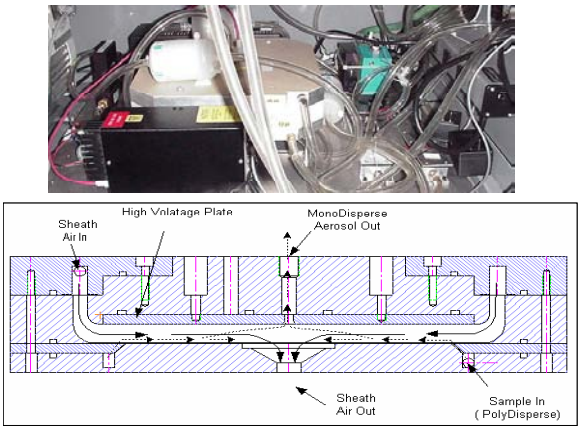

Figure 8: RDMA

Particle sizing is achieved by charging a polydisperse stream of aerosols and passing the stream through a well defined electric field. Charged particles within the aerosol will follow predetermined trajectories. The RDMA is designed to extract aerosols that follow one predetermined trajectory, while discarding all others. The particle number density was determined using the CNC sampling from the PFR in the WSR. A short stack configuration was used to minimize the PFR region for obtaining particulate, smoke and soot measurements close to the reactor. The sample from the PFR was extracted from a region 7 cm upstream of the PFR exit to capture the rich exhaust products before they could react with the ambient air.

The emissions system consists of a 150°C oil-cooled emissions probe and a 150°C heated sampling line that is 6.1 m long. The sample stream is then split into two streams. The first stream directly enters a flame ionization detector total hydrocarbon analyzer, while the second stream enters an Alpha Laval chiller, which provides the main sampling pump, condenses water vapor from the gas sample and sets the sample flow for the CO, CO_2, O_2 and NO_x analyzers. The analyzers are calibrated before each test using 2% certified standard gases and often spanned for verification of ~3% accuracy during the tests, using several calibration gas mixtures to check drift and maintain linearity.

TEST CONDITIONS

The air flow for the experiments was set at a constant 240 g/min with an inlet temperature set at 392 +/- 5K. The fuel/air equivalence ratio, ϕ, ranged from 1.9 to 2.6 for both fuels. The pressure inside the reactor section ranged from 1.1 to 1.7 kPa above the

ambient pressure for all of the experiments. The average residence time in the reactor, τ, which was calculated using: $\tau=\rho V/(m_a+m_f)$, was 9.7 +/- 0.3 ms for the experiment.

The gas temperature inside the reactor (uncorrected for the effects of radiation) ranged from 1480 to 1725 K. The temperatures are significantly lower than the adiabatic flame temperatures because of heat loss through the high-conductivity silicon carbide reactor walls to the nitrogen flow that is used to cool the jet ring.

EXPERIMENTAL RESULTS

The particle size distributions sampled from the plug flow region of the reactor are shown in Figure 9 for both the neat ethylene and the ethylene-ethanol mixtures over a range of ϕ from 2.0 to 2.6. The ethylene-ethanol mixture was shown to reduce particle concentration at all ϕ compared to the neat ethylene fuel. The highest particle concentrations for ethylene and the ethylene-ethanol were measured at ϕ = 2.4 and ϕ = 2.3, respectively.

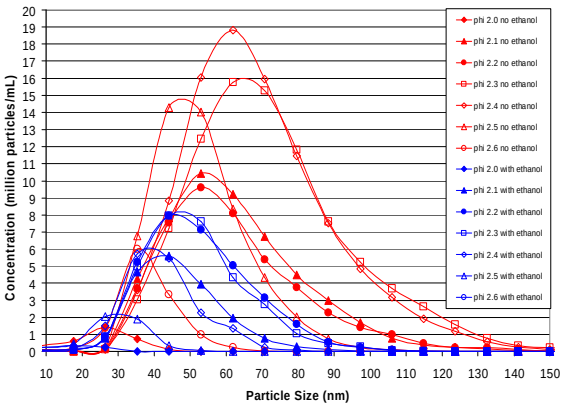

Figure 9: Particle Size Distribution

The diameter of the peak particle concentration for the size distributions is shown in Figure 10. The peak particle size increases as ϕ is increased from 1.9 to 2.3 for both fuels. As ϕ is further increased the peak particle size decreases. The ethylene-ethanol fuel resulted in smaller peak particle sizes compared to the ethylene fuel over the entire range of test conditions.

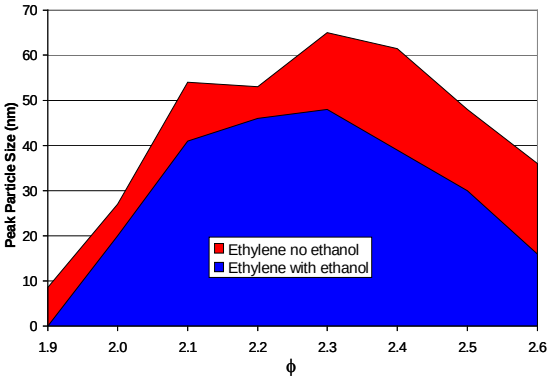

Figure 10: Peak Particle Size

The total particle concentration was calculated by integrating the area under the particle distribution curves for each ϕ, shown in Figure 11. The addition of ethanol resulted in a reduction in the total particle concentration measured over the entire range of ϕ tested. The bottom half of Figure 11 shows the stained quartz filters after the samples were acquired for both the neat ethylene fuel (top row) and ethylene-ethanol mixtures (bottom row) in order of increasing ϕ from left to right. The filter stains for both fuels are darker as ϕ is increased from 1.9 to 2.2 and then lightens as ϕ is further increased. For all ϕ the stains are darker for the ethylene fuel than they are for the ethylene-ethanol fuel.

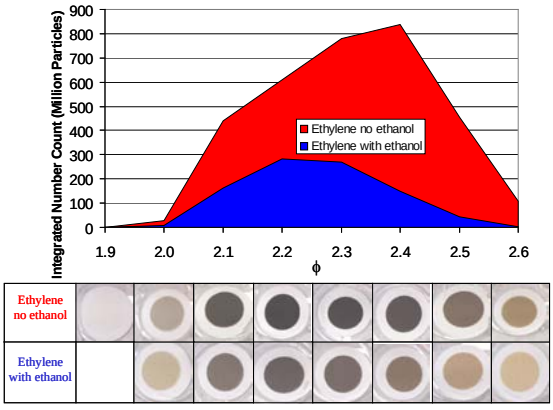

Figure 11: Total Particle Count (Top) and Corresponding Images of Filters from the Plug Flow Region (Bottom)

The GC/MS chromatogram resulting from direct injection of 500 µL of gas sampled from the WSR for a typical test is shown in Figure 12. Benzene was the most concentrated gaseous species detected followed by 1,3-cyclopentadiene and a series of other soot

precursors, whose structures are shown in the figure. These results were similar to those found by Lam et al.[10], where benzene was measured in highest concentration, followed by phenylacetylene, naphthalene, toluene and styrene. The mass chromatogram was magnified 100 times from 10.0-14.0 minutes to show the presence of trace PAH's in this range.

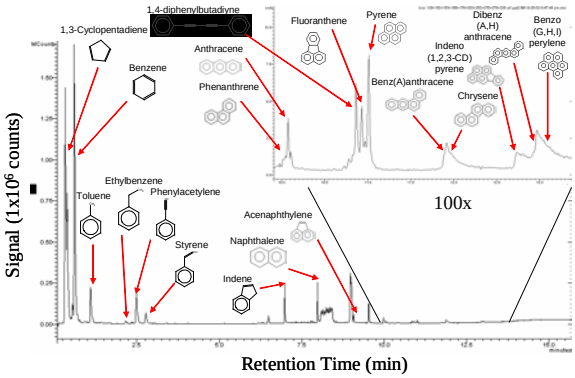

Figure 12: GC/MS Gas Analysis from WSR

A calibration curve was prepared for benzene by injecting 500 µL aliquots of benzene vapor at varying concentrations from a static dilution bottle. The mass of benzene per 500 µL sampled from the WSR is plotted for each ϕ, shown in Figure 13. The concentration of benzene increases linearly with increasing ϕ. The addition of ethanol resulted in no change in benzene content. All other gaseous soot precursors detected indicated a similar trend as benzene.

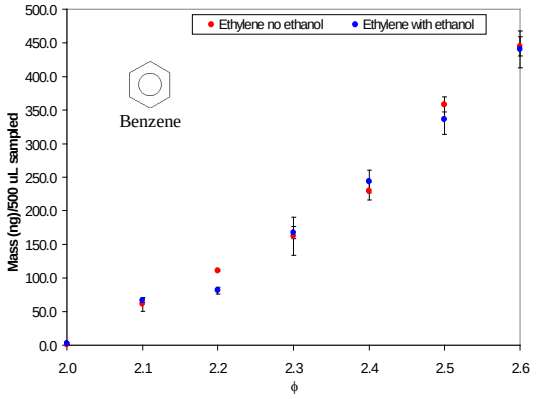

Figure 13: Benzene Concentration Sampled from the WSR

Figure 14 shows the smoke number measured from filter samples extracted from both the reactor and the plug flow section. For both fuels, the smoke number initially increases between ϕ = 1.9 and 2.2-2.3, and starts to decrease as ϕ is increased further. Although there is more fuel available for the formation of soot at higher ϕ, it is thought that the soot production is reduced due to decreasing temperatures and thus slower chemical reaction times. Note that the smoke number measured in both the reactor section and the plug flow regions are approximately equal for the same fuel at the same reactor conditions for ϕ < 2.4. As the fuel flow is further increased, the smoke number is seen to be lower in the reactor section than it is in the PFR.

The addition of ethanol results in a reduced smoke number for all ϕ measured, with the greatest reduction shown at ϕ = 2.2 and 2.3. This trend is different from the one observed previously in the study by Stouffer et al.[5] where the addition of ethanol was seen to slightly increase the soot production. However, it should be noted that the temperature inside the reactor in the previous study was higher (by approximately 110°C) than the reactor temperature in the current study because lower thermal conductivity ceramics were used for the wall materials in the previous study. It is thought that the combustion temperatures significantly affect the soot production mechanism.

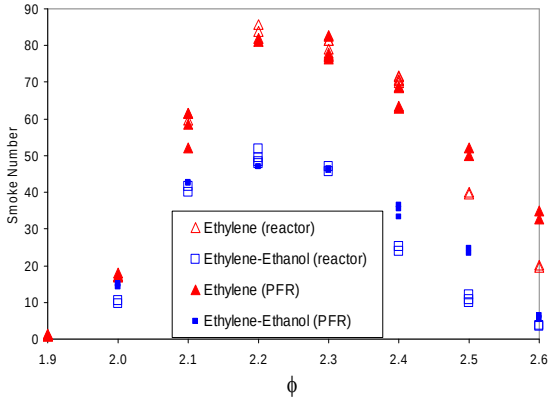

Figure 14: Smoke Number Results

Figure 15 shows total carbon analysis of the quartz filter samples extracted from both the reactor section and the plug flow sections of the WSR. The overall shape of the integrated carbon mass plot shown in Figure 15 shows trends similar to those shown for the smoke number plots in Figure 14. A significant difference is that there was an increase in the total carbon mass between the reactor and the plug flow section. The addition of ethanol decreases the

amount of carbon deposited on the quartz filters for all ϕ measured.

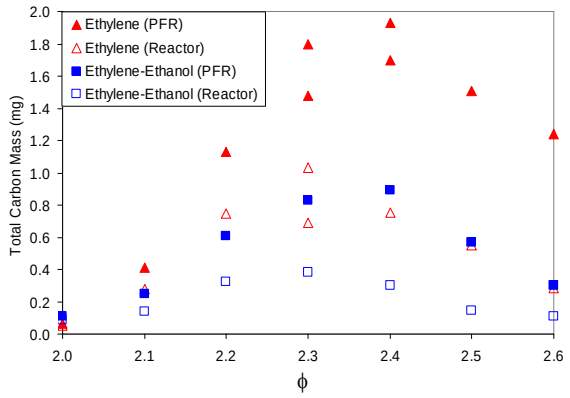

Figure 15: Total Carbon Mass

The relative carbon count plotted with increasing temperature for three equivalence ratios (ϕ = 2.1, ϕ = 2.3, and ϕ = 2.6) are shown in Figures 16A, 16B, and 16C, respectively, along with corresponding photographs of the filters before the carbon analysis was conducted. These figures show two distinct peaks, a low temperature peak located between 120 and 160°C, and a high temperature peak located between 450 and 560°C. The sample for the highest equivalence ratio (ϕ = 2.6 in Figure 16C) has the highest carbon content in the low temperature region and the filter stain is beige-colored while the high temperature carbon peak is highest for the ϕ = 2.3 case, shown in Figure 16B, which shows a much darker filter stain. It is thought that the low temperature peak is due to the presence of PAH's while the high temperature peak is due to the presence of carbonaceous soot.

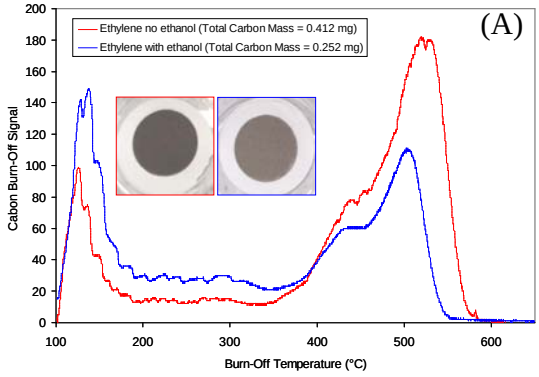

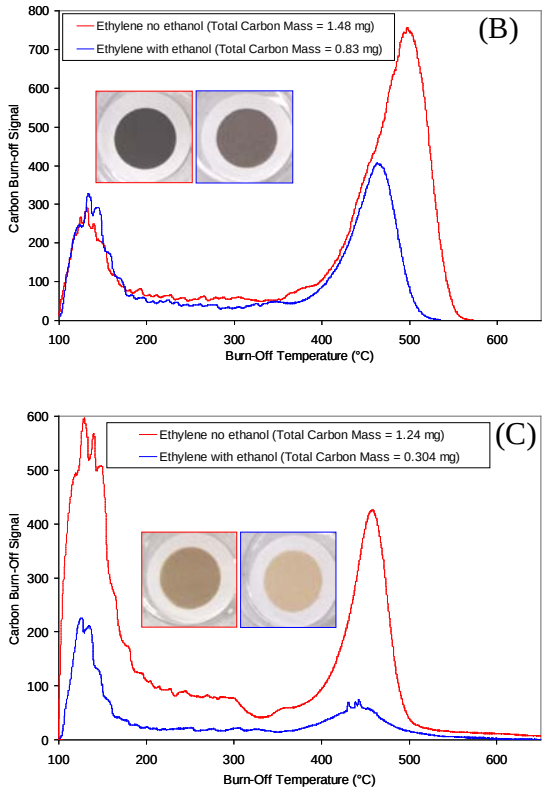

Figure 16: Carbon Vs. Filter Temperature, A (ϕ = 2.1), B (ϕ = 2.3), and C (ϕ = 2.6)

The chromatogram in Figure 17 was obtained from the GC/MS Chromatoprobe analysis of the particulate matter deposited on the quartz filters. Pyrene which is a known soot precursor was shown to be the most concentrated PAH detected and correlates well with total PAH content. Similar results were found by Lam et al.[10], where they saw large concentrations of acenaphthene, pyrene, and phenanthrene in the WSR plug-flow section.

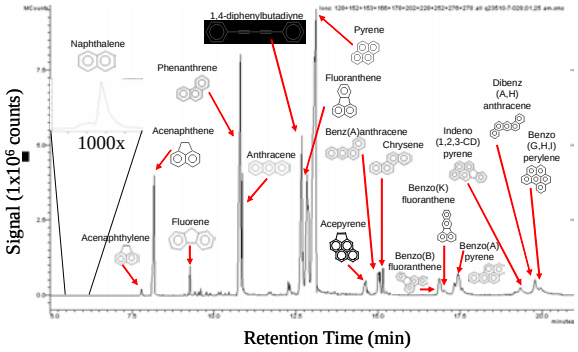

Figure 17: GC/MS Chromatogram of Species Thermally-Desorbed from Filter Samples

Pyrene concentration was determined from Chromatoprobe GC/MS analysis of quartz filters sampled at equivalence ratios (ϕ = 2.0 to 2.6). The concentration curve, Figure 18, follows a similar trend as the curve for total particle counts in Figure 11, indicating a relationship between pyrene and soot production - worthy of further examination. The addition of ethanol reduces the amount of pyrene deposited on the filters for ϕ > 2.2.

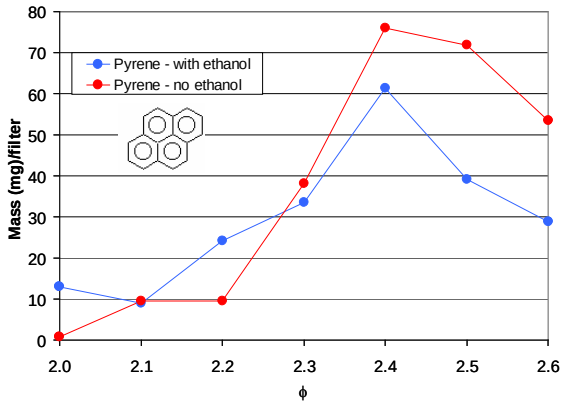

Figure 18: Pyrene Concentration

MODELING OF WSR FLOW

A time-dependent, axisymmetric mathematical model known as UNICORN[6,11] is developed to simulate the PAH's growth in unsteady flames. It solves for u- and v-momentum equations, continuity, and enthalpy- and species-conservation equations on a staggered-grid system. A detailed chemical-kinetics model of Wang and Frenklach[12] is incorporated in UNICORN for the investigation of PAH formation in acetylene and ethylene flames. It consists of 99 species and 1066 elementary-reaction steps. Thermo-physical properties such as enthalpy, viscosity, thermal conductivity, and binary molecular diffusion of all the species are calculated from the polynomial curve fits developed for the temperature range 300 – 5000 K. Molecular diffusion is assumed to be of the binary-diffusion type, and the diffusion velocity of a species is calculated using Fick's law and the effective-diffusion coefficient of that species in the mixture. A simple radiation model based on optically thin-media assumption was incorporated into the energy equation. Only radiation from CH_4, CO, CO_2, and H_2O was considered in the present study[13].

The finite-difference forms of the momentum equations are obtained using an implicit QUICKEST scheme, and those of the species and energy equations are obtained using a hybrid scheme of upwind and central differencing[11]. At every time-step, the pressure field is accurately calculated by solving all the pressure Poisson equations simultaneously and utilizing the LU (Lower and Upper diagonal) matrix-decomposition technique.

The WSR flow was modeled by assuming it as uniformly (in cross section) reacting gas flowing through a tube having a diameter and length of 51 and 150 mm, respectively. The formation of flame in the swirl section is highly three-dimensional and is not modeled in the present study, even though, it is believed to have significant influence on the generation of certain PAH species. These assumptions forced the model to make use of the prescribed temperature profile as input condition. The temperature distribution for each case along the length of the straight section of the WSR is constructed from the measurements made in the swirl section. A temperature drop of 100 K was assumed between the swirl and probe (150 mm) locations. Steady state calculations are performed for each case and the results are compared with the measurements in Figure 19.

The model predicts the CO concentration well, and over predicts the concentrations of stable species such as CO_2 (Figure 19A). As the model proved to predict CO_2 reasonably well in other systems such as burner-stabilized flames[14], the discrepancy noted in the present work could be attributed to the assumptions made in for the WSR flow. A good comparison between the predictions and measurements is obtained for benzene and acenaphthylene (Figure 19B). Note, samples of benzene were extracted from the reactor in gas phase while that of acenaphthylene were obtained in solid phase. On the other hand, the model seems to under predict the concentrations of heavier PAH species (Figure 19C). It is known that the inception of PAH species starts in the low temperature (~1200 K) region on the fuel side. Since the present model for WSR completely ignores the flame formation in the swirl section, prediction of lower amounts of PAH's should be expected.

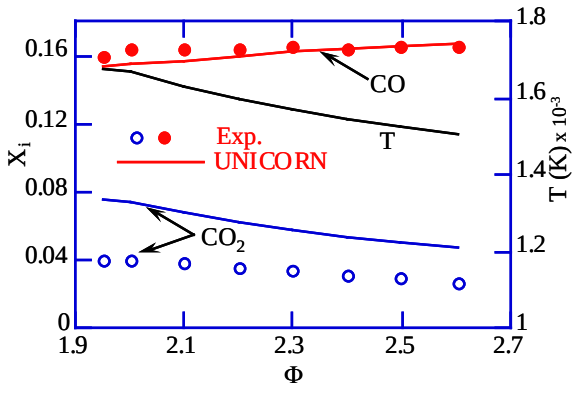

(A)

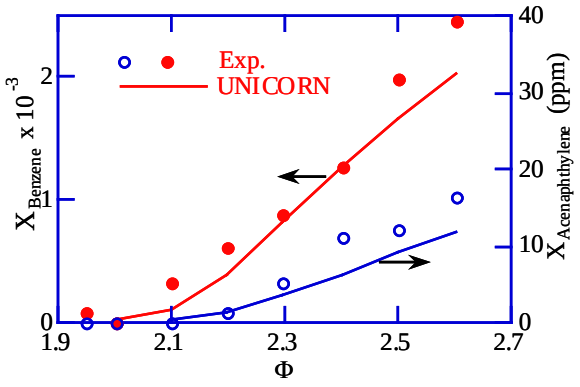

(B)

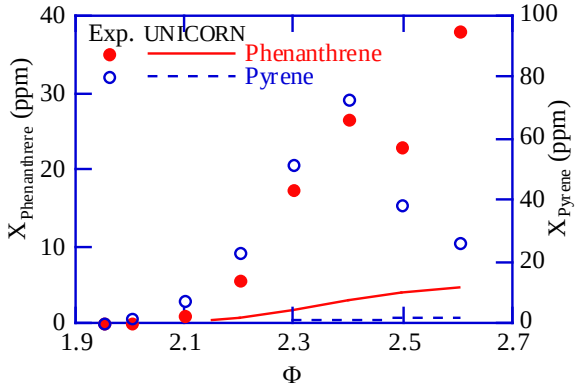

(C)

Figure 19: Predicted and Measured Species concentrations for Ethylene-Air Mixtures (A) Major species, (B) Benzene and Acenaphthylene, (C) Phenanthrene and Pyrene.

SUMMARY AND CONCLUSIONS

Experimental results from fuel-rich ethylene-air and ethylene-ethanol-air mixtures, where ethanol (5% of mixture) was used as a particulate reducing additive, were obtained using a WSR research combustor.

It was found that:

1. The PMCMS is capable of measuring particle size, particle distribution, and detailed chemical analysis of combustion products.
2. Particle count was reduced by 60% and peak particle size was reduced by 30% with ethanol addition to ethylene-air mixtures.
3. Large concentrations of benzene were found in the WSR, which increased linearly with increasing equivalence ratio. The benzene concentration was independent of additive addition.
4. A maximum 40% decrease in smoke number was observed with ethanol addition, with the maximum reduction occuring at $2.3 < \phi < 2.6$.
5. Carbon analysis of filter samples indicated two distinct carbon burn-off peaks attributed to PAH and carbonaceous soot deposits. These peaks shift in magnitude and temperature depending on the stoichiometry.
6. Pyrene was found to be a major PAH species, which correlates well with soot production.
7. These results suggest that pyrene, benzene and other PAH's can be used to predict soot formation in modeling and simulation routines for more complex practical combustion systems.

FUTURE RESEARCH PLANS

The WSR has been modified with the capability to vaporize heavier-hydrocarbon fuels such as heptane, toluene and JP-8 jet fuel. These pure compounds and practical fuels will be tested with various fuel additives to investigate soot mitigation processes. Long-term plans include the ability to predict soot formation in practical combustion systems by using detailed chemistry of soot precursors and the analysis of particle chemical content as a function of particle size.

ACKNOWLEGEMENTS

The authors are grateful for the contributions of the following personnel: Mr. Mike Arstingstall for his assistance with rig set-up, fabrication, assembly and test of the WSR, Mr. Richard Striebich for his assistance with the Chromatoprobe analysis, Mr. Ed Strader for assembly and set-up of the PMCMS, Dr. Matt Dewitt and Mr. David Brooks for the carbon burn-off analysis. The second author gratefully acknowledges the support of the Air Force through contract #F33615-97-C-2719.

REFERENCES

1. Nenniger, J. E., Kridiotis, A., Chomiak, J., Longwell, J. P., and Sarofim, A. F., "Characterization of a Toroidal Well Stirred Reactor," Twentieth Symposium (International) on Combustion, The Combustion Institute, pp. 473-479, 1984.

2. Zelina, J., "Combustion Studies in a Well-Stirred Reactor," Ph.D. Thesis, University of Dayton, Dayton, OH, 1995.

3. Zelina J. and Ballal, D. R., "Combustion Studies in a Well Stirred Reactor," AIAA Paper No. 94-0114, 1994.

4. "Development of a Particulate Matter On-Line Real Time Physical and Chemical Characterization and Monitoring System (PMCMS)," Final Report, SBIR Phase II, Contract No. F08637-99-C-6001, Deposition Research Laboratory Inc. Document No. 063001-01, 30 June 2001.

5. Stouffer, S. D., Streibich, R. C., Frayne, C. W., and Zelina, J., "Combustion Particulates Mitigation Investigations in a Well-Stirred Reactor," Paper No. AIAA 2002-3723, 38th Joint Propulsion Conference, 2002.

6. Roquemore, W. M. and Katta, V. R., "Role of Flow Visualization in the Development of UNICORN," *Journal of Visualization*, 2:257, 2000.

7. Society of Automotive Engineers (SAE), Aerospace Recommended Practice, "Aircraft Gas Turbine Engine Exhaust Smoke Measurement," *ARP 1179 Rev. C*, 1997.

8. Klosterman, J. R., Striebich, R. C. and Rubey, W. A., "Direct Thermal Desorption of Combustion Residues by GC-MS," Pittcon Paper No. 1034, New Orleans, LA, 5-8 March 2001.

9. Olson, D. D., Reed, X. B., and Whitefield, P. D., "The Design and Characterization of the Radial Differential Mobility Analyzer," Opportunity for Undergraduate Research Experience Final Report, University of Missouri-Rolla, 1998.

10. Lam, F. W., Howard, J. B., and Longwell, J. P., "The Behavior of Polycyclic Aromatic Hydrocarbons During the Early Stages of Soot Formation," Twenty-Second Symposium (International) on Combustion, The Combustion Institute, pp. 323-332, 1988.

11. Katta, V. R., Goss, L. P., and Roquemore, W. M., "Numerical Investigations of Transitional H_2/N_2 Jet Diffusion Flames," *AIAA Journal*, Vol. 32, No. 1, pp. 84-94, 1994.

12. Wang, H., and Frenklach, M., "A Detailed Kinetic Modeling Study of Aromatic Formation in Laminar Premixed Acetylene and Ethylene Flames," *Combustion and Flame*, Vol. 110, No. 1, p.173, 1997.

13. Annon., Computational Submodels, International Workshop on Measurement and Computation of Turbulent Nonpremixed Flames., http://www.ca.sandia.gov/tdf/Workshop/Submodels.html, 2001.

14. Katta, V. R., Blevins, L. G., and Roquemore, W. M., "PAH Formation in an Inverse Flame," AIAA Paper No. 2003-0666, Reno, NV, 6-9 January 2003.

Multi-Component LDV Measurements Downstream of a Gas Turbine Engine Nozzle/Air Swirler

J. Miller
Universal Technology Corporation

T. Meyer and M. Brown
Innovative Scientific Solutions, Inc.

A. Lynch, J. Gord, J. Zelina, D. Shouse, V. Belovich, and R. Hancock
Air Force Research Laboratory/PRTS

28th Annual Dayton-Cincinnati Aerospace Sciences Symposium
Dayton, Ohio 2003

Acknowledgments

Test Rig Build-Up and Operation:

- Richard Ryman, Steven Pennington, Glen Boggs, and Walter Balster (ISSI)

Modeling:

- Major gas turbine engine manufacturer

Funding:

- AFRL and engine manufacturer

Introduction

Motivation:

- Combustion modeling is essential in design and validation of advanced GT combustors
- Previous model calibrations not necessarily valid for new designs

Requirements:

- 3-component time-averaged velocity boundary conditions for 2 new fuel nozzle/air swirlers
- Downstream velocity profiles to compare with Reynolds averaged model and validate swirl angles

Approach:

- 2-component laser-Doppler velocimetry (LDV) for 3 components of velocity in each fuel nozzle/air swirler

Typical Swirl Combustor

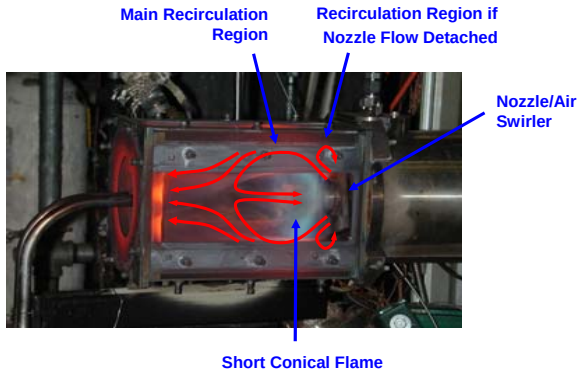

Experimental Schematic

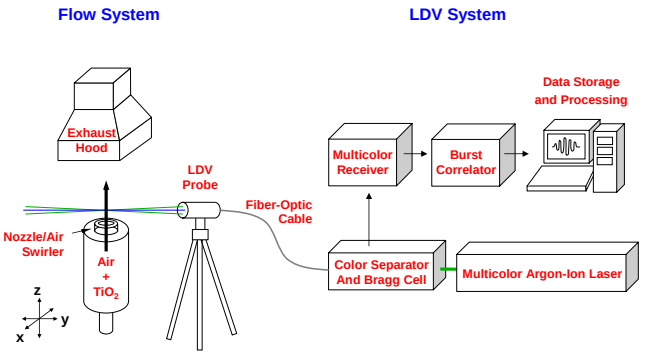

5

LDV Theory

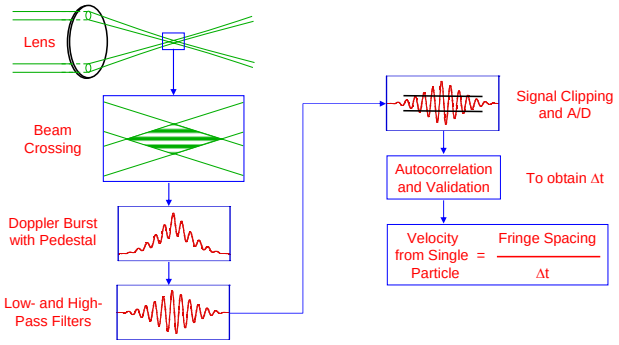

6

LDV Operation

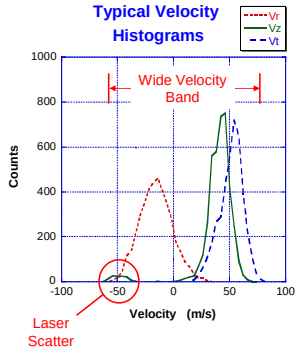

LDV Considerations:

- Wide velocity bandwidth requires wide range for low- and high-pass filters
- Post-processing required to eliminate laser scatter

LDV Parameters:

- Beam half angle: 3.95 deg.
- Green (514.5 nm) fringe spacing: 3.73 μm
- Blue (488 nm) fringe spacing: 3.54 μm
- Frequency shift: 40 MHz
- Frequency range: 10 – 100 MHz
- Allowed velocity range: -112 – 224 m/s
- Data points per position: 4096 points

7

3-Component Velocity Profiles

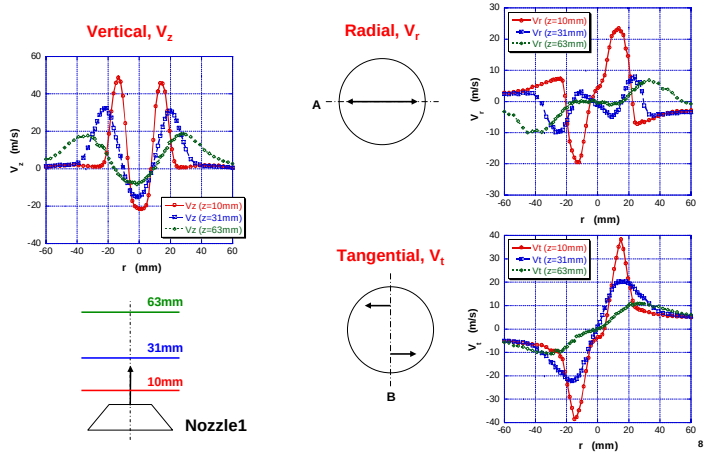

8

Validation of Axisymmetry

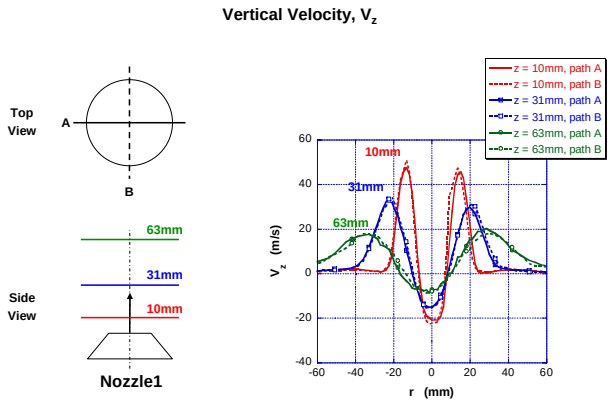

9

Run Conditions

	Nozzle1	Nozzle2
Pressure Drop	3.5%, 5.1%	3.5%, 5.1%
Geometry	Nozzle only Nozzle with swirler Swirler only	Nozzle only Nozzle with swirler Swirler only
Orientation	On Vane, Off Vane	On Vane, Off Vane

10

Pressure Drop of 3.5% vs. 5.1%

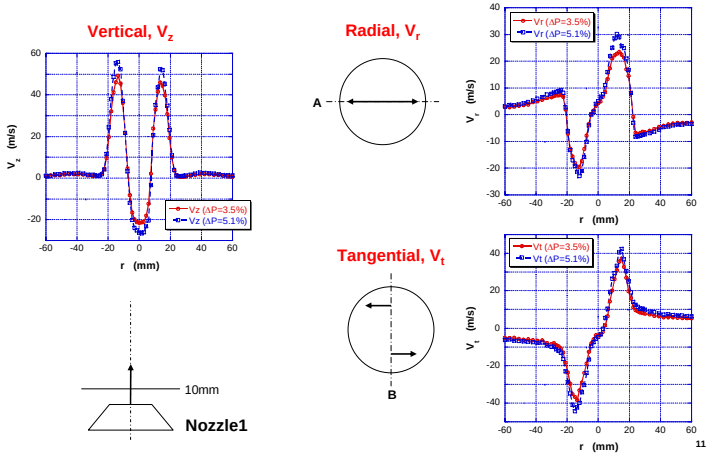

11

On Vane vs. Off Vane (18º Rot.)

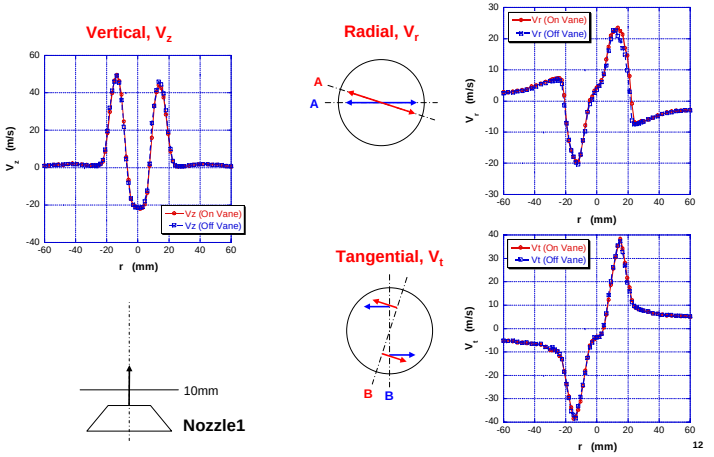

12

Nozzle1 vs. Nozzle2 (V_z)

Vertical, V_z

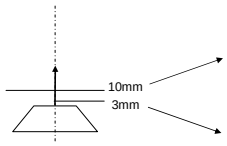

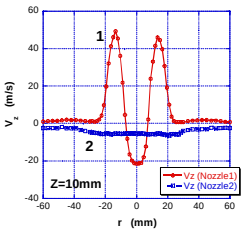

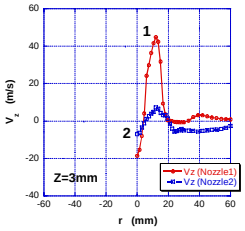

13

Nozzle1 vs. Nozzle2 (V_r and V_t)

Radial, V_r

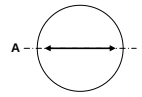

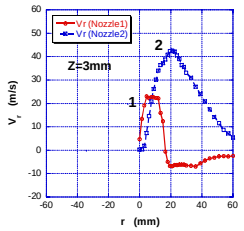

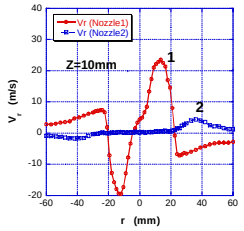

Tangential, V_t

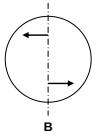

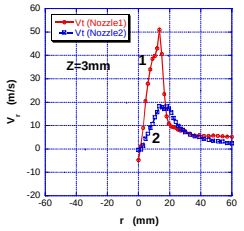

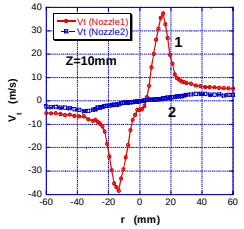

14

Summary

- Successfully performed 3-component velocity measurements in 2 nozzle/air swirlers using 2-component LDV
- Provided boundary conditions and verified swirl angles (not shown)
- Showed dependence of velocity profiles on pressure drop, vane location, and nozzle geometry
- Future Work: further comparison of LDV with numerical model

15

(c)2001 American Institute of Aeronautics & Astronautics or Published with Permission of Author(s) and/or Author(s)' Sponsoring Organization.

A01-16908

AIAA 2001-1129

Detonation Initiation Studies and Performance Results for Pulsed Detonation Engine Applications

Fred Schauer, Jeff Stutrud and Royce Bradley*
Air Force Research Laboratory, Propulsion Directorate
Wright-Patterson AFB, OH 45433
*Innovative Scientific Solutions, Inc.
Dayton, OH 45440

39th AIAA Aerospace Sciences Meeting & Exhibit
8-11 January 2001
Reno, NV

For permission to copy or to republish, contact the American Institute of Aeronautics and Astronautics, 1801 Alexander Bell Drive, Suite 500, Reston, VA, 20191-4344.

(c)2001 American Institute of Aeronautics & Astronautics or Published with Permission of Author(s) and/or Author(s)' Sponsoring Organization.

AIAA 2001-1129

DETONATION INITIATION STUDIES AND PERFORMANCE RESULTS FOR PULSED DETONATION ENGINE APPLICATIONS

Fred Schauer and Jeff Stutrud

Air Force Research Laboratory, Propulsion Directorate

Wright-Patterson AFB, OH 45433

Royce Bradley

Innovative Scientific Solutions, Inc.

Dayton, OH 45440

Abstract

An in-house computational and experimental program to investigate and develop an air breathing pulse detonation engine (PDE) that uses a practical fuel (kerosene based, fleet-wide use, "JP" type) is currently underway at the Combustion Sciences Branch of the Turbine Engine Division of the Air Force Research Laboratory (AFRL/PRTS). PDE's have the potential of high thrust, low weight, low cost, high scalability, and wide operating range, but several technological hurdles must be overcome before a practical engine can be designed. This research effort involves investigating such critical issues as: detonation initiation and propagation; valving, timing and control; instrumentation and diagnostics; purging, heat transfer, and repetition rate; noise and multi-tube effects; detonation and deflagration to detonation transition modeling; and performance prediction and analysis. An innovative, four-detonation-tube engine design is currently in test and evaluation. Preliminary data are obtained with premixed hydrogen/air as the fuel/oxidizer to demonstrate proof of concept and verify models. Techniques for initiating detonations in hydrogen/air mixtures are developed without the use of oxygen enriched air. An overview of the AFRL/PRTS PDE development research program and hydrogen/air results are presented.

Introduction

Recent renewed interest in pulsed detonation propulsion concepts has prompted a concerted effort being made by the U.S. Air Force (AFRL), U.S. Navy (NRL, ONR, and the Naval Post Graduate School), NASA, and several research contractors (Adroit Systems Inc., Advanced Projects Research, Inc., Pennsylvania State University, Enigmatics, and major engine manufacturers), to develop a low-cost, practical-fueled, pulse detonation engine. Conceptually, a pulse detonation engine (PDE) offers few moving parts, high efficiency, high thrust, low weight, low cost, and ease of scaling. These make the PDE an attractive alternatve to jet turbine engines for small disposable engines. A drawing that illustrates the simplicity of the PDE cycle is provided in Figure 1. The near constant volume heat addition process, along with the lack of a compression cycle, lend to the high efficiency and specific impulse, simplicity, and low-cost of pulse detonation engines. Pulse detonation engines have the potential for operation at speeds ranging from static to hypersonic, with competitive efficiencies, enabling supersonic operation beyond conventional gas turbine engine technology. Currently, no single cycle engine exists which has such a broad range of operability.

Pulsed detonation propulsion research has been funded by AFRL since the early 1990's, but most of the efforts have been performed out-of-house by contractors. In 1997, an AFRL/PRTS (the Combustion Sciences Branch of the Turbine Engine Division, Propulsion Directorate at Wright-Patterson AFB, Ohio) in-house PDE research and development program was created. Principal interests lie in the air-breathing arena; a similar pulsed detonation rocket engine (PDRE) program is being conducted by AFRL/PRSA at Edwards Air Force Base, California.

The in-house PDE program was established in order to make AFRL's unique resources available for the development of this technology. Traditionally, we

(c)2001 American Institute of Aeronautics & Astronautics or Published with Permission of Author(s) and/or Author(s)' Sponsoring Organization.

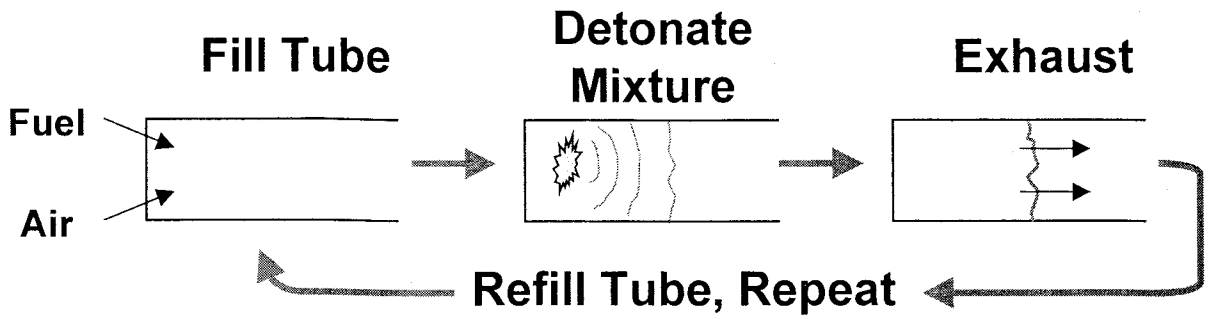

Figure 1. Conceptual pulsed detonation engine cycle.

have used AFRL's advanced computational modeling, diagnostic measurement techniques, and test facilities to work with government agencies and their contractors on the development of advanced combustor concepts. Much of this research was focused on deflagration phenomena while trying to avoid detonations. In order to work with pulsed detonation phenomena, AFRL has set out to develop the facilities, diagnostics, modeling tools, and experience necessary to contribute and provide unique resources for the maturation of pulse detonation technology.

The second motivation of the in-house program was to produce publishable PDE data from which codes and performance predictions can be anchored and/or validated. Currently, there is a great deal of dissension on PDE performance within the community.[1] Detonation physics and detonation engine blow-down are highly sensitive to initial conditions, boundary conditions, and multi-dimensional geometry effects. Most of the available data and models are proprietary and not shared across the community, making it difficult to assess the current status of PDE performance and capability.

For the Air Force, a practical-fueled PDE means JP/air detonation. This requirement creates several technological hurdles that must be overcome in order to field such a PDE. Complex hydrocarbon fuels, and particularly liquid hydrocarbons, are difficult to detonate in air, typically requiring hundreds of kilo-joules to directly initiate a detonation.[2] For this reason, a practically fueled PDE becomes a deflagration to detonation transition (DDT) minimization process since the fuel burned during detonation initiation does not produce thrust efficiently while it is burning at low pressures. Furthermore, since thrust is generated with each detonation cycle, Figure 1, it would be beneficial to raise the operating frequency in order to produce more thrust. Higher operating frequencies also have benefits from an unsteady inlet, nozzle, and noise generation perspective, but create complications in other areas including valving, mixing, shortened residence time requirements, and increased heat loads.

In cooperation with other government organizations performing PDE research and as the developer of one of two government in-house PDE research engines, AFRL/PRTS has established a niche for itself in tackling the above issues. The ONR funded research engine at the Naval Post Graduate School in Monterey, California is directed towards liquid fuel injection, atomization, and mixing[3] and AFRL's engine research is focused on detonation initiation and repetition. While there is crossover in the two programs, we are confident that if we can develop a premixed vapor-fueled/air PDE, the results of the Navy's research will provide the basis for making it work on liquid fuels.

Approach

AFRL's unique resources[4] have been used to develop three areas in which AFRL can contribute to the development of PDE technology. In broad terms, these areas are modeling, facilities and instrumentation, and research hardware development and testing.

AFRL's detonation modeling work is described in more detail elsewhere.[5] Recently this work has been extended to three dimensional calculations and studies of detonation initiation schemes such as the Shelkin spiral calculation in Figure 2. Both calculations employ weak initiation of hydrogen/air mixtures, but the upper frame is a straight channel and the lower contains a two dimensional representation of a Shelkin spiral. The brighter areas in Shelkin spiral calculation indicate that the "hot spots" critical for DDT events are more prevalent with the extra geometry. In the interest of space, further discussion of detonation modeling will not be addressed within this paper.

The Pulsed Combustor/Detonation Engine Research Facility (D-Bay) is capable of supporting up to 60,000 lbf thrust experiments, with integrated remote

(c)2001 American Institute of Aeronautics & Astronautics or Published with Permission of Author(s) and/or Author(s)' Sponsoring Organization.

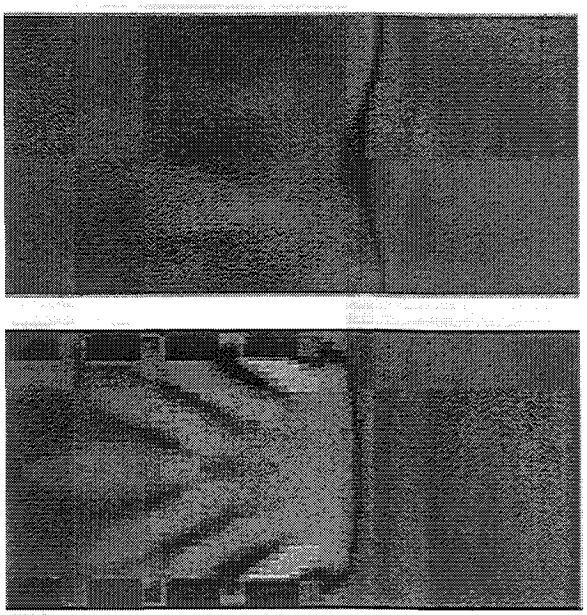

Figure 2. CFD pressure map of DDT event with 2D tube and Shelkin spiral.

control and instrumentation systems. Pulsed thrust measurements from 3 to 1,000+ lbf are accurately made with a damped thrust stand mounted on the existing engine thrust stand. Up to 6 lbm/sec (3 kg/sec) of 100 psi (680 kPa) air is available and high-capacity inlet and exhaust stacks are useful for self-aspirating designs and atmospheric exhaust. A direct connection to a liquid fuel farm via a high-pressure/high-capacity fuel pump retains the facilities ability to feed large-scale 60,000 lbf thrust engines. The facility test stand, damped thrust stand, with an installed research PDE are shown in Figure 3. The damped thrust stand itself sits upon the large capacity static thrust stand and the roll-up door to the exhaust tunnel is visible on the right.

A hardened remote-control room is adjacent to the

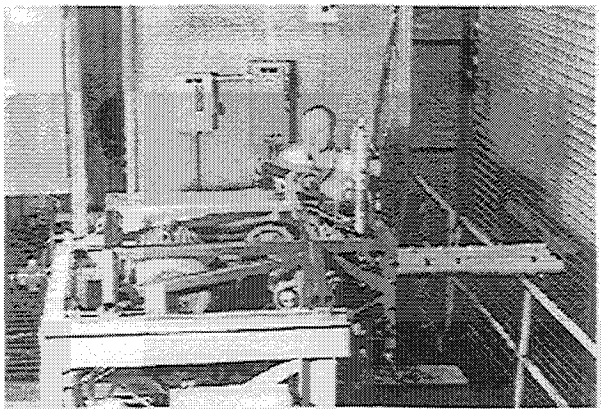

Figure 3. Pulsed combustor/detonation engine test stand, damped thrust stand, with installed research PDE.

750,000+ ft^3 test cell. A minimum of 2 feet of reinforced concrete is situated between the test cell and personnel during testing. Such precautions are necessary when dealing with the high noise levels associated with PDE operation. Control of all pulsed combustor/detonation engine operations and data acquisition is done via a LabVIEW based interface with duplicate manual emergency shutdown and safety system controls.

Choked flow measurements are employed to accurately regulate and measure oxidizer and fuel flow to pulsed engine experiments. These choke points isolate the measurements from the downstream pressure oscillations of pulsed valves. Each flow system contains a pressure controller, a choked orifice plate or critical flow nozzle, and a surge tank to set and hold a required flow rate even with unsteady combustor valve flows. As long as the flow is choked, flow rate can be varied by changing the pressure and choked area.

In addition to conventional (low Hz and kHz frequency) data acquisition and control systems which include intake, fuel, and purge system instrumentation, the facility is equipped with up to 16 channels of high-frequency data acquisition at up to 5MHz. These may be used for high-frequency pressure transducers, thermocouples, photodiodes, or advanced laser diagnostics. A 1Mhz framing rate digital camera is also available for advanced laser diagnostics and imaging techniques.[6] High frequency pressure transducers and photodiodes are currently installed with plans for digital Schlieren experiments to begin at a later date.

Due to the nature of this facility, testing is not limited to small-scale PDE experiments. Conventional full-scale turbine engine tests are possible making hybrid turbo-PDE's a future research possibility in this facility. It is envisioned that several smaller scale (<1,000 pound thrust) experiments could take place across the test deck or a single large-scale (10,000+ pound thrust) engine test could be performed. As with most of PRTS's test facilities, easy swap-out of test hardware is expected and accounted for in the initial test-facility design.

Due to the critical timing issues in pulsed detonation engine operations, the high frequency valving tends to be both expensive and highly constrained. During the design of a research PDE, many options were considered that were either too expensive, had severe limitations in operating range, or both. The research engine design selected is based upon valving found in a General Motors Quad 4, Dual Overhead Cam (DOHC) cylinder head commonly used in the Pontiac Grand Am automobile. This PDE design

(c)2001 American Institute of Aeronautics & Astronautics or Published with Permission of Author(s) and/or Author(s)' Sponsoring Organization.

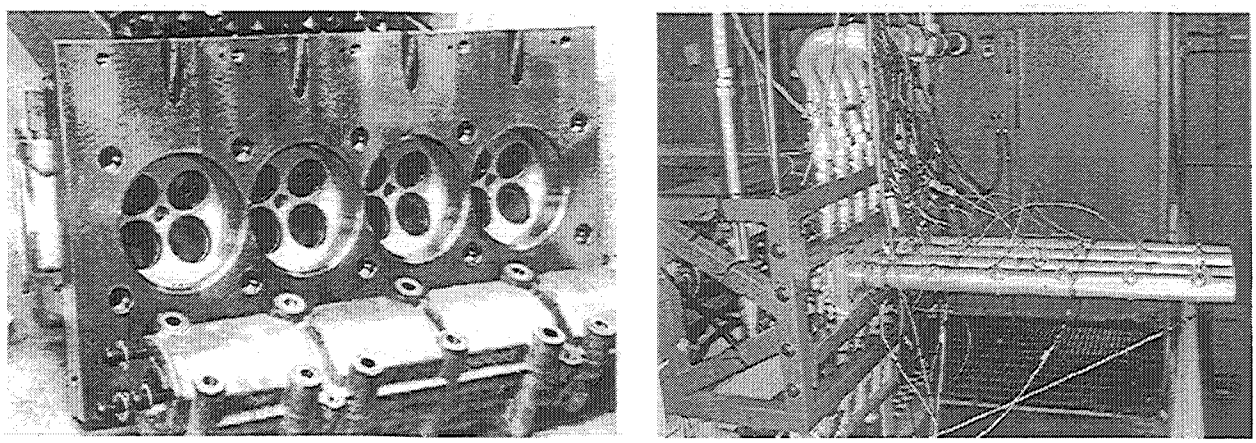

Figure 4. Second generation "Quad 4" based PDE during assembly (left) and as installed.

has an extremely broad operating range and configuration, with up to four detonation tubes operating at up to 100 Hz each. The engine has proven reliability and durability, although the loss of the first generation engine design did occur due to fatigue in the tube mount area after approximately 200 hours of hot time.[7] The head and tube mount systems have been redesigned to permit higher frequency operation, quick valve system and detonator tube configuration change-outs, and eliminate the areas where fatigue became a problem. The second generation engine is shown in Figure 4 during assembly and as installed in the damped thrust stand.

The operating conditions of PDE's are very similar to internal combustion engines and many of the components can be shared. By driving the overhead cams with an electric motor, the four valves in each of the four cylinders can be made to operate at between 0.5 and 50 Hz. With minor modifications, the frequency limit can be increased to 100 Hz for an aggregate maximum frequency of 400 Hz. Currently, several different detonator tube configurations are available including single 2" (50 mm) diameter by 3' (900 mm) tube, single 3.5" (90 mm) diameter by 3' (910 mm) tube, and multiple tube versions of each of the previous configurations. Provisions for lubrication, cooling, ignition, and fuel delivery are integral to the cylinder head/intake manifold assembly. The electric valve-train drive motor, which is grossly oversized but a readily available component, is clearly visible on the left side of the frame in Figure 3, along with the valve train drive parts.

The two intake valves in each cylinder, visible in Figure 5, are used to feed premixed air and fuel into detonation tubes, which are attached to an adapter plate secured by the head bolts. In the current configuration, the head and detonation tubes are installed horizontally, and the intake valves are the upper pair. Cold air flows through the exhaust valves in reverse as a purge gas to buffer hot products from igniting the next incoming charge and to convectively cool the inside of the detonation tube walls. The extra exhaust valve or valves in this four-valve-per-cylinder design could also be used for an axial predetonator or additional combustion air if necessary.

Somewhat uniquely, this PDE is operated premixed, minimizing mixing and stratification issues. The large pop-off valves and check valves visible in Figure 3 are some of the precautions used to prevent catastrophic failure in the event of an engine backfire through the premixed intake section. Up to four detonation tubes can be run at 90 degrees out of phase, with various diameters ranging up to ~3.5 inches (85mm). The main combustion air and purge air lines contain ball valves for each detonation tube feed system so that the engine can be run with one tube, two tubes 180 degrees out of phase, or all four tubes. A rotary

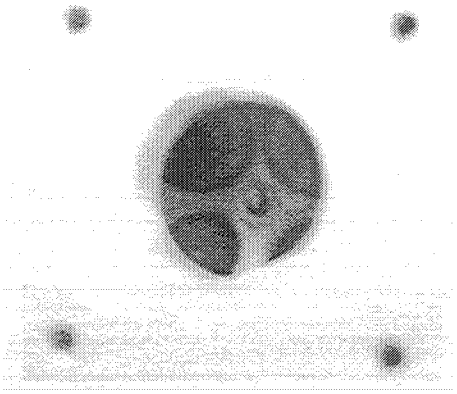

Figure 5. Research 'Quad 4' PDE detonation tube adapter plate with visible intake (upper) valve pair, purge air (lower) valve pair, and conventional spark igniter.

(c)2001 American Institute of Aeronautics & Astronautics or Published with Permission of Author(s) and/or Author(s)' Sponsoring Organization.

position sensor is adapted to the intake camshaft to provide both an index of the valve timing sequence and the relative position of the valves. This signal serves as the master timing signal for the ignition and data acquisition systems.

An eight-channel igniter/fuel injection control box is triggered off the rotary position sensor. Separate control of each detonation tubes igniter and/or fuel injector can be accomplished with this system, although currently vapor fuels are premixed with the combustion air via a separate critical flow nozzle and flow control system. Do to the high noise levels associated with PDE testing, all controls and data acquisition are performed remotely from an isolated control room. All of the control systems and data acquisition systems are LabVIEW based and integrated into one 'virtual instrument' with back-up manual shutdown and safety systems. This virtual control panel is extremely flexible and can control all aspects of the PDE's operation including: lubrication, operating valve drive motor speed, fuel flow, main combustion air flow, purge air flow, timing, ignition delays, and automatic shutdown in the event of a critical system failure. By changing the position of a few manual ball valves and pushing a few switches in the virtual control system, the engine configuration can be switched from one tube operating to four tubes in a matter of minutes.

The engine is to be used for performance prediction validations and serve as a test-bed for research of detonation initiation and DDT minimization, heat transfer, noise levels, pulsed ejector concepts, and multi-tube interactions. Initial testing and proof-of-concept is being done with hydrogen as the fuel due to the increased detonability versus practical liquid hydrocarbon fuels. A vapor propane fuel system has also been constructed in order to work with a complex-hydrocarbon that detonates much like kerosene based JP type fuels. This will eliminate the atomization and mixing of liquid fuel complications that increase the difficulty of practical PDE design and allow us to focus on detonation initiation and high frequency operation. As mentioned previously, ONR funded research is tackling the difficult problems of liquid fuel atomization and mixing for PDE applications.[3,8] Recently, active cooling has been implemented along with expanded fuel systems so that indefinite run times are possible. Further details on the research facility and engine are available elsewhere.[9]

Results and Discussion

Cold flow testing of the systems began in early 1999, with the first hot firing on 9 September. This initial test was done at low fuel flow conditions to minimize the amount of hydrogen in the test cell in event of a failure. The first test was done with fully instrumented intake and purge systems, detonation tube surface temperature thermocouples, four high frequency pressure transducers along the length of the tube, damped thrust, and two black & white video cameras. An image extracted from one of the video cameras is shown in Figure 6.

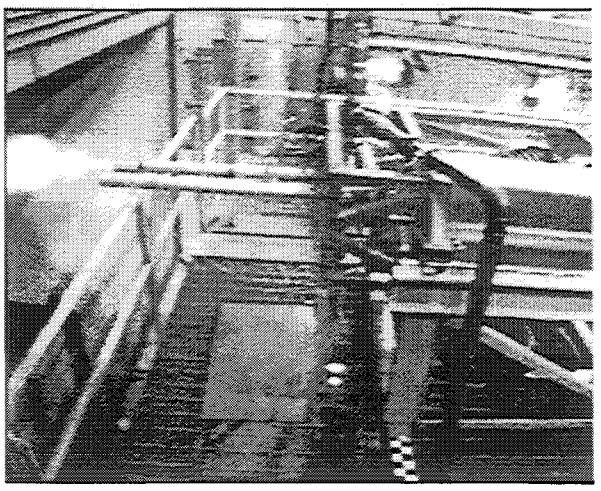

Figure 6. In-house research 'Quad-4' PDE, success on first attempt, 9 September, 1999: 91 second operation at 8Hz, single 2" diameter by 3' long tube, stoichiometric H_2/air, conventional ignition.

The initial testing produced very good qualitative results, with four runs of up to 91 seconds duration. These runs, which were un-cooled, were cut short because the tube surface thermocouples were epoxy mounted and the epoxy melted. The thermocouples have since been re-affixed more robustly. The sharp 'CRACK' sound and flash of the exhaust were qualitative indicators of detonations which contrasted with the softer 'wumpff' sound and flame visible out the back when the engine deflagrated due to off-stoichiometry conditions.

Although data has now been obtained with propane/air, the results presented herein will focus on hydrogen/air operation. Results presented were obtained with a single aluminum 2.0" (50.8mm) ID tube that was 36" (915mm) long. Conventional weak initiation was employed at the head end (via the spark plugs visible in Figures 4 and 5) with a 3.5 msec ignition delay. The fuel/oxidizer mixture was stoichiometric and premixed hydrogen/air with a 50% clean air purge fill ratio. The above operating parameters and an operating frequency of 16 Hz applies to all data herein unless otherwise stated.

(c)2001 American Institute of Aeronautics & Astronautics or Published with Permission of Author(s) and/or Author(s)' Sponsoring Organization.

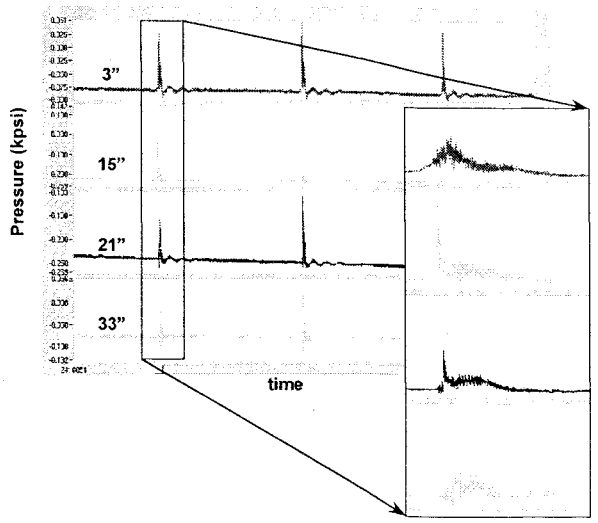

Figure 7. High frequency pressure traces from in-house PDE engine. Measurement locations at 3, 15, 21, 33" axial distances from head, ~200 msec duration shown.

Initially it was found that the detonation did not transition from deflagration until near the end of the detonation tubes. The addition of a Shelkin or shocking spiral produced much faster transitions and higher thrust levels. A 3/16" wire diameter spiral with a ~1.8" pitch was placed in the first 12" of the detonation tubes. This spiral produced overdriven detonations by the 9" axial location. High frequency pressure transducer measurements, as seen in Figure 7, indicate measured wave speeds of 1959 m/sec. Further experimental verification of detonation wave speeds was provided by photodiode measurements shown in Figure 8 with a derived wave speed of 1959 m/sec. These results are in excellent agreement with the stoichiometric hydrogen/air wave speed of 1968 m/sec published elsewhere.[10]

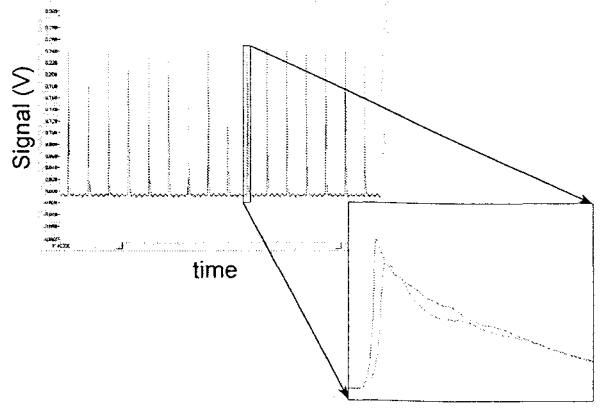

Figure 8. Photodiode results at 27 and 33" locations.

Since the initial single tube tests, the engine has been run in multi-tube mode, demonstrating both two-tube operation 180° out of phase and four tube operation 90° out of phase. A wide variety of frequencies have also been demonstrated along with operation of the tubes using partial fills.

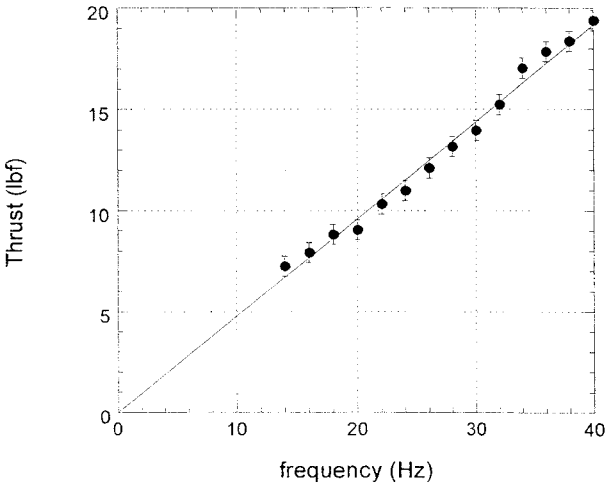

Figure. 9. Thrust versus frequency.

PDE's are highly scalable, as demonstrated in Figure 9. The thrust is observed to increase linearly with frequency, with the engine making no thrust when not operating as expected. This data also demonstrates the accuracy of the thrust measurements, as the error bars are +/- 0.5 lbf (+/- 2.2 N). Such thrust measurements have been demonstrated with the current system down to 3 lbf (13 N) but the accuracy and thrust range can be varied with configuration changes.

The impact of ignition delay can be assessed with

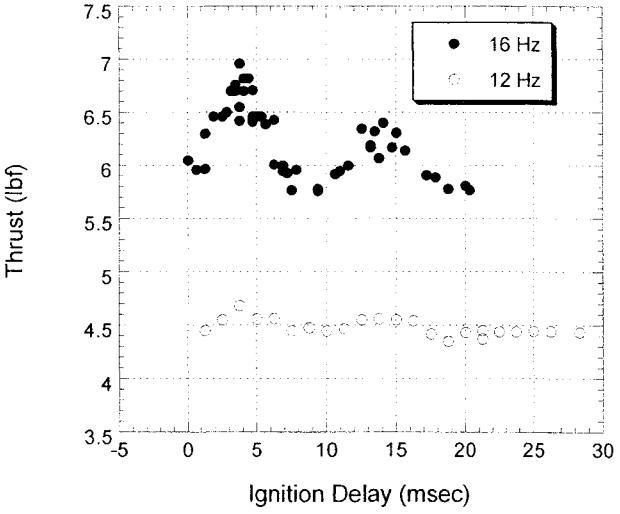

Figure. 10. Thrust versus ignition delay.

(c)2001 American Institute of Aeronautics & Astronautics or Published with Permission of Author(s) and/or Author(s)' Sponsoring Organization.

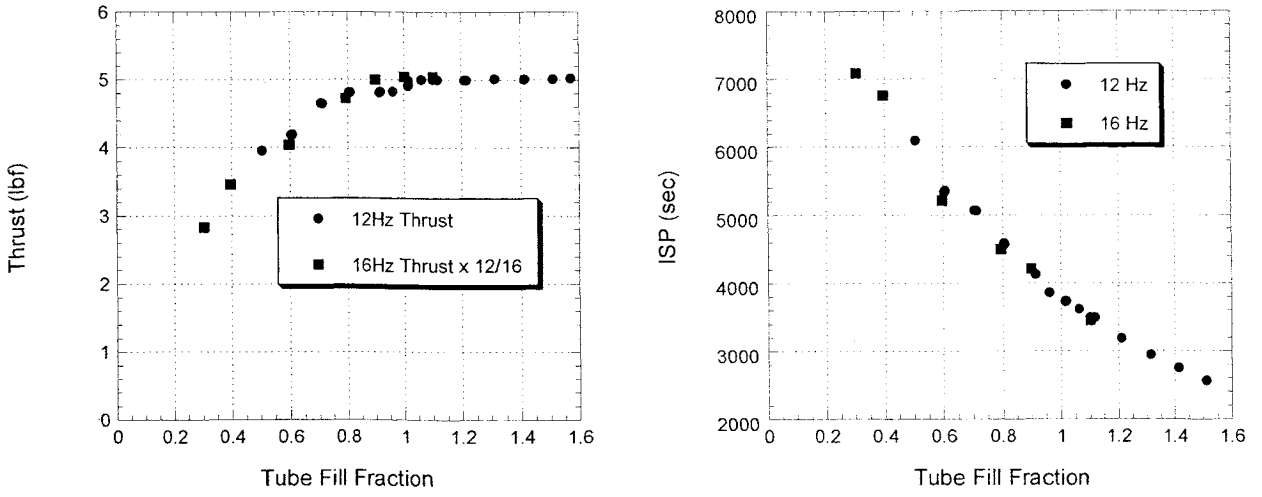

Figure 11. Thrust (left) and fuel specific (right) impulse versus tube fill fraction.

the data in Figure 10. The plot of thrust versus ignition delay contains data for two different frequencies. Ignition delay here is defined as the time in milliseconds between the intake valve closing completely and spark plug firing. Obviously, with premixed operation, negative ignition delays are to be avoided as they can result in combustion before the intake valves are closed with consequent backfiring through the intake system. It was found that premixed operation reduces the sensitivity of performance to ignition delay, as some PDE systems have been observed to detonate only within a narrow ignition delay window of only a few milliseconds. However, certain trends are apparent at both frequencies presented.

The ignition delay is observed to produce high and low spots. Because detonability is sensitive to changes in pressure, the initial low spot is surmised to be a result of attempting to initiate a detonation in the expansion resulting from the closing of the intake valve. The peaks at 3.5 msec ignition delay are believed to occur due to the presence of the subsequent compression wave. These behaviors are then observed to repeat at periods corresponding to the acoustic length of the detonator tube.

PDE scalability is also accomplished via variation of the volume of the tube filled with detonable mixture. Via volumetric flow control, the tube fill fraction was varied as shown in Figure 11. Results are shown for two frequencies to cover a range of fill fractions while remaining within the limits of a single choked-orifice volumetric flow control range. Thrust measurements on the left are scaled by frequency to 12 Hz. Due to the linear relationship of thrust and frequency, Figure 9, the differing frequencies collapse on one another when scaled by frequency. Further confirmation of this phenomenon is evident in the fuel specific impulse plot on the right in Figure 11. Here frequency is accounted for when dividing by the fuel flow and no other frequency scaling is required.

At a fill fraction of 1.0, the entire tube is filled with fresh reactants for each cycle. At fill fractions less than 1.0, only part of the tube is filled with fresh reactants with the remainder occupied by either a purge cycle or hot expanded products from the previous cycle. At fill fractions greater than 1.0, the entire tube is filled with the excess detonable mixture presumably forming a free cloud at the tube exit. Thrust versus tube fill fraction is plotted on the left in Figure 11. The thrust is observed to increase with tube fill fraction until abruptly leveling out at a fill fraction of 1.0. Since reactants detonating outside the tube are unconfined, they do not produce any thrust as shown for the fill fractions greater than 1.0. Note that even at tube fills corresponding to only 30%, more than half the peak thrust is still obtained. This results in up to double the efficiency as shown by the increased fuel specific impulse at fill fractions less than 1.0. This trend, which has been confirmed by Li, Kailasanath, and Patnaik using CFD,[11] is a result of longer blow down times produced by the increased acoustic relaxation length for partial tube fills. Effectively, purge air or previous cycle products are pumped by the detonation, resulting in the same higher mass/lower delta-velocity efficiency gains found in modern high-bypass turbofans. The remarkable efficiency gains are partly due to the increased efficiency of shock coupling in the PDE as compared to the viscous coupling in the turbofan.

In addition to the effects of frequency, ignition delay, and fill fraction, the impact of stoichiometry was

(c)2001 American Institute of Aeronautics & Astronautics or Published with Permission of Author(s) and/or Author(s)' Sponsoring Organization.

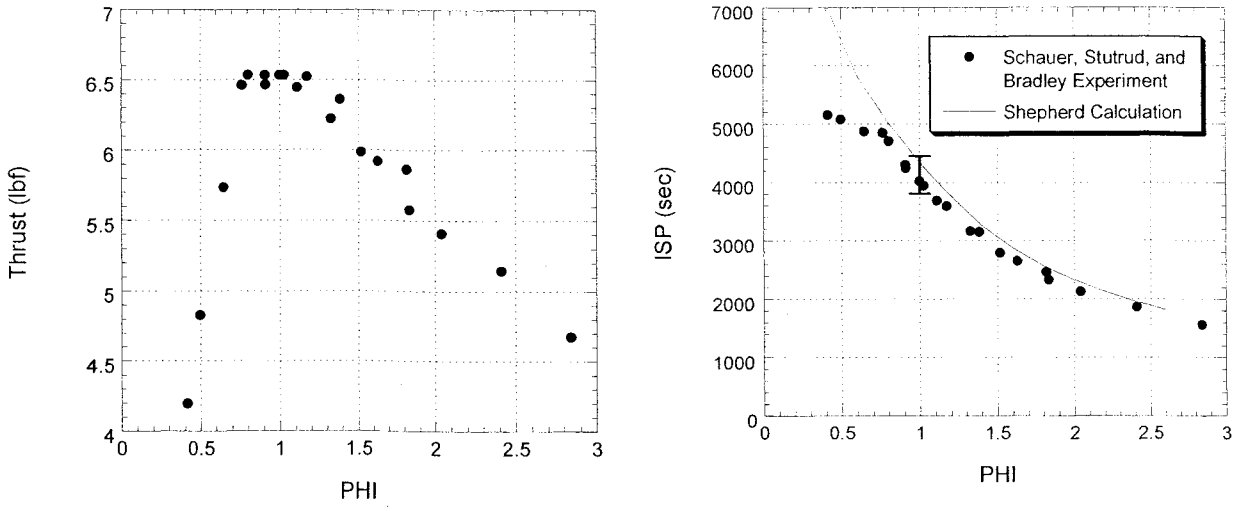

Figure. 12. Thrust and fuel specific impulse versus stoichiometry.

also examined as shown in Figure 12. Thrust on the left and fuel specific impulse on the right are plotted versus a wide range of stoichiometries. As expected from detonability data,[2] a stable region is observed at stoichiometries near 1.0. At fuel rich conditions, both the detonability and thrust are observed to fall off gradually with increasing fuel to air ratio. The detonability and thrust fall off more quickly on the fuel lean side of the stoichiometry curve. As with partial tube fills above, more than half the thrust is observed to occur even with only half the stoichiometric fuel to air ratio. This results in a higher efficiency for lean operation as confirmed on the specific impulse plot.

The current experiments are graphed in Figure 12 along with Joe Shepherd's analytical calculations[12] with excellent agreement across a wide range of equivalence ratios. The experimental error bar shown represents the variation in thrust possible by changes in ignition timing alone, Figure 10, as the data was collected with a constant ignition delay. Shepherd's results do not consider deflagration to detonation processes. The fall off in specific impulse observed experimentally for equivalence ratios less than 0.75 can be attributed to the rapid growth in DDT distance as the cell size gets much larger than the detonation tube size.

Summary and Conclusions

Pulse detonation engines are an extremely promising alternative to small, disposable-jet turbine engines. The Air Force Research Laboratory has supported PDE research for some time, and an in-house program of the Combustion Sciences Branch of the Turbine Engine Division at Wright-Patterson AFB has been established to produce shareable benchmark performance data. In addition, the in-house program has been used to harness AFRL's unique resources in order to contribute to the development of pulsed detonation propulsion technology in the form of modeling, facility, and research components.

It is expected that the deflagration to detonation transition modeling can be used as a tool in the development and design of a practical-fueled detonation initiator. The pulsed combustor/detonation engine test facility has been developed as a cost-effective test resource that meets many of the unique needs required for PDE testing. The remote controls and high frequency data-acquisition systems have been assembled to provide test support for researchers working in collaboration with AFRL. The facility can handle everything from bench scale experiments from academia to full-scale hybrid engine concepts from engine manufacturers. Moreover, it is hoped that researchers will take advantage of this national resource.

A research PDE was successfully designed, built, and operated under the in-house program using an innovative valve system based upon the "Quad-4", a 16 valve, four cylinder automobile engine from General Motors. The resulting engine is capable of a broad range of frequencies and configurations with up to four detonation tubes. Data from the engine is being published with the intent of providing non-proprietary PDE data against which performance codes and predictions can be benchmarked. The "Quad-4" PDE serves as a research tool and test-bed for detonation initiation concepts, high frequency operation, heat transfer studies, multi-tube detonation engine operation, and pulsed ejector research. The engine, which was

(c)2001 American Institute of Aeronautics & Astronautics or Published with Permission of Author(s) and/or Author(s)' Sponsoring Organization.

operated successfully for the first time in the fall of 1999, demonstrates the affordability and ease of scalability of PDE technology. The first generation engine operated for over 16 million cycles and approximately 200 hours of detonations before components failed due to fatigue. The engine demonstrated that PDE's can operate for extended durations even with low cost materials and designs. A second-generation engine design has been completed to replace the failed engine with numerous design improvements to durability and capability.

Hydrogen/air data have been presented on the effects of frequency, ignition delay, fill fraction, and fuel/air equivilance ratio. The resultant findings provide insight for scaling thrust and improving efficiency of PDE hardware. Data sets are available for collaborative studies, including flow conditions and heat transfer data not published herein. Additional data on propane/air detonations are available for qualified researchers.

There is much work to be done in developing valving, detonation initiators, noise suppression techniques, thermal protection systems, intake and exhaust nozzles, and control systems before a JP/air fueled PDE becomes practical. AFRL/PRTS would like to invite the community to consider AFRL resources for further PDE research. With high quality modeling, research facilities, and an in-house PDE engine, AFRL can work with other organizations and contractors, as done in the past with turbine engine technology, to maturate and transition PDE technology to the field.

Acknowledgements

Special appreciation must be expressed to the technicians and support personnel, both in-house government employees and on-site contractors who made this work possible, particularly Dwight Fox (ISSI) who helped build much of the research PDE engine and Walt Balster (ISSI) who recently joined us as a facility technician. Dr. Vish Katta and Dr. L.P. Chin have performed their usual miracles on the modeling side and are gratefully acknowledged for their contributions to this program. We also wish to acknowledge the technical leadership of Dr. Mel Roquemore and Dr. Robert Hancock (AFRL/PRTS).

References

1. Kailasanath, K., Patnaik, G. and Li, C., "Computational Studies of Pulse Detonation Engines: A Status Report," *AIAA 99-2634* (1999).
2. Kaneshige, M. and Shepherd, J. E., *Detonation database*, Technical Report FM97-8, GALCIT, (1997).
3. Brophy, C., Netzer, D. and Forster, D., "Detonation Studies of JP-10 with Oxygen and Air for Pulse Detonation Engine Development," *AIAA 98-4003* (1998).
4. Hancock, R. D., Gord, J. R., Shouse, D. T., Schauer, F. R., Belovich, V. M. and Roquemore, W. M., "AFRL Combustion Branch (PRSC) Aero-propulsion Research and Development Activities," *Proceedings of the International Test and Evaluation Association (ITEA) Conference* (1999).
5. Katta, V. R., Chin, L. P. and Schauer, F. R., "Numerical Studies on Cellular Detonation Wave Subjected to Sudden Expansion," *Proceedings of the 17th International Colloquium on the Dynamics of Explosions and Reactive Systems*. Heidelberg, Germany (1999).
6. Gord, J. R., Tyler, C., Grinstead, Jr., K. D., Fiechtner, G. J., Cochran, M. J. and Frus, J. R., "Imaging Strategies for the Study of Gas Turbine Spark Ignition," Presented at the SPIE's 44th Annual Meeting & Exhibition, Conference 3783 on Optical Diagnostics for Fluids/Heat/Combustion and Photomechanics of Solids, Denver CO, 23 Jul 99.
7. Schauer, F., Stutrud, J. and Bradley, R., "Pulse Detonation Engine In-House Research at AFRL," invited paper at the 13th ONR Propulsion Meeting, Edited by G. Roy and P. Strykowski, Minneapolis, MN, 10-12 August (2000).
8. Gabriel D. Roy, "Pulsed Detonation Phenomena for Air Breathing Propulsion," *ISABE 99-7127* (1999).
9. Schauer, F. R., Stutrud, J. S., Anthenien, R. A., Bradley, R. P., Chin, L. P. and Katta, V. R., "Development of a Research pulse detonation engine," invited paper at *Joint meeting of the CS/APS/PSHS JANNAF Subcommittees*, 18-22 October, Cocoa Beach, FL (1999).
10. Soloukhin, R. I., *Shock Waves and Detonations in Gases,* Mono Book Corp, Baltimore (1963).
11. Li, C., Kailasanath, K. and Patnaik, G., "A Numerical Study Of Flow Field Evolution In A Pulse Detonation Engine," AIAA Paper 2000-0314 (2000).
12. Shepherd, J., Personal Communication, California Institute of Technology, 24 August (2000).

AFRL/PRSC Pulse Detonation Engine Research Program

Fred Schauer and Jeff Stutrud
Air Force Research Laboratory, Propulsion Directorate
Wright-Patterson AFB, OH 45433

Royce Bradley and Vish Katta
Innovative Scientific Solutions, Inc.
Dayton, OH 45440

ABSTRACT

An in-house computational and experimental program to investigate and develop an air breathing pulse detonation engine (PDE) that uses a practical fuel (kerosene based, fleet-wide use, "JP" type) is currently underway at the Combustion Branch of Propulsion Sciences and Advanced Concepts Division of the Air Force Research Laboratory (AFRL/PRSC). PDEs have the potential of high thrust, low weight, low cost, high scalability, and wide operating range, but several technological hurdles must be overcome before a practical engine can be designed. This research effort involves investigating such critical issues as: detonation initiation and propagation; valving, timing and control; instrumentation and diagnostics; purging, heat transfer, and repetition rate; noise and multi-tube effects; detonation and deflagration to detonation transition modeling; and performance prediction and analysis. An innovative, four-detonation-tube engine design is currently in test and evaluation. Preliminary data are obtained with premixed hydrogen/air as the fuel/oxidizer to demonstrate proof of concept and verify model predictions while avoiding the detonation initiation problems associated with more complex hydrocarbon fuels. This paper presents an overview of the AFRL/PRSC PDE development research program as well as presents hydrogen/air results.

INTRODUCTION

Recent renewed interest in pulsed detonation propulsion concepts has prompted a concerted effort being made by the U.S. Air Force (AFRL), U.S. Navy (NRL, ONR, and the Naval Post Graduate School), NASA, and several research contractors (Adroit Systems Inc., Advanced Projects Research, Inc., Pennsylvania State University, Enigmatics, and major engine manufacturers), to develop a low-cost, practical-fueled, pulse detonation engine. Conceptually, a pulse detonation engine (PDE) offers few moving parts, high efficiency, high thrust, low weight, low cost, and ease and of scaling are an attractive alternative to jet turbine engines for small disposable engines. A cartoon that illustrates the simplicity of the PDE cycle is provided in Fig. 1 below. The near constant volume heat addition process, along with the lack of a compression cycle lend to the high efficiency and specific impulse, simplicity, and low-cost of pulse detonation engines. Pulse detonation engines have the potential for operation at speeds ranging from static to hypersonic, with competitive efficiencies enabling supersonic operation beyond conventional gas turbine engine technology. Currently, no single cycle engine exists which has such a broad range of operability.

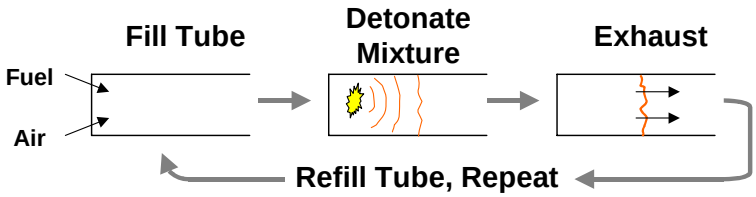

Fig. 1. Conceptual pulsed detonation engine cycle.

The in-house PDE program was established in order to make AFRL's unique resources available for the development of this technology. Traditionally, we have used our advanced computational modeling, diagnostic measurement techniques, and test facilities to work with government agencies and their contractors on the development of advanced combustor concepts. As such, much of our work was focused on deflagration phenomena while trying to avoid detonations. In order to work with pulsed detonation phenomena, we have set out to develop the necessary facilities, diagnostics, modeling tools, and experience so that we can contribute and provide our unique resources for the maturation of pulse detonation technology.

The second motivation of the in-house program was to produce publishable PDE data. Currently, there is a great deal of dissension on PDE performance within the community [1]. Detonation physics and detonation engine blow-down are highly sensitive to initial conditions, boundary conditions, and multi-dimensional geometry effects. Most of the available data and models are proprietary and not shared across the community, making it difficult to assess the current status of PDE performance and capability. As part of AFRL's research, an in-house research PDE has been developed to provide publishable data from which codes and performance predictions can be anchored and/or validated.

For the Air Force, a practical-fueled PDE means JP/air detonation. This requirement creates several technological hurdles which must be overcome in order to field such a PDE. Complex hydrocarbon fuels, and particularly liquid hydrocarbons, are difficult to detonate in air, typically requiring hundreds of kilo-joules to directly initiate a detonation [2]. For this reason, a practically fueled PDE becomes a deflagration to detonation transition (DDT) minimization process since the fuel burned during detonation initiation does not produce thrust efficiently while it is burning at low pressures. Furthermore, since thrust is generated with each detonation cycle, Fig. 1, it would be beneficial to raise the operating frequency in order to produce more thrust.

In cooperation with other government organizations performing PDE research and as the developer of one of two government in-house PDE research engines, AFRL/PRSC has attempted to establish a niche for itself in tackling the above issues. The ONR funded research engine at the Naval Post Graduate School in Monterey, California is directed towards liquid fuel injection, atomization, and mixing [3] and AFRL's engine research is focused on detonation initiation and repetition. While there is crossover in the two programs, we are confident that if we can develop a premixed vapor-fueled/air PDE, the Navy will make it work on liquid fuels.

APPROACH

Our unique resources [4] have been used to develop three areas in which AFRL can contribute to the development of PDE technology. In broad terms, these areas are: modeling, facilities and instrumentation, and research hardware development and testing.

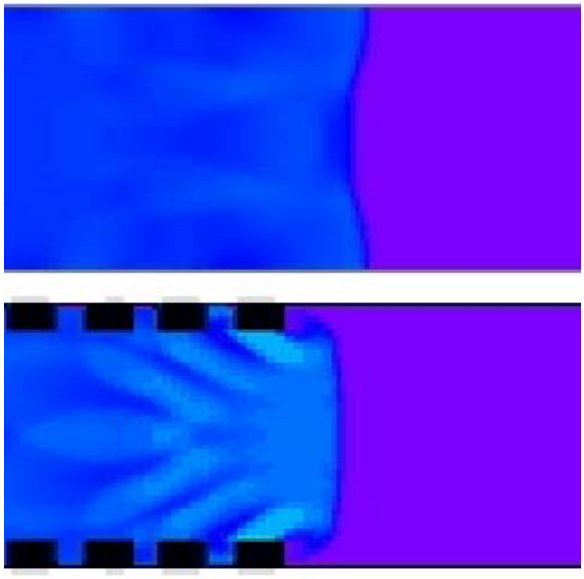

Fig. 2. CFD pressure map of DDT event with 2D tube and shelkin spiral.

Our detonation modeling work is described in more detail elsewhere [5]. Recently this work has been extended to three dimensional calculations and studies of detonation initiation schemes such as the Shelkin spiral calculation in Fig. 2. Both calculations employ weak initiation of hydrogen/air mixtures, but the upper frame is a straight channel and the lower contains a two dimensional representation of a Shelkin spiral. The brighter areas in Shelkin spiral calculation indicate that the "hot spots" critical for DDT events are more prevalent with the extra geometry. In the interest of space, further discussion of detonation modeling will not be addressed within this paper.

The Pulsed Combustor/Detonation Engine Research Facility (D-Bay) is capable of supporting up to 60,000 lbf thrust experiments, with integrated remote control and instrumentation systems. Choked flow measurements are employed to accurately regulate and measure oxidizer and fuel flow to pulsed experiments. Pulsed thrust measurements from 3 to 1,000+ lbf are accurately made with a damped thrust stand mounted on the existing engine thrust stand. Sixteen high speed analog channels (up to 5 MHz per channel) can be used to study the detonation

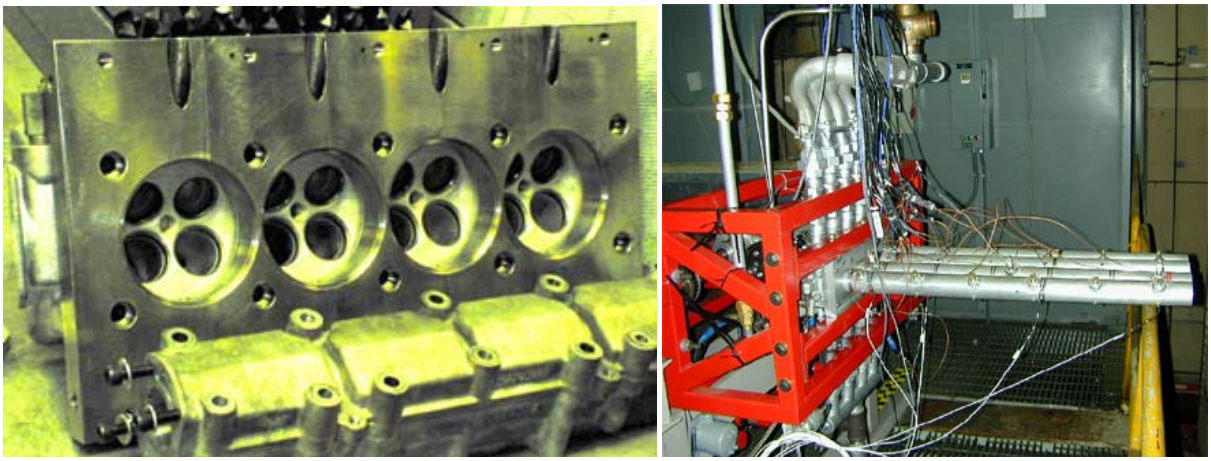

Fig. 3. Second generation "Quad 4" based PDE during assembly (left) and as installed.

phenomena. A digital imaging system operating at 1 Mhz is also available for high speed imaging [6].

The research engine is based upon valving found in a General Motors Quad 4, Dual Overhead Cam (DOHC) cylinder head commonly used in the Pontiac Grand Am. This PDE design has an extremely broad operating range and configuration, with up to four detonation tubes operating at up to 100 Hz each. The engine has proven reliability and durability, although the loss of the first generation engine design did occur due to fatigue in the tube mount area after approximately 200 hours of hot time [7].

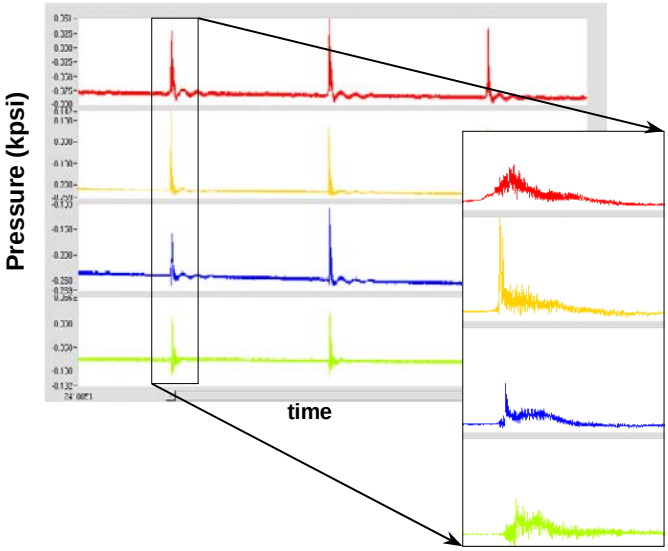

Fig. 4. High frequency pressure traces from in-house PDE engine. Measurement locations at 3, 15, 21, 33" axial distances from head (red, orange, blue, green respectively), 16 Hz Detonations, ~200 msec shown.

The head and tube mount systems have been redesigned to permit higher frequency operation, quick valve system and detonator tube configuration change-outs, and eliminate the areas where fatigue became a problem. The second generation engine is shown in Fig. 3 during assembly and as installed in the damped thrust stand. All of the control systems and data acquisition systems are LabVIEW™ based and integrated into one "virtual instrument" with back-up manual shutdown and safety systems. This virtual control panel is extremely flexible and can control all aspects of the PDE's operation including: lubrication, valve drive speed, fuel flow, main combustion air flow, purge air flow, timing, ignition delays, low and high frequency data collection as well as automatic shutdown in the event of a critical system failure. By changing the position of a few manual ball valves and pushing a few switches in the virtual control system, the engine configuration can be switched from one tube operating to four tubes in a matter of minutes.

Somewhat uniquely, the engine operates premixed. This has been found to increase the consistency of results by eliminating mixing issues. Recently, active cooling has been implemented along with expanded fuel systems so that indefinite run times are possible. Further details on the research facility and engine are available elsewhere [8].

RESULTS AND DISCUSSION

Although data has now been obtained with propane/air, the results presented herein will focus on hydrogen/air operation. Results presented were obtained with a single aluminum 2.0" (50.8mm) ID tube that was 36" (915mm) long. Conventional weak initiation was employed at the head end (via the spark plugs visible in Fig. 3) with a 3.5 msec ignition delay. The fuel/oxidizer mixture was stoichiometric and premixed hydrogen/air with a 50% clean air purge fill ratio. The above operating parameters and an operating frequency of 16 Hz applies to all data herein unless otherwise stated.

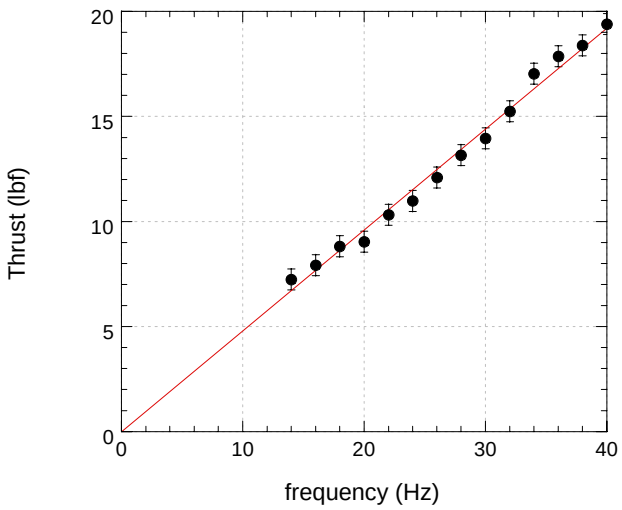

Fig. 5. Thrust versus frequency.

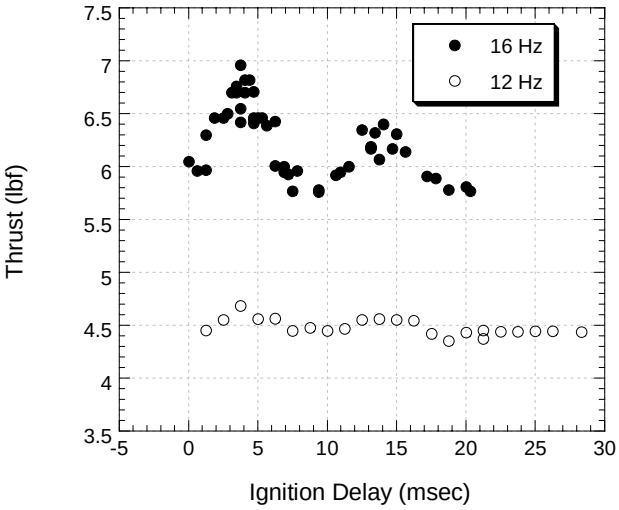

Fig. 6. Thrust versus ignition delay.

Initially it was found that the detonation did not transition from deflagration until near the end of the detonation tubes. The addition of a Shelkin or shocking spiral produced much faster transitions and higher thrust levels. A 3/16" wire diameter spiral with a ~1.8" pitch was placed in the first 12" of the detonation tubes. This spiral produced overdriven detonations by the 9" axial location. High frequency pressure transducer measurements, as seen in Fig. 4, indicate measured wave speeds of 1959 m/sec. This compares quite well with the stoichiometric hydrogen/air wave speed of 1968 m/sec published elsewhere [9]. Further experimental verification of detonation wave speeds was provided by photo diode measurements.

PDEs are highly scalable, as demonstrated in Fig. 5. The thrust is observed to increase linearly with frequency, with the engine making no thrust when not operating as expected. This data also demonstrates the accuracy of the thrust measurements as the error bars are +/- 0.5 lbf (+/- 2.2 N). Such thrust measurements have been demonstrated with the current system down to 3 lbf (13 N) but the accuracy and thrust range can be varied with configuration changes.

The impact of ignition delay can be assessed with the data in Fig. 6. The plot of thrust versus ignition delay contains data for two different frequencies. Ignition delay here is defined as the time in milliseconds between the intake valve closing completely and spark plug firing. Obviously, with premixed operation, negative ignition delays are to be avoided as they can result in combustion before the intake valves are closed with consequent backfiring through the intake system. It was found that premixed operation reduces the sensitivity of performance to ignition delay, as some PDE systems have been observed to detonate only within a narrow ignition delay window of only a few milliseconds. However, certain trends are apparent at both frequencies presented.

The ignition delay is observed to produce high and low spots. Because detonability is sensitive to changes in pressure, the initial low spot is surmised to be a result of attempting to initiate a detonation in the expansion resulting from the closing of the intake valve. The peaks at 3.5 msec ignition delay are believed to occur due to the presence of the subsequent compression wave.

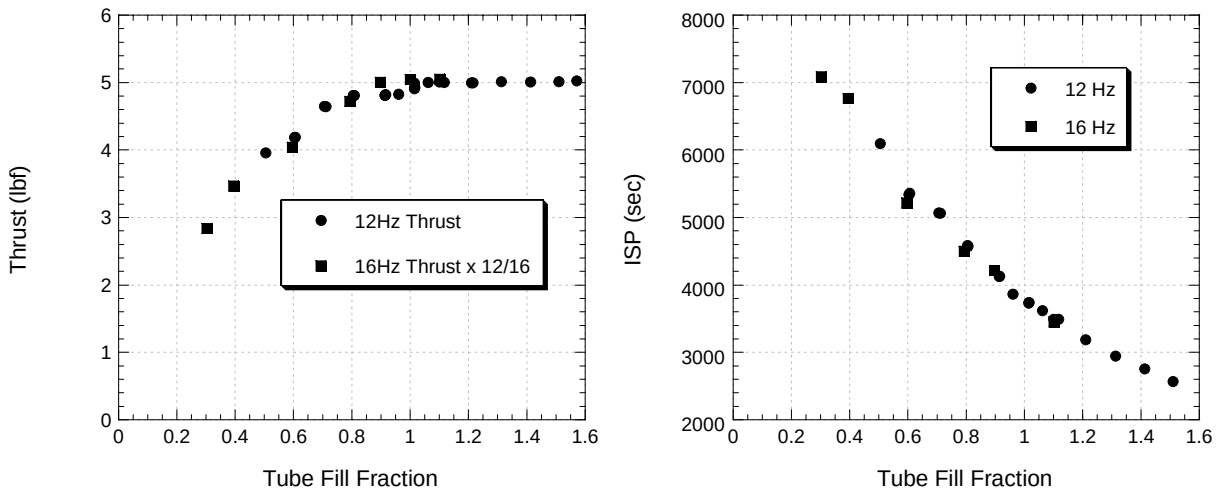

Fig. 7. Thrust and fuel specific impulse versus tube fill fraction.

These behaviors are then observed to repeat at periods corresponding to the acoustic length of the detonator tube.

PDE scalability is also accomplished via variation of the volume of the tube filled with detonable mixture. Via volumetric flow control, the tube fill fraction was varied as shown in Fig. 7. Results are shown for two frequencies to cover a range of fill fractions while remaining within the limits of a single choked-orifice volumetric flow control range. Thrust measurements on the left are scaled by frequency to 12 Hz. Due to the linear relationship of thrust and frequency, Fig. 5, the differing frequencies collapse on one another when scaled by frequency. Further confirmation of this phenomena is evident in the fuel specific impulse plot at the right of Fig. 7. Here frequency is accounted for when dividing by the fuel flow and no other frequency scaling is required.

At a fill fraction of 1.0, the entire tube is filled with fresh reactants for each cycle. At fill fractions less than 1.0, only part of the tube is filled with fresh reactants with the remainder occupied by either a purge cycle or hot expanded products from the previous cycle. At fill fractions greater than 1.0, the entire tube is filled with the excess detonable mixture presumably forming a free cloud at the tube exit. Thrust versus tube fill fraction is plotted on the left. The thrust is observed to increase with tube fill fraction until abruptly leveling out at a fill fraction of 1.0. Since reactants detonating outside the tube are unconfined, they do not produce any thrust as shown for the fill fractions greater than 1.0. Note that even at tube fills corresponding to only 30%, more than half the peak thrust is still obtained. This results in up to double the efficiency as shown by the increased fuel specific impulse at fill fractions less than 1.0. This trend, which has been confirmed by Li, Kailasanath, and Patnaik using CFD [10], is a result of longer blow down times produced by the increased acoustic relaxation length for partial tube fills. Effectively, purge air or previous cycle products are pumped by the detonation, resulting in the same higher mass/lower delta-velocity efficiency gains found in modern high-bypass turbofans. The remarkable efficiency gains are partly due to the increased efficiency of shock coupling in the PDE as compared to the viscous coupling in the turbofan.

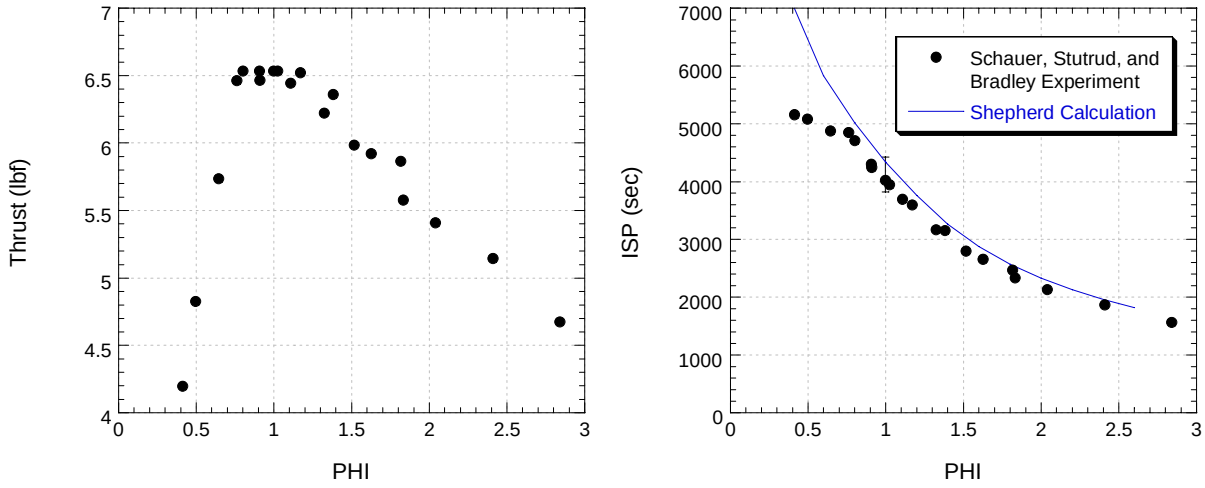

Fig. 8. Thrust (left) and fuel specific (right) impulse versus stoichiometry.

In addition to the effects of frequency, ignition delay, and fill fraction, the impact of stoichiometry was also examined as shown in Fig. 8. Thrust on the left and fuel specific impulse on the right are plotted versus a wide range of stoichiometries. As expected from detonability data [2], a stable region is observed near stoichiometries of 1.0. At fuel rich conditions, both the detonability and thrust are observed to fall off gradually with increasing fuel to air ratio. The detonability and thrust fall off more quickly on the fuel lean side of the stoichiometry curve. As with partial tube fills above, more than half the thrust is observed to occur even with only half the stoichiometric fuel to air ratio. This results in a higher efficiency for lean operation as confirmed on the specific impulse plot.

The current experiments are graphed along with Joe Shepherd's analytical calculations [11] with excellent agreement across a wide range of equivalence ratios. The experimental error bar shown represents the variation in thrust possible by changes in ignition timing alone, Fig. 6, as the data was collected with a constant ignition delay. Shepherd's results do not consider deflagration to detonation processes. The fall off in specific impulse observed experimentally for equivalence ratios less than 0.75 can be attributed to the rapid growth in DDT distance as the cell size gets much larger than the detonation tube size.

SUMMARY AND CONCLUSIONS

Pulse detonation engines are an extremely promising alternative to small, disposable-jet turbine engines. The Air Force Research Laboratory has supported PDE research for some time, and an in-house program of the Combustion Branch of the Propulsion Sciences and Advanced Concepts Division at Wright-Patterson AFB has been established to produce shareable benchmark performance data. In addition, the in-house program has been used to harness AFRL's unique resources in order to contribute to the development of pulsed detonation propulsion technology in the form of modeling, facility, and research components.

It is hoped that the contributions of our deflagration to detonation transition modeling can be used as a tool in the development and design of a practical-fueled detonation initiator. The pulsed combustor/detonation engine test facility has been developed as a cost-effective test

resource that meets many of the unique needs required for PDE testing. The remote controls and high frequency data-acquisition systems have been assembled to provide test support for researchers working in collaboration with AFRL. The facility can handle everything from bench scale experiments from academia to full-scale hybrid engine concepts from engine manufacturers. Moreover, it is hoped that researchers will take advantage of this national resource.

A research PDE was successfully designed, built, and operated under the in-house program using an innovative valve system based upon the "Quad-4", a 16 valve, four cylinder automobile engine from General Motors. The resulting engine is capable of a broad range of frequencies and configurations with up to four detonation tubes. Data from the engine is being published with the intent of providing non-proprietary PDE data against which performance codes and predictions can be benchmarked. The "Quad-4" PDE serves as a research tool and test-bed for detonation initiation concepts, high frequency operation, heat transfer studies, multi-tube detonation engine operation, and pulsed ejector research. The engine, which was operated successfully for the first time in the early fall of 1999, demonstrates the affordability and ease of scalability of PDE technology. The first generation engine operated for over 16 million cycles and approximately 200 hours of detonations before components failed due to fatigue. The engine demonstrated that PDEs can operate for extended durations even with low cost materials and designs. A second-generation engine design has been completed to replace the destroyed engine with numerous design improvements to durability and capability.

Hydrogen/air data have been presented on the effects of frequency, ignition delay, fill fraction, and fuel/air equivilance ratio. The resultant findings provide insight for scaling thrust and improving efficiency of PDE hardware. Data sets are available for collaborative studies, including flow conditions and heat transfer data not published herein. Additional data on propane/air detonations are available for qualified researchers.

There is much work to be done in developing valving, detonation initiators, noise suppression techniques, thermal protection systems, intake and exhaust nozzles, and control systems before a JP/air fueled PDE becomes practical. AFRL/PRSC would like to invite the community to consider our resources for further PDE research. With high quality modeling, research facilities, and an in-house PDE engine, we can work with other organizations and contractors, as we have in the past with turbine engine technology, to maturate and transition PDE technology to the field.

ACKNOWLEDGEMENTS

Special appreciation must be expressed to the technicians and support personnel, both in-house government employees and on-site contractors who made this work possible, particularly Dwight Fox (ISSI) who helped build much of the research PDE engine and Walt Balster (ISSI) who recently joined us as a facility technician. Dr. Vish Katta and Dr. L.P. Chin have performed their usual miracles on the modeling side and are gratefully acknowledged for their contributions to this program. We also wish to acknowledge the technical leadership of Dr. Mel Roquemore (AFRL/PRSC).

REFERENCES

[1] Kailasanath, K., Patnaik, G. and Li, C., "Computational Studies of Pulse Detonation Engines: A Status Report," *AIAA 99-2634* (1999).

[2] Kaneshige, M. and Shepherd, J. E., *Detonation database***,** Technical Report FM97-8, GALCIT, (1997).

[3] Brophy, C., Netzer, D. and Forster, D., "Detonation Studies of JP-10 with Oxygen and Air for Pulse Detonation Engine Development," *AIAA 98-4003* (1998).

[4] Hancock, R. D., Gord, J. R., Shouse, D. T., Schauer, F. R., Belovich, V. M. and Roquemore, W. M., "AFRL Combustion Branch (PRSC) Aero-propulsion Research and Development Activities," *Proceedings of the International Test and Evaluation Association (ITEA) Conference* (1999).

[5] Katta, V. R., Chin, L. P. and Schauer, F. R., "Numerical Studies on Cellular Detonation Wave Subjected to Sudden Expansion," *Proceedings of the 17th International Colloquium on the Dynamics of Explosions and Reactive Systems*. Heidelberg, Germany (1999).

[6] Gord, J. R., Tyler, C., Grinstead, Jr., K. D., Fiechtner, G. J., Cochran, M. J. and Frus, J. R., "Imaging Strategies for the Study of Gas Turbine Spark Ignition," Presented at the SPIE's 44th Annual Meeting & Exhibition, Conference 3783 on Optical Diagnostics for Fluids/Heat/Combustion and Photomechanics of Solids, Denver CO, 23 Jul 99.

[7] Schauer, F., Stutrud, J. and Bradley, R., "Pulse Detonation Engine In-House Research at AFRL," invited paper at the 13th ONR Propulsion Meeting, Edited by G. Roy and P. Strykowski, Minneapolis, MN, 10-12 August (2000).

[8] Schauer, F. R., Stutrud, J. S., Anthenien, R. A., Bradley, R. P., Chin, L. P. and Katta, V. R., "Development of a Research pulse detonation engine," invited paper at *Joint meeting of the CS/APS/PSHS JANNAF Subcommittees*, 18-22 October, Cocoa Beach, FL (1999).

[9] Soloukhin, R. I., *Shock Waves and Detonations in Gases*, Mono Book Corp, Baltimore (1963).

[10] Li, C., Kailasanath, K. and Patnaik, G., "A Numerical Study Of Flow Field Evolution In A Pulse Detonation Engine," AIAA Paper 2000-0314 (2000).

[11] Shepherd, J., Personal Communication, California Institute of Technology, 24 August (2000).

Evaluation of A Self-Aspirated Pulse Detonation Engine

30 March 2001

Dr. John Hoke (ISSI)
Jeff Stutrud
Royce Bradley
Dr. Fred Schauer
Air Force Research Laboratory

Introduction

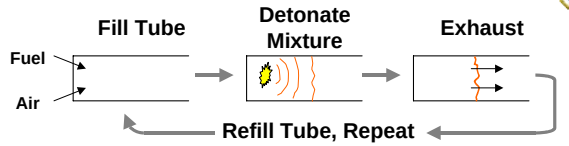

Goal: Develop air-breathing PDE's using practical fuels

Benefit: Cheap, simple, high performance engine that is highly scalable and efficient across a broad operating range (Mach 0-4+)

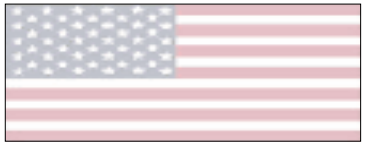

Issues

- Detonation Initiation
- Performance
- Proprietary Data

2

Self-Aspiration

- Supersonic Pulsed Ejector Pump
- Turbo-Charger
  - Can the PDE self-aspirate
  - How much thrust do you trade for self-aspiration?
  - Can a turbine withstand being placed at the exit of a PDE?

PDE Core

Replace HS/conventional combustor with PDE core

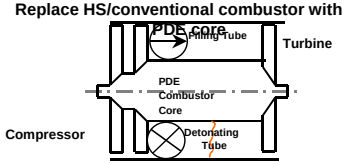

3

Turbo-Charger Configuration Schematic

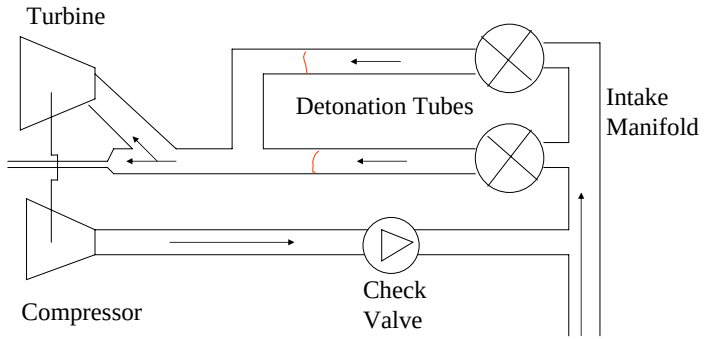

4

Turbo-Charger Configuration

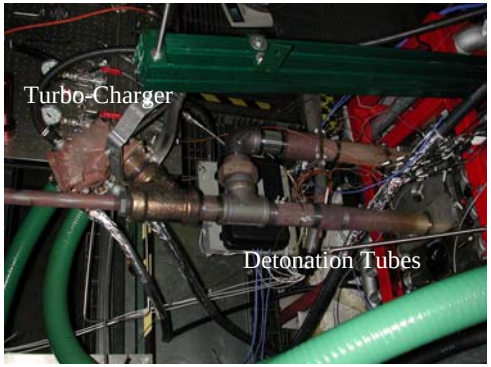

5

Self-Aspiration

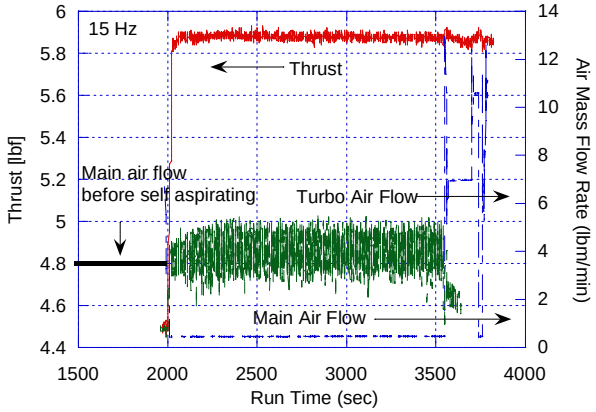

6

Temperatures During Self-Aspiration

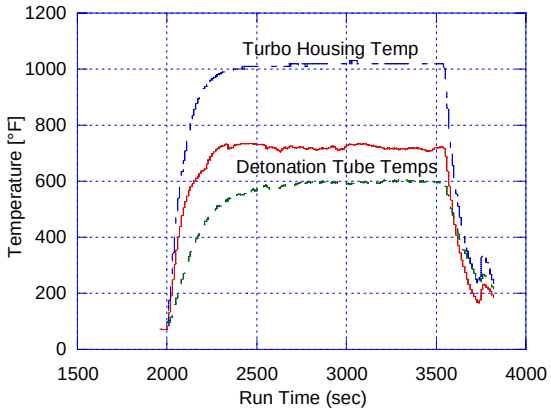

7

Turbine Blades After 35K Detonation Events

8

Turbo-Charger Performance

* Self Aspirating
¤ Other Conditions Achieved

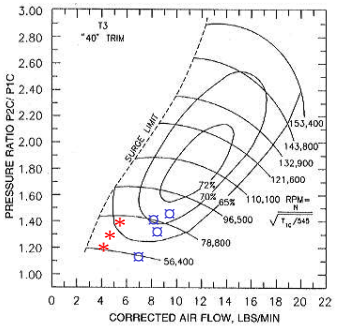

9

PDE Driven Ejector

- **High-bypass effect**
  - **Can a secondary flow be entrained**
  - **Does the entrained secondary flow increase thrust**
- **Noise reduction**
  - **Is the noise muffled by the ejector**

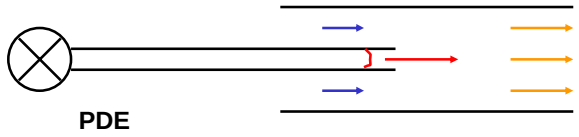

10

AFRL PDE-Ejector

11

Ejector Wall Pressure

Successfully Induced Secondary Airflow

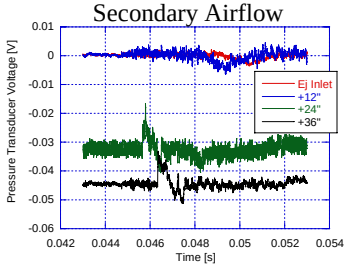

Failure to Induced Secondary Airflow

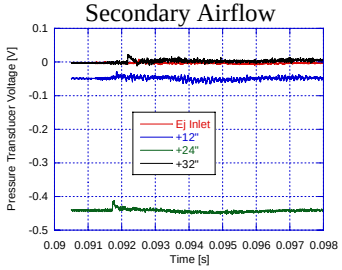

Stoichiometry and Primary-Tube Fill-Fraction Affect Induced Airflow

12

AFRL PDE-Ejector

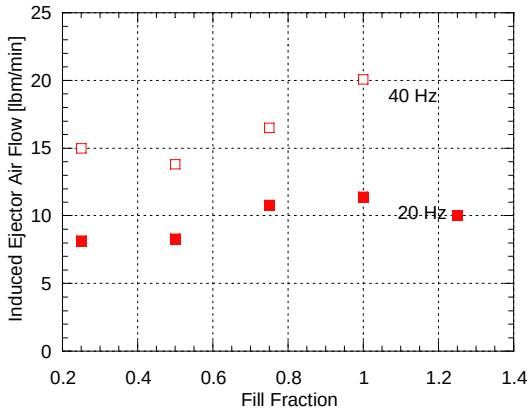

13

Ejector Performance

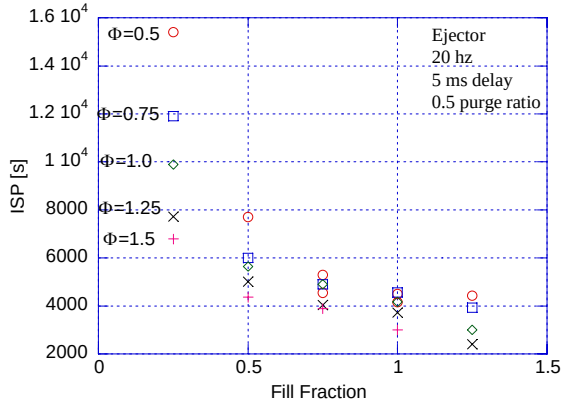

14

Summary and Conclusions

•Two methods to self-aspirate a PDE are currently being evaluated

•Self-aspiration has been achieved with a turbo-charger
- •No visible signs of wear on the turbine after 35K detonations
- •Experiments indicate that 20-25% of the thrust is traded for self-aspiration
- •25 minutes of continuous self-aspiration achieved

•Ejector pump successfully entrained secondary flow
- •Not all conditions entrain secondary flow
- •Thrust augmented 10-20%
- • A weighted noise level unaffected by ejector pump

Funded by: Propulsion Sciences and Advanced Concepts Division, AFRL, Industry, & AFOSR

15

Application of PDE Technology

Turbine-Based Hybrid Concepts

- **Turbo-PDE (PDE fan)**
  - **Clean, high-pressure air is more detonable**
  - **Combined fan/valving**
  - **Compressor stall?**
- **PDE Augmentor**
  - **Hot, high-pressure air is more detonable**
  - **Vitiated air is less detonable**
  - **Valving with turbine exit conditions?**
  - **Turbine back pressure interactions?**
- **PDE Core**
  - **Clean, high-pressure air more detonable**
  - **Combined compressor/valving**
  - **Firing PDE through turbine?**
  - **Compressor stall?**

16

Application of PDE Technology

Pure PDE

- first generation PDE missile, UAV/UCAV
- Future take-off through Supersonic propulsion

Advanced Propulsion Systems

- PDE Duct Burner
- PDE-PDRE Hybrid
- Single Flow-Path PDE-SCRAM
- PDE stabilized SCRAM
- PDE/PDRE-RBCC

17

PDE/Hybrid Cycles

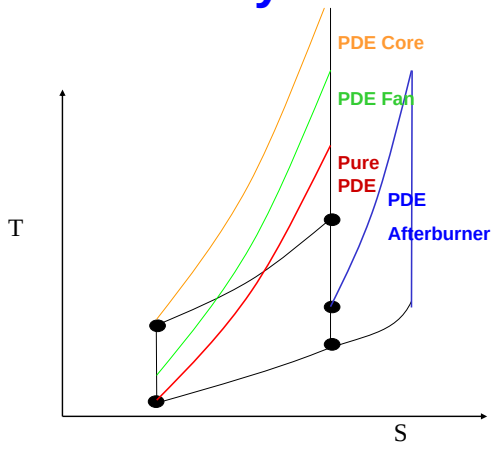

18

Tube Fill Fraction

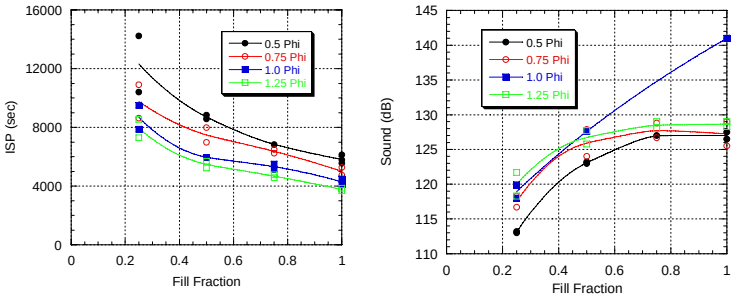

19

Hybrid Piston-Pulse Detonation Engine

30 Month 2001

Air Force Research Laboratory

Brian M. Frankey

Dr Fred Schauer

Jeff Stutrud

ISSI Contractors:

Dr John Hoke

Royce Bradly

PDE Background

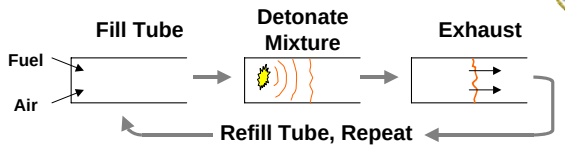

Goal: Develop air-breathing PDE's using practical fuels

Benefit: Cheap, simple, high performance engine that is highly scalable and efficient across a broad operating range (Mach 0-4+)

Previous Achievements

- Detonation Initiation
- Thrust

2

In-House PDE Research Engine

GM Quad 4 DOHC, 4 Cylinder Pulsed Detonation Engine

Current Quad-4 PDE

•Fed compressed air from external compressor

•Mechanized by external 10 hp DC motor

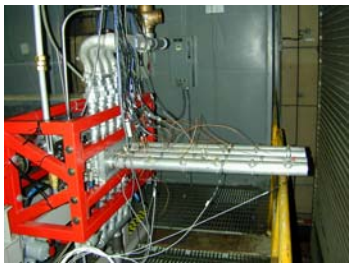

•Timing and valve system is stock cylinder head from scrapped Grand Am

•Next Step: Self actuated, self aspirated PDE…

3

Hybrid Piston-Pulse Detonation Engine
Self Actuated -- Self Aspirated

GOAL: Morph existing internal combustion engine into hybrid piston-pulse detonation engine.

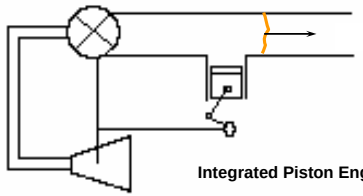

Integrated Piston Engine and Supercharger

4

HPPDE feasibility is dependent on detonation.

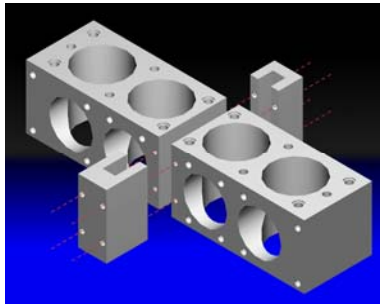

Aluminum Spacer

- Modification to allow integration of ICE with PDE to create HPPDE
- Cylinder is no longer a closed volume
  - No compression stroke
  - No pressure rise from deflagration

5

Hybrid Piston-Pulse Detonation Engine

Modified Suzuki Katana 1100

- **Third Generation PDE**
- **Designed to produce thrust and shaft work**
- **Self aspirated and self mechanized**

6

Head Pressure

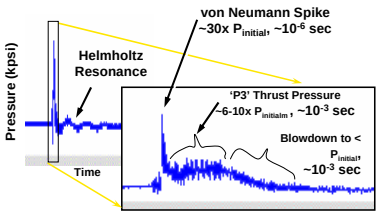

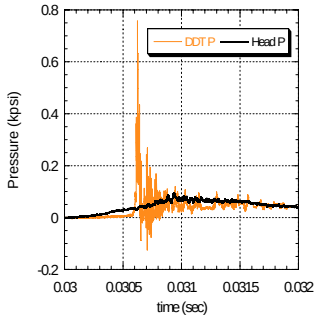

- Detonation wave travels faster than sound
- Detonation creates pressure rise of unconfined gas
- 6-10 times initial pressure for 2 ms
- Head pressures measured on the order of 100 psi in Quad-4 PDE

7

Theoretical Power

Vd	2.84E-04	m3	Rbs	1.345	
Vc	2.81485E-05	m3	a	29	mm
Cr	11.1		l	87	mm
B	78.01	mm	R	3	estimate
L	58	mm			

Ignition Delay	2.000E+01	ms
Max Pressure	7.000E+06	Pa

rpm	10000	
rev/s	166.6666667	
s/rev	0.006	ms

Total Work	1401.62	J
Watts	467207.51	Watts

Crank Angle (deg)	s [mm]	Cylinder Vol	Δv	Time [ms]	Pressure	ΔW
0	87	2.81485E-05		0	0.000E+00	0
1	86.99337487	2.81802E-05	3.16654E-08	0.016666667	0.000E+00	0
2	86.97350299	2.82752E-05	9.49794E-08	0.033333333	0.000E+00	0
3	86.94039498	2.84334E-05	1.58243E-07	0.05	0.000E+00	0
4	86.89406847	2.86548E-05	2.21422E-07	0.066666667	0.000E+00	0
5	86.83454818	2.89393E-05	2.84482E-07	0.083333333	0.000E+00	0
6	86.76186585	2.92867E-05	3.47392E-07	0.1	0.000E+00	0
7	86.67606027	2.96968E-05	4.10115E-07	0.116666667	0.000E+00	0
8	86.57717723	3.01694E-05	4.7262E-07	0.133333333	0.000E+00	0

8

Power

•Theoretical calculations of Power vs RPM over a range of ignition delays

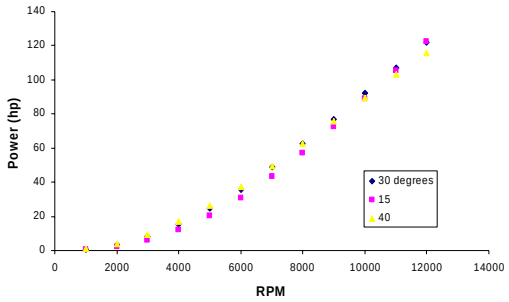

9

Getting Started

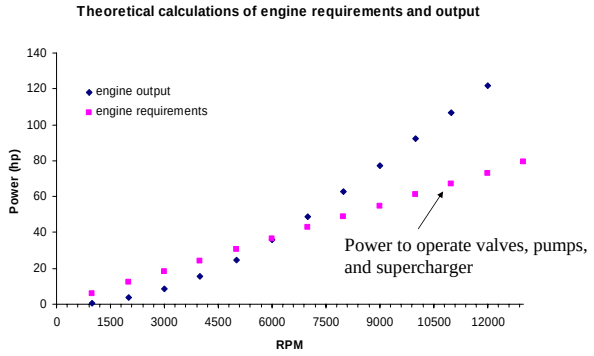

10

Summary and Conclusions

Beyond detonation initiation…

•Harness detonation energy

•self actuate

•self aspirate

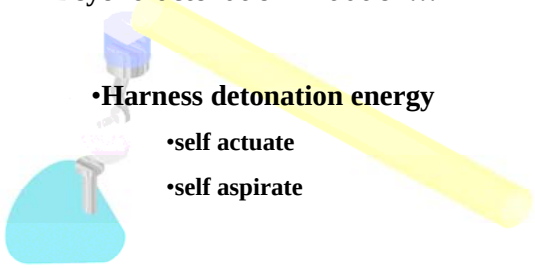

Funded by: AFRL & AFOSR

11

Self-Actuated Self-Aspirated PDE

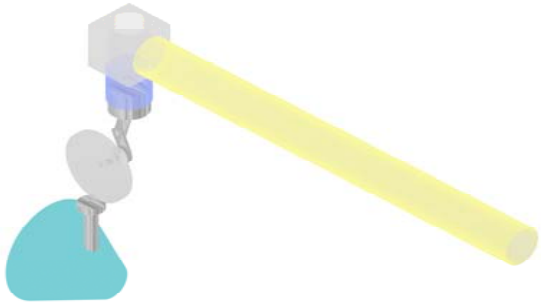

12

An Introduction to a Pulsed Detonation Engine

30 March 2001

Matthew Slagel
Wright State University
Dr. Fred Schauer
Jeffrey S. Stutrud
Research Engineers
Air Force Research Laboratory
Royce Bradley
ISSI

In-House PDE Research

Matthew Slagel
Wright State University

Dr. Fred Schauer
Jeffrey S. Stutrud
(937)255-1554
BLDG 490
1790 Loop Road North
Wright-Patterson AFB, OH 45433

Royce Bradley
Dr. John Hoke
Dr. Vish Katta
Innovative Scientific Solutions Inc.
Beavercreek, OH

2

Introduction

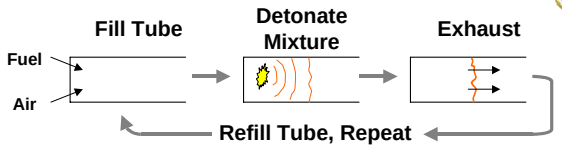

Goal: Develop air-breathing PDE's using practical fuels

Benefit: Cheap, simple, high performance engine that is highly scalable and efficient across a broad operating range (Mach 0-4+)

Issues

- **Detonation Initiation**
- **Performance**
- **Proprietary Data**

3

What is a PDE/Detonation?

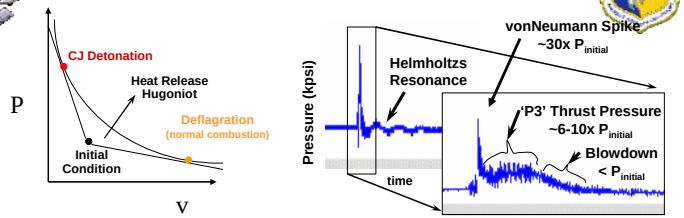

- **Detonation is one of two stable solutions to the combustion equations**
- **Temperatures typically 40% hotter than deflagration ('normal combustion')**
- **Flame/gas velocities are approximately Mach ~5/4 respectively**

Actual Detonation Processes have Complex Multi-Dimensional Cellular Structures Interacting with Gas Dynamics and Geometry

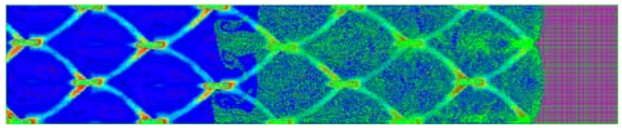

2-D CFD of Peak Pressure or 'Smoke Foil' Traces with Particle Traces

4

D-Bay: Pulsed Combustor/ Detonation Engine Facility

Formerly Mothballed, Full Scale Engine Research Facility

60,000 lbf Thrust Research Facility

Capabilities

- Explosion Proof Facility
- Up to 60 klbf Static Thrust
- 1,000+ lbf Damped Thrust
- 6 lb/sec 100 psi air supply
- High Capacity Inlet/Exhaust Stacks
- Direct Connection to Liquid Fuel Farm
- Choked Flow Measurements
  - Air
  - Hydrogen
  - Propane
- Hardened Remote Control Room
- 16 High Frequency DAC Channels, up to 5Mhz
- 1Mhz Digital Imaging System

Damped Thrust Measurements 1,000+ pound capacity

Isolated and Protected

Remote Control and High-Frequency DAC

Adapting OHC Cylinder Head to PDE

- Automotive Engines Designed for 8-20 Pressure Ratio
- Provisions for Valving, Fuel Injection, Timing, and Cooling
- Vapor Carburetor Available
- Bolt Flanged PDE Tubes to Cylinder Head
- Multiple Tubes/'Header' Effect
- Extra Valves for Predetonator or Purge Cycles
- Cheap/Mass Produced

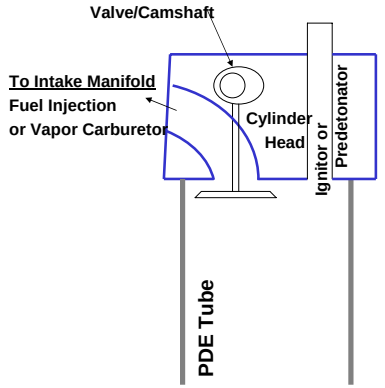

In-House PDE Research Engine

GM Quad 4 DOHC, 4 Cylinder Pulsed Detonation Engine

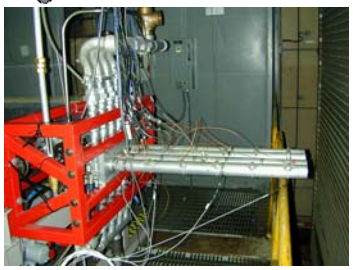

- Off The Shelf Technology - $2,000 Initial Hardware Investment
- Pontiac Grand Am Cylinder head (formerly 150 BHP) produces up to 3,000 lbf theoretical thrust as PDE
- Test-bed for PDE Research, Benchmarking
- Predetonator/Initiator Development
- High Frequency Operation
- Multi-tube Effects
- Pulsed Ejector Research

- Adapter Plate Mounts Detonation Tubes
  - 1-4 Tubes
  - 2" Diameter PDE Tubes for R&D
  - 3 1/2" Diameter PDE Tubes for Engine
- Electric Motor Driven Camshafts
  - 0.5-64 Hz currently (per tube)
  - 100 Hz possible
- Vapor Fuels: Hydrogen, Propane, etc.
- Liquid FI: Gasoline, Ethanol, JP, etc.

Stock Intake Manifold with Ball Valve Selection of 1-4 Detonation Tubes

(Purge Manifold Similar)

'Quad 4' PDE Valving and Air Systems

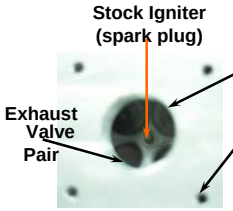

Adapter Plate with 4 Valves Per Cylinder

- Intake valves supply fuel/air
- Extra exhaust valves used for purge cycles, predetonator, or additional combustion air

Flow Rate across Valves versus Manifold Pressure (flow rate per cylinder)

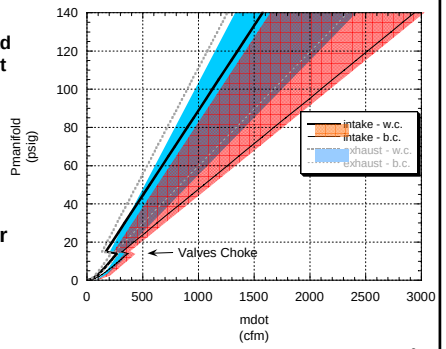

Integrated Remote Controls for: Facility, Engine, and Data Acquisition

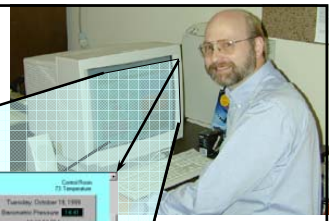

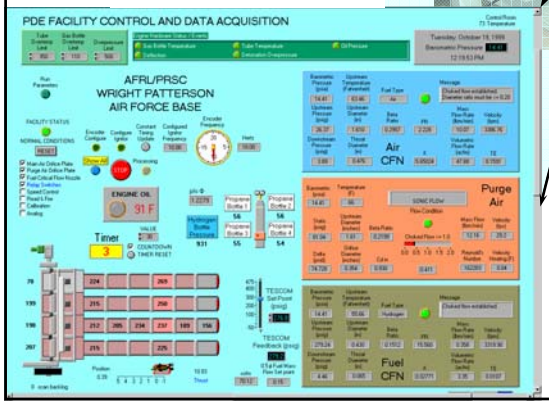

Jeffrey S. Stutrud

9

In-House Research 'Quad- 4' PDE

Tube 1 @ 16Hz

4 Tubes @ 4Hz each

2 Tubes @ High Frequency

High-Frequency Pressure Transducers

3, 15, 21, 33" locations (r,o,b,g)

16 Hz Detonations, ~200 msec shown

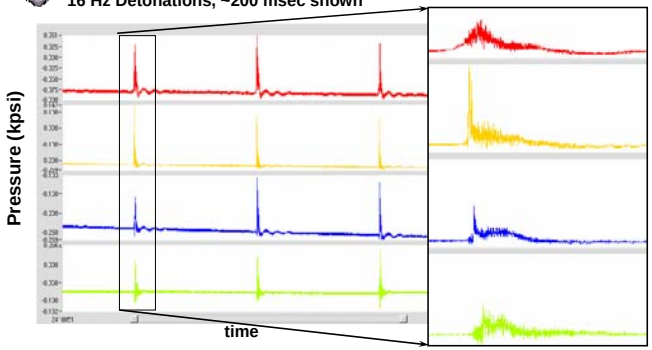

Measured Wave-speed is 1959 m/sec (CJ is 1968 m/sec)

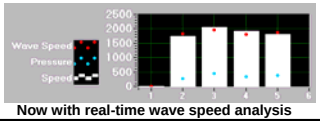

Now with real-time wave speed analysis

Shelkin Shocking Spirals

2" OD, 3/16" wire, ~1.8" pitch, 12" Long

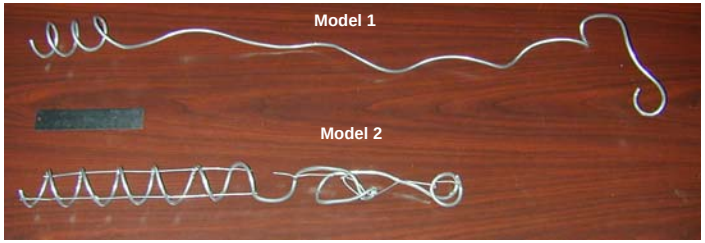

Model 3 is made of steel but survived ~100 hours of run time

RESULT: Dramatically increased thrust, DDT between 3 and 9" instead of ~36"

12

Thrust

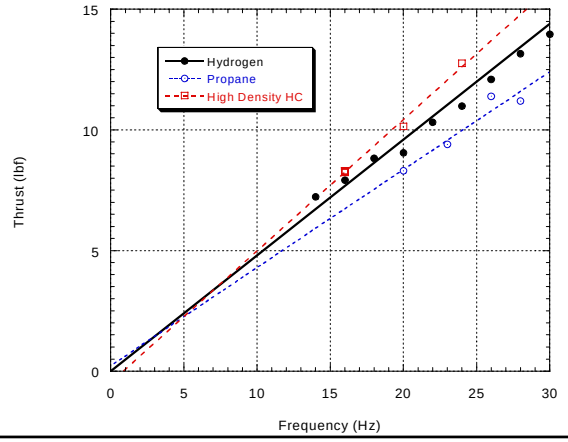

13

Fill Fraction

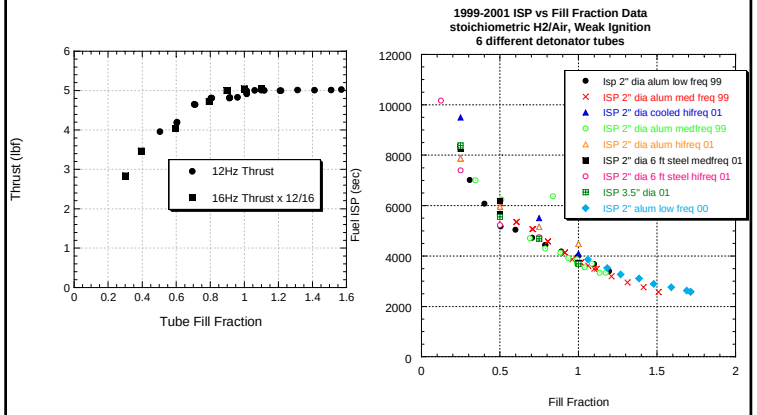

14

Stoichiometry

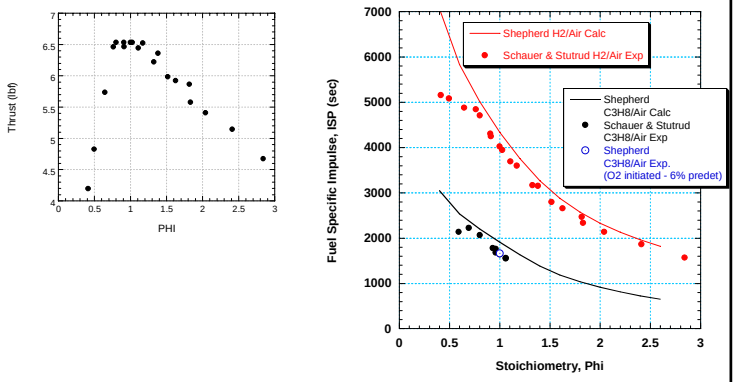

15

Summary and Conclusions

- Modeling
- Test Facility
- Research Engine

- **Benchmark PDE Data**
- **PDE R&D Capability for Technology Advancement**
- **Test - bed for In-House PDE Research**

Funded by:
AFRL & AFOSR

16

AFRL/PRSC

Detonation Wave Propagation through Tube Array

Capt. AJ Rolling
(937) 293-8695
AFIT/ENY
August.Rolling@afit.edu

Dr. Paul King
Dr. Fred Schauer
Dr. John Hoke
Royce Bradley
Matthew Slagel
Vish Katta
Jeff Stutrud

AFRL/PRSC

How does a PDE work?

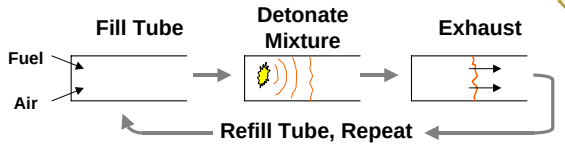

Single Tube Mechanism

Produces Thrust due to Mass Flux

AFRL/PRSC

How do we detonate a gas?

- **2 things can happen when we burn fuel**
  - •Deflagration (typical)
  - •Detonation

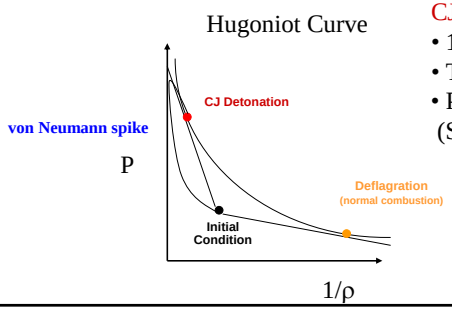

CJ Properties H2/air
- 1968 m/s
- T_2 ~ 2951 K
- P_2/P_p 15.62

(Soloukhin, 1966)

AFRL/PRSC

Detonation Mechanism

Deflagration to Detonation Mechanism (7 Steps, Kuo)

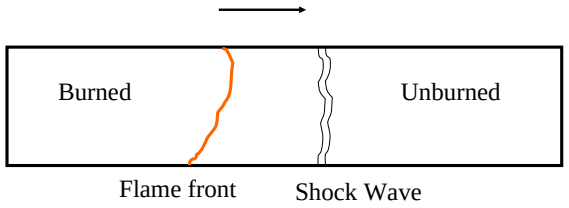

AFRL/PRSC

Detonation Mechanism

Deflagration to Detonation Mechanism (7 Steps, Kuo)

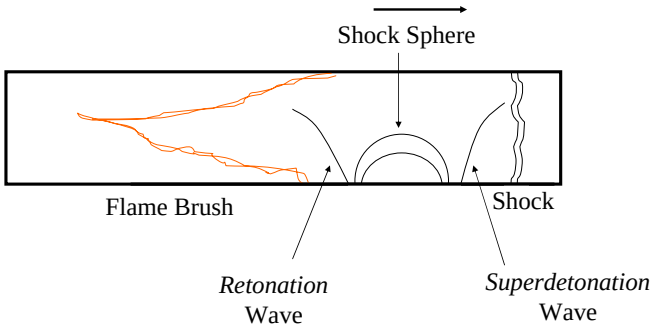

5

AFRL/PRSC

Detonation Combustion

Detonation Phenomena Observed in PDE

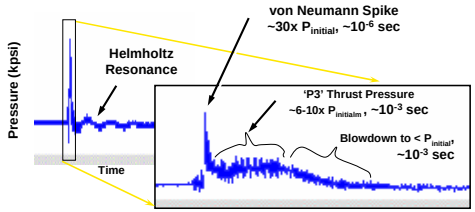

Actual Detonation Processes have Complex Multi-Dimensional Cellular Structures Interacting with Gas Dynamics and Geometry

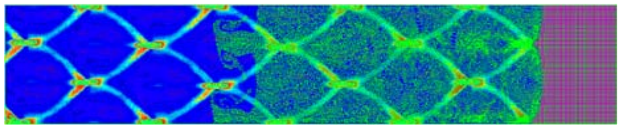

2-D CFD of Peak Pressure or 'Smoke Foil' Traces with Particle Traces

6

AFRL/PRSC

Methods

- **Long Tube (minimum diameter)**
- **Converging tube**
- **Shelkin Spiral**

7

AFRL/PRSC

Objective

- **Determine whether detonation wave can propagate through a "split tube"**

8

Detonation Splitter

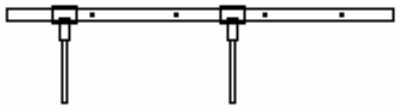

Test Set-up

- **8 Pressure Transducers**
- **3 Wall Thermocouples**
- **Thrust meter**

Splitter CFD

Vish Katta

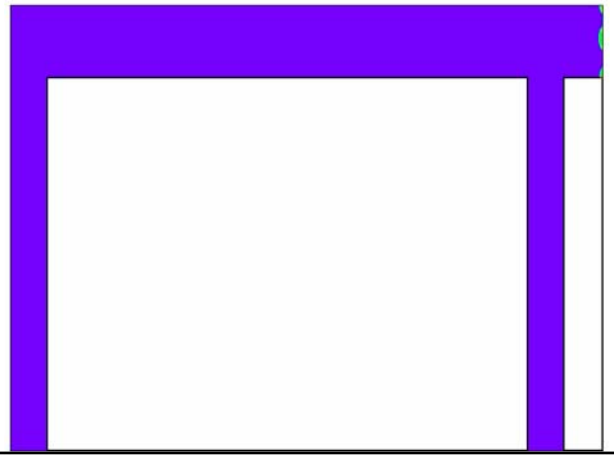

Experimental Configurations

- **Baseline**
- **Splitter**
- **Splitter with Reducer**

Experimental Parameters

- Fuel Fill 1.0
- Equivalent Length 50.464 in (Main Tube for all three configurations)
- Ignition Delay 0.0 s
- Frequency 20.0 Hz
- Equivalence Ratio 0.75, 1.0, 1.25

AFRL/PRSC

Pressure Traces

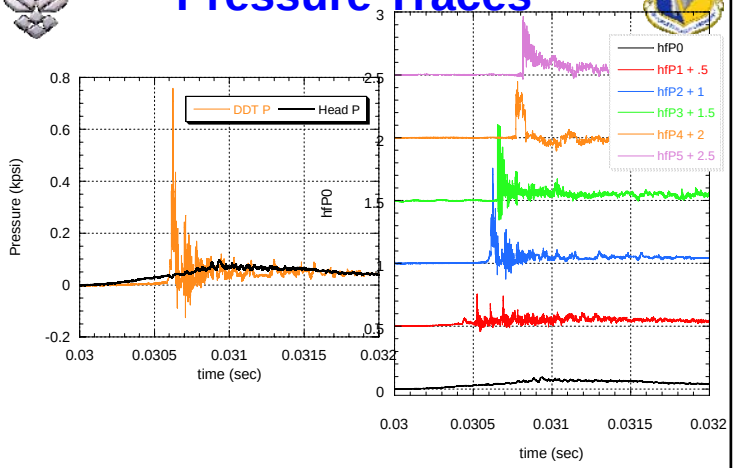

13

AFRL/PRSC

Actual Run

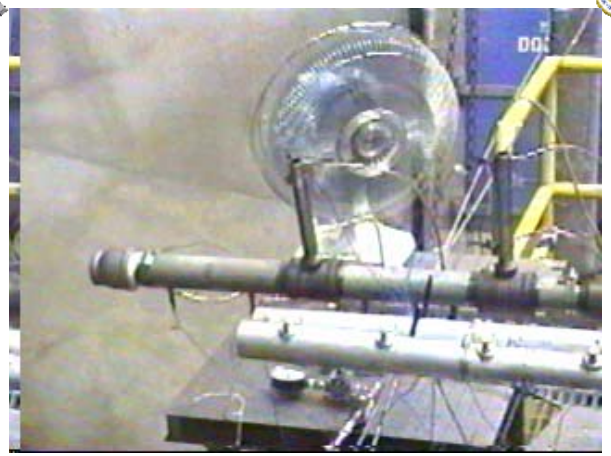

14

AFRL/PRSC

Results- Baseline

- **Baseline**
  - **Not at CJ point 1968 m/s**
    - **Point 1 to 2 1267 m/s**
    - **Point 2 to 3 1692 m/s**
    - **Point 3 to 4 1875 m/s**
  - **Clearly still accelerating through tube**
  - **Does not meet our initial objective**
  - **Question inlet conditions**

15

AFRL/PRSC

Results-Thrust

- **Thrust for stoichemetric (ϕ=1)**
  - **Baseline 9.96 lb**
  - **Split 9.4 lb**
  - **Split w/ Reducer 8.57 lb**
- **Trend for all configurations***
  - **Thrust increased with ϕ**

* **However, Consider Interaction with Fill Ratio**

16

Results-Splitter

AFRL/PRSC

Main Tube	Splitter	Baseline
– Point 1a* to 2	1382 m/s	1267 m/s
– Point 1b* to 2	1900 m/s	1267 m/s
– Point 2 to 3	1572 m/s	1692 m/s
– Point 3 to 4	1500 m/s	1875 m/s

- Split 1
  - Point 5 to 6 1000 m/s
- Split 2
  - Point 7 to 8 877 m/s

* Twin Peak Pressure Traces

17

Results-Splitter

AFRL/PRSC

- Comparison Points
  - Split 2 Point 2 to 7 1200 m/s
  - Main Tube Point 2 to 3 1562 m/s
- Deceleration making the 90 deg turn

18

Conclusions

AFRL/PRSC

- Do not know if detonation can split
  - Did not have detonation in main tube
  - Additionally require photodiode, carbon imprint, 3rd pressure transducer in split to determine if we have CJ detonation

19

AFRL Pulse Detonation Engine Research Application

Dr. John Hoke
Royce Bradley
Innovative Scientific Solutions, Inc.

Dr. Fred Schauer
Air Force Research Laboratory

Introduction

Issues

- Exit Boundary Condition Drives Performance
- Self Aspiration
- Extracting Shaft Power

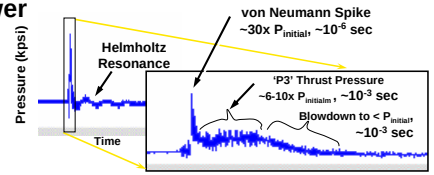

Studies

- Nozzles
- Supersonic Pulsed Ejector Pump
- Turbo-Charger
- Detonation-Driven Piston Engine

2

Nozzles and Blow Down

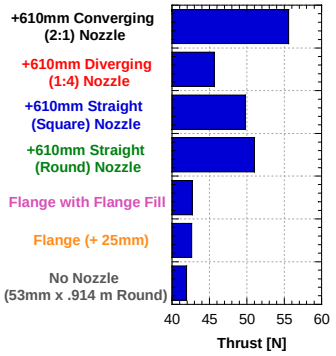

2D Nozzle Studies

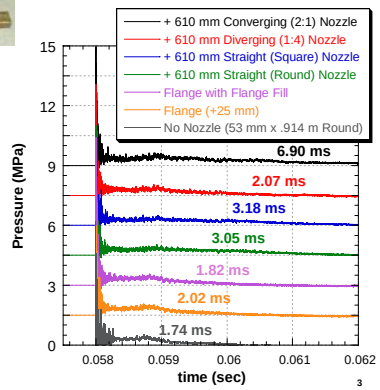

3

PDE Driven Ejector

- High-bypass effect
  - Can a secondary flow be entrained
  - Does the entrained secondary flow increase thrust
- Noise reduction
  - Is the noise muffled by the ejector

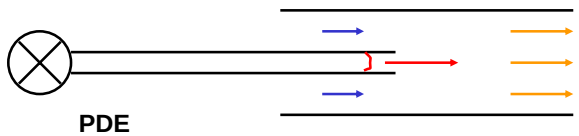

4

AFRL PDE-Ejector

AFRL PDE-Ejector

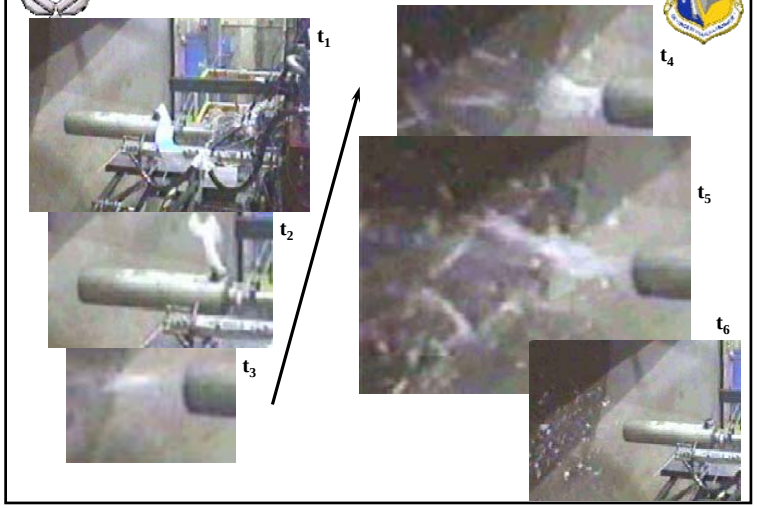

AFRL PDE-Ejector

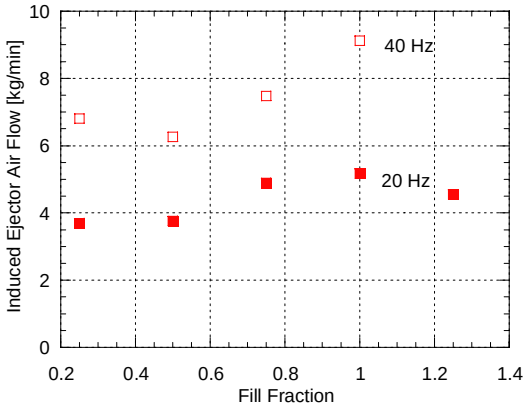

7

Ejector Performance

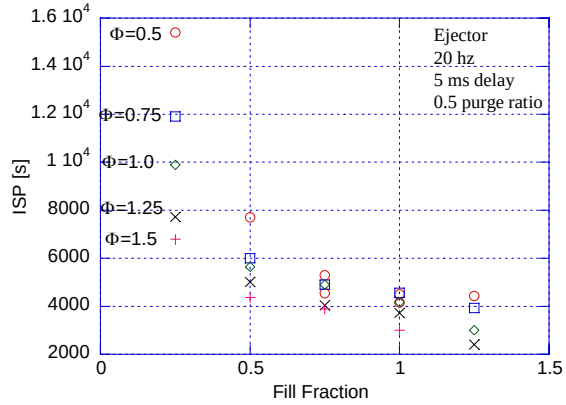

8

Ejector Wall Pressure

Successfully Induced Secondary Airflow

Failure to Induced Secondary Airflow

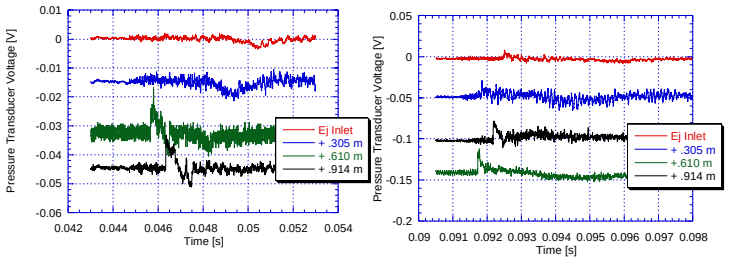

Equivalence Ratio and Primary-Tube Fill-Fraction Affect Induced Airflow

9

PDE in Core

Replace High Spool and / or Conventional Combustor with PDE Core

- **Clean, high-pressure air is more detonable**
- **Combined compressor / valving**
- **Firing PDE through turbine?**
- **Compressor stall?**

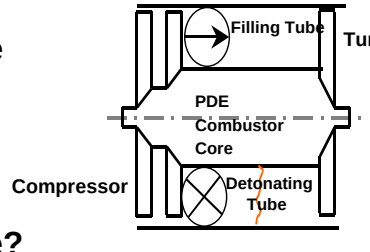

10

PDE Combustor in Turbine Core

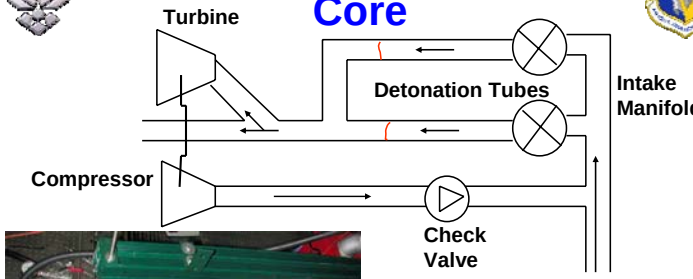

11

25 Minute Self-Aspirated Run to Thermal Equilibrium

with AFRL In-house Self-Aspirated PDE Core in Turbine

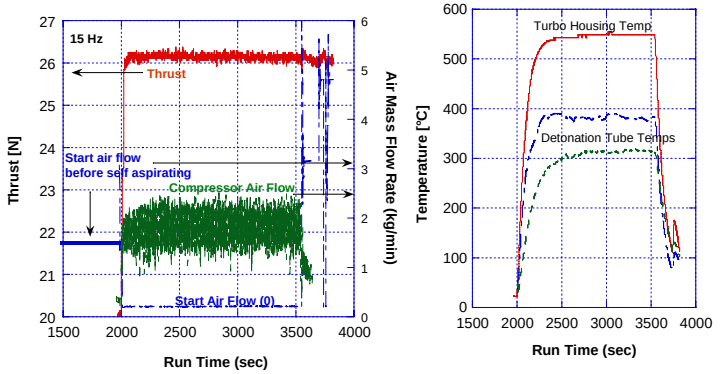

12

Detonation Driven Turbine

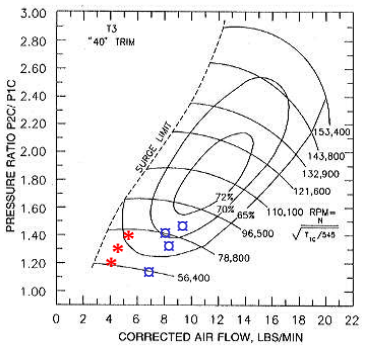

* Self Aspirating
¤ Other Conditions Achieved

- Preliminary results are very encouraging
- Detonation driven centrifugal-turbine spun to 80,000+ rpm
- No apparent turbine damage after 40+ minutes of operation and 30,000+ Detonations

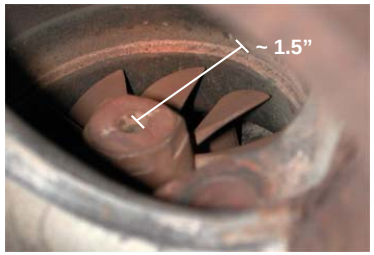

13

PDE-Piston Hybrid

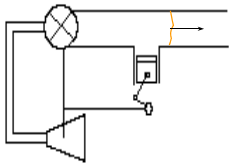

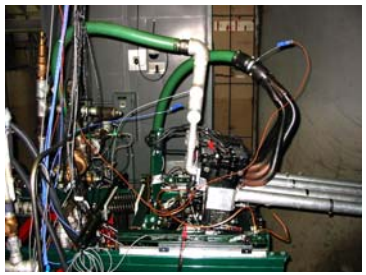

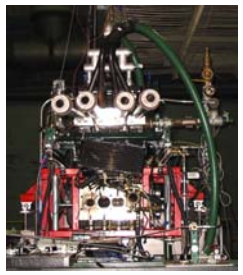

14

PDE-Piston Hybrid

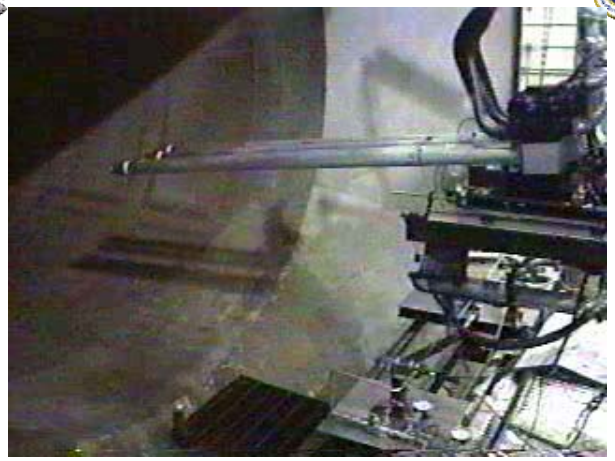

15

PDE-Piston Hybrid Results
(Tube 1 of 4)

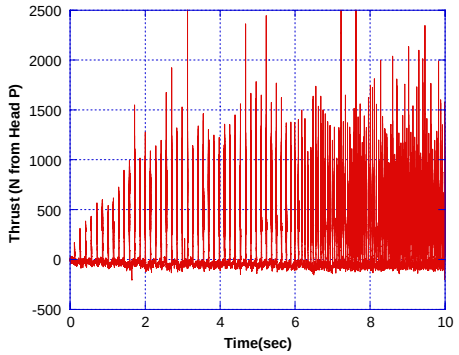

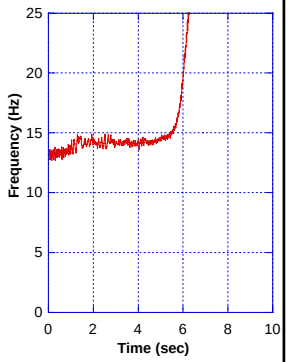

16

Summary and Conclusions

- Converging nozzle increases thrust
  - Blow down time doubled over straight round tube
  - Diverging nozzle desirable for higher operating frequencies
  - Increased thrust mechanism is being determined
- The interaction with three conventional systems has been evaluated
- Ejector pump successfully entrained secondary flow
  - Not all conditions entrain secondary flow
  - Thrust augmented 10-20%
  - A weighted noise level unaffected by ejector pump

Funded by: AFRL & AFOSR

Summary and Conclusions cont

- Self-aspiration has been achieved with a turbo-charger
  - No visible signs of wear on the turbine after 30K detonations
  - Experiments indicate that 20-25% of the thrust is traded for self-aspiration
  - 25 minutes of continuous self-aspiration achieved
- Hybrid Piston-PDE has been tested
  - Work can be extracted from PDE while still producing thrust
  - Self actuation achieved

(c)2002 American Institute of Aeronautics & Astronautics or Published with Permission of Author(s) and/or Author(s)' Sponsoring Organization.

A02-14344

AIAA 2002-0615
INTEGRATION OF A PULSED DETONATION ENGINE WITH AN EJECTOR PUMP AND WITH A TURBO-CHARGER AS METHODS TO SELF-ASPIRATE

John Hoke* Royce Bradley*, Jeff Stutrud and Fred Schauer
Air Force Research Laboratory, Propulsion Directorate
Wright-Patterson AFB, OH 45433
*Innovative Scientific Solutions, Inc.
Dayton, OH 45440

40th AIAA Aerospace Sciences Meeting & Exhibit
14-17 January 2002
Reno, NV

**For permission to copy or to republish, contact the copyright owner named on the first page.
For AIAA-held copyright, write to AIAA Permissions Department,
1801 Alexander Bell Drive, Suite 500, Reston, VA, 20191-4344.**

(c)2002 American Institute of Aeronautics & Astronautics or Published with Permission of Author(s) and/or Author(s)' Sponsoring Organization.

AIAA 2002-0615

INTEGRATION OF A PULSED DETONATION ENGINE WITH AN EJECTOR PUMP AND WITH A TURBO-CHARGER AS METHODS TO SELF-ASPIRATE

John Hoke and Royce Bradley

Innovative Scientific Solutions, Inc.

Dayton, OH 45440

Jeffrey Stutrud and Fred Schauer*

Air Force Research Laboratory, Propulsion Directorate

Wright-Patterson AFB, OH 45433

Abstract

Two methods, an ejector pump and a turbo-charger, are evaluated as a means to self-aspirate a Pulsed Detonation Engine (PDE). For the experiments pertaining to the ejector pump, a pulsed detonation engine is run on hydrogen and air at frequencies up to 40 Hz, equivalence ratios from 0.5 to 1.0, and fill fractions from 0.25 to 1.0. Flow visualization is used to determine the combination of fill fraction and equivalence ratio that successfully induced a secondary flow in the ejector pump. Pressure traces at the inlet and along the ejector pump are used to understand the performance of the ejector pump. The induced secondary flow is found to be approximately triple the primary detonation flow. Fill fraction and equivalence ratio are found to affect the performance of the ejector. High fill fractions and high equivalence ratios results in an oscillatory flow at the ejector inlet. Hydrogen and air are used as the fuel and oxidizer during the experiment with the turbo-charger also. Air flow and pressure at the exit of the compressor are used to evaluate the potential for self-aspirating the PDE. By running two detonation tubes simultaneously through the turbo-charger self-aspiration is achieved. The centrifugal style turbine and compressor of the turbo-charger showed no signs of discoloration or pitting after a 25 minute self-aspiration run where the detonation tube and turbo-charger attained thermal equilibrium. Throughout the course of the testing the turbine experienced 35K plus detonation events and reached a rotational operating speed of 80K rpm.

Introduction

Because of the simplicity and efficiency, research to develop a practical pulsed detonation engine (PDE) has persisted since the early 1940's[1]. The ability to detonate practical fuels, still remains as a technology hurdle; however, great strides have been made in the last decade[2-5]. Other technological hurdles include the ability to aspirate the PDE at subsonic speeds without significantly decreasing performance. Two methods to self-aspirate a PDE, an ejector pump and a turbo-charger, are investigated to determine the ability of these systems to survive and operate in the harsh supersonic environment of the PDE. Many studies have been conducted that show an increase in performance of an ejector in a pulsing environment; however, no published experimental studies were found that describe the operation of a ejector in the supersonic exhaust flow of a PDE[6-11]. No studies in the open literature describe the interaction of a turbine or a compressor operated in the high-temperature pulsing-supersonic flow of a PDE. In this study, both an ejector and a turbo-charger are experimentally evaluated as means to self-aspirate a PDE.

Experimental Apparatus

Two separate experiments were conducted; however, much of the experimental apparatus for the two experiments was identical. Both experiments were performed using the research PDE at the Air Force Research Labs (AFRL) at Wright-Patterson Air Force Base. The valves on a General Motors "Quad 4" automobile cylinder head were used to start and stop the

* Author to whom correspondence should be addressed: frederick.schauer@wpafb.af.mil, (937) 255-6462 Fax: (937) 656-4570

†This paper is declared a work of the U.S. Government and is not subject to copyright protection in the United States

(c)2002 American Institute of Aeronautics & Astronautics or Published with Permission of Author(s) and/or Author(s)' Sponsoring Organization.

fuel-air mixture and purge air flow into the detonation tube. The intake valves were used to fill the detonation tube with a hydrogen-air mixture and the exhaust valves were used to purge the detonation tube with air. The hydrogen and air was mixed upstream of the valves in the "intake" manifold, not in the detonation tube. The hydrogen-air mixture was ignited with a spark and a deflagration to detonation transition (DDT) process was used to achieve a detonation. Additional information concerning the AFRL research PDE is given by Schauer *et al.* [5]. The details that are specific to the ejector experiment and turbine-compressor experiment are described below.

Ejector experiment

Experiments on three ejector-detonator tube arrangements were conducted. In all the configurations, the ejector consisted of a 6″ (152 mm) diameter 36″ (914 mm) long pipe placed in line with the detonation tube. The detonation tube and ejector pipe overlapped for approximately 12″ (305 mm). In the first experiment, the detonator tube was 2″ (51 mm) in diameter and 36″ (914 mm) long, and the back end of the ejector was closed except for a 2″ (51 mm) diameter tube where the secondary airflow could be measured, see Fig. 1.

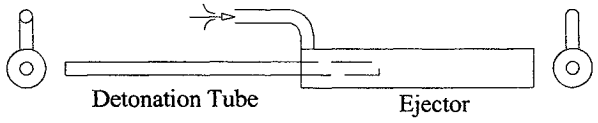

Figure 1. Schematic of 36" (914 mm) detonation tube and ejector for induced secondary flow measurement with ducted inlet

In the second experiment, the geometry was changed to increase the opening of the inlet of the ejector. The inlet of the ejector was open, except for the web that held the ejector in place, see Fig. 2. The geometry of the detonation tube in the second and third experiment was 2″ (51 mm) diameter and 72″ (1,829 mm) long.

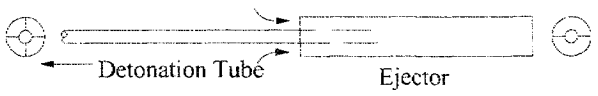

Figure 2. Schematic of 72" (1,829 mm) detonation tube and ejector with webbed ejector inlet

In the third experiment, the geometry was the same as the second experiment with the exception that a 5″ diameter disk was placed at the end of the detonator tube, see Fig. 3. This disk created a half-inch annular flow path for the induced secondary flow.

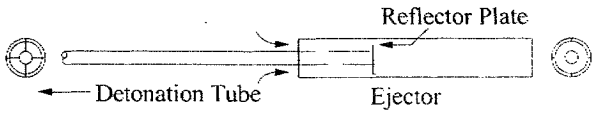

Figure 3. Schematic of 72" (1,829 mm) detonator tube and ejector with a 5" (127 mm) reflector plate

The induced airflow was measured with a "hot-wire" style velocity sensor. The output of this type of velocity sensor is not flow-direction sensitive. Flow visualization was used to determine if a secondary airflow was being induced or if exhaust products were flowing out of the intake of the ejector. Flow visualization was accomplished in two different ways for the two different styles of ejector inlets. For the ejector with the small inlet, a paper towel was wedged into the 2″ (51 mm) inlet prior to starting the engine. For the webbed-ejector-inlet, a weighted string was hung at the entrance of the ejector and observed during the experiment.

Turbine-compressor experiment

In this experiment, an automotive turbo-charger was attached to the detonation tube to examine whether a compressor and turbine could be used in the harsh pulsing flow of a pulse detonation engine. Two detonation tubes were connected and fired simultaneously. The purpose of using two detonation tubes in parallel was to increase the effective valve area. A 45 deg-lateral-pipe-fitting was used to split the exhaust flow. Part of the exhaust gas flowed through the turbine and part of the exhaust gas flowed through a nozzle, see Fig 4.

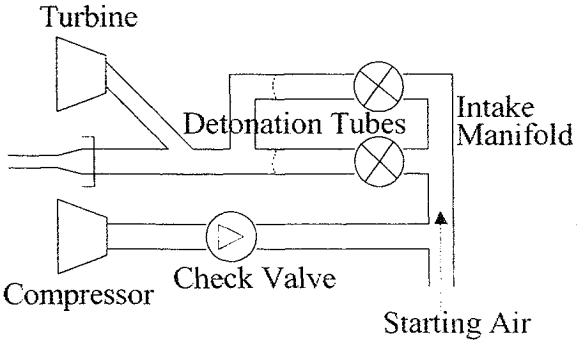

Figure 4. Schematic of turbine-compressor experiment

(c)2002 American Institute of Aeronautics & Astronautics or Published with Permission of Author(s) and/or Author(s)' Sponsoring Organization.

The inlet of the compressor was connected to a flow meter, while the exit of the compressor was connected to the inlet of the PDE. A check valve was used to prevent air from flowing backwards from the intake manifold of the PDE through the exit of the compressor, see Fig 4. In Fig. 5, a picture of the hardware is presented.

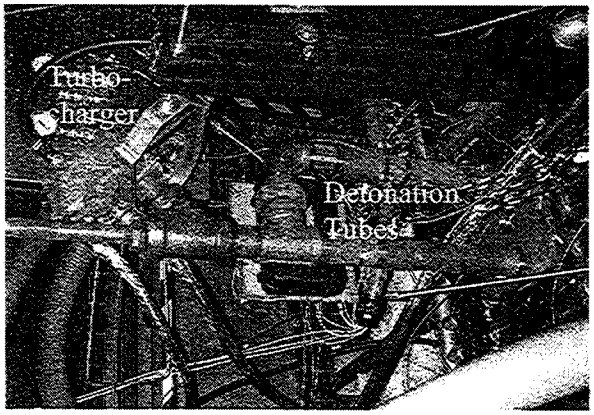

Figure 5. Photo of turbine/compressor experiment

Experimental Results and Discussion

Ejector results

The first experiments conducted on the ejector were used to determine the direction of flow at the ejector inlet. For the ducted inlet ejector, see Fig. 1, the flow direction was determined by placing a paper towel in the inlet. For some conditions, the flow at the inlet was bi-directional and at other conditions, a unidirectional secondary flow was induced. In Fig. 6 several images are presented of the successful induction of a secondary flow. In Fig. 6a, the ejector is shown with a paper towel wedged in the ducted inlet and a streamer extending several feet out of the inlet prior to the experiment. In Fig. 6b, the steamer is shown being pulled into the inlet of the ejector after the PDE began firing. In Fig. 6c, a large portion of the paper towel can be seen to have exited the ejector and when the exhaust gas from the next detonation exits the ejector, a diamond shaped expansion pattern can be seen as the paper towel had collected in the high-density region of the shock waves. Finally, in Fig. 6d, it is apparent that the entire steamer has been ingested and expelled by the ejector.

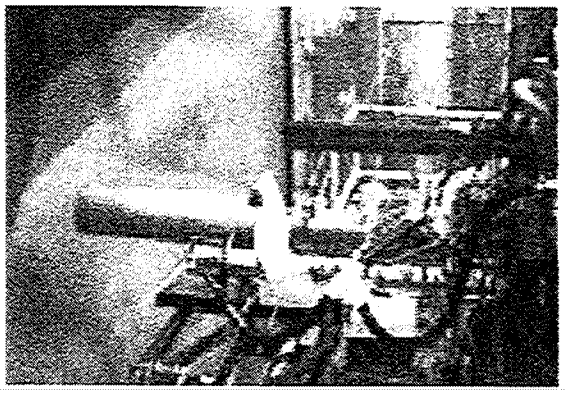

(a)

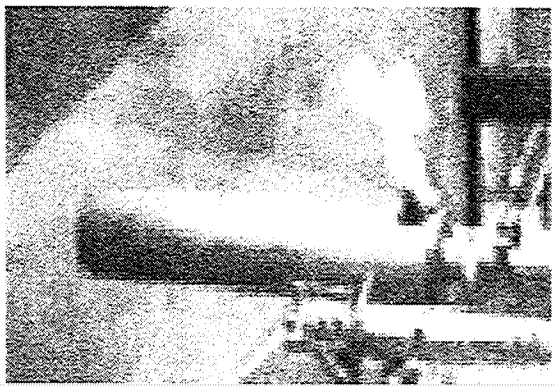

(b)

(c)

(c)2002 American Institute of Aeronautics & Astronautics or Published with Permission of Author(s) and/or Author(s)' Sponsoring Organization.

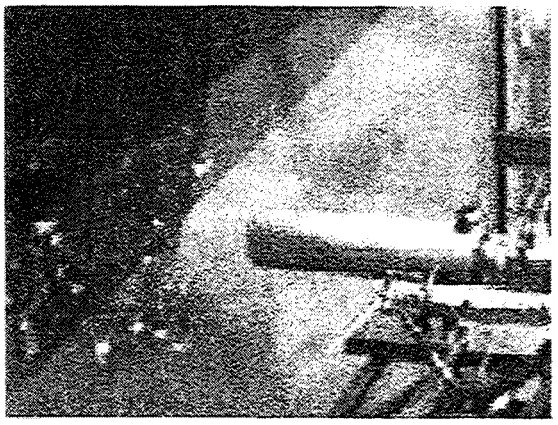

(d)

Figure 6. Flow visualization of secondary-air entrainment: (a) prior to firing the PDE, (b) the paper towel was steadily ingested, (c) diamond shock pattern visualized in exhaust, and (d) the entire paper towel and streamer was expelled out the end of the ejector

Not all conditions induced a secondary flow. In some experiments the paper towel would oscillate in the inlet of the ducted-inlet-ejector before being expelled out of the ejector inlet. The equivalence ratio and fill fraction (ff) were found to affect the induced flow. In Table 1, the conditions under which a secondary airflow was induced are given. At high fill fractions and high equivalence ratios, the flow at the inlet of the ejector was oscillatory, repeatedly flowing in and then out. The oscillatory flow was considered a failure.

Table 1. Conditions where a secondary flow was induced in the ejector and 36" detonation tube

	ff=1.0	ff=0.75	ff=0.5	ff=0.25
ϕ=1.0	Failure	Failure	Success	Success
ϕ=0.75	Failure	Failure	Success	Success
ϕ=0.5	Success	Success	Success	Success

In Figs. 7 and 8 are plotted the ejector wall pressure at four different locations along the ejector. Comparing the pressure traces at the inlet and 12″ (305 mm) downstream of the ejector inlet, it was apparent that in the case of failure to induce a secondary airflow, a shock wave propagated upstream in the ejector. In Fig. 7, the pressure at the inlet of the ejector was unaffected by the shock wave propagating from the end of the detonation tube.

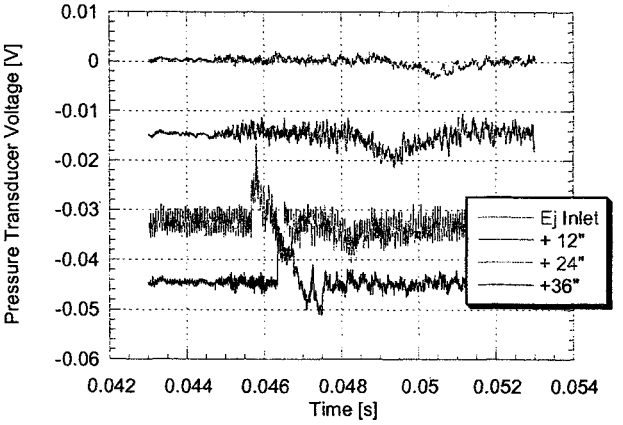

Figure 7. Ejector wall pressure: successful entrainment of secondary-air flow

The shock wave that propagated from the end of the detonation tube was evident in the pressure on the ejector wall at 24″ and 36″ (610 and 914 mm) from the ejector inlet. In Fig. 8, it was evident that the shock wave leaving the detonation tube traveled upstream in the ejector. Eventually the pressure at the ejector inlet decreases below the baseline. The shock wave followed by the suction at the inlet caused the oscillatory flow seen at the ejector inlet during some of the flow visualization experiments.

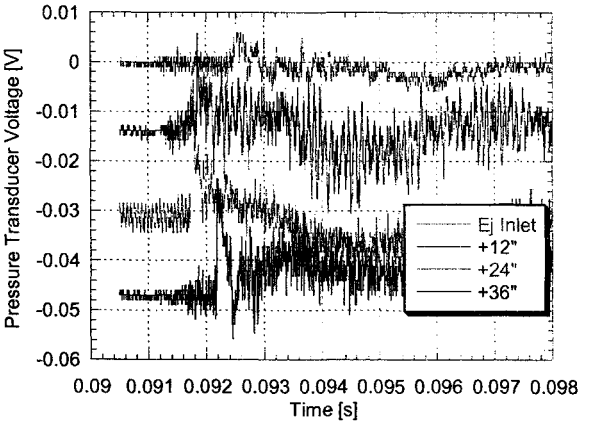

Figure 8. Ejector wall pressure: failure to entrain secondary-air flow

The induced airflow was measured as a function of fill fraction at two frequencies and an equivalence ratio of unity and presented in Fig. 9. Note that for fill fractions 0.75 and above, the flow at the injector inlet was oscillatory. At 20 Hz and a fill fraction of 0.5 the induced flow was approximately 3.4 times greater than the

(c)2002 American Institute of Aeronautics & Astronautics or Published with Permission of Author(s) and/or Author(s)' Sponsoring Organization.

primary airflow required by the PDE. At 40 Hz, and a fill fraction of 0.5 the induced airflow was approximately 3 times the primary airflow. For three of the four conditions tested at 40 Hz, the doubling of the frequency from 20 to 40 Hz resulted in an increase in the induced airflow of greater than 70%. For the case of a fill fraction of 0.75, the airflow increased by 50%.

The failure to induce a secondary flow at high fill fractions and high equivalence ratios was attributed to fuel burning or detonating at the exit of the detonation tube or inside the ejector. It was postulated that when the intake valve first opens, there was mixing between the fuel-air charge and the purge air. The mixing would decrease the equivalence ratio in this part of the charge and increase the volume of the air mixed with the fuel; thereby, over-filling the detonation tube. At low fill fractions this diluted charge was still in the detonation tube and a secondary flow was induced. At high fill fractions and low equivalence ratios, the equivalence ratio of the mixture at the exit or just outside the detonation tube may have been too low to detonate.

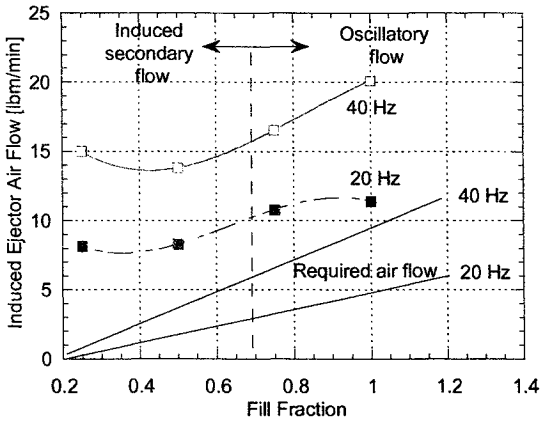

Figure 9. Induced secondary air flow, ϕ=1.0

In the last experiment conducted with the ejector a round disk was placed at the exit of the detonation tube and inside of the ejector, see Fig. 3. The purpose of the disk was to reflect the shock wave produced by the detonation at the exit of the detonation tube toward the exit of the ejector. In Table 2, flow visualization was used to determine if the ejector was inducing a secondary flow. With the reflector plate installed, the conditions of 0.75 fill fraction and an equivalence ratio of 0.75 was successful in inducing a secondary flow were previously, this condition created an oscillatory flow in the inlet of the ejector, cf. Table 1.

Table 2. Conditions where a secondary flow was induced in the ejector on a 72" (1,829 mm) detonation tube with reflector plate

	ff=1.0	ff=0.75	ff=0.5	Ff=0.25
ϕ=1.0	Failure	Failure	Success	Success
ϕ=0.75	Failure	Success	Success	Success
ϕ=0.5	Success	Success	Success	Success

Identical experiments were conducted on the 72" (1,829 mm) detonation tube and ejector without the reflector plate, see Fig. 2, and the results were identical to those shown in Table 1.

Turbine/compressor results

Several experiments were conducted with the turbo-charger connected to the detonation tube of the PDE. In Fig. 10, the conditions achieved with the compressor of the turbo-charger are plotted on a compressor map. The compressor operated at rotational speeds from 55K to 80K rpm. In most of the experiments, the PDE was run for 30 to 60 seconds; however, a 25-minute self-aspiration run was conducted.

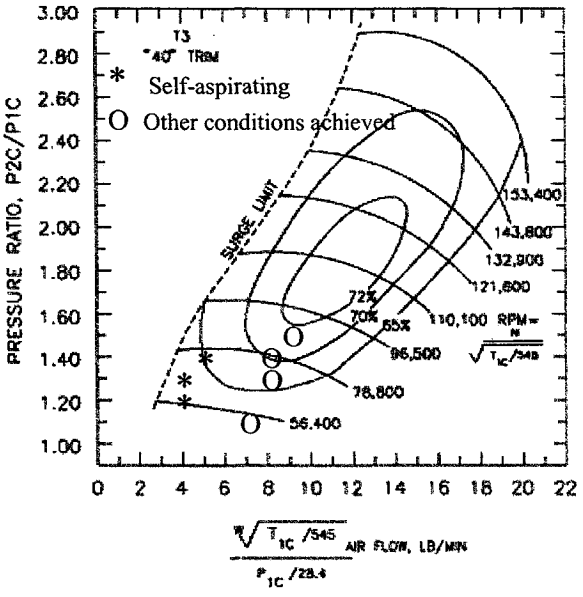

Figure 10. Compressor conditions achieved plotted on the compressor map (modified and reprinted from the website of Turbonetics Inc.)

In the self-aspiration experiment, the PDE was started using the facilities air supply system. After several

(c)2002 American Institute of Aeronautics & Astronautics or Published with Permission of Author(s) and/or Author(s)' Sponsoring Organization.

seconds of operation, the facility air flowing through the intake manifold was turned off, and the compressor on the turbo-charger was used to supply air. Purge air was still supplied by the facility compressors.

In Fig. 11, the airflow and thrust are plotted for this 25-minute self-aspirated run. The average measured airflow through the compressor driven by the turbine was very similar to the airflow rate used to start the engine. The fluctuations in the measured airflow rate through the turbine-driven-compressor were attributed to the oscillating check valve. The thrust of the PDE was reduced by approximately 20% while the PDE was self-aspirated via the turbo-charger

The temperature of the detonation tubes and turbine housing during this extended run were recorded and are presented in Fig. 12. The turbine housing temperature was significantly higher than the detonation tube wall temperature. The steady-state temperature of the detonation tube and turbine housing was reached in less than 500 seconds. A picture of the turbine after experiencing 35,000+ detonation cycles is presented in Fig 13. The turbine showed no signs of discoloration or pitting.

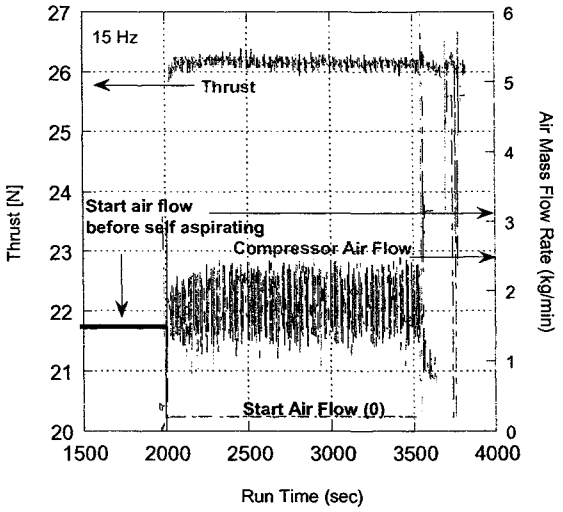

Figure 11. Airflow and thrust for a 25 minute self-aspirated run

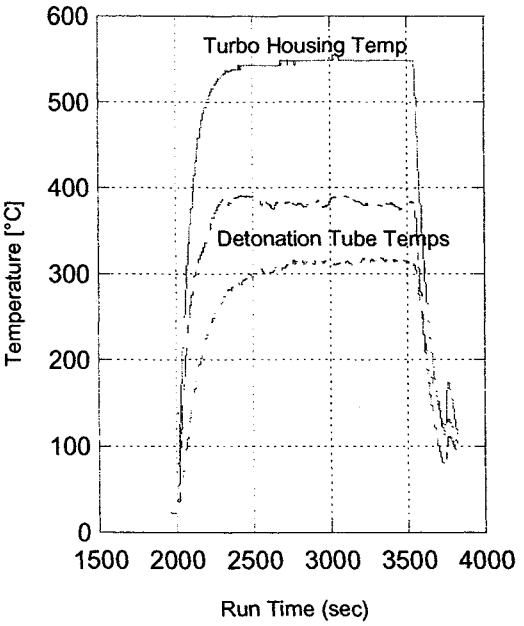

Figure 12. Detonation tube and turbine housing temperatures during the 25 minute self-aspirated run

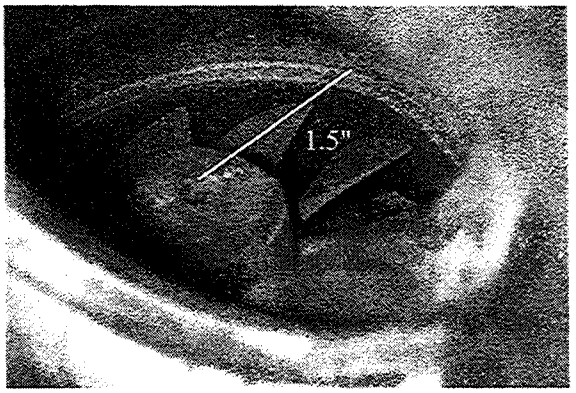

Figure 13. Turbine blades after over 35,000 detonation cycles

Summary and Conclusions

From these experiments, it has been shown that a PDE can be self-aspirated. The secondary flow can be induced in the supersonic-pulsing environment of a PDE. The fill fraction and equivalence ratio were found to be the primary variables affecting the success or failure of this ejector. The secondary induced flow was over 3 times the primary flow indicating that self-aspiration with an ejector pump was possible. Additional experiments

(c)2002 American Institute of Aeronautics & Astronautics or Published with Permission of Author(s) and/or Author(s)' Sponsoring Organization.

optimizing the ejector geometry and using the ejector to self-aspirate the PDE are planned

In the turbo-charger experiment, it was shown that a turbine and compressor survived and operated in the pulsing-shock-environment of a PDE. A 25-minute self-aspirated run was accomplished. Additional experiments with axial flow turbines and compressors are planned as well as experiments that use the turbine to increase the pressure in the detonation tube prior to detonation.

Acknowledgments

Appreciation is expressed to the technicians and facility personnel who made this work possible. We also would like to recognize the technical leadership of Dr. Mel Roquemore and Dr. Robert Hancock (AFRL/PRTS).

References

1. Proctor, P., "Pulse Detonation Technologies Advance". *Aviation Week and Space Technology*: p. 48(1998).

2. Brophy, C.M., D. Netzer, and D. Forster. "Detonation Studies of JP-10 with Oxygen and Air for Pulse Detonation Engine Development". in *34th Joint Propulsion Conference*. Cleveland: AIAA (1998).

3. Eckett, C.A., J.J. Quirk, and J. Shepherd, *The Role in Direct Initiation of Gaseous Detonations*. 2000.

4. Santoro, R.J. "PDE- Progress and Challenge". in *The 2001 Technical Meeting of the Eastern States Section of the Combustion Institute*. Hilton Head, SC (2001).

5. Schauer, F., J. Stutrud, and R. Bradley. "Detonation Initiation Studies and Performance Results for Pulsed Detonation Engine Applications". in *39th AIAA Aerospace Sciences Meeting and Exhibit*. Reno, NV (2001).

6. Collins, D.J., M.F. Platzer, J.C.S. Lai, and J.M. Simmons. "Experimental Investigation of Oscillating Subsonic Jets". in *Ejector Workshop for Aerospace Applications*. Dayton, OH (1982).

7. Irdmusa, J.Z. and C.A. Garris. "A Preliminary Study of Vortex Formation from Pulsed Jets". in *Ejector Workshop for Aerospace Applications*. Dayton, OH (1982).

8. Munipalli, R., V. Shankar, R. Wilson, H. Kim, F.K. Lu, and G.L. Liston. "Performance Assessment of Ejector Augmented Pulsed Detonation Rockets". in *AIAA*. (2001).

9. Parikh, P.G. and R.J. Moffat, "Resonant Entrainment of a Confined Pulsed Jet". *Journal of Fluids Engineering*. **104**: p. 482-488(1982).

10. Petrie, H.L., A.L. Addy, and J.C. Dutton, "Multiple Ducted Streams with a Periodic or a Steady Supersonic Driver Flow". *AIAA*. **23**(12): p. 1851-1852(1985).

11. Viets, H., M. Piatt, M. Ball, R. Bethke, and D. Bougine. "Unsteady Flows Applicable to Ejector Mechanics". in *Ejector Workshop for Aerospace Applications*. Dayton, OH (1982).

(c)2002 American Institute of Aeronautics & Astronautics or Published with Permission of Author(s) and/or Author(s)' Sponsoring Organization.

A02-13971

AIAA 2002-0474
EVALUATION OF A HYBRID-PISTON PULSED DETONATION ENGINE

Brian Frankey, Fred Schauer, Royce Bradley*, and John Hoke*
Air Force Research Laboratory, Propulsion Directorate
Wright-Patterson AFB, OH 45433
*Innovative Scientific Solutions, Inc.
Dayton, OH 45440

40th AIAA Aerospace Sciences Meeting & Exhibit
14-17 January 2002
Reno, NV

**For permission to copy or to republish, contact the copyright owner named on the first page.
For AIAA-held copyright, write to AIAA Permissions Department,
1801 Alexander Bell Drive, Suite 500, Reston, VA, 20191-4344.**

(c)2002 American Institute of Aeronautics & Astronautics or Published with Permission of Author(s) and/or Author(s)' Sponsoring Organization.

AIAA 2002-0474

EVALUATION OF A HYBRID PISTON-PULSED DETONATION ENGINE

Brian Frankey and Fred Schauer*

Air Force Research Laboratory, Propulsion Directorate

Wright-Patterson AFB, OH 45433

Royce Bradley and John Hoke

Innovative Scientific Solutions, Inc.

Dayton, OH 45440

Abstract

Experiments are conducted on a hybrid piston-pulsed detonation engine to evaluate the power extraction and system interaction issues. The hybrid engine is constructed using a four-cylinder motorcycle engine with a spacer block between the valves and pistons. Four detonation tubes, one for each cylinder, are placed perpendicular to the direction of the piston travel. A deflagration to detonation transition (DDT) is used to achieve detonations. The piston is in the deflagration region of the DDT. This hybrid engine has a critical starting frequency. Above this frequency the engine will self-actuate and produce excess power. Below this frequency, the power produced is less than that required to self-actuate and the engine decelerates after the starter motor is disengaged. The hybrid piston-pulsed-detonation-engine constructed for these experiments is capable of producing 20 hp and 50 lbf of thrust simultaneously.

Introduction

Over the past ten years, a resurgence of interest and research directed toward pulsed detonation engines (PDE's) has occurred[1]. Recent advances in computers and diagnostic tools have allowed researchers to overcome many of the technology hurdles hindering the construction of a practical PDE. Depending on the application, these obstacles include detonation initiation, valving, or flow control, aspiration, power extraction and others. Traditionally, the PDE has been viewed as a thrust-producing engine; however, for the PDE to work in an application like a commercial passenger jet, a second engine or power extraction from the PDE would be required to run sub-systems such as lights and air conditioning.

In this paper, a concept for extracting shaft-power from a pulsed detonation engine is described and the results of experiments conducted on the device are presented and analyzed.

Experimental Apparatus and Procedure

A hybrid piston-pulsed-detonation-engine (hybrid piston-PDE) was constructed by modifying a stock four-cylinder four-stroke motorcycle engine. A spacer block was placed between the "head" and "block" of the motorcycle to allow for the creation of four airflow passages for the four detonation tubes. The spacer block allowed one detonation tube, one for each cylinder, to be placed perpendicular to the travel of the piston. The 3-D CAD drawing of the spacer block is shown in Fig. 1a and a drawing of a cross section of the engine with the spacer block and detonation tube is given in Fig. 1b.

With the spacer block installed, the cam-chain and the oil supply and return lines to the "head" had to be extended. A picture of the assembled hybrid piston-PDE is shown in Fig 2. The spark and valve timing were altered from that of the stock engine. To maximize the power output of the hybrid engine the

* Author to whom correspondence should be addressed: frederick.schauer@wpafb.af.mil, (937) 255-6462 Fax: (937) 656-4570

†This paper is declared a work of the U.S. Government and is not subject to copyright protection in the United States

(c)2002 American Institute of Aeronautics & Astronautics or Published with Permission of Author(s) and/or Author(s)' Sponsoring Organization.

spark timing was adjusted so that the pressure from the detonation cycle occurred while the piston was traveling downward at its maximum velocity. The valve and spark timing relative to the piston position is depicted in Fig. 3.

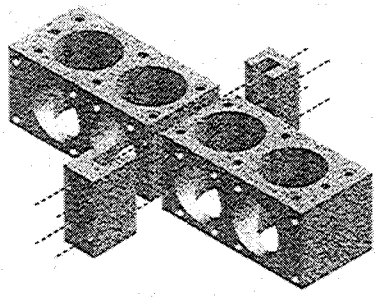

(a)

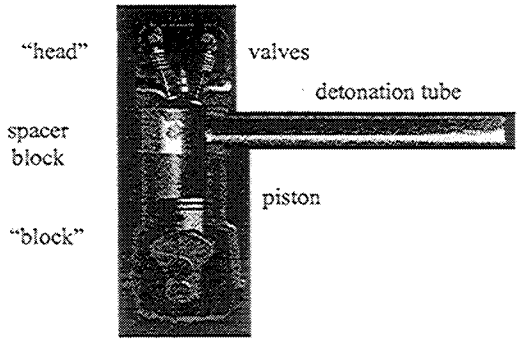

(b)

Figure 1. Spacer bock: a) 3D cad drawing and b) Drawing of a cross section of the assembled hybrid piston-PDE

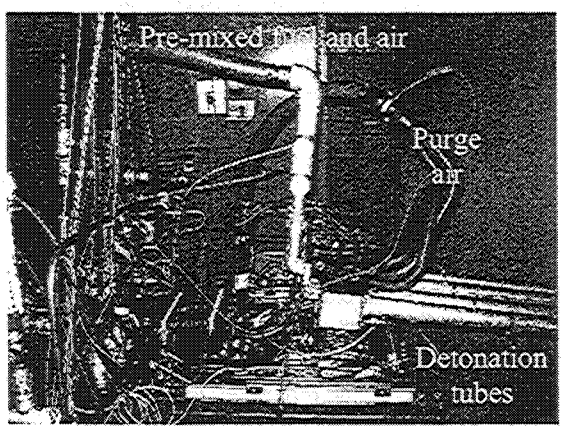

Figure 2. Picture of the hybrid piston-PDE

Starting at the top of the diagram in Fig. 3 and moving clockwise, the intake valve closed approximately 15 cam-degrees after the piston had reached top dead center (TDC). A stoichiometric mixture of hydrogen and air flowed through the intake valve when it was open. At approximately 30 cam-degrees, the spark plug was fired. The stock ignition system was used to initiate deflagration of the fuel air mixture. The timing of the spark was altered by adjusting the circumferential position of the Hall effect sensor around the crankshaft. A Shelkin shocking spiral was used to transition the deflagration to a detonation. For several milliseconds after the detonation wave exited the detonation tube, the pressure on the piston of the motorcycle was above atmospheric pressure. The spark timing was chosen to maximize the PdV work extracted by the piston.

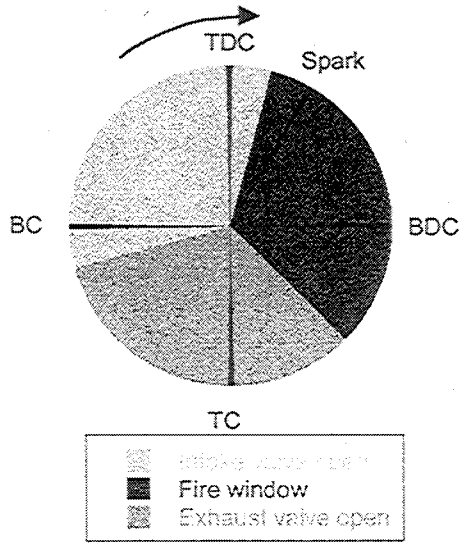

Figure 3. Valve and spark timing relative to piston position, note that the crankshaft makes two revolutions for every one that the camshaft makes. (TDC is top dead center, BDC is bottom dead center, TC is top center and BC is bottom center)

By the time the piston reached bottom dead center (BDC), the pressure on the piston had reached atmospheric pressure and the remainder of the possible "fire window" was not used. At approximately 135 cam degrees, the exhaust valve opened and purge air flowed into the cylinder and down the detonation tube to separate the hot exhaust products from the next air-fuel charge. Note that the motorcycle engine was a four-stroke, so the piston traveled up and down twice for each cycle of the camshaft. Since the exhaust products were not pushed out of the cylinder by the

(c)2002 American Institute of Aeronautics & Astronautics or Published with Permission of Author(s) and/or Author(s)' Sponsoring Organization.

piston, a two-stroke engine may have been better suited for this experiment. The intake valve opened at approximately 255 cam degrees after TDC and a pre-mixed charge of air and fuel filled the combustion chamber of the motorcycle and the detonation tube, repeating the cycle. Facility air compressors and controls were used to supply and regulate air and fuel flow to the hybrid piston-PDE. A good description of the facility is given by Schauer *et al.*[2]

A piston engine is often referred to as an air pump since the motion of the piston in concert with the valve train can be used to draw in fresh air and expel exhaust products. However in the hybrid piston-PDE, the piston cannot be used to pump air since the detonation tube and hence the cylinder was always open to the atmosphere, refer to Fig 1b.

As with almost any internal combustion engine, external power is supplied to "start" the engine. In this experiment, power to start the engine was supplied by a 20 hp variable speed electric motor. A chain was used to connect the electric motor to the output sprocket of the transmission. With the transmission in gear and the clutch engaged, power from the electric motor was transmitted to the crankshaft and from the crankshaft to the camshaft via the timing chain.

With the engine motored by the starter motor, the air and fuel flow rates were adjusted to match the detonation tube volume and engine frequency. A spark from the stock ignition system was used to ignite the fuel air mixture. Once the engine completed several cycles, the clutch was remotely disengaged—separating the "starting" electric motor from the hybrid piston-PDE. If the power extracted by the pistons was equal to the power required to rotate the crankshaft, camshaft and overcome the system friction, the rotational frequency of the hybrid piston-PDE would remain constant after the electric "starter" motor was disengaged. If excess power were produced, the rotational speed of the hybrid piston-PDE would increase. Conversely, the rotational speed of the hybrid piston-PDE would decelerate and quickly stop if the power produced was lower than the required power. As will be discussed in the "Analysis" section, a critical-starting-rotational speed must be obtained for this engine to produce enough power to self-actuate and continue to operate after the starter motor was disengaged.

Experimental Results

Experiments were conducted to determine if the hybrid piston-PDE would operate as anticipated and to determine the power and thrust produced by the engine. In Fig. 4, the instantaneous pressure at the head of the detonation tube is plotted verses time. From zero to three seconds, the fuel flow was gradually increased until the equivalence ratio was unity. The magnitude of the head pressure during this start-up time generally increased, see Fig. 4. At approximately 5.5 seconds, the clutch was disengaged separating the hybrid-piston PDE from the electric "starting" motor. In this particular configuration, the engine accelerated and the time between consecutive pressure spikes in Fig 4, decreased. From Fig, 4, it is evident from the magnitude of the pressure spikes that the fuel and air supply systems were being adjusted during the experiment to match the accelerating engine.

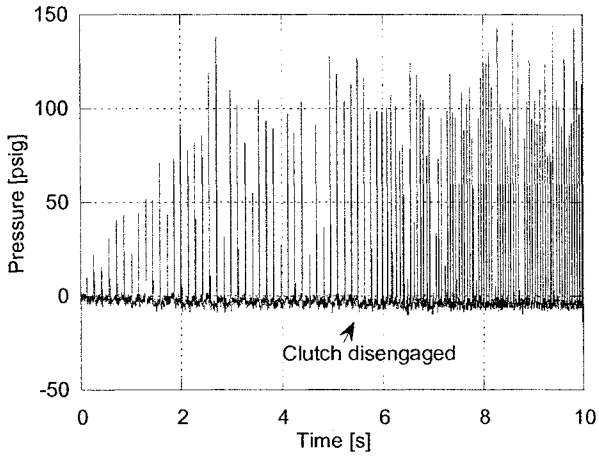

Figure 4. Instantaneous head pressure verses time: accelerating hybrid-piston-PDE

In Fig 5, the detonation frequency of a single tube is plotted versus time. In this experiment, the starting frequency was above the critical starting frequency. At approximately 3.5 seconds, the clutch was disengaged and the hybrid piston-PDE accelerated from a single tube detonation frequency of approximately 11 Hz to 21 Hz.

At 11 Hz, excess power was being produced which caused the rotational speed of the engine to accelerate. At 21 Hz, the hybrid engine reached a new equilibrium where the power required to actuate the

(c)2002 American Institute of Aeronautics & Astronautics or Published with Permission of Author(s) and/or Author(s)' Sponsoring Organization.

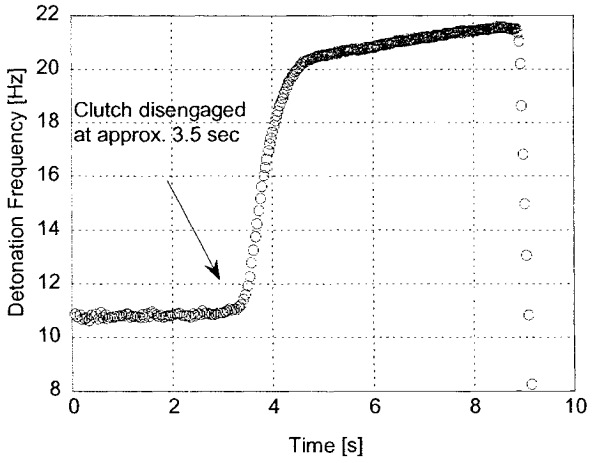

Figure 5. Detonation tube frequency verses time

engine was equal to the power produced by the engine. The air and fuel flow were set for operation at 11 Hz; therefore, at 21 Hz, the air and fuel flow were approximately half that required to completely fill the detonation tube prior to detonating. The control system for the air and fuel could not maintain ideal conditions with the rapid change in operating frequency of the hybrid engine. The experiment was automatically terminated at 9 seconds because the temperature of the detonation tubes exceeded a preset limit. In this experiment, the detonation tube consisted of a 72" long 2" diameter tube with a 1.84 to 1 bell reducer used as a converging nozzle.

At a starting frequency below the critical starting frequency for a 36" detonation tube without a nozzle, the engine did not self-actuate. In Fig. 6a, the frequency of the engine, normalized by the critical frequency determined experimentally, is plotted versus time. At approximately 1.7 seconds, the clutch was disengaged and the engine quickly decelerated. The power produced by this configuration is plotted in Fig. 6b. While the hybrid engine was being driven by the electric starter motor, the hybrid engine was producing approximately 8 hp—not enough to self-actuate at that starting frequency. The power produced was calculated by integrating the pressure in the cylinder head timed with the volume displaced by the piston movement.

The maximum power produced by this hybrid engine was approximately 20 hp while still producing 50 lbf of thrust. In Fig. 7a, the frequency of this run normalized by the critical frequency is plotted verses time. Notice that the engine was operating above the critical frequency. The power and thrust produced by

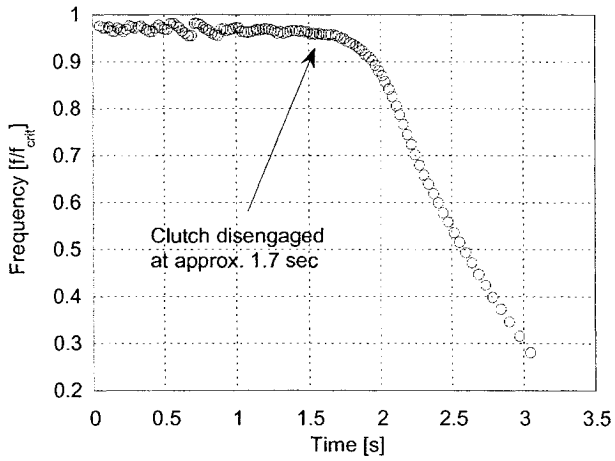

(a)

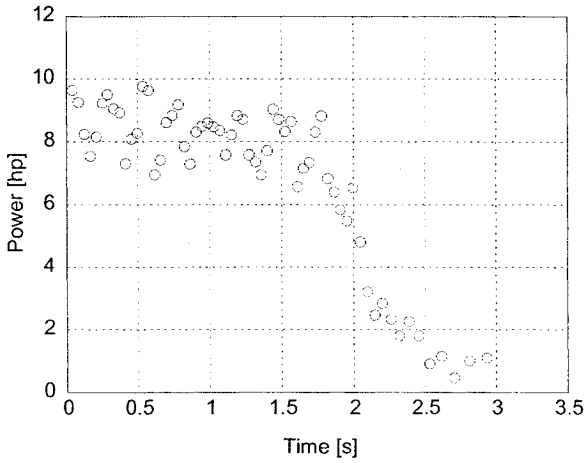

(b)

Figure 6. Below the critical starting frequency the hybrid piston-PDE failed to self-actuate, (a) normalized frequency verses time and (b) calculated power output during this experiment

this engine are plotted in Fig 7b and c respectively.

Analysis

As evident in the experimental results, there was a starting frequency, above which the hybrid piston-PDE would self-actuate and continue to operate after the electric "starter" motor was disengaged. Below this critical frequency the hybrid engine would quickly stop. The critical frequency for

(c)2002 American Institute of Aeronautics & Astronautics or Published with Permission of Author(s) and/or Author(s)' Sponsoring Organization.

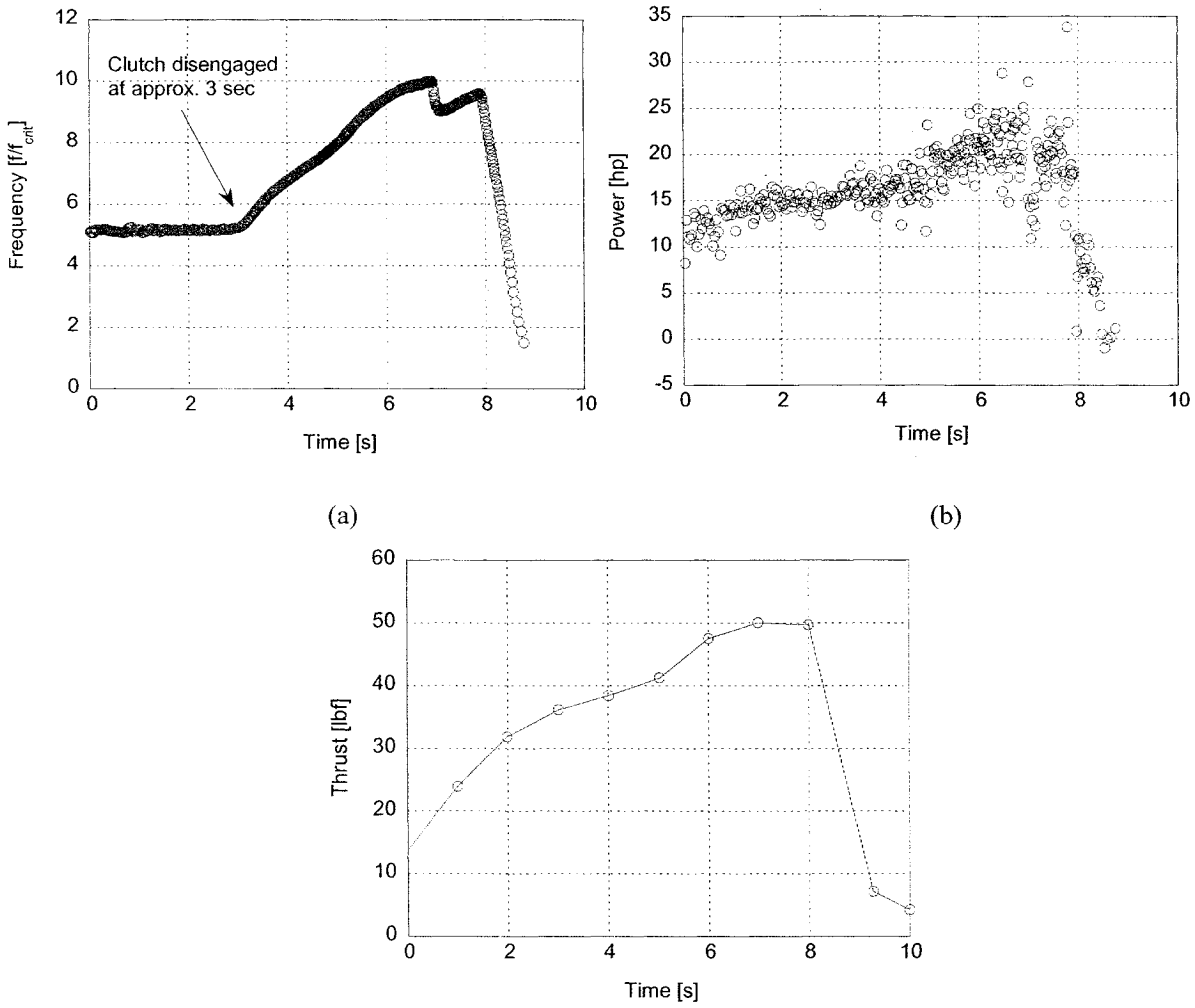

Figure 7. Above the critical starting frequency, the hybrid piston-PDE self actuated: (a) normalized frequency versus time showing self-actuation and acceleration of the hybrid engine, (b) calculated power output of the hybrid engine, and (c) thrust

this hybrid engine was a result of the different time constants for the piston movement and the detonation tube "blow down" event. The time constant for the piston engine is defined as

$$t_p = \frac{2}{f_{crank}} \qquad (1)$$

where f_{crank} is the frequency of the crankshaft. The time constant for the "blow down" event is the time required for the pressure in the detonation tube to decrease to 1/3 of the gage pressure behind the detonation wave.

The time constant of the blow-down event can be altered by changing the length of the detonation tube or installation of a nozzle on the end of the detonation tube. The time constant of the piston movement can be altered by changing the operating frequency of the engine.

For all of the conditions tested, the time constant of the detonation-tube-blow-down was smaller than that of the piston movement. If the difference between the magnitude of the time constants was too large, the blow down process would occur while the piston was effectively stationary; therefore little or no

(c)2002 American Institute of Aeronautics & Astronautics or Published with Permission of Author(s) and/or Author(s)' Sponsoring Organization.

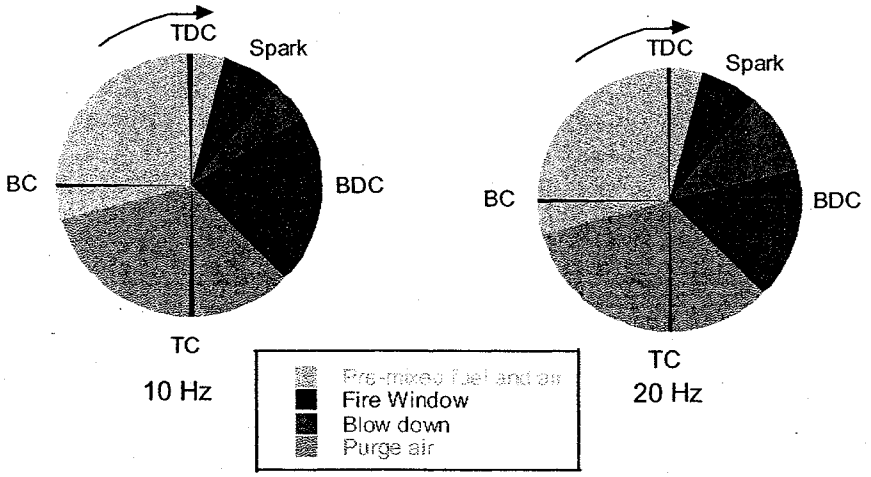

Figure 8 Engine timing and blow-down pressure during a cycle at two different frequencies

PdV work would be extracted from the detonation pressure. By increasing the starting frequency, and lengthening the detonation tube, the time constants of the piston movement and blow down process were similar enough that the power extracted by the piston exceeded the requirement to self-actuate. In Fig. 8, a diagram of the hybrid-engine-timing is given for two different operating frequencies. In these diagrams, the time constant for the piston travel is represented by 90 degrees of the circle from TDC to BDC. The time constant of the blow down process is represented by 18 degrees at 10 Hz and the 36 degree at 20 Hz. From these diagrams, it can be seen that at the higher frequencies, the blow down process occurs over a larger portion of the piston movement.

The critical frequency of the hybrid piston-PDE was calculated for each configuration by estimating the power required for self-actuation and equating that with the PdV work extracted as a function of frequency. The power required for self-actuation included the power required for the system friction and the power required to actuate the valves. Estimates for the power required were taken from Heywood[3]. Figure 9, shows the power required and the power produced plotted as a function of the frequency normalized by the critical frequency. The critical frequency for this particular configuration was calculated to be a detonation frequency of 5 Hz which was within a Hertz of the experimentally determined value. A better method for determining the parasitic system requirements would be to measure this power on a dynamometer.

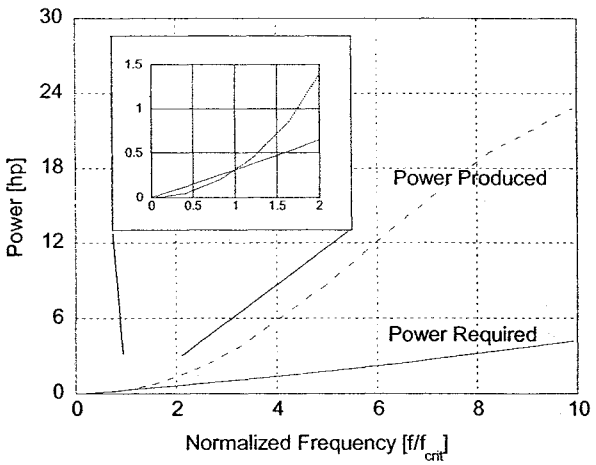

Figure 9. Hybrid piston-PDE critical frequency

In Fig. 10a the ideal T-s diagram for the hybrid piston-PDE is given and in Fig. 10b the ideal P-v diagram is given. The ideal thermodynamic piston-PDE cycle consists of a constant volume heat addition process (0-1) followed by an isentropic expansion process (1-2). This cycle is very similar to the Air-Standard Otto cycle except there is no isentropic compression of the working fluid before the constant volume heat addition. Of course the method for achieving constant volume combustion is significantly

(c)2002 American Institute of Aeronautics & Astronautics or Published with Permission of Author(s) and/or Author(s)' Sponsoring Organization.

different. This cycle would be impractical for constant pressure combustion. A general discussion of PDE cycle efficiency and the advantage of constant volume versus constant pressure combustion are given by Bussing and Pappas [4]. The ideal steady-cycle-thermal efficiency of the hybrid piston-PDE is given by Eq. (2).

$$\eta = 1 - \gamma \left[\frac{\left(\frac{T_1}{T_0}\right)^{\frac{1}{\gamma}} - 1}{\left(\frac{T_1}{T_0}\right) - 1} \right] \qquad (2)$$

Where γ is the ratio of specific heats and T is temperature.

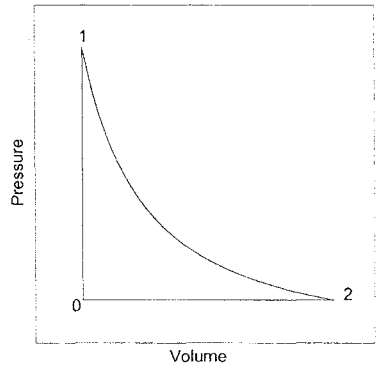

(a)

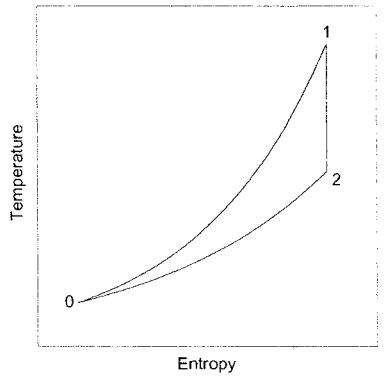

(b)

Figure 10. Ideal hybrid piston-PDE cycle: a) P-v diagram, b) T-s diagram

The measured thrust of the hybrid piston-PDE was lower compared to the conventional PDE[2]. The volume of the cylinder was approximately 10% of the detonation tube. Removing all of the work from the higher pressure gas prior to blow-down would ideally decrease the pressure in the detonation tube by 14.4%. However, experiments conducted on the hybrid piston-PDE showed that the thrust produced by the hybrid engine was approximately 1/2 that of the thrust on a PDE alone. A pressure trace for the two different engines is plotted in Fig. 11. The pressure of the shock wave traveling down the detonation tube was 2.6 times greater for the PDE alone. The blow-down pressure for the PDE was 20% higher than the blow-down pressure of the hybrid engine. In the hybrid piston-PDE the DDT was occurring as the piston was receding creating an expansion wave and hindering the DDT process. Additionally, there may have been some variability in the performance of the four detonation tubes on the hybrid-piston-PDE. These phenomena contribute to the difference in thrust between the two engines.

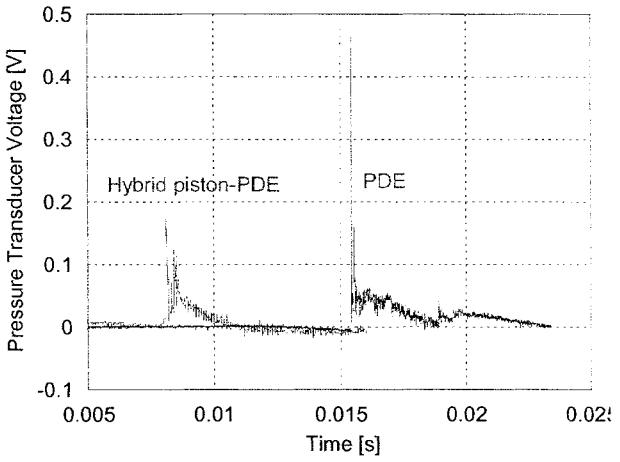

Figure 11. Pressure transducer voltage near the closed end of the detonation tube

No attempt was made to govern the frequency of the hybrid piston-PDE during these experiments. The rotational frequency of the hybrid piston-PDE could be governed in several ways. Reducing the fill fraction of the detonation tube is the most obvious. The equivalence ratio of the charge could also be used to govern the hybrid piston-PDE.

Perhaps one of the best ways to govern the hybrid engine is to alter the spark timing. There is an optimum-spark-timing, for extracting power from the detonation. By moving the spark off this optimum timing, less work is extracted from the detonation, which would control the rotational speed of the engine, and generate more thrust. Finally, the detonation tube

(c)2002 American Institute of Aeronautics & Astronautics or Published with Permission of Author(s) and/or Author(s)' Sponsoring Organization.

itself could be used to govern the rotational speed of the engine. Nozzle geometry and tube length affect the blow-down time, which affects the amount of work that is extracted by the pistons and also the thrust. Actively changing the geometry of the detonation tube while the engine is operating could be used to govern this hybrid engine.

Summary and Conclusions

A hybrid piston-pulse detonation engine was constructed. The device provided a means of extracting shaft power from a pulsed detonation engine while still providing significant thrust. The hybrid engine constructed was not optimized. It was a "proof-of-concept" engine. The performance of the hybrid piston-PDE can be improved by designing the piston engine specifically for this hybrid application. Additional experiments concerning power extraction, self-actuation and self-aspiration are planned.

Acknowledgements

Gratitude is expressed to the technicians who worked on this project: Walt Balster and Dwight Fox (ISSI). Some of the fabrication that was done was shear artwork. Thanks to Charley Smith (ISSI)for his consultations. The authors would also like to thank Jeff Stutrud (AFRL/PRTS) and Jason Parker (ISSI) for their computer programs used to collect and analyze the data, and Mike Bruggeman (AFRL/PROE)for his artistic drawing of the hybrid piston-PDE shown in Fig. 1b. The authors would also like to acknowledge the technical leadership of Dr. Mel Roquemore and Dr. Robert Hancock (AFRL/PRTS).

References

1. Santoro, R.J. "PDE- Progress and Challenge". in *The 2001 Technical Meeting of the Eastern States Section of the Combustion Institute*. Hilton Head, SC (2001).
2. Schauer, F., J. Stutrud, and R. Bradley. "Detonation Initiation Studies and Performance Results for Pulsed Detonation Engine Applications". in *39th AIAA Aerospace Sciences Meeting and Exhibit*. Reno, NV (2001).
3. Heywood, J.B., *Internal Combustion Engine Fundamentals*. 1988, New York: McGraw-Hill, Inc.
4. Bussing, T.R.A. and G. Pappas. "An Introduction to Pulse Detonation Engines". in *32nd Aerospace Sciences Meeting & Exhibit*. Reno: AIAA (1994).

(c)2002 American Institute of Aeronautics & Astronautics or Published with Permission of Author(s) and/or Author(s)' Sponsoring Organization.

A02-14342

AIAA 2002-0613
Effects of Exit Geometry on the Performance of a Pulse Detonation Engine

Daniel Allgood and Ephraim Gutmark
University of Cincinnati
Cincinnati, OH

Viswanath Katta
Innovative Scientific Solutions, Inc.
Dayton, OH

40th Aerospace Sciences Meetings and Exhibit
14-17 January 2002
Reno, Nevada

For permission to copy or to republish, contact the copyright owner named on the first page.
For AIAA-held copyright, write to AIAA Permissions Department,
1801 Alexander Bell Drive, Suite 500, Reston, VA, 20191-4344.

(c)2002 American Institute of Aeronautics & Astronautics or Published with Permission of Author(s) and/or Author(s)' Sponsoring Organization.

AIAA 2002-0613

EFFECTS OF EXIT GEOMETRY ON THE PERFORMANCE OF A PULSE DETONATION ENGINE

Daniel Allgood and Ephraim Gutmark
University of Cincinnati

Viswanath Katta
Innovative Scientific Solutions Inc.

Abstract

A preliminary analysis of a pulse detonation engine (PDE) driven ejector was performed. The thrust augmentation provided by a constant area cross-section ejector was computed. A range of partial-tube fill fractions and ejector diameters were simulated in this study. During the initial phase of this work, important issues associated with the imposed exit boundary conditions were addressed. Final analysis showed a rapid decrease in the PDE-ejector system performance as the ratio of the ejector to detonation tube diameter was increased. The thrust augmentation at the small ejector diameters was attributed to a compression wave that reflected off of the ejector wall and propagated back into the detonation tube. In addition, the sensitivity of the PDE-ejector system performance to the detonation tube fill fraction for all diameter ratios studied was seen to be similar to the case of the PDE without an ejector. Good agreement was observed between the simulations and available experimental data.

Introduction

Recent research on pulse detonation engines has revealed their potential as an efficient, low cost propulsion system. Conceptually, pulse detonation engines (PDE) offer few moving parts, high thrust to weight ratios, low cost, and ease of scaling. The fact that a PDE does not require a compression cycle eliminates the necessity for heavy and expensive compressor and turbine units. Due to the obvious potential advantages of the pulse detonation cycle, a PDE-based propulsion system is an attractive alternative to conventional propulsion systems. Potentially, the flight operating range of a PDE ranges from static conditions to hypersonic flight Mach numbers. As of today, there are no single-cycle propulsion systems available with such potential for a broad range of operability.

There have been many studies performed that have attempted to predict the performance characteristics of the PDE cycle. Kailasanath et al [1] found that the exit boundary condition specified in his computations can significantly impact the relaxation time required for the blow down process: the process in which the high-pressure post-detonation products inside the tube expand to the ambient pressure conditions. The sensitivity of the blow down process to the imposed boundary conditions can result in at least a 50% variation in the predicted performance values for the PDE due to the impact of the boundary condition on the relaxation length and time scales. It was concluded that the imposed exit boundary conditions are believed to be a major source of the performance controversy in the literature [1].

From an *experimental* view point, one method in which the effects of the pressure relaxation rate upon thrust can be studied, is by adjusting the percentage of the tube that is filled (fill fraction) with a detonable mixture as was done in the experimental work by Schauer et al [2] at the Air Force Research Laboratory (AFRL-WPAFB). Fill fraction is defined as the ratio of the tube volume that is initially filled with a fuel/air mixture to the overall tube volume. At fill fractions greater than 1.0, i.e. the detonable mixture over-fills the tube, no increase in performance was observed because the external detonation process has no thrust surface upon which to act. Conversely, if the tube is under-filled, essentially acting as a straight nozzle with either a purge cycle or previous cycle exhaust products filling the remainder of the tube, significant performance gains were observed. It is believed that "the unfilled portion of the tube acts

(c)2002 American Institute of Aeronautics & Astronautics or Published with Permission of Author(s) and/or Author(s)' Sponsoring Organization.

to increase the blow-down relaxation length and time scales" [2]. Alternatively, converging and/or diverging nozzles can be used to alter the blow-down process. Eidelman and Yang [3] have shown that various nozzle geometries dramatically affect the performance of the PDE.

In addition to exhaust nozzles, a conventional method of increasing thrust from an engine is by augmenting the engine with an ejector. The ejector is typically used to direct the entrainment of ambient air into the exhaust plume and promote the mixing of the hot combustion products with the relatively cooler ambient flow, whereby an increase in exhaust mass flow rate is obtained. Due to the increased exhaust mass flow, thrust augmentation can be achieved. Previous work by Bernardo and Gutmark [4] have shown the potential of using ejectors to entrain mass flow for steady-flow supersonic jets. The successful extension of this concept to pulse-detonation engine applications hinges upon rapid mixing between the primary (detonation) stream and the secondary (ambient) stream over a short distance. Due to the unsteady nature of the detonation, strong vortical structures (see Fig. 1) can develop which can aid in the mixing of the two streams thus providing additional thrust augmentation over steady-flow ejectors [5]. However, the benefits of pulsed vs. steady supersonic ejectors, as a function of frequency, is not known.

In addition to the viscous mixing generated by the ejector, an inviscid source of thrust augmentation may also be present due to the interaction of shock/expansion waves within the ejector and detonation tubes. The current study investigates the potential of using an ejector to favorably alter the blowdown process thereby increasing the thrust. However, due to the presence and interaction of complex shock and expansion waves, it is not clear what performance advantages, if any, will be provided by the ejector. The current work has attempted to address some of these issues.

In the present study, two-dimensional computational simulations were performed to develop a better understanding of the effects of a straight walled ejector on a PDE system's performance. The purpose of these simulations was to develop a fundamental understanding of the interaction of the unsteady compression/expansion wave dynamics within PDE-ejector providing the necessary guidance for optimizing the detonation tube blow-down process. The limitations and abilities of the code where seen by comparing the predicted performance values (thrust, Isp) to those measured in experiments performed at AFRL. Optimum geometrical configurations of the ejector relative to the single detonation tube dimensions and the effects of detonation tube fill fraction on thrust/Isp augmentation were investigated.

Description of Computational Simulations

The governing equations used in the present model are of the Euler type with exothermic chemical reactions. They can be expressed in the form presented in Figure 2. These equations are the conservation equations for mass, momentum, energy. The two progress variables depend on the q variables (ρ, ρu, ρv, e, $\rho\beta$, and $\rho\alpha$).

The gas mixture considered within this model is a stoichiometric hydrogen-oxygen fuel diluted with Ar/He by 70%. This mixture is known to generate a well-behaving detonation. The hydrogen-oxygen reactions are represented by the Korobeinikov model consisting of a two-step reaction mechanism; 1) a non-exothermic irreversible induction reaction where the progress variable (α) changes from 1 to 0, and 2) an exothermic reversible recombination reaction with its progress variable (β) changing from 1 to βeq. The rates of change of these variables are expressed in the Arrhenius form given in Figure 2. This two-step reaction model has been used in the past to address two-dimensional unsteady detonation problems [6-10]. The Chapman-Jouguet (C-J) Mach number of the premixed gas mixture considered is 4.8. A stationary grid system was used in the present work.

The numerical model for solving the governing equation uses an explicit 2nd-order MacCormack predictor-corrector technique with a 4th-order FCT (Flux Corrected Transport) scheme for capturing the shock waves accurately. Typically, the calculations are initiated from a

(c)2002 American Institute of Aeronautics & Astronautics or Published with Permission of Author(s) and/or Author(s)' Sponsoring Organization.

plain ZND detonation wave, from which a stable multi-dimensional detonation wave is generated by placing a few exothermic spots just upstream of the leading planar shock front. These exothermic spots perturb the plane C-J wave and develop transverse waves. Once the propagation of detonation becomes stable it is then subjected to different physical constrains, such as partial fill-fraction, sudden expansion, tube blockage, added cavities, etc. In this study, however, a small high pressure/temperature region near the head end of the tube was used to ignite the uniform mixture of combustible gases in the tube.

In previous work [11], the detonation code was proven to be successful in modeling the effects of spirals and cavities on the DDT process, as well as modeling the propagation of detonation waves through various tube geometries. Typical cellular detonation patterns predicted by the code are in good agreement with what has been observed experimentally through experimental soot-foil techniques.

Problem Description

The present work investigates a PDE driven ejector that has a constant cross-sectional area. Figure 3 is a schematic of the geometry that was used in the modeling. The flow properties at the inflow boundary (ejector inlet) were explicitly specified to be the freestream values, while the exit boundary conditions (ejector outlet) where obtained via a weighted extrapolation procedure. This configuration was chosen as a model for the ideal case of an "infinitely" long ejector. Future studies will address the effects of a finite-length ejector.

A detonation tube diameter (D_{tube}) of 2 inches was selected for the present computations in order to match the geometry used by the Air Force Research Laboratory (AFRL-WPAFB). At the end of this report, a comparison will be performed between some of the computational results and experimental data provided by AFRL and Innovative Scientific Solutions Inc. (ISSI). However, to accelerate the speed of the computations a shorter detonation tube length (L_{tube}=20 inches) compared to the experiments was used.

The ratio of ejector diameter to detonation tube diameter ($DR=D_{ejector}/D_{tube}$) was varied from 1.5 to 3.0 in most of the calculations, while the fill fraction ($ff=L_{tube_filled}/L_{tube}$) of the detonation tube, was varied from 0.25 to 1.0. All performance parameters were computed by intergrating over a fixed computational cycle time (T_{CYCLE}) of 100. This effectively set the operating frequency of the PDE. A constant baseline case (ff=1.0 and no ejector) was selected to normalize the thrust and Isp values.

Results

Effects of Imposed Exit Boundary Conditions

The ejector length ($L_{ejector}$) was found to be an important parameter since it dictated the effect of the exit boundary condition on the detonation tube head wall or thrust surface. A weighted extrapolation was used for the exit boundary condition ($P_i = 0.8*P_{i-1} + 0.2*P_{i-2}$). Since this type of boundary condition does not force the exit pressure to decay to the freestream value after some characteristic time, as in the case of some "characteristic" type boundary conditions, there is no free parameter to control the rate of relaxation in the case of subsonic exit flows.

Thus, in order to limit or remove the effects of the imposed boundary condition on the head wall (thrust), the exit boundary was systematically displaced farther away from the wall until it had no observable effect on the pressure trace during the selected PDE cycle time (T_{CYCLE}=100). This is in essence increasing the ratio of the ejector length ($L_{ejector}$) to the detonation tube length (L_{tube}), which was held constant (see Figure 3). Figure 4a shows the head wall pressure trace for $L_{ejector}/L_{tube}$ ratios ranging from 1.25 to 3.0 for a DR=1.5. This diameter ratio was seen to be the most influenced ("worst-case") by the boundary condition.

For small ejector lengths, the boundary condition produced weak reflections that propagated to the head wall of the tube. Increasing the $L_{ejector}/L_{tube}$ ratio to a value of 2 or greater produced no reflections during the detonation cycle. This translated into the thrust produced being independent of the boundary

(c)2002 American Institute of Aeronautics & Astronautics or Published with Permission of Author(s) and/or Author(s)' Sponsoring Organization.

condition as shown in Figure 4b. All the cases presented in this paper is for $L_{ejector}/L_{tube}$ = 2. Future work will investigate the feasibility of other types of boundary conditions in order to reduce the minimum computational grid size required to accurately model the PDE-ejector.

Effects of Fill-Fraction (ff)

The leading shock wave produced by a traveling detonation can be used to compress a noncombustible mixture. The resulting compressed flow will alter the blowdown process of the tube. Schauer et. al [2] have shown experimentally this can be accomplished by decreasing the amount of fuel/air mixture in the tube while maintaining the same detonation tube length. The additional tube volume behaves like a straight nozzle delaying the formation of the expansion wave at the exhaust that propagates back to the head wall. To validate our code and to observe how this partial fill effect behaved for the case of a PDE-ejector, fill fractions were varied from 0.375 to 1.0 for DR=1.5, 2.0, and 2.5. The pressure traces are shown in Figure 5, where the arrow in each figure represents the direction of increasing fill fraction (ff). As expected, the simulations showed that decreasing the fill fraction caused the blowdown process to occur sooner.

To quantify the effect of partial fill on performance parameters such as thrust and fuel-based Isp, the pressure at the head wall of the tube was integrated over its cross-sectional area and over the period of the cycle (T_{CYCLE}=100) and is given in Figure 6. The values are normalized by the baseline value as discussed in the previous section of this report. The thrust decreased with a decrease in fill fraction, but for the Isp, the fuel mass flow rate decreased more rapidly than the thrust creating an increase in Isp. In the case of DR=2.5, the Isp increased by 140% going from ff=1.0 to ff=0.25. The variation of Isp and thrust remained the same for all ejector diameters simulated.

Effects of the PDE-Ejector Diameter Ratio (DR)

Figure 6 showed that the thrust and Isp produced by the constant area PDE-ejector was a strong function of the fill fraction. However, there was not a very substantial effect of the diameter ratio (DR). To see the effect of DR more clearly, the fill fraction was held constant in the simulations at ff=1.0 and the DR was varied from 1.5 to 3.5. Figure 7 shows the thrust as a function of these ejector diameter ratios. At the smallest ratio (DR=1.5), a 14% increase in thrust was obtained over the baseline case. However, this thrust augmentation decreased rapidly as the ejector diameter ratio increased. Ejector diameter ratios above 2.25 showed no appreciable change in thrust over the baseline.

The head wall pressure traces for these cases, given in Figure 8, exhibited a pressure rise during the latter stages of the blowdown process. The timing of this pressure rise is seen to be a function of the diameter ratio and fill fraction, and thus could be due to a compression wave being reflected back into the tube by the collision of the leading shock wave of the detonation with the ejector wall and eventually impinging on the head wall of the detonation tube.

To support this argument, a series of pressure contour plots have been provided in Figures 9 (ff=1) and 10 (ff=0.375) for PDE-ejector diameter ratios of DR=1.5 and DR=2.5. For both fill fractions, the compression wave that reflects off of the small DR (1.5) ejector wall is more normal to the centerline of the PDE-ejector and will eventually propagate back into the detonation tube and impinge on the head wall. The larger DR ejector has an exiting detonation wave that was free to wrap around the detonation tube wall as in the case of the PDE without an ejector. Due to this effect and the fact that in this case the wave must travel along a longer path before impinging at the centerline of the PDE-ejector, the larger DR ejector did not generate as much augmentation. Also, the contour plots show that the DR=2.5 wave is much weaker and more oblique by the time it collides at the centerline of the PDE. This same process is observed in both the low and high fill fraction cases. Since these wave dynamics are governed by the geometry of the system, this might explain why the levels of thrust augmentation did not change as the fill fraction changed.

(c)2002 American Institute of Aeronautics & Astronautics or Published with Permission of Author(s) and/or Author(s)' Sponsoring Organization.

The pressure contours in Figures 9 and 10 also showed that the detonation wave exiting from the detonation tube created a spherical shock wave that propagated upstream to the entrance of the ejector. The strength of the backward propagating wave was a function of the ejector diameter and fill fraction of the detonation tube. Future studies will investigate how these parameters will affect the ability of an ejector to provide thrust augmentation through mass entrainment.

Comparison to AFRL/ISSI Experimental Data

Experimental tests were performed at AFRL/ISSI by Dr. Hoke [12] for a PDE-ejector configuration of DR=3.0 and various fill fractions. The simulations were performed for this DR at fill fractions ranging from 0.375 to 1.0. The predicted performance values were compared to the experimental data provided by AFRL/ISSI and plotted in Figure 11. Very good agreement was seen between the thrust and fuel-based Isp values in the experiments and simulations, giving further confidence in the accuracy of our code.

Conclusions

The preliminary analysis of a pulse detonation engine (PDE) augmented with a constant cross-sectional area ejector was presented. Important issues associated with the imposed exit boundary conditions were addressed and still require further analysis. However, good agreement was observed between the simulations and available experimental data for an ejector to detonation tube diameter ratio of 3.

The sensitivity of the performance of the PDE-ejector to changes in partial-tube fill fractions was seen to be the same as in the case of a PDE without an ejector. The final results also showed a rapid decrease in the PDE-ejector system performance as the ratio of the ejector to detonation tube diameter was increased. For the small ejector diameters, it was observed that the detonation wave reflected off of the ejector wall and propagated back into the tube during the blowdown process. This mechanism of thrust augmentation was seen to be independent of fill fraction for the ejector diameters simulated. However, the current work also showed that the detonation generated a compression wave that propagated around the tube and out the entrance of the ejector. This wave will alter the level of mass entrainment provided by the ejector. The strength and speed of this compression wave was seen to be a function of the ejector-to-tube diameter ratio and fill fraction.

Future work will investigate other issues that affect the performance of a PDE-ejector system such as finite length ejectors, direction ignition vs. deflagration-to-detonation transition (DDT), mass entrainment, and exit nozzles. Even though the viscosity does not play an appreciable role in the propagation of a detonation wave, it is necessary to accurately model the viscous effects for studying the mass entrainment of an ejector.

Acknowledgements

The authors would like to thank Dr. Hoke of ISSI and Dr. Schauer of AFRL at Wright-Patterson Air Force Base for the experimental data.

References

1. Kailasanath, K. "A Review of PDE Research – Performance Estimates," 39th AIAA Aerospace Sciences Meeting, AIAA 2001-0474.
2. Schauer, F., Stutrud, J., and Bradley, R., "Detonation Initiation Studies and Performance Results for Pulse Detonation Engine Applications," 39th AIAA Aerospace Sciences Meeting, AIAA 2001-1129.
3. Eidelman, S., Yang, X., "Analysis of the Pulse Detonation Engine Efficiency," 34th Joint Propulsion Conference, AIAA 98-3877.
4. Bernardo, A. and Gutmark, E., "Supersonic Rectangular Ejector", 30th AIAA Joint Propulsion Conference, Indianapolis, IN, June 1994.
5. Munipalli, R., Shankar, V., Wilson, D., Kim, H., Lu, F., and Liston, G., "Performance Assessment of Ejector Augmented PDRs," 39th AIAA Aerospace Sciences Meeting, AIAA 2001-0830.
6. Taki, S. and Fujiwara, T., "Numerical Analysis of Two-Dimensional Nonsteady Detonations," AIAA J. 16, 73 (1978).

(c)2002 American Institute of Aeronautics & Astronautics or Published with Permission of Author(s) and/or Author(s)' Sponsoring Organization.

7. Reddy, K. V., Fujiwara, T., and Lee, J. H., "Role of Transverse waves in a Detonation Wave--A Study Based on Propagation in a Porous Wall Chamber," Memoirs of the Faculty of Engineering, Nagoya University, Vol. 40, No. 1, 1988.
8. Oran, E. S., Young T. R., Boris J. P., Picone J. M., and Edwards, D. H., "A Study of Detonation Structure: The Formation of Unreacted Gas Pockets," Ninteenth Symposium (International) on Combustion, pg 573, The Combustion Institute, PA, 1982.
9. Erpenbeck, J. J., "Stability of Idealized One-Reaction Detonations," Physics of Fluids, 7, (1964).
10. Saint-Cloud, J. P., Guerraud, C., Brochet, C., and Manson, N., "Quelques Particulates des Detonations Tres Instables dans les Melanges Gazeux, Astronautica Acta., 17, 487 (1972).
11. V.R. Katta, L.P. Chin, and F.R. Schauer, "Numerical Studies on Cellular Detonation Wave Subjected to Sudden Expansion," Proceedings of the 17th International Colloquium on the Dynamics of Explosions and Reactive Systems. Heidelberg, Germany (1999).
12. Hoke, J. Personal Communication.

(c)2002 American Institute of Aeronautics & Astronautics or Published with Permission of Author(s) and/or Author(s)' Sponsoring Organization.

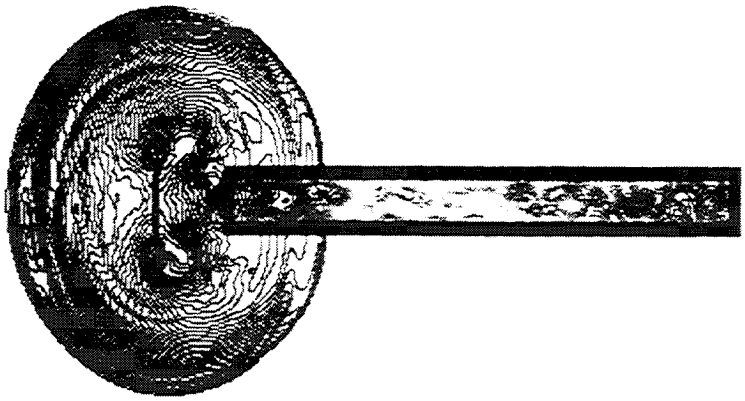

Figure 1: Exhaust Detonation Wave.

$$\frac{\partial q}{\partial t} + \frac{\partial E}{\partial x} + \frac{\partial F}{\partial y} + H = 0$$

$$q = \begin{pmatrix} \rho \\ \rho u \\ \rho v \\ e \\ \rho\beta \\ \rho\alpha \end{pmatrix}, \quad E = \begin{pmatrix} \rho u \\ \rho u^2 + p \\ \rho uv \\ (e+p)u \\ \rho u\beta \\ \rho u\alpha \end{pmatrix}, \quad F = \begin{pmatrix} \rho v \\ \rho uv \\ \rho v^2 + p \\ (e+p)v \\ \rho v\beta \\ \rho v\alpha \end{pmatrix}, \quad \text{and} \quad H = \begin{pmatrix} 0 \\ 0 \\ 0 \\ 0 \\ -\rho\dfrac{\partial\beta}{\partial t} \\ -\rho\dfrac{\partial\alpha}{\partial t} \end{pmatrix},$$

$$\frac{d\alpha}{dt} = -\frac{1}{\tau_{ind}} = -k_1\rho \exp\left(-E_1/RT\right)$$

$$\frac{d\beta}{dt} = \begin{cases} = 0, & \alpha > 0 \\ = -k_2 p^2 \left[\beta^2 \exp\left(\dfrac{E_2}{RT}\right) - (1-\beta)^2 \exp\left(-\dfrac{E_2+Q}{RT}\right)\right], & \alpha \le 0 \end{cases}$$

$$k_1 = 3.0\times10^{11} cm^3/g/s, \qquad k_2 = 1.5\times10^{-7} cm^4/dyn^2/s,$$
$$E_1/R = 9800K, \qquad E_2/R = 2000K, \qquad Q = 4.0\times10^{10} erg/g$$

Figure 2: Governing Equations and Detonation Model.

(c)2002 American Institute of Aeronautics & Astronautics or Published with Permission of Author(s) and/or Author(s)' Sponsoring Organization.

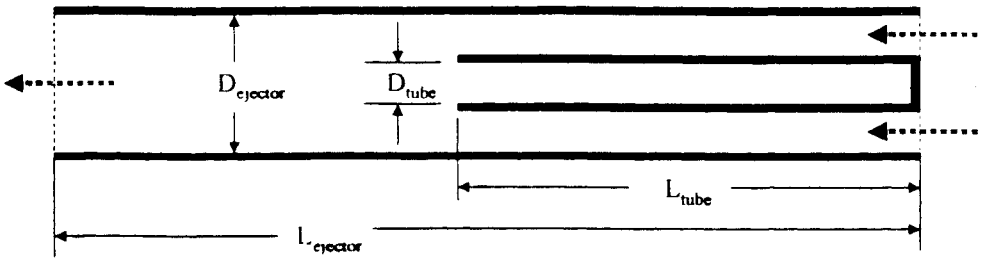

Figure 3: Pulse Detonation Engine Geometry.

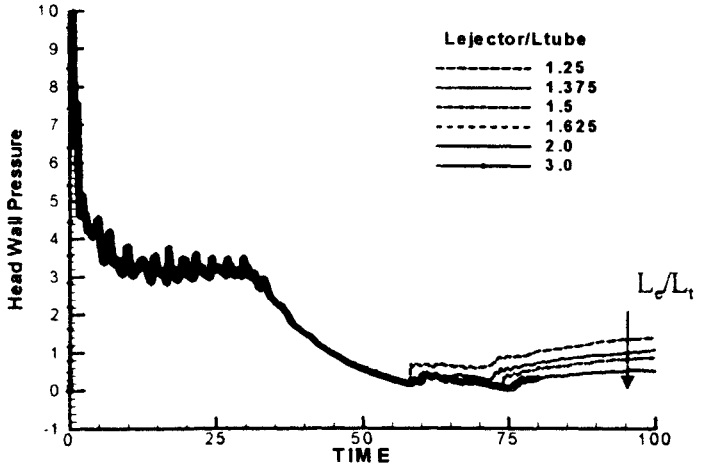

(a)

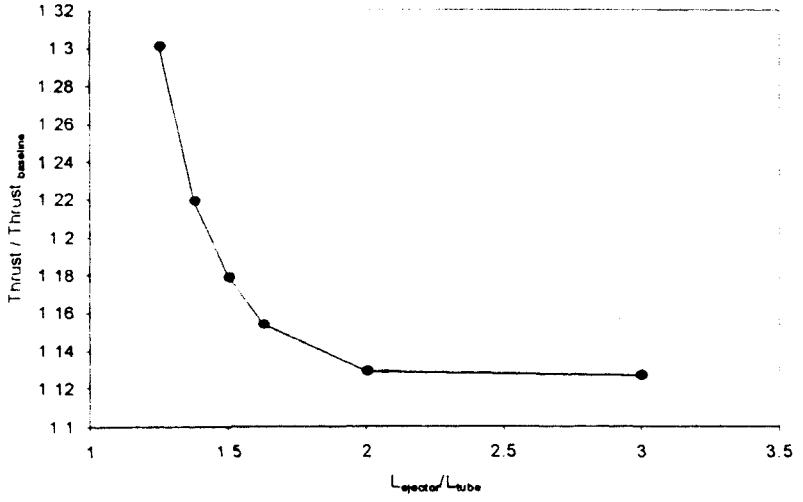

(b)

Figure 4: Effect of Exit Boundary Condition on
(a) head wall pressure trace and (b) normalized thrust. (DR=1.5)

(c)2002 American Institute of Aeronautics & Astronautics or Published with Permission of Author(s) and/or Author(s)' Sponsoring Organization.

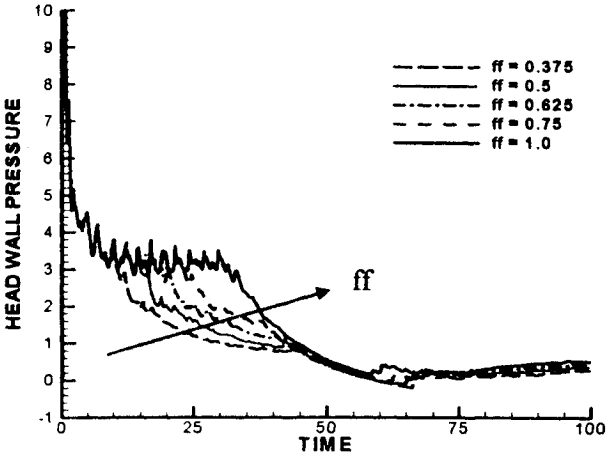

(a)

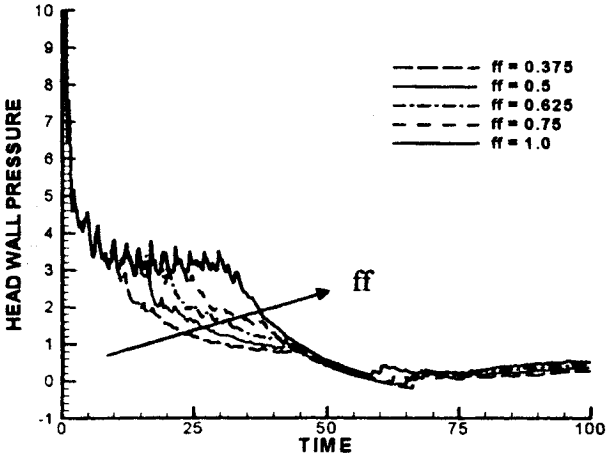

(b)

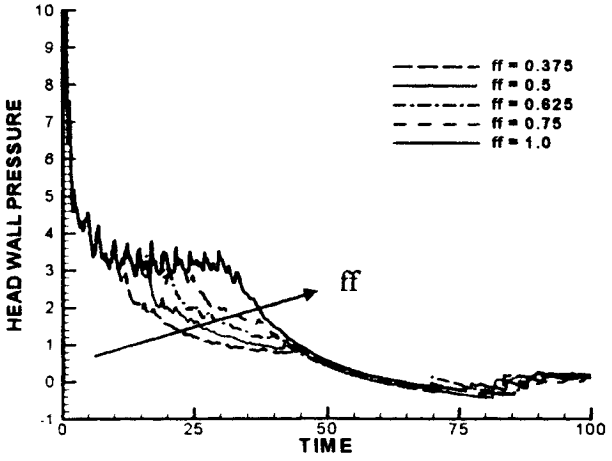

(c)

Figure 5: Partial Fill Effects (a) DR = 1.5, (b) DR = 2.0, (c) DR = 2.5.

(c)2002 American Institute of Aeronautics & Astronautics or Published with Permission of Author(s) and/or Author(s)' Sponsoring Organization.

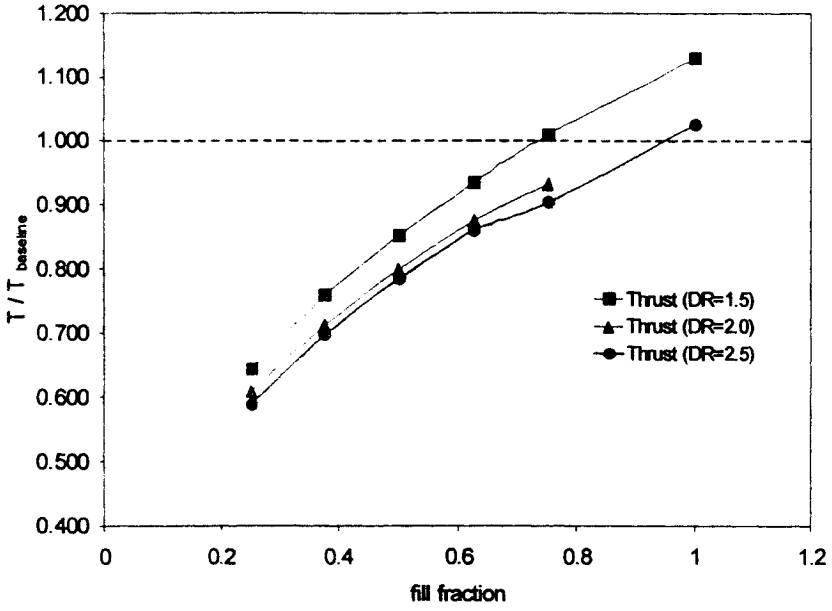

(a)

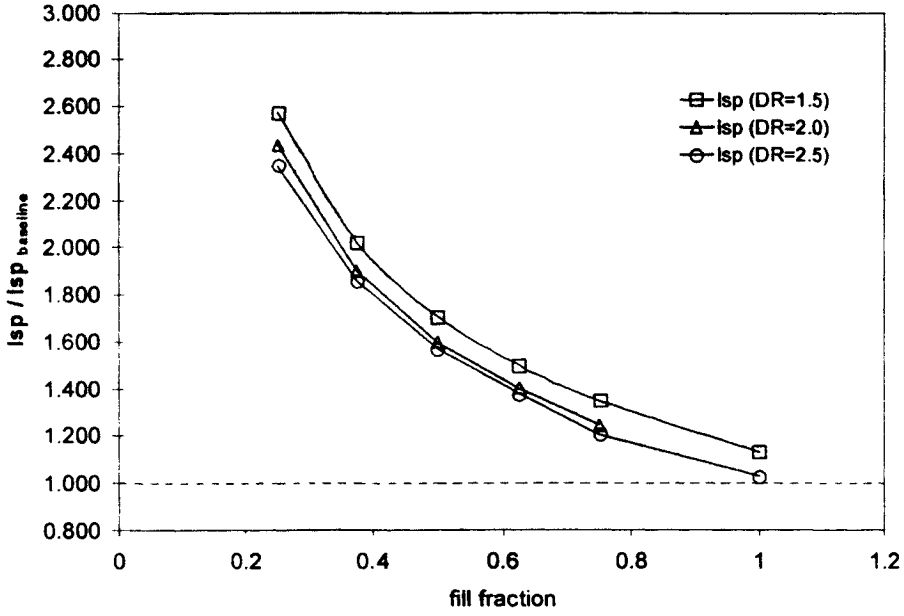

(b)

Figure 6: Partial Fill Effects on Normalized Thurst (a) and Isp (b).

(c)2002 American Institute of Aeronautics & Astronautics or Published with Permission of Author(s) and/or Author(s)' Sponsoring Organization.

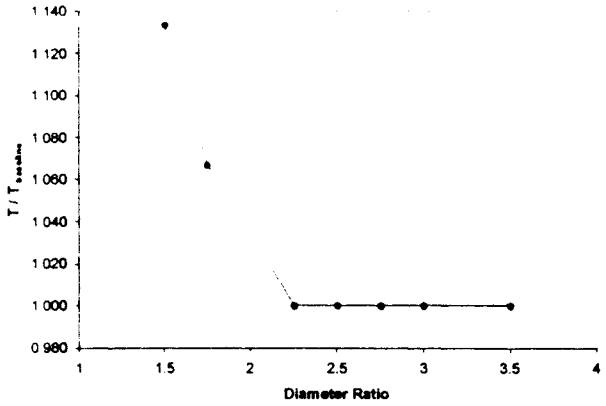

Figure 7: Normalized Thrust vs. Ejector Diameter Ratio (DR).

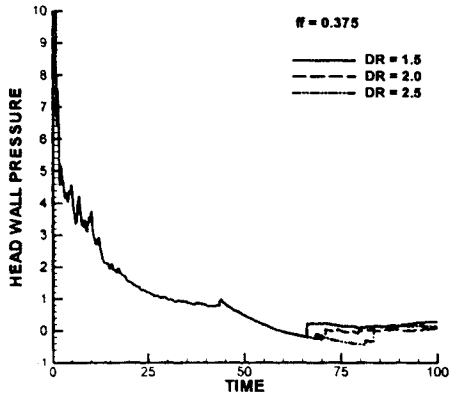

(a)

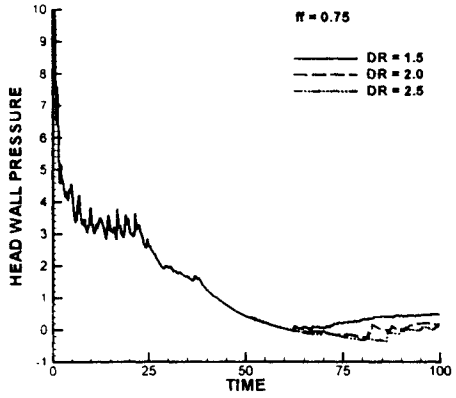

(b)

Figure 8: Effect of Ejector Diameter on Blow Down Process (a) ff=0.375, (b) ff=0.75.

(c)2002 American Institute of Aeronautics & Astronautics or Published with Permission of Author(s) and/or Author(s)' Sponsoring Organization.

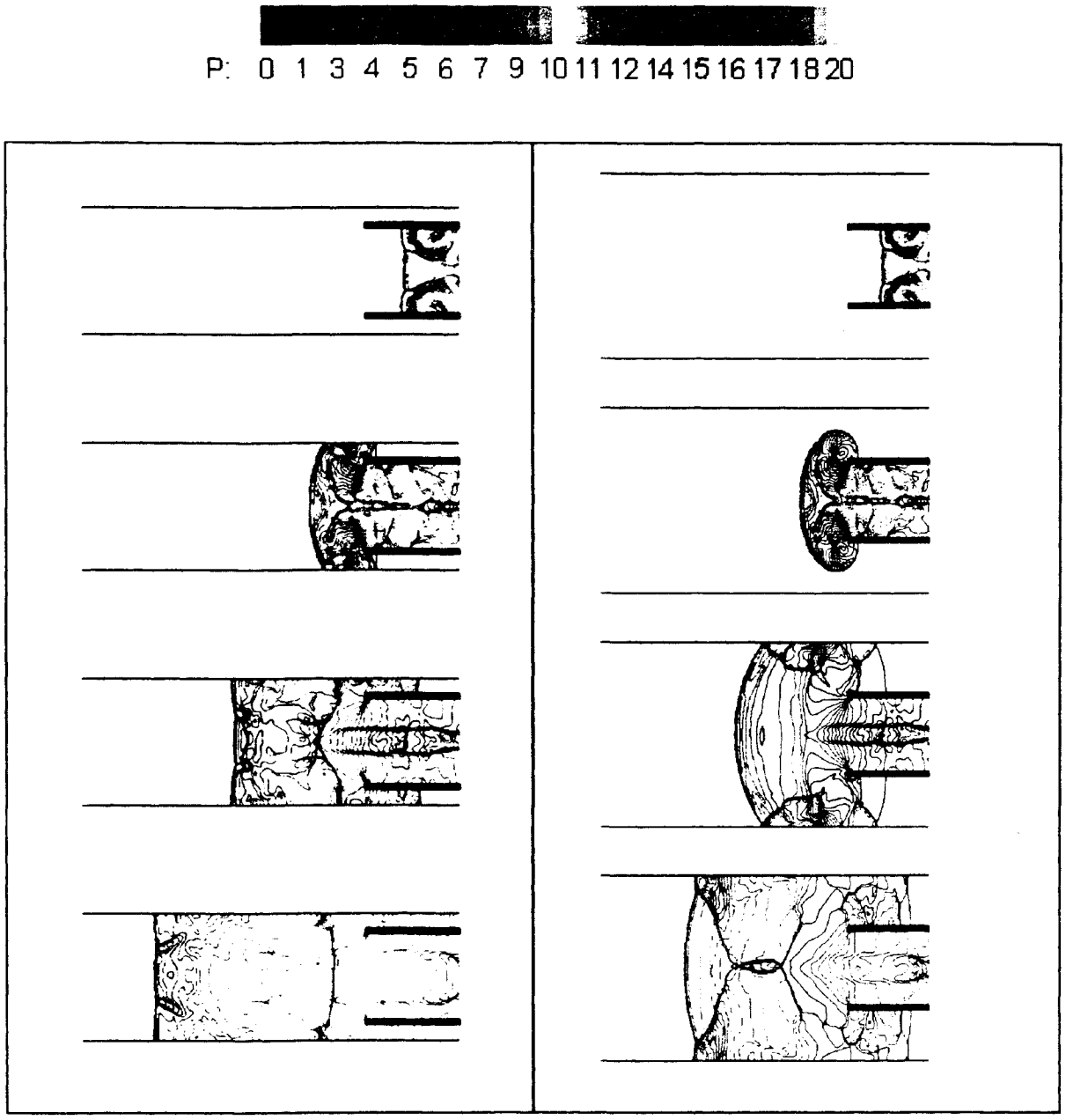

Figure 9: Pressure Contours for a Partial Fill Fraction of 1.0 and Ejector Diameter Ratios of (a) DR=1.5, (b) DR=2.5

(c)2002 American Institute of Aeronautics & Astronautics or Published with Permission of Author(s) and/or Author(s)' Sponsoring Organization.

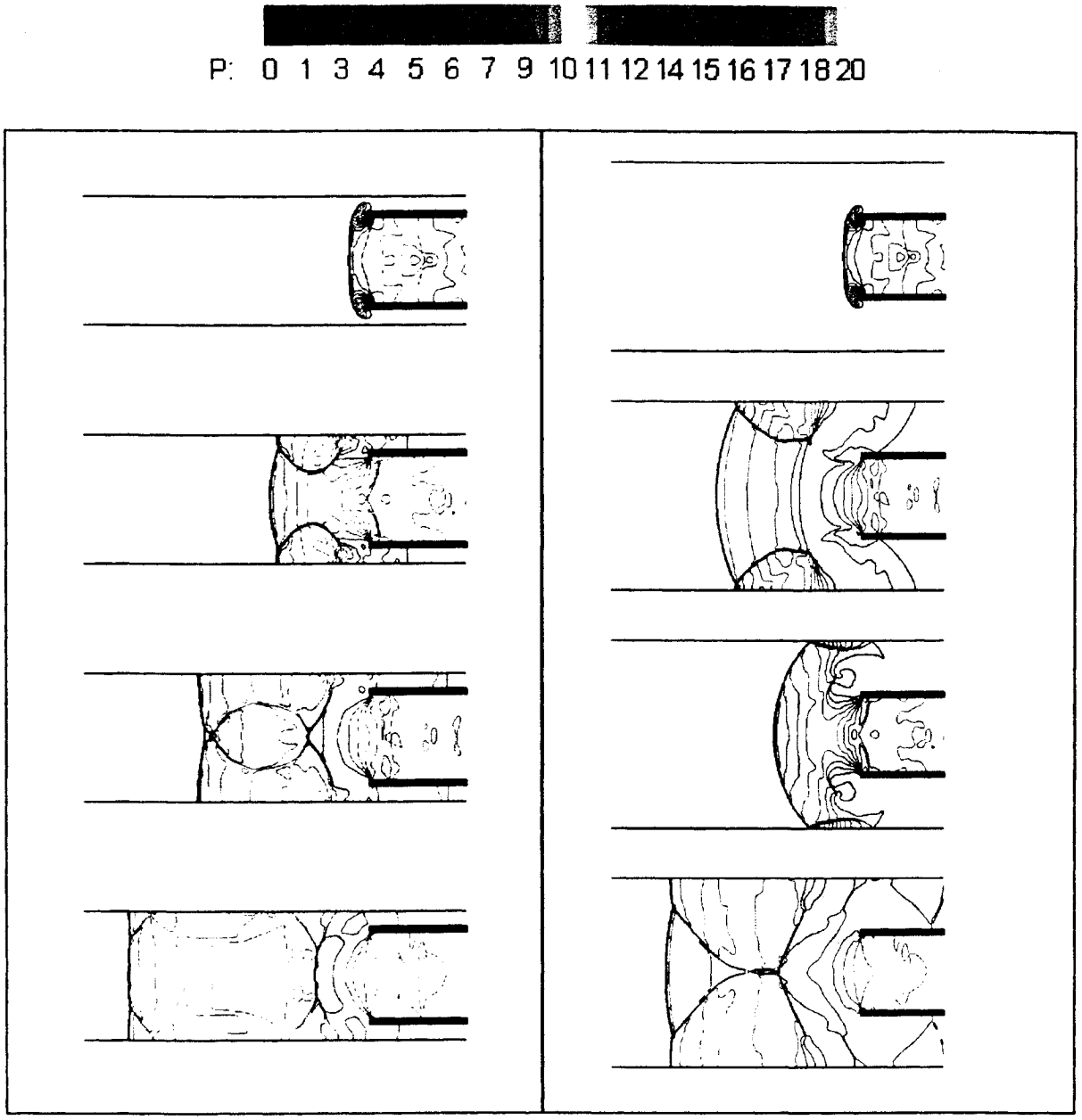

Figure 10: Pressure Contours for Partial Fill Fraction of 0.375 and Ejector Diameter Ratios of (a) DR=1.5, (b) DR=2.5.

(c)2002 American Institute of Aeronautics & Astronautics or Published with Permission of Author(s) and/or Author(s)' Sponsoring Organization.

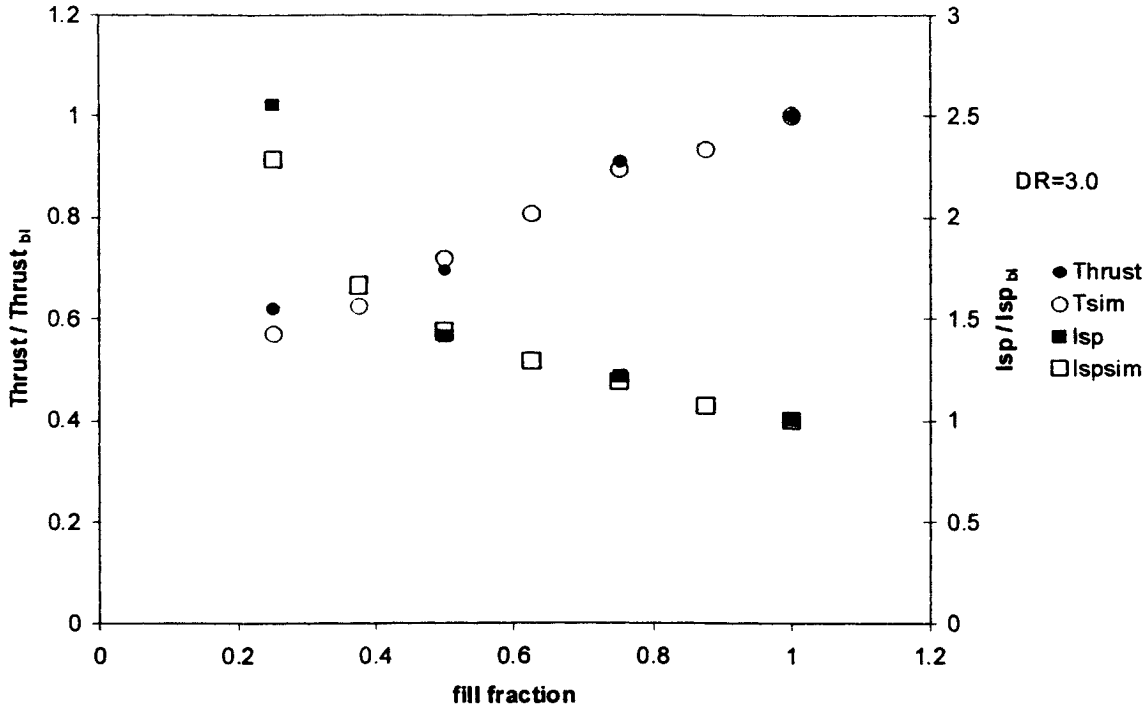

Figure 11: Predicted vs. Experimental Thrust and Isp Values for the AFRL PDE Ejector.

A Valve Pressure Drop Analysis of the PDE

5 March 2002

Matthew Slagel
ISSI
Dr. Fred Schauer
Research Engineers
Air Force Research Laboratory

In-House PDE Research

Matthew Slagel
Innovative Scientific Solutions Inc.
Beavercreek, OH
Dr. Fred Schauer
(937)255-1554
BLDG 490
1790 Loop Road North
Wright-Patterson AFB, OH 45433

Innovative Scientific Solutions Inc.
Beavercreek, OH

2

Introduction

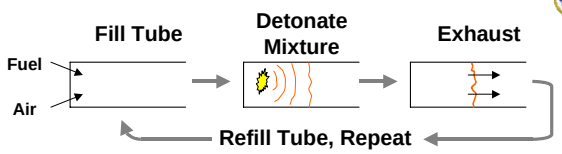

Goal: Develop air-breathing PDE's using practical fuels

Benefit: Cheap, simple, high performance engine that is highly scalable and efficient across a broad operating range (Mach 0-4+)

Issues

- Detonation Initiation
- Performance
- Proprietary Data

3

D-Bay: Pulsed Combustor/ Detonation Engine Facility

60,000 lbf Thrust Research Facility

Isolated and Protected

Formerly Mothballed, Full Scale Engine Research Facility

Capabilities

- Explosion Proof Facility
- Up to 60 klbf Static Thrust
- 1,000+ lbf Damped Thrust
- 6 lb/sec 100 psi air supply
- High Capacity Inlet/Exhaust Stacks
- Direct Connection to Liquid Fuel Farm
- Choked Flow Measurements
  - Air
  - Hydrogen
  - Propane
- Hardened Remote Control Room
- 16 High Frequency DAC Channels, up to 5Mhz
- 1Mhz Digital Imaging System

Damped Thrust Measurements
1,000+ pound capacity

Remote Control and High-Frequency DAC

4

Adapting OHC Cylinder Head to PDE

- Automotive Engines Designed for 8-20 Pressure Ratio
- Provisions for Valving, Fuel Injection, Timing, and Cooling
- Vapor Carburetor Available
- Bolt Flanged PDE Tubes to Cylinder Head
- Multiple Tubes/'Header' Effect
- Extra Valves for Predetonator or Purge Cycles
- Cheap/Mass Produced

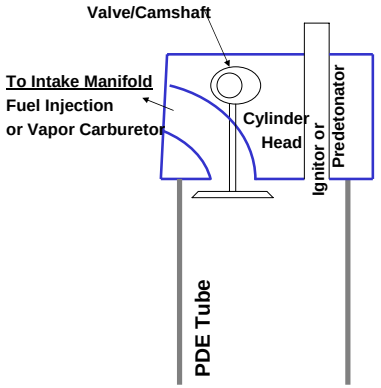

5

'Quad 4' PDE Valving and Air Systems

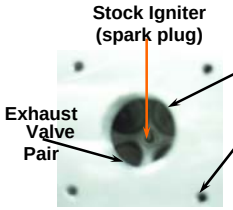

Adapter Plate with 4 Valves Per Cylinder

- Intake valves supply fuel/air
- Extra exhaust valves used for purge cycles, predetonator, or additional combustion air

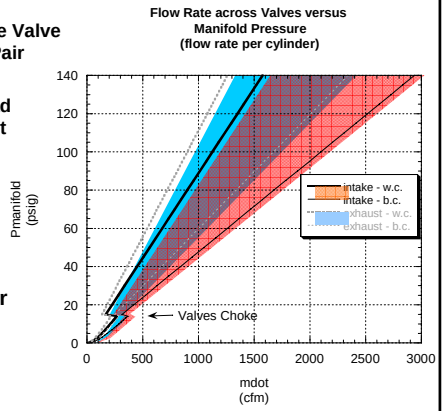

6

Pressure Experiment

Pressure Ratio found by calculating stagnation pressures at intake and tube

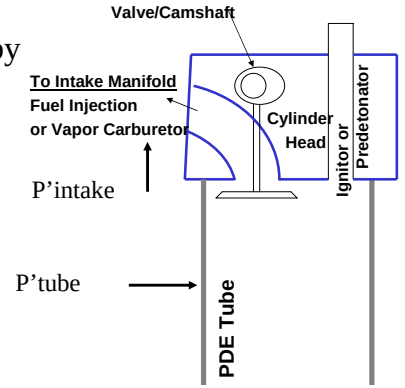

7

In-House Research 'Quad- 4' PDE

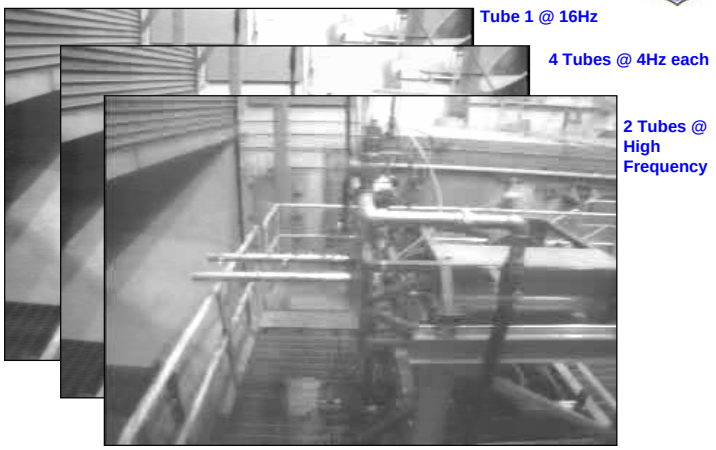

Thrust

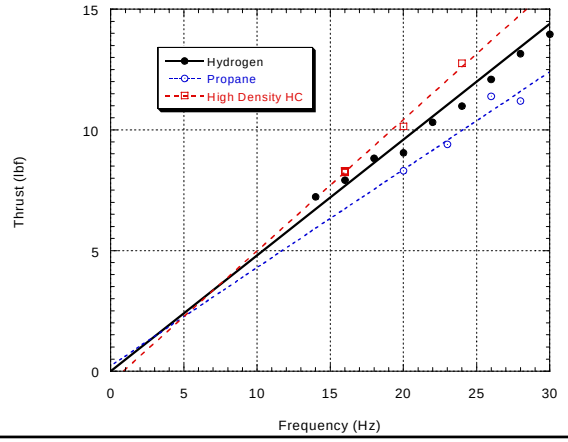

9

SCFM

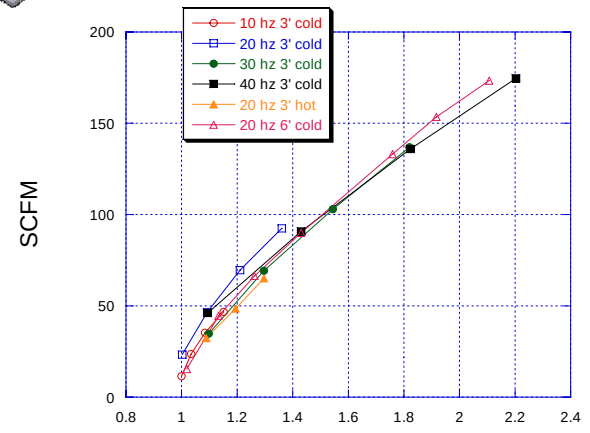

10

Mach Fill Number

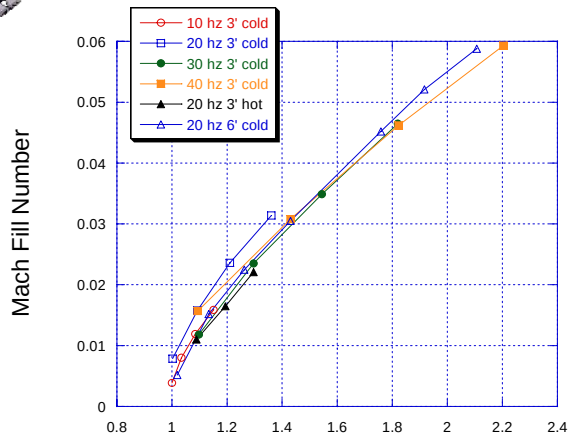

11

Effect of Tube Diameter

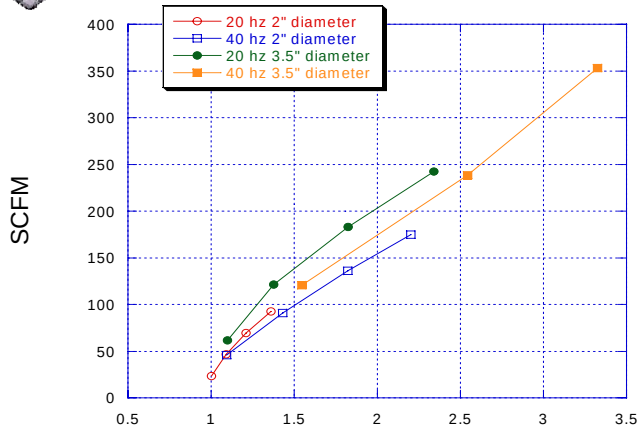

12

Effect of Tube Length

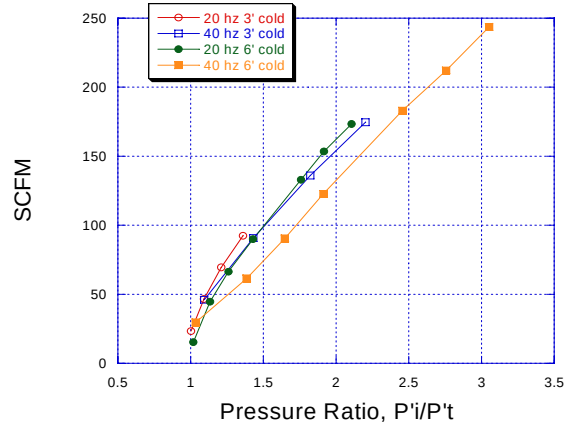

13

Tube vs. No Tube

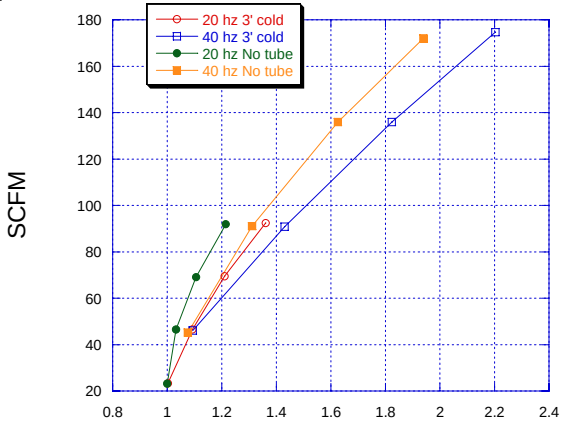

14

HOT vs. Cold

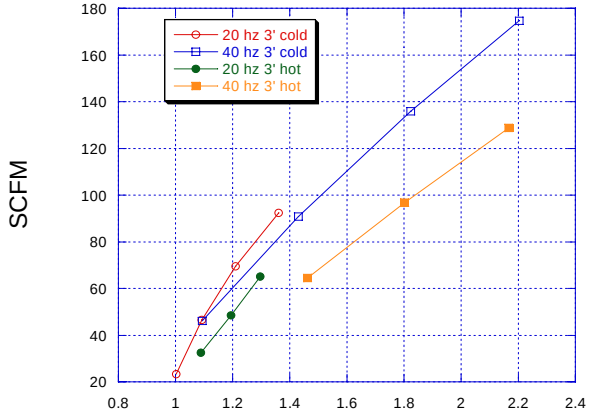

15

With Correction

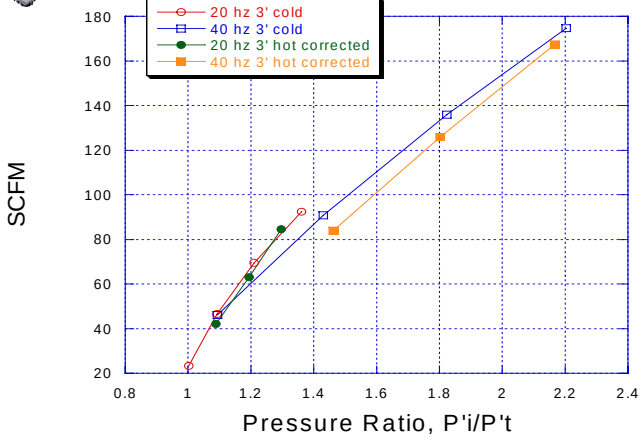

16

Summary

- Research engine using non-ideal valves
- Drop does not include Intake Manifold, Tube, Tube
- Effect of tube geometry , frequency, and fueling
- Similar trends are expected for realistic valve configurations
- Acknowledgements

Dr. John Hoke
Royce Bradley
Jeffrey Stutrud

17

Evaluation of a Hybrid Piston-Pulsed Detonation Engine

Brian Frankey
Dr. Fred Schauer
Air Force Research Laboratory
Dr. John Hoke
Royce Bradley
Innovative Scientific Solutions, Inc.

Outline

Pulse Detonation Engine Background

- PDE Cycle
- Detonation

Hybrid Piston Pulse Detonation Engine (HPPDE)

- Concept and Motivation
- Mechanical System
- Test Results

2

PDE Background

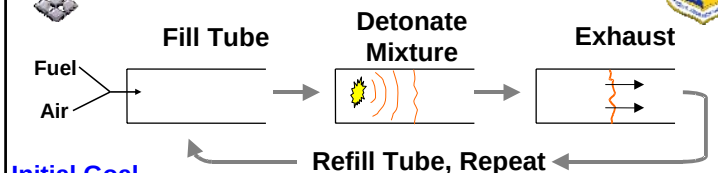

Initial Goal

- Develop air-breathing PDE's using practical fuels

Benefits

- Cheap, simple, high performance engine that is highly scalable and efficient across a broad operating range (Mach 0-4+)

Previous Achievements

- Detonation Initiation
- Thrust

3

Detonation

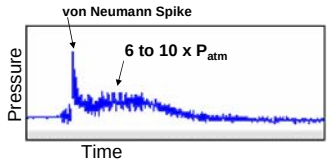

Detonation is critical to PDE success

- Detonation wave travels faster than sound
- Detonation creates pressure rise of unconfined gas
- 6-10 times initial pressure

4

First Generation PDE

THRUST

5

In-House PDE Research Engine

GM Quad 4 DOHC, 4 Cylinder Pulsed Detonation Engine

Current Quad-4 PDE

- Facility air compressors provide air mass flow
- Valves actuated by external 20 hp DC motor

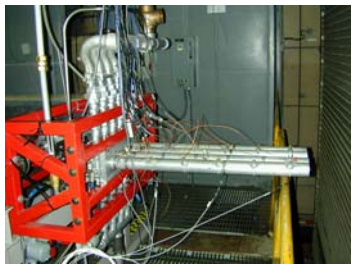

- Synchronized valve system: stock cylinder head from scrapped Grand Am
- Next Step: Self actuated, self aspirated PDE…

6

Hybrid Piston Pulse Detonation Engine

Goals

- **Extract Shaft Power**
  - **Self-Actuation**
  - **Self-Aspiration**

Method

- **Create a Detonation Driven Piston Engine**

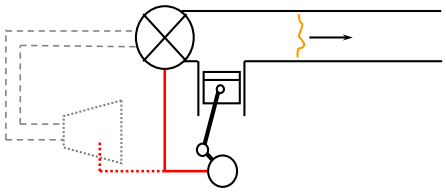

7

Hybrid Piston-PDE Cycle

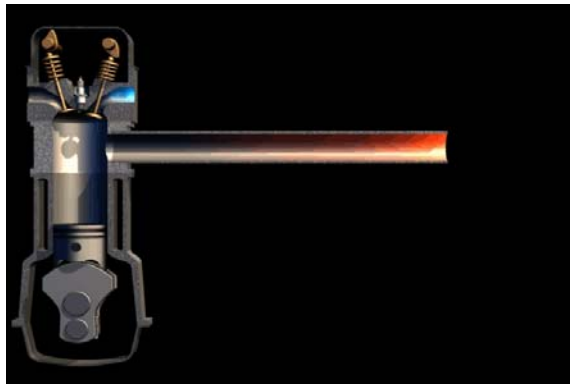

Animation created by Mike Bruggeman

8

Hybrid Piston Pulse Detonation Engine

Modified Suzuki Katana 1100

- Engine modified from ICE to HPPDE
- Cylinder no longer closed volume
  - No compression stroke
  - No pressure rise from deflagration

Aluminum Spacer

9

Engine and Timing

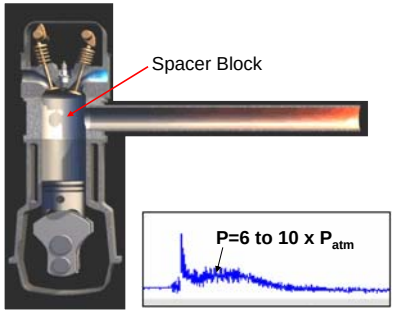

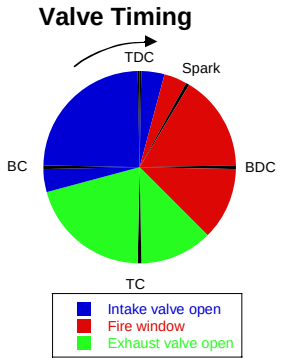

10

Critical Frequency (Calculated)

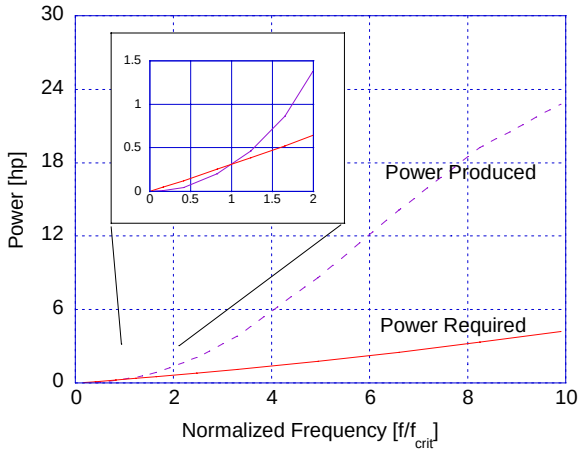

11

Experimental Engine

Suzuki Katana 1100 Modified with Spacer Block

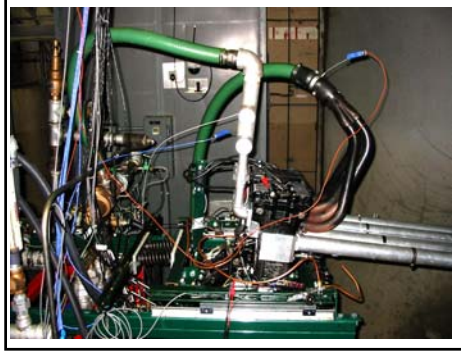

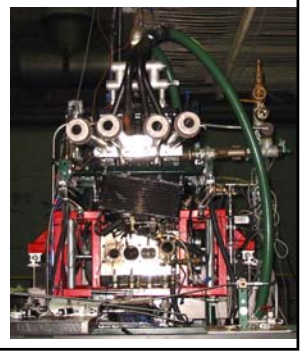

PDE-Piston Hybrid

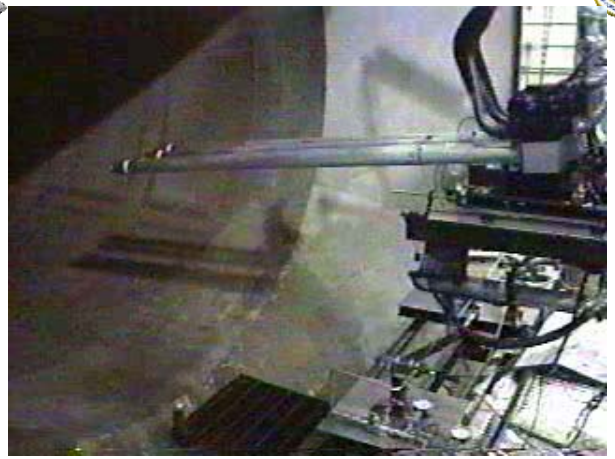

13

Self-actuation Above the Critical Starting Frequency

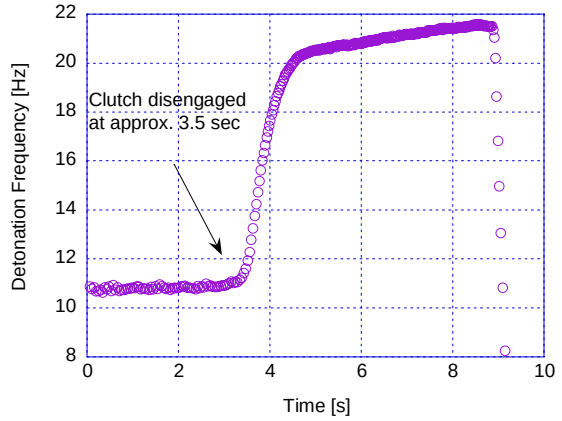

14

Frequency and Power Output During Failure to Self-Actuate

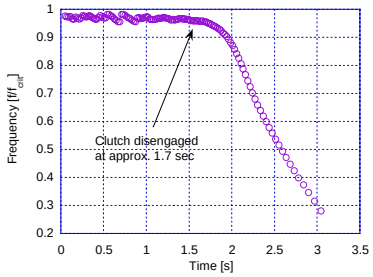

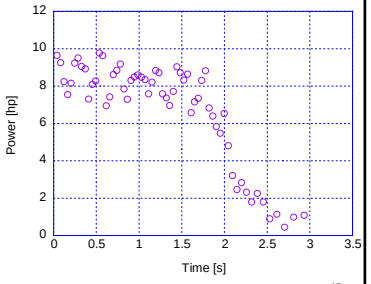

15

Frequency, Power and Thrust

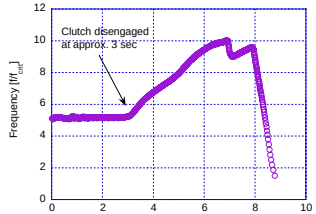

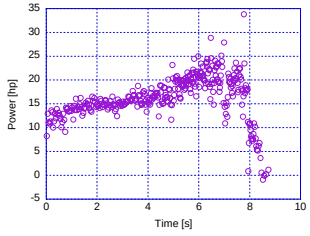

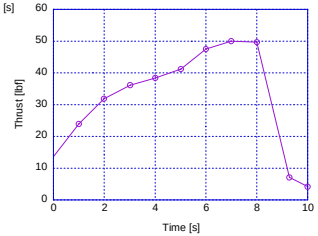

16

Summary and Conclusions

Hybrid Piston Pulse Detonation engine is a success

- Work can be extracted from PDE while still producing thrust
- Achieved 20 hp and 50 lbf of thrust simultaneously
- Critical starting frequency investigated and estimated

Funded by: AFRL & AFOSR

17

Ideal Steady Thermodynamic Cycle

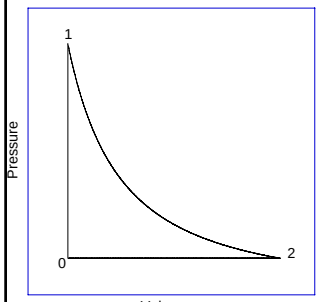

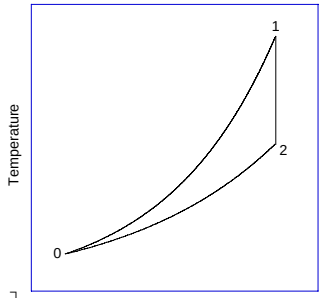

$$\eta = 1 - \gamma \left[\frac{\left(\frac{T_1}{T_0}\right)^{\frac{1}{\gamma}} - 1}{\left(\frac{T_1}{T_0}\right) - 1} \right]$$

18

Comparison of Pressure Traces of Hybrid Engine and Conventional PDE

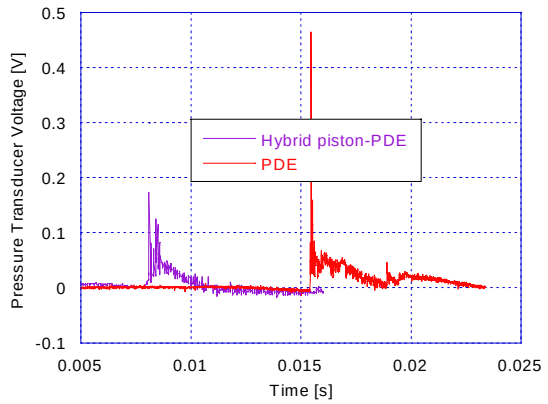

19

Critical Starting Frequency

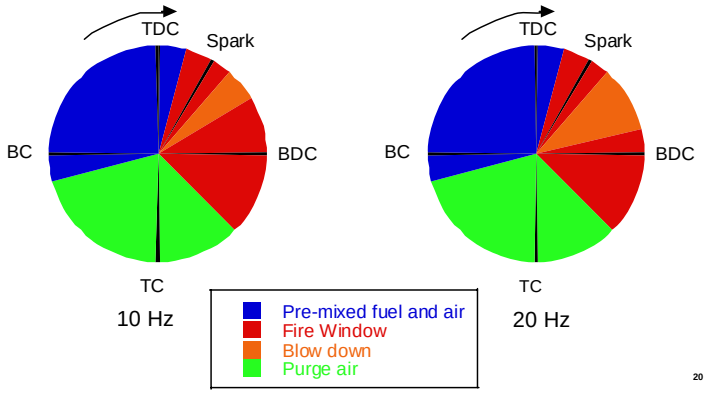

20

Spacer Block

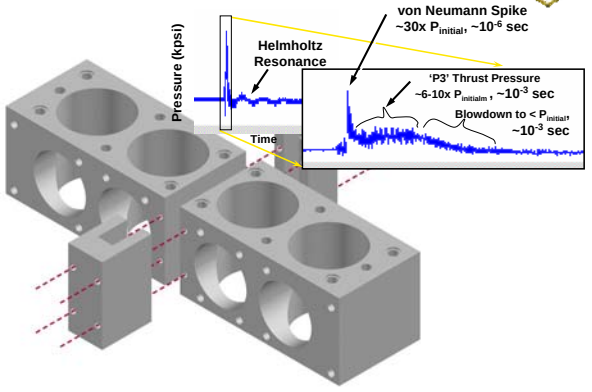

21

HPPDE Feasibility Is Dependent on Detonation.

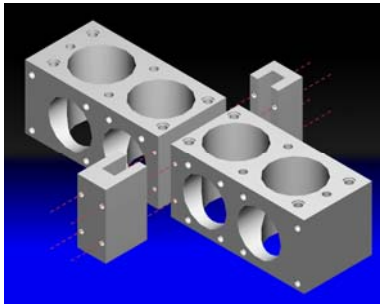

Aluminum Spacer

- Defining modification from ICE to HPPDE
- Cylinder no longer closed volume
  - No compression stroke
  - No pressure rise from deflagration

22

PDE-Piston Hybrid Results
(Tube 1 of 4)

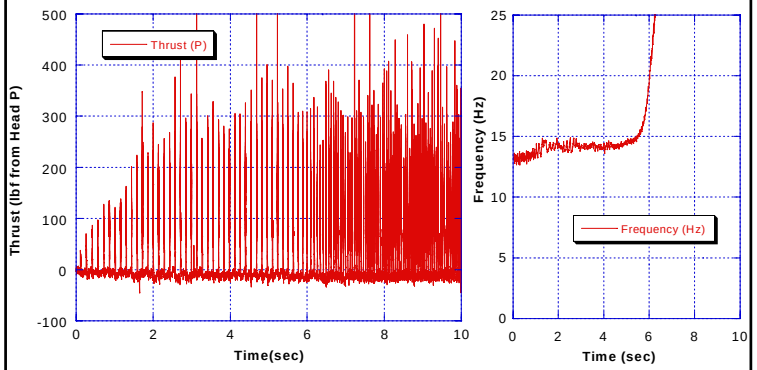

23

38th AIAA/ASME/SAE/ASEE Joint Propulsion Conference & Exhibit
7-10 July 2002, Indianapolis, Indiana

AIAA 2002-3720

EXPERIMENTAL STUDY OF DEFLAGRATION-TO-DETONATION ENHANCEMENT TECHNIQUES IN A H_2/AIR PULSED-DETONATION ENGINE

T. R. Meyer,* J. L. Hoke,* and M. S. Brown†
Innovative Scientific Solutions, Inc.
Dayton, OH 45440-3638, USA

J. R. Gord‡ and F. R. Schauer*
Air Force Research Laboratory, Propulsion Directorate
Wright-Patterson Air Force Base, OH 45433-7103, USA

Abstract

Experiments are performed on a number of deflagration-to-detonation (DDT) enhancement techniques for use in a H_2/Air pulsed-detonation engine (PDE). The mechanism, speed, and location of DDT for three configurations are considered, including a Shchelkin spiral, an extended cavity/spiral, and a co-annulus. High-speed digital imaging is used to track flame propagation, and simultaneous time-correlated pressure traces are used to record progress of the shock structure. It is found that DDT is initiated primarily through local explosions that are highly dependent on the particular geometry. In addition to various geometries, the effect of equivalence ratio and spark timing are also investigated.

Introduction

The pulsed-detonation engine (PDE) has experienced renewed interest due to its simplicity, low cost, low weight, scalability, and potential for a broad range of operability.[1] To optimize PDE performance and enable high operating frequencies, it is important to reduce the percentage of fuel that is burned during low-pressure deflagration and, thus, to minimize the time required for deflagration-to-detonation transition (DDT). Direct initiation offers an alternative approach, but requires high input energies that reduce the overall system efficiency.

Deflagration-to-detonation transition has been the subject of scientific study for over a hundred years.[2] It is by nature extremely complex and highly three-dimensional, involving non-repeatable flame interactions with shocks, reflections, and boundary layers. For this reason, it is not easily studied with multi-point probes, spatially averaged measurement techniques, or single-frame imaging. To capture various features of shock-wave-flame interaction, an impressive series of DDT experiments have used high-frequency stroboscopic schlieren photography in smooth tubes filled with H_2 and air.[3,4] A common feature of the observed DDT events is the occurrence of an 'explosion-in-the-explosion' that spreads transversely into the shock compressed fuel-air mixture and leads to a self-sustained detonation.

Although much has been done to characterize detonation behavior in smooth tubes, DDT enhancement through the addition of obstacles is inherently very difficult to study because it involves turbulent combustion with complex boundary conditions.[5] Conventional detonability criteria using cell-size properties can determine if DDT is possible, but cannot determine if DDT is likely to take place.[6] The Shchelkin spiral, for example, while greatly reducing the time required for DDT in most cases, can also destroy the cellular structure[5] of the detonation or destabilize the coupling between the flame and the shock.[7]

While parametric studies on various obstacles can be performed,[7] a satisfactory description of why certain geometries are more effective than others is not yet available. For the purposes of developing DDT enhancement techniques for PDE applications, it is important to improve the understanding of how such

*Research Engineer, Member AIAA
†Physicist, Senior Member AIAA
‡Principal Research Chemist, Associate Fellow AIAA

This material is declared a work of the U.S. Government and is not subject to copyright protection in the United States.

geometries interact with the flame and shock structures to produce conditions sufficient for DDT. The goal of the current investigation is to use short-exposure, high-speed digital imaging of flame luminosity and simultaneous pressure data to further this understanding for a number of DDT enhancement strategies. Emphasis is placed on visualizing the instantaneous flame front as a function of the geometry, operating conditions, and associated shock structure.

Experimental Set-Up

The test facility, shown in Fig. 1, has been described previously by Schauer et al.[1] A modified General Motors Quad-4, dual-overhead-cam cylinder head is used for premixed fuel-air intake and spark ignition. The PDE is capable of operating with one to four tubes, and it can run at frequencies from single shot to tens of Hz. Only one of the four tubes shown in Fig. 1 is studied in the current investigation, and it is replaced with polycarbonate or quartz for optical access. Data collection is typically performed in single-shot mode for quartz tubes and up to five shots per run with polycarbonate tubes.

Detonation enhancement is achieved in the current investigation using three main approaches, as shown schematically in Fig. 2. The Shchelkin spiral consists of 3/16-inch mild-steel rod shaped into a 19-inch spiral and inserted into the entrance of a 2-inch inner diameter PDE tube. The extended cavity configuration extends the 3.5-inch bore of the cylinder head by about 8 inch in length before tapering to the 2-inch tube diameter. Based on preliminary measurements, this configuration has been modified to include a 54-inch Shchelkin spiral in the 2-inch section. For the co-annular geometry, 5- and 12-inch long tubes of 5/8-inch outer diameter are inserted at the entrance of the 2-inch PDE tube for a staged DDT approach.

High-speed digital imaging at rates up to 62,500 frames-per-second (fps) is employed using a Phantom v5.0 CMOS-based digital camera. At this framing rate, it has a field-of-view 32 pixels in height and 256 pixels in length and enables viewing of 8 tube diameters. The slowest framing rate used with the Phantom camera in the current investigation is 27,900 fps, for which the field of view of 32×1024 allows viewing of 32 tube diameters. Exposure times are kept at a constant value of 10 μs for all run conditions and framing rates.

Since the field-of-view of the Phantom camera is reduced at the higher framing rates, a second NMOS-based high-speed digital camera is also utilized in the current investigation and will be referred to as the Photron camera. It is capable of framing rates up to 40,500 fps with 64×64 pixels and 18,000 fps with 64×256 pixels. Typically, 18,000 fps is used in the current experiment and image magnification is adjusted so as to achieve about 32 pixels across the PDE tube and 256 pixels in length.

Through the use of these high-speed digital cameras, a time-history of the DDT process can be recorded during a single engine cycle. In addition, time-dependent pressure traces are collected simultaneously at several locations along the length of the PDE tube. The pressure traces provide a limited but unambiguous measure of the strength of the detonation wave during initiation and propagation. The camera is triggered from a pressure transducer located sufficiently downstream to ensure that the shock structure is well developed. This is necessary because the detonation and propagation events occur on the sub-millisecond time scale, and inherent variability in DDT timing prevents a priori phase-locking of the high-speed camera and PDE control system.

Results

Shchelkin Spiral

The detonation process resulting from a Shchelkin spiral is shown in false color in Fig. 3 for a H_2/air equivalence ratio of 1.0. The deflagration first becomes visible as a hot spot along a single spiral. Subsequent hot spots quickly become visible, and detonation is marked by a large increase in flame luminosity. These measurements show that DDT for this condition occurs within about 200 μs after the first explosion is detected. The effects of the retonation wave are also evident in Fig. 3. Hot spots induced by pressure-wave coalescence propagate *upstream* and cause the luminosity to increase significantly. Since the flame remains near the spirals during the DDT process, it is also likely that unburned pockets of fuel and air are also combusting as the retonation wave passes. Because the camera exposure was selected to highlight the transition process, camera saturation quickly occurs in the detonation and retonation regions and precludes further quantitative study in this sequence of images. It is possible to detect in other data sets, however, that the retonation wave is reflected back downstream and recompresses the combustion products.

It is also possible to track flame propagation along the spirals by focusing on the DDT region only and using the highest framing rate of 62,500 fps, as shown in Fig. 4. An important question regarding the geometry of the Shchelkin spiral is whether the flame propagates across the spirals as it would in a series of orifice plates, or whether it propagates along the spirals in a continuous fashion. This sequence of images shows quite clearly that the hot spots are propagating along the spirals, and helps to explain differences with the

behavior of axisymmetric orifice plates (not presented here). If a single geometric obstacle can provide an explosion that can enhance the flame-shock interaction, then a spiral obstacle provides a continuous line of explosions surrounding the deflagration as it propagates along the center of the tube.

The success of the Shchelkin spiral over concentric rings may be due to another an important feature of the transition process as visualized by Urtiew and Oppenheim.[4] They observed that the 'explosion-in-the-explosion' in smooth tubes produces a bow-shaped shock which reflects off the side walls and intensifies the flame-shock interaction. Unlike axisymmetric obstacles, the Shchelkin spiral can support additional helical modes that can propagate upstream as they grow and interact with the side walls. Compelling evidence for this mode of interaction is provided by frame-by-frame animations which show helical fluctuations in flame luminosity within the spiral during and after DDT. This increases the probability of coupling between the shock structure and turbulent flame propagation, thereby increasing the likelihood of DDT.

To verify proper coupling of the flame front and shock wave, simultaneous high-speed images and pressure traces are shown in Figs. 5 and 6 respectively. Once the flame advances ahead of the Shchelkin spiral, as shown in Fig. 5, it attains a nearly flat profile. This is partial indication that the flame is well-coupled to the shock front, as confirmed by the pressure traces in Fig. 6 showing that the flame and shock fronts arrive nearly simultaneously at the pressure transducer locations. Note that the pressure traces follow the expected temporal profile, with a very high initial von Neumann spike and a subsequent Chapman-Jouguet (C-J) peak after the initial shock. The speed of the shock is such that it is possible to miss the peak of the pressure rise, as shown in the curve for PT4 in Fig. 6.

Extended Cavity / Shchelkin Spiral

Initial tests found that the extended cavity geometry did not significantly enhance DDT. Endview images were collected at several conditions for this configuration, and show that local hot spots are generated but produce weak detonations with speeds up to 800 m/s.

For the data presented here, a 54-inch spiral was added just after the extended cavity for the following reasons: (1) to determine if the increased initial heat release and hot spots generated by the extended cavity can reduce the time required for DDT and (2) to determine the effect of a lengthened spiral.

As shown in Fig. 7 for unity equivalence ratio, DDT is achieved shortly after the exit of the cavity (just to the left of each image). Since the flame is accelerated due to the geometry of the cavity, interaction with the spiral leads to an immediate transition. This case differs significantly from that of a pure Shchelkin spiral geometry. This is shown by the decaying detonation front, which begins as the flame front loses its flat character at PT3. This decay can be attributed to two main possibilities: (1) once DDT has taken place, the spiral interferes with the flame-shock coupling, or (2) the long spiral results in residual air remaining in the tube and causing lower than expected equivalence ratios.

Evidence for the former is provided in the pressure traces of Fig. 8. The pressure pulse for PT4 arrives several microseconds before the visible flame front, indicating that the primary flame-shock interaction has been disrupted. The flame-speed and luminosity quickly decay in the aftermath of this disruption, although local explosions are occurring which continue to drive the flame forward as a weak detonation. These local explosions are evident in the high-speed images of Fig. 7 as well as in the pressure spikes for PT5 in Fig. 8.

The flame speeds from the Shchelkin spiral geometry of Fig. 5 and the cavity/spiral geometry of Fig. 7 are shown for comparison in Figs. 9(a) and (b), respectively. For the Shchelkin spiral configuration of Fig. 9(a), the C-J velocity of about 2000 m/s is achieved after about seven tube diameters downstream of the engine block. This velocity is verified by measurements of the shock-wave speeds between pressure pulses, which are on the order of 2000 m/s as far as PT6 near the exit of the tube.

For the cavity/spiral configuration of Fig. 9(b), the flame enters the viewing area at nine tube diameters as a C-J detonation, but the flame speed varies tremendously. Velocities greater than the C-J velocity do not necessarily represent overdriven detonations, but could also represent the more intermittent nature of flame propagation via shock-induced local explosions. This intermittency indicates that the flame and shock are not well coupled, although strong local explosions drive the flame periodically to C-J velocities up to about 22 tube diameters downstream. Pressure traces indicate that the shock-wave is already below C-J conditions between PT3 and PT4, with a measured transit time corresponding to 1800 m/s. It drops further to about 900 m/s between PT4 and PT5.

Co-Annulus

The co-annulus shown previously in Fig. 2 was implemented due to promising results from numerical simulations. The idea is to initiate a detonation in the smaller tube first, which can then drive a detonation in the larger tube.

The results of a 5-inch long inner tube and a 12-inch long inner tube are shown in Figs. 10(a) and (b). The experimental data did not show a strong enhancement of

the DDT process. For the 5-inch tube, a hot spot develops *outside* the tube near its downstream tip. The flame from the central tube finally exits as a strong flame front, but it enters a burned-gas medium. For the 12-inch tube of Fig. 10(b), a hot spot occurs at the downstream tip of the inner tube, but in this case is also joined by the flame exiting the inner tube. Combustion pressures of nearly one-third that expected for a C-J detonation indicate that the flame is accelerated but does not achieve DDT. The measured flame velocity reaches about 520 m/s, which is well below the velocity of about 2000 m/s expected for stoichiometric mixtures of H_2/air.

Subsequent analysis of the numerical results indicates that the flame from the inner tube can be strongly dissipated unless its diameter is greater than one-half the diameter of the main tube. Subsequent experiments to verify this prediction are the subject of ongoing study.

Effects of Equivalence Ratio and Spark Timing

In addition to the effects of geometry on DDT, it is also of interest to study the effect of various operating conditions. For the Shchelkin spiral geometry, varying the equivalence ratio between 0.9 and 1.3 had an impact on the location of DDT, as expected, but did not affect the nature of the transition. The shortest distance required for DDT occurs at stoichiometric conditions and extends further downstream as the equivalence ratio becomes progressively lean or rich. For an equivalence ratio of 1.3, for example, DDT takes place three tube diameters further downstream near the end of the 19-inch Shchelkin spiral.

For the extended cavity/spiral configuration, varying the equivalence ratio between 0.75 and 1.0 had a similar effect. For stoichiometric conditions, the transition occurs almost immediately in the field-of-view, as shown in Fig. 7. At an equivalence ratio of 0.75, the transition occurs about two tube diameters further downstream. Despite these differences in location of DDT, the detonation speeds remain within about 2% of the theoretical C-J velocities once the self-sustained condition is achieved.

The primary effect of spark timing is to change the H_2/air mixture further downstream in the PDE tube. Large differences in the location of DDT are not detected in the current experiments, and it is found that the C-J velocities for early and late spark timings agree to within about 5%. The detonation wave for late spark timing, however, has difficulty propagating to the end the tube. This is attributed primarily to mixing with ambient air near the end of the tube caused by pulsing of the fresh H_2/air mixture. Thus, wave speeds near the end of the PDE tube drop to the level of weak detonations as the spark timing is progressively increased. These data highlight the importance of measuring fuel mixture fraction near the end of the PDE tube as a function of time during PDE operation.

Conclusions

An experimental study of three DDT enhancement techniques and different operating conditions has been performed using simultaneous high-speed digital imaging and pressure-transducer data. It is found that local explosions in the Shchelkin spiral geometry propagate along the spirals and behave in a fundamentally different manner when compared with local explosions produced by axisymmetric obstacles. In addition, it is shown that the continuous spiral geometry leads to transverse and helical modes that may enhance coupling between the flame and shock fronts. It is found that adding an extended cavity before the Shchelkin spiral leads to strong early detonations that then decay more quickly as compared with a simple Shchelkin spiral geometry. The co-annular geometry with inner tube diameters of less than half the main tube diameter did not lead to strong detonations and is under further investigation. Finally, equivalence ratio was found to change the location but not the nature of the transition, and spark timing was found to impact the progression of the detonation wave near the exit of the PDE tube. These studies provide a phenomenological description of the effects of geometry and various operating parameters on the flame-shock interaction during and after the DDT process.

Acknowledgments

The authors would like to acknowledge R. P. Bradley and C. Rice of ISSI and co-op students Matt Slagel, Jason Parker, and Brian Frankey for their assistance in the set-up and operation of the PDE facility. We also thank V. R. Katta of ISSI for his modeling efforts and for useful discussions regarding the deflagration-to-detonation transition process. This work is supported in part by U. S. Air Force Contract F33615-00-C-2068.

References

[1] F. Schauer, J. Stutrud, and R. Bradley, "Detonation Initiation Studies and Performance Results for Pulse Detonation Engine Applications," AIAA Paper No. 2001-1129, *39th AIAA Aerospace Sciences Meeting and Exhibit*, Reno, Nevada, Jan. 8-11, 2001.

[2] E. Mallard and H. Le Chatelier (1883), "Recherches Experimentales et Theoriques sur la Combustion des Melanges Gaseoux Explosifs," *Ann. Mines* 8(4): 274-568.

[3] A. K. Oppenheim, P. A. Urtiew, and F. J. Weinberg, (1966) "On the Use of Laser Light Sources in Schlieren-Interferometer Systems," *Proc. Roy. Soc. London*, A291:279.

[4] P. A. Urtiew and A. K. Oppenheim (1966), "Experimental Observations of the Transition to Detonation in an Explosive Gas," *Proc. Roy. Soc. London*, A291:13.

[5] J. H. S. Lee, "On the Transition from Deflagration to Detonation," Dynamics of Explosions, Vol. 106: Progress in Astronautics and Aeronautics, Martin Summerfield, Editor, American Institute of Aeronautics and Astronautics, Inc., New York, 1986.

[6] O. Peraldi, R. Knystautas, and J. H. Lee, "Criteria for Transition to Detonation in Tubes," 21st Symposium (International) on Combustion, The Combustion Institute, pp. 1629-1637.

[7] R. P. Lindstedt and H. J. Michels (1989), "Deflagration to Detonation Transitions and Strong Deflagrations in Alkane and Alkene Air Mixtures," *Combustion and Flame* 76:169-181.

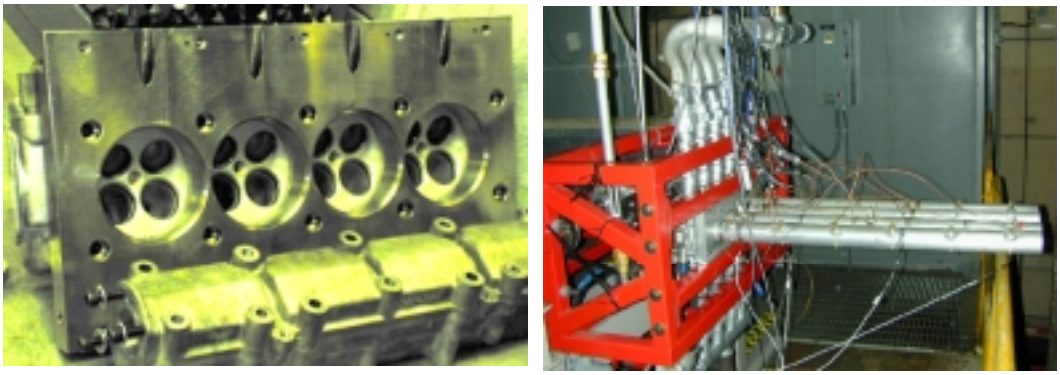

Fig. 1. Quad-4-based PDE during assembly (left) and as installed. Only one of the tubes is studied for the current investigation and is replaced with polycarbonate or quartz for optical access.

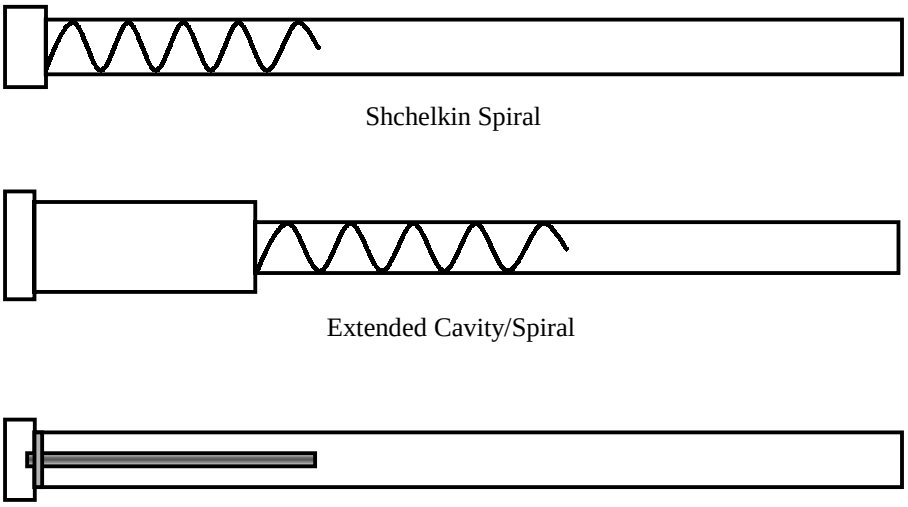

Fig. 2. Schematic of DDT enhancement techniques discussed in the current study. Sketches are not to scale.

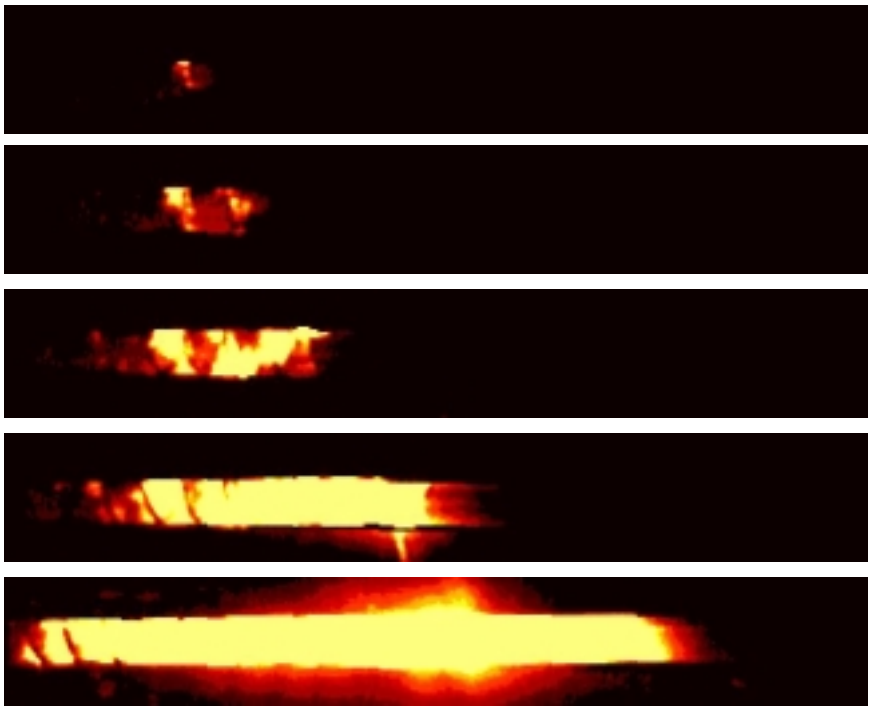

Fig. 3. High-speed images of DDT at 18,000 fps for a Shchelkin spiral at ϕ=1. Images are spaced 55.5 μs apart.

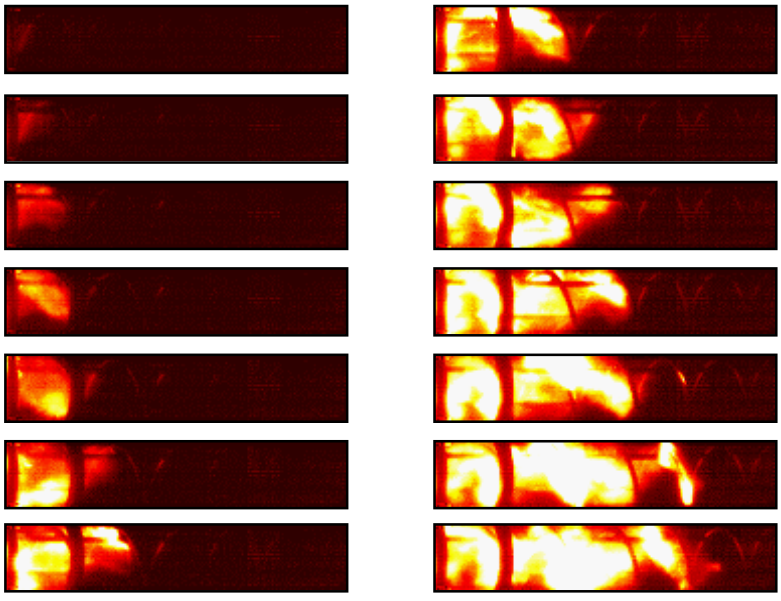

Fig. 4. Sequence of high-speed digital images at the highest framing rate of 62,500 fps for a Shchelkin spiral geometry. The flame front is clearly shown to take place along the spirals.

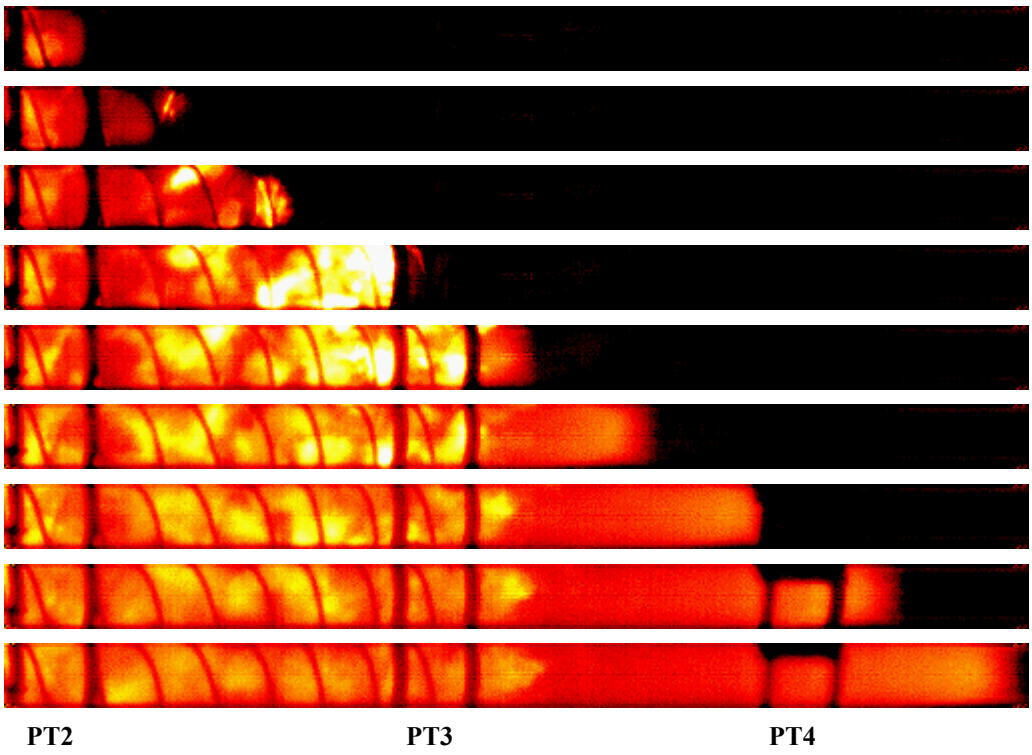

Fig. 5. Image sequence showing DDT initiated by a Shchelkin spiral with pitch of 1 tube diameter and length of 9.5 tube diameters. Images are spaced 50 μs apart in time and begin 5 μs after PT2 is triggered. Equivalence ratio is 1.0. Pressure transducer locations are labeled as PT2 to PT4.

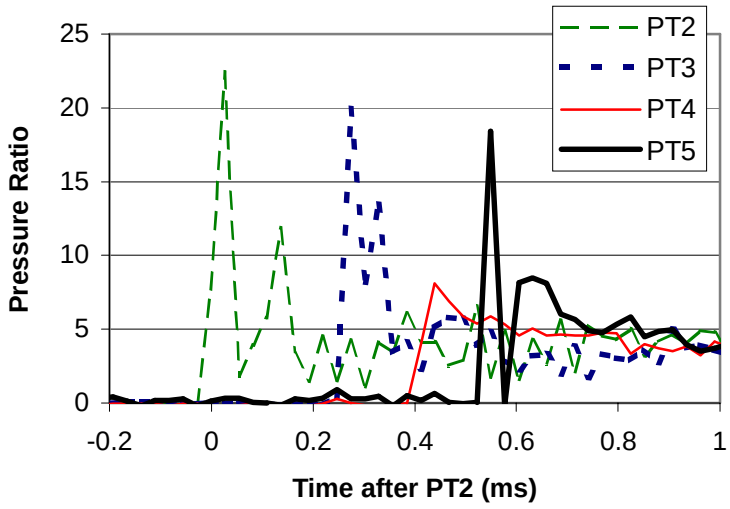

Fig. 6. Pressure traces for the Shchelkin spiral geometry of Fig. 5.

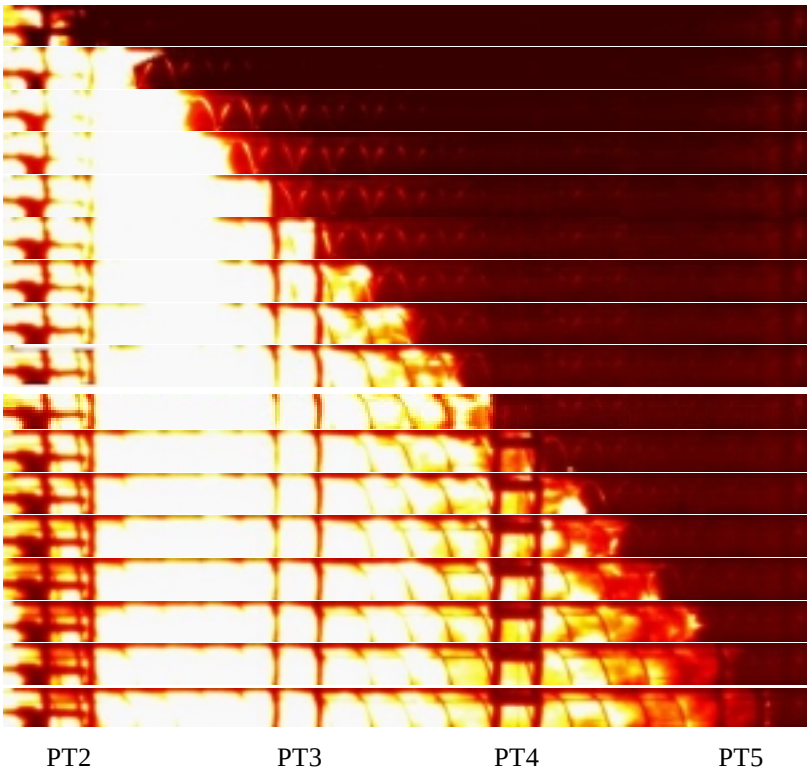

Fig. 7. Sequence of high-speed digital images for an extended cavity/spiral geometry.

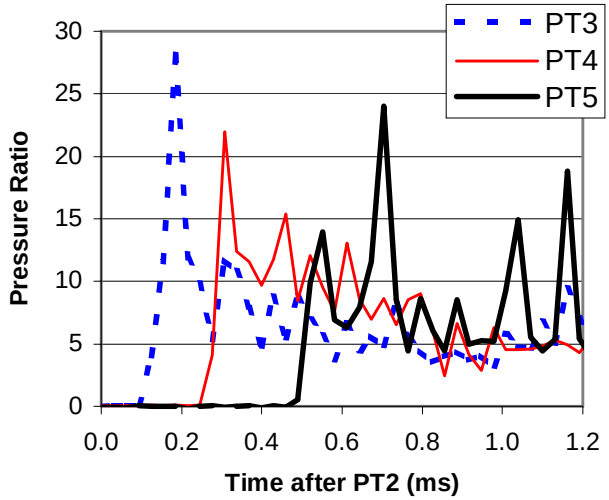

Fig. 8. Pressure traces for the extended cavity/spiral geometry of Fig. 7.

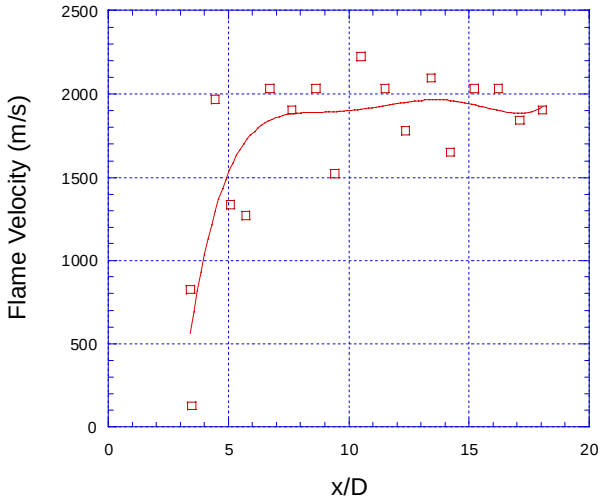

(a)

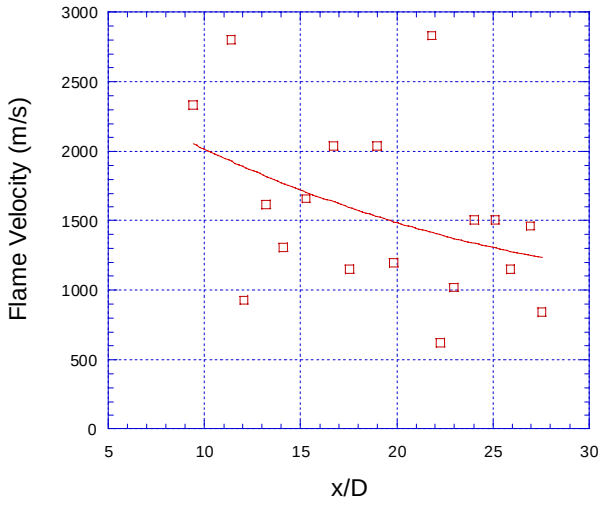

(b)

Fig. 9. Flame speeds for the (a) Shchelkin spiral geometry of Fig. 5 and (b) the extended cavity/spiral geometry of Fig. 7.

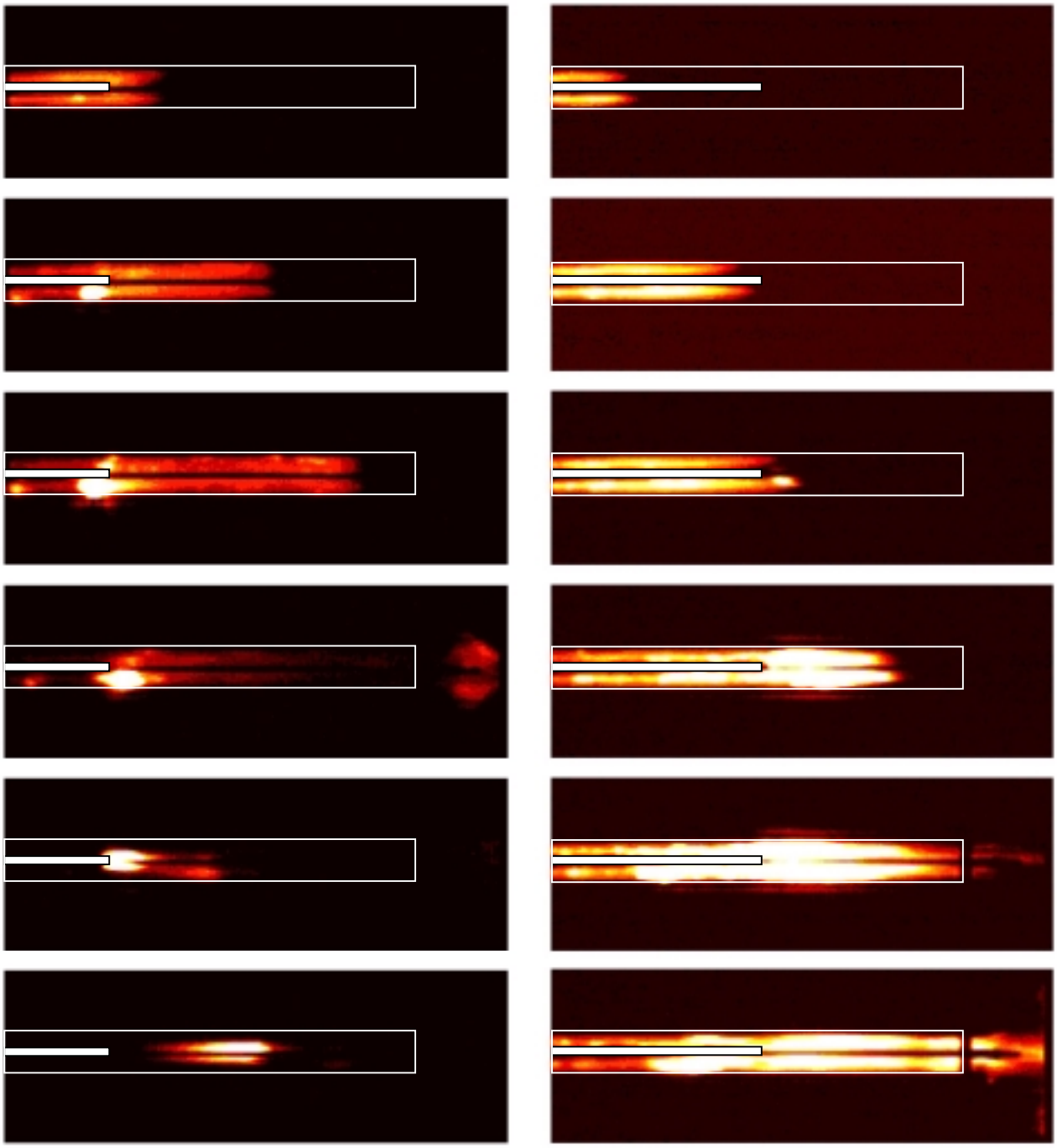

(a) (b)

Fig. 10. Image sequence showing co-annular tube DDT enhancement geometry with tube length of (a) 2.5 tube diameters and (b) 6 tube diameters. Equivalence ratio is 1.0. Maximum velocity of 520 m/s achieved for (b). Outlines of main and inner PDE tubes shown in white.

Detonation Studies And Performance Results For A Research Pulse Detonation Engine

Fred Schauer and Jeff Stutrud

Air Force Research Laboratory, Propulsion Directorate

Wright-Patterson AFB, Ohio 45433 USA

Royce Bradley, Vish Katta, and John Hoke

Innovative Scientific Solutions, Inc.

Dayton, Ohio 45440 USA

Abstract

Research results of a combined computational and experimental investigation of an air breathing pulsed-detonation engine (PDE) are presented. Models and hardware developed by the Air Force Research Laboratory in-house PDE program examine critical technology issues such as: detonation initiation and propagation; valving; timing and control; instrumentation and diagnostics; variation in tube fill, equivilance ratio, and repetition rate; detonation and deflagration to detonation transition; and performance prediction and analysis. An innovative, premixed four-detonation-tube engine design is currently employed for experimental research and evaluation. Specialized instrumentation and measurement techniques are developed to investigate the unsteady PDE processes. Research objectives include detonation initiation in air without the use of excess oxygen and performance results for various operating conditions. Data are obtained with hydrogen/air as well as hydrocarbon/air mixtures and compared with theoretical results.

Introduction

Renewed interest in pulsed detonation propulsion concepts has prompted recent efforts to develop a low-cost, practical-fueled, pulse detonation engine[1,2]. Conceptually, a pulse detonation engine (PDE) offers few moving parts, high efficiency, high thrust, low weight, low cost, and ease of scaling. These features make the PDE an attractive alternative to jet turbines for small disposable engines. The near constant volume heat addition process, along with the lack of a compression cycle, lend to the high efficiency and specific impulse, simplicity, and low-cost of pulse detonation engines. Theoretically, PDE's have the potential for operation at speeds ranging from static to hypersonic with competitive efficiencies, enabling supersonic operation beyond conventional gas turbine engine technology. Currently, no single cycle air-breathing engine exists which has such a broad range of operability.

A practical-fueled PDE likely requires kerosene/air detonation. This requirement creates several technological hurdles that must be overcome in order to develop such a PDE. Complex hydrocarbon fuels, and particularly liquid hydrocarbons, are difficult to detonate in air, typically requiring hundreds of kilo-joules to directly initiate a detonation[3]. For this reason, development of a practically fueled PDE may become a deflagration to detonation transition (DDT) minimization process since the fuel burned during detonation initiation does not produce thrust efficiently while it is burning at low pressures. Furthermore, since thrust is generated with each detonation cycle, it may be beneficial to raise the operating frequency in order to produce more thrust. Higher operating frequencies also have benefits from an unsteady inlet, nozzle, and noise generation perspective, but create complications in other areas including valving, mixing, shortened residence time requirements, and increased heat loads.

Technical Approach

The research approach combines use of analytical and numerical modeling with experimental research. The highly unsteady and severe conditions experienced during PDE operation dictate innovative methodologies to modeling, facilities and instrumentation, and research hardware development and testing, which are explained below.

AFRL's detonation modeling, described in detail elsewhere[4], has been extended to three dimensional calculations and studies of detonation initiation schemes such as the Shelkin spiral calculation in Figure 1. Both calculations employ weak initiation of hydrogen/air mixtures, but the upper frame is a straight channel and the lower contains a two dimensional representation of a Shelkin spiral. The brighter areas in Shelkin spiral calculation indicate that the "hot spots" critical for DDT events are more prevalent with the extra geometry.

The Pulsed Detonation Research Facility (D-Bay)[5] is capable of supporting full scale engine experiments, with integrated remote control and instrumentation systems. Pulsed thrust measurements from 3 to 1,000+ lbf (13-4500+ N) are made with a damped thrust stand mounted on a conventional static thrust stand. Up to 6 lbm/sec (3 kg/sec) of 100 psi (680 kPa) air is available and high-capacity inlet and exhaust stacks are useful for self-aspirating designs and atmospheric exhaust. A direct connection to a liquid fuel farm via a high-pressure/high-capacity fuel pump retains the facilities ability to feed large-scale engines.

A hardened remote-control room is adjacent to the 750,000+ ft^3 (25,000 m^3) test cell. A minimum of 2 feet (0.6 m) of reinforced concrete is situated between the test cell and personnel during testing. Such precautions are necessary when dealing with the high noise levels associated with PDE operation. Control of all pulsed combustor/detonation engine operations

and data acquisition is done via a National Instruments LabVIEW based interface with duplicate manual emergency shutdown and safety system controls.

Choked flow measurements are employed to accurately regulate and measure oxidizer and vapor fuel flow to pulsed engine experiments. These choke points isolate the measurements from the downstream pressure oscillations of pulsed valves. Each flow system contains a pressure controller, a choked orifice plate or critical flow nozzle, and a surge tank to set and hold a required flow rate even with unsteady combustor valve flows.

In addition to conventional (low Hz and kHz frequency) data acquisition and control systems which include intake, fuel, and purge system instrumentation, the facility is equipped with up to 16 channels of high-frequency data acquisition at up to 5MHz. These may be used for high-frequency pressure transducers, thermocouples, photodiodes, or advanced laser diagnostics. High speed digital imaging systems, with framing rates varying from khz to Mhz are used for imaging PDE phenomena. [6,7]

Due to the critical timing issues in pulsed detonation engine operations, the high frequency valving tends to be both expensive and highly constrained. During the design of a research PDE, many options were considered that were either expensive, had severe limitations in operating range, or both. The research engine design is based upon valving found in a General Motors Quad 4, Dual Overhead Cam (DOHC) cylinder head commonly used in the Pontiac Grand Am automobile. This PDE design has an extremely broad operating range and configuration, with up to four detonation tubes operating at up to 40+ Hz each with proven reliability and durability. Valving and tube mount systems have been redesigned to permit higher frequency operation, quick valve system and detonator tube configuration change-outs, and eliminate fatigue problem areas.

The operating conditions of PDE's are very similar to internal combustion engines and many of the components can be shared. By driving the overhead cams with an electric motor, the four valves in each of the four cylinders can be made to operate at between 0.5 and 40+ Hz. Many different detonator tube configurations are possible and interfaces are available including single and multiple tube configurations with tubes ranging from 0.75" (20 mm) to 6" (150 mm) in diameter and various lengths; 1 to 6' (0.3-2 meters) being typical. Provisions for lubrication, cooling, ignition, and fuel delivery are integral to the cylinder head/intake manifold assembly.

The two intake valves in each cylinder, visible in Figure 2, are used to feed premixed air and fuel into detonation tubes, which are attached to an adapter plate secured by the head bolts. In the current configuration, the head and detonation tubes are installed horizontally, and the intake valves are the upper pair. Cold air flows through the exhaust valves in reverse as a purge gas to buffer hot products from igniting the next incoming charge and to convectively cool the inside of the detonation tube walls.

Somewhat uniquely, the research PDE is operated premixed, minimizing mixing and stratification issues. The large pop-off valves and check valves visible in Figure 3 are some of the precautions used to prevent catastrophic failure in the event of an engine backfire through the premixed intake section. Up to four detonation tubes can be run at 90 degrees out of phase. The main combustion air and purge air lines contain ball valves for each detonation tube feed system so that the engine can be run with one tube, two tubes 180 degrees out of phase, or all four tubes. A rotary position sensor is adapted to the intake camshaft to provide both an index of the valve timing sequence and the relative position of the valves. This signal serves as the master timing signal for the ignition and data acquisition systems.

An eight-channel igniter/fuel injection control box is triggered off the rotary position sensor. Separate control of each detonation tubes igniter and/or fuel injector can be accomplished with this system. Vapor fuels are premixed with the combustion air via a separate critical flow nozzle and flow control system. Do to the high noise levels associated with PDE testing, all controls and data acquisition are performed remotely from an isolated control room. All of the control systems and data acquisition systems are LabVIEW based and integrated into one 'virtual instrument' with back-up manual shutdown and safety systems. This virtual control panel is extremely flexible and can control all aspects of the PDE's operation including: lubrication, operating valve drive motor speed, fuel flow, main combustion air flow, purge air flow, fuel systems, timing, ignition delays, and automatic shutdown in the event of a critical system failure.

The research engine is used for performance prediction validations and serves as a test-bed for research of detonation initiation and DDT minimization, heat transfer, noise levels, pulsed ejector concepts, and multi-tube interactions. A vapor propane system is utilized to conduct research on a complex-hydrocarbon that detonates much like kerosene based fuels, while avoiding atomization and mixing issues associated with liquid fuels. A variety of liquid fuel injection schemes have also been applied. Further details on the research facility and engine are available elsewhere[5,8].

Results and Discussion

Although a variety of mechanisms have studied for detonation initiation[9], only confinement and obstacles will be described briefly here. Confinement has long been a method of prompting detonation initiation via compression of a combustible mixture in an enclosed

space. Recently, cavities have been employed to accelerate the transition to detonation downstream of the cavity. Smirnov and co-workers were using cavities to promote DDT in gasoline-air mixtures[10].

Recent CFD models of this cavity effect have provided new insights into the mechanisms responsible for achieving DDT. A typical result in a model of such a cavity geometry is shown in Figure 4. Subsequent frames, from a.) through j.) depict pressure levels (red high / purple low). A channel corresponding to approximately 1 cell width in height is ignited via a small combusting channel propagating into a cavity approximately 3 cell widths in both height and width for this two dimensional simulation. In the first frame, a.), weak combustion ignition is achieved via the small channel entering the cavity. Unburned pockets of fuel-air mixture trapped in cavity in frame b.), 'explode' in frame c.), releasing heat behind the main combustion front. Compression waves from the cavity coalesce near the flame front in frames e.) through g.) and subsequently create the micro-explosion visible in g.), which then produces the multiple DDT events visible in frames h.) and i.). A right-running detonation wave and left-running retonation wave are then evident in frame j.). Similar results have been obtained experimentally as well[9].

In addition to looking at cavities, high speed digital imaging[6,7] was used to study the impact of obstacles such as the Schelkin spiral geometry which produced the hot spots evident in Figure 1. By utilizing a optically clear polycarbonate detonator tube, flame acceleration and formation of hotspots may be observed in footage such as the frames in Figure 5. Obtained at 18,000 frames per second, these images depict the classic micro-explosion formation of a DDT event, the detonation and retonation propagation, as well as the expansion process during tube blow down.

Utilizing detonation initiation methods developed using the techniques illustrated above, DDT is obtained. High frequency data acquisition systems verify detonative operation. High frequency pressure transducer measurements in a hydrogen/air detonator tube, as seen in Figure 6, indicate measured wave speeds of 1959 m/sec. Further experimental verification of detonation wave speeds was provided by photodiode measurements shown in Figure 7 with a derived wave speed of 1959 m/sec. These results are in excellent agreement with the stoichiometric hydrogen/air wave speed of 1968 m/sec published elsewhere[11].

Similar results are obtained for liquid hydrocarbon fuels (Figure 8), including the gradual pressure rise near the head wall, the overdriven wavespeeds obtained during DDT, and attainment of steady Chapman-Jouget values during detonation propagation down the detonator tube. Evidence of detonation may be observed in both the pressure magnitudes on the left side of Figure 8 and the time-of-flight wavespeed results on the right.

Typical performance results that follow were obtained with a single aluminum 2.0" (50.8mm) ID tube that was 36" (915mm) long, operated at 16 Hz. Conventional weak initiation was employed at the head end (via the spark plugs) with a 5 msec ignition delay. The fuel/oxidizer mixture was stoichiometric and premixed hydrogen/air with a 50% clean air purge fill ratio. The above operating parameters apply to all experimental data herein unless stated otherwise.

The research engine has been run in multi-tube mode, demonstrating both two-tube operation 180^o out of phase and four tube operation 90^o out of phase. A wide variety of frequencies have also been demonstrated indicating the simple linear scaling of thrust versus frequency as shown in Figure 9. This data also demonstrates the accuracy of the thrust measurements, as the deviation from linear is +/- 0.5 lbf (+/- 2.2 N). Such thrust measurements

have been demonstrated with the current system down to 3 lbf (13 N) but the accuracy and thrust range can be varied with configuration changes.

In addition to frequency alterations, thrust modulation may also be accomplished via variation of the volume of the tube filled with detonable mixture. Via volumetric flow control, the tube fill fraction was varied with the resulting impact upon thrust measured as shown in Figure 10. Similar results were observed with both hydrogen and liquid fuels. The ratio of the detonable mixture volume to tube volume is referred to as the fill fraction. Fill fractions greater than one typically result in a cloud of combustible mixture around the end of the detonator tube that does not contribute to thrust. Fill fractions less than one result in a detonation driving either purge cycle and/or products from the previous cycle. This results in the same effect as a bypass ratio in a turbo fan engine, in that a bigger mass is moved at a lower change in velocity with resultant gains in efficiency.

This effect has been observed both computationally and experimentally by a number of researchers[8,12] and has been analytically studied by Mitrofanov[13]. Mitrofanov's calculations, along with our experimental results, are plotted in Figure 11. Specific impulse was normalized via the specific impulse at a fill fraction of 1.0 to collapse the curves for the different fuels. Essentially, this permits data reduction with allowances for differences in the fuel heating value. As seen in the excellent match between the analytical results and the results with two different fuels, the correlation is quite good.

A similar correlation by Shepard[14] has been compared to a wide variety experimental data with various tube geometries, wall temperatures, and operating frequencies (Figure 12). Again, the results are in good agreement, indicating that performance is easily determined by tube volume and fill conditions.

Along with variations in fill conditions, tube geometry and dynamic effects have been found to dramatically impact the blow down behavior of detonator tubes. The sensitivity of performance to these exit conditions has been identified by Kailasanath and co-workers computationally as the source of much dissension in PDE performance comparisons[15]. Experimentally, high speed imaging of detonation blow down processes also revealed this sensitivity, as observed in Figure 13. Slight variations in conditions described above can result in either the spherical shock wrapping at the exit (left image) and resulting large scale vortices formation or the much different behavior depicted by the image on the right, where the detonation blow down appears to resemble a supersonic jet.

In addition to the effects of frequency and fill fraction, the impact of fuel/air ratio was also examined as shown in Figure 14. Thrust is plotted versus a wide range of equivilance ratios. As expected from detonability data[3], a stable region is observed at equivilance ratios near stoichiometric. At fuel rich conditions, both the detonability and thrust are observed to fall off gradually with increasing fuel to air ratio. The detonability and thrust fall off more quickly on the fuel lean side. Similar trends have been observed with other fuel/air mixtures. Despite the loss in thrust due to fuel lean operation, potential fuel efficiency gains may be made when fuel flow rates are also considered, such as in the following discussion of specific impulse.

Specific impulse versus a wide range of equivilance ratios are shown in Figure 15 with hydrogen, propane, and various liquid hydrocarbon fuels. Data is compared to analytical predictions by Shepard[16] along with one experimental point which was initiated with a conventional oxygen predetonator system. Shepard obtained this experimental data using a single-shot pendulum technique[16]. The heating values for the complex hydrocarbon fuels shown are all similar, except for ethanol, which has a lower heating value and a resultant, lower

specific impulse. The analytical predictions assume the mixture detonated from the start, while experimental results required DDT. Despite these differences, good agreement between model and experiments is observed for equivilance ratios above 0.7. Below phi=0.8, cell size increases rapidly making DDT difficult to obtain[3]; hence the low experimental values.

Concluding Remarks

A brief description of the modeling, research facility, and a research engine used to conduct pulsed detonation engine research has been provided. These tools provided results on detonation initiation, and performance for a wide variety of fuels, detonator tubes, and operating conditions. Results from variations in frequency, equivalence ratio, and tube fill conditions have been presented.

There is much work to be done in developing valving, detonation initiators, noise suppression techniques, thermal protection systems, intake and exhaust nozzles, and control systems before a kerosene/air fueled PDE becomes practical. The Air Force Research Laboratory is exploring PDE technology development (c.f. [17-19]) through in-house research and collaboration with other researchers.

Acknowledgements

This research was funded by the AFOSR and AFRL. Special appreciation must be expressed to the technicians and support personnel, both in-house government employees and on-site contractors who made this work possible, particularly Dwight Fox, Walt Balster, and Jason Parker. Dr. Terry Meyer, Dr. Mike Brown, and Dr. Jim Gord helped provide high speed

imaging. We also wish to acknowledge the technical leadership of Dr. Mel Roquemore and Dr. Robert Hancock.

References

1. Kailasanath, K., "Recent Developments in the Research on Pulse Detonation Engine," **AIAA 2002-0470**, Reno, NV (1999).
2. M.L. Coleman "Overview of Pulse Detonation Propulsion Technology," CPIA Technical Report CPTR 70, April (2001).
3. Kaneshige, M. and Shepherd, J. E., *Detonation database*, Technical Report FM97-8, GALCIT, (1997).
4. Katta, V. R., Chin, L. P. and Schauer, F. R., "Numerical Studies on Cellular Detonation Wave Subjected to Sudden Expansion," *Proceedings of the 17th International Colloquium on the Dynamics of Explosions and Reactive Systems*. Heidelberg, Germany (1999).
5. Hancock, R. D., Gord, J. R., Shouse, D. T., Schauer, F. R., Belovich, V. M. and Roquemore, W. M., "AFRL Combustion Branch (PRSC) Aero-propulsion Research and Development Activities," *Proceedings of the International Test and Evaluation Association (ITEA) Conference* (1999).
6. Gord, J. R., Tyler, C., Grinstead, Jr., K. D., Fiechtner, G. J., Cochran, M. J. and Frus, J. R., "Imaging Strategies for the Study of Gas Turbine Spark Ignition," Presented at the SPIE's 44th Annual Meeting & Exhibition, Conference 3783 on Optical Diagnostics for Fluids/Heat/Combustion and Photomechanics of Solids, Denver CO, 23 Jul 99.

7. T. R. Meyer, J. L. Hoke, M. S. Brown, J. R. Gord, and F. R. Schauer, "Experimental study of deflagration-to-detonation enhancement techniques in a h_2/air pulsed detonation engine," **AIAA-2002-3720**, Indianapolis IN (2002).

8. Fred Schauer, Jeff Stutrud, and Royce Bradley, "Detonation initiation studies and performance results for pulsed detonation engine applications," **AIAA 2001-1129**, Reno, NV (2001).

9. F. Schauer, J. Stutrud, R. Bradley, V. Katta, and J. Hoke, "Detonation Initiation and Performance in Complex Hydrocarbon Fueled Pulsed Detonation Engines," *50th JANNAF Propulsion Meeting*, paper **I-05**, 11-13 July, Salt Lake City UT (2001).

10. N.N. Smirnov, M.V. Tyurnikov, "Deflagration to detonation transition in gasoline-air mixtures," *Physics of Combustion and Explosion*, **22**:2, pg 65-68 (1986).

11. Soloukhin, R. I., *Shock Waves and Detonations in Gases,* Mono Book Corp, Baltimore (1963).

12. K. Kailasanath, G. Patnaik, and C. Li, "Computational Studies of Pulse Detonation Engines: A Status Report," *AIAA 99-2634* (1999).

13. Vladislav Mitrofanov, "Continuous Spin Detonation of Gases and Sprayed Liquid Fuels," Windows on Science Seminar, EAORD, Wright-Patterson AFB OH (2001).

14. Shepherd, J., presented at the ONR mid-term PDE MURI meeting, St Augustine FL, 11 February (2002).

15. K. Kailasanath, et al., Naval Research Laboratory, "Pulsed Detonation Engines-What is its Performance?" in *Proc. JANNAF 24th Airbreathing Propulsion Subcommittee and 36th Combustion Subcommittee Joint Meeting*, CPIA Publication 692, Vol. 1, pp. 131-140, Cocoa Beach FL, (1999).

16. Shepherd, J., Personal Communication, California Institute of Technology, 24 August (2000).

17. A.J. Rolling, P.I. King, and F.R. Schauer, “Propagationn of detonation waves in tubes split from a PDE thrust tube,” **AIAA 2002-3714**, Indianapolis (2002).

18. J. Hoke, R. Bradley, J. Stutrud, and F. Schauer, “Integration of a pulsed detonation engine with an ejector pump and with a turbo-charger as methods to self-aspirate,” **AIAA 2002-0615**, Reno (2002).

19. B. Frankey, Fred Schauer, R. Bradley, and J. Hoke, “Evaluation of a hybrid-piston pulsed detonation engine,” **AIAA 2002-0474**, Reno (2002).

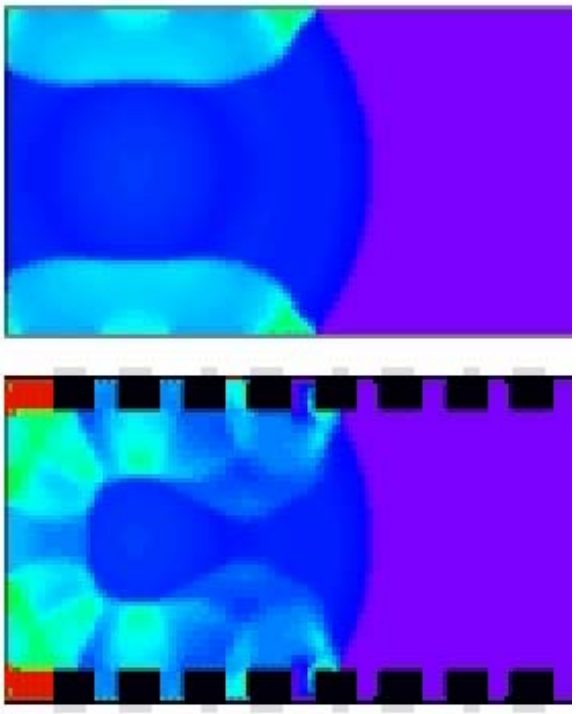

Figure 1. CFD model pressure map of deflagration to detonation transition event with two dimensional tube (upper) and Shelkin spiral (lower).

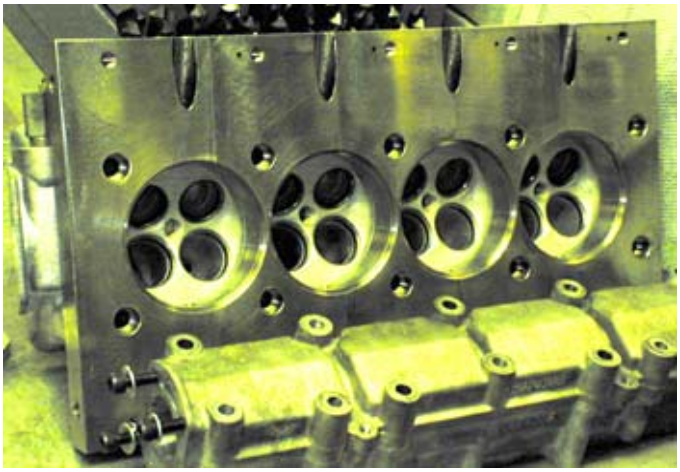

Figure 2. Quad 4 based research pulse detonation engine valving assembly. Each of the four tube positions contains two intake valves (the upper pairs) and two exhaust valves, which are currently used for purge cycles (the lower pairs of valves). The stock igniter location (smaller central hole between four valves) is typically used for ignition.

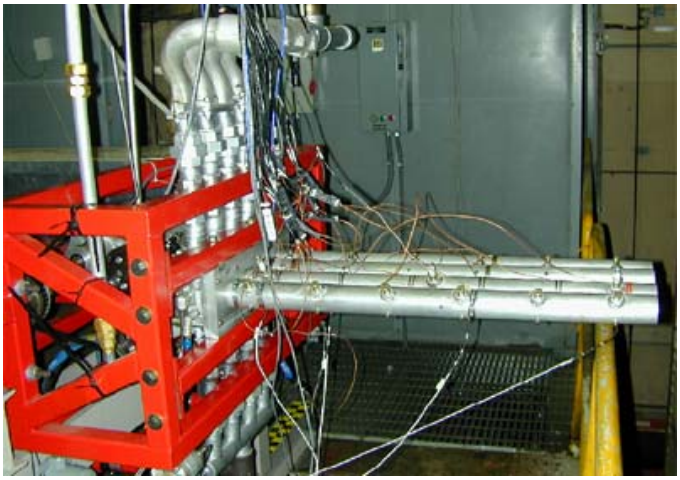

Figure 3. Four tube research pulsed detonation engine as installed on damped thrust stand. The upper manifold supplies premixed fuel and air; just visible below the frame is lower manifold which provides purge cycle of clean, unfueled air.

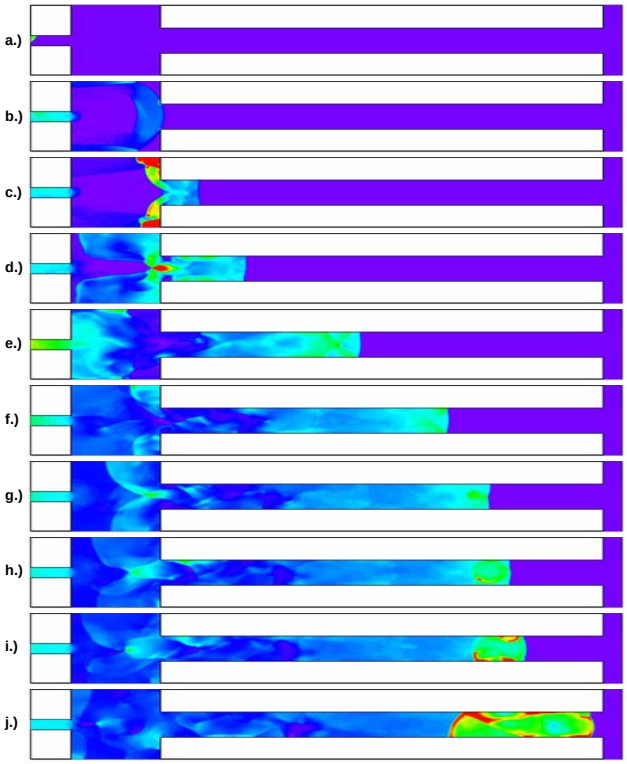

Figure 4. Sequential pressure images of weak ignition and subsequent DDT event in CFD model of cavity geometry.

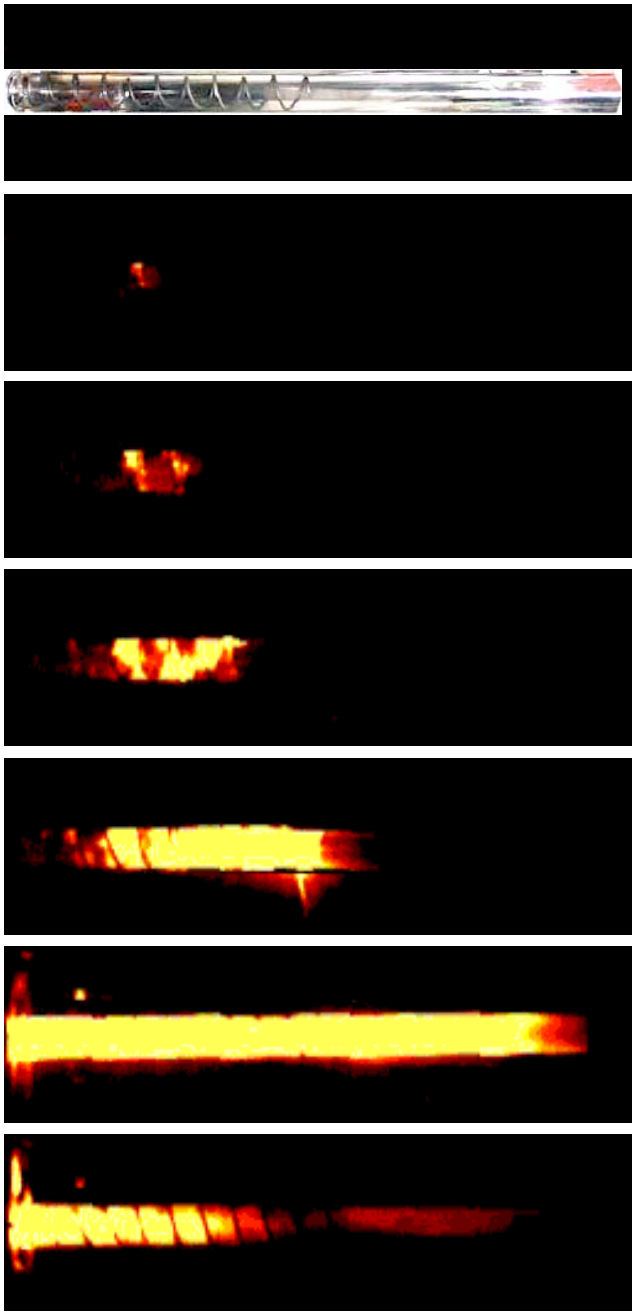

Figure 5. High speed digital imaging of deflagration to detonation transition process with Schelkin spiral in polycarbonate tube. From top to bottom: still of polycarbonate tube with Shelkin spiral, formation of hot spot, formation of multiple hot spots, micro explosion, DDT event, subsequent right running detonation and left running retonation, and in the last frame: left running expansion wave during blow down process.

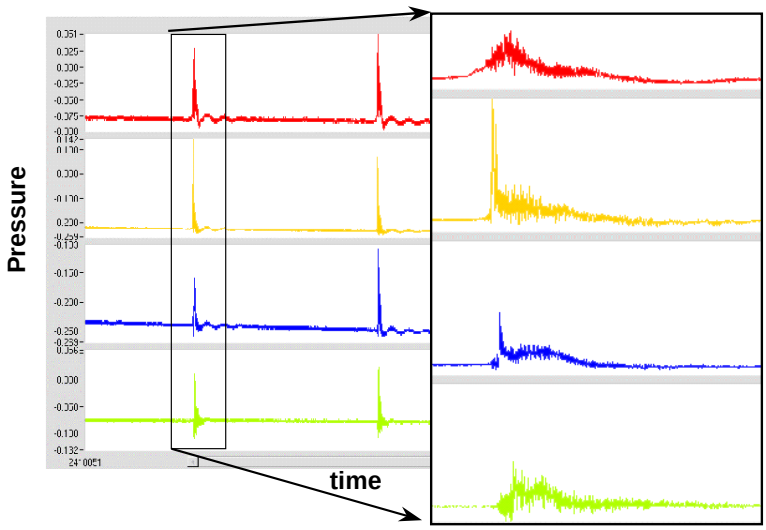

Figure 6. High frequency pressure traces from in-house PDE engine at 16 Hz detonation frequency. Measurement locations at 3, 15, 21, 33" (7, 38, 53, 83cm) axial distances from head; ~200 msec duration shown.

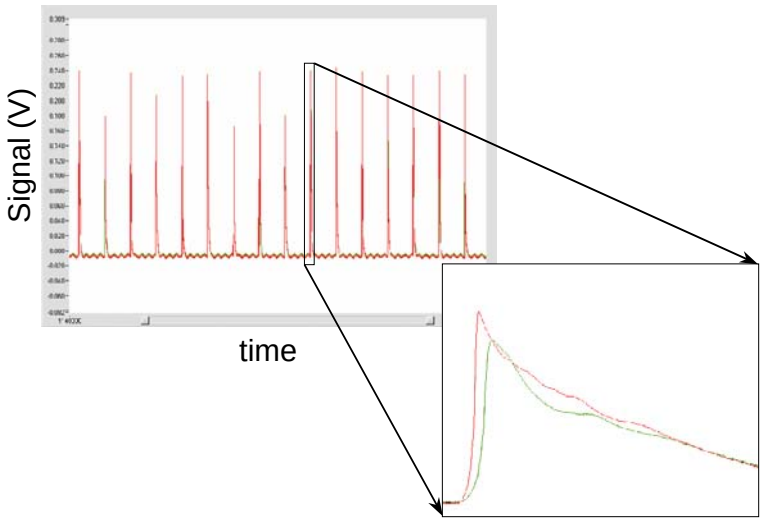

Figure 7. Photodiode measurements in PDE tube results at 27 and 33” (70 and 83cm) locations.

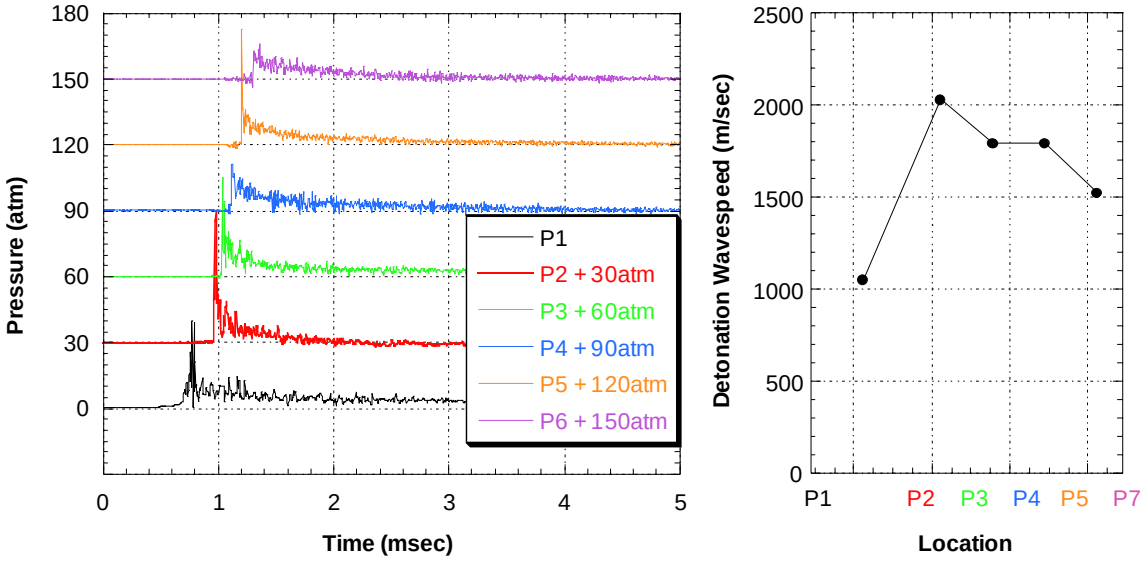

Figure 8. High frequency pressure traces from research PDE engine with aviation gasoline. Pressure transducers are distributed from near inlet to near detonator tube exit, P1 through P6 respectively. Wavespeeds on right are computed from time of flight between pressure transducers.

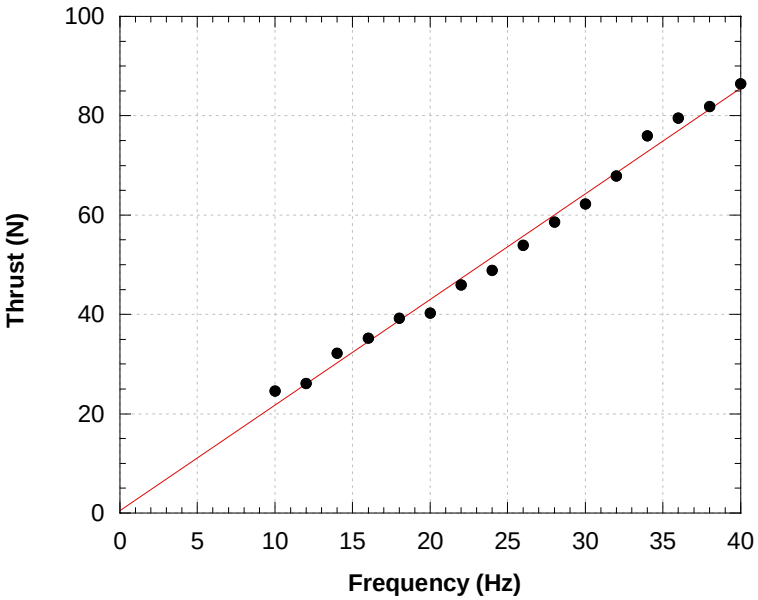

Figure 9. Thrust versus frequency.

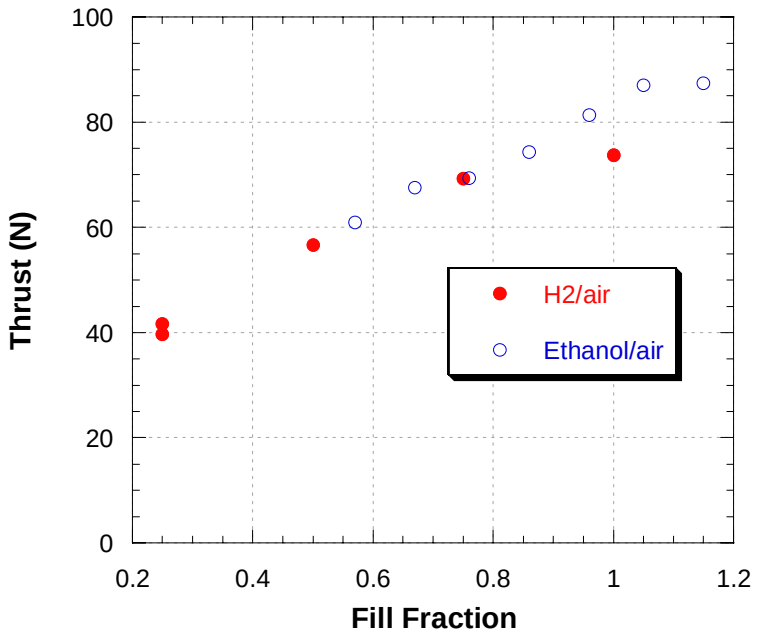

Figure 10. Thrust versus tube fill fraction for hydrogen/air and ethanol air. Fill fraction is defined as filled volume of detonable mixture divided by total tube volume.

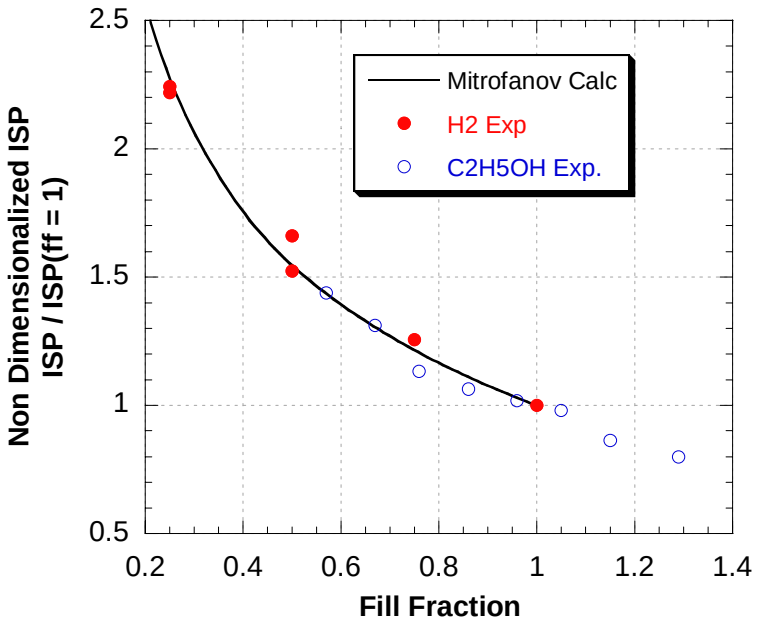

Figure 11. Effect of varying fill fraction (fueled tube length divided by total tube length) on fuel based specific impulse (non-dimensionalized by full tube fill). Experimental data is shown for hydrogen/air and ethanol/air mixtures along with the results of Mitrofanov[M].

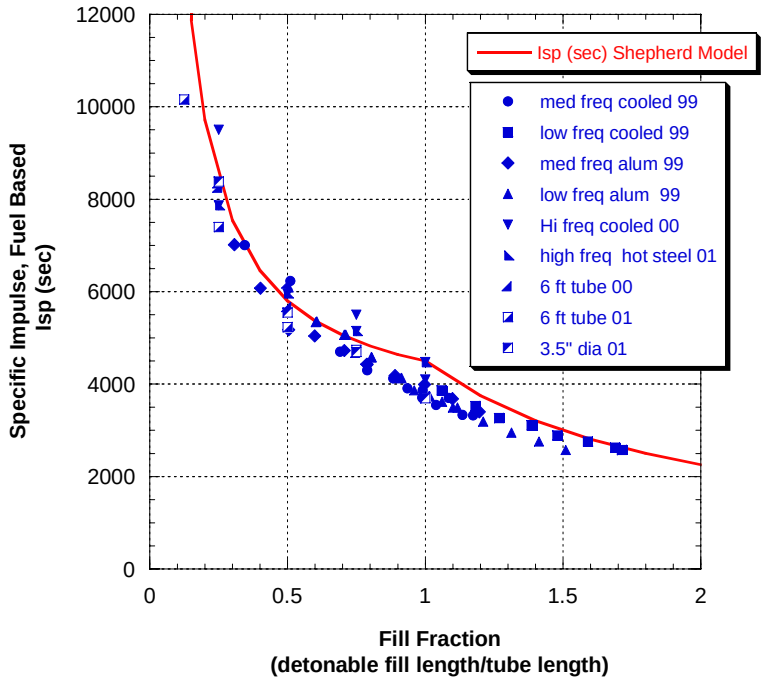

Figure 12. Variation of fuel based specific impulse versus tube fill fraction (fueled tube length divided by total tube length) for hydrogen/air. Experimental data from a variety of detonation tube sizes, wall temperatures, and operating frequencies are compared with the analytical model of Shepherd[N].

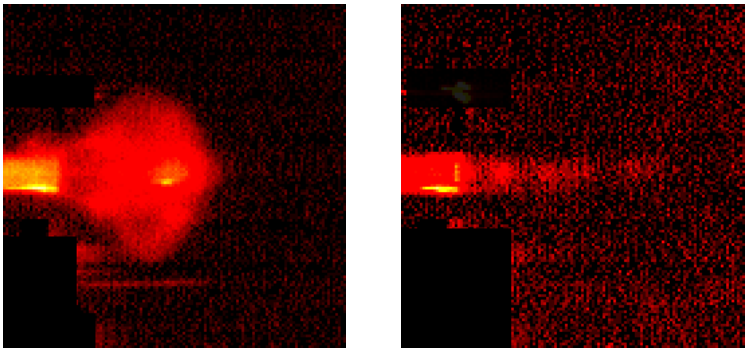

Figure 13. High speed images of detonation blow down. During blow down event on the left, a spherical compression wave and vortex roll up is evident. As a result of slight differences in operating conditions, the detonator tube imaged on the right resembles supersonic jet blow down.

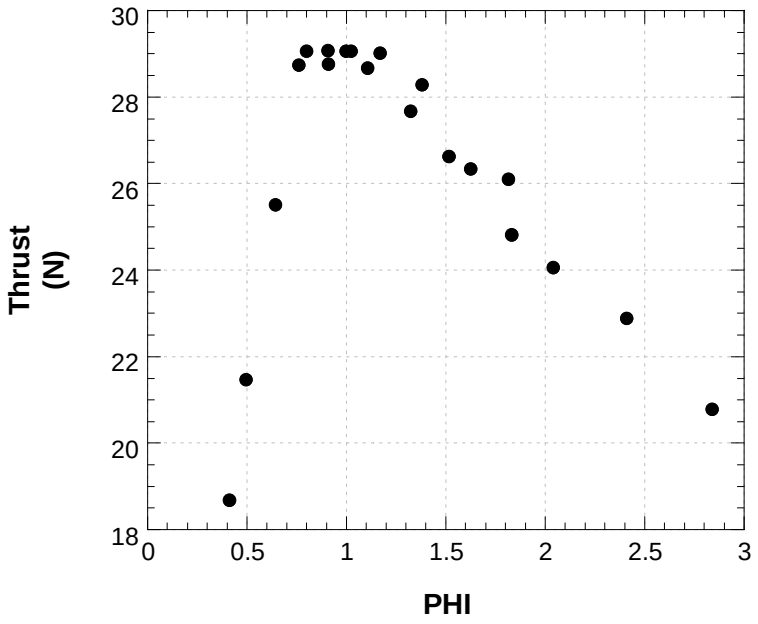

Figure. 14. Thrust versus equivalence ratio (PHI) for hydrogen/air PDE.

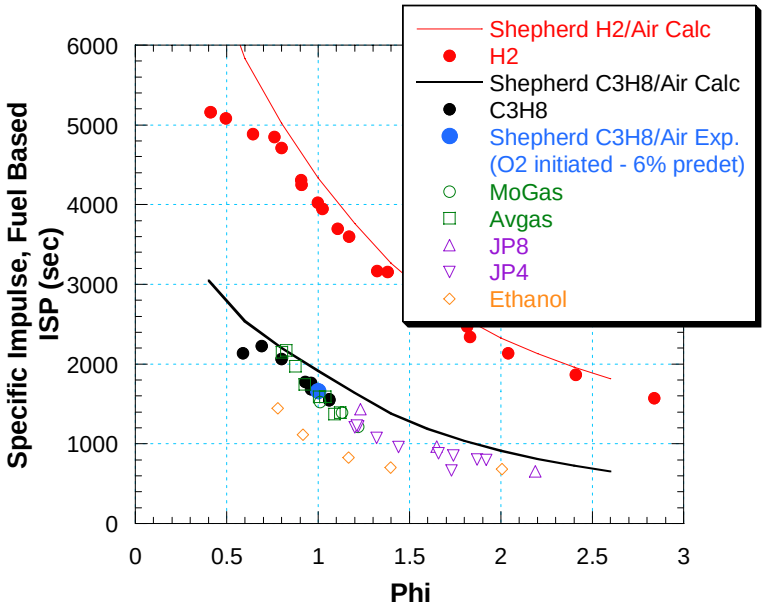

Figure 15. Fuel based specific impulse versus equivilance ratio (phi) for a variety of fuel/air mixtures. Calculations (Shepherd) and measurement of C3H8/air mixture initiated via conventional oxygen predetonator (big blue point) are provided by Shepherd[N]. All other experimental measurements were conducted with weak initiation in air. Fuels include hydrogen (H2), Propane (C3H8), 87 Octane motor gasoline (MoGas), 100 Octane low lead aviation gasoline (AvGas), standard USAF kerosene jet fuels (JP8 and JP4), and ethanol.

AIAA 2003-0891

INTERACTION OF A PULSED DETONATION ENGINE WITH A TURBINE

Fred Schauer, Royce Bradley*, and John Hoke*
Air Force Research Laboratory, Propulsion Directorate
Wright-Patterson AFB, OH 45433
*Innovative Scientific Solutions, Inc.
Dayton, OH 45440

41st AIAA Aerospace Sciences Meeting & Exhibit
6-9 January 2003
Reno, NV

**For permission to copy or to republish, contact the copyright owner named on the first page.
For AIAA-held copyright, write to AIAA Permissions Department,
1801 Alexander Bell Drive, Suite 500, Reston, VA, 20191-4344.**

AIAA 2003-0891

INTERACTION OF A PULSED DETONATION ENGINE WITH A TURBINE

Fred Schauer*

Air Force Research Laboratory, Propulsion Directorate

Wright-Patterson AFB, OH 45433

Royce Bradley and John Hoke

Innovative Scientific Solutions, Inc.

Dayton, OH 45440

Abstract

An evaluation of a pulsed detonation engine (PDE) blowing down through a turbine is presented. In previous experiments, a coupled PDE-turbocharger had demonstrated shaft power extraction and self aspiration. (**AIAA 2002-0615**). This more recent work adds additional instrumentation, configurations, and operating conditions in order to further study the detonation driven turbine. A PDE detonator tube exhaust drives a centrifugal turbine. A connected centrifugal compressor with regulated outlet pressure and measured inlet flow enables the determination of the achieved operating conditions. The turbine was spun to over 130,000 rpm and was studied at virtually all significant conditions on the turbine operating map, including such conditions as high compressor flow rates and outlet pressures. In addition, significant back-pressurization of the detonation tube was demonstrated under some operating conditions. Selected operating conditions, are compared to theoretical calculations, demonstrating high losses through the expansion throught the turbine. The turbine survived all testing despite detonation in the inlet. The turbine significantly attenuated the strength of detonation driven shocks in the exhaust nozzle.

Introduction

Because of the simplicity and efficiency, research to develop a practical pulsed detonation engine (PDE) has persisted since the early 1940's[1]. The ability to detonate practical fuels, still remains as a technology hurdle; however, great strides have been made in the last decade[2-5]. Other technological hurdles include the ability to aspirate the PDE at subsonic speeds without significantly decreasing performance and to extract auxiliary power for running accessories and exhange components. A turbine is evaluated to examine its performance when driven by detonation exhaust and to determine the ability of rotating machinery to survive and operate in the harsh supersonic environment of the PDE

Previously[6], an automotive turbo-charger (Garrett T3) was attached to a detonation tube to examine whether a compressor and turbine could be used in the harsh pulsing flow of a pulse detonation engine. Two detonation tubes were connected and fired simultaneously. The purpose of using two detonation tubes in parallel was to increase the effective valve area. A 45 deg-lateral-pipe-fitting was used to split the exhaust flow. Part of the exhaust gas flowed through the turbine and part of the exhaust gas flowed through a nozzle, see Fig 1.

The inlet of the compressor was connected to a flow meter, while the exit of the compressor was connected to the inlet of the PDE. The check valve was used to prevent air from flowing backwards from the intake manifold of the PDE through the exit of the compressor when self-aspirating.

The experimental configuration demonstrated the feasibility of utilizing a turbine in a pulsed detonation

* Author to whom correspondence should be addressed: frederick.schauer@wpafb.af.mil, (937) 255-6462 Fax: (937) 656-4570

†This paper is declared a work of the U.S. Government and is not subject to copyright protection in the United States

flow path. Further instrumentation and configurations were explored in order to quantify the turbine performance.

Experimental Setup

AFRL's research PDE at Wright-Patterson AFB was used to control the detonations. Further details on this engine, control system, and instrumentation are described in detail elsewhere[5]. A single 36" long, 2" inside diameter detonation tube was connected directly to the turbine inlet, forming an effective detonation tube of 38" length between the PDE valves and the turbine as shown in Figure 1.

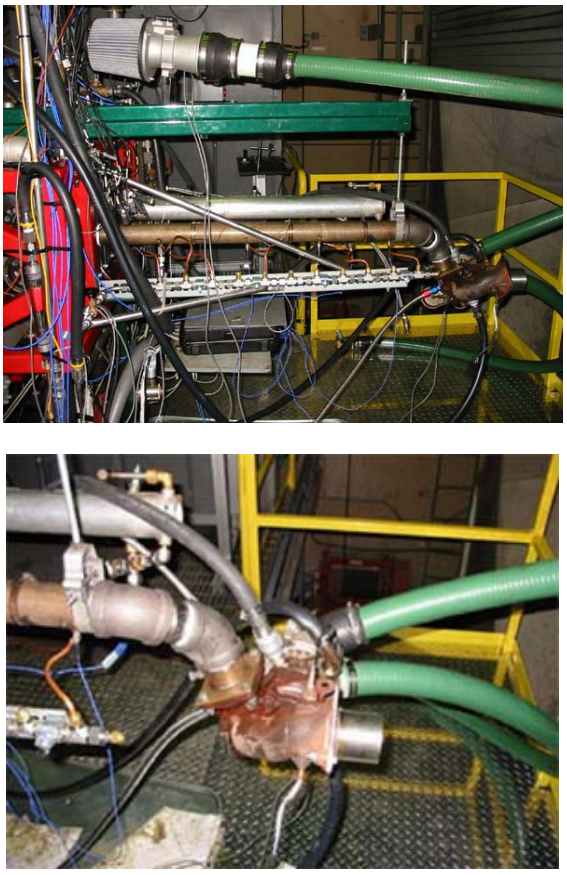

Figure 1. Photo of turbine/compressor experiment with research PDE and detonator tube connected directly to turbine. Lower photo shows detail of detonator tube entering turbine and mount for nozzle extensions (nozzle not installed). Green hoses are plumbing for compressor mass flow sensor on inlet (just down-stream of intake filter in top of upper photo) and connection of pressure regulator on compressor outlet.

Dynamic pressure transducers were located down the length of the detonation tube and beyond the turbine as indicated in Table 1. In a addition, a static pressure transducer was located near the head (P7 or trace 7) in the hopes of accurately measuring the initial pressure.

Location (in)	Label (Description)
-0.857	P1 (Detonator Tube Head)
3.75	P7 (Static Pressure near Head)
18.75	P2 (Detonator Tube)
24.69	P3 (Detonator Tube)
31.06	P4 (Detonator Tube)
37.06	P5 (Turbine Inlet)
38.75	Turbine Location
61.75	P7 (Turbine Exit)

Table 1. Location of pressure transducers.

The compressor outlet was not connected to the PDE inlet, but was dumped via a bleed valve in order to regulate compressor pressure ratio. The compressor flow was measured upstream of the compressor with a mass air flow sensor[6].

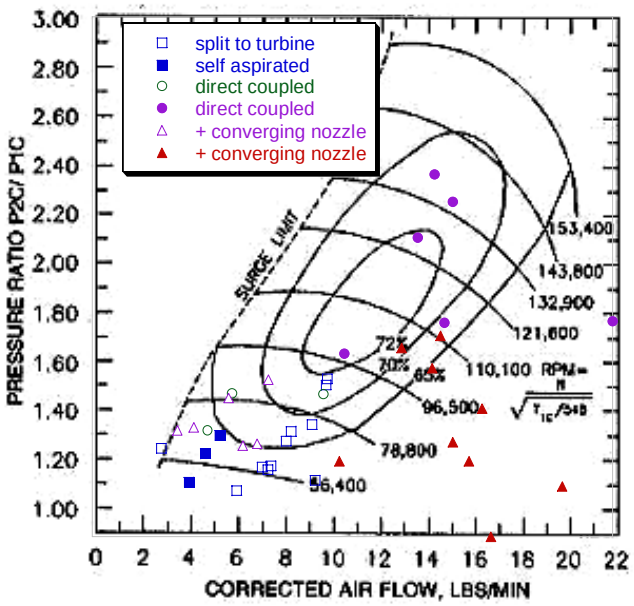

Figure 2. Compressor operating map with points achieved during testing. Filled triangles are points presented in detail.

As indicated in the compressor operating map shown in Figure 2, a wide variety of turbine/compressor operating conditions were obtained, including high flow rates, high compressor pressure ratios, and up to 135,000 rpm. The turbine relief valve was disabled so that the detonating flow was forced through the turbine. The points denoted by filled triangles will be analyzed in further detail. The remaining points include, the bypassed turbine configuration and self-aspiration discussed

elsewhere6, and additional direct connect tests which included various extensions and nozzles on the turbine exit. A preponderance of data drives the need to limit the data presented to the 9 points indicated in Table 2. All points were collected with stoichiometric hydrogen/air mixture.

Run (with Turbine)	freq	Tube Fill	Initial Pressure ~ psig	Thrust lbf	Compressor Flow lb/min	Compressor Pressure Ratio
1	20	1.0	9	3.72	16.86	1.05
2	20	2.0	24	8.81	15.94	1.29
3	30	1.0	8	6.44	10.45	1.29
4	30	2.0	11	12.53	13.08	1.73
6	40	1.0	14	8.36	19.87	1.19
7	40	1.0	13	8.94	15.24	1.36
8	40	1.5	16	13.92	16.49	1.49
9	40	1.5	22	13.98	14.37	1.65
10 (no nozzle)	40	1.5	12	12.05	14.72	1.77

Table 2. Operating conditions anaylyzed in this paper.

The indicated tube fill fraction assumes the detonator tube is completely filled to the turbine with detonable mixture at STP and does not take into account initial pressure variations. Thus, the tube fill fraction is an indcator of SCFM, and must be corrected to reflect ACFM and actual fill fraction accurately. The initial pressure as approximated in Table 2 may be used to find the actual fill fraction. However, the fill process is highly dynamic, and the initial tube pressure for each cycle is a function of time and location. In addition, previous measurements have indicated reactants do not flow down the tube smoothly without significant mixing with purge and/or exhaust products[7].

Except for run 10, the presented data was obtained with a 12” extension on the turbine outlet with a converging nozzle of 1.5” inside diameter with a short aspect ratio (consisting of a bell-mouthed pipe reducer screwed into a 12” nipple which was welded on a flange abutting the turbine exit). Run 10 is identical to the other geometries except the converging nozzle was removed.

Experimental Results

The data from each of the 10 runs discussed above, was reduced using the methods described elsewhere[8]. Results include pressure histories, wavespeeds, thrust, and compressor power output.

Shown in figure 3 are pressure traces from run 10. The traces are offset by 300psig for each location in order to clarify the detonation dynamics. Each of the other runs indicated similar results; generally: deflagration transistions to detonation befroe transducer location P2, and the resulting Chapman-Jouget detonation propagates to or near the turbine inlet. A backwards-propagating shock is observed as the relection of the detonation off the turbine. Only weak pressure rise is observed downstream of the turbine (P6).

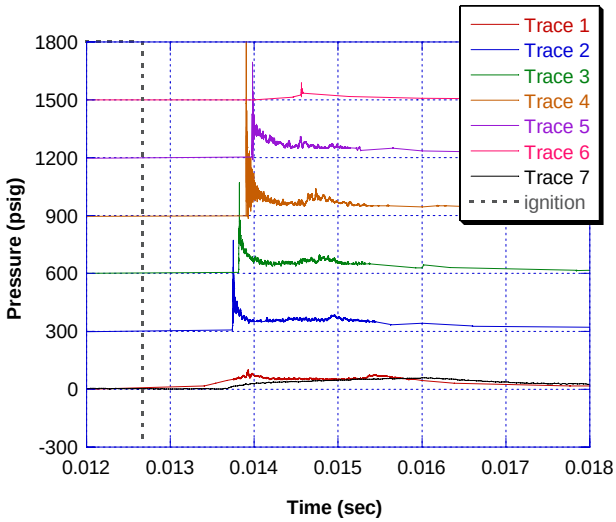

Figure 3. Pressure traces for run 10, showing detonation, schok reflection from turbine, and blow down. Note weakened shock beyond turbine exit (trace 7).

Wavespeeds are plotted versus location in Figure 4 for both runs 1 and 9 (runs 8, 9, and 10 were similar). From Table 2, it is readily apparent that the initial pressure during run 1 was higher than STP, resulting in the indicated fill fraction of 1.0 producing an under-filled condition. This may be the cause of the sub-Chapman-Jouget wavespeed shown near the turbine exit. Wavespeeds can be noted to fall off rapidly beyond the turbine location which is denoted via the dashed line and with the ‘TC’ label.

A closer look at head pressure traces reveals differences between the static (P7) and dynamic (P1) transducer measurements in Figure 5. The differences here are a result of the AC nature of the dynamic transducer, and the slow response time (kHz) of the static transducer. The static pressure transducer lags but maintains a quantitative voltage throughout the cycle, and perhaps measures some low frequency components that the dynamic measurement does not. The minimal difference in location (~ 4”) should not be a cause of trace differences at the plotted time scales. A complete PDE cycle is shown, with the sharp rise in pressure indicating arrival of the retonation wave, followed by detonation blow down, and the second and third smaller humps revealing the purge and fill cycles respectively. The fill

cycle continues on the next PDE cycle, as shown when it is followed back to the beginning of the plotted cycle.

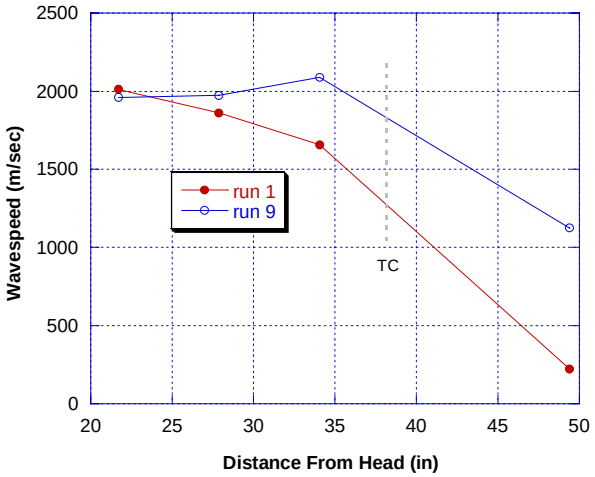

Figure 4. Wavespeed versus location for two operating conditions. Location of turbine is indicated by dashed line denoted 'TC'.

From the static transducer results, it is evident that the initial pressure before detonation varies from 5 to 18 psig in the 5 msec before detonation initiation. This is a source of uncertainty in a meaningful ACFM for calculating the real fill fraction of table 2. From spark to detonation initiation is on the order of 2 msec, making it difficult to know the actual fill pressure and mixture levels. Consequently, the fill fraction is calculated for SCFM as discussed above. Little effect upon the detonation was noted as a result of increased initial pressures other than perhaps a slight increase in pressures and wave speeds.

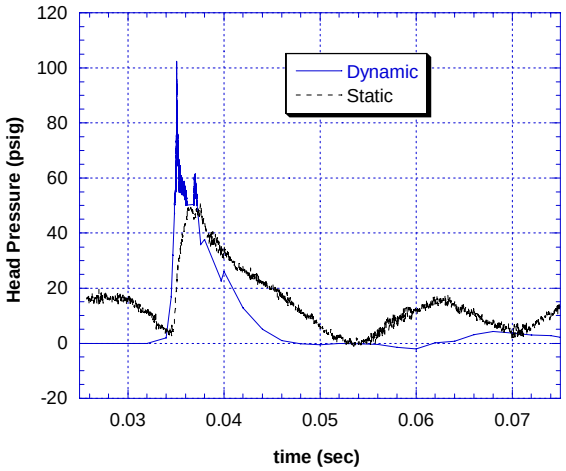

Figure 5. Dynamic and static head pressure transducers versus time.

One would expect that detonation blow times would be prolonged with the introduction of a turbine and nozzle to the detonator tube exit. The dramatic rise in blow down time is observed in Figure 6 where the detonation driven turbine blow down time is comparted with the blow down times from several other geometries. The simple PDE is similar to the geometry that would be present if the turbine and aft were removed. The PDE with straight extension (here a 2' extension was used to provide a similar overall length to the PDE-turbine geometry) can be compared to the effect of adding additional length post-turbine, but without the flow interactions of the turbine.

The turbine impedes the blow down in a manner similar to a contracting nozzle which tripled the blow down time for the 2:1 contraction presented here. However the detonation blow-down time of the PDE driven turbine extends into the fill cycle (after 17 msec for the 20 Hz detonations shown here), resulting in back pressurization. The back pressurization is observable via the higher than ambient initial pressures of Table 2. Note the differences in back- pressurization between runs 9 and 10 which have different exit areas only. The exit areas are significantly larger than the effective turbine flow area so it the sensitivity to exit area is suprising.

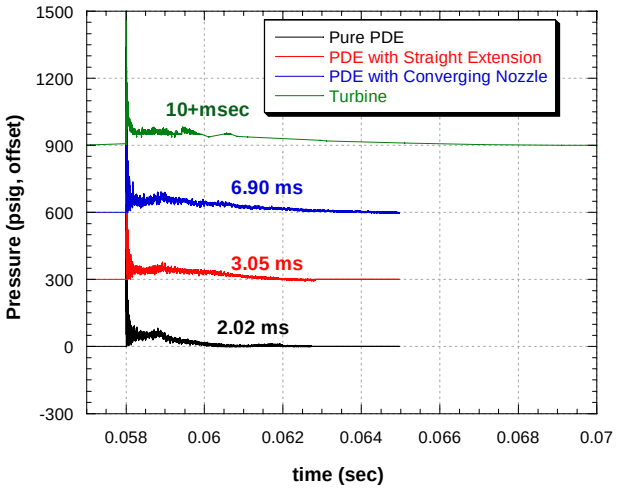

Figure 6. Detonation pressure blow down times for PDE, PDE with straight extension, PDE with 2:1 converging nozzle, and PDE exhausting through turbine.

In addition to the head pressures, the exit pressures provide some indication of the interaction of the turbine with the detonation process. Instead of the usual ~30 atm shock moving down the exit region, the turbine attenuates the shock. Peak turbine exit pressures and wavespeeds are in Table 3 for each run condition, as well as compared for extreme cases in figure 7 for runs 1 and 9. Again run 1, with a lower effective fill fraction due to

back-pressurization, has a weaker interaction with the turbine and a resultant weaker exit pressure wave. Even the stronger pressure waves of run 9 have significantly degraded from Chapman-Jouget conditions in going through the turbine.

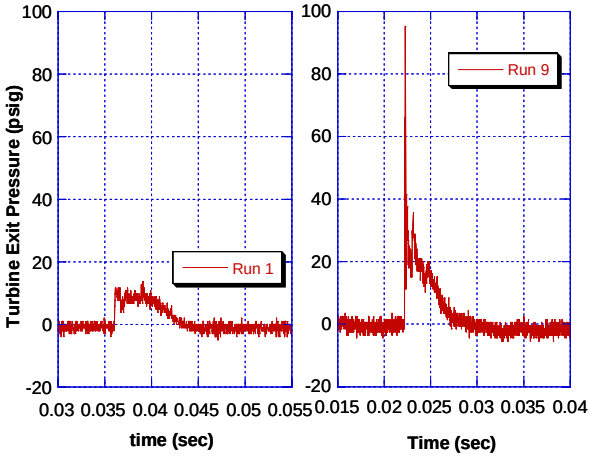

Figure 7. Turbine exit pressure profiles for two run conditions.

Performance Analysis

Performance values contained in Table 3, consisted of straightforward analysis of the PDE thrust[9,10] along with classical analysis of the steady compressor (Van Wylan and Sonnttag[11] among others). Heating value is from Povinelli and Yungsters' recent work which assumes recombination reactions[10]. The 'no turbine' PDE data point included at the bottom of Table 2 is from experimental data from the same engine with a conventional detonation tube which has been validated against various models [5,10].

The 'ideal' PDE performance assumes perfect isentropic expansion of the Chapman-Jouget conditions to the thrust wall and then to ambient conditions. Such an engine would require a loss-less 'rubber nozzle' and therefore no actual performance parameters are included for this idealized case.

Despite the same theoretical expansion of the detonation pressure through the turbine and for producing pure thrust, the performance is quite different. Even accounting for the 60-75% efficiency of the turbine/compressor in the total work, the overall efficiency of the detonation blowdown drops by a factor of ~ 4 when driving a turbine as opposed to making pure thrust (for all cases compared to the 'no turbine' PDE).

Run (with Turbine)	freq	Tube Fill	ST lb/lb/sec	ISP sec	Compressor Work kW	Total Work kW	Combustion Heat Release kW	Thermal Efficiency %
1	20	1.0	44	1526	0.5	4.5	120.4	3.7%
2	20	2.0	52	1807	2.7	14.3	240.8	5.9%
3	30	1.0	51	1761	1.8	10.0	180.6	5.5%
4	30	2.0	50	1713	5.0	21.2	361.3	5.9%
6	40	1.0	50	1715	2.3	12.7	240.8	5.3%
7	40	1.0	53	1834	3.2	15.3	240.8	6.4%
8	40	1.5	55	1903	4.5	23.8	361.3	6.6%
9	40	1.5	55	1911	5.0	24.6	361.3	6.8%
10 (no nozzle)	40	1.5	48	1648	5.9	21.4	361.3	5.9%
No Turbine								
PDE	40	1.0	119	4104		53.7	240.8	22.3%
Ideal								53.5%

Table 3. Performance results for PDE driving turbine, PDE with no turbine, and ideal pulsed detonation cycle.

Although the detonation driven turbine performance was poor, there is cause for optimism. Turbines such as the Garrett T3 were never designed to operate in such an environment. Fully developed detonations were propagating directly into the turbine inlet and yet the turbine still functioned despite 50,000+ detonations. No visible pitting or discoloration is visible as shown in Figure 8.

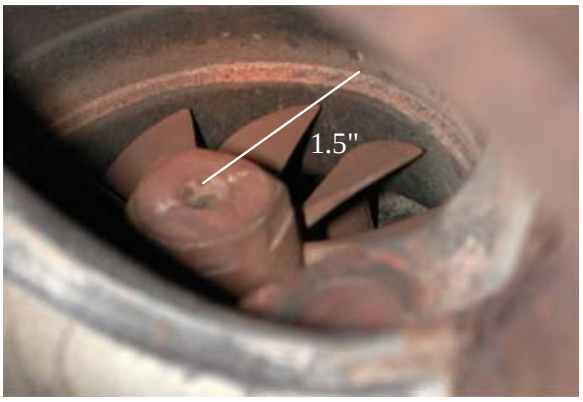

Figure 8. Turbine after 50,000+ detonations.

Summary and Conclusions

A Garret T3 turbine was driven by a pulsed detonation engine in order to simultaneously extract shaft power and produce thrust. The turbine was spun to over 130,000 rpm and was studied at virtually all significant conditions on the turbine operating map, including such conditions as high compressor flow rates and outlet pressures. In addition, significant back-pressurization of the detonation tube was demonstrated under some operating conditions. Selected operating conditions, are compared to theoretical calculations, demonstrating high losses through the turbine stage expansion. The turbine survived all detonation driven operation despite detonation in the inlet. The turbine significantly attenuated the strength of detonation driven shocks in the exhaust nozzle.

Acknowledgments

Appreciation is expressed to the technicians and facility personnel who made this work possible, particularly Jeff Stutrud. We also would like to recognize the technical leadership of Dr. Mel Roquemore and Dr. Robert Hancock (AFRL/PRTS). This work was performed under funding from AFOSR and AFRL.

References

1. Proctor, P., "Pulse Detonation Technologies Advance". *Aviation Week and Space Technology*: p. 48(1998).

2. Brophy, C.M., D. Netzer, and D. Forster. "Detonation Studies of JP-10 with Oxygen and Air for Pulse Detonation Engine Development". in *34th Joint Propulsion Conference*. Cleveland: AIAA (1998).

3. Eckett, C.A., J.J. Quirk, and J. Shepherd, *The Role in Direct Initiation of Gaseous Detonations*. 2000.

4. Santoro, R.J. "PDE- Progress and Challenge". in *The 2001 Technical Meeting of the Eastern States Section of the Combustion Institute*. Hilton Head, SC (2001).

5. Schauer, F., J. Stutrud, and R. Bradley. "Detonation Initiation Studies and Performance Results for Pulsed Detonation Engine Applications". in *39th AIAA Aerospace Sciences Meeting and Exhibit*. Reno, NV (2001).

6. J. Hoke, R. Bradley, J. Stutrud, and F. Schauer, "Integration of a pulsed detonation engine with an ejector pump and with a turbo-charger as methods to self-aspirate," **AIAA 2002-0615**, Reno (2002).

7. Brown, M.S., "Emission and absorption based sensors for the pulsed detonation engine," *Turbine Engine Technology Symposium*, Dayton Ohio (2002)

8. Parker, J. and Schauer, F., "Data analysis and compression algorithms for megabyte-data PDE experiments," **AIAA 2002-892**, Reno (2002).

9. Dyer, R.S., and Kaemming, T.A., "The thermodynamic basis of pulsed detonation engine thrust production," **AIAA 2002-4072**, Indianapolis (2002).

10. Povinelli, L.A., and Yungster, S., "Thermodynamic cycle and CFD analysis for hydrogen fueled air-breathing pulse detonation engines," **AIAA 2002-3629**, Indianapolis (2002).

11. Van Wylen, G. and Sonnttag, R., *Fundamentals of Classical Thermodynamics*, John Wiley and Sons, New York (1985).

AIAA 2003-6486
HEAT TRANSFER AND THERMAL MANAGEMENT IN A PULSED DETONATION ENGINE

John Hoke[*] Royce Bradley[*], and Frederick Schauer
Air Force Research Laboratory, Propulsion Directorate
Wright-Patterson AFB, OH 45433
[*]Innovative Scientific Solutions, Inc.
Dayton, OH 45440

41th AIAA Aerospace Sciences Meeting & Exhibit
6-9 January 2003
Reno, NV

For permission to copy or to republish, contact the copyright owner named on the first page.
For AIAA-held copyright, write to AIAA Permissions Department,
1801 Alexander Bell Drive, Suite 500, Reston, VA, 20191-4344.

AIAA 2003-6486

HEAT TRANSFER AND THERMAL MANAGEMENT IN A PULSED DETONATION ENGINE

John Hoke and Royce Bradley
Innovative Scientific Solutions Inc
2766 Indian Ripple Rd
Dayton, OH 45440

Frederick Schauer
Air Force Research Labs
Wright-Patterson Air Force Base
Dayton, OH 45433

Abstract

The unsteady nature of the Pulsed Detonation Engine (PDE) cycle creates a thermal environment fundamentally different from steady flow cycles. Gas velocities in a detonation tube range from O(-1) to O(1000) within a single cycle. This broad range of velocities and flow reversal make it difficult to determine analytically the contribution to the heat load from the purging, filling, detonating, and blow down portions of the cycle. In this paper, the overall heat load on a detonation tube is measured calorimetrically in an aluminum water-cooled detonation tube. The effects of operating parameters such as fill fraction, purge fraction, ignition delay, equivalence ratio, and cycle frequency are examined. Equivalence ratio and cycle frequency are found to have the largest effect on detonator tube heat load.

Introduction

Questions have arisen as to the thermal load of a pulsed detonation engine (PDE). Lower heat loads than experienced in conventional turbines are expected since the detonating portion of the cycle is relatively short; however, the temperatures and velocities of the flow during this period are higher than in conventional devices and potentially lead to higher heat loads. In this paper, heat-loads on the detonator tube of a PDE under several different operation conditions are experimentally measured and presented. Previously, Eidelman *et al*. (2001) have performed numerical simulations to determine the transient temperature profile, the rise time and steady state temperature along the detonation tube. Ajmani and Breisacher (2002) have modeled the heat flux to a detonator tube and present several measurements using heat flux gauges. Here, the overall heat load on the detonator tube is measured calorimetrically, while tube wall temperatures are measured in separate experiments using thermocouples spot-welded to the detonator tube.

Experimental Apparatus and Procedure

Experiments were performed on a 36" (0.91m) detonation tube at the Air Force Research Lab's Pulsed Detonation Research Facility. This facility was described in detail by Schauer *et al*.(2001), and only the details pertinent to this study are given here. The experiments were conducted with a spark-ignited hydrogen-air PDE. The cycle of the research Pulsed Detonation Engine (PDE) was divided into three temporally equal portions: i) detonation window, a third of the cycle is allotted for detonation initiation and blow-down. Depending on the cycle frequency, a portion of the time in this window was unused. ii) purge process, a third of the cycle was used to pump air into the detonation tube to separate the exhaust products from the pre-mixed fuel-air charge and to cool the internal geometry. iii) fill process, during the last third of the cycle, a pre-mixed charge of fuel and air was pumped into the detonation tube.

The fuel and airflow into the detonation tube were measured using a choked nozzle and choked orifices respectively. The flow rates were actively controlled by measuring the flow rate and adjusting the pressure upstream of the measuring devise to achieve the desired flow rate. The desired flow rates were calculated from the detonation tube volume, operating frequency and atmospheric pressure. With the flow control system, the equivalence ratio (ϕ), tube fill fraction (FF), and purge fraction (PF)

could be adjusted with the engine running. The FF and PF are defined as the fraction of the detonation tube volume filled during the filling and purging process respectively.

A water-cooled detonation tube was constructed by inserting the 2"schedule 40 aluminum detonation tube into a 2.5" schedule 40 aluminum tube of similar length. The tubes were oriented to be concentric and the space between the tubes at either end was welded closed. Water entered the cavity between the two concentric aluminum tubes at the head end of the detonation tube and exited at the tail of the detonation tube. Type T thermocouples inserted in the water flow were used to measure the inlet and exit temperatures of the cooling water. The water flow rate was measured by a rotometer. The heat load on the detonation tube could then be calculated. The absolute error in the heat load calculated was approximately 15% due to measurement error, conduction losses and convection losses from the outer water jacket. The relative error between experiments was much less being dominated by the measurement errors and was less than 7%.

Thermocouples were also used on un-cooled detonation tubes to determine thermal rise time and equilibrium temperatures. The thermocouples were spot-welded at intervals along the detonation tube. Accuracy of the high temperature thermocouple measurements was estimated to be ± 50 °F.

Experimental Results and Analysis

The effect of frequency, fill fraction, ignition delay, equivalence ration and purge fraction on the overall heat load was investigated. The equivalence ratio was found to have the largest impact on detonator tube heat load, see Fig. 1. The heat load at 20 Hz increased almost linearly from 0 to 21.8 kW as the equivalence ratio was increased from 0 to 1. Below an equivalence ratio of 0.5 it became increasingly difficult to achieve a detonation in the 36" (.91 m) detonation tube using a deflagration to detonation transition and the heat load measured was lower than that predicted using the measurements recorded at higher equivalence ratios. Experiments were not conducted above an equivalence ratio of one.

The influence that frequency has on heat load is shown in Fig. 2. Note that unlike thrust, doubling the frequency from 20 to 40 Hz does not double the detonator tube heat load but only increased the heat load by 58%. As the frequency increases the number of detonations

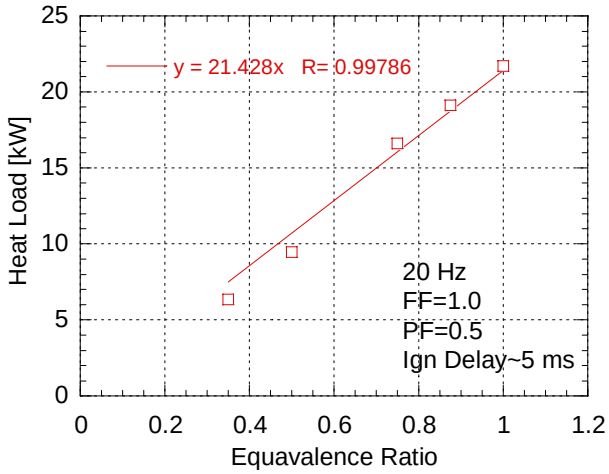

Figure 1 Heat load verses equivalence ratio, 36" (.91m) detonation tube

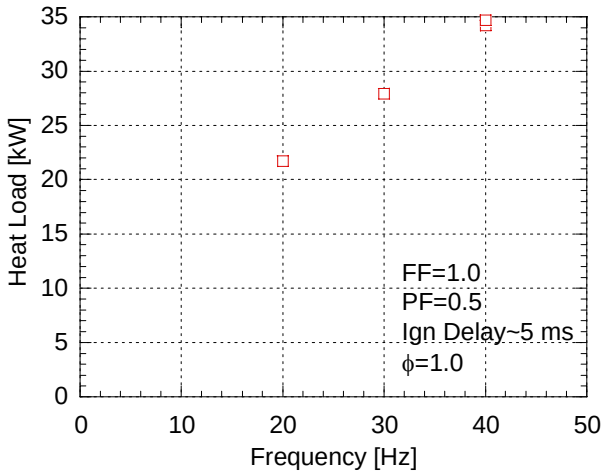

Figure 2. Heat load verses frequency, 36" (.91m) detonation tube

increased but the time for each portion of the cycle was fixed, and the time that the exhaust products (after blow-down) remained in the detonator tube decreased with increasing frequency. Additionally, the average velocity of the fill and purge increased with increasing frequency. For fully developed flow in a smooth pipe, the heat transfer coefficient increases by velocity to the 0.8 power according to the Dittus-Bolter correlation (White 1988). Therefore, at the higher frequencies, the purge and fill process would be more effective at removing heat from the detonation tube. Because of the developing boundary layer, the heat transfer coefficient was

expected to be significantly higher than that predicted by Dittus-Bolter. The heat flux during the fill and purge process was not measured in these experiments.

Decreasing the fill fraction of the detonation tube decreases the heat load; however, since the exhaust products must exit through the unfilled portion of the detonation tube, the decrease in heat load was not as pronounced as that found for equivalence ratio. If Fig. 3, the heat load on the detonation tube is shown to decrease by only 19% between a fill fraction of 1 and 0.5. At a fill fraction of 0.5, the PDE was consuming half of the fuel that it would be consuming at a fill fraction of 1, and 14% less fuel than it would consume at an equivalence ratio of 0.5 and a fill faction of 1. Even though the PDE was using 14% less fuel at a fill fraction of 0.5 than it was at an equivalence ratio of 0.5 and a full fill fraction, the fuel distribution in the detonation tube created a 62% difference in heat load. The lower fuel consumption condition of FF=0.5, ϕ =1 had the higher heat load. The majority of this difference was attributed to the theoretically lower exhaust temperatures of the 0.5 equivalence ratio condition.

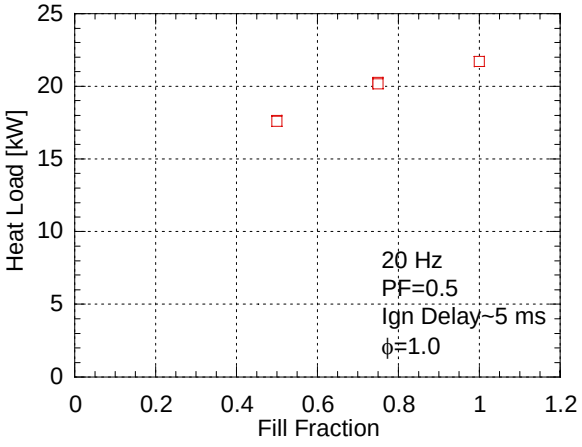

Figure 3. Heat load verses fill fraction, 36" (.91m) detonation tube

The purge fraction had a limited affect on tube heat load and in Fig. 4, the effect of purge faction on tube heat load is shown for two frequencies, 20 and 35 Hz. At 20 Hz, increasing the purge air from .25 to 1.25reduced the tube heat load by a kilo-watt. At 35 Hz, this effect was almost doubled and attributed to the higher purge velocities and greater purge mass flow required for the higher frequency.

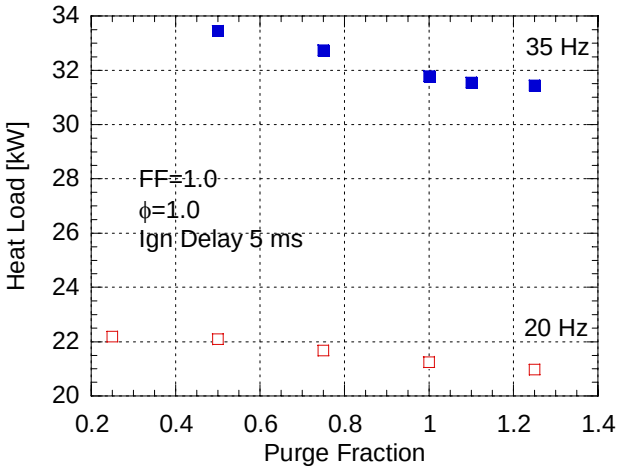

Figure 4. Heat load verses purge fraction, 36" (.91m) detonation tube

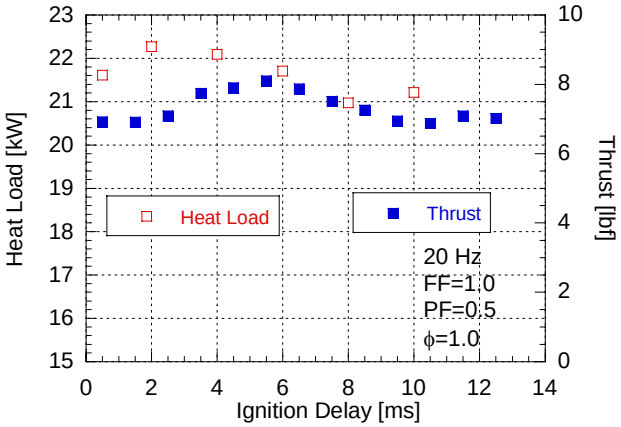

Figure 5. Heat load verses ignition delay, 36" (.91m) detonation tube

Lastly, the tube heat load was measured as a function of ignition delay. This parameter affects the time that the exhaust products remain in the detonation tube as well as the initial pressure at which the mixture was detonated, see Hoke *et al*. (2002). The heat load on the detonation tube varied approximately 1.5 kW with ignition delay, see Fig. 5. The maximum thrust occurred at an ignition delay of approximately 5 ms and the maximum heat load occurred earlier, between 2 and 4 ms. There are only small differences in the combustion temperatures with initial pressure, however, there can be a significant difference in thrust pressure. The higher thrust pressure leads to higher heat transfer however, the longer residence time of

the early ignition will also contribute to higher heat loads. Therefore, the peak of heat load occurs before the peak in thrust.

The heat load on an un-cooled detonation tube should be lower than that measured for the cooled detonation tube because the temperature difference between the exhaust gases and tube walls will be smaller. Shown in Fig.6 are outside wall temperatures along the length of a 72" detonation tube that was run to thermal equilibrium. The temperature along the detonation tube varied over 300 °F and thermal equilibrium was reached in approximately 2

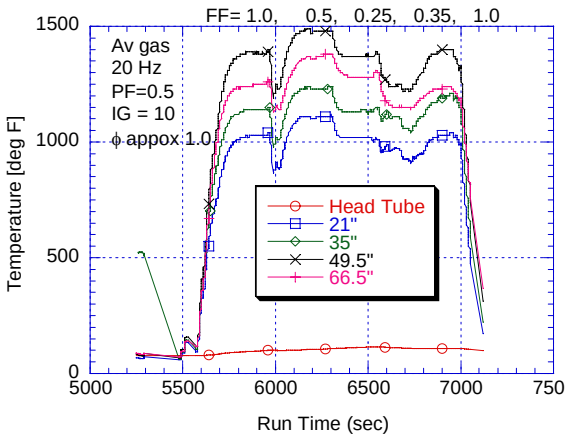

Figure 6. Detonation tube temperatures verses run time for several fill fractions, 72" (1.83m) detonation tube

minutes. The hottest region on the detonation tube occured in the region where transition from deflagration to detonation occurred. In this transition region, an overdriven detonation, with higher wave velocities, and pressures, increased the heat transfer to the tube wall. The fill fraction of the detonation was varied during this experiment and the heat load for a 72" detonation tube appeared to be higher at a fill fraction of 0.5 than at a fill fraction of 1. This was contrary to the results found for the shorter 36" detonation tube. At lower fill fractions, the peak temperatures decreased and a detonation wave was not produces since transition from deflagration to detonation occurred around 48" from the closed end of the detonation tube.

Summary and Conclusions

Although cooled-wall heat load measurements will not produce identical results to hot wall tests, the results found in this study give some indication as to the sensitivity of heat load to the significant parameters. From this study, it is evident that PDE's should be run at lower frequencies for lower heat loads; however, the heat load per unit thrust is lower at higher frequencies. Additionally, throttling of the PDE resulted in lower tube heat loads if the throttling is done by lowering the equivalence ratio rather than decreasing the fill fraction. The ignition delay or cycle of the PDE should be designed to minimize the length of time the exhaust products remain in the detonation tube after blow-down. Additionally, there are aspiration issues that encourage minimization of the time the exhaust gasses stay in the detonation tube after blow-down. Experiments with longer and larger diameter detonation tubes are planned as well as a numerical model.

Acknowledgements

Gratitude is expressed to the technicians who worked on this project: Curtis Rice, Walt Balster and Dwight Fox (ISSI). The authors would also like to thank Jeff Stutrud (AFRL/PRTS) for his computer programs used to collect and analyze the data. The technical leadership of Dr. Mel Roquemore and Dr. Robert Hancock (AFRL/PRTS) continues to be invaluable. Funding was provided by the propulsion directorate and Dr. Julian Tishkoff at AFOSR.

References

Ajmani, K. and K. J. Breisacher (2002). Qualitative Study of Cooling Methods for a Pulse-Detonation Engine. 51st JANNAF Propulsion Meeting, Lake Buena Vista, Florida, Chemical Propulsion Information Agency.

Eidelman, S., D. Sharov and D. Book (2001). The Thermal Balance of PDE. Computational Methods and Experimental Measures**:** 711-720.

Hoke, J. L., R. P. Bradley and F. R. Schauer (2002). The Effect of the Dynamic Filling Process on PDE Perfomance and Nozzle Selection. 51st JANNAF Propulsion Meeting, Lake Buena Vista, Florida, Chemical Propulsion Information Agency.

Schauer, F., J. Stutrud and R. Bradley (2001). Detonation Initiation Studies and Performance results for PDE Applications. 39th AIAA Aerospace Sciences Meeting and Exhibit, Reno, AIAA.

White, F. M. (1988). Heat and Mass Transfer. New York, Addison-Wesley Publishing Co.

22nd AIAA Aerodynamic Measurement Technology and Ground Testing Conference
24-26 June 2002, St. Louis, Missouri

AIAA 2002-3039

OPTICAL DIAGNOSTICS FOR CHARACTERIZING ADVANCED COMBUSTORS AND PULSED-DETONATION ENGINES

James R. Gord*
Air Force Research Laboratory
Propulsion Directorate
Wright-Patterson Air Force Base OH

Michael S. Brown† and Terrence R. Meyer‡
Innovative Scientific Solutions, Inc.
2766 Indian Ripple Road
Dayton OH

Abstract

While optical diagnostic techniques have been applied with great success to the fundamental study of combustion chemistry and physics in the laboratory, the challenges afforded by real-world propulsion systems demand continuing innovation if such techniques are to be adapted and transitioned for use in engineering tests and on-board monitoring and control applications. This paper documents continuing efforts to transition aerodynamic measurement technologies from diagnostics-development laboratories to combustor test-and-evaluation facilities in the Propulsion Directorate's Combustion Science Branch (Turbine Engine Division). Applications of various optical diagnostic techniques for visualizing flowfields and quantifying temperatures and key species concentrations in several advanced combustors are described. A number of next-generation diagnostics targeted for laboratory-to-facility transition in the near future are highlighted as well.

Introduction

Propulsions systems represent a substantial fraction of the cost, weight, and complexity of Air-Force aircraft, spacecraft, and other weapon-system platforms. The vast majority of these propulsion systems are powered through combustion of fuel; therefore, the detailed study of combustion has emerged as a highly relevant and important field of endeavor. Much of the work performed by today's combustion scientists and engineers is devoted to the task of improving propulsion-system performance while simultaneously reducing pollutant emissions. Increasing the affordability, maintainability, and reliability of these propulsion systems is also a driver of activity.

While improved performance can be described quantitatively in many terms (*e.g.*, specific fuel consumption, thrust-to-weight ratio, etc.), it often involves efforts to increase heat release during the combustion process. Improvements may be achieved as well by reducing the length and/or weight of the combustor through informed design decisions. Engine emissions that might adversely impact the environment and the military signature of Air-Force systems must be reduced while striving to improve performance. Judicious design and control of the combustor can significantly impact the affordability, maintainability, and reliability of the propulsion system by extending the useful life of engine components or by permitting the incorporation of less-expensive materials in combustor construction, for example. Pursuing these goals requires a thorough understanding of the fundamental physics and chemistry of combustion processes.

The Combustion Science Branch of the Air Force Research Laboratory's Propulsion Directorate (Turbine Engine Division) has adopted a philosophy for combustor-technology development aimed at achieving these goals. At the basic-research level, new diagnostic approaches are developed and tested in conjunction with extensive modeling-and-simulation efforts. Techniques are "cross-validated" through studies of fundamental combustion processes in laboratory rigs that provide favorable optical conditions while remaining computationally tractable. Axisymmetric burners with ample optical access and well-defined boundary conditions represent such test articles. The

*Principal Research Chemist, Associate Fellow AIAA
†Physicist, Senior Member AIAA
‡Research Engineer, Member AIAA

This material is declared a work of the U.S. Government and is not subject to copyright protection in the United States.

measurement and computational tools designed, tested, and matured through this basic research are applied subsequently to hardware testing and evaluation. Ultimately, sensor platforms based on these diagnostic approaches and algorithms derived in part from the combustion models are incorporated for on-board propulsion-system monitoring and control.

Development, demonstration, and application of laser-based and other optical diagnostic techniques are integral elements of this research plan. Advanced measurement techniques that exploit lasers and optics have become well-established tools for characterizing combustion.[1] Non-invasive measurement approaches are often ideally suited for visualizing complex reacting flowfields and quantifying key chemical-species concentrations and fluid-dynamic parameters. The fundamental information these techniques provide is essential for achieving a detailed understanding of the chemistry and physics of combustion processes. Furthermore, these data are critical for validating combustion models and combustor-design codes with tremendous potential for propulsion-system development. At a more applied level, hardened diagnostics provide the designer with performance data for the systems-engineering process. Diagnostics also promise to play an important role in fielded propulsion systems as elements in control and optimization schemes.

These characteristics of optical diagnostic techniques suggest a three-phased evolutionary process for their development and application. In the first phase, emphasis is placed on the diagnostic technique itself—on the chemistry and physics that define the measurement and the hardware (sources, optics, detectors, etc.) and software necessary to accomplish that measurement. During this phase of the process, a research-grade instrument is typically employed to study a well-characterized flowfield in a laboratory environment. While this phase of the diagnostics-development process is certainly essential and exciting, the ultimate utility of a diagnostic technique is significantly limited if it never sees application beyond the laboratory.

During the second phase of the process, a hardened version of the research-grade instrument is applied to achieving measurements in an engineering facility. The emphasis in this phase shifts from the diagnostic technique to the engineering application. In the third phase, a miniaturized and robust diagnostic device is incorporated into the final product, such as an actual gas turbine or internal-combustion engine, for on-board sensing and control.

The transitions from laboratory to facility to fielded systems are fraught with significant challenges that must be addressed. During the laboratory phase of diagnostics development, conditions are typically ideal and well controlled. They might involve vibrationally isolated laser tables, humidity- and temperature-controlled environments, and sufficient space to accommodate sources, optics, mounts, and detectors required to achieve the desired measurements. Test articles often feature ample optical access and support clean-burning, gas-fueled, laminar flames operating under atmospheric or sub-atmospheric conditions. In contrast, facilities applications involve conditions characteristic of actual engine hardware. Challenges include extreme environmental conditions (heat, vibration, acoustics, etc.), limited optical access, tight geometric constraints, little operational space, fully developed turbulence, two-phase flows, soot formation, high pressure, collisional quenching, energy redistribution, optical thickness, beam steering, high background luminosity, and scattering and spectral interferences. These challenges are amplified on moving from the facility to the on-board environment. Successful transitions, first from the laboratory to the facility and then from the facility to the field, require thoughtful attention to these issues.

This paper continues with brief descriptions of the various facilities throughout the Combustion Science Branch engaged in diagnostics development and subsequent test-cell applications. A number of advanced propulsion concepts currently under development in those facilities are highlighted as well. These include a trapped-vortex combustor (TVC), a pulsed-detonation engine (PDE), a CFM56-based model combustor, and an ultra-compact combustor (UCC). Amongst the diagnostics transitioned from the development laboratories to the test facilities are experimental methodologies for flow visualization, including high-speed digital imaging, planar laser-induced fluorescence (PLIF), particle-image velocimetry (PIV), coherent-structure velocimetry (CSV), and laser-induced incandescence (LII). Quantitative measurements of temperature and species concentrations have been achieved in the test cells with dual-pump coherent anti-Stokes Raman scattering (DP-CARS). Measurements of chemiluminescent emission have been applied for the determination of equivalence ratios. Next-generation diagnostics slated for test-cell applications in the very near future include triple-pump CARS (TP-CARS) for simultaneous determination of temperature and species concentrations, and line-of-sight absorption measurements based on the tunable output of diode-laser-based platforms that exploit various frequency-mixing schemes.

Combustion-Science-Branch Facilities

The Propulsion Directorate's Combustion Science Branch is an integral element of the Directorate's Turbine Engine Division. As such, all of the facilities

associated with the branch are considered part of the division's Turbine Engine Research Center (TERC). These branch facilities include the Combustion and Laser Diagnostics Research Complex (CLDRC), the Atmospheric-Pressure Combustor Research Complex (APCRC), the High-Pressure Combustor Research Facility (HPCRF), and the Pulsed-Detonation Research Facility (PDRF).

Combustion and Laser Diagnostics Research Complex

The CLDRC supports experimental and computational study of fundamental combustion phenomena to expand the scientific knowledge base; validate combustor-design codes; and improve the performance, reduce the pollutant emissions, and enhance the affordability, maintainability, and reliability of current and future-generation propulsion systems for military and commercial aviation. This state-of-the-art complex provides unique laboratory tools for the experimental characterization of combustion through the development, demonstration, and application of advanced laser-based/optical diagnostic techniques. These capabilities are complemented by a suite of specialized modeling and simulation methodologies for assessing and predicting the detailed chemistry and physics of combustion processes. Diagnostics developed in the CLDRC are transitioned to the other facilities for testing and evaluation of advanced propulsion-system concepts.

Atmospheric-Pressure Combustor Research Complex

The APCRC includes three separate laboratories for studies of propulsion-system performance under atmospheric-pressure conditions: 1) a well-stirred reactor (WSR) laboratory, 2) a fuel-additive-evaluation laboratory equipped with a CFM56-based model combustor, and 3) an advanced combustor research laboratory for exploring new concepts such as the TVC and the UCC. Each laboratory is fully instrumented with thermocouples, pressure transducers, and gas-sampling rakes for emissions measurements. In addition, each is configured to provide generous optical access.

The fuel-additive-evaluation laboratory is equipped to provide air flows to 45 lbm/min and heat-release rates to 500 kW. The advanced combustor research laboratory is equipped to provide air flows to 60 lbm/sec through three separate legs, heat release rates to 750-kW, and heated air temperatures to 700°F. Two independent liquid fuel systems are driven by fuel pumps rated to 417 psig that provide flow rates in the range 0.0667-0.667 gpm.

High-Pressure Combustor Research Facility

The HPCRF is designed for the experimental exploration of advanced combustor concepts under conditions simulating actual gas turbine engine operation. Like the APCRC, the HPCRF is fully equipped with test instrumentation and features ample optical access. Process and supervisory facility control is achieved by using proportional, integral, derivative (PID) controllers and programmable logic controllers (PLC's), respectively.

The HPCRF features two separate flow paths—one for sector combustor tests and another for single-nozzle combustor tests. The sector leg, which can accommodate a single- or dual-dome 60-degree arc sector or a 12-inch-wide planar combustor, is designed for combustor pressures from 2 to 325 psia with inlet air temperatures to 1200°F and air flows to 25 lbm/sec. The single-nozzle leg is designed for combustor pressures from 2 to 600 psia, with inlet air temperatures to 1150°F and air flows to 25 lbm/sec. Both legs can be configured to operate at combustor-test-section pressures as low as 0.25 atm, simulating altitudes beyond 40,000 ft.

The facility has two identical fuel systems that supply liquid fuel to each test section at rates to 6 gpm and pressures to 1000 psig. The two systems are configured to accommodate fuel for staged combustor systems operating in the facility.

Pulsed-Detonation Research Facility

The PDRF is a converted full-scale gas turbine engine research facility designed for testing hardware producing thrusts to 60,000 lbf. Like the other facilities, it features integrated remote control and instrumentation systems and affords substantial optical access for incorporation of advanced diagnostics. Pulsed-thrust measurements in the range 3-1,000 lbf are achieved with a damped thrust stand mounted to the existing engine thrust stand. Up to 6 lbm/sec of 100 psi air is available, and high-capacity inlet and exhaust stacks are useful for self-aspirating designs and atmospheric exhaust. The facility is connected directly to a liquid-fuel farm via the high-pressure/high-capacity pump that fueled past large-scale engine tests on the 60,000-lbf thrust stand.

Flow Visualization

Experimental and computational techniques for the visualization of fluid flows have emerged as essential tools for increasing our understanding of the physics and chemistry of these flows. Indeed, many—if not most—of the breakthroughs in fluid mechanics and dynamics can be attributed to the understanding achieved through imaging of the various multidimensional structures in fluid flow. High-speed digital imaging, PLIF, PIV, CSV, and LII are amongst the diagnostic tools routinely employed for two-

dimensional flow visualization in the test facilities of the Combustion Science Branch.

Flow Visualization in the Trapped-Vortex Combustor

The unique geometry of the TVC has been designed to bring improved overall performance, enhanced stability, and reduced pollutant emissions to current and next-generation propulsion systems.[2-4] It also promises benefits in terms of combustor length and pressure drop. The key features of the TVC design are evident in Fig. 1, which depicts a natural-gas-fueled TVC sector operating in the APCRC. Cavities at the top and bottom of the sector promote aerodynamic trapping of a combusting vortex. Injection of fuel and air into these cavities maintains continuous pilot flames therein, enhancing fuel-air mixing and flame stability. These trapped pilot flames interact with the main fuel-air flow situated between the two cavities.

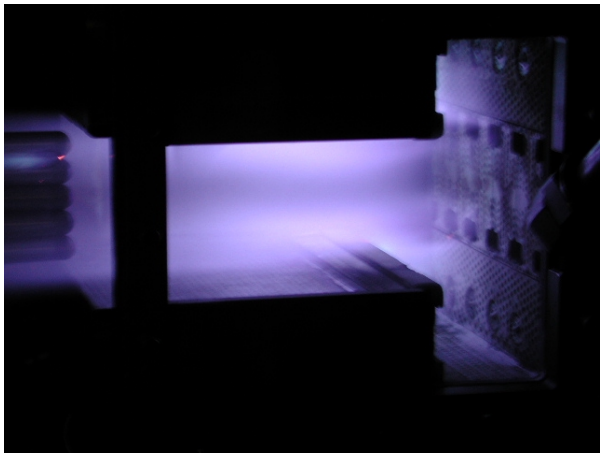

Figure 1. Natural-gas-fueled TVC sector operating in the APCRC. Flow is from right to left.

Originally conceived and explored in the Propulsion Directorate's Combustion Science Branch, the TVC has since evolved to a current research configuration under joint development by the Air Force and General Electric. Ongoing testing of various TVC sectors in the APCRF and HPCRF is aimed at establishing design rules and assessing the performance impacts of such drivers as cavity and main geometry, fuel-injector design and placement, and air flow. Enhanced mixing techniques aimed at reducing pollutant emissions and combustor size are also under study. These efforts are supported by flow visualization achieved through high-speed digital imaging, PLIF, PIV, and CSV.[4]

High-speed digital images of the TVC have been acquired using a Phantom v5.0 CMOS-based high-framing-rate digital camera available from Photo-Sonics International Ltd. During this study, the camera was operated at 11,200 frames per second (fps) with a resolution of 256×256 pixels and an exposure time of 10 μs. Frame captures of the normalized flame luminosity in a JP-8-fueled TVC sector operating at pressures of 8.5 and 12 atm are depicted in Figs. 2 and 3. These high-speed visualizations provide real-time feedback during TVC testing regarding the flow pattern and flame distribution within the cavities and main sections of the combustors. Exposure times as low as 10 μs enable flow freezing not achievable through conventional videography.

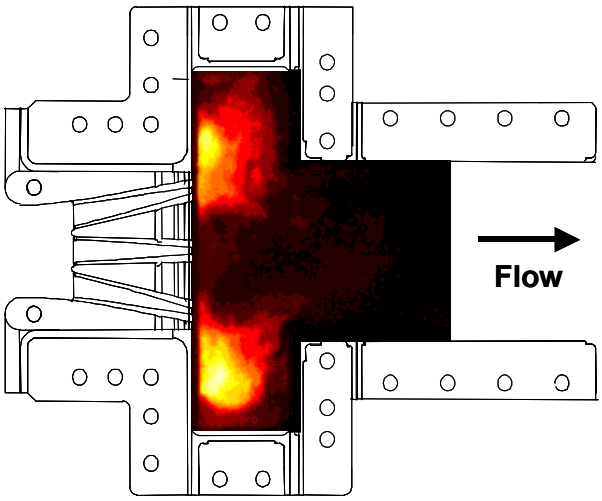

Figure 2. Flame luminosity captured with a high-speed digital camera from a JP-8-fueled TVC sector operating at 8.5 atm.

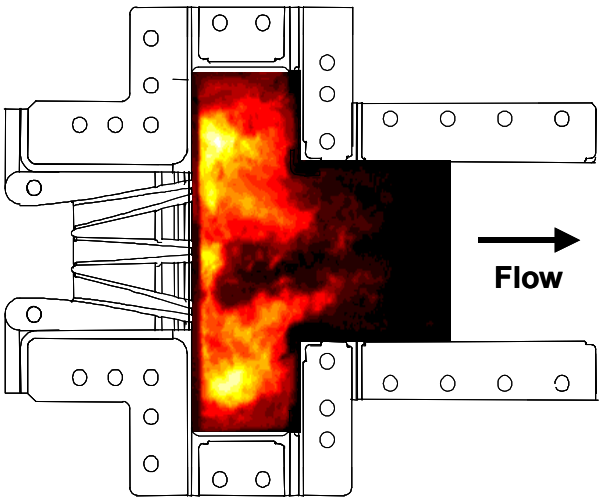

Figure 3. Flame luminosity captured with a high-speed digital camera from a JP-8-fueled TVC sector operating at 12 atm.

When viewed in a time-correlated sequence, such images clearly show vortical flame structures in the upper and lower cavities. These vortices act as flame holders that promote flame stability and enhance fuel-air mixing by increasing the turbulence level and the time available for fuel vaporization and molecular diffusion.

While high-speed digital imaging provides a qualitative description of flame location and dynamics, PLIF can be used to visualize specific flame species.[5] This yields a more accurate measurement of flame location and eliminates the spatial ambiguity associated with line-of-sight averaging. In the current work, PLIF of the hydroxyl radical (OH) was accomplished by exciting the $R_1(8)$ transition of the (1,0) band in the A-X system. The requisite 281.3414-nm laser sheet was generated using the frequency-doubled output of a Nd:YAG-pumped dye laser, and fluorescence from the A-X (1,1) and (0,0) bands was detected using an intensified charge-coupled device (ICCD) camera equipped with a UG-11 and two WG-295 colored glass filters to reduce visible and laser-scattered light, respectively.

OH-PLIF images were acquired in a natural-gas-fueled TVC sector for a number of fuel-injection configurations. The flame pattern obtained through fuel injection in the cavity and main sections is depicted in Fig. 4. Injection in the cavity alone produces the flame pattern in Fig. 5. These data are employed to verify calculations using a conventional k-ε-based CFD code with chemistry.

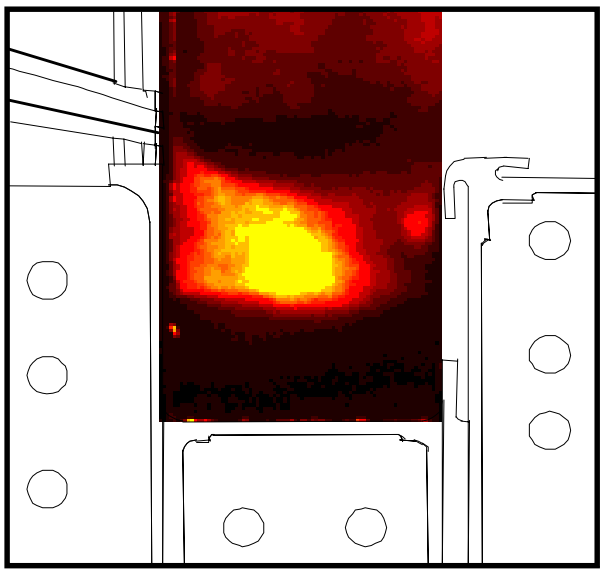

Figure 4. OH-PLIF signal obtained in the lower cavity of a natural-gas-fueled TVC with fuel injection in the cavity and main sections.

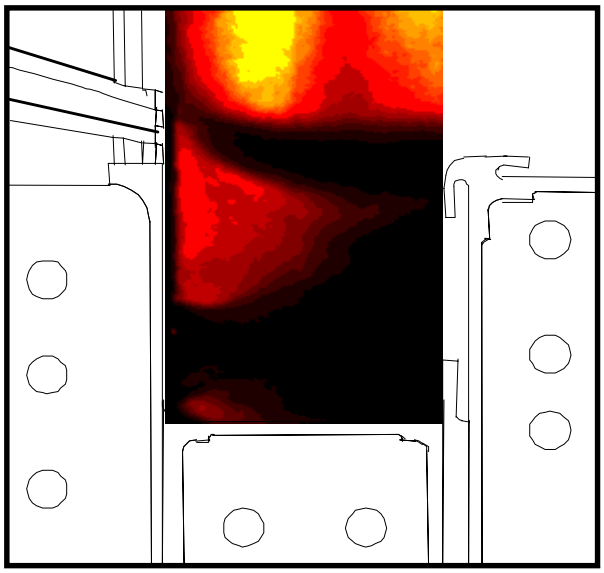

Figure 5. OH-PLIF signal obtained in the lower cavity of a natural-gas-fueled TVC with fuel injection in the cavity alone.

Velocimetry data have been acquired to complement these flame visualizations. PIV was achieved using a dual-image, digital cross-correlation configuration with two Nd:YAG lasers and a dual-frame Kodak ES4 2000×2000 pixel CCD camera. Vectors were computed using the dPIV code developed by AFRL and Innovative Scientific Solutions, Inc. An average of several image pairs was employed to generate the data in Fig. 6, where the velocities determined by PIV in the lower cavity of the TVC sector are compared with those computed using a commercial CFD package.

The short-exposure images acquired with the high-speed digital camera can also be used to estimate flow velocities subject to certain assumptions using CSV.[6,7] In the current work, this is achieved using an approach that involves several image-processing steps, including the generation of isoline contours to define structure boundaries, the selection of an optimal interrogation window and overlap parameter, and cross-correlation between image pairs for determination of the local displacement vectors.[4] It must be stressed that CSV in combusting flows cannot provide a true measure of convective velocity due to inherent non-convective flame-intensity variations. Nonetheless, slowly varying flame structures can provide a qualitative picture of the flow structure. Such a technique can be highly valuable for flow analysis on-demand and can supplement more difficult, laser-based methods such as PIV. The latter is valuable for quantitative velocimetry and code validation, but it is not conducive to continuous operation due to window fouling and seed build-up in small passages.

The CSV image in Fig. 7 depicts the combusting flow pattern with a cavity geometry very similar to that in which the PIV data of Fig. 6 were acquired. Qualitative agreement between the two velocity fields is quite good.

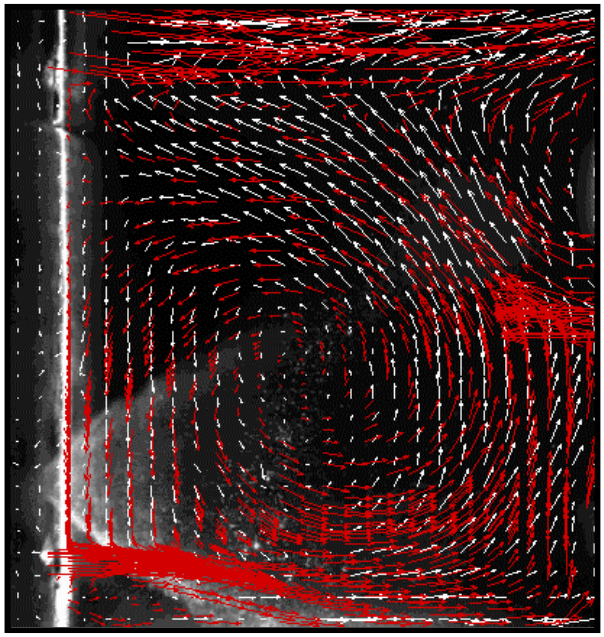

Figure 6. Comparison of PIV data (white vectors) and CFD data (red vectors) acquired in the lower cavity of a TVC sector under non-combusting conditions.

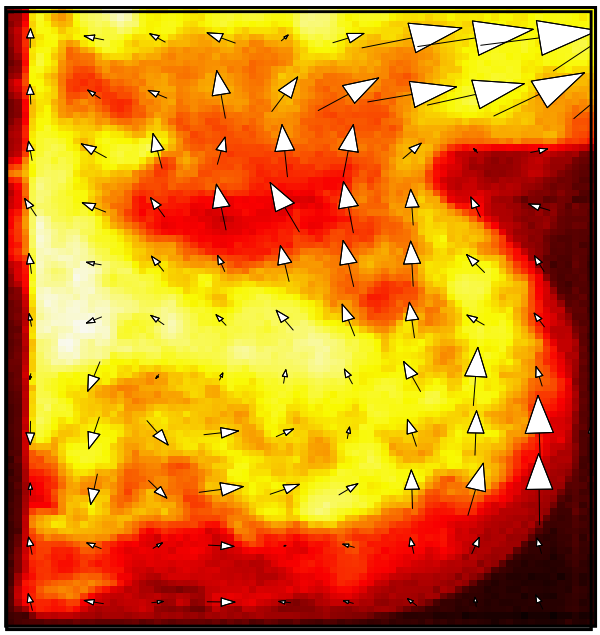

Figure 7. CSV data overlayed on a high-speed digital image of combustion in the lower cavity of a TVC sector.

Flow Visualization in a Pulsed-Detonation Engine

The PDRF at Wright-Patterson Air Force Base is equipped with a highly versatile research PDE that has been employed to explore a host of fundamental and engineering issues surrounding the development of an air-breathing PDE capable of operating with practical JP-type liquid fuels.[8] A four-tube configuration of that research PDE is shown in Fig. 8.

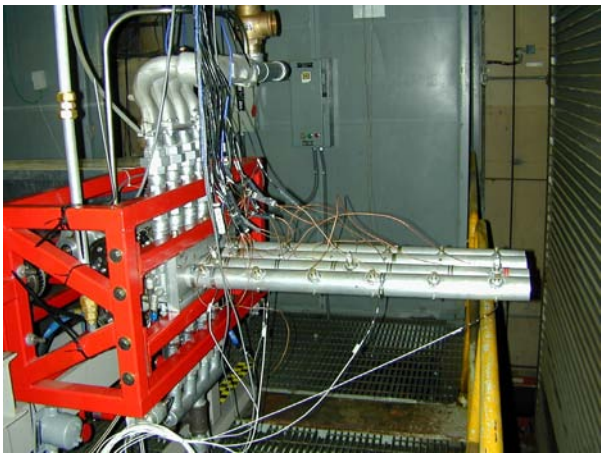

Figure 8. Four-tube configuration of the research PDE in the PDRF.

The success of this development effort is critically dependent upon enhancing the deflagration-to-detonation transition (DDT) at the heart of PDE operation. Various schemes for enhancing DDT have been investigated in the PDRF and elsewhere by experimental and computational means.[9] The DDT process is extremely complex and highly three-dimensional, involving flame interactions with shocks, reflections, and boundary layers.[10] Because of this complexity and DDT variability in time and space from shot-to-shot, the process is not easily studied with multi-point probes, spatially averaged measurement techniques, or conventional single-frame imaging. High-speed digital imaging, however, shows great promise for studying DDT because a time history of the process can be captured during the course of a single engine cycle.

In the current work, high-speed digital imaging of DDT in the PDE has been accomplished at rates to 40,500 fps using two Photron Fastcam Ultima 40K high-speed cameras. The conventional metal PDE tubes are replaced with tubes of quartz or polycarbonate to provide optical access during such studies.

The Shchelkin spiral is one device employed to enhance DDT in a PDE.[11] High-speed digital imaging was accomplished in a H_2-fueled research PDE configured for optical access with a Shchelkin spiral installed. Figure 9 includes side views and end views

captured using the high-speed cameras at various times during the DDT process. These images show that DDT begins with localized explosions along the Shchelkin spiral. The pressure waves that emanate from these explosions propagate ahead of the flame front, causing subsequent explosions further downstream. The transition to detonation takes place as subsequent explosions occur with increased intensity. End-view images confirm that the flame propagates along the spiral during the DDT process.

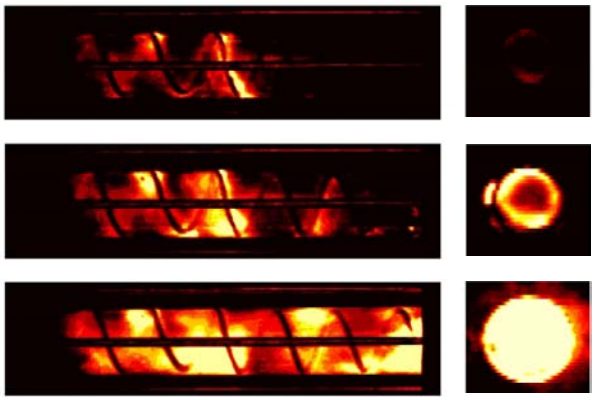

Figure 9. Side views (left) and end views (right) acquired by high-speed digital imaging during DDT in a research PDE equipped with a Shchelkin spiral. Images were recorded at relative timings of 0 μs (top), 55.5 μs (middle), and 111 μs (bottom).

Flow Visualization in a CFM56-Based Combustor

As part of a continuing effort funded through the Strategic Environmental Research and Development Program (SERDP), researchers in the Combustion Science and Fuels Branches have been exploring the impacts of various fuel additives on the characteristics of particulates formed during combustion. One of the key rigs employed in conjunction with these studies is a generic, optically accessible combustor in the APCRC designed around a single CFM56 fuel injector. This is a single swirl-cup combustor with a central nozzle designed to operate at atmospheric pressure with JP-type liquid fuels and fuel additives. A photograph of the rig is provided in Fig. 10.

Two forms of flow visualization—high-speed digital imaging and LII[12-15]—have been accomplished in concert with this Air-Force program to study the effects of additives on particulate production. Both reveal a complex, three-dimensional soot structure that varies dramatically from shot to shot. The sequence of images in Fig. 11, which were acquired using a high-speed digital camera, illustrate the temporal evolution of the soot field that arises due to the vortex-shedding processes associated with the fuel injector. A group of

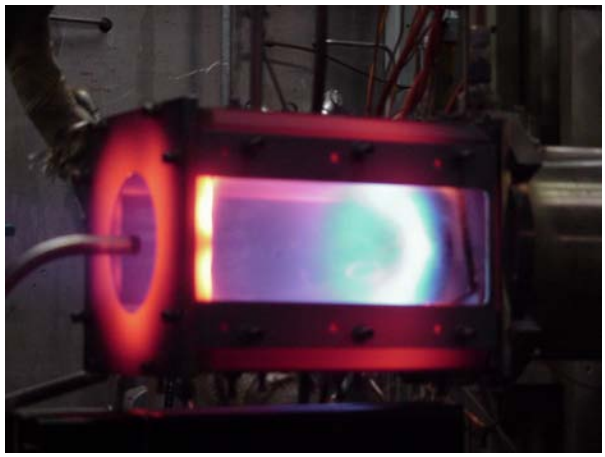

Figure 10. CFM56-based model combustor for evaluation of particulate-mitigating fuel additives. Flow is from right to left.

four uncorrelated, single-shot LII images in Fig. 12 show strong, sharply localized soot incandescence throughout the flowfield. These data were acquired by superheating nascent soot with the frequency-doubled output of a Q-switched Nd:YAG laser and recording the resulting incandescence using an ICCD equipped with spectral filters to limit signal contributions from laser-

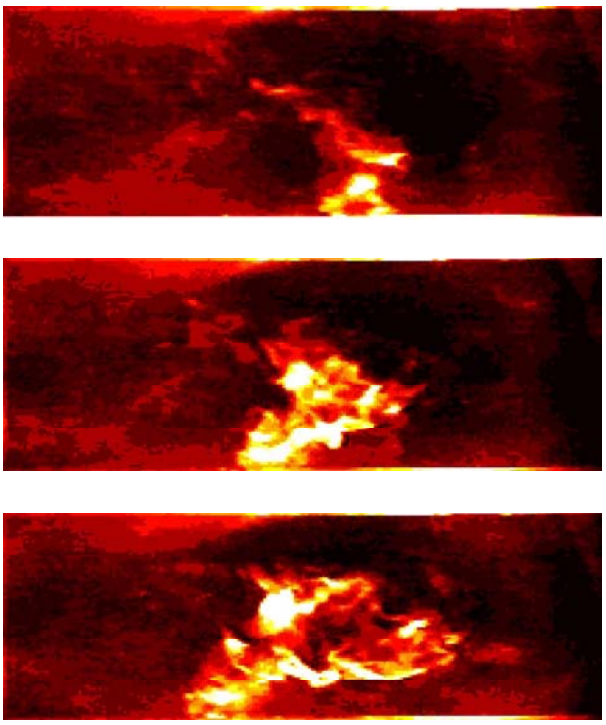

Figure 11. Time-correlated three-image sequence of nascent soot luminescence in a CFM56-based model combustor. Separation between images is 5.6 ms. Flow is from right to left.

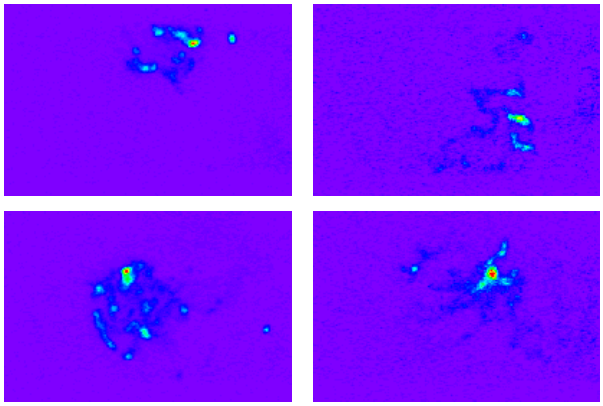

Figure 12. Uncorrelated, single-shot LII images acquired in a CFM56-based model combustor. Flow is from right to left.

induced fluorescence of C_2 and polycyclic aromatic hydrocarbons in the flame. The isolated, convoluted structures observed in the LII data are consistent with the instantaneous images of nascent-soot luminescence recorded with the high-speed camera.

In light of the shot-to-shot fluctuations in the LII images, it was necessary to average signals over many laser shots to acquire meaningful values for optimizing the LII signal and assessing the merits of various particulate-mitigating additives. An LII image averaged over 800 laser shots is shown in Fig. 13. The white box in the figure indicates a region over which signal intensities were averaged to yield a single value for each experimental condition and fuel additive studied. These average LII values are plotted in Fig. 14 as a function of equivalence ratio in comparison with particle number densities determined by extractive gas sampling. The data in Fig. 15 demonstrate the impact of a fuel-additive on soot formation as measured by LII over the course of eight experimental cycles.

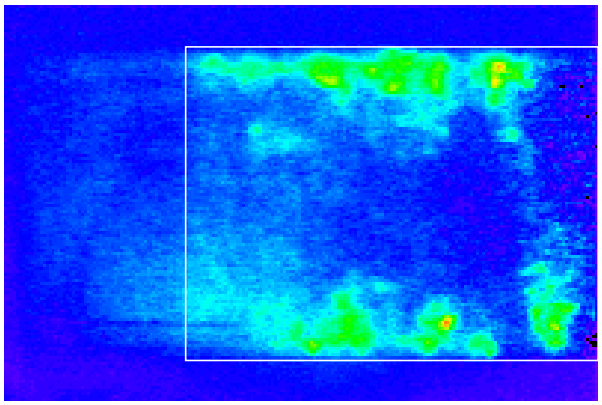

Figure 13. Average LII image acquired in a CFM56-based model combustor over 800 laser shots. Flow is from right to left. The white box is explained in the text.

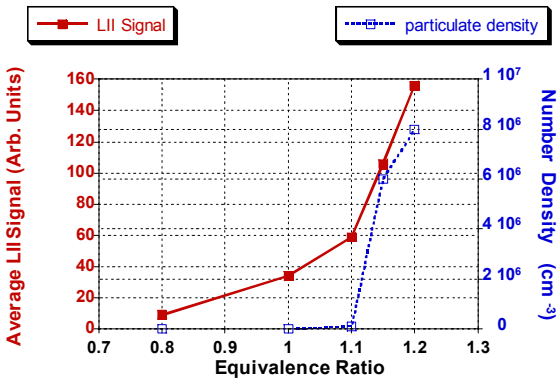

Figure 14. Average LII signals and particle number densities determined by extractive gas sampling as a function of equivalence ratio in a CFM56-based model combustor.

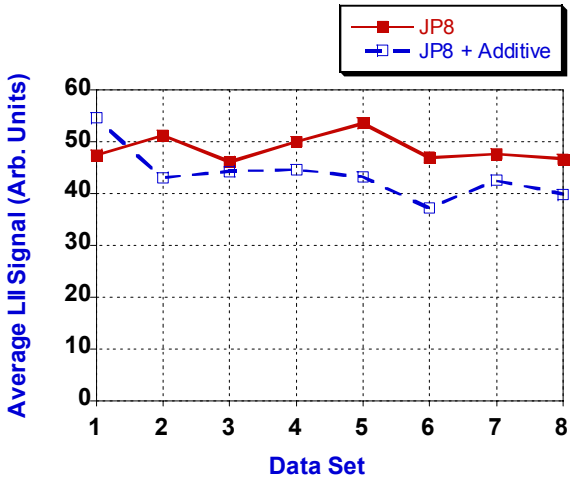

Figure 15. Average LII signals with and without a particulate-mitigating fuel additive in JP-8 as measured in a CFM56-based model combustor.

Dual-Pump Coherent Anti-Stokes Raman Scattering

While flow visualization can provide tremendous insights regarding the performance of advanced propulsion systems, quantitative measurements of critical parameters such as temperature and key species concentrations are also essential. Efforts to transition DP-CARS from the laboratory to the APCRC have been motivated by a desire to acquire these data on a single-shot basis in real-world combustors. One goal of such efforts is obtaining necessary aerothermodynamic data to determine combustion efficiencies for various propulsion platforms, including high fuel/air ratio systems and PDE's, in which traditional probe-based sampling approaches prove insufficient or unsatisfactory.

While CARS is now a well-established technique for measuring gas temperature in reacting flows,[16-21] considerably less attention has been paid to the development of CARS approaches for quantifying key combustion species.[22-29] Through the use of DP-CARS, researchers have achieved simultaneous measurements of temperature and multiple species, including N_2/O_2, N_2/H_2, N_2/CH_4, and N_2/CO_2. Simultaneous measurements of temperature and pressure have been realized as well.[30]

DP-CARS enjoys some significant advantages over other forms of the technique. Measurements are accomplished by incorporating a second, narrowband dye laser into the experimental apparatus traditionally used for broadband CARS, which includes two 532-nm beams from a Nd:YAG laser and a third beam from a YAG-pumped, broadband dye laser. In the DP-CARS arrangement, one of the 532-nm pump beams is replaced with the narrowband dye-laser beam. The narrowband and broadband dye lasers in the dual-pump configuration are tuned to generate CARS signals from two species such that the signal frequencies are very nearly the same. This situation serves to mitigate potential difficulties introduced by frequency-dependent characteristics of the optics and detectors employed to capture the signal. Because the CARS signals are generated using the same three laser pulses (one each from the YAG, the broadband dye laser, and the narrowband dye laser) and acquired simultaneously, the signals are highly correlated, reducing the impact of shot-to-shot variations in the laser intensity and other time-varying characteristics of the hardware. These advantages tend to improve the quality and simplify the post processing of dual-pump CARS data.

Single-shot measurements of temperature, N_2, and CO_2 were demonstrated in the APCRC using DP-CARS in a modified version of the CFM56-based model combustor operating with JP-8 and JP-8+100 fuels. The instrumentation included an injection-seeded, single-mode, Q-switched Nd:YAG laser; a narrowband dye laser; a modeless, broadband dye laser; and an unintensified, thinned, back-illuminated CCD camera. A typical single-shot spectrum is displayed in Fig. 16.

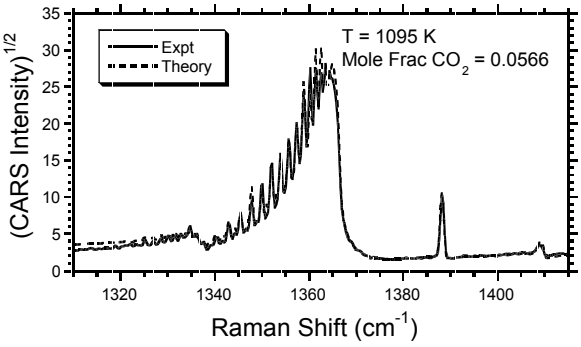

Figure 16. Typical single-shot DP-CARS data acquired in the CFM56-based model combustor.

Chemiluminescent Emission Measurements

Often the simplest diagnostic schemes show the greatest promise for transition from the laboratory to the test facility and thereafter from the test facility to fielded systems. Passive measurements of flame emission show great promise in this capacity. The strengths of numerous molecular and broadband optical emissions are sensitive to variations in local fuel/air ratios that are manifested in terms of local combustion chemistry and concentrations of key radical species.[31] These observations suggest the possibility of employing simple passive sensing of flame emission for determination of local equivalence ratios and for active combustion control.[32-34]

The potential utility of chemiluminescent emission measurements has been explored using the UCC in the APCRC.[35] Some additional preliminary studies have been performed with the research PDE in the PDRF. The UCC is a next-generation system designed to exploit unique geometry and new materials to yield a dramatically shortened combustor. Such a system would yield tangible benefits as a main combustor, and also holds promise as an inter-turbine burner for reheat in gas turbine engines.[36] The research UCC under study in the APCRC is depicted in Fig. 17. Key features include the combustor center body and circumferential injection of fuel into an annular ring at the front of the combustor that acts as a pilot similar to the cavities in the TVC. This unique geometry demands a thorough understanding of high-g effects on the combustion process in the annular ring. In addition, the development of new, high-temperature, ceramic

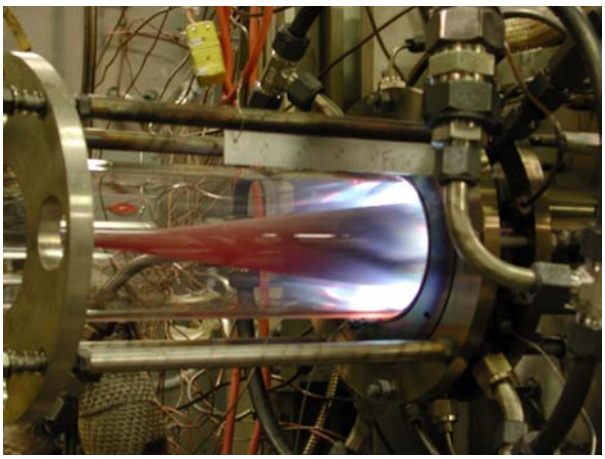

Figure 17. Research UCC operating in the APCRC. Flow is from right to left.

materials is essential to the successful evolution of the UCC.

Emission spectra were acquired in the UCC by using a silica-core/silica-cladding fiber bundle coupled to a small, fixed-grating spectrometer package available through Ocean Optics that operates over the spectral range 190-870 nm. The collection end of the fiber bundle was mounted using ceramic standoffs, stainless-steel tubing, and associated fittings to sample emission from the flame-holding annular cavity of the UCC. A typical emission spectrum collected in this fashion is depicted in Fig. 18.

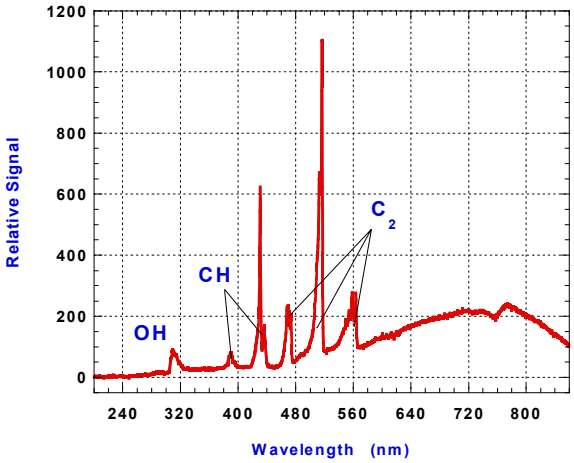

Figure 18. Typical flame emission spectrum acquired in the UCC operating at a local equivalence ratio of ~1.5.

This spectrum includes emission features for three key combustion radicals (OH, CH, and C_2) as well as a broad, structureless background that appears with increasing equivalence ratio. For the combustor conditions of Fig. 18, this background extends over the range 480-900 nm and likely includes contributions from polycyclic-aromatic-hydrocarbon emission and particulate incandescence. As the local equivalence ratio changes, the relative strengths of these emission features and the broad background are impacted as a consequence of variations in the local combustion chemistry, particularly the production and destruction rates of chemical intermediates. Development of a practical sensor rests on identifying spectral signals or ratios of spectral signals that correlate well with changes in the local equivalence ratio.

To explore potential correlations between emission-signal ratios and the local equivalence ratio, the fiber-coupled spectrometer was employed to acquire a series of emission spectra in a laminar, propane-air flame established with a Hencken burner. Calibrated mass-flow controllers were used to adjust the equivalence ratio over the stable operating envelope of the burner, and flame emission was collected from a region roughly one centimeter above the surface of the burner where the flame gases are well mixed but little or no co-flow (N_2) has been drawn into the flame.

The data in Fig. 19 illustrate the effects of equivalence ratio on the measured emission-signal ratios for CH at 435 nm to OH at 308 nm and for C_2 at 550 nm to OH at 308 nm. Both emission-signal ratios increase monotonically with equivalence ratio. Similar data are displayed in Fig. 20 for emission-signal ratios of C_2 at 550 nm to CH at 435 nm and OH at 308 nm to the total emission signal (molecular and broadband). Once again, these data show promising correlations with equivalence ratio.

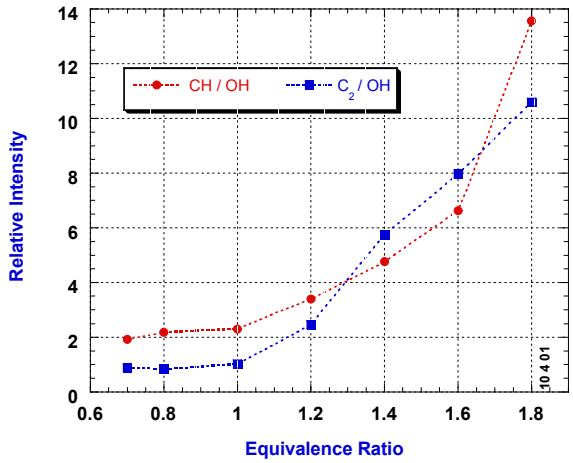

Figure 19. Plots of emission-signal ratios for CH (435 nm)/OH (308 nm) and C_2 (550 nm)/OH (308 nm) as a function of Hencken-burner equivalence ratio.

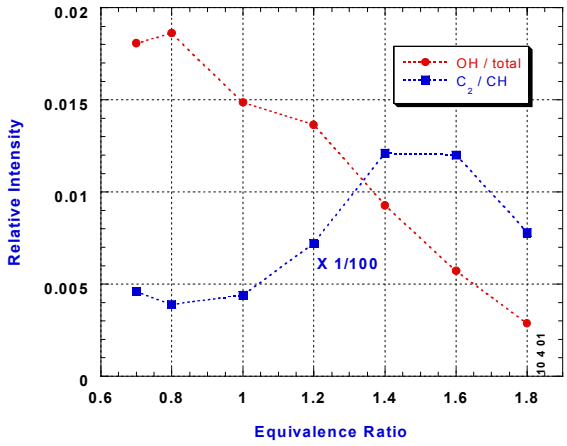

Figure 20. Plots of emission-signal ratios for C_2 (550 nm)/CH (435 nm) and OH (308 nm)/Total Emission as a function of Hencken-burner equivalence ratio.

Ongoing studies in the Hencken flame, the UCC, and the research PDE are aimed at correlating emission data with combustor operating parameters to enhance understanding of the underlying combustion chemistry and associated fluid-dynamic behavior while providing design feedback for combustor engineers. In addition to equivalence-ratio measurements, various emission-based schemes for determining combustion temperatures are under development as well.

Upcoming Lab-to-Facilities Transitions

Triple-Pump Coherent Anti-Stokes Raman Scattering

The successes achieved in transitioning DP-CARS from lab to facility have inspired similar efforts with TP-CARS for simultaneous measurements of temperature and multiple species concentrations with high spatial and temporal resolution. The TP-CARS approach employs four laser beams to generate CARS signals near two distinct wavelengths. Temperature and relative concentrations of the target species (with respect to N_2) are extracted by fitting the measured CARS spectra in each wavelength region. For the proof-of-concept measurements, CARS signals from N_2/O_2 and N_2/H_2 pairings were collected. Single-shot and time-averaged measurements were performed in an atmospheric-pressure H_2-air diffusion flame. Representative spectra are depicted in Figs. 21 and 22. Demonstration of this measurement capability in a practical combustor rig at WPAFB is scheduled for this fall.

Absorption Sensors in the Ultraviolet and Mid-Infrared Based on Diode-Laser Frequency-Mixing Schemes

Like the passive emission measurements described above, straightforward line-of-sight absorption techniques show great promise for transition beyond the facility into the field. To capitalize on such opportunities, two all-solid-state continuous-wave (cw) laser systems, one for ultraviolet absorption measurements of nitric oxide (NO) and another for mid-infrared absorption measurements of carbon monoxide (CO), have been developed and demonstrated. In the NO system, the single-mode tunable output of a 10-mW, 395-nm external-cavity diode laser (ECDL) is sum-frequency mixed with the output of a 115-mW, frequency-doubled, diode-pumped cw Nd:YAG laser in a beta-barium borate (BBO) crystal to produce ~40 nW of tunable cw radiation at 226.8 nm. The wavelength of the 395-nm ECDL is scanned over NO absorption lines to produce a fully resolved absorption spectrum. Initial results with mixtures of NO and N_2 in a room-temperature gas cell suggest an NO detection limit of 0.2 ppm per meter path length based on a demonstrated absorption sensitivity of 2×10^{-3}. Representative data are presented in Fig. 23.

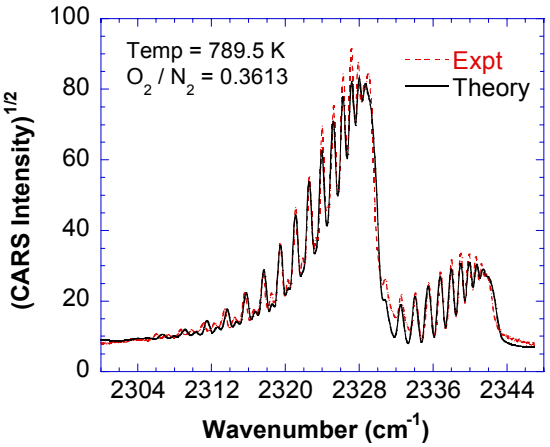

Figure 21. N_2/O_2 TP-CARS signal obtained near 491 nm in a H_2-air diffusion flame (fuel-lean side).

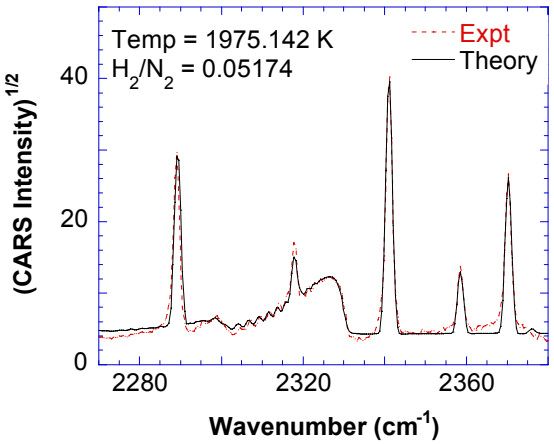

Figure 22. H_2/N_2 TP-CARS signal obtained near 437 nm in a H_2-air diffusion flame (fuel-rich side).

In the CO system, the single-mode, tunable output of a 70-mW, 860-nm ECDL is difference-frequency mixed with the output of a 550-mW diode-pumped cw Nd:YAG laser in a periodically-poled lithium-niobate (PPLN) crystal to produce ~1 μW of tunable cw radiation at 4.5 μm. The wavelength of the 860-nm ECDL is scanned over a CO absorption line to produce a fully resolved absorption spectrum.

Both the NO and CO sensors are currently being tested in the exhaust of the WSR in the APCRC at WPAFB. Comparisons with computational predictions and physical-sampling-probe measurements are underway.

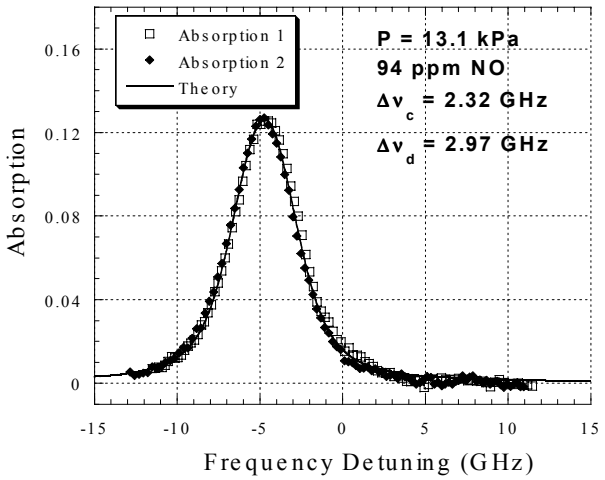

Figure 23. NO absorption spectrum of the $P_2(10)$ and ${}^{P}Q_{12}(10)$ overlapped absorption lines.

Summary

Tremendous time and energy have been invested in the development of advanced optical diagnostics for the fundamental study of combustion chemistry and physics. The techniques developed for these important basic-research activities also have enormous potential for impacting the design, development, test, evaluation, operation, and maintenance of current and next-generation propulsion systems when those techniques are transitioned from the laboratory to the test facility and ultimately to the field.

This paper summarizes some recent efforts to transition diagnostics for use in the combustor-test facilities of the Combustion Science Branch at Wright-Patterson Air Force Base. Various techniques for flow visualization, including high-speed digital imaging, PLIF, PIV, CSV, and LII, as well as methods for measuring temperatures and species (DP-CARS) and equivalence ratio (chemiluminescent emission) have been applied in these facilities. Future lab-to-facilities transitions will include TP-CARS and line-of-sight absorption measurements based on frequency-mixing schemes with tunable diode lasers.

Acknowledgments

The collected works described in this paper represent the efforts of many government researchers and valued collaborators from industry and academia. The authors gratefully acknowledge the contributions of Mel Roquemore and Robert Hancock (AFRL) and Sukesh Roy (ISSI), who impacted much of this activity. Those contributing in specific areas include: Dale Shouse (AFRL), Clay Cooper and Eun Kim (GEAE), Joel Haynes (GE Global Research Center), and Larry Goss and Darryl Trump (ISSI)—TVC; Fred Schauer and Jeff Stutrud (AFRL) and John Hoke and Royce Bradley (ISSI)—PDE; Vince Belovich and Edwin Corporan (AFRL)—CFM56-based combustor; Joe Zelina and Jeff Ehret (AFRL) and Glen Boggs and Dwight Fox (ISSI)—UCC; Bob Lucht, Jerry Caton, Viswa Velur, and Waruna Kulatilaka (Texas A&M), Greg Fiechtner and Roger Farrow (Sandia CRF), Keith Grinstead and Paul Danehy (NASA Langley), and Cam Carter (AFRL)—CARS; Geoff Sturgess (ISSI)—chemiluminescent emission; Bob Lucht, Thomas Walther, Jerry Caton, Thomas Anderson, Sherif Hanna, and Rodolfo Barron-Jimenez (Texas A&M)—diode-laser-based sensors. Funding for the propulsion-system development activities described in this paper was provided by numerous organizations, including the Strategic Environmental Research and Development Program (SERDP), which supports efforts to develop particulate-mitigating additives, and the Department of Energy's National Energy Technology Laboratory (NETL), which supports development of the natural-gas-fueled TVC through General Electric (Contract No. DE-FC2601NT41020). ISSI's contributions are funded in part through USAF Contract No. F33615-00-C-2068 (Vince Belovich, Contract Monitor). Finally the authors thank Julian Tishkoff (Air Force Office of Scientific Research) for his continued generous funding of our diagnostics-development efforts.

References

1. A. C. Eckbreth, *Laser Diagnostics for Combustion, Temperature, and Species*, 2nd Edition, Gordon & Breach, 1996.
2. W. M. Roquemore, D. Shouse, D. Burrus, A. Johnson, C. Cooper, B. Duncan, K.-Y. Hsu, V. R. Katta, G. J. Sturgess, and I. Vihinen, "Trapped Vortex Combustor Concept for Gas Turbine Engines," AIAA 2001-0483 (2001).
3. D. Burrus, A. Johnson, W. M. Roquemore, and D. Shouse, "Performance Assessment of a Prototype Trapped Vortex Combustor Concept for Gas Turbine Application," ASME 2001-GT-0087 (2001).
4. T. R. Meyer, M. S. Brown, S. Fonov, L. P. Goss, J. R. Gord, D. T. Shouse, V. M. Belovich, W. M. Roquemore, C. S. Cooper, E. S. Kim, and J. Haynes, "Optical Diagnostics and Numerical Characterization of a Trapped-Vortex Combustor," AIAA 2002-3863 (2002).
5. G. J. Fiechtner, C. D. Carter, K. D. Grinstead, J. R. Gord, W. M. Roquemore, and J. C. Rolon, "Flame-Vortex Interactions in a Non-Premixed H_2/N_2/Air Counterflow Burner," AIAA 98-3770 (1998).

6. P. T. Tokumaru and P. E. Dimotakis, "Image Correlation Velocimetry," Experiments in Fluids, Vol. 19, pp. 1-15 (1995).
7. W. J. A. Dahm, L. K. Su, and K. B. Southerland, "A Scalar Imaging Velocimetry Technique for Fully Resolved Four-Dimensional Vector Field Measurements in Turbulent Flows," Physics of Fluids, Vol. 4, No. 10, pp. 2191-2206 (1992).
8. F. Schauer, J. Stutrud, and R. Bradley, "Detonation Initiation Studies and Performance Results for Pulsed Detonation Engine Applications," AIAA 2001-1129 (2001).
9. C. M. Brophy and D. W. Netzer, "Effects of Ignition Characteristics and Geometry on the Performance of a JP-10/O_2 Fueled Pulse Detonation Engine," AIAA 99-2635 (1999).
10. K. Kailasanath, G. Patnaik, and C. Li, "Computational Studies of Pulse Detonation Engines: A Status Report," AIAA 99-2634 (1999).
11. R. P. Lindstedt and H. J. Michels, "Deflagration to Detonation Transitions and Strong Deflagrations in Alkane and Alkene Air Mixtures," Combustion and Flame, Vol. 76, pp. 169-181 (1989).
12. M. S. Brown, T. R. Meyer, J. R. Gord, V. M. Belovich, and W. M. Roquemore, "Laser-Induced Incandescence Measurements in the Reaction Zone of a Model Gas Turbine Combustor," AIAA 2002-0393 (2002).
13. R. T. Wainner, J. M. Seitzman, S. R. Martin, "Soot Measurements in a Simulated Engine Exhaust Using Laser-Induced Incandescence," AIAA Journal, Vol. 37, pp. 738-743 (1999).
14. S. Will, S. Schraml, and A. Leipertz, "Two-Dimensional Soot-Particle Sizing by Time-Resolved Laser-Induced Incandescence," Optics Letters, Vol. 20, pp. 2342-2344 (1995).
15. P. Roth and A. V. Filippov, "In Situ Ultrafine Particle Sizing by a Combination of Pulsed Laser Heatup and Particle Thermal Emission," Journal of Aerosol Science, Vol. 27, pp. 95-104 (1996).
16. A. C. Eckbreth, "CARS Thermometry in Practical Combustors," Combustion and Flame, Vol. 39, pp. 133-147 (1980).
17. L. P. Goss, D. D. Trump, B. G. MacDonald, and G. L. Switzer, "10-Hz Coherent Anti-Stokes Raman Spectroscopy Apparatus for Turbulent Combustion Studies," Review of Scientific Instruments, Vol. 54, pp. 563-571 (1983).
18. D. A. Greenhalgh, F. M. Porter, and W. A. England, "The Application of Coherent Anti-Stokes Raman Scattering to Turbulent Combustion Thermometry," Combustion and Flame, Vol. 49, pp. 171-181 (1983).
19. M. Aldén, and S. Wallin, "CARS Experiments in a Full-Scale (10 m x 10 m) Industrial Coal Furnace," Applied Optics, Vol. 24, pp. 3434-3437 (1985).
20. P.-E. Bengtsson, L. Martinsson, M. Aldén, B. Johansson, B. Lassesson, K. Marforio, and G. Lundholm, "Dual-Broadband Rotational CARS Measurements in an IC Engine," Proceedings of the Combustion Institute, Vol. 25, pp. 1735-1742 (1994).
21. G. Switzer, G. Sturgess, D. Sloan, and D. Shouse, "Relation of CARS Temperature Fields to Lean Blowout Performance in an Aircraft Gas Turbine Generic Combustor," AIAA Paper No. 94-3271 (1994).
22. A. C. Eckbreth, G. M. Dobbs, J. H. Stufflebeam, and P. A. Tellex, "CARS Temperature and Species Measurements in Augmented Jet Engine Exhausts," Applied Optics, Vol. 23, pp. 1328-1339 (1984).
23. A. C. Eckbreth, T. J. Anderson, and G. M. Dobbs, "Multi-Color CARS for Hydrogen-Fueled Scramjet Applications," Applied Physics B, Vol. 45, pp. 215-223 (1988).
24. R. R. Antcliff and O. Jarrett, Jr., "Multispecies Coherent Anti-Stokes Raman Scattering Instrument for Turbulent Combustion," Review of Scientific Instruments, Vol. 58, pp. 2075-2080 (1987).
25. S. M. Green, P. J. Rubas, M. A. Paul, J. E. Peters, and R. P. Lucht, "An Annular Phase-Matched Dual-Pump CARS System for the Simultaneous Detection of Nitrogen and Methane," Applied Optics, Vol. 37, pp. 1690-1701 (1998).
26. P.-E. Bengtsson, L. Martinsson, and M. Aldén, "Combined Vibrational and Rotational CARS for Simultaneous Measurements of Temperature and Concentrations of Fuel, Oxygen, and Nitrogen," Applied Spectroscopy, Vol. 49, No. 2, pp. 188-192 (1995).
27. R. P. Lucht, "Three-Laser Coherent Anti-Stokes Raman Scattering Measurements of Two Species," Optics Letters, Vol. 12, pp. 78-80 (1987).
28. R. D. Hancock, F. R. Schauer, R. P. Lucht, and R. L. Farrow, "Dual-Pump Coherent Anti-Stokes Raman Scattering (CARS) Measurements of Hydrogen and Oxygen in a Laminar Jet Diffusion Flame," Applied Optics, Vol. 36, pp. 3217-3226 (1997).
29. D. Brüggemann, B. Wies, X. X. Zhang, T. Heinze, and K. F. Knoche, "CARS Spectroscopy for Temperature and Concentration Measurements in a Spark Ignition Engine," in Combustion Flow Diagnostics, D. F. G. Durão, M. V. Heitor, J. H. Whitelaw, and P. O. Witze, Editors, Kluwer Academic, pp. 495-511 (1992).
30. R. E. Foglesong, S. M. Green, R. P. Lucht, and J. C. Dutton, "Dual-Pump Coherent Anti-Stokes Raman Scattering Technique for Simultaneous Measurement of Pressure and Temperature," AIAA Journal, Vol. 36, pp. 234-240 (1998).

31. A. G. Gaydon, *The Spectroscopy of Flames*, Wiley and Sons, 1974.
32. Y. Ikeda, J. Kojima, and T. Nakajima, "Chemiluminescene Based Local Equivalence Ratio Measurement in Turbulent Premixed Flames," AIAA 2002-0193 (2002).
33. A. Scott, G. B. King, and N. M. Laurendeau, "Chemiluminescence-Based Feedback Control of Equivalence Ratio for a Continuous Combustor," J. Propulsion and Power, Vol. 18, pp. 376-382 (2002).
34. M. G. Allen, C. T. Butler, S. A. Johnson, E. Y. Lo, and F. Russo, "An Imaging Neural Network Combustion Control System for Utility Boiler Applications" Combustion and Flame, Vol. 94, pp. 205-214 (1993).
35. M. S. Brown, T. R. Meyer, G. J. Sturgess, J. Zelina and J. R. Gord, "Chemiluminescence as a Measurement of Local Equivalence Ratio," AIAA 2002-3865 (2002).
36. J. Zelina, J. Ehret, R. Hancock, W. Roquemore, D. Shouse, and G. Sturgess, "Ultra-Compact Combustion Technology Using High Swirl for Enhanced Burning Rate," AIAA-2002-3725 (2002).

EMISSION- AND ABSORPTION-BASED SENSORS FOR THE PULSED DETONATION ENGINE

Turbine Engine Technology Symposium
Dayton, Ohio
12 September 2002

Michael S. Brown
Innovative Scientific Solutions, Inc.

Acknowledgments

- Diagnostics team: Jim Gord (AFRL); Terry Meyer (ISSI); Heidi Meicenheimer (Summer intern); Amy Lynch (co-op)
- PDE: Fred Schauer, Jeff Stutrud (AFRL); John Hoke, Royce Bradley, Jason Parker (ISSI)
- Funding: Julian Tishkoff (AFOSR)

2

Overall Approach

PDE Needs: – ground-based sensors for
tube fill history
equivalence ratio

– on-board sensor for active control of fill

Response: – OH^* emission monitor for
equivalence ratio (can be relative)
active control

– absorption-based fuel sensor
tube fill history
equivalence ratio

3

Research Pulsed-Detonation Engine

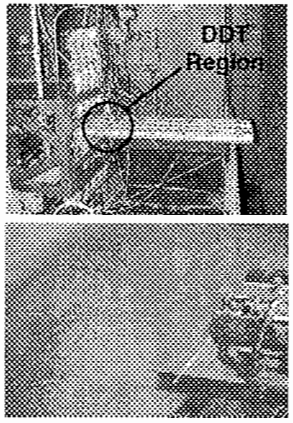

- Hydrogen-Fueled PDE
- High-Speed Digital Imaging
- Quartz or Polycarbonate PDE Tubes
- Shchelkin Spiral

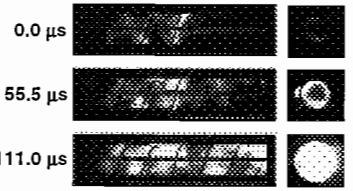

4

Control System Diagram

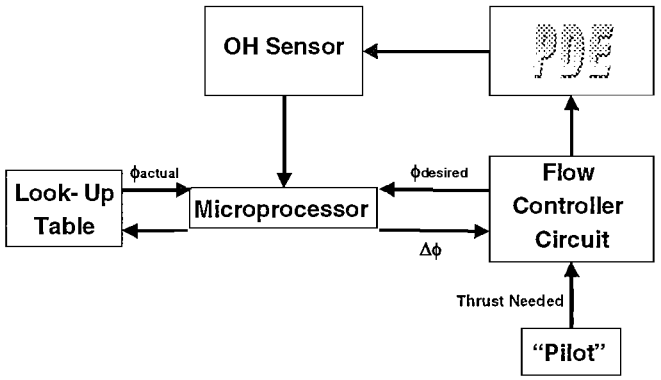

Sensor Sensitivity?

PDE Operating Params \ Sensor	Signal Amplitude	Signal Temporal Behavior
Equivalence Ratio	?	?
Fill Fraction	?	?
Ignition Delay	?	?
Repetition Rate	Independent	Independent

Emission Probe Location

End of Collection Fiber Mounted Normal to Tube Body & Flush With Inner Surface of Body

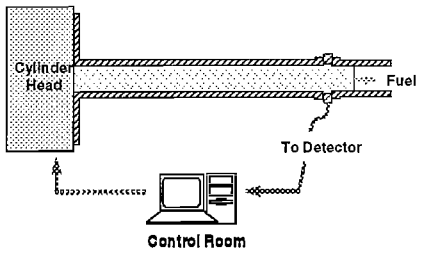

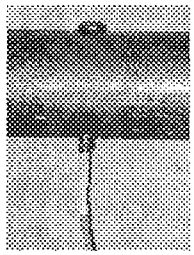

Using a silica multi-mode fiber for light collection

Emission Detection Schemes

All Emission Signals Collected Using a Silica Multi-Mode Fiber

	Detection Scheme #1	Detection Scheme #2
Detector	Filtered PMT	Si CCD Linear Array*
Spectral Range	10 nm @ 310 nm	200 – 870 nm (1.3-nm res)
Sampling Frequency	1 MHz	~ 33 Hz

*Coupled to Commercial Fixed-Grating Spectrometer

Typical Emission Spectrum

PDE Sequence of 11 Shots (ϕ = 1, 20 Hz, H_2/Air)

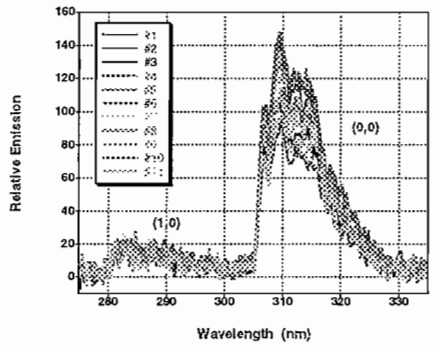

9

Raw OH* Emission Signal

Avgas/air near stoichiometry
78-inch tube, sensor at 50.75 inches
rep. rate - 17 Hz, fill fraction 1,

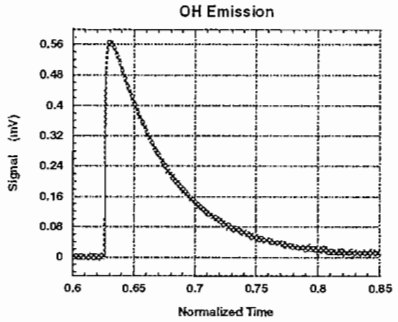

10

Temporal Signature

Temporal behavior of signal reflects OH dynamics & plug flow of PDE

OH:
chemical destruction, quenching, & fluorescent lifetime

PDE:
plug flow of distributed sample volume

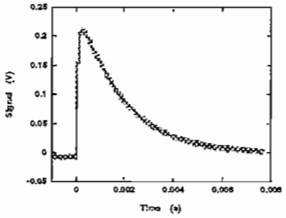

11

Single-Shot Signals

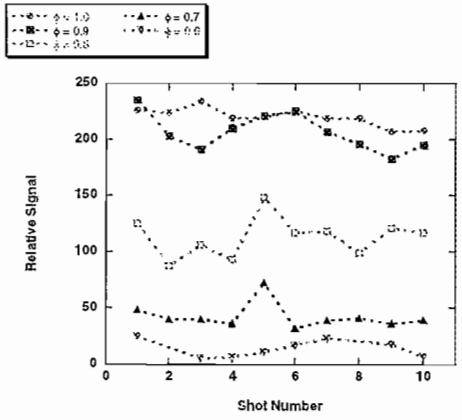

12

Fill Fraction Study

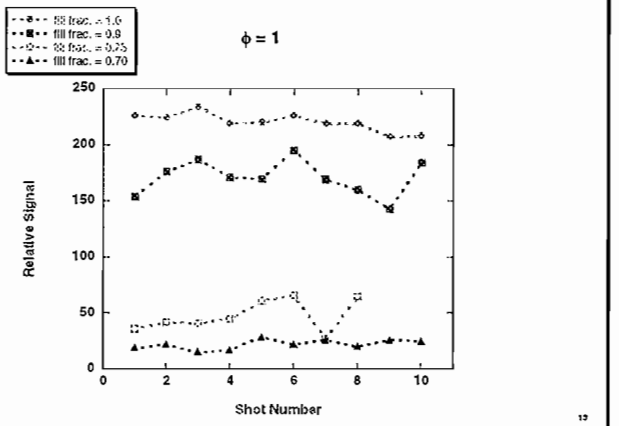

13

Time-Averaged Emission Signals

Hydrogen/air, 20 Hz, fill fraction of 1

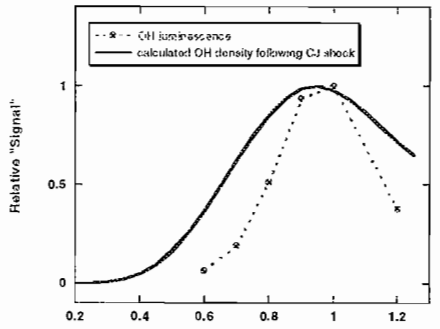

14

OH* in Propane/Air

78-inch tube, sensor at 50.75 inches
rep. rate - 20 Hz, fill fraction 1,

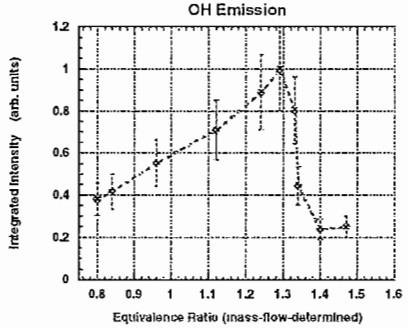

15

Integrated OH* Emission

Avgas/air near stoichiometry
78-inch tube, sensor at 50.75 inches
rep. rate – 17-20 Hz, fill fraction 1,

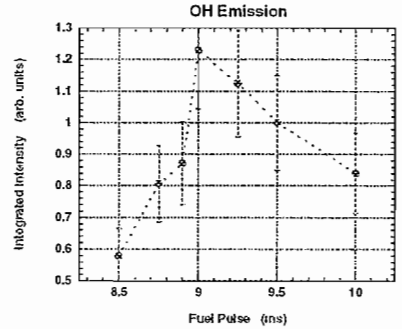

16

Summary

Chemiluminescence spectra of OH have been acquired in a single-tube pulse detonation engine.

The OH signals show a strong correlation with global equivalence ratio.

Sensor / PDE Operating Params	Signal Amplitude	Signal Temporal Behavior
Equivalence Ratio	Strong	Independent
Fill Fraction	Strong	Independent
Ignition Delay	Weak	Independent
Repetition Rate	Independent	Independent

17

Fuel Sensor Studies for the PDE

Goals –

1) evaluate simple hardware configuration for absorption-based detection of fuel

2) record time history of fuel in PDE tube at various locations

3) determine equivalence ratio in tube

Take advantage of overlap of HeNe 3.39-μm output And hydrocarbon resonance at 3.39 μm

Target species to date – propane and aviation gasoline (avgas)

18

Fuel Sensor Hardware

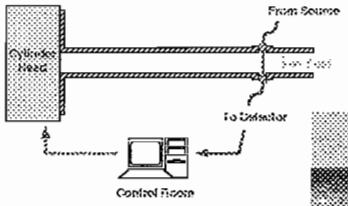

Fiber-Optic Absorption-Based *Hydrocarbon* Fuel Sensor

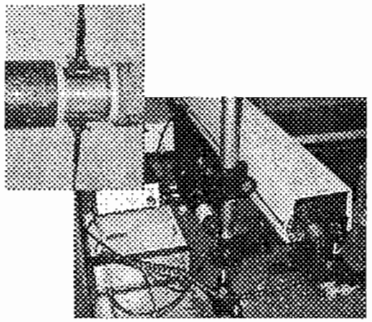

- IR Source - 3.39-μm commercial-grade cw laser
- Detector – uncooled lead selenide
- 1.5 - 3 kHz acquisition rate

Sample Sensor Signal

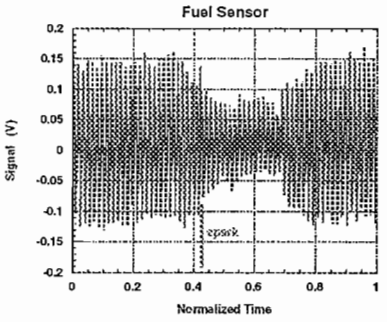

HeNe output chopped, 1.5 – 3 kHz

PbSe detector AC-coupled to DAQ

Closeup of raw signal

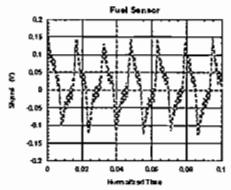

20

Signal Conversion to Equiv. Ratio

Sensor located near the middle of the tube

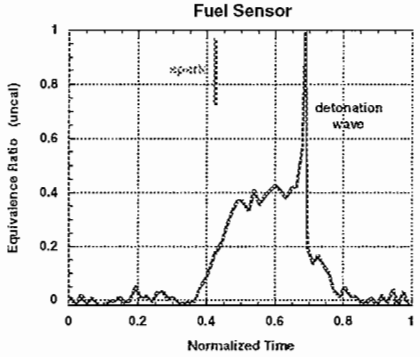

21

Fuel Sensor at End of Tube

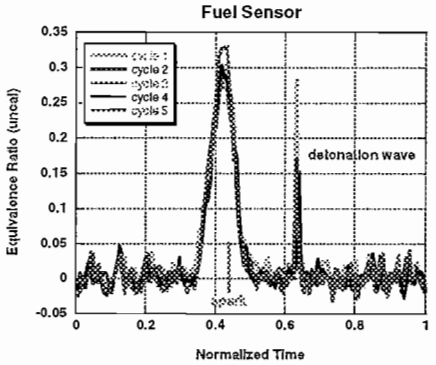

22

Propane Sensor (Cold Flow)

Measured Φ Versus Mass Flow Φ

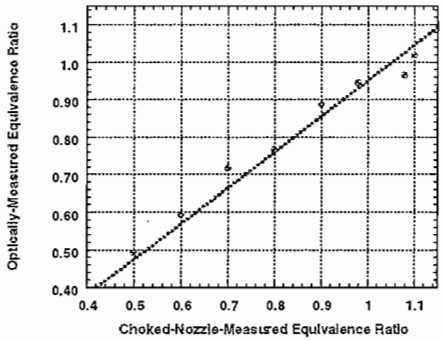

23

Fuel Sensor in Hot Flow

78-Inch tube, sensor at 44.75 inches
rep. rate - 10 Hz, fill fraction 1,

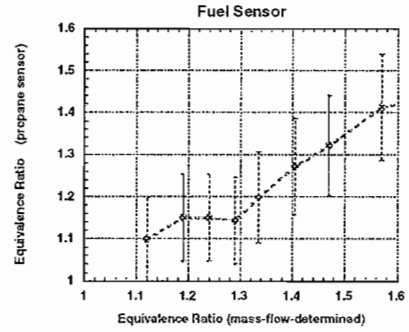

24

Aviation Gas Detection

Avgas/air near stoichiometry
78-inch tube, sensor at 50.75 inches
rep. rate - 17 Hz, fill fraction 1,

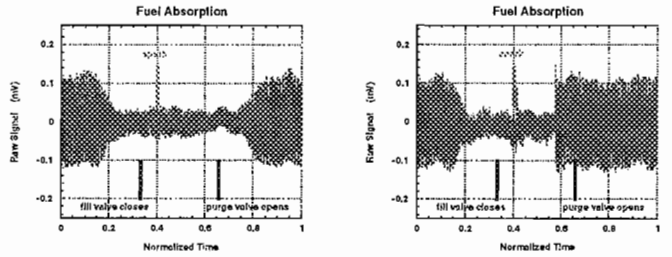

25

Stratified Charge Detection

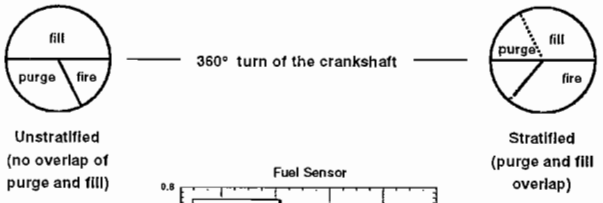

Unstratified (no overlap of purge and fill)

Stratified (purge and fill overlap)

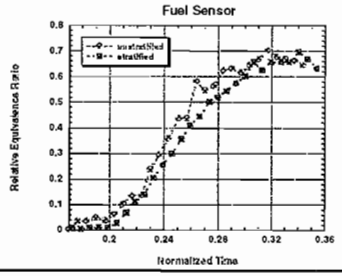

26

Particulate Sensor

Use fuel sensor platform with visible HeNe
Cold flow in avgas/air

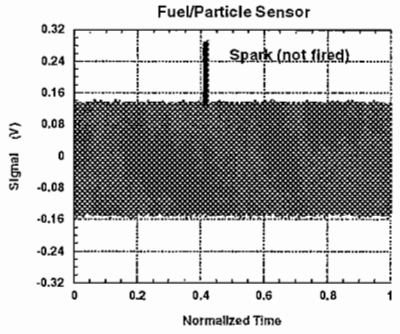

27

Fuel Sensor Summary

- Successfully recorded time traces of tube fill for propane and avgas
- Extracted sensible equivalence ratios from propane time histories
- Inferred fluid behavior from time histories including stratified charge
- Found no evidence of particulate or droplet presence

28

Conclusions & Future Work

- Successfully demonstrated emission and absorption sensors for tube fill and equivalence ratio measurements
- Simple hardware platforms used repeatedly without failure

Future Efforts

OH* sensor – construct a small inexpensive package including feedback algorithm for flying platform

Fuel sensor – acquire laboratory absorption data on avgas for absolute equivalence ratio measurements; due simultaneous particulate and fuel sensor measurements

29

41st Aerospace Sciences Meeting and Exhibit
6-9 January 2003, Reno, Nevada

AIAA 2003-889

COMPUTATIONAL AND EXPERIMENTAL STUDIES OF PULSE DETONATION ENGINES

Daniel Allgood and Ephraim Gutmark†
University of Cincinnati, Aerospace Engineering
Cincinnati, OH 45221

Terry Meyer, John Hoke, and Viswanath Katta
Innovative Scientific Solutions Inc.
Dayton, OH 45440

Fred Schauer
Air Force Research Laboratory, Propulsion Directorate
Wright-Patterson AFB, OH 45433

Abstract

Shadowgraph visualizations of pulse detonation engine (PDE) exhaust flowfields were performed using a new nanosecond duration light source. The shadowgraph system was developed at the University of Cincinnati and tested using the research PDE at the Air Force Research Laboratory. The complete detonation and blow-down process of the PDE was visualized and reconstructed by synchronizing the shadowgraph system with separate but repeatable detonation events. No visible smear or distortion of the detonation front and shock waves was observed due to the extremely short duration of each light pulse. Preliminary comparisons between the experimental visualizations and computational modeling results also showed good agreement. The structure and development of the exiting detonation wave was accurately predicted in the modeling.

Introduction

Recent research on pulse detonation engines has revealed their potential as an efficient, low cost propulsion system. Conceptually, pulse detonation engines (PDE) offer few moving parts, high thrust to weight ratios, low cost, and ease of scaling. The fact that a PDE does not require a high pressure-ratio compression cycle eliminates the necessity for heavy and expensive compressor and turbine units. Due to the obvious potential advantages of the pulse detonation cycle, a PDE-based propulsion system is an attractive alternative to conventional propulsion systems. The flight operating range of a PDE ranges from static conditions to hypersonic flight Mach numbers. As of today, there are no single-cycle propulsion systems available with such potential for a broad range of operability. A recent review on PDE research efforts has been given by Kailasanath [1].

Researchers have discovered that one method of controlling thrust and specific impulse of a pulse detonation engine is to alter the pressure relaxation rate by adjusting the percentage of the tube that is filled (fill fraction) with a detonable mixture [2]. Fill fraction is defined as the ratio of the tube volume that is initially filled with a fuel/air mixture to the overall tube volume. At fill fractions greater than 1.0, i.e. the detonable mixture over-fills the tube, no increase in performance was observed because the external detonation process has no thrust surface upon which to act. Conversely, if the tube is under-filled, essentially acting as a straight nozzle with either a purge cycle or previous cycle exhaust products filling the remainder of the tube, significant performance gains were observed. It is believed that "the unfilled portion of the tube acts to increase the blow-down relaxation length and time scales" [2]. Alternatively, converging and/or diverging nozzles can be used to alter the blow-down process. Eidelman and Yang [3] have shown that various nozzle geometries dramatically affect the performance of a PDE.

Another conventional method of increasing thrust from an engine is by augmenting the engine with an ejector. The ejector is typically used to direct the entrainment of ambient air into the exhaust plume and promote the mixing of the hot combustion products with the relatively cooler

†Corresponding Author: Ephraim.Gutmark@uc.edu

Copyright © 2003 by Daniel Allgood. Published by the American Institute of Aeronautics and Astronautics, Inc., with permission.

ambient flow, whereby an increase in exhaust mass flow rate is obtained. Due to the increased exhaust mass flow, thrust augmentation can be achieved with an appropriately contoured ejector. Previous work by Bernardo and Gutmark [4] have shown the potential of using ejectors to entrain mass flow for steady-flow supersonic jets. However, the benefits of pulsed vs. steady supersonic ejectors, as a function of frequency, is not known.

The successful extension of this concept to pulse-detonation engine applications hinges upon rapid mixing between the primary (detonation) stream and the secondary (ambient) stream over a short distance. Due to the unsteady nature of the detonation, strong vortical structures can develop which can aid in the mixing of the two streams thus providing additional thrust augmentation over steady-flow ejectors [5]. In addition to the thrust augmentation due to mass entrainment, an ejector for a PDE can provide thrust by favorably altering the blow-down process. Preliminary investigations of pulse detonation driven ejectors have been performed computationally by Allgood et al. [6] and experimentally by Hoke et al. [7].

Insight into how devices such as nozzles and ejectors affect the thrust production of a PDE can be obtained by visualizing the exhaust jet. Development of design guidelines for optimization of PDE systems requires a complete understanding of this complex and dynamic jet flow and the ability to predict its behavior. Although separate experimental and computational studies on PDE's have been performed and are published in the literature, there has been a lack of direct comparison between data produced from experimental flow diagnostic techniques, such as shadowgraph/schlieren visualizations, and computational modeling predictions. The current work is presented as a preliminary contribution in this area. The first objective was to develop a shadowgraph/schlieren system that was capable of capturing the fast moving detonation wave without any visible smearing or distortions of the shock waves. This required nanosecond duration of light pulses from the shadowgraph light source that must be synchronized with the detonation event. The second objective was then to compare these results to direct numerical simulation predictions. This direct comparison would provide guidance and validation towards the development of accurate tools for modeling pulse detonation engines.

Experimental Facility

The experimental data presented here was obtained through the use of the research pulse detonation engine (PDE) at the Air Force Research Laboratory located at Wright-Patterson Air Force Base. The PDE test facility was located in a 750,000 cubic feet test cell that was enclosed by 2ft reinforced concrete walls. The valve system of the PDE was constructed from a modified automotive cylinder head. Hydrogen and air were metered through choked flow nozzles and premixed before being injected into the PDE tube. The pressure and flow rate data was collected via a remote 5MHz 16-channel ADC system. The PDE was mounted on a 1000 lbf maximum damped thrust stand. However, during these tests the thrust stand was prevented from moving to allow accurate and repeatable shadowgraph visualizations of the exhaust flow to be obtained. For a more detailed description of the PDE test facility the reader is referred to the recent paper by Schauer et al. [8].

A detonation tube of 2-inch diameter and 40-inch length was used in the current work. The PDE was operated at stoichiometric conditions of premixed hydrogen/air and the tube was completely filled with a detonable mixture before being ignited. Two pressure transducers were mounted 6 inches apart to monitor the speed of the detonation wave. The measured wave speed was confirmed to be approximately the Chapman-Jouget wave speed of 1966 m/s. One of the two transducers were mounted 12 inches upstream of the exit of the PDE and was used to trigger the shadowgraph system.

In addition to the straight tube experiments, the effects of exit-area reduction on the structure of the detonation wave and dynamic blow-down process was visualized. A standard 1.84:1 diameter ratio pipe reducer (3.5 inches long) served as a converging nozzle and was mounted at the end of the detonation tube.

Nanopulser Shadowgraph System

A shadowgraph imaging system for visualizing pulse detonation engine flowfields was designed and constructed at the University of Cincinnati. This unique imaging system utilizes a nanopulser arc light source (XENON CORP.) that delivers 10 nanosecond duration light pulses. Light pulses of this time scale were necessary to capture traveling detonation waves without excessive smear of the leading shock wave. For example, for a Chapman-Jouget wave speed of 2000 m/s, the shock wave will only have moved 0.02 mm in the image. Figure 1 shows a schematic of the UC shadowgraph system aligned to visualize the exhaust flow of the AFRL PDE test rig. The light was collimated by 6" f/8 parabolic mirrors and refocused onto a high-speed CCD imager using a modified z-configuration. This arrangement was selected due to physical limitations of the laboratory. To avoid CCD saturation, neutral density filters were used to attenuate the light before entering the camera. During the testing, both the camera and the light source were triggered using a pressure transducer mounted 12-inches upstream of the exhaust of the PDE. When the pressure transducer recorded the event of a passing detonation wave (i.e. the voltage exceeded a given threshold) a TTL signal was sent to both the camera and the light source. By varying the delay of the light source, successive images could be captured to reconstruct the dynamic blow-down process of one complete detonation cycle from separate detonation events. The repeatability of the detonations was evident in the consistency of the images that will be shown in the experimental results section of this paper.

Description of Computational Simulations

A two-dimensional Navier-Stokes solver was written in generalized coordinates (figure 2) at the University of Cincinnati. The numerical method for solving the governing equations was the explicit 2nd-order MacCormack predictor-corrector technique with the nonlinear monotonicity preserving 4th-order FCT (Flux-Corrected Transport) scheme [9]. The artificial damping and anti-diffusion coefficients used in the FCT algorithm were those recommended by Boris and Book [9] for minimum residual diffusion.

The chemical reactions are represented by the parametric Korobeinikov model [10] consisting of a two-step reaction mechanism: 1) a non-exothermic irreversible induction reaction where the progress variable (α) changes from 1 to 0, and 2) an exothermic reversible recombination reaction with its progress variable (β) changing from 1 to βeq (0.23). The rates of change of these variables were expressed in the Arrhenius form given in figure 2. This two-step reaction model has been used successfully in the past to address two-dimensional unsteady detonation problems [11-13]. The parameters of the model were chosen to represent a stoichiometric hydrogen-oxygen mixture diluted with argon ($2H_2+O_2+7Ar$) [10]. This mixture is known to generate a well-behaving detonation with a Chapman-Jouguet (C-J) detonation wave Mach number of 4.8.

The computational grid used in the simulations is outlined in figure 3. A uniform mesh with a grid spacing of 0.02933 cm (0.011547 inches) was selected. This resolution provided at least 10 points within the induction zone of a CJ detonation wave, which has been shown in previous studies to be more than adequate for resolving the correct cell size of the regular two-dimensional cellular detonation wave [14]. The time-step was chosen based on a CFL number of 0.2.

Due to the near symmetry of the problem, symmetry-boundary conditions were imposed at the bottom boundary of the computational domain (see figure 3). This allowed a smaller grid size to be used in the simulations. The top and bottom of the domain were modeled as exit boundaries with 1st order extrapolations being imposed. The left boundary was modeled as a reflective wall. The pulse-detonation engine tube and head wall were also modeled as reflective free-slip walls. Wall boundary layer effects were not modeled in the simulations. The diameter of the PDE tube was matched to the 2-inch diameter tube used in the experiments. However, due to computer memory restrictions, a shorter detonation tube of 10 inches was used in the modeling. Thus, only the data for the initial blow-down process was compared to the experiments.

The detonation was initiated in the simulations by an initial condition of two small high pressure/temperature regions near the head end of the tube. The energy level and size of the ignition regions were chosen to produce a fast and stable cellular detonation wave. The entire domain was modeled as a stationary uniformly filled mixture of combustible gases. This uniform mixture distribution was selected since the tube was being generously overfilled during the experiments, and because the level of overfilling could not be accurately determined, the entire computational domain was initially filled with a detonable mixture. Future computational and experimental efforts will investigate the effects of overfilling/underfilling the tube on the structure of the PDE exhaust flow.

Experimental Results

Two PDE configurations were tested in the current work. The first configuration was a 2-inch diameter straight tube of 40-inch length with no exit nozzle present. The tube was completely filled with a detonable mixture of H2 and air (fill fraction ≥ 1). Only single shot detonations were run in these experiments. The second configuration had the same geometry as the first except for a 1.84:1 diameter ratio converging nozzle at the exit of the PDE. Sample pressure traces recorded by the pressure transducer are given in figure 4. The figure shows that the converging nozzle maintained the pressure in the PDE tube for a longer time period. By restricting the mass flow and thereby delaying the blow-down process, a converging nozzle improved the thrust production of a PDE but could limit its maximum operating frequency due to the increased blow-down time.

Figures 5a and 5b are series of shadowgraph images for configuration 1 with no exhaust nozzle present. The numbers below each image correspond to the time delay in milliseconds that was added to the light source. For example, the first image in Figure 5a shows the detonation wave exiting from the detonation tube 0.3125 ms after the wave had passed the pressure transducer. This image also shows that very strong gradients were produced by the leading shock wave as indicated by the thick black band in front of the leading shock wave. As the detonation front exited from the tube, the shock wave wrapped itself around the tube and traveled both upstream and downstream of the PDE. Behind this leading shock wave was a small zone of gas that separated the shock front from the combustion products (see the 0.45ms image). This is believed to be the well-known induction region of a detonation wave.

As the combustion products expanded out of the PDE into a large plume, a well-defined vortex formed and a strong Mach disk developed approximately 1 diameter downstream of the exit as shown in the 0.51ms image. The continued decay in tube pressure to atmospheric pressure caused the Mach disk to weaken into oblique shocks, which at this time have now propagated upstream closer to the exit of the PDE (t=0.62ms). At a delay of 0.7ms, the oblique shock waves were no longer visible. At 3ms, the pressure recorded by the upstream transducer had dropped to atmospheric pressure and the exhaust flow resembled that of a turbulent jet. When the pressure inside the tube over-expanded below atmospheric pressure, the jet was observed to contract in diameter resembling a venturi effect. Finally, 6.5 ms later no combustion gases were seen to exit from the tube.

The converging nozzle was then placed at the exit of the PDE tube to observe the effects of the reduction in area on the exhaust flow. Figure 6 is a collection of shadowgraph images obtained for this configuration. Several differences in the flow structures were observed. First, the detonation wave exiting from the converging nozzle appeared to have a more oblong shape, in that the leading shock wave moved much more rapidly along the centerline of the PDE than in the radial direction along its outer periphery. This was a result of the constriction accelerating the detonation wave before exiting the PDE. Second, the vortex produced by the detonation wave was initially smaller than in the case without the constriction. This change in vortex size was expected since the exit jet diameter was smaller with the converging nozzle. However, the size of the vortex is an important parameter in the operability of a PDE driven ejector [6]. The ejector should be properly sized so as to be able to ingest the vortex plume.

Thus, optimum ejector dimensions will be a function of the PDE exit nozzle geometry.

The final observation that can be made from these results is that Mach wave radiation during the blow-down process was more visible with a converging nozzle at the exit of the PDE. This might suggest that a converging nozzle would produce more turbulent jet noise. In future PDE noise studies, detailed acoustic measurements will be obtained to quantify any difference in the noise levels due to exit nozzle geometry and correlate these differences to the observations made in the shadowgraph visualizations.

Computational Results

The results obtained from the computational modeling were processed to visualize the gradients in density and species (mass fraction) concentrations. This provided a means for qualitatively comparing the simulations to the shadowgraph data shown previously. It should be noted that shadowgraph images are a result of line-of-sight integration. No corrections in the data were made for this difference. Also, due to the limitation of the computational grid size and the small viewing range of the shadowgraph system, only the initial exiting of the detonation wave was compared.

Figure 7 is a collection of images of experimental (top-half of each image) and computational (bottom-half of each image) visualizations for the straight tube configuration. The first image in figure 7 corresponds to a delay of 0.325ms from when the detonation wave passed the upstream pressure transducer. Both the experimental and computational results showed qualitatively the same structure and size of the exiting detonation wave – a strong leading shock wave closely followed by a region of hot combustion products. The leading shock wave of the detonation wave was observed to be nearly planar near the centerline of the PDE tube and more spherical near the outer periphery of the tube. Furthermore, both results showed a strong backward propagating shock wave.

The second and third images in figure 7 begin to show clearly that as the detonation wave exited the tube, the leading shock increased its detachment distance from the trailing combustion gases. This separation distance of the leading shock from the combustion gases was accurately predicted by the modeling. Inside the detachment region, both the experiments and modeling visualizations depict the formation of randomly spaced compression waves.

The final observation that can be made from this comparison is that the computations model correctly the relative rate of growth of the leading shock wave and the formation and size of the trailing vortex. Future studies will investigate the ability of the modeling in simulating the latter stages of the blow-down process for this case and other exit nozzle configurations.

Conclusions

Shadowgraph visualizations of a pulse detonation engine exhaust flowfield were performed using a new 10 nanosecond duration light source. The complete blowdown cycle was reconstructed by synchronizing the shadowgraph system with the detonation event. Images of the highest quality were obtained with this new visualization system due to the short pulse of light produced by the source. No smear or distortion of the detonation front and shock waves was observed. The experimental visualizations were then compared to preliminary computational modeling results obtained from a newly developed code at the University of Cincinnati. Very good agreement on the structure and development of the exiting detonation wave was obtained.

The dynamic structure of the exhaust flow of a PDE was visualized. Strong gradients were produced by the leading shock wave of the detonation front. This shock wave was observed to wrap itself around the tube and travel both upstream and downstream of the PDE. Behind the leading shock, a small zone of unreacted gas separated the shock from the combustion products. The combustion products exited the PDE initially as a large vortex ring followed by an under-expanded turbulent jet. During the early stages of the blowdown process, a strong Mach disk formed in the turbulent jet approximately 1 diameter downstream of the exit of the PDE. When a

converging nozzle was placed at the exit of the PDE, a more elliptical detonation front was produced due to the centerline acceleration of the shock wave. Mach wave radiation was also more visible with the converging nozzle, signifying possible changes in jet noise levels. Acoustic flowfield measurements will be performed in future studies.

Currently, tests are being performed to study the effects of various nozzle geometries (converging, diverging, etc.) and system parameters such as fill fraction, ignition timing and equivalence ratio on the exhaust flow and correlating these effects to changes in performance levels. Preliminary tests on ignition timing however showed little affect on the structure of the detonation wave. These tests are being conducted with our new system that utilizes 12-inch diameter mirrors to provide a larger viewing area. With this system, we will be able to investigate the flow field under the presence of an exhaust ejector. In parallel to the shadowgraph/schlieren visualizations, we will perform simultaneous OH PLIF visualizations to investigate the coupling between the chemical reactions and gas dynamics.

Acknowledgements

The authors would like to extend our appreciation to Richard DeLoof from NASA Glenn Research Center for sponsoring this research under grant NAG3-2669.

References

1. Kailasanath, K. “Recent Developments in the Research on Pulse Detonation Engines,” 40th AIAA Aerospace Sciences Meeting, AIAA 2002-0470.

2. Schauer, F., Stutrud, J., and Bradley, R., “Detonation Initiation Studies and Performance Results for Pulse Detonation Engine Applications,” 39th AIAA Aerospace Sciences Meeting, AIAA 2001-1129.

3. Eidelman, S., Yang, X., “Analysis of the Pulse Detonation Engine Efficiency,” 34th Joint Propulsion Conference, AIAA 98-3877.

4. Bernardo, A. and Gutmark, E., "Supersonic Rectangular Ejector”, 30th AIAA Joint Propulsion Conference, Indianapolis, IN, June 1994.

5. Munipalli, R., Shankar, V., Wilson, D., Kim, H., Lu, F., and Liston, G., “Performance Assessment of Ejector Augmented PDRs,” 39th AIAA Aerospace Sciences Meeting, AIAA 2001-0830.

6. Allgood, D., Gutmark, E., and Viswanath, K. “Effects of Exit Geometry on the Performance of a Pulse Detonation Engine”, AIAA 2002-0613, 40th Aerospace Sciences Meetings and Exhibit, Reno NV, Jan. 14-17.

7. Hoke, J., Bradley, R., Stutrud, J., and Schauer, F. “Integration of a Pulsed Detonation Engine With an Ejector Pump and With a Turbo-charger as Methods to Self-Aspirate”, AIAA 2002-0615, 40th AIAA Aerospace Sciences Meeting and Exhibit, Reno NV, Jan. 14-17.

8. Schauer, F., Stutrud, J., and Bradley, R. “Detonation Initiation Studies and Performance Results for Pulsed Detonation Engine Applications”, AIAA 2001-1129, 39th AIAA Aerospace Sciences Meeting & Exhibit, Reno, NV.

9. Boris, J. P. and Book, D. L. “Solution of Continuity Equations by the Method of Flux-Corrected Transport”, *Methods of Computational Physics*, Vol. 16, Academic Press, NY, pp. 85-129, 1976.

10. Korobeinikov, V., Levin, V., Markov, V. and Chernyi, G. “Propagation of Blast Waves in a Combustible Gas”, Astronautica Acta, Vol. 17, No. 4 & 5, pp. 529-536, 1972.

11. Taki, S. and Fujiwara, T., “Numerical Analysis of Two-Dimensional Nonsteady Detonations,” AIAA J. 16, 73 (1978).

12. Reddy, K. V., Fujiwara, T., and Lee, J. H., “Role of Transverse waves in a Detonation Wave--A Study Based on Propagation in a Porous Wall Chamber,” Memoirs of the

Faculty of Engineering, Nagoya University, Vol. 40, No. 1, 1988.

13. Oran, E. S., Young T. R., Boris J. P., Picone J. M., and Edwards, D. H., "A Study of Detonation Structure: The Formation of Unreacted Gas Pockets," Ninteenth Symposium (International) on Combustion, pg. 573, The Combustion Institute, PA, 1982.

14. Kawai, S. and Fujiwara, T., "Numerical Analysis of 1st and 2nd Cycles of Oxyhydrogen PDE", AIAA 2002-0929, 40th AIAA Aerospace Sciences Meeting and Exhibit, Reno NV, Jan. 14-17.

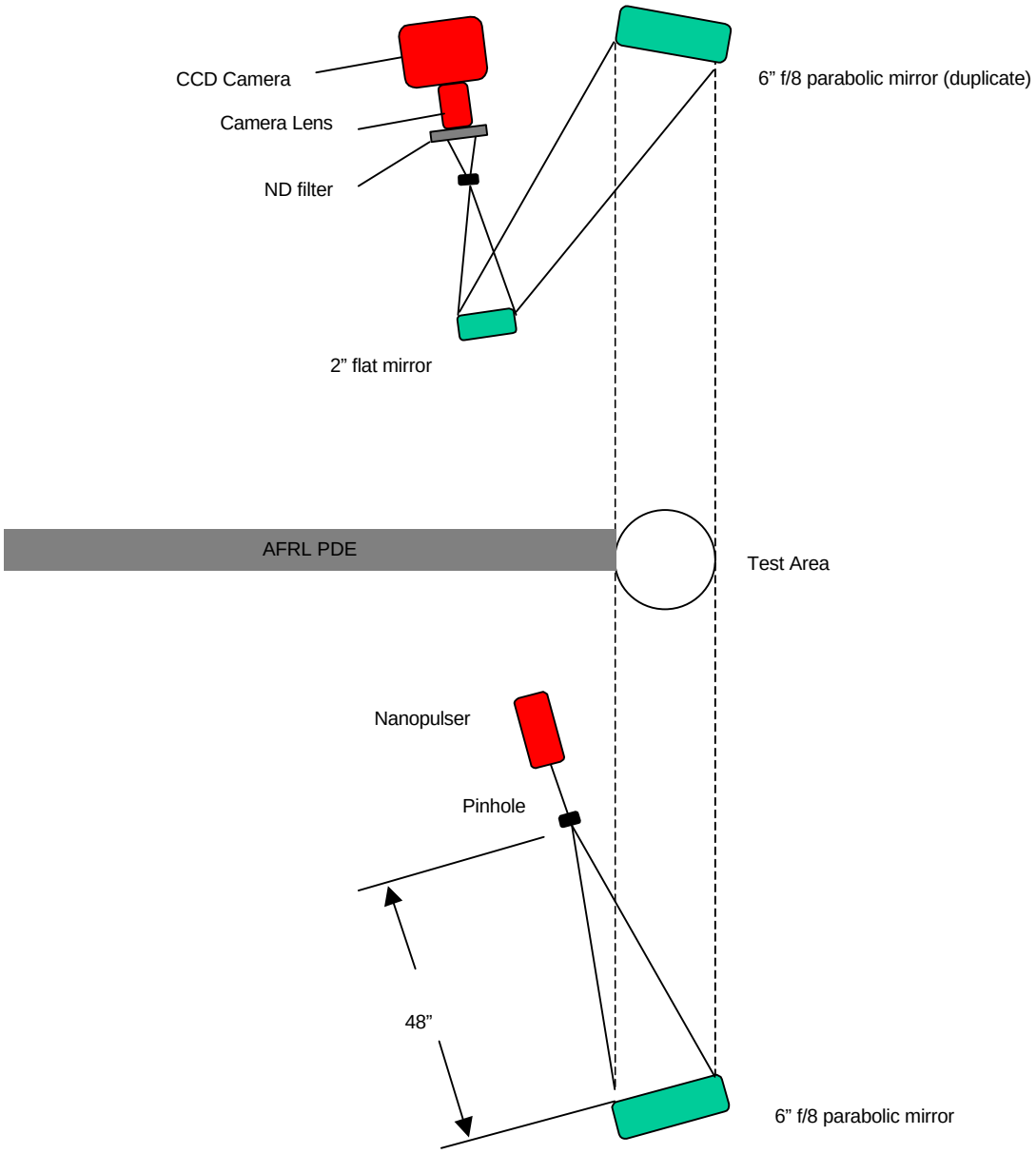

Figure 1: University of Cincinnati Shadowgraph/Schlieren Visualization System

$$\frac{\partial \bar{U}}{\partial \tau}+\frac{\partial \bar{E}}{\partial \xi}+\frac{\partial \bar{F}}{\partial \eta}=\frac{\partial \bar{E}_v}{\partial \xi}+\frac{\partial \bar{F}_v}{\partial \eta}+\bar{H}$$

$$\bar{U}=\frac{U}{J},\qquad \bar{E}=\frac{1}{J}\left(\xi_t U+\xi_x E+\xi_y F\right),\qquad \bar{F}=\frac{1}{J}\left(\eta_t U+\eta_x E+\eta_y F\right),\qquad \bar{H}=\frac{H}{J},$$

$$\bar{E}_v=\frac{1}{J}\left(\xi_x E_v+\xi_y F_v\right),\qquad \bar{F}_v=\frac{1}{J}\left(\eta_x E_v+\eta_y F_v\right),\qquad J=\frac{1}{x_\xi y_\eta - y_\xi x_\eta}$$

$$U=\begin{bmatrix}\rho\\ \rho u\\ \rho v\\ E\\ \rho\beta\\ \rho\alpha\end{bmatrix},\qquad E=\begin{bmatrix}\rho u\\ \rho u^2+p\\ \rho uv\\ u(E+p)\\ \rho\beta u\\ \rho\alpha u\end{bmatrix},\qquad F=\begin{bmatrix}\rho v\\ \rho uv\\ \rho v^2+p\\ v(E+p)\\ \rho\beta v\\ \rho\alpha v\end{bmatrix},\qquad H=\begin{bmatrix}0\\ 0\\ 0\\ 0\\ \rho\dfrac{\partial\beta}{\partial\tau}\\ \rho\dfrac{\partial\alpha}{\partial\tau}\end{bmatrix}$$

$$E_v=\begin{bmatrix}0\\ \tau_{xx}\\ \tau_{xy}\\ u\tau_{xx}+v\tau_{xy}-q_x\\ 0\\ 0\end{bmatrix},\qquad F_v=\begin{bmatrix}0\\ \tau_{yx}\\ \tau_{yy}\\ u\tau_{yx}+v\tau_{yy}-q_y\\ 0\\ 0\end{bmatrix}$$

$$\frac{\partial\alpha}{\partial\tau}=-\frac{1}{\tau_{\text{induction}}}=-k_1\rho\exp\left(\frac{-E_1}{RT}\right)$$

$$\frac{\partial\beta}{\partial\tau}=\begin{cases}0, & \alpha>0\\ -k_2 p^2\left[\beta^2\exp\left(\dfrac{-E_2}{RT}\right)-(1-\beta)^2\exp\left(\dfrac{-E_2-Q}{RT}\right)\right], & \alpha\le 0\end{cases}$$

$$k_1=3.0\times10^{11}\frac{cm^3}{g\cdot s},\quad k_2=1.5\times10^{-7}\frac{cm^4}{dyn^2\cdot s},$$

$$\frac{E_1}{R}=9800K,\quad \frac{E_2}{R}=2000K,\qquad Q=4.0\times10^{10}\frac{erg}{g}$$

Figure 2: Governing Equations In The Generalized Coordinate System

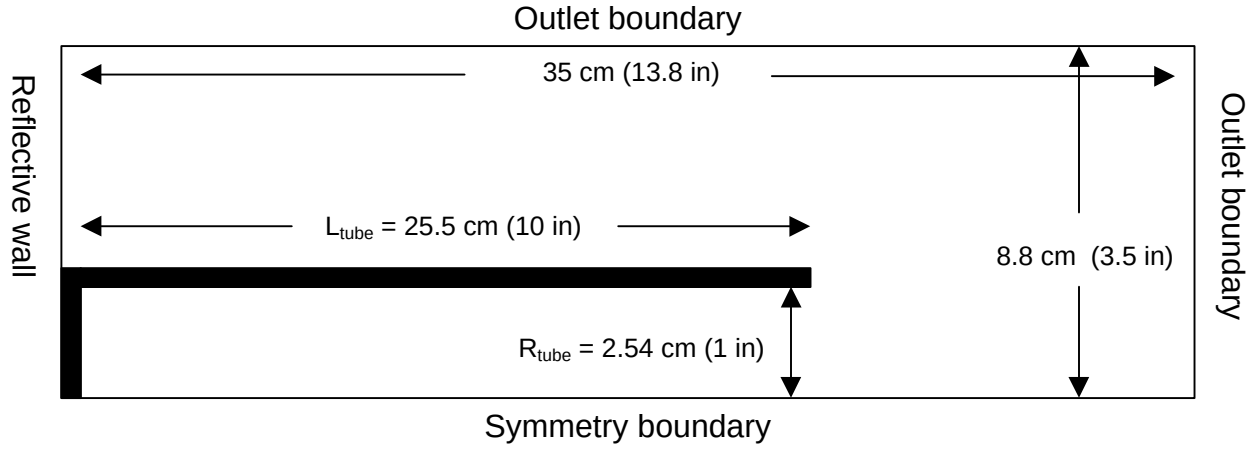

Figure 3: Computational Grid (dx=dy=0.02933cm=0.0115 in)

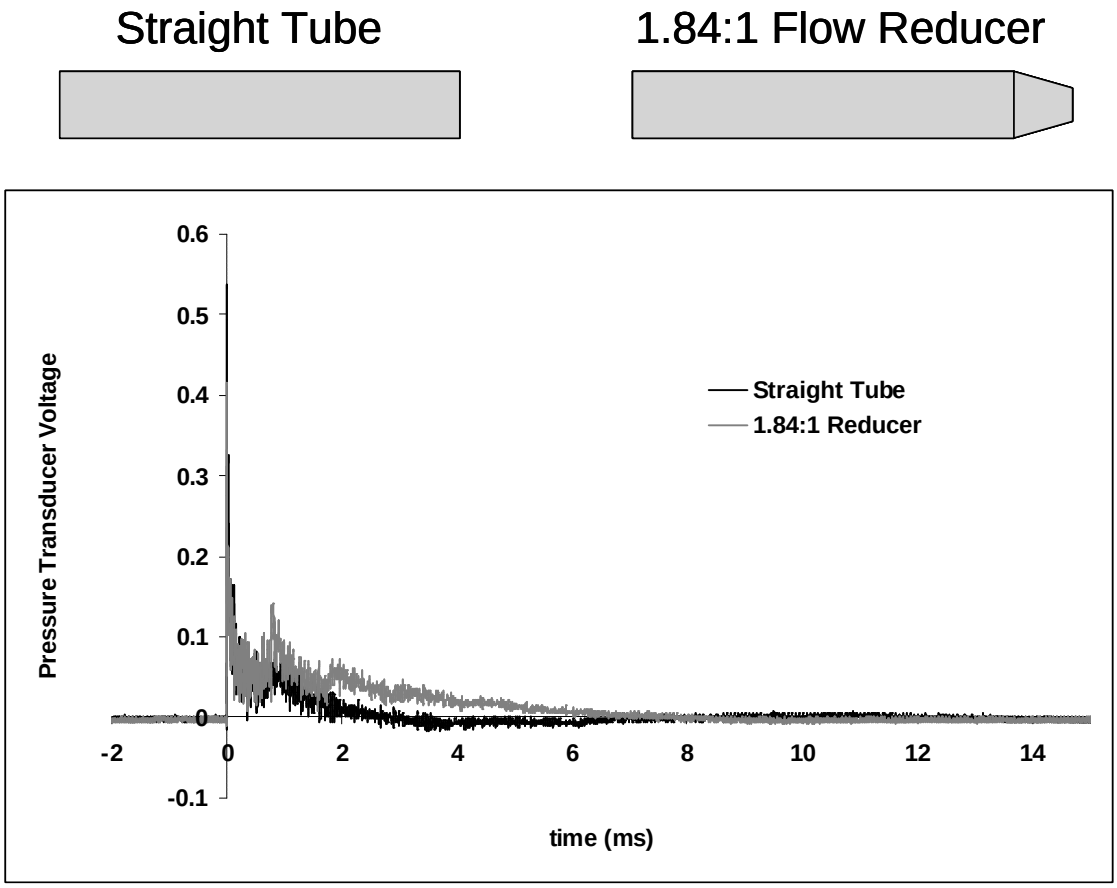

Figure 4: Pressure Traces of PDE Test Cases 1 and 2

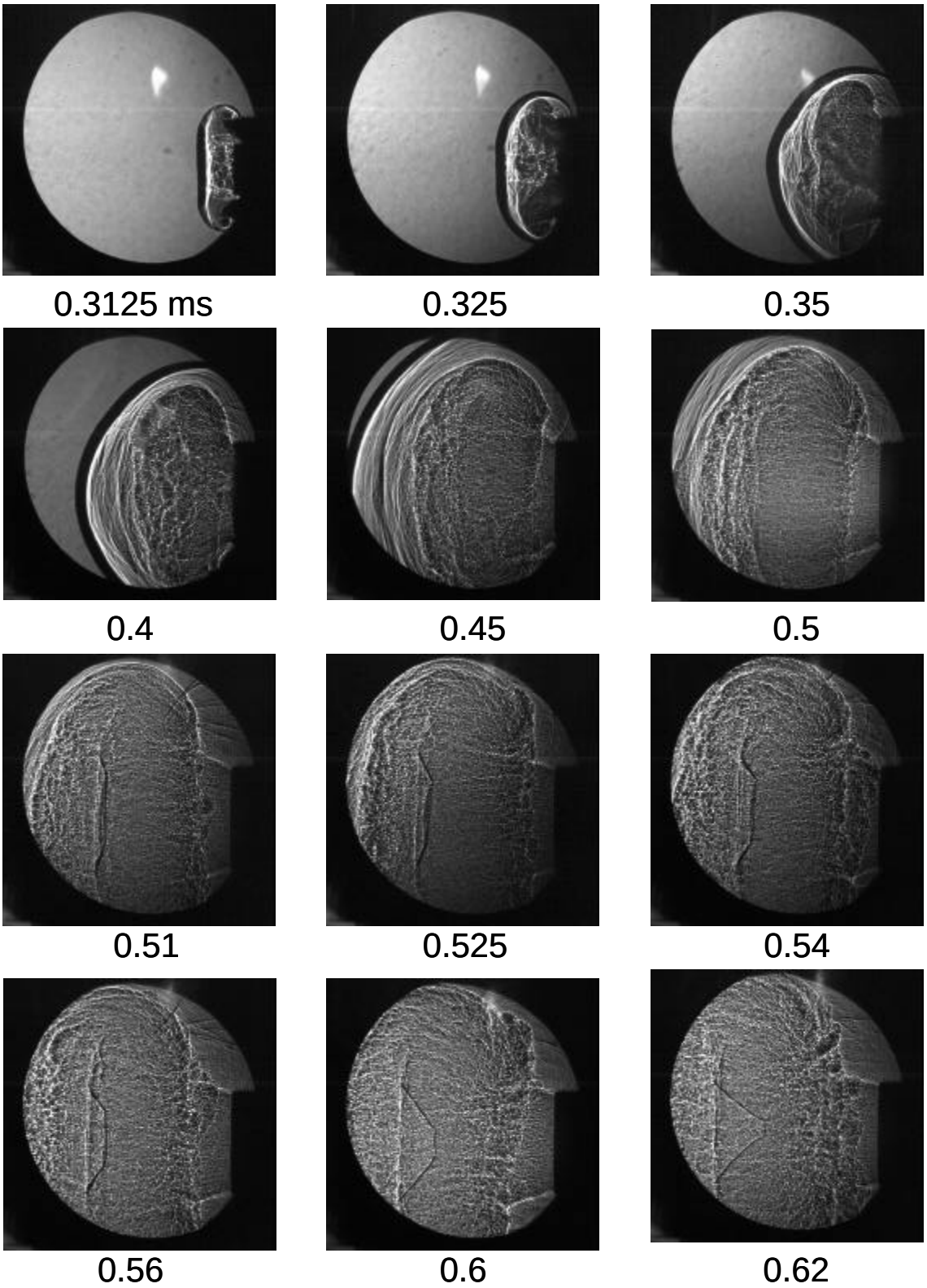

Figure 5a: Shadowgraph Images of Straight Tube (time in milliseconds)

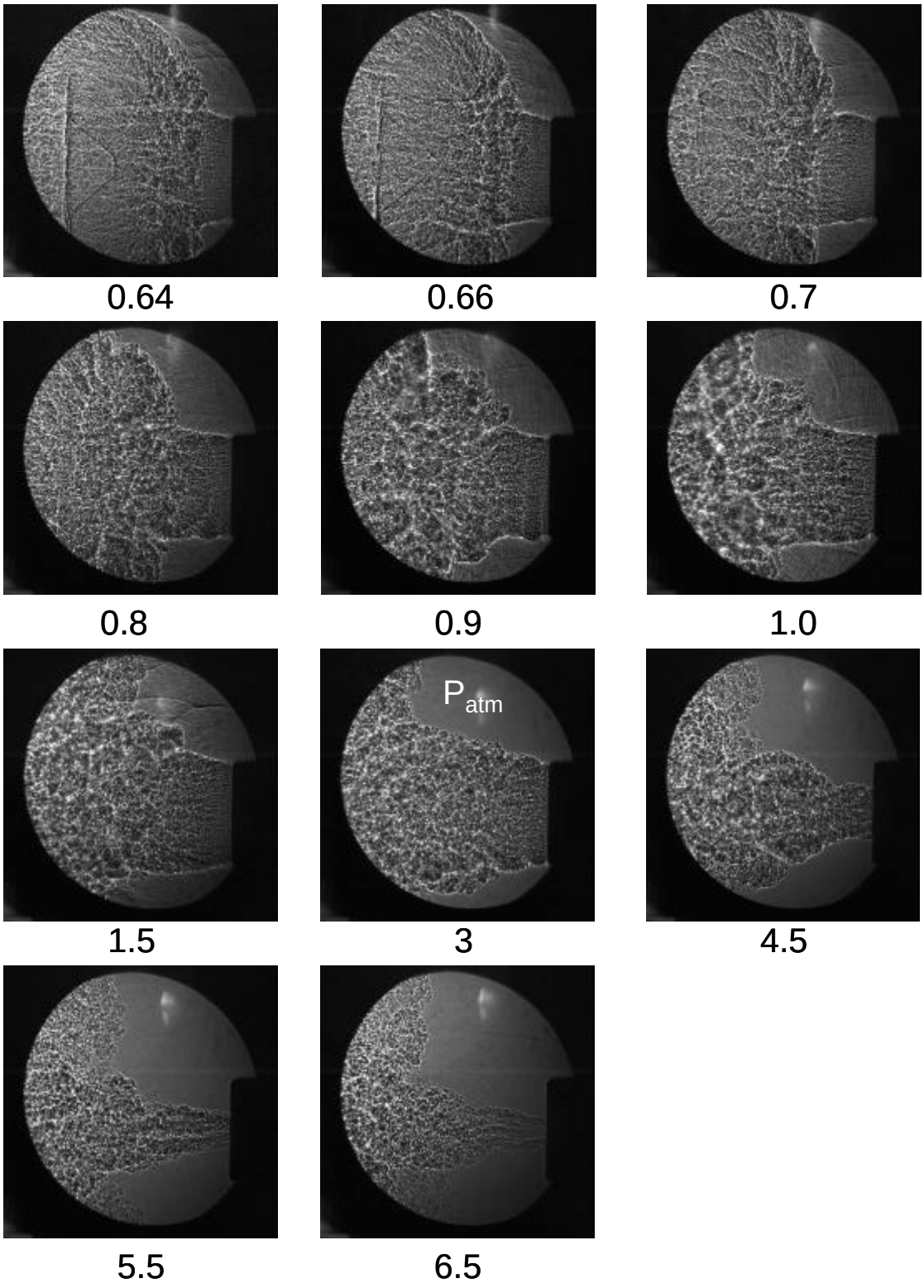

Figure 5b: Shadowgraph Images of Straight Tube (time in milliseconds)

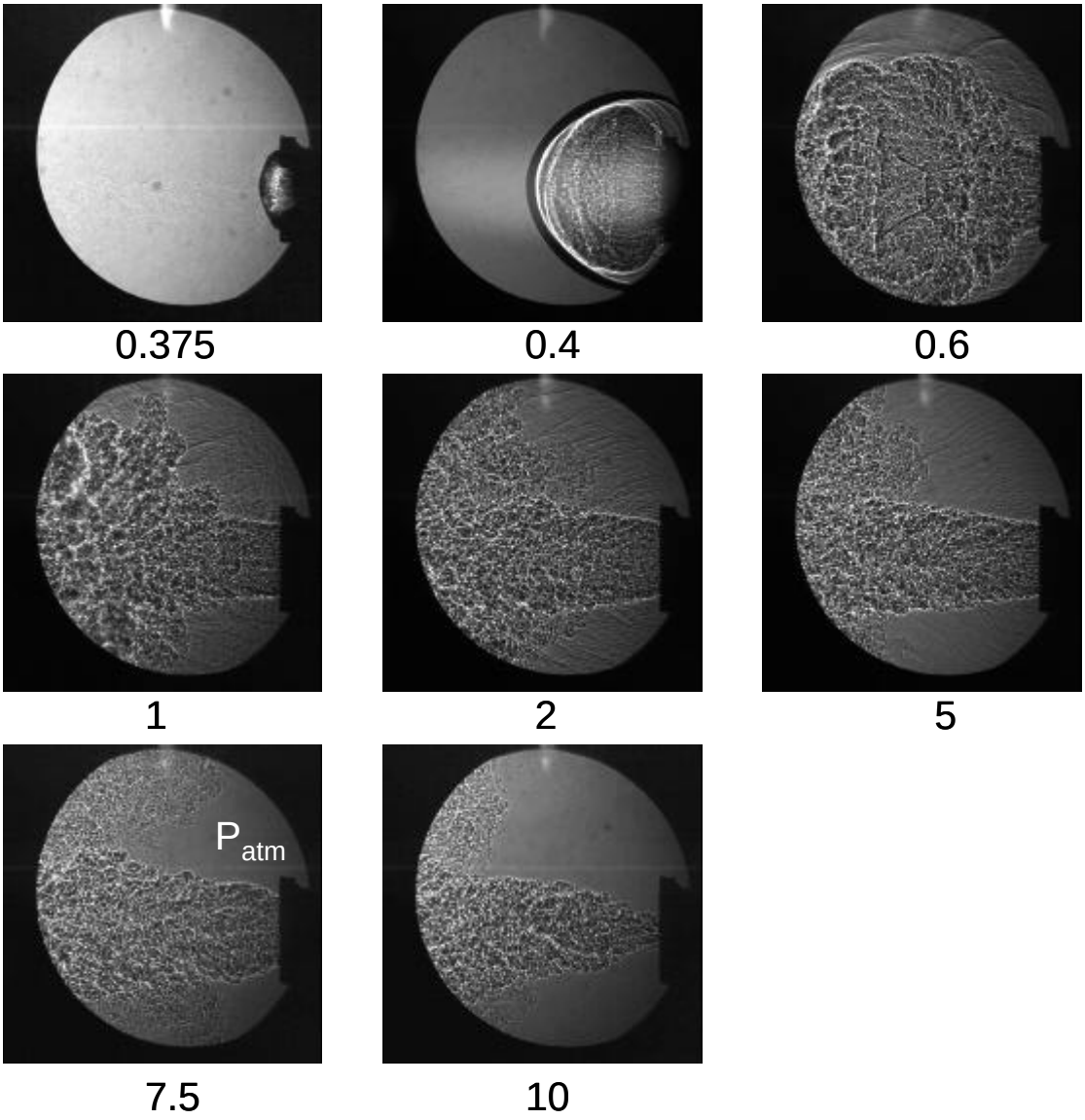

Figure 6: Shadowgraph Images of Converging Nozzle (time in milliseconds)

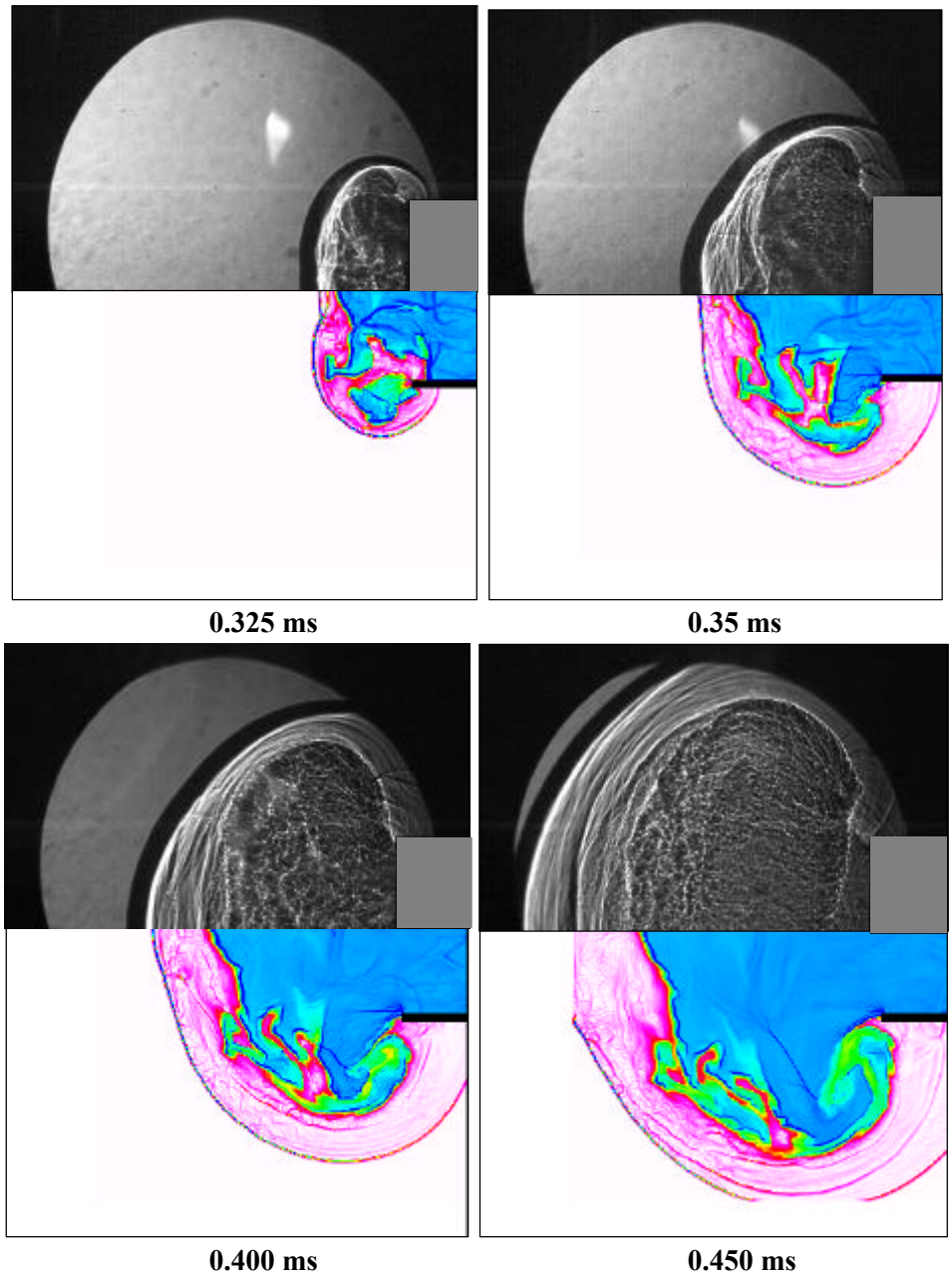

Figure 7: Comparison of Computational Predictions to Experimental Shadowgraphs

OH-BASED FUEL/AIR RATIO MONITOR FOR THE PULSED-DETONATION ENGINE

AIAA Dayton-Cincinnati Aerospace Sciences Symposium
Dayton, Ohio
4 March 2003

Michael S. Brown, Terrence R. Meyer, John L. Hoke, and Jason T. Parker
Innovative Scientific Solutions, Inc.,
Dayton, OH

James R. Gord and Frederick R. Schauer
Propulsion Directorate, Wright-Patterson
Air Force Base

Acknowledgments

- PDE: Jeff Stutrud (AFRL); Royce Bradley (ISSI)
- Funding: Julian Tishkoff (AFOSR)

Overall Approach

PDE Needs: – ground-based sensors for equivalence ratio (EQR)

– on-board sensor for active control of EQR

Response: – OH* emission monitor for equivalence ratio (can be relative) active control

Research Pulsed-Detonation Engine

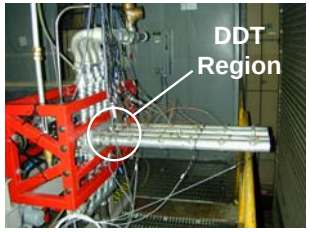

- Hydrogen-Fueled PDE
- High-Speed Digital Imaging
- Quartz or Polycarbonate PDE Tubes
- Shchelkin Spiral

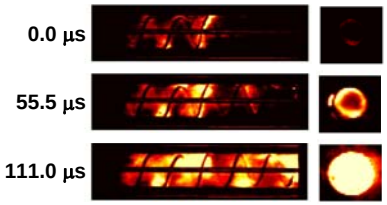

Control System Diagram

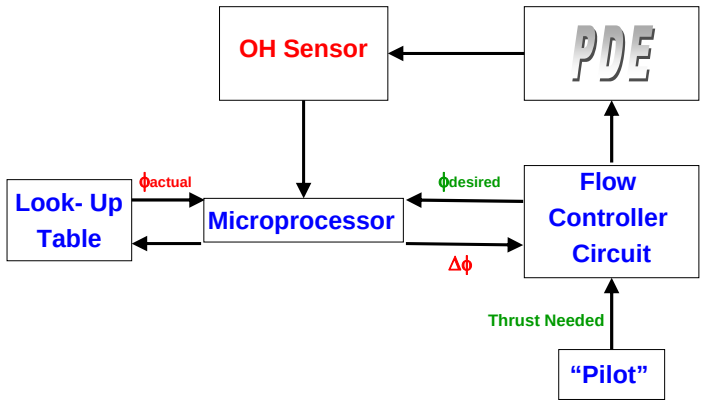

5

Sensor Sensitivity?

PDE Operating Params \ Sensor	Signal Amplitude	Signal Temporal Behavior
Equivalence Ratio	?	?
Fill Fraction	?	?
Ignition Delay	?	?
Repetition Rate	Independent	Independent

Emission Probe Location

End of Collection Fiber Mounted Normal to Tube Body & Flush With Inner Surface of Body

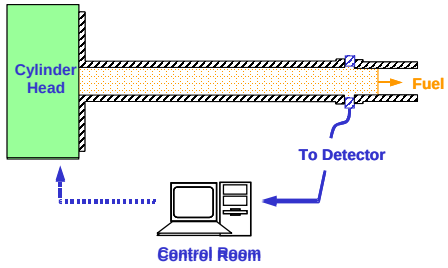

Using a silica multi-mode fiber for light collection

Emission Detection Schemes

All Emission Signals Collected Using a Silica Multi-Mode Fiber

	Detection Scheme #1	Detection Scheme #2
Detector	Filtered PMT	Si CCD Linear Array*
Spectral Range	10 nm @ 310 nm	200 – 870 nm (1.3-nm res)
Sampling Frequency	1 MHz	~ 33 Hz

*Coupled to Commercial Fixed-Grating Spectrometer

8

Typical Emission Spectrum

PDE Sequence of 11 Shots (ϕ = 1, 20 Hz, H_2/Air)

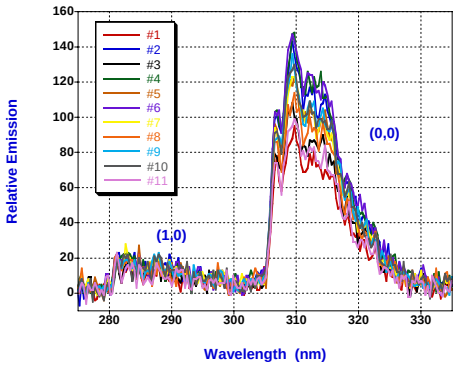

9

Raw OH* Emission Signal

Avgas/air near stoichiometry
78-inch tube, sensor at 50.75 inches
rep. rate - 17 Hz, fill fraction 1,

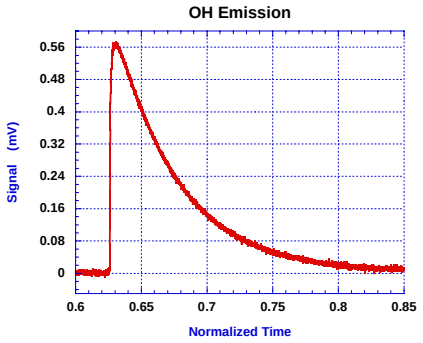

10

Temporal Signature

Temporal behavior of signal reflects OH dynamics & plug flow of PDE

OH:
chemical destruction, quenching, & fluorescent lifetime

PDE:
plug flow of distributed sample volume

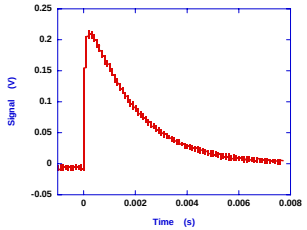

11

Single-Shot Signals

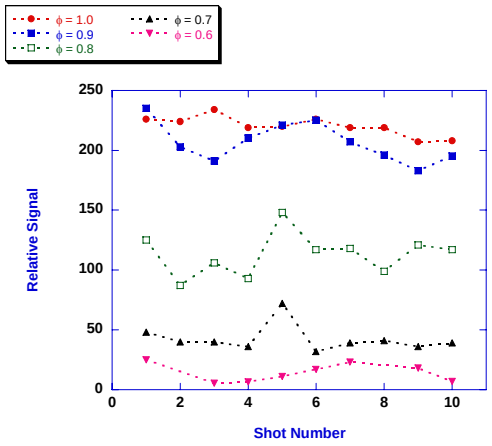

12

Fill Fraction Study

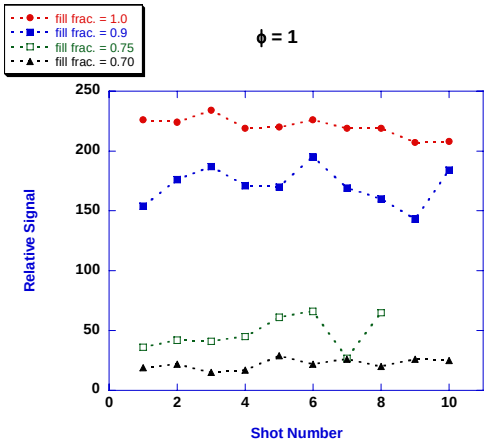

13

Time-Averaged Emission Signals

Hydrogen/air, 20 Hz, fill fraction of 1

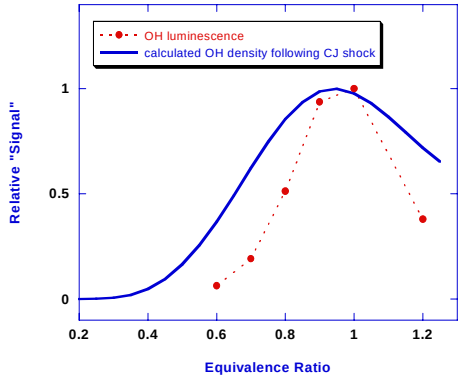

14

OH* in Propane/Air

78-inch tube, sensor at 50.75 inches
rep. rate - 20 Hz, fill fraction 1,

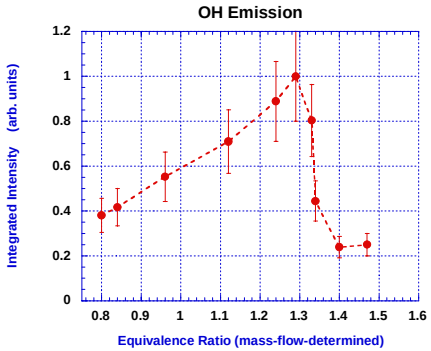

15

Integrated OH* Emission

Avgas/air near stoichiometry
78-inch tube, sensor at 50.75 inches
rep. rate – 17-20 Hz, fill fraction 1,

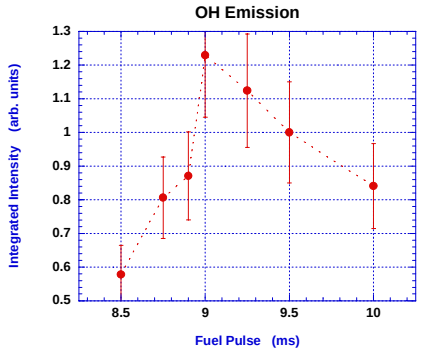

16

Summary

Chemiluminescence spectra of OH have been acquired in a single-tube pulse detonation engine.

The OH signals show a strong correlation with global equivalence ratio.

Sensor / PDE Operating Params	Signal Amplitude	Signal Temporal Behavior
Equivalence Ratio	Strong	Independent
Fill Fraction	Strong	Independent
Ignition Delay	Weak	Independent
Repetition Rate	Independent	Independent

17

Conclusions & Future Work

Conclusions

•Successfully demonstrated emission sensor for equivalence ratio measurements

• Simple hardware platforms used repeatedly without failure

Future Efforts

•Construct a small inexpensive package including feedback algorithm for flying platform

18

Fiber-Coupled Laser Sensor for In-Situ Measurement of Hydrocarbon Fuels in Pulsed-Detonation Engines

T. R. Meyer, M. S. Brown, J. L. Hoke, and J. T. Parker
Innovative Scientific Solutions, Inc.

J. R. Gord and F. R. Schauer
Air Force Research Laboratory/PRTS

28th Annual Dayton-Cincinnati Aerospace Sciences Symposium
Dayton, Ohio 2003

Acknowledgments

Air Force Research Laboratory / ISSI:

- Royce Bradley and Curtis Rice

Boeing:

- Mark Younger

Funding:

- Air Force Research Laboratory and NASA

Introduction

PDE Sensor Needs:

- Ground-based sensor for tube fill history & equivalence ratio
- Capable of surviving detonating conditions
- Flexibility for use in different fuels and tube geometries
- Ease of use and speed of implementation

Approach:

- Line-of-sight laser absorption at HC resonance of 3.39 μm
- Fiber coupled
- Species to date: propane and aviation gasoline

Theory of Operation

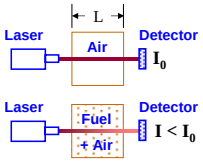

$$\frac{I}{I_0} = \mathrm{Exp}(-\varepsilon cL)$$

c = concentration
L = path length
ε = absorption coefficient
= fcn (species, T,P)

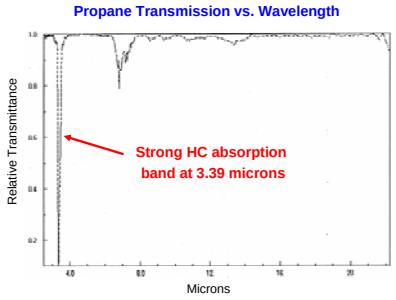

T and P Dependence

P dependence of $\varepsilon_{Propane}$ at 3.39μm:

- Varies by about 10% at 10atm
- Varies by about 20% at 100atm

T dependence of ε_{HC} at 3.39 μm:

- 1 atm: 5% per 100K
- 10 atm: 2.5% per 100K
- 20 atm: less than 1% per 100K

T-P dependence of equiv. ratio:

$$\text{Equiv. Ratio} = \phi = \frac{-\log(I/I_0)}{0.042[\varepsilon L\rho + \log(I/I_0)]}$$

Measured P dependence of ε_{avgas}:

- Fixed-path-length pressure cell
- Fused-silica windows
- Pressurized with nitrogen gas

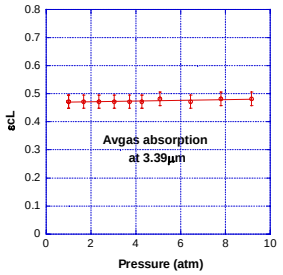

5

Experimental Set-Up

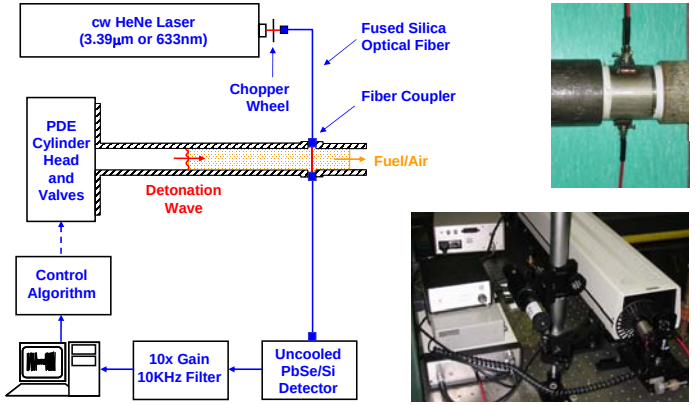

6

Adjustable Path-Length Sensor

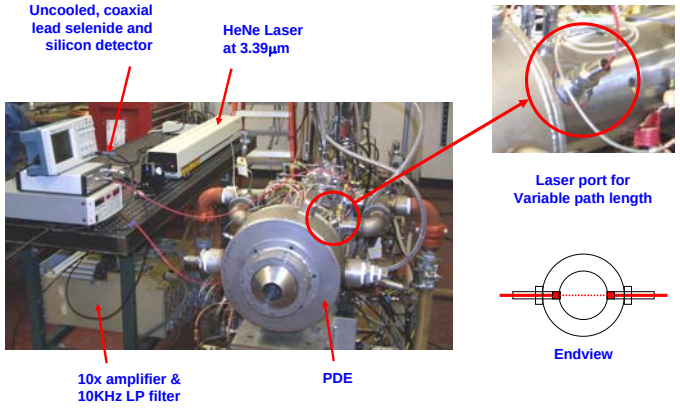

7

Raw Cold-Cycle Propane Signal

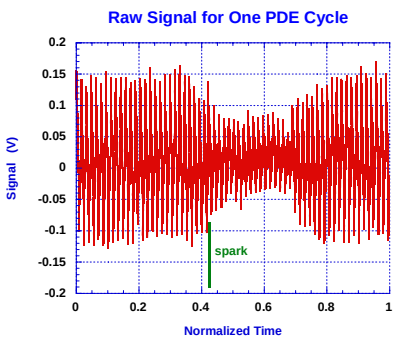

- HeNe output chopped at 1.5 – 4 kHz
- PbSe detector AC coupled to DAQ

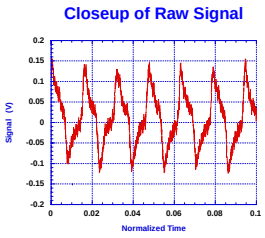

8

Extraction of Equivalence Ratio

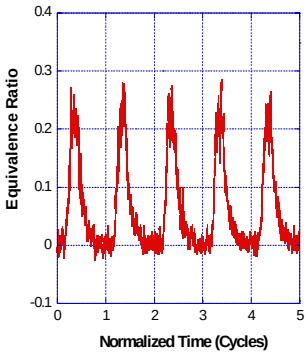

- Expected phi = 0.21
- Sensor near end of tube
- Fuel valve on at time = 0

Closeup of Cycle 1

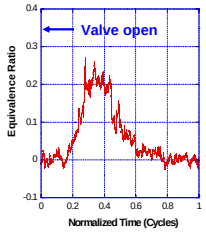

9

Propane Cold Cycle

Measured Φ Versus Mass Flow Φ

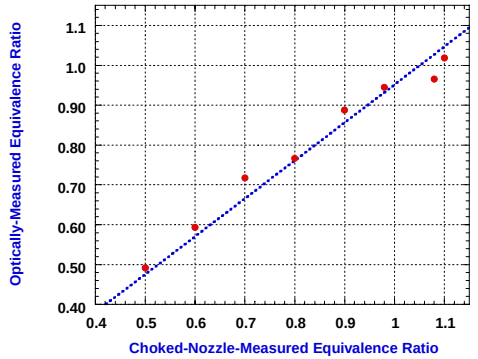

10

Propane Hot Cycle

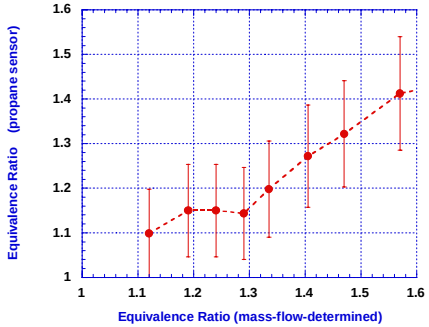

- Sensor located 4/7th down length of tube
- Propane under rich conditions

11

End of Tube Conditions

High-speed movie of PDE detonation decaying near the end of the tube

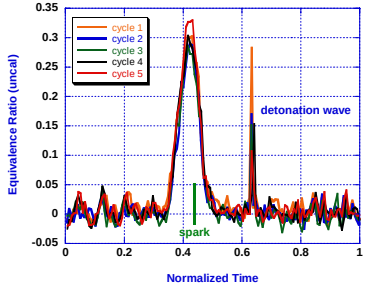

Sensor located 2 inches from end of tube

12

Stratified Charge Detection

Unstratified
(no overlap of
purge and fill)

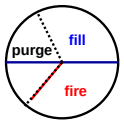

Stratified
(purge and fill
overlap)

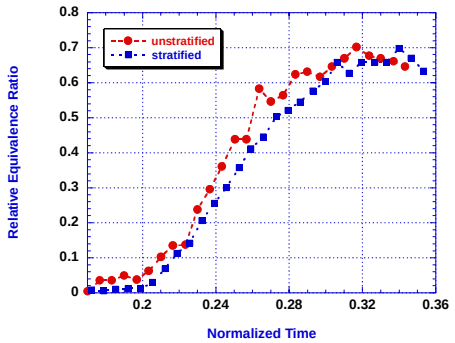

13

Sensor Power Spectrum

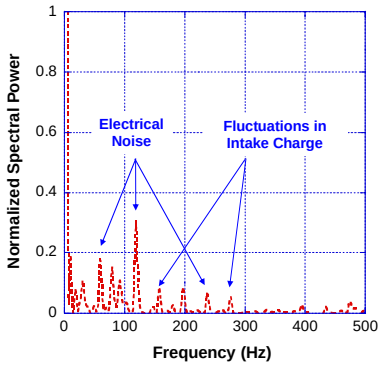

- Cold-flow study of avgas/air Intake flow system
- Spectral analysis reveals sources of signal fluctuation
- Used to fine tune intake system and ignition timing

14

Sample Av-Gas Signal

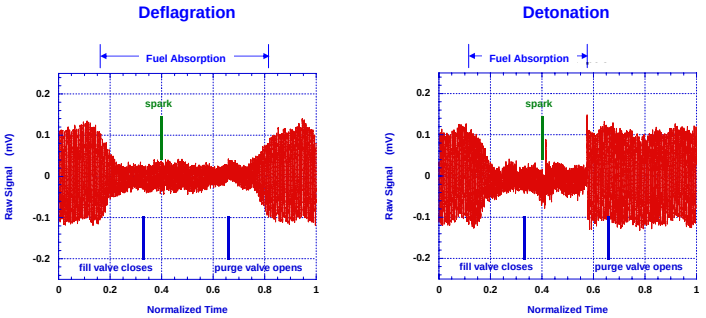

Sensor located 2/3 down
length of tube

15

Av-Gas Hot-Cycle Analysis

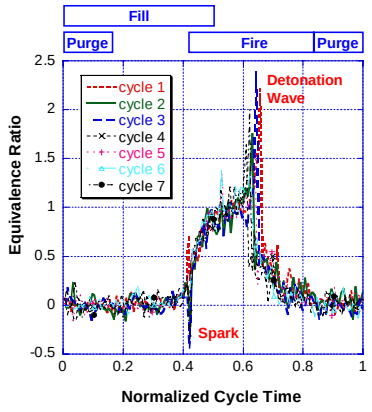

- Sensor located 2/3 down length of tube
- Spark initiated 4ms before end of fill cycle

Closeup of Filling Process

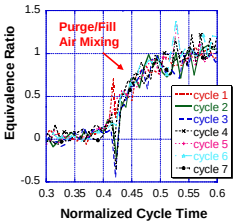

16

Droplets and Particulates

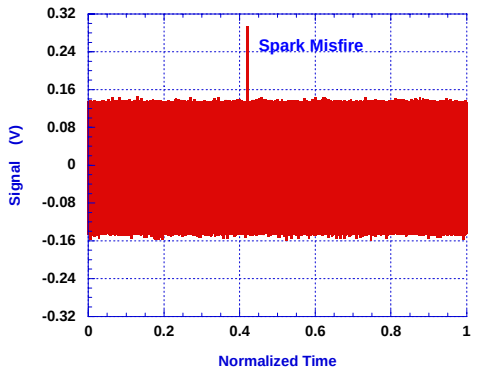

- 633 nm HeNe to detect scattering
- Av-gas cold cycle

17

Summary of Sensor Features

- Fiber coupled for windowless operation and minimal alignment
- Low T and P dependence of certain HC's (e.g., propane and avgas)
- Self-calibrated for each PDE cycle
- No need to scan across single or multiple absorption lines
  - Reduces error due to background subtraction and normalization
  - Can be extended for high-speed operation (currently 4 KHz)
- Ease of use and speed of implementation (< 1 day)
- Can be extended for simultaneous droplet/particulate detection

18

Summary of Sensor Performance

- Successfully recorded time traces of tube fill for propane and avgas
- Extracted equivalence ratios from propane time histories
- Inferred fluid behavior from time histories including stratified charge
- Found no evidence of particulate or droplet interference
- Future work: implement in upcoming NASA tests, calibrate sensor for other HC fuels, implement simultaneous dual-wavelength sensor

19

①

Computational and Experimental Studies of Pulse Detonation Engines

Daniel Allgood and Ephraim Gutmark
University of Cincinnati, Aerospace Engineering

Terry Meyer, John Hoke and Viswanath Katta
Innovative Scientific Solutions Inc.

Fred Schauer and James Gord
AFRL, Wright Patterson AFB

28th Annual Dayton-Cincinnati Aerospace Science Symposium
March 4, 2003

②

COMPUTATIONAL AND EXPERIMENTAL STUDIES OF PULSE DETONATION ENGINES

- Objectives
- Description of Experimental Facility
- Development of the UC Nanopulser Shadowgraph System
- Computational Modeling Approach
- Shadowgraph Visualizations of PDE Exhaust Flows
- Comparison to Computational Modeling Predictions
- Conclusions and Future Work

③

COMPUTATIONAL AND EXPERIMENTAL STUDIES OF PULSE DETONATION ENGINES

- The design of efficient pulse detonation engines (PDE) requires a complete understanding of how components such as exhaust nozzles and ejectors generate thrust and the ability to predict the performance enhancement by these devices.
- Insight into the manner in which these devices produce work can be obtained by visualizing the flowfield.
- Two primary objectives of the current work:
  - Develop the capability of visualizing the complex and dynamic flowfield of a pulse detonation engine (PDE)
  - Develop the ability to predict the PDE flow using computational modeling.

④

COMPUTATIONAL AND EXPERIMENTAL STUDIES OF PULSE DETONATION ENGINES

- Approach:
  - A nano-second shadowgraph/schlieren visualization system was built at the University of Cincinnati that is capable of capturing the fast moving detonation waves without any visible smearing or distortion of the shock structure.
  - A new 2D Navier-Stokes detonation code was written in the generalized coordinates system for modeling contoured geometries.
  - Preliminary comparisons of the computations to the experiments were performed.

AFRL EXPERIMENTAL PDE FACILITY

Capabilities

- Explosion Proof Facility
- Up to 60 klbf Static Thrust / 1,000+ lbf Damped Thrust
- 6 lb/sec 100 psi air supply
- Choked H_2/Air Flow Regulation
- Hardened Remote Control Room
- 16 High Frequency DAC Channels, up to 5Mhz each

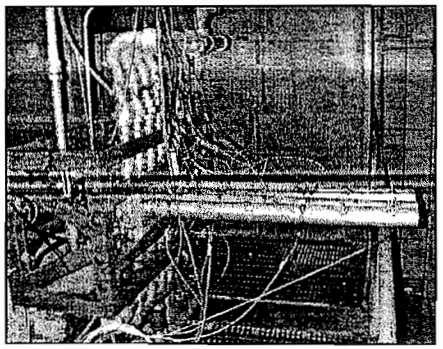

Current Experimental Setup

- PDE Tube: 2 inch diameter, 40 inches long
- Stoichiometric H_2/Air Premixed Mixture
- Fill Fraction of 1
- Measured wave speeds of approximately 1960 m/s (C-J Detonation Wave)
- 2 exit nozzle geometries tested

PULSE DETONATION ENGINE EXHAUST NOZZLES
COMPARISON OF STRAIGHT TUBE TO CONVERGING NOZZLE

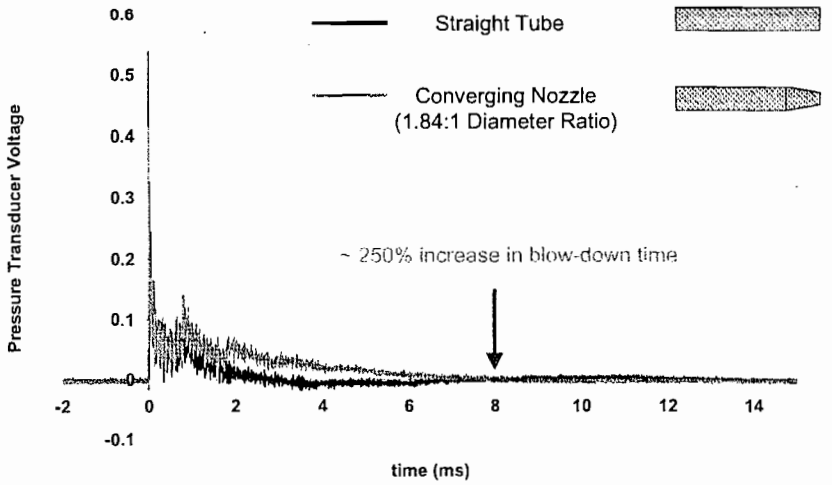

PDE FLOW VISUALIZATION
NANOSECOND SHADOWGRAPH/SCHLIEREN SYSTEM

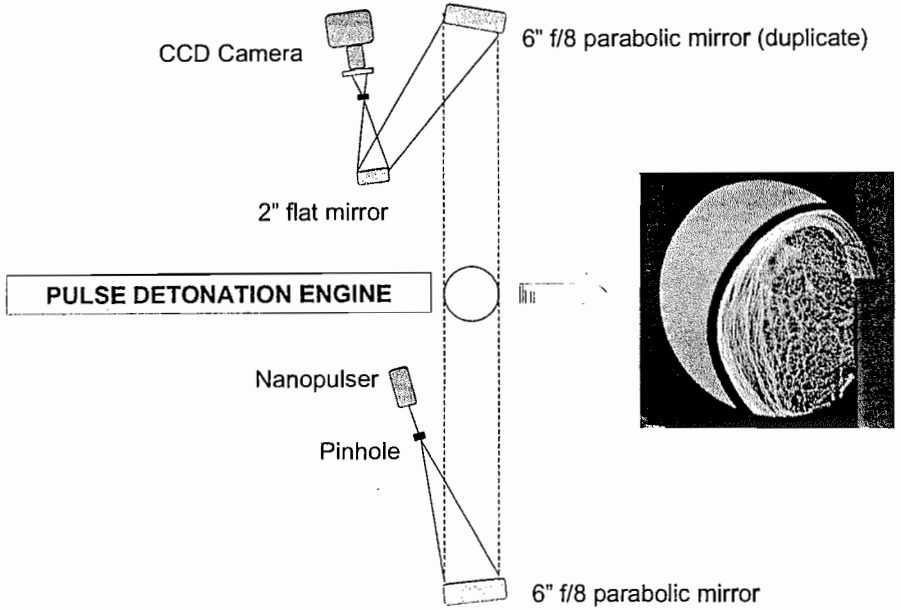

COMPUTATIONAL MODELING

- 2D unsteady Navier-Stokes code with chemical reaction models
- Generalized coordinates
- Explicit 2nd order MacCormack Predictor-Corrector Scheme with 4th order Multi-Dimensional Flux-Corrected Transport (FCT)
- Two-step induction parametric model for chemical reactions (Korobeinikov, Katta)
- Stoichiometric H_2/O_2 mixture diluted with argon by 70%

$$\frac{d\alpha}{dt} = -\frac{1}{\tau_{ind}} = -k_1 \rho \exp\left(-E_1/RT\right)$$

$$\frac{d\beta}{dt} = \begin{cases} = 0, & \alpha > 0 \\ = -k_2 p^2 \left[\beta^2 \exp\left(\frac{E_2}{RT}\right) - (1-\beta)^2 \exp\left(-\frac{E_2+Q}{RT}\right)\right], & \alpha \le 0 \end{cases}$$

$$k_1 = 3.0 \times 10^{11}\, cm^3/g/s, \qquad k_2 = 1.5 \times 10^{-7}\, cm^4/dyn^2/s,$$
$$E_1/R = 9800\ K, \qquad E_2/R = 2000\ K, \qquad Q = 4.0 \times 10^{10}\, erg/g$$

COMPUTATIONAL GRID

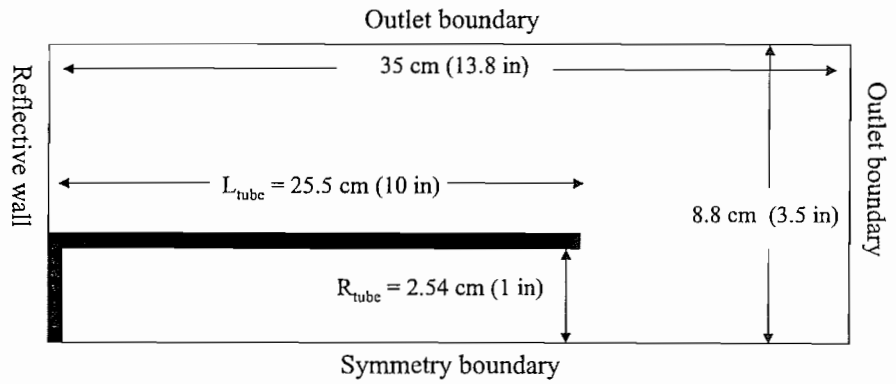

- Uniform grid spacing: 10*induction length = 0.02933 cm (0.0115 in)
- CFL # = 0.2
- Initial Conditions:
  Uniform stationary premixed mixture ignited by high temperature / pressure zones near head-wall of tube.

STRAIGHT TUBE PDE EXHAUST FLOW

10 ns light pulses, 3 ms blow-down

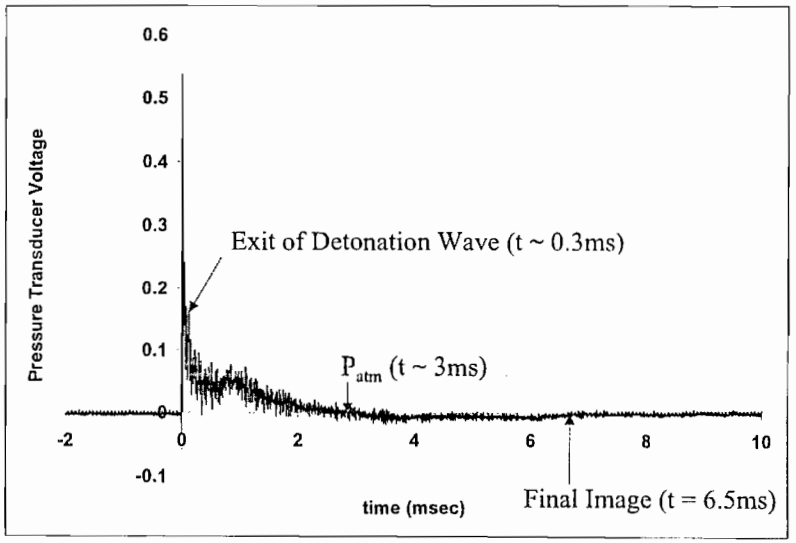

STRAIGHT TUBE PDE EXHAUST FLOW

10 ns light pulses, 3 ms blow-down

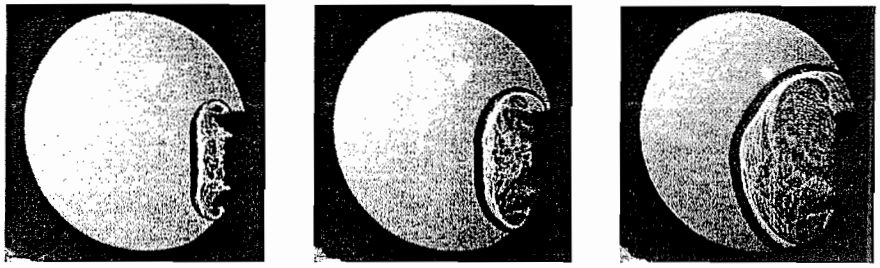

STRAIGHT TUBE PDE EXHAUST FLOW

10 ns light pulses, 3 ms blow-down

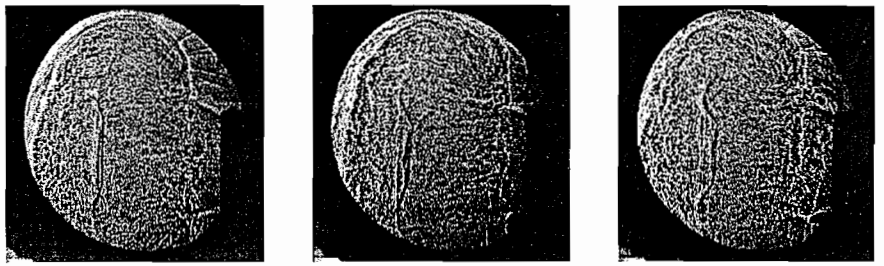

STRAIGHT TUBE PDE EXHAUST FLOW

10 ns light pulses, 3 ms blow-down

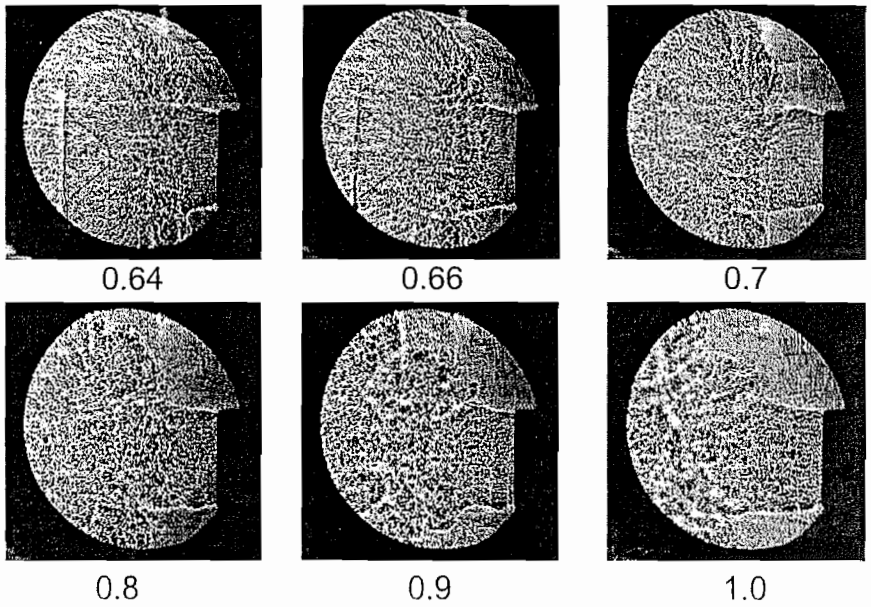

STRAIGHT TUBE PDE EXHAUST FLOW

10 ns light pulses, 3 ms blow-down

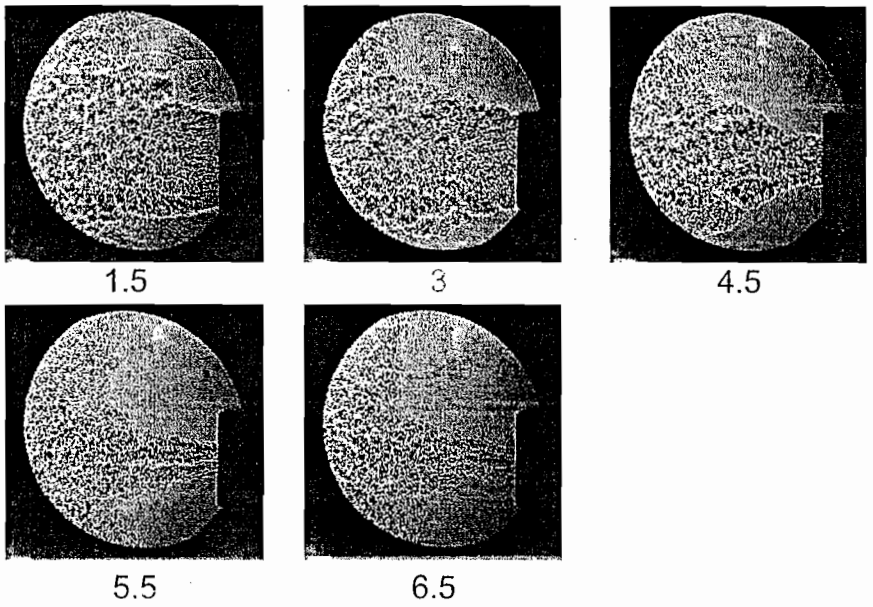

STRAIGHT TUBE PDE EXHAUST FLOW

10 ns light pulses, 3 ms blow-down

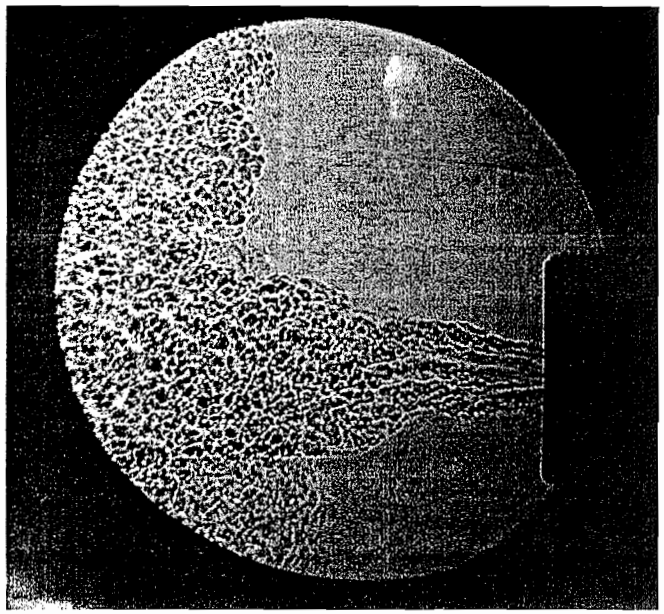

COMPARISON OF STRAIGHT TUBE TO CONVERGING NOZZLE

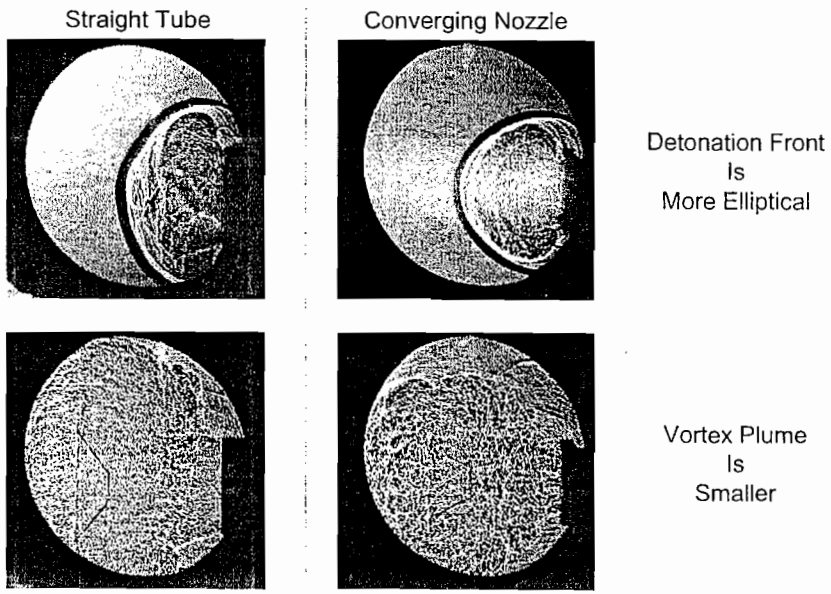

COMPARISON OF STRAIGHT TUBE TO CONVERGING NOZZLE

Straight Tube

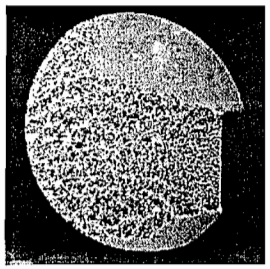

Converging Nozzle

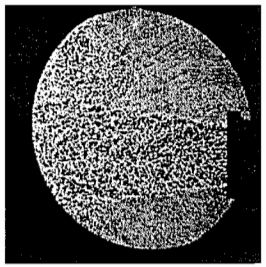

Mach Wave Radiation
Is
More Visible

CONVERGING NOZZLE PDE EXHAUST FLOW

1.84:1 Diameter Ratio, 10 ns light pulses, 7 ms blow-down

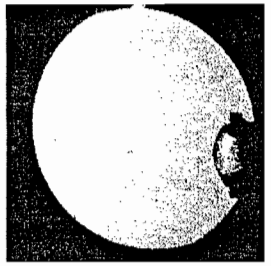

0.375 ms

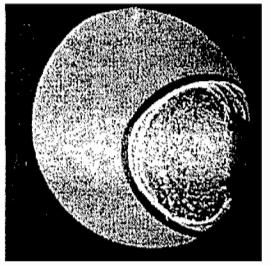

0.4

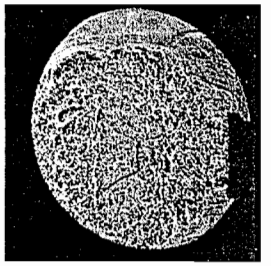

0.6

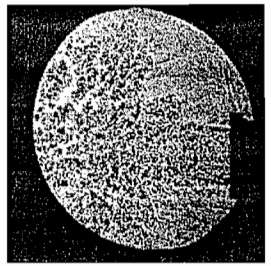

1

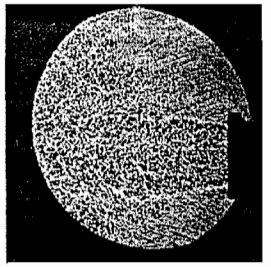

2

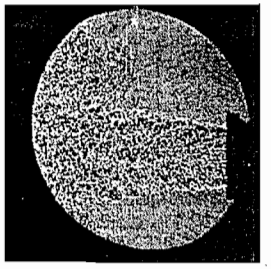

5

CONVERGING NOZZLE PDE EXHAUST FLOW

1.84:1 Diameter Ratio, 10 ns light pulses, 7 ms blow-down

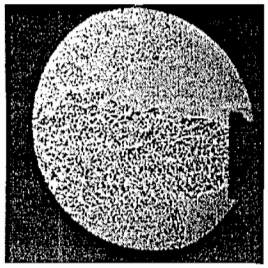

7.5

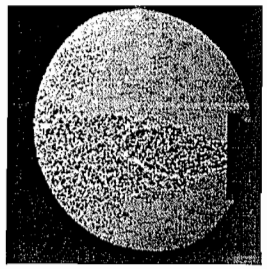

10

PULSE DETONATION ENGINE EXHAUST NOZZLES

EXPERIMENTS VS. SIMULATIONS

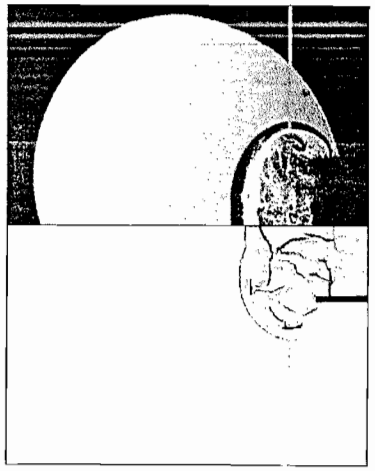

time = 0.3 ms

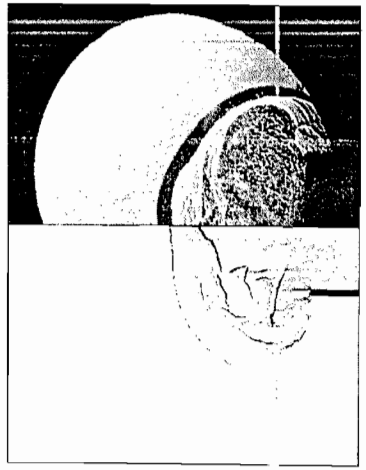

time = 0.325 ms

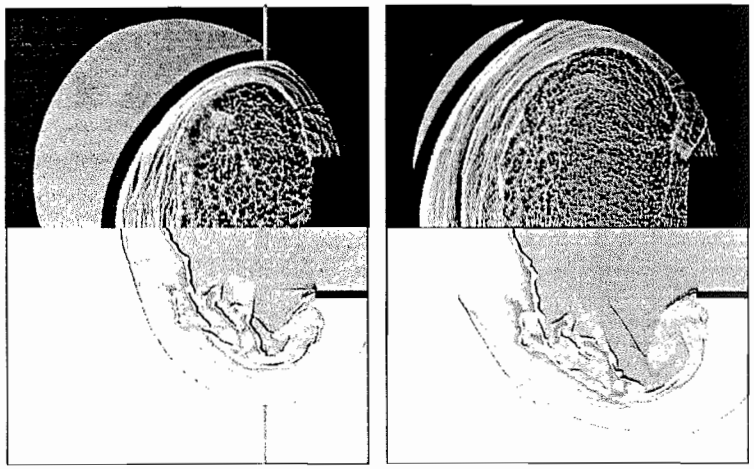

FUTURE WORK

1. Perform experimental and computational visualizations of various contoured exit nozzle geometries and ejector flowfields. These experiments will make use of new 12 inch diameter mirrors.
2. Study the effects of system parameters (fill fraction, ignition timing, and equivalence ratio) on exhaust jet structure and correlate with changes in performance values.
3. Acquire simultaneous OH-PLIF visualizations to investigate the coupling between the chemical reactions and gas dynamics.

ACKNOWLEDGEMENTS

• Special thanks to Richard DeLoof from NASA Glenn Research Center for sponsoring this research under grant NAG3-2669.

CONCLUSIONS

1. Shadowgraph visualizations of PDE exhaust flowfields were performed using a new 10 nanosecond duration light source.
2. The dynamic structure of the PDE exhaust flow was visualized for the complete detonation cycle.
   - Strong gradients was observed by the detonation front.
   - A large vortex plume was created by the detonation wave and a mach disk was observed to form in the underexpanded jet approximately 1 diameter downstream of the exit of the PDE.
   - A converging nozzle produced a more elliptically shaped detonation front, a smaller vortex plume and more visible Mach wave radiation.
3. Good agreement was observed between the modeling and experimental visualizations. Additional features were observed in the simulations that was masked by the line of sight of the shadowgraph visualizations.

(c)2001 American Institute of Aeronautics & Astronautics or Published with Permission of Author(s) and/or Author(s)' Sponsoring Organization.

A01-16774

AIAA 2001-0976
Computational and Experimental Study of Aerodynamics and Heat Release in a Liquid Fueled Combustor

A. Brankovic[1], R.C. Ryder, Jr.[1]
G.J. Sturgess[2]
J. Lee[3], A. Kushari[3], E. Lubarsky[3], B.T. Zinn[3]

(1) Flow Parametrics, LLC, Bear, DE
(2) Innovative Scientific Solutions, Inc., Dayton, OH
(3) Georgia Institute of Technology, Atlanta, GA

39th Aerospace Sciences Meeting & Exhibit
January 8-11, 2001 / Reno, NV

For permission to copy or republish, contact the American Institute of Aeronautics and Astronautics
1801 Alexander Bell Drive, Suite 500, Reston, Virginia 20191-4344

(c)2001 American Institute of Aeronautics & Astronautics or Published with Permission of Author(s) and/or Author(s)' Sponsoring Organization.

Computational and Experimental Study of Aerodynamics and Heat Release in a Liquid Fueled Combustor *

A. Brankovic[1], R.C. Ryder, Jr[1].
Flow Parametrics, LLC
Bear, Delaware 19701

G. J. Sturgess[2]
Innovative Scientific Solutions, Inc.
Dayton, Ohio 45440-3638

J. Lee[3], A. Kushari[4], E. Lubarsky[5], and B. T. Zinn[6]
School of Aerospace Engineering
Georgia Institute of Technology
Atlanta, Georgia 30332-0150

INTRODUCTION

The present work takes a diverse look at the computational fluid dynamics (CFD) modeling issues related to the prediction of multi-phase, reacting flows as applied to combustion system research and development. The objectives of the work are two-fold and include: 1) Performing validation simulations for the CFD flow solver for two-phase flow dynamics and chemically reacting flows, and: 2) Applying the CFD code in support of an experimental program to develop instrumentation for *in-situ* optical measurement of combustion instabilities, for the purpose of developing active combustion control systems to dampen or eliminate the large amplitude combustion oscillations. The flow solver used in this study is the second-generation solver of the NASA Glenn Research Center (GRC) National Combustion Code (NCC) called FPVortex™. Flow Parametrics, LLC independently developed this solver.

To achieve the first objective FPVortex™ is applied to simulate gas-phase and particle dynamics in a swirling, co-annular, particle-laden sudden pipe expansion flow. Detailed comparisons with experimental data for gas-phase and particulate mean velocities are provided. Good agreement is observed for mean axial and tangential velocity components of both phases, at various downstream measurement locations.

In support of the second objective a staged approach is taken, starting with validation studies of the liquid spray droplet flow, calculations of gaseous fueled combustion, and finally simulations of the full liquid spray droplet fueled combustion flow. Comparisons of predictions with data are made for gas-phase velocity in the liquid spray droplet flow, and also for axial heat release in the liquid-fueled combustor. The combustion system, developed at the Georgia Tech Combustion Laboratory, was measured experimentally using an optical CH* emissions measurement technique, in which the output voltage is proportional to heat release in a reacting flow. Comparisons are made at two equivalence ratios, characteristic of stable and unstable modes of combustion. The measured heat release profile is discussed with respect to the CFD results.

Near-term experimental work under this collaborative effort is aimed at acquiring more detailed gas-phase and liquid droplet data, including all three components of mean and RMS velocities for both phases. Additional experimental data acquisition and data reduction for CH* emissions in the combustor is also in progress. Near-term computational work under this program consists of parametric studies on the sensitivity of results due to variations of inlet liquid spray droplet boundary conditions, including use of stochastic methods for initial velocities

---

[1] AIAA Member
[2] AIAA Associate Fellow
[3] Ph.D. Student and Graduate Research Assistant
[4] Post-Doctoral Fellow
[5] Research Engineer and AIAA Member
[6] David S. Lewis Jr. Chair, Regents Professor, and AIAA Fellow

* This work is supported in part by Air Force Contracts F33615-99-C-2978 and F49620-99-1-0142. Contract monitors Carlos Arana and Dr. Mitat Birkan.

Copyright © AIAA. Published by American Institute of Aeronautics and Astronautics, Inc. with permission.

(c)2001 American Institute of Aeronautics & Astronautics or Published with Permission of Author(s) and/or Author(s)' Sponsoring Organization.

and starting locations. Fundamental studies of single liquid droplet dynamics and evaporation are being conducted, using existing experimental data for comparison. The experimental and computational efforts are being coordinated and are targeted at unsteady, multi-phase combustion dynamics cases, providing data and design guidance for the active control of combustion instabilities.

BACKGROUND

Liquid Fueled Combustor

The experimental apparatus is a combustor designed and built by E. Lubarsky and colleagues at the Georgia Tech Combustion Laboratory. The combustor was developed for the purpose of studying the combustion processes of modulated liquid fuel sprays, the combustion instabilities that can arise, and the active damping of these instabilities under closed-loop control. Applications of this information include the design and development of active combustion control systems for commercial and military gas turbine engine combustors, military gas turbine augmentors, and rocket, ramjet and scramjet propulsion flowpaths (see Lubarsky and Levy, Ref. 1, Heising et al., Ref. 2, and Kappei et al., Ref. 3). The instabilities of interest include longitudinal acoustic oscillations in the frequency range of 100-500 Hz., which can exhibit peak-to-peak pressure variances up to 30% of the mean pressure. Such excessive high amplitude pressure oscillations, which often occur in liquid-fueled combustors using bluff body or sudden expansion for stabilization, can cause loss of engine performance and excessive vibrational loads on the system.

With these design purposes the combustor uses *n*-heptane liquid fuel spray, provides optical access, and under appropriate operating conditions, has large amplitude heat release oscillations. A Phase Doppler Particle Analyzer (PDPA) is used to provide measurements of droplet velocity, droplet diameter probability density functions (PDF's), and droplet diameter oscillations. Under the assumption that liquid fuel spray droplets under 10 microns in diameter follow the gas-phase flow for both mean velocity and turbulent fluctuations, the PDPA system also provides the gas-phase velocity, measured concurrently with the liquid spray droplet flow. A special optical diagnostic system based on the chemiluminescence of CH radicals is used for direct determination of heat release in the combustor. With good optical access, the CH* imaging technique is suitable for providing primary zone combustor measurement, and thus sensing for active combustion control. Details of the experiment are provided in the sections on Combustor Design Features and Measurement Systems.

Computational Fluid Dynamics

The CFD modeling approach described in Ryder and McDivitt (Ref. 4) is followed. A major feature of this approach is to model the combustion system geometry precisely as it is installed on the test stand. Developing a CAD solid model representation of the hardware, and automatically meshing the flow volume, or "air-solid" using tetrahedral meshing software accomplishes this. The resulting grid is output into an unstructured geometry database, and read in by the flow solver. Intermediate results databases are created, and can be viewed automatically in graphics post-processing packages.

The physics-based modeling for the aerodynamics and the combustion processes includes the two-equation k-ε model of turbulence, together with eddy breakup combustion model. Liquid fuel spray droplet dynamics and evaporation were computed using the Lagrangian droplet software package developed by Raju (Ref. 5), which was added to the FPVortex™ flow solver. The spray droplet model includes physics-based correlations for drag, heat and mass transfer, internal circulation within the liquid droplets, and simple particle-wall interactions. The Lagrangian spray droplet equations are coupled to the gas-phase continuity, momentum and energy equations through source terms.

A test of the accuracy of the Lagrangian particle dynamics code was conducted for a turbulent, two-phase, swirling flow through a sudden pipe expansion. Computed results were compared with benchmark quality experimental data, and showed excellent agreement. Further comparisons of two-phase flow dynamics were made by comparing predictions to unconfined cold flow, spray droplet data obtained from the Georgia Tech combustor. Finally, the entire computational model including turbulence, droplet dynamics, evaporation and combustion, was applied to the three-dimensional combustor flow. Combustion was simulated at two distinct operating conditions, the first at lean, and the second at stoichiometric fueling conditions. These preliminary simulations are compared to heat release measurements at both fuel-air ratios. Further experimental measurements, simulations, and comparisons are currently in progress based on the experience gained to date.

PARTICLE DYNAMICS MODEL

Confined, Particle Laden, Swirling Annular Flow Through a Pipe Expansion: Simulations and Experiment

As a preliminary step towards computing the liquid spray droplet combustor with heat release, the Lagrangian particle dynamics model of Raju (Ref. 5) was applied to predict a well-documented particulate two-phase flow. The

(c)2001 American Institute of Aeronautics & Astronautics or Published with Permission of Author(s) and/or Author(s)' Sponsoring Organization.

selected test case was the confined, particle laden swirling flow described in the papers by Sommerfeld and co-workers (Refs. 6, 7, and 8). A schematic diagram of the injector is shown in Figure 1, indicating the two-phase core flow, and the gas-phase annular, swirling flow. A 3 mm thick, blunt trailing edge splitter plate separates the two flows. The outer step height is 65 mm, slightly larger than the diameter of the annular flow passage. The air mass flow rate of the primary jet was 9.9 g/s, while that of the secondary jet was 38.3 g/s. Swirl number for the annular flow was 0.47.

The particles were made of glass with a mass density of 2500 kg/m^3, and a mass flow rate of 0.34 g/s. PDPA measurements of the particles downstream of the injector yielded the diameter probability distribution shown in Figure 2, which shows the particle diameters ranging from 3 to 120 microns, with a mean diameter of 45.5 microns. Also included in the referenced papers are the particle velocity and particle number density PDF's, which help establish the stochastic initial conditions for the flow simulation. For the gas-phase measurements, particles with diameter less than 10 microns are considered to follow the airflow. The PDPA output is thus interpreted as providing simultaneous measurement of the larger, discrete phase particles, and smaller particles with mean and RMS velocities representative of the gas-phase.

The simulation is initialized 150 mm upstream of the sudden pipe expansion so that the turbulent boundary layers, wall turbulence quantities, and axial pressure gradients are allowed to develop as in the experiment. The exit plane of the computational model is located 1200 mm, or 18.5 step heights, downstream of the expansion. The shear layer formed by the interaction between the core and annular flows attaches to the outer pipe wall at about 1 step height downstream of the sudden expansion. The exit plane is thus well downstream of any significant axial gradients in the flow quantities.

Simulation results for the gas-phase flow are shown in Figure 3, including (a) axial velocity, (b) tangential velocity, and (c) turbulent kinetic energy distributions in the pipe. At the sudden expansion, the axial velocity decelerates rapidly, with the formation of a large recirculation zone along the central axis, and a corner recirculation region. The swirling annular flow expands radially outwards, impinging on the pipe outer wall. Turbulent kinetic energy peaks in the shear layers formed between the core and annular swirling flow. Accuracy in predicting the gas-phase turbulent kinetic energy is crucial, as this quantity is used directly in the particle turbulent dispersion model to determine particle velocity fluctuations and thus changes in particle position due to gas-phase turbulence.

The instantaneous particle positions are shown in Figure 4, which is a snapshot of the time-dependent motion of the particles through the flow field. For clarity, every 5th particle is shown in the Figure, to simply indicate overall trajectories and the accumulation of particles in the duct. Particles are well mixed within the core flow, and closely follow the turbulent boundary layer development of the airflow.

Quantitative comparisons between simulations and experimental data are shown in Figure 5, in terms of radial profiles taken at various downstream axial locations. In Figure 5 (a), the gas-phase mean axial velocity profile closely matches the profile at the first measurement plane, X = 0 mm. Both the magnitude and radial location of peak velocity are well predicted. The evolution of the axial velocity profile is well predicted at X = 52 mm, with CFD correctly predicting the reduction in peak core flow velocity, and the continued high axial velocity in the shear layers. At X = 112 mm, overall agreement in the velocity profiles is good, however, there is a cusp in the measurements along the central axis. This is due to the rapid variation of axial velocity at that location, coincident with the upstream stagnation point of the core flow. Previous modeling experience for highly swirled, recirculating flows (Brankovic et al., Refs. 9 and 10, Ryder, Ref. 11) has shown that the velocity profiles are very sensitive to the axial location of the stagnation point, and even small variances in the sampling location for the predictions can results in large difference in the profiles. Further downstream the agreement between predictions and experiment is satisfactory. Gas-phase mean tangential velocity profiles are shown in Figure 5 (b). Generally, agreement is good, with the exception of some discrepancy in the outer regions of the profile in the near field.

Quantitative comparisons with particle phase measurements are shown in Figure 5 (c) and (d). For the mean axial velocity, agreement at the inlet plane is excellent, with the turbulent velocity profile of the particles well predicted by the two-phase flow model. This agreement extends downstream, as the Lagrangian trajectory model predicts the particle axial velocity behavior closely. The mean tangential velocity component of the particles is also well predicted, as seen in Figure 5 (d) at two downstream locations.

The test of the Lagrangian particle trajectory model presented here serves to underscore the expected accuracy for the liquid spray droplet simulations for the combustor. It established the basic methods for determining the second-phase inlet boundary conditions, number of particle starting locations and overall number of particles needed for steady state, statistically valid solutions. With this information, preliminary simulations of the Georgia Tech

(c)2001 American Institute of Aeronautics & Astronautics or Published with Permission of Author(s) and/or Author(s)' Sponsoring Organization.

combustor, for both unconfined, cold flow and confined flow with heat release were initiated.

GEORGIA TECH LIQUID-FUELED COMBUSTOR

Combustor Design Features

The investigated combustor consisted of the air supply system, which was integrated with the liquid fuel injector, a conical flame holder, and a quartz pipe section open at its downstream end, as shown schematically in Figure 1 (a). The air flow was divided into two streams. One-third of the air mass flow was injected with swirl into the primary air passage also containing the liquid fuel spray, through a set of tangentially oriented orifices. The primary air passage also included the pintle of the fuel nozzle, through which liquid fuel was atomized and mixed with the primary air jet. The remaining two-thirds of the air was supplied into the flame region as an annular secondary stream that flowed into the combustor around the periphery of the conical flame holder. The mass flow split between the primary and secondary air jets is regulated by choking the primary jet air flow at the tangential injection orifices, and diverting the remaining flow around a racetrack which feeds the subsonic-entry, secondary airflow ports. The maximum total air mass flow rate was 15 g/s, and the maximum air temperature was 200° C.

The use of a quartz combustor tube, with inner diameter and thickness of 42 mm and 2 mm, respectively, allowed optical access to the spray and flame. The resulting combustion process was stabilized by the interaction of the fuel spray with the primary swirling air stream and subsequent interactions of the resulting fuel-air mixture with the secondary annular air stream near the downstream end of the conical flame holder. The fuel in all of the experiments was *n*-heptane (C_7H_{16}) and the maximum investigated fuel flow rate was 1 g/s.

Measurement Systems

The time dependence of the heat release at various axial locations along the flame, which is proportional to the local reaction rate, was determined from measurements of the spatial dependence of CH* radicals (λ = 431.5 nm) chemiluminescence. This was measured using the set up shown in Figure 6 (b). It consisted of a photomultiplier (PMT), a narrow band pass filter centered at wavelength λ = 430 ± 5 nm, and an appropriate system of lenses and apertures. CH* emissions from a narrow "slice" of the flame passed through two 1.5 x 40 mm slot apertures, a 50 mm focal length lens (d = 70 mm) and was then focused through the filter onto the PMT. The distance between the two apertures was 120 mm, and the distance from the first aperture to the combustor was also 120 mm. This design limited the PMT's instantaneous line of sight to a 3 mm thick section of the reaction zone. The PMT was mounted on the remotely controlled traversing system and slowly moved upwards or downwards along the combustor as it measured the axial spatial dependence of the CH* radicals chemiluminescence's. The PMT signal and a signal indicative of the PMT position were measured and sampled by a computerized data acquisition system using LabView™ software.

The PDPA and CH* emissions measurements were complemented by high-speed photography of the combustion zone. This was performed with a Kodak EktaPro Intensified Imager Camera with a controllable shutter speed up to 4000 Hz. The camera recorded the combustion zone characteristics by recording its emissions after they passed through a narrow band pass interference filter centered at λ = 430 ± 5 nm, corresponding to the wavelength measured by the PMT.

Photographs of the combustor hardware and various flow fields are shown in Figure 7. In (a), an overhead view of the conical flame holder and secondary flow passage is shown, with the quartz tube removed. In (b), the unconfined, cold spray droplet flow is shown, with the flow field illuminated using a red He-Ne laser sheet, and the PDPA laser beam passing though. Although faint, the radial spreading of the spray droplets can be seen. In (c), the confined, cold liquid spray droplet flow field is shown. The intermittent filming of the liquid fuel on the pipe side wall is evident. Measurement of confined, cold flow liquid spray droplets will therefore be a challenge, and an optical access port will likely be required to allow beam penetration into the combustor tube for detailed, *in-situ* droplet measurements. The confined, liquid spray droplet reacting flow is shown in Figure 7 (d).

An Aerometrics™ PDPA in cold flow experiments measured the spray droplet diameters and velocities. The combustor was mounted on a traversing mechanism that can be precisely moved along three mutually perpendicular coordinates, thus providing capabilities for placing any point in the spray at the intersection of the PDPA's laser beams. Analysis of the mean diameters of the spray results can be output based on either the arithmetic or the Sauter mean diameter definitions. Analysis of the PDPA data also determined the mean and RMS components of the spray droplet velocities at the measurement locations. In the current study, the PDPA will also be used in hot flow experiments for measurements of the host flow velocities (air stream will be seeded with alumina particles). Typical PDPA outputs for this experiment are shown in Figure 8, including droplet diameter and velocity PDF's for the cold flow spray droplet cases. The *n*-heptane droplet diameters ranged from 10 to 100 microns, with an arithmetic mean of 26.9, and a Sauter mean diameter of 47.7 microns. Mean droplet velocity was 4.187 m/s, with an RMS velocity of

(c)2001 American Institute of Aeronautics & Astronautics or Published with Permission of Author(s) and/or Author(s)' Sponsoring Organization.

1.964 m/s. This data was used to establish initial conditions for the liquid spray droplet streams at the injection locations.

CASE 1: Aerodynamics and Spray Droplet Dynamics for the Unconfined, Cold, Swirling Flow Test Case.

Unconfined, cold liquid spray droplet dynamics were studied first. Using the FPVortex™ code augmented with the Lagrangian two-phase flow model, simulations were performed to match the PDPA data for a test run with an overall fuel equivalence ratio of $\varphi = 0.6$. Since the flow exhausted into a hood situated in the open lab room, an entrainment boundary condition for the numerical simulation was implemented. This included specifying velocities at the combustor base, and also radially along the external pipe walls. To enable spreading of the spray droplet jet as in the unconfined experiment, the diameter of the quartz tube was doubled, and the entrainment condition applied along the extended pipe walls. For these simulations, a base velocity of 1.0 m/s at X = 0 mm, and a radial velocity of 2.0 m/s inward were used.

The inlet conditions for the Georgia Tech combustor are described in Figure 9. In Figure 9 (a), the tangential swirling flow for the primary air jet is shown. Air is fed normally into the four intake ports, and is choked at the intersection of the ports with the primary jet cavity. The choked flow results in supersonic flow inside the primary jet cavity, with local Mach numbers peaking at about 2.0. The supersonic cell structure wraps circumferentially around the cavity, and terminates upon impinging the adjacent jet. The flow is then forced into the axial direction.

A cross-section through the nozzle base is shown in Figure 9 (b). This view illustrates that flow reversal extends down to the very base of the primary jet cavity. The supersonic flow issuing from the tangential ports becomes axial, and stays attached to the perimeter of the primary jet cavity wall, until reaching the conical flame holder. There, the flow expands radially, anchored to the flame holder base, and forms the primary recirculation region that stabilizes the flame under reacting flow conditions.

Instantaneous droplet positions for the cold flow, spray droplet dynamics test case are shown in Figure 9 (c). The liquid droplets mix rapidly in the base, but are swept radially toward the outer wall of the primary jet flow due to centrifugal forces in the airflow. Upon exiting into the conical flame holder region, the droplets are swirled into the classic hollow spray cone configuration. Some stripping of droplets along the external branch of the spray cone occurs, together with some droplet dispersion radially inwards toward the flow central axis.

Using the PDPA measurements for 10-micron diameter (or smaller) liquid *n*-heptane droplets, gas-phase velocity data were recorded. Representative profiles are shown in Figure 10 (a) for mean axial velocity along the combustor centerline, and in (b) for a radial profile taken 35 mm downstream of the flame holder exit plane. Although some scatter is present in the experimental data, agreement is generally good in terms of the velocity recovery along the centerline, and in terms of the peak reverse flow velocity. Further experiments to characterize this flow are underway, and include measurements of the mean and RMS axial and tangential velocities for both phases.

CASE 2: Aerodynamics and Heat Release Characteristics of the Confined, Swirling Flow, Liquid Fueled Combustor: Lean and Stoichiometric Fueled Cases.

To establish the flow structure for the reacting flow calculations, a preliminary gaseous fueled simulation was performed at an equivalence ratio of $\varphi = 1.125$. This simulation demonstrated that the solver could easily compute the flow field despite flow conditions that included complex geometry, three-dimensional effects, regions of supersonic flow near the tangential entry ports, and flame holding along the periphery of the conical flame holder. Two CFD images of this calculation are shown in Figure 11. In Figure 11 (a), velocity vectors colored by static temperature are shown, indicating the counter-rotating vortex pattern at the flame holder base, upstream stagnation region for the central recirculation zone, and cooling due to the secondary flow issuing from the perimeter of the flame holder. Figure 11 (b) shows the temperature iso-contours of the same flow field.

With the gaseous combustion flow structure established, reacting flow cases for the liquid spray droplet combustion were performed, at equivalence ratios of $\varphi = 0.6$ and $\varphi = 1.0$. These fuel levels were selected as they result in two different heat release modes in the combustor. At the lower equivalence ratio, the resulting flame is aerodynamically stabilized along the base of the conical flame holder. At the higher ratio, the flame is lifted, the combustion zone is significantly larger in extent, and the mixture burns at a higher temperature.

The computed aerodynamic flow fields for the two cases are shown in Figure 12 (a) and (b). The axial velocity contour is broadly similar for the two cases, including features such as the streamline pattern, size and velocity magnitudes of the central recirculation region, and the particle trajectories. In both case, the droplets are injected axially into the combustor, and are then rapidly swirled outward and impinge on the pipe outer wall. Fuel is evaporated from the droplets, and is entrained into the central recirculation zone for combustion. In these

(c)2001 American Institute of Aeronautics & Astronautics or Published with Permission of Author(s) and/or Author(s)' Sponsoring Organization.

simulations, inspection of the droplet statistics indicates that no large droplets were entrained into the central recirculation region.

The computed temperature fields for the two cases are shown in Figure 13 (a) and (b), and indicate large differences in flow behavior. For the leaner case at $\varphi = 0.6$, a small, stabilized flame is anchored along the flame holder cup. For the stoichiometric case at $\varphi = 1.0$, the flame is lifted rather high off the flame holder, although two thin legs stretches of flame appear attached to the base near the intersection of the primary and secondary jet shear layers.

Emission scanning results

The measured and predicted axial heat release profiles for the two cases are compared in Figure 14. Each of the Figures is coincident with the combustor-imaging region, namely, from 0 mm to 100 mm downstream of the flame holder exit plane. In the upper two Figures, (a) and (b), the computed temperature fields for the 100 mm length of the combustor tube are shown. As seen previously in Figure 13, the flame at $\varphi = 0.6$ is aerodynamically stabilized along the conical flame holder face, with secondary air keeping the outer pipe region relatively cool. For the $\varphi = 1.0$ case, the flame is lifted, and in the experimental combustor, highly unsteady and oscillatory, with large amplitude fluctuations in flame front.

The CH* emissions data for the runs are shown in Figure 14 (d). Also included in the graph is a profile for a case near the lean blow out limit, at $\varphi = 0.4$, with only intermittent, low-level heat release. The case at this fuel condition was not computed in this series of simulations. The measured voltages are in proportion to the intensity of heat release rate, and in direct proportion to the CH* emission from the flame. Thus, the CH* results are most nearly comparable to the spatial derivative of the temperature. These results must be anchored to a known temperature data point; further data reduction is in progress.

The experimental heat release results for the $\varphi = 0.6$ run reach a peak at 25 mm downstream of the flame holder, while the CFD prediction peaks in temperature at about 12 mm. The CH* results decrease with axial distance, whereas the CFD predictions in Figure 14 (c) asymptote towards the fully mixed out temperatures for the given equivalence ratio. As the CFD model uses adiabatic walls, all heat released during combustion remains conserved in the computational domain.

For the $\varphi = 1.0$ case, the CH* emissions data show a broad peak at about 35 mm downstream of the flame holder, with large scale inflection at about 60 mm. This is indicative of the high amplitude combustion instability observed experimentally in this case. Also, the overall length of the combustion zone increases substantially at the larger equivalence ratio. The CFD prediction in Figure 14 (c) starts at a low temperature, indicative of the ignition delay, and subsequently asymptotes towards the adiabatic limit with increasing downstream distance.

Images

Figure 15 presents a series of images of "stable" flames at $\varphi = 0.6$, and "unstable" flames $\varphi = 1.0$, obtained by high-speed photography of these flames. An examination of Figure 15 (a) shows that during "stable" operation the flame is visible during the entire period, while exhibiting small variations of CH* emissions intensity and the magnitude of the flame. In contrast, Figure 15 (b) shows that during unstable operation the extent of the combustion region and intensity of flames emissions significantly changed during the cycle, and that the combustion region was longer than the "stable" combustion region. The information provided by these images is consistent with that obtained from analyses of their CH* emission scanning experiments, indicated by the CH* emissions voltages shown in Figure 14 (d), as well as the CFD predictions for the combustion zone lengths as shown in Figures 14 (a) and (b). For the unstable combustion case at $\varphi = 1.0$ in Figure 15 (b), one full cycle of the longitudinal instability is imaged over a period of 2.25 milliseconds, for an oscillation frequency of 440 Hz. This results falls within the range of frequencies cited earlier (100-500 Hz.) as producing large peak-to-peak variances in pressure amplitude, relative to mean flow pressure. For the stable combustion case at $\varphi = 0.6$, no distinct variations in the intensity of heat release are observed.

SUMMARY AND CONCLUSIONS

This paper described work in progress in applying the FPVortex™ flow solver to predict multi-phase reacting flows, and specifically towards supporting the design and development of instrumentation and systems suitable for active combustion control. The accuracy of the code in predicting the gas-phase and particulate phase fluid dynamics in a cold, swirling particle laden flow was established, based on detailed comparisons of predicted and measured velocity profiles for both phases, and analysis of the droplet trajectories. The code was further applied to predict liquid fuel spray droplet fluid dynamics in the Georgia Tech combustor. The limited comparisons of flow velocity for an unconfined, cold flow of the combustor are encouraging. The investigated combustor featured complex, three-dimensional geometry, regions of supersonic flow, and high levels of swirl and turbulence. Following cold flow and gaseous combustion flow simulations, liquid fuel spray droplet cases were run at two equivalence ratios, $\varphi = 0.6$ and $\varphi = 1.0$, which were representative of "stable"

(c)2001 American Institute of Aeronautics & Astronautics or Published with Permission of Author(s) and/or Author(s)' Sponsoring Organization.

combustion and "unstable" combustion modes. CH* emissions data, and high-speed photography of the combustion zone were presented and discussed.

Extensions of the modeling and experimental work are in progress in several areas. For the modeling, the stochastic representation of the droplet initial diameter and velocity is being further studied. Detailed simulations of single droplet dynamics, including final velocity, dispersion and spread angle are underway. Detailed comparisons with the gas-phase turbulent kinetic energy fields of the combustor are also being investigated. The coupling of the Lagrangian spray droplet model with gas-phase parameters such as turbulence are key to accurately calculating the overall spray droplet flow field, which together with the gaseous combustion model, govern the heat release characteristics of the combustion system. Sturgess et al. (Ref. 12) have provided a useful framework for numerical validation studies of liquid spray droplets dynamics, with application to predicting hollow-cone liquid sprays formed by fuel nozzles in gas turbine combustors.

Additional experiments are in progress to provide more detailed data for code comparisons. The tangential mean and RMS velocity components for both gas-phase and liquid droplet phase are chief among the flow quantities to be measured. Measurements in the dense spray region close to the flame holder will be attempted, to provide improvements for the spray droplet boundary conditions. The feasibility of modifying the quartz tube for optical access is also being investigated. This is necessary to enable PDPA and laser velocimetry measurements of the gas-phase aerodynamics and spray droplet trajectories for the confined, cold flow case. Confined flow measurements, which require the laser beams to pass through the quartz tube, are error prone. This is because the liquid spray impinges on the tube wall, forming a swirling, highly unsteady and non-uniform liquid film on the tube. This distorts and obscures the beams much of the time. Optical access into the quartz tube will enable application of the PDPA and LV systems to acquire local gas-phase and droplet information in the combustion cases as well. The optical access ports must be shaped and positioned in such a way to be as non-invasive of the combustor tube as possible, to avoid altering the aerodynamic and combustion flow patterns.

Following the extensions to the modeling and experimental programs described, the prediction and measurement methodologies will be applied towards unsteady, liquid spray droplet combustion flows in the Georgia Tech combustor, over a range of equivalence ratios. The CFD simulations will provide insights into the combustion flow structure, resulting in detailed design guidance and support for the active combustion control devices.

REFERENCES

1. Lubarsky, E. and Levy, Y., "Experimental Investigation of Flame-Holding System for the Suppression of Ramjet Rumble", Twenty-Seventh Symposium (International) on Combustion, pp. 2033-2037, 1998.

2. Heising, R., Lubarsky, E., Neumaier, M., Neumeier, Y., and Zinn, B.T., "Periodic Liquid Fuel Spray Combustion Processes and Their Damping of Combustion Instabilities", AIAA Paper 2000-1024, 2000.

3. Kappei, F., Lee, J.Y., Johnson, C.E., Lubarsky, E., Neumeier, Y., and Zinn, B.T., "Investigation of Oscillatory Combustion Processes in Actively Controlled Liquid Fuel Combustor", AIAA Paper 2000-3348, 2000.

4. Ryder, Jr. R.C. and McDivitt, T., "Application of the National Combustion Code Towards Industrial Gas Fired Heaters", AIAA Paper 2000-0456, 2000.

5. Raju, M.S., "An Overview of the NCC Spray / Monte Carlo PDF Computations", AIAA Paper 2000-0337, 2000.

6. Sommerfeld, M. and Qiu, H. -H., "Detailed Measurements in a Swirling Particulate Two-Phase Flow by a Phase-Doppler Anemometer", *Int. J. Heat and Fluid Flow*, Vol. 12, pp. 20-28, 1991.

7. Sommerfeld, M., Ando, A. and Wennerberg, D., "Swirling, Particle-Laden Flows Through a Pipe Expansion", *J. Fluids Engineering*, Vol. 114, pp. 648-656, 1992.

8. Sommerfeld, M. and Qiu, H. -H., "Characterization of Particle-Laden, Confined Swirling Flows by Phase-Doppler Anemometry and Numerical Calculation", *Int. J. Multiphase Flow*, Vol. 19, pp. 1093-1127, 1993.

9. Brankovic, A., Ryder, Jr., R.C. and Syed, S.A., "Mixing and Combustion Modeling for Gas Turbine Combustors Using Unstructured CFD Technology", AIAA Paper 98-3854, 1998.

10. Brankovic, A., McKinney, R., Ouyang, H., Porter, L., Kennedy, J., Madabhushi, R., Colket, M., "Comparison of Measurements and Predictions of Flow in a Gas Turbine Engine Fuel Nozzle", AIAA Paper 2000-0331, 2000.

11. Ryder, Jr. R.C., "Application of the National Combustion Code Towards Unsteady Mixing and Combustion Modeling", AIAA Paper 2000-0335, 2000.

12. Sturgess, G.J., Syed, S.A. and McManus, K.R., "Calculation of a Hollow-Cone Liquid Spray in a Uniform Air Stream", AIAA Paper 84-1322, 1984.

(c)2001 American Institute of Aeronautics & Astronautics or Published with Permission of Author(s) and/or Author(s)' Sponsoring Organization.

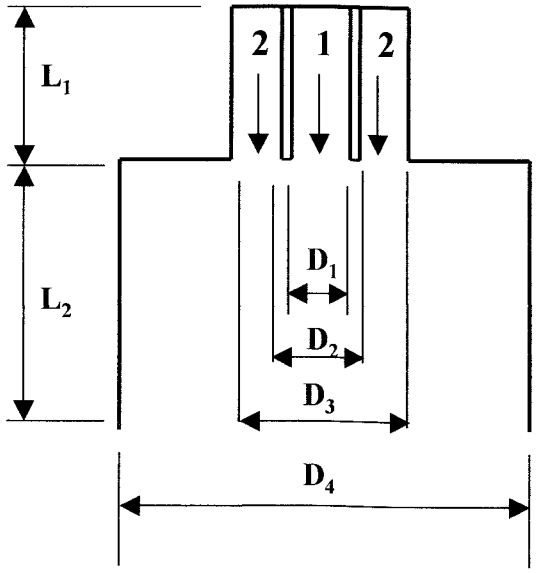

Dimensions:
$L_1 = 150$ mm
$L_2 = 1200$ mm
$D_1 = 32$ mm
$D_2 = 38$ mm
$D_3 = 64$ mm
$D_4 = 194$ mm

(1) Primary Flow: Gas Phase + Particle Flow
(2) Secondary Flow: Gas Phase, Annular Swirling Flow

Figure 1. Definition sketch for the particle laden, swirling annular flow through sudden pipe expansion experiment of Sommerfeld et al. (Refs. 6, 7 and 8)

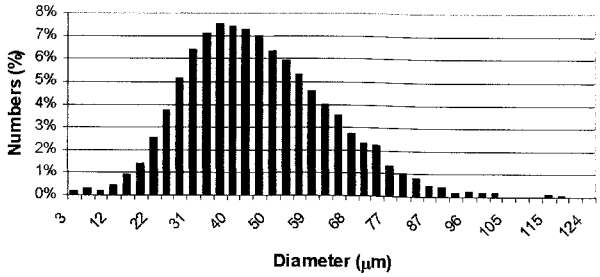

Figure 2. Measured particle size distribution using PDPA. Additional particle statistical information includes mean and RMS velocity distributions, used to establish stochastic particle velocities for the simulations.

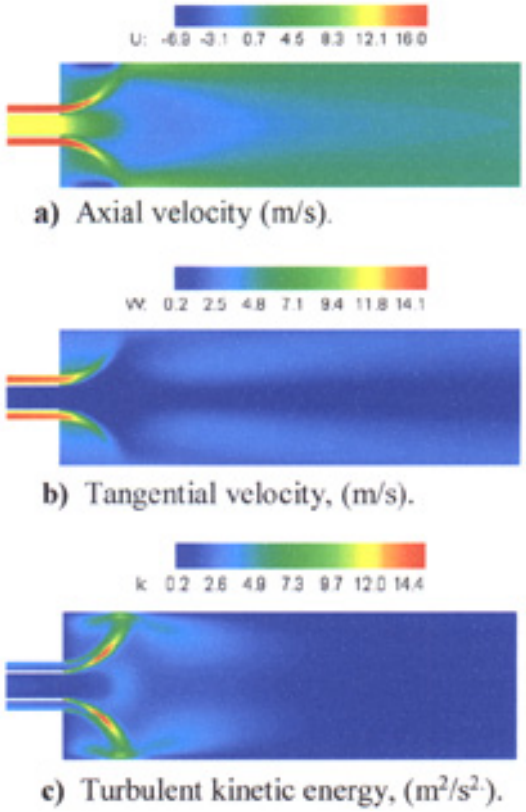

Figure 3. Computed gas-phase flow solutions, showing **(a)** axial and **(b)** tangential velocity, and **(c)** turbulent kinetic energy distributions.

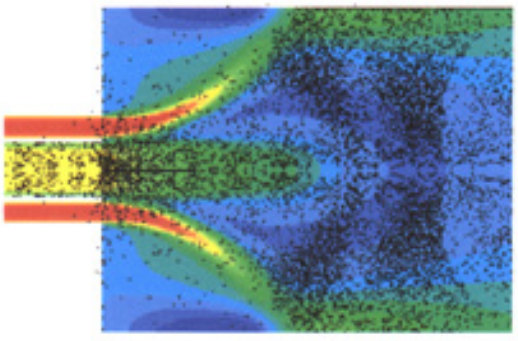

Figure 4. Computed instantaneous particle positions, superimposed on contour of gas-phase axial velocity.

(c)2001 American Institute of Aeronautics & Astronautics or Published with Permission of Author(s) and/or Author(s)' Sponsoring Organization.

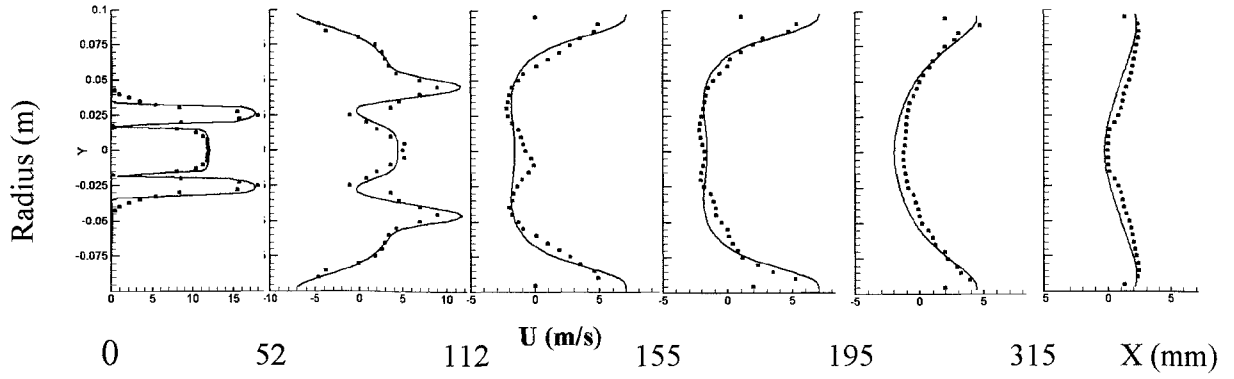

(a) Axial mean velocity of air (m/s): ■ Experiment. — Prediction.

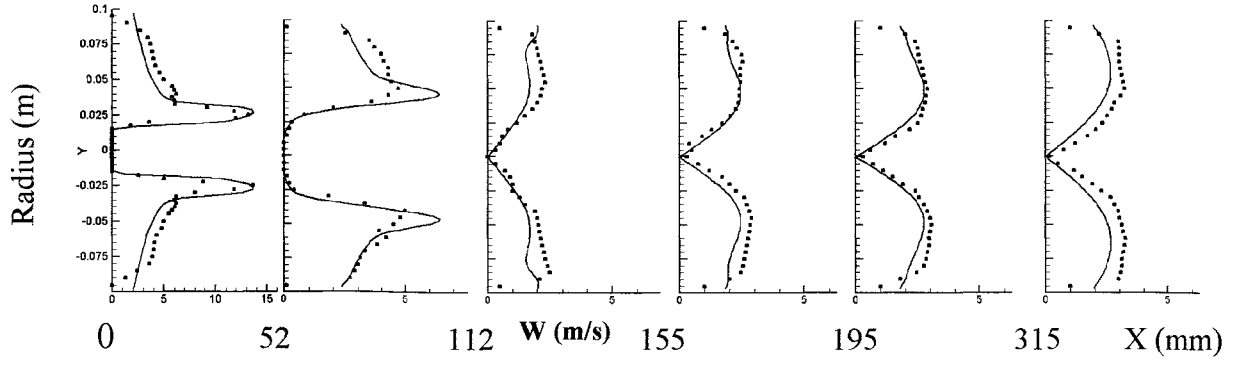

(b) Tangential mean velocity of air (m/s): ■ Experiment. — Prediction.

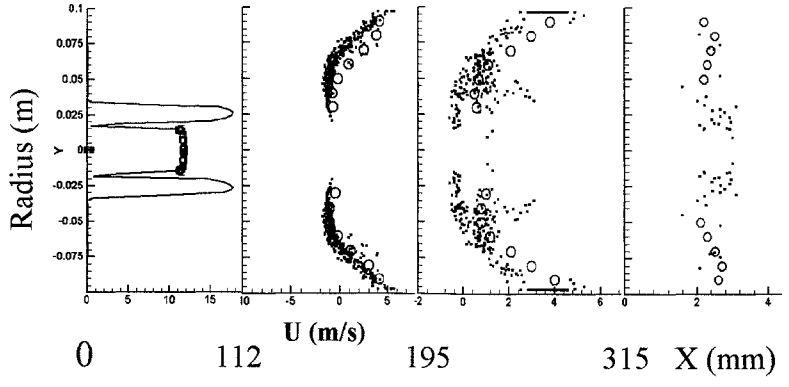

(c) Particle axial velocity (m/s):
○ Experiment. ■ Prediction.

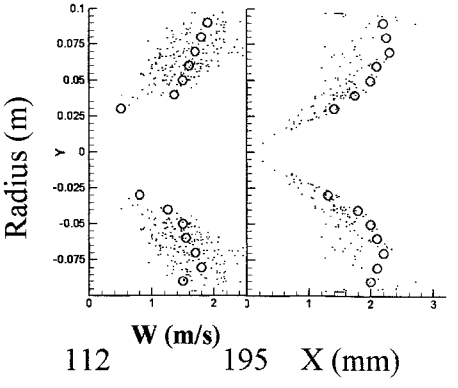

(d) Particle tangential velocity (m/s):
○ Experiment. ■ Prediction.

Figure 5. Comparison of experimental results and simulations: radial profiles.
(a) Gas-phase axial mean velocity. **(b)** Gas-phase tangential mean velocity.
(c) Particle axial mean velocity. **(d)** Particle tangential mean velocity.

(c)2001 American Institute of Aeronautics & Astronautics or Published with Permission of Author(s) and/or Author(s)' Sponsoring Organization.

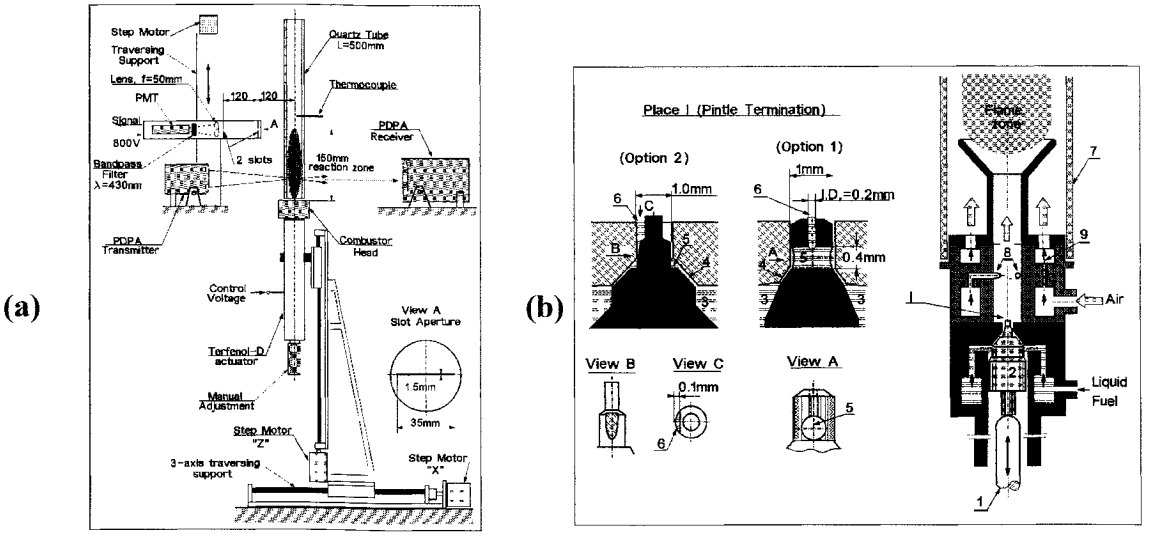

Figure 6. Details of the diagnostic equipment. **(a)** Overall view of test rig, showing layout of PDPA system. **(b)** Schematic of the model combustor: 1 – actuator rod; 2 – pintle; 3 – fuel supply lines; 4 – annular clearance; 5 – plenum; 6 – nozzle; 7 – quartz pipe section; 8 – air swirl holes; 9 – annular air holes.

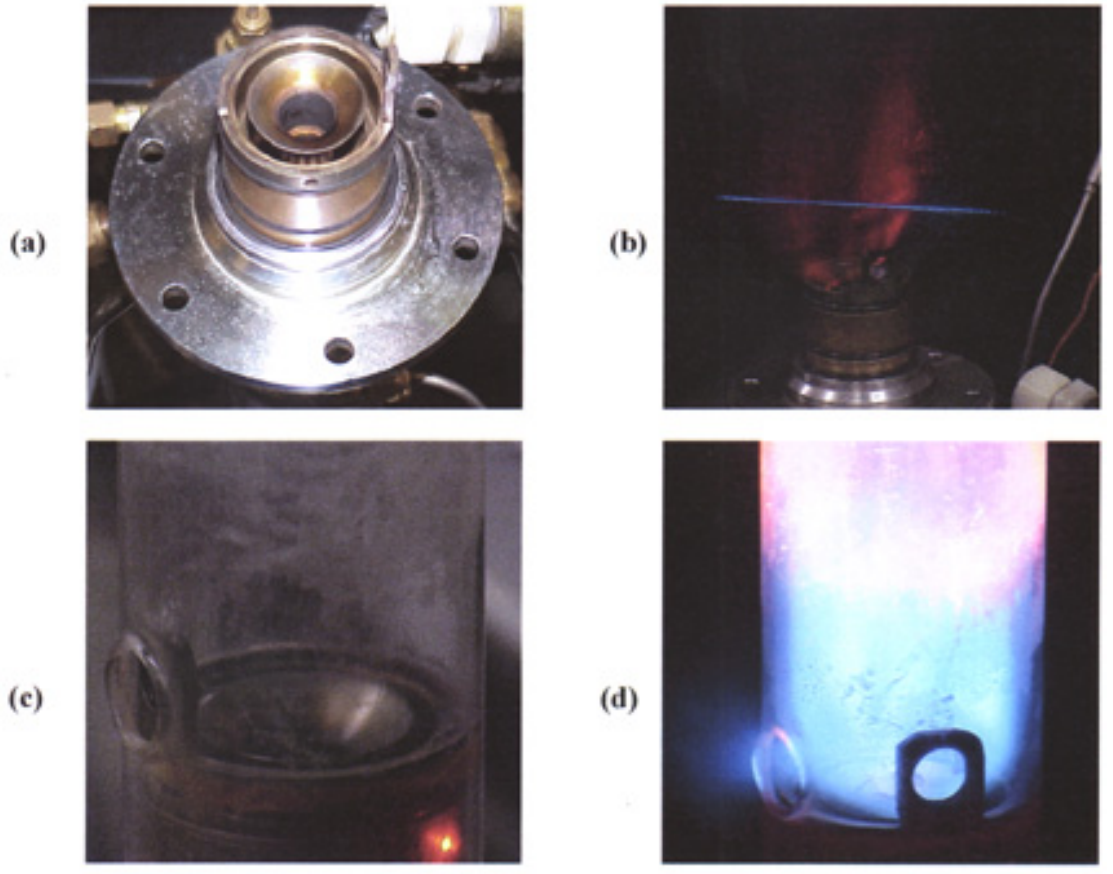

Figure 7. Photographs of combustor hardware and flow fields. **(a)** Overhead view of flame holder, with quartz tube removed. **(b)** Unconfined, cold spray droplet flow field, with sheet illumination by He-Ne laser, and PDPA measurement by Ar-ion blue-line laser beam. **(c)** Confined, cold spray droplet flow field, with intermittent liquid filming along quartz tube. **(d)** Confined, reacting spray droplet flow field.

(c)2001 American Institute of Aeronautics & Astronautics or Published with Permission of Author(s) and/or Author(s)' Sponsoring Organization.

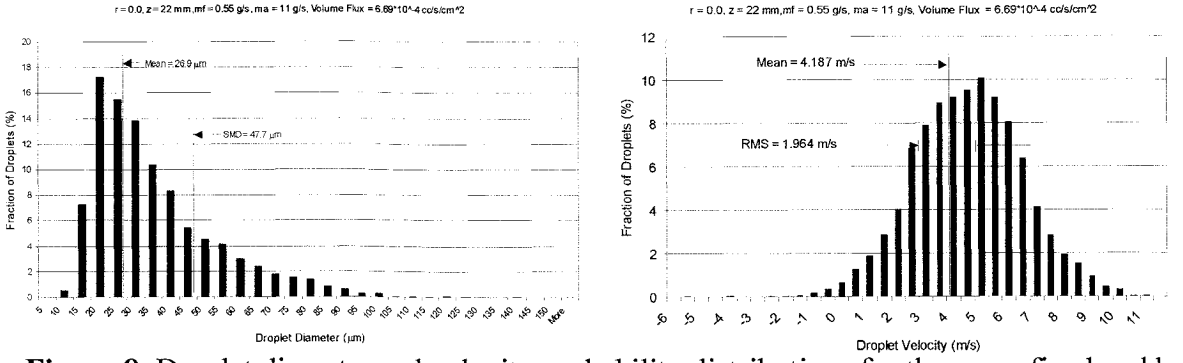

Figure 8. Droplet diameter and velocity probability distributions for the unconfined, cold spray droplet flow field in the Georgia Tech combustor. PDF's measured using PDPA along the combustor central axis, at 22 mm downstream of flame holder.

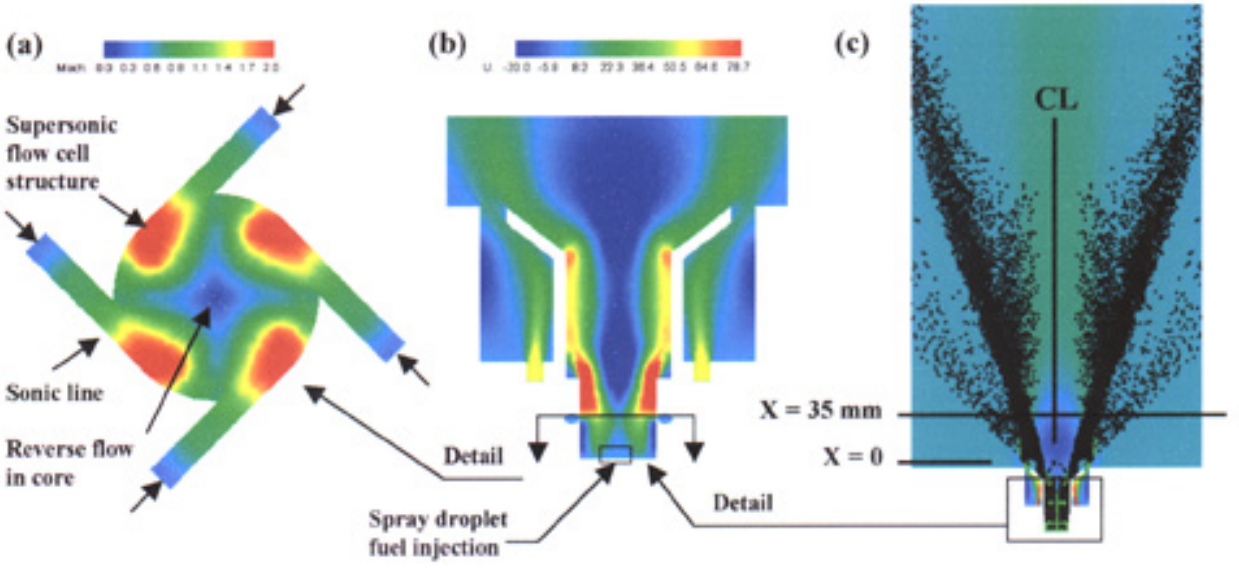

Figure 9. Injector near-field geometry, boundary conditions and computed flow field. **(a)** Slice through tangential entry swirlers, producing primary flow. **(b)** Slice through injector base. **(c)** Instantaneous spray droplet positions for the unconfined, cold flow test run.

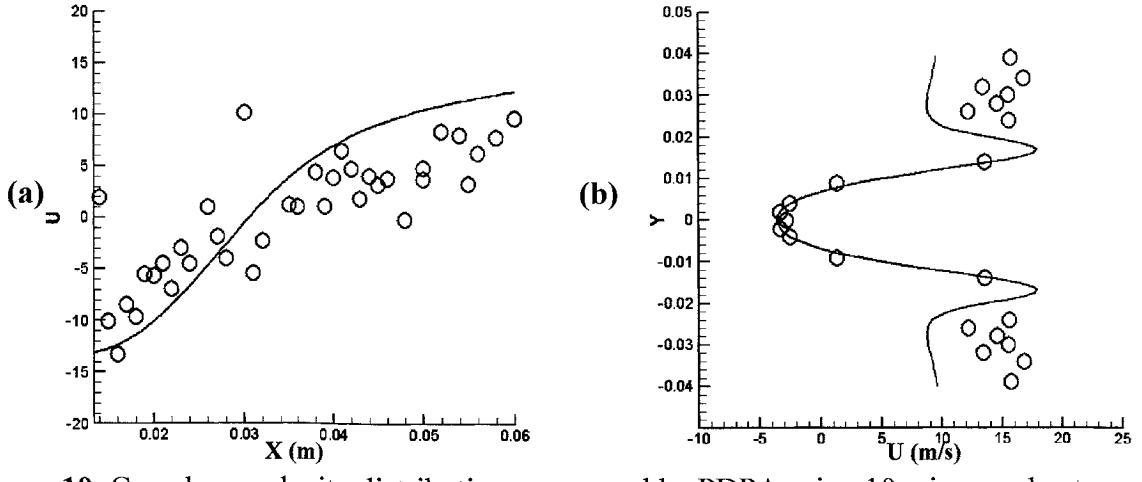

Figure 10. Gas-phase velocity distributions measured by PDPA using 10 micron *n*-heptane droplets as tracer particles. **(a)** Centerline distribution of gas-phase axial velocity. U in m/s, X in m, measured downstream from injector exit plane. **(b)** Radial distribution of gas-phase velocity at X = 35 mm.

(c)2001 American Institute of Aeronautics & Astronautics or Published with Permission of Author(s) and/or Author(s)' Sponsoring Organization.

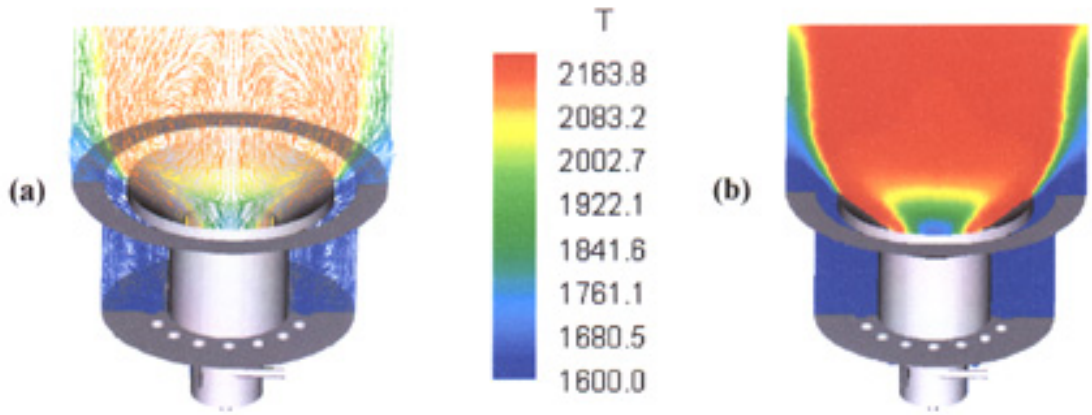

Figure 11. Preliminary gaseous fuel combustion calculation at $\varphi = 1.125$. **(a)** Velocity vectors colored by temperature. **(b)** Temperature contours at combustor midplane.

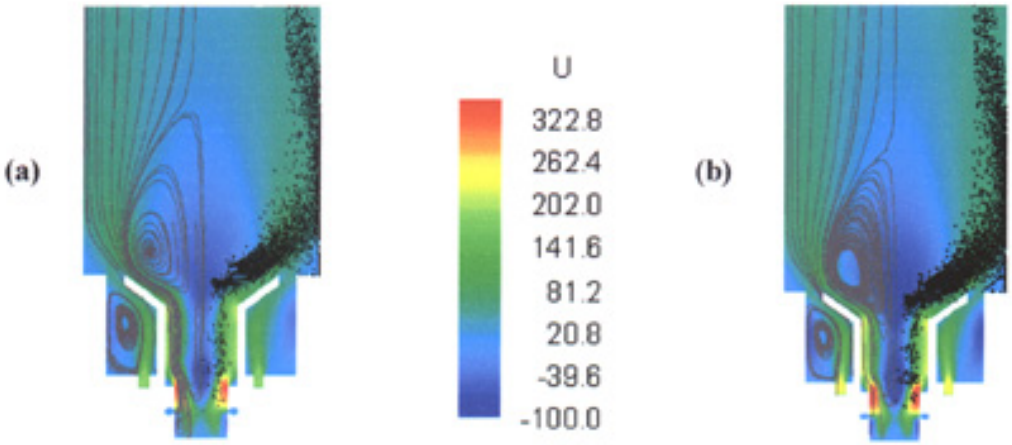

Figure 12. Preliminary liquid spray droplet combustion calculations, showing instantaneous droplet positions and flow streamlines superimposed on axial velocity contours. **(a)** $\varphi = 0.6$ results. **(b)** $\varphi = 1.0$ results.

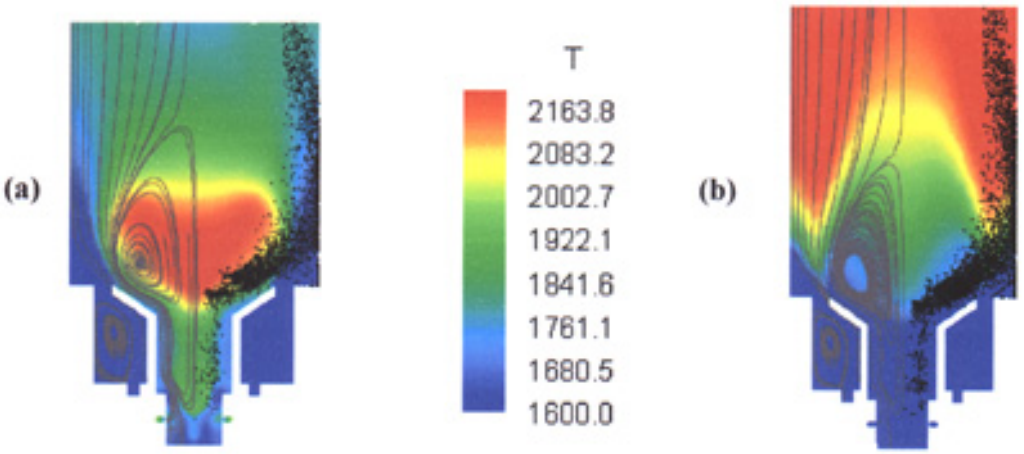

Figure 13. Preliminary liquid spray droplet combustion calculations, showing instantaneous droplet positions and flow streamlines superimposed on temperature field. **(a)** $\varphi = 0.6$ results. **(b)** $\varphi = 1.0$ results.

(c)2001 American Institute of Aeronautics & Astronautics or Published with Permission of Author(s) and/or Author(s)' Sponsoring Organization.

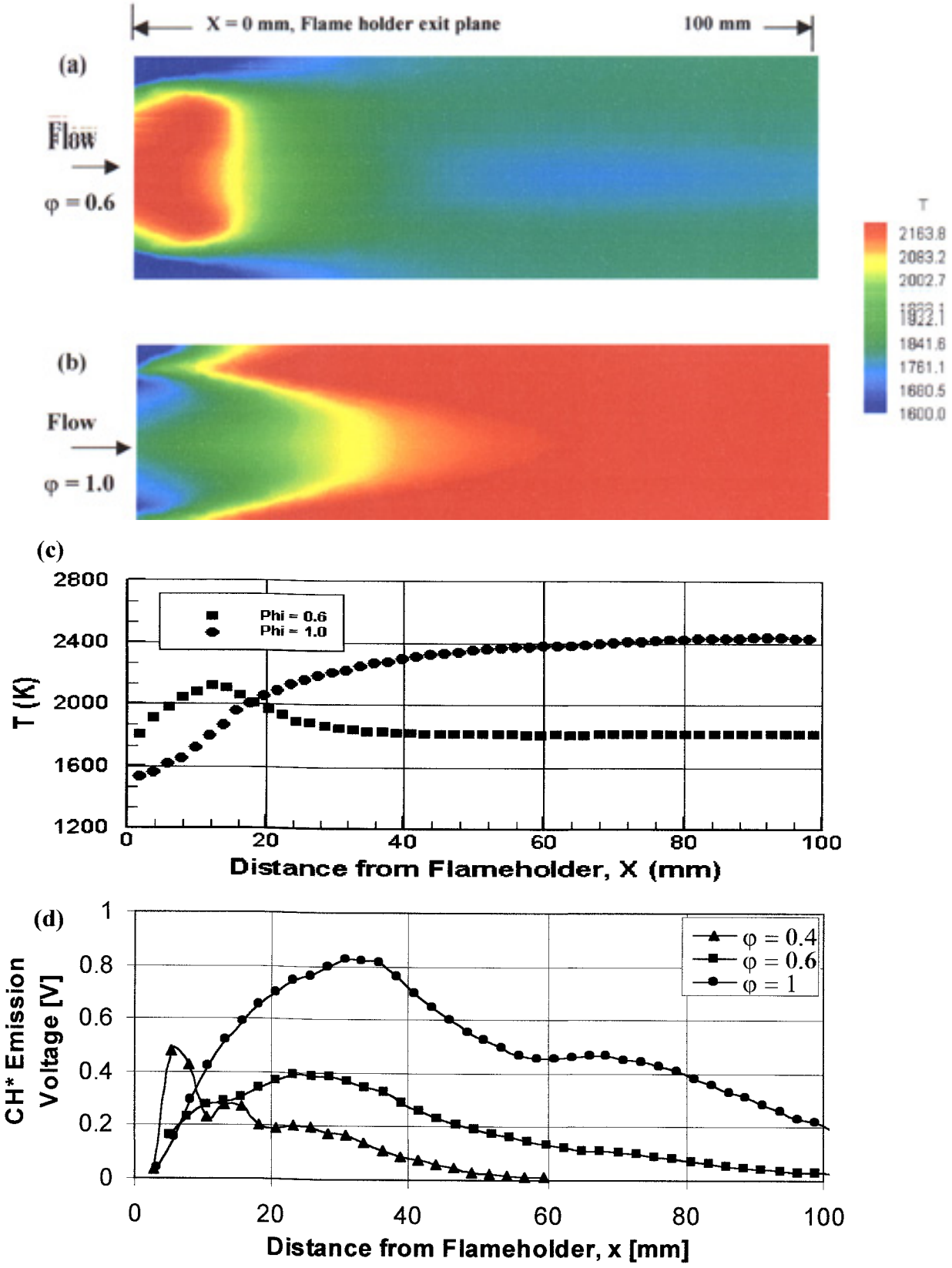

Figure 14. Comparison of predicted axial temperature distributions with CH* emissions results. **(a)** Computed temperature field at φ = 0.6. **(b)** Computed temperature field at φ = 1.0. **(c)** Post-processed results from the simulations. **(d)** Experimental CH* emissions data for three cases, at φ = 0.4, 0.6 and 1.0 test conditions.

(c)2001 American Institute of Aeronautics & Astronautics or Published with Permission of Author(s) and/or Author(s)' Sponsoring Organization.

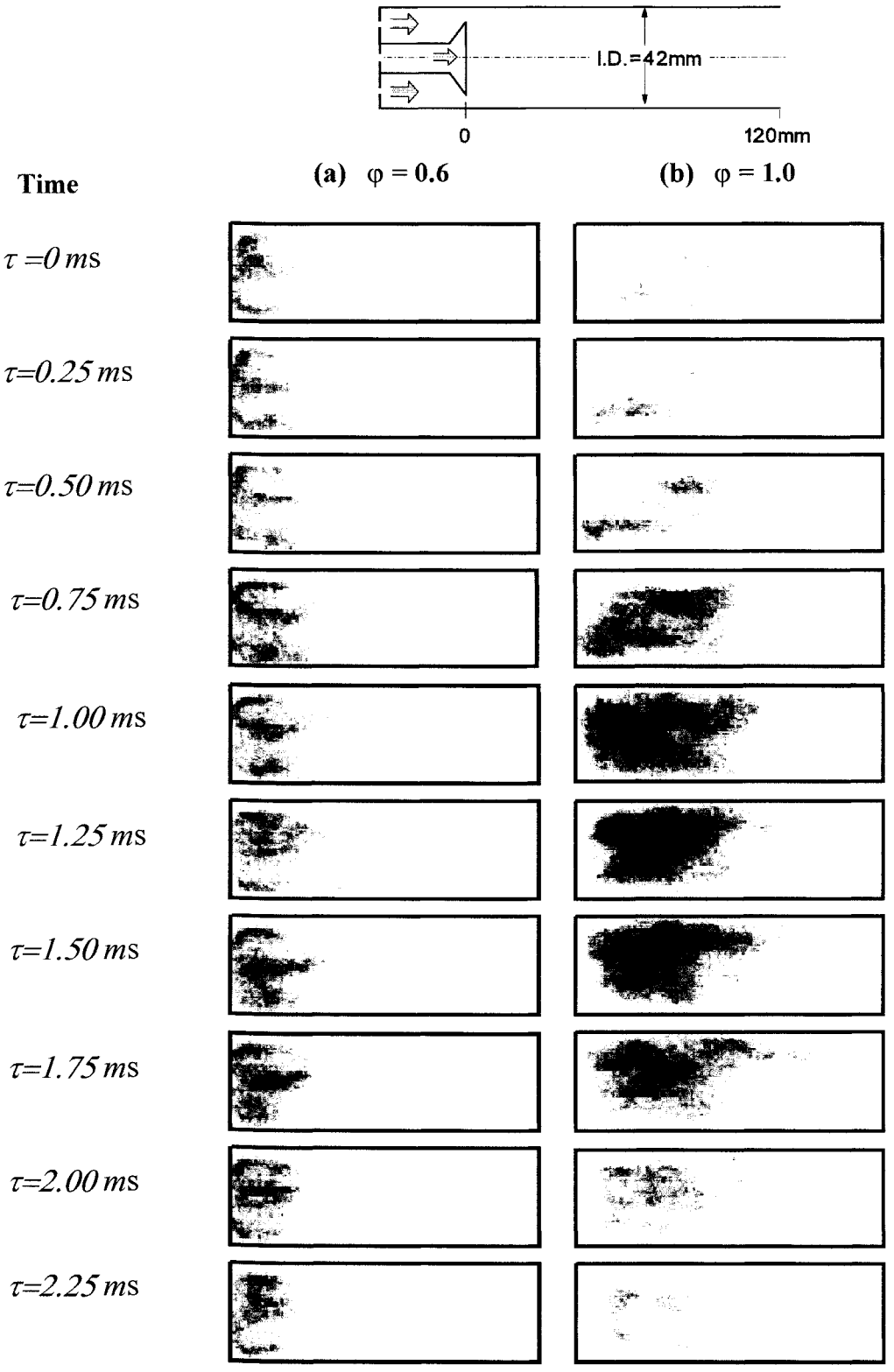

Figure 15. High speed photographs of the combustion zone in the Georgia Tech combustor, taken at 0.25 ms time intervals. The flow images indicate stable flames at **(a)** φ = 0.6, and unstable flames at **(b)** φ = 1.0. The photo sequence on the right illustrates one full cycle of the combustion oscillation.

Georgia Institute of Technology

MITE Workshop on Goals and Technologies for Future Gas Turbines

ULTRA COMPACT COMBUSTORS: MAIN AND INTER-TURBINE BURNER CONCEPTS

Dr. Geoffrey J. Sturgess AFRL/ISSI,
Capt. (Dr.) Ralph A. Anthenien U.S. Air Force/AFRL
and Dr. W. M Roquemore AFRL

4 December 2000

TO BE DISCUSSED

- Why ultra-compact combustors
- Potential possibilities and penalties for inter-turbine combustion
- Turbine constraints for inter-turbine combustion
- Concepts for inter-turbine combustors
- Concepts for ultra-compact main combustors
- AFRL ultra-compact combustor programs

WHY ULTRA-COMPACT COMBUSTORS?

- Main Combustors:
  - reduce engine length to increase thrust/weight ratio
- Inter-Turbine Combustors (two combustors in series, requiring that each be compact):
  - increase engine power density
  - decrease SFC through increased bypass ratio
  - reduced gaseous emissions in exhaust
  - improved turbine durability without excess cooling air

CONSTANT TEMPERATURE CYCLE ENGINE

- Ideal Constant Temperature Cycle:
  - continuous heat addition during expansion through H.P. And L.P. turbines

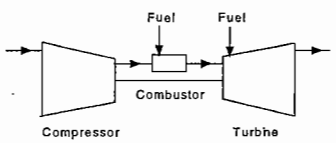

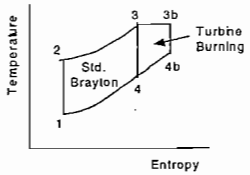

- Quasi-Constant Temperature Cycle:
  - reheat between H.P. and L.P. turbines

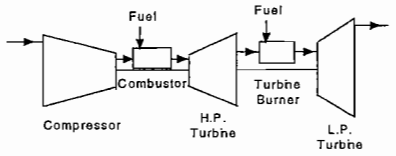

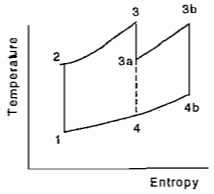

EXAMPLE OF INTER-TURBINE COMBUSTION

- Baseline Engine: SLS, 100% speed; Std. Day
  FPR = 1.84; CPR = 23.25; OPR = 42.78; BPR = 6.4;
  Fan Dia. = 112 inches; Installed F_n = 91,915 lbf; CET = 3008 °F

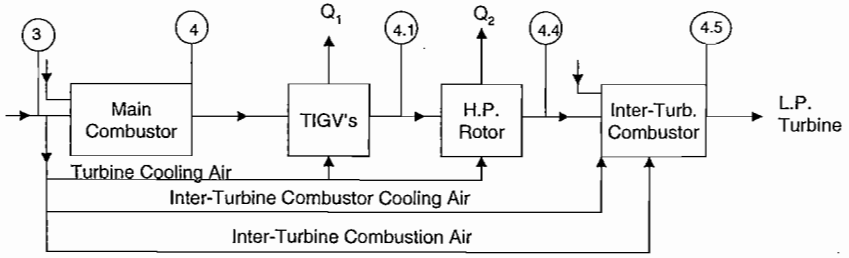

- With inter-turbine combustion, $T_{4.5} = T_4$ = 3008 °F; ϕ_{main} = 0.4706; ϕ_{ITC} = 0.5015: Additional heat release increases BPR to 19 while maintaining OPR (flexibility)
- For same overall heat release in a single combustor, ϕ_{main} = 0.868 and CET = 4107.3 °F; OPR increases also

EXAMPLE OPTIMIZED FOR SFC

- Cycle studies indicate for a transport aircraft application, minimum SFC obtained for BPR ≈ 11.0
- Inter-turbine combustion applied to baseline engine to give BPR of 11.0 while maintaining OPR gives,
  $T_{4.5}$ = 2254 °F and ϕ_{ITC} = 0.1546
- This is a lean burn situation with high inlet temperature combustion situation. Hence, flame stability is not difficult. Also, virtually zero additional NOx is generated in the inter-turbine combustor. However, since overall fuel flow is increased, NOx emission indices go down, and because SFC is reduced and thrust increased also, the NOx EPAP for the engine goes down dramatically.
- With the relative low $T_{4.5}$ little increase in L.P. turbine cooling air is needed.

Win/win situation

POSSIBLE PENALTIES contin/

- Best performance achieved at very high bypass ratios. However, since fan tip speed must be approximately constant, as BPR increases fan speed must decrease accordingly. Therefore, the number of L.P. turbine stages increases. Also, matching almost certainly requires use of a gear-driven fan. The fan gear box is not a trivial item in terms of design difficulty, weight and cost.
- An engine with inter-turbine combustion will have an increased part count and cost.

Each must be addressed and satisfactorily managed

POSSIBLE PENALTIES FOR INTER-TURBINE COMBUSTION

- Excessive pressure losses due to heat addition in relatively high Mach number flows
- Difficulty of burning efficiently in highly-strained flows
- Dangers of poor turbine durability:
  - cycle and turbine design pushing current material limits for highly stressed parts
  - concentration of cooler burnables on suction sides and tips of airfoils due to high gee forces

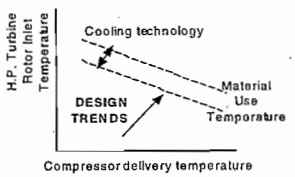

- Need to provide adequate cooling for L.P. turbine

HIGH BPR GEARED TURBOFAN

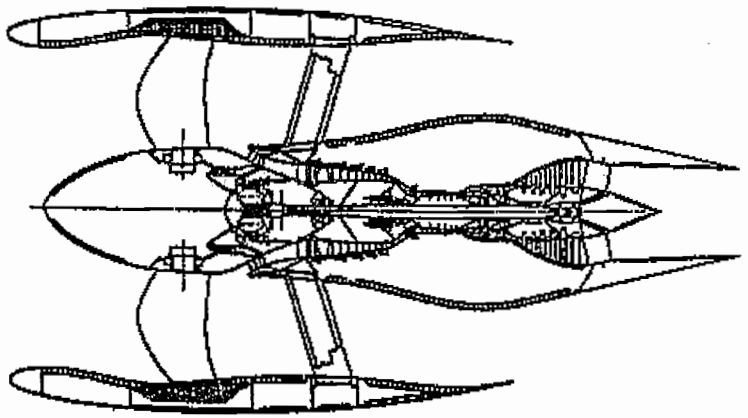

TURBINE CONSTRAINTS WITH INTER-TURBINE COMBUSTION

- Initial stages of L.P. turbine will require cooling with air from compressor intermediate stages. Damage-tolerant ceramic matrix composites (CMC's) might be used to minimize cooling air requirements

- L.P. turbines, like H.P. turbines, like to operate with a near-choked inlet at their design point. Depending on how the inter-turbine combustor is operated, some form of variable area control of the L.P. turbine might be needed

- The conventional definition of "degree of reaction" for the turbine airfoils might not apply where heat release takes place around them. Care will have to be taken therefore, to design airfoils to avoid boundary layer separation on suction sides, and to maintain high efficiency over wide ranges of blade to gas velocity ratios, while managing the heat transfer processes

LOCATION OF INTER-TURBINE COMBUSTOR

- Closely-Coupled H.P. and L.P. Turbines:

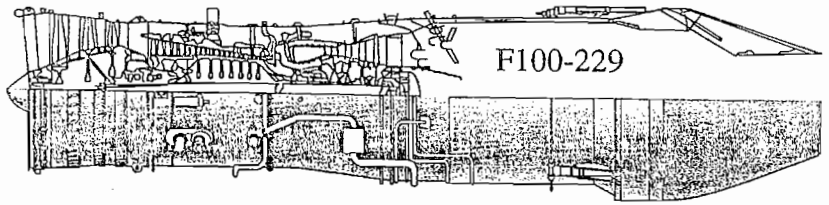

Combustor has to be integrated into turbines

INTEGRATED COMBUSTOR

- Minus:

  - relies on auto-ignition for light-off
  - no light-round capability
  - complicated internal fuel manifolding necessary
  - no direct control of gas exit temperature distributions
  - combustion efficiency uncertain
  - pressure losses might be high

- Plus:

  - no engine length increases
  - minimum effects on engine control
  - parts count increase minimal

LOCATION OF INTER-TURBINE COMBUSTOR contin/

- H.P. and L.P. Turbines Separated by Inter-Turbine Duct:

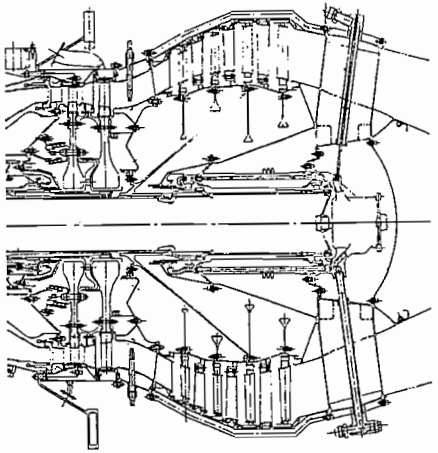

Space between turbines for separate combustor

CONCEPT DRAWING

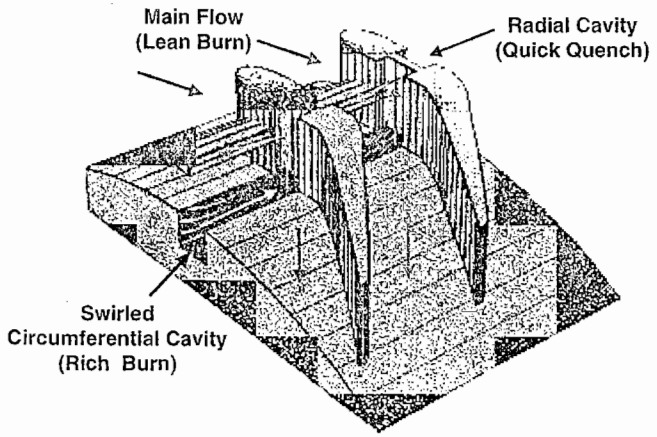

INTER-TURBINE DUCT COMBUSTOR

- Minus:
  - increased pressure losses in inter-turbine duct (but manageable)
  - durability issues (requires cooled CMC's)
  - increased parts count
  - inter-segment seal issues
  - might require variable area L.P. turbine (depending on how combustor is operated)

- Plus:
  - no engine length increases due to combined functions, folded flow path and high burning rates
  - fully capable combustor (i.e. independent light-off, light round, good combustion efficiency and flame stability)
  - only requires 10-15 relatively small fuel injectors, inserted radially through casing
  - modular construction eases strip and rebuild, as well as replacement and repair

COMPACT COMBUSTOR CONCEPT FOR INTER-TURBINE DUCT

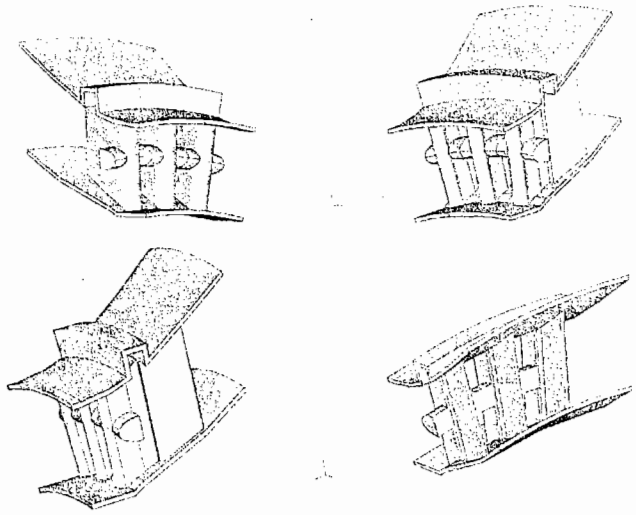

APPLICATION TO MAIN COMBUSTORS

- Inter-turbine duct combustor concept is directly applicable to main combustors, and results in engine length and weight reductions, and a reduced parts count
  - replaces H.P. turbine TIGV's with reduced number of wide chord vanes
  - eliminates need for compressor exit guide vanes since designed to accept swirling flow (saves 1.5+% pressure loss)
  - uses only 10-15 short length fuel injectors due to tangential swirl flow path in cavity and short throw, easy radial insertion
  - holds or reduces combustion section pressure loss
  - no increase in H.P. turbine cooling air (vane leading-edges see only T_3 temperatures)

Check on g-enhanced combustion.

Ultra-Compact Combustors

EVALUATION OF COMPOUND SWIRL CAVITY

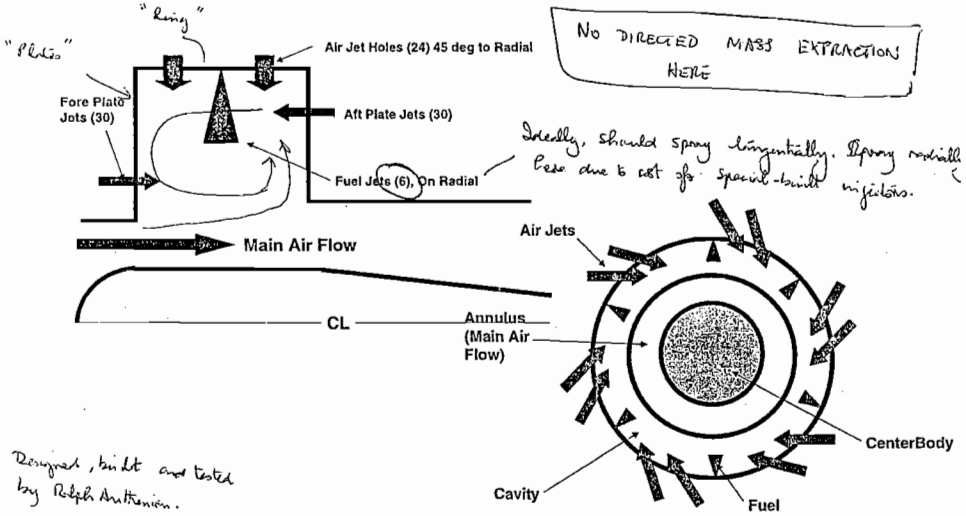

NO DIRECTED MASS EXTRACTIONS HERE

Ideally, should spray tangentially. Spray radially here due to cost of special-built injectors.

Designed, built and tested by Ralph Anderson.

Atom. pressure rig configuration

(AGTR Presentation, Sept. 2000)

Ultra-Compact Combustor

SWIRL EVALUATION contin/

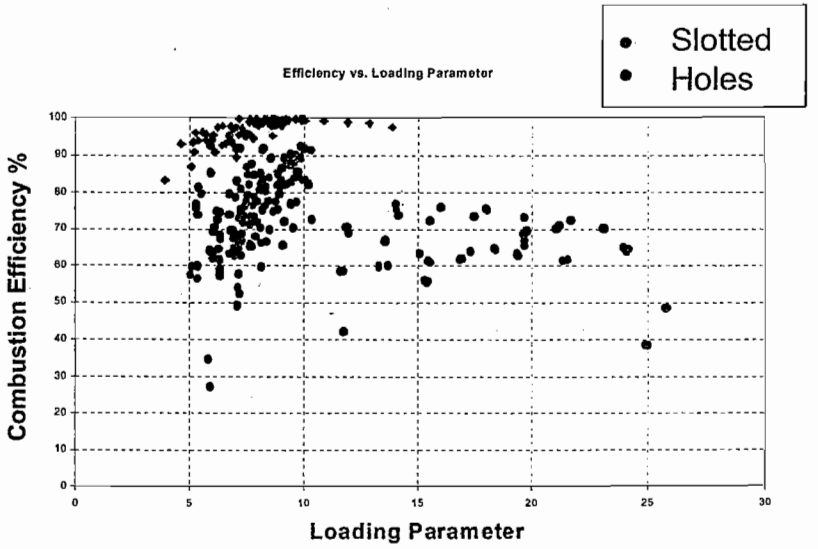

(AGTR Presentation, Sept. 2000)

Ultra-Compact Combustors

SWIRL EVALUATION contin/

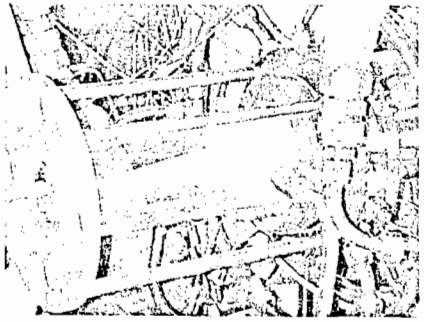

Phi Cavity = 1.2
Phi Overall = 0.36
Cavity Loading = 9.0

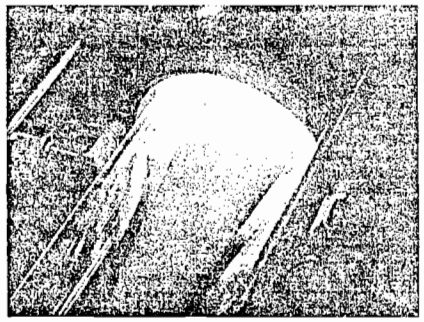

Phi Cavity = 0.74
Phi Overall = 0.26
Cavity Loading = 10.5

1,000 g's at highest cavity loading

(AGTR Presentation, Sept. 2000)

is similar to that of the Rolls Royce vaporizers, except for an increased sensitivity of combustion efficiency to both equivalence ratio and loading parameter. Figures IV-33 and 34 are both for Jet-A, JP-5 or JP-8 fuels.

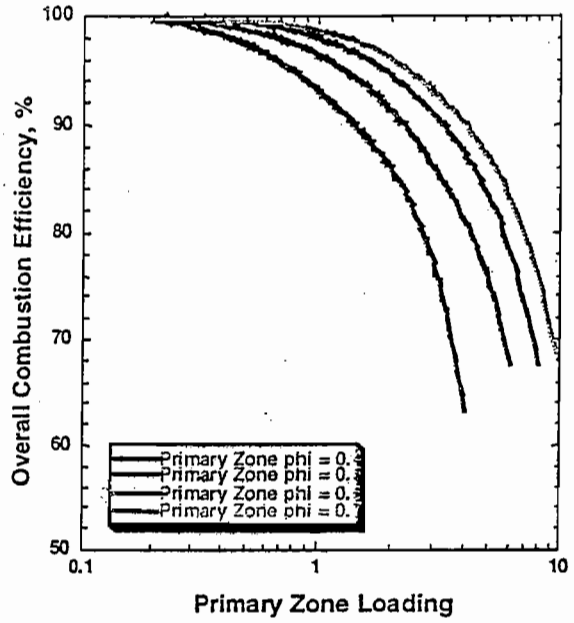

Figure IV-34: Combustion Efficiency for Swirl-Stabilized Combustors

It can be seen from Figure IV-34 that combustion efficiency decreases with decreasing equivalence ratio. At any equivalence ratio the combustion efficiency falls off precipitously as loading rises above about 3.0 (lbm/s)/(ft.^{3}atm$^{1.8}$) at 400 °K inlet. temperature. The impacts of this behavior on a blowout curve may be seen by using Figure IV- 34 together with Figure IV-15 to make a cross-plot. Figure IV-35 is a plot for this combustor of combustion efficiency at blowout against primary zone loading.

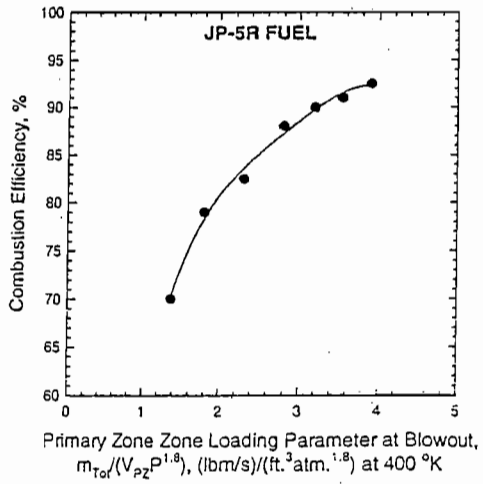

Figure IV-35: Combustion Efficiency at Blowout - Swirl Combustor

The presence of combustion decreases the reattachment length, for propane/air pre-mixtures to 4.3 to 5.3 step heights for Reynolds Numbers of 15,000 and 37,000 respectively at 0.57 equivalence ratio (Pitz & Daily, 1983), i.e. a 30% reduction from isothermal flow. Stevenson et al., 1982, for 113,000 Reynolds Number and 0.28 equivalence ratio, found a reattachment length of 7.5 step-heights, i.e. 12% less than the isothermal case. Swirling the jet tends to reduce the isothermal flow reattachment length. For swirling, combusting flow, the reattachment length is around 3.0 step-heights for Figure IV-29.

Combustion efficiency

Combustion efficiency can be expressed as a function of combustor loading parameter and equivalence ratio, just like blowout, and this is extremely convenient. An example is presented in Figure IV-33 for Rolls Royce vaporizer combustors, (Parnell & Williams, 1971), in terms of overall air loading parameter, with an apparent reaction order of 1.8 and corrected to 400 °K inlet temperature. The combustors shown all had about the same overall pressure drop of about 5-6 % inlet total pressure. Higher pressure drops affect the combustion efficiency through improving the fuel/air mixing. The data points include designs with different primary zone bulk equivalence ratios, all on the fuel-lean side. Note the relative insensitivity to equivalence ratio, and the retained combustion efficiency over a fairly wide range of loading parameter. These are characteristics of vaporizer combustors.

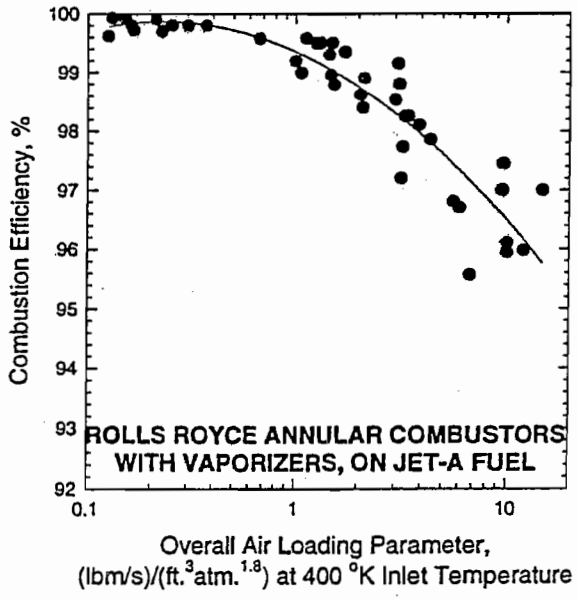

Figure IV-33: Correlation of Combustion Efficiency for Many Vaporizer-Tube Combustors

Figure IV-34 gives a similar plot for Pratt & Whitney swirl-stabilized combustors of conventional design; here, the loading parameter is for the primary zone. The behavior

INTER-TURBINE DUCT FEATURES

- Between H.P. turbine rotor exit and L.P. turbine inlet guide vanes
- Length 1-2 inlet annular heights - several inches total in big engines
- Flow Mach number in range 0.3-0.55
- Loss coefficients between 0.05-0.2 inlet dynamic heads
- Path canted due to increased diameter of L.P. turbine
- Flow contains exit swirl from H.P. turbine rotor

INTER-TURBINE DUCT POSSIBILITIES

- Length constraints and need to accept high inlet swirl suggest functions of L.P. turbine inlet guide vanes and inter-turbine combustor be combined
- The combined-function blade would have a wide chord, that should reduce the required number of them
- Wide-chord vanes necessitate an increased gap between their trailing edges and L.P. turbine rotor inlet

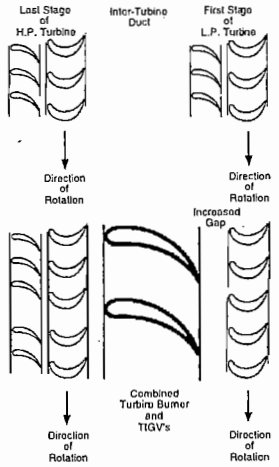

PRESSURE LOSS AND FLAME-HOLDING

- Conventional main combustors require about 25 dynamic heads of "useful pressure loss" to achieve fuel/air mixing, high turbulence generation for high turbulent burning velocities, and to set up flow patterns for flame-holding The blockage represented by this level of loss is too high for the inter-turbine duct
- Afterburner technology (spray bars and vee-gutters) has low loss but requires too much length to achieve adequate combustion efficiency. Also, it is difficult for such systems to handle the passage cant
- Trapped vortex combustors (TVC's) have demonstrated excellent flame-holding and good efficiencies with low pressure losses and very short axial burning lengths

Utilize TVC concepts for inter-turbine combustor

ENHANCED TVC FEATURE

- A conventional TVC utilizes a contained vortex system with a spin axis parallel to but across, the mainstream flow direction
- It has been shown that turbulent burning velocities increase with the square root of the gee-forces applied to the mixture, i.e.

$$S_T \propto (\rho_u/\rho_b)^{1/2} R_{max}^{1/2} \sqrt{g}$$

where R_{max} is maximum radius of swirling vortex and $g = \omega^2 R_{max}$ This is one reason why swirlers are used in conventional combustors; however, $g \approx 40\text{-}50$ is best achieved and the affect on flame speed is weak. If the whole dome flow is swirled about an axis parallel to but across, the mainstream flow direction (as in TVC) g's of several hundred might be achieved.

- It is proposed that the TVC concept to be used for the inter-turbine combustor be provided with an additional swirl component about an axis co-incident with the engine axis. This result in g's in the vortex cavity becoming 1,000-3,000. Exptl. results of Lewis show flame speed reaches a maximum at 3,500-4,200 g's.

ASSESSMENT OF 3-INCH RIG RESULTS

- Slotted Ring Jets Configuration:
  - very poor performance
  - could not load cavity over 1 lb/min air (10% of total)
  - very little warning to blowout; believed to be due to collapse of the fuel jet spray cone

- Straddle Jet Configuration:
  - good efficiency; can achieve loading parameters >12 at 99+% efficiency

this is what was expected

- Comments:
  - combustor performs better with more air thru ring, less thru plates
  - higher inlet velocities lead to lower efficiencies, (with plate air, effect is greater than when using ring air)

no control over mass exchange in cavity

HIGH-PRESSURE RIG

- Concept can only be evaluated in full axisymmetric form due to swirl cavity; 10 inch dia. for available airflow

3,000 g's should be achieved in cavity.

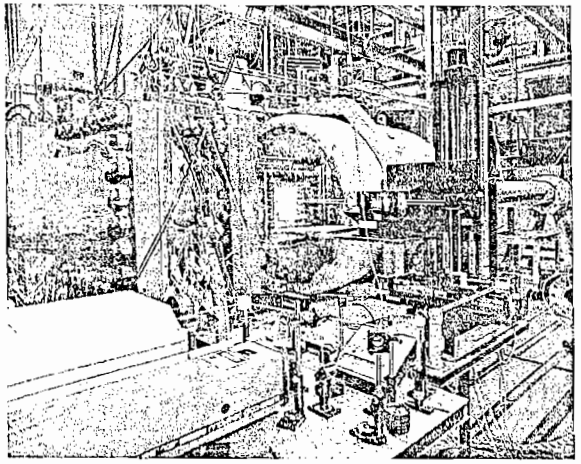

Air Flow Rate: 20 lbm/s

Air Temperature: 1100 F

Air Pressure: 0.25 to 20 atmospheres

Full Optical Access to 220 psia

CLOSURE

- Performance of constant temperature cycle engine (not discussed here) continues to look promising.

- Realization of performance gains through an engine layout study remains to be done.

- Combustion concept for inter-turbine duct combustor shows promise at atmospheric pressure, and concept appears feasible; parallel material development program (not discussed here) is proceeding.

- Rig design for high-pressure evaluation of concept is in progress.

- Inter-turbine duct combustor concept also could serve as an ultra-compact main combustor

38th AIAA/ASME/SAE/ASEE Joint Propulsion Conference & Exhibit
7-10 July 2002, Indianapolis, Indiana

AIAA 2002-3725

ULTRA-COMPACT COMBUSTION TECHNOLOGY USING HIGH SWIRL FOR ENHANCED BURNING RATE

J. Zelina**, J. Ehret, R. D. Hancock, D. T. Shouse and W. M. Roquemore***
Air Force Research Laboratory
WPAFB, OH 45433

G. J. Sturgess***
Innovative Scientific Solutions, Inc.
Indian Ripple Road,
Dayton, OH 45440-3638

**Senior Member AIAA ***Fellow AIAA

Abstract

A gas turbine engine is proposed that uses a near constant temperature (CT) cycle and an Inter-Turbine Burner (ITB) to provide large amounts of power extraction from the low-pressure turbine. This level of energy is achieved with a modest temperature rise across the ITB. The additional energy can be used to power a large fan for a high bypass ratio transport aircraft or to drive a generator for electrical power extraction. Conventional gas turbines engines cannot meet such power extraction demands without a loss of engine thrust. A second power source to provide energy for such applications would be necessary, adding considerable cost and weight to the system. This paper will describe efforts that focus on Ultra-Compact Combustor (UCC) technology to serve as an ITB or main combustor in the CT engine. Reducing the size of the main combustor and ITB is essential to reducing or maintaining overall engine weight and size.

Concepts for a UCC are being explored experimentally. Computational Fluid Dynamics (CFD) is used to guide combustor design modifications. The modified combustor hardware is being tested in the Atmospheric Pressure Combustor Research Complex (APCRC) at the Air Force Research Laboratory (AFRL). Experimental results indicate that the combustion system flame holding zone operated at 99+% combustion efficiency over a wide range of operating conditions. Flame lengths were extremely short, at about 50% that of conventional systems. High heat release rates were seen while maintaining high combustion efficiencies. Combustor cavity g-loading enhanced reaction rates thereby increasing the combustion efficiency.

Nomenclature

CFD	computational fluid dynamics
CT	constant temperature
EI	emissions index (g/kg)
g	g-loading
HRR	heat release rate (MBtu/atm-ft^3)
ICAO	International Civil Aviation Organization
ITB	inter turbine burner
LP	loading parameter (lb/sec-atm^n-ft^3)
m	mass flow rate (lb/sec)
OFAR	overall fuel-to-air ratio
P	pressure (psia)
T	temperature (F)
TVC	trapped vortex combustor
UCC	ultra-compact combustor
V	volume (ft^3)
WSR	well-stirred reactor

Symbols

ϕ	metered equivalence ratio
ρ	density (lb/ft^3)
τ	residence time

Subscripts

cav	cavity
f	fuel
a	air

Introduction

To meet the conflicting requirements of higher compression ratio, high heat release rates, reduced weight and low emissions, with improved engine durability requires revolutionary combustion systems. For example, advanced combustors are becoming shorter and utilize non-metallic materials to meet the required thrust-to-weight ratio goals. Shorter residence times in the combustion chamber may reduce the NOx emissions, but the CO and UHC emissions then increase due to inadequate reaction time. Also, the unburned fuel could escape the combustion chamber and continue to burn in the turbine machinery,

This material is declared a work of the U.S. Government and is not subject to copyright protection in the United States.

which could pose a series of rotating component challenges such as vane and blade durability, and pressure loss increases.

Recently, Sirignano and Liu[1,2,3] and others have proposed the idea of a turbine burner gas turbine engine to operate on a constant temperature (CT) cycle. The efficiency of a CT cycle approaches that of a Carnot cycle. The cycle analysis indicates that additional work can be gained with CT cycle engine without large performance penalties. Key to this cycle is that sufficient heat is added in the turbine to compensate for the work extracted to drive the compressor. Combustion in the inter-turbine duct has three major requirements: First, the inter-turbine burner (ITB) must be short enough to successfully accomplish its function without resulting in an increase in overall engine length. Second, the ITB must achieve the required heat release without introducing a large loss in total pressure. Third, the ITB must accomplish its function without adversely affecting the low-pressure turbine durability. If a successful ITB can be devised with these attributes, then the combustion concept may also become a candidate for the main combustor of the engine. Incorporation of an ultra-compact combustor (UCC) as a main combustor would provide sufficient length savings as to guarantee that a quasi-constant temperature cycle could be achieved without any increase in overall engine length. If an ITB was not included for some reason, adoption of a UCC would still allow a reduction in overall engine weight.

The ITB concept is clearly attractive, but a conventional combustor is much too large to fit between the stages of a turbine. A UCC is needed in order to implement the ITB concept without significantly increasing the engine length and thereby negating much of its benefit. In this work, we present preliminary experimental results of a UCC concept that utilizes high "g" swirl to shorten the overall flame length. Furthermore, it provides for the majority of the heat release to take place at low Mach numbers, thereby containing Rayleigh losses.

The effects of acceleration, specifically centrifugal acceleration, on combustion have been previously studied by Lewis[4]. He found that flame speed increases with increasing acceleration up to approximately 3000-6000g. Above this limit, flame speed abruptly decreased prior to being extinguished. He found that for regions of increasing flame speed, the laminar flame speed follows the relation:

$$S_L \propto g^{1/2} \qquad \text{Eq. 1}$$

Yonezawa et al.[5] applied this concept to design and analyze a jet-swirled combustor in the 800-1300 g range. This concept looks very much like a conventional annular combustor, but with a series of injection ducts inclined both axially and circumferentially to drive a swirling flow within the combustor liner. A qualitative flow analysis was undertaken to optimize the angles of the injection duct and a prototype was developed to test the concept. It was shown that a much higher loading factor could be obtained in this combustor design with high efficiency, and for a given loading factor, this jet swirl combustor had a higher efficiency over a conventional combustor. This work demonstrated that the rate of combustion could be sufficiently enhanced so that the length of a combustor could be reduced by ~33% while maintaining high combustion efficiency. Combustion is enhanced because the pressure gradient associated with the centrifugal acceleration of a rotating flow causes rapid mixing and transport of the hot gases towards the central axis of the flow. The accumulation of the hot gases near the central axis becomes a source of high temperature that promotes rapid combustion.

Here, we have proposed and have begun experiments on a UCC which will combine the combustor with the compressor exit guide vanes and the turbine inlet guide vanes. A trench, or cavity, will run around the outer circumference of the vanes (Fig. 1). Aligned with this cavity, within each vane, will be a radial cavity. The idea is to burn rich in the circumferential cavity, allowing much of the required combustion residence time to take place in the circumferential direction of the engine, rather than the axial as is done conventionally. The flow within this cavity will be swirled to generate high "g" loading and reduce the chemical residence time. Flame stabilization occurs as combustion products are recirculated in the cavity. The intermediate products of combustion will be transported into the radial cavity in the vane where combustion will continue at reduced equivalence ratio. Finally, across the leading edge of the vanes, again in a circumferential orientation, there will be a flame holder (if necessary) where products will be entrained and distributed into the main flow and complete the combustion process. Functionally, the circumferential cavity may be regarded as a primary zone, the radial cavities as constituting an intermediate zone, and the flameholder as the dilution zone. Swirl from either the compressor (if used as a main combustor) or the turbine stage ahead of the ITB may be used to drive the swirl in the cavity. This will negate the need for a stator ahead of the combustor, further shortening the system. The increased residence time of the combustion products in the cavities will contribute significantly to achieving complete combustion in a short distance. The cavities are a folded combustion system so that the quick-quench, lean-burn process actually starts at the inlet of the combustor with the rich burn process taking place in parallel in the cavities, and is accomplished without

extending the length of the combustion system. We estimate that an ultra-compact combustor, of design as described above, would be at least 66% shorter than a conventional combustion system defined as the diffuser, combustor, and the turbine inlet guide vanes. The heat release takes place within the sheltered cavities, out of the high velocity flow through the vanes. All heat release is to be completed upstream of the gauge point of the vanes. By this means, Rayleigh losses will be minimized and only mixing losses will be encountered.

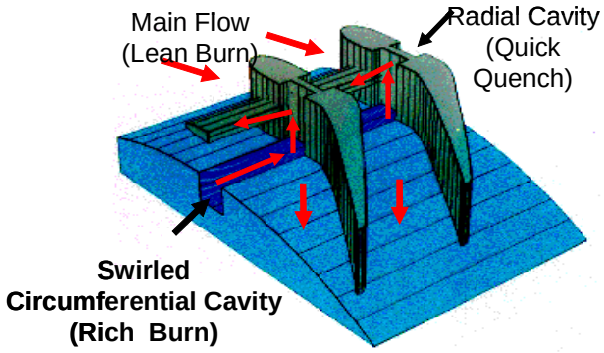

Figure 1: UCC/ITB Concept for Advanced Combustion Systems.

Experimental Setup

Test Facility

The facility can supply a total of up to 44 lbm/min of heated air at atmospheric pressure, with three independently controllable air systems available to allow for different air splits supplied to the combustor (*i.e.* a main air supply and two smaller systems for controlling cavity and cooling air supplies). The air can be heated to temperatures ranging from room temperature to 500 F. Two independently controlled fuel systems are available, each supplying flow at up to 400 psia and 5 lbm/min flow rate. The facility is fully instrumented for pressure, temperature and flow rates. Emissions analyzing equipment is available to detect CO, CO_2, NO_x, O_2, and total unburned hydrocarbons at the combustor exit plane.

Test Matrix

Based on a conceptual design study of a UCC for a conventional engine, and preliminary results from CFD calculations, three configurations were chosen for investigation. Additional configurations will be explored later. Both experimental tests and CFD modeling and simulation were conducted for each configuration. These tests were conducted to provide insight into combustor design parameters to improve the system performance and to provide data to anchor our CFD models. Three designs included a 16%, 22%, and 27% total airflow split to the cavity. The investigation included cavity and main pressure drop from 2-5% and cavity equivalence ratios from 0.75 to 2.2.

Atmospheric Pressure Rig Design

The purpose of this initial rig is to explore the functionality of the circumferential cavity. It is therefore not meant as a complete combustor. However, practical assembly and support considerations resulted in some additional functional features appearing, albeit in non-optimized form (Anthenien et al.[6]). The combustor is axi-symmetric and constructed of stainless steel, with a quartz tube in the exhaust section to allow for viewing of the flame. The center-body is bullet nosed at its leading edge, is of constant radius in line with the cavity of the combustor and has a tapered trailing edge. The main airflow enters the combustor from a settling chamber, and flows around the bullet nose of the center body (Fig. 2). Six support spiders locate the center body and allow for some limited mass transport out of the cavity into the main flow. Exhaust gases exit through an orifice section at the rig exit. This orifice prevents recirculation of ambient air back into the rig.

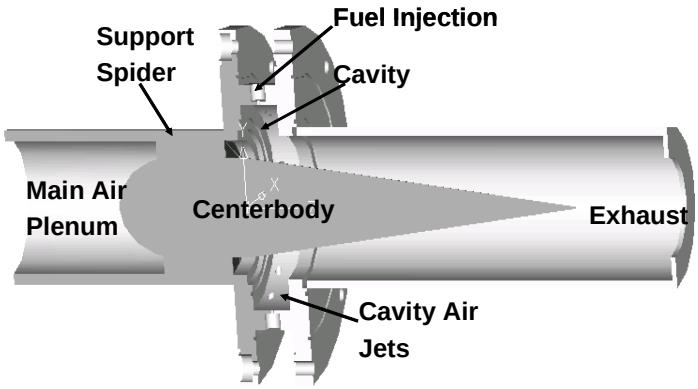

Figure 2: The UCC/ITB Combustor Rig Schematic.

Fuel is radically sprayed into the cavity at 6 equally spaced points around the circumference of the cavity. Simplex pressure atomizing nozzles are used. The nozzles have a flow number of FN = 0.4 and a 70º spray angle, and the injectors are fueled with JP-8+100 fuel.

Modeling and Simulation

Combustor Grid and Boundary Conditions

Computer Aided Design (CAD) and numerical simulation techniques were utilized to enable optimization of the UCC concept and, also to afford greater understanding of the behavior inside the combustor section. The UCC was modeled using AutoCAD2001. A full assembly drawing of the test rig was created and imported into Gambit, which is a pre-processing, mesh generation program. The full combustor was decomposed into a 60-degree section. This makes use of the axi-symmetric nature

of the UCC by implementing periodic boundary conditions in the test section. The section was also further decomposed to allow for a better mesh without a large number of highly skewed cells. The numerical test section was restricted to 55mm upstream from the combustor ring and 76mm downstream. The mesh was generated using approximately 350-400k hexagonal cells. Surface meshes were created with a hexagonal pave scheme in the region of the combustor and with hexagonal map in the outlying regions on either side of the combustor ring. A volume mesh was then generated employing the Cooper scheme. Cell spacing ranged from .635mm in the combustor ring to 2.032mm at the main air inlet and pressure outlet. This provided a dense grid in the area of interest, while keeping a somewhat coarse grid in the inlet and exit zones and keeping the total number of cells down to a manageable number for currently available computer capabilities at AFRL. The maximum skewness of cells in the model ranged from 0.72-0.74 on a normalized scale, and occurred in less than 1% of the cells.

Fluent, a commercially available CFD code, was used for the numerical simulation of the UCC. A steady state, 3-D, implicit model was created with a segregated numerical solver. A standard k-epsilon turbulence model was chosen employing the following turbulent Prandtl Numbers.

The TKE and TDR Prandtl numbers were chosen to be 0.2 in order to better stimulate mixing in the cavity to better reflect real life conditions. Initial work was conducted using the baseline UCC combustor data to calibrate the CFD code. Initial CFD calculations indicated that most of the burning was taking place far downstream of the cavity. Since the CFD model chemistry uses an infinitely-fast reaction rate, the mixing rates were adjusted to match combustor flame length by changing the Pr/Sc numbers. It was found that values of Pr=0.2 gave good agreement with experimental results. This assumption can be verified by He et al.[7], which showed that turbulent Prandtl-Schmidt number variations produced changes in the jet mixing rate for low momentum flux ratios. Standard wall functions were used and viscous heating was not taken into account.

A PDF lookup table was created for species properties and equilibrium chemistry was used. The fuel injection model was set up so that a discrete phase iteration would occur every twenty continuous phase iterations. A 70-degree injection cone with 500 particle streams was utilized. This fuel injection cone contained droplets with a radius of 1.2E-02 mm and a particle velocity of 39.6 m/s, injected at 0-degrees to the radial of the combustor model.

Temperature Calculations

Fig. 4 shows temperature calculations through the combustor plane in-line with the support spiders where ϕ_{cav} ~ 1.0. As seen, the flame region extends around the shear layer between the fuel injector spray, and along the shear layer between the main air and the swirling cavity airflow. Fig. 4a shows the temperature profile for the 16% cavity air case. The high temperature region is located around the fuel injection point at the top of the cavity, and propagates down to the shear layer between the cavity and main stream airflow. Notice, however, in Fig. 4b that the transport down the spider is greater for the higher cavity airflow case. In the complete combustor configuration, this hot gas transport along the spider is critical to maintain acceptable turbine pattern factor, and to provide a stability zone to complete the burning process.

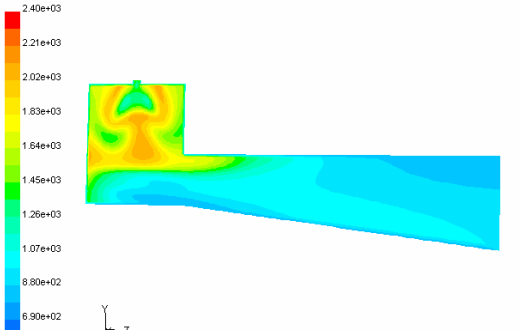

(a)

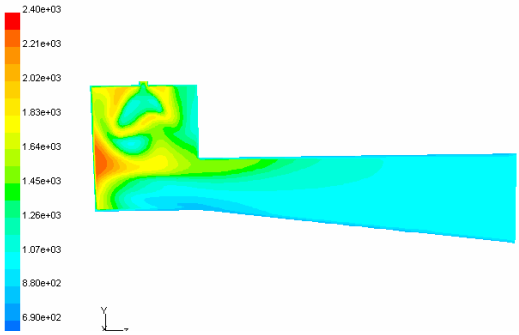

(b)

Figure 4: Temperature Calculations (°K) Along a Combustor Cross-Section at the Spider Location for (a) 16% Air and (b) 22% Air Configurations.

Fig. 5 shows the velocity vector, colored by gas temperature along the spider to show the transport mechanism. As seen, the hot gases move radially downward along the spider, and the gases are distributed along the radial main air channel. The transport mechanism is similar to that of the trapped vortex combustor (TVC) where the hot gases migrate along a series of radial and circumferential struts which distribute

the mixture to the main flow (Roquemore et al.[8]). Flame lengths, as indicated by high temperature location, is similar to experimental results. Typical flames extend about one cavity axial distance downstream of the cavity.

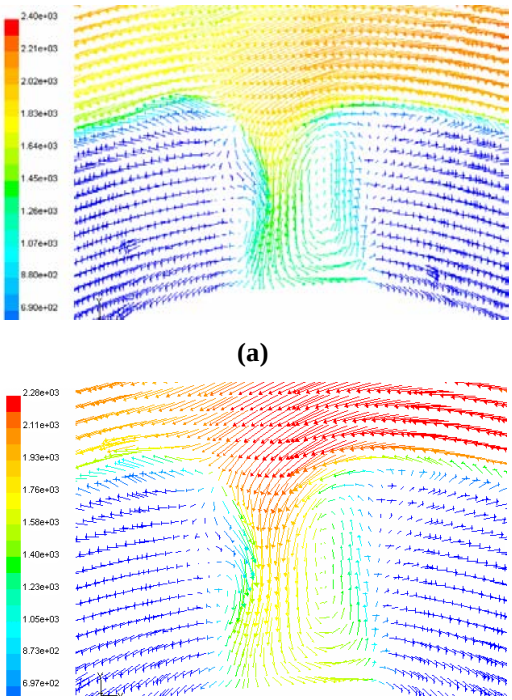

(a)

(b)

Figure 5: Velocity Vectors Colored by Temperature (°K) Showing Combustion Product Transport Along the Spider for (a) 16% Air and (b) 22% Air Configurations.

Fuel and air mixing in the cavity and flame zone communication to the adjacent fuel injection region is critical to the successful operation of this combustion system. Ideally, the previous burning zone would act as an ignition source for the following zone downstream, therefore maintaining a continuous flame in the cavity. Fig 6 shows temperature calculations in-line with the cavity air jets for the 16% and 22% cavity air configurations. In general, the flame location is similar, but the overall cavity temperature appears to be slightly lower for the 22% cavity air configuration.

Pollutant Emissions

Atmospheric pollution is a problem that encompasses the military and civil-aviation business. International standards for pollutant emissions from civil aircraft are currently set by the International Civil Aviation Organization (ICAO). Civil and military aircraft engines will undoubtedly come under greater scrutiny in the future as more stringent emissions standards are set and regulated. Aside from having to meet emissions standards, engines will also have to provide operation that is more efficient and direct operating costs that are lower than current designs. To meet these future requirements, turbine engines are being developed that are low in gaseous pollutants, but that also have improved operability and durability over current engines. The goal is to develop the technology to readiness level that allows a smooth transition to production engines.

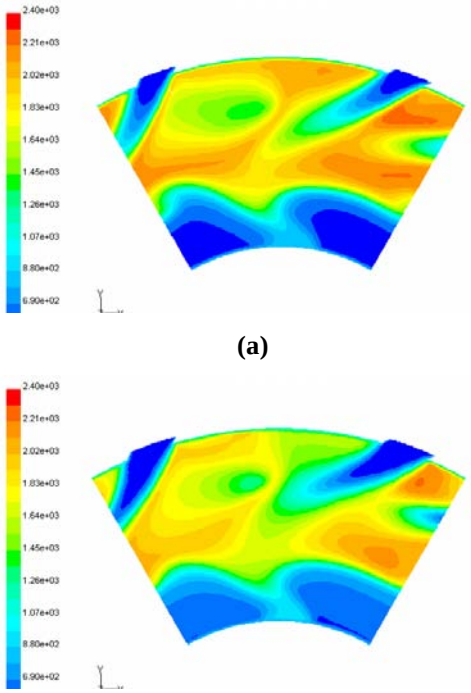

(a)

(b)

Figure 6: Temperature Calculations (°K) Along a Combustor Cross-Section in-Line with Cavity Air Jets for (a) 16% Air and (b) 22% Air Configurations.

Atmospheric Pressure Test Results

Three configurations at various flow splits between the cavity and the main air stream were investigated in the atmospheric pressure test facility. Figure 7 shows Emissions Index of unburned hydrocarbons (UHC) as a function of cavity equivalence ratio. As expected, the UHC EI increases steadily as the ϕ_{cav} increases from 0.8 to 2.0. With only 16% total airflow to the cavity, however, UHC emissions were considerably higher. With 22% cavity air, the UHC emissions were following similar trends compared to the 16% case, but they were an order of magnitude less than the baseline configuration, indicating the superior performance of the 22% case compared to the baseline configuration. Also shown in the figure is UHC EI for a well-stirred reactor (WSR) operating at atmospheric pressure and premixed, pre-vaporized JP-8 fuel. As expected, the UHC EI emissions decrease with increasing equivalence ratio. A minimum value will be reached at equivalence ratios slightly below stoichiometric. UHC

emissions will again increase as the equivalence ratio increases due to lack of oxygen (not shown in the figure).

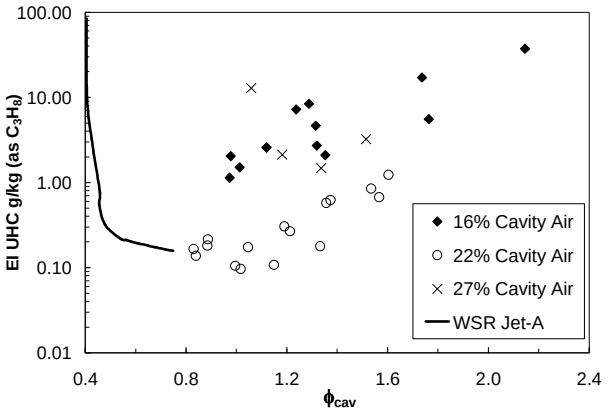

Figure 7: Total Hydrocarbon Emissions Index as a Function of Cavity Equivalence Ratio.

In a similar fashion, CO EI was plotted against cavity equivalence ratio for the three combustor designs in Fig. 8. Also shown is WSR emissions data burning JP-8 fuel from Zelina[9]. The 22% cavity air case had the lowest CO emissions of the three configurations tested. The CO emissions reach a minimum at ϕ_{cav} = 1.3 for each configuration. Of interest, however, is the typical CO vs. ϕ curves that indicate a minimum CO at ϕ = 0.8 for premixed, pre-vaporized systems.

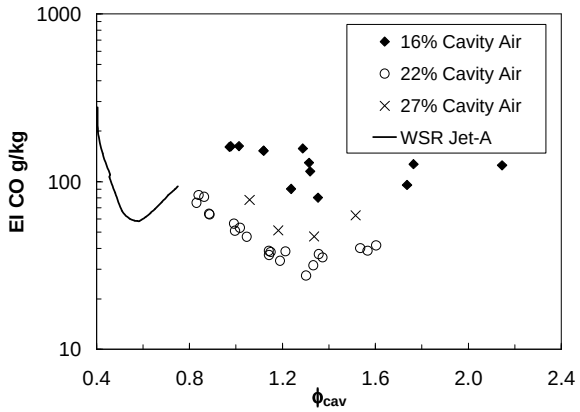

Figure 8: Carbon Monoxide (CO) Emissions Index as a Function of Cavity Equivalence Ratio.

Although these experiments were conducted at near-atmospheric conditions where NOx emissions are low, these emissions data were collected to compare the performance of the three configurations. Fig. 9 shows the NOx EI vs. ϕ_{cav} for the three design conditions along with WSR data for JP-8 combustion. The 16% cavity air case produced the highest NOx emissions over the range of equivalence ratios while the 27% cavity air case produced the lowest NOx emissions. For premixed systems, the greatest NOx emissions would occur slightly below stoichiometric, where temperature is high and oxygen is available to form NOx. As seen in Fig. 9, the WSR data shows a rapid increase in NOx, with ϕ, but tend to be more peaked than a spray combustion system due to the unmixedness effects.

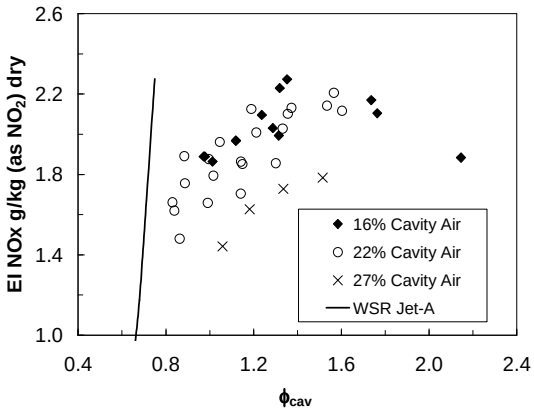

Figure 9: NOx Emissions Index as a Function of Cavity Equivalence Ratio.

The NOx, CO, and UHC data all suggest that the burning is taking place in the high shear layer between the cavity and main airflow, or that there is entrainment into the cavity from the main air stream. Recently, Sturgess and Hsu[10] found that as much as 40% of the mainstream air can be entrained into the cavity for a TVC-type design. The entrainment was a function of cavity-to-main momentum ratio and cavity geometry. Although the swirl direction of the cavity air is considerably different for the TVC compared to the UCC, the TVC data suggests that for the UCC design, there is positive entrainment of main air into the cavity. The emissions data would indicate 20-30% entrainment, which would shift the emissions vs. ϕ_{cav} curves to expected values. This entrainment value corresponds well with Sturgess and Hsu[10] experimental results. Further tests will be conducted with the UCC design to estimate the air entrainment into the cavity.

Figure 10 shows NOx emissions as a function of ϕ_{cav}. As seen, increasing the pressure drop in the cavity reduces NOx emissions since the mixing is enhanced. Also seen, as the mixing improves (dP/P increases) the NOx emissions tend to peak at ϕ_{cav} ~ 1.0, similar to a WSR. As the pressure drop is reduced, the mixing intensity is reduced and the NOx emissions peak at more fuel rich conditions.

EI NOx is also plotted as a function of cavity residence time at different pressure drops as seen in Fig. 11. Along lines of constant ϕ_{cav} the NOx emissions steadily rise with residence time at a rate of $\tau^{1/2}$. Also, higher NOx emissions are formed as ϕ_{cav} increases from 0.85 to 1.3, then the NOx emissions decrease with

increasing equivalence ratio in the cavity. The plot highlights the complex nature that equivalence ratio, residence time, and pressure drop have on NOx emissions production.

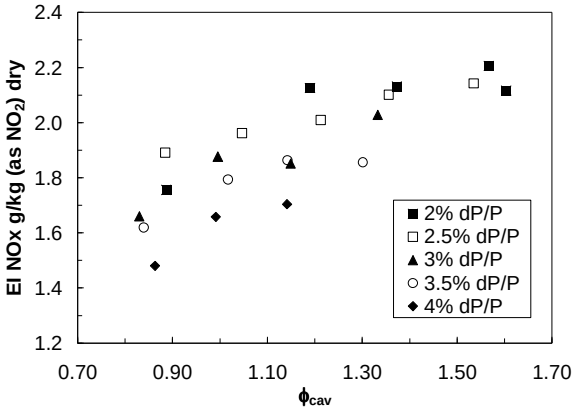

Figure 10: NOx Emissions Index as a Function of Cavity Equivalence Ratio.

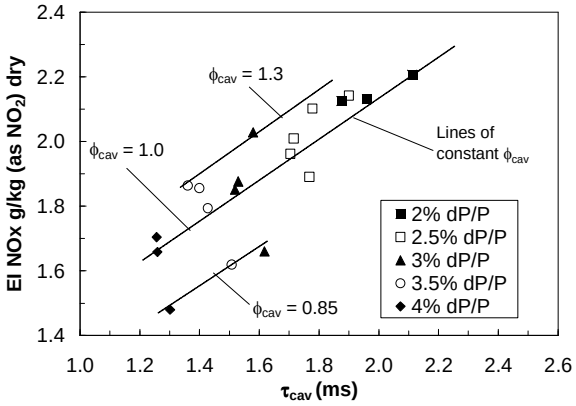

Figure 11: NOx Emissions Index as a Function of Cavity Residence Time at Different Pressure Drop Conditions.

Finally, emission maps in Fig. 12 show the relation between CO and NO_x in a way that distinguishes between design advances in emissions reduction technology and mere emissions compromises. As seen in Fig. 12, moving to the lower left of the graph would indicate superior emissions performance, while designs reaching the upper right corner would show poor combustor designs. Based on the current data at atmospheric conditions, increasing cavity air tends to reduce NOx emissions *and* reduce CO emissions. In conventional systems, trades usually exist between CO and NOx, where minimizing one species causes an increase in the other. The UCC design shows that both emissions can be minimized. This is believed to be due to the enhanced reaction rates of hydrocarbon fuels, especially the CO = CO_2 reaction by the high –g loaded nature of the design. Further experiments will be conducted at both atmospheric and high pressure to verify this trend.

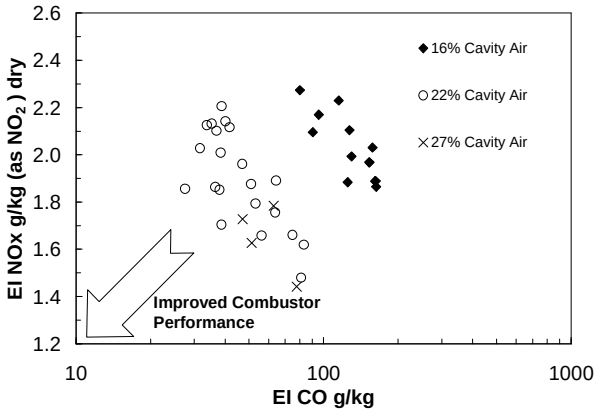

Figure 12: Emissions Maps of Three Combustor Designs.

Heat Release Rate

Cavity space heating rate (HRR) was calculated for the 22% cavity air configuration and plotted as a function of the cavity temperature rise and cavity pressure drop, as seen in Fig. 13. As expected, as the temperature rise increases in the cavity, the heat release rate increases. Interestingly, the HRR is also a strong function of the pressure drop. The data suggests that for a given HRR in the cavity, the cavity volume can be reduced while still maintaining a constant temperature rise if the pressure drop is increased. The HRR for the cavity is 20-40 MBtu/atm-ft^3. Also plotted are data from two gas turbine engine manufacturers, estimating the primary zone space heating rate. Both combustion systems, from Company A and Company B, required a much higher primary zone temperature rise to reach the level of space heating rate of the UCC cavity. In general, the UCC operates at higher space heating rates compared to conventional gas turbine combustor primary zones.

Flame Length

Minimizing the combustor flame length by increasing reaction rates is essential in the design of an ultra-compact combustor. High performance gas turbine combustor volume has decreased and overall fuel-to-air ratio (OFAR) has increased. This high OFAR translates to higher combustion zone temperatures which result in shorter chemical residence times. However, some of the heat release in these systems occurs in the turbine components, leading to durability issues. Therefore, a combustion system that utilizes the acceleration of reaction rates via high g-loading is attractive.

Figure 14 shows photographs of the UCC in operation with JP-8+100 fuel. As seen, the combustion

zone only occupies the cavity and a short volume downstream of the cavity. Estimations are that the flame extends about 25 mm downstream of the cavity. The UCC flame length is only 50-70% of the conventional swirl-stabilized combustors, which can lead to shorter gas turbine engines, saving cost and weight.

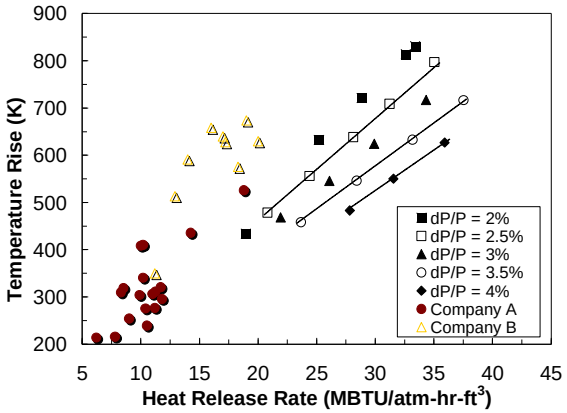

Figure 13: Cavity Heat Release Rate as a Function of Cavity Temperature Rise.

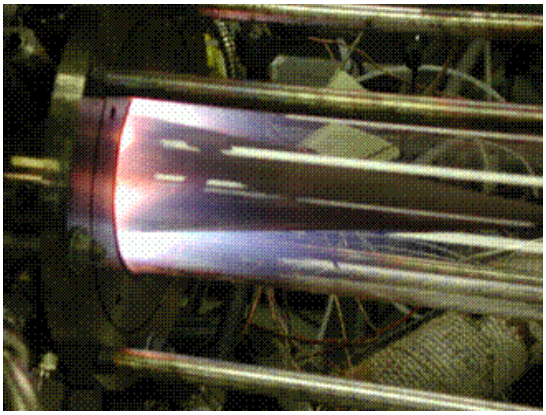

Figure 14: Photograph of the UCC Showing the Short, Compact Flame Even at High Equivalence Ratio.

Combustion Efficiency

Combustion efficiency is an important parameter to track in combustion system design since it represents the fuel burn of the engine. Figure 15 shows the combustion efficiency as a function of cavity residence time τ cav, where;

$$\tau_{cav} = \left(\frac{\rho V}{\dot{m}_f + \dot{m}_a} \right) \qquad \text{Eq. 2}$$

As shown, the 16% airflow case shows an efficiency peak at 2-3 ms residence time. This long residence time was not possible with the increased cavity airflow since the pressure drop would be well below 1%. However, combustor efficiency was greatest for the higher airflow, indicating enhanced reaction rates due to high g-loading.

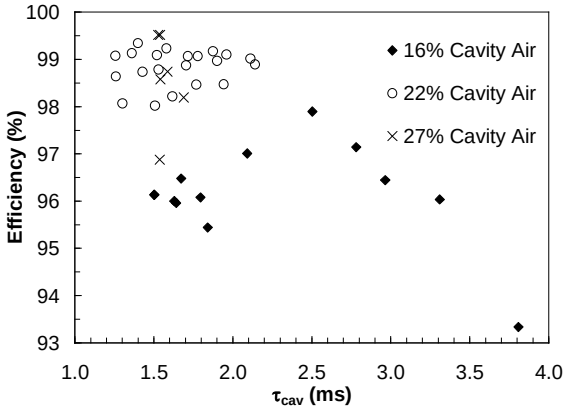

Figure 15: Combustion Efficiency as a Function of Cavity Residence Time for Three Combustor Designs.

Estimations based on CFD calculations were made for the circumferential velocity in the cavity to estimate the g-loading in this region. Based on the calculations, the g-loading increased from 1600 g's for the 16% cavity case, to 2300 g's for the 22% cavity air case. Based on earlier results from Lewis[4] the increased g-loading resulted in a 50% increase in flame speed which translates to accelerated reaction rates of the same magnitude. Using the estimated g-loading, the combustor efficiency was plotted as a function of cavity loading (LP) where,

$$LP = \frac{\dot{m}_f + \dot{m}_a}{V P^n F} \text{ (lbm/s)/(ft}^3\text{atm}^n\text{)} \qquad \text{Eq. 3}$$

where,

$$F = \frac{10^{\frac{T_3}{700}}}{3.72} \qquad \text{Eq. 4}$$

and , n=2ϕ for ϕ < 1.0 and n = 2.0 for ϕ > 1.0. This definitions of LP is described elsewhere (Sturgess and Hsu[11]). The results are shown in Fig. 16. Also included in the plot is efficiency data the Rolls Royce vaporizer combustor[12]. The plot includes UCC data for the three designs at constant ϕ_{cav}. It was expected that, at constant ϕ_{cav}, the curves would collapse independent of cavity airflow., but instead, the results indicates that efficiency increases as the cavity air flow increases from 16% to 27% at a constant cavity loading. Trends with loading are

similar to vaporizer systems, where increasing cavity loading results in a decrease in combustion efficiency.

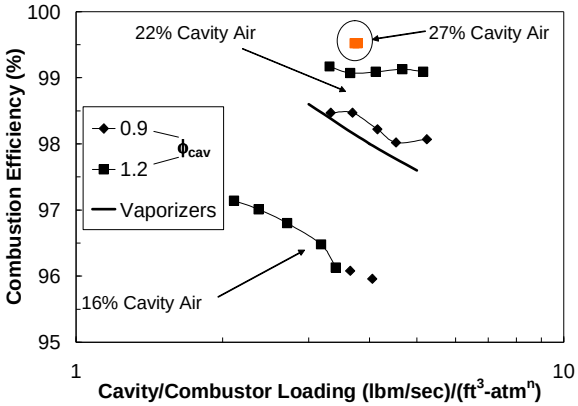

Figure 16: Combustion Efficiency as a Function of Cavity Loading at Different g-loadings and Cavity Equivalence Ratios.

This finding leads to the hypothesis that the cavity g-loading could indeed be improving either the mixing or the reaction rates as we had hoped. This, in turn, leads to higher efficiencies. The level of efficiency from the UCC straddles the performance achieved by Rolls Royce vaporizer combustors. When it is realized that the Rolls Royce vaporizer data are for complete and fully-developed combustors, the performance of the cavity (primary zone) is seen in context.

Investigation of cavity pressure drop, as it relates to combustion efficiency, was conducted during the 22% cavity air test series. As seen in Fig. 17, the efficiency is not strongly affected by the pressure drop, but rather ϕ_{cav}. Surprisingly, the combustion efficiency is well over 98% for all test conditions despite the fact that these were atmospheric-pressure tests and the rig only simulates the combustor primary zone.

Combustion Stability

While reducing pollutant emissions, advanced combustors must maintain or improve operability including enhancements to lean blowout and ignition. Fig. 18 shows a lean blowout stability loop for the 22% cavity air configuration. It can be seen that as the loading is reduced in the combustor, the blowout limits of the combustor are expanded. This behavior is similar to conventional combustor designs. Also shown is a loading limit in the combustor which is a value of LP = 5.0, again, similar to conventional combustor designs. The loading values correspond to roughly a dP/P = 2 to 4%. Plotted along with the UCC data is the WSR loading curve burning propane-air mixtures from Zelina and Ballal[13,14], a practical swirl stabilized conventional combustor in service, and the experimental results from the TVC of Sturgess and Hsu[11] for cavity-contained blowout limits. The UCC data suggests that the cavity is more well-mixed compared to the practical system and even the TVC, since the UCC curve falls closer to the WSR line. Further tests will be conducted with additional configurations to improve the peak heat release rate in the cavity.

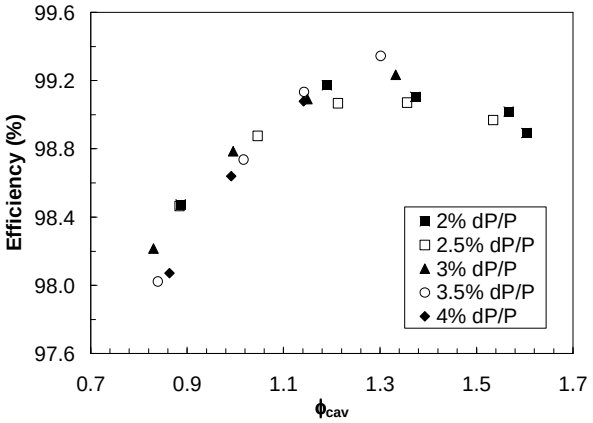

Figure 17: Combustion Efficiency as a Function of Cavity Equivalence Ratio at Various Combustor Pressure Drop.

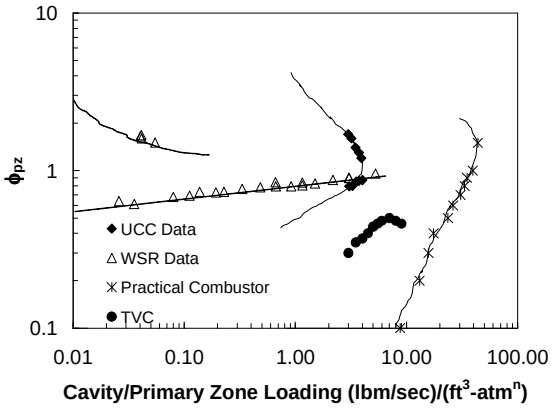

Figure 18: Stability Loop for 22% Cavity Air Configuration.

Conclusions

A high g-loaded combustion system has been successfully tested in an atmospheric pressure rig. The preliminary results indicate that this type of combustion system has the potential to be used as part of an ultra-compact combustor (UCC) for a main burner, or an inter-turbine burner (ITB) for use as a reheat cycle engine. Key features of the combustion system include:

1. High combustion efficiencies (99+%) over a wide operating range.

2. Short flame lengths (50%) compared to conventional combustor designs.

3. High heat release rate compared to conventional combustor designs by a factor of 2.

4. Improved fuel-air mixing as indicated by the stability curve approaching a WSR stability curve.

5. Emissions maps indicate that increasing cavity loading improves CO and NOx emission performance.

6. Stable, efficient operation at relatively low pressure drop (2%).

7. Increased g-loading resulted in improved combustion efficiencies.

CFD tools were used successfully to determine test matrix designs. The test data was then used to tune the CFD models to improve predictive capability. The tuned CFD tools will be used in further analysis to improve the combustor design. Further configurations, including angled fuel injection and airblast-type fuel injectors will be tested as part of the follow-on combustor research and development program.

Acknowledgements

The authors would like to thank Mr. Dwight Fox and Mr. Glenn Boggs for their assistance in fabrication, assembly and test of the combustion rigs. The authors are grateful for the preliminary design and testing of the UCC concept conducted by Capt. Ralph Anthenien. This work is supported by Air Force Office of Scientific Research (AFOSR) with Dr. Julian Tishkoff serving as Program Manager.

References:

1. Sirignano, W.A., Delplanque, J.P., and Liu, F., "Selected Challenges in Jet and Rocket Engine Combustion Research," *33rd AIAA/ASME/SAE/ASEE Joint Propulsion Conference*, Seattle, WA AIAA-97-2701 (1997).

2. Sirignano, W.A., and Liu, F., "Performance Increases for Gas-Turbine Engines Through Combustion Inside the Turbine," *Journal of Propulsion and Power*, **15**:1 pp.111-118 (1999).

3. Liu, F., and Sirignano, W.A., "Turbojet and Turbofan Engine Performance Increases Through Turbine Burners," *38th Aerospace Sciences Meeting & Exhibit*, Reno, NV, AIAA-2000-0741.

4. Lewis, G.D., "Centrifugal-Force Effects on Combustion," *14th Symposium (International) on Combustion*, The Combustion Institute, pp.413-419, 1973.

5. Yonezawa, Y., Toh, H., Goto, S., and Obata, M., "Development of the Jet-Swirl High Loading Combustor," *26th AIAA/SAE/ASME/ASEE Joint Propulsion Conference*, Orlando, FL, AIAA-90-2451, 1990.

6. Anthenien, R. A., Mantz, R. A., Roquemore, W. M., and Sturgess, G. J., "Experimental Results for a Novel, High Swirl, Ultra Compact Combustor for Gas Turbine Engines," Presented at the Western States Section Combustion Institute Meeting, Berkeley, CA, April, 2001.

7. He, G., Guo, Y., Hsu, A. T., Brankovic, A., Syed, S., and Liu, N-S, "The Effect of Schmidt Number on Turbulent Scalar Mixing in a Jet-in-Crossflow," *ASME 99-GT-137*.

8. Roquemore, W. M., Shouse, D. T., Burrus, D., Johnson, A., Cooper, C., Duncan, B, Hsu, K-Y., Katta, V. R., Sturgess, G. J., and Vihinen, I., "Trapped Vortex Combustor Concept for Gas Turbine Engines," *AIAA 2001-0483*.

9. Zelina, J., "Combustion Studies in a Well-Stirred Reactor," Ph.D. Thesis, *University of Dayton, Dayton, OH 1995*.

10. Sturgess, G. J., and Hsu, K-Y, "Entrainment of Mainstream Flow in a Trapped-Vortex Combustor," *AIAA 97-0261*.

11. Sturgess, G. J. and Hsu, K. – Y, "Combustion Characteristics of a Trapped Vortex Combustor," RTO Meeting Proceedings 14 of Gas Turbine Combustion, Emissions and Alternative Fuels, Applied Vehicle Technology Panel (AVI) Symposium, Lisbon, Portugal, pp. 44.1- 44.13, 1998.

12. Parnell, E. C., and Williams, M. R., "A Survey of Annular Vaporizing Combustion Chambers," Cranfield Intl. Symposium Series, Vol. II, Combustion and Heat Transfer in Gas Turbine Systems, Pergamon Press, 1971, pp. 91-104.

13. Zelina, J. and Ballal, D. R., "Combustor Stability and Emissions Research Using a Well-Stirred Reactor," *ASME IGTI 95-GT-109*.

14. Ballal, D. R., and Zelina, J., "Assessment of Gas Turbine Combustor Performance and Emissions Using a Well-Stirred Reactor," *ISABE-2001-1065*.

(c)2001 American Institute of Aeronautics & Astronautics or Published with Permission of Author(s) and/or Author(s)' Sponsoring Organization.

A01-16361

AIAA 2001-0483
Trapped Vortex Combustor Concept for Gas Turbine Engines

W.M. Roquemore, Dale Shouse, Dave Burrus*,Art Johnson*,
Clayton Cooper*, Beverly Duncan*, K.-Y. Hsu**,
V.R. Katta**, G. J. Sturgess**, and Illari Vihinen***
Air Force Research Laboratory, Propulsion Directorate
Wright-Patterson AFB, OH 45433
*General Electric Aircraft Engines, Cincinnati OH
**Innovative Scientific Solutions, Inc., Dayton OH
***General Electric Industrial Products, Hartford CT

39th AIAA Aerospace Sciences Meeting & Exhibit
8-11 January 2001 / Reno, NV

For permission to copy or republish, contact the American Institute of Aeronautics and Astronautics
1801 Alexander Bell Drive, Suite 500, Reston, VA 20191

(c)2001 American Institute of Aeronautics & Astronautics or Published with Permission of Author(s) and/or Author(s)' Sponsoring Organization.

AIAA 2001-0483

TRAPPED VORTEX COMBUSTOR CONCEPT FOR GAS TURBINE ENGINES

W. M. Roquemore[1], Dale Shouse[2], Dave Burrus[3], Art Johnson[4], Clayton Cooper[4], Beverly Duncan [5], K.-Y. Hsu[6], V. R. Katta[6], G. J. Sturgess[7], and Illari Vihinen[8]
Air Force Research Laboratory
AFRL/PRSC
1790 Loop Road North, Bldg 490
WPAFB OH 45433-7103
937-255-6813
melr@ward.appl.wpafb.af.mil

ABSTRACT

This paper presents an overview of the development and evaluation of a trapped vortex combustor (TVC) concept for low-emissions, high-performance gas turbine combustors. The TVC concept was first evaluated in an Air Force Office of Scientific Research program in 1993. Since then, it has evolved from a fundamental study to a development/evaluation program involving sector-rig experiments at realistic operating conditions. Its development is motivated, in part, by concerns about NOx emissions generated by gas turbine engines used for aircraft and stationary power. TVC offers the potential of a simple, compact, and less-expensive low-emissions combustor. It departs from the traditional swirl stabilized designs used in gas turbine engines for the past 40 years. It has two parts, a pilot combustor for stability and a main combustor for power. The pilot utilizes cavities to establish the recirculation zones needed for stable combustion. Each cavity is sized to provide a stable recirculation zone that is referred to as a "trapped vortex". Fuel and air are injected into the cavities in a way that reinforces the vortex that is naturally formed in the cavities. The following characteristics of a TVC have been demonstrated at realistic condition: 1) up to a 50% improvement in ignition, blow out, and altitude re-light over current-technology (conventional swirl stabilized combustors); 2) NOx emissions reduction ranging from 40% to 60% of the 1996 ICAO standard; and (3) an operating range that is 40% wider than conventional combustors with a combustion efficiency at or above 99%.

INTRODUCTION

Combustion stability is often achieved through the use of recirculation zones to provide continuous sources of ignition by mixing hot products with the incoming fuel and air. Swirl vanes, bluff-bodies, and rearward-facing steps are commonly used to establish recirculation zones for flame stabilization. The literature base that has been established on these techniques is sizable as can be noted in any textbook on combustion.[1]

A TVC employs cavities to stabilize the flame. Flow over cavities has been studied for many years, as evident from the large volume of literature on this subject.[2,3,4] Much of this effort has concerned understanding and controlling oscillations established by cavities. The motivation for this work is the result of practical concerns about oscillations that can occur in wheel wells, bomb bays, and other external cavity structures on aircraft. Cavities have also been studied as a means of cooling and reducing drag on projectiles.[5] A large body of literature is associated with the use of cavities to stabilize flames in scramjets.[6] Cavity burners have also been investigated for purposes of waste destruction.[7]

1. Senior Scientist, Fellow, AIAA
2. Project Engineer, Member, AIAA
3. Manager of Adv. Military Technology, GE Aircraft Engines, Non member
4. Engineer, GE Aircraft Engines, Nonmembers
5. TVC Team Leader, GE Aircraft Engines, Member, AIAA
6. Senior Scientists, ISSI, Inc. Associate Member, AIAA
7. Vice President, ISSI, Inc. Associate Fellow, AIAA
8. Engineer, GE Industrial Products, Member, AIAA

(c)2001 American Institute of Aeronautics & Astronautics or Published with Permission of Author(s) and/or Author(s)' Sponsoring Organization.

However, very few studies have been performed on cavity flameholders for subsonic flows where both fuel and air are injected into the cavity. This paper presents an overview of important results that have been obtained during the past eight years on a program designed to develop and evaluate the TVC concept for gas turbine engine applications.

TRAPPED VORTEX CONCEPT

Before outlining the features of a TVC, it is useful to briefly describe essential features of a typical gas turbine combustor. The generic swirl-stabilized combustor shown in Fig. 1(a) has a primary recirculation zone that is established by swirlers located around the fuel injector. This zone transports some of the hot combustion products back towards the combustor face and ignites the incoming fuel and air as they are mixed in the combustion chamber, thus providing a continuously lit, stable flame. The recirculation zones in the forward corners of the combustor also provide combustion stability. If the velocity of the air entering the combustion chamber is excessive, the primary recirculation zone becomes unstable, resulting in poor flame stability and low combustion efficiency. An unstable primary zone is avoided by the use of a diffuser to slow down the combustor inlet air. Air injected into the combustion chamber through the liner air jets is used to establish the length of the primary zone, and also used to mix and shape the temperature profile of the exhaust gases as they enter the turbine vanes. Although most aircraft and power-generation gas turbine combustors function in this way, many different combustor designs exist because of the need to satisfy specific aircraft-mission or power-generation objectives.

The similarities and significant differences between a TVC and a conventional combustor will now be discussed. The TVC shown in Fig. 1(b) is a staged combustion system with a trapped vortex pilot and a main combustor. The pilot employs a cavity to provide a stable recirculation zone. The cavity is sized so that it has a stable recirculation zone over a wide range of main airflow conditions. This can be accomplished with a relatively low-pressure drop across the combustor. The primary fuel and air are injected directly into the cavities such that the vortex is reinforced. Because the pilot flame is shielded from the main flow by the cavities, stable combustion can be achieved, even when the main air velocities are high.

In the annular version of the TVC depicted in Fig. 1(b), the diffuser consists of one or more circumferentially distributed splitter plates that direct the main air through different passages in the diffuser. The main fuel nozzles are located near the exit of the diffuser. The inlet to the main combustion chamber is a flat surface that is in the same plane as the front face of the cavities. The combustor inlet plane consists of passages where the fuel and air enter the main combustion chamber and a matrix of radial and circumferential struts. The struts act as conduits for transporting hot products out of the cavities. Ignition of the main combustor is achieved as the main fuel and air mix with the hot products from the pilot. The recirculation zones behind the struts serve as flameholders that are similar to those used in afterburners. The rapid mixing in the wakes behind the struts promote rapid combustion. The struts also distribute the exit gases such that an acceptable radial profile and pattern-factor can be achieved without using liner jets.

The TVC is a simple design that has the potential to provide high performance and low emissions. Because of the stable recirculation zones in the cavities, one should expect a TVC to have low lean-blow-out (LBO) limits and good altitude relight capabilities. Also, if rapid mixing can be achieved in the cavities, a TVC should have high combustion efficiencies over a wide operating range. Low NOx should also result from the rapid mixing between the fuel and air in the cavities and the main. Low NOx emissions can also be achieved by operating a TVC as a staged system with lean or premixed combustion. If a TVC could be operated at high inlet velocities, low thermal NOx could be achieved as a result of the reduced residence time. A TVC can also be operated as a rich-burn quick-quench lean-burn (RQL) combustor with the cavities providing the rich-burn mode and the rapid mixing with the main air (no main fuel) providing the quick-quench lean-burn modes. Thus, several strategies can be employed to reduce NOx emissions in a TVC. Whether these strategies can be implemented in a TVC designed is a question that will be addressed in this overview.

(c)2001 American Institute of Aeronautics & Astronautics or Published with Permission of Author(s) and/or Author(s)' Sponsoring Organization.

FIRST GENERATION TVC

The TVC discussed here was conceived and evaluated on an Air Force Office of Scientific Research (AFOSR) program with the Aerospace Sciences Division. In the first attempts to evaluate the TVC concept, an axisymmetric configuration similar to that in Fig. 1(b) was used accept that only an outer cavity and no diffuser or struts were employed. Stable combustion could not be obtained with this configuration because the cavities were too large. It became evident that a configuration was needed where the cavity size could be changed as one observed the flame. This was achieved in what we call the first generation TVC, shown in Fig. 2. The cavity is formed between the two disks in tandem. The length of the cavities could be easily changed by sliding the tube attached to the cavity back face in or out. Propane fuel and air are injected separately through a showerhead arrangement from the back face of the cavity, as shown in Fig. 2(a). Washers are used to change the diameter of the after disk. It was found by trial an error that stable combustion is achieved with a cavity length of $0.59D_o$ and an afterdisk diameter of 0.73 D_o where Do is the diameter for the forward disk. After achieving the proper cavity size, stable flames like those in Figure 2(b) were obtained. Visual observations confirm that a stable flame is achieved when a vortex appears to be trapped in the cavity.[8,9]

After determining the proper size of the cavity in the first generation TVC, we became aware[10] of the work of Mair[11] and Little and Whipkey[12] who investigated the rules for sizing cavities to reduce the drag of bluff-bodies in nonreacting flows. They studied cavities formed between two axisymmetric disks spaced along a central spindle, similar to those illustrated in Fig 3. Mair showed that for a ratio of afterbody-to-forebody disk diameters less than 1, an optimal separation distance existed where the drag was a minimum. Furthermore, the minimum drag was considerably lower than that of the forebody disk alone. Mair also found that for a given afterbody diameter, separation distances existed where the drag increased dramatically above that of the forebody alone. Little and Whipkey showed that the minimum drag corresponds to the condition where the recirculation zone is stable.

Katta and Roquemore[13] used a time-dependent, axisymmetric mathematical model to predict the results of Mair and Little and Whipkey and the combusting results of the first generation TVC. The results of nonreacting flow calculations for cavities of three different sizes are shown in Fig. 3. The top half of the figures contains the velocity vector plots, with color indicating the magnitude of the velocities. The lower half shows how fluid particles released in the boundary layer of the forward disk are entrained into the cavity.

In Fig. 3(a) the cavity is undersized and the drag is relatively large because shedding from the afterdisk. In Fig. 3(b), a stable vortex is formed in the cavity and in the near-wake region of the afterdisk, and the drag is a minimum. Also, very little fluid is entrained into the cavity. It is also noted that when the vortex is trapped in the cavity, the stagnation point is located at the downstream corner of the cavity. This observation is similar to that of Gharib and Roshko.[14] When the cavity is too large, the vortex in the cavity is unsteady and the drag is large.

Mair and Little and Whipkey established the conditions for minimum drag using a correlation between the disk separation distance and the afterbody disk diameter, both being normalized by the forebody disk diameter. A vortex is trapped in a cavity that is sized for minimum drag. Katta and Roquemore obtained the same correlation from the simulation results. These correlations are shown (see Fig. 4). An average of these correlations can be approximated by (1).

$$(1)\quad L/Do = -(1.62)D_1/D_0 + 1.79$$

When this equation is applied to the first generation TVC, L/Do is estimated to be 0.60. In the combusting flow experiments, an L/D_0 of 0.59 was obtained. Thus, it appears that a cavity sized for minimum drag for nonreacting flows also gives the optimum size for good combustion stability in a reacting flow. Indeed, the first generation TVC had LBO limits considerably below those of convention combustors and could operate stably over a wide range of inlet air velocities and fuel to air ratios. Other results obtained with the first generation TVC can be found in Refs. 15-19. The first generation TVC demonstrate the fundamental idea of trapping a vortex in a cavity to achieve a stable flame.

(c)2001 American Institute of Aeronautics & Astronautics or Published with Permission of Author(s) and/or Author(s)' Sponsoring Organization.

SECOND GENERATION TVC

Once we had demonstrated that a stable flame could be achieved with a properly sized cavity, we returned to a configuration with the cavities on the outside. The second generation TVC, shown in Fig. 5, is an axisymmetric can-type configuration, with a cavity surrounding the main burner. The depth of the cavity is about the same as that for the optimum first generation TVC. The depth of the forward wall is 29.8 mm and that of the back wall is 21.5 mm. The length of the cavity is 50.5 mm somewhat longer than of the first generation TVC. A quartz, 152.4mm diameter tube is used as the outer circumferential wall of the cavity. The struts result in a 50% blockage of the inlet area to the main combustor.

Gaseous propane and air are injected from the back face of the cavity, as indicated in Fig. 5(b). Four air jets surround each fuel jet. The cavity airflow could be controlled and metered independently of the main airflow.

The two radial struts shown in the end-view of Fig. 5c are used to transport the hot products out of the cavy. The circumferential struts or splitters promote mixing, ignition, flameholding, and distribution of the heat for the main burner. The main fuel and air are premixed upstream of the burner entrance.

Figure 6 shows side- and end-view images of the flame in the second generation TVC. The combustor is operating at overall stoichiometric condition. The inlet air temperature is 558K, the inlet pressure is slightly above atmospheric. The inlet airflow rate is 7 kg/min, with a velocity of 70 m/s at the entrance to the combustion chamber. The primary airflow rate is 0.57 kg/min. The glow from the flame in the cavity is evident in Fig. 6(a). The flame length is approximately 60 cm, which is surprisingly short considering the low operating pressure.

A single stable vortex can be observed through the cavity window. This vortex is not dramatically affected by the main airflow rate. The TVC has operated at main air inlet velocities as high as 150 m/s (maximum achievable in the facility) without disruption of the pilot flame. The vortex appeared to be more stable with the higher inlet velocities. However, the most impressive aspect of the second generation TVC is its large dynamic operating range. The overall equivalence ratio could be rapidly changed from 1 to 0.05 and then back to 1 by turning the main fuel on and off while leaving the pilot on. The rapid ignition of the main is thought to be due to the effectiveness of the struts in mixing hot products from the cavity with the main fuel and air.

The image in Fig. 6(b) is an end view of the flame. It is taken from a video and the quality is not good. The dark cross pattern illustrates the location of the radial struts. The four bright bands are flames that have been distributed by the circumferential struts. No hot spots are evident in the actual video, indicating that the struts were effective in uniformly distributing the reaction products.

The LBO results for the second generation TVC are shown in Fig. 7(a). Only the cavity is fueled. The primary airflow rate is fixed at 0.45 kg/min. The LBO experiments are conducted by establishing a flame in the cavity with a fixed main airflow rate. The fuel flow rate is slowly reduced until the visible flame in the cavity is extinguished. This process is repeated at a different main airflow rate. The second generation TVC exhibited LBO limits significantly below those of an advanced combustor that used swirl to stabilize the flame. Both the advanced and TVC combustors are operated at atmospheric pressure. The inlet air temperature is varied, as noted in the figure. The LBO limits of the TVC are independent of the main airflow rate. This characteristic was observed for the first generation TVC.

Figure 7(b) compares the combustion efficiency of the second generation TVC, an advanced combustor, and a current combustor as a function of total fuel flow. The inlet pressure is atmospheric. The average value of the primary equivalence ratio in the TVC is 1.0, as calculated from the measured fuel and airflow rates. The second generation TVC operated efficiently over a much wider range of fuel loadings than the current and advanced combustors. It is thought that the struts make a significant contribution to the wide operation limits of the TVC. It should also be pointed out that the pressure drop across the different combustor systems was approximately (4%) even though the airflow rate for the second generation TVC was considerably larger than that for the other two combustors.

In summary, the second generation TVC exhibited excellent LBO capabilities and efficient operation over a

(c)2001 American Institute of Aeronautics & Astronautics or Published with Permission of Author(s) and/or Author(s)' Sponsoring Organization.

wide dynamic range. This was accomplished without encountering combustion instabilities. However, the experiments were conducted with a can-type combustor that burned gaseous fuel at atmospheric pressure. The next step was to develop an annular-type TVC combustor burning liquid fuel.

THIRD GENERATION TVC

Injection of liquid fuel into the cavity in a way that can be easily implemented in practice is a challenge. Since the main fuel would be injected near the main combustor inlet, the number of penetrations through the high-pressure case should be kept to a minimum, and the plumbing should be as simple as possible, it seemed advantageous to inject the liquid fuel from the front face of the cavity. Thus, the challenge is to determine where in the cavity to locate the fuel nozzles and primary combustion air jets.

The third generation TVC shown in Fig. 8 is a two-dimensional sector designed for easy replacement and optical viewing of the cavities. The air for the cavities is plenum fed from square tubing with sealed ends. The cavities result from proper placement of the square tubes. This design allowed easy fabrication of cavities with different patterns of air jets and pressure atomizer fuel nozzles. Illustrations of the air- and fuel-injection sites are shown in Fig. 8(a). Vertical struts are used to transport the combustion products out of the cavities, and a splitter plate is employed in the diffuser to separate the incoming air into two channels. The faces of the struts and splitter plate provide bluff-body surfaces that aid in mixing and igniting the hot products transported from the cavities with the premixed fuel and air of the main combustor. They also serve as flame holders for the main combustor and have a blockage of 50%. A photograph of the partly assembled third generation TVC sector is shown in Fig. 8(b) and the operation of this TVC is shown in Fig. 8(c). The air supply for the cavities is separate from that of the main combustor and has its own controls. The main air and cavity air have separate air heaters that heat the airflow to 650K. All experiments were conducted at atmospheric pressure.

A detailed evaluation has been conducted of the third generation TVC, with the objective of determining the optimum location of air and fuel injection sites in the cavities. Nineteen cavity configurations with different air and fuel injection patterns have been evaluated. Visual inspection of the flame in the first combustors tested showed that a stable vortex could be formed in the cavities. Thus, very little effort has been devoted to investigating the impact of different cavity sizes and strut/main-burner designs on combustor performance. From the operation of the second generation TVC, it appeared that the most challenging design point would be the low power, idle condition, with high power conditions being relatively easy to achieve. Thus, the philosophy in designing the experiments with the third generation TVC was to find cavity designs that optimize the LBO and combustion efficiency near engine idle conditions, the assumption being that if a cavity design provides good low power performance, the high power conditions will be easy to achieve. This design philosophy has proven to be correct.

A design of experiments methodology was used in evaluating the 19 cavity designs. In all of the designs, the fuel is injected from the front face of the cavity. Ethanol fuel was used in the experiment because of its low heating value. JP-8 has also been used. Test run times with JP-8 are kept low because the combustor is uncooled, and considerable damage can result from the high heating value of JP-8.

The two cavity designs that exhibited the optimum overall performance are shown in Figs 9(a) and (b). A cooling approach for the back face and corners of the cavities was also evaluated; this scheme is illustrated in Fig. 9(c). The double vortex is generated by a line of air jets located deep on the front face of the cavity and near the center of the aft face of the cavity. A small vortex is also generated near the aft corner of the cavity. Locating the fuel deep in the cavity seems to be a critical requirement for good idle performance. If the fuel escapes from the cavity without burning it is readily quenched by the cool main, which leads to poor combustion efficiency. Thus, it is desirable to burn all of the fuel in the cavity before it is entrained into the main airflow. The single vortex design is shown in Fig. 9(b); the fuel injectors are located just above the centerline of the front face of the cavity. Small up or down variations in the location of fuel injectors can have a major impact on combustor performance.

(c)2001 American Institute of Aeronautics & Astronautics or Published with Permission of Author(s) and/or Author(s)' Sponsoring Organization.

Three vortices could be observed in the double vortex cavity design. The small vortex near the aft corner of the cavity results from an upward deflection of the back-face air jets. Part of the back-face air, along with some combustion products, is shed over the aft corner of the cavity. This in effect provides some cooling of the aft-corner cooling-nugget. A significant portion of the combustion products is transported along the faces of the struts. This provides a grid of flame that fills the face of the struts and splitter plate and readily ignites the main fuel and air. The main vortices in the double vortex and the single vortex configurations appeared to be "trapped" in the cavities for all operating conditions. No combustion instabilities have been observed from these two configurations. However, instabilities have been observed for several other configurations. Instabilities appear to be related to the location of the fuel nozzles.

Some results obtained with the third generation TVC are shown in Fig. 10. As shown in Fig. 10(a), the double vortex cavity design provided the lowest LBO limits. Indeed, all three TVC designs shown in Fig. 9 had LBO limits below those of conventional combustion system operating at the same conditions. The LBO limits are not strongly dependent on the Longwell loading parameter, which is defined as:

$$(2)\quad LP = W_{comb} / [\text{Volume} \times (P_3/14.7)1.75 \times e(T_3/540)]$$

W_{comb} is the combustor air mass flow rate (lbm/s); Volume is the volume of the combustor (cu-in); P_3 is the operating pressure (psia); and T_3 is the inlet air temperature (°R). In the experiments the main airflow rate was the key parameter varied. Thus, the LBO limits given in Fig. 10(a) are not very sensitive to the main airflow rate. This characteristic had been observed in the first and second generation TVCs.

The combustion efficiency is shown in Fig. 10(b). Again the double vortex design exhibited the highest combustion efficiency at the lowest overall equivalence ratio. The vertical line in the figure illustrates the overall LBO equivalence ratio for the double vortex cavity. The combustion efficiency of a conventional combustor operating at 1 atm pressure is also shown in the figure. Both TVC designs yielded considerably higher combustion efficiency than the conventional combustor. This is not a result of burning ethanol fuel since burning JP-8 fuel in the TVC yielded similar results. The combustion efficiency of the two TVC designs is almost as good as that of a conventional combustor operating at a pressure of 5 atm. General Electric Aircraft Engines tested a second generation TVC burning JP-8 fuel at 5 atmospheres pressure. Even though there were some fabrication errors, the combustor performed extremely well. The two data points obtained with the second generation TVC are shown in Fig. 10(b) and indicate that a TVC could have a wide operating range.

Some interest has been expressed by different organizations in evaluating the TVC concept for a number of applications. The data shown in Fig. 10(c) were obtained on a joint Air Force/Department of Energy (DoE) program. The DoE National Energy Technology Laboratory (DoE/NETL) is interested in reducing NOx production in power-generation gas turbine engines that burn low-Btu fuels. These fuels contain fuel-bound nitrogen (FBN) compounds such as ammonia. An RQL combustor approach is one possible way of preventing the FBN from becoming NOx. Experiments have been conducted with the third generation TVC to determine whether the TVC, operated in a RQL mode, could suppress some of the NOx produced from the FBN. These experiments have been conducted at atmospheric conditions, with ethanol fuel. Pyridine or butylamine have been used as am additives to simulate FBN compounds. The results did not change significantly with equivalence ratios greater than 1.0 or type of FBN compound. Data for cavity equivalence ratio of 1.5 and pyridine are shown in Figure 10(c). Experiments were conducted with one cavity fueled and two cavities fueled. With combustion in both cavities, only about 17% of FBN was converted to NOx. These results are encouraging since these are the first FBN experiments performed with a TVC. NETL has designed an RQL/TVC combustor for performing additional experiments at their Morgantown laboratory.

The experiments with the third generation TVC provided the information needed to design two high-pressure TVC sectors for evaluation of the TVC concept under realistic pressure and inlet air temperature conditions. A description of the next generation TVCs is presented in the next section.

(c)2001 American Institute of Aeronautics & Astronautics or Published with Permission of Author(s) and/or Author(s)' Sponsoring Organization.

HIGH PRESSURE TVC SECTORS

A double vortex and a single vortex cavity were designed for use in a 2D high-pressure sector rig located at Wright-Patterson Air Force Base. Also, a dual-passage and a tri-passage diffuser were designed for this sector rig. The cavity and diffuser components were designed to be interchangeable. Thus, four TVC configurations could be studied. For example, one high pressure TVC configuration includes a dual-passage diffuser and a double vortex cavity arrangement. This arrangement is illustrated in Fig. 11(a) and is referred to as the 2P-2V TVC. The diffuser is fabricated in ten sections. The ten sections are pinned together to construct the sector shown in Fig. 11(b). A photograph of one of the dual-passage diffuser sections is shown in Fig. 11(c). Each diffuser section has one-half of an air passage on each side. The face of the diffuser serves as struts for transporting hot products out of the cavities, bluff-bodies for enhance mixing, and as the main combustor flameholder. The main combustor and cavity pilots are fueled from nine spray bars. Each spray bar is placed in a grove that is machined into the diffuser component, as shown in Fig. 11(c). Each fuel spray bar has two separate fuel circuits, one for the main and one for the pilot. A spray bar is located in the center of each air passage and has two-pressure atomizer nozzles per air passage mounted normal to the main flow direction. Also, each of the cavities has a pressure atomizer nozzle for a total of 54 fuel injectors in the 2P-2V TVC sector. This large number of fuel injectors facilitates good distribution and mixing of the fuel and air.

A tri-passage diffuser with double vortex cavities (3P-2V TVC) is shown in Fig. 12. It is constructed in essentially the same way as the 2P-2V TVC sector. The cavity and diffuser components could also be configured for 2P-1V and 3P-1V TVCs. These configurations are not shown because very few experiments have been conducted with them because of an instability that resulted with the single vortex cavity design. The cavity fuel injectors were located deep in the cavities. Some of the fuel was transported directly into the main air stream. This burning fuel appeared to couple to the small vortex that is shed over the aft-wall corner of the cavity. This small vortex resulted from the way in which air is used to cool the aft face of the cavity. A similar vortex occurs in the double vortex cavity design.

The Air Force combustion facility where the TVC sectors were evaluated is designed with full optical access to the inside of a TVC sector. The windows have been used in combusting flow at pressures up to 13.5 atms. The facility is capable of operating at conditions of 20 atm, 900 K inlet air temperature, and 9 kg/s airflow. The facility also has an exhauster that can lower the pressure to as low as 0.14 atm.

Figure 12(b) shows a side view of the 3P-2V TVC sector operating with the cavities (only) fueled with JP-8. Note that the flame is transported out of the cavities and along the struts. Figure 12(c) is a photograph of the 3P-2V TVC operating with the cavities and the main fueled. This photograph illustrates the importance of being able to observe the flame during testing. It is evident that the main fuel spray from the center air passage has collapsed. Indeed, close visual inspection of the flame showed that the fuel spray had collapsed for all of the main fuel nozzles. However, the center passage created the major problem because there was not adequate heat at the exit of the center air passage to vaporize the fuel. This resulted in poor combustion efficiencies at low overall equivalence ratios for this configuration. This problem can be solved partially by replacing the tri-passage fuel spray bars with the bi-passage spray bars. Thus, only the outer main air passages are fueled. The presented data were collected with the 3P-2V TVC using this fueling arrangement.

The prototype rig has been operated for a total of more than 300 run hours, including: (1) 60 hours of run time at pressures exceeding 13.6 atms and temperatures exceeding 672 K and (2) 12 hours of run time at pressures exceeding 15.3 atm and temperatures exceeding 850 K. Over 700 data points were obtained. Assessment of the demonstrated performance revealed that the prototype TVC test rig had exceeded all initial expectations. A more detailed description of the TVC sectors and the high-pressure test results can be found in Ref. 20. Some results from the 3P-2V TVC are presented below.

Figure 13(a) shows the LBO characteristics of the 3P-2V TVC. Also shown are blow out characteristics for two conventional swirl stabilized combustion systems. The LBO limits for the TVC are about 50%

(c)2001 American Institute of Aeronautics & Astronautics or Published with Permission of Author(s) and/or Author(s)' Sponsoring Organization.

below those for the conventional combustors. Also, the TVC LBO limits are not so strongly dependent on the loading parameter as those for conventional combustors. Although the data are not shown, the LBO limits for the 2P-2V TVC are about the same as those for the 3P-2V TVC.

Figure 13(b) illustrates the altitude relight capabilities of the TVC. Relight data have been obtained at absolute rig pressures as low as 0.2 atms. This pressure corresponds to the ram pressure of an aircraft engine that is windmilling at 14 km at M = 0.5. The ram air temperature and the fuel temperature could not be simulated in the facility. The pilot fuel to air ratio at ignition has been measured for various values of the air loading parameter. The relight data for a conventional and an advanced combustion system are also shown. Three different ignition systems have been investigated with the TVC - a conventional system and two advanced research quality spark ignition systems in which the spark discharge frequency and power spectrum could be varied. The conventional system had and energy of ~ 2-joules and a frequency of 2 sparks per second. Although significant scatter, the data contains evidence that the TVC altitude relight is considerably better than that for swirl stabilized combustors. Conventional combustors have a relight capability of about 9 km. There appears to be significant improvements in relight capability, even though the inlet air and fuel temperatures do not match those at altitude.

Figure 14(a) illustrates the large operating range of the TVC. The severity parameter is defined as:

$$(3)\quad SP = (P_3/14.7)^{.026808} \times e^{(T3/257.693)} \times FAR_4 \times (F_{cavity}/F_{overall})^{0.291096}$$

P_3 and T_3 are the operating pressure (psia) and temperature (°R), respectively; F_{cavity} represents the overall equivalence ratio in the cavity including primary air, driver air, and cooling air; FAR_4 is the combustor exit fuel to air ratio; and $F_{overall}$ is the combustor overall operating equivalence ratio. The effective combustion efficiency takes into account the CO_2 and H_2O dissociation reactions to CO and H_2, respectively. These equilibrium reactions do not become important until the equivalence ratio is above 0.7. Effective combustion efficiencies above 99% are achieved for an overall equivalence ratio between 0.12 and 0.82. This represents about a 40% wider range than that typically achieved by conventional gas turbine combustion systems.

Figure 14(b) shows the exit gas temperature profile across the duct height with cavity-only and with cavity-plus-main-combustor operations. Results are shown for two fuel to air ratios with the main and cavities operating. The temperature profiles are relatively flat, even with cavity only operation, which is a good indication that the struts are evenly distributing the hot products transported out of the cavities. Although the temperature profiles of rigs do not always accurately reflect those of annular combustors of the same design, the temperature data do offer the potential of achieving low pattern factors with the TVC without the use of liner jets.

Figure 15(a) illustrates that a TVC can be operated efficiently at high inlet velocities. These high-speed experiments were motivated by interest of NASA Glenn in evaluating the TVC as a ramjet and, possibly, a scramjet combustion system. The experiments have been conducted with cavities only fueled and at three overall fuel to air ratios. The high inlet velocities were obtained by increasing the pressure drop across the combustor, an unrealistic mode of operation for a gas turbine engine. At a pressure drop of 21% across the combustor the inlet air velocity was estimated to have achieved a Mach No. = 0.77. At a more typical pressure drop of 5% across the combustor the inlet air velocity has a Mach No. = 0.3. In a ramjet, this pressure would be generated by ram air, not by the upstream plenum. Although these experiments do not simulate a ramjet operation, they do provide some insight into the operation of the cavities at high inlet velocities. Visual observations of the cavity flames revealed that the vortex became more intense and smaller as the pressure drop (inlet velocity) increased. The vortices also appeared to remain trapped in the cavity. At the low fuel to air ratio, the combustion efficiency decreased dramatically at pressure drops above 5.2% (Mach No. 0.310). However, at the higher fuel to air ratios, the combustion efficiency remained above 98% up to the max inlet air velocity. These results offer some support that a TVC might be used as a ramjet combustor. A joint program is in

(c)2001 American Institute of Aeronautics & Astronautics or Published with Permission of Author(s) and/or Author(s)' Sponsoring Organization.

progress with NASA Glenn to further evaluate the TVC as a high-speed combustion system.

The NOx emission index is also plotted in Fig 15(a). Since the overall equivalence ratio remained fixed for each curve, large decreases in the NOx emissions index occur with increasing pressure drop or increasing inlet air velocity. This suggests that significant NOx reductions might be possible with a TVC operating with a high inlet-air velocity. However, this reduction must be achieved with a reasonable pressure drop across the combustor. This exciting possibility will be evaluated in future studies.

The third generation TVC has demonstrated the potential of using the TVC as an RQL combustor where all of the fuel is injected into the cavity. Here the rich products from the cavity are transported along the struts, rapidly mixed with the main air, and burned lean. This idea has also been evaluated with the 3P-2V TVC; the results are shown in Fig. 15(b). The experiment was conducted at a pressure of 4 atm and a pressure drop of 5%, with an inlet temperature of 544 K. Also, data are presented for an operating pressure of 10.2 atm and inlet temperature of 783 K, with a pressure drop of 4%. Although the combustion efficiency peaked for the low inlet-temperature conditions, it remained above 99% for a cavity equivalence ratio between 1.2 and 3.8. The efficiency for the higher inlet condition was essentially over the full range of primary equivalence ratios tested . The amount of NOx produced during these RQL experiments is also shown in Fig. 15(b). The NOx behavior for the high and low inlet-temperature conditions is very different. The NOx in an RQL is expected to decrease with increasing equivalence ratio. However, this trend was not observed. The data indicate that the mixing of the hot products from the cavities with the main air is not so rapid to reap the full benefits of an RQL combustor. The DoE is investigating TVC concepts for power-generation that would improve this mixing process.

Figure 16(a) shows the NOx emissions index for the third generation TVC operating with cavity only and with cavity and main. The severity parameter provides a good correlation with the NOx for all points except those circled. These points are associated with the circled points given in Fig. 14(a) where the combustion efficiency begins to decrease, and represent combustor operation near and at overall stoichiometric discharge. The severity parameter EINOx correlation has been used to estimate the Landing Take-off EPA Parameter (EPAP) used for regulating commercial aircraft. Three TVC data points are shown for a Dual Annular Combustor (DAC II) cycle and an advance commercial engine cycle in Fig. 16(b). Engine data for these and other cycles are also shown. The TVC gives a 45% reduction in NOx for the DAC II cycle and a 55% reduction for the advanced commercial engine cycle as compared to the 1996 ICAO standard. This is thought to be a significant accomplishment, considering the fact that this is the first high-pressure TVC built and tested. Also shown in Fig. 16(b) is a model calculation predicting a NOx reduction of 65% achievable if the problem of the collapsed main spray is corrected.

CONCLUSIONS

The feasibility of the TVC concept has been demonstrated in a practical gas turbine combustor design for realistic inlet temperature and pressure conditions using JP-8 fuel. Test results indicate that the TVC offers significant improvements in LBO and altitude relight, as compared to conventional swirl stabilized combustors. Also, a wider operating range has been demonstrated as well as the potential to achieve low NOx. The TVC can operate in a staged, main/pilot mode as well as in an RQL mode. The TVC has shown potential for operating efficiently with high inlet velocities. Even though encouraging results have been obtained to date, it must be realized that the TVC technology is in the early stages of development. A practical design and issues associated with cost, weight, and life, have not been addressed in any detail. Programs are currently underway to further develop the capabilities of the TVC and address these issues.

ACKNOWLEDGEMENTS

The authors would like to thank the following organizations and program managers for supporting the TVC program: Dr. Julian Tishkoff of the Aerospace Sciences Division of the Air Force Office of Scientific Research; Dr. Charles Pellerin of the Strategic Environmental Research and Development Program

(c)2001 American Institute of Aeronautics & Astronautics or Published with Permission of Author(s) and/or Author(s)' Sponsoring Organization.

(SERDP); Messrs, John Hartranft and Michael Osborn of NAVSEA; Messrs, Steve Hartle and Marc Richman of NAVAIR. The authors also express their appreciation to Messrs, Jeff Stutrud for development of data collection and analysis software, Chuck Frayne and Ronald Britton for making the emissions measurements; Messrs, Richard Ryman and Karl Shoffstall for installing the instrumentation and combustor hardware and participating in the experiments; and Mr. Barry Kiel for testing the third generation TVC; Messrs, Harold Day, Dwight Fox, Steve Pennington, and Charles Able for the design and fabrication of TVC hardware; and Dr. Robert Hancock, Carlos Arana, and Ted Fecke for the many useful discussions on the TVC. The high speed TVC research is supported by Drs. Robert C. Hendricks, Nan-Suey Liu from NASA Glenn, and Mr. Rob Ryder of Flow Parametrics, LLC; and the RQL research is supported by Drs. G. A. Richards, D. L. Straub, T. G. Sidewell, D. J. Maloney, and K. H. Casleton of the National Energy Technology Laboratory. We would also like to thank Ms. Marian Whitaker for her many helpful comments and editorial assistance.

REFERENCES

1. Lefebvre, A. H., "*Gas Turbine Combustion*," Hemisphere Publishing Company, 1983, pp. 448-451.

2. Komerath, N. M., Ahuja, K. K., and Chambers, F. W., "Predictions and Measurement of Flows Over Cavities – A Survey," AIAA Paper 87-0166, January 1987.

3. Rockwell, D. and Naudascher, E., "Self-sustained Oscillations of Impinging Shear Layers," Ann. Rev. Fluid Mech., 11:67-94, 1979.

4. Chokani, N., "Flow Induced Oscillations in Cavities – A Critical Survey", AIAA Paper 92-02-159, May 1992.

5. Parthasarathy, S. P., Cho, Y.I., and Back, L. H., "High-Intensity tone Generation by Axisymmetric Ring Cavities on Training Projectiles", AIAA Paper No. 84-2259, October 1984.

6. Ben-Yakar and Hanson, Ronald K., "Cavity Flameholders for Ignition and Flame Stabilization in Scramjets: Review and Experimental Study", AIAA Paper AIAA 98-3122, 34th AIAA Joint Propulsion Conference & Exhibit, Cleveland, OH, July 13-15, 1998.

7. Willis, J. W., Cadou, C., Mitchell, M., Karagozian, A. R., and Smith, O. I., "Destruction of Liquid and Gaseous Waste Surrogates in an Acoustically Excited Dump Combustor," *Combustion and Flame*, Vol. 99, pp. 280-287, 1994.

8. Hsu, K.-Y., Goss, L.P., and Trump, D.D., "Performance of a Trapped-Vortex Combustor", Paper No. 95-0810, *AIAA 33rd Aerospace Sciences Meeting & Exhibit*, Reno, Nevada, January 9-12, 1995.

9. Hsu, K.-Y., Goss, L.P., and Roquemore, W.M., "Characteristics of a Trapped-Vortex Combustor", *Journal of Propulsion and Power*, Vol. 14, No. 1, pp. 57-65, January-February 1998.

10. Professor Eric J. Jumper of Notre Dame University directed us to the papers of Mair and Little and Whipkey after observing the operation of the first generation TVC.

11. Mair, W. A., "The Effect of a Rear-Mounted Disc on the Drag of a Blunt-Based Body of Revolution," The Aeronautical Quarterly, pp. 350-360, November 1965.

12. Little, B. H. Jr., and Whipkey, R. R., "Locked Vortex Afterbodies," *Journal of Aircraft*, Vol. 16, No. 5, pp. 296-302, May 1979.

13. Katta, V. R. and Roquemore, W.M., "Numerical Studies on Trapped-Vortex Concepts for Stable Combustion", Paper No. 96-TA-19, *American Society of Mechanical Engineers Turbo Asia Conference*, Jakarta, Indonesia, November 5-7, 1996.

14. Gharib, M., and Roshko, A., "The Effect of Flow Oscillations on Cavity Drag," *Journal of Fluid Mechanics*, Vol. 177, pp. 501-530, 1987.

15. Sturgess, G.J. and Hsu, K.-Y., "Entrainment of Mainstream Flow in a Trapped-Vortex Combustor", Paper No. 97-0261, *AIAA 35th Aerospace Sciences Meeting & Exhibit*, Reno, Nevada, January 6-10, 1997.

16. Katta, V.R. and Roquemore, W.M., "Study on Trapped-Vortex Combustor – Effect of Injection on Flow Dynamics", Journal of Propulsion and Power (reprint), Vol. 14, No. 3, pp. 273-281, May-June 1998.

17. Sturgess, G.J. and Hsu, K.-Y., "Combustion Characteristics of a Trapped Vortex Combustor", *RTO AVT Symposium on Gas Turbine Engine Combustion,*

(c)2001 American Institute of Aeronautics & Astronautics or Published with Permission of Author(s) and/or Author(s)' Sponsoring Organization.

Emissions and Alternative Fuels, Lisbon, Portugal, October 12-16, 1998.

18. Hsu, K.-Y., Carter, C.D., Katta, V.R. and Roquemore, W.M., "Characteristics of Combustion Instability Associated with Trapped-Vortex Burner", AIAA Paper No. 99-0488, AIAA 37th Aerospace Sciences Meeting & Exhibit, Reno, Nevada, January 11-14, 1999.

19. Stone, C. and Menon, S., "Simulation of Fuel-Air Mixing and Combustion in a Trapped-Vortex Combustor", AIAA Paper No. 2000-0478, *AIAA 38th Aerospace Sciences Meeting & Exhibit*, Reno, Nevada, January 10-13, 2000.

20. Burrus, et al., "Performance Assessment of a Prototype Trapped Vortex Combustor Concept for Gas Turbine Applications", ASME Turbo Expo 2001, New Orleans, Louisiana, June 4-6, 2001.

(c)2001 American Institute of Aeronautics & Astronautics or Published with Permission of Author(s) and/or Author(s)' Sponsoring Organization.

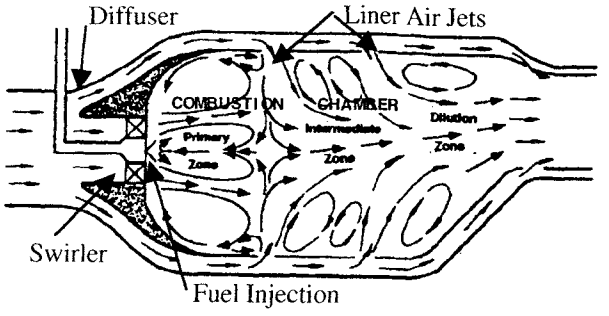

(a)

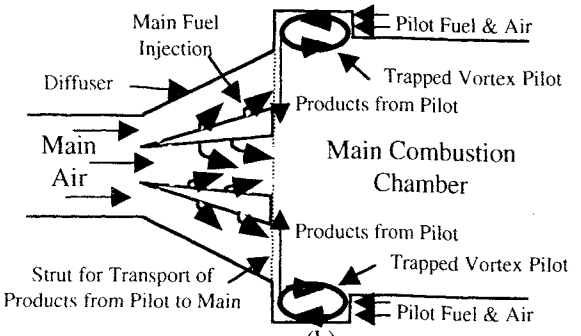

(b)

Figure 1. (a) Conventional and (b) TVC concepts.

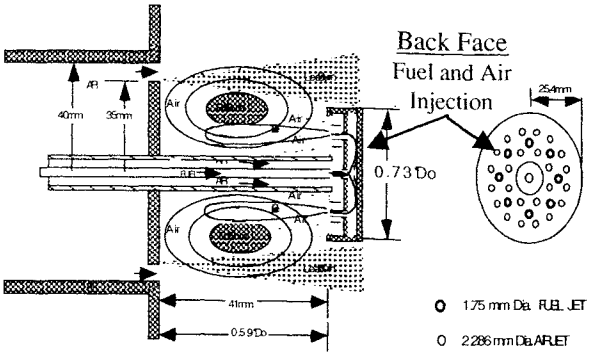

(a)

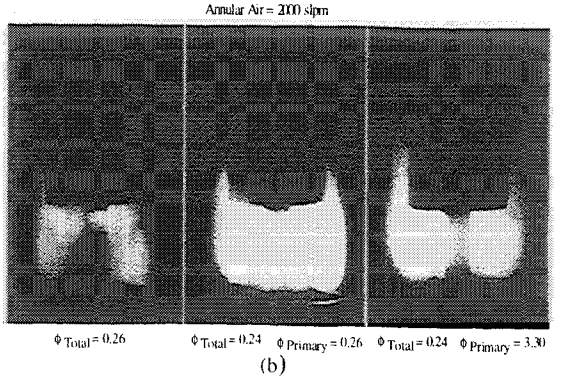

(b)

Figure 2. (a) First generation trapped vortex combustor with (b) flame photographs at different flow conditions.

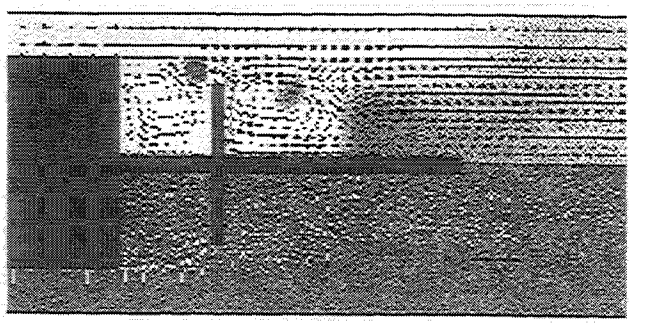

(a) Undersized Cavity

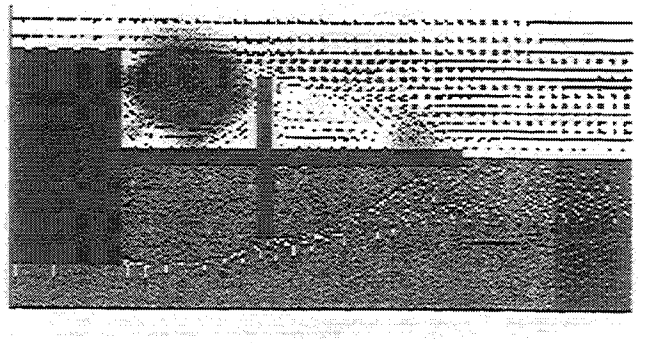

(b) Trapped Vortex Cavity

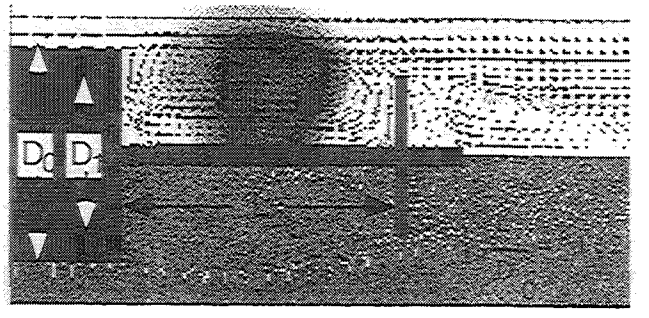

(c) Oversized Cavity

Figure 3. Calculations of Little and Mair experiments Ref. 12.

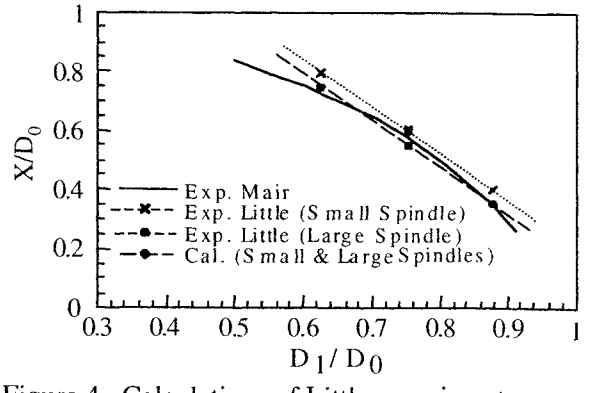

Figure 4. Calculations of Little experiments.

(c)2001 American Institute of Aeronautics & Astronautics or Published with Permission of Author(s) and/or Author(s)' Sponsoring Organization.

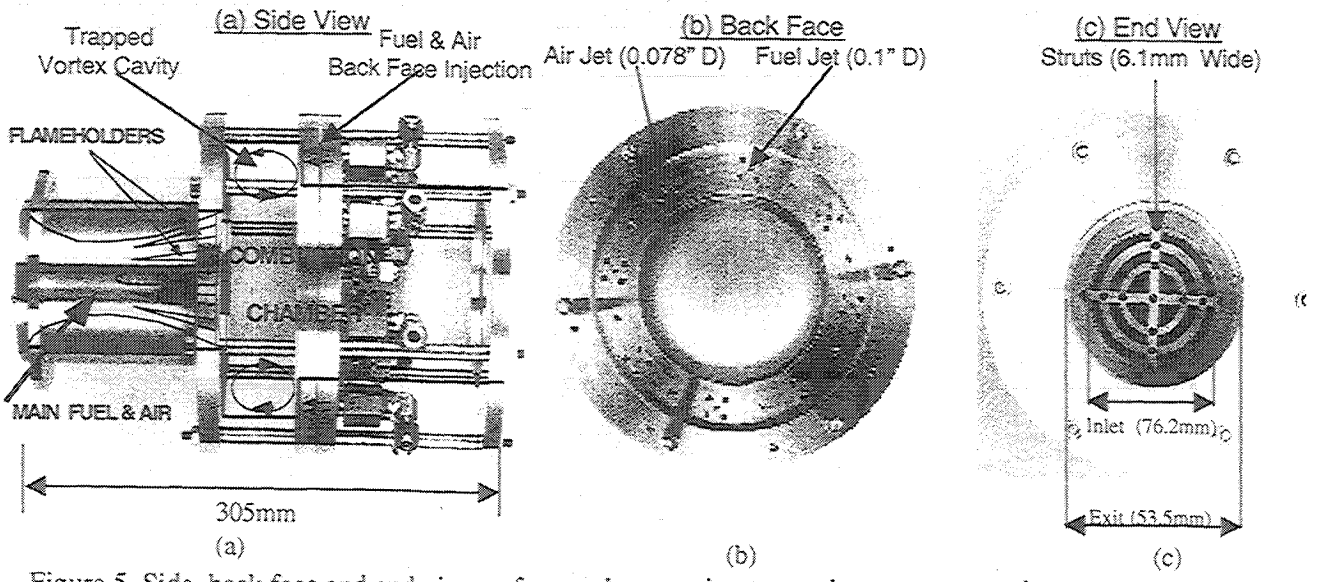

Figure 5. Side, back face and end views of second generation trapped vortex can combustor.

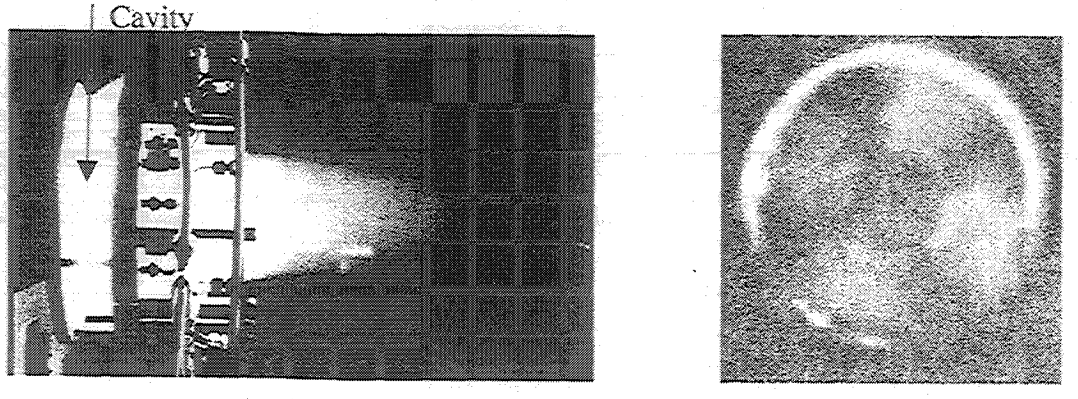

Figure 6. Side and end views of flame in second generation TVC can at equivalence ratio of 1.

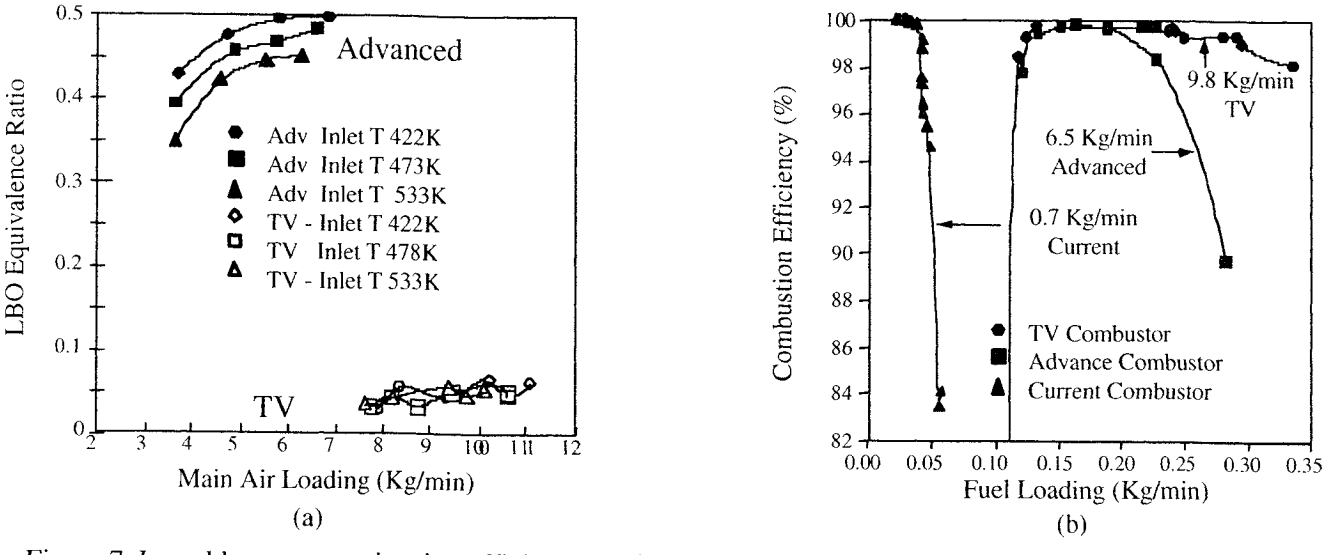

Figure 7. Lean-blow-out, combustion efficiency, and NOx emissions index for second generation TVC can with comparisons with current and advanced combustors.

(c)2001 American Institute of Aeronautics & Astronautics or Published with Permission of Author(s) and/or Author(s)' Sponsoring Organization.

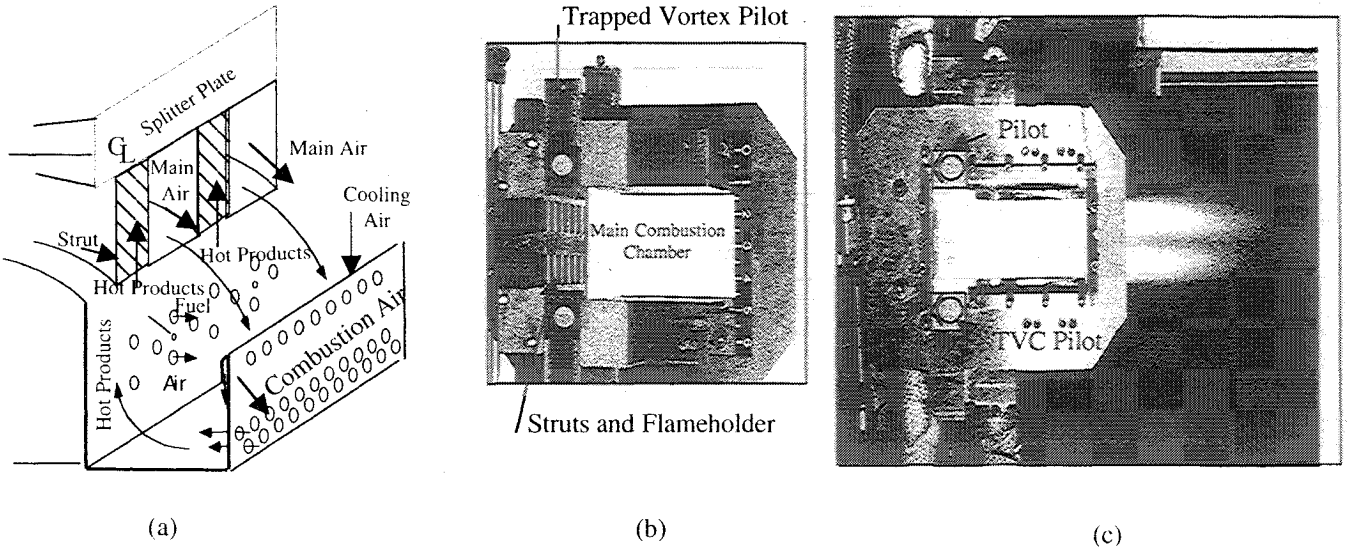

Figure 8. Illustration and side photographs of third generation trapped vortex combustor.

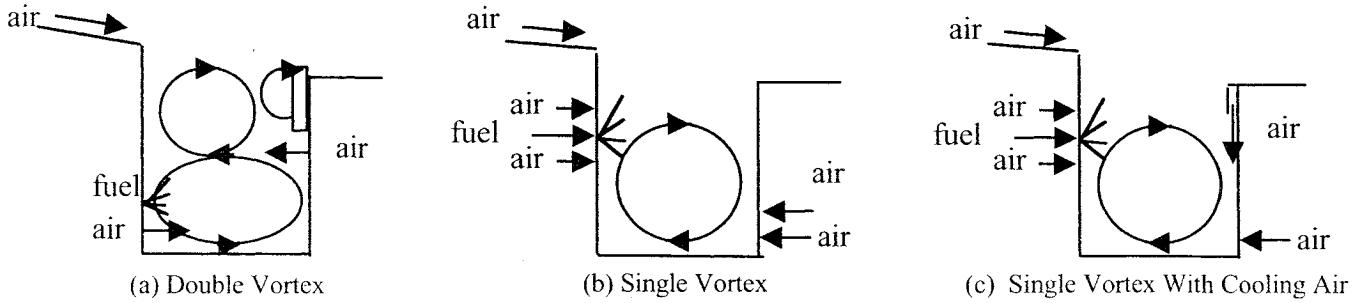

Figure 9. Three optimum configurations for injecting fuel and air into cavity.

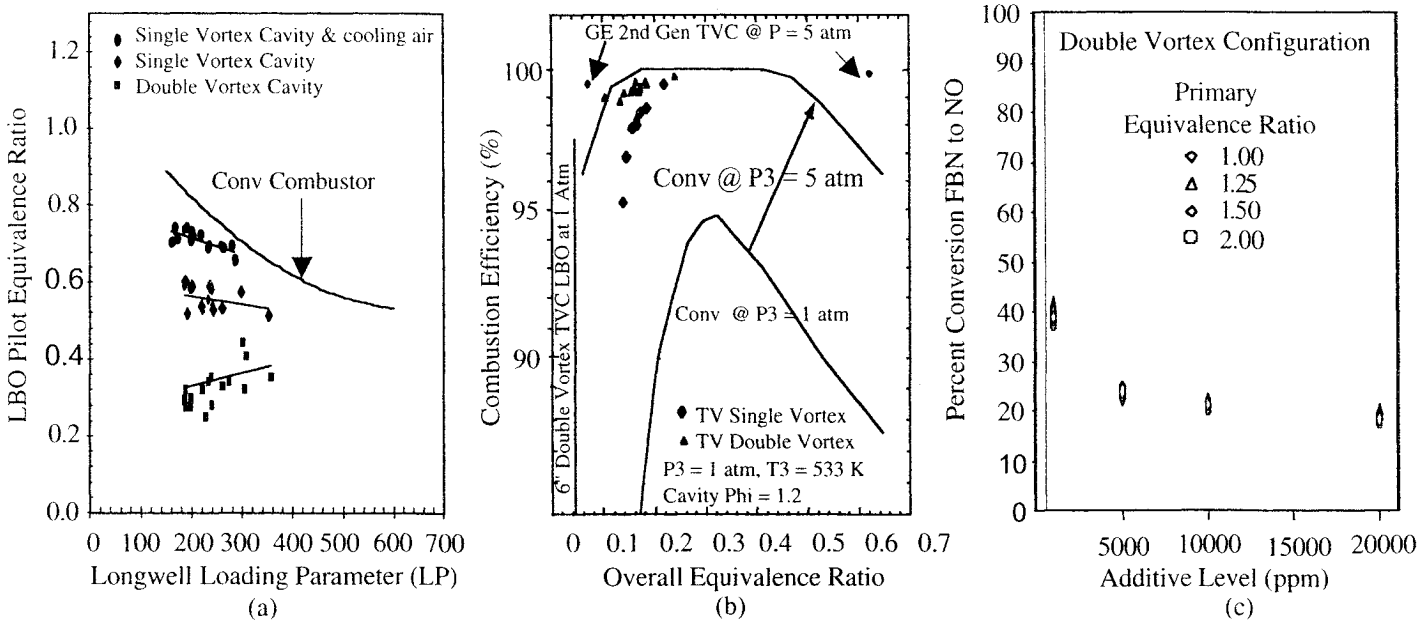

Figure10. Lean-blow-out,combustion efficiency, and fuel bound nitrogen (FBN) conversion to NO for third generation TVC
LP= $W_{comb}/[Vol \times (P_3/14.7)^{1.75} \times e^{(T3/540)}]$

(c)2001 American Institute of Aeronautics & Astronautics or Published with Permission of Author(s) and/or Author(s)' Sponsoring Organization.

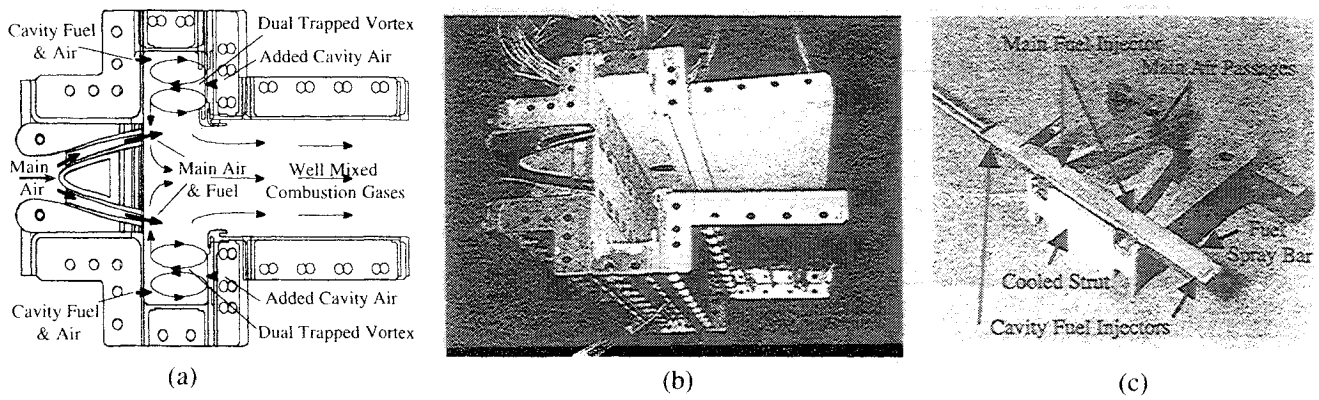

Figure11. Illustration and photographs of high-pressure, bi-pass diffuser, and double vortex (2P-2V) TVC .

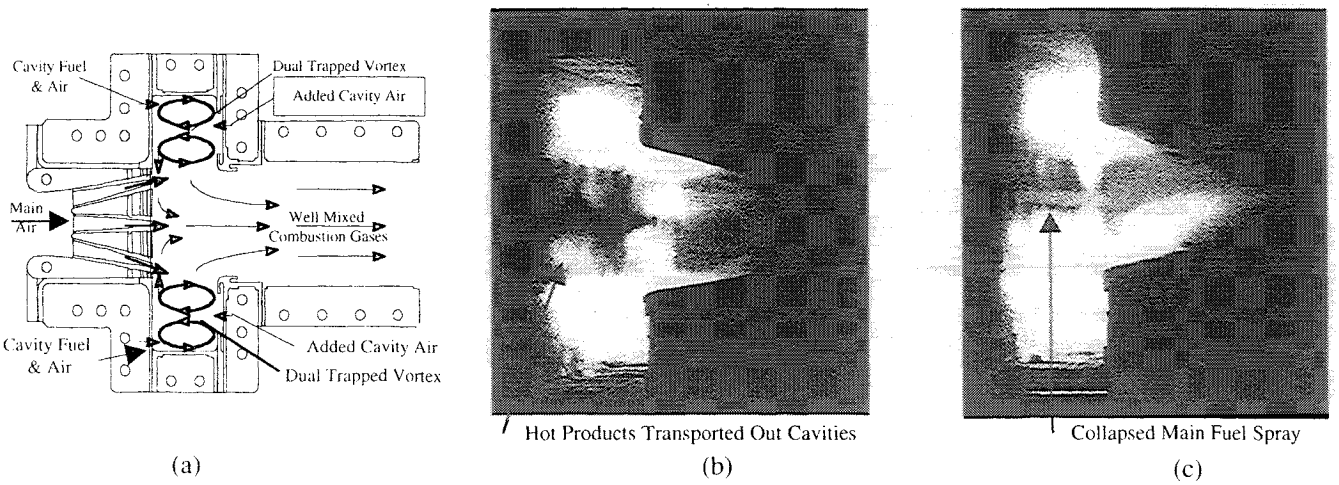

Figure12. Illustration and photographs of high-pressure, bi-pass diffuser, and double vortex (2P-2V) TVC .

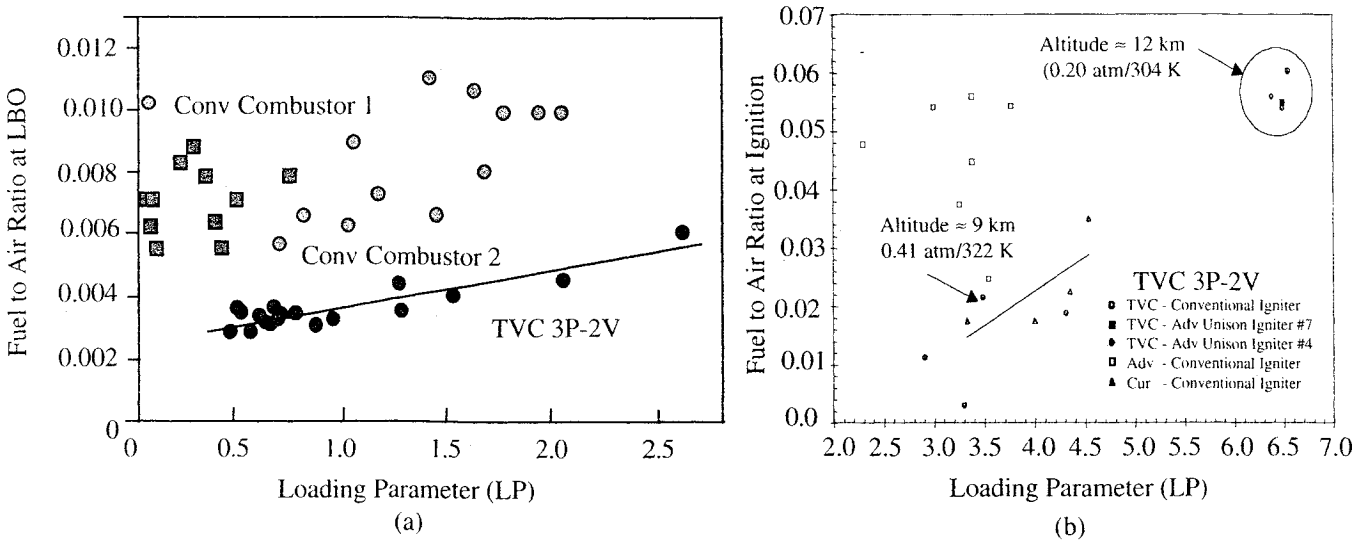

Figure13. (a) Lean-blow-out and, (b) altitude relight for high-pressure TVC 3P-2V.
LP= $W_{comb}/[Vol \times (P_3/14.7)^{1.75} \times e^{(T3/540)}]$

(c)2001 American Institute of Aeronautics & Astronautics or Published with Permission of Author(s) and/or Author(s)' Sponsoring Organization.

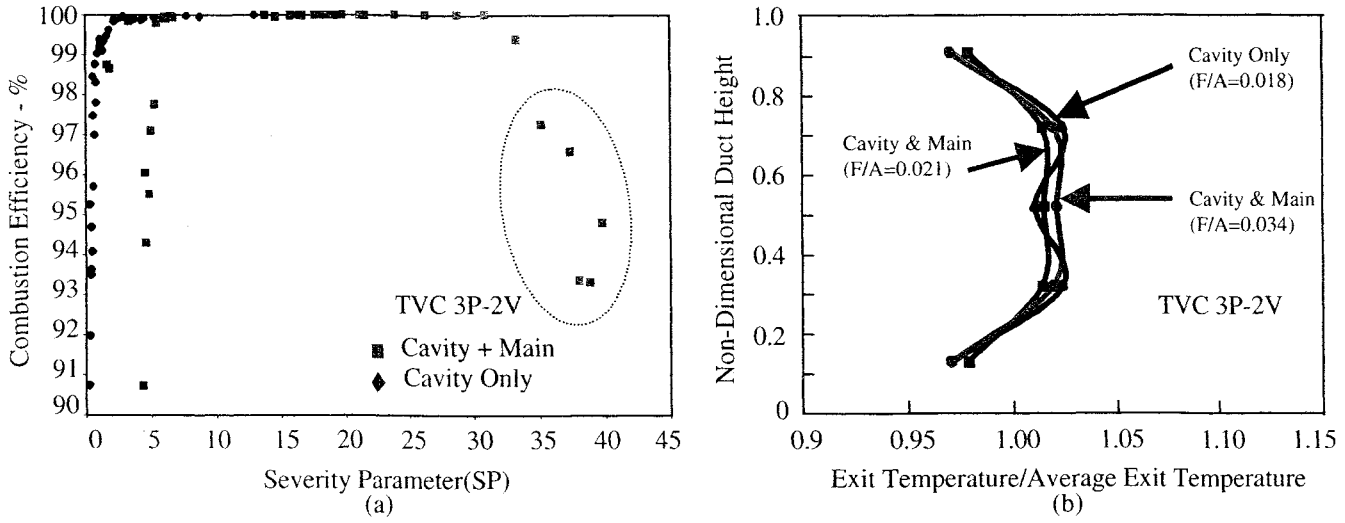

Figure14. (a) Combustion efficiency and radial profiles for 3P-2V TVC.
$SP = (P_3/14.7)^{0.26808} \times e^{(T3/257.693)} \times FAR4 \times (F_{cavity}/F_{overall})^{0.291096}$

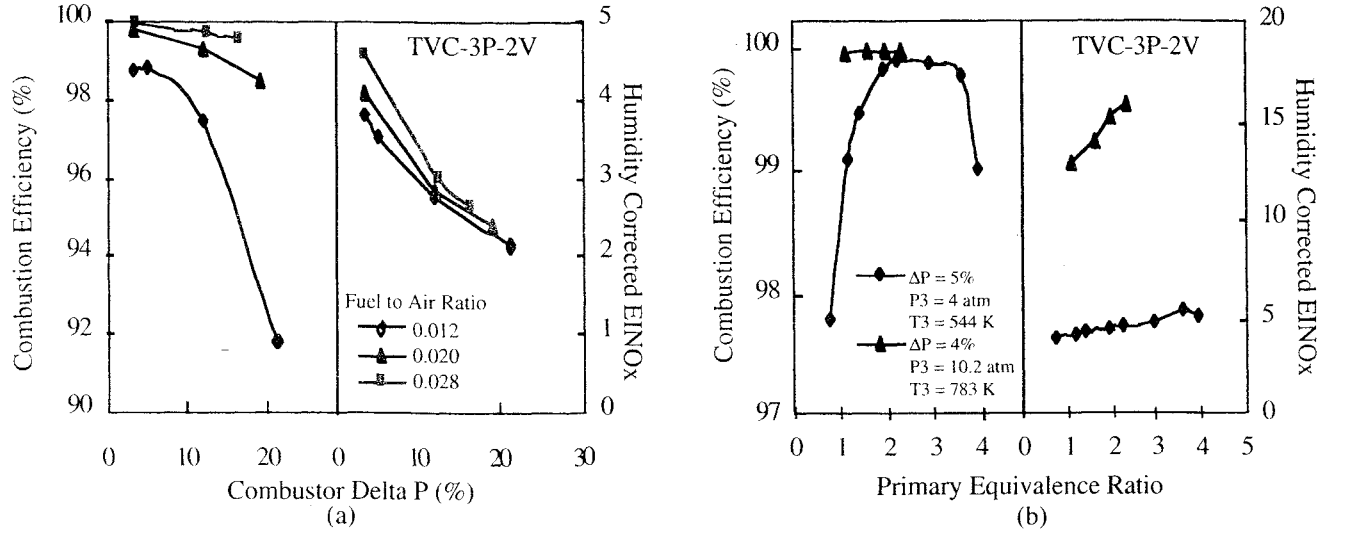

Figure15. Combustion efficiency and NOx EI for for (a) high speed inlet flows and (b) RQL TVC 3P-2V.

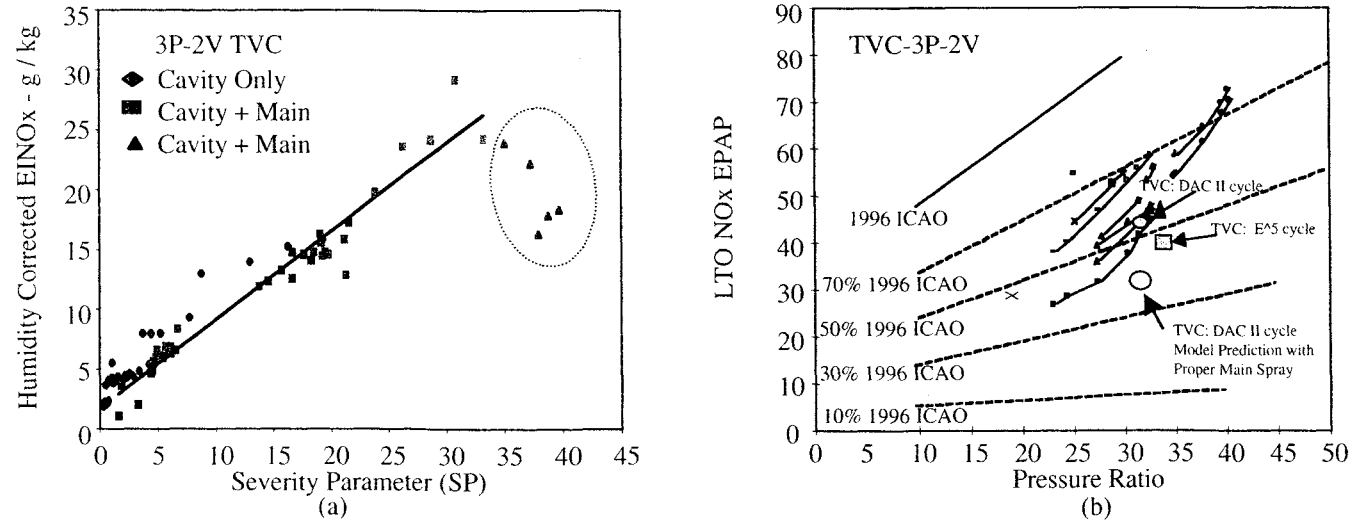

Figure16. (a) NOx emissions for 2P-2STVC and (b) estimates of TVC EPAP NOx for different engines.
$SP = (P_3/14.7)^{0.26808} \times e^{(T3/257.693)} \times FAR_4 \times (F_{cavity}/F_{overall})^{0.291096}$

38th AIAA/ASME/SAE/ASEE Joint Propulsion Conference & Exhibit
7-10 July 2002, Indianapolis, Indiana

AIAA 2002-3863

OPTICAL DIAGNOSTICS AND NUMERICAL CHARACTERIZATION OF A TRAPPED-VORTEX COMBUSTOR

T. R. Meyer,[*] M. S. Brown,[†] S. Fonov,[†] and L. P. Goss[‡]
Innovative Scientific Solutions, Inc., Dayton, OH 45440-3638, USA

J. R. Gord,[§] D. T. Shouse,[¶] V. M. Belovich,[*] and W. M. Roquemore[#]
Air Force Research Laboratory, Propulsion Directorate
Wright-Patterson Air Force Base, OH 45433-7103, USA

C. S. Cooper[**] and E. S. Kim[**]
GE Aircraft Engines, Cincinnati, OH 45215-1988, USA

J. M. Haynes[††]
GE Global Research, Niskayuna, NY 12309, USA

Abstract

Optical diagnostics are performed in concert with numerical simulations to characterize a new trapped-vortex combustor (TVC) for gas turbine engines. Variable parameters include the fuel composition, inlet pressure, inlet pressure drop, inlet temperature, and fuel-injection scheme. A number of experimental techniques are employed, such as high-speed digital imaging, coherent-structure velocimetry (CSV), particle-image velocimetry (PIV), and planar laser-induced fluorescence (PLIF) of hydroxyl (OH). The experimental data compare well with results from a computational fluid dynamics code (CFD) with chemistry, and are used to understand the flow pattern and flame location within the combustor. We discuss the utility of advanced diagnostics and simulations during the design and testing phase of combustor development.

---

[*]Research Engineer, Member AIAA
[†]Physicist, Senior Member AIAA
[‡]President, Member AIAA
[§]Principal Research Chemist, Associate Fellow AIAA
[¶]Senior Research Engineer
[#]Senior Scientist, Fellow AIAA
[**]Combustor Design Engineer
[††]Combustion Engineer

Introduction

The trapped vortex combustor (TVC), as illustrated in Fig. 1, is a new concept gas turbine combustor that utilizes cavity-stabilization rather than swirl-stabilization.[1,2] TVCs are currently being developed for low-emissions, high-performance combustion systems in aircraft and ground power gas turbine engines. Fuel and air are injected directly into the cavities in a way that reinforces stable recirculation zones that are established by properly sizing the cavities. Hot products are transported out of the cavities along struts that are flush with the forward walls of the cavities. The struts, with main air passages, form the inlet plane or face of the combustor. The main air and products from the cavities are mixed in the wakes of the struts. TVCs can be operated as rich-burn, quick-quench combustors or lean-burn combustors when all of the fuel is injected into the cavities. TVCs can also be operated as staged combustors if fuel is injected into both the cavities and the main airflow. TVCs have no liner jets to shape the temperature profile at the exit of the combustor. Instead, the temperature profile is controlled, at the face of the combustor, by the transport and mixing of the hot products along the struts.

Over the last 50 years, combustor designers have used swirl to stabilize the flame and promote mixing of the fuel and air. There is a large empirical database and considerable experience for designing swirl combustors. TVCs operate very differently from swirl combustors. Thus, designers cannot take advantage of established databases and design experience. Instead, computational fluid dynamics (CFD) based combustor design models along with visualizations and optical

This material is declared a work of the U.S. Government and is not subject to copyright protection in the United States.

measurements are being used in the design process.

The goal of this paper is to describe a number of advanced optical diagnostic and numerical approaches that are used to guide the development of the TVC. Such techniques include high-speed digital imaging, coherent-structure velocimetry (CSV), particle-image velocimetry (PIV), and planar laser-induced fluorescence (PLIF) of the hydroxyl radical (OH). In conjunction with experimental diagnostics, CFD with chemistry is performed for comparison with the CSV, PIV, and OH PLIF data. The current paper demonstrates how advanced diagnostics and numerical simulations can be applied to assess the performance of innovative combustor designs and can provide direct insight into the flame structure that contributes to their performance.

Experimental Method

Liquid-Fueled TVC

The liquid-fueled TVC has been under development by GE Aircraft Engines for use in high-performance, low-emissions gas turbine engines with sponsorship from the Air Force Research Laboratory (AFRL). A 6-inch rectangular TVC rig is used for laser-based diagnostics at atmospheric conditions, and a 12-inch rectangular TVC rig is used for high-speed digital imaging at high-pressure conditions. This rig is capable of operation at inlet pressures up to 20.5 atmospheres, inlet temperatures up to 900 K, and stoichiometric discharge conditions.[2] Regular testing includes emissions measurements using a five-element gas-sampling probe and smoke meter. Results of these tests can be found in other publications[1,2] and are not discussed in the current paper. The advanced optical diagnostics performed in the liquid-fueled TVC and reported in this paper include high-speed digital imaging, CSV, and PIV.

Gaseous-Fueled TVC

The objective of the gaseous-fueled TVC testing is to investigate the TVC performance with natural gas fuel using the existing 6-inch rectangular TVC rig. This program is led by GE Global Research Center under sponsorship by the Department of Energy with the overall goal of developing a prototype combustor that will reduce smog-causing nitrogen oxide emissions by 50% or more compared to state-of-the-art lean premixed gas turbine combustors. In the first phase of the program, the existing TVC, shown in Fig. 1, has been modified for gaseous fuel injection. Gaseous fuel is injected into the cavity through the primary injector, and gaseous fuel is premixed with the main air for the main injectors. Advanced diagnostics performed for this configuration include OH PLIF and PIV; only the OH PLIF results are presented here.

Optical Diagnostics

High-speed imaging of the TVC is accomplished in the High-Pressure Combustor Research Facility at Wright-Patterson Air Force Base. Initial work was performed with a Photron NMOS-based high-framing-rate digital camera capable of 40,500 fps. Additional data were collected using a Phantom v5.0 CMOS-based high-framing-rate digital camera capable of 60,000 fps by Photo-Sonics International Ltd. The latter camera is operated at 11,200 frames per second (fps) with a resolution of 256×256 pixels for imaging the entire combustor (main and 2 cavities), and at 19,800 fps with 128x256 pixels for imaging the lower half of the combustor. While conventional high-speed photographic cameras can easily accomplish framing rates of 10,000 fps or more, the 10 μs exposure time of the Phantom camera allows for unconventional flow-freezing capability, equivalent to a camera operating at 100,000 fps.

While providing qualitative volume-averaged information about flame behavior, the short-exposure, high-speed images can also be used to track flow patterns using coherent-structure velocimetry (CSV). Variations of this technique have been applied under cold-flow conditions.[3,4] To the extent that the *time-averaged* flow pattern in combusting flows is dominated by convection rather than the expansion caused by heat release, this approach provides a convenient alternative to particle-image velocimetry (PIV) in that it does not require extensive knowledge of laser diagnostics and does not require flow seeding. CSV is accomplished in the current work using images from the high-speed digital cameras. The image-processing procedure includes the selection of an optimal interrogation window and overlap parameter followed by cross-correlation between image pairs for determination of the local displacement vector. For more uniform flowfields, the generation of isoline contours to define structure boundaries may also be helpful. Finally, an adaptive grid may be necessary due to the disparate velocities between the cavity region and main section.

Laser-based diagnostics, including PIV and OH PLIF, are accomplished in the Atmospheric-Pressure Combustor Research Complex at Wright-Patterson Air Force Base. A schematic of the burner facility and diagnostics is shown in Fig. 3. The TVC and main supply duct is mounted on a translation stage for probing different cross-sections in the transverse direction. A coexisting optics set-up is used for both PIV and OH such that the research team could easily alternate between the two techniques.

PIV is achieved using a dual-image, digital cross-correlation configuration with two Nd:YAG lasers

(energy ~ 50 mJ) and a dual-frame Kodak ES4 2000×2000 pixel charge-coupled device (CCD) camera. Seeding particles into the flowfield is one of the main challenges of applying PIV in realistic combustors. One must avoid window fouling while attempting to achieve sufficient seed density in a combusting (low gas density) environment. For the current work, sufficient seeding is achieved by adding ceramic micro-spheres into the cavity-air feed paths. After capturing two time-correlated particle scattering images, vectors are computed using the dPIV code developed by AFRL and Innovative Scientific Solutions, Inc, with a 128×128 interrogation region and 75% overlap. Averaged vectors are calculated from 500 image pairs.

Planar laser-induced fluorescence of OH is performed by exciting the $R_1(8)$ transition of the (1,0) band in the A-X system at 281.3413 nm and collecting the subsequent fluorescence from the A-X (1,1) and (0,0) bands near 310 nm. Natural flame emission is reduced by using a short gate of ~100 ns and a UG-11 colored glass filter. Two WG-295 colored glass filters are required to reduce laser-scattered light off the bottom cavity while allowing fluorescence above 295 nm to be recorded. A 576×384 pixel Princeton Instruments ICCD and UV Nikkor 105-mm multi-element lens are used to collect the OH LIF signal. The 2-mJ OH laser sheet, which fills the lower cavity of the TVC, has a fairly tophat profile and no corrections for laser-sheet intensity variations are performed.

Computational Method

Steady-state numerical simulations of the TVC are developed at GE Aircraft Engines using the Fluent v5.5 commercial 3-D CFD code. The computational domain for the liquid-fueled TVC encompasses a single cavity meshed with a 413,000 hex-cell grid (average volume of 1.03 mm^3). A symmetry plane at the combustor center plane is used to reduce the model size by a factor of two; a periodic boundary is defined so that only a single sector encompassing one fuel injector is modeled. The governing equations are solved using a double-precision QUICK scheme, and the combustion model employs a Fluent-developed probability density function (PDF) method for direct fuel injection. Results from PIV measurements are used to anchor the CFD model, and the model is then used for parametric studies and for comparison with results from CSV. The 3-D Fluent CFD model of the gaseous-fueled TVC has been performed using a GE-developed Laminar Flame Model (LFM) for lean premixed fuel injection and a Fluent-developed PDF method for direct fuel injection. Temperature predictions for the gaseous-fueled TVC model are verified using results from OH PLIF.

Results and Discussion

Cavity Flow Structure

The flow pattern inside the cavity is a critical aspect of TVC performance. If fuel escapes from the cavity without burning during idle conditions, then it is easily quenched by the cool main air. This reduces overall combustion efficiency and leads to increased unburned hydrocarbon emissions. In the rich-burn quick-quench lean-burn (RQL) mode of operation, the cavities provide the rich-burn mode, and rapid mixing with the main air provides the quick-quench lean-burn modes. Thus, it is desirable to control the mixing and burning process inside the cavity, with the best performance typically being achieved when fuel is located deep within the cavity. The subsequent discussion of the TVC flow pattern is limited to the cavity-only liquid fuel-injection configuration (in RQL mode).

Initial TVC designs utilized fuel and air intake configurations that enhanced the natural vortex motion induced by flow over a cavity, as shown in Fig. 4(a). To improve the retention of unmixed fuel in the cavity, a design modification was implemented to sustain a second vortex in the cavity. As shown in Fig. 4(b), the second vortex would serve as a barrier between the vortex of fuel and air located deep in the cavity, as well as a secondary mixing stage. PIV measurements of the flow pattern in a non-combusting 6-inch liquid-fueled rig, shown in Fig. 5, indicate that the design of Fig. 4(b) may not, in fact, be able to sustain a double vortex. This was confirmed by high-speed digital imaging under combusting conditions, which provided excellent real-time feedback on the vortical motion within the cavity. The counter-clockwise flow patterns sketched in Fig. 6 agree with the non-combusting PIV/CFD results shown previously in Fig. 5, and helped combustor engineers tailor the cavity flow configuration. Differences in flame distribution for the two conditions of Fig. 6 are also evident in the high-speed images, with the case of Fig. 6(b) showing increased burning in the main due to unburned fuel escaping the cavity.

The flow pattern readily apparent to the eye (sketched in Fig. 6) is successfully tracked by CSV, providing qualitative confirmation of single-vortex cavity flow. The case of higher pressure and higher fuel load in Fig. 7(b) shows a slightly larger vortex circulation pattern as is consistent with the high-speed images. The absolute velocities of the front- and aft-wall air jets, shown previously in the PIV/CFD results of Fig. 5, are not captured by the CSV. This occurs for two main reasons: (1) air jets in non-combusting layers cannot be tracked by CSV and (2) the flow is three-dimensional and CSV is hampered by wall effects and line-of-sight averaging. The accuracy of CSV is expected to improve in the downstream main region where the flow is more two-

dimensional. Although not shown here, measurements in this region are 20% less than the CFD prediction. This is not surprising given that the flow velocity near the optical window is reduced by boundary layer effects not captured by the CFD.

Cavity and Main OH Species Distribution

The OH radical is an important flame marker in that it tracks high-temperatures within the reaction and post-reaction zones of premixed and non-premixed flames.[5] It can, therefore, be used to help validate temperature predictions from CFD calculations with simple chemistry models as it qualitatively marks the location of the flame. It must be kept in mind, however, that while OH signals indicate regions of high temperature (> 1100 K), regions of high temperature do not necessarily indicate regions of high OH number density.

A series of the OH-PLIF measurements has been performed for the gaseous-fueled TVC over a range of operating conditions. The OH-PLIF measurements are conducted at three different planes: one was aligned with the injector, the second plane was located between the injector and strut, and the third one was aligned with the strut. Here, only the OH images in the plane aligned with the injector are presented.

Figures 8 and 9 show average OH PLIF images and comparisons with CFD temperature predictions. To minimize the saturation level of the OH-PLIF images, OH images are plotted in different color scales for the purpose of illustration. In general, the CFD temperature predictions capture the qualitative differences between cavity/main injection (Fig. 8) and cavity-only injection (Fig. 9). Noticeable differences in terms of the flame structure, especially in the dome regions, are predicted between these two modes. For cavity/main injection (Fig. 8), the flame is concentrated in the cavity region because it is locally higher in equivalence ratio. The hot products are then convected downstream of the cavity by the incoming lean premixed main fuel and air. Due to limitations on optical access, it was not possible to determine the presence of OH downstream of the cavity. For cavity-only injection, high levels of OH can be detected in the dome region as higher levels of fuel escape the cavity and mix with the entrained air. Note the color scale is much higher for cavity-only injection, with OH PLIF signals significantly higher than cavity/main injection. The OH PLIF and CFD data help give physical insight into the reasons why splitting fuel injection from the cavity to the main (Fig. 8) allows for staged lean combustion and helps to reduce NO_x production at high-fueling conditions.

In addition to differences in the average OH distributions between the cavity/main and cavity-only injection modes, one can also identify differences in the instantaneous OH structure, as shown in Figs. 10 and 11, respectively. Note that a typical diffusion flame generates relatively thin reaction zones as marked by OH PLIF.[5] From the instantaneous images, only the main region of the cavity-only injection mode of Fig. 11 shows no evidence of thin reaction zones, indicating that the fuel and air are well mixed by this point.

Another noticeable feature of the instantaneous images is that the OH distribution for the case of cavity/main injection is much more intermittent than for cavity-only injection. This behavior is reflected in the PDFs of OH camera counts in Figs. 10 and 11, with each PDF having been generated from 200 OH images. The bimodal PDF of Fig. 10, with a large increase in probability toward zero camera counts, reflects the frequent occurrence of images in which no OH is present at the measurement location. This behavior is not evident in the PDFs of Fig. 11, indicating reduced intermittency for this condition.

It is not possible to distinguish such differences in OH structure from the *averaged* images of Figs. 8 and 9. It could not be determined, for example, whether the fairly uniform OH distribution occurs because of intermittent structures or a more uniform continuous flame. It is clear from Figs. 10 and 11 that the former is true for cavity/main injection and the latter is true for cavity-only injection. Such experimental data can be used to build information on how the instantaneous structure affects the final averaged predictions from the CFD model.

Conclusions

A number of advanced optical diagnostics and numerical simulations have been performed to help characterize the performance and aid in the design process of a trapped vortex combustor. Results from high-speed digital imaging, CSV, and PIV in a liquid-fueled combustor provided valuable information on the flow structure in the cavity and main regions of the TVC. A single vortex rotating in the opposite direction of the incoming flow was identified using these techniques, and appropriate design changes were implemented and tested to enhance the effectiveness of this flow pattern. Measurement of OH PLIF in a gaseous-fueled TVC has also been performed to help distinguish the combustor performance for two injection modes, as well as to validate a CFD model with chemistry. Experimental measurements of the flowfield and species generally agreed well with the numerical simulations, and demonstrated the importance and utility of advanced diagnostics for novel combustor designs.

Acknowledgments

The authors acknowledge D. D. Trump of ISSI for his help in setting up the PIV experiment, as well as C. Frayne, J. Stutrud, G. A. Boggs, R. L. Britton, R. E. Ryman, and K. O. Shoffstall for their help in operating the model gas turbine engine facilities. We thank C. Tenney of Instrumentation Marketing Corporation for his help in collecting some of the high-speed images, and acknowledge the project management of D. L. Burrus of GE Aircraft Engines. ISSI is supported in part by U. S. Air Force Contract F33615-00-C-2068.

References

[1] W. M. Roquemore, D. Shouse, D. Burrus, A. Johnson, C. Cooper, B. Duncan, K.-Y. Hsu, V. R. Katta, G. J. Sturgess, and I. Vihinen, "Trapped Vortex Combustor Concept for Gas Turbine Engines," AIAA Paper No. 2001-0483, *39th Aerospace Sciences Meeting and Exhibit*, Reno, Nevada, Jan. 8-11, 2001.

[2] D. Burrus, A. Johnson, W. M. Roquemore, and D. Shouse, "Performance Assessment of a Prototype Trapped Vortex Combustor Concept for Gas Turbine Application," ASME Paper No. 2001-GT-0087, *ASME ITGI Turbo Expo*, New Orleans, Louisiana, June 4-7, 2001.

[3] W. J. A. Dahm, L. K. Su, and K. B. Southerland, "A Scalar Imaging Velocimetry Technique for Fully Resolved Four-Dimensional Vector Velocity Field Measurements in Turbulent Flows," *Physics of Fluids A*, Vol. 4, No. 10, pp. 2191-2206, 1992.

[4] P. T. Tokumaru and P. E. Dimotakis, "Image Correlation Velocimetry," *Experiments in Fluids*, Vol. 19, pp. 1-15, 1995.

[5] K. A. Watson, K. M. Lyons, J. M. Donbar, and C. D. Carter, "Scalar and Velocity Field Measurements in a Lifted CH_4-Air Diffusion Flame," *Combustion and Flame*, Vol. 117, pp. 257-271, 1999.

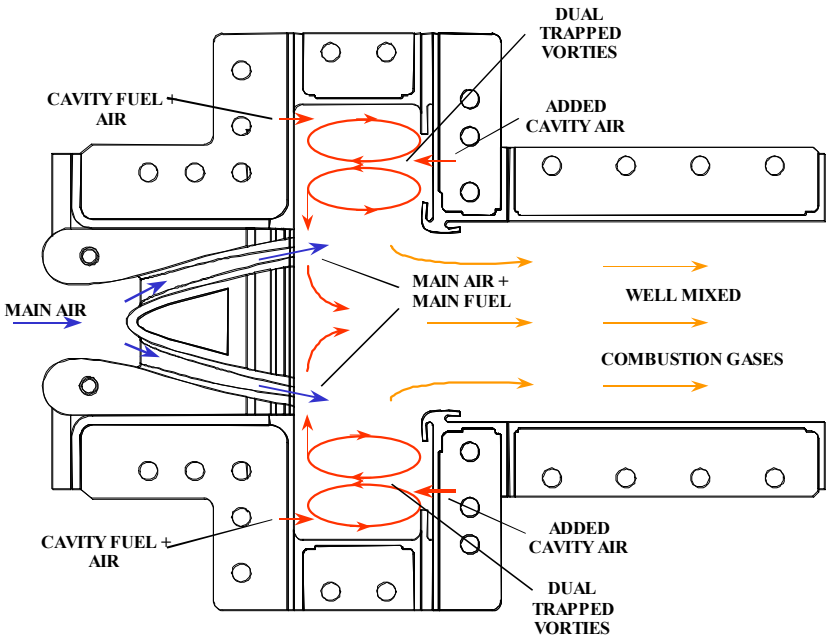

Fig. 1. Schematic of generic TVC geometry and flow configuration from Ref. 2.

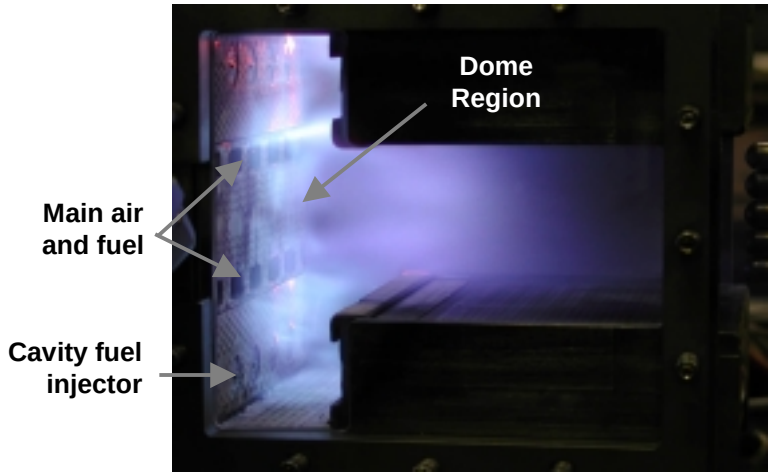

Fig. 2. Aft-wall-view of gaseous-fueled TVC operating in the Atmospheric-Pressure Combustor Research Complex at Wright-Patterson Air Force Base. Note the fuel and air inlet flow geometry leading to complex three-dimensional flow structure.

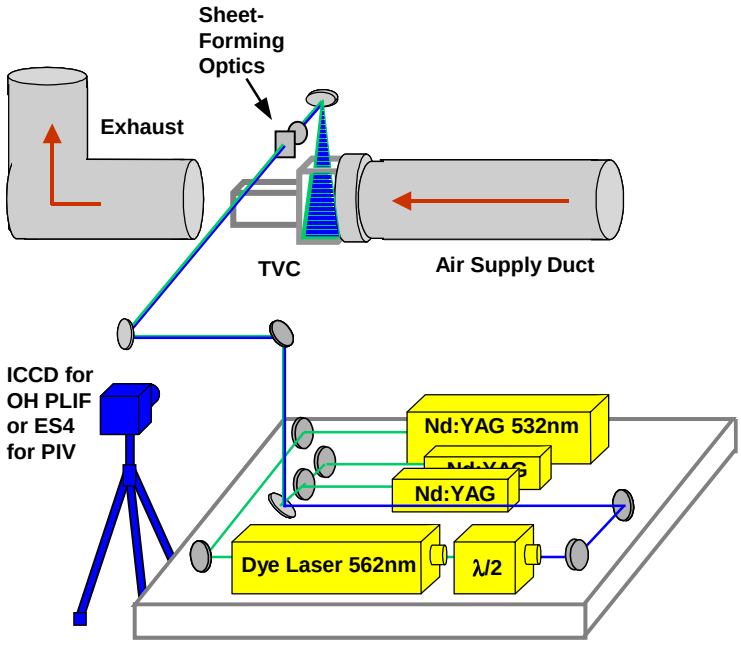

Fig. 3. Schematic of experimental set-up for non-simultaneous OH PLIF and PIV. Green beams represent 532 nm for PIV as well as pump beam for dye laser. Blue represents 281 nm for OH PLIF. Sheet-forming optics include a negative 50-mm focal-length cylindrical lens followed by a positive 500-mm focal-length spherical lens. Combustor is mounted on a translation stage for probing different transverse locations.

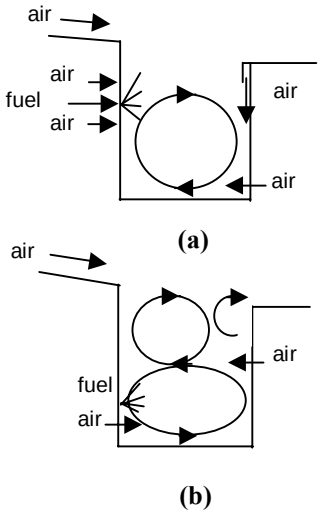

Fig. 4. Cavity flow pattern with (a) single enhanced clockwise-rotating vortex and (b) dual counter-rotating vortices to help retain unmixed fuel in the cavity. Liquid injection not present in gaseous TVC.

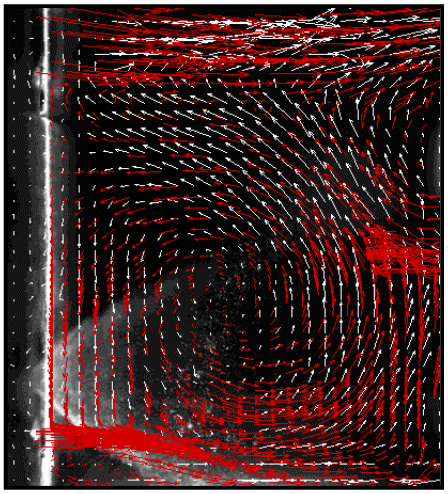

Fig. 5. Single counter-clockwise vortex pattern from PIV (white vectors) and CFD (red vectors) for design of Fig. 4(b). Flow is non-combusting and atmospheric. Inlet air temperature heated to T_3 = 450°F.

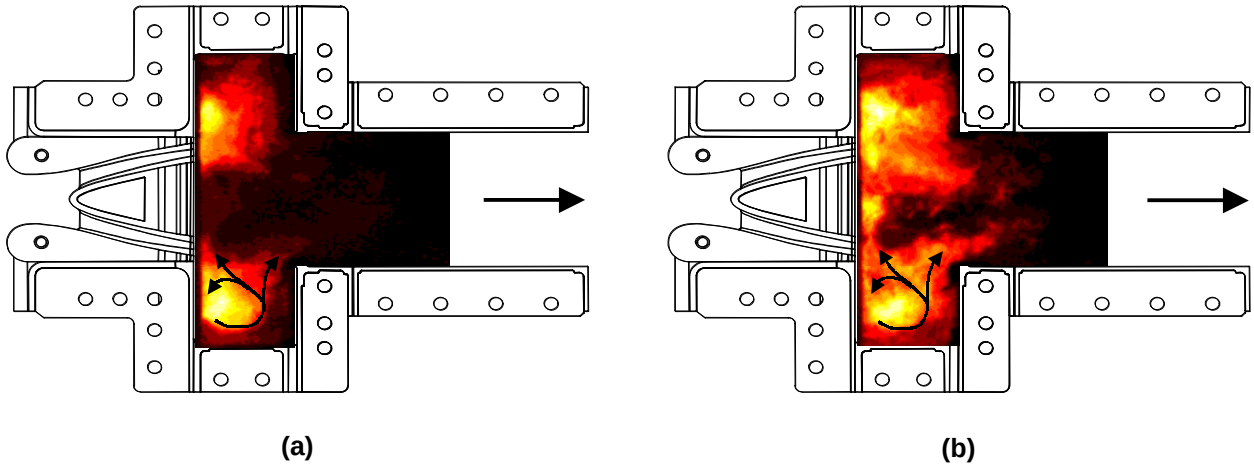

Fig. 6. Images from high-speed digital camera showing normalized flame luminosity in liquid-fueled 12-inch TVC at two conditions: (a) pressure of 125 psi, cavity equivalence ratio of 0.76, and inlet temperature of 575°F; (b) pressure of 175 psi, cavity equivalence ratio of 0.89, and inlet temperature of 700°F. Camera exposure time is 10 μs. Observed (sketched) flow patterns match that of Fig. 5.

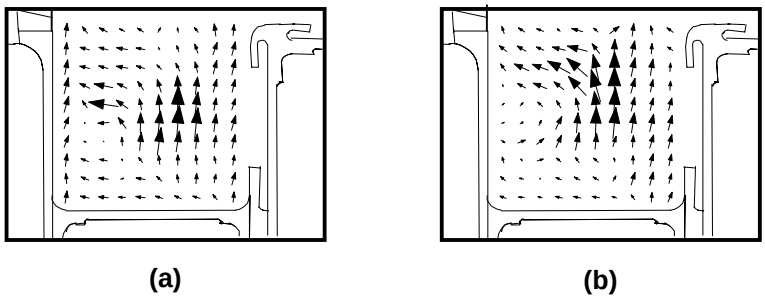

Fig. 7. Line-of-sight averaged velocity in cavity from CSV in liquid-fueled 12-inch TVC at two conditions corresponding to (a) Fig. 6(a) and (b) Fig. 6(b).

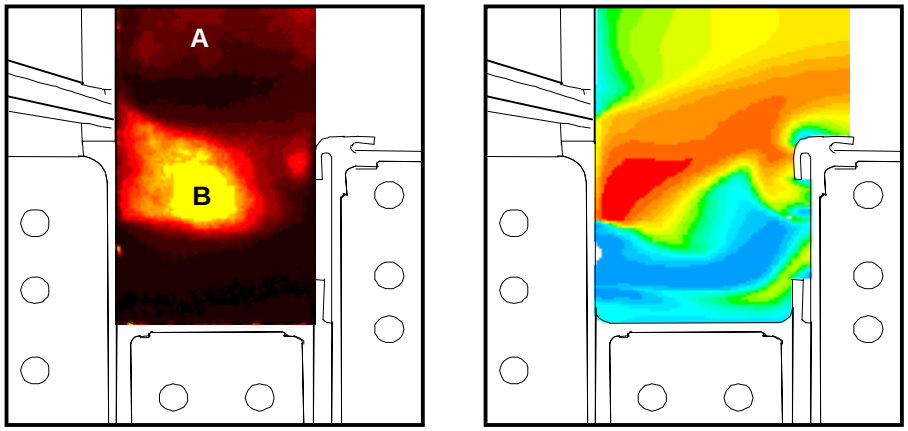

Fig. 8. Comparison between the measured OH-PLIF image (left) and predicted temperature contour (right) at the injector plane for cavity/main fuel-injection mode. Labels A and B mark the main and cavity regions, respectively. OH color scale is 0 to 1000 camera counts (black to yellow).

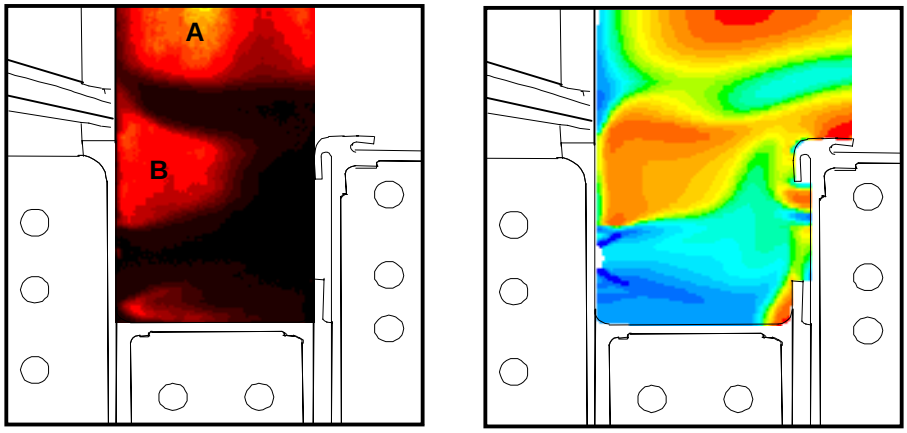

Fig. 9. Comparison between the measured OH-PLIF image (left) and predicted temperature contour (right) at the injector plane for cavity-only fuel-injection mode. Labels A and B mark the main and cavity regions, respectively. OH color scale is 0 to 2800 camera counts (black to yellow).

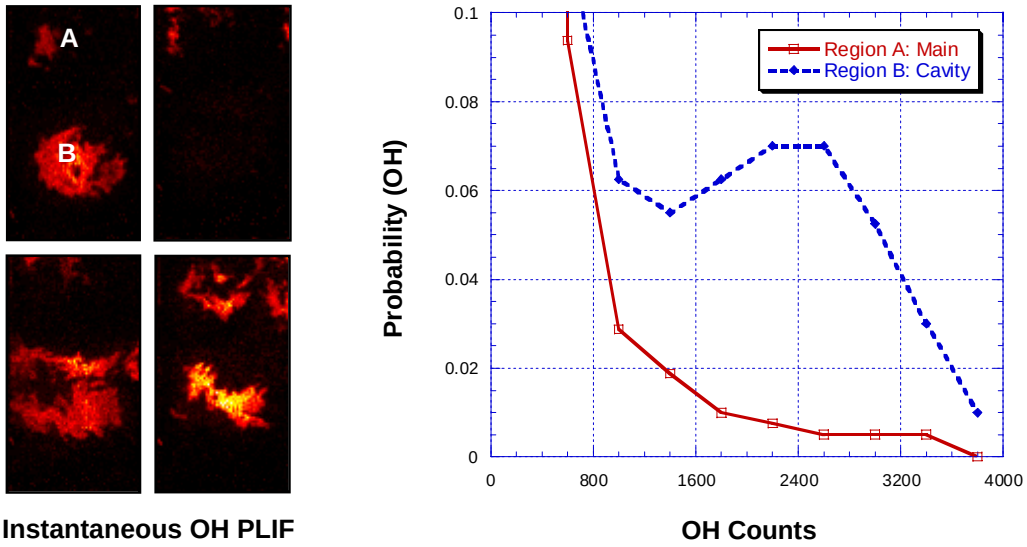

Fig. 10. Sample images of instantaneous OH PLIF and corresponding probability density functions (PDF) for Regions A and B shown previously in Fig. 8 (cavity/main fuel-injection mode). Two hundred instantaneous images are used to generate the PDF with ten bins between 0 and 4000 counts.

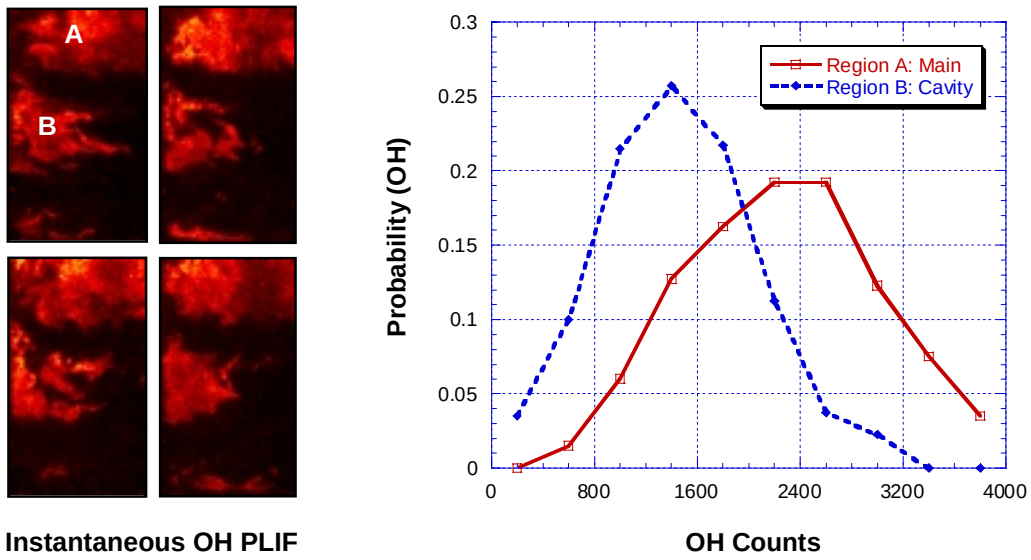

Fig. 11. Sample images of instantaneous OH PLIF and corresponding probability density functions (PDF) for Regions A and B shown previously in Fig. 9 (cavity-only fuel-injection mode). Two hundred instantaneous images are used to generate the PDF with 10 bins between 0 and 4000 counts.

①

Computational and Experimental Studies of Pulse Detonation Engines

Daniel Allgood and Ephraim Gutmark
University of Cincinnati, Aerospace Engineering

Terry Meyer, John Hoke and Viswanath Katta
Innovative Scientific Solutions Inc.

Fred Schauer and James Gord
AFRL, Wright Patterson AFB

28th Annual Dayton-Cincinnati Aerospace Science Symposium
March 4, 2003

②

COMPUTATIONAL AND EXPERIMENTAL STUDIES OF PULSE DETONATION ENGINES

- Objectives
- Description of Experimental Facility
- Development of the UC Nanopulser Shadowgraph System
- Computational Modeling Approach
- Shadowgraph Visualizations of PDE Exhaust Flows
- Comparison to Computational Modeling Predictions
- Conclusions and Future Work

③

COMPUTATIONAL AND EXPERIMENTAL STUDIES OF PULSE DETONATION ENGINES

- The design of efficient pulse detonation engines (PDE) requires a complete understanding of how components such as exhaust nozzles and ejectors generate thrust and the ability to predict the performance enhancement by these devices.
- Insight into the manner in which these devices produce work can be obtained by visualizing the flowfield.
- Two primary objectives of the current work:
  - Develop the capability of visualizing the complex and dynamic flowfield of a pulse detonation engine (PDE)
  - Develop the ability to predict the PDE flow using computational modeling.

④

COMPUTATIONAL AND EXPERIMENTAL STUDIES OF PULSE DETONATION ENGINES

- Approach:
  - A nano-second shadowgraph/schlieren visualization system was built at the University of Cincinnati that is capable of capturing the fast moving detonation waves without any visible smearing or distortion of the shock structure.
  - A new 2D Navier-Stokes detonation code was written in the generalized coordinates system for modeling contoured geometries.
  - Preliminary comparisons of the computations to the experiments were performed.

AFRL EXPERIMENTAL PDE FACILITY

Capabilities

- Explosion Proof Facility
- Up to 60 klbf Static Thrust / 1,000+ lbf Damped Thrust
- 6 lb/sec 100 psi air supply
- Choked H_2/Air Flow Regulation
- Hardened Remote Control Room
- 16 High Frequency DAC Channels, up to 5Mhz each

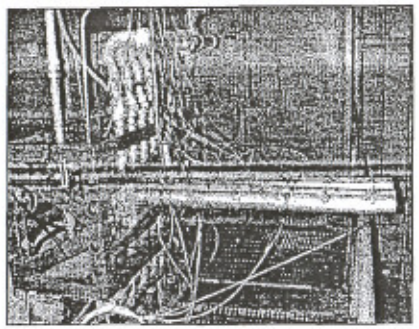

Current Experimental Setup

- PDE Tube: 2 inch diameter, 40 inches long
- Stoichiometric H_2/Air Premixed Mixture
- Fill Fraction of 1
- Measured wave speeds of approximately 1960 m/s (C-J Detonation Wave)
- 2 exit nozzle geometries tested

PULSE DETONATION ENGINE EXHAUST NOZZLES
COMPARISON OF STRAIGHT TUBE TO CONVERGING NOZZLE

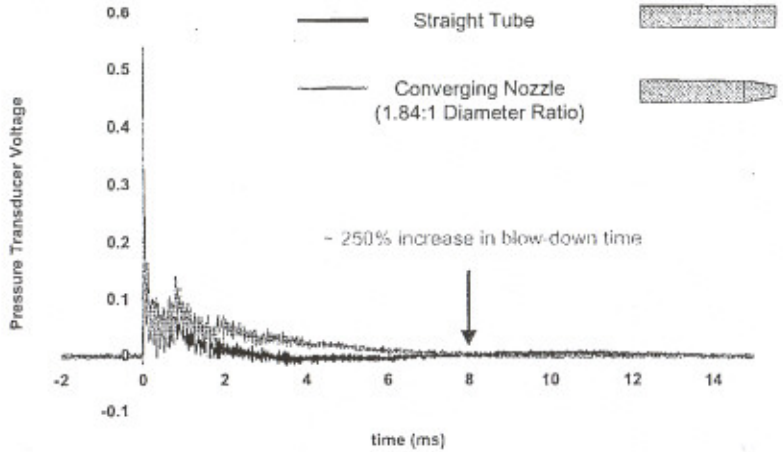

PDE FLOW VISUALIZATION
NANOSECOND SHADOWGRAPH/SCHLIEREN SYSTEM

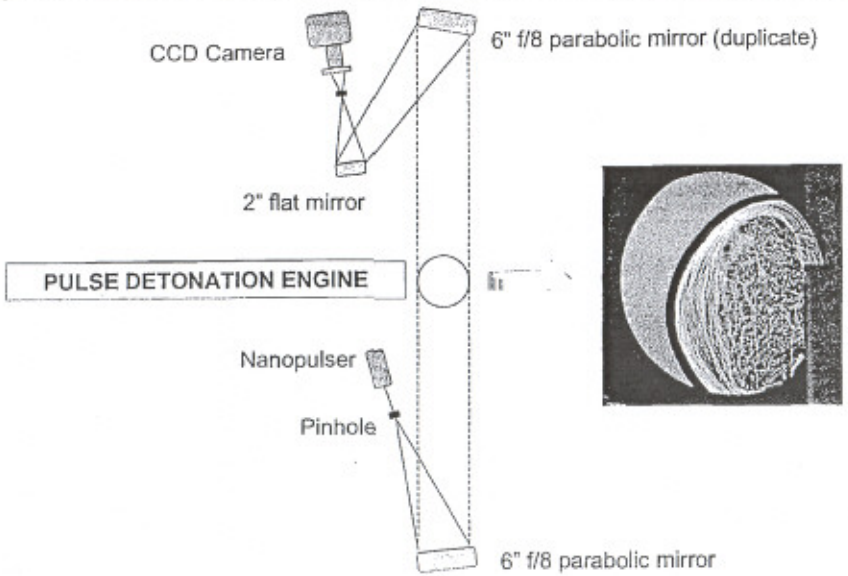

COMPUTATIONAL MODELING

- 2D unsteady Navier-Stokes code with chemical reaction models
- Generalized coordinates
- Explicit 2nd order MacCormack Predictor-Corrector Scheme with 4th order Multi-Dimensional Flux-Corrected Transport (FCT)
- Two-step induction parametric model for chemical reactions (Korobeinikov, Katta)
- Stoichiometric H_2/O_2 mixture diluted with argon by 70%

$$\frac{d\alpha}{dt} = -\frac{1}{\tau_{ind}} = -k_1 \rho \exp\left(-E_1/RT\right)$$

$$\frac{d\beta}{dt} = \begin{cases} = 0, & \alpha > 0 \\ = -k_2 \rho^2 \left[\beta^2 \exp\left(\frac{E_2}{RT}\right) - (1-\beta)^2 \exp\left(-\frac{E_2+Q}{RT}\right)\right], & \alpha \le 0 \end{cases}$$

$k_1 = 3.0 \times 10^{11}\, cm^3/g/s, \quad k_2 = 1.5 \times 10^{-7}\, cm^4/dyn^2/s,$
$E_1/R = 9800\ K, \quad E_2/R = 2000\ K, \quad Q = 4.0 \times 10^{10}\, erg/g$

COMPUTATIONAL GRID

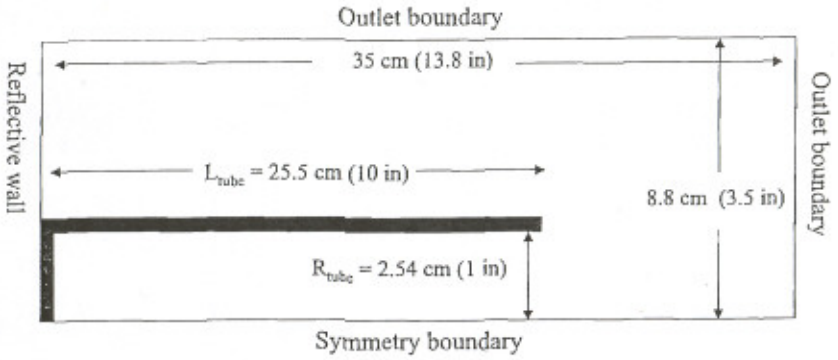

- Uniform grid spacing: 10*induction length = 0.02933 cm (0.0115 in)
- CFL # = 0.2
- Initial Conditions:
  Uniform stationary premixed mixture ignited by high temperature / pressure zones near head-wall of tube.

STRAIGHT TUBE PDE EXHAUST FLOW

10 ns light pulses, 3 ms blow-down

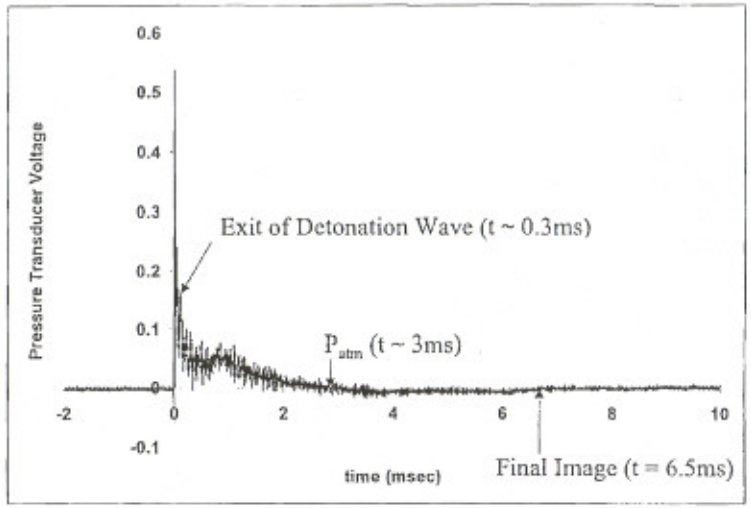

STRAIGHT TUBE PDE EXHAUST FLOW

10 ns light pulses, 3 ms blow-down

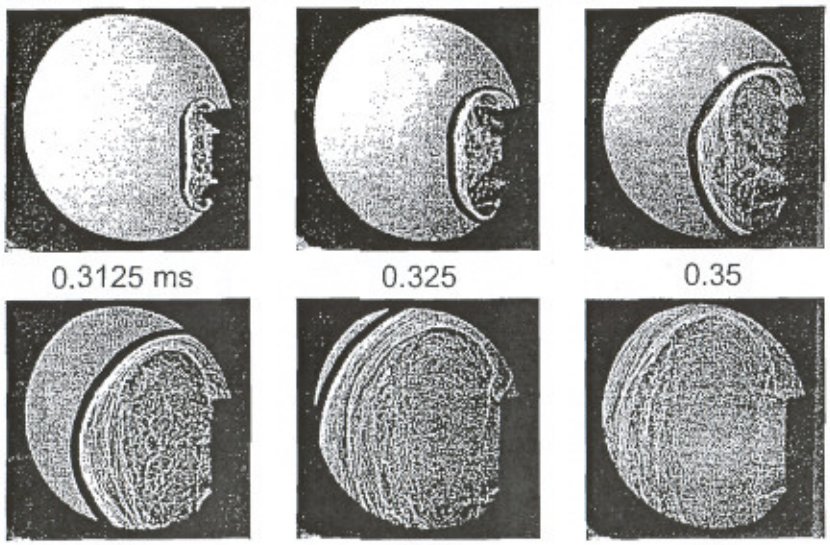

STRAIGHT TUBE PDE EXHAUST FLOW

10 ns light pulses, 3 ms blow-down

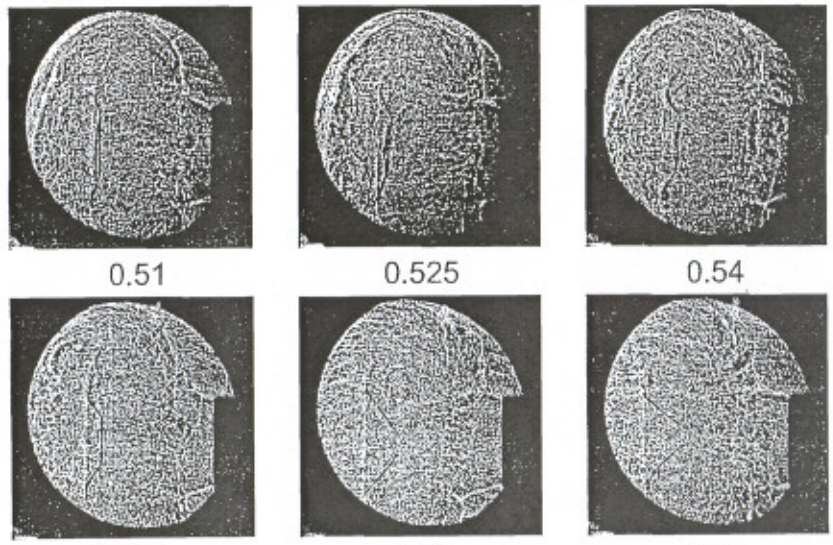

STRAIGHT TUBE PDE EXHAUST FLOW

10 ns light pulses, 3 ms blow-down

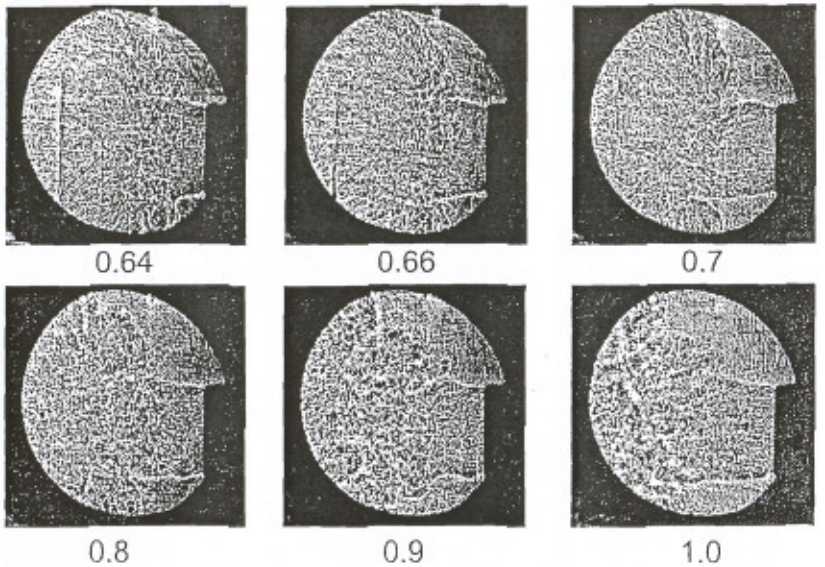

STRAIGHT TUBE PDE EXHAUST FLOW

10 ns light pulses, 3 ms blow-down

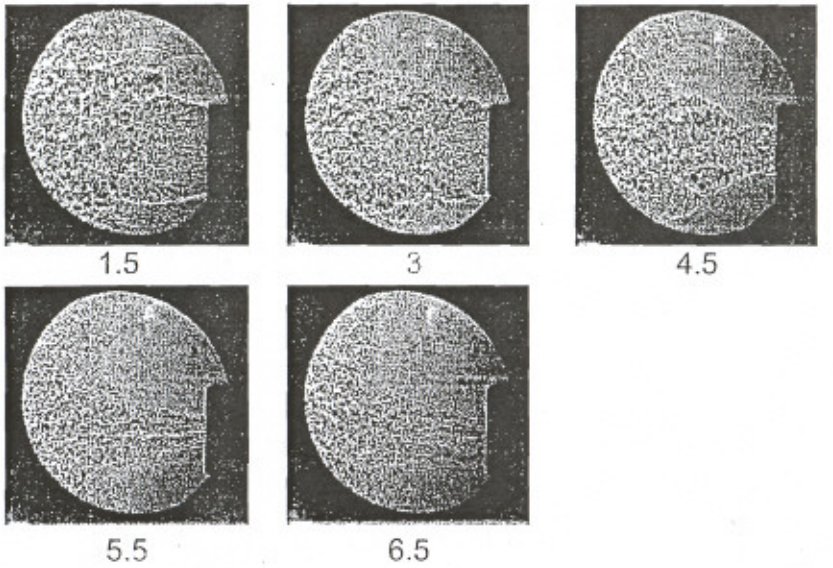

STRAIGHT TUBE PDE EXHAUST FLOW

10 ns light pulses, 3 ms blow-down

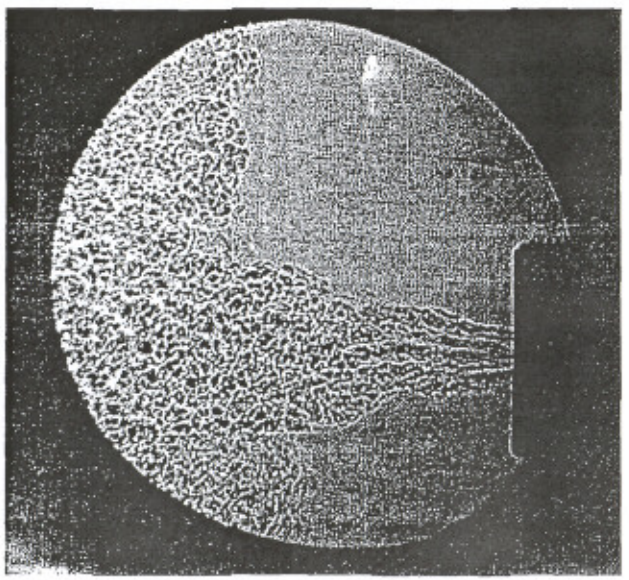

COMPARISON OF STRAIGHT TUBE TO CONVERGING NOZZLE

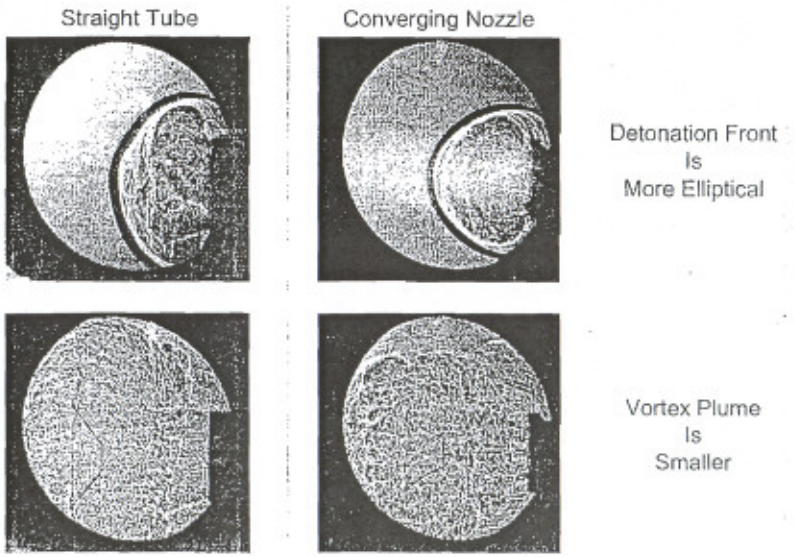

COMPARISON OF STRAIGHT TUBE TO CONVERGING NOZZLE

Straight Tube

Converging Nozzle

Mach Wave Radiation
Is
More Visible

CONVERGING NOZZLE PDE EXHAUST FLOW

1.84:1 Diameter Ratio, 10 ns light pulses, 7 ms blow-down

0.375 ms

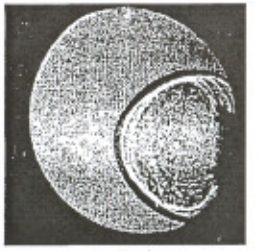

0.4

0.6

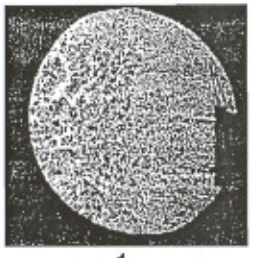

1

2

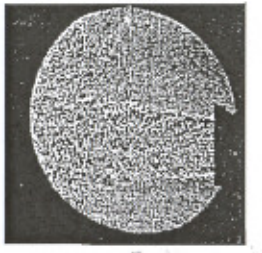

5

CONVERGING NOZZLE PDE EXHAUST FLOW

1.84:1 Diameter Ratio, 10 ns light pulses, 7 ms blow-down

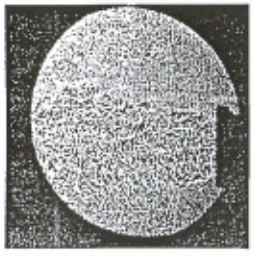

7.5

10

PULSE DETONATION ENGINE EXHAUST NOZZLES

EXPERIMENTS VS. SIMULATIONS

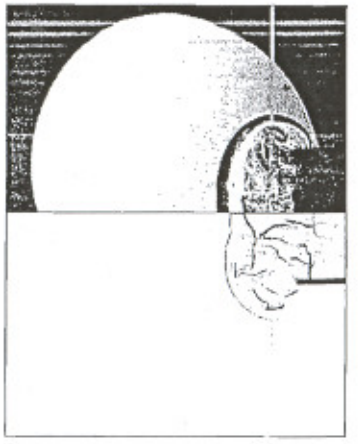

time = 0.3 ms

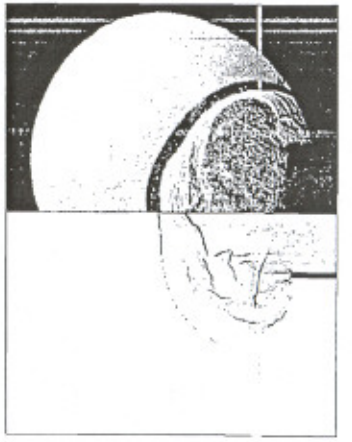

time = 0.325 ms

PULSE DETONATION ENGINE EXHAUST NOZZLES
EXPERIMENTS VS. SIMULATIONS

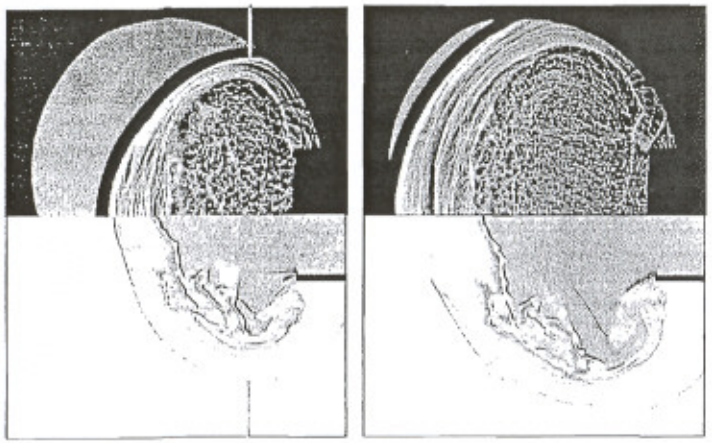

FUTURE WORK

1. Perform experimental and computational visualizations of various contoured exit nozzle geometries and ejector flowfields. These experiments will make use of new 12 inch diameter mirrors.
2. Study the effects of system parameters (fill fraction, ignition timing, and equivalence ratio) on exhaust jet structure and correlate with changes in performance values.
3. Acquire simultaneous OH-PLIF visualizations to investigate the coupling between the chemical reactions and gas dynamics.

ACKNOWLEDGEMENTS

• Special thanks to Richard DeLoof from NASA Glenn Research Center for sponsoring this research under grant NAG3-2669.

CONCLUSIONS

1. Shadowgraph visualizations of PDE exhaust flowfields were performed using a new 10 nanosecond duration light source.
2. The dynamic structure of the PDE exhaust flow was visualized for the complete detonation cycle.
   - Strong gradients was observed by the detonation front.
   - A large vortex plume was created by the detonation wave and a mach disk was observed to form in the underexpanded jet approximately 1 diameter downstream of the exit of the PDE.
   - A converging nozzle produced a more elliptically shaped detonation front, a smaller vortex plume and more visible Mach wave radiation.
3. Good agreement was observed between the modeling and experimental visualizations. Additional features were observed in the simulations that was masked by the line of sight of the shadowgraph visualizations.

Proceedings of PSFVIP-4
June 3-5, 2003, Chamonix, France.
F4009

Experimental study of two-phase vortex-flame interactions by laser induced fluorescence of OH and CH

A. Lemaire [1], K. Zähringer [1,2], T. R. Meyer [3], J. R. Gord,[4] and J. C. Rolon [1]

[1] Laboratoire d'EM2C, CNRS/École Centrale Paris, Grande Voie des Vignes, 92295 Chatenay-Malabry Cedex, France.
[2] now at : Lehrstuhl für Strömungsmechanik und Strömungstechnik, Universität Magdeburg, 39106 Magdeburg, Germany.
[3] Innovative Scientific Solutions Inc., 2766 Indian Ripple Road, Dayton, OH 45440, USA.
[4] Air Force Research Laboratory, Propulsion Directorate Wright-Patterson Air Force Base, OH 45433-7103, USA

KEYWORDS:
Main subject(s): *Combustion,*
Fluid: *Aerodynamics,*
Visualisation method: Laser Induced Fluorescence

ABSTRACT : The interaction between a vortex and a flat laminar diffusion flame is generally used to simulate a number of features that are common in turbulent combustion, such as dynamic strain, stretch, and curvature. Using well-controlled experiments to verify numerical simulations, phenomena such as flame extinction and micro-vortex-flame behaviour can be studied. The dynamic interaction between a laminar flame and a vortex may be examined by laser induced fluorescence of the hydroxyl (OH) layer produced by the flame, OH being a marker of long living intermediates, or by the CH radical which is considered to be a good marker of the primary reaction zone and a representative of the flame surface. The goal of the present investigation is to study two-phase vortex-flame interactions using both, OH and CH planar laser-induced fluorescence (PLIF). Like previous measurements in premixed flames, our results indicate that gaps in the CH PLIF layer do not always correspond to gaps in the OH layer.

1. Introduction

In the flamelet model for turbulent non-premixed combustion the flame surface is supposed to interact with turbulent vortices. The induced local strain and curvature can result in reduced overall reaction rates, local flame extinction, and decreased flame stability. Using well-controlled vortex injection to perturb steady counterflow diffusion flames and simulate the mentioned unsteady local extinction process in a repeatable manner, helped to generate turbulent combustion diagrams (Thévenin et al., 2000), and to study the time evolution of flame surface area during vortex-flame interaction (Renard et al., 1999). Two-phase vortex-flame interactions in counterflow diffusion flames were reported by Santoro et al. (2000 and 2002), who used methanol-air spray flames to capture flame phenomena found in practical devices.

Nguyen and Paul (1996) showed through measurements of OH and CH PLIF in premixed flames, that breakage of the CH radical front during vortex interaction may not be associated with a rupture of the OH-front. Donbar et al. (2000) showed the different features of the CH and OH layers in a turbulent nonpremixed methane-air flame. The CH layer can be considered as a proof that the flame exists. It appears in a narrow region of the flame near the location of peak temperature. OH may show either a flame location, an interface between OH and entrained air or a fuel-air interface where the flame is extinguished. In our study, the controlled vortex-flame interaction in a two-phase methane/n-heptane flame is visualised by these two radicals.

The goal of the current investigation is to study the flame structure and shape during two-phase vortex-flame interaction with a vortex coming from the droplet laden fuel side of the burner. CH and OH planar laser-induced fluorescence (PLIF) is used to visualise the flame front during vortex impingement and the different behaviour of these radicals as representatives of the reaction zone is discussed. Flame-surface evolution and relative radical mole fractions as a function of time relative to vortex perturbation can be determined from these images for different flame and vortex conditions.

Copyright ©2003 by PSFVIP-4

2. Experimental device

The burner apparatus and diagnostic approach have previously been described by Lemaire et al. (2002) for CH PLIF experiments. Thus, only a brief description is included here, with the changes necessary for the OH-PLIF study.

2-1 Burner apparatus and flow conditions

The experimental device used for this work was previously modified from a gaseous counterflow burner design (Rolon et al. 1991) to include a piston-actuated vortex injection system (Rolon et al. 1995). Several experimental studies using this apparatus have been reported previously in the literature (Renard, et al. 1999; Fiechtner et al. 2000). The burner consists of two axisymmetric, 20-mm diameter counterflow nozzles, with air in the upper flow and a nitrogen-fuel mixture in the lower flow. A two-phase methane with n-heptane fuel mixture is produced inside an atomizer system, creating a mono-disperse field of droplets (2.43-2.83 □m in diameter) for the current flow conditions. The spray is diluted to a non-dense condition. A 40-mm diameter flow of nitrogen surrounds each nozzle to shield the flame from ambient disturbances. The nozzle separation is set to 30 mm in this study. A vortex tube of 2 mm is added along the centerline of the fuel nozzle, fed by an electronically controlled piston-actuation system. Vortices of varying strength can be generated by controlling the stroke, and rise time of the piston. In this paper we concentrate on flames with an overall mixture ratio of 3.44 and a vortex size of 2 mm with a piston rise time of 10 ms. The initial mass fraction of fuel is 0.21 and the mass fraction of methane in the fuel is 0.48. The steady nozzle velocities of the fuel and oxyder stream are respectively 0.59 m/s and 0.61 m/s. The varying vortex parameters are given in table 1 including the ejected volume ΔV. The vortex propagation velocity U_T has been determined previously by PIV measurements (Lemaire et al., 2002). The 2-mm-tube vortices structure showing a spherical pattern, the vortex circulation (Γ_{Vort} is calculated using a spherical vortex model (($\Gamma_{Vort} = U_T D/5$ where D is the vortex diameter equal to 4mm).

Vortex	ΔV (mm^3)	U_T ($m.s^{-1}$)	Γ_{Vort} ($cm^2.s^{-1}$)
A	10	0.4	3.2
B	14	0.7	5.6
C	38	1.0	8.0

Table 1 : Vortex features.

2-2 LIF-System

CH PLIF is achieved using the $Q_1(5)$ transition (389.5 nm) in the $B^2\bar{\square}\square^2\square$ (0,0) absorption band of CH. The OH-PLIF technique uses the $Q_1(6)$ band of the $A^2\square^+$--$X^2\square$(1,0) transition of OH at 283 nm. The laser pulses of about 7 ns in duration and mean energies between 15 and 20 mJ for both CH and OH are formed into 0.3 mm thick sheets of 20-mm height for CH and of 50-mm height for OH. The power density variation inside the measurement region has been minimised by controlling it with Rayleigh scattering from nitrogen and Mie scattering from the droplets, by centering the laser sheet on the flame region during the entire vortex-flame interaction and by partially saturating the transitions. The high laser energy allows to diminish quenching and pulse-to-pulse laser fluctuation. Thus laser-sheet intensity variations did not exceed 5% in the whole measurement region.

Fluorescence of CH is collected from the A--X(0,0) and A--X(1,1) bands around 430 nm by using a combination of a 410 nm high-pass and a 450 nm low-pass filter. OH-Fluorescence is observed from the A--X(0,0) and A--X(1,1) bands through a filter combination of a 250-400-nm band-pass filter and a 285-nm high-pass filter. The CH PLIF signal is collected during 20 ns using a 2 x 2 binned 512 x 512 array PI-Max intensified CCD camera with a 58-mm f/1.2 Noct-Nikkor lens and 20-mm extension ring, while the OH signal is recorded during 80 ns using the same camera with a UV 105-mm f/4.5 Nikkor lens and a 36-mm extension ring. The region of interest is of 25 x 25 mm for CH detection and of 20 x 20 mm for OH.

Observation of vortex interactions also requires the synchronisation of several events, including vortex generation, laser pulse, and camera exposure. The vortex-flame interaction can then be imaged at various phases of its development by adjusting relative timing of piston actuation and laser diagnostics. The OH and CH PLIF measurements have not been realised simultaneously, but on similar vortices whose parameters are controlled and repeatable. The propagation velocities and circulations have been deduced from PIV measurements simultaneously with the CH-LIF.

Copyright ©2003 by PSFVIP-4

3. Results and discussion

Figures 1 to 3 show the series of LIF images for three different vortex conditions. These images are raw images, where no background has been subtracted and no normalisation with respect to the laser power has been done. The CH images are mean images of 10 raw images due to the low signal level of CH-LIF, the OH images are single-shot images. On the left side the CH-LIF images are represented, on the right side the OH-LIF is shown together with Mie diffusion on the n-heptane droplets. This allows the visualisation of the evaporation front, which is situated under the flame front represented by the OH layer, and the vortex position and structure.

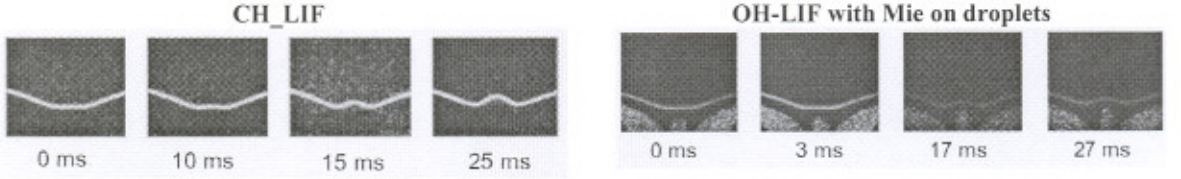

Fig. 1 : Vortex-flame interaction with weak deformation and no extinction (Vortex A)

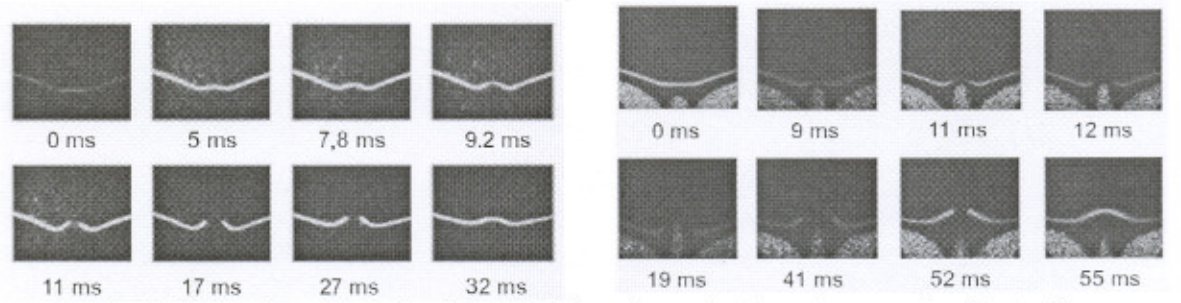

Fig. 2 : Vortex-flame interaction with weak deformation, extinction and reconnection (Vortex B)

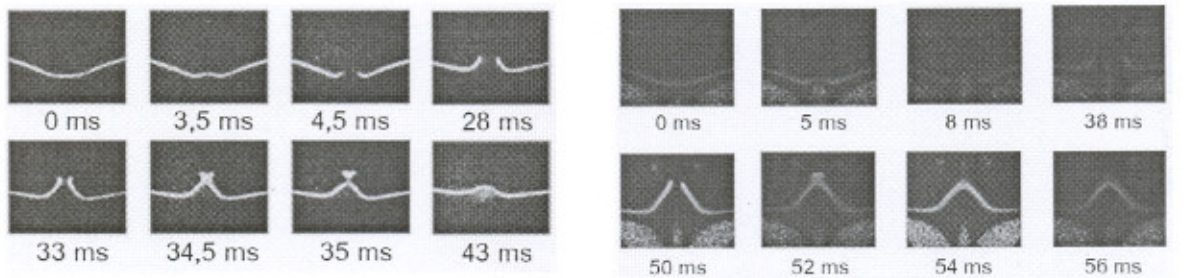

Fig. 3 : Vortex-flame interaction with weak deformation, extinction, elongation, junction and formation of small flame pocket (Vortex C)

In the first case (Fig.1) the flame is deformed very weakly during vortex impingement (Vortex □). There is no extinction and after about 40 ms the flame has once more its initial form. Figure 2 shows a series of images with flame extinction. The vortex (Vortex B) first weakly deforms the flame, which thins in the centre and disrupts. The initial OH-layer thickness is about 1 mm, the CH-layer is much thinner (0.2 mm). The vortex passes through the flame but is not strong enough to propagate against the air flow. The flame edges at the extinction hole remain in the vortex core, and non–vaporized droplets continue to feed the flame (Fig 2, time 41 ms). Then the flame reconnects propagating towards the mixed reactants accumulated by the absence of flame interface. If the vortex circulation is rather strong (Vortex C), flame extinction takes place much earlier. Then the vortex core propagates far inside the air flow, elongating strongly the flame edges. The conical flame shape elongates strongly under the induced vortex strain with its upper side becoming smaller; so that the flame fronts collapse. This collapse highly increases the flame intensity, leading rapidly to the formation of a small flame pocket. These is entrained by the vortex inside the air flow until extinction by lack of fuel. The OH and CH behaviours are slightly different during the collapse process. The CH signal clearly disappears at the collapse point separating a small flame pocket, while OH does not disappear completely and is present, with a weak signal, in a wide area from the collapse point to the flame pocket.

When comparing the two corresponding series for CH and OH, one can recognise that the CH-layer seems to extinguish before the OH-layer. For vortex B the CH front disrupts between 9 and 11 ms, for OH this takes place

Copyright ©2003 by PSFVIP-4

about 2 ms later. In the case of vortex C the difference is even bigger, CH-extinction is visualised after about 4 ms, whereas the OH-layer stays intact nearly until 8ms. The same fact can be remarked for the reconnection or junction of the flame front. The CH layer is re-established before the OH-layer.
These differences between OH and CH are known in the literature for local extinction processes in turbulent premixed jet flames (Nguyen and Paul,1996; Donbar et al.,2000). Here the same differences are found during dynamic vortex-flame interactions in diffusion flames. The earlier extinction of the CH-layer is due to the kinetic differences of CH and OH formation in the flame. CH is formed in the very early stage of the chemical reaction on the fuel-side of the flame and thus touched first by the vortex. OH is formed later, has a longer lifetime and diffuses into the hot burnt gasses. Therefore the OH layer is broader and it can exist for a while even after extinction of the primary reaction, as it can be seen during the collapse process. Watson et al. (1999) showed some images of reconnected CH-layers wrapping around broken OH-layers in their study of turbulent diffusion jet flames. This could corresponds to our finding of a later reconnection of the extinguished OH front compared to CH. The CH-layer has a faster chemistry and seems to be more sensitive to the vortex movement and therefore re-establishes earlier after the vortex has passed.

4. Conclusions and prospects

Laser-induced fluorescence measurements of CH and OH in a two-phase, laminar, non-premixed counterflow flame, interacting with a vortex have been done in this study. Different interaction regimes exhibit different ways of flame surface evolution with wrinkling, elongation, extinction and collapse processes. Both radicals are representatives of the reaction region, CH on the fuel-rich side, OH for the fuel-lean side of the flame. They show global behaviour similarities, however their local behaviour during transient process is clearly different. In order to get a more accurate depiction of the regions of extinction and reconnection or junction of disrupted flame fronts, simultaneous CH and OH measurements would be necessary on the same configuration. This would finally exclude any doubt about repeatability of the vortex generation and its influence on the interaction behaviour.

Acknowledgments

This work was supported by French DGA / ONERA PEA-number 98703-TITAN and by U.S. Air Force Contract F33615-00-C-2068 in a French-U.S. collaborative program.

References

Donbar J.M., Driscoll J.F., and Carter C.D.: Reaction Zone Structure in Turbulent Nonpremixed Jet Flames - From CH-OH PLIF Images, *Combustion and Flame,* Vol. 122, pp. 1-19, 2000.

Fiechtner G. J., Renard P. H., Carter C. D., Gord J. R. and Rolon J. C.: Injection of Single and Multiple Vortices in an Opposed-Jet Burner, *Journal of Visualization,* Vol. 2, pp. 331-341, 2000.

Lemaire, A., Meyer, T. R., Zähringer, K., Gord, J. R. and Rolon, J.-C.: PIV/PLIF-Investigation of two-phase vortex-flame interactions : effects of vortex size and strength, *Experiments in Fluids*, accepted for publication, 2002.

Nguyen Q.-V., Paul P. H.: The time evolution of a vortex-flame interaction observed via planar imaging of CH and OH, *Proceedings of the Combustion Institute*, Vol. 26, pp. 357-364, 1996.

Renard P. H., Rolon, J. C., Thevenin, D., and Candel, S.: Investigations of heat release, extinction, and time evolution of the flame surface for a non-premixed flame interacting with a vortex, *Combustion and Flame*, Vol. 117, pp. 189-205, 1999.

Rolon J.C., Veynante, D., Martin, J.-P. and Durst F.: Counter Jet Stagnation Flows, *Experiments in Fluids,* Vol. 11, pp. 313-324, 1991.

Rolon, J. C., Aguerre, F. and Candel, S. Experiments on the Interaction between a Vortex and a Strained Diffusion Flame, *Combustion and Flame*, Vol. 100, pp. 422-429, 1995.

Santoro V.S., Kyritsis D.C. and Gomez A.: An Experimental Study of Vortex-Flame Interaction in Counterflow Spray Diffusion Flames, *Proc. Combust. Inst.*, Vol. 28, pp. 1023-1030, 2000.

Santoro V.S. and Gomez A.: Extinction and Reignition in Counterflow Diffusion Spray Flames interacting with Laminar Vortices, *Proc. Combust. Inst.,* Vol. 29, 2002.

Thévenin D., Renard P.-H., Fiechtner G.J., Gord J.R. and Rolon J.C.: Regimes of Non-Premixed Flame-Vortex Interactions, *Proc. Combust. Inst.*, Vol. 28, pp. 2101-2108, 2000.

Watson K.A., Lyons K.M., Donbar J.M., and Carter C.D.: Scalar and velocity measurements in a lifted CH4-air diffusion Flame, *Combustion and Flame,* Vol. 117, pp. 257-271, 1999.

Copyright ©2003 by PSFVIP-4

REAL-TIME COMBUSTOR DIAGNOSTICS USING HIGH-SPEED DIGITAL IMAGING

ISSI

Terrence R. Meyer, Michael S. Brown, John L. Hoke, and Sergey Fonov
Innovative Scientific Solutions, Inc.

Frederick R. Schauer and James R. Gord
Air Force Research Laboratory / PRTS

27th Annual Dayton-Cincinnati Aerospace Sciences Symposium
Dayton, Ohio, March 5, 2002

Acknowledgements

ISSI

D. Shouse, V. Belovich, and M. Roquemore
Air Force Research Laboratory / PRTS

R. Bradley, G. Boggs, R. Britton, R. Ryman, K. Shoffstall, B. Day, J. Parker, and M. Slagel
Innovative Scientific Solutions, Inc.

C. Cooper
GE Aircraft Engines

C. Tenney
Photo-sonics / IMC

U.S. Air Force Contract F33615-00-C-2068

Background and Motivation

ISSI

- Many combustors of practical interest are highly intermittent and three-dimensional.
- Such combustors are difficult to study with single-frame laser-based imaging.
- High-speed digital imaging is now capable of 60,000 fps with 10 μs exposure.
- High-speed digital imaging can offer convenient real-time diagnostics for combustor research and development.

Applications

ISSI

Pulsed-Detonation Engine

- Supersonic combustion
- High pressure flame structure
- Dynamics of soot formation

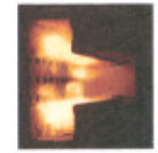

Trapped-Vortex High-Pressure Combustor

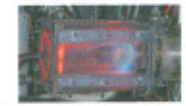

Single Swirl Cup CFM-56 Atmospheric Combustor

Equipment

ISSI

	Photron FASTCAM-Ultima SE 1	Photo-sonics Phantom v5.0	Redlake HG-100K Imager
Maximum Speed	40,500 fps	60,000 fps	100,000 fps
Minimum Shutter	24.7 μs	10 μs (Indep.)	10 μs (Indep.)
Chip	NMOS 256 x 256	CMOS 1024 x 1024	CMOS 1508 x 1100
Sensitivity	Good Visible Only	Low Visible Only	Low Visible Only

PDE Exhaust

ISSI

Image from Conventional Video Camera

Exhaust Flow from High-Speed Camera (18,000 fps)

PDE Detonation Transition

ISSI

Side-View of Full Tube with Shelkin Spiral (18,000 fps)

0.0 μs

55.5 μs

111.0 μs

166.5 μs

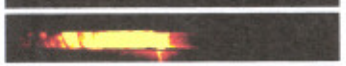

222.0 μs

PDE Detonation Transition

ISSI

Side-View of Transition Region with Shelkin Spiral (18,000 fps)

0.0 μs

55.5 μs

111.0 μs

166.5 μs

PDE Detonation Transition

ISSI

- Endview images collected in conjunction with high-speed pressure traces.

Endview of PDE Tube with Shelkin Spiral (40,500 fps)

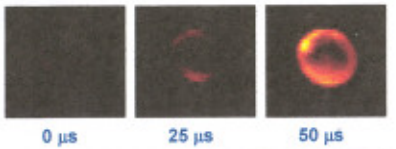

0 μs 25 μs 50 μs

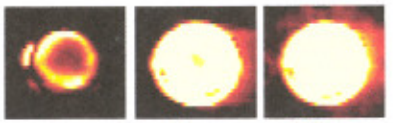

75 μs 100 μs 125 μs

Trapped-Vortex Combustor

ISSI

- High-speed imaging shows vortex circulation and roll-over time.
- High pressure leads to more uniformly distributed heat release.

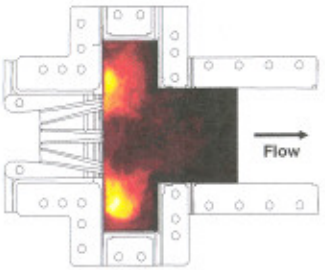

Atmospheric Pressure

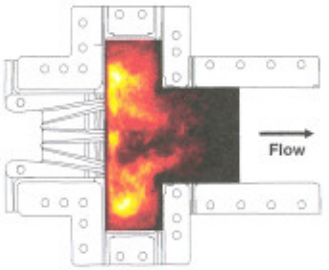

High Pressure

Coherent-Structure Velocimetry

ISSI

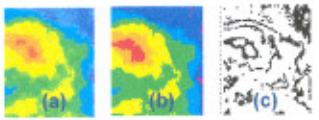

Step (a): Obtain source image.
Step (b): Increase contrast.
Step (c): Calculate iso-contours.
Step (d): Cross-correlate for velocity.

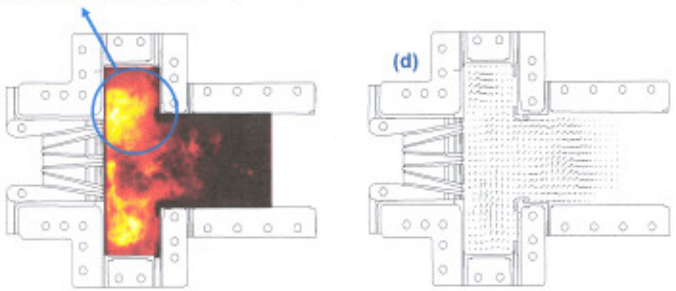

CFM56 Atmospheric Combustor

ISSI

- Filtered high-speed images can highlight CH^* fluorescence in the fuel-spray region.
- Fuel-spray intermittency evident in time-correlated images.

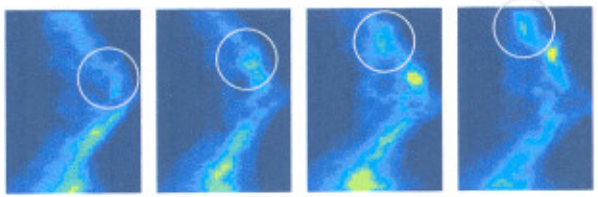

CFM56 Soot Formation

ISSI

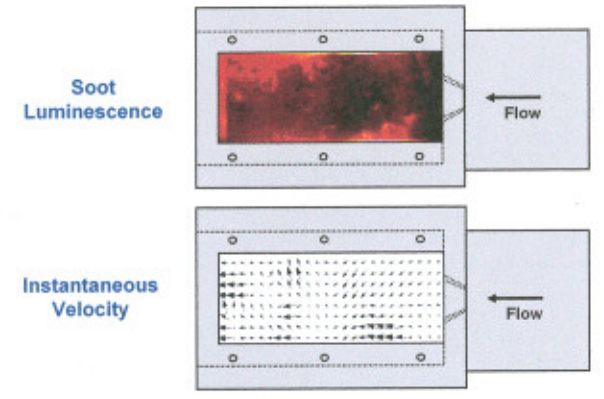

Influence of Streamwise Vortices in Soot Formation

ISSI

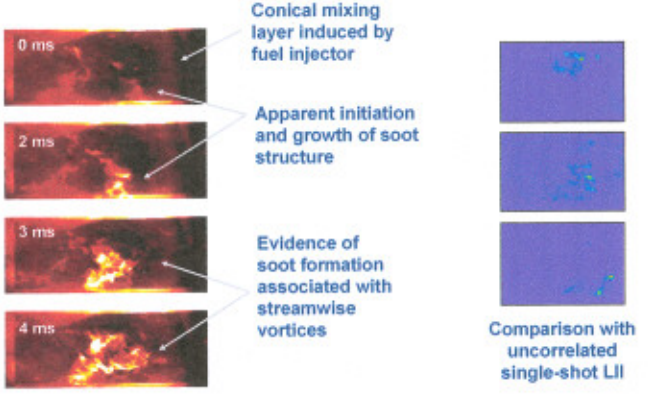

Conclusions

ISSI

High-speed digital imaging demonstrated in the following areas:

- Imaging highly transient processes in a pulsed-detonation engine.
- Analyzing the effect of various operating conditions on the flame structure of a high-pressure trapped-vortex combustor.
- Providing a time-averaged and instantaneous estimate of the velocity field using coherent-structure velocimetry.
- Analyzing the coupling of fluid dynamics and soot formation in a CFM56 atmospheric combustor.